

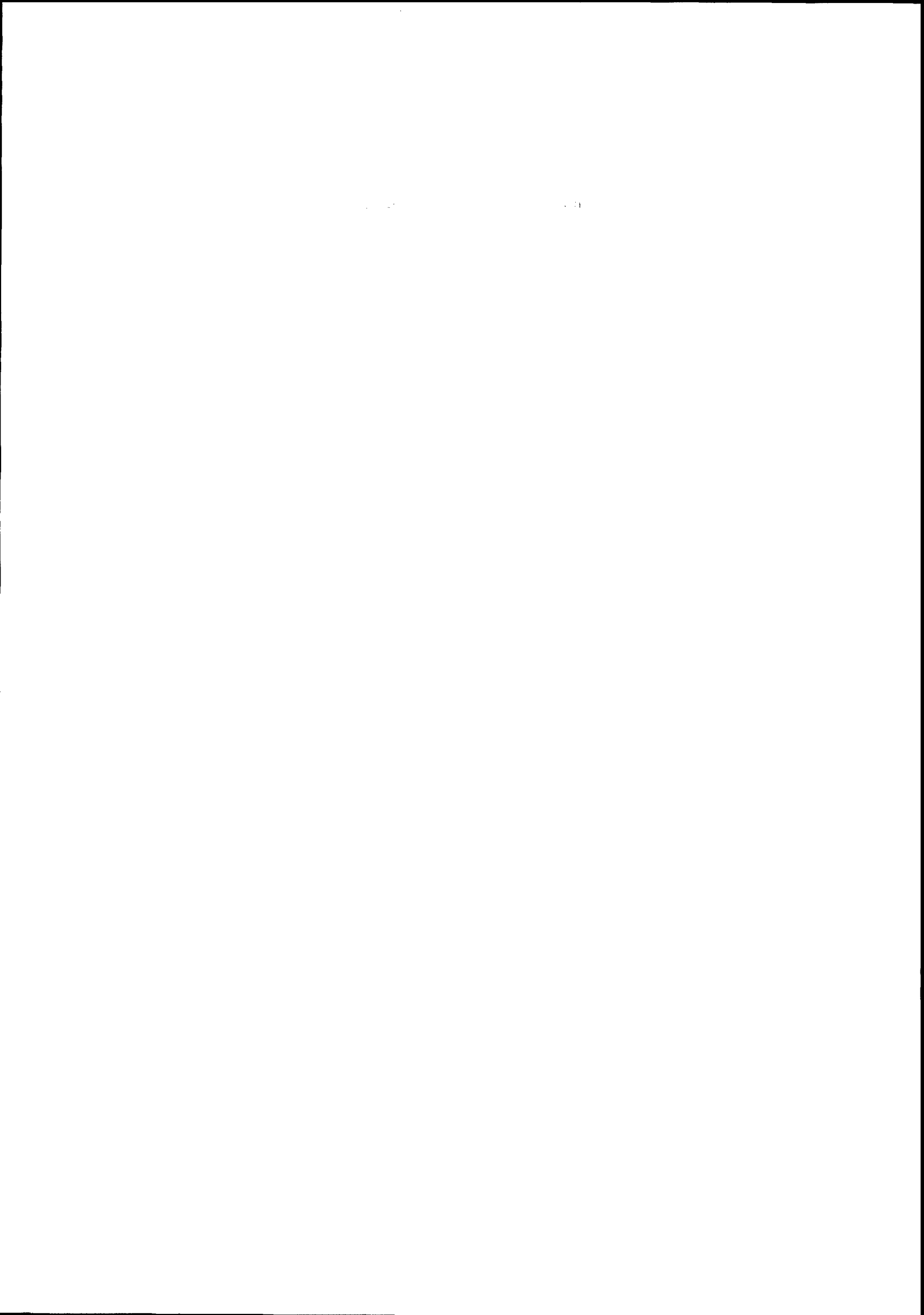


*SAR Workshop*

CEOS Committee  
on  
Earth Observation  
Satellites  
Working Group  
on Calibration  
and Validation

Toulouse, France  
26 - 29 October 1999





# CEOS SAR Workshop

*26-29 October 1999*  
*Toulouse, France*

*Organised by:*

European Space Agency  
and  
CNES, France



**European Space Agency**  
**Agence spatiale européenne**

**ORGANISING COMMITTEE****CNES:**

Jean-Claude Souyris  
Christine Correcher  
Frédéric Adragna  
Nadine Pourthié

**ESA:**

Evert Attema  
Maurice Borgeaud  
Yves-Louis Desnos  
Gonnie Elfering  
Henri Laur

**SCIENTIFIC COMMITTEE**

Jean-Paul Aguttes	CNES	France
Alain Arnaud	ESA/ESRIN	Italy
C.H. Buck	ESA/ESTEC	The Netherlands
Hubert Cantalloube	ONERA	France
Bertrand Chapron	IFREMER	France
Shane Cloude	University of Dundee	United Kingdom
Bruno Cugny	CNES	France
Mihia Datcu	DLR	Germany
Malcolm Davidson	CESBIO	France
Tom Farr	JPL	USA
Nicolas Floury	ESA/ESTEC	The Netherlands
Bob Hawkins	CCRS	Canada
Peter Hooeboom	TNO-FEL	The Netherlands
Harald Johnsen	NORUT IT	Norway
Gordon Keyte	DERA	United Kingdom
Thelma Krug	INPE	Brasil
Thuy Le Toan	CESBIO	France
Chung-Chi Lin	ESA/ESTEC	The Netherlands
Armand Lopes	CESBIO	France
Francesco Mattia	ITIS - CNR	Italy
Alberto Moreira	DLR	Germany
Soren Madsen	TUD	Denmark
Pierluigi Mancini	ESA/ESRIN	Italy
Didier Massonnet	CNES	France
Eric Pottier	IRESTE	France
Claudio Prati	University of Milan	Italy
Josep Rosello-Guasch	ESA/ESTEC	The Netherlands
Masanobu Shimada	NASDA/EORC	Japan
Satish Srivastava	CSA	Canada
Jean-Luc Suchail	ESA/ESTEC	The Netherlands
Eric Thouvenot	CNES	France
Ridha Touzi	CCRS	Canada
Lars Ulander	NDRE	Sweden
Paris Vachon	CCRS	Canada
Jason Williams	Alaskan SAR Facility	USA
Manfred Zink	DLR	Germany

Short Title: ***SP-450 CEOS SAR Workshop***

Published by: ESA Publications Division  
ESTEC, Keplerlaan 1  
2200 AG Noordwijk  
The Netherlands

Tel: +31 71 565 3400

Fax: +31 71 565 5433

Editors: R.A. Harris, L. Ouwehand

Price: 40 Euros

Copyright: © 2000 European Space Agency

ISBN No: 92-9092-641-4

Printed in: The Netherlands

## Contents

<b>Foreword</b> .....	xvii
<i>Y.-L. Desnos, Chairman CEOS SAR S/G and Head User Support Section (ESA/ESRIN), J.-C.Souyris, Workshop Local Organiser (CNES/QTIS)</i>	
<b>Introduction</b> .....	xix
<i>J.-L. Fellous, Delegate to the Earth Observation Programmes, CNES S. Briggs, Head of Earth Observation Exploitation Department (ESA/ESRIN)</i>	
 <b>Session 1: Land Applications</b> Chairman: T. Le Toan (CESBIO) Co-chairman/Report: M. Borgeaud (ESA)  	
LIGHTSAR: Convergence of Science, Applications and Commercial Requirements .....	3
<i>D. Evans, A. Freeman (Jet Propulsion Laboratory, USA)</i>	
Application of Polarimetric SAR Data Processing to Snow Cover Remote Sensing.....	5
Validation Using Optical Images and Ground Data. <i>L. Ferro-Famil, J. Saillard (IRESTE, University of Nantes, France), E. Pottier (University of Rennes, France), J.P. Dedieu, C. Corgier (LAMA-CNRS, Grenoble, France)</i>	
RADARSAT, ERS and EMISAR for Snow Monitoring in Mountainous Areas .....	11
<i>T. Guneriusssen, H. Johnsen, I. Lauknes (Norut IT Ltd, Norway)</i>	
Monitoring Terrain Deformations Using Multi-Temporal SAR Images .....	15
<i>A. Ferretti, C. Prati, F. Rocca (Politecnico Di Milano, Italy)</i>	
JERS SAR Processing for the Boreal Forest Mapping Project SIBERIA .....	19
<i>A. Wiesmann, U. Wegmüller, T. Strozzi (Gamma Remote Sensing, Switzerland)</i>	
Temporal Variations of Interferometric Coherence over a Deciduous Forest .....	25
<i>C. Proisy, E. Mougin, A. Lopes (CESBIO, Toulouse, France), F. Sarti, (CNES/DSO/OT/QTIS/SR, Toulouse, France), E. Dufrière, V. LeDantec (Université de Paris XI, France), P. Borderies, I. Chênerie (ONERA/CERT/DEMR, Toulouse, France)</i>	
Operational Use of SAR Images for Crop Surveillance – Issues Regarding.....	31
Identification and Congruency Accuracy <i>M. Chakraborty, J. Parihar, S. Panigrahy (Space Applications Centre (ISRO), India)</i>	

**Session 2: Ocean Applications**  
 Chairman: B. Chapron (IFREMER)  
 Co-chairman/Report: E. Attema (ESA)

Ocean Wave Measurements Using Complex ERS-2 Wave Mode Data.....	39
<i>J. Schulz-Stellenfleth, S. Lehmer, B. Schöttler, H. Breit (DLR, Wessling, Germany)</i>	
Wind Retrieval Over the Ocean Surface Using Synthetic Aperture Radars.....	45
<i>J. Horstmann, W. Koch (GKSS Research Center, Germany), S. Lehner, J. Schulz-Stellenfleth (DLR, Wessling, Germany), R. Tonboe (Danish Meteorological Institute, Copenhagen, Denmark)</i>	
Retrieval and Validation of Sea Surface Winds from Calibrated RADARSAT ScanSAR Images.....	53
<i>X. Li, W.G. Pichel, P. Clemente-Colón, K.S. Friedman (NOAA/NESDIS, Camp Springs, USA), F. Monaldo, R. Beal (The Johns Hopkins University, Laurel, USA), C. Wackerman (ERIM International Inc., Ann Arbor, USA)</i>	
Validation of Envisat ASAR Wave Mode Level 1b and Level 2 Products Using ERS SAR Data.....	59
<i>H. Johnsen, G. Engen, K.-A. Høgda (NORUT IT, Tromsø, Norway), B. Chapron (IFREMER, Plouzané, France), Y.-L. Desnos (ESA/ESTEC, Noordwijk, The Netherlands)</i>	
Sea Ice Thickness from Kinematics.....	65
<i>R. Kwok, B. Holt (Jet Propulsion Laboratory, Pasadena, USA)</i>	
SAR Research and Application Activities for Coastal Management in Norwegian Waters.....	71
<i>O. Johannessen, S. Sandven, H. Espedal, B. Furevik (Nansen Environmental and Remote Sensing Center, Bergen, Norway)</i>	

**Session 3: Geometry/Radiometry/Calibration**

Chairman: R.K. Hawkins (CCRS)  
 Co-chairman/Report: G. Keyte (DERA)

The ERS SAR Performances: an Update.....	79
<i>P. Meadows (Marconi Research Centre, Chelmsford, UK), D. Esteban Fernández (GAEL Consultant, Champs-sur-Marne, France), P. Mancini (ESA/ESRIN, Frascati, Italy)</i>	
RADARSAT-1 Image Quality – Update.....	85
<i>S. K. Srivastava, B.T. Banik, M. Adamovic, R. Gray (Canadian Space Agency, Quebec, Canada), R.K. Hawkins, T.I. Lukowski, K.P. Murnaghan (Canada Centre for Remote Sensing, Ontario, Canada), W.C. Jefferies (RADARSAT International, Cantley, Quebec, Canada)</i>	
Plans for Radiometric and Polarimetric Calibration of RADARSAT-2 Beams.....	89
<i>A. Luscombe (MacDonald Dettwiler, Richmond, Canada)</i>	

Calibration of the GEOSAR Dual Frequency Interferometric SAR.....	93
<i>E. Chapman, S. Hensley, D. Moller (Jet Propulsion Laboratory, USA)</i>	
Calibration of an X-Band Airborne Synthetic Aperture Radar with Active Radar .....	95
Calibrators and Corner Reflectors	
<i>M. Satake, T. Umehara, T. Kobayashi, A. Nadai, T. Matsuoka, S. Uratsuka (Communications Research Laboratory, Ministry of Posts and Telecommunications, Tokyo, Japan), H. Wakabayashi, M. Shimada (NASDA, Japan)</i>	
Stability of Amazon Backscatter at C-Band: Spaceborne Results from ERS-1/2 .....	99
and RADARSAT-1.	
<i>R. Hawkins (Canada Centre for Remote Sensing, Ottawa, Canada), E. Attema (ESA/ESTEC, Noordwijk, The Netherlands), R. Crapolichio, P. Lecomte (ESA/ESRIN, Frascati, Italy), J. Closa (SERCO Srl/ESA/ESRIN, Frascati, Italy), P.J. Meadows (Marconi Reseach Centre, Chelmsford, UK), S.K. Srivastava (Canadian Space Agency, Québec, Canada)</i>	
A New Method for Calibration of SAR Images .....	109
<i>G. Engen, H. Johnsen (Norut IT, Tromsø, Norway)</i>	
Use of Interferometric Phase for Co-Registration of ERS SAR and SPOT Images.....	113
<i>D. Raucoules, C. Carnec (BRGM DR/LGT, Marseille, France)</i>	
Localization Using ERS for Operational Mapping.....	119
<i>S. Gobert, I. Tannous (Thomson-CSF / SYSECA, Malakoff, France), P. Bally (SPOTIMAGE, Toulouse, France), H. Laur (ESA/ESRIN, Frascati, Italy)</i>	
On Accuracy of Attitude Estimation and Doppler Tracking .....	127
<i>M. Dragošević, (Satlantic Inc., Halifax, Canada)</i>	

#### Session 4: SAR Processing

Chairman: F. Adragna (CNES)

Co-chairman/Report: M. Shimada (NASDA)

The Shuttle Radar Topography Mission: Processing Scenario and Techniques.....	133
<i>H. Breit, N. Adam, M. Eineder, R. Bamler, S. Suchandt (DLR, Wessling, Germany)</i>	
Phase Preserving Extended Chirp Scaling Processing Techniques and First Results .....	137
<i>J. Mittermayer, A. Moreira (DLR, Germany), Y.-L. Desnos (ESA/ESRIN, Frascati, Italy)</i>	
Phase Screen Determination for the GEOSAR Interferometric Mapping Instrument.....	139
<i>S. Hensley, E. Chapman, B. Thomas, P. Siqueria, W. Brown, Y. Kim (Jet Propulsion Laboratory, USA)</i>	
New Results for Spaceborne Hybrid Strip-Map/Spotlight SAR High Resolution .....	141
Processing	
<i>S. Henrion (Alcatel, Toulouse, France / ENSICA, Toulouse, France), L. Savy, J.-G. Planès (Alcatel, Toulouse, France)</i>	

SAR Path Processor and Application to the Large Scale Mosaics .....	147
<i>M. Shimada, H. Wakabayashi, T. Tadono, V.B. Taylor (Earth Observation Research Center/National Space Development Agency of Japan, Tokyo-to, Japan), O. Isoguchi, H. Miyagawa (Remote Sensing Technology of Japan)</i>	
Some Applications of an Accurate Geometrical Error Model for Airborne SAR .....	153
<i>H. Cantalloube (ONERA, Palaiseau, France)</i>	
RADARSAT-1 Doppler Centroid Estimation Using Phase-Based Estimators .....	159
<i>I. Cumming (Remote Sensing Data Centre, DLR, Wessling, Germany), F. Wong (National University of Singapore), B. Hawkins (Canada Centre for Remote Sensing, Ottawa, Canada)</i>	
An Accurate Radargrammetric Chain for DEM Generation .....	167
<i>Y. Belgued (Alcatel / ENSEEIHT Informatique, Toulouse, France), E. Hervet, P. Marthon (ENSEEIHT Informatique, Toulouse, France), C. Lemaréchal (ENSEEIHT Informatique / CNES, Toulouse, France), L. Rognant (Alcatel, Toulouse, France) F. Adragna (CNES, Toulouse, France)</i>	
Potentiality of High-Resolution SAR Images for Radargrammetric Applications .....	173
<i>E. Simonetto, H. Oriot (ONERA, Châtillon, France), R. Garello (ENSTBr, Brest, France)</i>	

### **Session 5: Antenna Synthesis/Data Compression/ Post Processing Techniques**

#### **Sub-session: Antenna Synthesis**

Chairman and report: M. Brown (Marconi)

Performance-Based Elevation Gain Pattern Synthesis .....	183
<i>M. Brown (Marconi Research Centre, Chelmsford, UK), C. Buck (ESA/ESTEC, Noordwijk, The Netherlands)</i>	
Antenna Pattern Synthesis Optimization for the Elevation Pattern of the ASAR Instrument .....	189
<i>J. Mittermayer, A. Moreira (DLR, Germany), Y.-L. Desnos (ESA/ESRIN, Frascati, Italy)</i>	

#### **Sub session: Data Compression**

Chairman and report: I. Cumming (UBC)

SAR Raw Data Compression Techniques .....	193
<i>G. Schirinzi (DAEIMI – Università di Cassino, Italy / IRECE-CNR, Napoli, Italy)</i>	



Compression of Temporal Series of Registered SAR Images .....	199
<i>G. Mercier, M.-C. Mouchot, G. Cazuguel (ENST de Bretagne, Brest, France),</i>	
<i>J. Mvogo (IUT de Douala, Douala, Cameroun),</i>	
<i>J.-P. Rudant (Université de Marne-la Vallée, France)</i>	

Wavelet Based ScanSAR Image Compression Minimizing Block Effects .....	203
<i>J.V. Fischer, U.C. Benz, (DLR, Oberpfaffenhofen, Germany)</i>	

### **Sub-session: Post Processing Techniques**

Chairman and report J.S. Lee (NRL)

New Approaches in Speckle Filtering .....	211
<i>F. Adragna (CNES, France), A. Lopes, J. Bruniquel (CESBIO, France)</i>	

Sensitivity of SAR Speckle Filtering on the Assessment of Surface Roughness .....	213
and Soil Moisture Content	
<i>F. Zagolski (Privateers NV, Philipsburg, St. Maarten, Netherlands Antilles),</i>	
<i>S. Foucher (CARTEL, Université de Sherbrooke, Canada),</i>	
<i>C. Gaillard (Technologies SEPIA Inc., Saint-Jean-sur-Richelieu, Canada)</i>	

A Family of Distribution-Entropy MAP Speckle Filters for Polarimetric.....	219
SAR Data, and for Single or Multi-Channel Detected and Complex SAR Images	
<i>E. Nezry, F. Yakam-Simen (Privateers NV, Philipsburg, St. Maarten, Netherlands Antilles)</i>	

A Protocol for Speckle Filtering of SAR Images .....	225
<i>R. Touzi (Canada Centre for Remote Sensing, Ottawa, Canada)</i>	

### **Session 6: Instrument Design and New Concepts**

Chairman: J.P. Aguttes (CNES)

Co-chairman/Report: L. Ulander (SDRE)

Space-Borne SAR in Russia: SRIPI's Main Projects .....	233
<i>I. Neiman, S. Vnotchenko (Scientific &amp; Research Institute of Precise Instruments),</i>	
<i>A. Zakharov (Institute of Radioengineering &amp; Electronics),</i>	
<i>O. Goriachkin (Central Specialized Design Bureau)</i>	

Modular Design of SAR Electronics .....	235
<i>F.A. Petz, J. Rosello-Guasch, C. Mavrocordatos (ESA/ESTEC),</i>	
<i>Ch. V. Narasimha Rao (ISRO, Ahmedabad, India)</i>	

Status of the X-Band SAR Instrument Demonstrator Development .....	241
<i>R. Zahn, H. Braumann, (Dornier Satellite Systems, Friedrichshafen, Germany)</i>	

The RADARSAT II Mission: an Update Towards an End-to-End System.....	245
Performance	
<i>P.-P. Landry (Systèmes Néotech, Montreal, Canada),</i>	
<i>G. Séguin, R. Girard (Canadian Space Agency, St-Hubert, Canada)</i>	

Capabilities and Limitations of the Interferometric Cartwheel .....	251
<i>D. Massonnet (CNES, Toulouse, France)</i>	
PROSE: a Low Cost P Band Transponder Radar Satellite Based on the SAIL Concept .....	263
<i>J. Aguttes, L. Lapierre (CNES, Toulouse, France)</i>	
Radar Penetration in Soils: Towards a New System for Subsurface Earth Observation .....	267
<i>G. Grandjean, N. Baghdadi (BRGM, Orléans, France),</i>	
<i>P. Paillou (Observatoire de Bordeaux, Floirac, France),</i>	
<i>P. Dreuillet, (ONERA, Palaiseau, France), P. Dubois (DGA, Arcueil, France),</i>	
<i>J.C. Souyris (CNES, Toulouse, France), J. Achache (CNES, Paris, France)</i>	
Processing and Calibration of Ultra-Wideband SAR Data from Carabas-II .....	273
<i>L.M.H. Ulander, P.O. Frörlind, T. Martin</i>	
<i>(Swedish Defence Research Establishment, Linköping, Sweden)</i>	
HSRRA: an Advanced Radar Altimeter for Ocean and Cryosphere .....	279
Monitoring	
<i>L. Phalippou (Alcatel, Toulouse, France)</i>	
<i>D.J. Wingham (University College London, UK)</i>	
Spotlight SAR on Spaceborne Platform .....	285
<i>T. Misra, A.Jha, D. Dave (ISRO, India)</i>	
High Resolution SAR Constellation for Risk Management .....	287
<i>A. Herique, L. Phalippou, S. Ramongassie (Alcatel, Toulouse, France),</i>	
<i>C.C. Lin, (ESA ESTEC, Noordwijk, The Netherlands)</i>	
A Fully Polarimetric L-Band Spaceborne SAR Instrument Targeting .....	293
Land Applications	
<i>G.T.A. Burbidge, D.M. Simpson, C.H. Mathew (Matra Marconi Space, Portsmouth, UK)</i>	
A World - Metric- Cartography And Topography Mission.....	299
<i>F. Adragna (CNES, France)</i>	

### **Session 7: Envisat**

Chairman: Y.L. Desnos (ESA)

Co-chairman: S. Srivavasta (CSA)

Report: H. Laur (ESA)

The Envisat ASAR Instrument Verification and Characterisation .....	303
<i>R. Torres, C. Buck, J. Guijarro, J.-L. Suchail, A. Schönenberg</i>	
<i>(ESA/ESTEC, Noordwijk, The Netherlands)</i>	
Envisat/ASAR Precision Transponders .....	311
<i>H. Jackson (ESA/ESTEC, Noordwijk, The Netherlands),</i>	
<i>I. Sinclair, S. Tam (MPB Technologies Inc., Pointe Clair, Québec, Canada)</i>	

The Envisat ASAR Processor and Data Products.....	317
<i>Y.-L. Desnos (ESA/ESTEC, Noordwijk, The Netherlands),</i>	
<i>H. Laur, J. Closa (ESA/ESRIN, Frascati, Italy),</i>	
<i>P. Meisl (MacDonald Dettwiler, Richmond, Canada)</i>	
The Envisat ASAR Calibration and Validation Plan.....	323
<i>Y.-L. Desnos, C. Buck J.-L. Suchail, R. Torres, B. Duesmann</i>	
<i>(ESA/ESTEC, Noordwijk, The Netherlands)</i>	
<i>H. Laur, J. Closa (ESA/ESRIN, Frascati, Italy)</i>	
<b>Session 8: Polarimetry/Interferometry</b>	
Sub session Polarimetry: Chairman: E. Pottier, U. Rennes,	
Co-chairman; W. Boerner, U. Illinois at Chicago	
Application of the « H / A / $\alpha$ » Polarimetric Decomposition Theorem for Unsupervised.....	335
Classification of Fully Polarimetric SAR Data Based on the Wishart Distribution	
<i>E. Pottier (Université de Rennes I, France),</i>	
<i>J.-S. Lee (Naval Research Laboratory, Washington DC, USA)</i>	
Synoptic Representation of the Polarimetric Information .....	341
<i>P. Imbo (CESBIO / ENSEEITH, Toulouse, France),</i>	
<i>J.-C. Souyris (CNES, Toulouse, France), A. Lopes (CESBIO, Toulouse, France),</i>	
<i>Ph. Marthon (ENSEEITH, Toulouse, France)</i>	
Vegetation and Ground Parameter Estimation Using Polarimetric Interferometry.....	347
Part I: The Role of Polarisation	
<i>K.P. Papathanassiou, S.R. Cloude (Applied Electromagnetics, St Andrews, Fife, UK),</i>	
<i>A.Reigber, (DLR, Oberpfaffenhofen, Germany)</i>	
Vegetation and Ground Parameter Estimation Using Polarimetric Interferometry.....	353
Part II: Parameter Inversion and Optimal Polarisations	
<i>K.P. Papathanassiou, S.R. Cloude (Applied Electromagnetics, St Andrews, Fife, UK),</i>	
<i>A.Reigber, (DLR, Oberpfaffenhofen, Germany)</i>	
<b>Sub session: Interferometry</b>	
Chairman: D. Massonnet, CNES,	
Co-chairman: C. Prati, Politecnico di Milano	
The Shuttle Radar Topography Mission.....	361
<i>T.G. Farr, S. Hensley, E. Rodriguez, J. Martin, M. Kobrick</i>	
<i>(Jet Propulsion Laboratory, Pasadena, USA)</i>	
Interferometric Repeat-Pass SCANSAR Data Processing.....	365
<i>R. Bamler, A. Moreira, J. Mittermayer (DLR, Germany)</i>	
Radargrammetry and SAR Interferometry for DEM Generation: .....	367
Validation and Data Fusion.	
<i>M. Crosetto (Politecnico Di Milano, Milano, Italy),</i>	
<i>F. Pérez Aragües, (Institut Cartografic de Catalunya, Barcelona, Spain)</i>	

Accuracy Assessment of IINSAR Topographic Mapping.....	373
<i>P. Defourny, X. Blaes, C. Lucau (Université Catholique de Louvain, Belgium)</i>	
Calibration of the X-SAR System on SRTM.....	375
<i>M. Zink, D. Geudtner (DLR, Oberpfaffenhofen, Germany)</i>	
Recent Advances in Polarimetric- Interferometric SAR Theory & Technology .....	379
and its Applications	
<i>W.-M. Boerner, University of Illinois at Chicago, USA),</i>	
<i>J.S. Verdi (Naval Air Warfare Center, Patuxent River, MD, USA)</i>	
<b>Seed Questions</b> .....	399

### Session Syntheses and Recommendations

Chairman: Yves-Louis Desnos, Co-chairman: Jean-Claude Souyris

Land Applications, .....	M. Borgeaud.....	407
Ocean Applications, .....	E. Attema.....	409
Geometry,/Radiometry/Calibration, .....	G. Keyte .....	410
SAR Processing, .....	M. Shimada .....	412
Antenna Synthesis, .....	M. Brown .....	413
Data Compression, .....	I. Cumming.....	414
Post Processing Techniques, .....	J. Lee .....	415
Instrument Design and New Concepts, .....	L. Ulander.....	418
ENVISAT, .....	H. Laur .....	420
Polarimetry/ Interferometry, .....	W. Boerner/ C. Prati.....	421

<b>Summary and Conclusions</b> .....	429
Y.-L. Desnos	

### Poster Session

Geographic Data Base Enriching from ERS SAR Scenes:.....	433
Examples in French Guiana	
<i>N. Classeau, J.-P. Rudant (Université de Marne, France),</i>	
<i>H. Trebossen (Service Hydrographique et Océanographique de la Marine,</i>	
<i>Brest, France), I. Jeanne (Institut Pasteur de Madagascar, Madagascar),</i>	
<i>P. Geuillopé (CETE Normandie Centre, Le Grand Quevilly, France)</i>	
Contribution of RADAR SAT Imagery for Mapping Coastal Areas: .....	437
Examples of Sedimentational and Erosional Zones in French Guyana, Mauritania	
<i>H. Trebossen (Université de Marne la Vallée, France /</i>	
<i>Service Hydrographique et Océanographique de la Marine, Brest, France),</i>	
<i>J.-P. Rudant, B. Fruneau, N. Classeau (Université de Marne la Vallée, France)</i>	

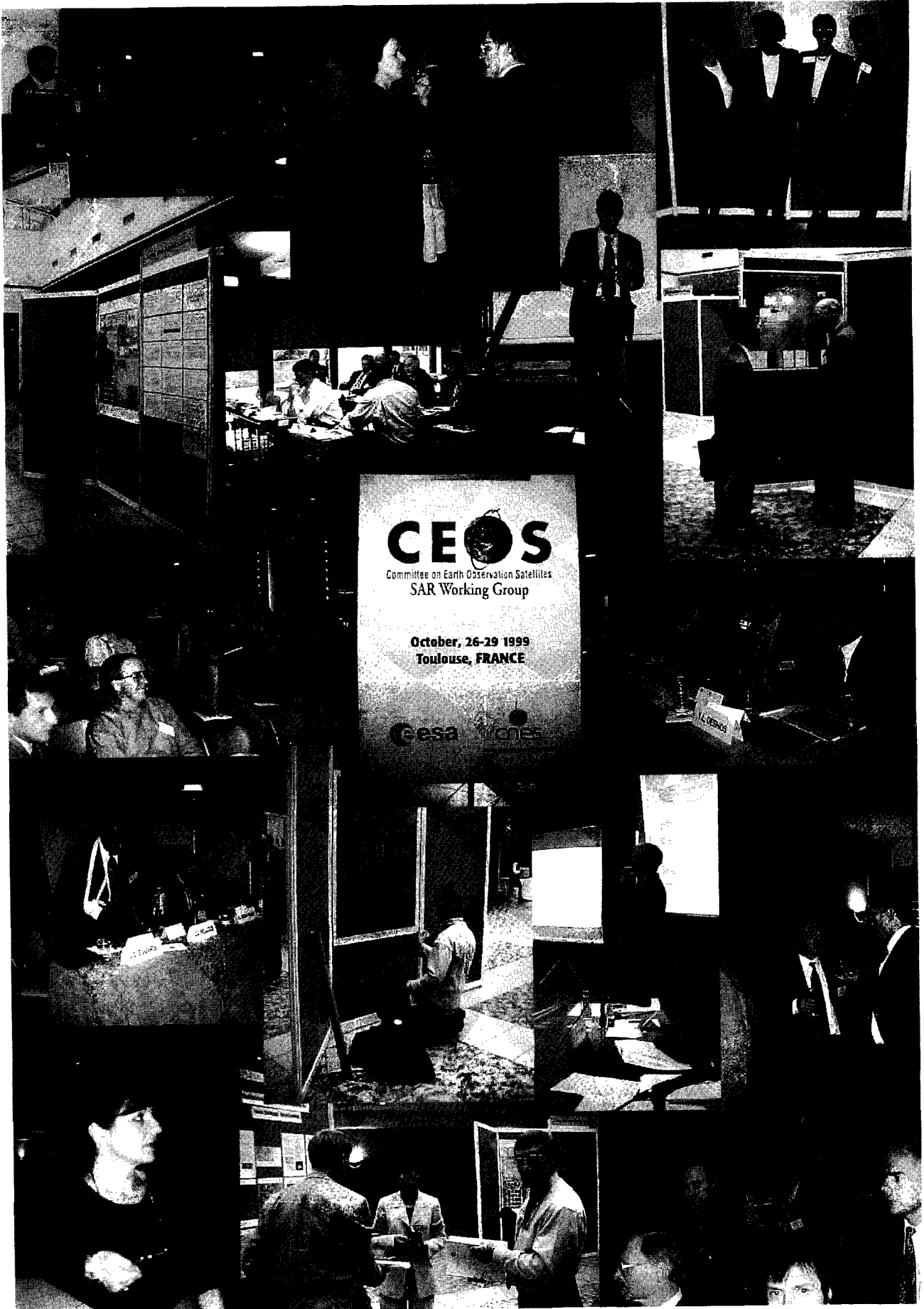
Crop Parameters Retrieval by SAR Phasimetry .....	443
<i>X. Blaes, P. Defourny (UCL, Louvain-la-Neuve, Belgium)</i>	
Geometric and Physical Constraints on Recovering Snow Covered Area from SAR.....	449
<i>R. Caves, S. Quegan (University of Sheffield, UK), T. Nagler (University of Innsbruck, Austria)</i>	
Assessment of Multi-Temporal products for Multi-Thematic Applications.....	455
with ERS SAR Data	
<i>J. Bruniquel, H. Sassier, S. Péraudeau, L. Rognant, S. Goze (Alcatel, Toulouse, France), G. Chust, D. Ducrot (CESBIO, Toulouse, France), K. Fellah (SERTIT, Illkirch, France), H. Laur (ESA/ESRIN, Frascati, Italy)</i>	
A Global NRCS Database Derived from ERS Scatterometer Data .....	461
<i>C. Lin (ESA/ESTEC, Noordwijk, The Netherlands), V. Wismann (Institute for Applied Remote Sensing, Freiburg, Germany)</i>	
On the Impact of C-Band SAR Calibration Errors on Soil Moisture Retrieval.....	467
<i>G. Satalino, G. Pasquariello (IESI-CNR, Bari, Italy), F. Mattia, G. De Carolis (ITIS-CNR, Matera, Italy), T. Le Toan, M. Davidson (CESBIO, Toulouse, France), M. Borgeaud (ESA/ESTEC, Noordwijk, The Netherlands)</i>	
Application of SAR Interferometry to Flood Damage Assessment.....	473
<i>C. Buck, S. Monni (ESA/ESTEC, Noordwijk, The Netherlands)</i>	
Potentiel de Détection des Traits Structuraux d'un Territoire Semi-Désertique .....	479
sur des Images RADARSAT: Le Cas du Macizo del Deseado, Argentina	
<i>D. Marchiommi, E. Rolleri (INREMI Universidad Nacional de La Plata, La Plata, Argentina), F. Cavayas (Université de Montréal, Canada)</i>	
Assimilation of ERS and RadarSat SAR Observations within the STICS Crop .....	485
Growth Model	
<i>H. Chauki, L. Prévot, D. Troufleau, N. Brisson, A. Oliosio, F. Baret (INRA, Avignon, France), M. Guérif (INRA, Laon, France)</i>	
Suivi de la Colonisation en Amazonie (Etat d'Amapa) a Partir d'Images ERS .....	491
<i>F.-M. Le Tourneau, M. Droulers (CREDAL, Paris, France), J.-P. Rudant (Université de Marne la Vallée, France)</i>	
Monitoring Urban Areas (Paris) with Multitemporal Multiincidence ERS Images .....	497
<i>A. Bianchin (Istituto Universitario di Architettura, Venezia, Italy), H. Maitre, J.-M. Nicolas, F. Tupin (ENST, Paris, France)</i>	
Using Layovers in Fusion of Optical and SAR Data: Application to .....	503
Mustang Landscape Analysis	
<i>L. Merlin, J.-M. Nicolas (ENST, Paris, France), D. Blamont (GRTS/LSIIT/ULP, Illkirch, France)</i>	
Boreal Forest INSAR Classification Properties.....	509
<i>D.L.A. Gaveau, H. Balzter, S. Plummer (Natural Environmental Research Council, Huntingdon, UK)</i>	

Analysis and Prediction of Internal Waves Using SAR Image and Non-Linear Model.....	513
<i>H. Hajji, S. Sole (MétéoMer, Puget/Argens, France) A. Ramamonjisoa (I.R.P.H.E., Marseille, France)</i>	
The Impact of RADARSAT ScanSAR Image Quality on Ocean Wind Retrieval .....	519
<i>P.W. Vachon, J. Wolfe, R.K. Hawkins (Canada Centre for Remote Sensing, Ottawa, Canada)</i>	
The Use of Ground Receiving Stations for ERS SAR Quality Assessment .....	525
<i>P. Meadows (Marconi Research Centre, Chelmsford, UK)</i>	
Maintenance of Radiometric Calibration Performance of RADARSAT-1 .....	531
<i>B.T. Banik, M. Adamovic, S.K. Srivastava (Canadian Space Agency, Saint Hubert, Canada), R.K. Hawkins, K.P. Murnaghan (Canada Centre for Remote Sensing, Ottawa, Canada)</i>	
The Radiometric Calibration Budget of RADARSAT-1 .....	539
<i>R. Hawkins (Canada Centre for Remote Sensing, Ottawa, Canada), S. Srivastava (Canadian Space Agency, Saint Hubert, Canada)</i>	
Roll Angle Measurement and Compensation Strategy for RADARSAT ScanSAR .....	545
<i>M. Dragošević, G. Davidson (IOSAT, Halifax, Canada)</i>	
Modelling of Electromagnetic Waves Interaction with Forest Canopies .....	551
<i>A. Ruiz (ONERA/CERT/DEMR / Université Paul Sabatier, Toulouse, France) P. Borderies (ONERA/CERT/DEMR, Toulouse, France), I. Chênerie (Université Paul Sabatier, Toulouse, France), E. Mougin, C. Proisy (CESBIO, Toulouse, France)</i>	
The Technology Development of a Spaceborne On-Board SAR-Processor .....	557
<i>and Storage Demonstrator M. Suess, C. Schaefer, R. Zahn (Dornier Satellite Systems, Friedrichshafen, Germany)</i>	
Simulator of Ocean Scenes Observed by Polarimetric SAR .....	563
<i>C. Cochin (DGA/CELAR, Bruz, France), T. Landeau (IRESTE/CNRS, Nantes, France), G. Delhommeau, B. Alessandrini (ECN/CNRS, Nantes, France)</i>	
On the Effect of Multi Scale Surface Roughness on SAR Data .....	569
<i>F. Mattia (ITIS-CNR, Matera, Italy), T. Le Toan, M. Davidson (CESBIO, Toulouse, France), P. Borderies, E. Bachelier (ONERA-DEMR, Toulouse, France), M. Borgeaud (ESA/ESTEC, Noordwijk, The Netherlands)</i>	
Stereo Vision Measurements of Soil Surface Characteristics and Their Use in Model.....	575
<i>Validation A. McDonald, S. Crossley, J. Bennet, S. Brown, G. Cookmartin, K. Morrison, S. Quegan (University of Sheffield, UK)</i>	
An Accurate Geometrical Error Model for Airborne SAR: A Design Example .....	581
<i>H. Cantalloube (ONERA, Palaiseau, France)</i>	

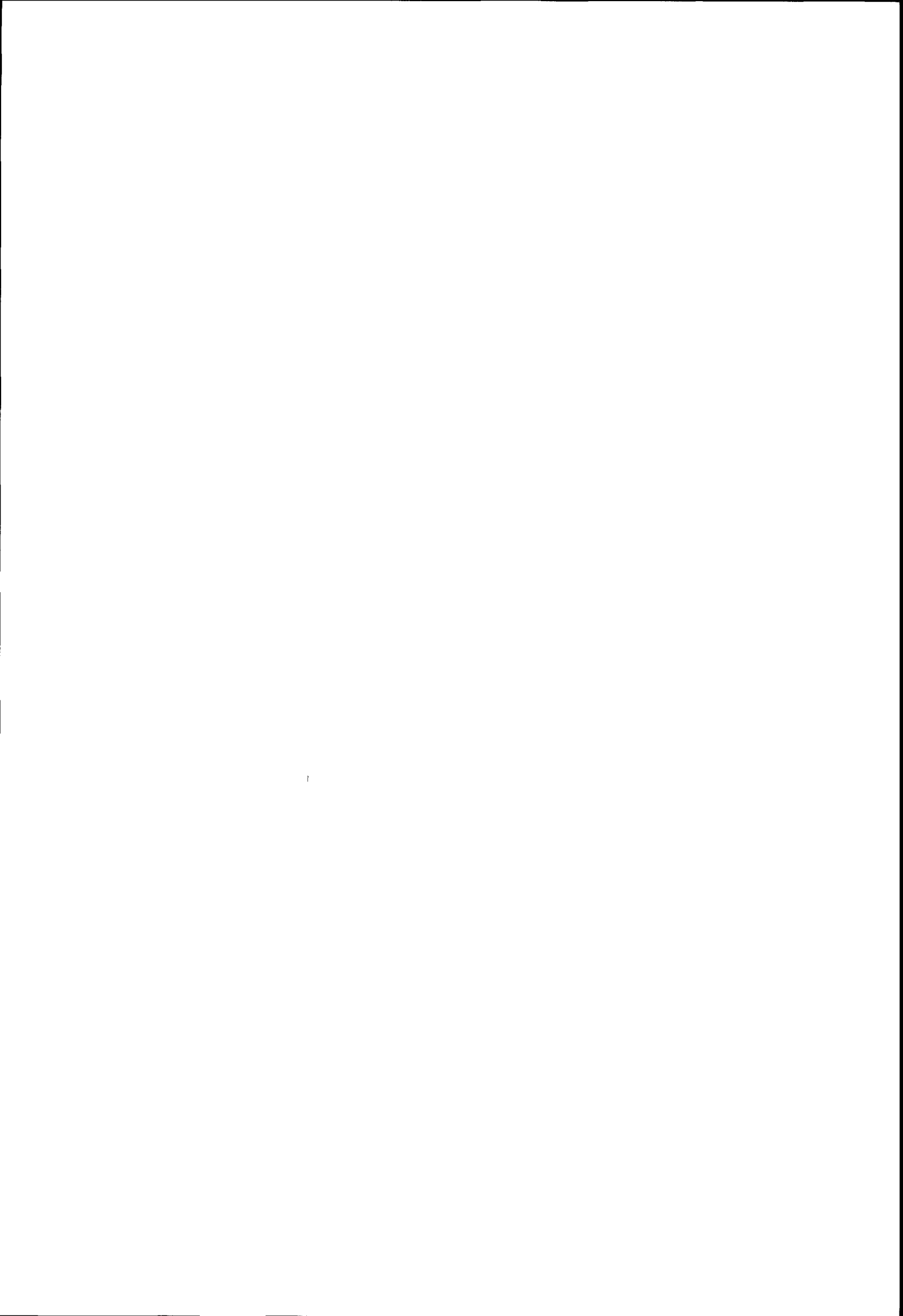
Airborne Imaging Radar Simulation in Realistic Environment Using Shooting and Bouncing Ray Technique <i>H. Mametsa, A. Berges (ONERA, Toulouse, France), T. Cathala, J. Latger (OKTAL, Toulouse, France)</i>	587
A New Interferogram Simulator: 2SIR. Study of Coherence Losses for Tortured Reliefs <i>D. Petit (IRIT, Toulouse, France), F. Adragna CNES, Toulouse, France)</i>	591
ERS Attitude Errors and its Impact on the Processing of SAR Data <i>D. Esteban Fernández (GAEL Consultant, Champs-sur-Marne, France), P. Meadows (Marconi Research Centre, Chelmsford, UK), B. Schättler (DLR, Oberpfaffenhofen, Germany), P. Mancini ESA/ESRIN, Frascati, Italy)</i>	597
Mosaic Generation Using ERS SAR Imagery <i>P. Meadows, P. Wright (Marconi Research Centre, Chelmsford, UK)</i>	607
Location Accuracy of Edge Detectors for SAR Images <i>O. Germain, P. Réfrégier (ENSP de Marseille, France)</i>	613
Analysis of Complex SAR Raw Data Compression <i>S. Peskova, S. Vnotchenko (Tsyolkovsky Russian State Technological University, Moscow, Russia)</i>	619
High Resolution Spectral Analysis Applied to SAR Images <i>L. Savy, J.-G. Planès (Alcatel, Toulouse, France), C. Moal (ENSICA, Toulouse, France)</i>	625
Data Compression for Transmission of Polarimetric SAR Signal by Vector Quantization – Performance Evaluation <i>N. de Beauhoudrey, T. Seren, D. Barba (IRESTE, Nantes, France), X. Morin (Institut Français pour la Recherche et la Technologie Polaires, Plouzané, France)</i>	631
How to Compute a Multi-Look SAR Image? <i>H. Cantalloube, C. Nahum (ONERA, Palaiseau, France)</i>	635
Get Out of the Black Box: Turn Remote Sensing Data into Useful Information and Knowledge! <i>M. Oddou (StorageTek SBG Europe, Toulouse, France)</i>	641
A Spaceborne Ground Penetrating Radar: MIMOSA <i>A. Herique, L. Phalippou (Alcatel, Toulouse, France), W. Kofman (LPG UJF, Grenoble, France), P. Bäuer (CNES, Toulouse, France), F. Remy (LEGOS, Toulouse, France)</i>	645
Phase Unwrapping by Ground Slopes Estimation <i>X. Dupuis, P. Matthieu, M. Barlaud (Université de Nice, Sophia Antipolis, France)</i>	651
Operational Interferometric ERS Tandem Data Processing <i>B. Schättler, M. Eineder, W. Knöpfle, M. Hubig (DLR, Wessling, Germany)</i>	657

Insar Analysis of the Effects of the Izmit Earthquake with ERS Data .....	663
<i>F. Sarti, F. Adragna, N. Pourthié (CNES, QTIS/SR, Toulouse, France),</i>	
<i>B. Rosich, A. Arnaud (ESA/ESRIN, Frascati, Italy),</i>	
<i>K. Feigl (OMP/CNRS, Toulouse, France),</i>	
<i>M. Rosengren (ESA/ESOC, Darmstadt, Germany),</i>	
<i>P. Imbo (CESBIO, Toulouse, France), D. Petit(IRIT/UPS, Toulouse, France)</i>	
 The Spot Image Coherence Product and Dimap: A New Format for a New Product .....	 671
<i>P. Bally, C. Angleraud, Y. Somer (Spot Image, France)</i>	
 A Method for the Automatic Characterization of Interferometric Fringes Free .....	 679
Atmospheric Artifacts: Application to the Study of the Subsidences on the City of Paris	
<i>B. Fruneau (IFG, Université de Marne la Vallée, France),</i>	
<i>F. Sarti (CNES, QTIS/SR, Toulouse, France)</i>	
 Ship Detection Using Polarimetric SAR Data .....	 687
<i>R. Ringrose, N. Harris (DERA Farnborough, UK)</i>	
 An Eigenvector Method for the Extraction of Surface Parameters in .....	 693
Polarimetric SAR	
<i>S.R. Cloude, K. Papathanassiou(Applied Electromagnetics, St. Andrews, Scotland),</i>	
<i>I. Hajnsek (DLR, Wessling, Germany)</i>	
 Polarimetric Calibration Results and Error Budget for SAR-580 System .....	 699
<i>R. Hawkins, R. Touzi, A. Wind (Canada Centre for Remote Sensing, Ottawa, Canada), K.</i>	
<i>Murnaghan (Isoceles Information Solutions, Canada),</i>	
<i>C. Livingstone (Defense Research Establishment, Ottawa, Canada)</i>	
 Radar Polarimetry for Vegetation Observation .....	 705
<i>C. Titin-Schnaider (ONERA, Palaiseau, France)</i>	
 <b>List of Authors</b> .....	 713
 <b>List of Participants</b> .....	 719





**CEOS**  
Committee on Earth Observation Satellites  
**SAR Working Group**  
  
October, 26-29 1999  
Toulouse, FRANCE  
  
ESA CNES



## Foreword

In the framework of the *Committee on Earth Observation Satellites* (CEOS) Working Group on Calibration and Validation, a SAR Workshop jointly organised by ESA and CNES was held at the ATRIA Mercure hotel, in Toulouse from 26<sup>th</sup> to 29<sup>th</sup> October 1999. The meeting was hosted by the Radar Systems Department of CNES "Centre Spatial de Toulouse".

The workshop, attended by 180 participants (17 countries were represented) was organised in the form of plenary sessions allowing 20 minutes for presentations and 5 minutes for questions. For the first time, a poster session was also organised. The programme content and preparation was supported by an International Technical committee composed of 36 experts representing the various disciplines.

A web site was also prepared for the workshop and papers are available on-line at URL:

<http://www.estec.esa.nl/CONFANNOUN/99b02>.

120 presentations (65 orals and 55 posters) were given during the CEOS'99 meeting

Each workshop session was followed by a round table in order to allow further discussions on '*seed questions*' prepared by the session chairmen and rapporteurs, and on specific issues raised during the presentations. On the last day of the workshop, a session was organised to summarise the different sessions of the workshop and to draft recommendations for the CEOS WGCV.

This volume brings together the results presented at the workshop in the full length papers, the seed questions prepared for the round tables, the summary reports of the 8 sessions and finally the recommendations brought up to the CEOS WGCV. A synthesis of the discussions related to suggestions on the workshop format can be also be found at the end of the proceedings.

The CEOS SAR workshop was more than ever the forum for interchange at the highest level of the SAR Systems Engineering field. We were able to discuss in depth key technical problems and to help to better define future SAR instruments and their performances. These discussions confirmed that various technical issues remain to be solved and the SAR subgroup will continue to meet every year in order to address them. As a measure of the success of this workshop, three space agencies have already proposed to host the next meeting : NASDA (Japan), DLR (Germany) and CSA (Canada).

We would like to take this opportunity to thank all attendees for their effort in attending, presenting and contributing to the workshop. We should also thank also the organising committee, the scientific committee, the session chairmen and rapporteurs and the staff from the CNES and ESA conference bureaus who contributed to the success of this event. We look forward to seeing all of you at the next CEOS SAR workshop.

Yves-Louis Desnos (Chair CEOS SAR Subgroup)

Jean-Claude Souyris (Workshop Local Organiser)



## Introduction

S. Briggs, Head Earth Observation Applications Department (ESA/ESRIN)  
J-L. Fellous, Earth Science and Applications, CNES Programme Directorate

International collaboration on calibration and validation through the Cal/Val Working Group has been one of the signal successes of the CEOS organisation. The Working Group has created a mechanism for the sharing of effort in CAL/VAL between cooperating agencies, for the management of coherent programmes and campaigns and for the pooling of engineering and scientific information about the process of Earth observation through a variety of techniques. The success of the meeting of the SAR subgroup reported here is further evidence of the success of the coordinated approach adopted through CEOS.

The location of the meeting in Toulouse is also evidence of the interest and historical support for SAR work in Europe. SAR was central to the mission of the first two ESA EO satellites, ERS-1 and ERS-2, and the Advanced SAR (ASAR) on board ENVISAT will be a further step forward in technology and in the exploitation of SAR data. In addition, there have been significant European contributions to joint missions with NASA, culminating in the recent marvellously successful SRTM topographic mapping mission, developing interferometric techniques first demonstrated in space with the ERS missions. Recent developments in differential interferometry reported here are particularly exciting and are leading both to a better understanding of the geophysics of the Earth's crust and, of immediate practical benefit, to methods of monitoring and even perhaps predicting surface deformations caused by natural disasters such as earthquakes and landslides, as well as anthropogenic subsidence. Coherence mapping is also showing very encouraging results in other aspects of disaster monitoring.

The volume of business at this meeting shows the world-wide interest in SAR Cal/Val. Over 180 participants attended from 17 countries, with over 120 papers being presented. A particularly important and useful contribution came from the Round Table sessions, where the practical details of cooperative programmes and campaigns were discussed. Over 10 hours of Round Table talks were held during the course of the meeting.

Conclusions of the workshop will be presented to the next WGCV Plenary meeting in India and formal recommendations made to the CEOS Plenary in Sao Paulo in late 2000, for implementation through member space agencies.

We are very pleased that ESA has agreed to publish the proceedings as a volume in the ESA Special Publication Series; this will ensure that the workshop will have the widest possible impact.

We would like to congratulate the organisers on the outstanding success of the workshop and the quality of the subsequent publication.



## **Session 1: Land Applications**





**LIGHTSAR: Convergence of Science, Applications and Commercial Requirements**

Diane Evans, Anthony Freeman  
Jet Propulsion Laboratory, USA

This paper was not available for publication



## Application of Polarimetric SAR data processing to Snow Cover Remote Sensing. Validation using Optical images and Ground data.

L. FERRO-FAMIL<sup>1</sup>, E. POTTIER<sup>2</sup>, J.P. DEDIEU<sup>3</sup>, C. CORGIER<sup>3</sup>, J. SAILLARD<sup>1</sup>

<sup>1</sup> IRESTE, The University of Nantes, France. SEI Laboratory, EP CNRS 63  
Rue C. Pauc, 44306 NANTES Cedex

Ph/Fax : (+33) 2 40 68 32 30 / (+33) 2 40 68 32 33 E-mail: lferrofa@ireste.fr.

<sup>2</sup> The University of Rennes, L. A. T. Laboratory, UPRES-A CNRS 6075, "Structures Rayonnantes".

Campus de Beaulieu - Bat 22, 263 Av. Gal Leclerc, CS 74205, 35042 Rennes Cedex, France

Ph/Fax : (+33) 2 99 28 29 55 / (+33) 2 99 28 69 63, E-mail : eric.pottier@univ-rennes1.fr

<sup>3</sup> LAMA - CNRS (ESA 5068) 17, rue M. Gignoux, 38031 Grenoble cedex 09 - France.

Ph/Fax : (+33) 4 76 63 59 40 / (+33) 4 76 17 06 62, E-mail : dedieujp@iga.ujf-grenoble.fr

### ABSTRACT

In this paper is introduced a polarimetric approach to snow cover remote sensing based on techniques derived from polarimetric decomposition theorems dedicated to the analysis of natural media SAR images. Discriminant parameters are interpreted by the mean of polarimetric image comparison. The analysis of the changes from one image to the other are realized by construction of a unitary variation operator or through the classification of polarimetric representations gathering information from both images.

Results are compared to remotely sensed optical images, ground measurements and meteorological simulations.

### INTRODUCTION

Scattering from snow is function of many physical parameters of the snow pack itself such as depth, density, temperature, grain shape, but also of the underlying soil (roughness, moisture, ...). Backscattering may also vary in a significant way according to the frequency and the incidence angle at which the measurements are done.

Numerous studies have been done using both mono- and multi-polarized data.

In the case of single polarization data, the snow water equivalent of dry snow can be derived from the power ratio between summer and winter images [1]. This method requires the data to be accurately calibrated and geo-corrected.

Other approaches take into account several polarizations, giving rise to additional interpretation of the backscattering behavior of the snow pack. They are based on a model fitting strategy, or on the splitting of the scattering coefficients into a sum of contributions from the different regions of the snow layer [2].

These studies require the use of polarimetric coefficients but do not take into account the whole polarimetric information, the main reason being that the remaining coefficients do not contain useful information for target classification in these conditions [3].

SAR data for snow remote sensing is generally pre-processed in order to remove the effects of the scene topography. This correction consists in a slant range to ground range sampling and projection on an artificial flat surface, or on a Digital Elevation Model (DEM). The scattering coefficients are then weighted by a function depending on their local incidence angle with respect to the observing radar in order to attenuate differences due to orientation variations from one pixel to the other [4].

In this paper, we apply polarimetric techniques on SAR data in order to classify dry snow in mountain regions.

This work is based on the use of a polarimetric decomposition theorem [5], and in order to preserve the validity of the information and its interpretation, all the polarimetric incoherent terms must be considered.

Data sampling and correction imply operations that may corrupt the polarimetric information and modify the geographical location of the pixels. Such techniques are not very well adapted to full polarimetric data processing which is highly sensitive to power and phase sharing between the polarization channels.

The analysis of several images of a given scene significantly improves the observed medium characterization, and provides parameter variations strongly related to its physical properties.

In this paper, we propose several methods for polarimetric image comparison.

We first define the polarimetric variation from one pixel to the other using a special unitary operator parameterized by 8 real coefficients. We propose to extract these parameters by a least square optimization procedure.

We present the  $H/A/\bar{\alpha}$  decomposition used to initialize an unsupervised polarimetric Wishart classifier which permits to adapt the decision boundaries to data distribution. Images are classified sequentially and the pixel to pixel distance from one image to the other is used to give an interpretation of the changes in the

scattering phenomenon.

We introduce a polarimetric representation containing the information from both images. We then set up a unsupervised algorithm which directly classifies data according to their characteristics in both images and to the correlation of the polarimetric features between the images.

Finally, these classifications are applied on polarimetric data that was collected during two of the space shuttle missions in 1994, by the Jet Propulsion Laboratory SIR-C sensor over the French Alps during April and October at both L and C bands.

### UNITARY OPERATORS

In a monostatic configuration, the 3 by 3 hermitian coherency matrix  $[T]$  of a target is defined from the elements of the scattering matrix  $[S]$  as follows:

$$[T] = \underline{k}\underline{k}^{*T} \text{ with}$$

$$\underline{k} = \frac{1}{\sqrt{2}} [S_{HH} + S_{VV} \quad S_{HH} - S_{VV} \quad 2S_{HV}] \quad (1)$$

where  $\underline{k}$  is the target vector. The target is said to be pure if the 9 real coefficients used to parameterize  $[T]$  verify the 4 target equations as explained in [6]. In this case the matrix results in 5 degrees of freedom and its rank is 1. A pure matrix can be decomposed into its eigenvector basis in the following way

$$[T] = \lambda [V][\Sigma_0][V]^{-1} \text{ with } [\Sigma_0] = \begin{bmatrix} 1 & 0 & 0 \\ 0 & 0 & 0 \\ 0 & 0 & 0 \end{bmatrix} \quad (2)$$

$\lambda$  is the single eigenvalue different from zero and the eigenvector matrix  $[V]$  is special unitary, i.e. it verifies the conditions enounced in (3).

$$[V]^{-1} = [V]^{*T} \text{ and } \det([V]) = +1 \quad (3)$$

Two pure matrices  $[T_1]$  and  $[T_2]$  are linked by the way of a special unitary transformation defined from their eigenvector matrices, respectively  $[V_1]$  and  $[V_2]$ .

Defining  $[U] = [V_2][V_1]^{-1}$ , we obtain

$$[T_2] = \frac{\lambda_1}{\lambda_2} [U][T_1][U]^{-1} \Leftrightarrow \underline{k}_2 = \sqrt{\lambda_1/\lambda_2} [U]\underline{k}_1 \quad (4)$$

A 3 by 3 special unitary matrix is made of  $2*9 = 18$  real elements. Its 3 column vectors are mutually orthogonal, it has a unitary norm and its determinant equals 1. The number of real parameters needed to determine a special unitary operator is then  $18-6-3-1 = 8$ . By projection on the 8 Gell-Mann hermitian matrix set, this special unitary operator is parameterized in terms of complex matrix exponentials as expressed in (5) [7].

$$[U] = \exp\left(j \sum_{i=1}^8 \omega_i [\beta_i]\right) \quad (5)$$

with  $[\beta_i]$  the  $i$ th Gell-Mann matrix and  $\omega_i$  its real scalar weighting coefficient. These 8 parameters fully describe the change in polarization from  $[T_1]$  to  $[T_2]$ .

It can be easily shown that the eigenvector matrices used to built  $[U]$  are not unique, leading to an infinite number of Gell-Mann parameters verifying (4). The right hand side of (4) is an under-determined set with 8 unknowns and 5 equations since a target vector is an incoherent representation and does not depend on the absolute phase.

A solution is to increase the number of equations by assuming that a pixel and one of its neighbors undergo a similar polarimetric transformation from one image to the other. We then deal with an over-determined set with 8 unknowns and 10 equations, which can be resolved through a least square approximation procedure. The 8 Gell-Mann coefficients of  $[U]$  are the ones that minimize the scalar

$$\varepsilon^2 = |\underline{k}_2 - [U]\underline{k}_1|^2 + |\underline{k}_4 - [U]\underline{k}_3|^2 \quad (6)$$

In (6),  $\underline{k}_1$  and  $\underline{k}_3$  are the target vectors of neighbor pixels in the first image,  $\underline{k}_2$  and  $\underline{k}_4$  their respective corresponding target vectors in the second image.

### THE H/A/ $\bar{\alpha}$ DECOMPOSITION AND THE UNSUPERVISED WISHART CLASSIFIER

The application of the Gell-Mann decomposition procedure limits the polarimetric comparison to the case of pure images. In order to reduce the speckle, data are generally averaged and the resulting mean matrix  $\langle [T] \rangle$ , which represents a distributed target, has its rank superior to 1.  $\langle [T] \rangle$  cannot be related to a single scattering matrix  $[S]$  and has to be decomposed in order to identify the global mean scattering mechanism.

In [5] is enounced a polarimetric decomposition theorem based on the eigenvalue/eigenvector decomposition of a distributed coherency matrix.

$\langle [T] \rangle$  is decomposed into a weighted sum of three orthogonal unitary matrices representing each a pure scattering mechanism.

$$\langle [T] \rangle = \sum_{i=1}^3 \lambda_i \underline{V}_i \underline{V}_i^{*T} = \lambda_1 [T_1] + \lambda_2 [T_2] + \lambda_3 [T_3] \quad (7)$$

with  $\lambda_i$  the  $i$ th eigenvalue of  $\langle [T] \rangle$  and  $\underline{V}_i$  its related eigenvector.

The unitary eigenvectors are parameterized using 4

angular variables leading to an interpretation of the scattering phenomenon.

$$V_i = \left[ \cos \alpha_i \sin \alpha_i \cos \beta_i e^{j\delta_i} \sin \alpha_i \sin \beta_i e^{j\gamma_i} \right]^T \quad (8)$$

A statistical analysis of the eigenvector based decomposition theorem is used in order to extract the mean global scattering mechanism.

Each one of the three scattering mechanisms described in (7) is weighted by its pseudo-probability  $p_i$  corresponding to its relative power with respect to the total power.

The mean decomposition parameters are calculated according to (9).

$$(\bar{\alpha}, \bar{\beta}, \bar{\delta}, \bar{\gamma}) = \sum_{i=1}^3 p_i (\alpha_i, \beta_i, \delta_i, \gamma_i) \text{ with } p_i = \frac{\lambda_i}{\sum_{j=1}^3 \lambda_j} \quad (9)$$

The three main parameters of this decomposition are

- $\bar{\alpha}$  the indicator of the mean scattering mechanism. A value close to 0 relates surface reflection, for dipole scattering  $\bar{\alpha}$  equals  $\frac{\pi}{4}$ , and reaches  $\frac{\pi}{2}$  when the target consists in metallic dihedral scatter.

- The entropy H, an indicator of the random behavior of the global scattering.
- The anisotropy A which represents the relative importance of the two less significant terms.

H and A define the matrix probability spectrum.

The H- $\bar{\alpha}$  classification is achieved by projecting the pixels of an image onto a plane according to their (H,  $\bar{\alpha}$ ) coordinates. The anisotropy allows to distinguish between pixels belonging to the same class in the (H,  $\bar{\alpha}$ ) plane depicted in Fig. 1.

The decision borders in this classification plane have been chosen arbitrarily. The H axis is split into three zones depicting almost deterministic, moderately random and highly random scattering. The  $\bar{\alpha}$  regions have been set so as to contain slight variations around canonical limit behaviors.

The main advantage of this classification is to provide an interpretation of the global scattering that is refined enough to roughly characterize scenes made of targets with distinct scattering behaviors like the San-Francisco bay AirSAR image at L band which contains sea, urban and forest target types.

For complex scenes presenting more various and less spatially segmented behaviors, the H- $\bar{\alpha}$  approach fails to accurately classify the different media types.

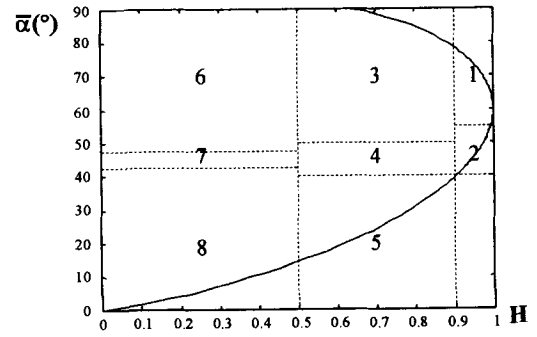


Fig. 1: H- $\bar{\alpha}$  classification plane.

This is mainly due to the use of linear arbitrarily fixed decision borders. Pixels from the same type of natural media may form a cluster in the H- $\bar{\alpha}$  plane belonging to two or more different classes. The classified data set is then noisy and may lead to misinterpretation. Furthermore, two or more natural clusters, for instance single bounce reflection on surfaces with different dielectric constants, may be contained within a single class, class number 9 in this example. This drawback is an important limitation in the case of snow remote sensing over slightly rough surfaces, since the slight modification of the backscattering due to the presence of snow is not detected.

In [8] is presented an unsupervised classification which adapts its decision to the distribution of the polarimetric data.

Under some conditions the coherency matrices of an image are shown to follow a Wishart distribution leading to the definition of a distance between a pixel coherency matrix and the center of the mth class.

$$d(\langle [T_m] \rangle, [T]) = \ln |\langle [T_m] \rangle| + \text{Tr}(\langle [T_m] \rangle^{-1} [T]) \quad (10)$$

where  $\langle [T_m] \rangle$  is the mth class center coherency matrix resulting of the averaging of all the coherency matrices belonging to the class m, and  $[T]$  is the matrix of the pixel to be classified.

A pixel belongs to the ith class if

$$d(\langle [T_i] \rangle, [T]) < d(\langle [T_j] \rangle, [T]) \quad \forall j \neq i \quad (11)$$

One can remark the indirect use of information related to the scattering degree of randomness in (10). The term  $|\langle [T_m] \rangle|$  is indeed the product of the eigenvalues of  $\langle [T_m] \rangle$  and is then closely related to the class center matrix entropy. Since this matrix results from the averaging of a large number of matrices, the class center has in general all its eigenvalues different from 0, involving that the distance from the class center to itself is not equal to the minimal value of 3 and depends on the resemblance of the whole class matrices.

Both (10) and (11) are used to perform an iterative k-mean classification with an initialization of the class centers using the H- $\bar{\alpha}$  segmented plane.

The algorithm is:

Step 1: Classify each pixel in one of the 8 classes  $C_i$  of the H- $\bar{\alpha}$  plane

Step 2: Calculate the mean matrix for each class  $\langle [T_i] \rangle = \frac{1}{n_i} \sum [T] \in C_i$ .

Step 3: For each pixel, apply (9) and (10) to find the nearest class  $C_j$ , and associate the pixel to this class. If a termination criterion is met go to Step 4, otherwise go to Step 2.

Step 4: End.

The number of classes is fixed to 8 due to the use of the H- $\bar{\alpha}$  segmented plane. The critical point when classifying with a k-mean procedure concerns the initialization step, which determines the quality of the whole classification. This algorithm was tested on many data sets, and gave satisfying results due to the relevance of the H and  $\bar{\alpha}$  initializing parameters. An estimation of the stability of the pixel distribution acts as a termination criterion. The process is stopped if the stability reaches a fixed threshold.

#### DIRECT UNSUPERVISED CLASSIFICATION OF TWO POLARIMETRIC IMAGES

The classification procedure mentioned above deals with one image at a time. When comparing polarimetric images, one has to classify each image, and then analyze differences by a class to class migration observation from one image to the other [6].

In order to directly perform the comparison, we build a polarimetric incoherent representation gathering information from both images.

From (1), we construct a 6 element target vector  $\underline{k}$  by superposing two target vectors,  $\underline{k}_1$  and  $\underline{k}_2$ , belonging to the different images.

$$\underline{k} = \begin{bmatrix} \underline{k}_1 \\ \underline{k}_2 \end{bmatrix} \quad (12)$$

The corresponding hermitian 6 by 6 coherency matrix,  $[T]_6$ , summarizes the information from both images and has the following structure.

$$[T]_6 = \underline{k} \underline{k}^{*T} = \begin{bmatrix} [T_1] & [\Omega] \\ [\Omega]^{*T} & [T_2] \end{bmatrix}, [\Omega] = \underline{k}_1 \underline{k}_2^{*T} \quad (13)$$

$[T_1]$  and  $[T_2]$  are the standard 3 by 3 hermitian coherency matrices for separate images.  $[\Omega]$  is a 3 by 3

complex matrix which contains information about the correlation of their polarimetric characteristics.

By construction,  $[T]_6$  is pure matrix with only one of its 6 eigenvalues different from 0.

After averaging, its entropy depends on the entropies of both  $[T_1]$  and  $[T_2]$  but also on the correlation between the target vectors  $\underline{k}_1$  and  $\underline{k}_2$ .

Similarly to the 3 by 3 matrix case, the 6 by 6 matrix image is classified by the way of an unsupervised Wishart classifier.

The classes are initialized with the results of the Wishart classification over the separate images which constitute stable segmentations adapted to the data distribution within each image. The resulting number of classes is then 64, involving the use of a class merging procedure to be able to interpret and visually represent the classified information.

Considering the whole class set, the clusters to be merged are the ones presenting the lowest degree of separability.

Two classes can be distinguished if they are compact and if the mean distance between their elements is high. We define the separability between classes  $i$  and  $j$  as the ratio of their between-class distance to their within-class dispersion.

The within-class dispersion for class  $C_i$  is defined as the mean distance from its elements to the class center  $\langle [T_i] \rangle$  as described in (14)

$$W_i = \frac{1}{n_i} \sum_{p=1}^{n_i} d(\langle [T_i] \rangle, [T]_i) \quad (14)$$

where  $[T]_i$  stands for  $[T] \in C_i$ .

Applying (10) in (14), we find

$$W_i = \ln |\langle [T_i] \rangle| + Tr([I]) = \ln(|\langle [T_i] \rangle|) + 6 \quad (15)$$

The distance between class  $C_i$  and class  $C_j$  is the mean distance from the element of each class to the center of the other class.

$$B_{ij} = \frac{1}{2} (\langle d(\langle [T_j] \rangle, [T]_i) \rangle + \langle d(\langle [T_i] \rangle, [T]_j) \rangle) \quad (16)$$

$$B_{ij} = \frac{W_i + W_j + Tr(\langle [T_i] \rangle^{-1} \langle [T_j] \rangle + \langle [T_j] \rangle^{-1} \langle [T_i] \rangle)}{2} \quad (17)$$

Consequently, two classes are to be merged if they present a low separability

$$Sp_{ij} = B_{ij} / (W_i + W_j) \quad (18)$$

Data sets are classified according to the algorithm described in the preceding section, and the number of classes is decreased using (18) till a fixed number of classes is reached.

## APPLICATIONS TO POLSAR DATA

We apply the classification procedures introduced in this paper to the polarimetric SAR images of Izoard test site in the southern Alps. Data has been collected at both April and October periods, which respectively correspond to snow and snow free conditions. The target generators color coded image describing the test scene in Fig. 2, is built from the diagonal elements of the coherence matrices.

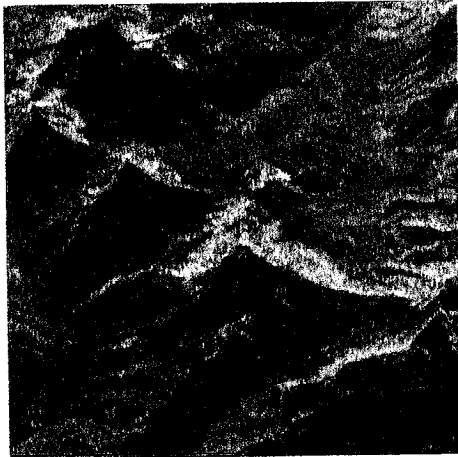


Fig. 2: Target generators color coded image of Izoard at L band, October 1994.

We first apply the  $H-\bar{\alpha}$  classification on the snow covered image at C band.

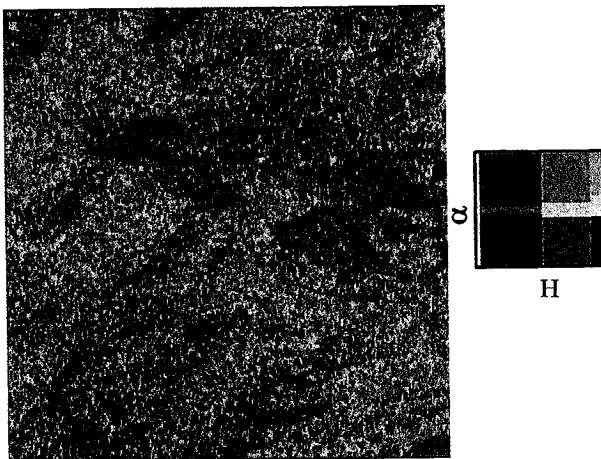


Fig. 3: April 1994 Izoard. Classified C band image using the  $H-\bar{\alpha}$  classification.

The classes corresponding to low and medium entropy single bounce scattering, coded dark and light blue, occupy a huge proportion of the classified image. The other main classes are double bounce scattering and scattering on anisotropic elements, respectively coded red and green. The noisy aspect of the classified image, and the concentration of the pixels in a small number of classes are due to the fact that the linear arbitrarily fixed

boundaries do not fit the pixels distribution.

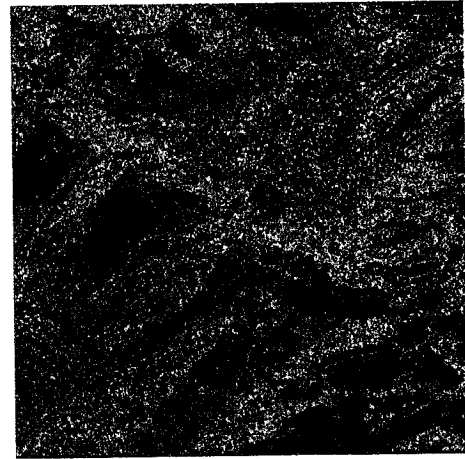


Fig. 4: October 1994, Izoard. Classified C band image using the Wishart classifier with anisotropy.

In Fig. 4 and Fig. 5 are shown the C band classification results obtained with the Wishart classifier including the anisotropy for both observation dates. This classification shows a lot more details and permits a refined analysis of the mean scattering phenomenon. Since this classifier adapts its decision borders to the polarimetric information distribution, the features of the class centers vary during the iterative process.

In order to characterize the nature of each class, we need to plot their spatial distribution and their occurrence in the  $H-\bar{\alpha}$  plane as shown in Fig. 6. Other indicators such as power or the distance for each pixel to its class center may also be used.

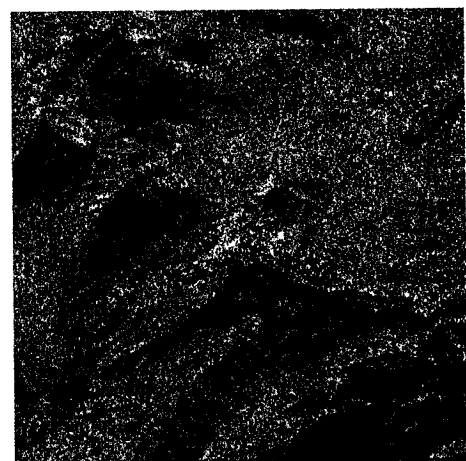


Fig. 5: April 1994, Izoard. Classified C band image using the Wishart classifier with anisotropy.

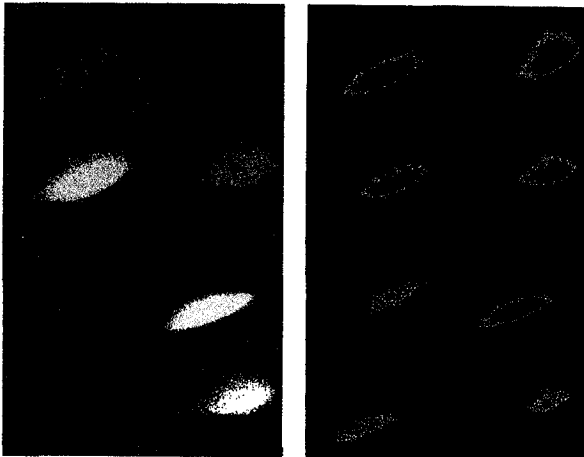


Fig. 6: Characteristics of the 8 first clusters from the classified image in Fig. 5. Each class spatial distribution (left) and occurrence (right) are plotted in a  $H-\bar{\alpha}$  plane.

Fig. 7 represents the classified image obtained with the direct Wishart classifier applied to 6 element target vectors made of C band polarimetric elements from both October and April data sets.

The results show more accuracy due to information given by the between image correlation term  $[\Omega]$ .



Fig. 7: C band, Izoard. Classified image using the direct Wishart classifier applied on 6 by 6 coherency matrices built from both April and October images.

### CONCLUSION

In this paper we presented several approaches to polarimetric image comparison. We first defined 8 real parameters which characterize the polarimetric variations between two pure matrices. We presented the unsupervised Wishart classifier which greatly improves the quality of the classification due to its adaptive nature. Finally, we developed a direct Wishart classifier which

merges information from both images to be compared and take into account the correlation between their polarimetric characteristics.

During the oral session, we will show detailed results and interpretations which will be compared to optical images from Landsat Thematic Mapper, and illustrated by meteorological snow conditions generated by the CROCUS simulator from Météo-France.

### REFERENCES

- [1] M. Bernier, J.P. Fortin, "The Potential of Time Series of C-Band SAR Data to Monitor Dry and Shallow Snow Cover", *IEEE Transactions on Geoscience and Remote Sensing*, Vol. 36, No 1, September 1996.
- [2] J. Shi, J. Dozier, "On estimation of Snow Water Equivalence using SIR-C/X-SAR", Second International Workshop on Retrieval of Bio- and Geo-physical Parameters from SAR Data for Land Application, Noordwijk, The Netherlands, October 1998.
- [3] D. M. Floricioiu, "Polarimetric Signatures and Classification of Alpine Terrain by Means of SIR-C/X-SAR", Ph. D. Thesis, Innsbruck, Austria, October 1997.
- [4] T. Guneriusson, "Backscattering properties of a wet snow cover derived for DEM corrected ERS-1 SAR Data", *International Journal of Remote Sensing*, Vol. 18, No. 2, 1997.
- [5] S. R. Cloude, E. Pottier, "A Review of Target Decomposition Theorems in Radar Polarimetry", *IEEE Transactions on Geoscience and Remote Sensing*, Vol. 34, No. 2, March 1996.
- [6] L. Ferro-Famil, T. Landeau, E. Pottier, J. Saillard, J.P. Dedieu, M. Bernier, J.P. Fortin, "Classification of Snow Scattering Behavior using Polarimetric Decomposition Theorems", International Workshop on Radar Polarimetry, PIERS'98, Nantes, France, July 1998.
- [7] S. R. Cloude, E. Pottier, "Matrix Difference Operators as Classifiers in Polarimetric Radar Imaging", RADAR'94, Paris, France, May 1994.
- [8] J. S. Lee, E. Pottier, "Application of the H/A/Alpha Polarimetric Decomposition Theorem for Unsupervised Classification of Fully Polarimetric SAR data based on the Wishart Distribution", CEOS Workshop, Toulouse, France, October 1999.



## RADARSAT, ERS and EMISAR data for snow monitoring in mountainous areas

Tore Guneriussen, Harald Johnsen and Inge Lauknes  
NORUT IT Ltd.,

Tromsø Science Park, 9005 Tromsø, Norway  
Tel: + 47 77 62 94 00, Fax: + 47 77 62 94 01, e-mail: tore@itek.norut.no

### ABSTRACT

This paper address the snow mapping capabilities of SAR instruments by presenting results from analysis of Polarimetric SAR (EMISAR), ERS and RADARSAT data acquired from two campaign.

Polarimetric SAR and ERS data were acquired as part of the Snow and Ice experiment within the European Multi-sensor Airborne Campaign (EMAC'95). The test area is the Kongsfjellet area, located in Norway, 66° N, 14° E. Fully polarimetric C- and L-band SAR data from EMISAR, an airborne instrument operated by the Danish Centre for Remote Sensing (DCR), were acquired in March, May, and July 1995. In addition, several ERS SAR, airborne photos, field, and auxiliary data were acquired. The difference in mean backscattering coefficient between wet snow and ground in July was found to be 4.5 - 6.5 dB and 7-11 dB for ERS SAR and EMISAR C-VV data, respectively. For EMISAR, higher difference was found at large incidence angle (55°) than at lower incidence angle (45°).

In another campaign, a total of 21 RADARSAT SLC data from Heimdalen area Norway (61° N, 9° E) during snowmelt in 1997 have been geocoded and recalibrated and analysed for temporal and incidence angle dependencies. The study area is 128 Km<sup>2</sup> catchment area covering altitudes from 1053 to 1853 m, where most of the area is above the treeline.

The difference between wet snow and bare ground was found to be 13 dB for RADARSAT Standard Beam Mode (S) S7, while the difference in S2 data the day after was 6 dB. The increase contrast confirmed the airborne observations and is explained by the difference in incidence angle. This increased contrast between wet snow and bare ground for higher incidence angle are supported by surface scattering model results.

Backscattering from dry snow is found to be 2-3 dB lower than for bare ground.

Temporal backscattering behaviour correspond to snow temperature measurements and demonstrates the capability of detecting the snow melt onset.

**KEY WORDS:** SAR, snow, angular dependency, backscattering

### INTRODUCTION

Synthetic Aperture Radar (SAR) has demonstrated the capability to detect the extent of wet snow cover. The contrast between wet snow and bare ground has been found to be in the order of 3 dB [1], [2] and [3].

#### Backscattering Theory

Backscattering from a snow covered terrain depends on 1) sensor parameters which includes frequency, polarization and viewing geometry, and 2) snowpack and ground parameters which includes snow density, liquid water content, ice particle size and shape, surface roughness parameters, stratification aso. Scattering from a snow cover is the sum of the scattering from the snow surface, the snow volume and the scattering from the underlying ground and is given by:

$$\sigma^o(\theta) = \sigma^o_{ss}(\theta) + \Psi(\theta)^2[\sigma^o_{sv}(\theta') + \sigma^o_{sg}(\theta')L^{-2}(\theta')]$$

where  $\sigma^o_{ss}(\theta)$  = snow surface backscattering coefficient,  $\Psi(\theta)$  = transmissivity of the snow pack,  $\sigma^o_{sv}(\theta')$  = backscattering coefficient of the snow volume,  $\sigma^o_{sg}(\theta')$  = the backscattering coefficient of the underlying ground, and  $L(\theta')$  the one way propagation loss in the snow volume.

In wet snow, the absorption loss is high and the scattering from the snow ground interface may be neglected. Thus, the scattering from wet snow is a combination of surface and volume scattering, and the relative strength between the two components depends on the snow properties- liquid water content, density ice particle size, and shape and surface roughness [4]. For a dry snow cover the backscattering from the snow surface may be neglected and the backscattering is a combination of volume scattering from snow and surface scattering from the ground.

#### EMISAR and ERS for snow parameter estimation

The Norwegian part of the European Multi-sensor Airborne Campaign (EMAC'95) Snow and Ice experiment test area is located at Kongsfjellet and at the Okstindan glacier, Norway, 66° N, 14° E. In this area snow is an important part of the annual precipitation. The snow test field cover altitudes from about 400 m to 1100 m and the size of the area is approximately 60 km<sup>2</sup>. Vegetation

types varies from sparsely forested peat land, forested areas to exposed rock.

Three combined remote sensing and ground data acquisition campaigns were conducted at March 22-23, May 1-3 and July 5-6 where fully polarimetric C- and L-band EMISAR airborne data were acquired. The EMISAR measurements were supported with 4 ERS-1 data. The area was completely covered with snow in March. At 400 m altitude the snow was wet while at 1000 m the snow was nearly dry. The depth of the snow range from 1 meter up to more than 4 meters. In May the area was completely covered with wet snow and in July the area was partly covered with wet snow. The EMISAR polarimeter data are one look slant range complex data (SLC) focused to a resolution of  $2 \times 2 \text{ m}^2$ . The data is motion compensated, imbalance compensated, and absolute calibrated to a flat earth [1]. The calibration is stable.

Nominal operation height is 1200 m with a swath width of 12 km resulting in incidence angle varying from  $35^\circ$  to  $60^\circ$  at the near and far range, respectively. The EMISAR data have been georeferenced to a UTM zone 33 WGS 84 map projection with 5m x 5m pixel size, using a high resolution DEM [5]. Figure 1 presents the EMISAR C-vv backscattering image from July acquisition, where the area is partly covered with wet snow, giving a low backscattering. The positions of the in-situ measurement stations is also shown.

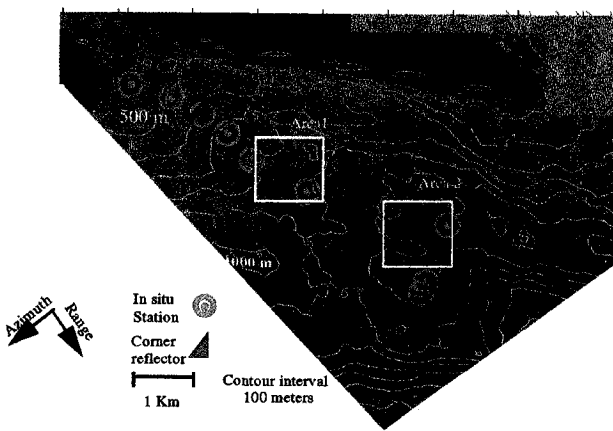


Figure 1. EmisarC-vv backscatter image from Kongsfjellet, July 1995.

Figure 2 presents the EMISAR C-VV mean backscattering coefficient with respect to local incidence angle, Probability Distribution Function (PDF) for local incidence angle and the PDF of the EMISAR backscattering coefficient for the data presented above, for Area1 and Area2, both for snow and bare ground, respectively. The angular dependencies for bare ground in Area 1 and Area 2 are similar, for the snow in Area 2 only small variations are shown. This weak angular dependency for snow at high incidence angles is an indication of volume scattering being the dominating scattering mechanism.

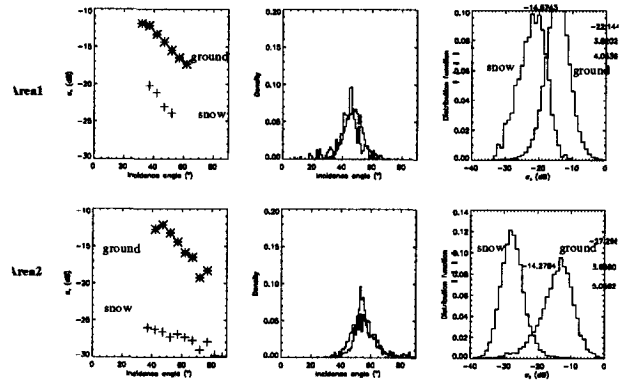


Figure 2. EMISAR C-VV statistics for Area1 and Area2. Left) mean backscattering coefficient vs local incidence angle, middle) local incidence angle PDF and right) backscattering PDF.

An increased difference between the mean backscattering value for snow and bare ground was observed when going from Area 1 (-7.8 dB) to Area 2 (-11.2).

Figure 3 presents the backscattering coefficient for snow derived from EMISAR C-VV July and ERS 11 July data, surface and volume scattering model for wet snow. The volume scattering have been modelled using Rayleigh scattering from a volume of ice particles with complex dielectric constant of 3.0, 0.1, and radius of 1mm. The surface scattering have been modelled using Kirchhoff stationary phase approximation with slope parameter  $m = 0.22$ . At high local incidence angle the EMISAR backscattering correspond to volume scattering while at low local incidence angle the data correspond more to surface scattering.

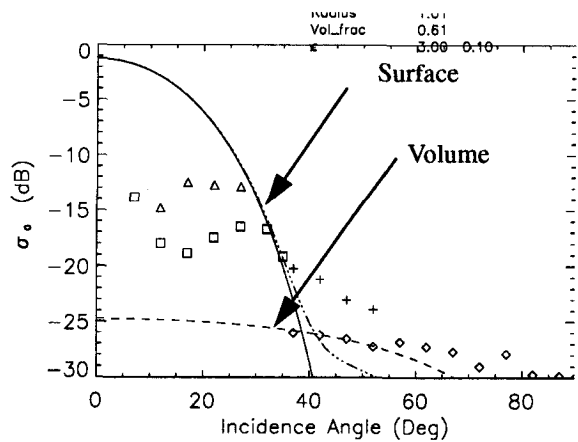


Figure 3. Scattering model overlaid snow data from ERS 11 July (square), ERS 12 July (triangle), and EMISAR 6 July C-VV (diamond and plus) from Area1 and Area2.

## RADARSAT EXPERIMENT

The Heimdalen area, Norway ( $61^{\circ}$  N,  $9^{\circ}$  E) is a  $128 \text{ Km}^2$  subcatchment to Vinstra river and cover altitudes from 1053 to 1853 m. The area has moderate topography. More than 64% of the area have slopes less  $10^{\circ}$ . Less than 8 % of the area is affected by slopes more than  $20^{\circ}$  and, 28% have slopes between  $10$ - $20^{\circ}$ . The main study area is above the treeline, which is approximately at 1200 meter elevations, consists of mostly sparsely vegetated areas (bare rocks and grass heaths) [4]. Three in-situ measurements campaign were carried out close in time to the RADARSAT overflights where measurements of snow temperature, snow density, snow grain size, and snow liquid water content were measured at more than 50 locations within the catchment. Mean snow depth, air temperature, and surface roughness were also measured. Air temperature data from meteorological stations within the study area at 1060 meters have been available. At several locations temperature loggers were deployed for measurement of snow temperature during the snow melt period.

The field was covered with dry snow in March 15, with a depth of the snow cover in the range 1-4 meters. Snow melt starts in mid May and the snow starts to become wet in the lower parts of the area. During the field campaign in mid May the area was cover with partly wet snow. In June the field was partly snow covered with wet snow. Fig. 4 presents the geocoded and recalibrated Radarsat backscattering image from 11 June. We clearly see the difference between wet snow (dark) and bare ground. The positions of some of the field sites are also shown.

## ANALYSIS

The RADARSAT data have been georeferenced to a UTM zone 32 WGS 84 map projection with  $10\text{m} \times 10\text{m}$  pixel size, using a high resolution DEM and inhouse developed geocoding software [6]. The geometric accuracy of the geocoded RADARSAT data have been checked by correlation analysis between SAR image and aerial photo. The rms difference in range and azimuth position was found to be approximately 10 m and the 16 m, respectively. To reduce the speckle level a  $5 \times 5$  median filter was applied to the geocoded and recalibrated RADARSAT backscattering coefficient image in dB.

The backscattering statistics was calculated for several small areas within the study site. The result from Area 1 (UL 492590, 6804735 UTM sone32) with an area of approximately  $30 \times 30$ . Fig. 5 presents the snow temperature and backscattering as a function of time. The snow temperature measurements are from station 5, 8 and 14 see Fig. 4. The backscattering coefficient is derived from Area 1 using all available S6 and S7 ascending pass data. From the snow temperature measurements at station 5 at 1200 meter altitude, we observe that the snow tempera-

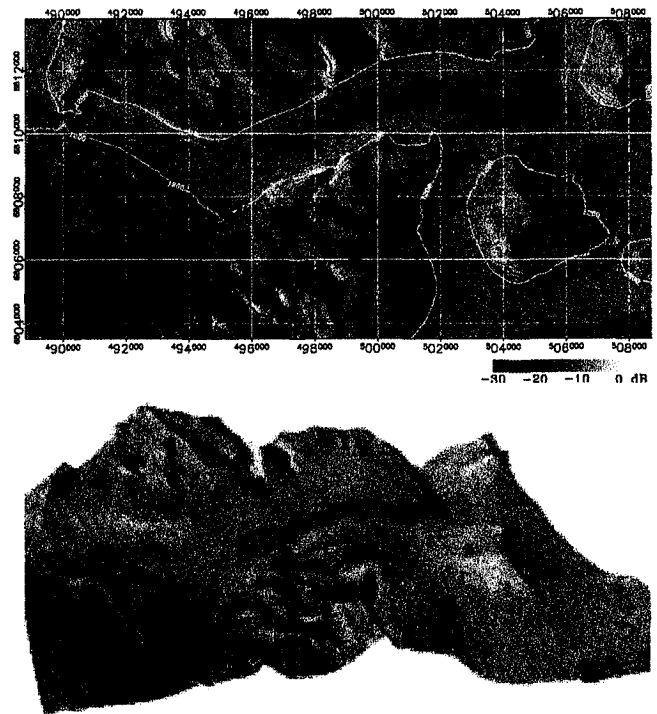


Figure 4. Geocoded Radarsat SLC backscattering image for Heimdalen 11 June, 1997 in UTM zone 32 map projection.

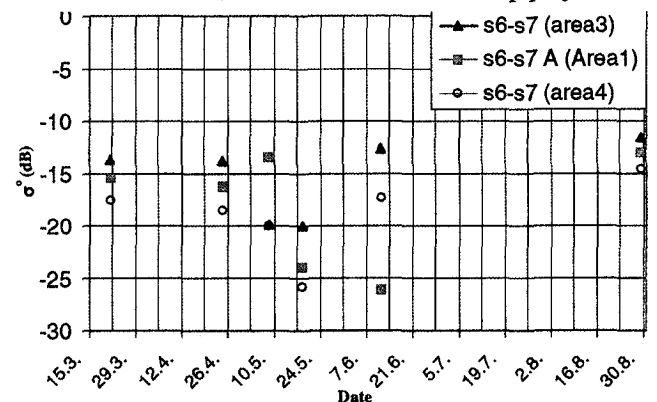


Figure 5. Backscattering as function of time for different elevations.

ture reach  $0^{\circ}\text{C}$  in mid May, while at station 14 at 1700 meter altitude the snow temperature reach  $0^{\circ}\text{C}$  approximately 14 day later. From the data, we observe that some snow melt takes place in end of April and beginning of May. From the temperature data and the field measurements we find that the snow is wet in mid May and June. Thus, at these times surface scattering is the main scattering component from the snow. For bare ground surface scattering is assumed to be the main scattering source. We observe a decrease in backscattering corresponding to the melt onset as observed by the snow temperature loggers. At 1100 meters a significant decrease is taking place between 24 April and 8 May, at 1300 the decrease in backscattering coefficient takes place between 8 May and 18 May.

In 11 June Radarsat Standard Beam Mode (S) S7 data the difference between wet snow and bare ground was

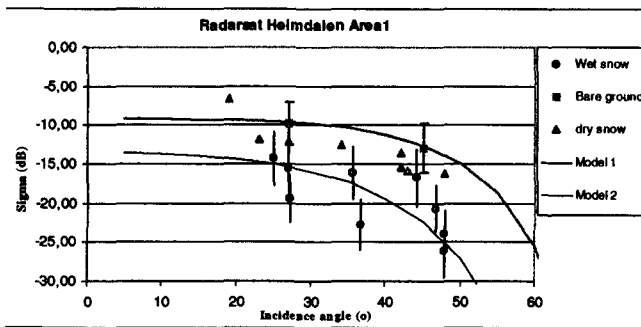


Figure 6. Backscattering vs local incidence angle.

found to be 13 dB, while the difference in S2 data one day later was 6 dB. Figure 6 presents the backscattering coefficient as function of local incidence angle derived from Area 1 using 18 Radarsat data. Surface scattering model data using Kirchhoff stationary phase approximation with slope parameter  $m = 0.48$  and  $0.38$ , respectively are also shown. The bare ground data are from 23 August (S2) and 29 August (S7), respectively, while the dry snow data are obtained using Radarsat data from March and April. We also observe that a reduction in surface roughness increase the incidence angle dependency. The effect on the backscattering coefficient for a wet snow covering the ground is a effective smoothing of the surface roughness in addition to having a lower reflection coefficient. We observe that the backscattering of wet snow show a stronger incidence angle dependency than bare ground. The difference in backscattering between bare ground and wet snow is 5 dB and 12 dB at  $25^\circ$  and  $45^\circ$ , respectively. Thus the difference between bare ground and wet snow is increased with 7 dB when observed with S7 instead of S2. The S2 beam mode correspond to the ERS SAR nominal incidence angle ( $23^\circ$  at mid swath).

We observe a difference between dry snow and bare ground of approximately 2 dB. An increase difference is observed for higher incidence angle. Theoretically the power reflection coefficient between dry snow and bare ground is smaller than the reflection coefficient of an air ground interface. In March and April when the snow is dry, the snow depth in the areas is 1-3 meters (site 5-8 in March). The ground is frozen and thus the lower ground reflection may cause this change.

An increased difference between the mean backscattering value for snow and bare ground was observed when going from june 12 data to june 11 data.

Since the contrast depend on the ground and snow properties, wet snow will show higher contrast to ground with high (rough surface) backscattering.

### CONCLUSIONS

Both from analysis of airborne SAR and Radarsat SLC data the difference in backscattering coefficient between snow and bare ground was found to be higher at large

incidence angle S7 ( $45^\circ$ ) than at lower incidence angle S2 ( $24^\circ$ ). The incidence angle dependency of the backscattering from bare ground and wet snow corresponded to surface scattering model. Thus, SAR images acquired with large incidence angle gives better separability between wet snow and bare ground. Thus previous proposed classification algorithms [1]

A difference of approximately 2-3 dB between bare ground, and dry snow is also observed in the RADARSAT data. A frozen ground and thus a lower ground reflection may explain this change.

The extent of wet snow cover is clearly observed in the SAR data. The temporal change in the extent of wet snow is also seen. The melt zone and its temporal development can also be seen in RADARSAT data.

These result documents the capabilities for using Radarsat and ENVISAT ASAR data in operational snow cover mapping for hydropower production planning and flood prediction.

### ACKNOWLEDGMENT

This work was carried out within SNOWTOOLS, an Environment and Climate project funded by Commission of the European Community Contract no ENV4-CT96-0304, Norwegian research Council, ENFO, Statkraft and Norwegian Water and Energy administration. Many thanks to all members of the field team at Heimdalen and Kongsfjellet. The RADARSAT data have been acquired as part of the ADRO project no 172. RADARSAT data are © Canadian Space Agency 1997.

### REFERENCES

- [1] Koskinen, J., Pulliainen, J. and Hallikainen, M., 1997, "The Use of ERS-1 SAR Data in Snow Melt Monitoring," *IEEE Trans. Geosci. Remote Sensing*, vol. 35, No 3, pp 601-610.
- [2] Guneriusen, T., 1997, "Backscattering properties of a wet snow cover derived from DEM corrected ERS-1 SAR data," *Int. J. Remote Sensing*, vol 18, No 2, 1997, pp. 375-392.
- [3] Nagler, T., Rott, H., and Glendinning, G., Snowmelt modelling using Radarsat data, 1998, Proc.of ADRO final symposium, Montreal
- [4] Karlsen, S. R., Johansen, B. and Guneriusen T., 1997, "Vegetation dependant backscattering properties observed with ERS and EMISAR," *Norut It report*, IT450/5-97.
- [5] Johnsen, H.,Lauknes, I., and Guneriusen T., 1998, Geometric and Radiometric Calibration of Synthetic Aperture Radar Imagery Acquired in Alpine Regions- Spaceborne and Airborne, *Norut It report IT431/32-98*.
- [6] Shi, J., and Dozier, J., 1995, "Inferring Snow Wetness Using C-band Data from SIR-C's Polarimetric Synthetic Aperture Radar," *IEEE Trans. Geosci. Remote Sensing*, vol. 33, No 4, pp 905-914.

# Monitoring Terrain Deformations Using Multi-Temporal SAR Images

A. Ferretti, C. Prati, F. Rocca

Dipartimento di Elettronica e Informazione - Politecnico di Milano

Piazza L. da Vinci, 32 - 20133 Milano - Italy

fax: +39-2-23993585, e-mail: aferre@elet.polimi.it

## Abstract

Stable natural reflectors (Permanent Scatterers) can be identified from long temporal series of interferometric SAR images even with baselines larger than the decorrelation one. We discuss the use of PS in urban areas, like Pomona (California) showing subsidence and absence effects. An estimation of the Atmospheric Phase Screen (APS) superimposed on each image and the displacement field in the area of interest is carried out. New solutions are presented in order to cope with non-linear motion of the targets.

## 1 Introduction

One of the main difficulties encountered in DInSAR applications is due to temporal and geometric decorrelation. The main goal of our research was the identification of single pixels (to be called Permanent Scatterers - PS) coherent over long time intervals and for wide look-angle variations [1]. This allows one to use all ERS acquisitions relative to an area of interest. In fact when the dimension of the PS is smaller than the resolution cell, the coherence is good (the speckle is the same) even for image pairs taken with baselines larger than the decorrelation one. Then, on those pixels, sub-meter DEM accuracy and millimetric terrain motion detection can be achieved, even if the coherence is low in the surrounding areas. Reliable elevation and deformation measurements can then be obtained on this subset of image pixels that can be used as a "natural" GPS network.

## 2 Method

The mathematical framework for this kind of estimation is rather simple. Let us suppose that  $N + 1$  ERS SAR images of the area of interest are available. Data are first coregistered on a unique master and a DEM of the area is estimated starting from low temporal baseline pairs [3]. Then,  $N$  differential interferograms between all SAR images and the

master are computed. After DEM compensation, the residual phase of interferogram  $i$  is [1]:

$$\varphi_i = \frac{4\pi}{\lambda} r_{Ti} + \alpha_i + n_i + \varepsilon_{topo-i} \quad (1)$$

where  $\lambda$  is the system wavelength,  $\alpha_i$  the atmospheric phase contribution,  $n_i$  the decorrelation noise,  $\varepsilon_{topo-i}$  the phase contribution due to possible errors in the DEM (proportional to the normal baseline of each image  $B_{n-i}$ ) and  $r_{Ti}$  is the possible target motion in the direction of the satellite line-of-sight (LOS).

The first term in Eq. (1) can then be written as follows:

$$\frac{4\pi}{\lambda} r_{Ti} = \frac{4\pi}{\lambda} \cdot v_r \cdot T_i + \mu_{NLi} = C_{vi} \cdot v + \mu_{NLi} \quad (2)$$

where  $v$  is the unknown component of the mean target velocity in the direction of LOS,  $\mu_{NL}$  is the phase term due to a possible non-linear target motion and  $T_i$  is the temporal baseline between the master acquisition and the generic  $i$ -th slave image.

Since we have  $N$  differential interferograms of the same area with different temporal and geometric baselines, we finally write, for each pixel, a linear system of  $N$  equations and 2 unknowns ( $\varepsilon_z, v_r$ ):

$$\varphi_i = C_{zi} \cdot \varepsilon_z + C_{vi} \cdot v \quad i = 1 \dots N \quad (3)$$

where  $\varepsilon_z$  is the DEM error and  $C_{zi}$  is proportional to  $B_{n-i}$ .

The problem would be linear if we knew the unwrapped phase values. Anyway, using a simple periodogram (albeit with an irregular sampling of the two dimensions: baselines and time) we can estimate both the residual elevation and the mean LOS velocity, provided that the signal-to-noise ratio is high enough.

Actually phase residues ( $w_i$ ) are the sum of three contributions: atmospheric components (Atmospheric Phase Screen - APS) of the master and the slave acquisitions, noise, and non linear motion:

$$w_i = \varphi_i - C_{zi} \cdot \varepsilon_z - C_{vi} \cdot v_r = \mu_{NLi} + \alpha_i + n_i \quad (4)$$

Since  $\mu_{NL}$ ,  $\alpha$  and  $n$  are independent random variates, the residual phase variance  $\sigma_w^2$  is the sum of three contributions too. As a matter of fact, a proper estimation of target motion and elevation is possible only if  $\sigma_w^2$  is low. To this end, the analysis is carried out in two steps. First a subset of image pixels is selected using the coherence maps of the area of interest: only locations of highly coherent targets are retained (low  $\sigma_n^2$ ). If now we consider a couple of targets not too far apart (distance less than, say, 1 km), it is usually possible to estimate  $\Delta v$  (relative mean velocity) and  $\Delta \varepsilon_z$  (relative elevation error) with a high degree of accuracy. In fact, low distance implies low variance of the atmospheric component: for points less than 1 km apart, values of  $\sigma_\alpha^2$  less than  $0.1 \text{ rad}^2$  are common [4]. Moreover, the motion of neighboring pixels is usually correlated. If this hypothesis is verified,  $\sigma_\mu^2$  should be low as well. Estimation of  $(v, \varepsilon_z)$  is then obtained integrating the values of  $(\Delta v, \Delta \varepsilon_z)$  previously estimated from couples of neighbor pixels [2].

Once the differential phase values  $\varphi_i$  have been compensated for  $\varepsilon_z$  and  $v$  (i.e. data have been detrended for the estimated DEM errors and the mean velocity field), we can start looking at their temporal evolution, to check for subsidence leakage. The low pass component of the phase residues should be considered as an estimation of the non-linear motion contribution  $\mu_{NL}$ , since atmospheric components are highly correlated in space but uncorrelated in time. APS estimation is then carried out smoothing spatially the high-pass filtered time series of the phase residues  $w_i$ . As described in [1] and [2], after estimation and removal of all the APS superimposed on the data, we can finally estimate the motion of each pixel in the image and identify more PS's.

### 3 Results

An interesting case of subsidence, already studied using differential interferometry and other techniques, is found in Pomona [5]. 41 ERS images were available (Track: 170. Frame: 2925). All were resampled on the same master acquisition (ERS2 - April 6th, 1996) and 40 interferograms were obtained. In Fig. 1 the incoherent average of all the data (close up of Los Serranos area) is reported: due to the high number of looks, the radiometric quality of this image is comparable to that of an optical one. Using 4 Tandem pairs, we also determined a reference DEM (about 10 m accuracy, also limited by building effects) of the area of interest using the wavelet approach [3], and the correspondent phase was removed from each single image.

After the initial selection of the PS set (about 3 PS/km<sup>2</sup> were identified), phase increments between

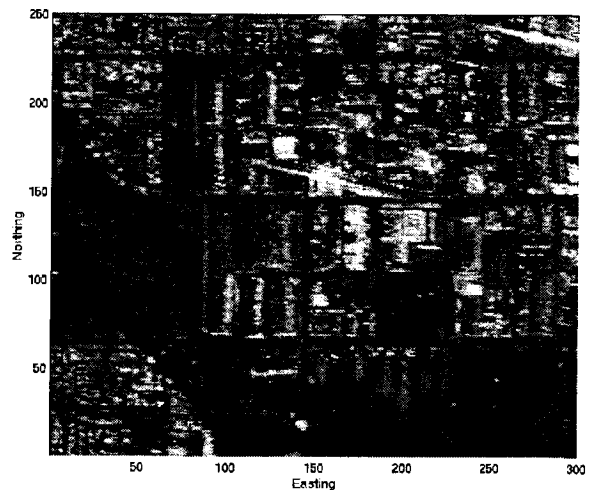


Figure 1: Geocoded multi-image reflectivity map of the test site (close up of Los Serranos area). The high radiometric quality is due to the incoherent data average.

each PS and all the others less than 1 km apart were estimated using the periodogram technique. To better illustrate this kind of approach, in Fig. 2 we show the temporal distribution of the takes together with their normal baselines, referred to the master image. The range of normal baselines is about  $\pm 1100$  m, while the maximum temporal baseline is more than 6 years. If a PS had a LOS velocity of, say, 2 cm/yr and a residual elevation difference of 5 m with respect to a neighboring scatterer, considered as a reference, its phase variations as a function of time and baseline would be a 2D sinusoid, also represented in the Fig. 2. If now we accept, temporarily, the hypothesis of constant LOS velocity of each pixel, then using a periodogram we can estimate both the residual elevation and the LOS velocity difference of the pixels. As already mentioned, this operation was carried out for all PS pairs less than 1 km apart, thus removing the effects of the residual elevation with respect to the average DEM and of the LOS velocity and estimating the unwrapped phase values [2].

After estimation of both elevation and mean velocity of the targets, time series analysis of the phase residues in correspondence of each PS was carried out. The target is to identify possible non-linear motion contributions. As discussed previously, for each PS we carried out a temporal smoothing using a triangular filter (300 days long) and we removed the low pass component. Phase residuals were then spatially filtered using a moving average on a  $2 \times 2$  km window. APS's were then interpolated on the original regular grid and removed from each datum. It should be noted that each APS is actually the difference of

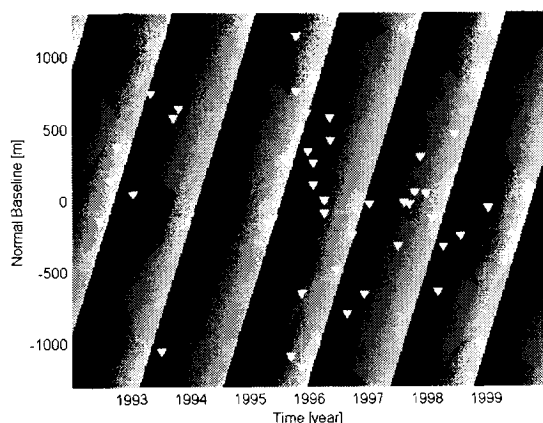


Figure 2: Space-Time distribution of the available data. The bidimensional sinusoid represent the phase contribution for a LOS velocity of  $2 \text{ cm/yr}$  and a DEM error of  $5 \text{ m}$  (see text).

the atmospheric component of the slave image and the APS of the master acquisition. Averaging the 40 APS's it was possible to get an estimation of the master contribution and then of each single contribution. An example of estimated APS is reported in Fig. 3.

After APS removal it is possible to estimate not only the mean velocity field of the area but a displacement field as a function of time, possibly interpolating the displacement maps on a regular temporal grid. Here we report a sequence of 4 spatial maps corresponding to 4 equally spaced time instants (Fig. 4, 5, 6 and 7). The non-linear motion behavior reflects into the change of shape of the contour lines. A perspective view of the displacement field of Fig. 4 is also reported in Fig. 8. Maximum positive and negative displacements are  $+6$  and  $-20 \text{ cm}$ , respectively. Of course, computer animation procedures can provide an improved visualization of the phenomenon under study. Two animations relative to the estimated displacement field in Pomona since June 1992 will be soon available on our web site (<http://www-dsp.elet.polimi.it>).

## 4 Conclusions

We have shown that in urban areas Permanent Scatterers exist that allow to generate interferograms on a sparse grid, even if the time lapse between the takes is many years long. The spatial dimensions of the scatterers can be selected to be small with respect to range resolution so that baselines longer than the critical one can be used. The density of those PS's, small enough to have sufficient phase stability with

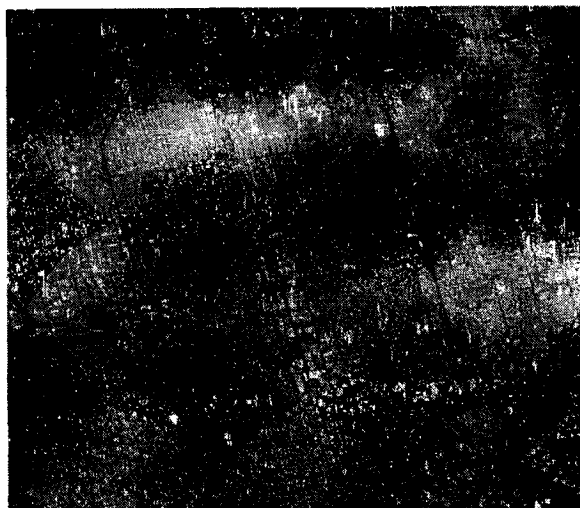


Figure 3: Example of APS estimated for April 6<sup>th</sup>, 1996. The APS has been superimposed on the multi-image reflectivity map of the area. APS standard deviation is  $0.86 \text{ rad}$ .

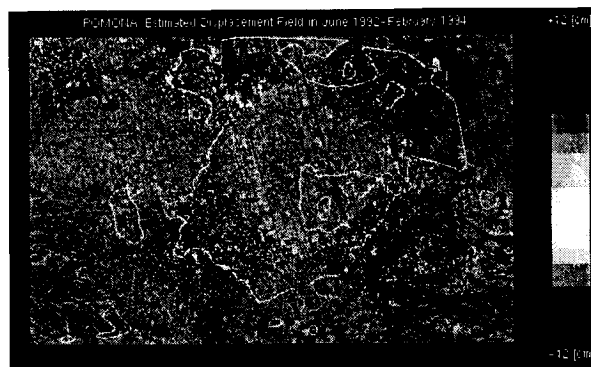


Figure 4: Pomona: estimated displacement field in  $\text{cm}$  relative to the time interval June 1992 - February 1994. Contour lines step:  $2.5 \text{ cm}$ .

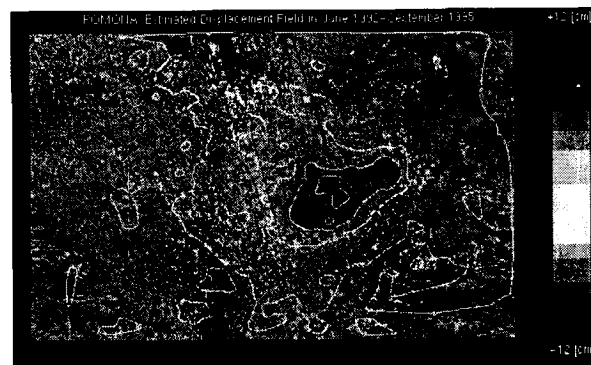


Figure 5: Pomona: estimated displacement field in  $\text{cm}$  relative to the time interval June 1992 - September 1995.

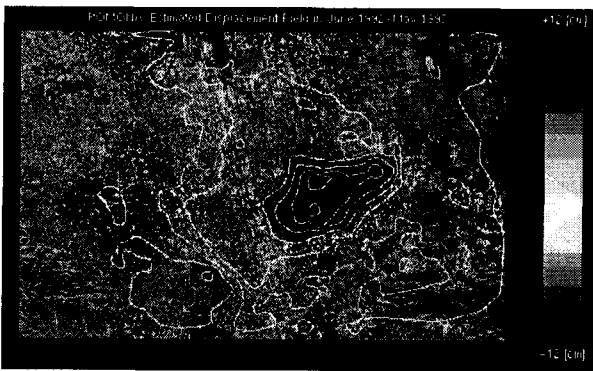


Figure 6: Pomona: estimated displacement field in *cm* relative to the time interval June 1992 - May 1997.

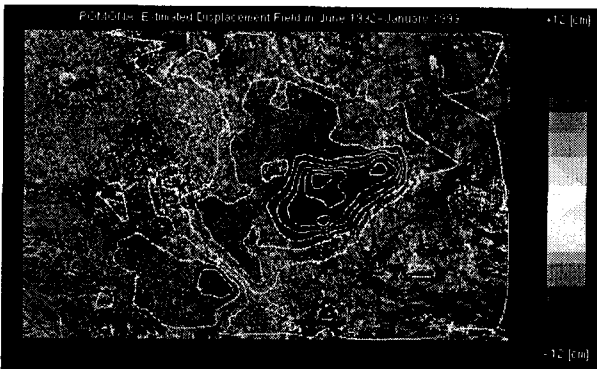


Figure 7: Pomona: estimated displacement field in *cm* relative to the time interval June 1992 - January 1999. Color scale has been saturated for visualization purposes (+/- 12 *cm*).

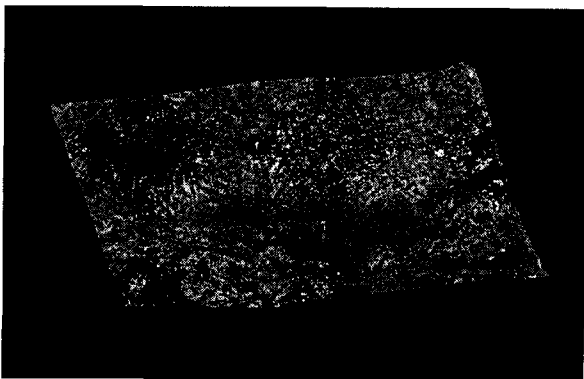


Figure 8: Perspective view of the displacement field relative to June 1992 - January 1999. Minimum negative value: -20 *cm*. Maximum positive displacement: +6 *cm*.

respect to the baseline, was seen to be sufficient (at least in urban areas) to be able to estimate the atmospheric disturbance (the APS) with a sufficient spatial resolution. Then, the estimated APS can be removed from the interferometric phase, improving the DEM estimates and improving the estimate of the pixel motion.

The long time lapse observations made available by this technique allow to estimate long term pixel motion with an accuracy that was previously attainable using optical techniques only. Sure enough, the density of the PS's may prove to be too low in vegetated areas, so that artificial PS's, namely corner reflectors, will have to be added in some locations. However, first tests indicate that rather small CR's, say with 1500 m<sup>2</sup> cross section, should suffice.

Several questions remain to be studied like: i) the distribution of PS's in different types of terrain, ii) the possibility of reducing the threshold coherence level to extend their number, iii) the physical nature of the PS's in towns and on rocky terrain, etc. iv) the quality of the APS estimates and their statistics.

## 5 Acknowledgments

We'd like to thank Dr. G. Rigamonti and Dr. R. Locatelli for their support in data processing and Dr N. Bienati for helpful discussions.

## References

- [1] A. Ferretti, C. Prati and F. Rocca, "Permanent Scatterers in SAR Interferometry", submitted for publication to *IEEE Trans. Geosci. Remote Sensing*, June 1999.
- [2] A. Ferretti, C. Prati and F. Rocca, "Non-linear Subsidence Rate Estimation Using Permanent Scatterers in Differential SAR Interferometry", submitted for publication to *IEEE Trans. Geosci. Remote Sensing*, September 1999.
- [3] A. Ferretti, C. Prati and F. Rocca, "Multibaseline InSAR DEM Reconstruction: the Wavelet Approach", *IEEE Trans. Geosci. Remote Sensing*, vol. 37, no. 2, pp. 705-715, Mar. 1999.
- [4] S. Williams, Y. Bock and P. Pang, "Integrated satellite interferometry: Tropospheric noise, GPS estimates and implications for interferometric synthetic aperture radar products," *J. Geophys. Res.*, 103, B11, pp. 27.051-27.067, 1998.
- [5] G. Peltzer, "Monitoring of Ground Subsidence," <http://www.esrin.esa.it/esrin/eos/mon2.html>



## JERS SAR processing for the boreal forest mapping project SIBERIA

Andreas Wiesmann, Urs Wegmüller, and Tazio Strozzi  
Gamma Remote Sensing

Thunstrasse 130, CH-3074 Muri b. Bern, Switzerland

Tel: +41 31 951 70 05, Fax: +41 31 951 70 08, email: wiesmann@gamma-rs.ch, <http://www.gamma-rs.ch>

### ABSTRACT

In the frame of the EC Environment and Climate Program project, SIBERIA, an extensive forest map for a part of Siberia will be produced using state-of-the-art satellite data and remote sensing techniques. Among other sensors the JERS SAR will be used. In this contribution important steps in the JERS processing will be discussed, including radiometric calibration, geocoding, and final products.

### INTRODUCTION

The main objective of the EC Environment and Climate Programme project "SAR Imaging for Boreal Ecology and RADAR Interferometry Applications" (SIBERIA) is the production of an extensive forest map for a part of Siberia using state-of-the-art satellite data and remote sensing techniques. The proposed forest map will serve as a unique planning and monitoring tool for the sustainable management of the natural resources of Siberia, for its socio-economic development and for a better understanding of the role of boreal forest in climate

change.

One of the sensors used for the production of the forest map is the L-band SAR on the JERS-1 satellite. JERS data over Siberia are available either from the onboard data recorder or by direct link-down at the mobile German receiving station, which was set up in Ulan Bator in 1997 and 1998. The JERS SAR data are of particular interest because of the sensitivity of the L-band backscatter to forest biomass. This permits a relatively good separation of forested and unforestated areas. Also of high interest are interferometric terrain height estimates and the degree of coherence.

In the following the processing chain set up at Gamma Remote Sensing for the required pre-operational JERS SAR and INSAR processing, radiometric calibration, and geocoding will be presented. Special attention is given to the radiometric calibration and to the geocoding. The radiometric calibration is important for the quantitative interpretation of the backscattering coefficients. Geocoding is required not only for the geographic reference of the results but also to facilitate the combination with ERS SAR based products and available

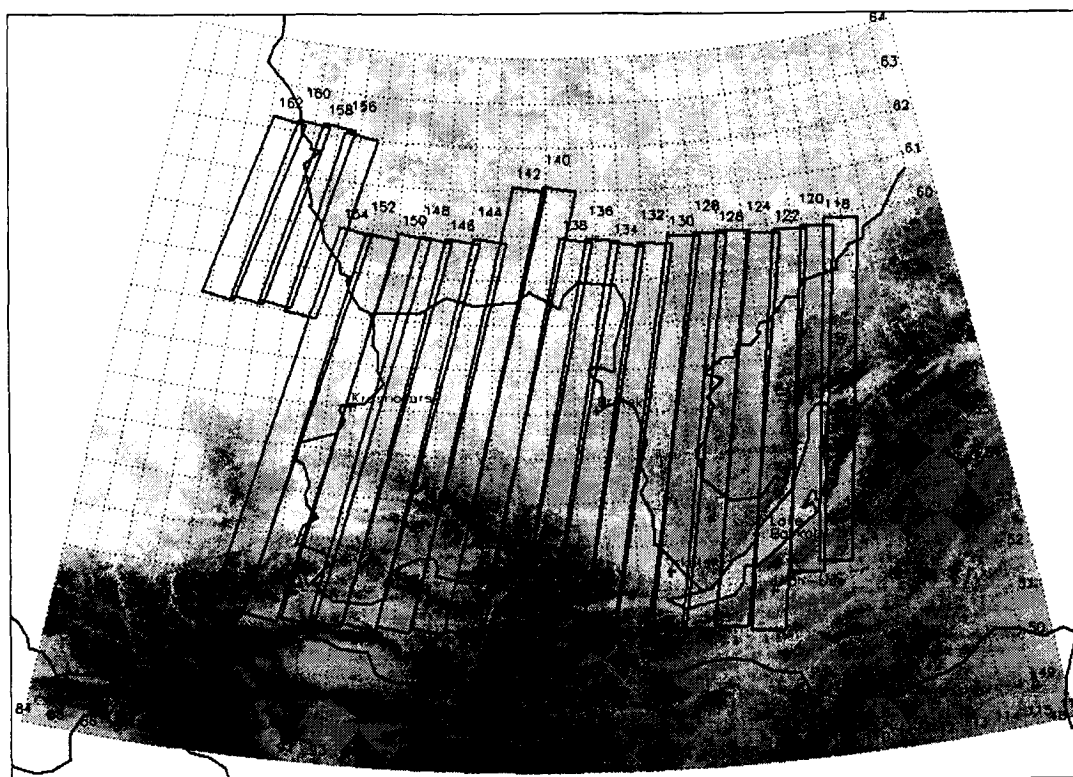


Fig 1: Map of the Siberia test area. The dark boxes indicate JERS tracks with even RSP (track) number.

in-situ data. In the second part we show some products that demonstrate the high potential of the JERS SAR data for boreal forest mapping.

### RADIOMETRIC CALIBRATION

The calibration factor required for the absolute radiometric calibration of JERS SAR processing was determined based on active calibrator data made available by M. Shimada (NASDA), and validated by cross-comparison with NASDA processed data over a tropical forest site (Figure 2). Good agreement was found.

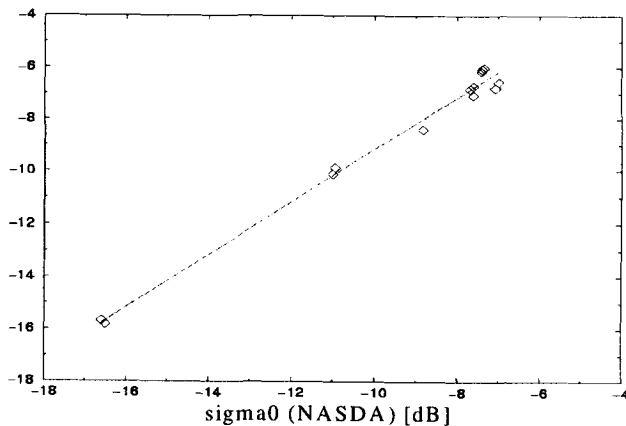


Figure 2: Averaged calibrated backscattering coefficients  $\sigma^0$  of image segments across JERS image processed by Gamma MSP versus corresponding value extracted from data processed by NASDA. The linear regression shown is  $y = 0.775 + 1.0007x$ .

### JERS PROCESSING

Figure 3 shows the JERS data processing chain. Data are processed track by track as indicated in Figure 1. Interferometric pairs are processed together.

#### Raw Data:

For the Siberia project the JERS data requirements are a) global coverage of the test area (see Figure 1 for a map), b) INSAR coverage of selected sites, and c) multi temporal coverage of selected test sites.

From the signal-interpretation point of view important criteria were:

- No melt-freeze or snowfall events in the data.
- Complete coverage of the test-area within one season.
- Small temporal baseline between in-situ observation and SAR data acquisition.

Additionally for interferometry:

- A spatial baseline of less than about 2 km.
- Succeeding orbits (44 days).

JERS data are available either from the NASDA JERS archive (up to summer 1997) or from the special mission

of the DLR receiving station in Ulan Bator (autumn 1997 to summer 1998). The Ulan Bator data were received and synchronized by DLR and processed to level 0 format by NASDA. In the Siberia project the Ulan Bator data are preferred for its almost complete coverage in spring and summer 1998. But also archive data have been processed to investigate temporal changes and because at the beginning of the project no Ulan Bator data were available.

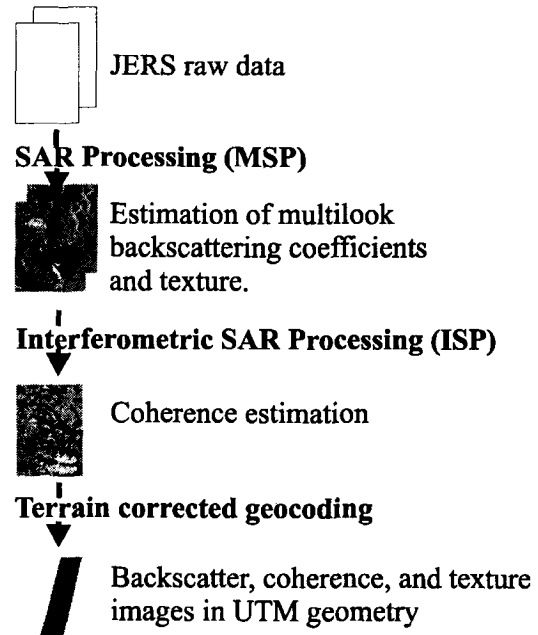


Figure 3: JERS data processing chain.

SAR processing, radiometric calibration, and fine registration:

The SAR processing with Gamma's Modular SAR Processor (MSP) [1] includes radio frequency interference (RFI) filtering. The radiometric calibration accounts for JERS sensitivity gain control (STC), and automatic gain control (AGC). In addition it corrects for JERS range antenna pattern. Gain saturation correction was not applied. A MSP calibration constant of 22.1 dB was used as derived in the calibration experiment.

Multitemporal SLC are registered to a common slant range geometry. For the backscattering images 4 looks in slant range and 12 looks in azimuth are taken. To investigate the information content of the texture for forest applications, a texture image is generated.

Interferometric SAR Processing:

The INSAR Processing is done with Gamma's Interferometric SAR Processor (ISP). Common band filtering is applied. As expected from the large temporal baseline of 44 days, the coherence is generally low. In

spite of the low coherence, we succeeded to generate INSAR DEM's for a few test areas.

#### Terrain corrected geocoding:

Geocoding is used for the registration of the JERS with the ERS images and the available in-situ data. During the map production phase geocoding will be an important step of the mosaicing process.

For the geocoding the GAMMA Differential Interferometry and Geocoding Software (DIFF&GEO) was used. The global DEM "gtopo30" was used as geometric reference. Quadratic spline interpolation algorithms were used for the data interpolation necessary in the single resampling step. The effective number of looks, determined with the method of moments, is about 25. An error of 200m in height in the "gtopo30" DEM results in an error of 220m (far range) to 270m (near range) in localization.

#### PRODUCTS

The final JERS data products are in UTM coordinates with pixel spacing of 50m in easting and northing. To keep the image files at a reasonable size, the data strips were cut into tiles of 100km x 100km. The products include backscatter coefficients, coherence maps, texture images and the interpolated "gtopo30" DEM (see Table 1). Figures 4 to 7 show the JERS data products for a subsection near Krasnoyarsk (RSP 148, June 18 and August 1, 1998). The backscatter images of June 18 (Figure 4) and August 1 (Figure 5) show detailed information about the ground state. The low backscattering indicates the agricultural areas at the bottom and on the right side of the image. Some fields change the backscattering due to farming activity. On the left side and in the center of the image the area is forested. Different forest types can be distinguished from the different backscatter levels. The classification of different forest types is one of the key issues of the Siberia project. Looking at the coherence image, presented in Figure 6, we find some relief dependence. The coherence is often low in the valleys. Forested area often exhibit higher coherence than open fields. Agricultural areas show a higher dynamic range due to the different crop types and growth stages. The texture image given in Figure 7 indicates the boundaries of large spatial backscatter changes. The borders of the river and the edges of the fields are indicated by high texture values.

#### CONCLUSIONS AND OUTLOOK

The JERS data processing chain in the Siberia project was presented. Geocoded and calibrated backscatter, texture, and coherence images in UTM geometry at 50m pixel spacing are generated.

Preliminary results confirm the expected potential of the JERS data with respect to forest/non-forest classification. Next steps of the project will be a more thorough investigation of the ERS and JERS signatures with available ground-truth, the definition of a robust classification algorithm, and the operational application of the entire processing chain from the raw data to the forest map for large parts of Siberia.

Additional data sets such as ERS Tandem coherence maps, and backscatter ratio images will be available for the landuse classification.

Table 1: Description of the final JERS data products

<p><i>Backscatter images:</i> Backscattering coefficient <math>\sigma^0</math> in short integer format. <math>\sigma^0 = 1.e-06*SQR(\text{value})</math></p>
<p><i>Coherence images:</i> Adaptive estimates of degree of coherence in unsigned character format. coherence = value/255.0</p>
<p><i>Texture images:</i> The texture is obtained from 5 x 15 sections using <math>\text{llog} \langle I \rangle - \langle \log I \rangle</math>, where <math>I</math> is the backscattering coefficient. Images are stored in unsigned character format. texture = 1.e-02*SQR(value)</p>
<p><i>DEM:</i> The interpolated global DEM is in short integer format. height [m] = value</p>

#### ACKNOWLEDGMENTS

The Swiss Federal Office for Education and Science supported this work in the frame of the EC Environment and Climate Programme Project SIBERIA.

The JERS data is copyright by NASDA.

Wolfgang Wagner DLR is acknowledged for the generation of Figure 1.

#### REFERENCES

- [1] U. Wegmüller and C.L. Werner, "Gamma SAR Processor and Interferometry Software", 3rd ERS Symposium, Florence, 18-21 March 1997.

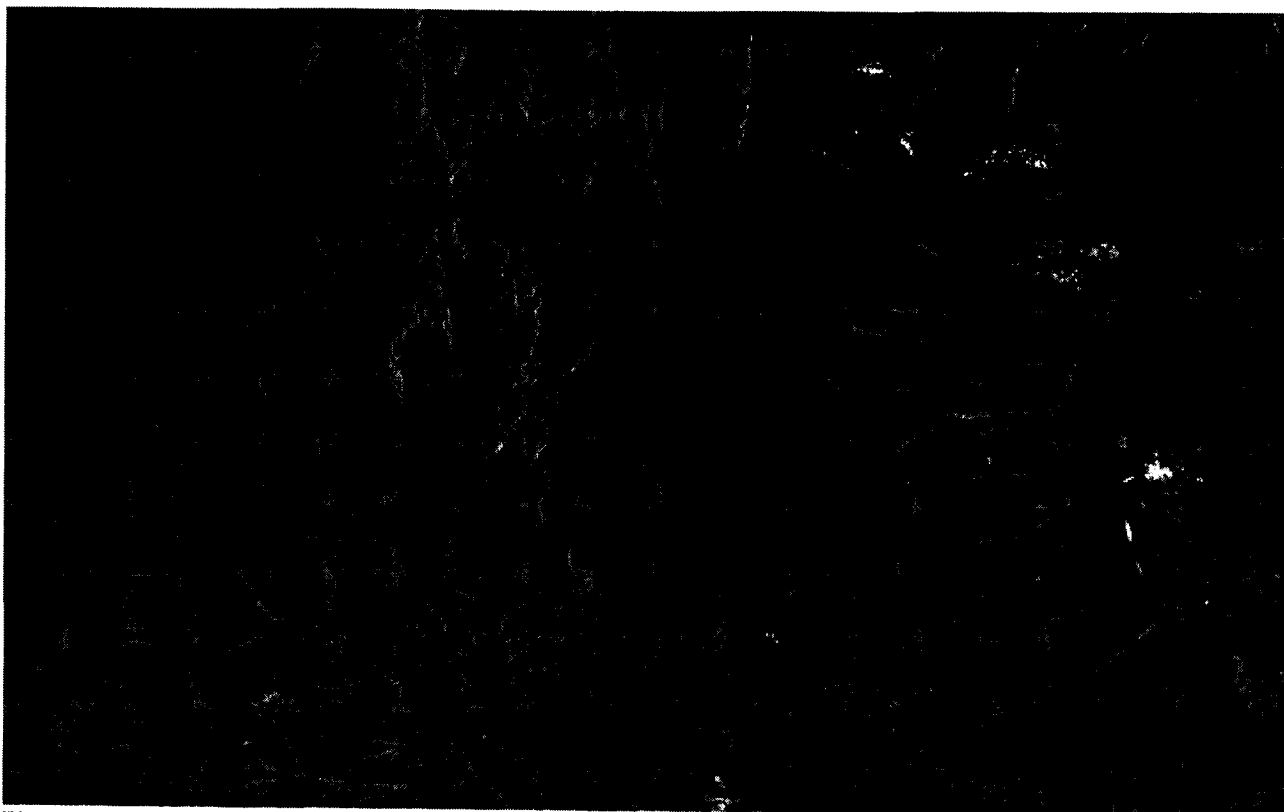


Figure 4: JERS backscatter image of 18. June 1998 near Krasnoyarsk. The image size is 65 x 40 km<sup>2</sup>.

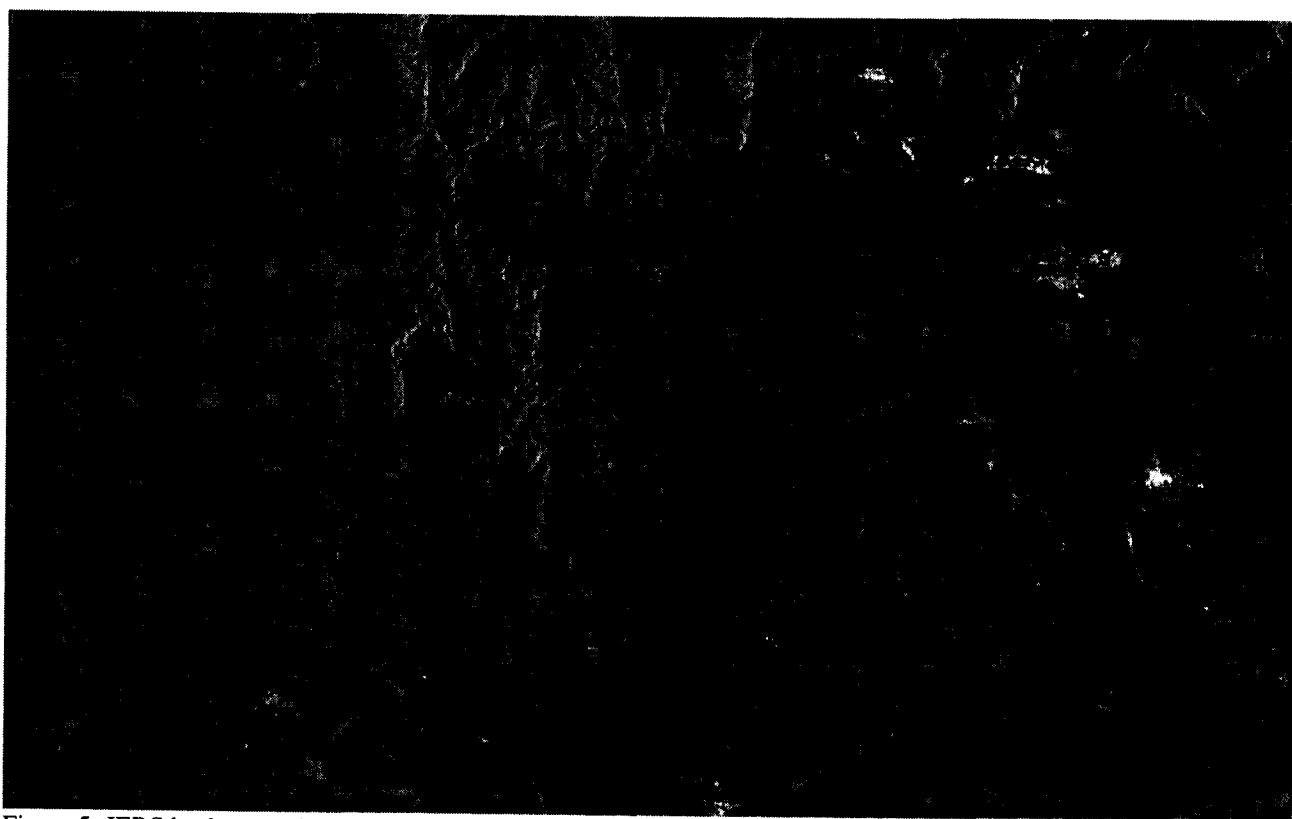


Figure 5: JERS backscatter image of 1. August 1998 near Krasnoyarsk.



Figure 6: Estimate of coherence between June 18, 1998 and August 1, 1998. The geometric baseline is 650m.

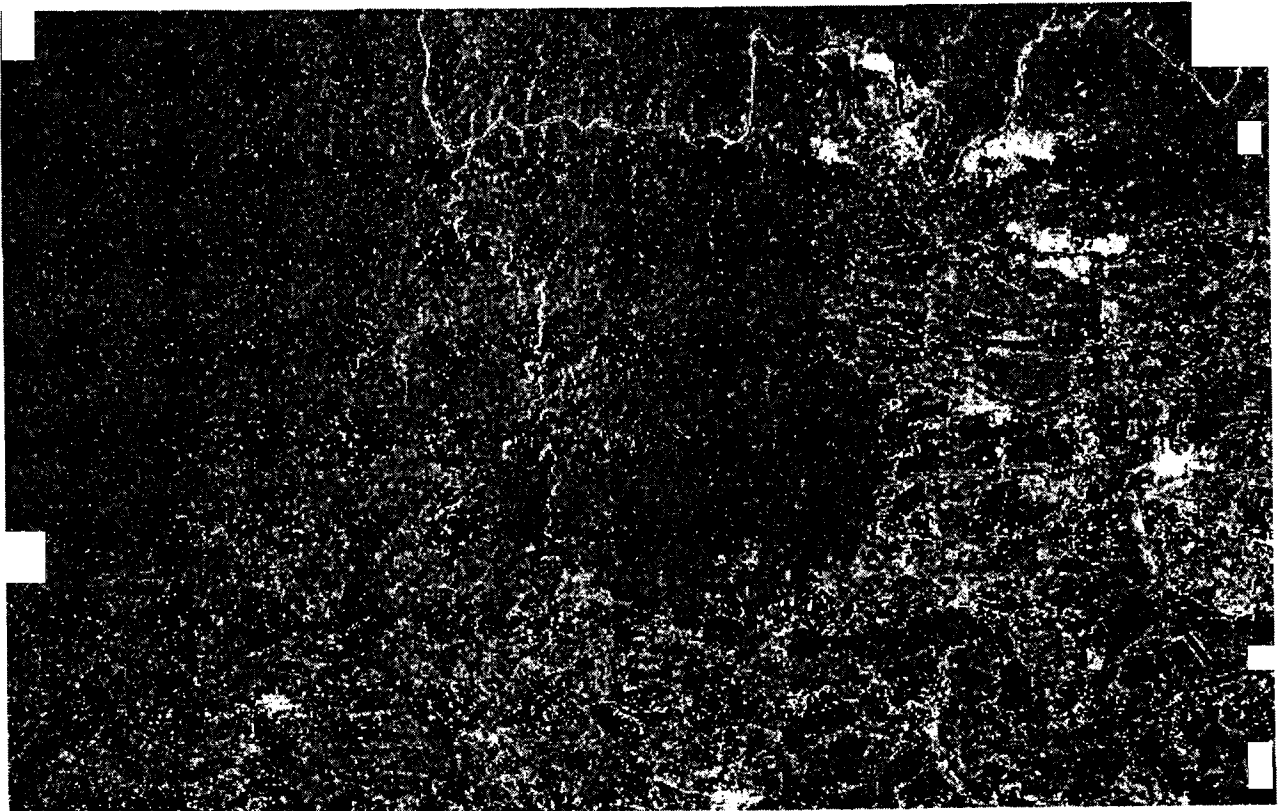
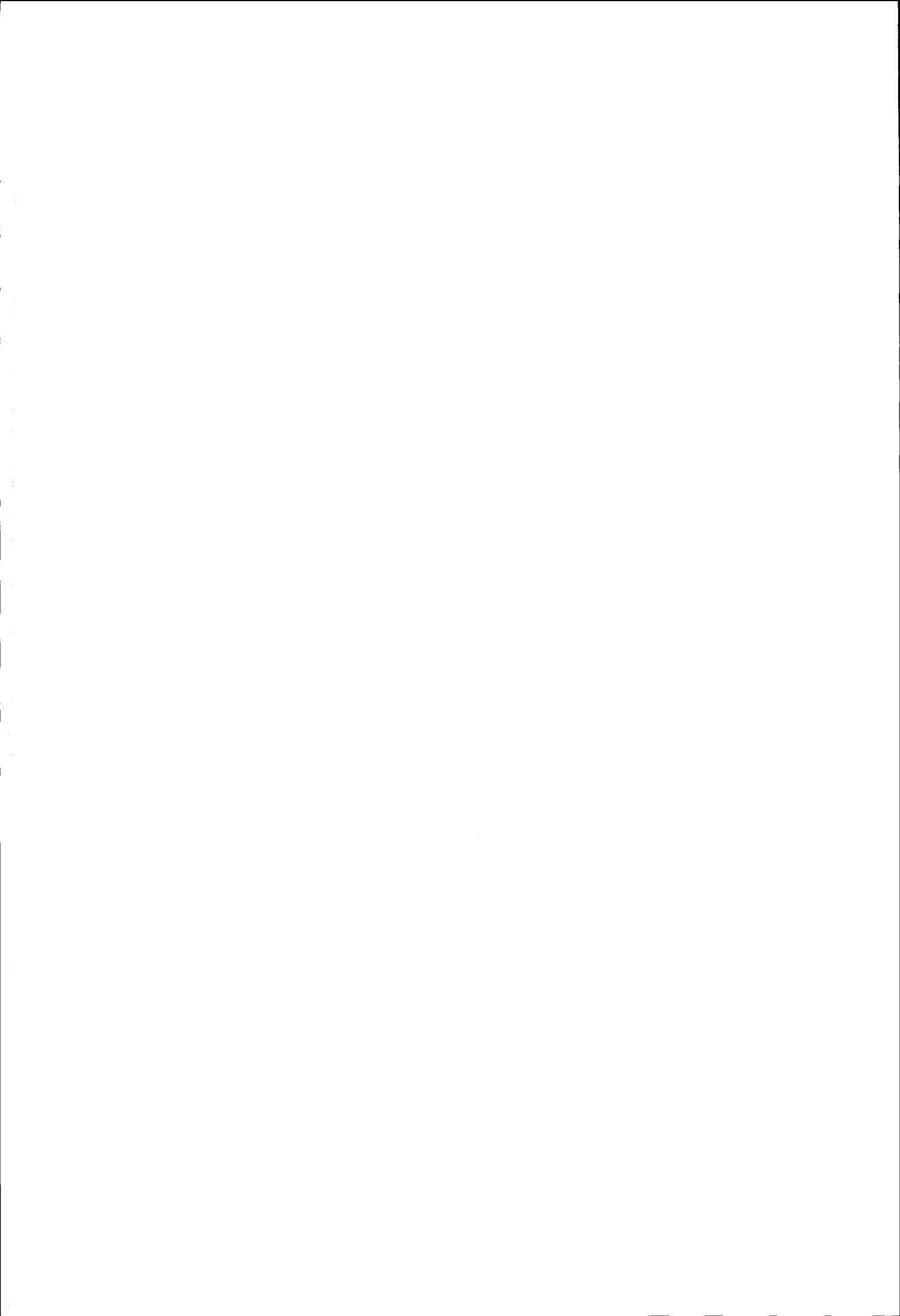


Figure 7: Texture image of 18. June 1998 near Krasnoyarsk.



## Temporal variations of interferometric coherence over a deciduous forest

<sup>1</sup>C. Proisy, <sup>2</sup>F. Sarti, <sup>1</sup>E. Mougin, <sup>1</sup>A. Lopes, <sup>3</sup>E. Dufrêne, <sup>3</sup>V. LeDantec, <sup>4</sup>C. Ruiz, <sup>4</sup>P. Borderies, <sup>4</sup>I. Chênerie

1 Centre d'Etudes Spatiales de la Biosphère, CNES/CNRS/UPS  
BPI 2801, 18, avenue E. Belin, 31401 Toulouse Cedex 4, France.  
Phone : 33.5.61.55.85.19, Fax: 33.5.61.55.85.00  
Email : proisy@cesbio.cnes.fr, <http://www-sv.cict.fr/cesbio/dynamic/>

2 Centre National d'Etudes Spatiales, CNES/DSO/OT/QTIS/SR  
B.P.I. 811, 18, avenue E. Belin, 31401 Toulouse Cedex 4, France.  
Phone : 33.5.61.28.21.33 Fax : 33.5.61.27.31.67, Email : sarti@cnes.fr

3 Laboratoire d'Ecologie Végétale, Université de Paris XI  
Bat. 362, 91405 Orsay Cedex, France.  
Phone: 33 1.69.15.56 80, Fax : 33.1.69.15.72.38  
Email: Eric.Dufrene@eco.u-psud.fr, <http://www.esu.u-psud.fr/evhome.htm>

4 ONERA/CERT/DEMR  
2, avenue. E. Belin, BP 4025, 31055 Toulouse Cedex, France.  
Phone: 33 5.62.25.27.18, E-mail: ruiz@oncert.fr

### ABSTRACT

This paper presents the first results concerning the use of ERS Tandem coherence time series for monitoring the dynamics of a mixed temperate forest ecosystem. The spatial and temporal sources of decorrelation are analyzed and we propose a preliminary explanation of the observed variation of coherence over the Fontainebleau forest.

The present study aims to evaluate the relevance of ERS-1/2 SAR instruments for monitoring temporal and structural changes in a mixed temperate forest ecosystem. Emphasis is put on the capability of InSar time series for detecting the leafy cycle of a deciduous forest. Firstly, we want to examine the different factors of decorrelation including system noise, spatial and temporal effects. Secondly, we investigate the possibility to relate the coherence variations to the structural and seasonal forest dynamics.

### INTRODUCTION

Recent studies, based on measurements of atmospheric CO<sub>2</sub> concentrations and on the use of atmospheric transport model, have suggested that temperate ecosystems, particularly forests, might presently act as major carbon sinks. This would mainly results from a human-induced effect of CO<sub>2</sub> fertilization on forest growth [1]. However, large uncertainties still exist for determining whether carbon sink or source occurs in temperate deciduous forests [2].

In this context, the potentialities of space-borne Synthetic Aperture Radars (SARs) for monitoring forest ecosystems must be investigated. Particularly, data acquired by existing C-band systems must be evaluated. Today, few studies are concerning with temperate deciduous forests. In addition, they all suffer from a lack of experimental data both in radar time series and in associated relevant ground data [3]-[5]. However, most of these studies demonstrate the potentialities of coherence information, especially for forest – non-forest classification [5]. They also point out the need of a better understanding of interferometric signatures over forests [6]-[7].

### SITE DESCRIPTION AND DATA COLLECTION

#### The Fontainebleau forest

The Fontainebleau forest, located 70 kilometers southeast of Paris, is a managed mixed deciduous-coniferous forest extending over 17 000 ha. Dominant species consist of oak, beech and Scots pine. Co-dominant species are hornbeam and birch.

This forest was used as a test site during several airborne and space-borne campaigns such as EMAC-94 (<http://www.estec.esa.nl/vrwww/emac/>). Within the frame of these campaigns, we have developed a large database dedicated to remote sensing studies and model validation. A detailed description of the forest and the associated ground data can be found elsewhere in [8] and [9].

#### Ground data collection

Besides the inventory measurements aimed at determining the structural parameters of about 55 test stands, intensive measurements were performed during each overpass of ERS-1/2 satellites [9]. They consisted of measurements of ephemeral biological forest

parameters like the PAI or the leaf water content on three representative test stands (oaks: C08, beeches: H13; pine trees: P08). As an illustration, Fig.1 shows the seasonal variation of the Plant Area Index (sum of Leaf Area Index and Wood Area Index) measured during the 96-growing season for oak, beech and pine trees, respectively. Throughout the year, deciduous trees exhibit a well pronounced seasonality, characterized by the leaf-on in April and the leaf-off in November.

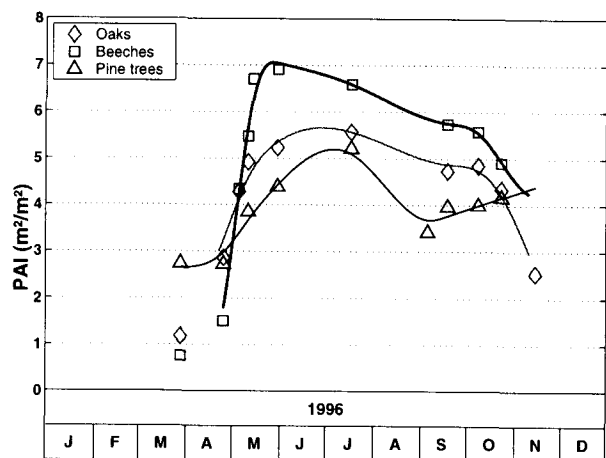


Fig. 1: Seasonal variation of PAI for oaks, beeches and pine trees.

On the whole, maximum Leaf Area Index (LAI) is reached 4-6 weeks after leaf-on and ranges from about 1 to 8, depending on stand development. For coniferous trees, LAI shows minimum values in winter and maximum values in July, ranging from 1 to 7.

### Meteorological data

It includes semi-hourly air temperature, precipitation and wind speed, parameters measured by the meteorological station of Fontainebleau.

## INTERFEROMETRIC PROCESSING

### Data

We have focused on 1-day time interval acquisitions provided by all the ERS Tandem pairs available on the Fontainebleau forest. The resulting dataset includes 9 Tandem images acquired in descending orbits from August 1995 to July 1996 and covers the critical phenological stages of vegetation development (Table 1). The Fontainebleau test site is totally imaged with a range of variation of the incidence angle of about 2 degrees around two mean incidence angles of 22.75° and 26.5°. The perpendicular components of all tandem baselines range from 27 m to 256 m.

Pair	Phenological State	ERS-1 date	Incidence angle (°)	Baseline (m)
1	Max. LAI	06 Aug. 95	22.75	83
2	LAI ↘	15 Oct. 95	22.75	256
3		19 Nov. 95	22.75	168
4	LAI = 0	24 Dec. 95	22.75	185
5		03 Mar. 96	22.75	35
6		19 Mar. 96	26.5	27
7	Bud burst	23 Apr. 96	26.5	82
8	LAI ↗	28 May 96	26.5	103
9	Max. LAI	02 Jul. 96	26.5	70

Table 1: Acquisition parameters for the 9 Tandem pairs.

### Coherence estimation

Interferometric processing of SLC data is achieved with the DIAPASON software developed at the Radar Department of CNES. The processing combines two SLC images into an interferogram including a coherence image. The interferometric coherence  $\gamma$  is calculated as:

$$\gamma = \frac{|\langle g_1 \cdot g_2^* \rangle|}{\sqrt{\langle g_1 \cdot g_1^* \rangle \cdot \langle g_2 \cdot g_2^* \rangle}} \quad (1)$$

where  $g_1$  and  $g_2$  are the complex pixel values of the ERS-1 image and ERS-2 image, respectively and

$$\langle g \rangle = \frac{1}{N} \sum_{i=1}^N g_i \quad (2)$$

indicates the spatial expectation over an N pixels window. Here, an optimal window size of 25 (azimuth) by 5 pixels is retained, insuring unbiased expectation of coherence values (Fig.2). According to [10], the estimated coherence bias is then negligible for  $\gamma > 0.4$  and below this threshold, the coherence values of forested areas can be also accurately estimated with uncertainty of about 0.08 for a 25x5 window as mentioned in [6].

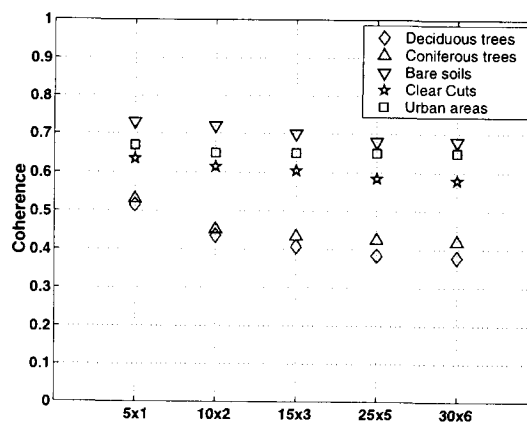


Fig 2 : Variation of the estimated coherence  $\gamma$  versus different window size (December 1996).



### Analysis of decorrelation factors

To compare the coherence estimates on forested areas within a time-series, a *normalization process* has to be carried out [11]-[13]. In a first step, the various non-forest sources of decorrelation are analyzed. The coherence values can be divided into three factors [13]:

$$|\gamma| = |\gamma|_{noise} \cdot |\gamma|_{spatial} \cdot |\gamma|_{temporal} \quad (2)$$

where  $|\gamma|_{noise}$  is related to the processor and the thermal noise decorrelation, which are normally negligible for reasonably high signal levels ( $\gamma >$ ,  $S/N >$ ),  $|\gamma|_{spatial}$  is the spatial decorrelation factor which includes decorrelation due to acquisition geometry, site topography and volume scattering within the forest medium. The third factor  $|\gamma|_{temporal}$  can be decomposed into one term related to meteorological effects and one term related to temporal changes in vegetation.

### ANALYSIS OF THE SPATIAL DECORRELATION

#### Influence of SAR acquisition geometry

Common band filtering of the azimuth and range spectra is applied in order to eliminate the non-common parts of spectra and to optimize the interferometric correlation. The baseline decorrelation is then compensated by normalizing the tandem coherences values with the theoretical profile given in [13]. For the largest baseline (256 m), the correction applied on the Tandem coherences values is about 0.08. The decorrelation effect due to different viewing angles is quite difficult to evaluate here since the 2 used incidence angles differ from only  $4^\circ$  (Table 1). Consequently, the effect is assumed to be negligible in this study, but will be analyzed in detail using a coherent model [14].

#### Influence of site topography

As well, the slope effect, which is expected to induce a coherence loss in the case of radar-oriented slopes, can be neglected here (flat area), except for pine trees stands generally located on hilly terrain. A simulated interferogram is generated by correlation with a DEM. The Fontainebleau forest of about  $15 \times 15 \text{ km}^2$  is a small enough area to accurately coregister DEM in Lambert II co-ordinate system with the slant-range-azimuth domain of the interferogram.

#### Influence of forest structure

Fig. 3 shows the variation of the coherence  $\gamma$  versus total aboveground biomass (expressed in tons of dry

matter per hectare) of deciduous and coniferous stands. Overall, there is a negative relationship between the coherence  $\gamma$  and total biomass. The statistical correlation coefficients of the different logarithmic relationships between  $\gamma$  and total biomass are smaller than 0.5 and 0.8 for deciduous and coniferous stands, respectively.

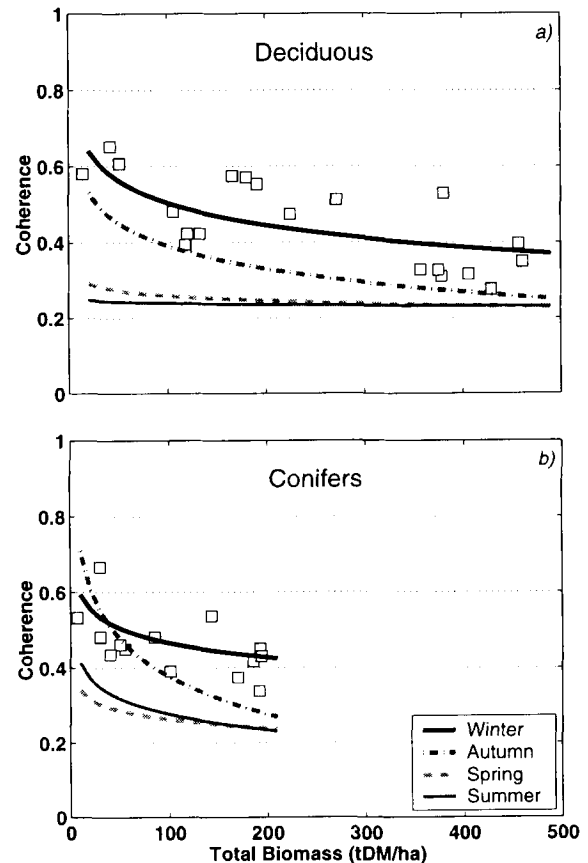


Fig. 3 : Decorrelation versus total biomass for deciduous trees and conifers. The mean trends are given for the 4 seasons. Only experimental data of wintertime are plotted ( $\square$ ).

Furthermore, it is observed a seasonal dependence of the relationships between coherence and biomass. For deciduous species,  $\gamma$  is a decreasing function of biomass in winter and autumn whereas it is almost independent of biomass in spring and summer. The leaf number, increasing volume scattering, is certainly one of the main driving factors of decorrelation. The absence of leaf therefore explains the highest coherence values observed during the winter season and the presence of leaves explains the lowest and stable coherence profile during summertime (where the number of leaves is maximal). At this time, these results are not fully understood and need to be interpreted by sensitivity analysis using a coherent model [14].

For coniferous species, the trends are all decreasing but compared to deciduous trees, the slopes are higher, especially in autumn. The increase of volume scattering as a function of biomass can certainly explain the  $\gamma$  decreasing profiles because the seasonality of LAI for conifers is not as marked as deciduous trees and needles are present at any season (Fig. 1). The observed seasonal variations need to be understood by taking into account other temporal changes occurring in the forests (e.g. in soil moisture).

## TEMPORAL DECORRELATION

### Influence of meteorological events

Random dislocation and dielectric changes of individual scatterers occurring during the time interval of the ERS-1/ERS-2 repeat pass tend to lower the interferometric correlation. Depending on the type of forest structure, effects of wind, temperature and rain will be more or less severe [11]. For a difference in wind speed smaller than 15 km/h, there is a slightly decrease of coherence as a function of wind difference for urban areas and for forested areas. The coherence values remains low and stable for water areas (Fig. 4).

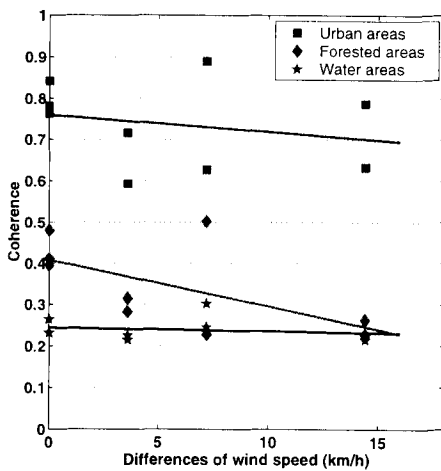


Fig. 4: Variation of coherence versus differences of wind speed between ERS-1 and ERS-2 acquisitions for urban, forested and water areas.

As well, there is no clear indication of an effect of temperature and rainfall on coherence. Because more than 9 tandem pairs are needed for a statistical analysis, it appears difficult to conclude now on the influence of a meteorological event on the decorrelation.

### Influence of seasonal changes in forests

#### Deciduous species

Fig. 5 shows the seasonal variation of coherence for 3 different deciduous stands corresponding to different

total biomass of 30 (thickets), 120 (pole stands) and 310 t DM ha<sup>-1</sup> (mature stands), respectively. On the whole, seasonal variation of coherence is well pronounced. The highest coherence values are observed in winter when leaves are absent whereas low and constant values of about 0.2-0.25 are found in spring and summer after leaf emergence. The decrease of coherence occurs during the period of leaf-on in March-April and an increase in coherence values is found again in autumn during leaf-fall. Furthermore, the seasonal variation of coherence strongly depends on stand development. The  $\gamma$  dynamic range is high for the youngest stands with low biomass whereas mature stands with high biomass exhibit a smaller dynamic range. This mainly results from the winter coherence values which decrease as biomass increases. Besides, the summer values are almost identical at about 0.2, indicating no correlation at all. Indeed, this value corresponds to minimal ERS system signal to noise ratio.

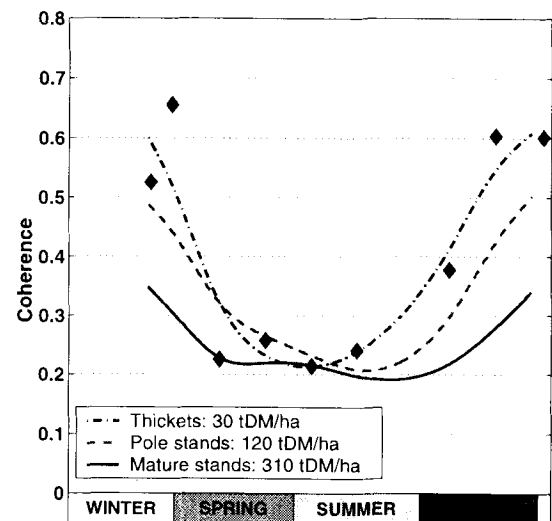


Fig. 5: Seasonal decorrelation observed over deciduous trees for different stand development. The corresponding mean biomass for the thickets and the tendency lines are also indicated.

#### Coniferous species

The seasonal variation of coherence for conifers is compared to that of deciduous trees (Fig. 6). Surprisingly, the seasonal variation is quite the same for both tree types. However, the same interpretation does not hold since conifers as evergreen trees do not exhibit large phenological variation throughout the year (see Fig. 1). Other factors of decorrelation including dielectric changes in canopy and soil must therefore be analyzed.

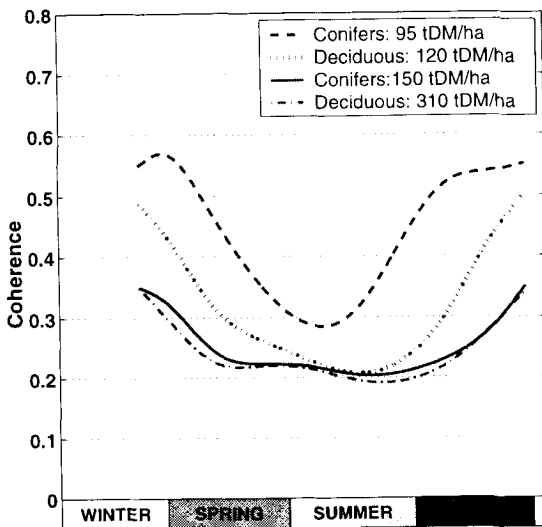


Fig. 6: Comparison between seasonal decorrelation observed over deciduous trees and conifers.

#### Influence of soil contribution

Observed coherence over bare soils are always high (see Fig. 2). As for backscattering coefficients, the importance of soil contribution to the scene coherence is a function of both the moisture status of the soil surface and the attenuation by the vegetation layer. This was demonstrated for  $\sigma^\circ$  on the Fontainebleau test site using multitemporal ERS data combined with a backscattering model [9]. For a beech stand, the analysis of the different contributions shows that the decrease in backscattering from January to March is mainly due to the drying of the soil surface (Fig. 7).

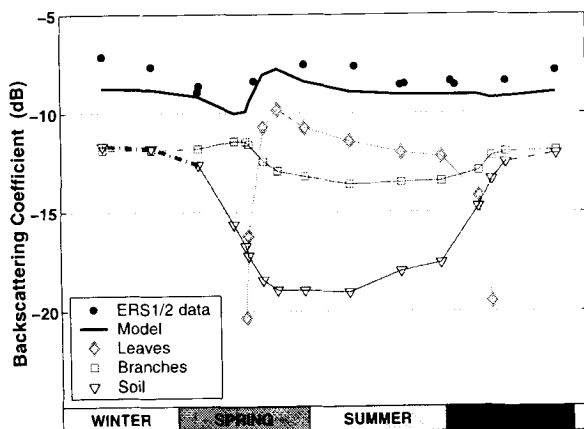


Fig. 7: Comparison between simulated  $\sigma^\circ$  and ERS-1/2 data for the H13 beech reference stand (from [9]).

Leaf emergence leads to an increase of about 2 dB during a short period when leaves contain a high percentage of water. Meanwhile, the contribution of the soil drops down due to the high attenuation by the foliage. As well, the seasonal profile of coherence

results from the contribution of each forest component at a given season. In winter, high values of coherence can be related to the high moisture content of the soil surface and low coherence values can be related to both the presence of leaves and the small contribution of the dry soil surface.

For conifers, the seasonal variation of backscattering was not yet simulated. However, one can observe similar temporal profiles between coherence and soil water content. The higher the soil humidity is, the higher the coherence value. The soil contribution is expected to be more important than for deciduous because the canopy structure of the P08 stand is more opened than that of the H13 stand.

#### Influence of foliage water content

The variation of mean summer coherence values as a function of foliage water content (expressed in  $t\ H_2O/ha$ ) is plotted on Fig. 8. As expected,  $\gamma$  is a decreasing function of the foliage water content. However, the sensitivity of coherence is weak, of the order of  $0.025/t\ H_2O/ha^{-1}$ .

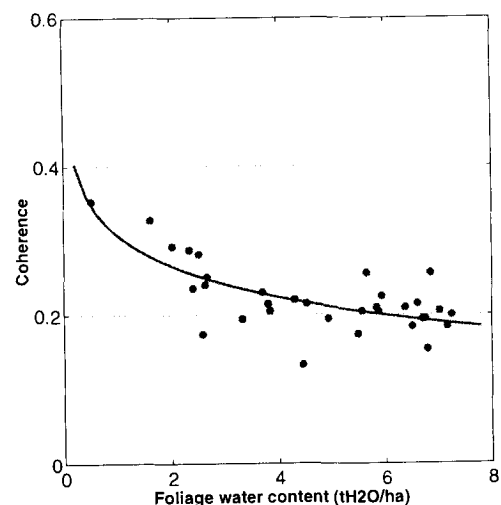


Fig. 8: Variation of coherence versus foliage water content (proportional to leaf biomass) during summertime.

### PRELIMINARY INTERPRETATION

From the above observations and following [7], the degree of coherence  $\gamma$  can be decomposed as a function of the contribution of each forest component as :

$$|\gamma| = |\gamma_{ground}| \frac{\sigma^\circ_{ground}}{\sigma^\circ_t} + |\gamma_{wood}| \frac{\sigma^\circ_{wood}}{\sigma^\circ_t} + |\gamma_{foliage}| \frac{\sigma^\circ_{foliage}}{\sigma^\circ_t}$$

where  $\gamma_{ground}$ ,  $\gamma_{wood}$  and  $\gamma_{foliage}$ , then  $\sigma^\circ_{ground}$ ,  $\sigma^\circ_{wood}$  and  $\sigma^\circ_{foliage}$  represent the forest ground, wood and foliage coherences and backscattering coefficients, respectively. Each coherence term is weighted by its effective

contribution related to the total backscattering of the forest  $\sigma^{\circ}_1$ .

In winter, the third term is null and the forest coherence is due to the strong contribution of the wet surface. From spring to autumn, the soil contribution decreases because of the drying conditions and of foliage attenuation. During summertime, the foliage as the main contributor in total backscattering, leads to small coherence values.

### CONCLUSION

The objective of the present paper was to analyze the potentialities of coherence time-series for monitoring the structural and temporal changes of a mixed temperate forest. Firstly, the decorrelation analysis points out some different results. Decorrelation factors like those due to SAR acquisition geometry can be taken into account and corrected whereas those due to meteorological effects are not obviously understood. Secondly, the analysis of decorrelation due to forest parameters shows very interesting experimental results, which need to be interpreted with an appropriate model.

Generally speaking, the results obtained over the Fontainebleau forest agree with previous observations and conclusions made for boreal forests [6]-[7]. Additionally, we also need to follow on with an experimental-theoretical approach aimed at interpreting the variation of coherence over forest covers. In this way, the Fontainebleau forest is a test site of particular interest.

### ACKNOWLEDGMENTS

This work was financially supported by the Radar Department of the French Space Agency (CNES). We would like to thank Jean Claude Souyris, for his permanent interest and support for our research works within the frame of the Fontainebleau project.

### REFERENCES

- [1] P. Ciais et al., "A large Northern Hemisphere terrestrial CO<sub>2</sub> sink indicated by the <sup>13</sup>C/<sup>12</sup>C ratio of atmospheric CO<sub>2</sub>", *Science*, 269: 1098-1102, 1995.
- [2] R.K. Dixon et al., "Carbon pools and flux of global forest ecosystems", *Science*, 263: 185-190, 1994.
- [3] G. Kattenborn et al., "High resolution detection and monitoring of changes using ERS-1 time series", *Proc. Second ERS-1 Symposium-Space at the service of our Environment*, Hamburg, Germany, October 11-14, pp. 635-642, 1993.
- [4] U. Wegmüller et al., "Interferometric signatures of temperate forest from ERS-1 SAR data", *Proc. IGARSS'94*, Pasadena, Aug. 8-12, pp. 292-294, 1994.
- [5] U. Wegmüller and C. Werner, "Retrieval of Vegetation parameters with SAR interferometry", *IEEE Trans. Geosci. Remote Sensing*, 35 (1): 18-24, 1997.

- [6] J. I. H. Askne et al., "C-band Repeat-Pass Interferometric SAR Observations of the Forest", *IEEE Trans. Geosci. Remote Sensing*, 35 (1): 25-35, 1997.
- [7] J. I. H. Askne et al. "Understanding ERS InSar Coherence of boreal forests", *Proc. IGARSS'99*, Hamburg, Germany, Jun. 28- Jul. 2, 1999.
- [8] E. Duffrène et al., "Remote sensing of the Fontainebleau forest during EMAC-94 : Objectives and data collection program", *Proc. EMAC 94/95 final results*, ESTEC, Noordwijk, NL, ESA SP-441, 14-16 April, pp. 91-95, 1997.
- [9] C. Proisy, et al., "Monitoring seasonal changes of a mixed temperate forest using ERS SAR observations", *IEEE Trans. on Geosci. Remote Sensing*, In press, 1999.
- [10] R. Touzi et al., "Coherence estimation for SAR imagery", *IEEE Trans. Geosci. Remote Sensing*, 37(1): 135-149, 1999.
- [11] O. Stebler et al., "Analysis of ERS-SAR tandem-time series using coherence and backscattering coefficient", *Proc. FRINGE 96 Workshop*, ERS SAR interferometry, Zürich, 1996.
- [12] P. B. G. Dammert, "Accuracy of INSAR measurements in forested areas", *Proc. FRINGE 96 Workshop*, ERS SAR interferometry, Zürich, 1996.
- [13] H. A. Zebker and J. Villasenor, "Decorrelation in interferometric radar echoes", *IEEE Trans. Geosci. Remote Sensing*, 30(5): 950-959, 1992.
- [14] C. Ruiz et al., "Modeling of electromagnetic waves interaction with forest canopies", *this issue*, 1999.

## Operational Use of SAR Images for Crop Surveillance - Issues Regarding Identification and Congruency Accuracy

M. Chakraborty, J. S. Parihar and S. Panigrahy  
 Space Applications Centre (ISRO)  
 SAC PO, Ahmedabad 380053, INDIA

Tel : +91 79 676 1188. Fax : +91 79 674 8813. Email : manabsac@yahoo.com

### ABSTRACT

Synthetic Aperture Radar (SAR) exhibits the combined advantages of fine resolution and all weather capability without serious degradation by atmosphere. Thus, the sensor has tremendous potential for agricultural surveillance. A large amount of data will be available by a number of SAR sensors in the coming years. Automated techniques for quick analysis of images are needed for timely use of such data in the field of agriculture surveillance. Three points need special attention in order to enhance the timeliness and accuracy of SAR image analysis, viz., accuracy of image location, image congruency of multi-date data and absolute calibration of SAR data. In SAR data, identification of ground control points both with reference to map to image registration and image to image registration are very difficult. Crop discrimination studies require precise location of fields used as reference ground truth for image analysis, which require precise geometric correction. Multi-temporal data set is essential for such studies. This requires precise image to image registration as that of multi-spectral optical data. Data calibrated in the absolute domain is essential as one uses data across the season, year and of different sensors for in-depth scientific investigations. Some of these aspects were put to test using RADARSAT ScanSAR data. ScanSAR is of particular interest for large area rice monitoring due to its large swath and shallow angle. 48 scenes of RADARSAT ScanSAR scenes were analysed during 1998-99 season to monitor rice crop in four states of eastern India. Four-date data acquired with 24-day repeat cycle were used to make multiple forecasts of crop acreage and condition as the crop season progressed. Use of satellite orbit and attitude information provided in the data header facilitated map to image correction. GCPs for image to image registration was scarce in most of the cases. RMSE error of within 0.5 pixel was achieved. This is considerably high to that provided by multi-spectral data set of optical sensors. The experience showed that maximum time was spent in data set preparation. Calibration accuracy within 2 dB was observed within the image and 4 dB between images of same pass. This facilitated development of generalised decision rules to classify the rice fields and apply it to the whole area with minor modifications. This paper highlights some of these issues which are found critical for such studies and will facilitate developing automated

procedures for crop surveillance. It is essential that these points are taken care at the data generation level to improve the format and nature of standard products to make it more user friendly and for near real time analysis.

### INTRODUCTION

Satellite remote sensing based crop production forecasting is one of the reliable methods towards large area crop production forecasting. The technical precision of such procedures has improved through years and at present is accepted to meet the requirement of routine gathering of timely information on crop prospects. In India, Crop Acreage and Production Estimation (CAPE) is an on-going project which uses optical remote sensing data to forecast production of major cereals, oilseeds, and fibre crops (SAC, 1995 [7]). However, data availability from optical sensors caused by cloud cover is the limitation of such studies particularly for crops like rice. It is observed that there are very few cloud-free images available during July to October, the entire 120 day growth period of the crop, with virtually no available images during the early vegetative stage (Currey et. al., 1987 [3]). Synthetic Aperture Radar (SAR) has a crucial role in operational crop surveillance. SAR exhibits the combined advantages of fine resolution and all weather capability without serious degradation by atmosphere. SAR data from ERS-1 and 2 had shown promising results for rice crop detection (ESA, 1995 [4], Patel *et. al.*, 1995 [6], Panigrahy *et al.*, 1997 [5], Chakraborty et al, 1997 [2]). The scope of utilising SAR data widened with the launch of RADARSAT in 1995. RADARSAT offers a wide range of data both in terms of incidence angle and resolution (RSI, 1995). Of these, ScanSAR Narrow data with its large swath and medium resolution is of particular interest for large area crop inventory. ScanSAR Narrow B (SNB) having a swath width of 300 km had shown promising results for large area rice crop monitoring. In near future a large amount of data will be available by a number of SAR sensors like RADARSAT 2, ENVISAT etc. Thus, the prospect of operational use of SAR for large area crop monitoring brightens. Automated techniques for quick analysis of images will be needed for timely use of such data in the field of agriculture surveillance. However, certain issues related to the preprocessing of data sets needs to be addressed to realise operational use by the users. This paper highlights some of these aspects

based on an experience of state level rice crop monitoring carried out using multi-date ScanSAR data during 1998-99 season in India..

### OBJECTIVES

Early acreage estimation of rice at state level using multi-date ScanSAR (SNB) data.

Multiple pre-harvest estimation as the crop growth progressed.

To monitor the progress of crop sowing and assess the crop condition.

To identify the parameters which needs further improvement for operational use of such data for crop surveillance.

### STUDY AREA AND DATA USED

Four states in India - Assam, Orissa, West Bengal and Tamil Nadu were selected as study area. All these four states belong to the traditional rice growing regions of eastern India, where rice is the dominant crop. Wetland rice practice prevails in these areas. The total geographic extent of the study area was around 35 million hectares.

RADARSAT ScanSAR Narrow Beam B data were used for analysis. Reasons for selection of this data were: (1) large swath with moderate spatial resolution (with lesser volume of data) and shallow incidence angle. ScanSAR SNB data is generated by combining the beams W2, S5 and S6 as given in Table-1.

Three and four-date data acquired at 24 day repeat cycle were used in the study as shown in Table-2. A total number of 48 images were used in this study. Data were acquired keeping in view the rice crop calendar of each state. The first-date data was acquired just before the transplanting operation.

### METHODOLOGY

The first two-date data were used to obtain an early estimate of area based on the signature of puddled / freshly transplanted fields.. The estimates were further updated using third and fourth-date data.. A specific software called 'SARCROPS' was developed for semi-automatic processing of SAR data using PCI EASI/PACE software on IBM workstation.

Broadly the steps of analysis were:

- (i) ScanSAR SNB Image data downloading (requires east-west reversal of data for descending mode). All header parameters including satellite orbit information are loaded.
- (ii) Data smoothening - spatial filtering to suppress speckle.
- (iii) Data calibration - conversion of digital numbers to

backscattering coefficient (dB). The header information was used to compute the backscattering coefficient from the digital number value by computing the radar brightness and incidence angle for each pixel and to create the dB image.

(iv). Dividing the image into four overlapping quadrants. This was carried out to keep the data volume manageable and achieve higher map to image and image to image accuracy.

(v). Image to Map registration - the first-date data was treated as base or master image. Image to map registration was carried out in this data.:

From the orbit information contained in the header file of the full ScanSAR data, latitude/longitude values of first, middle and last pixels of each scan line of data are generated. At least four appropriate bounding lat./long. coordinates are transferred into each quadrant image as header GCP segment. Few additional GCPs (obtained using GPS or from 1:50,000 scale maps) are used to validate the accuracy of the header GCPs. The GCPs are edited if required to develop the image to map fitting equation.

(vi). Multi-date data registration:

Since, the approach was to use multi-date data as one data set for classification of rice crop, it was essential to create a registered data set before the classification. Thus the second and subsequent date data were registered to the first-date data using image to image registration procedure. A first-order affine transformation is used to create multi-date registered data set using cubic convolution resampling.

(vii). Classification

A decision rule based classification was used to classify rice fields in temporal SAR data. The details of the procedure is as given by Chakraborty and Panigrahy, 1996 [1]. This classifier essentially uses the temporal backscatter to model the rice growth in three and four date data. The rules were developed using the statistics of ground truth sites for rice in the scene. Thus, specific rules for crops sown in different dates, different vigour and different field and soil status were developed. Working in the calibrated domain was essential for this.

### RESULTS AND DISCUSSION

Rice signature

RADARSAT ScanSAR Narrow -SNB data having an incidence angle of 31-46 degree was found to give distinct signature to lowland rice crop. The temporal behaviour was similar to that reported using ERS SAR data (Chakraborty et al., 1997). The freshly transplanted fields with standing water were characterised by low backscatter due to specular forward scattering surface of water. As the crop growth progressed (tillering stage),

backscatter increased due to volume scattering from the crop canopy. This separated rice fields from water bodies, forest areas, fallow fields and fields with other crops. The two-dimensional scatter-plots of the pixels belonging to various classes showed high separability of rice fields from water, homestead/forest classes in any combination of two-date data that includes the first-date. *This indicates that acquisition of SAR data during the early growth stage is very essential for rice crop identification.*

Decision rule classifiers performed well in the calibrated data sets and provided a meaningful classification of rice fields. It was also well suited to handle the large variability in the multi-date SAR signature. Hence, it was feasible to separate rice subclasses based on its growth stages and associated crop rotation practice using this classifier. Area estimates were obtained well in advance of the harvest of the crop. Estimates obtained with two-date data were used to assess the prospects of crop acreage. For example, in case of Orissa, a predominantly rainfed area, analysis of two-date data indicated subnormal crop prospects in the state. This agreed well with the reported deficit in rainfall in the region. The total acreage estimated was 3.9 million hectare out of which 3.5 million ha area indicated normal crop growth. This was much lower than the average 4.2 m ha in normal years.

#### Map to image transformation accuracy

Accurate map to image transformation is one of the critical requirement of such studies. Unlike optical sensors, it is difficult to identify well-defined GCPs in SAR data due to the presence of speckles and lack of contrast. Use of satellite header information was useful in minimising the required GCPs. In all cases the header information augmented with an average of 10 map GCPs collected in each quadrant, one could achieve the following RMS error using a second-order polynomial model:

- (i) Average residual RMS error less than 5 pixels
- (ii) Maximum residual RMS error less than 10 pixels

It can be mentioned that the four bounding GCPs obtained from the header was found to be essential to keep the overall error within these bounds throughout the image. The specified maximum *absolute error of image to map location* in RADARSAT data is 750 metres. Our observation for absolute error for ScanSAR data (satellite header information only) was within 500 metres. With the help of image to map GCPs, we could bring it down to 250 metres. The accuracy mentioned is for relatively flat terrains, which characterise the agricultural area (not valid for hilly regions). Table-3 shows map to image GCP fit obtained for one of the quadrant in Orissa.

Identification of map GCPs was the most time

consuming step in the study. Still one could not achieve the desirable target of maximum absolute error of 50 meter, with an average error of 25 metre required for such studies. Thus, it essential that such accuracy using the satellite ephemeris is obtained in order to meet the timeliness target of such studies.

#### Image to image registration accuracy

Multi-date SAR data was used as one combined data set similar to the multi-spectral data in optical sensor. Thus, it requires very accurate image to image registration. Lack of well-defined GCPs in SAR data coupled with their inconsistency in different dates was the major constraint to achieve this. We could achieve the following RMS error for each quadrant using on an average of 15 GCPs.

- (i) Average residual RMS error less than 0.5 pixel
- (ii) Maximum residual RMS error not exceeding 1 pixel

Example of image to image registration accuracy for one of the quadrant image is given in Table-4. It can be mentioned that the desirable error is less than 0.25 pixels (as in case of band to band registration of multi spectral optical sensors). This needs to be addressed at the software level using self-similarity detection algorithms (and other automated image to image fitting software). Also, the internal distortions of the images must be less than half a pixel (12.5 metres for ScanSAR Narrow). This has to be ensured at the data acquisition and subsequent data generation stage.

#### Shifts in multi-date images

It was observed that there is a shift of at least 8-10 km. between two multi-date acquisitions of ScanSAR Narrow B data of the same scene. This was observed both in the path (East-West) and row (North-South) direction. This resulted in loss of usable data around the perimeter of the scene leading to gaps in area coverage. The loss in row direction can be totally eliminated at the data processing level itself. The shift in the path, due to the instability of the satellite orbit, must also be reduced. There is a possibility of minimising this shift by beam angle adjustment and subsequent data processing. Though this can be avoided by taking overlapping scenes, it may be mentioned that RADARSAT ScanSAR Narrow data is available with 33% sidalap. This results in a large 33% increase in data cost and not preferred for operational studies. It is desirable to have at most 10% overlap for large area coverage with minimum increase in cost.

#### Data calibration

SAR data being an active sensor has the advantage of retrieving calibrated multi-temporal target property, which is essential for multi-date studies. This could be used for knowledge-based classification of the crops, modelling of the crop growth parameters and crop conditions. Thus it calls for high relative and absolute calibration. We observed a relative accuracy of  $\pm 4$  dB within a time period of 80 days. This may be reduced to 2-3 dB and needs to be maintained over the mission period for crop surveillance studies. Absolute calibration is required to compare data from different sensors. Originally ScanSAR data was not planned to be calibrated in absolute domain. However, as it showed promising result for quantitative study, steps had been taken to calibrate the data. Reported absolute accuracy of SNB is  $\pm 2$  dB.

### CONCLUSION

Rice crop was separable from most of the other land cover classes in two and three date data. ScanSAR Narrow B data was found to be cost effective for large area rice crop monitoring. This is of particular interest in the Indian context where rice is grown over 30 million hectares, often in large contiguous area as a single most dominant crop during the rainy season. This study showed the strong possibility of using ScanSAR Narrow B data to estimate total rice area, very early in the season, as well as assess the progress in sowing and crop growth as the season progressed.

However, since timeliness is the critical requirement for agricultural monitoring, certain issues need to be addressed for effective use of SAR data in regular crop surveillance. These issues are related to minimising the time taken for pre-classification data set preparation. It was observed that image to map and image to image registrations were the most time consuming steps in the whole procedure. Satellite header information has been found to be very useful, often essential in this direction. However, this needs to be further improved to enable the user to achieve better map accuracy with out supplementary GCPs. Similar efforts are needed to facilitate image to image data registration. This is of great importance, as use of SAR data requires either multi-date or multi-parameter data as one data set. High accuracy of relative calibration of data during the crop growth period was also essential to develop knowledge based crop discrimination classifier. High absolute accuracy will be essential to enable a user to compare multi sensor and ground based studies.

In addition to this, certain other aspects like temporal resolution needs to be addressed. Use of temporal SAR data essentially uses the temporal changes in growth for crop identification. In case of rice, the practice of growing rice in water filled puddled fields,

which gives an unique temporal SAR signature is used for identification of the crop. It showed that acquisition date has a strong bearing on the accuracy of crop identification. The 80 to 100 day crop calendar of rice require at least temporal resolution of 7-10 days which will give flexibility to select desirable dates of data acquisition suited to an area than the currently available 24-day cycle.

A number of SAR sensors with similar configuration will be available in near future. This brightens the prospects of taking up operational programmes based on SAR data for rice crop surveillance. However, it should be realised that the success of such programmes depend upon the relative ease with which an user can handle the data set and minimising the time taken for data set preparation. Thus, it is time to address some of these issues.

### ACKNOWLEDGMENTS

The authors would like to place on record a deep sense of gratitude to Dr. K. Kasturirangan, Chairman, ISRO, for his keen interest and providing this opportunity. His constant encouragement has been a great motivation for this work.

The authors are grateful to Shri AKS Gopalan, Director, SAC, for his constant support. Dr. George Joseph, Distinguished Professor, SAC, needs special mention for his keen interest and constant encouragement. The authors are grateful to Dr. RR Navalgund, Dy. Director, RESA for his constant guidance.

### REFERENCES

- [1] M. Chakraborty, and S. Panigrahy, 1996, Evaluation Of Four Per-pixel Classifiers Using ERS-1 SAR Data For Classification Of Rice Crop. In Proceedings Of Indo-us Symposium , I.I.T, Bombay, October, 1996.
- [2] Chakraborty, M., S. Panigrahy and S. A. Sharma, 1997, Discrimination Of Rice Crop Grown Under Different Cultural Practices Using Temporal ERS-1 SAR Data. ISPRS Photogramm. & Remote Sensing, 52:183-191.
- [3] Currey, B., A. S. Fraser and K. L. Bardsley, 1987, How Useful Is Landsat Monitoring. Nature, 328:587-590.
- [4] ESA, 1995. Satellite Radar In Agriculture, Experience With ERS-1, Sp-1185, ESA Publications, Pp66.
- [5] Panigrahy, S., M. Chakraborty, S. A. Sharma, N. Kundu, S. C. Ghose and M. Pal, 1997, Early Estimation Of Rice Acre Using Temporal ERS-1 Synthetic Aperture Radar Data - A Case Study For Howrah And Hughly Districts Of West Bengal, India. Int. J. Rem. Sens., 18:1827-1833.



[6] Patel, N. K, T. T. Medhavy, C. Patnaik and A. Hussain, 1995. Multi Temporal ERS-1 SAR Data For Identification Of Rice Crop. Journal Of Indian Society Of Remote Sensing, 23, 33-39.  
 [7] SAC, 1995, Manual For Crop Production Forecasting Using Spaceborne Remotely Sensed Data, A Joint Project Of Space And Ministry Of Agriculture,

Govt. Of India, Technical Note, RSAM/SAC/CAPE-II/TN/46/95, Space Applications Centre, Ahmedabad.  
 [8] RSI. (1995). RADARSAT Illuminated, Your Guide To Products And Services. RADARSAT International, Client Services, Richmond, Canada.

Pass details			
Period	Mode	Local Time	
July-October	Descending	0630 Hrs	
Satellite beam specification			
Incidence Angle (Degree)	31-46		
Beam Mode Combinations	W2	S5	S6
Resolution (Range*Azimuth)m	55.1*71.1	50.1*71.9	45.7*78.8
Nominal Swath (Km)	145-440		
Processing image specification			
Nominal Image Size (Km)		300 * 300	
Pixel Spacing (M)		25 * 25	
Number of Looks (Range*Azimuth)		2 * 2	
Digital file specifications			
Data Product		Path Image	
File Size (Mb)		144	
File Size (Pixel * Line)		12,000 * 12,000	
Bits/Pixel		8	

Table-1. Specification of ScanSAR Narrow-2 data used.

STATE	No. of Scenes	Data Acquisition period
ASSAM	3*4	July 01 to September 22, 1998
ORISSA	4*4	July 12 to October 02, 1998
WEST BENGAL	3*4	July 01 to September 22, 1998
TAMIL NADU	2*4	September 11 to November.22, 1998.

Table-2. Details of the data acquired

Model Parameters	FX	FY
1 CONS	-.329825E+06	.167508E+06
2 X	.405548E+04	-.800893E+03
3 Y	-.863466E+03	-.433709E+04

GCP's are ordered from worst to best residuals.

GCP No.	Set 2 GCP's		Set 1 GCP's		Residual		Distance
	LONG/LAT	E010	PIXEL	PIXEL	PIXEL	PIXEL	
11	86 53'19"E	21 33'04"N	3948.8	4443.2	7.05	-6.39	9.52
6	86 45'20"E	21 15'27"N	3662.5	5830.5	6.53	1.36	6.67
10	86 45'49"E	21 58'31"N	3074.2	2706.8	5.31	-3.37	6.29
16	87 01'51"E	21 39'18"N	4423.8	3887.8	-5.13	3.40	6.16
9	86 46'46"E	21 53'55"N	3194.2	3033.8	-4.57	3.42	5.71
17	87 14'09"E	21 40'58"N	5231.2	3597.8	-4.45	-2.44	5.08
12	87 02'54"E	21 28'28"N	4651.8	4650.2	-3.30	-3.79	5.03
8	86 47'22"E	21 50'20"N	3286.8	3278.8	-4.29	-2.53	4.98

7	86 56'01"E	21 31'12"N	4146.5	4547.5	-4.37	-1.09	4.51
14	87 08'10"E	21 47'33"N	4733.5	3206.5	-3.73	2.47	4.47
5	86 19'03"E	21 14'21"N	1891.5	6261.5	-3.69	2.07	4.23
18	87 20'47"E	21 37'27"N	5736.5	3769.5	1.96	3.41	3.93
15	87 14'16"E	21 51'10"N	5093.8	286 2.2	-3.13	.70	3.21
13	87 19'06"E	21 56'19"N	5349.2	2421.2	-.79	-2.72	2.83

Table-3. Example of Map to Image fit in one of the scenes in Eastern Orissa

Model Parameters		FX	FY				
1	CONS	-.315365E+02	-.405802E+02				
2	X	.999793E+00	.253111E-03				
3	Y	.154226E-04	.100010E+01				
GCP's are ordered from worst to best residuals.							
GCP No.	Set 2 GCP's		Set 1 GCP's		Residual		Distance
	PIXEL		PIXEL		PIXEL		
15	1155.8	4070.2	1123.2	4029.8	-0.79	-0.62	1.00
9	803.9	6110.1	773.1	6069.9	.86	-.48	0.98
1	5536.8	3493.8	5503.2	3455.2	-.87	.33	0.93
21	4529.2	2608.2	4497.2	2568.2	.43	-.83	0.93
2	1420.2	366.8	1388.8	325.8	.32	-.82	0.88
3	1098.2	6507.8	1065.8	6468.2	-.84	.16	0.85
4	4504.1	508.1	4471.1	469.4	-.54	.64	0.84
14	2942.8	713.8	2910.8	674.8	.13	.76	0.78
19	413.8	5151.8	382.8	5112.2	.54	.46	0.71
11	2302.8	3377.2	2271.2	3337.2	.46	-.34	0.57
5	4987.8	1538.2	4955.8	1499.2	.54	.17	0.57
22	428.5	649.5	396.5	609.5	-.38	.41	0.56
12	3259.5	2461.5	3227.5	2421.5	.17	-.49	0.52
17	2663.8	1695.2	2631.2	1655.8	-.44	.24	0.50
13	5701.8	770.8	5669.2	731.2	.20	-.44	0.48
18	2884.5	4342.5	2852.5	4303.5	.07	.42	0.42
16	3855.5	3518.5	3823.5	3479.5	.28	.26	0.38
23	735.5	3518.5	703.5	3478.5	-.37	.04	0.37
7	2327.1	5269.2	2295.1	5230.1	-.06	.34	0.35
8	3825.1	1636.9	3792.9	1597.1	.05	-.30	0.31
6	4254.8	4688.1	4222.2	4649.1	-.28	.04	0.28
20	4009.2	6268.8	3977.2	6229.8	.27	-.06	0.28
10	1066.8	2173.2	1035.2	2133.2	.22	.09	0.24

Table-4. Example of Image to Image fit for a quadrant image in Orissa.

## **Session 2: Ocean Applications**



## Ocean wave measurements using complex ERS-2 wave mode data

Johannes Schulz-Stellenfleh, Susanne Lehner, Birgitt Schättler, Helko Breit

German Aerospace Center (DLR), DFD, D-82234 Wessling, Germany

Tel. +49 8153 28 2828

Fax: +49 8153 28 2895

Email: Johannes.Schulz-Stellenfleh@dfd.dlr.de

### ABSTRACT

A global dataset of complex synthetic aperture (SAR) images processed from wave mode raw data acquired by the ERS-2 satellite is used to measure ocean waves.

Cross spectra of two looks extracted from the azimuth spectrum of wave mode imagettes are used to derive ocean wave propagation directions on a global basis. Energy, propagation direction and phase derived from wave mode cross spectra are compared with ECMWF ocean wave model data.

A new inversion scheme for the retrieval of two dimensional wave spectra from SAR cross spectra is presented. The algorithm is based on a maximum a posteriori estimation which combines the information from SAR measurements with a priori knowledge on short ocean waves. A new regularization approach is used to impose smoothness constraints on the retrieved wave spectra.

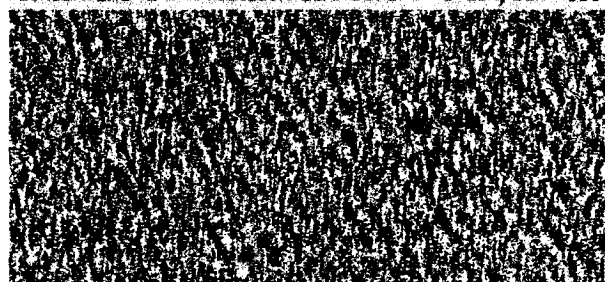
### INTRODUCTION

	ERS-1/2	ENVISAT
radar frequency	5.300 GHz	5.331 GHz
polarization	VV	HH or VV
sampling	every 200 km	every 100 km
coverage	≈ 10x5 km	6x5 km-10x5 km
daily coverage	≈ 1100 imag.	≈ 2200 imag.
incidence angle	19.3 / 23.5	14.1 - 42.3
R/V	110 s / 112 s	108 s - 142 s

Table 1: Comparison of different ENVISAT ASAR and ERS SAR wave mode parameters

Since the launch of the ERS-1 and ERS-2 satellites in 1991 and 1995, synthetic aperture radar (SAR) images have been acquired over the oceans on a continuous basis. Full swath scenes of 100 x 100 km size are taken where receiving stations are in line of sight (image mode), whereas 6 x 10 km images (imagettes) are acquired every 200 km along the orbit (wave mode). Due to their all weather capability and high resolution, SAR systems have become a valuable

Sensor: ERS-2 Processor: BSAR@DFD © ESA/DLR 1999



Raw Data ID: GSO27561-3-1-59  
UTC Time: 01-JUN-1997/05:00:45  
Coordinates: 5 58.00° / E 64.42°  
Processing Date: 20-MAY-1999

Flight North  
DLR

Figure 1: 10 x 6 km ERS-2 SAR imagette acquired on June 1, 1997, 05:00 UTC. The corresponding complex data were processed with the DLR processor BSAR

measurement tool for wind speed and ocean waves [1] [2], [3].

It is clear, that SAR imaging of the sea surface is a complex mechanism, influenced by many different processes, e.g. wave motion, wind, currents, slicks or rain. The basic imaging mechanisms are quite well understood by now [2], [4], [5], [3], [6], [7].

Quite a few studies were published about the use of ERS wave mode data for wind and wave measurements. These are mostly concerned with the analysis of UWA spectra which are the standard ESA product [1], [8], [9]. UWA spectra are coarsely gridded image power spectra derived from imagettes with a directional resolution of 15 degrees and 10 wavenumber bins logarithmically spaced between 66 m and 660 m (recently changed from 100 m to 1000 m) [10]. The complex imagettes themselves are so far not available from ESA as a standard product. However an analysis of intensity imagettes has been performed by Kerbaol [11].

Recently new algorithms were developed to derive wind speed and ocean wave spectra from complex SAR images [12], making use of the additional phase information contained in these data. Up to now these algorithms were only tested using image mode data [13], which are not suited for global statistical analysis as they can be acquired over the open ocean only

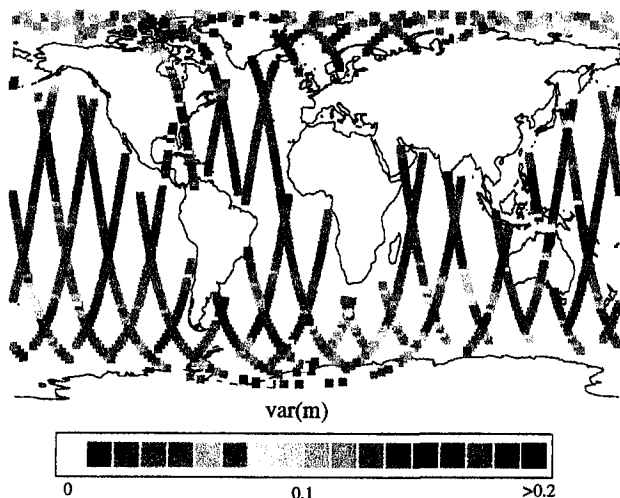


Figure 2: SAR image variance calculated for a global dataset of complex imaggettes acquired on June 1/2, 1997 (speckle contribution removed with multilook technique)

when in line of sight of antenna station.

This study is a preparation for the new data products available from the ASAR (advanced SAR) of the ENVISAT satellite to be launched in the year 2000. As the ERS SAR, the ASAR will operate at C-band and collect data in image mode and wave mode. The ENVISAT ASAR wave mode will have some advanced features as shown in table 1.

To prepare for ENVISAT data, ERS-2 wave mode raw data were processed to single look complex imaggettes using the BSAR processor developed at the German Remote Sensing Data Center (DFD). An example of an imaggette quicklook from this dataset showing ocean waves is given in figure 1.

In this study cross spectra computed from complex ERS-2 wave mode data are analyzed and a new method to retrieve two dimensional wave spectra is presented.

### Data analysis

The analyzed ERS-2 wave mode data set consists of about 1000 complex imaggettes acquired on June 1, 1997. Figure 2 shows a global map with the respective imaggette locations. The color coding corresponds to the observed coefficient of variation determined for the imaggettes (speckle removed by multilook technique). Collocated wave spectra were kindly provided by ECMWF with time gap less than 3 hours and spatial distance less than 100 km. Figure 3 shows a scatterplot between squared coefficient of variation (speckle included) and ECMWF significant wave heights. It can be seen that there is considerable correlation between the variation observed in the imaggettes and the ECMWF wave height. However as shown later, a proper wave height retrieval

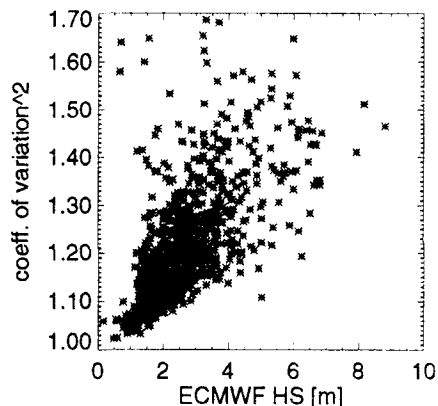


Figure 3: Scatterplot of coefficient of variation (squared) computed for ERS-2 imaggettes acquired on June 1, 1997 versus collocated ECMWF wave heights.

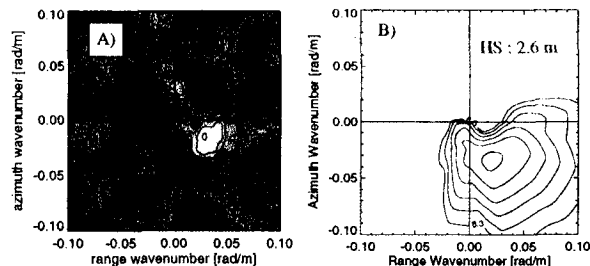


Figure 4: (A) Complex part of cross spectrum computed from complex ERS-2 imaggette acquired on June 1, 1997 06:27 UTC at lat -8.8 lon 56.51 (B) ECMWF ocean wave spectrum with 2.6 m significant wave height computed for June 1, 1997 06:00, -9 lat 56.63 lon

requires more sophisticated techniques, taking into account the complex SAR imaging process.

Complex SAR data allow to apply multilook techniques, which can be used to study the time evolution of the sea surface cross section during SAR integration time. The idea of the method is to use subintervals of the integration time to process two images with a time offset of about 0.4 s in the case of ERS-2. These looks have a lower azimuthal resolution and can be used to detect the ocean wave phase shift taking place between look acquisitions. An example of a look cross spectrum observed over the ocean is shown in figure 4. Figure 4 (A) shows the imaginary part of the azimuth look cross spectrum derived from an ERS-2 imaggette acquired on June 1, 1997, 06:27 UTC indicating a wave system of about 200 m length propagating to the right. In Figure 4 (B) the collocated ECMWF wave spectrum with 2.6 m significant wave height is plotted, confirming the SAR observation.

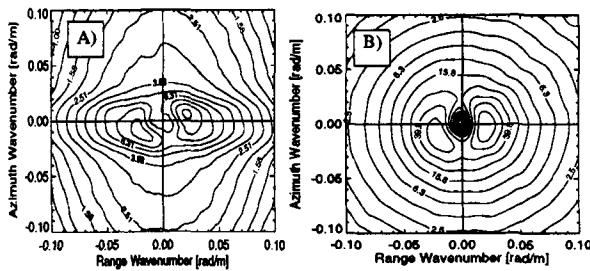


Figure 5: (A) Average ocean wave spectrum derived from  $n=1089$  imagette collocated ECMWF spectra. (B) Average Cross Spectrum energy derived from  $n=1089$  ERS-2 imagettes

The imagette cross spectra  $p_{m_1 m_2}$  were analyzed on a statistical basis using all imagettes with collocated ECMWF ocean wave spectra ( $n=1089$ ). Figure 5 (A) shows the average cross spectrum energy computed as

$$\zeta(k) = \frac{1}{n} \sum_{\text{im}(\rho^i(k)) > 0} |p_{m_1 m_2}^i(k)| \quad (1)$$

An azimuthal low pass filtering of the cross spectra caused by wave motion [4] is clearly visible. In addition the average spectrum is nearly symmetric indicating wave systems of about 300 m wavelength propagating in approximate range direction. The corresponding average ECMWF ocean wave spectrum is given in figure 5 (B), showing remarkable agreement with the observed cross spectra.

To study the phase of the measured cross spectrum the energy distribution over the interval  $[0, 2\pi]$  was analyzed. To avoid distortions caused by velocity bunching effects the analysis is concentrated on the phase observed along the range axis of the cross spectrum. Figure 7 shows the distribution of the cross spectrum energy  $|\phi_{m_1 m_2}|$  in the range wavenumber - phase plane. The dashed lines represent the phase expected for ocean waves propagating in very deep water. The phases scatter considerably, showing four week local maxima at a wavenumber of  $\pm 0.025$  rad/m and phase values of  $\pm 1$  rad and  $\pm 0.8$  rad respectively. The location of the local maxima with respect to the dashed line shows, that the phase shift of range waves derived from the ERS imagettes tends to be smaller than predicted by the deep water dispersion relation.

This leads to the question, whether despite of the strong scattering in the phase of the cross spectrum phase, a reasonable resolution of wave propagation ambiguity can be achieved. The problem is analyzed by studying the cross correlation of the cross spectrum imaginary part ( $> 0$ ) and the collocated ECMWF spectrum from the WAM model [14]. Only one dimensional spectra obtained by averaging over

range and azimuth respectively are considered. Figure 6 shows the analysis of the cross spectrum for one day of complex data. Figure 6 (A) shows a contour plot of the cross correlation between the range cross spectrum imaginary part ( $> 0$ ) and the corresponding range wave spectrum. It can be seen that the highest correlations are found along the diagonal plotted in dashed, while negative correlations are found in the upper left and bottom right quarter. Although the absolute correlation values are relatively small, showing a maximum of about 0.6, this pattern indicates a reasonable propagation direction ambiguity resolution for waves travelling in range direction. For the azimuth case figure 6 (B) shows a similar behavior, although the correlation pattern is more stretched in the azimuth direction of the ECMWF wave spectrum. This is due to the velocity bunching mechanism, which causes short wave systems travelling in the azimuth direction to be shifted towards lower azimuth wavenumbers in the SAR spectrum.

### Cross spectra forward model

Retrieval of ocean wave information from SAR cross spectra requires a good understanding of the physical processes involved in the imaging process. The forward model used for the inversion algorithm presented in this study is mainly based on an integral transform developed by Engen and Johnson [12]. Some simplifications were made to keep consistent with the forward model for SAR image power spectra used in the MPI scheme [15].

Let the modulation of two looks  $I_1, I_2$  extracted from the SAR azimuth spectrum with time separation  $\Delta t$  be denoted by  $m_1, m_2$

$$m_i = \frac{I_i - \langle I_i \rangle}{\langle I_i \rangle} \quad i = 1, 2 \quad (2)$$

It can then be shown [12] that the cross spectrum  $p_{m_1, m_2}$  of  $m_1$  and  $m_2$  is connected to the ocean wave spectrum  $F$  by the following integral transform:

$$p_{m_1, m_2}^{\Delta t}(k) = \frac{1}{4\pi^2} \exp(-k_x^2 \beta^2 \int^v(0)) \int dx \exp(-i k x) \exp(k_x^2 \beta^2 \int^v(x)) \cdot (1 + \int^R(x) + i k_x \beta (\int^Rv(x) - \int^Rv(-x)) + (k_x \beta)^2 (\int^Rv(x) - \int^Rv(0))(\int^Rv(-x) - \int^Rv(0))) \quad (3)$$

Here  $\beta$  is the slant range to platform velocity ratio and  $k_x$  is the azimuth wavenumber component. The autocovariance and cross covariance functions  $\int^v, \int^Rv$  and  $\int^R$  are defined as follows.

$$\int^R(x) = 0.5 \int dx (F(k) |T_k^R|^2 \exp(i\omega \Delta t)) \quad (4)$$

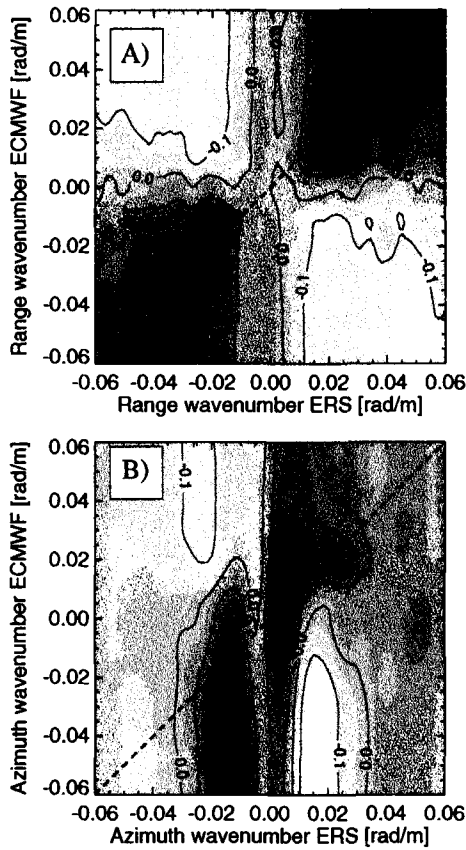


Figure 6: (A) Cross Correlation in range direction between cross spectrum imaginary part ( $> 0$ ) and collocated ECMWF ocean wave spectrum. (B) Cross Correlation in azimuth direction between cross spectrum imaginary part ( $> 0$ ) and collocated ECMWF ocean wave spectrum.

$$\begin{aligned} & + F(-k) |T_{-k}^R|^2 \exp(-i\omega\Delta t) \exp(i k x) \\ \tilde{f}^{Rv}(x) & = 0.5 \int dx (F(k) T_k^R \overline{T_k^v} \exp(i\omega\Delta t) \quad (5) \\ & + F(-k) \overline{T_k^R} T_{-k}^v \exp(-i\omega\Delta t)) \exp(i k x) \end{aligned}$$

$$\begin{aligned} \tilde{f}^v(x) & = 0.5 \int dx (F(k) |T_k^v|^2 \exp(i\omega\Delta t) \quad (6) \\ & + F(-k) |T_{-k}^v|^2 \exp(-i\omega\Delta t)) \exp(i k x) \end{aligned}$$

Here  $T^R$  and  $T^v$  are transfer functions for the real aperture modulation and the orbital velocity and  $\omega$  is the ocean wave frequency. To simplify eq. 4 the integral part in eq. 4 can be expanded in a Taylor series with respect to the wave spectrum  $F$ . Keeping only the linear term yields the following simple quasi linear transform

$$\begin{aligned} p_{m_1, m_2}^{\Delta t}(k) & \approx \exp(-k_x^2 \beta^2 \tilde{f}^v(0)) \\ & \cdot (|T_k^{SAR}|^2 \exp(i\omega\Delta t) F_k \quad (7) \\ & + |T_{-k}^{SAR}|^2 \exp(-i\omega\Delta t) F_{-k}) \end{aligned}$$

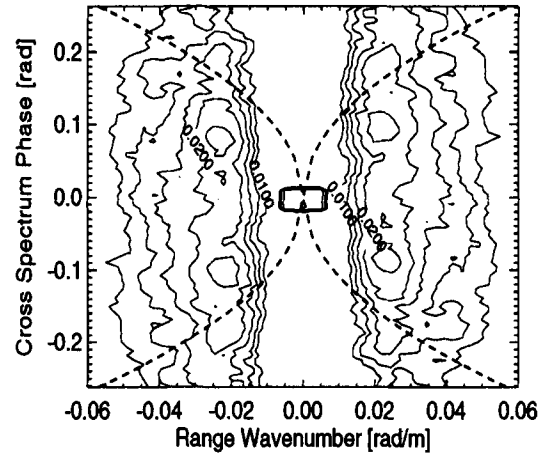


Figure 7: Distribution of energy of the cross spectrum in the range wavenumber/phase plane. The dashed lines represent the theoretical phase for ocean waves propagating in deep water

with transfer function  $T^{SAR}$ . The quasilinear transform reveals the basic nature of the SAR ocean wave imaging process, which is an azimuthal low pass filtering of the SAR spectrum.

### Inversion problem

As shown in the data analysis of the second section (fig. 5), information is lost on short waves propagating in flight direction. The retrieval of two dimensional ocean wave spectra from SAR data therefore requires some sort of a priori information to fill this gap. The question then is how the measurement and the a priori knowledge are combined to yield a wave spectrum which makes optimal use of all the available information. One approach to solve this problem is based on the so called maximum a posteriori estimation. The goal in this approach is to find an ocean wave spectrum  $F$  such that the conditional probability  $P(F|p)$  of  $F$  given a measured cross spectrum  $p$  is maximized. According to the Bayes formula this probability can be written as

$$P(F|p) = \frac{P(p|F) P(F)}{P(p)} \quad (8)$$

with  $P(p|F)$  describing the measurement error and  $P(F)$  and  $P(p)$  being the a priori probabilities of the wave spectrum and the observation respectively. As  $P(F|p)$  is regarded as a function of  $F$ , maximizing the probability  $P(F|p)$  is equivalent to minimizing the cost function:

$$J(F) = -\log(P(p|F)) - \log(P(F)) \quad (9)$$

Following other studies [4] a Gaussian probability



distribution with uncoupled wave components is assumed for the measurement error.

$$P(p|F) = c_2 \prod_k \exp[-|p^k(F) - \hat{p}^k|^2 / 2\sigma_k^2] \quad (10)$$

Here  $p(F)$  represents the forward model to simulate cross spectra from given wave spectra  $F$  (eq.4) and  $\hat{p}$  is the observed cross spectrum.

For the a priori distribution a new approach is taken, which introduces a coupling between wave components to achieve a more realistic representation of the prior knowledge than approaches taken so far [4], [3]. The idea is to regularize only the shape of the spectrum rather than the spectral energies. To make the optimization problem given by eq.9 feasible from the numerical point of view, the inversion is performed on a polar grid with  $m$  angles  $\Phi$  and  $n$  wavenumbers  $k$ . The used polar grids have a resolution comparable to the grids used in ocean wave models like WAM (e.g.  $m=12$ ,  $n=24$ ). Let the wave spectrum  $F$  be given as

$$F = (F_{\Phi_1, k_1}, \dots, F_{\Phi_1, k_n}, \dots, F_{\Phi_m, k_1}, \dots, F_{\Phi_m, k_n}) \quad (11)$$

The a priori distribution can then be written as

$$P(F) = c_3 \exp(-(F - \hat{F})^T G (F - \hat{F})) \quad (12)$$

with inverse covariance matrix  $G$  and a priori wave spectrum  $\hat{F}$ . The matrix  $G$  was chosen such that deviations between the derivatives of  $F$  and  $\hat{F}$  are penalized. Denoting the derivative operators acting in  $\Phi$  and  $k$  direction with  $L_\Phi$  and  $L_k$  respectively, this can be achieved by setting

$$G = L_k^T L_k + \gamma L_\Phi^T L_\Phi \quad (13)$$

The side condition  $F \geq 0$  was taken into account by using a transformation

$$F \rightarrow \exp(F) \quad (14)$$

This transformation also causes invariance of the probability given by eq.12 with respect to rescaling, e.g. a rescaled version of the a priori spectrum  $\hat{F}$  has the same a priori probability as  $\hat{F}$  itself. This is in accordance with the primary objective of the inversion scheme to regularize only spectral shape and not spectral energy.

Figure 8 shows two examples of inverted wave spectra (A),(C) and a priori wave spectra (B) and (D). It can be seen that the wave height and direction is slightly changed by the SAR observation in both cases. The second example in addition shows a weak wave system propagating in the opposite direction of the original wave. This is an artifact caused by a mismatch between the observed and the theoretical cross spectrum phase, which can be avoided by

modifying the a priori probability distribution (eq. 12).

## CONCLUSIONS

In the present study a first statistical analysis of ERS-2 wave mode cross spectra is given. It was shown that the ocean wave propagation directions derived from cross spectra are in reasonable good agreement with ECMWF data. However considerable scattering was observed of the cross spectrum phase showing poor agreement with theoretical predictions.

A new inversion scheme was presented, which uses a priori information on the spectral shape of the high frequency part of the wave spectrum. Ocean wave spectra retrievals using ERS-2 cross spectra and a priori information from the ECMWF wave model were presented.

## ACKNOWLEDGEMENTS

We would like to thank ESA for providing ERS-2 wave mode raw data in the framework of the ERS AO project COMPLEX. We also thank the ECMWF for providing collocated ocean wave spectra

## References

- [1] P. Heimbach, S. Hasselmann, and K. Hasselmann, "Statistical analysis and intercomparison with WAM model data of three years of global ERS-1 SAR wave Mode Spectral retrievals," *J. Geophys. Res.*, vol. 103, pp. 7931-7977, 1998.
- [2] W. R. Alpers, D. B. Ross, and C. L. Rufenach, "On the detectability of ocean surface waves by real and synthetic aperture radar," *J. Geophys. Res.*, vol. 86, pp. 6481-6498, 1981.
- [3] H. Krogstad, O. Samset, and P. W. Vachon, "Generalizations of the nonlinear ocean-SAR transformation and a simplified SAR inversion algorithm," *Atmos. Ocean*, vol. 32, pp. 61-82, 1994.
- [4] K. Hasselmann and S. Hasselmann, "On the nonlinear mapping of an ocean wave spectrum into a synthetic aperture radar image spectrum," *J. Geophys. Res.*, vol. 96, pp. 10713-10729, 1991.
- [5] H. Krogstad, "A simple derivation of Hasselmann's nonlinear ocean-synthetic aperture

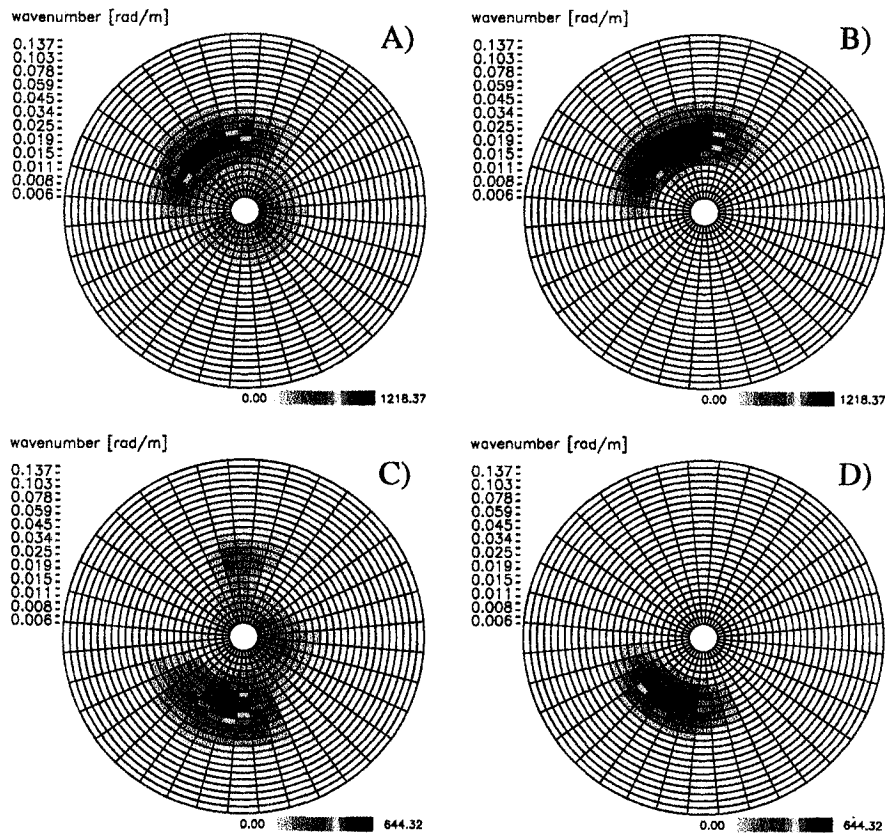


Figure 8: (A): Inverted ocean wave spectrum derived from complex ERS-2 wave mode cross spectrum acquired at lat -47.4, lon 19.2 on June 1, 1997 08:19 UTC with 4.7 m waveheight (B): Collocated ECMWF spectrum with 5.2 m waveheight (C) Inverted ocean wave spectrum derived from complex ERS-2 wave mode cross spectrum acquired at lat -29.0, lon 184.9 on June 1, 1997 21:38 UTC with 3 m waveheight (D) : Collocated ECMWF spectrum with 3.4 m waveheight

radar transform," *J. Geophys. Res.*, vol. 97, pp. 2421–2425, 1992.

- [6] P. W. Vachon and H. E. Krogstad, "Airborne and spaceborne synthetic aperture radar observations of ocean waves," *Atmosphere-Ocean*, pp. 83–112, 1994.
- [7] "Advances in oceanography and sea ice research using ERS observations," *J. Geophys. Res.*, vol. 103, C4, 1998.
- [8] C. Mastenbroek and C. F. Valk, "Wave spectra from SAR imageries," *J. Geophys. Res.*, 1996.
- [9] C. Mastenbroek and C. F. de Valk, "A semi-parametric algorithm to retrieve ocean wave spectra from SAR," *J. Geophys. Res.*, 1998.
- [10] G. Brooker, "UWA processing algorithm specification, version 2.0," Tech. Rep., ESTEC/NWP, ESA, 1995.
- [11] V. Kerbaol, B. Chapron, and P. W. Vachon, "Analysis of ERS-1/2 synthetic aperture radar wave mode imageries," *J. Geophys. Res.*, vol. 103, pp. 7833–7846, 1998.
- [12] G. Engen and H. Johnson, "SAR-ocean wave inversion using image cross spectra," *IEEE Trans. Geosci. Rem. Sens.*, vol. 33, pp. 1047–1056, 1995.
- [13] H. Johnsen and Y.-L. Desnos, "Expected performance of the ENVISAT ASAR wave mode cross spectra product," in *Proceedings of the IGARSS 99 conference, Hamburg, 1999*.
- [14] WAMDI Group, "The WAM model—a third generation ocean wave prediction model," *J. Phys. Oceanogr.*, pp. 1775–1810, 1988.
- [15] S. Hasselmann, C. Brüning, K. Hasselmann, and P. Heimbach, "An improved algorithm for the retrieval of ocean wave spectra from synthetic aperture radar image spectra," *J. Geophys. Res.*, vol. 101, pp. 16615–16629, 1996.

## Wind Retrieval over the Ocean Surface using Synthetic Aperture Radars

J. Horstmann<sup>(1)</sup>, S. Lehner<sup>(2)</sup>, W. Koch<sup>(1)</sup>, J. Schulz-Stellenfleth<sup>(2)</sup>, and R. Tonboe<sup>(3)</sup>

<sup>(1)</sup>GKSS Research Center  
Max-Planck-Str.  
D-21502 Geesthacht,  
Tel. +49 4152 87 1567  
Fax: +49 4152 87 1565  
Email horstmann@gkss.de

<sup>(2)</sup>Deutsches Zentrum für Luft und  
Raumfahrt  
D-Wessling,  
Tel. +49 8153 28 2828  
Fax: +49 8153 28 2895  
Email Susanne.Lehner@dfd.dlr.de

<sup>(3)</sup>Danish Meteorological Institute  
Lyngbyvej 100  
Dk-2100 Copenhagen  
Tel: +45 39157349  
Fax: +45 39157300  
Email rtt@dmi.dk

### ABSTRACT

The high resolution and large coverage of satellite borne **synthetic aperture radars** (SAR) offer an unique opportunity to derive **mesoscale wind fields over the ocean surface**. For this purpose, several algorithms have been developed and tested using SAR images from the European remote sensing satellites **ERS-1** and **ERS-2** and from the Canadian satellite **RADARSAT**. For retrieving wind speeds from SAR images empirical **C-band models** that give the relation of the local wind to the normalized radar cross section (NRCS) can be used. Another method is based on the measure of the **azimuthal smearing** which is related to wind speed. The methods are applied to ERS-2 **SAR imagerettes** and RADARSAT **ScanSAR images**. The results of SAR retrieved wind measurements are compared to winds retrieved from ERS-2 **scatterometer** (SCAT) and in case of the ScanSAR also to the **atmospheric high resolution limited area model** (HIRLAM) operated at the Danish Meteorological Institute (DMI). Furthermore the **vertical to horizontal polarization ratio** is studied using RADARSAT ScanSAR images together with the ERS-2 SCAT data. Finally the different **sources of errors** using the wind retrieval methods are discussed and estimated considering resolution and polarization of the SAR.

### INTRODUCTION

Since the launch of the European remote sensing satellites ERS-1 and ERS-2, and the Canadian satellite RADARSAT, synthetic aperture radar (SAR) images have been acquired over the oceans on a continuous basis. Their all-weather capability and independence on daylight together with their high resolution and large spatial coverage make them to a valuable tool for measuring geophysical parameters like ocean surface winds. In the past few years much effort has been undertaken to develop algorithms for derivation of wind vectors from SAR images. Wind direction is estimated by measuring the orientation of wind induced streaks visible in most SAR images [1] [2] [3]. For retrieval of wind speed, two main approaches are pursued. In the first, wind speed is estimated from the measured normalized radar cross section (NRCS), in-

cidence angle of radar beam and wind direction [4] [5] [6] [7]. For this purpose the NRCS has to be accurately calibrated and a model function is required that relates the ocean surface wind speed to the NRCS. In the second method wind speed is estimated from the spectral width of the the image spectrum in azimuth [8]. For this method a model is needed that describes the relationship between the spectral width of the azimuth spectrum, the ocean wave spectrum and the wind speed. The latter method has been applied to SAR intensity images of the European remote sensing satellites ERS-1 and ERS-2 [9] [10].

In the first part of this paper the investigated data sets are introduced followed by a short description of the applied SAR wind retrieval methods. Thereafter comparisons of different SAR data to scatterometer (SCAT) data and results of the atmospheric high resolution limited area model (HIRLAM) are performed using ERS-2 SAR imagerettes and RADARSAT ScanSAR images. Finally the main sources of errors using the wind retrieval methods are discussed and estimated considering resolution and polarization of the SAR.

### INVESTIGATED DATA SETS

#### ERS-2 SAR Single Look Complex Imagerettes

The C-band VV-polarized SAR aboard ERS-2 can acquire full swath scenes of 100 × 100 km size if a receiving station is in line of sight (imaging mode) or 6 × 10 km images (imagerettes) every 200 km along the entire orbit (wave mode), which results in ~ 1100 global distributed imagerettes per day. The later are up to day distributed as coarsely gridded image power spectra (UWA) derived from the intensity imagerettes [11]. Single look complex imagerettes themselves are so far not available from the European space agency (ESA) as a standard product, but will be available as a product of the ASAR aboard the ENVISAT satellite to be launched in the year 2000. To prepare for the ENVISAT wave mode data, ERS-2 SAR wave mode raw data were processed to single look complex (SLC) imagerettes using the BSAR processor [12] [13] developed at the German remote sensing data center. These SAR SLC imagerettes have a resolution of approximately 10 × 10 m and are nearly equivalent to

the ENVISAT ASAR wave mode product and therefore offer an ideal opportunity to test ENVISAT ASAR algorithms on a global scale.

#### RADARSAT ScanSAR Images

The SAR aboard the Canadian satellite RADARSAT can operate in various different acquisition modes. For this study, the HH polarized C-band SAR acquired images in the ScanSAR wide swath mode having the largest possible range of incidence angles between 20° and 50° perpendicular to flight direction. All ScanSAR data were processed by Gatineau Processing Facility in Canada into calibrated ScanSAR images. A ScanSAR wide swath comprises four beams (W1, W2, W3, and S7) which cover four areas in range with sequential scans. Each processed image covers an area of approximately 500 × 500 km with a pixel size of 50 m. The resolution of the four beams differs from 86.5 to 146.8 m in range and 93.1 to 117.5 m in azimuth. Since February 1999 the RADARSAT ScanSAR beams processed at Gatineau have been calibrated, with a nominal radiometric accuracy of ± 1.35 dB [14], although in specific areas with occurrence of scalloping, an effect caused by a too high variation in the satellite yaw angle, calibration may degrade further. The geometric accuracy of the ScanSAR data are in the order of approximately 100 m. The RADARSAT ScanSAR data were transformed to NRCS with a calibration scheme proposed by Shepherd [15], which compensates for scaling performed during processing and incidence angle dependencies.

#### ERS-2 SCAT Data

In addition to a SAR, ERS-2 is equipped with a scatterometer (SCAT) operating at the same wave length and polarization. The SCAT transmits and receives the signal at three antennae orientated at 45° forward, perpendicular, and 45° backwards with respect to the satellite flight track. The SCAT covers incidence angles between 18° and 59° illuminating a swath of 500 km. The spatial resolution is ~45 km and each data area is viewed from the three directions with different incidence angles. The SCAT data are processed by the European Space Agency (ESA) to wind fields using the C-band model CMOD4 [16]. The resulting wind field is available on a grid of 25 × 25 km covering a 500 km wide swath along the orbit.

#### HIRLAM Model Results

HIRLAM is a mesoscale atmospheric model which is in operational use at the Danish Meteorological Institute. It is a semi-implicit model, with Eulerian advection and leap frog time stepping (details are provided by [17] and [18]). For the Greenland area it was set up with a time step of 240 s and a horizontal resolution of 0.45°. The analysis of the model is performed every six hours using

the optimum interpolation method, which is a statistical procedure to minimize the difference between observations and first guess from the model. The lateral boundary values for the model are obtained from the global European center for medium range weather forecast (ECMWF) model.

## WIND RETRIEVAL FROM SAR

#### Wind Direction from SAR

The wind direction can be derived from the orientation of wind-induced streaks, such as boundary layer rolls in the atmosphere [4], visible in most SAR images. Therefore SAR subimages are transformed into the wavenumber domain, where the wind direction corresponds to the direction perpendicular to the line connecting the maximum of spectral energy. A spectral filter is applied for wave lengths between 500 and 1500 m to distinguish wind induced stripes from ocean waves and from larger-scale atmospheric structures such as atmospheric gravity waves. Due to the symmetry of the spectrum, the wind direction can only be computed with a 180° ambiguity. The algorithm shows good results applied to ERS-1 and ERS-2 SAR images [3] [19].

#### Wind Speed Retrieval using the Cross Correlation Algorithm

The wind speed can be estimated from the spectral width of the image spectrum in azimuth with the cross correlation algorithm (CCA) [8] [9]. The CCA is based on the azimuthal low pass character of the SAR ocean wave imaging process, which is caused by sea surface motion. The basic mechanism is an azimuthal shift and smearing of SAR image points due to slant range velocity and acceleration components of the backscattering facets. To remove the speckle peak in the CCA and to obtain a better performance of the fit procedure it was proposed in [9] to use the cross correlation between different looks having uncorrelated speckle noise. However in contrast to the proposed method which uses azimuth multilooking, looks extracted from the range chirp spectrum are preferred [10]. This approach has the major advantages that the azimuth resolution is not degraded, and the cross correlation function is not distorted by the phase shift of long azimuth ocean waves.

#### Wind Speed Retrieval using C-band Models

Another method for retrieving wind speeds from SAR is based on a model function relating the NRCS of the ocean surface to wind speed  $u$  and wind direction versus antenna look direction  $\phi$  according to

$$\sigma_0^{pol} = a u^\gamma (1 + b \cos \phi + c \cos 2\phi), \quad (1)$$

where  $a$ ,  $b$ ,  $c$ , and  $\gamma$  are coefficients that in general depend on radar frequency, polarization, and incidence an-

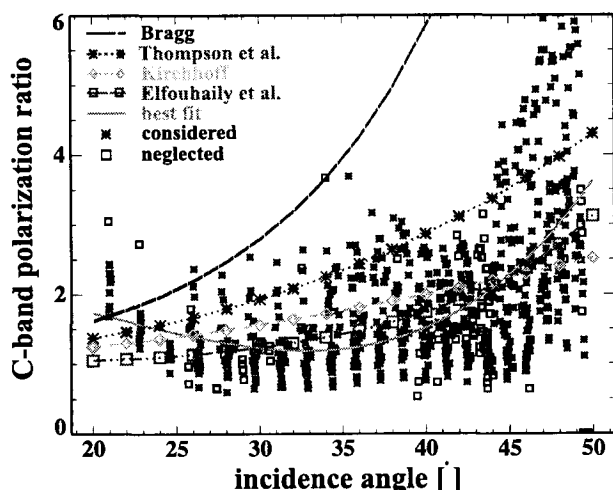


Figure 1: The incidence angles are plotted versus the C-band polarization ratio according to some theoretical models. Crosses and squares indicate polarization ratios retrieved from the normalized radar cross section (NRCS) from the HH-polarized RADARSAT ScanSAR images and the NRCS from the VV-polarized ERS-2 SCAT data.

gle. These coefficients were determined empirically in case of the model functions CMOD4 and CMOD\_IFR2 which were developed for the VV-polarized C-band SCAT aboard ERS-1 [16] [20]. Both models have been applied successfully to ERS-1 and ERS-2 SAR images [6] [2] [1] [7] [3]. So far there are no similarly well-developed and validated C-band models for HH polarization available. For that reason a hybrid model function has to be applied to RADARSAT ScanSAR data, consisting of the CMOD4 model and the C-band polarization ratio. The C-band polarization ratio has been measured with a SCAT by Unal et al. [21] for incidence angles of 20°, 30°, and 45° for wind speeds from 2 to 14 ms<sup>-1</sup>. Their work shows that the ratio, defined as VV/HH hereafter, is mainly dependent on incidence angles. However for wind speeds below 6 ms<sup>-1</sup> the authors also observed a wind speed dependency. Thompson et al. [22] proposed a polarization ratio model independent on wind speed and fitted the model to the data of [21]. The model has the following form:

$$\sigma_0^{\text{HH}} = \frac{(1 + \alpha \tan^2 \theta)^2}{(1 + 2 \tan^2 \theta)^2} \sigma_0^{\text{VV}}(u, \phi, \theta), \quad (2)$$

here  $\sigma_0^{\text{HH}}$  is the HH polarized NRCS,  $\sigma_0^{\text{VV}}$  is the VV polarized NRCS,  $\theta$  is the incidence angle and  $\alpha$  is a constant which was set to 0.6 fitting the data of Unal et al. [21] quite well. Changing  $\alpha$  in (2) to 0 gives the theoretical polarization ratio for Bragg scattering [23] and setting  $\alpha$  to 1 results in Kirchhoff scattering [24] [25]. The polarization ratios of (2) are plotted in Fig. 1 together with an additional model proposed by Elfouhaily [26].

## COMPARISON OF WIND SPEEDS

### Comparison of ERS-2 SAR Imagettes to SCAT

Up to now the SLC SAR imagettes are only relatively calibrated and absolute calibration will be difficult to achieve due to a power loss caused by the saturation of the analogue to digital convertor. However for the next generation of data from the ENVISAT satellite, saturation will be no longer a problem. The upper plot of Fig. 2 shows a scatterplot of mean intensity (log scale) versus scatterometer wind speeds. Triangles indicate imagettes on which sea ice, slicks or atmospheric effects were found by inspection. As can be seen these imagettes are characterized by relatively low intensities. In addition it can be observed that most of the corresponding SCAT wind speeds are also on the lower level, suggesting that these measurements are disturbed by the phenomena seen on the imagettes. A revision of the ERS SCAT flagging is thus

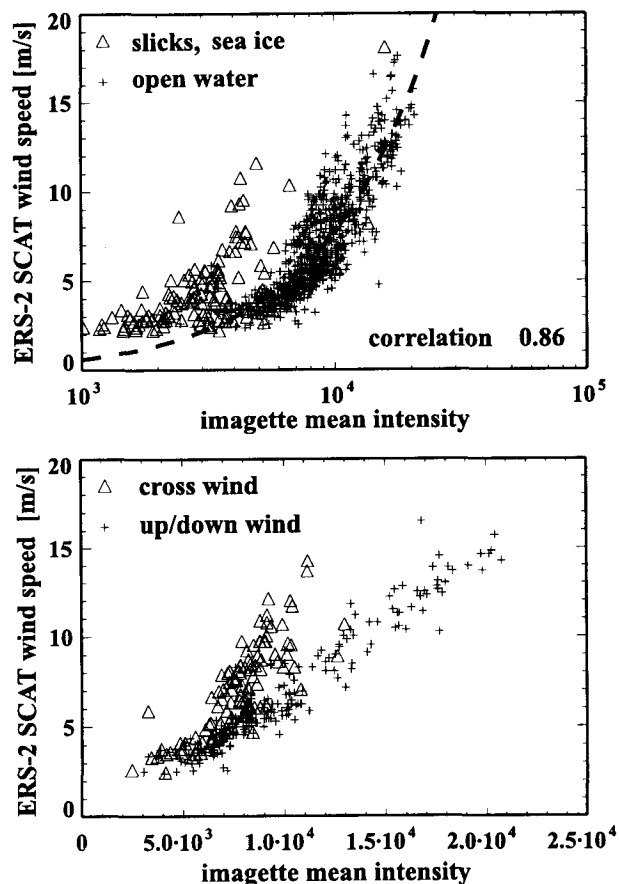


Figure 2: The mean intensity of each ERS-2 complex single look (SLC) synthetic aperture radar (SAR) imagette is plotted versus the corresponding ERS-2 scatterometer (SCAT) wind speed. On the left hand side homogeneous imagettes are denoted by a + and imagettes affected by slicks, sea ice or atmospheric phenomena by a  $\Delta$ . On the right hand side the + denotes cross wind and the  $\Delta$  up and down wind with respect to the SAR antenna.

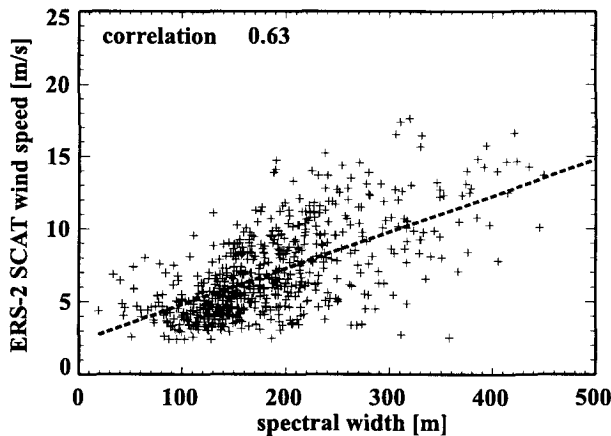


Figure 3: The spectral width is retrieved via the cross correlation algorithm (CCA) and plotted versus colocated ERS-2 SCAT wind speeds.

strongly suggested. The linear regression line (dashed line) was computed for the remaining homogeneous imagettes. The corresponding correlation is 0.86. The lower plot of Fig.2 shows the mean imagette intensity versus SCAT wind speed for cross wind (+) and up/down wind ( $\Delta$ ) respectively, where wind direction is taken from the ERS-2 SCAT. Only wind directions with a maximum deviation of  $25^\circ$  from range and azimuth direction respectively, are considered in this plot. As predicted by the CMOD models, it clearly shows up that the imagette intensities are higher for cross wind than up/downwind given the same wind speed. These results strongly suggest that C-band models applied to the ERS wave mode will yield a reliable and stable wind speed algorithm.

To analyze the CCA, simultaneous measurements of the ERS-2 SCAT are used. To check for the homogeneity of the imagette and the stability of the fit procedure, the spectral width was not only estimated for the area of the entire imagette, but also for quarter subimages. Fig.3 shows a scatterplot of the spectral width versus SCAT wind speed and its regression line (dashed line). Only imagettes having a standard deviation of the spectral width below 50 m were considered for the plot. The correlation of 0.63 indicates a reasonable close relationship. However the CCA method has to be further improved to obtain sufficient accuracy. This implies in particular a better understanding of the shape of the SAR spectrum and its dependence on wind speed.

#### Comparison of RADARSAT ScanSAR to ERS-2 SCAT and HIRLAM

Retrieving wind directions from RADARSAT ScanSAR images using the method described above failed in most cases and is due to the inadequate spatial resolution of the images. Therefore additional use of other information such as atmospheric models, weather charts, or measurements are required when using RADARSAT ScanSAR

images for wind speed retrieval applying the C-band models. Furthermore the resolution of the ScanSAR is insufficient for applying the CCA.

However wind speeds from ScanSAR can be retrieved using the hybrid C-band model function composed of the CMOD4 and the C-band polarization ratio [27] [28] [29]. To get an estimate of a suitable polarization ratio, the NRCS for HH polarization is taken from ScanSAR and the VV polarization is estimated from SCAT data. Therefore, the NRCS and incidence angles of the RADARSAT ScanSAR images are averaged over  $25 \times 25$  km on the grid used by the ERS-2 SCAT. At each point of the grid, the SCAT wind speed and wind direction measurement is put together with the ScanSAR incidence angle as input to the CMOD4 model, which then gives an estimate of the VV polarized NRCS. Taking the corresponding NRCS from the HH polarized ScanSAR data the VV/HH polarization ratio of each grid cell is derived. In Fig.1 the resulting polarization ratio is plotted versus incidence angle, considering 4 ScanSAR scenes and their colocated SCAT data, which were acquired 4.5 hours later. Stars represent results of areas where the backscatter is dominated by the wind and squares indicate data which were strongly affected by other features, e.g. sea ice. The decrease of polarization ratio in near range cannot be explained by the theoretical approaches and is most likely due to calibration inaccuracies. For higher incidence angles the polarization ratio shows the same trend as from Kirchhoff scattering and the approach of Elfouhaily.

Fig. 4 shows a scatter plot where SCAT wind speeds are compared to ScanSAR wind speeds. Therefore ScanSAR

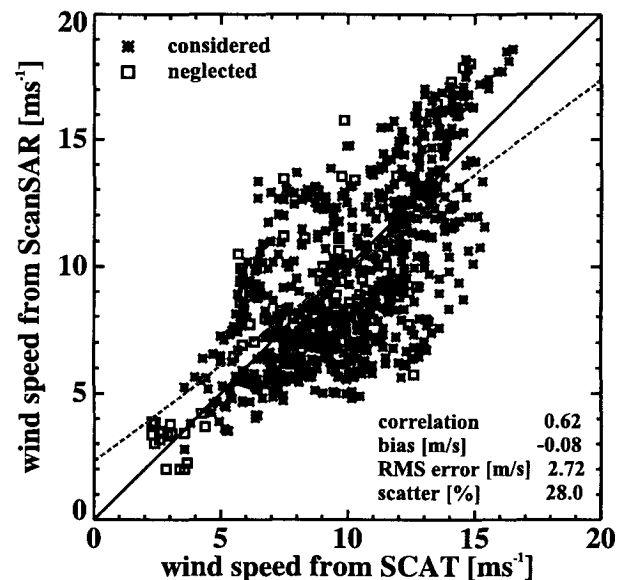


Figure 4: Scatter plot of comparison between wind speeds from the SCAT and from RADARSAT ScanSAR using the hybrid model function consisting of the CMOD4 and the polarization ratio according to Kirchhoff.

NRCS and incidence angles are used together with the wind direction from the corresponding SCAT grid cell as input to the hybrid model function, with the polarization ratio according to Kirchhoff scattering. The stars represent again results of grid cells which are open water and dominated by the wind while the squares are associated to grid cells which are affected by other ocean surface features. Although the ScanSAR and SCAT data are acquired 4.5 hours apart, the results are in fair agreement, having a correlation of 0.62 with nearly no bias. These results show the applicability of RADARSAT ScanSAR for wind speed retrieval, though efforts for better calibration have to be undertaken.

To test the applicability of the hybrid model function for a large range of wind situations, a comparison was performed using a data set of 10 ScanSAR scenes all in the Cape Farewell area. The images were acquired at approximately 2030 UTC and compared to the HIRLAM forecast of 2100 UTC. For this comparison, the ScanSAR images were averaged to the grid of HIRLAM, resulting in an average grid cell size of approximately  $28 \times 55$  km. Again wind speeds were retrieved from ScanSAR using the hybrid model function. The comparison was performed considering the polarization ratio according to Kirchhoff scattering and the best fit from ScanSAR and the corresponding SCAT measurements (Fig.1). For each grid cell, the wind speeds were derived using the NRCS and incidence angle from the ScanSAR together with the wind direction from the HIRLAM model. In Fig.5 wind speed from HIRLAM is plotted versus wind speed retrieved from ScanSAR, assuming the polarization ratio

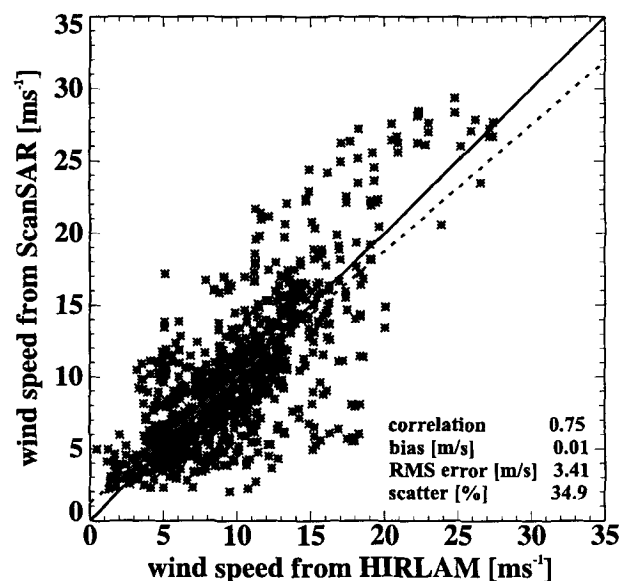


Figure 5: Scatter plot of comparison between wind speeds from HIRLAM and from RADARSAT ScanSAR using the hybrid model function consisting of the CMOD4 and the polarization ratio according to Kirchhoff.

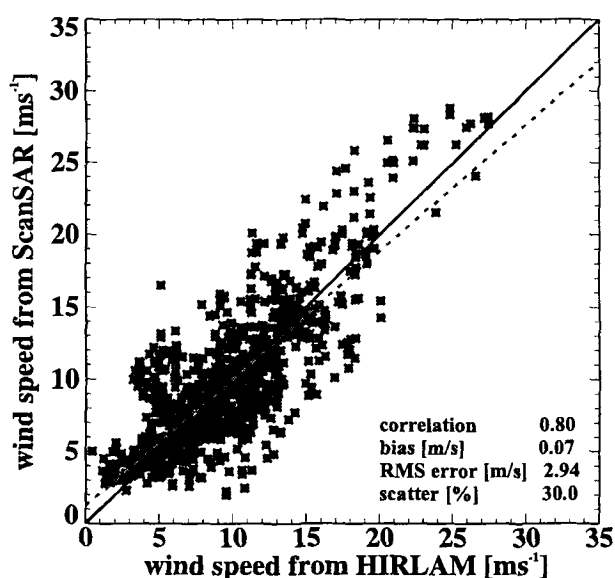


Figure 6: Scatter plot of comparison between wind speeds from HIRLAM and from RADARSAT ScanSAR using the hybrid model function consisting of the CMOD4 and the polarization ratio according to the best fit shown in Fig.1.

according to Kirchhoff scattering. The correlation is 0.75 with a bias of  $0.01 \text{ ms}^{-1}$ . Using the polarization ratio proposed by Elfouhaily gives very similar results, though with a bias of  $-0.81 \text{ ms}^{-1}$ . The same scatter plot is shown in Fig.6 where the polarization ratio resulting from the best fit (Fig.1) was used for wind speed retrieval. Both plots look very alike, though the statistics of Fig.6 look more reasonable. The correlations of the comparison is for all of the 3 ratios  $\geq 0.74$  and significantly better than the correlation of 0.62 resulting from the comparison to SCAT. This is most likely due to changes of the wind situation in the 4.5 hour time difference. However, the results from both polarization models are quite similar, and we cannot conclude which model is better.

In a next step, the difference in wind speed retrieved from ScanSAR and HIRLAM is derived for each ScanSAR image at every grid cell. The results are coded in grey levels and plotted at its location as a square superimposed on the ScanSAR image. In Fig.7 four typical ScanSAR images are shown. The grey scale of the image represents the NRCS. The main differences in wind speed occur in near range of the image (between 0 and 70 km), in lee of the coast, and at atmospheric fronts. The first is most likely due to calibration inaccuracies in near range. However, the other two phenomena cannot be caused by calibration errors or a wrong choice of the transfer function. In 8 of the 10 studied ScanSAR images, the wind speed in near range was significantly underestimated. In all images distinct differences in wind speed were observed near to the coast, especially in presence of wind shadowing, which shows that ScanSAR can significantly improve the infor-

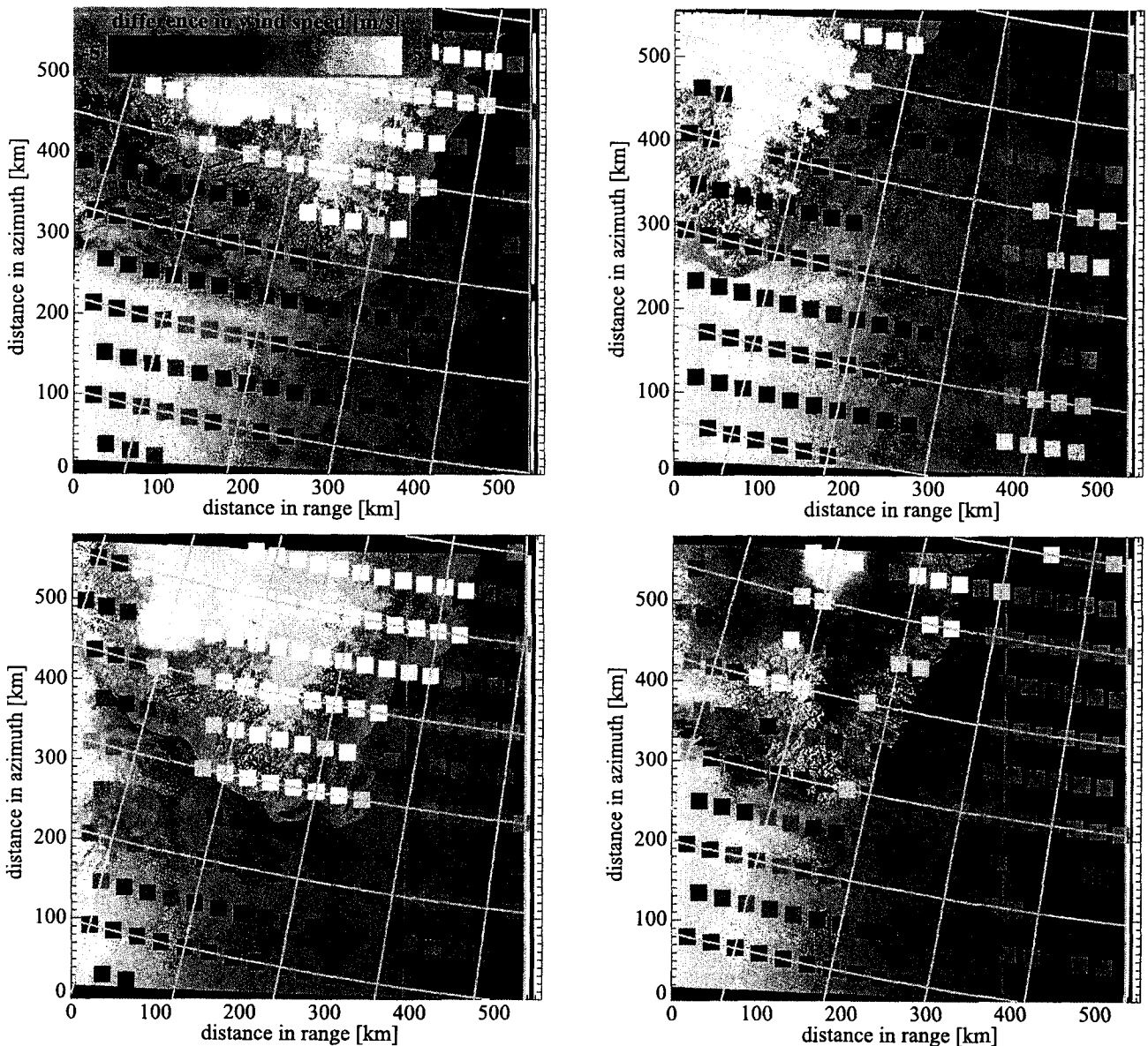


Figure 7: Four RADARSAT ScanSAR images from the Cape Farewell area. The images represent the NRCS of the ScanSAR data and the superimposed squares represent the difference in wind speed between ScanSAR and HIRLAM. ©Danish Meteorologic Institute and RADARSAT International.

mation on the wind field, especially in such unattainable areas.

### ERROR SOURCES

When computing wind speeds from ScanSAR images with the C-band hybrid model function the accuracy is strongly dependent on the input to the algorithm, NRCS, wind direction, and incidence angle. Main errors are caused by: the effect of speckle, uncertainty in wind direction, and calibration accuracy of NRCS. The granular appearance of SAR images is the effect of speckle, a small-scale fluctuating component of the backscatter. In the case of RADARSAT ScanSAR images, speckle can be  $\pm 3$  dB on

a single pixel. Therefore the NRCS of the images have to be averaged over at least  $2 \text{ km} \times 2 \text{ km}$  to reduce the effect of speckle.

More important is the necessity to have information on wind direction for retrieval of the wind speed. The NRCS is strongly dependent on wind direction and therefore uncertainties in wind direction can lead to significant errors in wind speed. The relative error in wind speed is plotted in Fig.8 assuming an uncertainty in wind direction of  $\pm 10^\circ$ . The computations were performed for incidence angles of  $20^\circ$ ,  $35^\circ$ , and  $50^\circ$ , using the CMOD4 with the Kirchhoff model polarization ratio. The largest relative errors result from wind directions near to  $45^\circ$  and  $135^\circ$ , respectively, and near to  $225^\circ$  and  $315^\circ$ , due to the



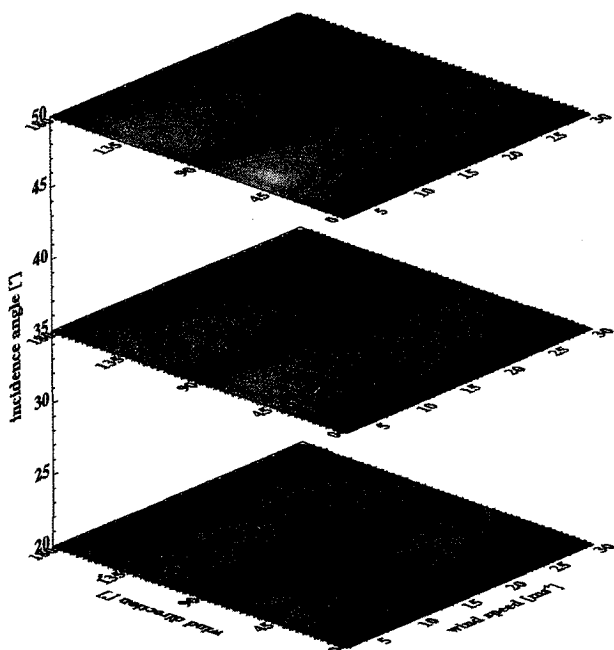


Figure 8: The computed relative error in percentage of wind speed due to an uncertainty in wind direction of  $\pm 10^\circ$  for incidence angles of  $20^\circ$ ,  $35^\circ$ , and  $50^\circ$ . The error is computed for wind speeds between 2 and  $30 \text{ ms}^{-1}$ , and wind directions from  $0^\circ$  to  $180^\circ$ .

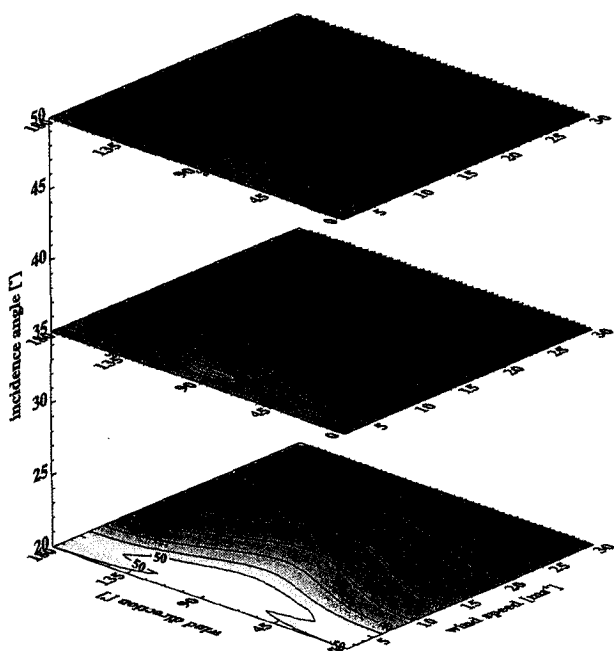


Figure 9: The computed relative error in percentage of wind speed due to an uncertainty in NRCS of  $\pm 0.5 \text{ dB}$  for incidence angles of  $20^\circ$ ,  $35^\circ$ , and  $50^\circ$ . The error was computed for wind speeds between 2 and  $30 \text{ ms}^{-1}$ , and wind directions from  $0^\circ$  to  $180^\circ$ .

symmetry of the hybrid model function. With increasing incidence angles and for low wind speeds, the error increases, however for higher wind speeds there is a dis-

tinct decrease of error with increasing incidence angles. The error in wind speed due to the accuracy of the NRCS is strongly dependent on the sensor performance and its calibration. In Fig.9 the error in wind speed is plotted assuming an accuracy of  $\pm 0.5 \text{ dB}$ . The computations were performed with the same model and the same ranges of input parameters used for the results of Fig.8. The relative error decreases significantly with increasing wind speed and is slightly lower for cross wind than for up- and downwind. This behavior also results for increasing incidence angles, though the error decreases significantly with increasing incidence angle.

## CONCLUSIONS

The derivation of wind speed from SAR data was considered using both ERS-2 SAR globally distributed wave mode imagettes and RADARSAT ScanSAR data. The measurements were compared to ERS-2 SCAT wind-data and wind field from an atmospheric model. The technique relating the image intensities to wind speeds show good results for both data sets. Measurement of wind direction is still a problem, as the features needed for the determination of wind direction are sometimes not present in SAR images.

Overall the investigation of the RADARSAT ScanSAR images showed the applicability of the hybrid model function for mesoscale wind speed retrieval over the ocean surface. It was found that the best fitting theoretical polarization ratios were according to Kirchhoff scattering and an extended model proposed by Elfouhaily. However, there are significant differences between the measured and the theoretical polarization ratios so that an empirical ratio was used in addition. Investigation of location of the largest deviations between ScanSAR and HIRLAM results showed a significant underestimation of the shadowing effect of Greenland by the HIRLAM model and calibration inaccuracies in the ScanSAR data at near range (0 - 70 km). Due to the inadequate resolution wind direction cannot be retrieved so far from ScanSAR images. However, the operational use of RADARSAT ScanSAR wind maps retrieved using the hybrid model function together with the wind directions from HIRLAM is planned at the Danish Meteorological Institute to help improve weather and especially ice drift forecast in the area around Greenland.

For the next European satellite ENVISAT ASAR radar measurements of the sea surface are available as well in wave mode as in ScanSAR mode. The present study is therefore one preparation step to test the wind algorithms for the planned operational use of ENVISAT ASAR data at meteorological weather centers.

## ACKNOWLEDGEMENTS

The authors from the GKSS Research Center (GKSS) and from the Deutsches Zentrum für Luft und Raum-

fahrt (DLR) were supported by the German Bundesministerium für Bildung und Forschung (BMBF) in the framework of the project ENVOC. The ERS-2 data were kindly provided by the European Space Agency (ESA) as part of the ERS AO3 COMPLEX714.

## REFERENCES

- [1] P. W. Vachon and F.W. Dobson. Validation of wind vector retrieval from ERS-1 SAR images over the ocean. *The Global Atm. and Ocean Syst.*, 5:177–187, 1996.
- [2] C.C. Wackerman, C.L. Rufenach, R. Schuchman, J.A. Johannessen, and K. Davidson. Wind vector retrieval using ERS-1 synthetic aperture radar imagery. *J. Geophys. Res.*, 34:1343–1352, 1996.
- [3] S. Lehner, J. Horstmann, W. Koch, and W. Rosenthal. Mesoscale wind measurements using recalibrated ERS SAR images. *J. Geophys. Res.*, 103:7847–7856, 1998.
- [4] W. Alpers and B. Brümmer. Atmospheric boundary layer rolls observed by the synthetic aperture radar aboard the ERS-1 satellite. *J. Geophys. Res.*, 99:12 613–12 621, 1994.
- [5] W. Rosenthal, S. Lehner, J. Horstmann, and W. Koch. Wind measurements using ERS-1 SAR. in *Proc. of Second ERS Applications Workshop*, ESA SP-383:355–358, 1995.
- [6] A. Scoon, I. S. Robinson, and P.J. Meadows. Demonstration of an improved calibration scheme for ERS-1 SAR imagery using a scatterometer wind model. *Int. J. of Rem. Sens.*, 17(2):413–418, 1995.
- [7] J. Horstmann. Untersuchung zur Windgeschwindigkeitsbestimmung aus dem Radar mit synthetischer Apertur ann Bord der ERS-1/2 Satelliten. *external GKSS report, GKSS 97/E/55, ISSN 0344-9629*, 1997.
- [8] B. Chapron, T. Elfouhaily, and V. Kerbaol. A SAR speckle wind algorithm. In *Proceedings of the Second ERS-1 Workshop*, IFREMER, Brest, 29280 Plouzane, France, 1994. BP 70.
- [9] V. Kerbaol, B. Chapron, and P. W. Vachon. Analysis of ERS-1/2 synthetic aperture radar wave mode imageries. *J. Geophys. Res.*, 103:7833–7846, 1998.
- [10] S. Lehner, J. Schulz-Stellenfleth, B. Schättler, H. Breit, and J. Horstmann. Wind and wave measurements using complex ERS-2 SAR wave mode data. *IEEE Trans. Geosci. Remote Sensing*, submitted 1999.
- [11] G. Brooker. UWA processing algorithm specification, Version 2.0. Technical report, ESTEC/NWP,ESA, 1995.
- [12] H. Breit, B. Schättler, and U. Steinbrecher. A high precision workstation-based chirp scaling SAR processor. In *Proceedings of the International Geosc. and Rem. Sens. Sym. 1997*, Singapore, 1997.
- [13] S. Lehner, B. Schättler, J. Schulz-Stellenfleth, and H. Breit. Processing and calibration of ERS SAR single look complex imageries – Extraction of wind and sea state parameters. In *Proceedings of the CEOS SAR Calibration and Validation Workshop '98*, Noordwijk, The Netherlands, 1998.
- [14] S.K. Srivastava, B.T. Banik, M. Adamovic, and R.Gray. Maintaining image quality and calibration of RADARSAT-1 CDPF products. In *Proceedings of the International Geosc. and Rem. Sens. Sym. 1999*, pages 443–445, Hamburg, Germany, 1999.
- [15] N. Shepherd. Extraction of beta nought and sigma nought from RADARSAT CDPF products. *Report AS97-5001 Rev. 2*, 1998.
- [16] A. Stoffelen. *Scatterometry*. PhD thesis, Universiteit Utrecht, 1998. ISBN 90-393-1708-9.
- [17] N. Gustafsson. HIRLAM 2 final report. *HIRLAM Tech. Report No.9, 126pp.*, Available from SMHI, S-60176 Norrköping, Sweden, 1994.
- [18] L. Wolters, G. Cats, N. Gustafsson, and T. Wilhelmsson. Data-parallel numerical methods in a weather forecast model. *Applied Numerical Mathematics*, 19:159–171, 1995.
- [19] J. Horstmann, I. Weinreich, D.Hauser, S. Lehner, and W. Koch. SAR wind measurements during the FETCH experiment. *Elsevier Oceanography Series*, submitted 1999.
- [20] Y. Quilfen and A. Bentamy. Calibration / validation of ERS-1 scatterometer precision products. In *Proceedings of the International Geosc. and Rem. Sens. Sym. 1994*, pages 945–947, Pasadena, USA, 1994.
- [21] C.M.H. Unal, P. Snooiji, and P.J.F. Swart. The polarization-dependent relation between radar backscatter from the ocean surface and surface wind vectors at frequencies between 1 and 18 GHz. *IEEE Trans. Geosci. Remote Sensing*, 29:621–626, 1991.
- [22] D.R. Thompson, T.M. Elfouhaily, and B. Chapron. Polarization ratio for microwave backscattering from the ocean surface at low to moderate incidence angles. In *Proceedings of the International Geosc. and Rem. Sens. Sym. 1998*, Seattle, USA, 1998.
- [23] J. W. Wright. Backscattering from capillary waves with applications to sea clutter. *IEEE Trans. Antennas Propag.*, AP-14(6):749–754, 1966.
- [24] F.T. Ulaby, R.K. Moore, and A.K. Fung. *Microwave remote sensing and surface scattering and emission theory*, chapter Introduction to random surface scattering and emission, pages 922–1033. Addison Wesley Publishing Company, 1982.
- [25] T. Elfouhaily, D.R. Thompson, D. Vandemark, and B. Chapron. A new bistatic model for electromagnetic scattering from perfectly conducting random surfaces. *Waves in Random Media*, in press 1999.
- [26] T. Elfouhaily. Physical modeling of electromagnetic backscatter from the ocean surface; Application to retrieval of wind fields and wind stress by remote sensing of the marine atmospheric boundary layer. *Phd thesis, Travail de recherche effectué au sein Département d'Océanographie Spatiale de l'Institut Français de Recherche pour l'Exploitation de la mer (IFREMER)*, 1997.
- [27] D.R. Thompson and R.C. Beal. Mapping of mesoscale and submesoscale wind fields using synthetic aperture radar. *Applied Physics Laboratory Technical Digest*, in press 1999.
- [28] J. Horstmann, W. Koch, S. Lehner, and R. Tonboe. Computation of wind vectors over the ocean using spaceborne synthetic aperture radar. *Applied Physics Laboratory Technical Digest*, in press 1999.
- [29] J. Horstmann, W. Koch, S. Lehner, and R. Tonboe. Wind retrieval over the ocean using synthetic aperture radar with C-band HH polarization. *IEEE Trans. Geosci. Remote Sensing*, submitted 1999.

## Retrieval and validation of sea surface winds from calibrated RADARSAT ScanSAR images

Xiaofeng Li<sup>1</sup>, W. G. Pichel<sup>1</sup>, F. Monaldo<sup>2</sup>, C. Wackerman<sup>3</sup>, R. Beal<sup>2</sup>, P. Clemente-Colón<sup>1</sup>, and K. S. Friedman<sup>1</sup>

<sup>1</sup>NOAA/NESDIS, E/RA3, Room 102 WWBG, 5200 Auth Road,  
Camp Springs, MD 20746-4304, USA

Tel: (301)763-8177; Fax: (301)763-8020; Email: [xiaofeng.li@noaa.gov](mailto:xiaofeng.li@noaa.gov)

<sup>2</sup>The Johns Hopkins University Applied Physics Laboratory, Laurel, MD, 20723-6099, USA

<sup>3</sup>ERIM International, Inc., Ann Arbor, MI 48113-4008, USA

### ABSTRACT

Two SAR ocean surface wind retrieval procedures have been developed by The Johns Hopkins University Applied Physics Laboratory (APL procedure) and ERIM International Inc. (ERIM procedure). The APL procedure estimates the SAR wind direction from temporally coincident meteorological model output, and then a SAR wind speed image is computed from the SAR radar cross section (RCS) measurements using the CMOD4 algorithm modified for HH polarization. The ERIM procedure first estimates the wind direction from wind-aligned feature in the SAR image and then estimates the wind speed in a manner similar to the APL model. The wind vector retrieved from the ERIM model has 180 degree wind direction ambiguity.

The APL procedure winds were compared with meteorological model winds, and the RMS error is about 3.49m/s. The ERIM model winds were compared with buoy winds and the RMS error in wind direction was about 31 degrees. The RMS error in wind speed was about 3.5 m/s.

### 1. INTRODUCTION

The retrieval of sea surface wind speed from high-resolution, wide-swath SAR images has been a focus of study in the SAR research community for the past few years. A research and development program at NOAA/NESDIS with partners in government, academia, and industry has endeavored to develop coastal ocean SAR applications, in particular wind measurement and hard target detection. These applications are being prepared for a preoperational demonstration in Alaska (the Alaska SAR Demonstration) starting in the fall of 1999. The primary data source will be quick-look, wide-swath SAR (i.e., ScanSAR Wide B) imagery processed at the Alaska SAR Facility (ASF) located at the University of Alaska, Fairbanks. Calibration coefficients (available beginning October 1998) for calculation of normalized radar cross section (RCS) for RADARSAT ScanSAR imagery, as well as calibration and mapping techniques and software

have been supplied by the ASF and used in the data processing.

In support of the Alaska SAR Demonstration project, two wind retrieval models have been developed by The Johns Hopkins University Applied Physics Laboratory (APL procedure) and ERIM International Inc. (ERIM procedure). The APL model estimates the SAR wind direction from temporally coincident meteorological model output, and thus SAR wind direction accuracy depends directly on model wind accuracy. A SAR wind speed image is then estimated from the SAR RCS measurements using the CMOD4 wind speed algorithm modified for HH polarization. The ERIM procedure first estimates the wind direction from wind-aligned features in the SAR image (e.g., wind rows, convective cells, surfactants, etc.) and then estimates the wind speed in a manner similar to the APL approach, although with different radar cross section models. The wind vector retrieved from the ERIM procedure has 180 degree wind direction ambiguity.

### 2. RADARSAT SAR CALIBRATION

The retrieval of ocean surface wind from SAR imagery is dependent upon the knowledge of RCS obtained from calibrated imagery. Since late 1998, RADARSAT ScanSAR Wide B SAR imagery processed at the ASF has been certified as calibrated. Calibrated imagery provided in the Committee on Earth Observation Satellites (CEOS) SAR data format is accompanied by a leader file containing the appropriate coefficients for converting the digital value in the image into RCS using the following equation (for data processed at ASF):

$$\sigma_0 = a_2(d^2 - a_1n(\theta)) + a_3 \quad (1)$$

where  $a_1=21947.9$ ,  $a_2=1.1026 \times 10^{-5}$ , and  $a_3 = 0.00000$  are typical values. The quantity  $d$  is the digital value in the image, and  $n(\theta)$  is a noise value represented by a lookup table that describes the noise floor as a function of ground range (values are typically in the range  $0.0093 < n < 0.2417$ ). The noise floor information in the leader

file, however, is not correct. The effect of an incorrect noise floor in the leader file is shown in Figure 1. The wind speed image in the left panel was derived from SAR data calibrated to RCS using the leader file information. Using wind directions obtained from the NOGAPS model, a wind speed at each pixel location was computed. The right panel was computed the same way except that the RCS values came from the ASF calibrate program, software made available on the ASF web site (<http://www.images.alaska.edu/software.html>). The overall structure and the range of the wind speeds are the same in the two images. However, at the very lowest wind speeds, the left image exhibits a rather unrealistically large region of zero wind speed.

Although the calibration scheme using the leader file produces reasonable cross sections values, the difference in the noise floor guarantees systematic problems, particularly at low wind speeds. For the Alaska SAR Demonstration, both the APL and ERIM procedures incorporate the ASF calibration software rather than using the leader file in order to produce accurately calibrated images for wind calculation.

Most of the SAR data to be used in the Alaska SAR Demonstration are ScanSAR data geocoded at the ASF to polar stereographic projection with a standard latitude of 70°N and a prime longitude of 45°W. Using Earth location information found in the map projection data record of the ASF SAR leader file, latitude and longitude are calculated for any pixel in the image using software obtained from ASF and incorporated into the wind processing modules.

### 3. SAR DERIVED OCEAN SURFACE WIND

Measurement of ocean surface winds from satellite scatterometer data is now quasi-operational. Routine availability of ERS-1/2 C-band scatterometer and the ADEOS Ku-band scatterometer data have fostered the development of mature algorithms for derivation of wind speed and direction from this type of data. But SAR instruments also have the potential for wind measurement. Like scatterometers, a SAR instrument measures variations in radar backscatter from the wind-roughened ocean, variations that are a function of wind speed and direction. Unlike scatterometers, SAR instruments only have one azimuth viewing angle, so wind direction must be obtained using a technique that differs from the multiple-azimuth measurement algorithm in use with modern scatterometers. An independent estimate of local wind direction, either from model output or from another source, is required for accurate wind measurement. Under the right

conditions, wind-aligned patterns in the SAR data itself can be used to infer wind direction with 180-degree ambiguity [1]. SAR wind measurements have the advantage of being at very high spatial resolution (in the range of 300 m to 1 km as opposed to the normal scatterometer resolution of 25-50 km) and can be made right up to the coast or in bays and estuaries without suffering from the land contamination evident in scatterometers and passive microwave radiometers. Two SAR wind products are being generated for the Alaska SAR Demonstration. Both products will be evaluated as to their utility to operational weather forecast and analysis activities; and ways of combining both algorithms to improve the wind product will be investigated.

#### 3.1 APL WIND ALGORITHM

The APL wind algorithm is based on the CMOD4 algorithm [4,8]. The relationship between wind speed and direction and RCS is given by the CMOD4 algorithm as:

$$\sigma_0^V = a(\theta)f(U)^c [1 + b(\theta)\cos\phi + c(\theta,U)\cos 2\phi]^{1.6} \quad (2)$$

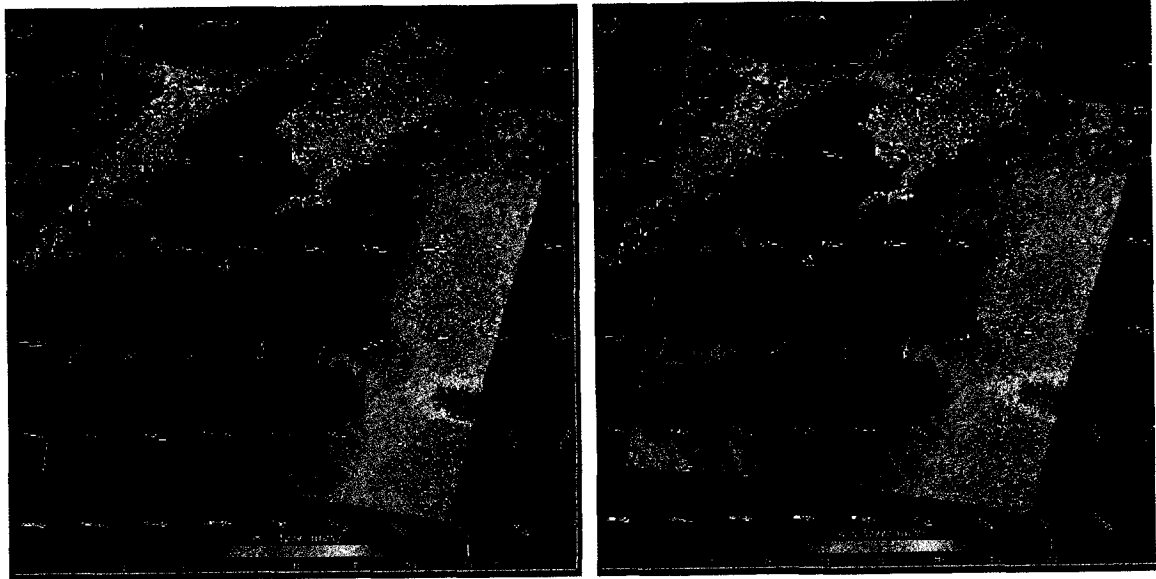
where  $\sigma_0^V$  is the vertical RCS,  $U$  is the wind speed,  $\theta$  is the local incidence angle, and  $\phi$  is the angle between the SAR look direction and the local wind direction. This model was developed for the ERS-1 C-band vertically polarized scatterometer (C-VV). Since RADARSAT SAR imagery is acquired at C-band horizontal polarization (C-HH), the CMOD4 algorithm needs to be modified for use with RADARSAT. The following relation between RCS for C-VV and C-HH has been derived at JHU/APL [5]:

$$\sigma_0^H = \sigma_0^V \frac{(1 + \alpha \tan^2 \theta)^2}{(1 + 2 \tan^2 \theta)^2} \quad (3)$$

where  $\alpha$  is a parameter that is still an area of research, and has been empirically estimated to be 0.6 [2,5]. Note that for an incidence angle of 0,  $\theta = 0$ ,  $\sigma_0^H = \sigma_0^V$ .

Figure 1 is an example of the APL wind image product derived from SAR data using Equations (2) and (3). The RADARSAT ScanSAR Wide B geocoded polar stereographic image data are averaged to 400 m pixels and calibrated to RCS. Wind direction is obtained from the 1° × 1° latitude/longitude grid NOGAPS (Naval Operational Global Atmospheric Prediction System) meteorological model analysis or forecast closest in time to the SAR image. The model wind directions are interpolated down to the 400 m SAR pixels with a bilinear

Figure 1. Sample wind image derived from APL wind algorithm. Left image was calibrated with data from leader file. Right image was calibrated with ASF software. Image is of the Gulf of Alaska with Kodiak Island in the top center of the image. North is up.



interpolation scheme. Equations (2) and (3) are used to prepare a lookup table that returns wind speed output given RCS horizontal polarization input. In Figure 1, SAR wind speed is shown in the image color value. Arrows in the wind image are wind vectors from the NOGAPS model [2].

### 3.2 ERIM WIND ALGORITHM

The ERIM ocean surface wind product is derived with a different approach to the problem of measuring winds from SAR. SAR images over the ocean contain signatures of atmospheric effects due to the local changes to surface wind speed and direction. These signatures are often elongated in the general direction of the local wind. Examples are wind rows and island wind shadows [1]. In the ERIM procedure, land is first masked out of a RADARSAT SAR image using a coastline map (a 2 km uncertainty is added to take care of navigation errors). Multiple spatial frequency spectra are generated within a 48 km region of the SAR image with Fast Fourier Transforms. These spectra are then averaged to form a smooth spectrum. Next, the elongation direction of the spectral energy over large scales (3-20 km) is calculated with the elongation direction determined in two ways: (1) by fitting a quadratic polynomial to the spectrum and calculating the direction of smallest curvature, and (2) by finding the spectrum peak value. The wind direction is rotated 90 degrees from this elongation direction. This procedure is repeated with slightly overlapping regions

to form a 32 km grid of wind directions with 180-degree ambiguity. For each 48 km region used to estimate a wind direction, the average RCS of the region is also calculated, and then a 3 x 3 smoothing operation is applied to the wind directions where each direction is replaced by the weighted average of nine wind directions surrounding it with the average RCS values providing the weights. Finally, for each grid location the wind speed is estimated as follows. Given some model for the RADARSAT C-HH  $\sigma_0^H$ , wind speeds from 1 m/s to 30 m/s every 0.2 m/s are put into the model along with the estimated wind direction to generate an estimated  $\sigma_0^H$ . The wind speed that generated the estimated  $\sigma_0^H$  closest to the actual  $\sigma_0^H$  is chosen as the wind speed for that grid location. Currently, three RADARSAT C-HH  $\sigma_0^H$  models are being evaluated. The first is the same as in Equation (3) above. The second is similar to Equation (3), but where the CMOD4 scale factor is a cubic polynomial in  $\tan(\theta)$  and the polynomial coefficients are empirically derived so that

$$\sigma_0^H = \sigma_0^V (\alpha_3 \tan^3 \theta_i + \alpha_2 \tan^2 \theta_i + \alpha_1 \tan \theta_i + a_0) \quad (4)$$

The third model is a two-scale model with hydrodynamic effects that is being investigated to obtain a refined C-HH  $\sigma_0^H$  model [3,6,7]. This is defined as

$$\sigma_0^H = \iint \sigma_b(s_u, s_c) [1 + s(u)h(s_u, s_c)] \rho(s_u, s_c) ds_u ds_c \quad (5)$$

where  $s_u$ ,  $s_c$  are the wave height slopes in the upwind and crosswind directions respectively,  $\sigma_b(s_u, s_c)$  is the tilted bragg RCS for an ocean surface with the given slopes,  $s(u)h(s_u, s_c)$  represents a modulation to the bragg RCS due to hydrodynamic effects (with  $u$  representing wind speed,  $s(u)$  a scale factor based on wind speed, and  $h(s_u, s_c)$  a linearization of the hydrodynamic effects in upwind and crosswind slopes), and  $\rho(s_u, s_c)$  is the probability that a facet with slopes  $s_u$  and  $s_c$  occurs on the ocean surface.

Since the underlying RADARSAT C-HH  $\sigma_0^H$  model is so important to the final wind vector product, a study is underway to validate the different models and perhaps combine them into a final version. Figure 2 shows a plot of each model versus actual RADARSAT C-HH values calculated from 46 samples where the wind information came from an *in situ* buoy and the radar cross section value came from an average of the calibrated RADARSAT image over a 1 km square around the buoy. In Figure 2, the Two-Scale Model refers to the model in Equation (5), the Empirical Scaling Model refers to Equation (4), and the bragg Scaling Model refers to Equation (3). The normalized root mean square error (NRMSE in the figure) represents the mean square of the error between the model and RADARSAT RCS values (calculated in energy, not dB) normalized by the total energy in the RADARSAT values. Note that the NRMSE values are between 0.35 to 0.39 with the two-scale model performing slightly better than the other two. However it should be noted that the two-scale model takes much longer to calculate than the other two models. Work is ongoing to finalize these models.

Figure 2. Comparison of the various RADARSAT C-HH radar cross section models to RCS values calculated from calibrated RADARSAT images.

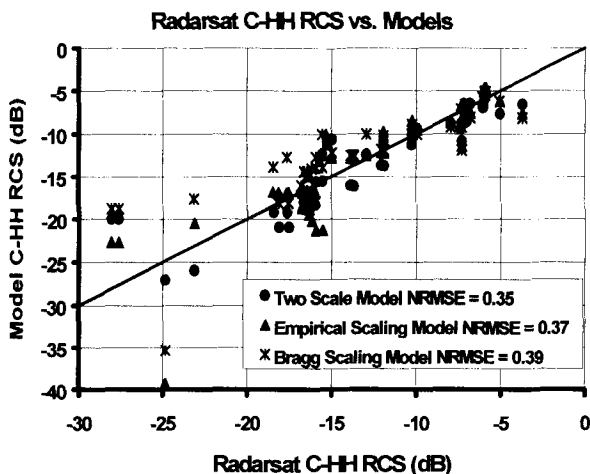
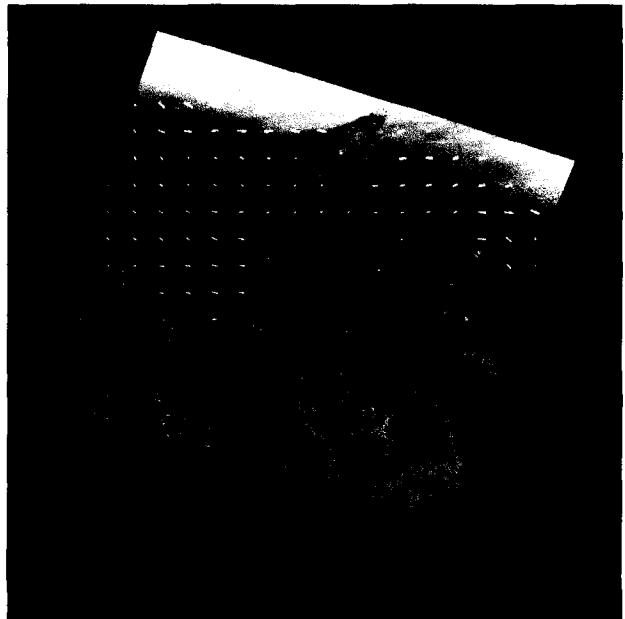


Figure 3 is an illustration of the ERIM wind product. The actual product is a text file of wind speed and direction for each grid point. In Figure 3, the vectors have been plotted on the SAR image from which they were derived to visualize the result.

Figure 3. A sample ERIM wind vector product derived from the SAR image. Image is of the Bering Sea. Nunivak Island is at the top center of the image. North is to the lower left portion of the image. SAR image Copyright, Canadian Space Agency, 1999.



#### 4. VALIDATION OF SAR WIND PRODUCTS

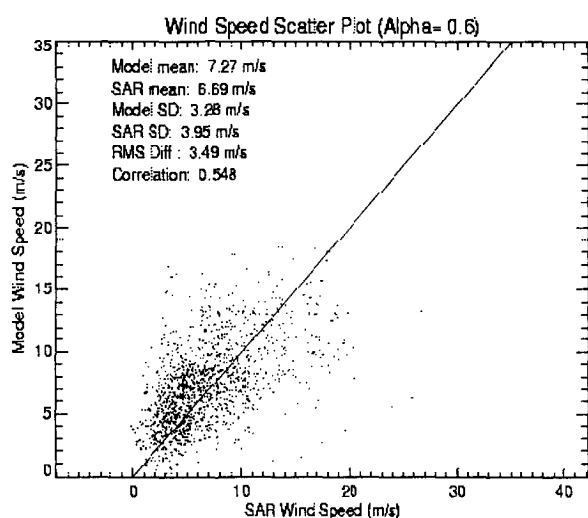
A validation system has been developed such that for each calibrated SAR image containing a meteorological buoy, the simultaneous buoy measurements ( $\pm 30$  minutes) for the SAR image are extracted. A SAR wind image and SAR wind vectors are then processed from the calibrated SAR image. Finally, the wind measurements calculated from the SAR image at the buoy locations are extracted together with the buoy report to form a matchup file. In addition, the APL SAR winds are compared with the Navy NOGAPS meteorological model winds.

##### 4.1 VALIDATION OF APL WIND IMAGES USING THE NAVY NOGAPS NUMERICAL MODEL

As a preliminary validation of the APL wind product, a comparison is made with the NOGAPS model winds that provide the directional information for the APL

model. The NOGAPS wind speeds are compared with the SAR wind speeds to detect any systematic errors. Figure 4 is a scatter plot of model wind speed derived from approximately 200 ScanSAR Wide B images versus SAR wind speed. The RMS difference is 3.49 m/s, with the mean of the SAR winds being 0.58 m/s lower than the model winds.

Figure 4. Comparison between the APL wind product with NOGAPS model wind.



#### 4.2 VALIDATION OF THE ERIM WIND VECTORS USING NOAA MOORED METEOROLOGICAL BUOY DATA

Ten-meter winds measured by NOAA moored buoys are used as ground truth. The wind vector derived from RADARSAT SAR using the ERIM algorithms are compared with co-located buoy data. To date only ten matchup points have been used for wind direction comparisons whereas 46 have been used to estimate wind speed errors; wind direction validation utilizing the full 46 matches is currently underway. The wind direction comparison is given in Figure 5. Because of the 180 degree ambiguity in wind direction generated from the ERIM procedure, the error between the estimated and actual wind direction is always defined to be between  $\pm 90$  degrees. Thus the dashed lines in Figure 5 show the region within which the error must be by definition. One can see that the RMSE of the wind direction is 44 degrees with the peak algorithm and 33 degrees with the polynomial algorithm. In general we have found that the polynomial algorithm performs better than the peak algorithm, and routinely use that algorithm.

Figure 5. Comparison between wind direction derived from RADARSAT SAR using the ERIM algorithm and co-located NOAA moored buoy data.

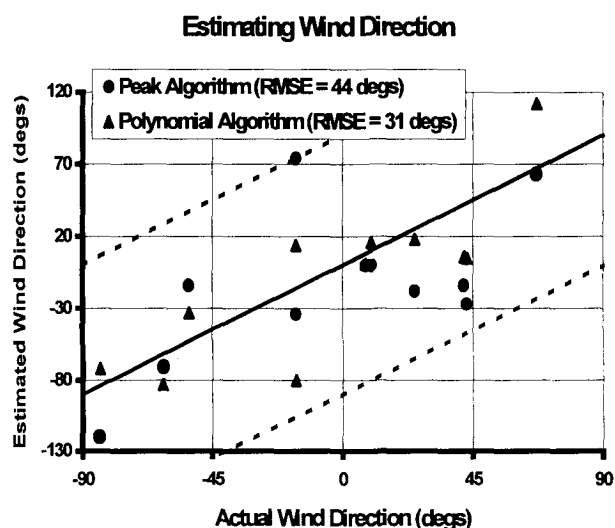
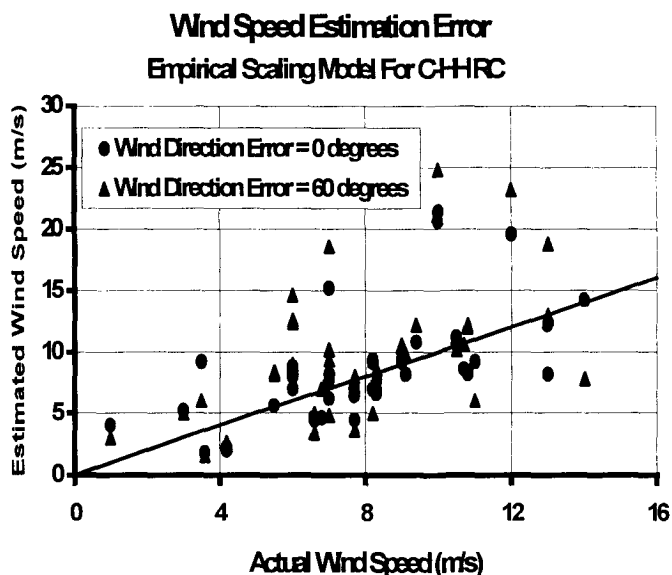


Figure 6 shows the resulting wind speed errors for the full 46 points where we have assumed an average wind direction error of 0 degrees and 60 degrees. For an average direction error of 0 degrees the wind speed RMSE was 3.41 m/s whereas for an average error of 60 degrees (which is much larger than expected) the wind speed RMSE was 4.85 m/s. A full validation for both wind direction and speed is underway, but we anticipate that the final wind speed RMSE will be close to 3.5 m/s.

Figure 6. Wind speed errors for the ERIM procedure for two different wind direction errors.



## 5. SUMMARY

Two wind retrieval procedures have been developed by The Johns Hopkins University Applied Physics Laboratory (APL procedure) and ERIM International Inc. (ERIM procedure) in support of the Alaska SAR Demonstration project. In this paper we give brief outlines of these models and some preliminary validation results. The APL procedure wind speed was compared with model wind measurements, and the RMSE in wind speed is about 3.49m/s. The ERIM model winds were compared with buoy winds and the RMS error in wind direction was between 31 and 44 degrees. The RMS error in wind speed was around 3.5 m/s.

## 6. ACKNOWLEDGEMENTS

Funding for the Alaska SAR Demonstration and research preceding the demonstration was provided by the NOAA/NESDIS Ocean Remote Sensing Program. RADARSAT data were provided under the NASA RADARSAT Applications Development and Research Opportunity (ADRO) Project 396.

## 7. REFERENCES

- [1] Fetterer, F, D. Gineris, and C. Wackerman, "Validating a wind Algorithm for ERS-1 SAR," *IEEE Trans. Geosci. and Remote Sens.*, 36, 479-492, 1998.
- [2] Monaldo, F., and R. Beal, "RADARSAT applications demonstration in the Gulf of Alaska," *Johns Hopkins University Applied Physics Laboratory Tech. Rep.*, SRO-99-07, PP. 1-18, 1999.
- [3] Romeiser, R. and V. Wismann, "An improved composite surface model for the radar backscattering cross section of the ocean surface 1. Theory of the model and optimization/validation by scatterometer data," *J. G. R.*, Vol. 102, No. C11, 25,237-25,250, 1997.
- [4] Stoffelen, A and D. L. T. Anderson, "Wind retrieval and ERS scatterometer radar backscatter measurements", *Adv. Space Res.*, 13, 53-60, 1993
- [5] Thompson, D. R., T. M. Elfouhaily, and B. Chapron, "Polarization ratio for microwave backscattering from the ocean surface at low to moderate incidence angles," *Proc. 1998 International Geoscience and Remote Sensing Symposium*, 1671-1673, 1998.
- [6] Valenzuela, G.R., "Theories for the interaction of electromagnetic and ocean waves – A review," *Boundary Layer Meteorol.*, 13, 61-85, 1978.
- [7] Wackerman, C., "Incorporating hydrodynamic effects into an analytic two-scale model to predict C-VV and C-HH observation," Unpublished, 1999.
- [8] Wismann, V., "A C-band scatterometer model derived from data obtained during the ERS-1 calibration/validation campaign," *Proc. First ERS-1 Symposium*, Cannes, 55-59, 1992.



## Validation of Envisat ASAR Wave Mode Level 1b and Level 2 Products Using ERS SAR Data

by

Harald Johnsen<sup>1</sup>, Geir Engen<sup>1</sup>, Kjell-Arild Høgda<sup>1</sup>, Bertrand Chapron<sup>2</sup>, Yves-Louis Desnos<sup>3</sup>

<sup>1</sup> NORUT IT, N-9005 Tromsø, Norway, tlf: 4777629400, e-mail: harald.johnsen@itek.norut.no

<sup>2</sup> Dpt. DRO/Océanographie Spatiale, IFREMER, BP 70, 29280 Plouzane, France, e-mail: bchapron@ifremer.fr

<sup>3</sup> ESA/ESTEC, Box 299, 2200 AG Noordwijk, The Netherlands, e-mail: ydesnos@estec.esa.nl

### ABSTRACT

A pre-liminary validation of the ASAR Level 1b (cross spectra) product and the Level 2 (wave spectra retrieval) algorithm have been conducted using ERS Wave and Image Mode SLC data collocated with in-situ measurements and numerical wave model. The objectives of the validation have been to optimize the algorithms, the processing settings and to predict the performance of the new products and algorithms. New methodologies for wind retrieval have also been considered and tested against in-situ observations.

For the Level 1b product, the main focus of the validation test has been on the resolution of the propagation direction and the establishment of RMS errors (as compared to simulated spectra) for the main swell spectral parameters. The main result is that when ocean swell system was detected the propagation ambiguity was resolved in 93% of the cases. The spectral peak wavelength and propagation direction RMS were 50m and 40°, respectively. The mean peak wavelength was for this data set 265m, and the average azimuth cut-off value was 256m. We conclude that the cross spectra product of the ENVISAT Wave Mode is superior to the existing ERS Wave Mode product in terms of signal-to-clutter ratio and propagation ambiguity.

For the Level 2 development the pre-liminary results shows that a consistent inversion scheme can be formulated without using any apriori information or first guess spectrum. Initial validation results shows that the wave spectrum within the SAR domain are unambiguously resolved in 80% of the cases processed. In the remaining 20% of the cases, ocean swell is not present (does not exist or not detected by the SAR) or directional informations not resolved. The Level 2 development also shows that wind related informations can be achieved from the SAR Image Mode SLC data, and new methodologies are proposed and tested versus in-situ observations.

### INTRODUCTION

The ERS global wave spectra measurements will be extended and improved by the ENVISAT mission scheduled for launch in year 2000. The improvements will be achieved by better coverage, greater flexibility and new products. The limitations in the existing ERS Wave Mode products require the wave retrieval schemes to

extensively rely on in-situ wind and wave informations [9]. The Envisat ASAR Wave Mode, however, will provide the users with a new wave mode product based on the cross spectra methodology. This has lead to the possibility of developing an improved Level 2 algorithm available for the user community.

The main advantages of Level 1 products are expected to be the 180 degree propagation ambiguity, the speckle bias compensation and improved SNR. The expected performance of the ENVISAT Wave Mode cross spectra product has been set by using more than 70 ERS SLC images collocated with in-situ data from the North Atlantic and North Sea, and a limited number of ASAR Wave Mode Level 1b products generated from ERS Wave Mode data. The data are used to simulate the performance of, and to optimize the processing of ENVISAT ASAR Wave Mode data. The optimization and performance test were done by simulating Envisat ASAR SLC imaggettes by means of ERS SLC image mode data, generation of the cross spectra product, and inversion. The collocated in-situ wave and wind informations allow us to compute the corresponding synthetic cross spectra product for comparison. The in-situ data consist of directional wave spectra and wind vector, and were provided by either wave models, directional buoys, platform wave radar or weather ship observations. The SAR data were acquired under various wind and sea state conditions ranging from 2 - 20 m/s wind speed and 1.2 - 7.8 m significant waveheight. The main focus of the performance test has been on the resolution of the propagation direction and the establishment of RMS errors for the main swell spectral parameters, and to verify the Level 2 algorithm.

### DATA ANALYSIS

The data used in the analysis are ERS-1/2 Image Mode and ERS-2 Wave Mode SLC data, collocated with wave model, or buoy or in-situ observations. The ERS data were provided by ESA and the in-situ data by the Norwegian Meteorological Institute, IFREMER, and Oceanor Ltd. The Image Mode data were collected mainly in the period 1993-1995, 1997-1999 from the Norwegian Sea and the North Sea. The Wave Mode data were collected during 1998 globally.

## Image Mode Analysis

Procedure for analyzing the Image Mode data:

- simulation of Envisat ASAR SLC imagerettes from ERS SLC Image Mode Data
- processing of cross-spectra from the simulated Envisat ASAR SLC imagerettes using the ASAR software [1], [3]
- simulation of cross-spectra from collocated ocean wave spectra using in-house simulation software [2]
- comparison of observed and simulated cross-spectra and Level 1b processing optimization
- development and testing of Level 2 algorithm and new wind retrieval methodologies

## Wave Mode Data Analysis

- analysis of Envisat ASAR Level 1b product generated from ERS Wave Mode data
- spectral and propagation characteristics

The cross spectra processing is illustrated in Figure 1 showing the look filters within the azimuth bandwidth.

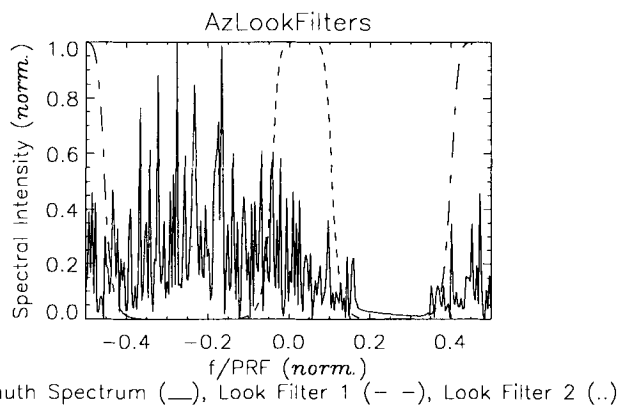


Figure 1. Optimal look filter selection for ASAR Wave Mode Level 1b processing. Filter bandwidth  $\sigma = 0.18\text{PRF}$ , and look separation  $\Delta f = |f_{\text{bw}}/f_{\text{PRF}} - (7/4)\sigma|$  corresponding to 250Hz and 0.40sec, respectively. Here  $f_{\text{bw}}$  is the azimuth bandwidth and  $f_{\text{PRF}}$  is pulse-repetition frequency.

## RESULTS

### Level 1b Validation

#### Image Mode Data

One example of Envisat ASAR Wave Mode cross spectra generated from ERS Image Mode SLC image, and the corresponding spectra simulated using the wave model (WINCH) is shown in Figure 2. Such data are used to establish the performance of the Level 1b processing that was the basis for generating the ASAR Level 1b products from the ERS Wave Mode data.

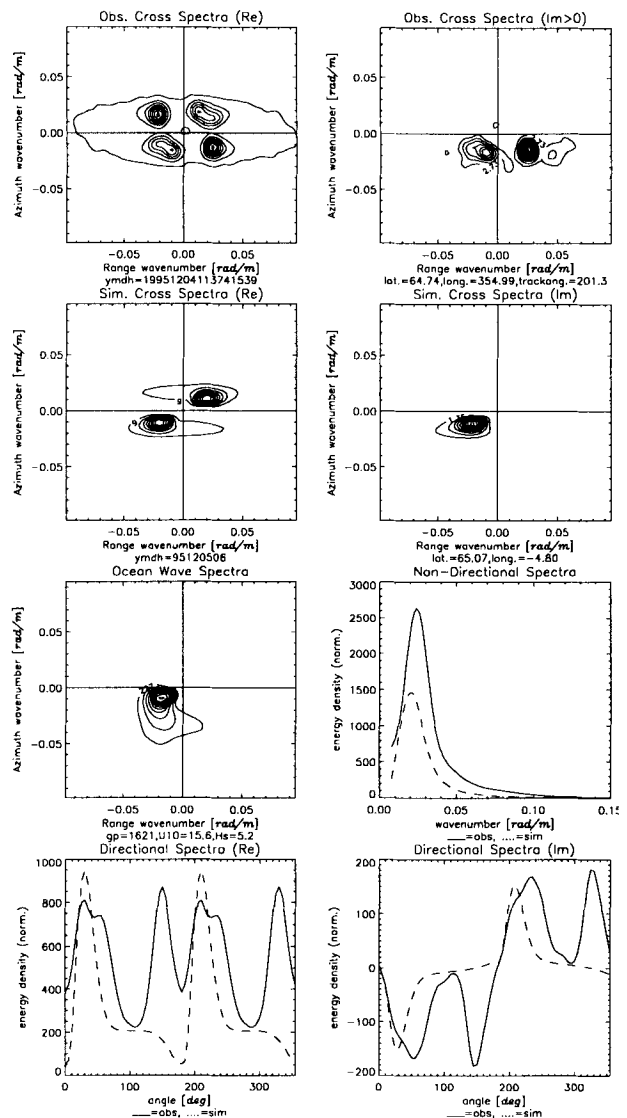


Figure 2. ASAR Wave Mode cross spectra processed from ERS SLC data together with cross spectra simulated using collocate wave model spectra. Non-directional and directional spectra are also shown.

In Figure 2 the SAR detects two wave systems while the wave model predicts only one of them. Results as shown in Figure 2 are generated from about 70 SLC scenes and used to establish RMS error and performance statistics as summarized below:

- Swell system detected, and propagation ambiguity resolved in 80% of the cases
- Swell system detected, but propagation ambiguity not resolved in 7% of the cases
- No swell system detected, and no swell predicted in 13% of the cases
- No swell system detected, but predicted in 2% of the cases
- Input data statistics outside confidence interval in 1.5% of the cases

The clutter values were in the range 1.5393E-8 to 1.2153E-7, with an average value of 5.8785E-8. The imaginary and real peak values were on average 7.0E-5 and 3.5E-4, respectively.

The mean peak wavelength was 265m, and the average azimuth cut-off value was 256m.

For those data sets where collocated wave spectra are available, the RMS error of the measured spectral parameters versus the simulated are as follows:

- Spectral Peak Wavelength RMS = 50m
- Spectral Peak Propagation Direction RMS = 40°
- Spectral Peak Phase Value RMS = 0.10 rad

It is concluded that the overall performance is good.

#### Wave Mode Data

A limited number of ERS Wave Mode data were processed into ASAR Level 1b product at ESA/ERSRIN collocated with Scatterometer observations. The results of the analysis is tabulated in Table 1.

Table 1. Cross spectra parameters of the ASAR\_WVI\_1b products generated from ERS Wave Mode data

YMDH	$\langle \lambda \rangle$ m	$\lambda_{\min}$ m	$\lambda_{\max}$ m	$\langle \phi \rangle$ deg	$\phi_{\min}$ deg	$\phi_{\max}$ deg	$\langle \lambda_c \rangle$ m
98030221	113	105	121	267	260	270	242
98030807	137	130	139	268	260	275	361
98030808	110	98	150	101	95	110	240
98039809	227	197	261	242	230	260	200
98030915	129	121	130	265	260	270	335
98031220	96	74	113	269	260	275	297
98031320	250	243	265	230	225	235	220
98031409	361	345	370	219	205	235	262
98031719	224	212	243	98	90	100	306

In Table 1  $\langle \lambda \rangle$  = average peak wavelength,  $\lambda_{\min}$  = minimum peak wavelength,  $\lambda_{\max}$  = maximum peak wavelength,  $\langle \phi \rangle$  = average peak wave direction,  $\phi_{\min}$  = minimum peak wave direction,  $\phi_{\max}$  = maximum peak wave direction, and  $\langle \lambda_c \rangle$  = average azimuth cut-off wavelength, of each of the data sets. Each of the data sets contained 6 or 5 spectra, separated a distance of 200km along track.

The overall performance of the Wave Mode generated Level 1b products was that in 75% of the cases, wave systems are detected and propagation direction resolved. In 18% of the cases no wave systems are detected, and in 7% of the cases wave systems are detected but the propagation direction not resolved.

We concluded that the preliminary analysis of the Wave Mode data shows that the Level 1b products performs

well in producing unique wave spectral and propagation characteristics within the SAR imaging domain.

## Level 2 Development

### Wave Retrieval Algorithm

A retrieval algorithm generally attempts to reconstruct the ocean wave spectrum by minimizing the difference between its corresponding theoretical SAR spectrum (obtained with a forward transformation) and the satellite observation. The exact derivative of the nonlinear transform being to cumbersome to carry out, most of the inversion schemes partially ignore the complete non linear mapping and mostly use the simplifying gradient of a so-called optimized SAR quasi-linear transform that best matches the full non linear transform.

After the first inversion algorithm proposed in 1991[8], improved and/or alternative methods have been developed [9], [10]. Common to these are that they require an a priori guess of the wave spectrum. The most recent inversion algorithm is based on separating the retrieval scheme into two steps [11]: one for the wind sea part of the spectrum, the other for the swell contribution. This algorithm does not require any a priori wave spectrum but only an estimate of the local wind vector. None of these algorithms are at present designed for utilizing the complex cross spectra that will be available from the Envisat mission, and non of them incorporate backscatter models.

The philosophy of the Level 2 development [12] is to design an wave retrieval algorithm that does not necessarily require apriori information. The basic idea is to separate the retrieval scheme into two steps: one for the non-linear part of the spectrum, the other for the quasi-linear part. The idea is then to estimate the non-linear part and then to remove it from the observed cross spectra. The remaining part is then the quasi-linear contribution which easily can be solved with respect to the swell spectrum if the RAR MTF is known. The procedure is as follows step wise:

- remove the window function (any instrumental effects) of the SLC data, define the look filters, and extract independent looks (at least two) from the available bandwidth
- compute the various cross covariance functions and cross spectra
- compute the system transfer function

The cross spectrum is then inverted with respect to the ocean swell wave spectrum by the following steps:

- provide an estimate of wind field or use the backscatter from the image, and compute the RAR MTF
- measure the non-linear azimuth spectral (asymptotic) width from the cross spectra.

- estimate the correct quasi-linear azimuth cut-off (variance of azimuth orbital velocity shift) from a set of values by fitting the corresponding tabulated non-linear profiles to the observed cross spectra profile.

- select the tabulated non-linear spectra corresponding to the estimated quasi-linear azimuth cut-off value and the measured spectral width.

- express the cross spectrum as a sum of the non-linear approximation and the well known quasi-linear part given by the exponential cut-off factor, transfer functions and swell spectrum

- remove the non-linear contribution and solve the quasi-linear part linearly with respect to the swell spectrum inside the SAR imaging domain

The computation of the non-linear contribution to the SAR image cross spectrum will be based on pre-computed look-up tables. This is done in order to simplify the algorithm and to decrease the processing load. The estimation of the non-linear part is the crucial point of the algorithm. The tabulated non-linear part of spectra is generated for a wide range of wind sea parameters using a full non-linear implementation of the SAR transform using log-polar fourier transform.

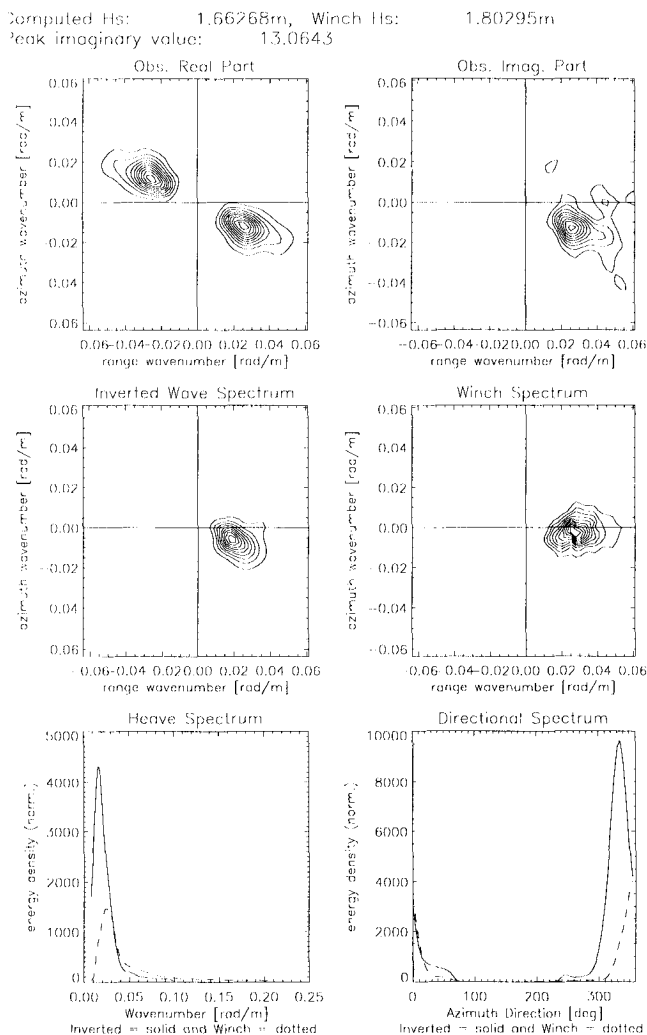


Figure 3. Example of inversion of ERS cross spectrum with respect to ocean wave spectrum within the SAR imaging domain. The collocated wave model spectrum is shown for comparison.

About 40 cross spectra generated from imagettes from ERS Image Mode SLC data were inverted using the approach above, and the overall results can be summarized as follows:

- The swell spectrum within the SAR domain are unambiguously resolved in 80% of the cases processed. In the remaining 20% of the cases, ocean swell is not present (does not exist or not detected by the SAR) or directional informations not resolved.

- The important point for correct inversion is the prediction/measurement of the non-linear part of the cross spectra, the non-linear asymptotic spectral width, and the variance of azimuth orbital velocity shift

### Wind Retrieval

Access to well calibrated SAR images i.e. radar cross section images, has led to an increased research activity of utilizing the SAR for high-resolution wind field measurements. The near surface wind speed may be estimated (on scales 1-10km) from SAR images using a scatterometer empirically derived radar cross section model function (CMOD)[5], provided an estimate of the wind direction is known. The wind direction is estimated either by identifying shadowing effects for near shore scenes or by analyzing very small wavenumber spectral component orientations. However, investigations show that wind streaks are only observed in roughly 40% of the SAR images [6]. Furthermore, these method will obviously suffer from non-wind low wavenumber spectral signature such as in the presence of slicks.

It has also been demonstrated that another source of spectral information exist to further help to complement SAR scatterometry-like analysis [7]. This is based on analysis of the observed spectral azimuth cut-off which again is caused by the wind generated wave random motions. However, the SAR cut-off parameter estimates are also carrying long wave orbital motion information, and that biases may be caused by the inertia of gravity waves in the case of fetch limited or relaxation conditions, as well as in the presence of large swell systems.

We propose a new look on the SAR wind field retrieval by considering the time decorrelation and phase spectra computed from inter-look processing of SLC data. The methods shown below have been developed using advanced simulation tools. The results from the real data are estimated from an area of 16kmx20km.

### Wind Direction

Assume we have computed the cross spectra,  $P(k, t)$  from the single-look complex images. The phase spectra is then obtained by smoothing the cross spectra and then computing the ratio as:

$$\Phi(\underline{k}) = \text{atan} \left\{ \frac{\text{Im}\{P(\underline{k}, t)\}}{\text{Re}\{P(\underline{k}, t)\}} \right\} \quad (1)$$

The wind direction will be given as the normal to the line separating the negative and the positive part of the phase plane,  $\Phi$ . The fitting to the phase plane with respect to the angle  $\varphi_w$  is given as:

$$\min_{\underline{a} \in \mathfrak{R}} \left\{ \int d\underline{k} |\psi(\underline{k}) - \underline{a} \cdot \underline{k}|^2 W_1(\underline{k}) \right\} \quad (2)$$

$$\varphi_w = \text{atan} \frac{a_y}{a_x} \quad (3)$$

The angle,  $\varphi_w$  is then proposed to provide an ambiguity free estimate of the wind direction relative to the positive range axis. The use of phase spectra requires that the SAR processing is precisely done since the phase ratio is used. Example of ERS-2 cross spectra and corresponding phase spectra is shown in Figure 4.

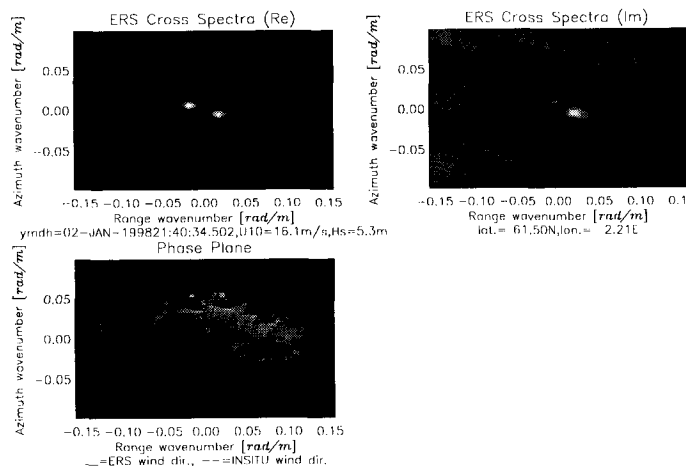


Figure 4. Example of ERS-2 cross spectra (upper plots) and the corresponding phase spectra (lower plot). The lines in the phase spectra indicate the SAR and the in-situ measured wind direction.

Figure 4 shows a successful retrieval of wind speed from the phase spectra. Note that the extracted wind direction is not aligned with the direction of the main swell wave system (white spot) detected by the SAR. Statistics from comparison with in-situ measurements from the Gullfaks C platform in the Norwegian Sea is shown in Figure 5.

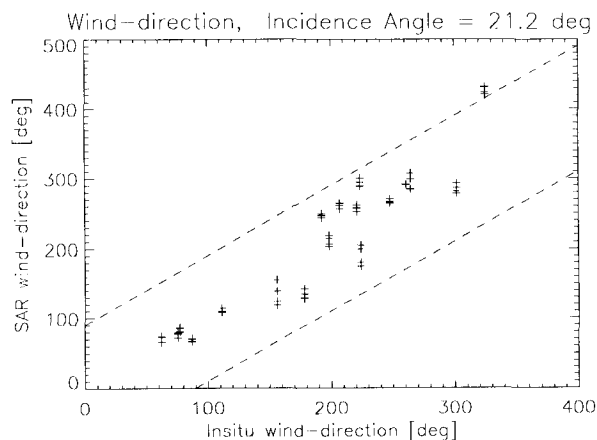


Figure 5. Wind direction derived from ERS SAR SLC images versus in-situ measured wind direction.

Figure 5 shows a good correlation between SAR and in-situ measured wind direction. The RMS error is around 35 degrees.

#### Wind Speed

The azimuth cut-off estimator estimate the width of the ratio of the azimuth cross spectra profiles obtained at two different look separation times. The idea is that during the short time separation the difference in azimuth spectral width can only be caused by the very small waves, which again are highly correlated to the wind field. This method actually measure the variability of the wind field, and is expected to be less dependent of the wind direction than the backscatter.

The ratio of the spectra is given as:

$$r(\underline{k}) = \frac{|P(\underline{k}, 2t)|}{|P(\underline{k}, t)|} \quad (4)$$

where  $P(\underline{k}, 2t)$  and  $P(\underline{k}, t)$  are cross spectra computed at two different look separation times, a large and a small separation.

The spectral ratio can be fitted to theoretical functional form using the relation:

$$\min_{b \in \mathfrak{R}} \left\{ \int d\underline{k} |P(\underline{k}, 2t) - g_b(\underline{k})P(\underline{k}, t)|^2 W_2(\underline{k}) \right\} \quad (5)$$

where

$$g_b = e^{-k_y^2/b^2} (1 + k_y^2/b^2) \quad (6)$$

The fitting to the spectral ratio is done with respect to the parameter,  $b$ , and the wind speed is related to this parameter. Examples of azimuth cut-off ratio

(Equation 4) obtained from ERS-2 Image Mode data are shown in Figure 6 for different wind speeds.

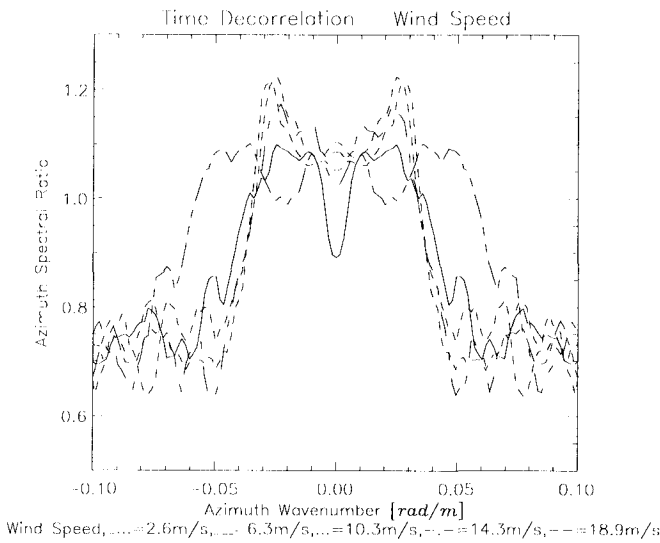


Figure 6. Azimuth power ratio profiles obtained from ERS cross spectra (real part) for different wind speeds.

Statistics obtained by fitting such curves to Equation 6 is plotted in Figure 7 versus in-situ measured wind speed.

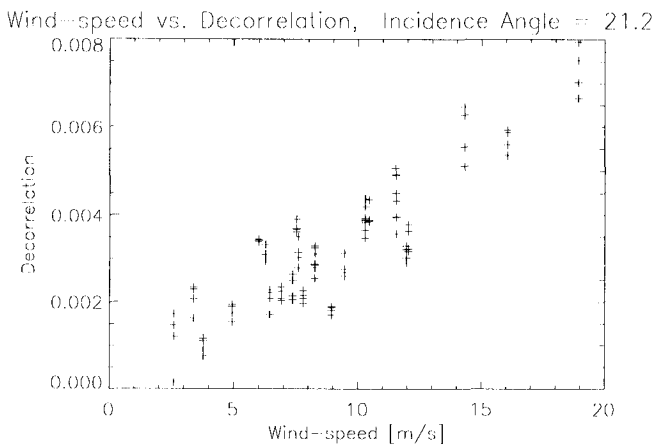


Figure 7. Temporal decorrelation measured versus in-situ measured wind speed.

Figure 7 shows a good correlation between the time decorrelation measured using two look separation times and the in-situ wind speed.

### CONCLUSION

The ASAR Wave Mode Level 1b cross spectra product is shown to be superior to the existing ERS Wave Mode product. The main advantages are achieved for the SNR and the resolution of the 180 degree propagation ambiguity. The latter also makes the product well suited for obtaining a unique solution for the underlying swell

spectrum. In 80% of the cases waves systems are detected and a unique solution of the wave inversion problem is achievable without using external informations.

### REFERENCES

- [1] The Envisat ASAR Wave Mode Cross Spectra Algorithm - Software Requirements Document, NORUT IT report: ASAR-D6-NT-01, Version 1.3.6, 27 June 1997.
- [2] G. Engen, H. Johnsen; SAR-Ocean Wave Inversion Using Image Cross Spectra, *IEEE Transc. on Geo. Science and Remote Sensing*, Vol. 33, No. 4, pp.1047-1056, 1995.
- [3] Johnsen H., Engen G., Lauknes I., The Envisat ASAR Wave Mode Cross Spectra Algorithm, *Proc. CEOS SAR Workshop*, WPP-138, ESTEC 3-6 February 1998.
- [4] Hasselmann, S., C. Brüning, K. Hasselmann, P. Heimbach, An improved algorithm for the retrieval of ocean wave spectra from synthetic aperture image spectra. *Journal of Geophysical Research*, 101(C7):16615-16629, 1996.
- [5] Stoffelen A., Anderson D.L.T. (1993), ERS-1 Scatterometer data characteristics and wind retrieval skill, *Adv. Space Res.*, 13, 553-560.
- [6] Vachon P.W., Dobson F.W., (1996), Validation of wind vector retrieval from ERS-1 SAR images over the ocean, *The Global Atmos. and Ocean Sys.*, 5, 177-187.
- [7] Chapron B., Elfouhaily T., Quilfen Y., (1994), Speckle wind speed algorithm from the ERS-1 SAR wave mode images, *CERSAT News*, CERSAT, BP 70, Plouzane, France
- [8] K. Hasselmann, S. Hasselmann, "On the nonlinear mapping of an ocean wave spectrum into a synthetic aperture radar image spectrum and its inversion", *J. Geophys. Res.*, Vol.96, No. C6, pp.10713-10729, 1991
- [9] S. Hasselmann, C. Brüning, K. Hasselmann, P. Heimbach, An improved algorithm for the retrieval of ocean wave spectra from SAR image spectra. *J. Geophys. Res.*, 101, 16615-16629.
- [10] L.A. Breivik, M. Reistad, H. Schyberg, J. Sunde, H.E. Krogstad, H. Johnsen, "Assimilation of ERS SAR wave spectra in an operational wave model", *J. Geophys. Res.*, Vol.103, No. C4, pp.7887-7900, 1998
- [11] K. Mastenbroek, "Ocean Wave Spectra from Space-Born SAR", to be published, 1998.
- [12] Envisat ASAR Level 2 Wave Mode Product Algorithm Specification - Software Requirements Document, Norut IT Doc. No. IT544/5-98, Ver. 1.0, October 1999.

## Sea Ice Thickness from Kinematics

R. Kwok and B. Holt  
 Jet Propulsion Laboratory  
 California Institute of Technology  
 MS 300-235  
 4800 Oak Grove Drive  
 Pasadena, California 91109  
 USA

Tel: (818) 354-5614 Fax: (818) 393-3077 email: Ronald.Kwok@jpl.nasa.gov

### ABSTRACT

High resolution 3-day surveys of the Arctic Ocean are currently being obtained using the Canadian RADARSAT synthetic aperture radar with its wide-swath ScanSAR mode. For the first time, we can produce basin-scale estimates of sea ice age and thickness from Lagrangian observations of ice motion derived from sequential SAR images of the Arctic Ocean. The deformation of material elements (cells) on the SAR imagery is computed using strain rates from ice motion. From the record of deformation of each cell, we estimate the ice age and thickness. In the winter, open water and thin ice are created when there is a positive change in area while negative area changes are associated with ridging. The deformation of the ice cover is sampled by cells with an initial area of approximately 10 km by 10 km. More than 60,000 of cells are used to cover the entire Arctic Ocean. These geophysical products can be put to a variety of uses: analyzing new ice climatologies, testing ice models or new ideas about sea ice rheology, and for assimilating into sea ice models.

Thus far, we have produced estimates of sea ice deformation, thickness and age from five months of SAR data of the Arctic Ocean (November 1996 through March 1997). These data products are available on a web site at the Jet Propulsion Laboratory (<http://www-radar.jpl.nasa.gov/rgps>). Here, we describe this data set, their use for studies of the sea ice cover and the potential of using ENVISAT to extend these observations into the future.

### INTRODUCTION

The scientific goal of remote sensing of the polar regions is to provide data sets to improve our current understanding of the impact of sea ice on climate and to monitor changes in the Arctic Ocean sea ice cover. Interactions between sea-ice, ocean and atmosphere in the polar regions strongly affect the Earth's climate. Sea ice growth, movement and decay affect energy and mass

balance of the polar ocean system. The surface heat and brine fluxes associated with sea-ice growth contribute significantly to convection of the ocean and thermohaline circulation. Snow covered sea-ice reflects most of the incident solar radiation back into space, while fresh water fluxes associated with melting ice serve as stabilizing elements in the circulation of the North Atlantic waters. Processes along the ice margin and coastlines participate in water-mass formation, upwelling, convection sediment transport and other phenomena.

Global climate models project the largest greenhouse warming in the polar regions [e.g. *Kattenberg et al.*, 1996]. The high-latitude sensitivity displayed by existing climate models has been attributed to positive feedbacks involving surface albedo and reduced sea ice extent and thickness [*Ingram et al.*, 1989; *Rind et al.*, 1995]. Recent years have seen significant changes in the sea level pressure in the Arctic (e.g., *Walsh et al.*, 1996). Correspondingly, buoy data and satellite ice motion data from the 1990s indicate a weakened Beaufort Gyre and a migration of the Transpolar Drift Stream [*Rigor*, per. comm., 1999; *Kwok*, 1999] and variability in ice export that is connected to the North Atlantic Oscillation [*Kwok and Rothrock*, 1999]. A decreasing trend in the Arctic Ocean ice extent is observed in satellite passive microwave observations [*Parkinson et al.*, 1999]. Hydrographic data from recent submarine and icebreaker cruises reveal large-scale changes in the structure of the Arctic upper ocean (e.g., *Steele and Boyd* 1998; *Morison et al.*, 1998). In fact, model simulations show regime shifts in the general surface ocean circulation [*Proshutinsky and Johnson*, 1997; *Zhang et al.* 1998] and the circulation of river water [*Maslowski*, per. comm., 1998]. These changes would undoubtedly be reflected in the surface heat and mass balance of the Arctic Ocean. Understanding and modeling these phenomena require information of sea-ice motion, thickness and concentration.

The remote sensing data set described here addresses the requirement of ice motion and ice thickness observations. The technique (described below) utilizes large volumes sequential SAR imagery. From the Lagrangian observations of sea ice motion, we derive

ice age and ice thickness histograms of the thin ice fraction of the ice cover in the winter. In the summer, we also estimate the open water fraction. The time of melt-onset in the spring and freeze-up in the late fall are estimated from changes in backscatter signature of the ice cover.

These algorithms are implemented in the RADARSAT Geophysical Processor System (RGPS) - a system dedicated to the analysis of SAR data of sea ice collected by the Canadian RADARSAT satellite. RADARSAT was launched in November of 1995 into a 24-day repeat cycle. This orbit configuration and the wide swath (500 km) ScanSAR mode allow the repeat coverage of the Arctic Ocean every 3 to 7 days. To support the data needs of the RGPS, we have been using this mode, termed ScanSAR, to acquire repeat coverage of the Arctic Ocean since November of 1996. Over a 24-day repeat cycle of the satellite, we have close to eight observations of the western Arctic Ocean within the Alaska SAR Facility (ASF) Reception mask in Fairbanks, Alaska. The repeat coverage of the Eurasian Basin is less frequent (6-days) due to the additional cost of RADARSAT data down-linked at the Tromsø Satellite Station in Norway. We expect to continue this acquisition process over the life of the RADARSAT mission. The input SAR imagery is processed to a spatial resolution of approximately 100 m by 100 m, and is calibrated and archived at ASF.

## MOTION, AGE AND THICKNESS

This new method estimates ice age and thickness from repeated observations of Lagrangian elements or cells of sea ice in sequential SAR imagery [Kwok *et al.*, 1995]. Fig. 1 shows the time series of observations of one cell within a matrix of such cells, strain ellipses describing the deformation, graphs of the history of cell area, and the thin ice coverage within that cell at the end of a 41-day period. Line segments connecting the four vertices of a cell define its boundaries. The drift and deformation of a cell over time are obtained by tracking the displacement of its vertices in the SAR imagery. The motion tracking procedure is described in Kwok *et al.* (1995). The underlying deformation of the cell evolved from a circle on 8 November 1996 through a series of increasingly eccentric ellipses. The steady evolution of the ellipse, or equivalently the nearly monotonic nature of the invariants, are remarkable. This sequence of observations demonstrates that lead ice controls the mechanical behavior through its orientation and yield strength. This orientation dependence gives the ice cover an anisotropic character.

The age histogram of the ice in a cell is computed from the temporal record of area changes. An age histogram

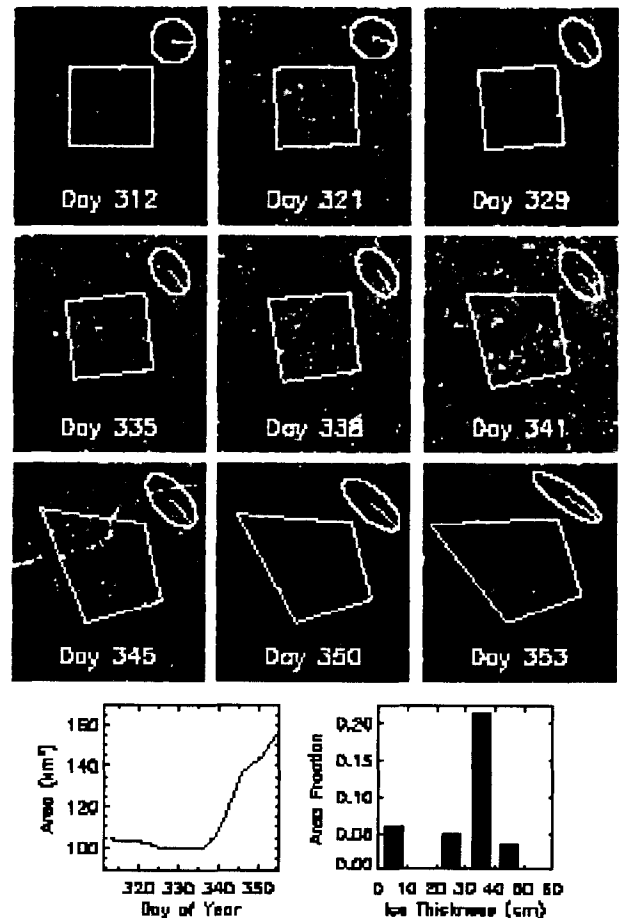


Figure 1. The deformation of a 10 km by 10 km cell over a 41-day period. The record of area changes reflect the opening of the lead running through the cell. The strain ellipses are computed from strain rates.

of sea ice specifies the fractional area covered by ice of different chronological ages. To construct this histogram from sequential observations, we follow the steps below. Every time a new observation is available, we interpret a positive area change as the creation of an area of open water. New ice is assumed to grow over this area immediately after opening. The uncertainty of the ice age occupying this area is dependent on the time interval between observations. This age range is recorded as a new age category in the histogram. At the same time a new category is introduced, existing age categories are 'aged' by the same time interval. In Fig. 1, this procedure created five ice age categories from the sequence of positive area changes since Day 335. A negative change is assumed to have ridged the youngest ice in the cell, reducing its area. The assumption here is that once ridging starts, the deformation tends to be localized in the recently-formed thinner and weaker ice in leads. This area of ridged ice is tracked as a separate category in the age histogram.



Ice age is converted to ice thickness using an empirical ice growth formula. We approximate the growth rate as a function of the number of freezing-degree days (FDD) associated with each age category using Lebedev's parameterization (discussed in *Maykut*, 1986) with  $H = 1.33 F^{0.58}$ , where  $H$  is thickness and  $F$  is the accumulated freezing-degree days of that category. Volume is conserved when ice is ridged. We assume that all ridged ice is five times its original thickness and occupies a quarter of the area [*Parmeter and Coon*, 1972].

We start this scheme at fall freeze-up by covering the entire Arctic Ocean with initial 10 km by 10 km square elements, except near the ice margins where 25 km by 25 km are used. Complete coverage of the Arctic takes approximately 70,000 cells. At start up, the ice age/thickness histograms within the cells are unknown. In the process described, the ice volume created over a season is recorded in the thin ice thickness distribution and the ridge volumes. Since we do not melt ice in our scheme, the procedures above work only during the winter ice growth season. The results provide fine age/thickness resolution of only the young/thin end of the age/thickness distributions, but this is the crucial range that produces the most ice growth, the most turbulent heat flux to the atmosphere and the most salt flux to the ocean.

The backscatter intensity of each SAR sample is used to provide an independent estimate of the multiyear (MY) fraction within each cell. The MY algorithm [*Kwok et al.*, 1995] uses a maximum likelihood classifier and a look-up table of expected backscatter characteristics to assign an image pixel to one of two classes: multiyear ice and first-year ice. We assume that the area of MY ice fraction within a cell remains constant throughout the winter (by definition, no multiyear ice is created). Any anomaly in the classification process due to the backscatter variability of other ice types would show up as transients or spikes. These anomalies are filtered out in the time series of MY fraction estimates in each cell.

## RGPS DATA PRODUCTS

A brief description of the RGPS data product is given below.

*Ice Motion (Lagrangian trajectories).* A regular array of points is defined initially on the first image of a long time series of SAR images and an ice tracker finds the positions of those points in all subsequent images of the series. This product contains a record of the trajectories or an array of position measurements of the 'ice particles' that are located on an initial grid which covers the entire Arctic Ocean. The sampling interval is determined by the available repeat coverage of these

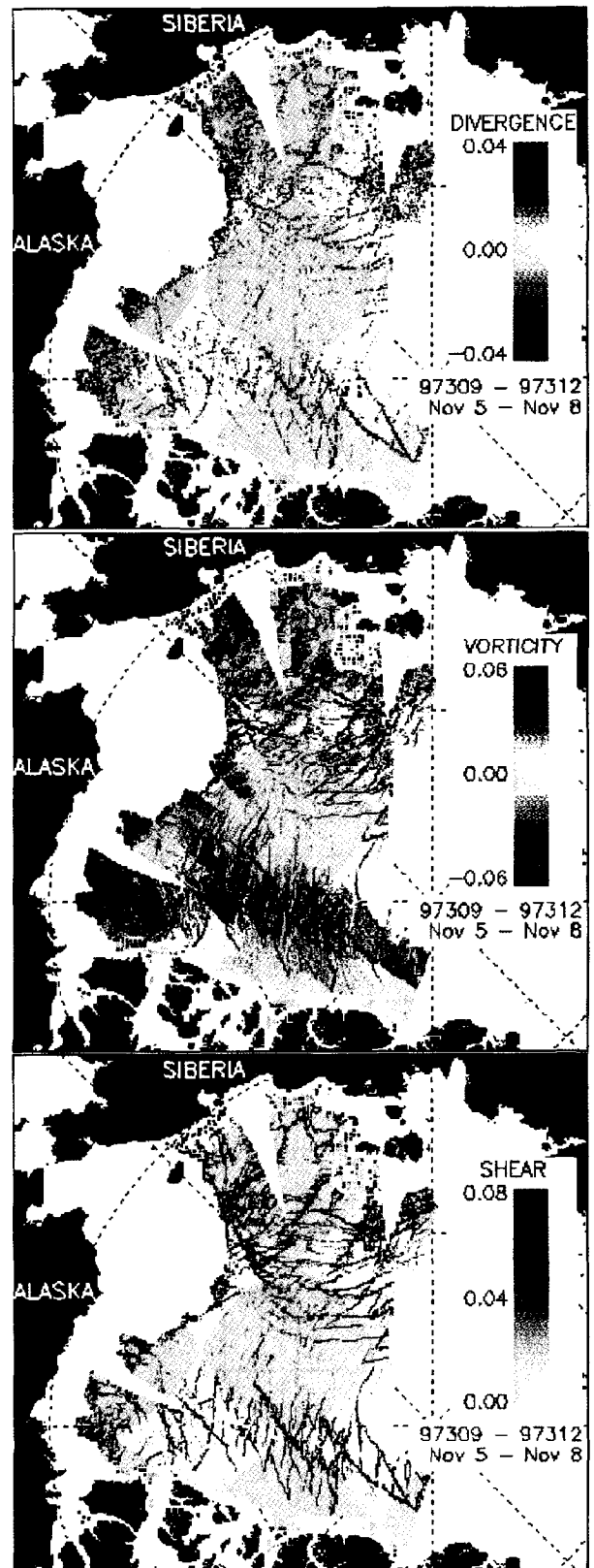


Figure 2. The deformation of the ice cover over three days between Day 309 and 312 in 1997. (a) Divergence. (b) Vorticity. (c) Shear.

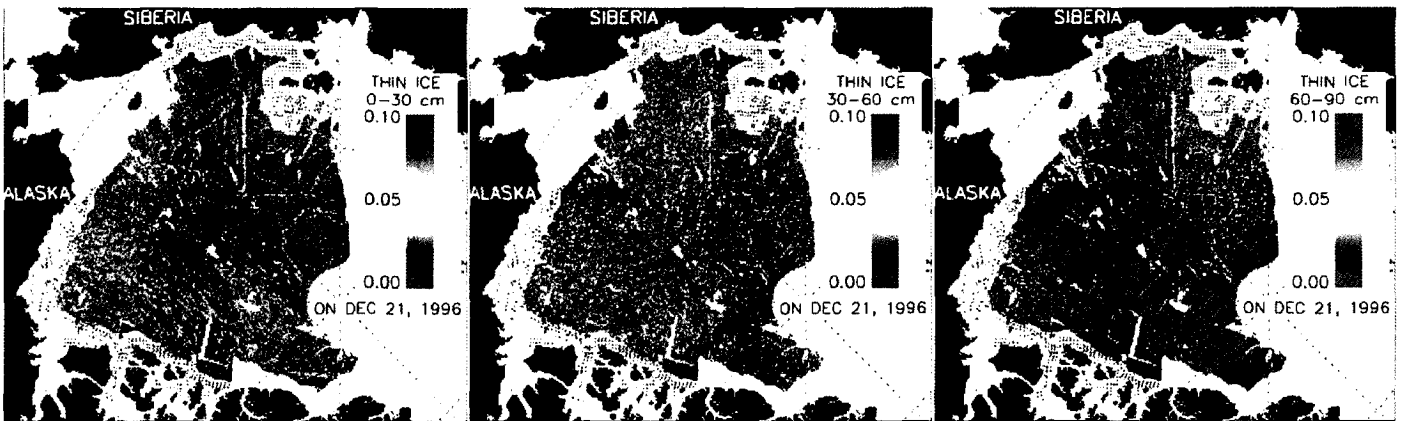


Figure 3. The fractional coverage of thin ice within each grid cell on December 21, 1996.

points by the SAR sensor. The initial grid spacing is 10 km. The accuracy of the position measurements is typically 300m in areas with moderate deformation with higher uncertainties in areas with intense deformation.

**Ice Deformation.** The local deformation of the ice is computed using the velocity gradients at the vertices of the cells. Fig. 2 shows a basin-scale view of the divergence, vorticity, and shear of the ice cover sampled by the RGPS cells. The deformation fields show linear kinematic features (LKF) that characterize the opening, closing, and shear of the ice cover.

**Ice Age Histogram.** The ice age distribution of sea ice specifies the fractional area covered by ice in different age categories as a function of time. This ice age distribution is computed from the field of Lagrangian trajectories described above. The algorithm for determining ice age works only in the winter: the assumption is that there is ice growth in all new leads. It is initialized shortly after fall freeze-up and is operated till the onset of melt. The resolution of age is dependent on the sampling interval of the area of interest. As an example, for a series of images with, say, seven days between successive images, the age classes would be: 0-7 days, 7-14 days, 14-21 days, 21-28 days, ..., first-year ice and multiyear ice. The multiyear ice fraction is obtained with a backscatter-based ice classification algorithm. We keep track of the accumulated freezing-degree days associated with each age class. The surface air temperatures for computing the freezing-degree days are extracted from analyzed air temperature fields. Closings are interpreted as ridging events and the amount of ice that participates in this processes is recorded. This product contains records of local ice age distributions and the accumulated freezing-degree days of each age category within the distributions, and the ridged ice area.

**Ice Thickness Histogram.** The ice thickness distribution specifies the fractional area covered by ice in different

thickness ranges within a given region as a function of time. The ice thickness distribution is estimated from the ice age distribution using an empirical relationship between the accumulated freezing-degree days and ice thickness. The local age distributions are converted to ice thickness distributions and accumulated over large areas to provide regional scale products; A sampling interval of seven days would cause an uncertainty in the thickness of the thinnest ice of about 23cm (if the air temperature were  $-20^{\circ}\text{C}$ ) using Lebedev's parameterization (in Maykut, 1986) of the dependence of ice growth on freezing-degree days. Fig. 3 shows the amount of thin ice in different thickness categories on December 21, 1996. The evolution of the basin scale distribution of thin ice thickness and ridged ice can be seen in the histograms in Fig. 4.

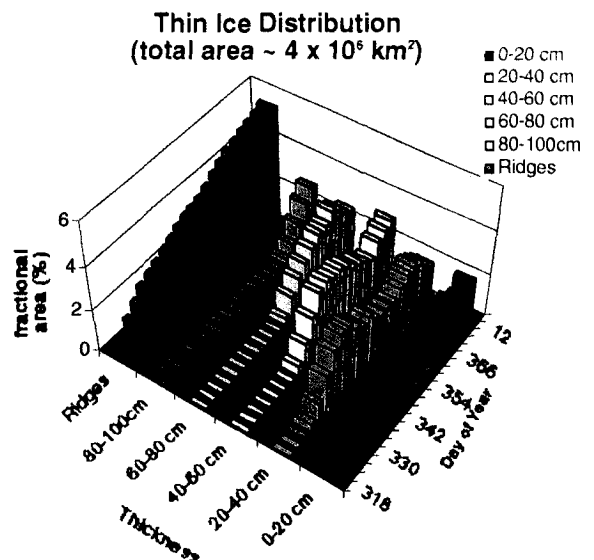


Figure 4. The distribution of thin ice within different thickness ranges and the coverage of ridged ice formed since Day 318.

*Open Water Fraction.* Summer ice conditions are characterized by an open water fraction. The summer open water fraction in a Lagrangian cell (defined by line segments connecting the tiepoints) is estimated from kinematics and backscatter data.

*Backscatter Histogram of Lagrangian cells.* The backscatter histograms of the Lagrangian cells are recorded in this product.

*Date of Melt-onset in Spring/ Freeze-up in Fall.* There is a fairly well-defined change in the backscatter of the snow/ice to the onset of melt and freeze-up. The analysis algorithm will detect and estimate the date this seasonal transition using the time series of backscatter product. Different parts of the Arctic go through these transitions at different dates and this product would provide a high spatial resolution of the date of transition although the temporal resolution is dependent on the repeat observations of the Lagrangian cells.

## RGPS STATUS

*Status and schedule.* Currently the RGPS is processing the winter of 1996/97, which is expected to be completed by December, 1999. With the commissioning of a second operational system this summer, the winter of 1997/98 has been initiated. By the end of year 2000 we expect to have completed both of these winters plus analysis of the summers of 1997 and 1998. We expect to continue to obtain RADARSAT imagery only until November, 2000.

## ENVISAT

The RGPS basin-scale products of sea ice age and thickness are truly unique and we anticipate that these data products will have important utility for use in comparisons with climate models and other sensors and data sets. Also, the Arctic is undergoing measurable change this decade in several key indicators of climate warming. The 4-year time record from RADARSAT is fortuitously timed to also potentially provide indicators of climate change through ice motion and age/thickness derivations which are used to determine the surface heat and mass balance of the Arctic Ocean. It therefore seems both desirable and justifiable to continue the unique RGPS derivations over an extended time period. The ENVISAT ASAR wide swath mode presents an excellent opportunity for continued acquisition of high-resolution SAR mapping of the Arctic Ocean. Here we present a brief description of the RGPS requirements and the utility of the ENVISAT ASAR imagery.

In terms of general SAR requirements for the RGPS, repeat wide-swath SAR surveys of the entire Arctic at preferably 3-day near repeat sub-cycles are needed to determine the motion field of the ice cover. Resolution on the order of 100-200 m will resolve moderate deformation and opening/closing of important size-scale of leads. From these, ice age and thickness can be derived over comparatively short time periods. Relative radiometric accuracy of 1 dB or less across the swath provides adequate stability needed for maintaining high areal correlation of ice features between successive images. Geometric location of 300 m or better is needed to reduce feature tracking errors. For frequency, C-band SAR is preferred due to the high radar contrast between first-year, multiyear, and wind-roughened open water, which improves feature tracking. One caveat is that the Lagrangian tracking approach used to obtain ice age places high demand on successful and regular repeating mappings. If an 'ice particle' is not imaged every 3 or 6 days, a time step uncertainty is imparted that particularly affects new ice and ridged ice production. In fact, a time gap of more than 15 days requires that a grid cell be stopped and not propagated or reinitialized with a new grid cell at a later time.

The characteristics of the ENVISAT ASAR wide swath image mode provides excellent compatibility with the RGPS input image requirements, including frequency and resolution. The 400 km swath enables nearly 100% mapping of the Arctic basin every 3-days or 12 mappings every 35-day orbit repeat cycle. Several key calibration parameters will be improvements on the RADARSAT data quality and should likewise improve the RGPS output quality. These include absolute location accuracy due to 2 pixels (150 m) and radiometric error of 0.2 dB. Also, the availability of strip map will reduce data manipulation requirements within the RGPS. The RGPS would ingest ASAR Level 1 image data and make the output products globally available. With dedicated and long-term mappings, this Arctic data would enable monitoring of the climatic changes of the Arctic sea ice cover.

## CONCLUSIONS

From Arctic Ocean SAR mappings provided to date by the RADARSAT ScanSAR mode, a geophysical processor system has been developed to make the data-derived estimates of ice age and thickness for the first time ever. Continuing such mappings with ENVISAT ASAR wide swath mode would enable these critical observations of the sea ice cover to continue during a time of significant climate change that is presently taking place in the Arctic.

## ACKNOWLEDGMENTS

The RADARSAT imagery is provided by the Alaska SAR Facility, Fairbanks, AK. R. Kwok and B. Holt performed this work at the Jet Propulsion Laboratory, California Institute of Technology under contract with the National Aeronautics and Space Administration.

## REFERENCES

- Ingram, W. J., C. A. Wilson, and J. F. B. Mitchell, Modeling climate change: An assessment of sea ice surface albedo feedbacks, *J. Geophys. Res.*, 94, 8690-8622, 1989.
- Kattenberg, A., F. Giorgi, H. Grassl, G. A. Meehl, J. F. B. Mitchell, R. J. Stouffer, T. Tokioka, A. J. Weaver, and T. M. L. Wigley. Climate models: Projections of Future Climate. In: J. T. Houghton, L. G. Miera Filho, B. A. Callander, N. Harris, A. Kattenberg, and K. Maskell, eds., *Climate Change 1995*, Cambridge, 285-357, 1996.
- Kwok, R., D. A. Rothrock, H. L. Stern and G. F. Cunningham, Determination of Ice Age using Lagrangian Observations of Ice Motion, *IEEE Trans. Geosci. Remote Sens.*, Vol. 33(2), 392-400, 1995.
- Kwok, R. The RADARSAT Geophysical Processor System, in *Analysis of SAR data of the Polar Oceans: Recent Advances*, Tsatsoulis, C. and R. Kwok, Eds., Springer-Verlag, 235-258, 1998.
- Kwok, R. and D. A. Rothrock, Variability of Fram Strait Flux and North Atlantic Oscillation, *J. Geophys. Res.*, 104(C3), 5177-5189, 1999.
- Kwok, R. Recent changes in the Arctic Ocean sea ice circulation associated with the NAO, *Geophys. Res. Lett.*, in press.
- Maykut, G. A., The Surface Heat and Mass Balance, in *Geophysics of Sea Ice*, Ed. N. Untersteiner, 395-463, Series B: Physics Vol. 146, Plenum Press, 1986.
- Morison, J. H., M. Steele, and R. Andersen, 1998: Hydrography of the upper Arctic Ocean measured from the nuclear submarine USS Pargo. *Deep Sea Res.*, 45, 15-38.
- Parkinson, C. L., D. J. Cavalieri, P. Gloersen, H. J. Zwally, and J. Comiso, Arctic sea ice extents, areas, and trends, 1978-1996, *J. Geophys. Res.*, 104(C9), 20837-20856, 1999.
- Parmerter, R. R. and M. Coon, Model of pressure ridge formation in sea ice, *J. Geophys. Res.*, 77, 6565-6575, 1972.
- Proshutinsky, A. Y. and M. A. Johnson, Two circulation regimes of the wind-driven Arctic Ocean, *J. Geophys. Res.*, 102, 12,493-12,514, 1997.
- Rind, D., R. Healy, C. Parkinson, and D. Martinson, The role of sea ice in 2xCO<sub>2</sub> climate model sensitivity. Part I: The total influence of sea ice thickness and extent, *J. Climate*, 8, 449-463, 1995.
- Steele, M. and T. Boyd, Retreat of the cold halocline layer in the Arctic Ocean, *J. Geophys. Res.* 103(55), 10,419-10,435, 1998.
- Walsh, J. E., W. L. Chapman, and T.L. Shy, 1996: Recent decrease of sea level pressure in the central Arctic. Notes and Correspondence, *J. Climate*, 9, 480-486.
- Winebrenner, D. P., D. G. Long and B. Holt, Mapping the progression of melt onset and freeze-up on Arctic sea ice using SAR and scatterometry, in *Analysis of SAR data of the Polar Oceans: Recent Advances*, Tsatsoulis, C. and R. Kwok, Eds., Springer-Verlag, 129-144, 1998.
- Zhang, J., D. Rothrock, and M. Steele, Warming of the Arctic Ocean by a strengthened Atlantic inflow: Model results, *Geophys. Res. Lett.*, 25, 1745-1748, 1998.

## SAR research and application activities for coastal management in Norwegian waters

O. M. Johannessen, S. Sandven, Heidi Espedal and Birgitte Furevik

Nansen Environmental and Remote Sensing Center  
 Edvard Griegsvei 3a, N-5059 Bergen, Norway  
 Tel: + 47 55 29 72 88, fax: + 47 55 20 00 50,  
 e-mail: [stein.sandven@nrsc.no](mailto:stein.sandven@nrsc.no)  
<http://www.nrsc.no>

### ABSTRACT

The SAR research activities at the Nansen Environmental and Remote Sensing Center are focused on ocean and coastal applications such as mapping of currents, fronts eddies and wind field retrieval. SAR has also capability to detect oil spill as well as natural oil seeps which require discrimination algorithms to distinguish man-made oil spills and natural film. A SAR simulation model is used to study the SAR signatures of various surface processes: wind, waves, currents, fronts and slick. The simulation model is useful in the interpretation and classification of SAR images of sea surfaces. In ice-covered waters SAR has been developed into an important tool in operational ice monitoring. Industrial applications of SAR are under development for the following markets: SAR-derived wind energy maps for the wind mill industry, mapping of currents and front for deep offshore drilling and ice service for Arctic operations. In addition, SAR-derived products for wave forecasting, oil spill monitoring and ship detection are already established in operational public monitoring services.

### INTRODUCTION

This paper describes the ongoing efforts at the Nansen Center to develop SAR applications for coastal waters including integration of SAR-derived information into operational monitoring systems. The work has been focused on retrieval of current patterns, mesoscale eddies, fronts, natural film, oil slicks and high-resolution wind fields. In order to develop retrieval algorithms and other quantitative SAR products ERS SAR imagery have obtained along the coast of Norway since the start of the ERS programme, and images have been analyzed in conjunction with in situ information, SAR simulation models and other available remote sensing data [1].

### COASTAL CURRENTS IMAGED BY SAR

It is well known that SAR can image current patterns such as eddies, fronts and shear zones, but to obtain

quantitative estimates from SAR for these parameters is difficult. The approach is therefore to combine SAR data with in situ field observations and backscatter models of profiles across such fronts. Previous results [2] based on a one-dimensional smoothed current data set from ADCP measurements at 20 m depth, when crossing an ocean front with a shear of  $10^{-4} \text{ s}^{-1}$  (current variation  $\sim 50 \text{ cm/s}$  over a horizontal distance of 5 km), indicated that the front showed up only weakly in the modeled backscatter using the old version of Environmental Research Institute of Michigan (ERIM) Ocean Model (EOM) [3,4] compared to the SAR imagery (Fig.1).

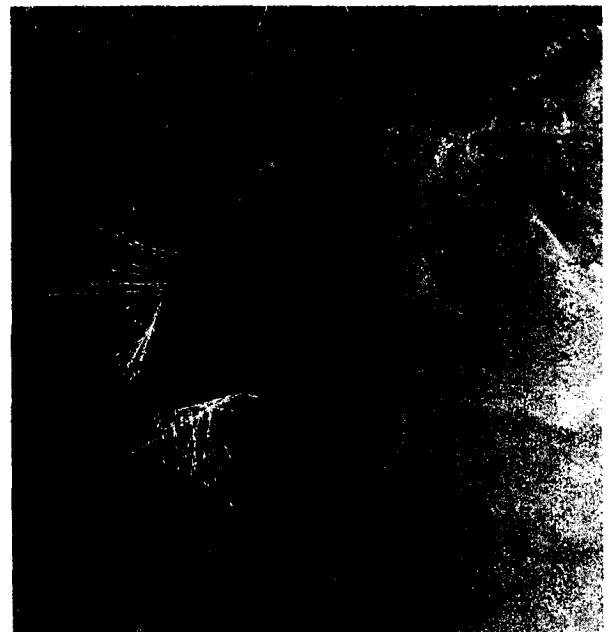


Fig.1. ERS SAR scene from 27 September 1995 obtained during the COASTWATCH experiment off the south coast of Norway. Two ocean fronts were studied by *in situ* data from R/V Håkon Mosby, measuring ocean current profiles by ADCP (indicated by the arrows). The northern front was observed by the vessel at the same time as the SAR image was taken. ©ESA/TSS, 1995.

Model results using a simplified current field indicated that unrealistic shear rates of nearly  $10^{-2} \text{ s}^{-1}$  are required before the shear itself leads to backscatter enhancement of the same order of magnitude as that actually observed in the SAR imagery. In an extended version of the EOM [5], the mean effect of the hydrodynamic modulation of the Bragg waves by longer waves (0.5 – 2 m) is included. This will increase the Bragg wave intensity at places where the intermediate-scale waves are steep. Due to this interaction with the intermediate-scale waves, the total intensity variations of the Bragg waves will become much larger than the variations that result from direct interaction between Bragg waves and the current field. The extended version of EOM [5] has been tested on some current fronts crossed during the COASTWATCH'95 experiment.

The modeling was one-dimensional with the axis directed along the ship track. The subsections of the ADCP profiles (at 8 m depth) comprising the fronts were extracted for the each case. These subsections were the inputs to the hydrodynamic module of EOM. Grid spacing was set to the average value between ADCP measurements, i.e. 550 m. The values of salinity, sea surface temperature and radar incidence angle were chosen to be the same (typical for the data set) for all the cases since their variability was small. Wind speed and direction for the model were taken from the ship meteorological station at the time of the satellite passage. Wind and current vectors were rotated to reflect angles between North, ship track and radar look direction. These will differ from front to front.

The output of the hydrodynamic module of EOM, directional ocean wave spectrum for each grid point, was given as input of the new extension to EOM. In turn, it calculated for each point an enhancement factor for 5 cm waves due to interaction with intermediate scale waves. This factor is to be multiplied by the equilibrium wave spectrum and added to the local spectrum. For this procedure to improve modeling results (i.e. provide more modulation for the local spectrum as a function of distance) the factor itself should vary with distance, significantly and not randomly. These factor profiles, along with real and simulated (using old EOM version) NRCS profiles and currents were calculated for each front. An example of modeling results is shown in Fig. 2. We observed the previously documented fact that EOM gives too high absolute backscatter values compared to SAR [2]. However, more importantly the modulation across the front is too small. While the change in backscatter across the front is  $\sim 1\text{-}2$  dB in the SAR image, it is 0.4

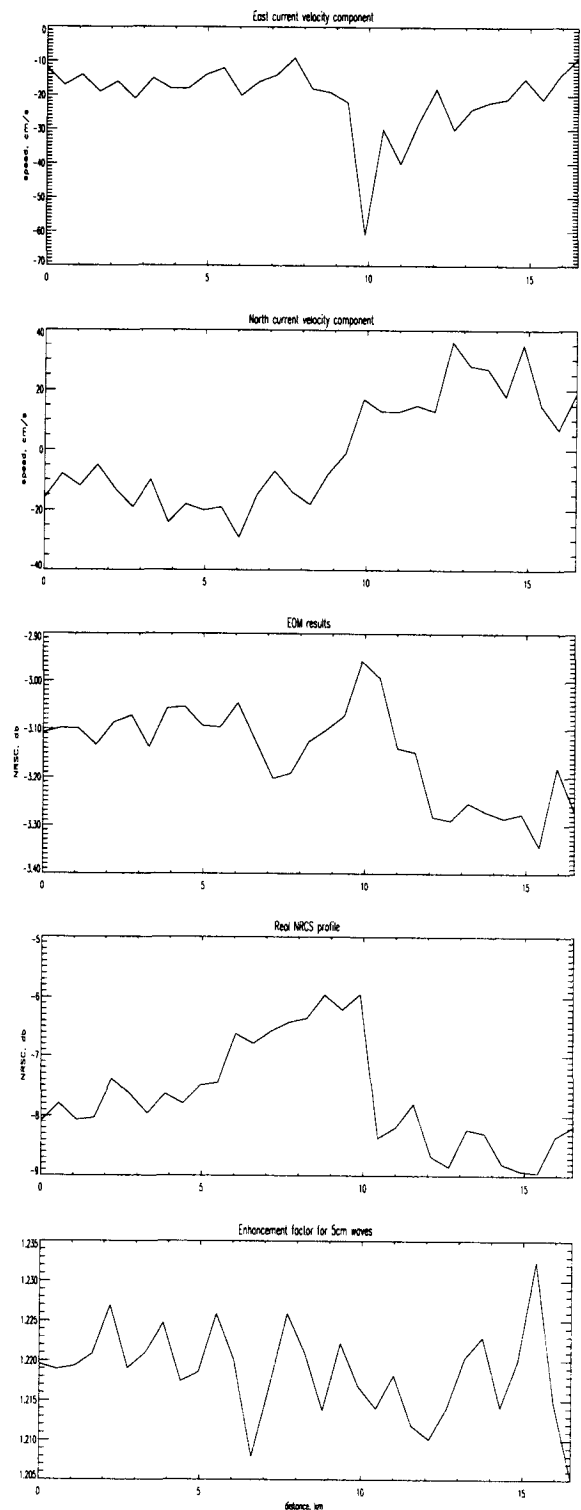


Fig. 2. Simulation study of a 16 km long section across the northern front in Fig. 1. The plots from top to bottom are: current components (east and north velocity components), EOM old version Normalized Radar Cross Section (NRCS), SAR NRCS, and the new enhancement factor.

dB in the EOM result (old version). The variation of the enhancement factor was found to be in the second (or sometimes even the third) decimal, and appears quite random. The result is a modulation across a front that at best becomes e.g. 0.7 dB instead of 0.4 dB. Therefore, the enhancement factor does not seem to be able to sufficiently improve the EOM results for the fronts presented here and we conclude that the EOM model needs improvement.

#### WIND FROM SAR COMPARED TO SCATTEROMETER

Wind retrieval from SAR will become more important since RADARSAT and ENVISAT carry wide swath SAR can provide wind fields along 500 km wide swaths, but no wind scatterometer. SAR derived wind field can be used in operational weather forecasting, particularly in coastal regions and in the marginal ice zone, but is yet not implemented. NERSC has also suggested to use this method to make detailed wind energy maps for coastal regions to be used in planning of wind mills along the Norwegian coast as well as abroad [6].

A systematic analysis has been performed on the mesoscale coastal wind field conditions expressed in the SAR imagery obtained during the COASTWATCH'95 experiment [7]. Two different wind retrieval models, the SAR wind algorithm (SWA) and the CMOD4, were applied to the data.

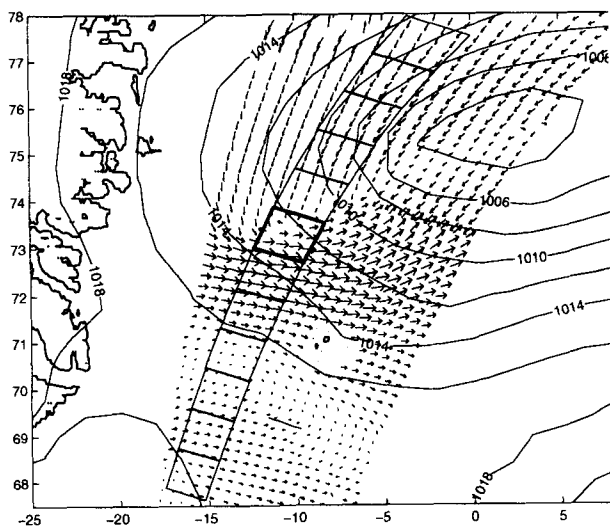


Figure 3. Wind field in the Greenland Sea measured from ERS-1 WSC on Sept. 1, 1995. The atmospheric sea level pressure (indicated by the contours) are provided by Norwegian Meteorological Institute. The frames indicate where SAR images were obtained

about 30 minutes later by ERS-2.

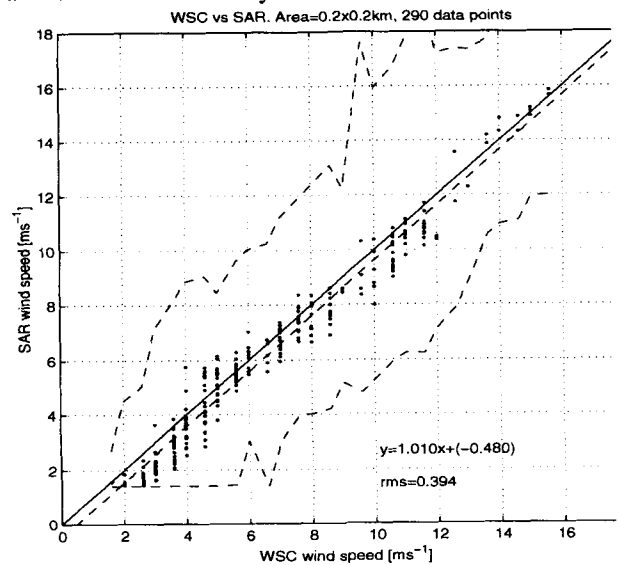


Fig. 4. Comparison of WSC wind speeds to SAR CMOD-IF2 wind speeds when these are calculated in a subimage of 25 x 25 km. The straight dashed line is the best fit to the data, while the straight solid line indicates a perfect correlation. An underestimation of <math><0.5\text{ m/s}</math> is found. (Also note the dashed curved lines; these are the envelopes of all the derived wind speeds from the SAR sub-images with with 200m resolution, giving the character of the mesoscale variability).

Comparison of the SWA and CMOD4 results indicates a wind speed difference less than 2 m/s. When comparing with in situ observations, the SAR generally underestimated the wind speed.

In one recent study performed at the Nansen Center, the extracted wind field from SAR precision images (PRI) has been compared with the Wind Scatterometer (WSC) wind field product during the ERS-1/2 Tandem Phase [8]. In this phase the ERS-1 WSC and the ERS-2 SAR covered the same area on the sea surface north of 63° in open ocean with only 30 minutes time lag. Wind vectors from approximately 290 WSC data points were compared with the wind speed extracted from corresponding 25 x 25 km areas in the SAR images (Fig. 3 and 4). The CMOD IF2 model was used for both data sets. This model is used operationally on the WSC data at IFREMER [9]. When using CMOD models on SAR data the wind direction is needed as input. Since comparison is done towards the WSC the wind direction from this instrument is used. A very good correlation was found. An underestimation by the SAR of <math><0.5\text{ m/s}</math> is unexplained. This offset is believed to be due to a difference in incidence angles of the two sensors. If this is the case, it means that the

C band model used to extract the wind from SAR and WSC has to be adjusted in its dependence on the incidence angle. This subject is under investigation.

### SAR SURFACE FILM AND OIL SLICKS

A sea surface slick experiment was also conducted during COASTWATCH'95, using two microlayer samplers with teflon drums; the INTERFACE I and II [10]. The INTERFACE II was also fitted with a GPS system, temperature probes, an anemometer and a data logger. In addition, a C-band Doppler scatterometer was used to acquire shipborne radar backscatter measurements from the bow of the research vessel R/V Håkon Mosby.

For one of the verified natural films, surface drifters and the Doppler radar data showed that a convergence was responsible for the film accumulation. Another verified natural film case showed no clear convergence or shear. In a third case, no samples were obtained for chemical analysis, but a slick with finger-like extensions was investigated using the Doppler radar, and also found in the ERS-1 SAR image 6 hours later (with prevailing low winds). The slick had totally disappeared in the ERS-2 SAR image the next day. During this period the wind speed increased from 2-3 m/s to 5-10 m/s.

Using a supervised slick discrimination algorithm [11] estimates of natural film coverage and damping were found, based on the 71 SAR images covering the experiment region. The results showed that for increasing wind speed, the percentage of film coverage in the SAR scenes expectedly decreases (Fig. 5). The largest film coverage (40 %) was found for winds near the detection threshold (2.5 m/s), while already at 5-10 m/s wind the film coverage had decreased below 5 % in all cases. Increasing wind speeds also lead to decreasing damping by the natural films. The wide range of damping values, especially at low wind speeds, were believed to be due to varying film composition and thickness. Of the 71 SAR scenes, 27 were classified as containing no natural film. They all had a wind speed of 5 m/s or more.

When comparing the results to a previous experiment conducted in 1994 in Korsfjord [12] the slicks investigated during COASTWATCH'95 contained smaller fatty acid molecules indicating marine organisms as their source. The fjord slicks were dominated by terrestrial sources. The COASTWATCH'95 slicks also had lower concentration of fatty acids, resulting in slightly lower damping values in the SAR imagery, 2-11dB, compared to 6-17dB for the fjord cases.

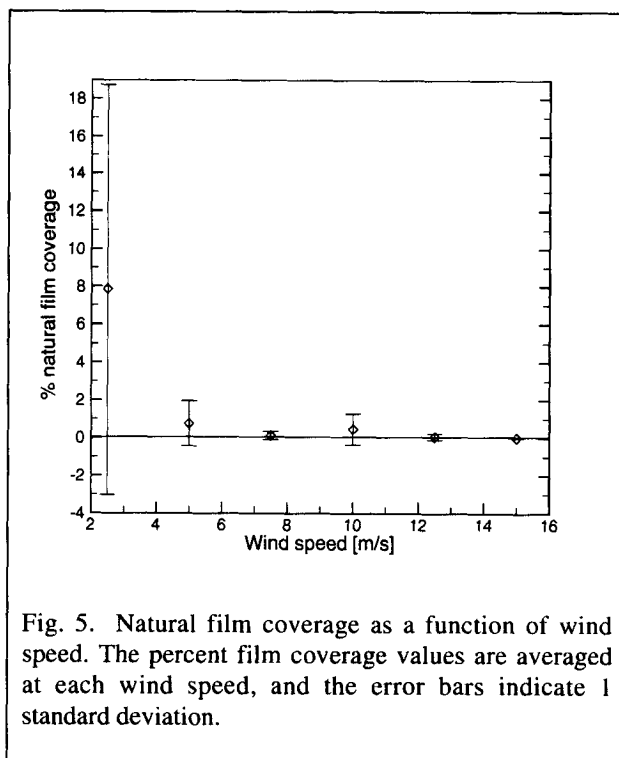


Fig. 5. Natural film coverage as a function of wind speed. The percent film coverage values are averaged at each wind speed, and the error bars indicate 1 standard deviation.

SAR imagery are used routinely in combination with aircraft surveys for pollution monitoring of Norwegian coastal waters. The SAR imagery are primarily used to optimize use of the aircraft, especially to scan areas where the aircraft does not need to fly because there are no apparent pollution. If a potential pollution is observed in a SAR image, the aircraft normally flies to spot to decide if there is a real pollution. Since there are many signatures in a SAR image which look like pollution, it is necessary to develop classification schemes which takes into the shape, size and drift of the feature in response to winds and currents.

One technique to help in classification of a slick signature is analysis of the wind history prior to the SAR observation. Fig. 6 shows an example of such analysis where a confirmed oil spill in the North Sea from a platform (bright spot) and the wind history in the preceding days is indicated in the lower panel. The shape of the elongated dark feature is characteristic for a spill which has been exposed to a shift in wind direction. The wind analysis prior to the SAR image acquisition is useful to help determine the age of the slick and to what extent the release of the slick has been continuous or a short-time event. In addition to wind history it is also necessary to take into account the effect of currents, especially tidal currents which in areas like the north sea can transport a spill several km during a tidal cycle of about 12 hours.



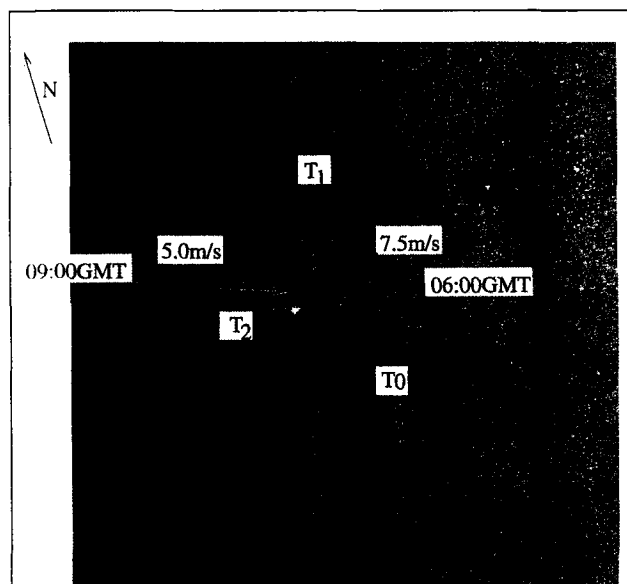


Fig. 6 a ERS SAR image covering 25 by 25 km in the North Sea, showing an oil spill which drifted in different directions in response to varying winds. The wind vectors for the periods T0 – T1 and T1 – T2 are superimposed.

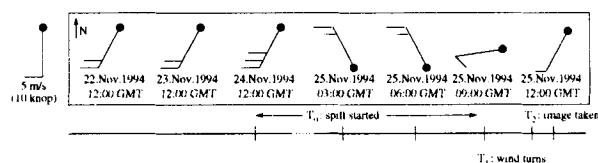


Fig. 6 b Wind analysis of the period before the SAR image above was acquired. T0 – T1 indicates the period from beginning of the spill until the wind changed from northwesterly to southwesterly direction.

#### OPERALT: SYNERGY BETWEEN SAR AND RADAR ALTIMETER

In OPERALT, an EU-supported demonstration project the needs of the offshore industry to obtain ocean current data from altimetry has been investigated. As oil exploration and production move from the continental shelves to deeper waters information about ocean currents becomes increasingly important, and altimeter data can provide valuable data on mean currents and eddy kinetic energy. The spatial and temporal scales covered by altimetry is insufficient to map fronts, current shears and eddies which represent the highest current velocities and are therefore of particular interest for offshore operations. SAR images

were collected in the same area as altimeter analysis was performed, off the west coast of Norway where oil companies are drilling at depths above 1000 m.

Estimates of precise mean sea surface has been produced from ERS-1/2 and Topex/Poseidon data which have been merged to produce a continuous, 7 year data set gridded at approximately 10 km and 10 day intervals [xx].

The study shows that altimeter-derived eddy fields can be recognized in SAR imagery (Fig. 7), but the time scale between the two data sets must be taken into account. The altimeter derived velocity field is averaged over 10 days, whereas the SAR image shows an instantaneous picture of patterns associated with fronts and eddies. In order to compare data taken on similar time scale, geostrophic velocity from one altimeter profile is plotted across the image, showing the velocity component perpendicular to the altimeter track. The altimeter track was taken on the same day as the SAR image, both showing northward propagating current on the right side and a southward propagating current on the left side.

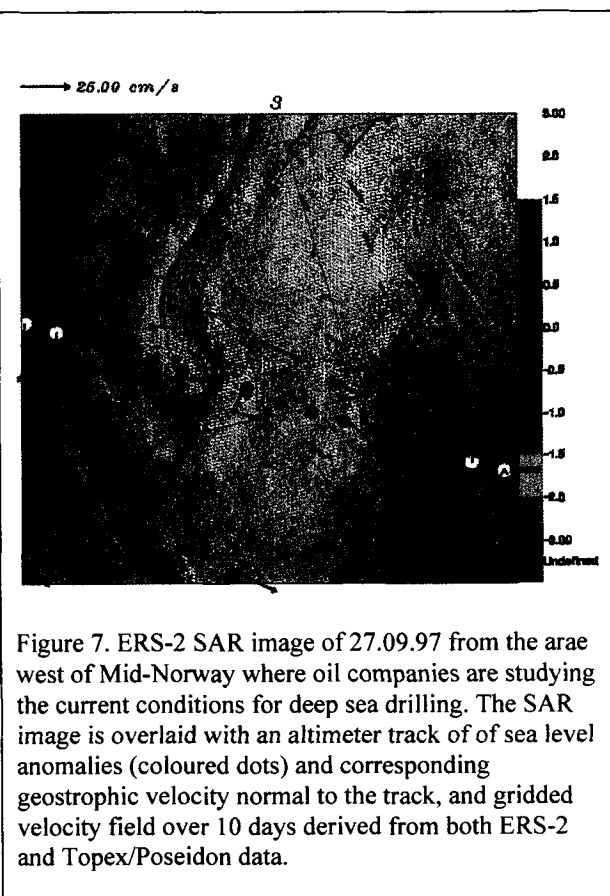


Figure 7. ERS-2 SAR image of 27.09.97 from the area west of Mid-Norway where oil companies are studying the current conditions for deep sea drilling. The SAR image is overlaid with an altimeter track of sea level anomalies (coloured dots) and corresponding geostrophic velocity normal to the track, and gridded velocity field over 10 days derived from both ERS-2 and Topex/Poseidon data.

## CONCLUSION

We have presented examples of SAR products that have been developed and tested for use in ocean and coastal monitoring systems. Satellite SAR has proven to be a useful technique for monitoring a number of sea surface processes such as wind, waves, current patterns and fronts, oil spill and natural films. In addition to SAR retrieval algorithms, it is necessary to include use of in situ data, SAR simulation models and other available data sources in monitoring systems. With improved temporal and spatial SAR coverage over ocean areas by RADARSAT and ENVISAT it is foreseen that SAR-derived products will become increasingly important in coastal areas. Several operational applications of SAR are under development including tailored products for industry such as wind energy mapping, oil seep detection, mapping of ocean eddies and fronts.

## ACKNOWLEDGEMENTS

The SAR coastal studies have been supported by Strategic Program for SAR remote sensing at NERSC, funded by the Research Council of Norway, and EU projects COASTMON and OPERALT and Norske Shell a.s. ERS data were obtained under the ESA Program AO2.N108.

## REFERENCES

- [1] Johannessen, O. M., *et al.*, COASTWATCH: Using SAR imagery in an operational system for monitoring coastal currents, wind, surfactants and oil spills. In "Operational Oceanography. The Challenge for European Co-operation" (Editor in Chief: J. H. Stel). Proceedings of the First International Conference on EuroGOOS, 7 -11 October 1996, The Hague, The Netherlands. Elsevier Oceanography Series, No. 62, pp. 234-242, 1997.
- [2] Jenkins, A. D, *et al.*, Intercomparison and improvement of SAR ocean imaging interaction models. ESA Contract No. 11969/96/NL/CN. NERSC Technical Report no. 132. February 1998.
- [3] Lyzenga, D. R., and J.R. Bennett, Full spectrum modeling of SAR internal wave signatures, *J. Geophys. Res.* Vol.93 no.C10, 1988.
- [4] Tanis, F. J., J.R. Bennett and D.R. Lyzenga, "Physics of EOM", Tech. Rep. no.028, ERIM, USA, 1989.
- [5] Lyzenga, D. R., Effects of intermediate-scale waves on radar signatures of ocean fronts and internal waves, *J. Geophys. Res.* Vol.103 no.C9, 1998.
- [6] Johannessen, O. M., E. Korsbakken and E. Bjørgo. Determination of wind energy from synthetic aperture radar for wind mill siting. Proceedings of the 27th International Symposium on Remote Sensing of Environment, Tromsø, Norway, pp. 217-220, 1998.
- [7] Korsbakken, E., J.A. Johannessen and O.M. Johannessen, Coastal wind field retrievals from ERS synthetic aperture radar images. *J. Geophys. Res.*, vol.13 no C4, 1998.
- [8] Furevik, B. and E. Korsbakken. Wind field retrieval from Synthetic Aperture Radar compared to Scatterometer wind field during the ERS Tanem Phase. Proceedings of the 27th International Symposium on Remote Sensing of Environment, Tromsø, Norway, pp. 201 - 204, 1998.
- [9] Quilfen, Y., *et al.*, Observation of tropical cyclones by high-resolution scatterometry, *J. Geophys. Res.*, vol.103 no.C4, pp.7767-7786, 1998.
- [10] Espedal, H. A. *et al.*, COASTWATCH'95: ERS-1/2 SAR detection of natural film on ocean surface, *J. Geophys. Res.*, vol.103 no.C11, pp.24969-24982, 1998.
- [11] Espedal, H. A., Detection of oil spill and natural film in the marine environment by spaceborne SAR, PhD. Thesis, University of Bergen, Norway, 1998.
- [12] Espedal, H. A., *et al.*, Satellite detection of natural film on the ocean surface, *Geophys. Res. Letters*, vol.23 no.22, pp.3151-3154, 1996.
- [13] <http://www.nrsc.no/Operalt>

## **Session 3: Geometry/Radiometry/Calibration**



## The ERS SAR Performances: An Update

P.J. Meadows<sup>1</sup>, D. Esteban Fernández<sup>2</sup> and P. Mancini<sup>3</sup>

<sup>1</sup>Marconi Research Centre, West Hanningfield Road,  
Chelmsford, Essex, CM2 8HN, United Kingdom.  
Email: peter.meadows@gecm.com

<sup>2</sup>GAEL Consultant, Cité Descaetes, 18 rue Albert Einstein,  
77420 Champs-sur-Marne, France.

<sup>3</sup>European Space Agency, Directorate of Application Programmes,  
ESRIN, 00044 Frascati, Italy.

### ABSTRACT

The performance of the ERS-1 and ERS-2 Synthetic Aperture Radars (SARs) are routinely assessed at the ESA Product and Archiving Facilities (PAFs) via a variety of quality assessment and calibration measures. At the previous CEOS SAR workshop details of the performance of the ERS SARs were given [1]. This paper gives the latest ERS SAR quality assessment and calibration results including updates to ERS-1 and ERS-2 SAR internal calibration and stability results and updates to the ERS-2 nominal replica pulse correction table. Also given are image localisation results, noise equivalent radar cross-section measurements and a comparison of the calibration of the three-look PRI and complex SLCI products.

### INTRODUCTION

The ERS-1 and ERS-2 SAR missions have been in operation since July 1991 and April 1995 respectively. They have fully lived up to their expectations by successfully demonstrating the ability of imaging radars to provide valuable long-term earth observation data to many categories of users.

Users require the SAR products from the ERS-1 and ERS-2 SARs to be calibrated (absolutely or relatively). Absolute calibration supports the geophysical interpretation of SAR data by relating the digital values in data products to the physical and meaningful estimation of the normalised radar cross-section  $\sigma^0$  (also referred to as the backscattering coefficient). Relative calibration enables SAR products from either ERS-1 or ERS-2 to be compared with each other. The importance of using calibrated ERS SAR imagery has been demonstrated for the application of ocean wind speed extraction [1] and land applications [2, 3]. Equations to calculate the radar cross-section of point and distributed targets from the ESA three look detected PRI product

and the single look complex SLCI/SLC product can also be found in [2, 3].

### ERS SAR QUALITY ASSESSMENT

The quality of ERS SAR imagery has been assessed via impulse response function measurements using the three ESA transponders deployed in The Netherlands. These measurements include the azimuth and range spatial resolutions, peak sidelobe ratio and integrated sidelobe ratio (see [1] for definitions). Table 1 gives values for these parameters from the PRI and SLCI products. In addition, Fig 1 and Fig 2 show the azimuth resolution as a function of acquisition date and the range resolution as a function of incidence angle for ERS-1 and ERS-2 PRI products respectively. The solid line and curve in these figures show the theoretical spatial resolutions. The PRI results have been derived for measurements taken throughout the lifetime of both ERS-1 and ERS-2. The ERS-1 SLCI results are derived from a set of 15 products acquired between January and March 1994 and the ERS-2 SLCI results are derived from a set of 10 products acquired between August 1995 and February 1997.

Parameter	ERS-1 PRI	ERS-2 PRI
Azimuth resolution (m)	21.58±0.43	21.61±0.38
Peak sidelobe ratio	-15.9±0.8dB	-15.9±0.8dB
Integrated sidelobe ratio	-12.1±1.6dB	-12.1±1.5dB

Table 1(a). ERS-1 and ERS-2 SAR PRI image quality parameters.

Parameter	ERS-1 SLCI	ERS-2 SLCI
Azimuth resolution (m)	5.32±0.02	5.33±0.03
Range resolution (m)	9.66±0.06	9.83±0.07
Peak sidelobe ratio	-20.4±0.6dB	-21.9±0.6
Integrated sidelobe ratio	-14.8±1.2dB	-14.9±0.5

Table 1(b). ERS-1 and ERS-2 SAR SLCI image quality parameters.

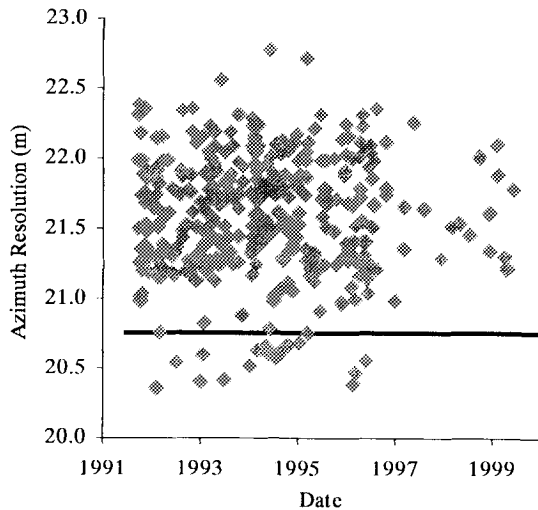


Fig 1(a): ERS-1.SAR.PRI azimuth resolution (the line is the theoretical azimuth resolution).

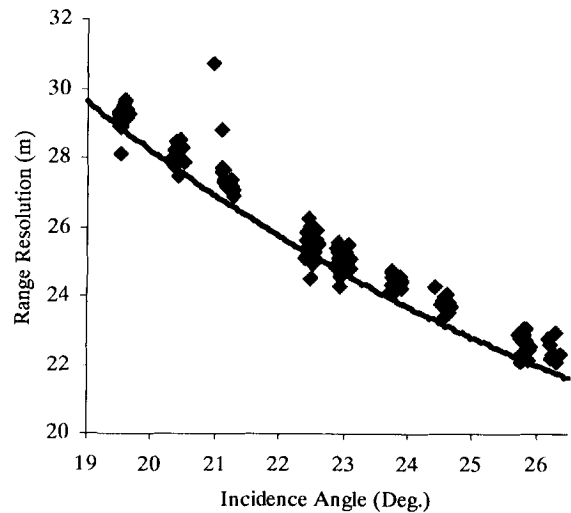


Fig 2(b): ERS-2.SAR.PRI range resolution (the curve is the theoretical range resolution).

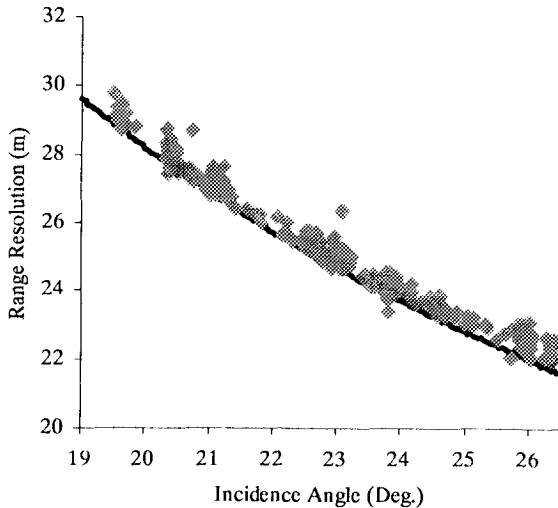


Fig 1(b): ERS-1.SAR.PRI range resolution (the curve is the theoretical range resolution).

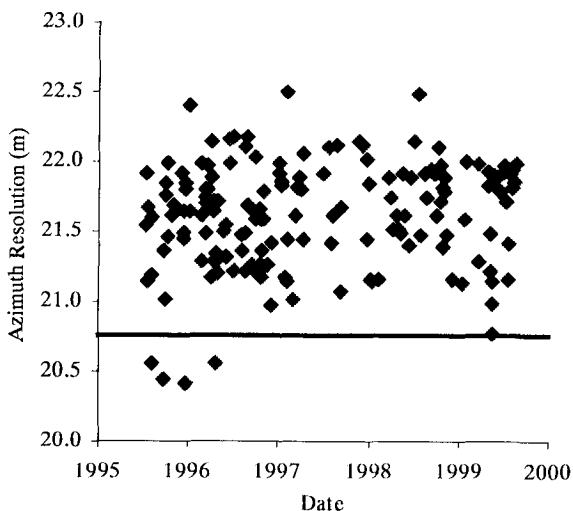


Fig 2(a): ERS-2.SAR.PRI azimuth resolution (the line is the theoretical azimuth resolution).

Table 1 and Figs 1 and 2 show that the measured azimuth and range resolutions compare well with theoretical values (20.76m for PRI azimuth resolution, 24.67m for PRI mid range resolution, 4.82m for SLCI azimuth resolution and 9.64m for SLCI slant range resolution). The sidelobe ratios are all low and acceptable.

The ESA transponders have also been used to derive the point target azimuth ambiguity ratio when the ambiguity background is sufficiently low to enable a measurement to be made (see [1] for further details). Based on the measurement of 13 ERS-1 SAR ambiguities in PRI products, the average azimuth ambiguity ratio is  $-27.8 \pm 3.1$  dB while the average difference in the measured and theoretical azimuth locations of the ambiguities is only  $7.8 \pm 4.8$  m (i.e. less than one pixel). The corresponding values for 10 ERS-2 SAR azimuth ambiguities is  $-24.5 \pm 2.9$  dB and  $4.1 \pm 2.2$  m. These results indicate an excellent ambiguity performance for both the ERS-1 and ERS-2 SARs.

Large uniform distributed targets can be used to estimate the image radiometric resolution. ERS-1 and ERS-2 PRI and SLCI products give radiometric resolutions of 2.07dB and 3.03dB respectively. The theoretical values are 1.98dB for the PRI product and 3.01dB for the SLCI product (these values assume perfectly uniform distributed targets).

#### ERS SAR RADIOMETRIC CALIBRATION

The radiometric calibration of ERS SAR products is achieved via internal and external calibration to determine equations that can be used to calculate the radar cross-section of point and distributed targets. External calibration comprised elevation antenna pattern

derivation using the Amazon rain forest [5] and the use of the ESA transponders for derivation of the image product calibration constants. Some radiometric calibration corrections are required to be carried out by the user: the ERS-1 replica pulse power and the ERS-1 and ERS-2 ADC power loss corrections [1, 2, 3, 6].

#### Internal Calibration

The internal calibration of the ERS SARs are assessed via calibration and replica pulse powers. The calibration pulse measures the majority of any gain drift from image sequence to image sequence while the replica pulse monitors any gain drift during the imaging sequence when the more representative calibration pulse is not available. In fact, the power of the calibration pulse is the best guide we have for the transmitted pulse power. The SAR processors at the PAFs make no direct use of the calibration pulse power while the replica pulse is used for the range compression part of the processing.

Calibration and replica pulse powers from ERS-1 SAR data archived at the UK-PAF are shown in Fig 3. Note that ERS-1 was placed in standby mode in June 1996; after this date the amount of data archived by the UK-PAF reduced significantly. For the period up to early 1998, the calibration pulse power was, for the most part, stable. The replica pulse power, during the same period showed variation of up to 2dB. It has been concluded that the ERS-1 SAR calibration pulse power (and hence the transmitter pulse power) is independent of the replica pulse. This is of particular importance for ERS-1 SAR image calibration as the image variations introduced by the range compression part of the processing (which uses a replica pulse) need to be removed. This is achieved via a replica pulse correction in the expression used for the calculation of radar cross-section.

During the period from early 1998, the calibration pulse power has been consistently high compared to before this date. This change indicates that the transmitter pulse power increased shortly after a 38% reduction in available power from the ERS-1 solar panels that occurred on 29<sup>th</sup> December 1997 [7]. A consequence of the change in transmitter pulse power is that the ERS-1 SAR calibration constant needed to be revised for data acquired from early 1998. Using ERS-1 SAR transponder measurements from 24<sup>th</sup> February 1998, a revised calibration constant was measured to be 0.79dB higher than previously. Thus, for example, ERS-1 VMP PRI products processed at the UK-PAF have a revised calibration constant of 59.03dB (799000) cf. 58.24dB (666110) previously while for the SLCI products, the revised K is 48.92dB (78000) cf. 48.13dB (65026). The decrease in replica pulse power (Fig 3(b)) for the same

period is compensated for by the ERS-1 SAR replica pulse power correction.

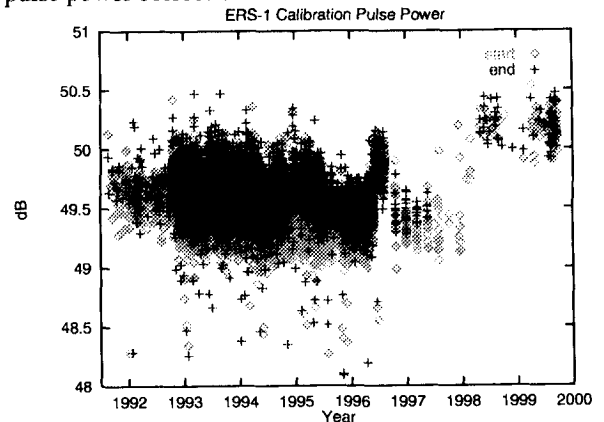


Fig. 3(a): ERS-1 SAR calibration pulse powers.

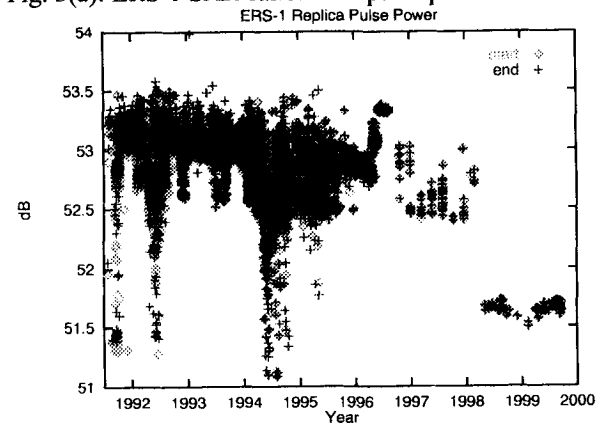


Fig. 3(b): ERS-1 SAR replica pulse powers.

The calibration and replica pulse powers for the ERS-2 SAR are shown in Fig 4. Here both the calibration and replica pulse powers show a drop in power as a function of time. The rate of decrease for both powers is approximately 0.63dB per year. Unlike the ERS-1 SAR, the ERS-2 calibration and replica pulse powers are correlated and hence no replica pulse correction is required when obtaining the radar cross-section from ERS-2 SAR imagery (as any reduction in transmitter power is removed by the reduced power of the replica pulse used for range compression).

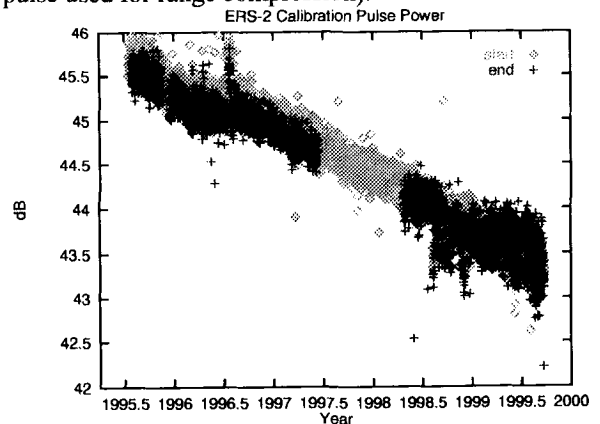


Fig. 4(a): ERS-2 SAR calibration pulse powers.

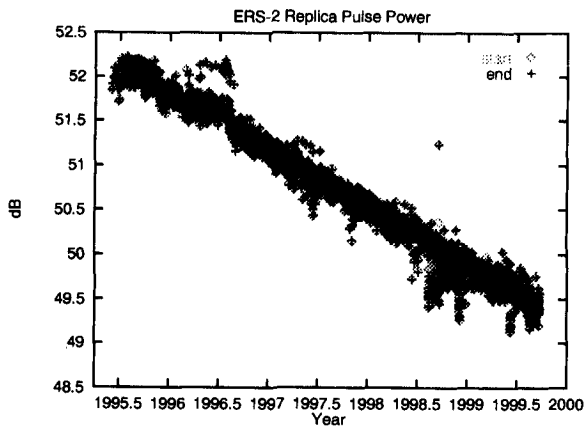


Fig. 4(b): ERS-2 SAR replica pulse powers.

Stability

The stability of the ERS-1 and ERS-2 SARs has been measured using the three ESA transponders deployed in The Netherlands. In particular, the measured radar cross-sections of the transponders have been compared to their actual radar cross-section values. This relative transponder radar cross-section (after all calibration corrections have been applied [6]) has been routinely calculated as is shown in Fig 5. The ERS-1 stability measurements include the revised ERS-1 SAR calibration constant since February 1998 as discussed above.

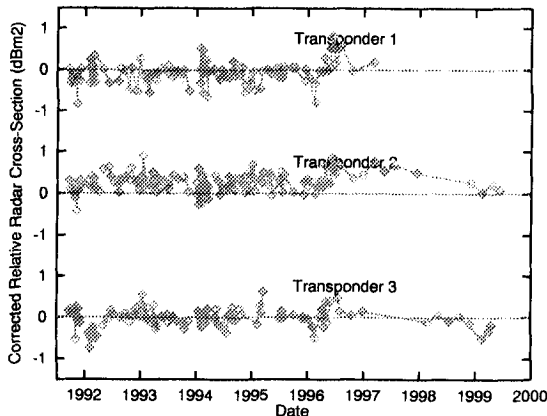


Fig. 5(a): ERS-1 SAR corrected relative radar cross-sections for the ESA transponders.

The measured mean radiometric results for the ERS-1 and ERS-2 SARs over their lifetimes are shown in Table 2. This table indicates an excellent stability for both SARs. In addition, the radiometric accuracy values are very good while the peak to peak values are acceptable.

Parameter	ERS-1	ERS-2
Radiometric Stability	0.24dB	0.27dB
Radiometric Accuracy	0.05dB	0.15dB
Peak to Peak RCS	1.42dB	1.23dB

Table 2: ERS-1 and ERS-2 SAR radiometric results.

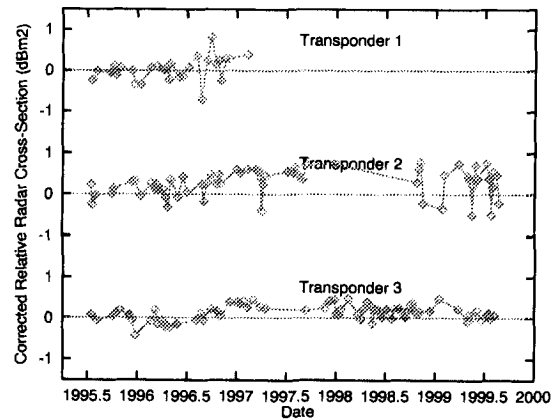


Fig. 5(b): ERS-2 SAR corrected relative radar cross-sections for the ESA transponders.

Noise Equivalent  $\sigma^0$

The upper limit to the noise equivalent  $\sigma^0$  ( $NE\sigma^0$ ) of an image can be estimated by measuring the radar cross-section of low intensity regions (usually ocean/inland water regions). A small number of ERS-1 SAR PRI products with suitable regions present give an estimated  $NE\sigma^0$  of -26.2dB. For ERS-2, the reducing transmitter power gives a  $NE\sigma^0$  that is increasing with time. Fig 6(a) shows low intensity region radar cross-section measurements from ERS-2.SAR.PRI images. In terms of estimating the  $NE\sigma^0$ , the important data points are those towards to bottom of the plot (as these include the smallest distributed target contribution to the radar cross-section measurement). These measurements indicate an estimated ERS-2  $NE\sigma^0$  of -25.2dB in July 1995 and -23.2dB in June 1999 (i.e. a reduction of 2dB in 4 years). This is similar to the reduction in transmitter pulse power over the same period (as measured by the calibration pulse power).

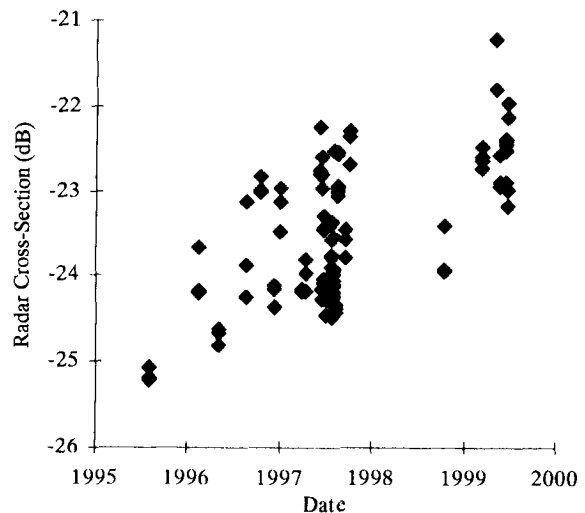


Fig. 6(a): ERS-2.SAR.PRI Noise Equivalent  $\sigma^0$ .

The  $NE\sigma^0$  is expected to change across the swath due to the antenna pattern gain. Figure 6(b) shows the ERS-2



SAR low radar cross-section  $\sigma^0$  measurements as a function of incidence angle. There is some evidence that  $\sigma^0$  is higher at the swath edges, especially at far range, but this is probably masked out by the reduction in transmitter power during the 4 year time interval of the data.

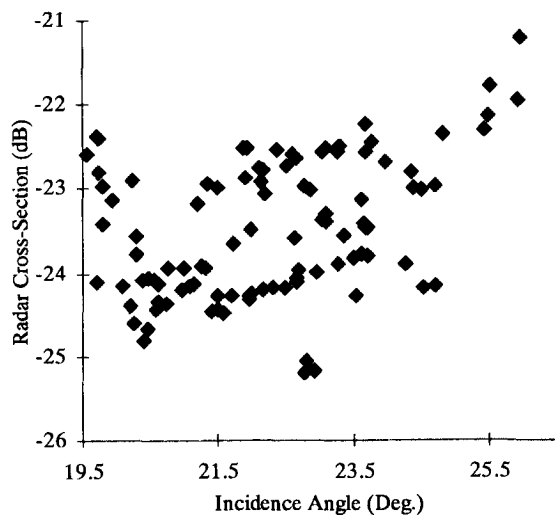


Fig 6(b): ERS-2.SAR.PRI Noise Equivalent  $\sigma^0$  as a function of incidence angle.

#### Nominal Replica Pulse Products

A small number of PAF SAR Verification Mode Processor (VMP) products (< 1%) are generated using a nominal replica pulse rather than a replica generated at the time of imaging (an extracted replica). Products generated with a nominal replica have significantly higher pixel values than products generated using an extracted replica. These products can be corrected but the correction is different for ERS-1 and ERS-2 SAR products.

For ERS-1 SAR products the image intensity needs to be reduced by factor of 291.52 (24.65dB). For ERS-2 SAR products the correction depends on the extracted replica pulse power at the time of data acquisition. This can be estimated from the quarterly averaged values given in Table 3. The correction factor is applied such that the image intensity values need to be reduced. More details can be found in [1, 6].

Year	Q1	Q2	Q3	Q4
1995			23.57	23.38
1996	23.23	23.15	23.05	22.78
1997	22.61	22.43	22.29	22.11
1998	21.97	21.81	21.57	21.42
1999	21.29	21.15	20.98	

Table 3: Quarterly averaged nominal replica pulse correction (dB) for the ERS-2 SAR.

## ERS SAR IMAGE LOCALISATION

Localisation of ERS SAR imagery can be assessed by using the measured pixel coordinates of known point targets. This is achieved by converting the point target pixel coordinate to cartographic coordinates (x, y in a UTM map projection) via the image corner latitude and longitudes. The distribution of point target cartographic coordinates gives the image localisation (after compensation of terrain height has been included). More details on the derivation of the image localisation can be found in [4].

The ESA transponders deployed in The Netherlands have been used to assess the ERS-2 SAR image localisation. Fig 7 shows the displacement of each transponder in cartographic coordinates after compensating for terrain height and for the transponder time delay. The mean displacement, i.e. the image localisation, from all measurements is 26.4m.

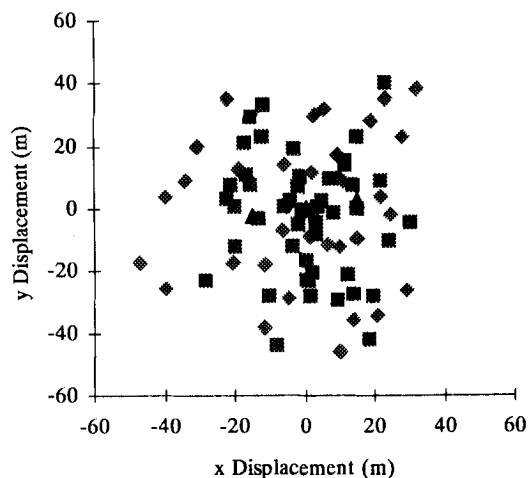


Fig. 7: ERS-2.SAR.PRI image localisation using the ESA transponders (triangles for transponder#1, diamonds for transponder#2 and squares for transponder#3).

## ERS SAR PRI/SLCI PRODUCT CALIBRATION

On order to assess the relative calibration of PRI and complex SLCI products, the corrected relative radar cross-section of the ESA transponders has been measured for the same scene in each product type. Details of SLCI calibration can be found in [2, 6]. Fig 8(a) shows the ERS-1 PRI and SLCI radar cross-section results (based on 15 scenes acquired between January and March 1994). The straight line in this figure is a least squares fit assuming a slope of one – this indicates an offset of 0.12dB between the PRI and SLCI measurements with the SLCI measurement being the slightly greater. Fig 8(b) shows the ERS-2 PRI and SLCI results (based on 10 scenes acquired between

August 1995 and February 1997). The offset between the PRI and SLCI measurements is 0.06dB with the PRI measurements being the greater. Both the ERS-1 and ERS-2 measurements indicate a good agreement between radar cross-section values derived from PRI and SLCI data (although there is some scatter for individual transponder measurements).

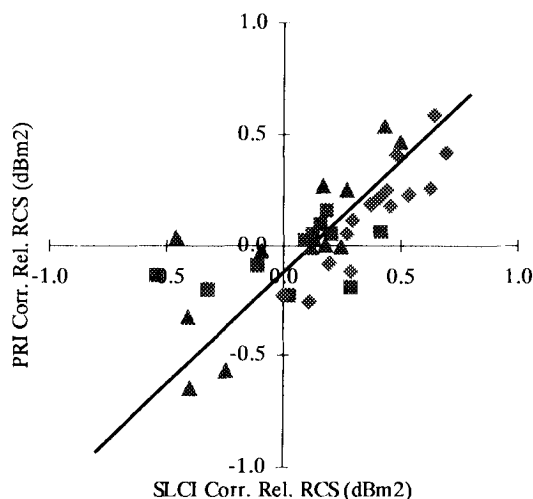


Fig. 8(a): ERS-1 PRI and SLCI product relative calibration (triangles for transponder#1, diamonds for transponder#2 and squares for transponder#3).

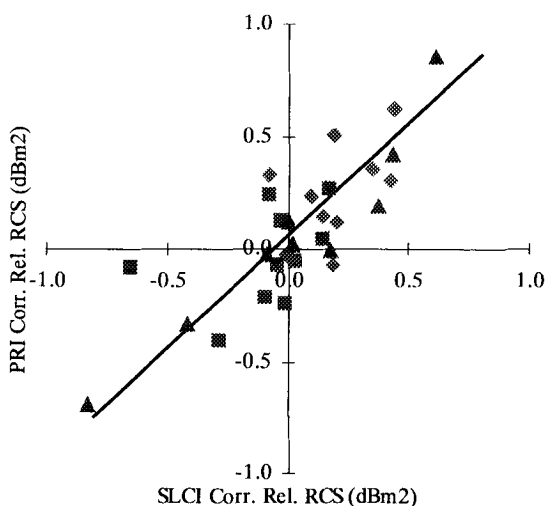


Fig. 8(b): ERS-2 PRI and SLCI product relative calibration (triangles for transponder#1, diamonds for transponder#2 and squares for transponder#3).

#### CONCLUSIONS

This paper has updated details of the performances of the ERS-1 and ERS-2 SAR since the last CEOS SAR workshop in February 1998. Results presented show that both SARs continue to work well with excellent quality assessment and radiometric calibration results. For the ERS-1 SAR it has been shown that the calibration constant has had to be increased for data

acquired since February 1998 due to a change in transmitter pulse power. For ERS-2, the decrease in SAR transmitter pulse power continues at the rate of 0.63dB per year. The only consequence of this has been an increase in the noise equivalent radar cross-section (in mid 1999 it was estimated to be an acceptable -23dB).

Image localisation using the ESA transponders has given measured to be an excellent 26.4m. A comparison between transponder radar cross-sections derived using PRI and SLCI product types has shown a very small difference, averaged over a number of measurements, between the two product types.

#### REFERENCES

- [1] Meadows, P.J., Laur, H., Sánchez, J.I. & Schättler, B., 'The ERS SAR Performances', Proceedings of the CEOS SAR Workshop, 3-6 February 1998, ESTEC, Noordwijk, The Netherlands, ESA WPP-138, pp 223-232.
- [2] Meadows, P.J., Laur, H. & Schättler, B., 'The Calibration of ERS SAR Imagery for Land Applications', Proceedings of the 2<sup>nd</sup> International Workshop on Retrieval of Bio- & Geo-physical Parameters from SAR Data for Land Applications, 21-23 October 1998, ESTEC, Noordwijk, The Netherlands, ESA SP-441, pp 35-42.
- [3] Meadows P.J., Laur, H. & Schättler, B., 'The Calibration of ERS SAR Imagery for Land Applications', Earth Observation Quarterly, No 62, June 1999.
- [4] Meadows, P.J., 'The Use of Ground Receiving Stations for ERS SAR Quality Assessment', Proceedings of the CEOS SAR Workshop, 26-29 October 1999, Toulouse, France.
- [5] Laycock, J.E. & Laur, H., 'ERS-1 SAR Antenna Pattern Estimation', ESA/ESRIN, ES-TN-DPE-OM-JL01, Issue 1, Rev. 1, September 1994.
- [6] Laur, H., Bally, P., Meadows, P., Sánchez, J., Schättler, B., Lopinto, E. & Esteban, D., 'ERS SAR Calibration: Derivation of  $\sigma^0$  in ESA ERS SAR PRI Product', ESA/ESRIN, ES-TN-RS-PM-HL09, Issue 2, Rev. 5b, September 1998.
- [7] Earth Observation Programme Board, 'ERS Mission Status following partial ERS-1 Solar Array Failure', ESA Information Note ESA/PB-EO/DOSTAG(98)3, April 1998.

## RADARSAT-1 Image Quality - Update

S. K. Srivastava, B. T. Banik, M. Adamovic<sup>1</sup> and R. Gray<sup>2</sup>  
 Satellite Operations, Canadian Space Agency  
 6767 Route de l'aéroport, Saint Hubert, Quebec, Canada J3Y 8Y9  
 Tel: (450) 926-5133 Fax: (450) 926-4433 E-Mail: [satish.srivastava@space.gc.ca](mailto:satish.srivastava@space.gc.ca)

R. K. Hawkins, T. I. Lukowski and K. P. Murnaghan<sup>3</sup>  
 Canada Centre for Remote Sensing  
 588 Booth Street, Ottawa, Ontario, Canada K1A 0Y7  
 Tel: (613) 995-1067 Fax: (613) 947-1383 E-Mail: [Robert.Hawkins@CCRS.NRCan.gc.ca](mailto:Robert.Hawkins@CCRS.NRCan.gc.ca)

W. C. Jefferies  
 RADARSAT International  
 75 A McClelland Road, Cantley, Quebec, Canada J8V 2Y8  
 Tel: (819) 827-3001 Fax: (819) 827-1955 E-Mail: [bjefferies@rsi.ca](mailto:bjefferies@rsi.ca)

### ABSTRACT

The Canadian earth observation satellite, RADARSAT-1 was launched on November 4, 1995 and put into routine operations on April 1, 1996. Since then almost four years of successful operation have been completed, utilizing data for their intended applications. In this paper, we are primarily concerned with image quality associated with the image products generated by the Canadian Data Processing Facility (CDPF) for different SAR operating beams and modes. A chronology is presented which reviews the image quality evolution of RADARSAT-1 since launch, complementing previously presented reviews on this subject. Data will be given on various image quality parameters related to impulse response, location error, antenna pattern, and radiometric stability.

### INTRODUCTION

RADARSAT-1 was launched in November 1995, commissioned in March 1996, and put into routine operation on April 1, 1996. Since then almost four years of successful operation have been completed, utilizing data for their intended applications. The end-to-end image quality specifications and goals are set out in the RADARSAT System Specification document [1]. Previous publications on RADARSAT-1 performance may be consulted for further information describing image quality and calibration performance since launch [2],[3],[4]. This paper discusses radiometric and image quality performance since the start of the Maintenance Phase after the products were declared calibrated.

### RADIOMETRIC CALIBRATION AND IMAGE QUALITY PERFORMANCE

RADARSAT-1 has been under the Maintenance Phase since the end of the Radiometric Calibration Phase. Maintenance Phase started in February 1997. Tracking of beam calibration and image quality parameters is performed on a routine basis. Measurement parameters include point target impulse response measures: range and azimuth impulse response widths (IRW), range and azimuth peak sidelobe ratios (PSLR), integrated sidelobe ratio (ISLR), and absolute location error (ALE), using images of RADARSAT Precision Transponders (RPT). Radiometric accuracy performance is tracked by measuring deviations in measured pattern when compared to the calibrated pattern for any given beam, using images of the Amazon Rainforest. Special purpose software tools have been developed to track performance of radiometric and image quality parameters, and to compare those values against RADARSAT System Specifications. Some of them are described in [5].

Fig. 1 shows typical results for relative radiometric accuracy as measured for Beam S3 since its calibration date of May 1997. It also shows the period when the beam shape changed which resulted in its re-calibration. The re-calibration task for the beam S3 was completed in April 1999, but the resultant payload file was made effective October 1998 when a degradation in radiometric accuracy was first noticed. Details of re-calibration process are presented in another paper in these proceedings [5]. Figs. 2, 3 and 4 show IRW results for all three chirps, for all single beams. PSLR, ISLR

<sup>1</sup> On contract from *Lockheed Martin Canada*

<sup>2</sup> On contract from *Altrix Systems*

<sup>3</sup> On contract from *Isosceles Information Solutions Inc.*

and ALE measured results, each combined for all three chirps, are shown in Figs. 5, 6 and 7, respectively.

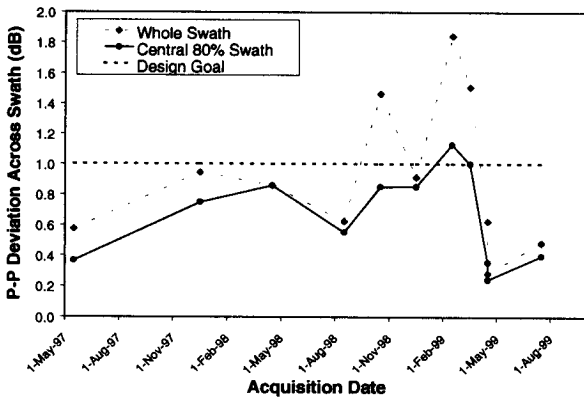


Fig. 1: Radiometric Accuracy Performance for Beam S3

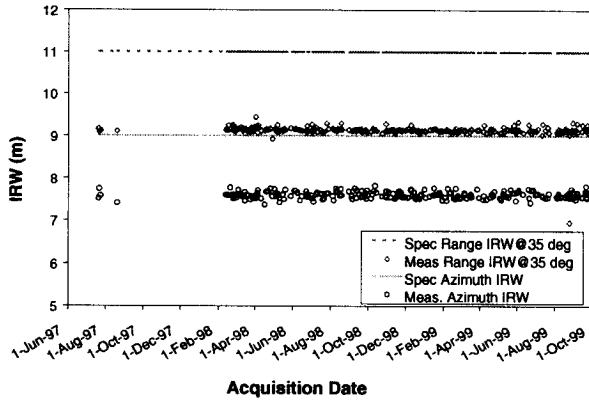


Fig. 2: Range and Azimuth Impulse Response Width for Chirp 1 Beams (BW=30.00 MHz)

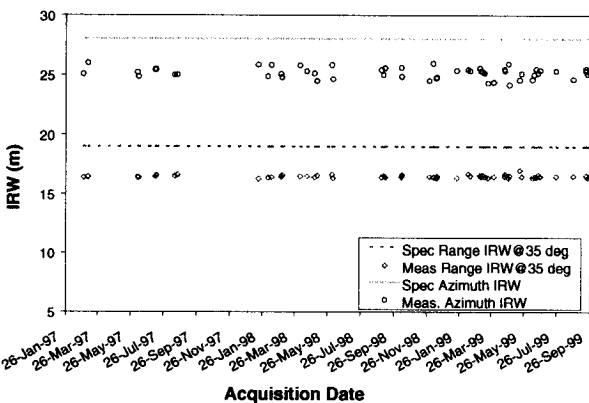


Fig. 3: Range and Azimuth Impulse Response Width for Chirp 2 Beams (BW=17.28 MHz)

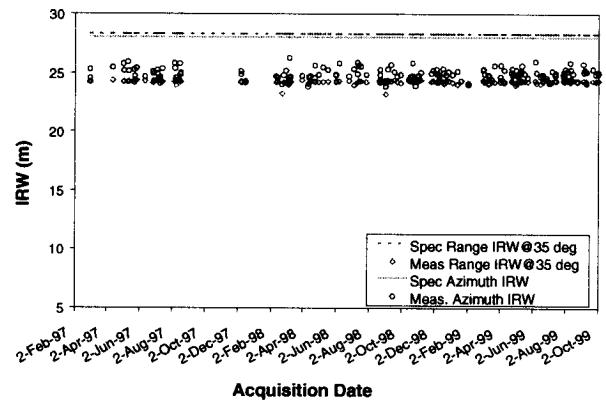


Fig. 4: Range and Azimuth Impulse Response Width for Chirp 3 Beams (BW=11.58 MHz)

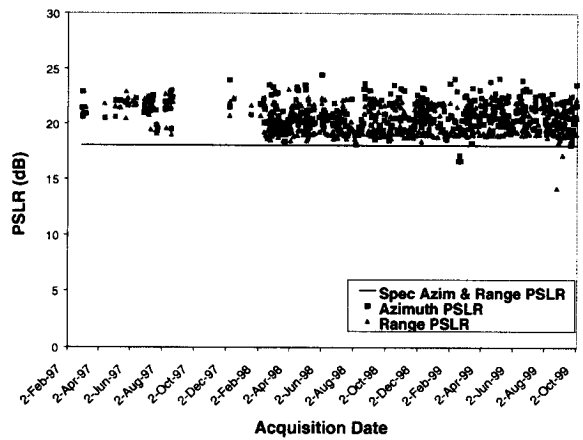


Fig. 5: Peak Sidelobe Ratio for all Beams

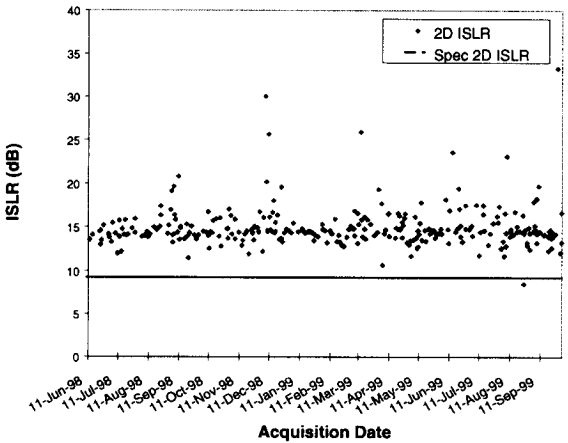


Fig. 6: Integrated Sidelobe Ratio for all Beams

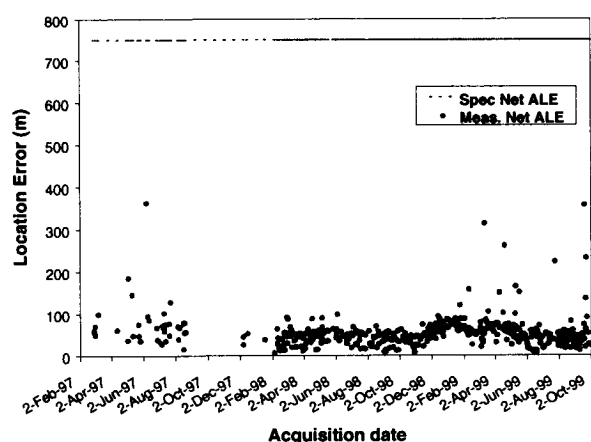


Fig. 7. Absolute Location Error for all Beams

All measured results for radiometry and point target indicate that both radiometric and image quality performance of RADARSAT-1 SAR are within the system specification, except when beams are being re-calibrated.

#### SCANSAR CALIBRATION

The CDPF ScanSAR processor has some problems in estimating the Doppler centroid and elevation beam pointing. As a result, scalloping effects and beam boundaries are observed in a number of ScanSAR images. Some improvements have already been made and work is continuing to upgrade the processing software, minimizing these problems. However, effective February 1, 1999, all ScanSAR images generated by the CDPF are radiometrically calibrated. As an illustration, a gamma-nought measurement for the Amazon Rainforest from a recent Narrow ScanSAR product is shown in Fig. 8. Based on a limited set of Amazon Rainforest data it is found that the worst case absolute accuracy is  $\pm 1.35$  dB, and relative accuracy is 2.7 dB within any image or between any two images. Users will most typically have imagery with radiometric accuracy of  $\pm 1$  dB, or better in absolute level (2 dB or better in relative level).

In addition to radiometric errors, some parts of some ScanSAR imagery may suffer from scalloping errors. Typical scalloping error when present is about 1.5 dB peak to peak, but in some cases it could be worse depending upon the terrain features. The scalloping errors are expected to be reduced when planned upgrades to the CDPF are completed. It should be noted that a constant Gamma-Nought of  $-6.5$  dB was used for the Amazon Rainforest for all ScanSAR incidence angles as a reference in calibrating ScanSAR.

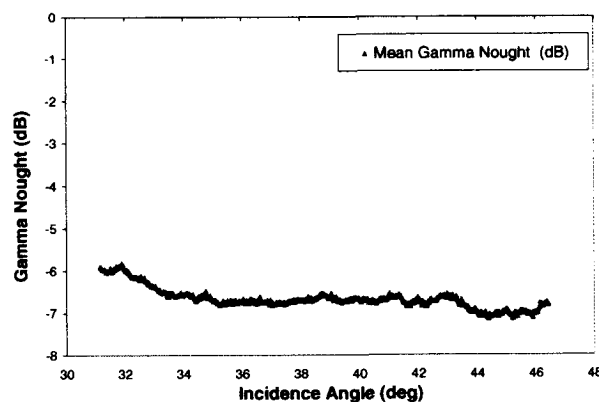


Fig. 8. Gamma-Nought for a ScanSAR Narrow Image of the Amazon Rainforest

#### RE-CALIBRATION OF SINGLE BEAMS

By the process of tracking the beam radiometric accuracy performance on a routine basis as part of the Maintenance Phase, a few beams were recently observed to have relative radiometric accuracy within a scene more than the design goal of 1 dB. The affected beams were W1 and F4. When investigated in detail it was found that the radiometric degradation was caused by changes in elevation beam pattern for these two beams. The beams were then re-calibrated in December 1998. Subsequently, additional measurements made on these beams indicate improved radiometric accuracy, which is well within the design goal. Similar behaviour was later noticed on beams S3 and S6. These beams were re-calibrated in April 1999. More recently beam S1 was re-calibrated in June 1999.

#### CONCLUSIONS

The measured relative radiometric accuracy in calibrated single beams is within the design goal. Beams W1, F4, S3, S6 and S1 have been re-calibrated due to changes in their elevation beam patterns. All other Image Quality parameters are performing better than the system specification. ScanSAR calibration has been completed and further improvements to the CDPF ScanSAR processor are forthcoming to improve radiometry and scalloping effects.

#### REFERENCES

- [1] "RADARSAT System Specification", *Canadian Space Agency Document RSCSA-SP0002, Rev. C, 1996.*
- [2] Proceedings of Committee on Earth Observation Satellites (CEOS) Workshop on RADARSAT Data

Quality, Canadian Space Agency, St. Hubert, Feb. 4-6, 1997.

- [3] R.K. Hawkins, et al, "Evolution of RADARSAT Calibration to Date", *Proceedings of CEOS SAR Workshop*, Noordwijk, the Netherlands, Feb. 3-6, 1998.
- [4] S.K. Srivastava, et al, "RADARSAT Image Quality and Calibration Performance", *Proceedings of*

*CEOS SAR Workshop*, Noordwijk, the Netherlands, Feb. 3-6, 1998.

- [5] B.T. Banik, et al, "Maintenance of Radiometric Calibration Performance of RADARSAT-1", these proceedings.

## Plans for Radiometric and Polarimetric Calibration of RADARSAT-2 Beams

Anthony Luscombe  
 MacDonald Dettwiler  
 13800 Commerce Parkway  
 Richmond, BC, V6V 2J3, Canada  
 Tel: +1 604 231 2448 Fax: +1 604 276 2856 Email: apl@mda.ca

### ABSTRACT

The RADARSAT-2 SAR currently under development will be required to operate in many modes, including a fully polarimetric mode and a selection of single and dual-polarization options for all other modes.

Radiometric calibration will therefore be required for many more beams than RADARSAT-1, and polarimetric calibration must also be performed for at least 30 beams.

This paper describes the plans that are being developed for radiometric and polarimetric calibration of these large sets of beams through intensive campaigns of data acquisition and analysis. The plans are based on an approach in which measurements are performed over a sufficient subset of the beams to allow modelling (or interpolation) to derive the equivalent information for other beams.

The aim is to complete initial calibration operations within a few months starting during the Commissioning Phase, with ongoing calibration measurement and analysis to refine and update the calibration throughout the mission.

Images of distributed target areas such as Amazon are being considered for use in both radiometric and polarimetric calibration. Because of the rapid switching time that can be achieved between modes, measurements can be performed for several beams during a single pass over the Amazon areas. Active transponders with appropriate polarization capabilities are highly desirable, but the availability of these devices is yet to be confirmed.

### RADARSAT-2 IMAGING MODES

The RADARSAT-2 system is designed to provide all the imaging modes of RADARSAT-1, with single-polarization (co- or cross-) and dual-polarization (co- and cross-) options, as well as some new modes. All imaging modes are available in either left- or right-looking orientation for the satellite.

The UltraFine Resolution mode will provide single-look single-polarization images with approximately 3m resolution covering swath widths of 20km. This mode

is available for incidence angles from 30° to 40° with possible extension to 50° and beyond. In this mode, the synthetic aperture is formed by alternating signals received simultaneously by the leading and trailing wings of the antenna.

The Quad-Polarization mode will provide full polarimetric data for swaths of at least 20km up to an incidence angle of 41°. Resolution options similar to the RADARSAT-1 Standard and Fine Resolution modes are available. Imaging is performed in a standard polarimetric mode with alternating H and V transmissions, and simultaneous H and V receptions.

Although these new modes involve a large number of beams, all these beams are simple focussed beams unlike the shaped beams used for all the heritage modes from RADARSAT-1. Pencil beams are less liable to distortion, and all beams of the Quad-Pol and UltraFine sets are similar in form. Both features are expected to simplify the calibration task.

### THE RADARSAT-2 SAR

The antenna dimensions and many of the operating parameters from RADARSAT-1 have been retained for RADARSAT-2, but the antenna technology is fundamentally different and other features have been extended and enhanced. The following are some of the key features of the RADARSAT-2 sensor:

- Pulse generation with bandwidths up to 100MHz
- Active phased array antenna with 16 rows of 32 T/R modules, each feeding a subarray of 20 elements
- T/R modules with two power settings and temperature compensation of phase and amplitude
- Two full receive channels used either for H and V polarizations or leading and trailing antenna wings
- Block Adaptive Quantization (BAQ) of all signal data with selectable wordlength (normally 4 bits I + 4 bits Q)
- High data rate (400Mbps) solid state recorders used for all data, with subsequent downlink on two 105 Mbps links
- Gaps between images reduced to less than 1s.
- Internal calibration capabilities, still to be defined.

## RADIOMETRIC CALIBRATION

### Requirements and Goals

The radiometric accuracy specifications for RADARSAT-2 are the same as for RADARSAT-1: relative errors (peak-to-peak) of no more than

- 1dB within a scene
- 1.5dB between points imaged within an orbit
- 2dB between points imaged within 3 days
- 3dB between points imaged during the mission

The aim is to achieve significantly better performance than this specification, particularly over longer timescales. It is also a goal to provide images with preliminary calibration information within a month or two of the end of the Commissioning Phase.

### Characteristics of the sensor

The antenna design allows independent phase control of an array of 16x32 T/R modules on transmit, and amplitude and phase control on receive. Beams will therefore have non-reciprocal transmit and receive patterns.

### Proposed Approach to Calibration

The radiometric calibration will be based on a similar type of measurement as RADARSAT-1, using images of specific uniform areas of the Amazon (and possibly other distributed target types). Beam patterns will be estimated from these data, and parameters in an antenna model will be adjusted to match the measured data from a representational set of beams. This set of beams will include a number of the wider, shaped beams, which are more susceptible to distortion, and therefore generally of greater value in characterising the cause of the distortion. If the adjusted model can be shown to predict other patterns with sufficient accuracy, an initial set of patterns for the full set of beams will be generated from the model for use in processing.

If it proves impossible to find a model which simultaneously matches all the measured data, or which fails to provide adequate predictions of other patterns, the measurement campaign will be continued until all shaped beams and a subset of the pencil beams have been measured.

Amazon imaging will be performed routinely throughout the mission to allow the model (or beam set) to be refined, and to enable radiometric performance to be monitored. These regular

measurements will also be used to track any systematic variations in the set, and to apply appropriate updates.

### Timeline

The following is a target (but very challenging) schedule for collection and analysis of calibration data:

- Collection of multiple images with a subset of beams within 24 days
- Adjustment and validation (if possible) of model within 48 days
- Measurement of all shaped beams within 96 days.

This schedule is based on:

- Imaging of only the Amazon area currently used for RADARSAT-1
- Multiple images with different beams within each pass over this area (approx. 5 seconds per beam)
- Collection of maximum number of polarizations (dual- or quad-) with each data take.
- Potentially 33 imaging passes and 128 images within 24-day orbit cycle.

## POLARIMETRIC CALIBRATION

### Goal

The goals for polarimetric calibration are channel imbalance of better than  $\pm 0.5\text{dB}$  and co-channel relative phase error of less than  $10^\circ$ .

### Characteristics of the Sensor

The following are some relevant features of the radar design, which have been taken into account in the preliminary polarimetric calibration plans:

- Common transmit path for H and V pulses up to the T/R modules
- Switch between H and V within the T/R module providing very good isolation ( $< -40\text{dB}$ )
- Simultaneous H and V reception by T/R modules
- Separate H and V receive paths from T/R modules right through to digital segment, with potential leakage only within switch matrix ( $< -40\text{dB}$ )
- The dominant cross-polarization leakage ( $-23\text{dB}$  or less) should be in the radiating patches on transmit and receive.
- H and V receive path distortion and leakage expected to be independent of whether previous transmission was H or V.

Based on these characteristics, it should be possible to represent the transmit distortion and receive distortion each as a 2x2 matrix containing imbalance and cross-talk terms. All terms may be beam- and elevation-angle



dependent, but these dependencies are expected to be systematic and progressive.

#### Approach to calibration

Various alternative methods are under consideration, and the final choice of baseline method will depend on the calibration targets available for regular imaging. Transponders with polarization versatility are desirable, but no commitment has yet been made to provide them.

Current studies are aimed at determining the amount of polarimetric calibration information that can be extracted from polarimetric imagery of the Amazon. Key characteristics of C-band Amazon data, in theory at least, are:

- Uniform, known  $\gamma^0$  for co-pol returns ( $S_{HH}$ ,  $S_{VV}$ )
- Significant cross-pol ( $S_{HV}$ ,  $S_{VH}$ ) return
- Backscatter reciprocity,  $S_{HV} = S_{VH}$
- Uncorrelated co- and cross-pol return,  $\langle S_{HH} \cdot S_{HV}^* \rangle = \langle S_{VV} \cdot S_{HV}^* \rangle = 0$
- Mean phase correlation of co-pol returns,  $\arg(\langle S_{HH} \cdot S_{VV}^* \rangle) = 0$

The accuracy of this characterisation, and the precision with which imbalance and cross-talk terms can be estimated from these data, are being assessed. The use of active and/or passive point calibration targets to supplement these data, or to validate results is also being examined.

On the basis of current information on the instrument design and hardware characteristics, it is anticipated that the polarization distortion matrices will vary systematically with beam and angle. (SIR-C experience gives credibility to this.) Current planning is therefore for collection and analysis of data from a subset of beams spanning the full range of elevation angles to be used for polarimetry. If a systematic variation can be identified across these data sets, the characteristics for intermediate beams will be predicted by interpolation, and validated using data actually collected with these beams. If no systematic variation can be identified, data will be collected and analysed for all polarimetric beams.

A specification has been placed on the payload for polarimetric (inter-channel amplitude and phase) stability to ensure that any polarimetric calibration data will remain valid over a period sufficient to allow tracking of variations.

Once an initial database of polarimetric distortion and correction data has been established, there will be

regular imaging of calibration sites to refine the database and track changes.

#### Timeline

The following is a target schedule for collection and analysis of polarimetric calibration data. The schedule is likely to be revised when the combination of point and distributed targets to be used has been decided. If polarimetric calibration is heavily reliant on Amazon imaging, the major collection campaign will have to be coordinated with the radiometric data collection, and may therefore be delayed:

- Collection of multiple images with a subset of beams within 24 days
- Analysis of data for subset of beams, interpolation to other beams, and preliminary validation (if possible) within 48 days
- Measurement with all beams (if necessary) within 72 days.

This schedule is based on:

- Imaging of distributed target in the Amazon area currently used for RADARSAT-1 and of transponders (if available) in the current locations
- Multiple images using different beams within each pass over the Amazon area
- Potentially 33 imaging passes and 128 images within 24-day orbit cycle for Amazon.
- Potentially 112 imaging opportunities for transponders within 24-day orbit cycle

#### ONGOING AND FUTURE WORK

The calibration plans for RADARSAT-2 are still under development. The following are some key items of work which are currently underway, or are planned for the near future.

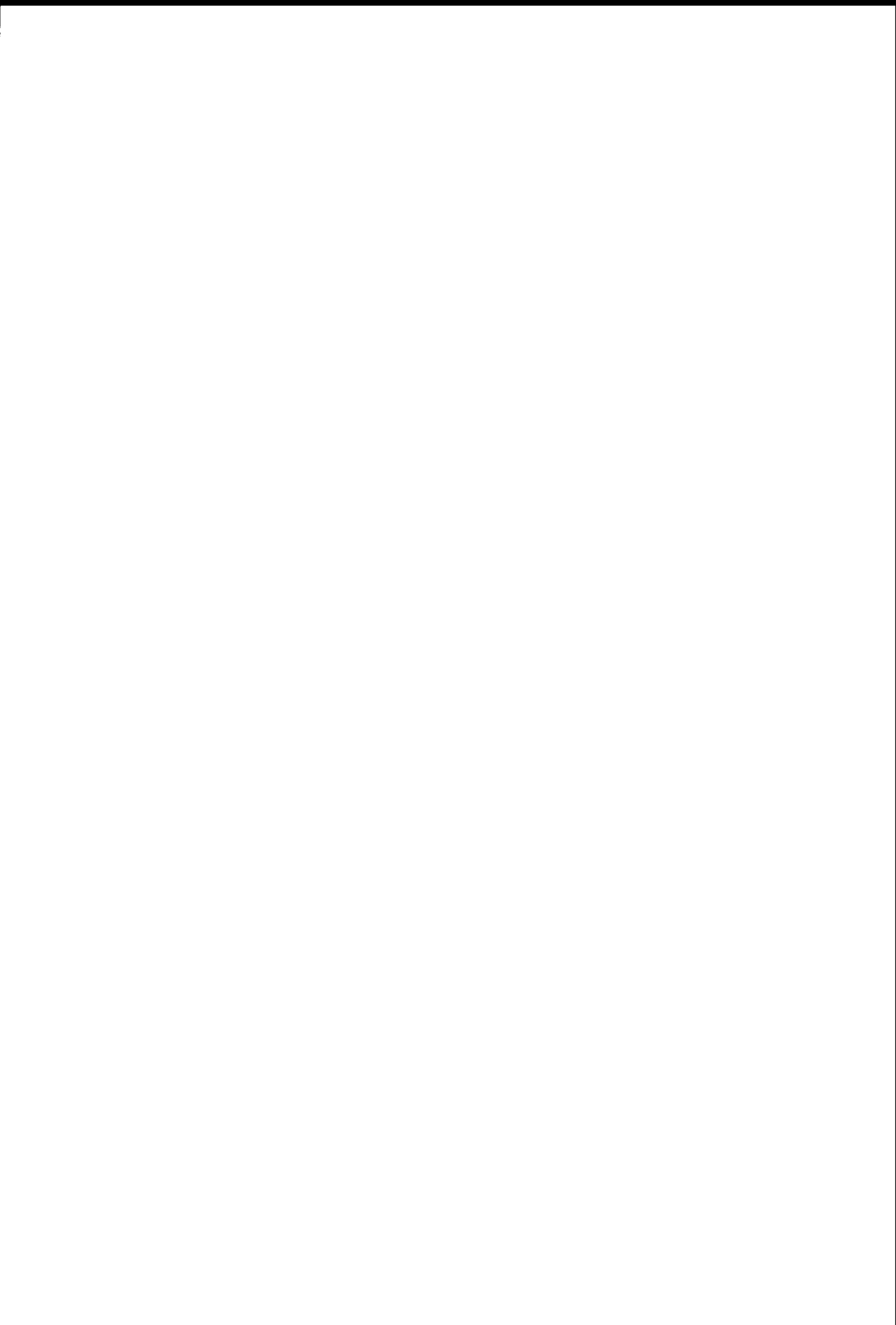
- Examination of SIR-C Amazon data sets to determine the accuracy and stability of theoretical data characteristics. Experimentation with polarimetric analysis routines using these data sets.
- Refinement of the instrument model as sensor design is firmed up and hardware measurement data become available.
- Decision on provision of point calibration targets.
- Inclusion of calibration imaging campaigns in operations planning documents for Commissioning Phase and the early Operational Phase. Inclusion of routine calibration data collection in operations planning for the full mission.
- Assessment of what polarimetric calibration information can be extracted from general scenes as a backup.



## **Calibration of the GEOSAR Dual Frequency Interferometric SAR**

Elaine Chapman, Scott Hensley, Delwyn Moller  
(Jet Propulsion Laboratory, USA)

This paper was not available for publication.



## Calibration of an X-band Airborne Synthetic Aperture Radar with Active Radar Calibrators and Corner Reflectors

Makoto SATAKE, Toshihiko UMEHARA, Tatsuharu KOBAYASHI, Akitsugu NADAI, Takeshi MATSUOKA, Seiho URATSUKA, Hiroyuki WAKABAYASHI\*, and Masanobu SHIMADA\*

Earth Environment Division, Communications Research Laboratory (CRL)  
Ministry of Posts and Telecommunications  
Koganei, Tokyo 184-8795, JAPAN  
Tel. +81.42.327.6101 / Fax. +81.42.327.5521 / Email: satake@crl.go.jp

\* National Space Development Agency of Japan (NASDA)

### ABSTRACT

Communications Research Laboratory (CRL) and National Space Development Agency of Japan (NASDA) developed an airborne imaging radar system consisting of an X-band (polarimetric/ interferometric) SAR and an L-band (polarimetric) SAR, to acquire SAR data for the research of monitoring earth environments and disasters surveillance. To obtain normalized radar cross-section ( $\sigma_0$ ) of earth surfaces from the data precisely, CRL and NASDA are making external calibrations of the SAR's using calibration reflectors. This paper describes the X-band SAR calibration using corner reflectors (CR) and active radar calibrators (ARC). CR of a triangle trihedral is used for radiometric calibration of like-polarization (HH and VV) and to estimate imbalance between HH and VV components. ARC that can select polarization (H or V) in reception and transmission is used for calibration of cross-polarization (HV and VH) components. We made a calibration experiment in October 1998 deploying those reflectors in the Tottori dune, Japan. Preliminary results of the experiment are presented, including CR responses when SAR signals were, unexpectedly, saturated.

### INTRODUCTION

An airborne imaging radar system consisting of an X-band and an L-band synthetic aperture radar (SAR) had been developed jointly by Communications Research Laboratory (CRL) and National Space Development Agency of Japan (NASDA). With polarimetric function for both the X-band and L-band SAR's and interferometric function for the X-band one, it was named 'PI-SAR' as abbreviation of Polarimetric and Interferometric Airborne Synthetic Aperture Radar. Since completion of its fundamental hardware development in 1996, we have been making flight experiments with this radar system to

obtain SAR images in Japan for the purpose of the research, especially on monitoring earth environments and disasters surveillance.

External calibration of the SAR's are also proceeded by CRL and NASDA using calibration targets, to obtain normalized radar cross-section ( $\sigma_0$ ) of the surface from the data precisely. This paper is on calibration of the X-band SAR by CRL using corner reflectors (CR) and active radar calibrators (transponder) (ARC).

### PI-SAR SYSTEM

PI-SAR is a multi-parameter airborne imaging radar. Features of the PI-SAR are:

- Multi-frequency observation of X- and L-bands,
- High resolution of 1.5 m for X-band and 3.0 m for L-band,
- Polarimetric observation both for X- and L-bands,
- Interferometric observation (one pass) for X-band.

Mounted on the Gulfstream II jet airplane as shown in Fig. 1, it is operated to observe earth surfaces in about 10 km swath, from 6000 to 12,000 m altitudes, at about 200 m/sec navigation speeds. Main characteristics of PI-SAR are summarized in Table 1.

### CALIBRATION STRATEGY

Reliable calibration is necessary for PI-SAR, not only for our research, but also for wide use of its data in science community. Although radiometric performance such as antenna patterns and losses in each channel were thoroughly measured while it had been manufactured and it has internal calibration mode to monitor its transmitter-to-receiver performances routinely, we had decided to make external calibration with calibration targets to estimate normalized radar cross-section ( $\sigma_0$ ) of earth surfaces precisely from measured data on the fly.

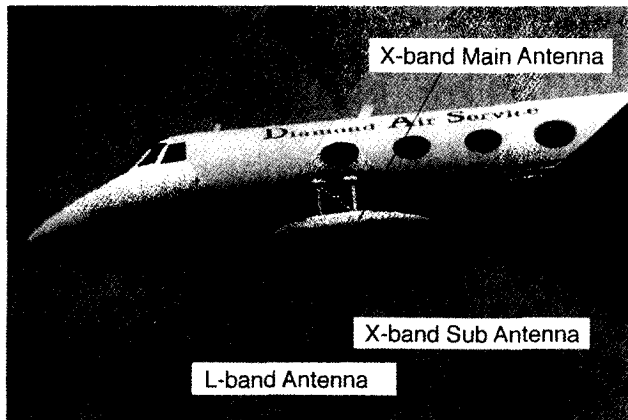


Fig. 1 PI-SAR antennas mounted on Gulfstream II.

In order to make the external calibration, we had developed corner reflectors (CR) and active radar calibrators (ARC) as calibration targets.

*Corner reflector (CR)*

CR is used to make radiometric calibration of like-polarization (HH/VV) components. We had developed triangle trihedrals of 10, 15, 20, 30 cm leg length, corresponding to radar cross sections of -3.7, 3.3, 8.3, 15.4 dBm<sup>2</sup> for the X-band respectively. Five CR's of each size (20 in total) had prepared and used in the calibration experiment to obtain many data samples.

*Active Radar Calibrator (ARC)*

ARC was developed to obtain cross-polarization (HV/VH) signals for polarimetric calibration. Key

parameters of the ARC are shown in Table 2 and its appearances in Fig. 2. The ARC is capable to select

Table 2 ARC parameters.

Frequency	9.4 ~ 9.7 GHz
Antenna	Square Horn
-Type	15 dB
-Gain	~ 25 deg.
-3-dB beam width	-30 dB (H plane)/ -20 dB (V plane)
-Peak Sidelobe	1 Rx and 2 Tx
-Number used	0 (H), 45 (H and V), 90 deg. (V)
-Polarization	~16 dB
-Pol. isolation	+30 ~ -30 dBm <sup>2</sup>
Sigma (cross section)	

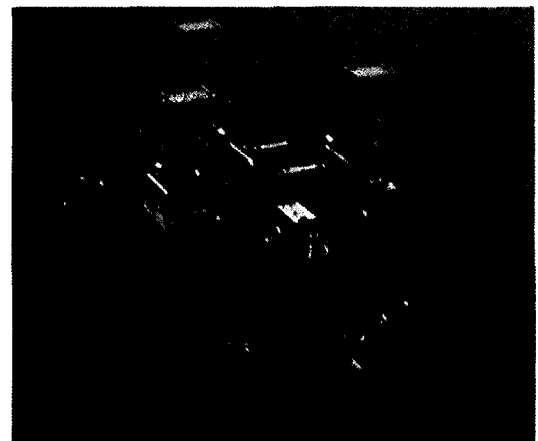


Fig. 2 ARC deployed in the experiment.

Table 1 Main characteristics of PI-SAR.

	X-band SAR			L-band SAR	
Frequency	9.55 GHz			1.27 GHz	
Transmit. Power (HPA peak)	8.3 kW			3.5 kW	
Bandwidth	100 MHz			50 MHz	
Antenna, Length x Width	1.05 m L x 0.19 m W (2 for V pol. & 1 for H)			1.55 m L x 0.65 m W	
Off-nadir Look Angle	10 -75 deg. (Variable)			20 -60 deg. (Fix)	
Observation Mode	2-Ch. <sup>*2</sup> Pol./ Int'fero.	4-Ch. <sup>*3</sup> Pol.	6-Ch. <sup>*4</sup> Pol.&Int'fero.	1-Ch. <sup>*1</sup>	4-Ch. <sup>*3</sup> Pol.
Swath Width (12,000m Alt.)	19.6/ 42.5 km	8.2/ 19.6 km	4.3 / 11.9 km	42.5 km	19.6 km
Slant Range Resolution	1.5/ 3 m	1.5/ 3 m	1.5/ 3 m	3/ 5/ 10/ 20 m	3/ 5/ 10/ 20 m
Azimuth Resolution (4/8-look)	1.5/ 3 m			3/ 6 m	
Interferometry - Baseline - Topographic Accuracy	2.3 m ≤ 2 m (rms.)			N/A	
Data Sampling	123.45 / 61.725 MHz			61.7 / 30.9 MHz	
Data Quantization	8 bits (I and Q)			8 bits (I and Q)	
Data Rate	512 Mbps			256 Mbps	

\*1) 1-Ch [L] (HH) or (VV)  
 \*2) 2-Ch [X] Polarimetry: (HH, HV) or (VV, VH) / Interferometry : (Vmain, Vsub)  
 \*3) 4-Ch [X, L] Polarimetry: (HH, HV, VH, VV)  
 \*4) 6-Ch [X] Polarimetry & Interferometry: (HH, HV, VH, VV, Vmain, Vsub)

polarization to receive and to transmit between H and V by rotating antennas. The polarimetric ARC (or PARC) is needed to generate cross-polarization components, but its response could be unstable due to temperature and misalignment. To correct the response of the PARC, response of a CR may be useful, although a CR reflects only like-polarization. While most of other PARC's have one transmitting channel only for cross-polarization, our PARC has two channels to re-transmit both like- and cross-polarization. Its like-polarization component can be corrected by a CR's response, which makes the cross-polarization component also corrected. As a result, accuracy of the polarimetric calibration with the PARC will be improved. Two PARC's had prepared and used in the experiment to assign H reception to the one and V reception to the another.

### CALIBRATION EXPERIMENT

In October 1998, we deployed several types of calibration targets (both for X and L-band), including the CR's and the ARC's mentioned above, in the Tottori dune. X- and L-SAR images of the area with those targets were taken several times from the altitude of 6,000/12,000m at the incidence angle of 55/40 degrees [1].

Although the dune is the largest in Japan, the site of a sand surface where we deployed array of calibration targets had small topography, undulation and gentle slope along azimuth direction. Also in the area were scattered grass, near-by trees (within 100m) and a building (within 500m). Those inhomogeneity in the background may affect the calibration targets' responses in SAR images.

### EXPERIMENTAL RESULTS

Examples of CR's responses in the data-take #1805 and #1901 are shown in Fig. 3 and 4. In the data-take #1805 from 6,000m altitude at 55 deg. incidence angles (at the peak of range pattern of the antenna gain), Fig. 3, responses of the same size CR fluctuates largely as much as 7 dB (much larger in HH than VV). We have found it is due to saturation of SAR signals, further discussed later. Meanwhile in #1901 from 12,000m altitude at 40 degree incidence angles (15 deg. near from the peak), Fig. 4, responses are rather stable within 1 dB in the same size CR, except for the smaller (10 cm, 15 cm) CR's. Responses of smaller CR's are unstable and larger than expected. It may be explained by larger noise level at higher altitude and lower antenna gain (compared with #1805).

Detailed analysis of the results including ARC's responses is ongoing.

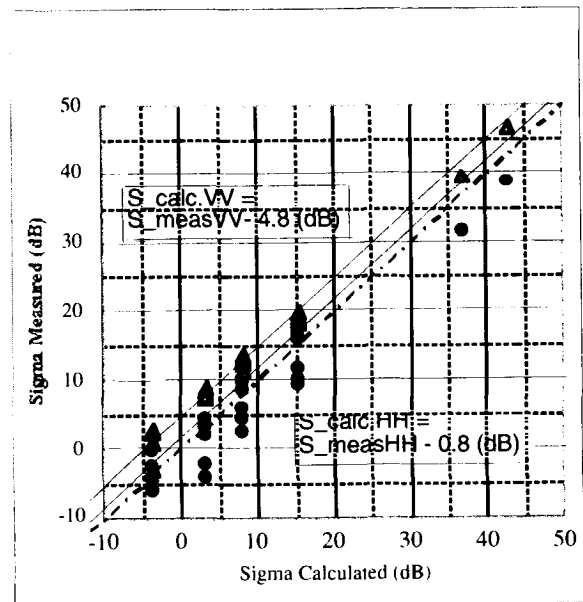


Fig. 3 CR's responses in data-take #1805: altitude 6000m, at range peak. [O: HH,  $\Delta$ :VV]

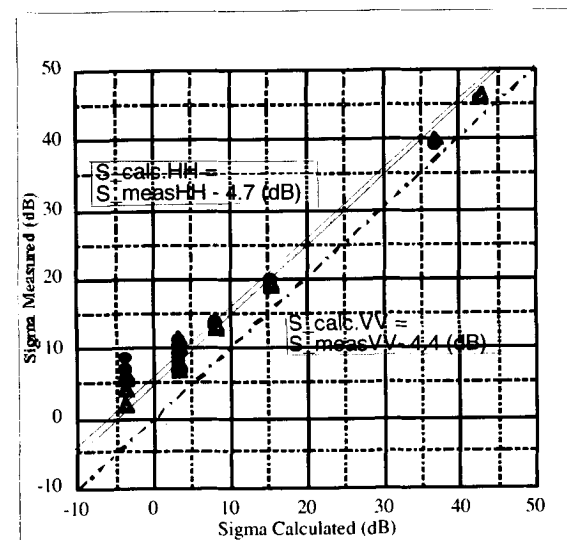


Fig. 4 CR's responses in data-take #1901: altitude 12,000m, 15 deg. near from range peak. [O: HH,  $\Delta$ :VV]

### SATURATION OF SAR SIGNALS

Fig. 5 shows CR responses plotted by each size along the position in azimuth ('a' is located at the earliest in azimuth and 'e' is the latest) for the data-take #1805, the same data as shown in Fig. 3. We see a decline of reflected power of CR depends on location in azimuth.

Fig. 6 shows saturation rate of the SAR data in each azimuth line over the corresponding area of CR's. The rate was estimated from the number of outliers of analog-to-digital conversion range (8 bit) in the receiver. Higher saturation rates are seen in later in azimuth, corresponding to smaller CR's responses in Fig. 5. Saturation in SAR signals (before compression) makes its image (after range and azimuth compression) deteriorated [2]. Therefore it can be said that the unusual fluctuations of CR's responses in #1805 result from saturation in received power due to improper gain control.

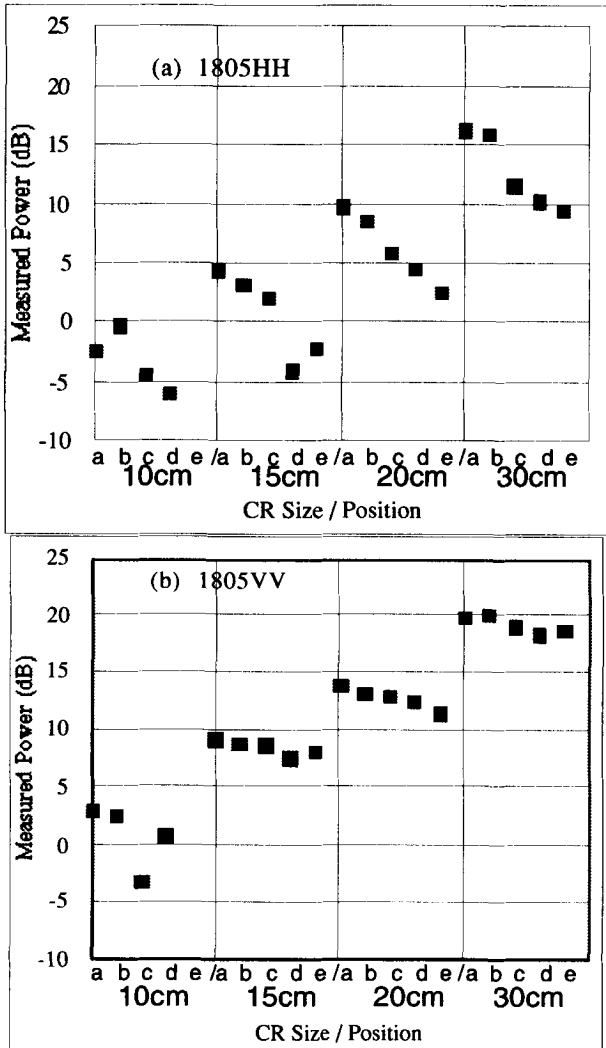


Fig. 5 Corner reflectors (CR) responses in (a) HH, (b) VV image (after compression) in data-take #1805.

CONCLUDING REMARKS

The paper describes the calibration of the X-SAR of PI-SAR system with a preliminary results of the calibration experiments. Detailed analysis of the experimental results is ongoing and calibration coefficients including polarimetric ones will be announced for use of quantitative data analysis in near future.

REFERENCES

- [1] M. Satake, et al., Corner Reflector's Responses Observed by X-band Polarimetric Airborne Synthetic Aperture Radar, Proc. of IGARSS'99, pp.2667-2669, 1999
- [2] M. Shimada, Radiometric Correction of Saturated SAR Data, IEEE Trans. GRS, vol. 37, pp. 467-478, 1999.

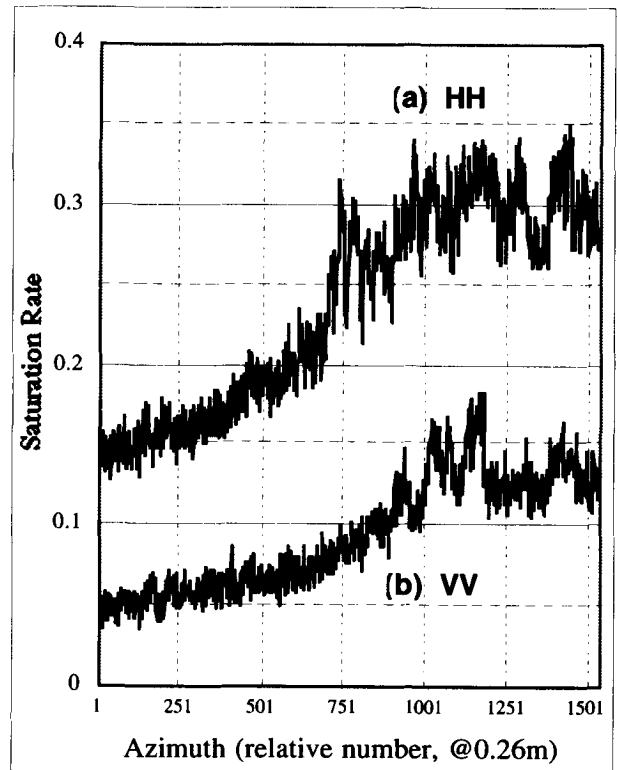


Fig. 6 Saturation rates of (a) HH, (b) VV Level-0 data (before compression) in data-take #1805.



## Stability of Amazon Backscatter at C-band: Spaceborne Results from ERS-1/2 and RADARSAT-1

RK Hawkins<sup>†</sup>, E Attema<sup>‡</sup>, R Crapolicchio\*, P Lecomte\*, J Closa<sup>♥</sup>, PJ Meadows<sup>†</sup>,  
and SK Srivastava<sup>††</sup>

<sup>†</sup>Canada Centre for Remote Sensing, 588 Booth St, Ottawa, K1A 0Y7, Canada;  
Email: robert.hawkins@ccrs.nrcan.gc.ca

<sup>‡</sup>European Space Agency, ESTEC, PO Box 299, 2200 AG Noordwijk, The Netherlands;  
Email: eattema@estec.esa.nl

\*European Space Agency, ESRIN/PCS, 00044 Frascati, Italy; Email: rcrapolicchio@esrin.esa.it,  
plecomte@esrin.esa.it, Josep.Closa@esrin.esa.it

♥ SERCO Srl /ESA/ESRIN, 00044 Frascati, Italy; Email: Josep.Closa@esrin.esa.it

<sup>†</sup>Marconi Research Centre, West Hanningfield Rd, Chelmsford, Essex, CME 8HN, United Kingdom;  
Email: peter.meadows@gecm.com

<sup>††</sup>Canadian Space Agency, 6767 Route de l'aéroport, Saint Hubert, Québec, Canada;  
Email: satish.srivastava@space.gc.ca

### ABSTRACT

This paper looks at the question of the temporal and spatial stability of the Amazon rainforest as a distributed target calibration source. The Amazon rainforest has been established by a number of investigators as a useful means of determining the in-orbit antenna pattern of spaceborne SAR and scatterometers. It was used for ERS-1 and ERS-2, J-ERS-1, and RADARSAT-1 providing a large isotropic backscattering reference over a wide range of incidence angle. In this paper, we look at a long series of results from ERS and RADARSAT to examine the temporal and spatial stability of this target class. These properties are supported by a simple radar signature model.

In any radar measurement, uncompensated variation in the sensor may be included with changes in target backscatter. Results from independent measurements from precision transponders are used to assess the size and characteristics of these inherent systematic variations before discussing the implications of the Amazon backscatter measurements.

The implications of the results for future missions are also explored.

### INTRODUCTION

The Amazon rainforest is a vast area comprising over  $3 \times 10^6$  km<sup>2</sup> located along the equator, mostly (2/3) in Brazil but extending into Peru, Colombia and Ecuador. It consists of a high, dense canopy stretching to

approximately 30 m although there is considerable diversity in types and stages [1,2]. Biomass ranges from 100 to 300 tons/ha with annual precipitation, approximately 3 m. This region is popularly understood as the source of ~30% of the oxygen flux, a storehouse of biodiversity and a natural indicator of climate and other ecological changes.

To the incident radar frequencies used in remote sensing satellites and many airborne systems which operate at X, C and L-band, most of the scattered radiation is from the crown area and tends to have a slow incidence angle,  $\theta_{inc}$ , variation which can be characterized by the relation:

$$\gamma = \text{constant} = \sigma^o / \cos \theta_{inc} = \beta^o \tan \theta_{inc} \quad (1)$$

Here  $\gamma$ ,  $\sigma^o$ , and  $\beta^o$  are forms of the backscattering coefficient and radar brightness used to define the scattering properties of a distributed target [3]. This property and small temporal variation, first noted with Seasat and Skylab [2], together with a number of logistic advantages which include the large areal extent and low relief of the area (<200 m) make the use of the Amazon forest a favoured site for the determination of in-flight antenna patterns for the synthetic aperture radars (SAR) and scatterometers: Seasat [4], ERS-1 [5], ERS-2, RADARSAT [6], JERS-1 and Sir-C [7]. In these instances, property (1) is used to invert the radar equation allowing a determination of the relative antenna pattern in the elevation plane. The details of that inversion depend on the normalization used in the

SAR processor and other implementation factors of the system.

Despite the fact that the Amazon basin constitutes a wide area of relatively high homogeneity, care is taken in practise to assure that any local departures are handled by appropriate statistical filtering [8] when antenna pattern shapes are derived. Fig. 1 is a J-ERS-1 composite of the entire Amazon basin [9] showing the homogeneity and variability of the region.

Table 1: Characteristics of operational instruments

Instrument	Freq (GHz)	Pol	$\theta_{inc}$	Res <sup>†</sup> (m)
ERS-1/2 SAR	5.30	VV	19-27°	25
ERS-1/2 Scatterometer	5.30	VV	18-59°	50000
J-ERS-1	1.275	VV	36-41°	18
RADARSAT-1	5.30	HH	10-59°	25



Fig. 1: J-ERS-1 mosaic of the Amazon basin. Descending passes from over 60 swaths are combined in the mosaic comprised of approximately 2000 individual scenes.

Operational satellites have had an opportunity to repeatedly view the region and should be able to provide some sort of seasonal if not longer term basis. This is particularly true of J-ERS-1, ERS-1/2, and RADARSAT-1. Table 1 gives a summary of some overall parameters of these instruments germane to this discussion.

We note differences in frequency, polarization, and incidence angles. For this study, we will restrict our focus to the C-band instruments. In the sections below, we comment on the scattering theory which leads to property (1) and then go on to discuss the results from ERS and RADARSAT.

<sup>†</sup> Resolution here is of a typically processed product for this analysis.

## MICROWAVE SIGNATURE MODEL OF DENSE FOREST

Because the microwave dielectric constant of dry vegetative matter is much smaller than the dielectric constant of water, and because a canopy (even a dense forest) is composed of more than 99% air by volume, a radar signature model for vegetation canopies has been proposed in which the canopy is represented by a water cloud whose droplets are held in place by the vegetative matter [10]. Applying radiative transfer theory to this model, the radar backscattering coefficient per unit projected area,  $\gamma$  for dense forests simply depends on the biomass,  $B$  (tons/ha), incidence angle and two empirical parameters,  $C$  and  $D$ . These parameters depend on a number of physical quantities such as target structure, radar wavelength, and polarisation. According to the cloud model, the equation for  $\gamma$  can be written as

$$\gamma = C \left[ 1 - \exp\left(\frac{-BD}{\cos \theta_{inc}}\right) \right] \quad (2)$$

Fig. 2 shows that this simple model nicely predicts the well known saturation of the radar echo for higher values of biomass as well as the smooth variation with incidence angle already expressed in (1). In the example shown,  $C=0.23$  and  $D=0.05$ , are values

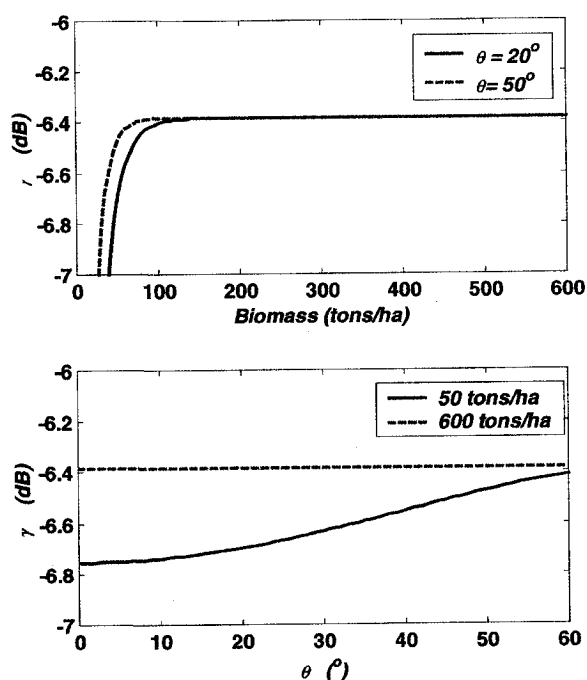


Fig. 2: Dense forest model of  $\gamma$  as a function of biomass and incidence angle

considered appropriate for C-band, VV polarisation.

For the biomass appropriate to the rainforest, this theory suggests asymptotic (constant) behaviour for the backscatter with biomass and incidence angle.

## ERS-1/2 SCATTEROMETER RESULTS

Some of the most complete data sets from the Amazon rainforest come from the ERS-1/2 scatterometers [11] which have been in continuous operation since 1991. The instrument has three side looking beams with a swath of 500 km with diversity in azimuth look direction. Ongoing monitoring of the area [12] located between  $2.5^{\circ}\text{N}$  and  $5.0^{\circ}\text{S}$  and  $62.5^{\circ}\text{W}$  and  $75.0^{\circ}\text{W}$  occurs with weekly synopses for each of the beams in ascending and descending geometries. Fig. 3 shows a monthly synopsis and Fig. 4, an associated histogram providing weekly statistics from approximately the same time frame. From these figures, we note:

- The three beams appear to be measuring slightly different properties but differ by as little as 0.1 dB.
- There is significant ( $> 1$  dB) spatial variation over the test region.
- Ascending (night) and descending (day) passes also show strongly varying spatial distributions.

Fig. 5 shows the variation of the weekly means from each of the ERS-2 scatterometer beams for the period January, 1996 to April 1999. We note:

- Both ascending and descending passes show an annual cycle with amplitude approximately 0.15 dB modulating more noise like variations about 0.05 dB. (The large step in the early part of the data stream is due to a calibration adjustment.)
- The annual variation is thought to be geophysical in nature since it has been shown to be uncorrelated with annual variations in the antenna temperature ( $2^{\circ}\text{C}$ ) [13]. Similar annual variations with ERS-1 *could not* be correlated with specific rainfall events at Benjamin Constant [16]. This result is not necessarily at odds with ERS-1 scatterometer results recently published [14] which show *strong* seasonal correlation between accumulative precipitation over a period of about 30 days. These authors have shown variations as much as 0.5 dB during 1993 from a Guyanain rainforest test site of  $50 \times 50$  km. More typical global RMS variations [15], determined from ERS-1, are 0.59 dB.

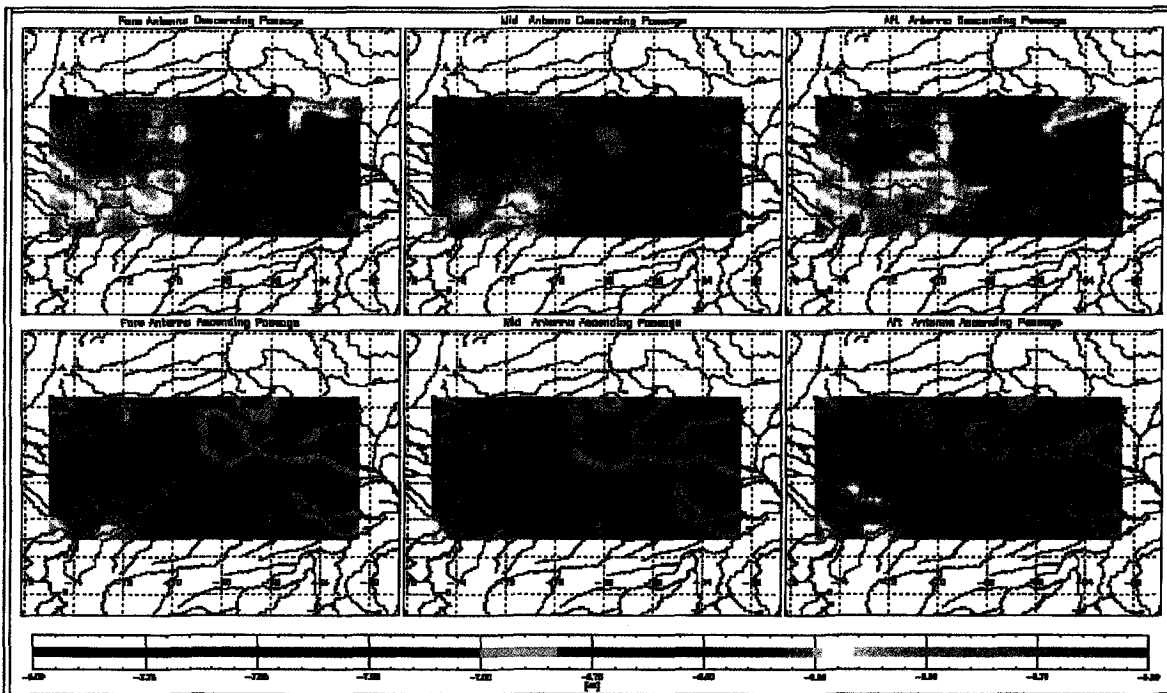


Fig. 3: ERS-2 winds scatterometer monthly synopsis  $\gamma$  image of Amazon basin March 13 to April 18, 1999

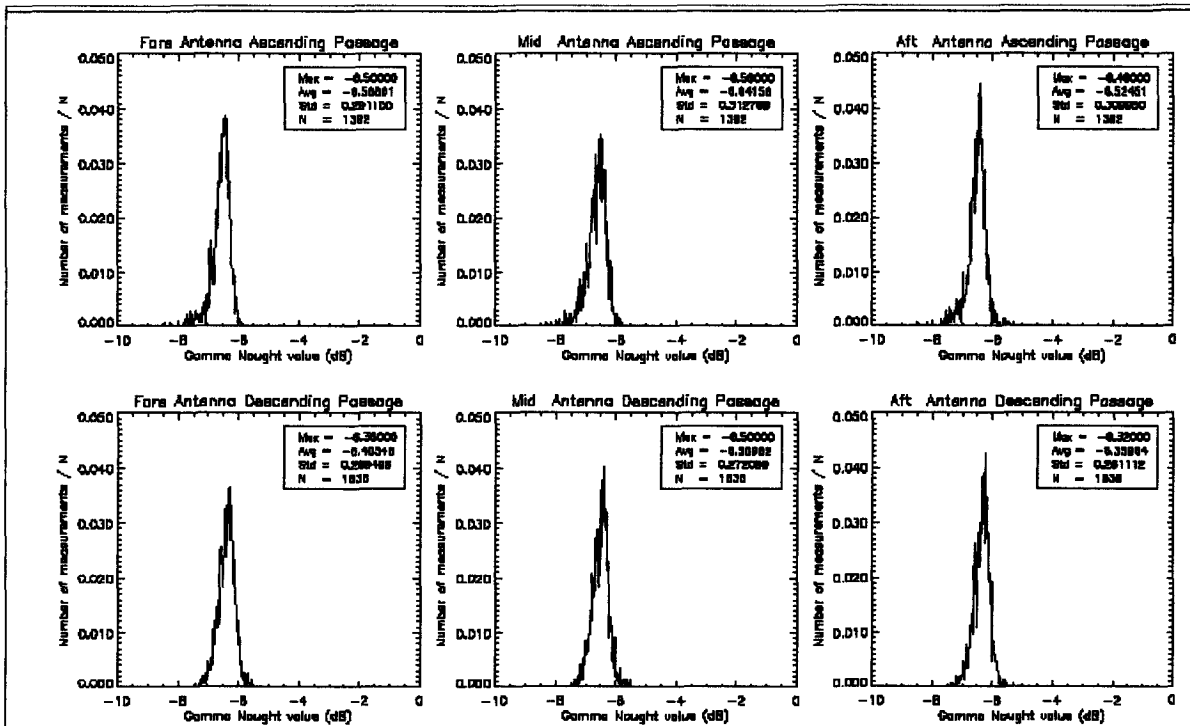


Fig.4: Weekly  $\gamma$  histogram synopsis from ERS-2 from April 12 to April 18, 1999

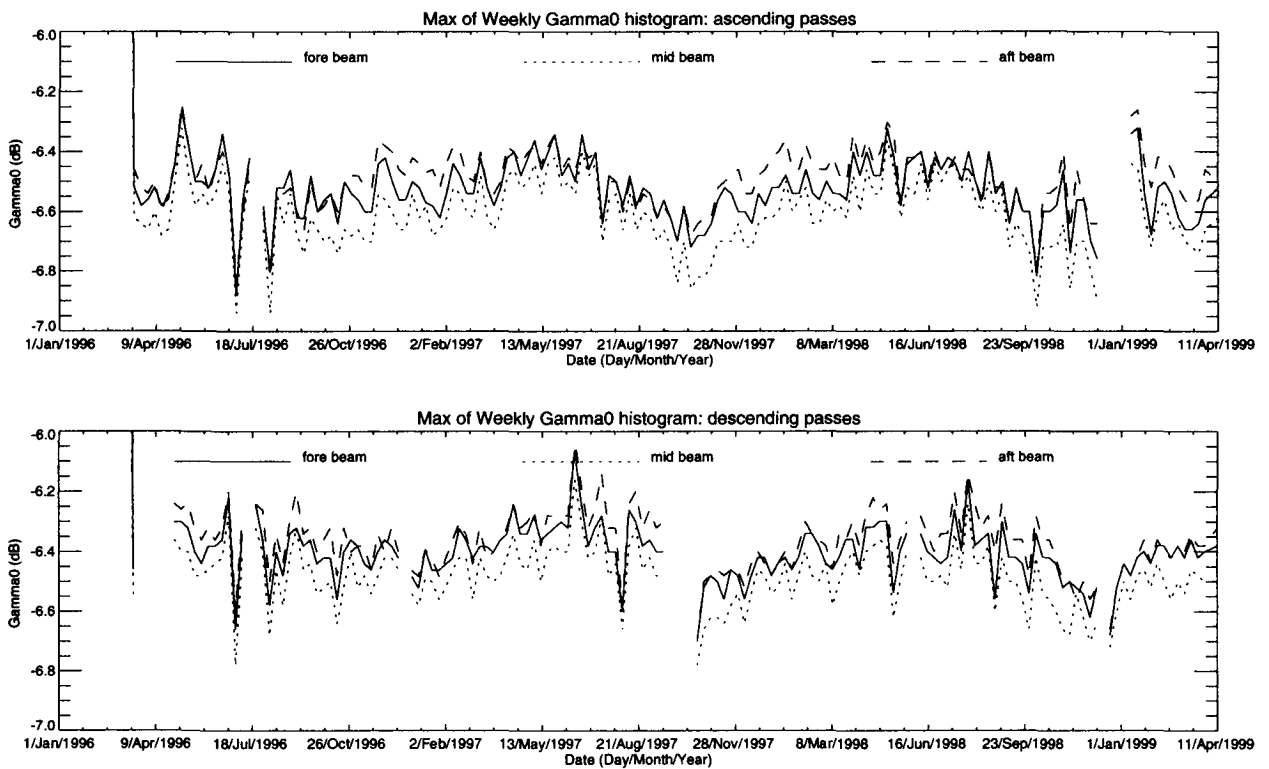


Fig. 5: History of weekly  $\gamma$  maxima from ERS-2 scatterometer from Jan 1996 to April 1999

### ERS Scatterometer Stability

The ERS scatterometer was calibrated [16] using the Amazon to derive antenna patterns and transponders to derive the absolute levels. The small differences in the mean levels in the three beams are believed related to the measurements biases introduced in the calibration. Compared to the ERS SAR, these instruments have had less attention paid to their calibration [17], and relatively fewer measurements [18] have been taken during the commissioning phase of the instrument.

In Fig. 6, features of the ESA scatterometer transponder calibration data for the *forebeam* are shown, as the *DGCF* (differential gain correction factor) defined as:

$$DGCF = \frac{\text{Measured RCS}}{\text{Actual RCS}} \quad (3)$$

Variation in the *DGCF* reflects uncertainty in the instrument calibration for an individual scene at the incidence angle of the point target measurement. It is a measure of the total number of interrelated uncertainties including S/C roll, recovery of the point target impulse response, processing as well as systematic drifts in both the calibrator and the radar. We can only discuss the variation in Amazon data in the wider context of the stability shown with these point target references since they are a measure of our ability to characterize the

overall performance of the system. At the top, is the dependence of *DGCF* across the 10 scatterometer beam segments showing individual measurements; in the middle, is a time history irrespective of beam; and, at the bottom a histogram of that data measuring a RMS variation of 0.20 dB. This is our best direct knowledge of the scatterometer stability and is very much better than the system specification of 0.7 dB.

The data are combined across the swath to obtain this statistic to compare with the weekly synoptic averages discussed above. We believe that this figure represents a pessimistic estimation of the scatterometer stability because of limitations in the instrumentation and techniques employed. Indeed, data from the Greenland ice cap [19] have shown stabilities better than 0.1 dB over an extended time. Fig. 7 shows the temporal backscatter stability in the interior of Greenland [20].

Given these results, it is likely that, of the three instruments studied in this paper, the ERS scatterometer has the most sensitivity to small changes in the backscatter of the Amazon. The measurements are however for larger area footprints than the 'imaging' SAR sensors.

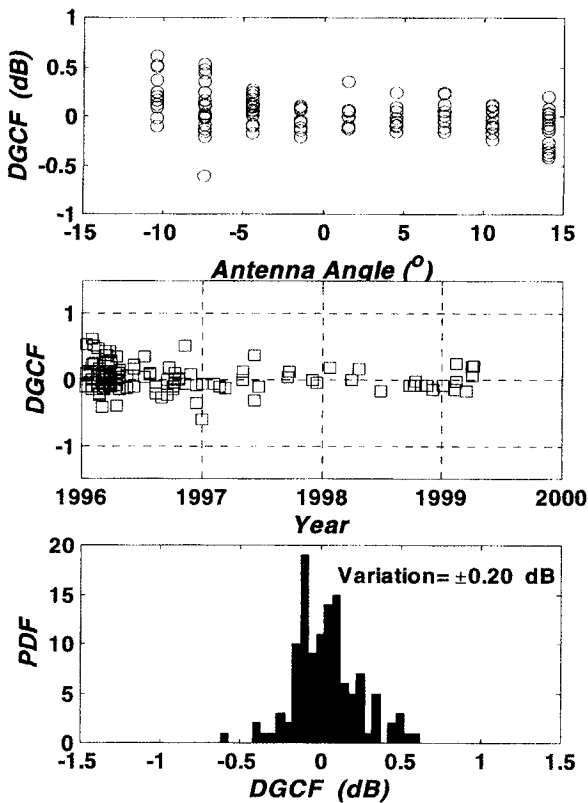


Fig. 6: ERS-2 scatterometer forebeam transponder results

### RADARSAT-1 RESULTS

Fig. 8 is a time history of RADARSAT-1 data at HH-polarization over the Amazon for the first 20000 orbits. It is a composite of over 400 data takes from the 16 single beams classes which are plotted as individual colours. The area studied roughly bounded by: 66.5°W, 68.5°W, and 6.0°S and 8.0°S. Each point represents the spatial average of the data used to monitor the antenna pattern, calibrated using the best knowledge of the system and antenna gains and corrected for any S/C roll. The error bars represent the standard deviation of 512 azimuth averages across the swath. The history spans four calendar years. It is difficult to observe any cyclical trend in these results or dependency on beam type.

Fig. 9 is a histogram of the constituent data represented in the ensemble of the points shown in Fig. 7. The mean and standard deviation of the data are indicated. We note that although the mean is close to the ERS-1/2 VV scatterometer, there is considerably more variation. This cannot be due to speckle as each estimate includes

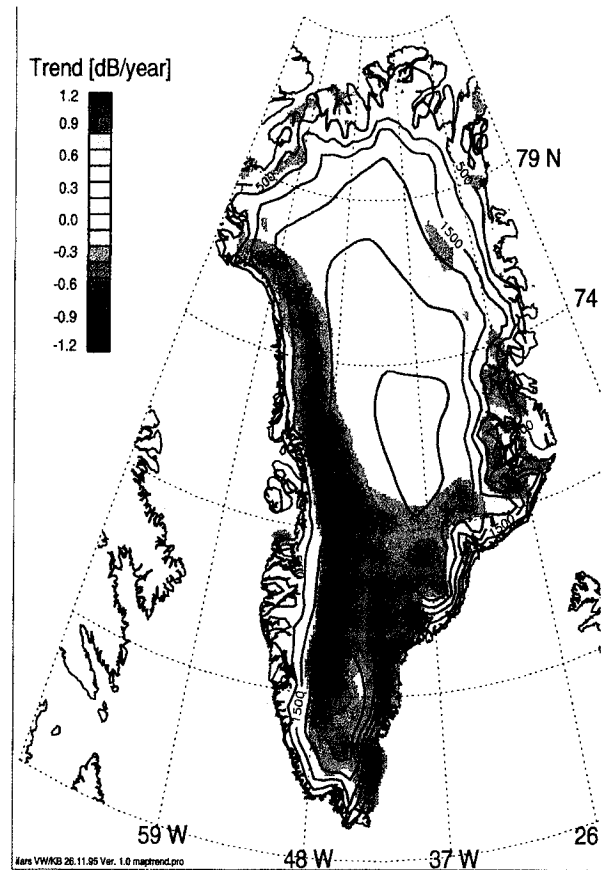


Fig. 7: Temporal backscattering stability measured by the ERS scatterometers over Greenland

many thousands of individual measurements. The absolute levels in each case are determined from precision transponder data [21].

### RADARSAT-1 Instrumental Stability

The question of spatial and temporal stability of RADARSAT-1 can be partially answered from statistics of the internal and external calibration data for the instrument. The error budget for individual measurements is discussed in [22]. Fig. 10 shows a time series from the calibration measurements from precision transponders. Following the analysis done on the ERS SAR [23], we plot the DGCF for the four precision transponders used for RADARSAT-1 in Fig. 9 where the RMS variation is 0.42 dB. Assuming the transponders themselves [22] have a radiometric RMS variation of 0.25 dB, we can assess the RMS stability of RADARSAT itself to be less than 0.34 dB since this number includes analysis and processing uncertainty.

Combining this number with the observations over the Amazon (including instrumental variation) shown in Fig. 8, we obtain a RMS variation for the Amazon alone of 0.60 dB.

## ERS-2 SAR RESULTS

There are no routine ERS-2 SAR calibration measurements of the Brazilian rainforest as the ERS-2 SAR calibration is performed using the ESA transponders located in the Netherlands (see paragraph on ERS SAR stability). The Amazon rainforest is only used to derive the antenna pattern [5]. For the purpose of this paper, we have analyzed a set of ten ERS SAR PRI images covering an area of the Amazon rainforest which corresponds to the frame used to derive the antenna pattern, located in Brazil and centered at 7.25° S and 67.43° W. The images were acquired by ERS-2 between April 1996 and April 1999 and processed at the German Processing Facility and at ESA/ESRIN.

Each point in Fig 11 represents the mean  $\gamma$  of a PRI image (100 × 100 km), while the error bars show the standard deviation of the azimuth averaged profiles for each image. The  $\gamma$  values were obtained using the ERS SAR Toolbox [24].

The measurements in Fig. 11 confirm the temporal radiometric stability of the rainforest in C-band. They also show the high stability of the ERS-2 SAR instrument as the standard variation of the  $\gamma$  values is 0.23 dB comparable to those obtained with the transponders measurements. Note that two images have a higher  $\gamma$  values which cannot be explained by a visual examination of the images. The temporal standard deviation of  $\gamma$  without these two images is 0.06 dB. The  $\gamma$  range profiles of the images are flat, confirming the model shown in Fig. 2.

The  $\gamma$  measurements of Fig. 11 are however slightly higher than those obtained from the ERS-2 scatterometer and RADARSAT (by about 0.2 dB). Although they fall within the distribution envelope of each of the above data sets, the ERS SAR dataset might not be large enough to adequately represent the statistics for three years and more ERS SAR images should be analyzed before making final conclusions.

## ERS-2 SAR Stability

Fig. 12 gives the time series of three ESA transponder measurements for the ERS-2 SAR since 1995. The overall RMS variation of the DGCF is 0.28 dB with a bias of 0.17 dB against the nominal calibration constant of 59.75 dB. This variation arises from a temporal stability due to a combined SAR and transponder stability and from a spatial stability due to variations within a scene caused by the SAR processor and measurement of the transponder total power. Examination of data from simultaneous pairs and triplets of the transponders located in the Flevoland gives a spatial RMS stability of 0.19 dB. Assuming that the temporal and spatial stabilities are independent, then the temporal RMS stability is 0.21 dB. Included in this temporal stability is the transponder RMS stability; this is estimated [25] to be approximately 0.08 dB.

Combining the uncertainties from the Amazon and transponder data suggest that the rainforest RMS variation is small although a larger Amazon data set is required to adequately access its value.

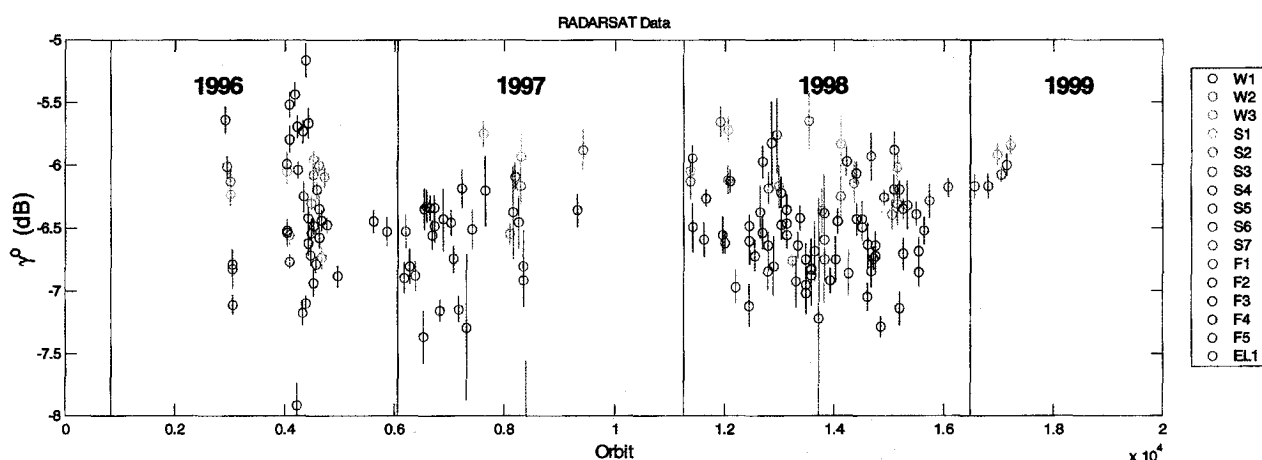


Fig. 8: History of  $\gamma$  measurements from RADARSAT-1. The colours represent different single beam results and the error bars the standard deviations of the scene distributions.

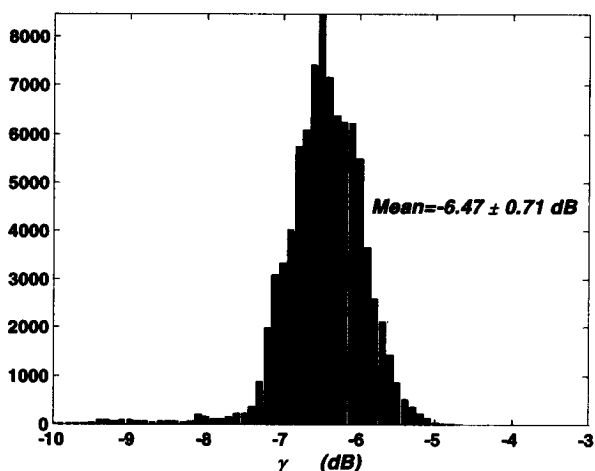


Fig. 9: Distribution of  $\gamma$  from RADARSAT-1

DISCUSSION AND CONCLUSIONS

In this study, we have tried to present a clear picture of the observations of the Amazon rainforest obtained from ERS and RADARSAT together with independent measurements of the respective instrument stabilities. The region is important from many perspectives; however, the aspect emphasized here is the stability of the region as a standard for calibration of spaceborne radars. The validity of property (1) has been unchallenged in making antenna pattern estimates for these instruments over limited angular ranges and is indeed corroborated by transponder measurements taken

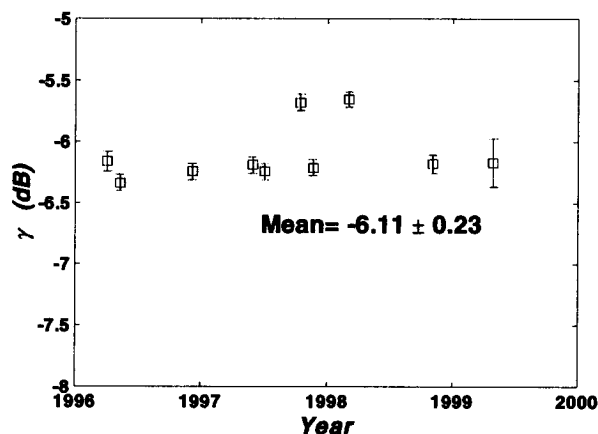


Fig. 11: ERS-2 SAR results from Amazon rainforest

with both ERS and RADARSAT within the limitations of their calibration.

Because the stability of the Amazon measurements is high, it is difficult to separate variations in backscatter measurements from those of the measuring instrument; however, we have been able to demonstrate that on average, each of the instruments has more inherent stability than individual measurements from the Amazon.

In Table 2, we summarize the observed long term backscatter and calibration variations discussed in this study. Where these are available (ERS-2 SAR only), we have computed the constituent parts of the calibration

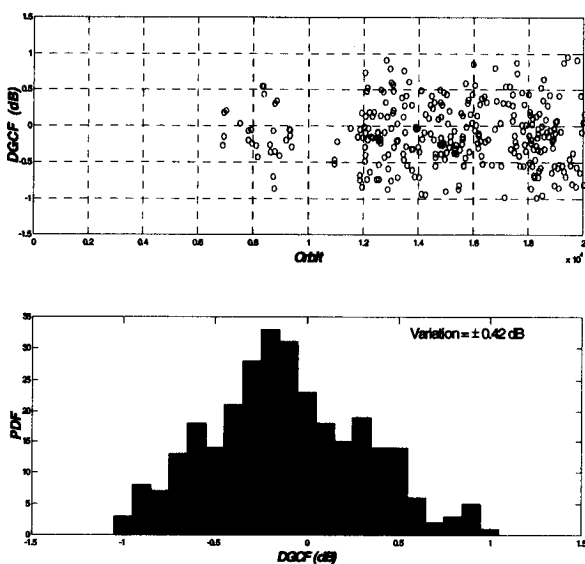


Fig. 10: RADARSAT-1 stability from CSA transponders

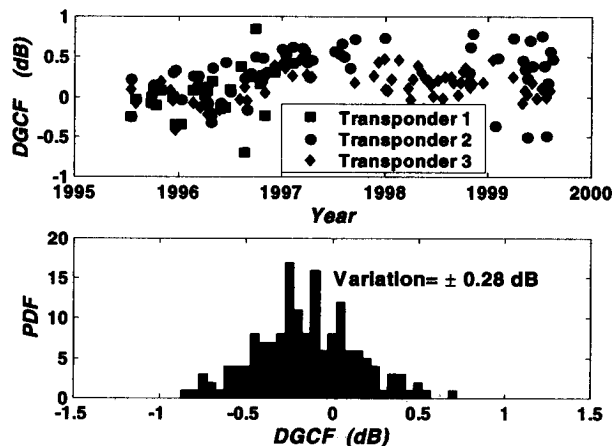


Fig. 12: ERS-2 SAR stability from ESA transponders



due to instrument and calibrator together with analysis. We need to stress that these results are from long term measurements from area samples all greater than  $10^4$  km<sup>2</sup> and time period greater than 1 year.

Individual measurements may vary considerably from the mean spatial and temporal averages represented in Table 2 and care must be taken in extrapolating results from the longer term/wider area to particular data sets

which can be influenced by local precipitation and ground conditions.

The use of Amazon rainforest results for spacecraft mission calibration therefore needs to be confined to those cases where sufficient data samples have been analyzed to assess the variation and associated uncertainty. Otherwise, precision calibrators appear to be the best absolute standard.

Table 2: Long term summary statistics from Amazon rainforest and instrumental calibration

RMS Variation	SPACEBORNE INSTRUMENT		
	ERS Scatterometer	ERS-2 SAR	RADARSAT
	(dB)	(dB)	(dB)
Rainforest + Instrument	0.59	0.23	0.72
Calibrator + Instrument + analysis	0.20	0.28	0.42
Calibrator + analysis	NA	0.19	NA
Instrument	NA	0.21	NA
Rainforest alone	0.56	0.10	0.60

#### ACKNOWLEDGEMENTS

We thank Kevin Murnaghan and Andrew Wind (CCRS), Bob Banik and Marko Adamovic (CSA) in the preparing the data for this document. The cooperation of RADARSAT International is also appreciated. Robert Landry and Frank Ahern supplied the J-ERS-1 mosaic of the Amazon. We would also like to acknowledge the cooperation of Henri Laur in facilitating data acquisition and Harry Jackson for his sharing of his intimate knowledge of the ERS transponders. Comments by Joost van der Sanden and Andrew Wind were very helpful in reviewing the manuscript.

#### REFERENCES

- JJ van der Sanden, *Radar Remote Sensing To Support Tropical Forest Management*, PhD thesis, Wageningen Agriculture University, Tropenbos-Guyana Programme, 1997, 330p.
- IJ Birrer *et al.*, " $\sigma^0$  Signature of the amazon rain forest obtained from the Seasat scatterometer," *IEEE GSRS*, GE-20, No. 1, 1992, pp. 11-17.
- RK Raney, *et al.*, "A plea for radar brightness," *Proc. IGARSS'94*, vol. II, 1994, pp. 1090-1092.
- DG Long and GB Skouson, "Calibration of spaceborne scatterometers using tropical rain forests," *IEEE GSRS*, vol. 34, 1996, pp 413-424.
- JE Laycock and H Laur, "ERS-1 SAR Antenna Pattern Estimation", ESA/ESRIN, ES-TN-DPE-OM-JL01, Issue 1, Rev. 1, September 1994, 32p.
- K Murnaghan, RK Hawkins, and TI Lukowski, "Combination procedure for RADARSAT antenna generation," *Proc. of 20<sup>th</sup> Canadian Symposium on Remote Sensing*, Calgary, Alberta, 1998, 6p.
- Y Fang and RK Moore, "Inflight vertical antenna patterns for SIR-C from Amazon rain-forest observations," *Remote Sens. Environ*, vol. 5, 1997, pp. 407-414.
- M Shimada and A Freeman, "A technique for measurement of spaceborne antenna patterns using distributed targets," *IEEE GSRS*, vol. 33, 1995, pp. 100-114.
- South America JERS-1 SAR mosaic courtesy STA/NASDA, made available as a contribution to the CEOS/IGOS-P pilot project "Global Observation of Forest Cover".
- EPW Attema and FT Ulaby, "Vegetation modelled as a water cloud," *Radio Science*, vol. 13, no. 2 1978, pp. 1299-1307.

- 11 P Lecomte, "The ERS scatterometer instrument and the on-ground processing of its data," in *SP-424: Proceedings of a joint ESA-Eumetsat Workshop on Emerging Scatterometer Applications - From Research to Operations*, ESTEC, Noordwijk, The Netherlands, 5-7 October 1998, pp. 241-260.
- 12 PCS team, "ERS-2 wind scatterometer cyclic report, from 28th June to 2nd August, Cycle 44," APP-AEM/PCS/WS99-006, Issue 1, ESA Technical Document, ESRIN, Frascati, Italy, 1999, 31p.
- 13 A Stoffelen, "Antenna gain variation caused by the sun's irradiation." KNMI technical note presented to the ESA Scatterometer Scientific Advisory Group, 1996, 6p.
- 14 IH Woodhouse, JJ van der Sanden and DH Hoekman, "Scatterometer observations of seasonal backscatter variation over tropical rainforest," *IEEE TGRS*, vol. 37, 1999, pp. 859-861.
- 15 P Lecomte and EPW Attema, "Calibration and Validation of the ERS-1 Wind Scatterometer", in *Proceedings First ERS-1 Symposium - Space at the Service of our Environment*, Cannes, France, 4-6 Nov, 1992, ESA SP-359, p.19.
- 16 P Lecomte and W Wagner, "ERS wind scatterometer commissioning and in-flight calibration," in *SP-424: Proceedings of a joint ESA-Eumetsat Workshop on Emerging Scatterometer Applications - From Research to Operations*, ESTEC, Noordwijk, The Netherlands, 5-7 October 1998, pp. 261-270.
- 17 H Jackson, (1999) personal communication.
- 18 PCS team, "ERS-2 wind scatterometer cyclic report, from 19th April to 24th May, Cycle 42," APP-AEM/PCS/WS99-004, Issue 1, ESA Technical Document, ESRIN, Frascati, Italy, 1999, 42p
- 19 V Wisman, "A global NRCS database derived from ERS Scatterometer data," in *Proc of IGARSS'99*, Hamburg, Germany, 1999, pp. 2722-2724.
- 20 ---, "New views of the earth: Engineering achievements of ERS-1," ESA SP-1176/III, October 1997, ISBN 92-9092-141-2, p. 41.
- 21 RK Hawkins *et al.*, "RADARSAT precision transponders", *Adv. Space Res.*, vol. 19, 1997, pp. 1455-1465.
- 22 RK Hawkins and SK Srivastava, "Radiometric calibration budget of RADARSAT-1," this proceedings.
- 23 PJ Meadows *et al.*, "The ERS SAR performances," CEOS SAR Workshop, ESA publication WPP-138, 1998, pp. 223-232.
- 24 ESA, Earthnet Online, , "ERS SAR Toolbox," <http://earth1.esrin.esa.it/STBX>
- 25 H Jackson and A Woode, "Development of the ERS-1 active radar calibration unit," *IEEE Trans Microwave Theory and Techniques*, 1992, pp. 1063-1069.

## A New Method for Calibration of SAR images

Geir Engen, Harald Johnsen  
 NORUT IT, N-9291 Tromsø, Norway,  
 e-mail:geir.engen@itek.norut.no

### ABSTRACT

A methodology for calibration of Synthetic Aperture Radar (SAR) images is given based on combining first and second order statistics from ocean images. It is shown to be, compatible with transponders in accuracy, easy to use, and low cost operational. ERS-1 and ERS-2 data are used in this study to demonstrate the performance and potential of the methodology. An accuracy of 0.47dB is obtained from using only one ERS-2 image. Improvements of accuracy can be obtained by using several independent images. The method can be used to monitor and update the absolute calibration constant of spaceborne SAR images.

### INTRODUCTION

Absolute calibrated SAR images are required for an increasing number of applications both over land, ocean and ice surfaces. Extensive efforts are undertaken to make the SAR data calibrated to better than 0.5dB. Traditionally, deployed transponders, corner reflectors and rain forest are used for this purpose. With the increase complexity of SAR antennas (such as Envisat ASAR) and products, a cheap and easy way to establish, monitor and update the absolute calibration constant is required.

We propose a new concept for automatic calibration and monitoring of SAR data that are cheap, easy and very precise. It is based on using SAR observations over ocean where the backscatter intensity and the asymptotic inverse spectral width of cross spectra are considered. It can be shown that these two parameters statistically have the same wind field dependency. This means that they statistically align with each other. The relation can be established for a certain radar frequency, polarization, and incidence angle and locked once and for all to an absolute backscattering coefficient by a single transponder, corner reflector or rain forest measurement. The algorithm can then be applied to any SAR system (present or future) with the corresponding configuration (without any use of transponders). For instance, we can use the existing ERS data sets to establish an absolute calibration algorithm for the Envisat ASAR modes corresponding to the ERS configuration. For the remaining ASAR configurations only a single overpass with transponders is required for each configuration. For the remaining life time of the satellite, the proposed algorithm can be easily

used to automatically ensure monitoring and absolute calibration of the various modes.

Statistical relations between backscatter intensity and asymptotic inverse spectral width are established from using ERS-1 and ERS-2 data sets. Results show that the method gives an accuracy of 0.47 dB for the radar backscattering cross section established using only one single ERS-2 image. The accuracy can further be improved by increasing the number of independent images.

### METHODOLOGY

#### Theoretical Model

The method is based on the ocean-to-SAR cross-spectral transform given as [1], [2]:

$$P(\underline{k}, \tau) = \int d\underline{x} e^{-i\underline{k} \cdot \underline{x}} e^{k_y^2 (\phi_{\xi\xi}(\underline{x}, \tau) - \phi_{\xi\xi}(0, 0))} \times \{1 + \phi_{II}(\underline{x}, \tau)\} - \delta(\underline{k}) \quad (1)$$

where  $I$  is the SAR image, and  $\xi$  is the ocean orbital velocity generated shift field. It can be shown that the asymptotic behavior for  $k_y \rightarrow \infty$  is given as:

$$P(k) \rightarrow \frac{1}{(\alpha k_y)^4} \quad (2)$$

for some parameter  $\alpha$ , which is the inverse spectral width in the azimuth direction.

The inverse spectral width,  $\alpha$  is compared with the backscatter intensity,  $E\{I_{SAR}\}$ .

#### Data Processing

First a relation,  $f$  between the radar backscatter cross section,  $\sigma_0$  and the inverse spectral width,  $\alpha$  needs to be established from real data:

$$\sigma_0 = f_{\theta, \omega_c}(\alpha) \quad (3)$$

where  $\theta$  is the incidence angle, and  $\omega_c$  is the radar frequency. The radar cross section is furthermore related to the backscatter intensity through the absolute calibration constant,  $K$  as:

$$\sigma_0 = KE\{I_{SAR}\} \quad (4)$$

The average backscattering intensity,  $E\{I_{SAR}\}$  is computed from typically an area of 18kmx14km within the SLC image. The inverse spectral width,  $\alpha$  is found by fitting the a  $k_y^{-4}$  function to the average azimuth profile

$$P_{k_y} = \int dk_x |\text{Re}\{P(k)\}| \quad (5)$$

within the asymptotic region. This is illustrated in Figure 1 showing a cross spectrum, the average azimuth profile and the  $k_y^{-4}$  function.

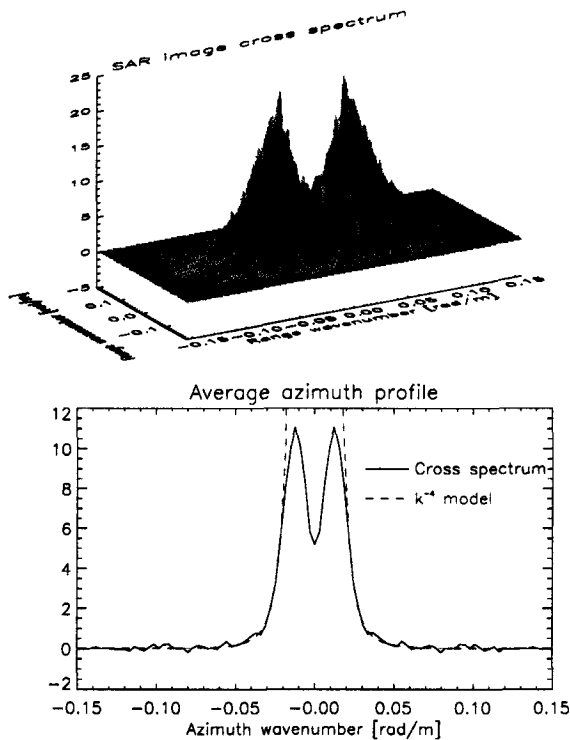


Figure 1. Typical cross spectrum (upper), average azimuth profile overlapped the  $k_y^{-4}$  function (lower).

Once the relation in Equation 3 is established, which requires knowledge of the absolute calibration constant, a procedure for updating or monitoring of the calibration constant can be established. This is done by the following steps:

- compute the image intensity  $E\{I_{SAR}\}$  and the inverse spectral width,  $\alpha$  from a given set of SLC SAR images
- use the established relation,  $f$  to calculate or update the calibration constant using the formula:

$$K = E \left\{ \frac{f_{\theta, \omega_c}(\alpha)}{E\{I_{SAR}\}} \right\} \quad (6)$$

The algorithm is easy to implement. It requires inter-look processing (cross spectra computation), similar to what is implemented for Level 1 processing of ASAR Wave Mode data [3].

## DATA

The methodology was tested using 33 ERS-2 and 24 ERS-1 SLC images acquired in North Atlantic (Norwegian Sea) in the period 1993 - 1999.

From each images, 5x7 (range x azimuth) cross spectra are processed each covering an area of 18km x 14km. This will cover five incidence angles, 20.6, 21.8, 23, 24.2 and 25.4 degrees. The total number of estimation points obtained from this data set for each incidence angle are 231 (ERS-2) and 168 (ERS-1).

## RESULTS

We present the results obtained for applying the calibration algorithm on ERS-2 and ERS-1 SLC data. First we show the results on ERS-2 data, and secondly we make comparison between ERS-1 and ERS-2 data. In Figure 2 is shown the relation  $\sigma_0 = f_{\theta, \omega_c}(\alpha)$  obtained from one ERS-2 SLC image at the incidence angle of 24.2 degrees. The full line represent the polynomial fit to the data points and represent the relation to be found. The standard deviation obtained is 0.67dB.

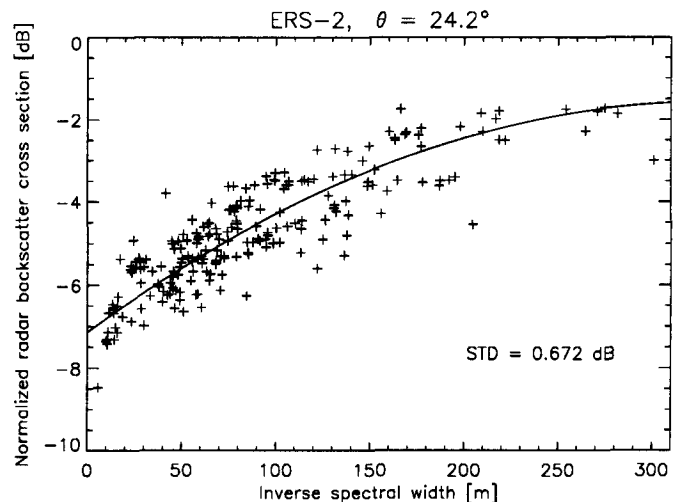


Figure 2. Normalized radar cross section versus inverse spectral width obtained from one single ERS-2 SLC image at the incidence angle of 24.2 degrees. The full line is the polynomial fit to the data points.

If we average the data points with same incidence angle in the azimuth direction, we improve the standard deviation. The result is shown in Figure 3, yielding now a standard deviation of only 0.47dB. This is the accuracy obtained from using only one SLC image.

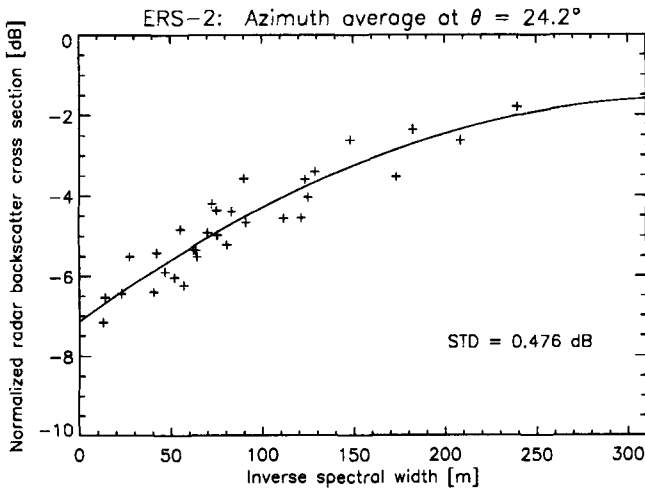


Figure 3. Same data as in Figure 2, but now averaged in azimuth direction. The full line is the polynomial fit to the data points.

The standard deviation can further be improved by averaging more independent observations (images). This is shown in Figure 4, and illustrates the potential of the method and what accuracy can be achieved with the method.

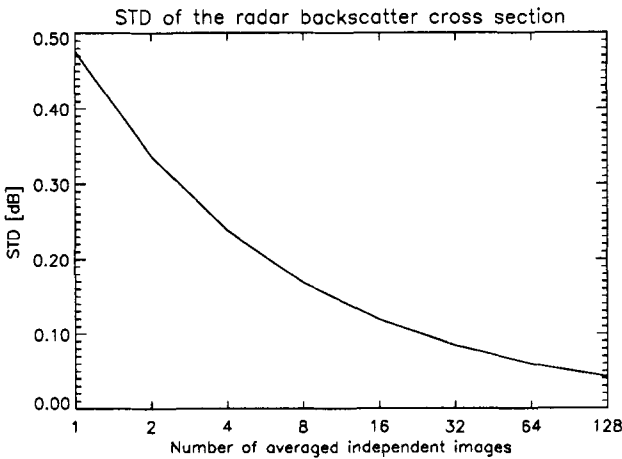


Figure 4. Standard deviation of radar cross section versus number of averaged independent observations (images).

In the next figures we show results of comparing the methods on the ERS-1 and ERS-2 data. We present the results for three different incidence angles, 20.6, 24.2, and 25.4 degrees. In Figure 5 is shown the radar cross section versus inverse spectral width from ERS-1 and ERS-2 data, and the corresponding offset. The results are obtained from processing all the images available (33 ERS-2 and 24 ERS-2 images).

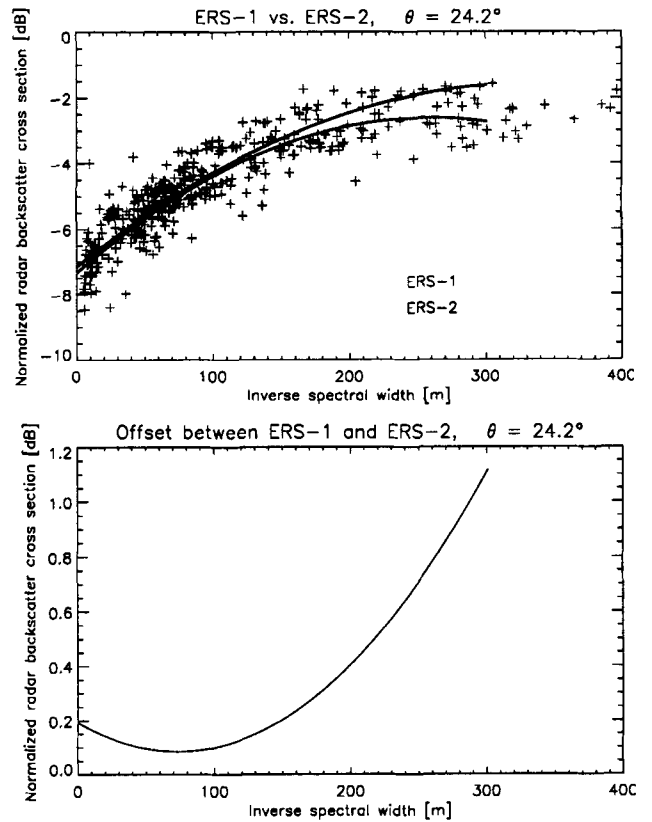


Figure 5. Normalized radar cross section versus inverse spectral width obtained from ERS-2 and ERS-1 SLC images at the incidence angle of 24.2 degrees. The full lines are the polynomial fit to the data points. Lower plot: Offset obtained between ERS-1 and ERS-2 data obtained at incidence angle 24.2 degrees.

We see from Figure 5, that ERS-1 and ERS-2 are reasonable well calibrated until the saturation starts to influence the ERS-1 data. This effect should increase if we go to a lower incidence angle, and decrease if we increase the incidence angle. This is exactly what happens as shown in Figure 6 and Figure 7, respectively.

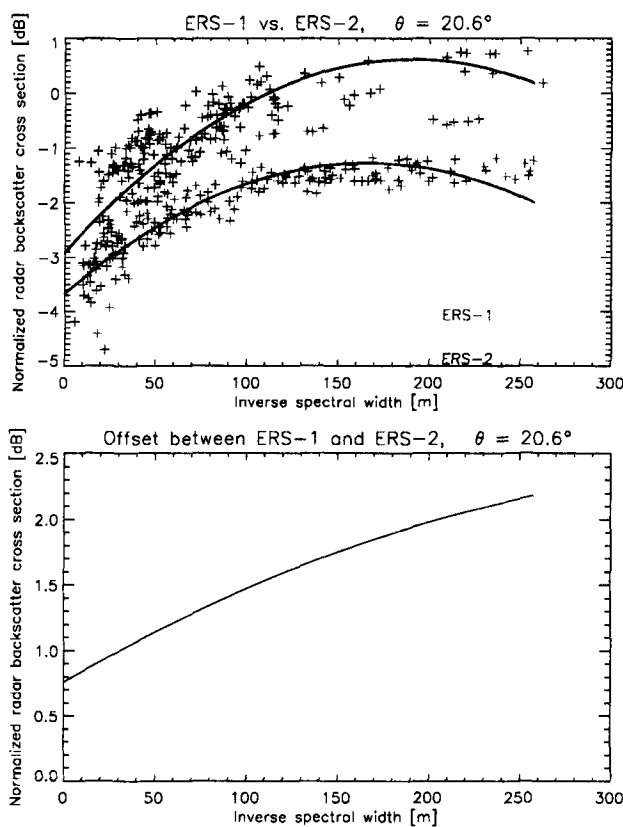


Figure 6. Normalized radar cross section versus inverse spectral width obtained from ERS-2 and ERS-1 SLC images at the incidence angle of 20.6 degrees. The full lines are the polynomial fit to the data points. Lower plot: Offset obtained between ERS-1 and ERS-2 data obtained at incidence angle 20.6 degrees.

From Figure 6 we see that even ERS-2 have saturation effects at low incidence angles. If we go to high incidence angle, the saturation becomes less and the ERS-1 and ERS-2 curves become quite equal. This is shown in Figure 7.

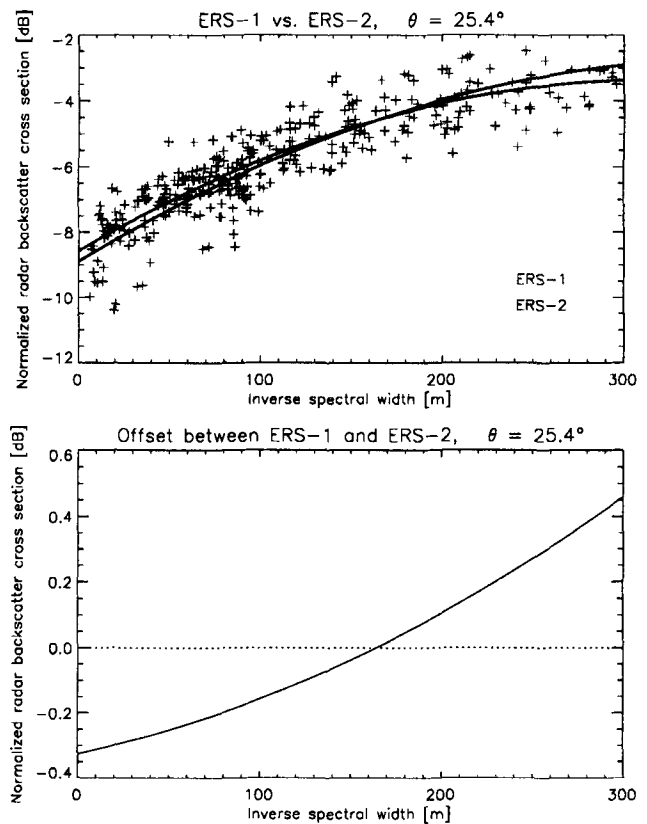


Figure 7. Normalized radar cross section versus inverse spectral width obtained from ERS-2 and ERS-1 SLC images at the incidence angle of 20.6 degrees. The full lines are the polynomial fit to the data points. Lower plot: Offset obtained between ERS-1 and ERS-2 data obtained at incidence angle 20.6 degrees.

## CONCLUSION

A new methodology for calibration of SAR images is proposed and applied to ERS data. The methodology shows that an accuracy of 0.47dB is obtained from using only one ERS-2 image. The accuracy can furthermore be improved by combining more images.

**Acknowledgement:** We thank Yves-Louis Desnos at ESTEC for providing us with the ERS data, and Bertrand Chapron at IFREMER for many fruitful discussions.

## REFERENCES

- [1] K. Hasselmann, S. Hasselmann, "On the nonlinear mapping of an ocean wave spectrum into a synthetic aperture radar image spectrum and its inversion", *J. Geophys. Res.*, Vol.96, No. C6, pp.10713-10729, 1991
- [2] G. Engen, H. Johnsen; SAR-Ocean Wave Inversion Using Image Cross Spectra, *IEEE Trans. on Geo. Science and Remote Sensing*, Vol. 33, No. 4, pp.1047-1056, 1995.
- [3] Johnsen H., Engen G., Lauknes I., The Envisat ASAR Wave Mode Cross Spectra Algorithm, *Proc. CEOS SAR Workshop*, WPP-138, ESTEC 3-6 February 1998.

## Use of interferometric phase for co-registration of ERS SAR and SPOT images

Daniel RAUCOULES, Claudie CARNEC  
BRGM DR/LGT, 117 avenue de Luminy - BP 167 - 13276 Marseille cedex 9, France

Tel (33) 4 91 17 22 92 / Fax (33) 4 91 17 74 75 / email: d.raucoules@brgm.fr

### ABSTRACT

Without altimetric information, the co-registration between ERS SAR and orthorectified image (in our case SPOT ortho-image) can be an alternative for the geocoding processing. We propose the use of local correlation to deal with the co-registration problem, taking into account the interferometric phases as additional information. The SPOT image is fitted to the SAR (slant range) geometry using the orbital parameters of the SAR acquisition. Local correlation co-registration between this image and the original SAR image allows to refine the geometric transformation. Local offsets estimated in the new ground referenced geometry with some constraints on possible values interval and local correlations SNR can be used for specific correction.

The initial transformation can be improved by introducing the phases (previously unwrapped). This method is less sensitive to the relief and then there is no need of local correction.

The two methods have been evaluated on test sites with smooth relief conditions.

### INTRODUCTION

To compare and merge spatial data from different sources - in our case SAR and SPOT orthorectified data -, they have to be converted to a common geometry (coregistration) as a planimetric reference system (geocoding). Because of the particular geometry (azimuth/slant range) of the SAR imagery, Digital Elevation Models and Ground Control Points are needed to geocode it.

In addition, the co-registration between a SAR image and an other sensor image is made difficult due to both noise (speckle noise)

hampering the SAR signal and incorrect orbital information.

We propose to use local correlation to deal with this problem but also the inclusion of interferometric phases as additional input. The two techniques were evaluated on Hanoi with a resulting estimated accuracy close to the pixel size. Our interest for using these procedures on the Hanoi region comes from the difficulties to get reliable DEM on the sector. Fig.1 shows the SAR and SPOT data used.

### REGISTRATION USING LOCAL CORRELATION

The coregistration is done using a tool from the GAMMA interferometric processing software designed to adjust the slant range geometry image with a simulation derived from a DEM in order to geocode the SAR image [1]. Instead of using the SAR intensity image simulation, we introduce the SPOT image transferred into the SAR geometry. For this purpose, we use the orbital information to transform the SPOT image. That allows us to deal with a first step: to obtain similar geometry to make possible local correlation computations. The obtained images are then coregistered.

An argument to select the slant range/azimuth geometry instead of the geographic reference is shown in Fig. 2. The dependency between azimuth component and topography is negligible therefore the azimuth only depends on planimetric position. The consequence is that the error which affects this component can be corrected even if we have no altimetric information. It is different in a geographic reference system where the altimetric variable affects both components and therefore prevents independent corrections.

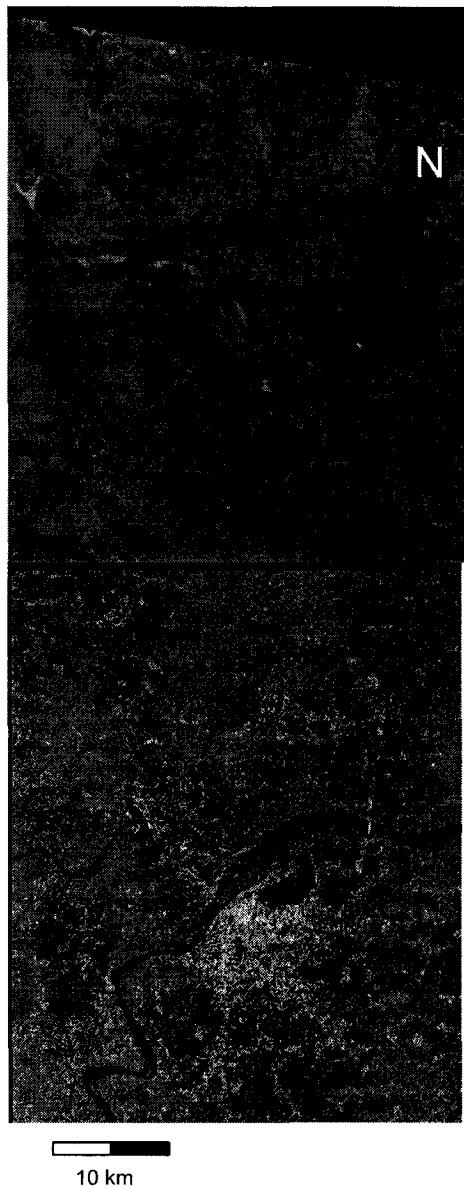


Fig. 1: Panchromatic SPOT ortho-image (26/10/95) and ERS1 SAR intensity image (excerpt from frame 3186 orbit 24426 - 17/03/96) on the same Hanoi sector. Note the difference (rotation and left-right inversion) between the geometric references. The SAR image is sampled in distance target/sensor  
 Resolutions: SPOT image 10mx10m, ERS1 image about 20mx20m (ground projected estimation)

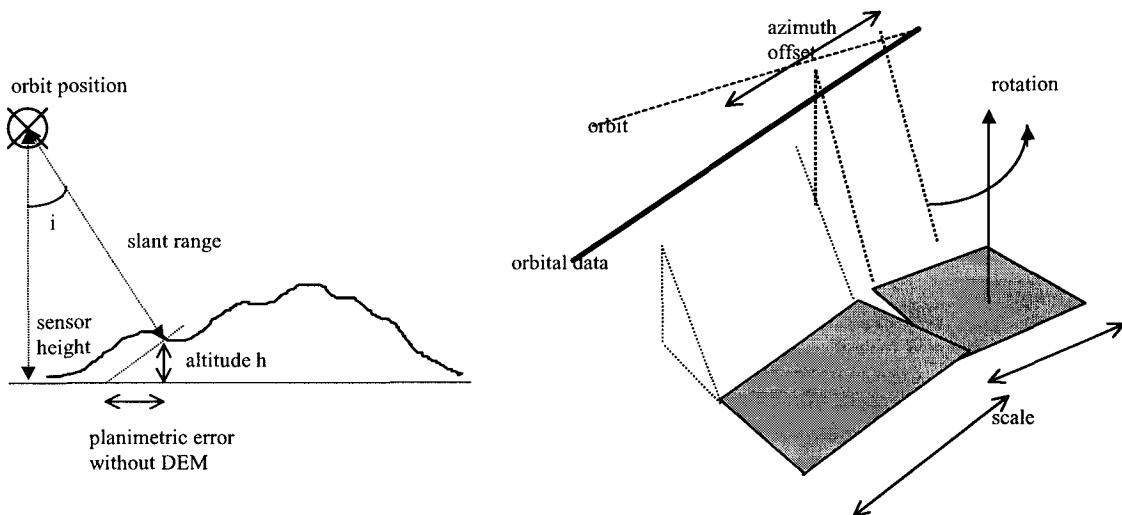




Fig. 2. a) The topography affects the cross-track direction. The ground error if we do not take into account the topography is approximately  $h / \tan i$ .

b) The azimuth errors are only due to inaccuracies in the satellite orbital information (state vectors and data starting time) which produce slight distortions (rotation, offsets and scaling effects) between the SPOT and SAR images. This distortions can be corrected using a bilinear transformation without altimetric information.

The geometric correction is made by computing the correlations between small windows on both images centred on points from a regular grid extracted from the SAR image. From these correlations values, local offsets are derived and fitted by a bilinear offsets model. The offsets best-fit function permits to correct the model and then to rectify the SAR image to the SPOT image geometry. In this processing we have not taken into account the topography which is an important element for any change of reference geometry of a SAR image [2].

However, scale effects, like those introduced by having not considered the mean altitude and the influence of average ramp of the topography should be corrected by using this procedure owing to the fact that the model correction uses a bilinear fit of the offsets.

In a next step, we have refined the coregistration by repeating the local correlations processing in the SPOT image geometry with the corrected SAR image. The new computed offsets have been rejected if greater than a 60 metres threshold (roughly the amplitude of topography on all the image coverage - the offsets should not be greater) or for low SNR on correlation estimations (less than 5.5). The offsets have been interpolated to obtain a new correction to be applied to the SAR image (Fig.3)



Fig. 3 : ERS SAR image registered to the SPOT image geometry

#### REGISTRATION USING INTERFEROMETRIC PHASES

Interferometric phases can be an alternative to altimetric information for geometric corrections. Altimetric information can be derived from interferometric phase data [3] but GCPs are indispensable to obtain a correct DEM. The reasons are the indetermination of the phase unwrapping - the unwrapped phases are obtained with a constant bias - and the orbital inaccuracy which induces distortions on the resulting DEM and the homogeneous atmospheric bias expressed by regular fringe patterns. These limitations affect the extraction

of altimetric information from inSAR phases [4].

As we have at our disposal a ERS tandem pair - orbits 4753 (ERS2) and 24426 (ERS1), one day between images (Fig. 4) - we will introduce it in the process as additional information. As the phases are obtained modulo  $2\pi$ , an unwrapping step is needed [5]. We make the assumption that the previous shortcomings affect the data at the image scale.

Therefore, using the phases corrected - if possible - by introducing the average altitude to obtain a first geocoding model without additional altimetric information, we can correct local height related images deformations but not the previous large scale shortcomings. The use of the first step of the precedent procedure - the correction of the geocoding model using the coregistration with the SPOT image in the satellite geometry - implies a correction of those biases.

We have to note that the altitude of ambiguity is a bit larger than the amplitude of the topography therefore we are close to the limit of efficiency of the interferometric techniques for deriving heights - typically the accuracy is  $1/5$  to  $1/4$  the altitude of ambiguity -. But no tandem pair with lower altitude of ambiguity were available.



Fig. 4: Interferometric phases from tandem pair 4753/24426 . The phases in  $[-\pi, \pi[$  are represented by the image hue; the darker zones correspond to low coherence. The altitude of ambiguity is 85 metres.

## EVALUATION OF THE COREGISTRATION ACCURACY

The planimetric accuracy is evaluated by comparing the positions of ten points on the coregistered SAR image and on the SPOT image. The points have been located manually taking care of selecting them regularly distributed on the image.

The estimated accuracy is 30 metres - the maximum offset detected is 40 metres - for the second method (about 1.5 SAR image pixel) and 30 metres - the maximum offset is 60 metres - for the first one. Those precisions are both compatible with the initial resolution of the SAR data and with a precise use of the data.

Though the methods seem equivalent some restrictions against the first method must be taken in consideration. The region relief is moderated. With a more important relief the size of the windows for local correlation must be increased in relation with the offsets interval, which will be increased proportionally with heights. The number of points of the correlation grid should be increased too with the variability of the topography.

An other point is the need to have reliable correlation computations to have similar features on both images. Therefore if on urban or agricultural zones the coregistration is good, we think an extraction of features like texture information [6] could be a useful pre-processing in zones like forests characterised more by texture than intensity values.

A last point to be tackled is the possibility of using edge detection filtered images to make more efficient the correlation step. It is a frequently used method for image coregistration [7]. That could increase the correlation performances and we shall test it in further developments. However we can already point the fact that the edge extraction is difficult on SAR images because of the specificity of the noise [8] but also the SAR geometry and illumination properties can have as consequence the displacement of image features, specially on pixels close to important slopes [9] and corrupt the result.

## CONCLUSION

The local correlation methods allow, in the conditions of the study, a good coregistration between SAR images and other sensor data (in

our case SPOT data) with an accuracy close to the SAR resolution. On the other hand the introduction of interferometric phases seems an interesting additional information which increase the efficiency of the processing. That can be a possible alternative for the geocoding of a SAR image when no DEM is available.

#### ACKNOWLEDGEMENTS

This study was carried out under scientific collaboration agreements between BRGM, VTGEO and SCOT Conseil. The study was supported by the European Space Agency (Contract 1-3199/97/I-HGE) and the Research Division of BRGM. For this study we have used the Gamma Software from Gamma Remote Sensing Research.

#### REFERENCES

- [1] Gamma Remote Sensing Research & Consulting, 1997, <http://www.gamma-rs.ch/diff.htm>
- [2] Toutin, T., Carbonneau, Y., Saint-Laurent, L., 1992, An integrated method to rectify airborne radar imagery using DEM. *Photogrammetric Engineering and Remote Sensing*, vol. **58**, pp 417-422
- [3] Graham, L., 1974, Synthetic Interferometer Radar for topographic Mapping, *proceedings of IEEE*, vol. **62**, pp 763-771
- [4] Tarayre, H., 1996, Extraction de Modèles Numériques de Terrain par Interférométrie Radar Satellitaire: Algorithmie et Artefacts Atmosphériques, Thèse de doctorat. Toulouse: INPT
- [5] Goldstein, R., Zebker, H., and Werner, C., 1988, Satellite radar interferometry: two-dimensional phase unwrapping. *Radio Science*, vol. **23**, pp 713-725
- [6] Simard, M., De Grandi, G., Thomson, K., 1998, Adaptation of the Wavelet Transform for the Construction of Multiscale Texture Maps of SAR Images. *Canadian Journal of Remote Sensing*, vol. **24**, pp 264-285
- [7] Paillou, P. and Gelautz, M., 1998, The Optimal Gradient Matching Method: Application to X-SAR and Magellan Stereo Images, In *Proceedings of IGARSS'98*, CDROM . Seattle: IEEE
- [8] Beauchemin, M., Thomson, K., and Edwards, G., 1995 The ratio of the arithmetic to geometric mean: an efficient first order statistical test for multi-look SAR image homogeneity. *IEEE transactions on geoscience and Remote Sensing*, vol. **34**, pp 604-606
- [9] Toutin, T., et al, 1998, GCPs Selection from Multi-source Data Over Mountainous Topography, In *Proceedings of IGARSS'98*, CDROM . Seattle: IEEE



## Localization using ERS for Operational Mapping

Stéphane GOBERT<sup>(1)</sup>, Issam TANNOUS<sup>(1)</sup>, Philippe BALLY<sup>(2)</sup>, Henri LAUR<sup>(3)</sup>

<sup>(1)</sup> Thomson-CSF / SYSECA

66 avenue P. Brossolette  
92247 Malakoff, FRANCE  
tel : (+33) (0)1.41.48.07.93  
fax : (+33) (0)1.41.48.02.54

email : [stephane.gobert@syseca.thomson-csf.com](mailto:stephane.gobert@syseca.thomson-csf.com)

<sup>(2)</sup> SPOTIMAGE

5, rue des Satellites - BP 4359  
31030 Toulouse Cedex, FRANCE  
tel.: (+33) (0)5 62 19 40 40  
fax: (+33) (0)5 62 19 40 11

email : [philippe.bally@spotimage.fr](mailto:philippe.bally@spotimage.fr)

<sup>(3)</sup> ESA/ESRIN

Via Galileo Galilei  
I-00044 Frascati, Italy  
tel: (+39) 6 94180 1

fax : (+39) 6 94180 280  
email : [henri.laur@esrin.esa.it](mailto:henri.laur@esrin.esa.it)

### ABSTRACT

This paper focuses on the use of ERS SAR images to provide absolute geographic localization. It presents an operational validation of a technique allowing the absolute localization of ground points, using a descending and an ascending ERS images, whatever the Processing and Archiving Facility (PAF) providing the images. The main goal of such technique is to generate accurate ground control points, without any other georeferenced data, in order to register SPOT image data and produce level 2 images. The results we obtained show that such technique has high performances, but with some limitations, due to the presence of a bias in altimetric measurements. Nevertheless, this study has demonstrated, taking into account operational constraints, the technical feasibility of absolute localization using ERS.

### INTRODUCTION

The aim of the study was to assess the capability of ERS SAR to produce absolute 3D localized points. The 3D points can then be used in several applications. One possible application is considered in this study; it concerns the geocoding of SPOT images using the 3D points as ground control points for the production of image products level 2B and 3.

The capability to localize ground point from ERS images rely on an approach based on the physical modeling of the sensor viewing geometry. Such an

approach allows the computation of the 3D localization of a ground point given its position in two different ERS images acquired with two different angle of view.

The theoretical feasibility of the technique is well known. Our goal was to demonstrate its feasibility in a typical operational context, and its repeatability with different PAFs.

The evaluation of the localization technique is performed over a large test area, covered with cartographic data (ground truth), using several ERS SAR images provided by ESA and non ESA processing facilities.

The principle of the localization technique and its predicted performance is described in section 1. The description of the data and the method proposed for the evaluation are then given in section 2. Section 3 presents the results of this experimentation with an operational point of view (qualitative feasibility). The quantitative results using ESA products and non-ESA products are presented in sections 4 and 5. Finally, we give a general conclusion on the study.

### 1. PRINCIPLES OF THE LOCALIZATION TECHNIQUE

#### Physical Geometric Modelling of ERS images

The imaging process of sensors like ERS or SPOT can be geometrically modeled in a reliable way, with respect to a set of well known physical parameters: the

instrument parameters (PRF, sampling frequency, near range time, reference acquisition time, Doppler Centroid for a SAR system, focal length, detector size and detectors position for a sensor like SPOT) and the trajectory of the satellite. Such a modeling leads to the derivation of the *localization function*, linking the position of the point P in the images and their absolute ground localization (X in planimetry, z in altimetry):

$$X = G_{\theta}(P, z)$$

where  $\theta$  is the geometric model parameters vector. Similarly, we define the so-called *projection function* as the inverse of the localization function :

$$P = F_{\theta}(X, z)$$

The accuracy of the localization function depends on the accuracy of the knowledge of the parameters of acquisition. With most commercial products (SPOT, ERS, Radarsat), the image is provided with an estimation of these parameters, known by construction, or measured by the sensor exploitation center. For optical sensors like SPOT, the lack of accurate attitude measurements leads to a bias of some hundreds of meters in the localization function. The true parameters have to be estimated more precisely to have an accurate georeferencing, using ground control points measured on maps or with GPS.

With SAR sensors, the accuracy of the a priori localization function doesn't suffer from the same problem as SPOT, because of the independancy of the localization function with respect to the satellite attitude. As a result, we can hope that the localization function computed with the auxiliary data is accurate (better than one pixel in absolute), although some parameters are known to be slightly biased.

Principles of ground point localization from images

The ground point localization from images is based on the same concept as triangulation in photogrammetry. If a point is viewed on an image, the form of the localization function gives a continuous set of possible ground location for the point (a 3D circle for SAR). With only one image, the 3D position of this point cannot be determined, unless an additional information is known (e.g. its elevation). But if the same point is imaged from another point of view, the ground point can be accurately determined as the intersection of two geometric curves. The accuracy of the determination of the intersection is given by the differences between the angle of view of both images.

The orbit of ERS allows the acquisition of a same ground point from two configurations two similar orbits (ascending/ascending, or descending/descending), or the two opposite-sides orbits (ascending/descending).

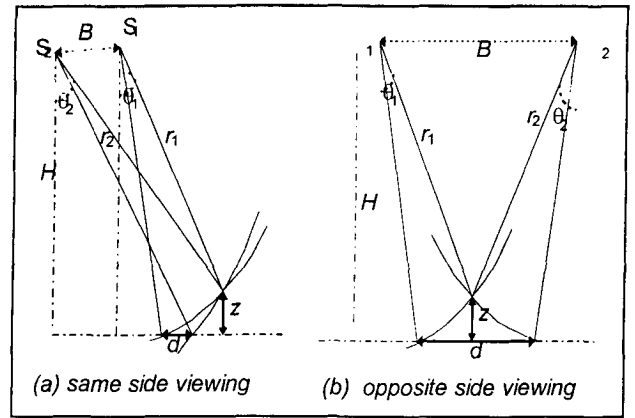


Figure 1: ERS configurations for 3D point localization

For the (a) case, the difference between the two viewing geometries is small; and the precision of determination of the intersection is not as high as in the (b). Even if the similarity of the viewing geometry eases the homologous point determination, which is an important point with respect to the operational feasibility of the technique, we will see in the next section that the **(b) case will be preferred** to the (a) one for accurate localization purpose with ERS.

Theoretical Performance

The evaluation of the theoretical performance of the localization technique rely on the geometric modeling functions of the images. We assume that a pair of homologous pixels have been selected on the images ( $P_1$  on image 1, and  $P_2$  on image 2). The ground point ( $X, z$ ) corresponding to the image pixels satisfies :

$$\begin{cases} X = G_{\theta_1}(P_1, z) \\ X = G_{\theta_2}(P_2, z) \end{cases} \quad (1)$$

The theoretical performance of the technique will be assessed assuming that the sensor and orbit parameters are well known (in fact, these parameters can be responsible for bias and noise in the final true localization results).

With this hypothesis, the only error in the process is introduced by the selection of point  $P_2$  in image 2 corresponding to point  $P_1$ . Equation (eq1) shows that this error introduces directly an error in the 3D localization of the corresponding ground point **across track**. The error on the ground point ( $\delta X, \delta z$ ) and the selection error of point  $P_2$  ( $\delta P_2$ ) are thus related by the following equations set (derivation of (1)) :

$$\begin{cases} \delta X = \frac{\partial G_{\theta_1}}{\partial z} \cdot \frac{1}{\chi} \cdot \frac{\partial G_{\theta_2}}{\partial P} \delta P_2 \\ \delta z = \frac{1}{\chi} \cdot \frac{\partial G_{\theta_2}}{\partial P} \delta P_2 \end{cases} \quad (2)$$

where  $\chi$ , the imaging configuration parameter that determines the height measurement capability of the system, is given by :

$$\chi = \frac{\partial G_{\theta_1}}{\partial z} - \frac{\partial G_{\theta_2}}{\partial z}$$

This parameter depends on the imaging configuration (see figure 1) :

$$\chi \cong \cot(\theta_1) - \cot(\theta_2) \text{ for the (a) case and}$$

$$\chi \cong \cot(\theta_1) + \cot(\theta_2) \text{ for the (b) case}$$

For ERS, the (a) configuration gives a maximum of 0.7 for (a) and 4.7 for (b). It is clear that the best precision is obtained with the (b) configuration.

The pixel selection precision for an human operator is generally taken close to one pixel. But it can be worse, especially on SAR images because of speckle. In practice, one can say that the pixel pointing precision on ERS image is about 1 to 2 pixels.

By using PRI products, the pixel size (along-track and cross-track) is 12.5 meters.

The final precision of the **across-track** localization method (without considering the potential geometric model error), is then given by :

$$\begin{cases} \delta X \geq 6.3m \\ \delta z \geq 2.7m \end{cases} \text{ for a one pixel pointing error}$$

$$\begin{cases} \delta X \geq 12.6m \\ \delta z \geq 5.4m \end{cases} \text{ for a two pixel pointing error}$$

These values can be considered as the inferior limit for the localization precision.

Note that this result applies to the across track component of the localization technique. For **along track** component, we know that the computed point is located with **half the pointing error** (6.25m for one pixel error, 12.5m for two pixel error).

#### Effects of geometric model errors on localization

The derivation of the precision given on the previous section have assumed that the only source of error was the pointing error. In practice, the geometric model of the images can be not accurate enough. We recall that the geometric modelization of the images is two-folded ; it comprises :

1. the instrument model,
2. the orbit model.

Because their parameters are not always well known, errors can be introduced in the geometric model of the images through parameters  $\theta$ , which entails errors in the final localization of the ground points.

#### Effects of Errors in the Instrument Parameters

The errors in the instrument model are mainly limited to both following parameters :

- the start time of sampling in range for each line, also called « near range time » ;

— the start time of acquisition along the orbit.

Both parameters are known to be biased, and will introduce measurement errors. These bias are not accurately known. They can be caused by unstability on the on-board instrument, but can also be introduced in the ground processing.

The effect of start time acquisition error along the orbit will consist in a translation error in both images, but in opposite direction. If this bias is systematic and stable, the ground point determination process will choose a point which compensates for the bias along this direction, and as a result, will find the right point if this bias is systematic (otherwise, a bias in localization along the azimuth axis will appear).

The effect of near range time error is more critical. As it can be seen on figure 2, such errors have impacts on vertical localization as well as localization on the across-track direction. The main effect is located on vertical axis. It remains even if the bias is systematic ( $\Delta r_1 = \Delta r_2$ ). The other effect, located on along-track axis, is only observed when bias is different from one orbit to the other (non systematic bias). The expression of these effects can easily be derived from figure 2:

$$\varepsilon_z = \Delta r_1 / \cos \theta + (\Delta r_2 - \Delta r_1) / 2 \cos \theta$$

$$\varepsilon_x = (\Delta r_2 - \Delta r_1) / 2 \sin \theta$$

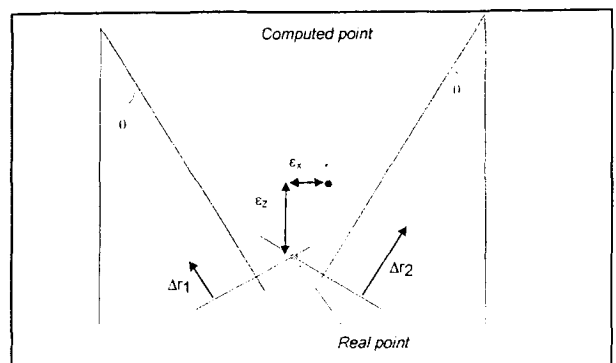


Figure 2 : Effects of errors in near range time

We will see during the experimentations if such biases are present in ERS image products, and if they can be considered as systematic.

#### Effects of orbit errors

The errors introduced on the localization technique by the orbit will be the same as the satellite localization errors (absolute translation). The precision of the ephemerids used to modelize the orbit is a priori known. We know that 4 levels of orbits can be provided for ERS image products (in increasing order of precision):

- Predicted orbits (25 to 400m precision);
- Restituted orbits (1 to 4m precision, 1 value/minute);
- Preliminary orbits (10cm, one value / 2 minutes);

— Precise orbits (10cm, one value / 30s).

The main characteristic is that predicted orbits have poor precision, whereas restituted to precise orbit give precision compliant with the requirements of the localization technique. The ERS image product contains ephemerids that may be computed from predicted, restituted, preliminary or precise orbits (information available in the CEOS file header). It seems that most of ESA products contain restituted to precise orbit level, but this may not be the case for other products. Nevertheless, for any ERS image products, the use of precise orbits product in complement with the image product can insure the use of optimal orbital data.

#### Description of the GCP generation functions

SYSECA implemented a software tool allowing the computation of ground control points from ERS images pairs, using a user friendly man machine interface. This chain takes as inputs the original image products (in CEOS format), on CDROM or tape. The output is a set of identified georeferenced ground points. It comprises the following steps.

##### *Image Import and Geometric Model computation*

This driver software module reads data that respects the CEOS format definition, to extract the relevant informations on the stored data, and to convert the data in the SYSECA's internal format. The import software extracts the ancillary data, like the orbit or the sensor parameters, to generate the geometric model of the imported image (the orbit is modeled by Kepler representation, computed from the ephemerids).

##### *Image points acquisition*

Whereas the previous step was fully automatic, this one is highly interactive. Because of the opposite viewing angles configuration, the automatic acquisition of pairs of homologous points cannot be done automatically. This task is only possible with human interpretation. Though, it remains a tedious task, and represents a bottleneck for the operability of the technique. This functionality is mainly used for further processing called aero/spatio-triangulation (bundle adjustment of the imaging parameters using the selected points).

##### *Ground point computation*

The ground point computation step uses the geometric models of the images to derive the georeferenced localization of the ground point corresponding to a pair of homologous points. This computation algorithm is based on an optimal approach, estimating by iterations the 3D coordinates minimizing the image residues. Mathematically, this problem takes the following form:

$$(\hat{X}, \hat{z}) = \arg \min \left[ \|F_{\theta_2}(X, z) - P_2\|^2 + \|F_{\theta_1}(X, z) - P_1\|^2 \right]$$

This minimization is done with a quasi-Newton algorithm. This approach is the only solution for a rigorous estimation the ground location, and doesn't rely on any first order approximation.

## 2. EVALUATION METHOD

In order to assess the technical feasibility, it is necessary to focus on two criterions :

- The qualitative performance of the technique : we will analyze whether the selection and acquisition of interest points in both images is possible; moreover, we will see if the ground points computed can be used to play the role of ground control points in a SPOT image on the same area.
- The quantitative performance of the technique: we will quantify the absolute geometry quality of the generated ground points, with respect to a ground truth.

The reference ground points have been measured on 1/25000 standard maps of the area, provided by the french Institut Géographique National. The accuracy of such measurements is approximately 10 meters (0.4mm on the map). For ground referential, our measures will be expressed in a referential based on Clarke80 ellipsoid, Lambert 3 as projection, and the z-datum is the standard geoid (IGN's map standard referential). A rigorous geographic knowledge has to be used to insure the coherency between such referential and the images, whose ephemerids are expressed in totally different referentials (WGS84 ellipsoid, also for z datum).

## 3. OPERATIONAL FEASIBILITY EVALUATION

#### Description of the data

We experimented the technique on a set of ERS data provided by SPOTIMAGE. The area of interest was centered on the south-east of France, from Marseille to Carpentras.

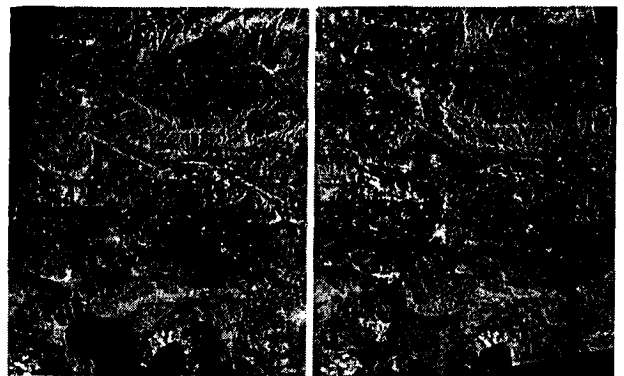


Figure 3 : Crossed orbit ERS images pair (A1/M1)



One ascending ERS image, acquired on 5 July 1998, and two descending images, acquired respectively on 18 July 1998 and 22 August 1998, have been used. We also used another ascending image, whose date was 8 December 1998. Although a long delay was present between this last image and the others, the identification of ground control points with this image and the former ones have revealed to be possible, which illustrates the robustness of the technique. One of the pair is shown on the figure below. One can see the important dissimilarity between both images, especially in mountainous areas.

#### Ground Point selection and acquisition

##### *Type of selected points*

The points which are going to be used as ground control points for further exploitation must respect two constraints :

1. they must be viewed and accurately detected on both images of the ERS image pairs ;
2. they must be significant enough and no radar specific to be also detected in optical images (in order to be used to register SPOT images).

Obviously, no moving feature can be used as ground control points. Constraint 1 entails the rejection of points located in valleys, or surrounded by embankments, because of the opposite side viewing geometry with such active sensors., and constraint 2 prevents from using points which are well detected with radar wavelength, but are barely seen on optical images : for example, some small-sized man made features give rise to bright points on radar images : whereas in optical images, they are not detectable.

The result is that our points are mainly defined by cross-roads, bridges, coastlines details. It hasn't been possible to detect candidates points in uninhabited mountainous areas (Luberon region for example).

##### *Difficulties of the points selection task*

The selection of candidates points hasn't been straightforward. ERS images don't insure systematically the visibility of features like roads, rivers or coastlines. We suspect that difference in weather conditions between two of the images used in this experimentation are responsible for the degradation of image quality with respect to our purpose. The detection of ground points has been a very tough task, because of the resolution of ERS images, combined with speckle : road networks are not always clearly seen, and selection of points can only be done with a high level of human interpretations and extrapolation.

As a result, the selected points are corrupted with errors. The error can be modeled as a random gaussian noise with zero mean and a standard deviation which is worse than one pixel (say 2 pixels).

##### *Ground coverage*

One of the requirements for the operational use of the technique is its ability for generating a sufficient number of ground control points to register SPOT images. Typically, one needs about ten points, uniformly distributed across the images.

In our experimentation, the number and density of ground points in urbanized area (near Marseille) is good enough. Nevertheless, the area of Cavaillon, on the top of the image, is really poor, which is due to the mountainous aspect and the lack of road or river network visible in this area.

We can then conclude that the localization technique will not be efficient for georeferencing SPOT images in areas where no detectable feature are present. This technique will probably fail for images over deserted areas, mountainous areas, or deep tropical forests areas.

##### *Examples of selected points*

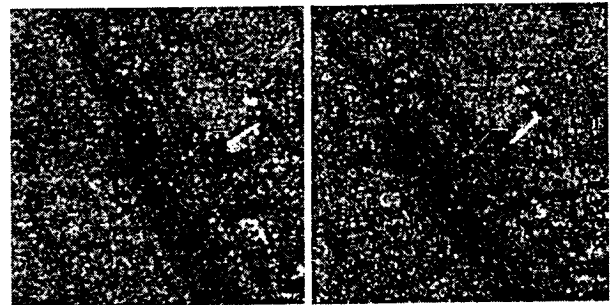


Figure 4 : Crossing of taxiways on an airport

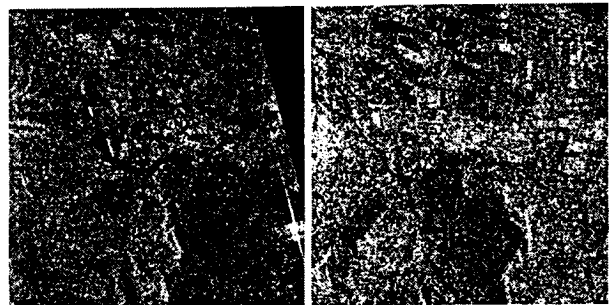


Figure 5 : Middle of a bridge over a river

#### Operational use of the generated GCPs with SPOT

The feasibility of the technique used for SPOT image registration imposes that ground points computed from ERS must be visible on SPOT images. We insisted on this point in previous chapter. We present here some examples on the application of the technique, illustrating the operational use of ERS ground points for SPOT images. In each case, we present the points selected on ERS image pairs, and the point selected on SPOT images.

On figure 6, one can see an easy case, where the point is found as the crossing of taxiways on an airport. As expected, the point is easily found on the SPOT image.

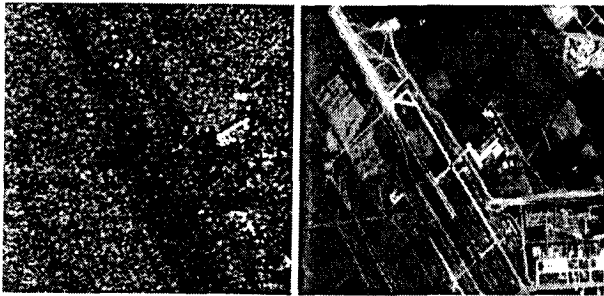


Figure 6 : Taxiways crossing on ERS and SPOT

In the next example, the determination of the point selected on the ERS pair is not as easy. Although the identification of the same point on both ERS images is straightforward, because of its nature (a crossing between two roads), the identification of this point on the SPOT image is not easy because the roads don't appear clearly enough.

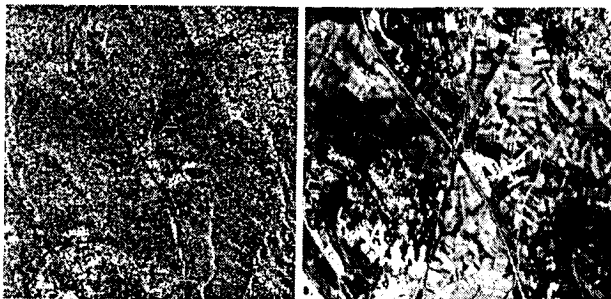


Figure 7 : crossroad on ERS and SPOT

Nevertheless, we can say that most of the generated ground points from ERS images can be identified on SPOT with a precision about 1 to 2 pixels. For some very difficult points, the pointing precision can get worse (a few pixels).

#### 4. LOCALIZATION RESULTS USING ESA DATA

The performances of the 3D localization technique have been evaluated on 4 pairs, using 4 images :

- Ascending: M1 (05/07/98) and M2 (08/12/98);
- Descending : D1 (18/07/98) and D2 (22/08/98);

The images, provided in PRI format, have been processed at the I-PAF. This evaluation has been done using on the one hand the ephemerids provided with the images, and on the other the ephemerids from precise orbit products (ORB.PRC). We did not observe significant differences in the results with both orbit data type (ESA products generally provide preliminary or predicted orbit level data with images).

Table 1 gives the estimated accuracy of the localization technique as the absolute 3D error, represented by its mean ( $\Delta X_m, \Delta Y_m, \Delta Z_m$ ), standard deviation ( $\sigma_{\Delta X}, \sigma_{\Delta Y}, \sigma_{\Delta Z}$ ) and RMS ( $\Delta X_{RMS}, \Delta Y_{RMS}, \Delta Z_{RMS}$ ). N is the number of reference points used.

Config.	M1/D1	M1/D2	M2/D1	M2/D2
N	24	21	13	11
$\Delta X_m$	+1.3	-2.5	+3.2	-1.1
$\Delta Y_m$	+6.7	+8.8	+1.5	+1.5
$\Delta Z_m$	-36.6	-37.3	-33.4	-33.9
$\sigma_{\Delta X}$	14.6	13.5	11.9	15.5
$\sigma_{\Delta Y}$	14.0	16.0	15.8	17.5
$\sigma_{\Delta Z}$	5.0	5.0	5.4	4.7
$\Delta X_{RMS}$	14.7	13.8	12.3	15.6
$\Delta Y_{RMS}$	15.5	18.3	15.9	17.5
$\Delta Z_{RMS}$	36.9	37.6	33.9	34.3

Table 1 : Localization errors for ESA products (meters)

The performances in **planimetric** localization are **compliant with the theoretical performances**. The bias in the X-axis (East axis, roughly the across-track direction) is close to 0, and the bias in the Y-axis (North axis, roughly the along-track direction) is small with respect to standard deviation values.

The **altimetric** performances are not compliant with theory. They suffer from an **important bias** (about -35 meters). Nevertheless, the standard deviation is compliant with the theoretical value. The planimetric performances aren't affected by this bias, which leads to the conclusion that the bias in range is a **systematic** error which planimetric effects offset each other because of the opposite-side viewing.

The bias in altitude measurement seems to be induced by a near range time measurement error in the ancillary data provided with the images (this error corresponds to +33 meters in range).

#### 5. LOCALIZATION RESULTS USING NON ESA PRODUCTS

The evaluation of the technique on non-ESA products was aiming at highlighting potential differences between several acquisition and diffusion stations. Our approach was to compare results obtained with ESA data to results on the same raw data processed by different stations.

Only one set of data was available, processed by the ACS company. The processor used was based on the « omega-k » algorithm. The three images acquired on summer 1998 have been processed (A1, D1, D2).

Like the experiments with ESA products, we used the different combinations with our 3 images.

We compared the results obtained with the initial orbit data and with precise orbit products (ORB.PRC). The

results were very bad without precise orbit data, showing that ephemerids provided with ACS PRI products are not restituted nor precise orbits (in fact, predicted orbit data according to the CEOS header). We can conclude that the precise orbit product is necessary with ACS data.

The results, using precise orbit data, are given in the table below.

Config.	M1/D1	M1/D2
N	23	18
$\Delta X_m$	+8	+3.6
$\Delta Y_m$	+13.7	+11.9
$\Delta Z_m$	+48	+46.6
$\sigma_{\Delta X}$	16.3	19.6
$\sigma_{\Delta Y}$	12.2	13.9
$\sigma_{\Delta Z}$	4.5	4.2
$\Delta X_{RMS}$	18.2	19.9
$\Delta Y_{RMS}$	18.3	18.3
$\Delta Z_{RMS}$	48.3	46.7

Table 2 : Localization errors for ACS products (meters)

The localization errors behavior is similar to the ESA case. The performances in **planimetric** localization are **close to theoretical performances**. The bias in the across-track axis (X) is close to 0, and the bias in the along-track axis (Y) is of the order of the standard deviation values. The values for standard deviation are slightly higher than the theoretical ones (15 meters) for a two pixel pointing precision. As a result the RMS values are slightly higher than the theoretical value (18 meters).

The results of our experiments with ACS data show that the technique is also able to generate, from ERS products, ground control points accurately located in planimetry (unbiased coordinates, with standard deviation close to 18 meters), but with an important bias in altimetry (+48m) despite of the accuracy of the altitude measurement (standard deviation close to 5m). The bias in altitude measurement seems to be due to a near range time measurements error in the data provided with the images. A residual bias in localization along the orbit can be observed, probably due to random errors on the start time of acquisition.

## CONCLUSION

During this study, we implemented a localization technique allowing the generation of ground control points from an ascending orbit image and a descending orbit image acquired with ERS SAR sensor. We evaluated the performances of this technique by comparing the results of the 3D localization technique with reference points given by a map with 1/25000 scale.

We observed that the technique is able to provide ground control points with the following performances :

- planimetric localization precision :  $\sigma = 15$  to 18 meters, no bias ;
- altimetric localization precision :  $\sigma = 5$  meters , but with an important bias value (about -33m for ESA products, +46m for ACS products).

The bias in altimetry is probably due to a systematic bias in the near range time of the images.

The technique has proven to be repeatable with ESA as well as non-ESA products (ACS). The only influence of the processor is the value of the near range time bias. Nevertheless, we found that ACS products give slightly worse results than ESA ones (a few meters degradation).

The bias in near range time has been commonly observed by ERS users. It is known that there is an instability in the sampling start time in distance for ERS. Though, the dependency of the observed bias to the processor is emphasized by the use of PRI products, which have been submitted to important resampling. Maybe this problem is less critical with SLC data. More experiments have to be led to confirm this. Moreover, we cannot conclude that this bias is systematic unless more data sets are exploited, but the results obtained on images with large differences in acquisition time (july to december) seem to confirm this characteristic.

For SPOT geocoding, the accuracy of measurements of the 3D points is compliant with respect to SPOT resolution. Nevertheless, the bias in altitude will cause errors in the geocoding process. But our situation is not as critical as it may appear : we do not have ground control points with bad altimetric precision, but points with good precision, and an unknown bias. Hence, this bias has to be introduced in the geocoding process as an additional variable to be estimated. Several approaches can then be used :

- The estimation can be performed using one reference altitude (example : on the sea coast, the altitude is known to be zero).
- The bias can be known by accurate calibration of the instrument and the processor by ESA or receiving station (if it really systematic and stable enough).
- The accurate knowledge of the orbit can lead to the estimation of the bias. Because of the precision of the knowledge of SPOT orbit (best than 10 meters for SPOT4), we have a constraint that can compensate for this bias during the estimation process.

Hence, we can conclude that the technique of localization using ERS for SPOT registration is very close to operability, although further experiments have to be done to confirm our results. A specific approach will be necessary to cope for the bias problem in altitude measurement, and we identified several solutions to that problem, and they have to be tested.



# On Accuracy of Attitude Estimation and Doppler Tracking

Marina V. Dragošević

SATLANTIC Inc. Richmond Terminal, Pier 9 Halifax, NS, Canada B3K 5V8

Tel: 1 902 492-4780 Fax: 1 902 492-4781 marina.dragosevic@satlantic.com

## Abstract

A precise physical model of the Doppler effect is based on the spacecraft state vectors, Earth model and spacecraft attitude. Thus, the problem of Doppler tracking can be posed as the problem of adaptive estimation of the satellite attitude. The same physical model and general approach to Doppler/attitude tracking can be applied to ERS and RADARSAT, single beam mode and scan mode SAR. For ERS, zero Doppler steering is taken into account. For RADARSAT, two effects are a major concern: i) PRF (pulse repetition frequency) ambiguity resolution and ii) elevation dependent azimuthal displacement of the beam peak illumination. This paper presents some results related to these issues.

## INTRODUCTION

Many scientific SAR applications require very high image quality, [5]. Proper attitude and DC (Doppler centroid) tracking is necessary in order to insure radiometric and geographic accuracy. This work is based on a concept in which attitude and Doppler tracking are closely related. The first two sections describe the mathematical model for the DC and the overview of the Doppler tracker implemented in the IOSAT's SAR processor (Sentry-SAR), which successfully combines the kinematic and the echo-adaptive approach to DC estimation. Further sections are devoted to the analysis of the estimation variance, observed RADARSAT attitude variability and tuning of the coefficients in the model of the elevation dependent beam peak displacement.

## THE DOPPLER CENTROID MODEL

The following is the expression for the DC vs. elevation angle  $\gamma$ , given the attitude angles yaw  $\phi_y$

and pitch  $\phi_p$ , satellite position  $\mathbf{r} = [r_x \ r_y \ r_z]^T$  and velocity  $\mathbf{v} = [v_x \ v_y \ v_z]^T$  in the ECI (Earth Centered Inertial) coordinate system. Geodetic position  $\mathbf{s}$  of the satellite is also needed (it is the vector from the Earth rotation axis to the spacecraft, locally orthogonal to the Earth surface). It determines the vertical  $v_v$  and the horizontal  $v_h$  components of the satellite velocity.

$$f(\gamma, \phi_y, \phi_p) = f_0(\gamma) + f_\phi(\gamma, \phi_y, \phi_p) \quad (1)$$

where the zero attitude component is

$$f_0(\gamma) = -\frac{2}{\lambda} \left( v_v \cos \gamma + \omega \frac{s v_z - s_z v_v}{v_h} \sin \gamma \right) \quad (2)$$

and the attitude dependent component is

$$f_\phi(\gamma, \phi_y, \phi_p) = f_n (\phi_y \sin \gamma - \phi_p \cos \gamma) \quad (3)$$

$$f_n = -\frac{2}{\lambda} (v_h - \omega \frac{r_x v_y - r_y v_x}{v_h}) \quad (4)$$

DC can be zeroed all across the swath by proper steering in both yaw and pitch. The required attitude values are easily derived by equating the coefficients of the sine and cosine terms of  $f_0(\gamma)$  and  $f_\phi(\gamma, \phi_y, \phi_p)$ .

RADARSAT attitude is not steered. Although it is close to zero, there is an additional offset of the beam center (and peak) in azimuth and the amount of this offset depends on the elevation angle. Originally, the dependence was modeled as a third order polynomial  $\phi(\gamma) = P(\gamma - \gamma_{ref})$ , defining a cone with the vertex at the satellite position, [1]. The tangent plane to this cone, at any elevation angle, can be viewed as corresponding to a local pair of yaw and pitch angles given by

$$\tilde{\phi}_y(\gamma) = \phi(\gamma) + \frac{d\phi(\gamma)}{d\gamma} \sin \gamma \cos \gamma \quad (5)$$

$$\tilde{\phi}_p(\gamma) = \frac{d\phi(\gamma)}{d\gamma} (\sin \gamma)^2 \quad (6)$$

When these values are fed back into the generic DC equation, we can establish the following decomposition of the DC:

$$f(\gamma, \phi_y, \phi_p) = f_b(\gamma) + f_\phi(\gamma, \phi_y, \phi_p) \quad (7)$$

where the expected (spacecraft zero-attitude) DC term

$$f_b(\gamma) = f_0(\gamma) + f_\phi(\gamma, \tilde{\phi}_y(\gamma), \tilde{\phi}_p(\gamma)) \quad (8)$$

reflects the beam behavior, while the other term corresponds to physical attitude only.

The problem is that the original (preflight) beam model does not perform quite well, especially for the extended beams and for the scan SAR.

## AN OVERVIEW OF THE DOPPLER TRACKER

There are many techniques to estimate DC from the pulse returns, unrelated to the underlying geometry. Within this work, we will classify them as coarse methods and refinement methods. As coarse we will consider those methods that are based on spectral analysis (e.g. periodogram, autoregressive) of the range compressed echo samples, [2]. They may be biased in the case of along track discontinuities of the surface reflectivity. The refinement methods provide more accurate and more consistent DC estimates, but they work on the azimuth compressed data, usually in an iterative manner. In strip map mode, the same algorithms can be used as in coarse estimation. For scan modes, as well as strip map, other image domain techniques are available, such as Jin's ratio algorithm [3] or similar, but simpler, radiometric balance (weighted difference) algorithm (used in SentrySAR).

Several principles can be used to resolve the PRF ambiguity. They are based on  $\lambda$  (wavelength) diversity (from range looks) [2], PRF diversity, rate of DC change with elevation angle.

SentrySAR Doppler tracker uses a combination of practically all of the above mentioned methods and practically all of the available data. DC is estimated

across range before and after azimuth compression. In single beam mode, a block of 2048 or 4096 range lines is used. In scanning mode, all beams, several bursts of each, are used in combination. For single beam modes, PRF ambiguity is resolved based on  $\lambda$  diversity. Attitude is fitted to the DC estimates. For scan mode of SAR, all beams are taken into account at once, including the range overlaps, and the PRF ambiguity is estimated together with the two attitude angles. It utilizes both the PRF diversity in the overlaps and the cross track shape of the DC curve. Also, processing blocks are combined. Attitude is smoothed along track, over the processing blocks. To make this procedure very efficient, the coarse DC estimates are used for the current block and refined DC estimates are used for all previous blocks. Thus, no reprocessing of any block is ever done and still the post-compression refinement of DC estimates is utilized.

## VARIANCE OF THE ESTIMATES

In the case of  $N$  independent, zero-mean DC estimates with variance  $\sigma_f^2$  taken across the swath and LS (least squares) fitting of  $\Phi = [\phi_y \phi_p]^T$ , the error covariance matrix is

$$\frac{\sigma_f^2}{f_n^2} \frac{2}{N} \left( \frac{1}{N^2} \sum_{i=1}^N \sum_{j=1}^N \sin^2(\gamma_i - \gamma_j) \right)^{-1} \mathbf{V} \quad (9)$$

where

$$\mathbf{V} = \begin{bmatrix} \frac{1}{N} \sum_{i=1}^N \cos^2 \gamma_i & \frac{1}{N} \sum_{i=1}^N \cos \gamma_i \sin \gamma_i \\ \frac{1}{N} \sum_{i=1}^N \cos \gamma_i \sin \gamma_i & \frac{1}{N} \sum_{i=1}^N \sin^2 \gamma_i \end{bmatrix} \quad (10)$$

Yaw and pitch estimates are highly correlated, which explains their similarity as seen e.g. in [4].

In the special case of equidistant estimation points in the elevation angle space

$$\sigma_y^2 = \frac{\sigma_f^2}{f_n^2} \frac{2}{N} \frac{1 + \text{sinc}(\gamma_f - \gamma_n) \cos(\gamma_f + \gamma_n)}{1 - \text{sinc}^2(\gamma_f - \gamma_n)} \quad (11)$$

$$\sigma_p^2 = \frac{\sigma_f^2}{f_n^2} \frac{2}{N} \frac{1 - \text{sinc}(\gamma_f - \gamma_n) \cos(\gamma_f + \gamma_n)}{1 - \text{sinc}^2(\gamma_f - \gamma_n)} \quad (12)$$

where  $\gamma_f$  and  $\gamma_n$  are far and near elevation angle, respectively. The variance is highly dependent on

the elevation aperture. The LS fitting may become an ill conditioned problem for small apertures. It is difficult to separate the contribution of yaw and pitch to the measured DC. The following tables illustrate the significance of the elevation dependent factor in yaw and pitch variance (last factor in (11) and (12)).

Asymptotic variance factor						
	W1	W2	W3	S5	S6	S7
Yaw	178	270	543	604	714	864
Pitch	31	95	230	280	436	630

Asymptotic variance factor			
	SCWA	SCWB	SCNB
Yaw	24.6	30.3	57.2
Pitch	8.5	9.6	14.0

It is interesting to note that the weighted difference

$$\phi_y \frac{1}{N} \sum_{i=1}^N \sin \gamma_i - \phi_p \frac{1}{N} \sum_{i=1}^N \cos \gamma_i \quad (13)$$

can be estimated with much lower variance  $\sigma_f^2/(N f_n^2)$ . This again explains why the estimates of yaw and pitch follow approximately the same patterns along track.

When such attitude estimates are used to recompute the DC via (7), (3), due to the well behaved nature of the weighted difference (13), the variance of the recomputed DC is reduced to  $\sigma_f^2/N$ , which can be notably better than the original DC estimation (coarse or refined) variance.

If attitude stays constant or varies slowly, it can be averaged over the processing blocks. Then the variance of the recomputed DC is further reduced, since the effective value of  $N$  increases.

In conclusion, SentrySAR map and scan SAR processors can provide good Doppler tracking. Attitude tracking will achieve very good accuracy (standard deviation in of the order of thousandths of a degree, confirmed by real data tests) for SCW (scan wide) modes.

## ATTITUDE VARIABILITY

In most cases we have observed variability of RADARSAT yaw and pitch in the order of the hundredths of a degree within a scene (about minute and a half worth of data). In some cases the change was in the order of a tenth of a degree. For example,

during the orbit 12204 in descending pass over the Great Lakes (07.03.1998.), pitch rate was close to 0.4 degrees per minute in the last 15 s of the scene. This emphasizes the need to closely track attitude. Otherwise strong scalloping will occur in the image.

Long term stability of RADARSAT attitude has also been monitored by the Sentry ground station. Yaw tends to be slightly negative (about -0.1 degree), while pitch changes from small positive to small negative values depending on the pass orientation (ascending/descending). The SentrySAR processor has found the early RADARSAT orbits to be characterized by yaw in the range of about 0.8 to 0.9 degrees and pitch around 0.4 degrees.

## TUNING THE BEAM DISPLACEMENT MODEL

The original beam model for RADARSAT was determined on the preflight fine and standard beam measurements. The coefficients (increasing power) are:

$$[0.001037356 \ -0.000185 \ -0.10330429 \ 0.1986098]$$

and  $\gamma_{ref} = 0.52010812$ , all in radians.

Extended high beams largely deviate from this model. Scan mode of SAR can be used to test the model in the following way. Attitude can be estimated for particular beams separately and independently and compared to the attitude obtained by over-all fitting. It has been noticed that certain beams have a bias relative to the over-all estimates of yaw and pitch. The bias is persistent and on the average it is about the same for the same beams in various data files. This lead to the conclusion that the beam model is incorrect.

Fitting the beam coefficients together with the yaw and pitch within the same LS procedure does not seem to be an option, since the system for attitude estimation alone is already poorly conditioned. We have taken a different approach.

The refinement algorithm provides corrections for the DC estimates cross swath. In the case of maritime scenes it usually corrects a possible offset and the slope of the coarse DC estimates (because they are sensitive to the scene content). But there are non-negligible corrections even for radiometrically uniform scenes, such as ocean and the rain forest. Those DC corrections vs. elevation angle,  $\Delta f(\gamma)$ , were collected and plotted for many blocks and for many data files. They exhibit ripples of about 10

to 20 Hz in magnitude. A pattern was noticed and attributed to the beam model deficiency via

$$\Delta\phi(\gamma) = \frac{\Delta f(\gamma)}{f_n \sin \gamma} \quad (14)$$

$\Delta\phi(\gamma)$  also had a characteristic shape, including two maxima and a minimum, in the range of 0.01 degree to -0.01 degree. It was modeled as a fourth order polynomial in  $\gamma - \gamma_{ref}$ . These coefficients were then averaged over many blocks and data sets. The corrections were then added to the beam model. This procedure has resulted in a fourth order beam polynomial model with coefficients:

[0.0009678 0.00025 -0.0886317 0.1822822 -0.366262]

This particular set of coefficients has been obtained from five different data sets which were not all ideal for this purpose. For example, the meritime and Great Lakes scenes were used, as well as some more uniform ones of the Atlantic ocean and Saskatchewan.

In order to verify the procedure, all data sets were reprocessed with the new beam model. The separately estimated values for yaw and pitch were now closer, on the average, to the values estimated for all beams jointly. This is shown in the table below. A test case is included as well. It is an image of Amazon, not used within the training set. The improvement for the test case is comparable to the improvement for the two cases from the training set shown in the table. Attitude values are in degrees.

	From the training set		Test case
Orbit	2322	11367	9173
Type	SCWB	SCWA	SCWB
Orientation	asc.	asc.	dsc.
$\sigma_{\Delta yaw}$ old	0.0216	0.0565	0.0222
$\sigma_{\Delta yaw}$ new	0.0081	0.0098	0.0069
$\sigma_{\Delta pitch}$ old	0.0157	0.0462	0.0161
$\sigma_{\Delta pitch}$ new	0.0044	0.0079	0.0069

## CONCLUSION

IOSAT has incorporated a sophisticated Doppler tracker into the SentrySAR processor. It has several useful features. All algorithms are simple, numerically efficient. No iterations or reprocessing are needed, it is a track-while-process or flow-through implementation. It works unsupervised. Updates are

frequent to capture attitude variations. The procedure is independent of the swath length. Accuracy is owing to massive averaging in the proper way. The tracker does not presume any particular features of the scene. Modeling of DC (and DR) as a function of range is in terms of the attitude angles, not by an arbitrary function such as a polynomial. Thus, fewer parameters need to be fitted, namely only yaw and pitch. Meaningful physical constraints can be imposed on yaw and pitch and built into the tracking algorithm (related to the rate of change of the spacecraft attitude) and monitored. For scan mode, estimation of yaw and pitch simultaneously uses all of the beams. For RADARSAT, the tracker handles the beam shape problem. On the other hand, this type of DC modeling is sensitive to the beam characteristics. Due to this same sensitivity, it is possible to devise a method for beam model correction and tuning. When combined with a very accurate, unbiased DC estimator, the presented scan SAR tracker algorithms can be a useful tool for precise measurements and monitoring of RADARSAT attitude and the beam shape characteristics. This can even be achieved in routine operation, over any scenes. Better results can be expected in controlled conditions.

## References

- [1] S. Marandi, "RADARSAT Attitude Estimates Based on Doppler Centroid Measurements", *CEOS Workshop on RADARSAT Data Quality*, Montreal, Québec, Feb. 1997.
- [2] F. Wong and I. G. Cumming, "A Combined SAR Doppler Centroid Estimation Scheme Based upon Signal Phase", *IEEE Trans. on GE*, vol. 34, pp.696-707, May 1996.
- [3] M. Y. Jin, "Optimal Range and Doppler Centroid Estimation for a ScanSAR System", *IEEE Trans. on GE*, vol. 34, pp. 479-488, March 1996.
- [4] K. Eldhuset, "Accurate Attitude Estimation Using ERS-1 SAR Raw Data", *Int. J. Remote Sensing*, vol. 17, no. 14, pp. 2827-2844, 1996.
- [5] P.W. Vachon, J. Wolfe, R.K. Hawkins, "The impact of RADARSAT ScanSAR image quality on ocean wind retrieval", this proceedings



## **Session 4: SAR Processing**



## The Shuttle Radar Topography Mission: Processing Scenario and Techniques

Helko Breit, Nico Adam, Michael Eineder, Richard Bamler and Steffen Suchandt

German Aerospace Center (DLR)  
P.O. Box 1116, D-82230 Wessling, Germany  
Phone: +49-8153-28-1365 Fax: +49-8153-28-1446  
e-mail: [Helko.Breit@dlr.de](mailto:Helko.Breit@dlr.de)

### ABSTRACT

The Shuttle Radar Topography Mission (SRTM), now being scheduled for January 2000, will perform a global topographic mapping of the earth's surface by the first space-borne single pass C- and X-band SAR interferometers [4]. DLR will process the X-band data to a unique DEM data set with a height accuracy in the order of 6 m [5].

The generation of a global DEM requires algorithms optimized for both accuracy and throughput. The paper presents the processing scenario and the processing system's architecture and algorithms.

### INTRODUCTION

During the 11 days mission about 156 orbits will be flown, with a distance between equator crossings of about 220 km. There will be about 650 data take acquisitions over the land mass between latitudes  $\pm 60^\circ$ , with a swath width of 48 km comprising about 2.8 Terabytes of raw data. Fig. 1 gives an quantitative impression of the SRTM / X-SAR coverage over Central Europe. The final geositions of the data takes may differ from this graphic.



Fig. 1: SRTM / X-SAR coverage over Central Europe

The X-SAR interferometer consists of the 12 m primary transmit/receive antenna, which has been flown in the two SIRC/X-SAR missions in 1994, and an receive-only antenna of 6 m length, which is electronically steerable in the

along track direction. The key parameters for the instrument and the mission are given in Table 1.

wavelength	0.03122 m
polarization	VV
chirp bandwidth	9.5 MHz
raw data quantization	4 bit / 4 bit
PRF	1674 Hz
look angle	52°
swath width	48 km, 2878 samples
baseline (nominal)	60.96 m
baseline tilt angle (nominal)	45°
flight height	233 km
mean range	390 km
synthetic aperture	0.15 s, 254 samples
wavenumber shift	0.5 MHz

Table 1: SRTM / X-SAR system and mission parameters

### PROCESSING SCENARIO

The scenario for X-SAR data processing in the frame of the SRTM / X-SAR project is subdivided into three phases:

#### Raw Data Screening

The screening process comprises the extraction of instrument mode parameters and auxiliary data out of the SAR raw data stream as well as the derivation of SAR processing parameters from signal data itself. The resulting parameters are stored in the mission data base MDB, which is subsequently accessed by the InSAR processor. Further on, the SAR raw data which has been demultiplexed, frame synchronized and transcribed from tape to disk, will be stored in the robot archive in segments of one minute length. Thus, the InSAR processor has direct access to about 8000 raw data files via the file system.

The instrument mode parameters and auxiliary data are contained in the first 32 byte of each range line. The most essential parameters are codes for PRF, raw data quantization and chirp bandwidth, which are kept constant for one data take (= continuous acquisition sequence), and instrument settings for the receiver gain, data window position

and phase shifters, which will be kept constant for at least one second.

Signal processing comprises Doppler centroid estimation [1] and PRF-band ambiguity resolving [2] as well as the determination of raw data signal statistics, revealing ADC biases, gain imbalance and non-orthogonality.

Furthermore, time varying phase offsets introduced by the secondary channel receiving hardware, especially by the two 100 mast cables, are estimated by analyzing the phase differences of a sinusoidal calibration signal (3.5 MHz cal-tone) which will be fed into the primary and secondary channel's receiving electronics [9], [12].

All acquired SAR raw data will be screened within a three month time period.

### Commissioning and Calibration Phase

During the commissioning phase, the results of the Doppler centroid estimation and PRF band tracking will be semi automatically validated and corrected, if necessary. Thus, reliable Doppler values for SAR focussing will be obtained, even for areas (deserts and calm ocean) characterized by low SNR.

The InSAR imaging geometry will be measured by the Attitude and Orbit Determination Avionics system (AODA) mounted on the antenna structure with a sampling rate of one second during the Space Shuttle flight. After the mission the AODA data will be processed and provided as Position and Attitude Data Record (PADR) by JPL. This information, labeled as uncalibrated, is stored in the orbit and attitude section of the MDB.

The calibration of the X-SAR instrument and InSAR imaging geometry will be performed by the Calibration Team for X-SAR [12]. For that purpose, interferograms acquired over the almost flat ocean surface will be processed. Time varying correction parameters for electrical phase offsets, and calibrated baseline length and tilt angles will supplement the orbit and attitude data in the MDB, now being calibrated.

From PADR, the secondary antenna motion will be determined and parameters for motion compensation are fed into the mission data base.

### Operational InSAR processing and DEM generation

After the InSAR processor checkout during the commissioning phase all X-SAR raw data will be systematically processed to so called Interferometric Data Sets consisting of 4 data files, all in slant range geometry:

- single look complex primary channel image,
- coherence
- unwrapped phase,

- segmentation mask, describing invalid samples and independently unwrapped regions of the interferogram

About 13.000 IFDS will be stored in the robot archive. Each IFDS covers 150 km by 48 km and serves as input data for the DEM generation. The archiving step uncouples the DEM generation, which is most efficiently done in a geographically oriented schedule, from IFDS generation which is most efficiently performed in data acquisition time order.

All the data will be processed to interferograms and DEM tiles in a two years time frame following the commissioning phase.

### PROCESSOR ARCHITECTURE AND ALGORITHMS

The processing chain consists of the three DLR / DFD developed processing system BSAR, GENESIS and GeMoS. Based on their multi-threaded scaleable architecture BSAR and GENESIS are predestinated to operate on multi-CPU hardware. Utilizing a SUN ET4000, equipped with 12 CPUs, 250 MHz each, and two Gigabytes of RAM, the generation of an unwrapped interferogram (about 38.000 x 3.000 pixel) starting from unfocussed SAR raw data will take less then 50 minutes.

### SAR Focussing

The high-precision multi-sensor chirp scaling SAR processor BSAR generates the two single look, slant range, complex data sets for subsequent interferogram generation [3], [6]. This system is characterized by the following features:

- All focussing parameters are updated for each block to minimize the effect of approximations between the blocks
- The sampling grid in range and azimuth of adjacent scenes is kept coherent, so that the scenes can be coregistered without resampling.

BSAR has been extended with SRTM specific features:

- Mission data base access module
- Application of azimuth and range varying phase corrections on the SAR raw data. This allows for the correction of electrical phase offsets as well as the compensation of secondary antenna motion introduced by mast roll bending.
- Suppression of the cal-tone during range compression.
- Optional coregistration in range direction (shift and scale) and azimuth direction (shift) during focussing avoiding explicit interpolation.

The most critical component of the outboard antenna motion is mast roll bending. The first order oscillation is

characterized by a cycle time of 8.4 s and a peak amplitude of 3.3 cm. It is obvious that this displacement, which is in the order of the wavelength, has to be corrected. The phase variation of  $30^\circ$  within the aperture time is in the order of  $\pi/8$  where the focussing quality begins to deteriorate. The uncompensated linear motion in the line of sight within one aperture leads to an azimuth position error oscillating between  $\pm 0.7$  m within 8.4 s. A resulting constant phase offset of  $0.012^\circ$  can be neglected. The oscillating azimuth positioning error can not be compensated by an azimuth coregistration. Depending on the Doppler centroid, the resulting misregistration may lead to phase errors higher than the phase SNR. As a conclusion the compensation of the mast roll bending is foreseen in the processor [5], [13].

### Interferogram Generation

The interferometric processor GENESIS is a flexible designed system supporting different sensors like ERS 1 / 2 [15], X-SAR and Radarsat, and has been adapted to meet the requirements of SRTM [7]. Adaptations for the single pass data acquisition mode were necessary since all spaceborne InSAR systems so far work in repeat pass mode. These systems perform very stable flight paths. Their position is determined by external systems and the accuracy is optimized by orbit propagators. Consequently, a small number of state vectors proved to be sufficient to represent the orbit. Now the AODA system delivers the exact position and attitude of the shuttle and the baseline every second. The orbit module of GENESIS has been adapted to make optimal use of this different orbit representation. The processing sequence is depicted in fig. 2.

The interferogram generation steps are

- Reconstruction of the InSAR imaging geometry in order to estimate the flat earth's phase and the spectral shift.
- Spectral shift filtering improves the SNR of the interferogram, filtering the data of both scenes to their common azimuth and range spectra.
- Measurement of the misregistration between the two complex images and optional coregistration.
- Multilooking and interferogram generation. In order to simplify subsequent phase unwrapping (PU) the flat earth's phase is subtracted.
- Generation of cost maps in order to guide the phase unwrapping's underlying minimum cost flow algorithm in a robust manner. These maps are obtained from the phase, amplitude and residues density. The cost maps have been optimized utilizing experiences with ERS tandem data and simulated SRTM data as well. The cost values consist of macro and micro costs. Respective contributions result from large and small scale analysis. Macro costs take large scale

topographic features into account, while micro costs minimize the roughness of the unwrapped phase.

- PU and segmentation mask formation. PU utilizes the minimum cost flow algorithm guided by the previously derived cost maps [10]. The segmentation mask indicates invalid phase samples and separately unwrapped regions.
- Coherence estimation as a quality check, indicating the SNR of the phase. The coherence is corrected for the expected topography by feedback unwrapped and smoothed phase.
- So far all processing steps are performed independently scene by scene. The concluding phase matching step connects separately unwrapped regions of adjacent scenes. The phase  $2\pi$  ambiguity for regions within one scene can be optionally solved by the incorporation of tie points from an external low resolution DEM.

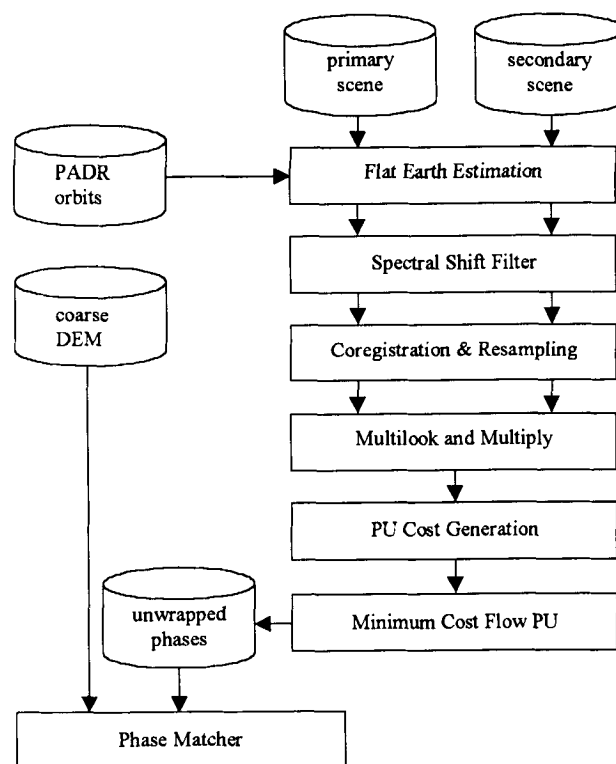


Fig. 2: InSAR processing chain

### DEM Generation

The Geocoding and Mosaiking System GeMoS finally generates the DEM and geocoded products. The following steps are performed:

- Homologue points, which have to be identified in the continuous mesh of crossing ascending and descending data takes, serve as input for the block adjustment

algorithm. This way, the orbit and baseline parameters are further refined.

- The geocoding of the unwrapped phase is done in two steps. First a slant representation  $X(r,t)$ ,  $Y(r,t)$ ,  $Z(r,t)$  is calculated by geolocating each pixel [8]. In a second step the slant range representation is resampled onto a regular grid of geo-coordinates (universal transverse mercator, geographic, etc.) by using an efficient lookup-table approach [11].

The screening system, the InSAR processor BSAR/GENESIS and GeMoS are fully embedded in the newly developed Data and Information Management System DIMS at DLR / DFD. DIMS provides the tools and services for operating, production control, cataloguing and archiving. The processed data will be stored in an online robot archive and all catalogue information will be accessible via web-based interfaces.

### OUTLOOK

The presented system for processing of interferometric SRTM / X-SAR data has been tested with simulated data from the SIRC / X-SAR mission in 1994. The fine tuning of the algorithms for motion compensation, electrical phase corrections, coregistration, cost map generation and block adjustment strongly depend on the stability of the instrument attitude, baseline and electrical phase.

We are looking forward to this unprecedented Space Shuttle mission SRTM and the unique and challenging data set it will provide.

### REFERENCES

- [1] S. N. Madsen, "Estimating The Doppler Centroid of SAR Data", IEEE Transactions on Aerospace and Electronic Systems, Vol. AES-25, No. 2, pp. 134 - 140, 1989
- [2] R. Bamler, "PRF-ambiguity resolving by wavelength diversity", IEEE Transactions on Geoscience and Remote Sensing, vol. 29, pp. 997-1001, 1991
- [3] R. K. Raney, H. Runge, R. Bamler, I. G. Cumming, F. H. Wong, "Precision SAR processing using chirp scaling", IEEE Transactions on Geoscience and Remote Sensing, vol. 32, pp. 786-799, 1994
- [4] R.L. Jordan, E.R. Caro, Y. Kim, M. Kobrick, Y. Shen, F.V. Stuhr, M.U. Werner, "Shuttle Radar Topography Mapper (SRTM), Proc. SPIE 2958, pp. 412-422, 1996
- [5] R. Bamler, M. Eineder, H. Breit, "The X-SAR Single Pass Interferometer on SRTM, Expected Performance and Processing Concept", Proc. EUSAR'96, pp. 181-184, 1996
- [6] H. Breit, B. Schättler, U. Steinbrecher, "A High-Precision Workstation-Based Chirp Scaling SAR Processor", Proc. IGARSS'97, Singapore, 465-467, 1997.
- [7] M. Eineder, N. Adam, "A Flexible System for the Generation of Interferometric SAR Products", IGARSS'97, Singapore, 1341 - 1343, 1997.
- [8] W. Goblirsch, "The Exact Solution of the Imaging Equations for Crosstrack Interferometers", Proc. IGARSS'97, Singapore, 439-441, 1997.
- [9] K.-B. Klein, M.U. Werner, "System Performance Monitoring for X-SAR/SRTM", Proc. EUSAR'98, Friedrichshafen, 1998
- [10] M. Eineder, M. Hubig, Björn Milcke, "Unwrapping Large Interferograms Using the Minimum Cost Flow Algorithm", Proc. IGARSS'98, Seattle, pp. 83-87, 1998.
- [11] A. Roth, W. Knöpfle, M. Hubig, N. Adam, "Operational Interferometric SAR Products", Proc. IGARSS'98, Seattle, pp. 324-326, 1998.
- [12] M. Zink, D. Geudtner, "Calibration of the Interferometric X-SAR System on SRTM", Proc. IGARSS'99, Hamburg, pp. 227-229, 1999.
- [13] G. Franceschetti, A. Iodice, S. Maddaluno, D. Riccio, "Effects of Secondary Antenna Oscillations on X-SAR / SRTM Performance", Proc. IGARSS'99, Hamburg, 1999.
- [14] R. Bamler, "The SRTM Mission: A World-Wide 30m Resolution DEM from SAR Interferometry in 11 Days", Proc. 47<sup>th</sup> Photogrammetric Week, Stuttgart, 1999.
- [15] B. Schättler, et al, "Operational Interferometric ERS Tandem Data Processing", to be presented at CEOS SAR Workshop, Toulouse, 1999, unpublished.

## **Phase Preserving Extended Chirp Scaling Processing Techniques and First Results**

Josef Mittermayer, Alberto Moreira  
DLR, Germany

Yves-Louis Desnos  
ESA/ESRIN, Frascati, Italy

This paper was not available for publication

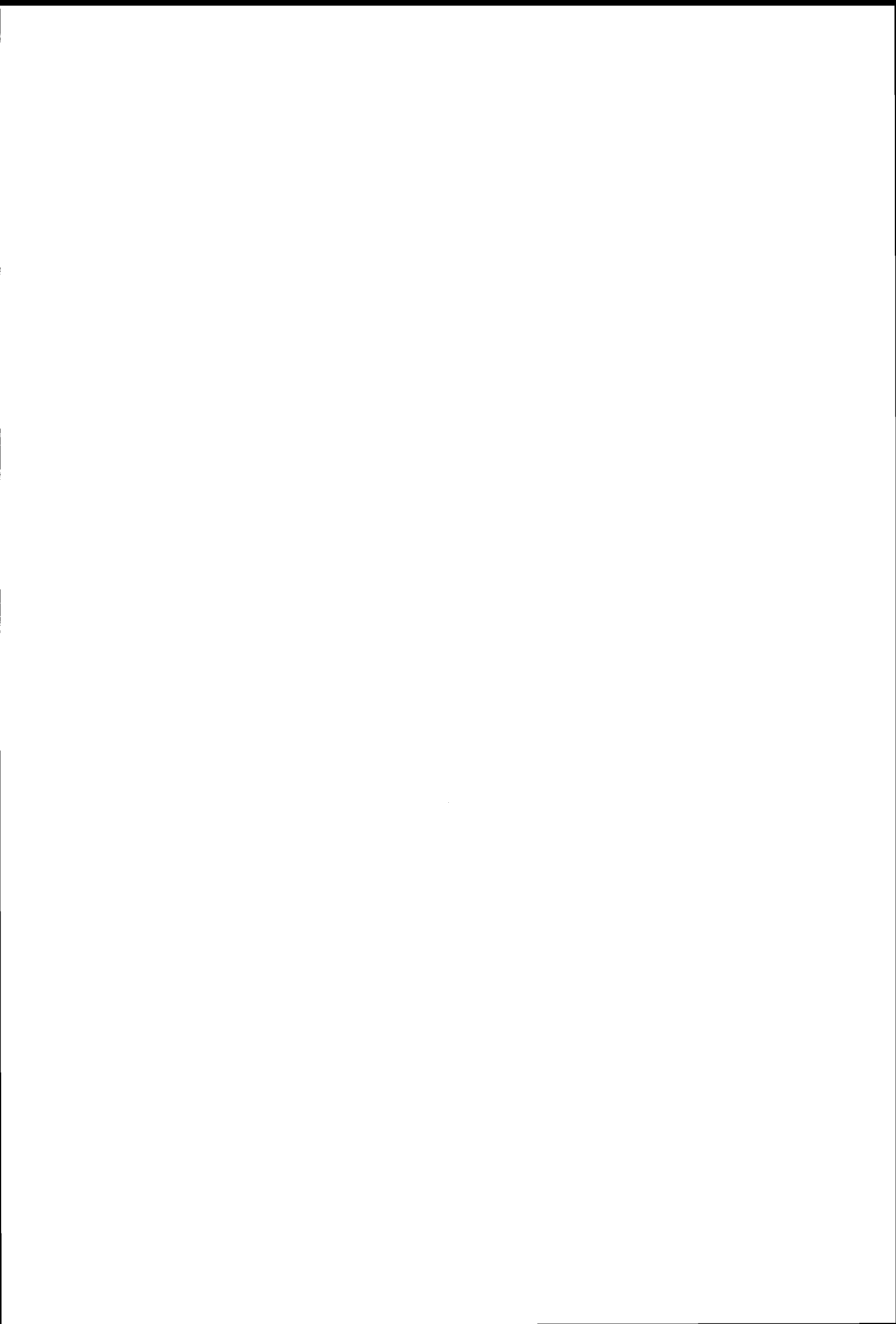




## **Phase Screen Determination for the GEOSAR Interferometric Mapping Instrument**

Scott Hensley, Elaine Chapman, Bob Thomas, Paul Siqueria, Walt Brown, Yunjin Kim  
Jet Propulsion Laboratory, USA

This paper was not available for publication



## New results for Spaceborne Hybrid Strip-map/Spotlight SAR High Resolution Processing

Stéphane Henrion<sup>(1),(2)</sup>, Laurent Savy<sup>(1)</sup>, Jean-Guy Planès<sup>(1)</sup>

(1) Alcatel Space Industries, 26 avenue J.F. Champollion, BP 1187 Toulouse Cedex, France  
Tel (33) 05.34.35.53.94, Fax (33) 05.34.35.61.63.

(2) ENSICA (Ecole Nationale Supérieure d'Ingénieurs en Constructions Aéronautiques),  
1 place Emile Blouin, 31056 Toulouse, France. Tel (33) 05.61.61.86.34.

Email : shenrion@ensica.fr, laurent.savy@space.alcatel.fr, jean-guy.planès@space.alcatel.fr

### ABSTRACT

The aim of this paper is to highlight the spatial configuration specificities against the airborne ones and to draw up the consequences for a High Resolution SAR processing. By considering a more exact geometry for the spaceborne case, we rewrite the usual high resolution processing algorithms ( $\omega$ -k algorithm, Chirp Scaling Algorithm ...). Then we present a global algorithm that allows to process hybrid strip-map/spotlight SAR data, and we give some results about the processing parameters (memory size...).

### 1. INTRODUCTION

The usual Strip-map operating mode of air- and spaceborne SAR limits physically the azimuth spatial resolution to the half of the antenna length.

Today, the need for metric or sub-metric resolution is now increasing with the emergence of more constraining requirements in detection and classification, but unachievable with a Strip-map spaceborne SAR whose antenna length is about a few meters to ensure an efficient power statement

The spotlight mode, which consists in exactly compensating the radar displacement by training the antenna beam onto the same scene, answers the strip-map limitation by increasing the illumination time over each target inside the beam ground footprint. But if this allows to consider higher resolutions, it reduces the image size to the antenna beam footprint.

So that the only way to obtain high resolution for spaceborne SARs with larger image sizes is to use hybrid strip-map/spotlight mode. Such a mode has already been studied for airborne SARs and associated algorithms have been defined, but their implementation in the spaceborne case is not straightforward. Indeed the high precision required during the processing is incompatible with the simplifying hypothesis adopted for the airborne configuration.

So before considering a global algorithm to process hybrid spatial SAR data, it is important to carefully reconsider classic high resolution processing in a more precise geometry than the airborne one.

The goal of the proposed paper is then to highlight the main consequences of a more exact model on signal processing to finally define a complete algorithm.

This paper will focus on the two main stages of a hybrid SAR data processing that are:

- a data formatting step to remove the Doppler aliasing
- a high resolution processing over strip-map like data

In a first section, the paper will touch on the complex satellite-earth range expression with time what will help us to model the signal to be processed.

In a second section the paper will remind the consequences of this new signal modelling by extending the matched filtering and the usual SAR algorithms ( $\omega$ -k technique, Chirp Scaling Algorithm,...) to the spaceborne case, by means of analytical results and analysis of impulse response function.

In a third section, the paper will focus on Doppler spectrum aliasing (several times the PRF value). This data formatting step is characteristic of the hybrid operating mode, and aliasing removing have been already proposed in the airborne case.

After having underlined the specificities and the issues of the spatial configuration, we will then propose a reference algorithm which accommodates with the complexity of a Spaceborne Hybrid Strip-map/Spotlight SAR High Resolution Processing and answers the high memory costs.

### 2. SPATIAL CONFIGURATION AND ANALYTICAL SIGNAL MODELLING

We first insist on the differences between the air and space expressions of the radar-target distance, which is the origin of the propagation delay in the received signal expression.

#### 2.1 Airborne and Spaceborne respective assumptions.

In order to exactly underline the main differences between airborne and spaceborne received echoes, this section will first remind the simplifying geometry and hypothesis usually adopted for the airborne configuration and then present the specific assumptions that characterise the spaceborne one.

Because of the relative velocity, the size of the observed scene and the illumination time required, the airborne case assumes the hypothesis of flat earth model, stationary earth and linear and uniform sensor trajectory. From there it

immediately comes the following expression of the relative radar-target distance :

$$R_x^2(t) = R_0^2 + V_s^2 \cdot \left(t - \frac{x}{V_s}\right)^2 = R_0^2 \left(t - \frac{x}{V_s}\right)_{write}^2 = R^2(t) \quad (1)$$

where  $x$  is the azimuth position of the ground target,  $V_s$  the relative radar-target velocity, and  $R_0$  a reference distance [1].

But for a spatial configuration, associated to a hybrid operating mode involving higher analysis time, such hypothesis are no longer valid, and more precise assumptions shall be considered. So we decided to adopt a more accurate and complete model of the spatial configuration. Such a model leads to a complex slant range expression depending on several space mechanics parameters as it is shown on the figure below :

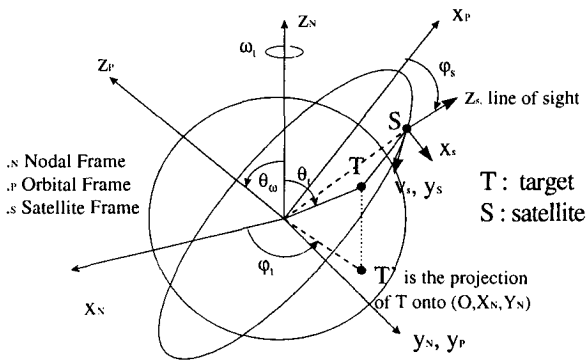


Fig 1 : Space imaging geometry

From this we obtain a complex expression of the slant range as a function of many parameters :

$$R(t) = h(\omega_s, \omega_t, V_s, y, z...) \quad (2)$$

The velocity  $V_s$  mentioned in the previous equations is the relative SAR-target velocity on the « ground footprint » (cf. [1] for details).

Now we keep on following the usual step of the airborne processing building, by expanding the previous radar-target range as a function of time  $t$ .

### 2.2 Slant Range expansion.

In accordance with the usual notations for « short time » (or range time)  $t_1 = t - n \cdot T_R$  (with  $T_R = 1/PRF$ , Pulse Repetition Frequency and  $n$  the number of the considered impulse), and « long time » (or azimuth time)  $t_2 = n \cdot T_R$ , we also introduce

$$\text{« azimuth delay » } \tau_2 = \frac{x}{V_s} \text{ and « range delay » } \tau_1 = \frac{2R_0}{c}$$

With airborne model a Taylor expansion of the Nth order approximates the relative earth-sensor range as follow :

$$R(t) = R_0 + \sum_{n=1}^N b_n \cdot \frac{t^n}{R_0^{n-1}} = \frac{c}{2} \left( \tau_1 + \sum_{n=1}^N \underbrace{b_n \left(\frac{c}{2}\right)^n}_{c_n} \cdot \frac{t^n}{\tau_1^{n-1}} \right) \quad (3)$$

In practice,  $R(t)$  is obtained from an high precision orbit restitution, and its Taylor expansion is derived from a polynomial fit on.

$$\text{that we can expressed : } R(t) = R_0 \left( 1 + \sum_{n=1}^N c_n \cdot \left(\frac{t}{\tau_1}\right)^n \right) \quad (4)$$

For the second model the relative distance expansion becomes :

$$R(t) = h(\omega_s, \omega_t, t, y, z...) = R_0 + \sum_{n=1}^N b_n(R_0) \cdot \frac{t^n}{R_0^{n-1}} \quad (5)$$

$$\text{that can be written : } R(t) = R_0 \left( 1 + \sum_{n=1}^N c_n(\tau_1) \cdot \left(\frac{t}{\tau_1}\right)^n \right) \quad (6)$$

where  $c_n(\tau_1) = \left(\frac{2}{c}\right)^n \cdot b_n(R_0)$ . The dependency on  $R_0$  (or  $\tau_1$ ) of the Taylor coefficients is at the origin of the fundamental difference between airborne and spaceborne received signals. Indeed, for the airborne case, Taylor coefficients no longer depend on the slant range  $R_0$ . This leads to specific properties in signal processing for the airborne case (see [1]).

### 2.3 Received signals.

We now use the previous results to obtain the expression of the signal that we have to process in the spatial case.

As the literature widely develops the steps to get the final expression, we just remind it, using our formalism, for the whole burst of emitted pulses in the time domain :

$$\text{emitted signal : } e(t) = \sum_n u(t - nT_R) \exp(i2\pi f_0 t) \quad (7)$$

$$\text{with } f_0 \text{ the carrier frequency and } u(t) = \text{rect}\left(\frac{t}{T_i}\right) \exp(i\pi \gamma t^2)$$

In the two dimensional space defined by the variables  $(t_1, t_2)$  introduced previously, the received signal expression after demodulation is given by:

$$S_r(t_1, t_2) = A \cdot u\left(t_1 - \frac{2}{c} R(t_2 - \tau_2, t_1)\right) \cdot \exp\left(-i \frac{4\pi}{\lambda} R(t_2 - \tau_2, t_1)\right) \quad (8)$$

where  $A$  is a complex constant, including all the gains and power losses; it can be assumed constant because slowly varying with time.

With the expanded distance (6) we can express the phase of the returned signal in the spatial context:

$$\frac{2}{c}R(t_2 - \tau_2, \tau_1) = \tau_1 \cdot \left( 1 + \sum_{n=1}^N c_n(\tau_1) \cdot \underbrace{\left( \frac{t_2 - \tau_2}{\tau_1} \right)^n}_{\alpha} \right) \quad (8)$$

### 3. SIGNAL AND TRANSFER FUNCTIONS EXPRESSIONS

#### 3.1 Expression of the classical High resolution processing

With the expanded writing of the received signal we can now remind the expression of the main processing Transfer Functions (TF) that derive from approximation of the exact transfer function (ETF). This one comes from the expression of the matched filtering.

##### 3.1.1 Exact Transfer Function

Optimal detection procedure (in case of white noise) results in matched filtering in both temporal and frequential :

$$\begin{aligned} X(\tau_1, \tau_2) &= \iint x(t_1, t_2) g^*(t_1, t_2, \tau_1, \tau_2) dt_1 dt_2 \\ &= \iint \tilde{x}(f_1, f_2) \tilde{g}^*(f_1, f_2, \tau_1, \tau_2) df_1 df_2 \end{aligned} \quad (9)$$

where  $g$  is the signal replica,  $f_1$  is the frequency associated with range time,  $t_1$ , or **radial frequency** and  $f_2$  is the frequency associated with azimuth time,  $t_2$ , or Doppler frequency or **azimuth frequency**.

We will derive the ETF from matched filtering in the frequency domain. Using the stationary phase principle, we can express the signal replica as follow :

$$\begin{aligned} \tilde{g}(f_1, f_2, \tau_1, \tau_2) &= \frac{\sqrt{2\pi}}{\sqrt{\Phi''(\alpha_0 \tau_1 + \tau_2)}} \cdot \tilde{u}(f_1) \\ &\cdot e^{-i2\pi(f_1 + f_0)(1 + \sum_{n=1}^N (1-n)c_n(\tau_1)\alpha_0^n)\tau_1} \cdot e^{-i2\pi f_2 \tau_2} \end{aligned} \quad (10)$$

$$\text{where } \alpha_0 \text{ is solution of } \sum_{n=1}^N n c_n(\tau_1) \alpha^{n-1} + \frac{f_2}{f_1 + f_0} = 0 \quad (11)$$

The Exact Transfer Function,  $H_{ETF}$ , is obtained when writing the matched filtering as a two dimensional Fourier transform :

$$H_{ETF}^* e^{i2\pi(f_1 + f_0)\tau_1} e^{i2\pi f_2 \tau_2} = \tilde{u}(f_1) \cdot \tilde{g}^*(f_1, f_2, \tau_1, \tau_2) \quad (12)$$

So that :

$$H_{ETF}(f_1, f_2, \tau_1) = e^{i2\pi(f_1 + f_0)(1 + \sum_{n=1}^N (1-n)c_n(\tau_1)\alpha_0^n)\tau_1} \quad (13)$$

Whatever the configuration, the ETF depends on slant range

$R_0 = \frac{c\tau_1}{2}$ . It is this dependency that all the focusing SAR algorithms have to deal with, [2]. But for the spaceborne case, an extra difficulty occurs with the dependency of the coefficients  $c_n$  on  $\tau_1$ .

Now we focus on the others algorithms TF expression.

##### 3.1.2 $\Omega$ -K technique

This algorithm achieves the ETF by a change of variables  $f_1 \rightarrow f_1'$  (Stolt Mapping) :

$$f_1' = (f_1 + f_0) \left( 1 + \sum_{n=1}^N (1-n)c_n(\tau_1)\alpha_0^n(f_1, f_2) \right) \quad (14)$$

followed by a two dimensional inverse Fourier Transform in the new frequency domain  $(f_1', f_2)$ .

##### 3.1.3 ETF approximations : Chirp Scaling Algorithm (CSA) and Secondary Range Compression (SRC)

These algorithms involve more or less approximations of the ETF. As it is shown in [2] and [3], CSA (as the Range Doppler Algorithm (RDA)) assumes a linear approximation of the Stolt mapping change of variables, while a parabolic approximation is assumed when CSA is associated with SRC.

The most general approximation (the parabolic one) leads to a quadratic expansion of the ETF phase :

$$f_1' = a_0(f_2, \tau_1) + a_1(f_2, \tau_1)f_1 + a_2(f_2, \tau_1)f_1^2 \quad (15)$$

The coefficients  $a_0, a_1, a_2$ , can be obtained by a polynomial fit on (14).

The transfer function for CSA,  $H_{CSA}$ , becomes :

$$H_{CSA}(f_1, f_2, \tau_1) = e^{i2\pi a_0(f_2, \tau_1)} e^{i2\pi(1+a_1(f_2, \tau_1))f_1 \tau_1} \quad (16)$$

and the transfer function of CSA associated with SRC is :

$$H_{SRC}(f_1, f_2, \tau_1) = H_{CSA} e^{i2\pi a_2(f_2, \tau_1)f_1^2 \tau_1^2} \quad (17)$$

The coefficients  $a_0, a_1, a_2$ , no longer depend on slant range

$$R_0 = \frac{c\tau_1}{2} \text{ for the airborne case.}$$

##### 3.1.4 Main results concerning with these expressions

Along all we describe previously, we have seen that the Taylor coefficients dependency on  $\tau_1$  is the main difference between air and spatial processing. As a result all the expressed algorithm are still range dependant in the new domain  $(f_1', f_2)$ , whereas in airborne case all the Transfer functions where range independent

This result induce an updating of the built Transfer function over a certain number of azimuth lines (forming a range block) over which ones the coefficients  $c_n$  can be assumed nearly constant with  $\tau_1$ .

To illustrate the previous analytical results, we decided to first conclude about the theoretical limits in resolution that can be obtained with the different algorithms. We consider here a spaceborne sidelooking SAR with an ERS2 like orbit (altitude 790 Km, inclination 98°). To achieve at least a spatial resolution of half a meter (with 20° incidence), a fourth order Taylor expansion (N=4) of the satellite-earth range in azimuth

time  $t_2$  is required. The two dimensional impulse response functions obtained from CSA with SRC is plotted respectively

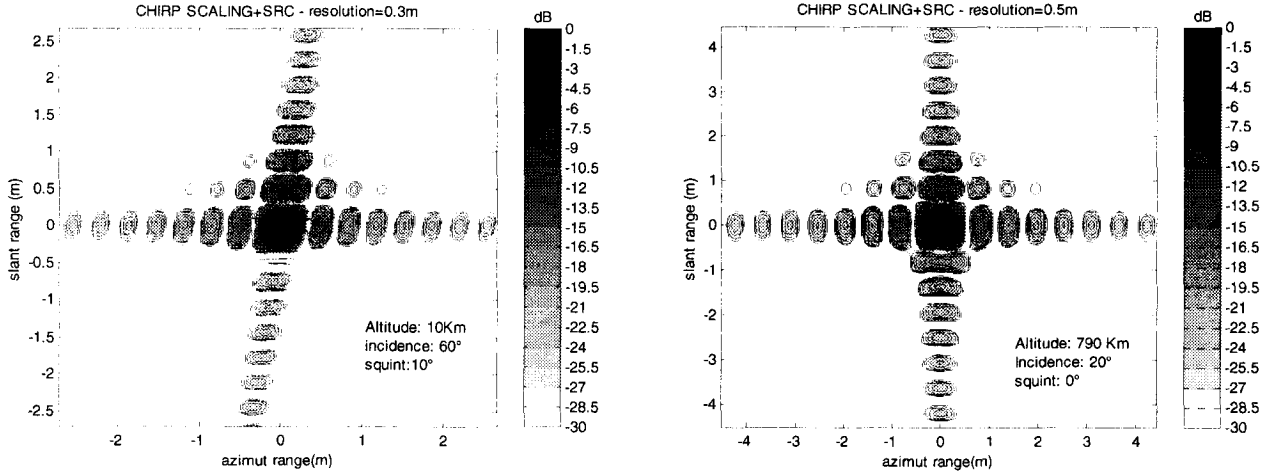


Fig.2 : Limits in resolution of CSA+SRC : airborne (left) vs. spaceborne case (right)

To conclude we can say that only the ETF (via  $\Omega$ -K) performs a perfect focusing. Systematic simulations have also shown that only a range block of a few hundred meters extension could be processed with the same ETF, without introducing defocusing.

But the updating of the Transfer function is a very calculus step, so we tried to eliminate this drawback by rewriting the previous algorithm with a new assumption.

### 3.1.5 Transfer Function dependency removing

It is worth noting that one of the main advantage offers by the different focusing algorithms expressed in the new domain  $(f'_1, f_2)$  for the airborne case is they are range invariant. But this property is lost for the spaceborne case, due to the dependency of coefficients with slant range ( $\tau_1$ ).

But the coefficients  $c_n$  are slightly dependent on  $\tau_1$  (that is why range blocks of few hundred meters can be processed with the same TF).

This slight dependency allows us to consider a Taylor expansion of phase expression with  $\tau_1$  around  $\tau_0$  as follow :

$$\Phi(\tau_1) = 2\pi(f_1 + f_0)\tau_1 \underbrace{\left(1 + \sum_{n=1}^N (1-n)c_n(\tau_1)\alpha_0^n(f_1, f_2, \tau_1)\right)}_{\varphi(\tau_1)} = \underbrace{2\pi f'_1 \tau_1}_{\text{from } \Omega-K}$$

$$\begin{aligned} \tau_1 \varphi(\tau_1) &= \tau_0 \varphi(\tau_0) + (\tau_1 - \tau_0) \cdot (\varphi(\tau_0) + \tau_0 \cdot \varphi'(\tau_0)) \\ &= \underbrace{\tau_0^2 \varphi'(\tau_0)}_{\varphi_1(\tau_0)} + \tau_1 \cdot \underbrace{(\varphi(\tau_0) + \tau_0 \varphi'(\tau_0))}_{\varphi_2(\tau_0)} \end{aligned} \quad (18)$$

From this we can rewrite the phase of the received signal :

on figures (2) for airborne and spaceborne case.

$$\Phi(\tau_1) = -2\pi(f_1 + f_0) \left( \underbrace{\varphi_1(\tau_0)}_{\text{constant term}} + \underbrace{\tau_1 \varphi_2(\tau_0)}_{\text{linear term with } \tau_1} \right) \quad (19)$$

With this new phase expression, while the first term can be easily compensate by a single phase term multiplication, the resulting phase term is linear with  $\tau_1$  what leads to the ETF shape similar to the airborne case :

$$H_{ETF}(f_1, f_2, \tau_1) = e^{i2\pi(f_1 + f_0) \left(1 + \sum_{n=1}^N (1-n)d_n(\tau_0)\alpha_0^n\right) \tau_1} \quad (20)$$

Finally we remove the range dependency of the coefficients, and consequently the Transfer functions of all the previous algorithms follow an expression close to the ones of the airborne configuration. But this invariance is only valid for limited scene extension about 10 Km swath only.

Now we have removed the slant range dependency, we interest in a very dimensional stage (from a calculus and memory point of view) of the Hybrid data processing : the formatting step.

## 4. DOPPLER ALIASING PROCESSING

### 4.1 The common formatting step

The formatting stage is characteristic of the Hybrid mode. As it is shown in [1], the aim of this step is to remove the Doppler aliasing that occurs within the antenna beam rotation. Fig.3 illustrates the common technique to remove the Doppler aliasing.

With the usual low resolution processing (it means for resolution superior to one meter), we can assume the linearity

of the azimuth echoes and of the Doppler centroid evolution with the time (because a second order expansion of the slant range is acceptable).

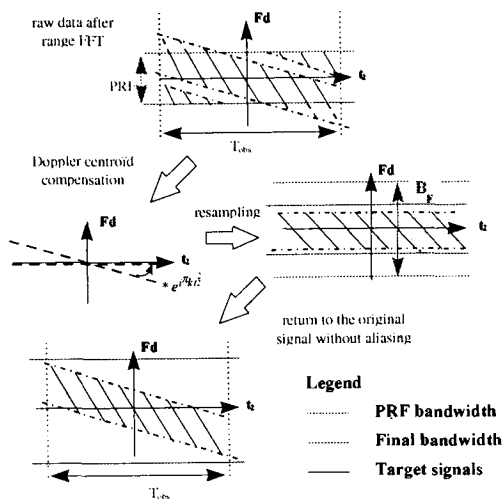


Fig.3: over sampling step

The previous figure illustrates the most known data aliasing processing which consists in compensating the Doppler centroid evolution (because we know the rotating speed of the antenna beam), before resampling the data [1].

But this method has a high memory cost ; indeed if we consider the same spaceborne SAR as in section 2.4 (ERS2, PRF is about 1700 Hz), for an azimuth resolution of 0.5m and a scene of 5 by 5 Km extension, we could easily have an idea about the increase of the data size :

- The real signal bandwidth is about 40 KHz
- The illumination time over the scene is near 16.3 sec
- A single target illumination time about 5.6 sec
- A single target bandwidth is about 11 KHz
- Range migrations follows the next curve.

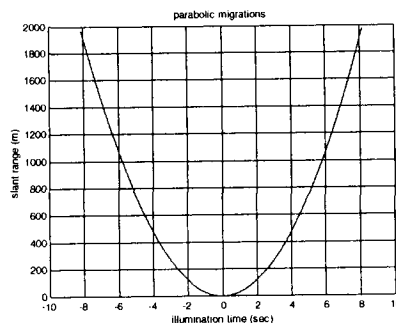


Fig.4 Parabolic migrations for the whole observation

So the processor that uses the global over sampling technique requires a memory size closed to 75 Goctets to process the whole scene.

This high memory cost involve enormous computational requirements ; that is why we interested in another step.

#### 4.2 The parallel formatting step

That is why we decided to define another formatting step.

The principle of this one is to divide the azimuth processing into elementary blocks, as the above scheme illustrates :

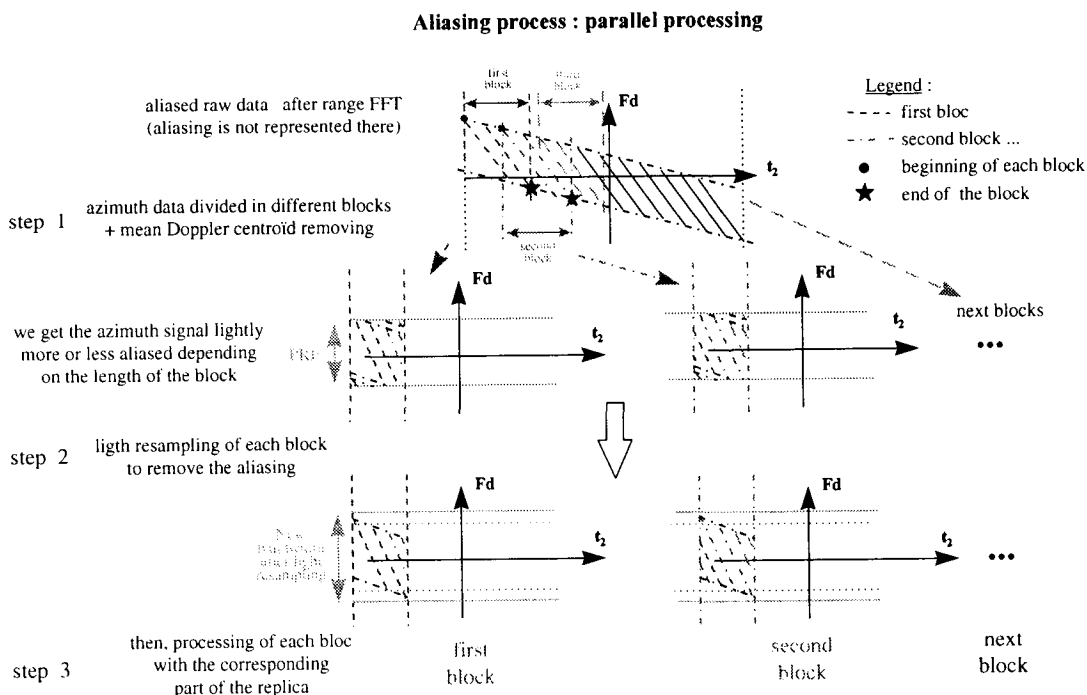


Fig.6: « Parallel processing » scheme

This technique limits the resample (step2) which is responsible for the high calculus cost. This method doesn't induce any displacement in the resulting image because the Doppler centroid compensation is also apply to the replica, what also authorises the parallel processing.

The blocks length is a major point to study. If a block should at least contain an entire target, the optimal size of the block between one target and the whole observation time is not trivial, because if we take the smallest block length (a single target) we minimise the resampling step but we maximise the number of blocks to process.

The following figures illustrates the existence of an optimal block length, that minimises the global data size to be processed.

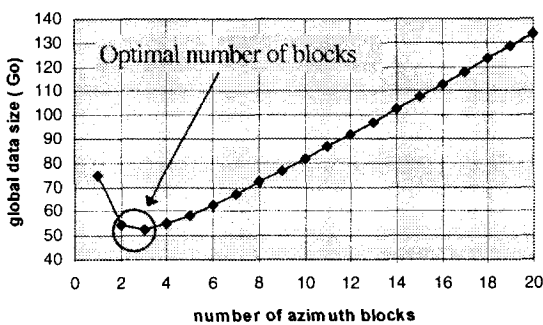


Fig.7 : Global data size to process and its optimum :  
global data =(data size per block)\*(Nbr of blocks to process)

We can clearly see an optimal number of blocks that minimises the whole data to process. This optimal is of course particular to the adopted configuration (ERS...).

Moreover, if this technique allows to decrease the global data size to process, the memory gain can be improved if we decide to process the data sequentially. Indeed if we process each block separately, the memory needed obviously decrease with the number of block.

As shown on the following figure this gain is very important as soon as we decide to adopt more than one block :

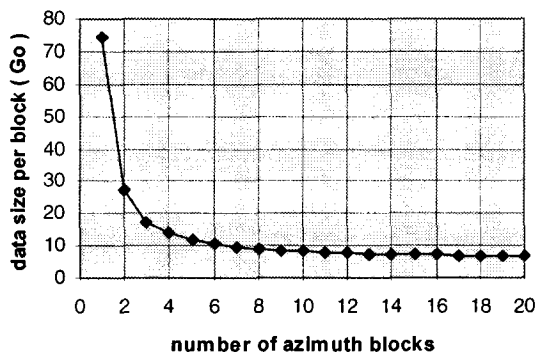


Fig.8 : data size to process a single block according to the global number of blocks.

## 5. CONCLUSION

Our study led us to describe the usual high resolution processing in an uniform formalism for a spaceborne SAR. According to this writing, we underlined the slant range dependency of the Transfer functions for the spaceborne case. We investigated this main issue and solved it with what can be called an « extended  $\Omega$ -K ».

Then we discussed the formatting step of a Hybrid mode data acquisition, which is a critical stage (from the data size point of view). The global (over all the illumination time) oversample has a high memory cost, and is not adapted to spaceborne data.

So we present a formatting step lower in memory cost, that leads to a reference algorithm, that will help us to validate and evaluate the performances of the different high processing scheme with real data ( by taking into account the SNR, the antenna gain, and propagation losses).

The main advantage of the parallel processing is to give us reference results that can be compared to any other algorithms (such as sub-aperture processing), which are not easy to obtain in an analytical way for a spatial configuration.

## REFERENCES

- [1] S.Henrion, L.Savy, J-G Planès, « Properties of hybrid Strip-Map/Spotlight Spaceborne SAR processing », IGARSS 99.
- [2] Richard Bamler, « A comparison of range-Doppler and wavenumber Domain SAR focusing algorithms », IEEE Transactions on geoscience and remote sensing, vol. 30, N° 4, july 1992.
- [3] D.P. Belcher, C.J. Baker, « High resolution processing of hybrid strip-map/spotlight mode SAR », IEE Proc. Radar, Sonar Navig., Vol 143, N° 6, December 1996.
- [4] Alberto Moreira, Josef Mittermayer, and Rolf Scheiber, « Extended chirp scaling algorithm for air- and spaceborne SAR data processing in strip-map and scansar imaging modes », IEEE Transactions on geoscience and remote sensing, vol. 34, N° 5, september 1996.
- [5] Josef Mittermayer, Alberto Moreira and Otmar Loffeld, « Spotlight processing of wide-beam strip-map SAR data using the frequency scaling Algorithm », IGARSS 98.
- [6] Knut Eldhuset, « A new fourth-order processing algorithm for spaceborne SAR », IEEE Transactions on Aerospace and Electronic Systems, vol.34, N° 3,july 1998.



## SAR Path Processor and Application to the large scale Mosaics

Masanobu Shimada, Hiroyuki Wakabayashi, Takeo Tadono, Victor B. Taylor, Osamu Isoguchi\*, Hiroyuki Miyagawa\*

Earth Observation Research Center/National Space Development Agency of Japan

Roppongi first building 13F, Roppongi 1-6-6, Minato-Ku, Tokyo-to, Japan. Tel 81-3-3224-7056, FAX: 81-3-3224-7052,

e\_mail: shimada@eorc.nasda.go.jp

\*Remote Sensing Technology of Japan

### ABSTRACT

Producing a large-scale mosaic image has concerns on geo-location accuracy and radiometric uniformity, since there are so many number of freedoms (scenes as a components) balancing in a mosaic frame. To improve the geo-location error and the radiometric uniformity, we tried to start from the SAR path proceedings (and images) for mosaicing. In this paper, we summarize the keys of the SAR path processing's, the generated mosaic, and the image quality.

### INTRODUCTION

The rainforest and boreal forest, as sharing the most of the world forest, plays an important roll to all the habitants' life and world climate change (carbon cycle). Its global understanding on land use change, deforestation, inundation, etc. is crucial for us to do next for saving the earth environment.

Since L-band signal is superior in penetrating the forest over the land and not attenuated by the weather condition so much, L-band SAR on a suitable orbit enables the time (season) - consistent observation. L-band SAR on Japanese Earth Resources Satellite - 1 (JERS-1) meets these conditions, where the path shifts 60 Km in west at

the equator 44-days over the globe. JERS-1, which was operated from April 15 1992 to Oct. 12 1998, has collected more than 700,000 SAR scenes of the world land/ocean using mission data recorder. The large forested areas were intensively observed in wet and dry seasons, and these data must contribute the more on the forest understanding.

For the sake of the study, SAR mosaics were produced as NASDA-NASA (JPL and ASF)-EU (JRC) joint project on 1995 [5],[6]. First, the rainforest mosaics for South America, Central Africa, and Southeast Asia, were being generated. Second, these for the boreal forests of North America, Siberia, and north Europe are being generated.

Although SAR of RADARSAT, SIR-C, ASAR of ENVISAT, PALSAR of ALOS have ScanSAR modes that enable wider field of view than the contemporary strip mode, their radiometric accuracy and image quality do not exceed those of strip mode. Moreover, a dependence of backscattering coefficient on incidence angle can not be as small as ignorance. Thus, its correction is a topic problem on generating mosaic from the ScanSAR data. Strip mode data, however, has smaller incidence angle variance in a swath, then, these data should be the most suitable source for the mosaic.

There are two mosaic ways from the strip mode SAR, 1) to use many small scenes and 2) to use path images. The former can use a small size of image. However, geometry among neighbor (surrounding) scenes should be strictly defined among many unknowns on shift and rotation [2]. It breaks once an isolated island exists. The latter decreases a number of scenes (paths) and can succeed even an isolated island is included.

There are two co-registration ways for two neighboring scenes, 1) just believes the orbit data, and 2) tunes the minute dislocation by finding the common texture within neighbor scenes. Discontinuity of the sigma-zero over two consecutive scenes (paths) is a serious problem as it can be visible as stripes along paths over land and/or ocean. The former is caused by 1) incorrect antenna gain without considering the topography [3], 2) incorrect antenna elevation pattern. The latter is the natural phenomena. Selection of the map projection, re-sampling, speckle reduction filter, remain as the specific problem on high qualified mosaic. Here, we discuss a mosaicing from the SAR path images.

## SAR MOSAIC PROCESSING

### SAR Path Processing

The SAR path processor adopted the standard Range-Doppler method for an image correlation with the Doppler bandwidth of 1200 Hz. Radiometric correction routine deals with, a recoupage of the power loss due to saturation, interference from the ground radar [4], correction for Sensitivity Time Control (STC)/Automatic Gain Control (AGC), antenna elevation pattern correction, calibration using the calibrator, checking the telemetry continuity and recovering the lost part

(sampling window width, synchronization loss, automatic gain values) [1].

The antenna gain is calculated as an image sits on the reference ellipsoid (GRS80). Thus the stripes becomes visible at the moderate-to-high relief region. Stripes are eliminated empirically (described later). Processing parameters, i.e., Doppler frequency and the rate, depend on the latitude (Fig.1), then, the parameters are modeled (statistically) as a function of the along-path. The radiometric accuracy is 1.1 dB. Geometric correction can be available by tuning the azimuth and range shift if necessary.

This processor prepares two map models (UTM and Mercator) and generates slant range, ground range, geo-referenced, and geo-coded images. In order to simplify the coordinate, first sampling window start time (SWST) of the beginning of the path is the reference to the all the path product. This can correct the several jumps of the start time within a long path. As a preprocessing, the continuity check is conducted for AGC and SWST through the whole path.

The original image is processed in four-look, 16-bit amplitude, high resolution of 24-m in azimuth and 10-m in range. To meet the mosaic's resolution requirement of 100-m, 64 pixels, 8 azimuth and 8 range, are averaged and obtained 144m azimuth resolution and 70m range resolution image. Speckle noise is suppressed by this averaging. Lat/lon of the image is calculated sparsely on the earth ellipsoid. The geometric accuracy of the path image is summarized in Table 1 and error distributions are shown in Fig 2. A digital elevation model of the Japanese geographical survey of institute was used as a reference.

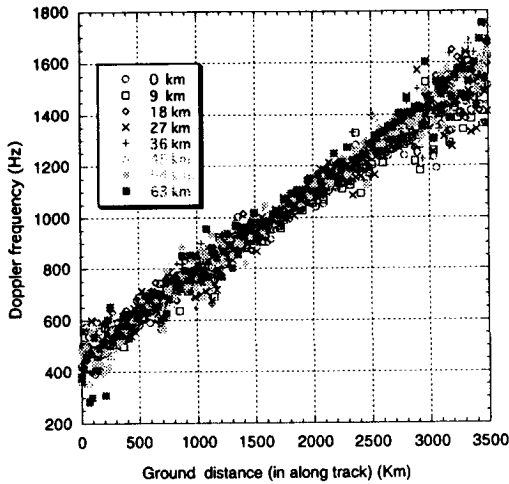


Fig.1 Dependence of the Doppler frequency on the latitude is shown for the image of Siberia. Each observation data are evaluated at eight different slant ranges. Doppler's are generally higher at far ranges.

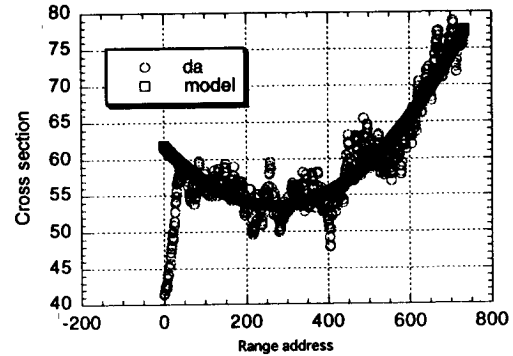


Fig. 2 An averaged cross range pattern is shown for path 139. It shows that excess property can be approximated by a squared power of range

Table 1 Image of JERS-1 SAR image produced by this path processor [1]

Item	Azimuth	Range
Resolution	6.5m	9.6
PSLR	-15.56 dB	-15.53
ISLR	-8.70 dB	
Ambiguity	22 dB	
G-Error	24.0m	204.0m
Error of CF	0.6 dB (Integral)	0.7 dB (Peak)
R-Error	1.1 dB (Integral)	1.4 dB (Peak)
Uniformity	0.2 dB	
Saturation	0%	
Interference	27%	

Remarks SAR images were acquired in the single transmitter mode (325 W). Resolution, PSLR, and ISLR were calculated by evaluating the impulse responses from ARCs.

### Stripe Elimination

Other than the way that eliminates the stripes using a digital elevation model (DEM), we have examined another stripe elimination in empirical way.

We assume

- 1) SAR instrument is stable.
- 2) Generally, a radiometric error across the swath is approximated by a second order function of the slant range (Fig. 2).
- 3) Sigma-zero of the overlapped area (near range of the left path and the far range of the right path) is the same at any place.

Then,

- 1) Divide a path image into several. Each segment is represented by a path number (I) and sub-segment number (J), i.e., I and J. Na and Nb are roughly 500.
- 2) Define a represented cross range pattern of the amplitude by  $P_{I,J}(Y) \equiv \frac{1}{N} \sum_{X_{I-1} < X < X_I} P(Y)$ , where X is along track and Y is range track coordinate.
- 3) approximate the above pattern by

$$P_{l,j}(Y) \leftarrow a_{l,j}(Y - Y_0)^2 + b_{l,j}(Y - Y_0) + c_{l,j},$$

where  $Y_0$  is the center of the cross track ( $\sim 3000$ ).

4) Interpolate the coefficients,  $a$ , and  $b$  as a function of along track.

5) Apply  $(a_{l,j}(Y - Y_0)^2 + b_{l,j}(Y - Y_0))^{-1}$  to the uncorrected image and we have the destriped image.

A simplified block diagram of the mosaicing is shown in Fig. 3. The small mosaics of corrected and uncorrected cases are shown in Fig.4.

### Mosaicing

Mosaic processing combines the following two methods:

1) by believing the accuracy of the orbit data, map the each pixel on to a selected coordinate. 2) Obtaining initial values from the orbit, then more accurate co-registration is done by the area correlation method. As the output of path processor, slant range path images are given with the geometric files, which enables the projection of the pixel data to the map.

## RESULTS AND IMAGE QUALITY

Mosaic image over a part of the south East Asia is shown in Fig. 4-b) (Stripe existing version is shown in Fig. 4-a)). The image is projected on the Mercator coordinate with a pixel spacing of 100m at the equator. The geometric accuracy was evaluated by comparing with the coastline data (Table 2). And, the standard deviations of X (east west) and Y (north south) are 463 m and 1669m. Their offsets error of X and Y are 323m and 1449m respectively. As shown in Fig. 5, the enhanced image keeps a detail of the texture information.

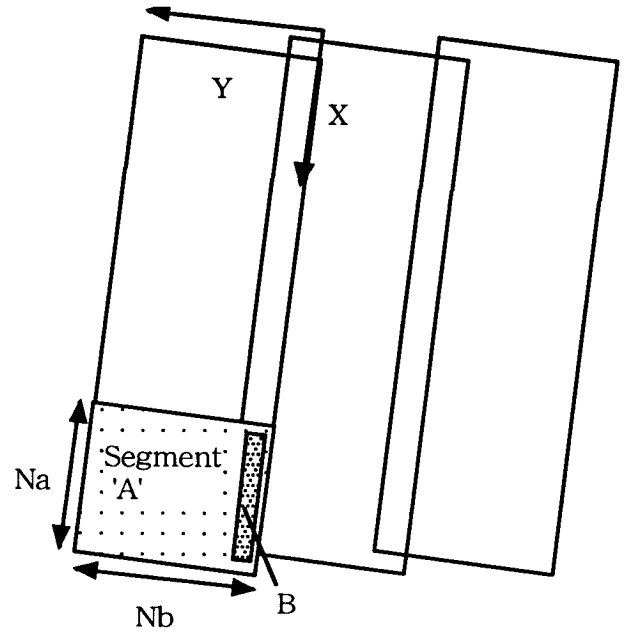


Fig. 3 In this sample, three consecutive path images are in mosaic process. The segment A (left bottom) is represented by an averaged cross section of slant range. Each segment has  $N_b$  pixel in slant range, and  $N_a$  pixel in along track. The overlapped area "B" is used to equalize the intensity of the corrected images of both paths.

## EVALUATION

Using the method introduced in this paper, we have generated a mosaic of the Southeast Asia. It covers 1500 Km in north south and 350 Km in east west. The stripes were eliminated from the mosaics and the image quality is satisfactory. As the enlarged image is given Fig. 6, image keeps the good quality for the further analysis. The mis-registration at the coast area is not recognized. Since this method works even if the area includes the isolated islands from the continent, the mosaic generation using the path images is powerful. As shown in Table 2 for the geometric accuracy, a standard deviation and difference of total 16 GCP data exceeds 1500m. We should tune the algorithm. A mosaic of the

sigma-zero map is useful for the further analysis. Based on this study, we should continue the following studies for generating the high accurate mosaics.

- 1) Correction of the foreshortening effect.
- 2) Correction of the scattering area (correction of the incidence angle in geometric calibration)
- 3) Antenna pattern correction using DEM
- 4) Correction of the water vapor when deriving the DEM from interferometry

### CONCLUSIONS

The mosaic generation using path images was introduced. It was confirmed that path processing can easily generate the SAR image data for wide area mosaicing, 2) Orbit error of 100 m can generate the high accurate mosaics.

### REFERENCES

- [1] M. Shimada, "Verification Processor for SAR Calibration and Interferometry," Advanced Space Research (COSPAR'98), in press 1999.
- [2] P. Siqueira, "Global Rain Forest Mapping Project-Creation of the JPL Amazon Mosaic-", 1997 GRFM/GBFM and InSAR PI Meeting at JPL, November 4-7, 1997.
- [3] F. Holecz, P. Pasquali, "Radiometric calibration issues in the JRC GRFM Africa mosaic", 1998 GRFM/GBFM and InSAR PI Meeting at JRC, Nov. 16-20, 1998.
- [4] M. Shimada, et al., "Removal of the Interference Appeared Within the SAR Images," Advanced Space Research (COSPAR'98), in press 1999.
- [5] O. Isoguchi, et al., "JERS-1 SAR south East Asia mosaic," Hamburg, IGARSS'99.
- [6] B. Chapman, M. Alves, M. Shimada, A. Freeman, A.

Rosenqvist, and P. Siqueira, "Data Quality of the JERS-1 SAR Global Rain Forest Mapping project (GRFM)", submitted to Int. Journal Rem. Sensing, 1998.

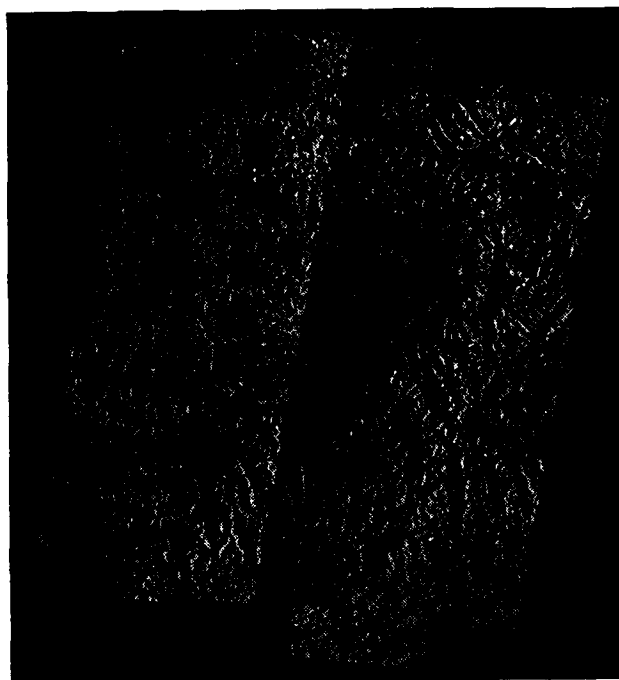


Fig. 4-a) A northern part of the Southeast Asia (Myammer) is mosaic-processed (before destriping).

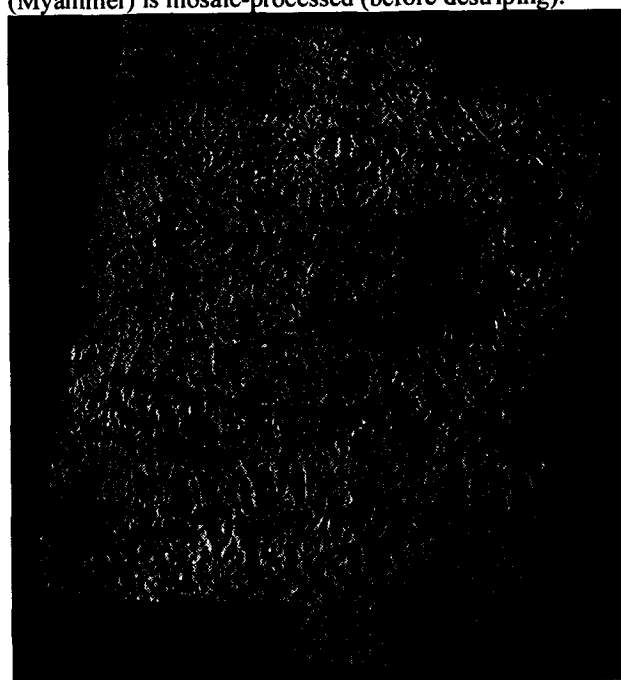


Fig. 4-b) Final mosaic image (after destriping).

Table 2 Geometric evaluation results

	X (m)	Y (m)	no.of GCP
Std. Dev.	-463	1669	16
Mean	-323	1449	16

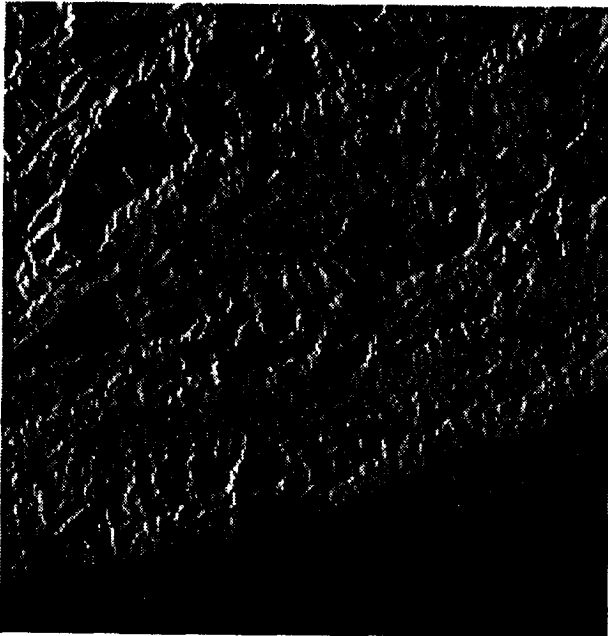


Fig. 6 A part of the mosaic image is shown. Image size is 22km in east west, and 23km in north south.

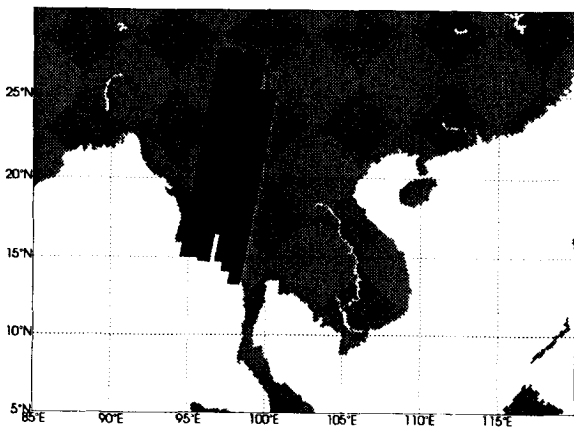


Fig. 8 Location of the Fig. 7.

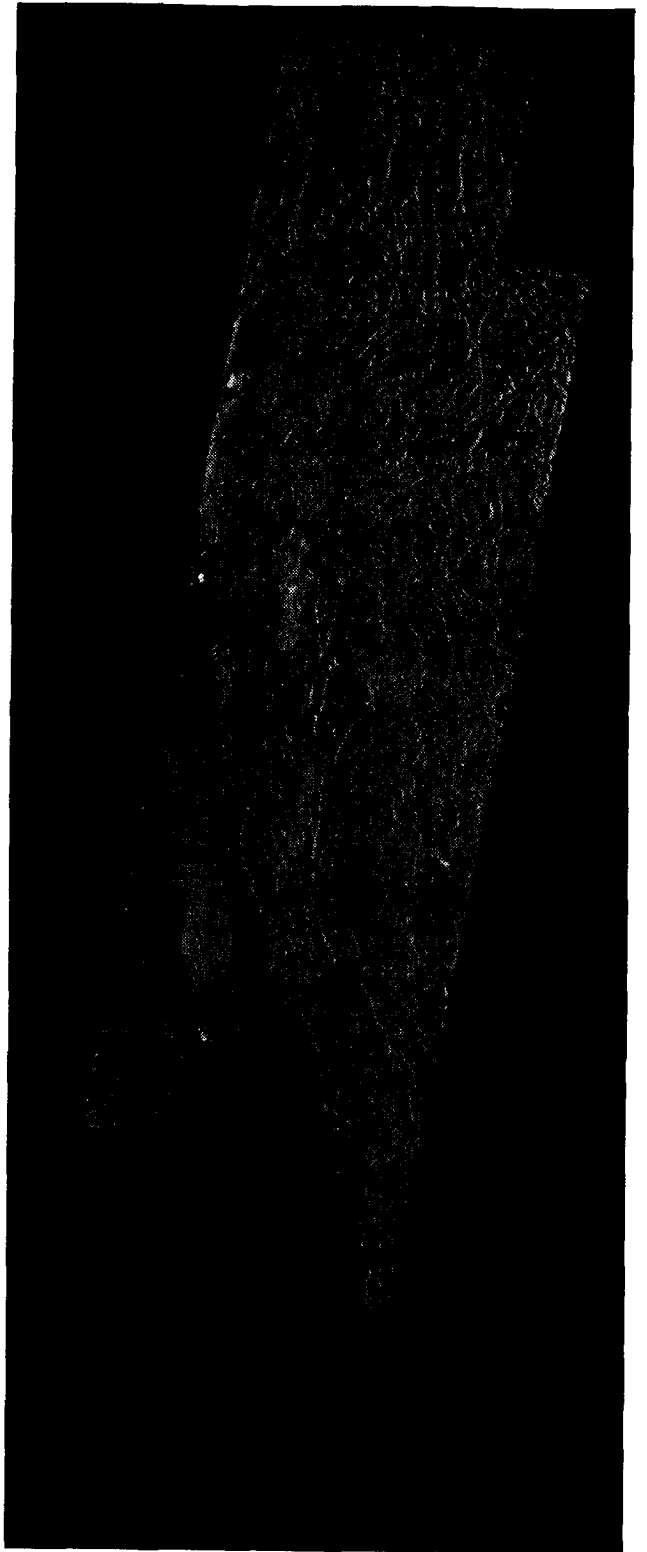


Fig. 7 JERS-1 SAR mosaic of the Southeast Asia.

## Some Applications of an Accurate Geometrical Error Model for Airborne SAR

Hubert CANTALLOUBE

ONERA, Chemin de la Hunière, 91761 PALAISEAU Cedex, France.

Phone: (33)1 69 93 62 14, Fax: (33)1 69 93 62 69, E-mail: nahum@onera.fr

### ABSTRACT

The accurate knowledge of the geometry of an airborne SAR image is crucial for many applications and in particular those involving a registration step:

Coherent techniques, such as repeat-pass SAR interferometry, require an accurate image matching to the  $10^{\text{th}}$  of a pixel. On the other hand, incoherent processings seem less demanding. Wide area coverage by multi-pass composite or image geocoding tolerate mismatches of pixels.

Compared to spaceborne SAR, those accuracy requirements are stronger since airborne SAR provide higher resolution images. Moreover, irregularities in aircraft motion due to air turbulence introduce severe geometrical distortions in the images. Unfortunately, these distortions are tightly coupled with the signal processing algorithm used for computing SAR images.

We have implemented a geometrical error model for our generic off-line SAR processor. The details of the design are given in reference [1]. This paper addresses some relevant application examples. It is illustrated with images obtained with the airborne SAR RAMSÈS, operated by ONERA.

### 1. INTRODUCTION

A geometrical error model (GEM) is a routine that establishes the direct coordinate transform rule from a geographical referential to the image coordinates, the inverse coordinate transform rule from the image coordinates to a geographical referential. Those transforms should involve an error parameter vector modelling the low frequencies trajectory errors and some radar parameters errors. In order to increase the numerical efficiency of the routine, the GEM also provides the derivatives of the transforms as well as their partial derivatives with respect to error parameters. The design of a GEM is detailed in [1]. This paper addresses some relevant applications of GEM. The SAR images were obtained from acquisitions of the ONERA airborne SAR RAMSÈS with linear-chirp deramped-on-receive waveforms, in either S or X band. Images are synthesised using a BiD SAR

processor, with flat-terrain hypothesis. Trajectories are estimated by an inertial navigation unit with an error of the order of one nautical mile per hour.

### 2. INCOHERENT APPLICATIONS

#### 2.1 Multi-Look Imaging

This is certainly the basic application of GEM's. Due to the low directivity of the radar antenna onboard the aircraft, one given target on the ground is illuminated by the radar during a much longer time than the necessary integration time. The principle of this technique and its interests are detailed in [2].

The accurate matching of the single-look images requires a good geometrical model, especially if the aircraft trajectory is far from linear (in case the trajectory is linear uniform, a simple skewing maps one single-look to the other).

To illustrate this application, three single-look images in X-band, have been calculated with a trajectory hybridisation between GPS and INU. The GPS correction on the velocity is about 10 cm/s. The cut-off frequency (resolution) is 0.71 m along both range axis and azimuth axis (no windowing). After geocoding, the cut-off frequency along the projection of the range axis becomes 0.82 m. The incidence angle is  $60^\circ$  at mid-swath. Each look has been processed at a constant squint angle. In order to keep an homogeneous azimuth resolution on the whole image, the integration time increases with distance, from 0.71 s at the near range to 0.98 s at the far range end of swath.

Then the first and the third single-looks have been registered to the middle look geometry and a linear combination of the looks, which optimises the signal to noise ratio, has been computed yielding a smoother 3-look image displayed on Fig. 1.

#### 2.2 Autofocusing

Some errors in the radar parameters or in the estimated aircraft trajectory, result in mismatches in the single-look images registration, and as a consequence, the multi-look image will be blurred. If the mismatch between the single-looks is measured at several diffe-

rent locations on the image, the GEM will allow to find the error parameter vector that would minimise the resulting mismatch, once integrated to the GEM. The initial mismatch can be computed by correlating a small patch of one single-look into another single-look. Then the partial derivatives of the coordinate transform rules with respect to the error parameters allow to estimate some values of the error parameters which decrease the mismatch. Reiteration of the process yields an estimation of error parameters that optimises the single-look matching.

This technique called "time variant frame-drift autofocus" (meaning that trajectory correction is not a constant velocity bias, since variations of the mismatch with azimuth are taken into account) is illustrated on Fig.3. The image obtained by the flight 0607, (45° from the runway axis) has been focused with this technique.

### 2.3 Precise image registration

To compute precise registered images (PRI), the error parameters are adjusted in order to minimize the distance between ground control points (GCP) and the projection on the ground of their location on the SAR image. Recall that a GCP is a landscape feature of which geographical and altitude coordinates are very accurately known. Once the error parameters are precisely evaluated, the SAR image is projected onto the ground exploiting a DEM of the area, yielding geocoded image of cartographic quality.

The three-look image of Fig.1 has been matched with a scanned map of the same region assuming that the terrain was flat with an altitude chosen as the mean value given by the radio-altimeter (309 m) (left hand-side of Fig.2). The same three-look image has also been mapped using terrain elevation data from NATO's DLMS/DTED data base. Its planimetric gridding is 62 m x 92 m, its vertical sampling is 1 m, and its altitude values ranges from 250 m to 335 m on the area. One can observe that mismatches remain between map and image, mostly because the DEM smoothes away altitude features thinner than 100 m wide.

### 2.4 Aircraft trajectory estimation

As a byproduct of the above error parameters estimation, the determination of the aircraft trajectory can be improved and lead to a better image focusing. This process named single-look to map autofocus, requires however either extremely accurate GCP or a very large number of automatically detected linear features from both map and SAR image because

features on paper maps are always displaced to allow printing and reading of the map. If roads were drawn to scale they would be much thinner. And buildings on their sides are always shifted away from the roads!

### 2.5 Elevation-dependent motion compensation

Once the trajectory is accurately deduced in 3-D space, it is possible to use the most appropriate terrain elevation model in the focusing. This allows elevation-dependent motion compensation of the SAR-processor.

### 2.6 Combination of images

PRI from multiple acquisition flights can be combined to create a composite image covering a region larger than the radar swath. The only difficulty is to join without visible seams, portions of images corresponding to different incidence angles. One solution is again to use the GEM for locally calibrating the image to an arbitrary incidence angle. The GEM provides the "viewing direction" from the radar and the DEM gives the local normal to the terrain. With those vectors and the range (or "viewing distance") the local calibration factor can be deduced. This assumes that the surface follows the Lambert's law, which is generally (at least approximatively) the case for extended landscape features. Seamless joints are then generated by using linear combinations of which the weights are calculated in order to minimise the thermal noise of the result, (their sum equals 1).

Fig.3 shows a coverage assembly from three acquisition flights with respective heading 059°, 104° and 149°. For each pass, the focusing has been performed by hybridisation GPS-INU except for the pass at 104° (which had been focused by the autofocus technique described above). These images have been registered to the scanned map using ground control points and the DLMS/DTED DEM.

For each flight, three looks have been synthesised, hence the common part corresponds to a 9-look image. On purpose, we did not crop away the extreme ranges of the swath (where signal to noise ratio is low and which are contaminated by range ambiguity replicas) for keeping the seams apparent.

### 2.7 SAR stereogrammetry

When composing SAR images from different acquisition flights, the DEM quality is extremely critical: Any elevation error induces a projection error in the geographical coordinates system, but this error is oriented towards the aircraft trajectory and its magni-



tude depends on the incidence angle. Therefore, if the viewing angles or headings of overlapping images are different, there is a mismatch in the super-imposition of the composite image. On the other hand, a measure of this mismatch gives an estimation of the elevation error. This is the principle of the SAR stereogrammetry. Classically, two SAR images obtained from parallel flight directions thus for two distinct incidence angles are used. But with airborne SAR the flight direction can be changed (unlike the fixed polar orbit plane of satellites such as ERS or RadarSat) so that one can also compute the elevation of the terrain with SAR multi-heading stereogrammetry.

### 3. COHERENT APPLICATIONS

#### 3.1 Repeat-pass interferometry

In case the trajectories of the different flight acquisitions (on the same area) are too close to deduce a measure of the elevation from super-imposition mismatches, it is still possible to evaluate DEM errors from repeat-pass SAR interferometry. This method exploits the interference pattern between the two images in order to derive the elevation error.

This application is certainly the most demanding in terms of registration accuracy. To understand the reason why, just consider two corresponding pixels in each image of the interferometric pair. Each pixel value stands for the sum of ground point contributions around the nominal pixel centre multiplied by a bell-shaped instrumental function (or point-spread function) whose shape and width depend on the radar bandwidth, the integration time and the windowing functions. The "geometrical coherency conditions" on a SAR image pair, allowing it to be used for interferogram generation, is that on the area of the "nominal ground surface" covered by the bell-shaped curve, the optical pathway difference between the two antenna positions shifts the phase difference by a fraction of a turn. A slight misregistration (even below one pixel) reduces dramatically the product of the bell-shaped functions for each image, thus reducing the "meaningful" part of the interferogram. Since the energy of the interferogram is roughly the same (provided area is homogeneous) the signal to noise ratio drops, hence so does the accuracy of the phase difference estimation which is highly sensitive to noise.

This sub-pixel registration is much more difficult to achieve in the airborne case. The resolution of the images is higher than in the spaceborne case, and the non-linearities in the trajectories make the geometry

of the registration non uniform (an accurate GEM is therefore required).

The second difficulty comes from the fact that the maximum number of fringes in the interferogram is generally lower. Indeed, one fringe corresponds to a shift of one image with respect to the other of  $\lambda/2$  along the range axis! This shift is not visible at first because the resolution is much lower than  $\lambda/2$ . But as the fringes add-up the shift increases to a substantial fraction of a pixel. Since the resolution (width of the bell-shaped curve called "pulse response") is inversely proportional to the radar bandwidth, it is clear that the maximum number of fringes is about twice the inverse of the relative bandwidth (bandwidth divided by the frequency).

This limits the elevation correction from prior knowledge that we can deal with. In practice, the elevation is first evaluated by maximising the coherency between the two images (this is really a coherent version of the SAR-stereogrammetry, but its sensitivity is much higher and it is not ambiguous) and thereafter, the interferogram is computed.

The method is illustrated on Fig. 4: Two S-band images have been acquired along the same flight path but ten days apart. In fact, the acquisition flight was done twice because the harsh meteorological conditions (32 knots of wind) ruined the simultaneous acquisition in X-band (for which the antenna is too directive to accommodate heavy turbulences). The strong back-wind explains why the first image of the pair covers a longer area on the ground though the acquisition duration was the same: the aircraft speed was increased by 18%. The relative bandwidth is 0.07, hence we cannot get more than about 30 fringes (for highest available resolution, the radar can modulate with a relative bandwidth of 0.2 yielding only 10 fringes!).

Prior elevation estimation is done by computing coherency for the elevation of the interpolated DLMS/DTED DEM and a set of shifted elevations (by  $-30$  m up to  $+30$  m with 10 m steps)

#### 3.2 Change detection

Mismatches due to elevation errors in composite image super-imposition were mentioned above. But the origin of those mismatches can come from changes in the landscape. This might be the case if the time elapsed between the SAR signal acquisitions is of the order of the hour or the day, or the month. The mismatches may be automatically detected by incoherent change detection ("activity detection" or post-strike "damage assessment" for example). But this requires a precise regis-

tration of the images which, since successive flight trajectories could not be exactly identical, requires an accurate GEM.

In case the conditions for repeat-pass SAR interferometry are met, we could also perform a coherent change detection as a byproduct of interferogram generation. Loss of the coherency even if the radiometry remains similar allows to detect that a vehicle or aircraft has been used and parked back (its location has changed at the  $\lambda$ -scale though it is not visible at the SAR image resolution). The loss of coherency may also help to decide between growing vegetation and a similar man-made object. It may also signal surface work (ploughing, mine burial...) and sometimes subterranean activities by the slight vertical motion it causes above it (geosynclinal gas storage or retrieval, nuclear testing...) Fig. 5 shows the incoherent and coherent change detection in the interferometric image pair of Fig. 4.

Coherency loss areas (appearing as darker spots in the bottom image) are of three kinds: Moved vehicles (dark sharp spots), low backscatter areas (diffuse dark areas as roads and runways or sharp areas as building shadows) and volumetric or wind-sensitive reflectors (forest and the strange rectangular shaped field). Recall that meteorological conditions changed between the acquisitions (rain with 32 knots wind versus calm with a slight snow cover)

#### 4. SINGLE-CHANNEL MTI

Instead of using SAR images from two separate flights for stereogrammetry or interferometry, one could think of using different looks of the same acquisition. The reason why this strategy would not work is that only non-linearities in the trajectory induce mismatches. To get convinced, just consider that the trajectory is a perfect straight line: The SAR imaging geometrical problem is now axially symmetrical around the trajectory line! Therefore, mismatches are almost negligible in usual situations (this explains why "flat ground" focusing gives acceptable results except in very high resolution cases).

Nevertheless, multi-look mismatch detection has one application: a given target point is imaged under squint angle 2 a few seconds after having been imaged under squint angle 1, and during this time lapse, the object behind the target point might have moved. Thus the comparison of looks may help to perform a kind of Moving Target Indication, the single-channel MTI. Of course, there are other more accurate MTI techniques

(Adaptive pulse repetition frequency, Space-time adapted processing...) that require multi-channel *i.e.* several antennae separated along the flight direction.

In practice, the locations of moving targets are also erroneous on the single-look images. This is due to the interference of their motion with the image synthesis (which extracts signal according to the radial velocity). However, the GEM can be used to compute the "apparent" positions of a moving target on the different single-look images (simply subtracting the target proper velocity from the aircraft velocity as if it were a "trajectory error")

#### 5. CONCLUSION

Because of the high resolution of the airborne SAR images and the irregularities of the aircraft trajectory which may distort them, a Geometrical Error Model (GEM) must be defined.

The GEM gives the transformation from image position to geographical coordinates together with the inverse transformation and the derivatives with respect to some error parameters.

This paper has been illustrated with some images obtained by the airborne SAR RAMSES designed and operated at ONERA. Among the numerous applications of a GEM, multi-look processing, elevation dependent motion compensation, combination of images, repeat-pass interferometry and change detection have been addressed.

#### BIBLIOGRAPHY

- [1] Cantalloube H., Accurate Geometrical Model for an Airborne SAR: A Design Example, CEOS 99.
- [2] Cantalloube H., How to compute a multi-look SAR image? CEOS 99

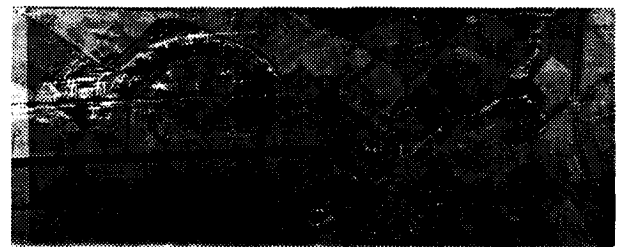


Fig. 1 : Three single-look images in X band, at constant squint angles (+3.46°, +4.77° and +6.08°) have been matched in the middle look slant-range geometry. Range increases to the bottom and azimuth (time) increases to the right.

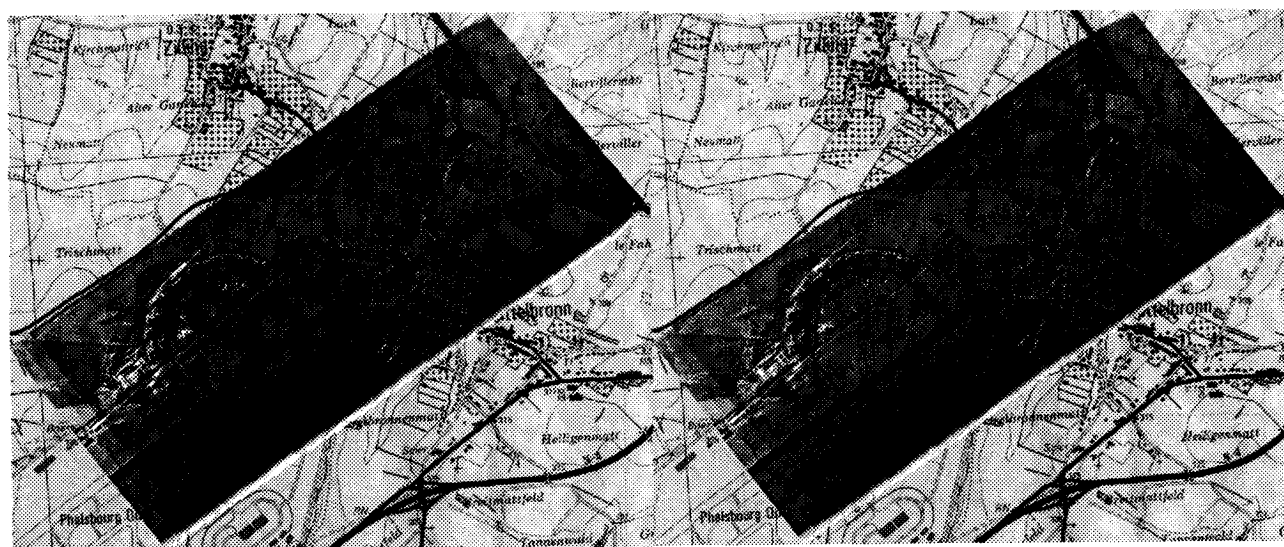


Fig. 2 : Projection of the image of Fig. 1 on a flat terrain (left) then on on a Digital Elevation Model (right). © IGN (French National Geographical Institute) for the map background.

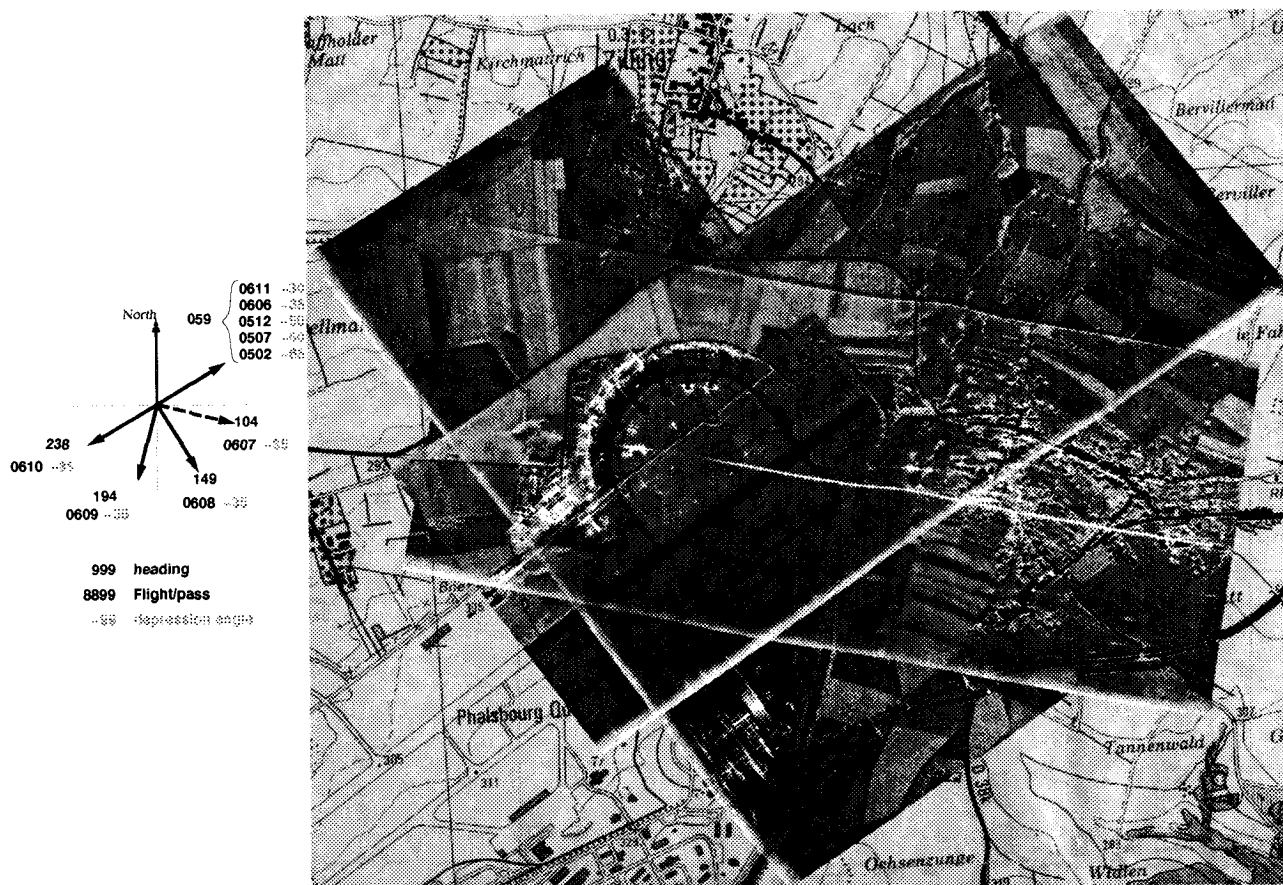


Fig. 3 : Repeat-pass image composing with two other X-band acquisitions. © IGN (French National Geographical Institute) for the map background.



Fig. 4 : Repeat-pass interferometry with two successively acquired S-band images (left). Interference patterns are computed for the interpolated DEM (right).



Fig. 5 : Change detection between the images of Fig.4. Difference image on top (Reflector disappearances and apparitions are depicted as darker and lighter spots respectively), maximum coherency among the elevation-shifted interferograms, and the same image thresholded (coherency losses appear black).

# RADARSAT-1 Doppler Centroid Estimation Using Phase-Based Estimators

Ian Cumming<sup>(1)</sup>, Frank Wong<sup>(2)</sup> and Bob Hawkins<sup>(3)</sup>

(1) Remote Sensing Data Centre (DFD)  
Deutschen Zentrum für Luft und Raumfahrt (DLR)  
Postfach 11116, D-82234 Wessling, Germany. Ian.Cumming@dlr.de

(2) The National University Of Singapore  
Electrical Engineering, 10 Kent Ridge Crescent, Singapore 119260  
Email: elewongf@nus.edu.sg

(3) Canada Centre For Remote Sensing  
Data Acquisition Division, 588 Booth St, Ottawa, Canada K1A 0Y7  
Email: Robert.Hawkins@ccrs.nrcan.gc.ca

**ABSTRACT<sup>1</sup>:** — When processing satellite SAR scenes in a production environment, it has been found that image quality distortions (radiometric, geometric, and phase) that occur in a few percent of the scenes can be traced to errors in the Doppler centroid (DOPCEN) estimators. Radiometric scalloping is particularly an issue with ScanSAR scenes as they have more sensitive DOPCEN tolerances.

In this paper, we examine some troublesome RADARSAT-1 scenes, in which Doppler centroid estimation errors are frequently caused by radiometric discontinuities in the scene. After reviewing the operation and performance of several current Doppler estimators, we propose a scheme based on a spatial diversity concept, in which areas that cause poor estimates are removed from the estimation process.

## 1 Introduction

Doppler Centroid (DOPCEN) estimation continues to be an important [1] and sometimes overlooked component of SAR processing. The issue is especially acute in the case of RADARSAT-1 ScanSAR processing, where the estimate must be accurate to approximately 5 Hz in order to avoid radiometric artifacts such as scalloping in the processed images [2].

In the last 10 years, a new class of estimator has been developed based on the phase of the received signal, rather than on the spectral amplitude. The concepts were developed by Madsen [3], Bamler and Runge [4], and more recently by Wong and Cumming [5]. It is generally acknowledged that the phase-based estimators can be more accurate than the amplitude-

based estimators, provided their limitations are understood, and they are applied properly.

We consider the DLR [4], the MLCC and the MLBF [5] algorithms, as well as the classic spectral-fit algorithm. We have found that their performance differs as a function of radiometric discontinuities, partially-exposed targets, noise levels, and scene contrast.

In this paper, we review the operation of the DOPCEN algorithms, compare their performance, explain why it is advantageous to combine estimates from more than one algorithm, and propose a new estimation scheme that uses spatially diverse parts of the scene to obtain reliable estimates.

## 2 Review of Estimators

In this section, we will review the algorithms used in the most common DOPCEN estimators. Because of space limitations, we will concentrate on estimates of the "fractional-PRF" part of the Doppler centroid. Obtaining a good fractional-PRF estimate is a prerequisite to obtaining a good Doppler ambiguity estimate, and in many cases, the associated Doppler ambiguity estimator has similar estimation properties with respect to data anomalies.

### 2.1 Classic spectral amplitude fit

This was the first DOPCEN estimator [6] used for satellite SAR data, and is still in common use. The shape of the azimuth magnitude spectrum is averaged over a suitable range/azimuth window, and compared with the expected shape based on the azimuth beam pattern and received SNR [6, 7]. A correlation is done between the measured and modelled azimuth spectrum to determine the Doppler frequency of the peak of the measured spectrum. Accuracies are typically a few tens of Hz when a million samples are analyzed.

<sup>1</sup>Presented at the CEOS'99 SAR Workshop, Toulouse, October 26-29, 1999. Dr. Cumming is currently on sabbatical leave from the University of British Columbia (ianc@ece.ubc.ca). Dr. Wong is currently on leave of absence from MacDonald Dettwiler and Associates.

## 2.2 Phase increment methods

In 1989, Madsen recognized that the centroid could be measured by finding the average phase increment in the azimuth data [3]. Later, Bamler and Runge of DLR, and Wong and Cumming applied the same principle to Doppler ambiguity resolvers [4, 5]. We refer to the latter algorithms as the DLR and the MLCC (for Multi-Look Cross-Correlation) algorithms.

Considering a point target, the change in phase between one azimuth sample and the next varies linearly with time along the exposure of the target, as shown in the top panel of Fig. 1. In the bottom panel, we show the individual phase increments in the complex plane, going from the beginning of the exposure A to the end B. We also show their vector sum (the longer vector with the circle at its end). Since the target is strongest at the Doppler centroid, and its exposure is symmetrical about the centroid; finding the average phase increment (vector sum) along the whole exposure will then give the Doppler centroid. A target which is only partially exposed in the estimation window (or any other non-symmetry in the exposure) will bias the estimate. Accuracies of the phase increment methods are generally a little better than the classic method.

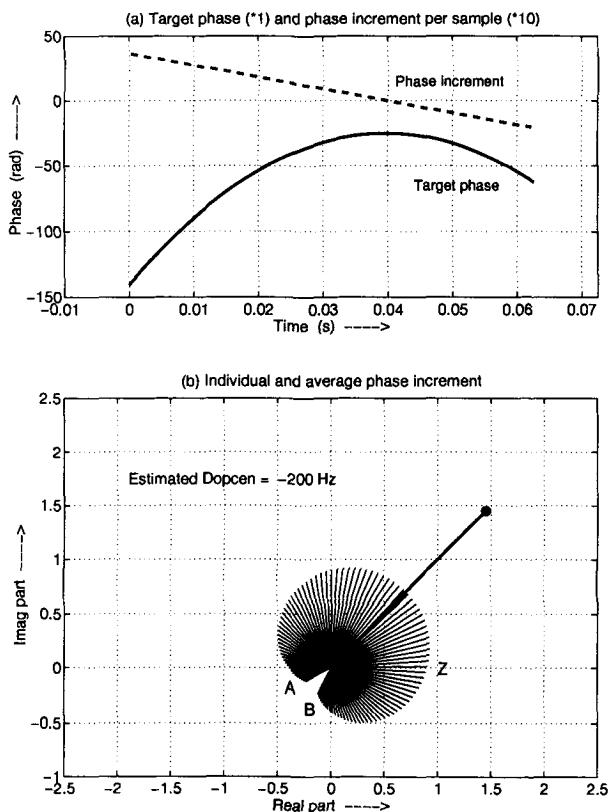


Figure 1: Principles of phase increment methods.

## 2.3 MLBF algorithm

Wong and Cumming developed an additional method of finding the Doppler ambiguity when a colleague at MacDonald Dettwiler, Robert Deane, recognised that the beat frequency formed by multiplying the received signal from radar systems of slightly different centre frequencies was proportional to the unaliased Doppler centroid [8]. The different radar frequencies are obtained by extracting two looks from the range spectrum. The method is not accurate enough to estimate the fractional-PRF centroid to a useful accuracy, but it is generally accurate enough to estimate the ambiguity.

## 3 RADARSAT-1 Data

We investigated four RADARSAT-1 scenes which had DOPCEN estimation errors. They all had severe azimuth radiometric discontinuities. An example is the standard beam 7 scene shown in Fig. 2. The scene is centred at  $49.94^\circ$  N,  $63.09^\circ$  W, and the data were collected on the 142nd day of 1996, at 10:13:15 UTC. The spacecraft heading was  $195.6^\circ$  (descending orbit). The scene contains part of the north shore of the St. Lawrence River in eastern Canada (top) and Anticosti Island (bottom). The bright land beside the dark water creates a radiometric discontinuity of up to 16 dB.

Also noted in the left of the scene is a darkening of a portion of the land area caused by raw data saturation. This occurs because the Automatic Gain Control (AGC) scheme adopted for RADARSAT-1 measures the signal strength in the first quarter of the range swath [9], and cannot adapt to the bright land in the far range (left) part of the scene with the four bits available. This artifact, which is not uncommon in coastal scenes, presents a special DOPCEN estimation case.

### 3.1 What upsets estimators

If the radar SNR is high enough, and equal-strength targets are spread uniformly throughout the estimation window, then most DOPCEN estimators give excellent results. In examining scenes which gave poor Doppler estimates, the following scene characteristics were identified as having a possible effect upon the estimation accuracy:

- Azimuth radiometric discontinuities
- Range radiometric discontinuities
- The level of scene contrast
- Low SNR

It was soon found, as indicated in Section 4.2, that azimuth radiometric discontinuities were the most troublesome. We concentrate on these in this paper.

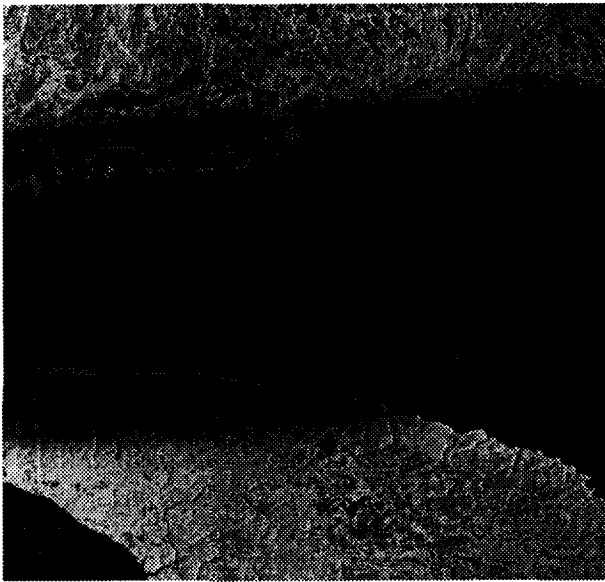


Figure 2: RADARSAT-1 Anticosti scene (beam S7) ©CSA.

## 4 Initial Estimator Tests

Most estimators work on a block basis, e.g. on  $4096 \times 4096$  samples. To examine the behaviour of the estimators on different scene features, we divided the scene of Fig. 2 into relatively small blocks ( $256 \times 1024$  samples or 4.1 km in range by 5.2 km in azimuth), and applied the estimators to each block individually. The data were range compressed but not azimuth compressed. This is the point in the SAR processing flow where the DOPCEN estimation is usually carried out.

### 4.1 Measuring scene statistics

Before running the estimators, we measured the radiometric gradients, the spectral distortion, the energy (SNR) and the contrast of each block. The range and azimuth radiometric gradients are shown in Fig. 3, where the prominent edges of the land/water boundaries are clearly seen. To observe the SNR and the spectral distortion, it is useful to plot the azimuth magnitude spectra averaged over each block. In Fig. 4, the spectra of azimuth block numbers (rows) 17–24 are plotted, taken down the left-hand side in Fig. 3 (range block (column) 28). Low signal strength can be observed in rows 21–24, and spectral distortion can be seen in row 20.

### 4.2 Simulation tests

The estimators were first tested on simulated data. Millions of point targets were used to simulate different scene contrasts and radiometric discontinuities [10].

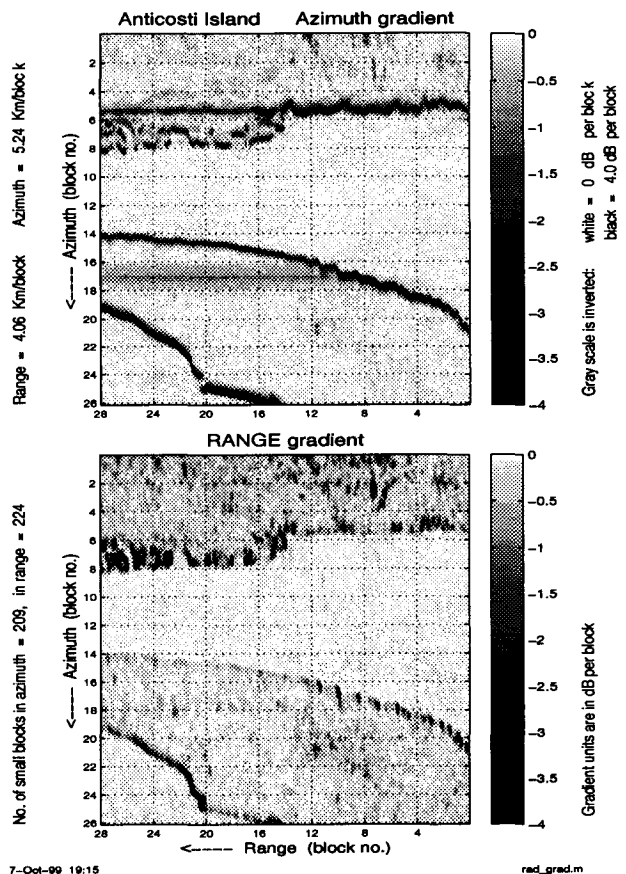


Figure 3: Range and azimuth radiometric gradients of range compressed Anticosti scene.

Simulated data were first tested with different levels of contrast by inserting strong targets between average strength targets. It was found that the DLR and MLCC algorithms worked best with low contrast scenes in which the data are more uniform and the azimuth spectrum is undistorted. In low contrast scenes, partial exposures are not so damaging, as the partially-exposed targets at the start of the estimation window are compensated by others of similar strength at the end of the window.

On the other hand, the MLBF algorithm was found to work best on scenes with high contrast. In fact, the MLBF algorithm works best when only one dominant target is present in each range cell when the beat frequency is clearest. When many targets of roughly equal strength exist in a range cell, they mix with one another and the beat frequency becomes 'smeared out'. The MLBF algorithm is not as sensitive to partial exposures, as the beat frequency does not change so much along the target's exposure.

When uniform scenes were simulated, but with range and azimuth radiometric discontinuities, it was found that the range discontinuities had little effect on es-

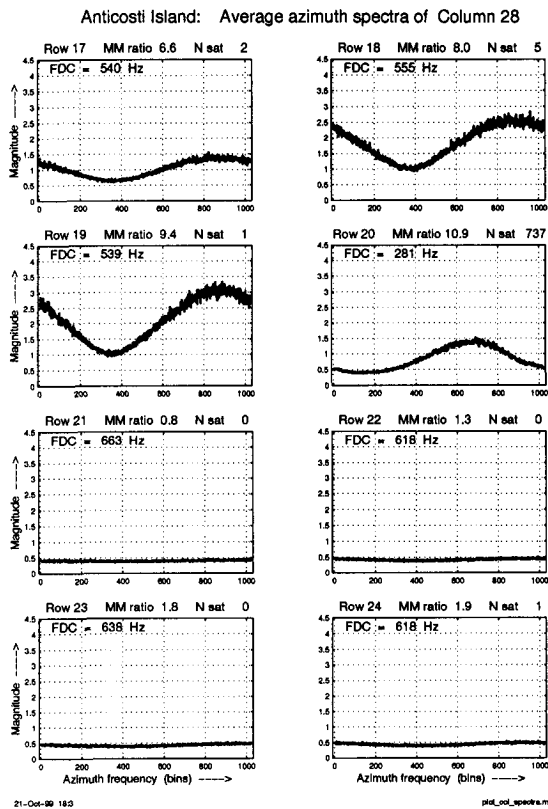


Figure 4: Azimuth spectra of column 28 of the Anticosti scene.

estimator performance. However, the azimuth discontinuities had a pronounced effect on the estimators, particularly with the classic, DLR and MLCC estimators. When the data SNR was low, the standard deviation of the estimates increased, but the estimates were not biased as long as the spectrum was symmetrical. Because of the different sensitivities to scene features, we recommend running the complementary MLCC and MLBF algorithms in parallel, and using statistical quality measures to select the best estimate [5].

Based on these tests, it was determined that the major impact on the estimators was caused by partial azimuth exposures. Partial exposures occur when a strong target is present, but only part of the target is present within the estimation window.

### 4.3 RADARSAT-1 data tests

The  $256 \times 1024$  sample data blocks were arranged in 26 rows and 28 columns, as indicated by the annotation in Fig. 3. This was convenient to run the estimators down columns or across rows, to allow unwrapping of estimates where necessary, and to provide a useful display format.

Figs. 4 and 5 show a typical set of results, when the

estimators were run on the blocks going down column 28 (the left hand column). This column spans a representative set of radiometric discontinuities and we can observe the estimator behaviour on these scene features. In this case, the spectral fit estimator was used.

The upper panel of Fig. 5 shows the fractional-PRF DOPCEN estimates, along with a straight line fit (it has been found that DOPCEN estimates are typically linear with azimuth time, over periods of tens of seconds). The next three panels of Fig. 5 show: the block rms value; how close the magnitude spectrum fits the expected high-SNR shape; the max/min ratio of the spectra in dB (almost the same as the "goodness of fit" curve); and the range and azimuth gradients.

The following points can be observed in this typical data set:

- The estimates conform well to the expected linear behaviour with azimuth time, except where the data undergoes substantial azimuth discontinuities. The discontinuities can be observed in the second and fourth panels (solid line) of Fig. 5, in the top panel of Fig. 3, as well as in the image itself, Fig. 2.
- The estimates taken in the low-energy water regions seem to be quite good despite the lower SNR and the poor spectral fit. See rows 10 to 13 and 22 to 26. The poor fit is due to the high noise floor, but the symmetry of the spectrum still yields good estimates.
- The AGC change around rows 16 and 17 does not affect the estimator appreciably in this case.

We ran similar tests on the other rows and columns of this scene. We also used the MLCC, DLR and MLBF estimators, and examined three RADARSAT-1 fine beam scenes with DOPCEN estimation difficulties. From this experience, we deduce that the azimuth radiometric gradient, as shown in the solid line in Fig. 5, is the best single predictor of poor estimator performance. We observe that if we can avoid the blocks which upset the estimators, a good global estimate can be made from the set of "good" blocks.

## 5 Global Fitting Strategy

Because we can recognize which blocks are likely to bias the DOPCEN estimate, and the estimates should be taken over as wide an area as possible, we propose a *global-fitting* algorithm based on the following strategy:

1. Use of spatial diversity:
  - Use as large an area as possible;



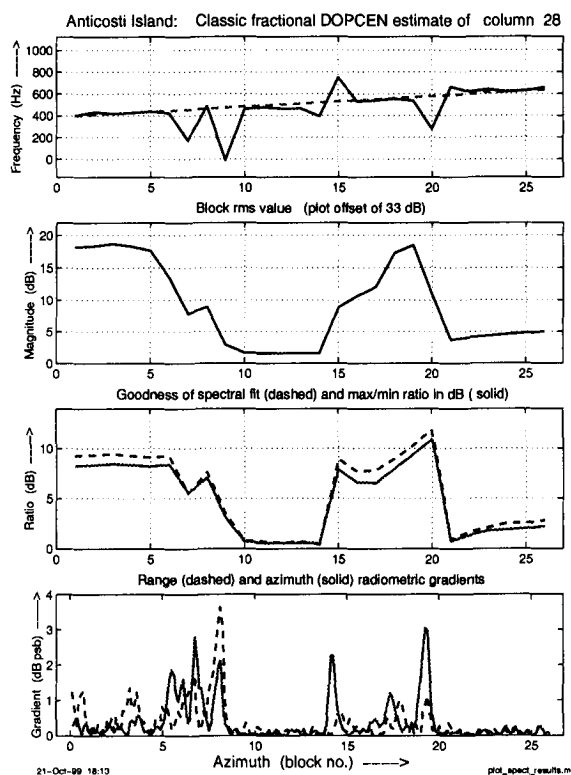


Figure 5: Summary of results of column 28 of the Anticosti scene.

- Divide the area into small blocks.
2. Reject blocks based on quality criteria such as:
  - scene statistics, and/or
  - estimator deviations.
3. Fit DOPCEN model globally over blocks:
  - constrain the fit to a sensible shape;
  - weight the blocks based on quality criteria.

The structure of the algorithm is outlined in Fig. 6. The key to the success of the algorithm is to begin with as large an area as possible, and to make a careful choice of the quality criteria used to exclude bad blocks from the final estimate (a mask is used to exclude bad blocks during the iterations). It was found best to begin by excluding blocks which had a higher than normal azimuth radiometric gradient, which ensures a reasonable initial fit, then finish by excluding additional blocks on a "worst-deviation" basis.

The maximum number of blocks that can be excluded is set to an upper limit, and if this number is exceeded, the iterations are redone with a different block size. Physical models for the Doppler based on the satellite attitude (along with the orbit and earth

rotation) can be successfully used to predict the functional form of the DOPCEN curve [11, 12, 13], and constrain the estimate to a plausible shape.

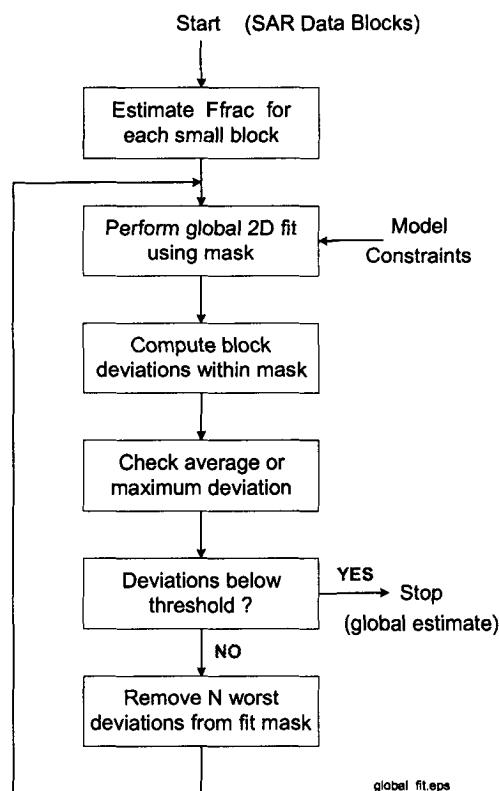


Figure 6: Global fit DOPCEN estimation algorithm.

## 5.1 Global fit results

The spectral fit estimator was run on blocks from every row and the results are shown in Fig. 7. The results of each block are reasonably smooth except when the azimuth gradient is large (compare Fig. 7 with Fig. 3).

We then applied the global fitting strategy of Fig. 6 with the bad blocks removed according to their azimuth gradient. More and more blocks are removed until the deviations from the fit of the remaining block estimates are less than a selected threshold (70 blocks of 728 were removed). For this scene, we recognized that the water areas had a Doppler bias (see below), and we also removed these from the global estimation. The following linear/quadratic fit was performed:

$$F_{DC} = \alpha_1 + \alpha_2 a + \alpha_3 r + \alpha_4 r^2 \text{ Hz} \quad (1)$$

where  $a$  is the azimuth block number centred on row 21.5 and  $r$  is the range block number centred on column 14.5. The fit coefficients are:

$$\alpha = [1415.3 \quad 8.4 \quad 34.4 \quad -0.07] \quad (2)$$

and the result is shown in Fig. 8. Fig. 9 shows the deviations of each of the blocks from the fitted surface. Examining the 66 "good" blocks near the middle of Anticosti Island, the bias between the fitted surface and the 66 blocks is 0.006 Hz, and the rms deviation is 7.3 Hz. In the top 4 rows (112 blocks covering the northern mainland area), the bias between the fitted surface and the 66 blocks is -0.03 Hz, and the rms deviation is 12.7 Hz.

Note that the deviations shown in Fig. 9 do not directly relate to the error in the global fit. However, if the functional form of the fit is correct (i.e. the linear and quadratic terms are correct), and the block estimates are uncorrelated and unbiased, then the standard deviation of the global fit would be  $1/\sqrt{N}$ , when  $N$  blocks are used in the fit. Using this line of reasoning, we can say the small block deviations observed suggest that the global fit is likely good to 5 Hz or better over the land area.

An interesting observation is that there is a small bias of 35 Hz in the river area south-west of the island, which could be attributed to a current of 1.5 m/s. A smaller bias of 18 Hz exists in the water area in the centre right of the scene, presumably where the current is less. Other investigations [14, 2] suggest this is reasonable.

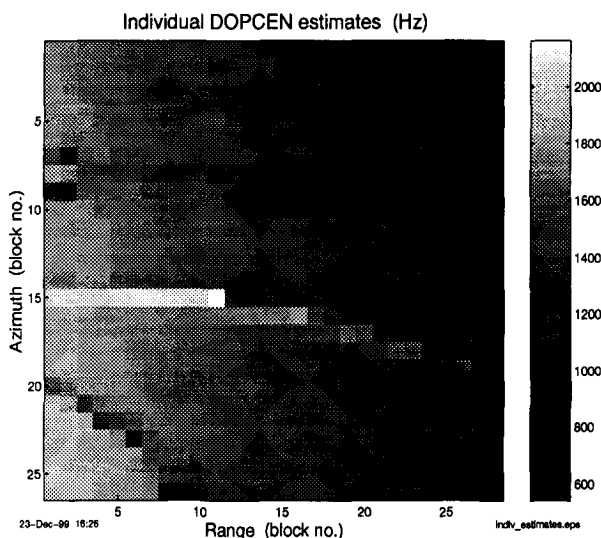


Figure 7: Individual DOPCEN estimates of each block.

## 6 Conclusions

In this paper, we have worked on the problem of bad DOPCEN estimates in RADARSAT-1 scenes. These occur most often when the radar passes over prolonged scene features where there is a prominent

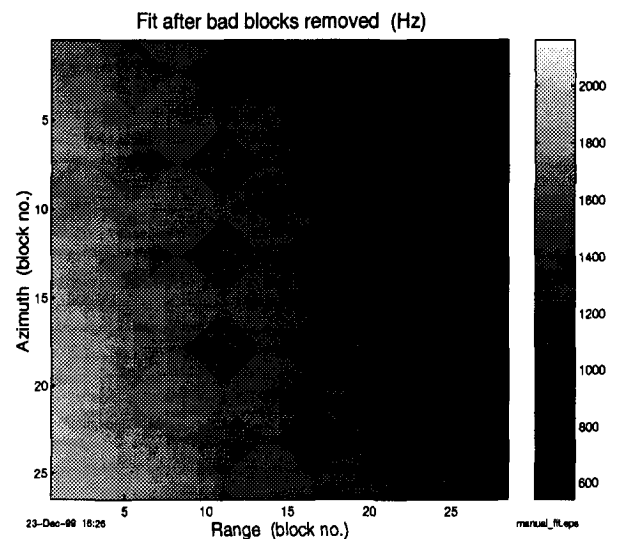


Figure 8: Quadratic surface fitted to good block estimates.

change in radiometry, as often happens on land/sea boundaries.

We have taken the approach of finding out what scene features upset the estimators most, and designing a global estimation scheme which excludes areas of the scene which cause bad estimates. The key to success of the algorithm is to work with as large an area as possible, and to choose a quality criteria which reliably identifies the bad blocks. There may also be a requirement to use adaptive methods where local altitude [15] or currents [2] may exist.

The algorithm is ideally suited to ScanSAR data, because of the large area available to the estimator. The large area increases the probability that bad areas can be avoided by the estimator. Also, ScanSAR has particularly demanding DOPCEN accuracy requirements, and we have shown that the global fit estimator shows the promise of meeting the ScanSAR estimation requirements of 5 Hz.

## Acknowledgements

The authors would like to acknowledge the assistance of Kevin Murnaghan in providing some results from one of the CCRS standard processors; Julius Princz for providing range compressed data from the standard 'raw' product from the CDPF processor; Tommy Zhang of UBC for performing the simulation experiments; Bill Jefferies of RADARSAT International for supplying the raw data which were used in the study; and Paris Vachon for reviewing the manuscript. Funding to support this research came from a number of sources including the RSDDP pro-

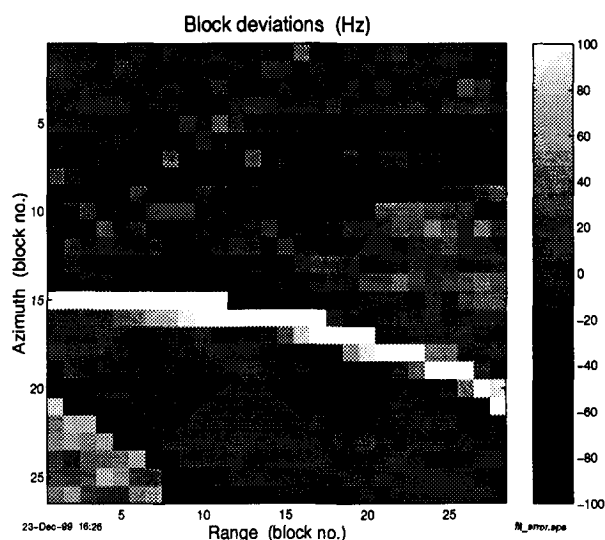


Figure 9: Deviations of individual estimates from quadratic fit (expanded scale).

gram, CSA, CCRS and MacDonald Dettwiler, and we are grateful for their support.

## References

- [1] R. K. Hawkins, T. I. Lukowski, K. P. Murnaghan, and S. K. Srivastava, "The effects of Doppler processing errors in SAR Data," in *Proc. of the CEOS SAR Calibration Workshop*, (Noordwijk, The Netherlands), pp. 201–208, February 2–5, 1998.
- [2] D. C. Lancashire, "ScanSAR Calibration," in *Proc. of the CEOS SAR Calibration Workshop*, (Noordwijk, The Netherlands), pp. 241–245, February 2–5, 1998.
- [3] S. N. Madsen, "Estimating the Doppler Centroid of SAR Data," *IEEE Trans. Aerospace and Electronic Systems*, vol. AES-25, pp. 134–140, Mar. 1989.
- [4] R. Bamler and H. Runge, "PRF Ambiguity Resolving by Wavelength Diversity," *IEEE Trans. on Geoscience and Remote Sensing*, vol. 29, pp. 997–1003, Nov. 1991.
- [5] F. H. Wong and I. G. Cumming, "A Combined SAR Doppler Estimation Scheme Based Upon Signal Phase," *IEEE Trans. on Geoscience and Remote Sensing*, vol. 34, pp. 696–707, May 1996.
- [6] J. R. Bennett and I. G. Cumming, "A Digital Processor for the Production of SEASAT SAR Imagery," in *SURGE Workshop, ESA Publication SP-154*, (Frascati, Italy), July 16–18, 1979.
- [7] F. K. Li, D. N. Held, J. Curlander, and C. Wu, "Doppler Parameter Estimation for Spaceborne Synthetic Aperture Radars," *IEEE Trans. on Geoscience and Remote Sensing*, vol. 23, pp. 47–56, Jan. 1985.
- [8] F. H. Wong, I. G. Cumming, and R. A. Deane, "Doppler Ambiguity Resolver Based on Beat Frequency Between Range Looks," in *Proceedings of the Progress in Electromagnetics Research Symposium, PIERS'96*, (Innsbruck, Austria), p. 544 (abstract only), July 8–12, 1996.
- [9] P. W. Vachon, A. L. Gray, C. E. Livingstone, and A. P. Luscombe, "Adaptive compensation of RADARSAT SAR analogue-to-digital converter saturation power loss," in *Proceedings of GER'97 (on CD-ROM)*, (Ottawa, Canada), May 27–29, 1997.
- [10] T. Zhang, "Investigation of Biases in Doppler Centroid Estimation Algorithms," Master's thesis, Dept. of Electrical and Computer Engineering, The University of British Columbia, Aug. 1999.
- [11] M. Dragošević, "On Accuracy of Attitude Estimation and Doppler Tracking," in *Proc. of the CEOS SAR Workshop*, (Toulouse, France, paper #164), October 26–29 1999. <http://www.estec.esa.nl/CONFANNOUN/99b02/>.
- [12] V. Mitrovic, "RADARSAT CDPF single beam Doppler centroid estimation," Tech. Rep. RZ-TN-50-8357, MacDonald Dettwiler, Richmond, BC, Canada, 1997.
- [13] S. R. Marandi, "RADARSAT attitude estimates based on Doppler centroid measurements," in *Proceedings of a Workshop on RADARSAT Data Quality*, (St. Hubert, Quebec, Canada), February 4–6, 1997.
- [14] M. van der Kooij, W. Hughes, and S. Sato, "Doppler derived measurements of current velocity from spaceborne SAR data," *Can. J. Remote Sensing*, Submitted 1999.
- [15] G. W. Davidson and I. G. Cumming, "Signal Properties of Squint Mode SAR," *IEEE Trans. on Geoscience and Remote Sensing*, vol. 35, pp. 611–617, May 1997.



## An Accurate Radargrammetric Chain for DEM Generation

Youssef Belgued<sup>(1,2)</sup>, Eric Hervet<sup>(2)</sup>, Cédric Lemaréchal<sup>(2,3)</sup>, Loïc Rognant<sup>(1)</sup>, Philippe Marthon<sup>(2)</sup>, Frédéric Adragna<sup>(3)</sup>

<sup>(1)</sup>Alcatel Space Industries

26 avenue J. F. Champollion, BP 1187, 31037 Toulouse, France

Tel : 05 34 35 69 09, Fax : 05 34 35 61 63, Email : Youssef.Belgued@space.alcatel.fr

<sup>(2)</sup>ENSEEIH Informatique

2 rue Camichel, BP 7122, 31071 Toulouse, France

Email : Eric.Hervet@enseeiht.fr

<sup>(3)</sup>CNES

18 avenue Edouard Belin, 31401 Toulouse, France

Email : Cedric.Lemarechal@cnes.fr

### ABSTRACT

Radargrammetry is the automatic process of extracting DEM (Digital Elevation Model) from stereoscopic SAR (Synthetic Aperture Radar) images. In this paper, we break it down into a chain of independent tasks that are analyzed in depth to get the most accurate DEM as output. The two images are first resampled in epipolar geometry to simplify further computations. The matching step follows an original approach by estimating the correlation directly from unfiltered images. This estimation takes into account the statistics of the radar signal. Then, disparity estimation is performed by optimizing a global criterion that includes disparity gradient. Having the disparity map, we then go back to the initial images before epipolar transformation and calculate the three-dimensional position of each homologous pair. This is done by a space triangulation method through the adjusted geometric parameters of the sensor. The final result is a DEM whose accuracy is evaluated. Tests on RADARSAT images are performed to assess the DEM quality improvement in each step of our radargrammetric chain.

### INTRODUCTION

Radargrammetry is the automatic or semi-automatic process of extracting height information from more than two stereoscopic SAR images. It is equivalent to photogrammetry for optical images. The first research work on the spatial domain was with stereoscopic images from SIR-B mission. The development of radargrammetric techniques has been slowed down because of a new method for relief restitution (interferometry), and because of problems encountered due to geometric sources (layover, shadow...) and radiometric sources (speckle...). Now that more and more stereoscopic SAR images are available thanks to the growing number of multi-incidence sensors

(RADARSAT...), and that the operational status of interferometry has suffered a check, researchers and industrialists are again interested in radargrammetry. In this paper we propose a new description of the functional architecture of radargrammetric processing.

### PROCESSING STEPS

Fig. 1 shows the flow chart, which represents the different phases of our radargrammetric processing.

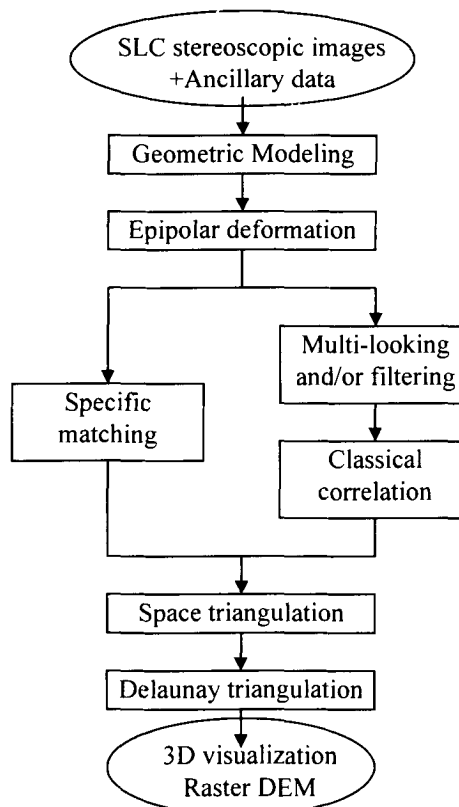


Fig. 1 : Flow diagram of the radargrammetric processing

We start with a couple of SLC (Single Look Complex) stereoscopic images and their ancillary data (ephemeris points, sensor parameters...). At the end, we obtain a regular DEM in a reference geometry. Next, every module of the diagram is described in detail, and illustrated on an example of RADARSAT couple of SAR images.

GEOMETRIC MODELING

The viewing geometric models are set for each image to tie them to the terrain using the leader files information.

The parameters of these models are generally inaccurate and need to be adjusted by means of GCP (Ground Control Points). At this time, this correction is restricted to two parameters per image : the time and the near range. Fig. 2 shows two RADARSAT images that have been geo-referenced, i.e. being subject to the previous handling.

For the images on fig. 2, two GCP were taken manually from the images and scanned topographic maps. Direct and inverse localization can then be computed to link image pixels and ground points [1].

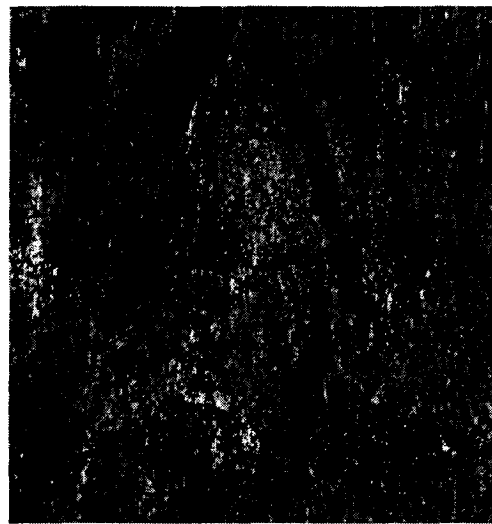
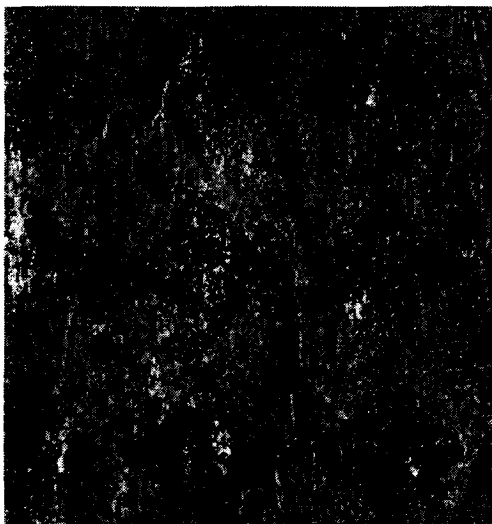


Fig. 2 : original RADARSAT stereoscopic images pair in standard mode, descending orbits, covering the region of Aix-Marseille, including Sainte Victoire mount. Left: standard 3. Right: standard 1

EPIPOLAR DEFORMATION

Computation of epipolar lines

Let us consider a point  $M_1$  with the altitude  $h$  in the first image and its homologous  $M_2$  in the second image. If we don't change  $M_1$  and let  $h$  vary and then perform a direct then an inverse localization, the different homologous of  $M_1$  in the second image describe a curve  $C_2$ . In the same way we obtain a curve  $C_1$  in the first image by letting  $h$  vary while fixing  $M_2$  in the second image. Every point on the curve  $C_1$  has its homologous on the curve  $C_2$  whatever the altitude  $h$  and reciprocally [2].

To compute the image points of the epipolar lines, a mean altitude and an altitude step are fixed. In fig. 3 and

fig. 4, we see the principle of epipolar lines computation.

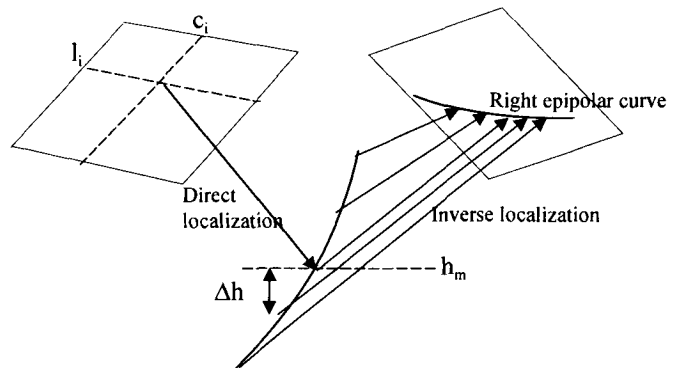


Fig. 3 : Computation of the epipolar curve containing the homologous of  $(l_i, c_i)$  in the right image

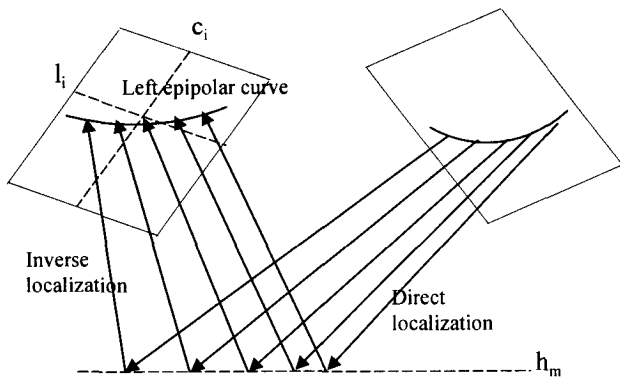


Fig. 4 : Computation of the epipolar curve containing  $(l_i, c_i)$  in the left image

From an initial point  $(l_i, c_i)$ , we first determine the homologous line (represented by a set of points) by direct localization on several altitudes  $(h_m + n\Delta h)$  followed by an inverse localization (fig. 3). Then the

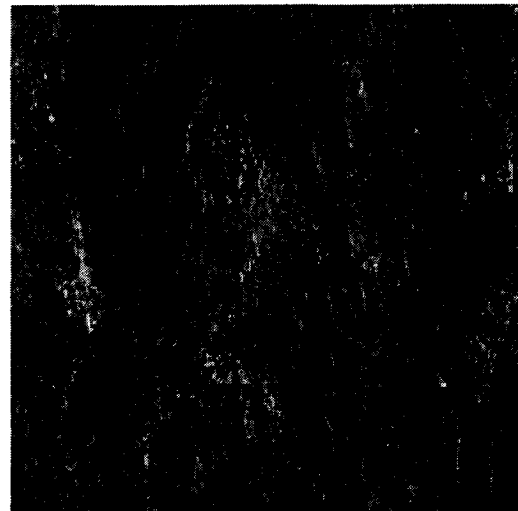
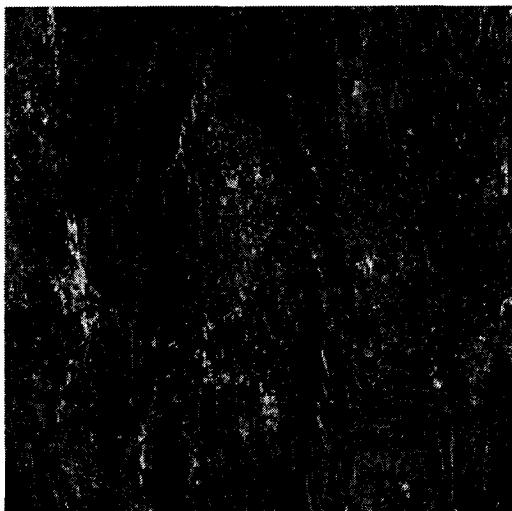


Fig. 5 : RADARSAT stereoscopic images resampled in epipolar geometry. The homologous point of any pixel on the left image (standard 3 mode) lies on the same line on the right image (standard 1 mode)

IMAGE MATCHING

Classical matching method

It consists on matching the two images of the stereoscopic pair after a multi-looking and filtering step to reduce the speckle and to accentuate the resemblance (fig. 6). The matching procedure is based on the correlation of the two intensities or modules images [3].

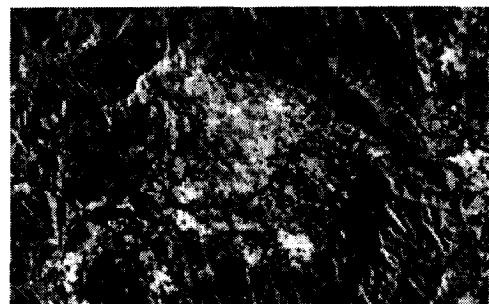


Fig. 6 : An extract from the standard 3 mode image in epipolar geometry, multi-looked 6 times in lines and twice in columns, then filtered by a frost filter.

curve that contains the initial point is similarly computed from each point of the previous set on the same altitude  $h_m$  (fig. 4).

Resampling in epipolar geometry

To resample the stereoscopic pair into epipolar geometry, we compute a deformation polynomial model by means of the previous homologous curves (set of points) for a number of initial points  $(l_i, c_i)$  by putting these curves as lines of the new couple of images. In fig. 5, we see the application of this resampling on the initial pair shown in fig. 2.

The deformation procedure takes into account the characteristics of the radar signal. Doppler centroid estimation, upsampling by zero-padding and nearest neighbor interpolation help to keep the phase information unchanged. Initial resolution is also unchanged after this deformation.

### Specific matching method

Filtering has the inconvenient of deleting some important information in the SAR images, especially structures and contours. Here we present our matching method that combines a global optimization technique with a SAR specific estimation of the correlation [4]. Input images are not filtered.

### Tabu Search

Now we are to describe an iterative matching algorithm based on an optimization technique: the Tabu search [5]. For the particular problem of matching images, we start with an initial solution (first approximation) of the disparity map. Then we converge by successive iterations towards a final solution as close as possible to the global solution of the problem. This one consists in minimizing a cost based on two fundamental criterions : an estimation of the correlation between the two images, as well as the disparity gradient used to measure the local continuity-regularity of the disparities.

### Estimation of the correlation

If we take into account two pixels with intensities  $A_1$  and  $A_2$ . We can write the probability distribution of the pair of pixels as in (1) :

$$p(A_1, A_2 / \rho, \alpha, b_1, b_2) = \frac{1}{(1-\rho^2)\Gamma(\alpha)\rho^{\alpha-1}} \left( \frac{A_1 A_2}{b_1 b_2} \right)^{\alpha-1} \exp \left[ -\frac{1}{1-\rho^2} \left( \frac{A_1}{b_1} + \frac{A_2}{b_2} \right) \right] I_{\alpha-1} \left[ \frac{2\rho}{1-\rho^2} \sqrt{\frac{A_1 A_2}{b_1 b_2}} \right] \quad (1)$$

Where  $\rho$  is the correlation between the two pixels and  $\alpha$ ,  $b_1$  and  $b_2$  are parameters estimated from the two images.  $I_\alpha$  denotes a modified Bessel function of first kind. If we suppose that the pairs of neighboring pixels have the same distribution and that every pair is independent, the maximum likelihood estimator of  $\rho$  is calculated as solution of (2) :

$$n(1-\rho^2)[(\alpha+1)\rho^2 - \alpha + 1] - 2\rho^2 \sum_i \left( \frac{A_1^i}{b_1} + \frac{A_2^i}{b_2} \right) + 2\rho(1+\rho^2) \sum_i \left( \sqrt{\frac{A_1^i A_2^i}{b_1 b_2}} \frac{I'_{\alpha-1} \left[ \frac{2\rho}{1-\rho^2} \sqrt{\frac{A_1^i A_2^i}{b_1 b_2}} \right]}{I_{\alpha-1} \left[ \frac{2\rho}{1-\rho^2} \sqrt{\frac{A_1^i A_2^i}{b_1 b_2}} \right]} \right) = 0 \quad (2)$$

We suppose in (2) to have  $n$  pairs of pixels, i.e.  $n$  independent realizations of a 2-dimensional Gamma law.

### Disparity gradient

The second fundamental criterion taking part in the computation of the global cost quantifies the local variations of the disparity. The aim is to express that the depth variations of a given surface are very small compared to the distance between it and the sensor. For that we use the disparity gradient defined by Julesz [6].

### Multiscaling strategy

The Tabu Search program works with three resolution levels. This cuts down the computation time since the disparities computed at a given resolution level guide the computations for the higher levels, so the interval of allowable disparities is reduced.

## 3D RESTITUTION

Given the disparity map and the inverse deformation model, we can identify homologous points in original images before epipolar transformation. Thus, by means of a space triangulation process (fig. 7) and the viewing models, we compute the three-dimensional position of each homologous pair.

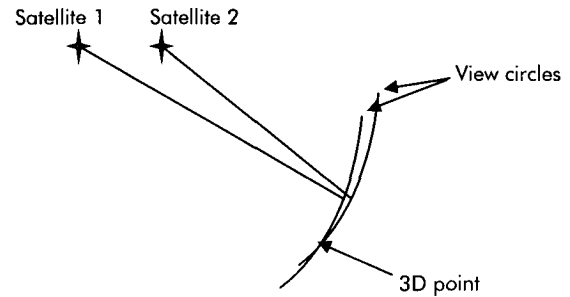


Fig. 7 : Computation of the 3D position of a pair of homologous pixels by intersecting the range sphere and the Doppler cone for each image

The result is a set of 3D points (longitude, latitude, and altitude) in a reference system (for example wgs84). This forms an irregular DEM.

## EVALUATION OF THE DEM QUALITY

### Test data

Stereoscopic SAR images used as input for the radargrammetric chain are RADARSAT SLC images in standard and fine modes covering the same region of



Aix-Marseille. Hereafter we show only results for the S1/S3 pair from descending orbit. A reference DEM is also available. The format of this DEM is dtd 1 (3" arc).

#### Test method

If a reference DEM is available, the evaluation of the altimetric precision of the radargrammetric DEM takes place after the 3D restitution step. Each 3D point generated by space triangulation is localized automatically on the reference DEM (line, column), then the point altitude is compared to the altitude read from the DEM after interpolation (because the line and column numbers are floats). This is done automatically for all the irregular radargrammetric DEM.

#### Results

We have tested the two matching methods : the specific matching for SAR images (fig. 8) and the classical correlation preceded by a filtering stage (fig. 9).

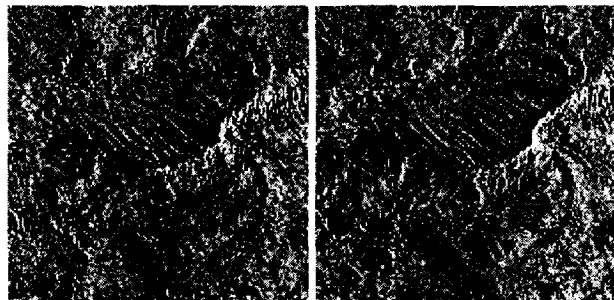


Fig. 8 : Extracts from the SAR pair unfiltered used as input of the specific matching

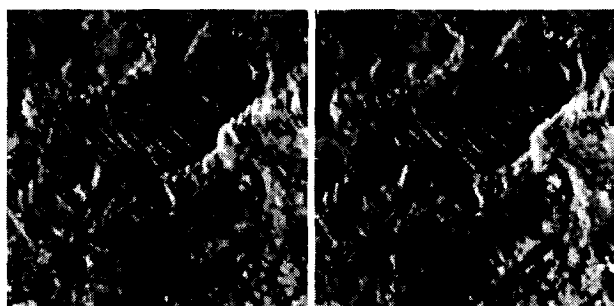


Fig. 9 : Extracts from the filtered pair used as input of the classical correlation

Fig. 10 shows extracts from the two disparity cards resulting from the specific matching stage (left image) and from the classical matching (right image). We point out that even that input images for the classical correlator are much more alike due to the filtering, the

correspondent disparity card is less regular and noisier than the one issued from the specific correlator. This is confirmed by table 1. In this table we have the results of the comparison between the two DEM generated by this radargrammetric chain and the reference DEM. This evaluation proves, for the two cases, the good accuracy of computation in each step of our radargrammetric processing. These results could be better if we had a fine-mesh DEM as reference.

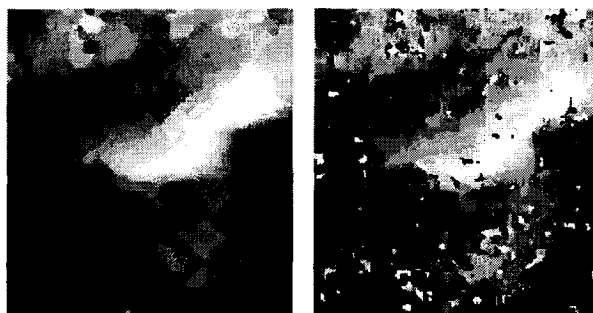


Fig. 10 : Extracts from the disparity cards generated after the specific matching step (left) and the classical matching step (right)

	Points with altimetric error					
	< 20 m		< 50 m		< 100 m	
	%	rmse	%	rmse	%	rmse
Chain with classical matching	38	11.1	74	24.7	89	35.5
Chain with specific matching	49	11.0	85	23.0	95	31.4

Table 1 : Results of the comparison of the two DEM generated by the radargrammetric processing on the S1/S3 RADARSAT pair and the reference DEM. The percentage of points and the root mean square error on those points. Statistics are performed on all points even uncorrelated ones.

#### DELAUNAY TRIANGULATION

The set of points generated from the 3D restitution step forms an irregular DEM due to the inverse epipolar transformation, the relief distortions and the unmatched points. Thus, we organize these points in a network of Delaunay triangles [7] to be able to handle the DEM.

### 3D visualization

After the Delaunay triangulation of the irregular DEM, we can put it in the VRML format (Virtual Reality Modeling Language) and then visualize it in three dimensions. Fig. 11 shows a 3D view of the triangulated DEM generated by radargrammetry.

### Raster DEM generation

A raster DEM can be generated from the triangulated one by putting a regular grid under it and giving each node of the grid the value on the triangle at the vertical.

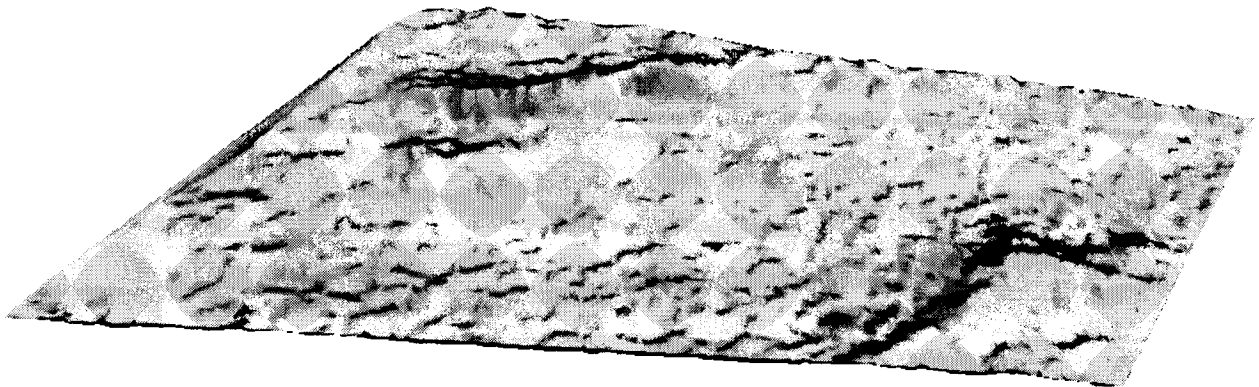


Fig. 11 : 3D view of the DEM generated by radargrammetry from the RADARSAT S1/S3 stereoscopic pair on the region of Aix-Marseille, east of Aix-en-Provence town

### CONCLUSION

In this paper, we have presented all the radargrammetric processing chain. Each step of treatment is analyzed to be the most rigorous possible. This chain is all automatic unless the taking of GCP for the geometric modeling, which also can be made automatic. Adjustment of parameters is restricted to range and time which is not sufficient in some cases. We are working on a block adjustment method correcting physical parameters of the models to improve the geometric accuracy. Concerning the matching step, our experiments have proved that the tabu search program is a robust and reliable tool for image matching. The Julesz' disparity gradient is used to produce regular disparity maps. The specific coherence estimation in original images permits to measure the underlying reflectivity, without pre-filtering the images in order to keep the whole useful information.

### REFERENCES

- [1] Y. Belgued, L. Rognant, L. Denise, S. Goze, J.G. Planès, "Application of space triangulation to the calibration of interferometric DEM", IGARSS'98, vol. 5, pp. 2665-7, Seattle.
- [2] H. Guichard, G. Ruckbush, E. Sueur, S. Wormser, "Stéréorestitution numérique SPOT: une approche originale de formation des images épipolaires et de mise en correspondance", colloque SPOT1 Utilisation des images: bilan et résultats, pp.1371-1392, Paris, France, November 1987.
- [3] L. Marinelli, T. Toutin, I. Dowman, "Génération de MNT par radargrammétrie: Etat de l'art et perspectives", SFPT bulletin no 148, pp.89-96, 1997.
- [4] E. Hervet, C. Lemaréchal, P. Marthon, Y. Belgued, A. Lopès, "SAR image registration without pre-filtering", Europto'99, Florence.
- [5] F. Glover, M. Laguna, "A user's guide to tabu search", in Annals of Operations Research, 1992.
- [6] P. Burt, B. Julesz, "Modifications of the classical notion of panum's fusional area", Perception (9), 1980.
- [7] L. Rognant, S. Goze, J.G. Planès, J.M. Chassery, "Triangulated Digital Elevation Model: definition of a new representation", ISPRS Commission IV Symposium, vol. 32, part 4, pp. 494-500, Stuttgart September 7-10, 1998.

[1] Y. Belgued, L. Rognant, L. Denise, S. Goze, J.G. Planès, "Application of space triangulation to the

## Potentiality of High-Resolution SAR Images for Radargrammetric Applications

Elisabeth Simonetto<sup>(1)</sup>, Hélène Oriot<sup>(1)</sup> and René Garello<sup>(2)</sup>

<sup>(1)</sup> ONERA, BP 72, 29 avenue de la Division Leclerc, 92322 Châtillon Cedex, France.

Tel: 33 1 46 73 49 59. Fax: 33 1 46 73 41 67. E-mail: simonetto@onera.fr

<sup>(2)</sup> ENSTBr, Technopole Brest-Iroise, BP 832, 29285 Brest Cedex, France.

### ABSTRACT

In the state-of-the-art of 3D SAR extraction, we can distinguish three main techniques: radarclinometry, interferometry and radargrammetry. Our project is to perform radargrammetry on high-resolution images recorded by the airborne sensor RAMSES. The goal of this paper is to verify that this method is adapted for such images. First, we are interested in the location errors due to sensor parameter and disparity errors. A theoretical error model is proposed and used to evaluate the geometric potentiality of RAMSES sensor for three stereoscopic configurations. We are then dealing with the pertinence of strong echoes. We show the first quantitative results of radargrammetry on two different strong reflectors in an industrial park.

### INTRODUCTION

Radarcinometry is often applied to completely developed speckle areas. Because of specular reflection, this hypothesis is no more valid in high-resolution. In airborne case, repeat-track interferometry is weakly sensitive to atmospheric artefacts but requires very accurate data. Cross-track interferometry needs two boarded antennae. For these reasons, we choose to operate radargrammetry on high-resolution images. Radargrammetry includes the matching process leading to the disparity map and the stereo computation where 3D point co-ordinates are deduced from disparities and viewing parameters. The extracted information leads to a Digital Elevation Model (DEM).

However, the location precision must be compatible with the expected DEM accuracy. Furthermore, strong echoes occur because of the specular backscattering of the radar beam on smooth surfaces. A study of these spots is important to understand if they correspond to the same reflectors and if they contain 3D information. Therefore, the RAMSES sensor aptitude is evaluated owing to a theoretical error model. In a second part, the pertinence of strong echoes for 3D is verified through the interpretation of the images of two different strong reflectors. This work completes the study of [1].

### VIEWING CONFIGURATION ASSESSMENT

The quality of the extracted topographic information is confronted to the well-known compromise between stereoscopic accuracy and radiometric dissimilarities

between the two views [2]. In order to evaluate quantitatively the viewing configuration, we deal with the effects of parameter errors (sensor position, velocity and range) and matching errors (column and row of corresponding points) on the ground point location. Such measures have already been made using ground control points (GCP) [3,4] or theoretically in particular cases (parallel trajectories, zero Doppler,... [2,5]). A more general theoretical error model is proposed, adapted for any viewing arrangement.

### Location by stereomodel

We note (Fig. 1):

- Earth referential  $(\vec{0}, \vec{u}_{x1}, \vec{u}_{x2}, \vec{u}_{x3})$
- $P$ -coordinates in this reference frame:  $X(x_1, x_2, x_3)^T$
- left and right parameters at  $P$ -imaging time:
  - position  $S_1(s_1^{x1}, s_1^{x2}, s_1^{x3})^T - S_2(s_2^{x1}, s_2^{x2}, s_2^{x3})^T$
  - velocity  $\vec{V}_1(v_1^{x1}, v_1^{x2}, v_1^{x3})^T - \vec{V}_2(v_2^{x1}, v_2^{x2}, v_2^{x3})^T$
  - slant range  $r_1 - r_2$
- left reference frame:  $(N_1, \vec{x}_1, \vec{y}_1, \vec{z}_1)$ ,  $N_1$  left nadir,
  - $\vec{x}_1 = \vec{V}_1 / V_1$ ,  $\vec{y}_1 = \vec{z}_1 \wedge \vec{x}_1$ ,  $\vec{z}_1 = \vec{S}_1 N_1 / S_1 N_1$
- crossing angle between trajectories,  $G$
- stereo angle,  $\Delta\theta$  (difference between incidence angles)

The  $P$ -coordinates result from the intersection of the two range-Doppler circles, that we resolve by non-linear least squares:

$$\begin{cases} r_1^2 = S_1 P^2, & r_1 \sin \tau_1 V_1 = \vec{S}_1 P \cdot \vec{V}_1 \\ r_2^2 = S_2 P^2, & r_2 \sin \tau_2 V_2 = \vec{S}_2 P \cdot \vec{V}_2 \end{cases}$$

### Method

We first look for the expression of the location errors due to parameter errors. For that purpose, we use the method presented in [1]. It provides the complete covariance matrix of the estimated coordinates from the parameter measures and the function minimized during the stereo intersection stage. The effects of matching errors are then deduced considering that these errors induce date (and so sensor position and velocity) errors and range errors.

### Parameter error model

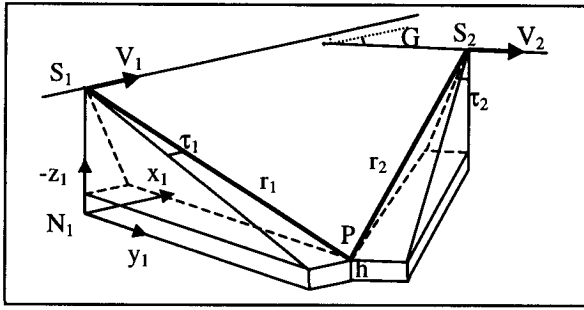


Fig. 1: Notation for any viewing configuration

We show that the covariance matrix of the estimated coordinates depends on scalar and vectorial products of position and velocity vectors (table 1). The vectorial function  $F_{ik}(x_p)$  ( $F_{vk}(x_p)$ ,  $F_{rk}$ ) defines the relationship between the  $P$ -coordinate and the position on  $\vec{u}_p$  axis (velocity, range) of the antenna  $k$ . We suppose that left and right measures are independant and range measure is independant from position and velocity measures.

#### Matching error model

Matching error includes row and column errors of the associated points. Column error causes range error according to:  $r = \text{NearRange} + \text{PixelSize} \cdot j$ . Then:

$$\sigma_j = \sigma_r / \text{PixelSize}$$

We suppose at first order that row error produces only sensor position error. Rigorously it might give rise to velocity error too. As,  $i - i_0 \approx \text{PRF} \cdot S_0 \cdot S / V$ ,  $\text{PRF}$  is the Pulse Repetition Frequency and  $S_0$  the initial sensor position related to the first row  $i_0$ , we have:

$$\sigma_i = \frac{\text{PRF}}{V S_0} \left[ (s^{x1} - s_0^{x1}) \sigma_{s^{x1}} + (s^{x2} - s_0^{x2}) \sigma_{s^{x2}} + (s^{x3} - s_0^{x3}) \sigma_{s^{x3}} \right]$$

Table 1: Covariance matrix of the estimated co-ordinates in terms of measures ( $i, j \in [1,3]^2$ ,  $t$  complementary of  $k$ )

$\text{cov}(x_i, x_j) = \frac{1}{D^2} \sum_{k=1}^2 \left[ \sum_{p=1}^3 \left[ (F_{sk}(x_p) \vec{u}_{xi}) (F_{sk}(x_p) \vec{u}_{xj}) \sigma_{s_k^{xp}}^2 + (F_{vk}(x_p) \vec{u}_{xi}) (F_{vk}(x_p) \vec{u}_{xj}) \sigma_{v_k^{xp}}^2 \right] + (F_{rk}(x_p) \vec{u}_{xi}) (F_{rk}(x_p) \vec{u}_{xj}) \sigma_{r_k}^2 + \sum_{p=1}^3 \sum_{q=1}^3 K_{p,q,i,j} \sigma_{s_k^{xp} v_k^{yq}}^2 \right]$	
$D = F_{s1}(x_1) \vec{u}_{x1} + F_{s2}(x_1) \vec{u}_{x1}$	$\vec{T}_k = \frac{(\vec{S}_1 \vec{P} \wedge \vec{S}_2 \vec{P}) (\vec{V}_k \cdot (\vec{S}_1 \vec{P} \wedge \vec{S}_2 \vec{P}))}{(\vec{V}_1 \wedge \vec{V}_2) (\vec{S}_k \vec{P} \cdot (\vec{V}_1 \wedge \vec{V}_2))}$
$F_{sk}(x_p) = 4 \left[ v_k^{xp} \vec{T}_k + (x_p - s_k^{xp}) \vec{M}_k \right] + \left[ (x_p - s_k^{xp}) \vec{U}_k + v_k^{xp} \vec{N}_k \right]$	$\vec{U}_k = \frac{(\vec{V}_1 \wedge \vec{V}_2) (\vec{S}_k \vec{P} \cdot (\vec{V}_1 \wedge \vec{V}_2))}{(\vec{V}_u \wedge \vec{S}_i \vec{P}) (\vec{S}_k \vec{P} \cdot (\vec{V}_u \wedge \vec{S}_i \vec{P}))}$
$F_{vk}(x_p) = -(x_p - s_k^{xp}) \left[ 4 \vec{T}_k + \vec{N}_k \right]$	$\vec{M}_k = \sum_{u=1}^2 \left[ (\vec{V}_u \wedge \vec{S}_i \vec{P}) (\vec{S}_k \vec{P} \cdot (\vec{V}_u \wedge \vec{S}_i \vec{P})) \right]$
$F_{rk} = 4 \left[ (f_{Dk} \lambda_k / 2) \vec{T}_k + r_k \vec{M}_k \right] + \left[ r_k \vec{U}_k + (f_{Dk} \lambda_k / 2) \vec{N}_k \right]$	$\vec{N}_k = \sum_{u=1}^2 \left[ (\vec{V}_u \wedge \vec{S}_u \vec{P}) (\vec{V}_k \cdot (\vec{V}_u \wedge \vec{S}_u \vec{P})) \right]$
$K_{p,q,i,j} = (F_{sk}(x_p) \vec{u}_{xi}) (F_{vk}(x_q) \vec{u}_{xj}) + (F_{sk}(x_p) \vec{u}_{xj}) (F_{vk}(x_q) \vec{u}_{xi})$	

When working in the left referential, we consider that row matching error only generates sensor position error on  $x_1$  axis (along track direction).

#### Influence of the crossing and stereo angles

We can observe that the error model depends on:

- stereo angle by  $(\vec{S}_1 \vec{P} \wedge \vec{S}_2 \vec{P})$
- crossing angle by  $(\vec{V}_1 \wedge \vec{V}_2)$
- Doppler angle by  $(\vec{V}_k \wedge \vec{S}_k \vec{P})$ .

We work in the left referential. Briefly, let us remind the parallel and zero Doppler case. Errors on  $y_1$  and  $z_1$   $P$ -coordinates are decorrelated from the  $x_1$   $P$ -coordinate error. The errors along  $y_1$  and  $z_1$  axes are due to look angle and range errors (so on  $r_k, s_k^{y1}, s_k^{z1}$ ), whereas  $x_1$  coordinate errors occur when a non-zero Doppler is introduced (so on  $s_k^{x1}, v_k^{y1}, v_k^{z1}$ ).

The analysis of the crossing and stereo angles is based on simulated trajectories. Starting from a reference trajectory, the other ones are built so that they define an increasing stereo angle from about 5 to 60° and a crossing angle of 0, 10 and 20°. The left incidence angle is around 30°.

The location errors are expressed in pixel unit per error on the measure of one unit (meter for position and range, meter/second for velocity). The pixel size on ground is used to convert the error coefficients in pixel unit.

In [1], the error effects are studied on each axis. We prefer here to distinguish error effects on planimetric and altimetric  $P$ -point location. As some measures are linked, we consider only effects of column, row and velocity (projected on  $y_1$  or  $z_1$  axis) errors (Fig. 2).

The following points are observed:

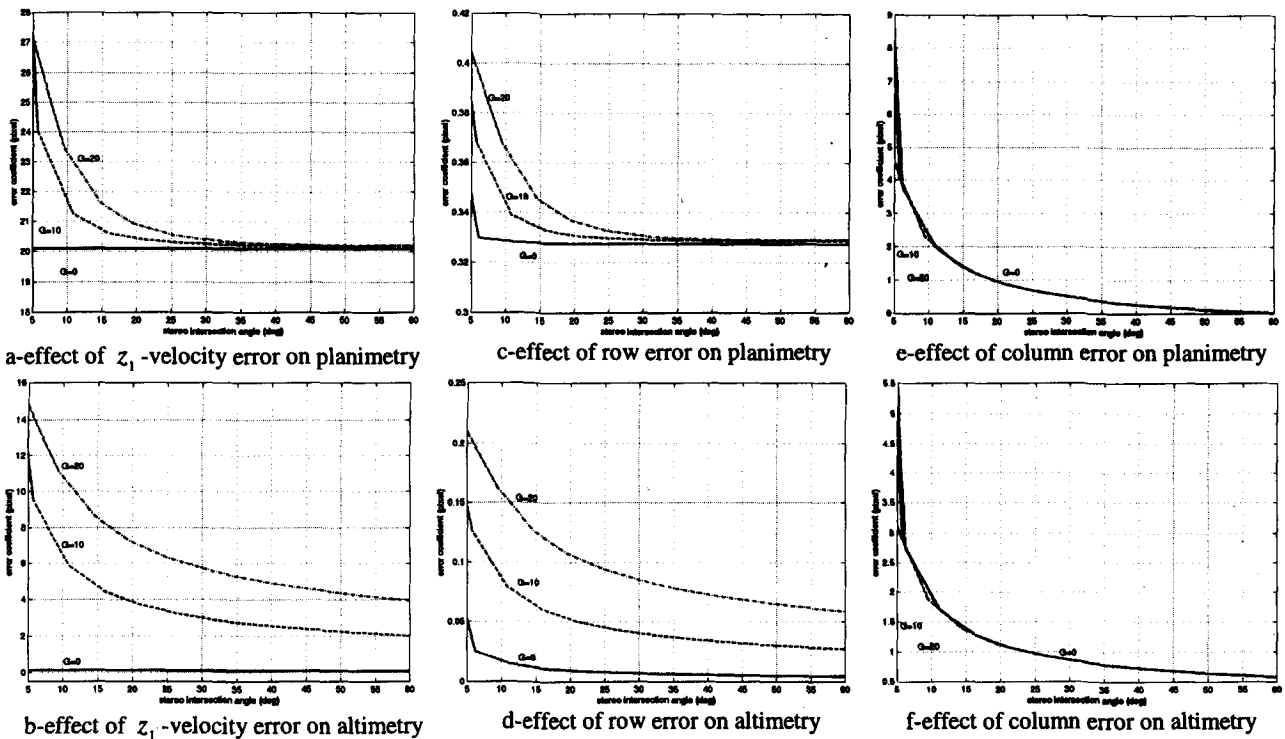


Fig. 2: Location errors due to velocity and matching errors according to stereo and crossing ( $G$ ) angles (in pixel unit)

Table 2: Parameter (velocity, position, range) precisions required for a theoretical location accuracy of one pixel

couple	view1-view3	view3-view2	view2-view1
$\Delta\theta$ (°)	30	20	10
$G$ (°)	0.22	0.50	0.38
velocity (m/s)	0.05	0.03	0.04
position (m)	0.75	0.32	0.26
range (m)	0.65	0.28	0.20

Table 3: Matching error effect in pixel unit/measure unit

couple	view1-view3	view3-view2	view2-view1
column error effect on:			
planimetry	0.48	1.99	2.77
altimetry	0.85	1.73	1.42
row error effect on:			
planimetry	0.33	0.64	0.49
altimetry	0.03	0.22	0.09

- Concerning the influence of the crossing angle: parameter errors in the orthogonal plane to the viewing direction (along-track and height axes) have less effect in parallel case, whereas the impact of parameter errors in the viewing direction (across-track axis) decreases with the crossing angle.
- Velocity measures must be particularly accurate.
- Row errors are less penalizing than column errors, producing location errors inferior to a half pixel.
- Thus column errors are limiting, but a precision of one pixel on altimetry and planimetry can be reached for a stereo angle greater than about 25°.

It derives that radargrammetry is theoretically possible with a one pixel precision in some viewing condition.

Application to RAMSES images

Presentation of the images

The images have been recorded by the RAMSES (Radar Aéroporté Multi-Spectral d'Etude de Signatures,

for more information see [6]) sensor of the ONERA. Three views of an industrial site are available (Fig. 3). These images allow the visualization of man-made structures such as tanks, buildings and streets.

Viewing parameter correction

To improve the geometric modelling that enables the image-to-ground correspondence, viewing parameters are corrected with GCP. It consists in adding an offset on sensor position. The offset is fitted by least squares. The GCP are selected on the BD TOPO® (IGN, 3D model with a one-meter accuracy).

Theoretical assessment of the three pairs

The error model is applied to the three possible pairs. We report in table 2 the required precisions on the parameters to obtain a one pixel location accuracy. The effect of matching error (table 3) confirm that the view1-view3 pair has the best potential. The other ones have a capacity limited by the effect of column errors.

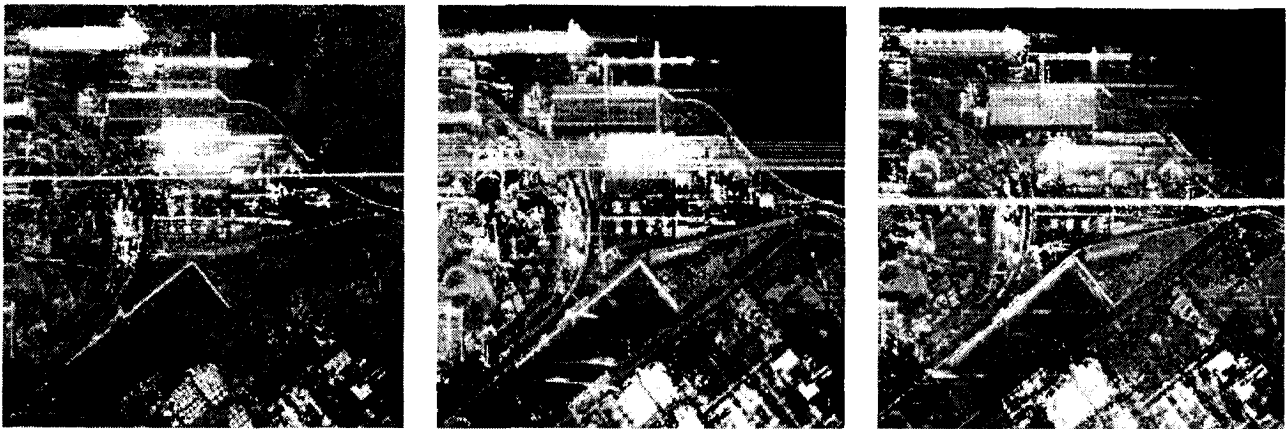


Fig. 3: Three views of an industrial park in ground-range geometry

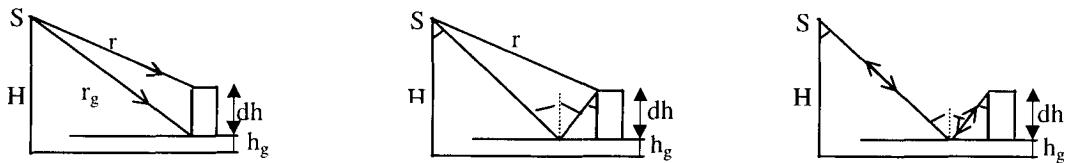


Fig. 4: Beam paths for direct, double and triple reflections

ANALYSIS OF STRONG REFLECTORS

The direct reflections

The surfaces backscatter the radar beam diffusely if they are rough or specularly if they are smooth. Definition of smoothness depends on the wave length [2]. Specular reflectors appear on radar images as one or more punctual strong echo. In the following study, we deal with the succession of echoes. This phenomenon can be observed for any high smooth component. In general, two successive strong echoes are visible (Fig. 5). Here is proposed a simplified interpretation of the phenomena, that could be included in our future radargrammetric chain.

The first echo is due to the specular backscattering from the top of the structure. The second echo corresponds to the corner between the structure and the ground (Fig. 4). Besides indirect mirror reflections occur because of a smooth surrounding ground. In this case, multiple reflections happen between the ground and the component [2]. Considering only dihedral reflections (between two smooth surfaces), we identify double and also triple reflections if the object is very reflective.

The double reflections

Theory

We note:

- $h_g$  base height (so ground height) and  $r_g$  its range
- $h$  absolute height of the object and  $r$  its range

- $dh$  relative height:  $dh = h - h_g$
- $\theta$  incidence angle on  $h$ -point
- $r_2(dh, r, \theta)$  range of the double reflection

The double reflection corresponds to the path of the radar beam as shown in Fig. 4, or to the similar path with a mirror angle on the structure. The beam first hits the ground or the structure.

In [1], we find that the double reflection corresponds to the second echo, as the direct reflection from the base. Let us study the theoretical expression of the difference of ranges,  $\Delta r = |r_2(dh, r, \theta) - r_g(dh, r, \theta)|$ .

Supposing that the ground is flat, we have:

$$r_2(dh, r, \theta) = (r/2) \cdot \left( 1 + \sqrt{1 + 4dh \cos \theta / r + 4dh^2 / r^2} \right)$$

(mirror angle on the ground)

$$r_g(dh, r, \theta) = r \left( 1 + \sqrt{1 + 2dh \cos \theta / r + dh^2 / r^2} \right)$$

For  $dh \ll r$ :  $\Delta r = dh^2 \sin^2 \theta / 2r$

So:

$$\Delta r < \delta \Rightarrow |dh| < \sqrt{2H\delta / \cos \theta \sin^2 \theta}$$

It means that the double reflection and the direct reflection from the base contribute to the same echo while the relative height is below a threshold. For any sensor height, this threshold corresponds to an incidence angle of  $54.7^\circ$  and is written:

$$dh_{max} = \sqrt{3\sqrt{3}H}$$

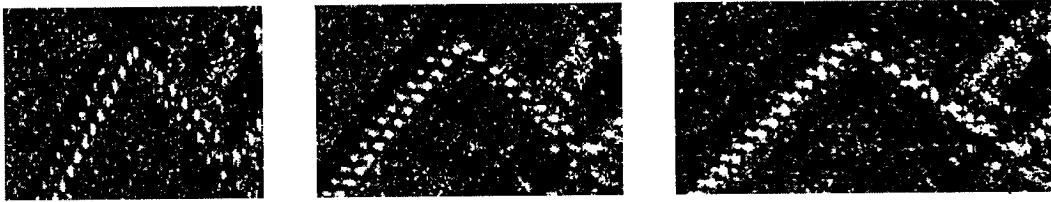


Fig. 5: three views of street lamps in slant-range geometry

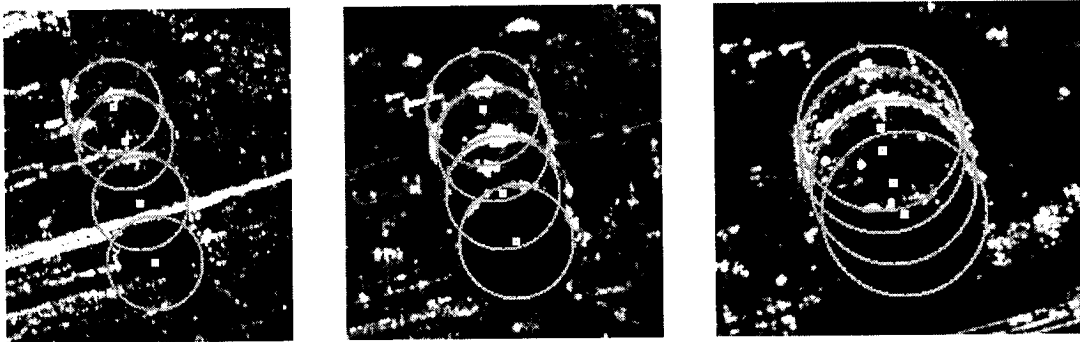


Fig. 6: Extracted Hough circles on the geocoded images (the pixel sizes are different)

Table 4: statistic on ten street lamps. Altimetric (A) and planimetric (P) distances between the two echoes of each street lamp

couple	view1-view3	view3-view2	view2-view1
(A) mean (m)	8.09	7.79	8.36
(A) std (m)	0.64	0.71	1.28
(P) mean (m)	0.72	0.65	0.60
(P) std (m)	0.22	0.28	0.81

Therefore, for a sensor height of 2000m, the difference of ranges is less than one meter while the relative altitude of the structure is inferior to about 100m.

#### Example of the street lamps

A street lamp induces two echoes (Fig. 5). The first one corresponds to the direct reflection from the top. The second echo is the sum of the direct reflection off the base and the double reflection via the ground as interpreted before. Of course, the double reflections can happen at any height of the structure and the corresponding ranges vary from  $r_2$ -range to  $r_g$ -range.

We match manually the maximum pixel value of each spot and compute their 3D location. According to the table 4, the stereoscopic pairs lead to very good location precisions with mean differences between pairs inferior to 60cm in altimetry and less than 15cm in planimetry.

The triple reflections: interpretation for a gas tank

#### Echo extraction and matching

Table 5: Reconstruction of the Hough circle centres (planimetry: distance to real point on BD TOPO®)

results (m)	view1-view3	view3-view2	view2-view1
echo 1 : height	41.60	46.46	36.84
planimetry	1.30	2.44	9.98
echo 2 : height	30.48	30.17	30.68
planimetry	2.35	1.98	2.85
echo 3 : height	8.78	7.84	9.32
planimetry	2.80	2.05	4.67
echo 4 : height	-12.73	-15.19	-10.91
planimetry	3.24	1.48	6.90

Here we are interested in a gas tank. Its image is composed of four successive echoes (Fig. 6). Only one side of the tank is visible. The mirror backscattering off the smooth roof away from the sensor explains this. So a circular Hough transform is used to define the tank boundaries on the four echoes and to perform the matching.

We use a Hough transform based on [7] and adapted so that the circles go through the highest pixel values under the bright arc [1]. Here, we look for four circles of same radiuses.

However as the tank appears to be oval in slant-range geometry, the Hough process is performed on the geocoded images (Fig. 6). The geocoding uses a null height for all points. The extracted centres are then reprojected in the slant-range geometry, matched and located by stereo computation (table 5).

We observe that the location of the first echo varies from one configuration to another. The three other echoes are quite consistent with a metric accuracy for the second echo. The imprecision of the circles explains the location differences for the two last echoes.

Table 6: difference between theoretical height deduced from altitudes of echoes 2 and 3, and height of echo 4

results (m)	view1-view3	view3-view2	view2-view1
height difference	0.19	-0.70	1.13

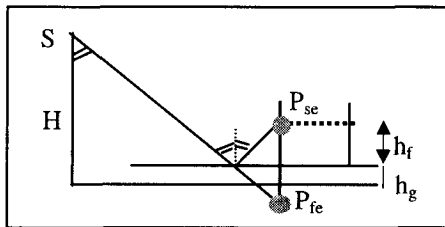


Fig. 8: Interpretation for triple reflection.  $P_{se}$  ( $P_{fe}$ ): intersection point of second (fourth) echo

#### Qualitative interpretation

The picture of Fig. 7 shows a footbridge surrounding the tank. It is responsible for the two unusual echoes. Besides, the roof is mobile. As one of the three images (view 2) has been taken at a very different date from the others, the inconsistency of the first echo reconstruction can be explained by a change of height.

We can find three possible specular reflectors:

- the crenelated top of the tank
- the metallic footbridge
- the corner at the base of the tank.

They give rise to direct backscattering with three different ranges that correspond to the three first echoes. The presence of a fourth echo means that indirect reflections occur, because of a smooth ground. As previously, double reflections are associated to the third echo, related to the base. The fourth echo is due to the footbridge that defines a corner underneath. A triple reflection then happens from the smooth ground (Fig.4).

#### Theoretical interpretation

For a flat ground, the range for a triple reflection is:

$$r_3(dh, r, \theta) = r\sqrt{1 + 4dh \cos\theta / r + 4dh^2 / r^2}$$

The negative height of the fourth echo can be explained geometrically [2]: the two range-Doppler circles intersect at the symmetric point of the footbridge reflector under the ground (Fig. 8). Consequently, supposing a flat ground, the triple reflection altitude is expressed in terms of the ground height and the footbridge height by:

$$h = -(h_f - 2h_g)$$

Table 6 proves the validity of this formula.

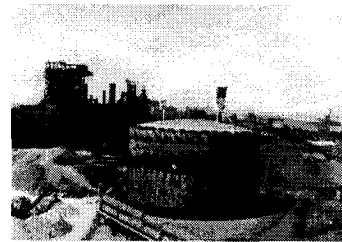


Fig. 7: Picture of the studied gas tank.

#### CONCLUSION

This study allows us to conclude that radargrammetry is adapted on high-resolution images. First, a one pixel location accuracy can be reached for viewing configurations with a stereo angle above around  $25^\circ$ . Then a succession of strong echoes, interpreted by direct and indirect reflections, contain pertinent 3D information. However the echoes indicate different altitudes: real height, ground height. Therefore a processing is necessary to enable echo association and attribution of the right altitude to the structure. However, as Doppler angles are different between images, the pixels of maximum value in spots are not exactly corresponding points. Their association leads to matching errors. Image rectification can then avoid this. Future work will concern automatic matching taking into account strong reflectors. In addition to strong echoes and the research of a robust matching, the complete DEM reconstruction must also consider typical L-shape buildings and half-circle-shape tanks.

#### REFERENCES

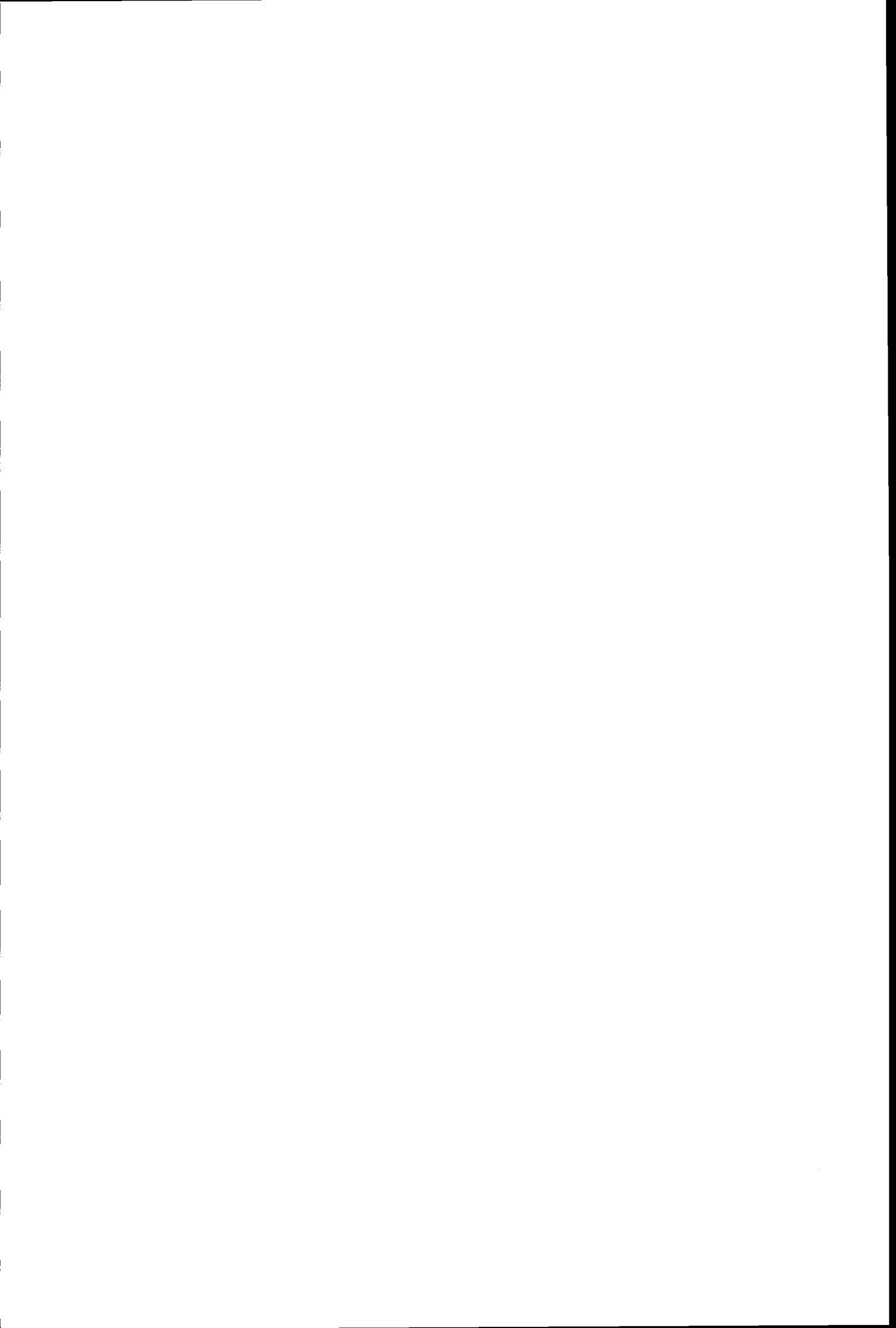
- [1] E. Simonetto, H. Oriot, R. Garello, "3D extraction from airborne SAR imagery", EUROPTO99, Florence, in press.
- [2] F.W. Leberl, *Radargrammetric image processing*, Artech House, 1990.
- [3] S. Sylvander, P. Gigord, P. Durand, "Evaluation of the geometric potential of RADARSAT images", ADRO98 Montreal, 1998.
- [4] H. Raggam, A. Almer, "Assessment of the potential of JERS-1 for relief mapping using optical and SAR data", *Int. Archives of Photogrammetry and Remote Sensing (IAPRS)*, vol. XXXI, part B4, pp. 671-676, Vienna, 1996.
- [5] Z-G. Twu, I.J. Dowman, "Automatic height extraction from ERS-1 SAR imagery", *IAPRS*, vol. XXXI, part B2, pp. 380-383, Vienna, 1996.
- [6] H. Cantalloube, C. Nahum, "Accurate Geometrical error model for airborne SAR", EUROPTO99, Florence, in press.
- [7] P. Kierkegaard, "A method for detection of circular arcs based on the Hough transform", *Machine Vision and Applications*, vol. 5, pp. 249-263, 1992.



**Session 5: Antenna Synthesis/Data Compression/  
Post Processing Techniques**



**Sub-session: Antenna Synthesis**



## Performance Based Elevation Gain Pattern Synthesis

M.A. Brown<sup>1</sup>, C.H. Buck<sup>2</sup>

<sup>1</sup>Marconi Research Centre, West Hanningfield Road,  
Chelmsford, Essex, CM2 8HN, United Kingdom.  
Email: [mike.a.brown@gecm.com](mailto:mike.a.brown@gecm.com)

<sup>2</sup>ESA/ESTEC, TOS-ETP, Keplerlaan 1, Postbus 299,  
2200AG Noordwijk, The Netherlands  
Email: [cbuck@estec.esa.nl](mailto:cbuck@estec.esa.nl)

### ABSTRACT

The performance of any synthetic aperture radar (SAR) is highly dependent on the gain patterns. In particular, the elevation patterns, which may be different on transmit and receive, contribute to the overall radiometric performance. Image quality measures such as sensitivity and ambiguity suppression determine the acceptable swath coverage. It is therefore extremely worthwhile to consider the resulting performance during the design process. The image quality requirements can be used as inputs to the gain pattern synthesis. This iterative process can then be driven by the user to produce the desired performance, either using a template or directly against the requirements. Both approaches are discussed using examples from the forthcoming ASAR.

### INTRODUCTION

Within the highly complex SAR design process one of the most critical elements is the elevation gain pattern optimisation. This has a major impact on a wide range of performance measures from swath coverage through radiometric sensitivity to ambiguity suppression. The trade-off process for the selection of individual swaths is inherently linked to the antenna size. It is therefore extremely important to ensure that the correct antenna dimensions are established early in the design process, prior to any breadboarding and manufacturing. Subsequently, monitoring of the performance prediction process allows the overall system design to be continually optimised against the evolving subsystem performance predictions.

Traditionally a template has been used as the basis to determine the required aperture excitations. The performance requirements for radiometric sensitivity and ambiguity suppression are translated into requirements on the mainlobe and sidelobe structure of the two-way elevation gain pattern. This approach was used on the ERS AMI, and has been used for ASAR. It

is a sensible approach when using different partners in a consortium, since it provides an interface between the beam pattern synthesis and the performance analysis.

Such an approach to the beam pattern synthesis process means that the optimisation process for the transmit and receive patterns may be independent of each other. Consequently, any over- or under-achievement of the synthesis against the template in one dimension can only be compensated in the other dimension by altering the template for the latter dimension. This results in a potentially time-consuming iterative process involving template manipulation and pattern synthesis for each dimension.

The use of a performance-based optimisation process removes the need for the template altogether. The radiometric performance, notably sensitivity and stability, imposes requirements on the mainlobe of the two-way pattern, whilst the ambiguity suppression imposes requirements on the sidelobe structure. Rather than using the template as the measure against which the synthesis is compared, the performance of the synthesised two-way pattern can be determined and used as the basis for the iterative process.

This paper describes the latest upgrades to the synthetic aperture radar (SAR) Instrument Modelling Software (IMS) package produced by the Marconi Research Centre (MRC) under contract to the European Space Research and Technology Centre (ESTEC). It represents the latest in a series of software tools used successfully in the development of spaceborne systems including the ERS-1 SAR, and the forthcoming ASAR. IMS provides a facility to support the high-level design and development of future SAR systems, and provides a capability to investigate various design options for multi-parameter SAR instruments. It can be used in both the design and performance assessment stages of programmes. Furthermore it is under continual development to incorporate the latest techniques (e.g. multi-polarisation operation and spotlight).

## TRADITIONAL TEMPLATE-BASED SYNTHESIS

Historically, the approach used in the beam pattern synthesis process has been to define a template. This places requirements on the mainlobe region and the ambiguity regions to either side.

IMS provides such a facility. Within the IMS template generation module the performance requirements for radiometric sensitivity and ambiguity suppression are translated into requirements on the mainlobe and sidelobe structure of the two-way elevation gain pattern. The two-way template is then split between the transmit and receive beams. Nominally, this is simply an equal division although the user may assign alternative splits for the mainlobe and/or sidelobe regions. This can be beneficial if the aperture constraints being applied to the transmit and receive pattern syntheses are different (for example, the transmit beam may only have a capability for phase variation, whereas the receive beam can vary both the phase and amplitude of each element).

The target swath and range ambiguity regions are considered in terms of the edges of the target swath. This equates to the extent of the mainlobe of the template (with allowances for a roll error). The target imaging geometry and the PRF then determines the ambiguity regions. The absolute gain requirement on the mainlobe is determined from the radiometric sensitivity requirements (e.g. radiometric resolution ( $\gamma$ ) or noise equivalent sigma zero ( $NE\sigma_0$ )). The link-loss budget is used to derive the two-way gain pattern contribution to the signal-to-noise ratio budget.

The relative sidelobe levels are then determined from the ambiguity suppression requirements. The point target range ambiguity ratio (PTRAR) imposes a limit on each ambiguity region individually, whilst the distributed target range ambiguity ratio (DTRAR) represents a cumulative measure and so the distribution amongst the sidelobe regions is somewhat arbitrary. Within the template generation process the user is given some guidance towards the distribution, notably equating to a constant sidelobe level for each ambiguous location, or a variable sidelobe level for each ambiguity corresponding to equal powers in the received signal from each.

The beam pattern synthesis then considers each of the (one-way) transmit and receive patterns separately. This means that the optimisation process for each is independent of the other. Consequently, any over- or under-achievement of the synthesis against the template in one dimension can only be compensated in the other dimension by altering the template for the latter dimension. This results in a potentially time-consuming

iterative process involving template manipulation and pattern synthesis for each dimension.

A simple improvement to this process is to consider both dimensions simultaneously. The synthesis still uses a (two-way) template as the main driver, but addresses the product of the transmit and receive beams. Both beams retain the option of separate aperture constraints. The key advantage to this approach is the removal of the template adjustment for each beam separately.

## PERFORMANCE-BASED SYNTHESIS

The use of the template introduces the possibility that the requirements on the synthesis process are over-specified. In particular, this relates to the distributed target ambiguity ratio as an input to the template generation process. The template is based on the radiometric sensitivity and ambiguity suppression requirements. As mentioned previously, the radiometric sensitivity imposes requirements on the mainlobe of the template, whilst the ambiguity suppression imposes requirements on the sidelobe structure. The point target ambiguity ratio requirement considers each ambiguity separately, and so imposes a unique requirement on each sidelobe section of the template. However, the distributed target ambiguity ratio considers the sum of the returns from the ambiguous regions. The user then has control of allocating the allowance from each ambiguity region. Consequently, the requirement placed on one particular ambiguity region may be over-specified (since the synthesis can over-perform in other regions). For the template-based approaches, this situation would require the template to be adjusted, and the synthesis performed again.

Relating the performance directly to the synthesis can circumvent this procedure. Rather than using the template as the measure against which the synthesis is compared, the performance of the synthesised two-way pattern can be determined and used as the basis for the iterative process. The user can then trade-off the different performance measures directly against each other. For example, they may prefer to improve ambiguity suppression at the expense of sensitivity.

The synthesis process is driven by the specification values for the performance measures. The far-field pattern needed to satisfy the performance requirements is computed every iteration and the appropriate adjustments made to the array weights. This approach is particularly suited to cases where different transmit and receive beams are being utilised. Relating the performance requirements directly to the synthesis process is particularly advantageous for those measures

which are based on a combination of gain values at different angles, notably the distributed target range ambiguity suppression. Indeed, the transmit and receive patterns can be used to compensate for variations in the other.

### BEAM PATTERN GENERATION

We assume that the two-way gain pattern can be expressed as the product of two separable 1-d cuts. This is based on underlying assumption of a rectangular lattice for the radiating elements. Furthermore, only the error-free syntheses are performed. The inclusion of errors can be accommodated as an off-line activity. This is a reasonable approach since the inclusion of errors tends to vary from case to case (and will depend upon the actual antenna layout in terms of T/R modules, sub-arrays etc.).

The elevation gain pattern is based on the co-polar element pattern and the array distribution. The synthesis process determines the latter settings. These are derived using the successive projections synthesis method. This is an iterative process that determines the phase and amplitude settings (weights) across the aperture. The initial array distribution can be user-defined or determined by the synthesis process itself. For a given set of weights the far-field gain pattern is determined. The far-field point for which the difference between the pattern and the template is greatest is found. A revised set of weights are produced which satisfy the template at this point and which also involve the minimum change to the previous set of weights. This process continues for a specified number of iterations or until the template is met.

### ONE-WAY TEMPLATE-BASED TRADE-OFFS

The template used on input to the beam pattern synthesis process represents the effective one-way gain pattern template, and is simply half of the two-way template. The 2 one-way templates can then be adjusted by updating two parameters. The first allows the user to define the proportional split in the two-way mainlobe gain requirement between transmit and receive. Similarly, the second allows the user to apportion the sidelobe contribution between transmit and receive. These adjustments tend to be useful when the transmit and receive beams use different aperture constraints.

For any given synthesis we can determine the performance. Thus, we have the potential to provide a trade-off capability within the synthesis process based on the resulting performance. This trade-off can be driven by adjustments to the array gain margin for each pattern.

Normally, the array gain margin is used to relate the directivity to the gain, and so can be thought of as the antenna losses. However, during the synthesis process they can be adjusted artificially as a means of aligning the achievable mainlobe gain with the template mainlobe requirement. This provides a useful short cut if the template mainlobe and achievable gain is significantly different, and does not require the template to be modified. By allowing the user to specify a range of adjustment margins in each dimension we can produce a 2-d trade-off for each performance measure. Note that the performance is then calculated using the appropriate phase and amplitude settings, but with the adjustment margins removed.

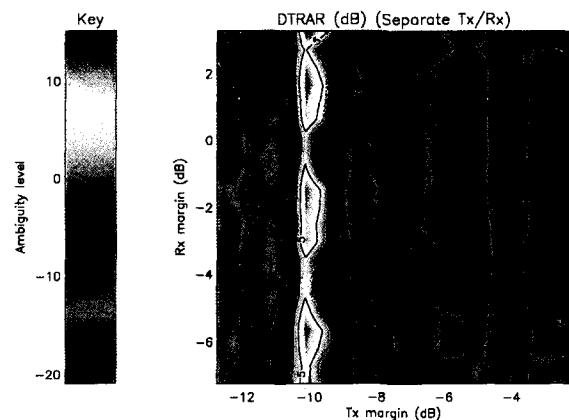


Fig. 1(a): One-way Template-based DTRAR Trade-off

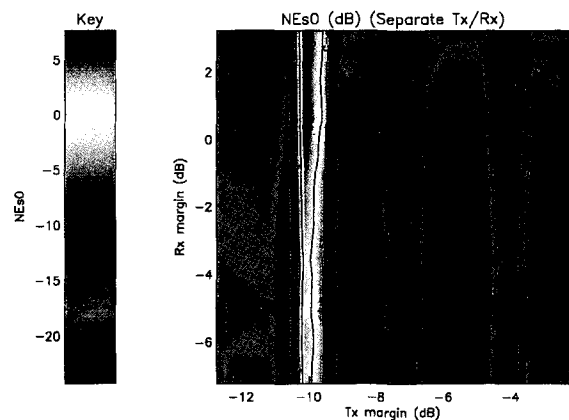


Fig. 1(b): One-way Template-based  $NE\sigma_0$  Trade-off

Figs 1(a-b) show the DTRAR and  $NE\sigma_0$  performance for the swath denoted IS3 in the ASAR Image mode. This swath has proved to be particularly problematic in achieving good performance. It is primarily due to the fact that the near range ambiguity lies very close to the nadir region (i.e. small incidence angle). In turn this leads to large ambiguous returns – the radar cross-section model used on ASAR is a combination of land

and sea models and represents quite a severe worst case scenario).

The diagrams show each performance measure in terms of contour levels, spaced at 5dB intervals. The legend beside each contour plot shows the data range in that plot. The colour range is normalised for each plot. The darker regions demonstrate good performance ( $< -20$ dB is compliant for each measure for this swath). The DTRAR has an optimum value of  $-21$ dB whilst  $NE\sigma_0$  reaches  $-24$ dB (but not simultaneously). It can be seen that the performance appears to be cyclical in nature with respect to the transmit margin. For the range considered optimal performance appears to be produced for a transmit margin of between  $-6$ dB and  $-5$ dB, coupled to a receive margin of  $-4.5$ dB.

### TWO-WAY TEMPLATE-BASED TRADE-OFFS

As discussed previously the main limitation of the one-way template-based beam pattern synthesis is that each dimension is considered separately. The optimisation process for each is independent of the other, and consequently any over- or under-achievement of the synthesis against the template in one dimension cannot directly be compensated in the other. This limitation is overcome if the synthesis considers the two-way template.

In this synthesis process the defined two-way template is compared with the two-way pattern product and the maximum error found. The weights of both the transmit and receive beams are adjusted to achieve the required two-way product (again using the method of successive projections). The synthesis process alternately attempts to optimise the transmit and receive patterns (using the current 'best' pattern for the other dimension when comparisons are made with the template).

This approach to the beam pattern synthesis is particularly suited to cases where different transmit and receive beams are being utilised. For example, it may only be possible to adjust the phase of the excitations on the transmit path. Often this is the case when maximum power is to be transmitted (although this does not necessarily lead to optimal performance). The power loss associated with the use of amplitude weighting on transmit (depending upon the antenna design) may mean that the optimal overall performance is achieved with two distinct patterns.

Figs. 2(a-b) show the corresponding performance for this two-way template case as considered for the one-way template approach shown in Figs 1(a-b).

This shows similar performance to the one-way template-based approach. However, the preferred solution can usually be found using fewer iterations (although each iteration takes longer to perform). These contour plots were produced using 50 iterations for each margin combination. This comprises 5 transmit pattern iterations coupled to 10 receive pattern iterations. This compares to 500 iterations for each dimension in the separate one-way template example.

This approach is better suited to producing flatter mainlobe characteristics. By synthesising both beams simultaneously the variations in one can be offset by the other. This is much harder to accomplish with the one-way template-based approach. There, the mainlobe characteristics are controlled by the mainlobe allowance (effectively the peak-to-peak variation).

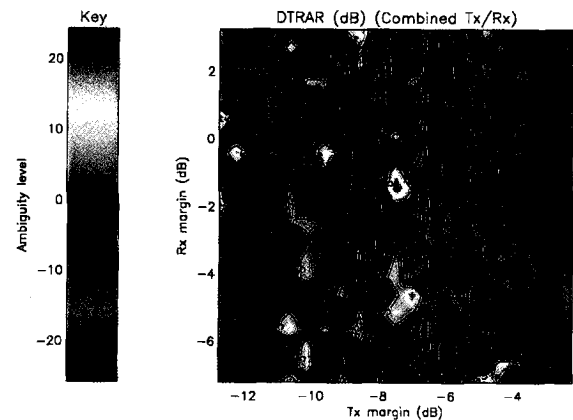


Fig. 2(a): Two-way Template-based DTRAR Trade-off

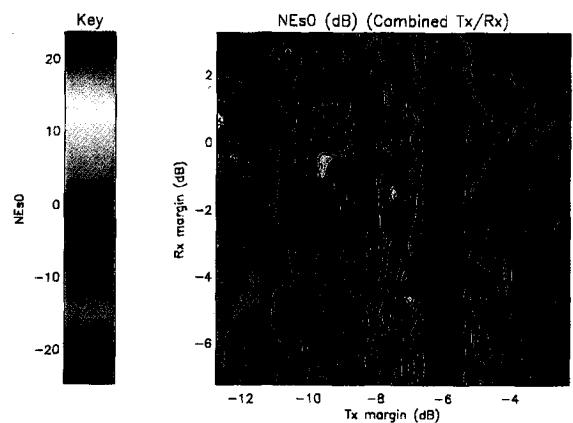


Fig. 2(b): Two-way Template-based  $NE\sigma_0$  Trade-off

The optimum DTRAR is  $-26$ dB whilst  $NE\sigma_0$  reaches  $-25$ dB. As with the one-way template case the user can use this 2-d trade-off capability to home-in on their preferred balance between the different performance measures.



The trade-off facility provides the user with a capability to select their preferred antenna patterns based on the resulting performance, which is ultimately the main aim. Compliance against the template is effectively an artificial requirement.

### PERFORMANCE-BASED SYNTHESIS

The preceding technique considers both propagation directions simultaneously, but still uses a template as the main driver. The key advantage to this approach is the removal of the template within the synthesis process. The use of the template allows the requirements on the synthesis process to be (possibly) over-specified. If the requirement on the template region is uniquely defined (e.g. by the PTRAR for the sidelobe regions, or the radiometric sensitivity for the mainlobe) then there is no freedom in the template definition. However, for the DTRAR the user essentially has control of allocating the distribution of the requirement between each ambiguity region. A template is a single example of a possible solution to the DTRAR requirement. By not using a template we allow the synthesis process greater freedom.

The complexity of this approach depends upon the number of performance measures used to drive the synthesis. We offer the user the basic case that uses the  $NE\sigma_0$  requirement to drive the mainlobe characteristics, coupled to the DTRAR requirement to control the sidelobe structure. Additionally, the PTRAR and Radiometric Stability (Rstab) can be specified. These drivers are included once the main two drivers have been met. The Rstab controls the gain slope at the edges of the mainlobe by imposing an additional constraint on the mainlobe (peak-to-peak) variation. The slope tends to be greatest at the edges of the swath.

The synthesis process uses the performance measures to define an internal template. This template is continually adjusted depending on the current synthesis performance. For example, if the ambiguity suppression is insufficient at one location the internal template will be adjusted for that location. The performance is determined for a number of positions across the target swath. These are used to adjust the mainlobe requirements on the internal template. For the sidelobe regions all the ambiguity locations corresponding to each particular target location are adjusted equally based on the performance shortfall.

This simplifies the procedure and is possible due to the fact that the performance measures and adjustments are made in decibels (i.e. on a relative scale).

The performance of this synthesis approach is ultimately dependent on the performance requirements.

Sensitivity is directly proportional to the system power budget, whilst DTRAR performance is highly dependent upon the radar cross-section model(s). The user should be aware of the trade-offs between the performance measures when specifying them. For example, if the aperture can produce more gain than is required to meet the sensitivity requirement, the synthesis process will attempt to distribute the remaining available gain across the sidelobe regions (principally in the 'don't care' gaps between the ambiguities) which may then lead to poorer ambiguity suppression. As with the template-based approaches a trade-off capability is provided to assist in the system design optimisation.

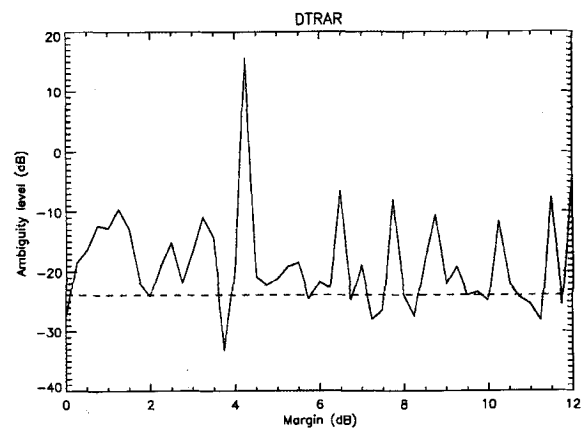


Fig. 3(a): Performance-based DTRAR Trade-off

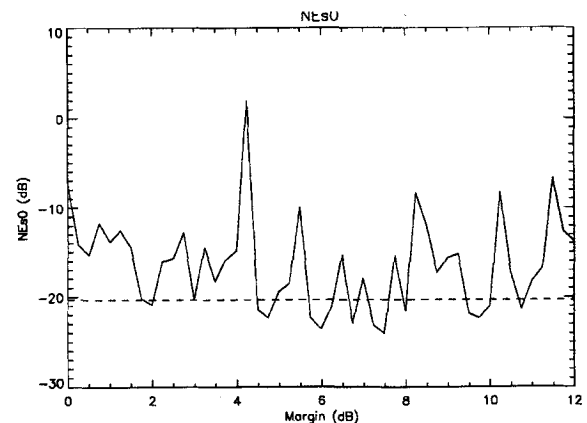


Fig. 3(b): Performance-based  $NE\sigma_0$  Trade-off

A single margin is offered to control the trade-off process. The lower bound on the mainlobe gain requirement is dependent on the sensitivity requirement. The user is offered the opportunity to vary this requirement. This leads to different synthesis solutions as the algorithm attempts to achieve the desired mainlobe gain whilst providing sufficient sidelobe suppression in the ambiguous directions. Figs 3(a-b) show an example of the 1-d trade-off for the

same case as shown previously. Similar plots can be produced for the template-based cases by taking cuts through the contour plots. For this synthesis requirements of  $-20\text{dB}$  for  $\text{NE}\sigma_0$  and  $-24\text{dB}$  for DTRAR were specified.

Fig. 4 shows the resulting 2-way beam pattern, which uses phase-only control for the transmit pattern. The suppression of the sidelobes in the ambiguous regions can clearly be seen.

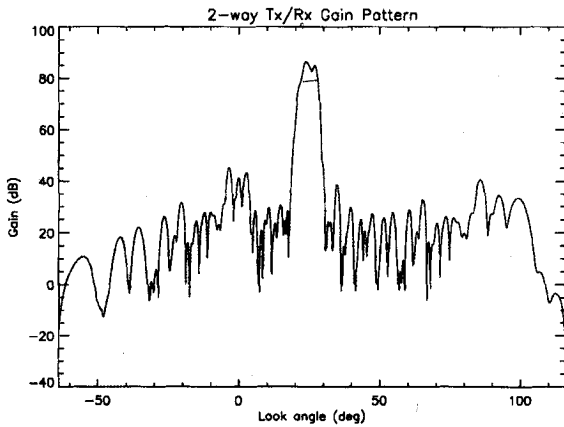


Fig. 4: Performance-based 2-way Gain Pattern

## CONCLUSIONS

The elevation beam pattern synthesis for SAR systems has been demonstrated. Techniques using a template to drive the synthesis process have been shown for cases using separate or combined transmit and receive patterns. A capability to trade-off the image quality performance is used to control the overall process.

An alternative approach using the performance measures to directly control the synthesis process, without the need to specify a template, has also been presented. This uses the radiometric performance (sensitivity and stability) to drive the mainlobe characteristics, whilst the ambiguity suppression is used to control the sidelobe structure.

All the techniques have been incorporated into the latest version of the MRC SAR Instrument Modelling Software (IMS). These techniques will be beneficial to the assessment of any future systems. They allow alternative optimisation of the beam patterns with direct assessment of the performance implications.

The performance-based approach allows the user to vary the performance requirements during the synthesis trade-off process and so examine the limits of achievable performance rapidly. Additionally, this provides a facility to design the error-free beam patterns to satisfy requirements which then accommodate some level of margin to allow for possible degradation during the instrument lifecycle.

**Antenna Pattern Synthesis Optimization for the Elevation Pattern of the ASAR  
Instrument**

Josef Mittermayer, Alberto Moreira  
DLR, Germany

Yves-Louis Desnos  
ESA/ESRIN, Frascati, Italy

**This paper was not available for publication**



**Sub session: Data Compression**



## SAR raw data compression techniques

Gilda Schirinzi

DAEIIMI - Università di Cassino, via Di Biasio, 43 - 03043 Cassino (FR)- Italy  
 and IRECE-CNR, via Diocleziano 328, 80124 Napoli - Italy  
 ☎ 39-081-5707999 - fax. 39-081-5705734 - e-mail: schirinzi@ing.unicas.it

### ABSTRACT

The use of wavelet and wavelet packets basis for synthetic aperture radar (SAR) raw data compression is investigated. Moreover, the performance of signum coding (SC) techniques, advantageously adopted for real time processing, is presented in terms of bit rate reduction and quality parameters evaluation.

### INTRODUCTION

The development of advanced SAR systems for earth observation from satellite, offers flexible microwave imaging sensors, capable of multiple imaging modes and resolutions. These features together with the wide swath requirement, determines the production of a huge amount of data, that have to be processed to generate the high resolution image. Due to the large amount of data to be processed, the received signal is quantized using from 3 to 8 bits, properly coded and transmitted to the ground, where the image formation process is performed. The amount of produced data is then constrained by on board storage and downlink bandwidth. To manage this problem, many efforts have been taken place in order to develop suitable compression techniques of the bit stream necessary for raw data coding [1-5], that well adapts to the particular raw data statistics.

To develop suitable compression techniques the particular statistics of received raw data has to be considered. The received signal can be viewed as a (complex) random process, whose real and imaginary parts are Gaussian, with zero mean and identical variance, and uncorrelated. It can be also shown that adjacent samples, in both range and azimuth directions, are low correlated. These features make conventional image compression techniques not very convenient.

The most widely used compression techniques is the Block Adaptive Quantization (BAQ), due to its simplicity for coding and decoding. This technique consists on an optimal scalar quantizer, which adapts to the changing levels of the signal to be quantized [2]. It can be used also a non-uniform quantizer (or Lloyd-Max quantizer) that minimizes the Mean Squared Error (MSE) for a given number of quantization levels [6]. The algorithm divides the raw data in blocks, and for

each block computes the standard deviation  $\sigma$ , in order to determine the optimum quantizer (see Fig. 1). The minimum block size is selected in order to guarantee a Gaussian statistic within a block; the maximum block size is limited by the fact that the signal power should be approximately constant in the block.

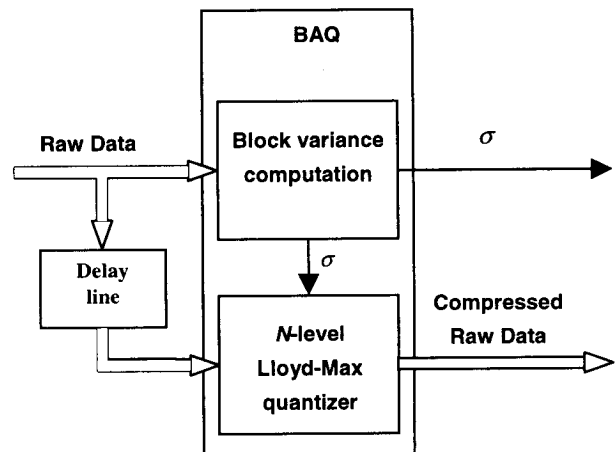


Fig. 1: BAQ quantization of the raw data

Vector quantization techniques [3], allows a small improvement at expenses of a noticeable increase of complexity.

In order to reduce the quantization error and to increase the compression ratio, other techniques combining the advantages of BAQ and vector quantization have been developed [2,4]. They allow a small improvement of the performances, at expenses of a noticeable increase of complexity.

Transform coding algorithms can be also applied. They are based on the decomposition of the signal to be encoded in an orthonormal basis. Then, to construct a finite code, each decomposition coefficient is approximated by a quantized variable. If a wavelet basis is adopted, different quantization strategies can be followed for the different resolution frames in which the data are decomposed.

Other techniques, which are based on signum coding (SC) of the raw signal [7], besides to data compression,

allow to deal with binary sequences, that can be processed in real time by using low-cost, low-weight and low-power consumption dedicated hardware [8].

The performance of the above mentioned compression techniques, applied to the SAR raw data signal of ERS-1 mission relative to Fleevoland (The Netherlands) test site, is presented. Different quality parameters are computed on the SAR images, obtained after processing the compressed data.

WAVELET TRANSFORM CODING

Transform coding algorithms decompose the signal to be encoded in an orthonormal basis. Let us consider for the sake of simplicity a one dimensional case. If we adopt a wavelet basis  $\psi_{n,m}$ , the SAR raw signal can be expressed as [9]:

$$y = \sum \sum c_{n,m} \psi_{n,m}, \tag{1}$$

where the orthonormal wavelet coefficients are given by the inner product:

$$c_{n,m} = \langle \psi_{n,m}, y \rangle. \tag{2}$$

In order to compute a separable two-dimensional wavelet decomposition of an image, one-dimensional quadrature mirror filters are used, in both horizontal and vertical directions, combined with downsampling. In multilevel octave-band decomposition, the coarse resolution image is then further decomposed in the same way (see Fig. 2). The tree in Fig. 3 is then spawned by the scaling/wavelet filter pairs.

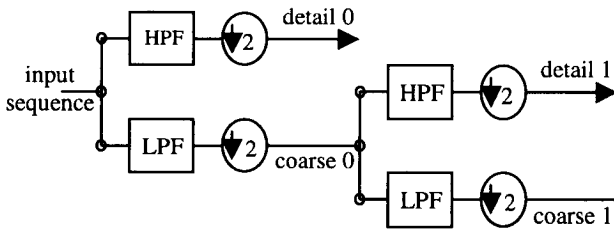


Fig. 2: Octave-band filter banks

To construct a finite code, each decomposition coefficient has to be approximated by a quantized variable  $\hat{c}_{n,m} = Q(c_{n,m})$ . An entropy constrained scalar quantizer has to be designed in such a way to minimize

the entropy of the quantized coefficients for a given distortion rate

$$D = \| y - \hat{y} \|^2 = \sum_{n,m} |c_{n,m} - \hat{c}_{n,m}|^2. \tag{3}$$

The distortion rate depends on the choice of the orthonormal basis and of the quantizer  $Q$ .

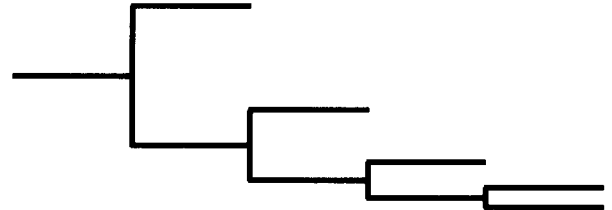


Fig. 3: Wavelet decomposition tree

An advantage of the application of a multiresolution decomposition is that we can use different quantizers and associated entropy coders, optimized for the statistic of each frequency band of wavelet coefficients. A bit allocation algorithm can then be used to distribute bits among the subbands.

A popular bit allocation criterion is given by [10]:

$$R_i = R + \frac{1}{2} \left( \log_2(w_i \sigma_i^2) - \sum_{j=1}^N \alpha_j \log(w_j \sigma_j^2) \right) \tag{4}$$

where  $R$  is the desired overall bit rate,  $R_i$  is the bit rate for the  $i$ th subband,  $\sigma_i^2$  is the variance of the  $i$ th subband,  $\alpha_i$  is the relative area of the  $i$ th subband

(normalized so that  $\sum_{i=1}^N \alpha_i = 1$ ), and  $w_i$  are weighting

factors accounting for the variable gain effects of the inverse transform among different subbands.

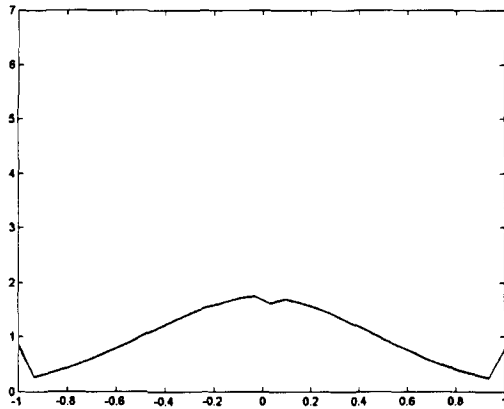
Given the bit allocation (bit rate) for each subband, the continuous-valued wavelet coefficients are converted to a set of symbols that can be transmitted with the available bits. As far as the choice of the quantizer is concerned, it is well known that at low bit rates uniform quantizer is not optimal [11]. A non-uniform quantizer consists in quantizing to zero the coefficients whose amplitude is outside a proper interval  $[-T, T]$  and uniformly quantizing the others. This is an optimal entropy constrained quantizer if the decomposition basis is chosen so that many coefficients are close to zero and few of them have a large amplitude. The position of zero versus nonzero quantized coefficients is stored in a



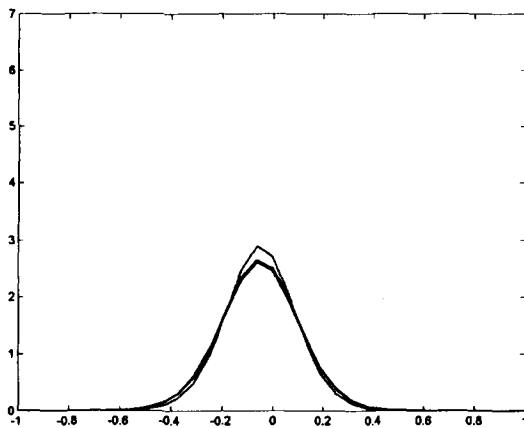
binary significance map. This map is commonly recorded with a run length coding, that is entropy encoded.

The wavelet coefficients are scanned in a predefined order, in such a way to properly exploit the energy correlation properties of the wavelet coefficient at different scale levels. In the same scanning order the amplitudes of the nonzero quantized coefficients are also entropy encoded with a Huffman or an arithmetic coding, and transmitted together with the coded map.

The total number of bits necessary to encode a data frame is then given by the number of bits necessary to encode the significance map plus the number of bits necessary to encode the significant wavelet coefficients. Of course, the total bit rates decreases as the coefficients *pdf*  $p(x)$  becomes more peaked, that is the number of significant coefficients decreases and the map becomes more correlated.



(a)



(b)

Fig. 4: (a) *pdf* of the raw data (b) *pdfs* of the wavelets coefficients for different subbands.

In our case, due to the particular nature of the SAR raw data to be quantized, the *pdf* of the wavelet coefficients in each subband is not as peaked like in common image compression applications (see Fig. 4), so that the number of significant coefficients is not very low and the bit rate required for map coding is commonly very close to one.

The wavelet transform, however, is only one of many possible transforms that are derived from the same scaling/wavelet filter pairs. A generalization of the wavelet transform basis is given by the family of the wavelet packets basis [12], whose complete decomposition tree (uniform decomposition) is shown in Fig. 5.

This generalization of the traditional wavelet filter bank structure permits the representation of a signal by one of many bases given by the ensemble of all possible scalings and translations of the same scaling/wavelet filters, that optimizes a given quality criterion. This *best* basis can be then obtained by properly pruning the complete wavelet packet tree (see Fig. 6) [12].

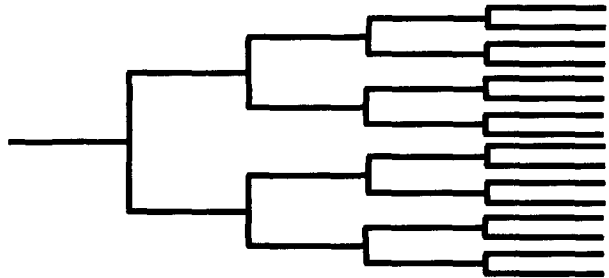


Fig. 5: Wavelet packets complete tree

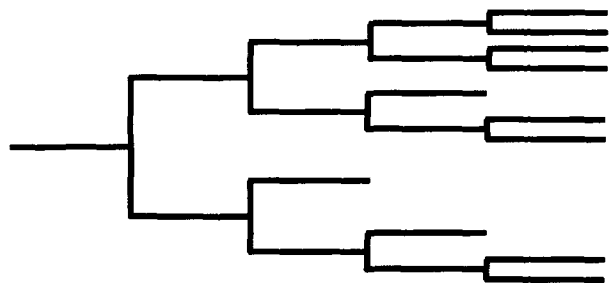


Fig. 6: Wavelet packets pruned tree

The *pdfs* of the subband coefficients obtained by applying a 3-level complete tree wavelet packets decomposition are shown in Fig. 7. The different statistical distribution of the coefficients in different subbands is evident.

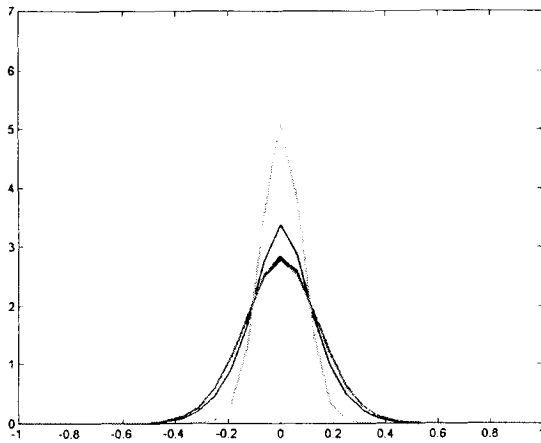


Fig. 7: pdf of the coefficients for different subbands obtained by a 3-level wavelet packets decomposition

#### SIGNUM CODING OF RAW DATA

Let us consider the expression of the raw signal  $\tilde{u}(t)$  received on board from the SAR antenna, in its analytical form:

$$\tilde{u}(t) = A(t) \exp\{j[2\pi f_0 t + \zeta(t)]\} + n(t) = u(t) + n(t), \quad (5)$$

constituted by a deterministic part  $u(t)$ , and by an additive Gaussian random component  $n(t)$  with zero mean, and variance  $\sigma_n^2$ .  $f_0$  is the intermediate frequency, and  $A(t)$  and  $\zeta(t)$  are envelope and phase of the analytical signal. Let us denote with  $B$  the signal bandwidth.

To quantize the received signal (5) at one bit is equivalent to take the signum of its real ( $\Re$ ) and imaginary ( $\Im$ ) parts. It has been shown [7] that, when the noise power is sufficiently large with respect to the signal power, like in common SAR applications, the signum coding (SC) quantization renders its spectrum as the sum of partial spectra related to the odd signal harmonics  $v_m$ , that are centered at frequencies  $j^{m-1}mf_0$ , and exhibit bandwidths  $mB$ , proportional to their order. Consequently, the partial spectra will be positioned accordingly to the values assumed by the three parameters  $f_0$ ,  $B$ , and  $m$ . In particular for an assigned value of  $B$ ,  $f_0$  can be properly chosen in such a way to avoid the overlapping between the most significant harmonics.

The normalized amplitude of the Fourier transform (FT) of the SC signal relative to a point scatterer response, averaged over the noise, with  $B = 6$  MHz and  $f_0 = 20$  MHz, is shown in Fig. 8(a). It is possible to distinguish the fundamental harmonic  $v_1$ , whose FT is

equal, but for a constant factor, to the FT of the original signal  $u$  (see Fig. 8(b)), and all the other (most significant) harmonics  $v_3, v_5, v_7, v_9, v_{11}$ , whose central positions on the frequency axes, and whose relative bandwidths assume the predicted values. Note that the value of  $f_0$  has been chosen sufficiently high, in such a way to avoid the overlapping of the harmonics of order lower than thirteen.

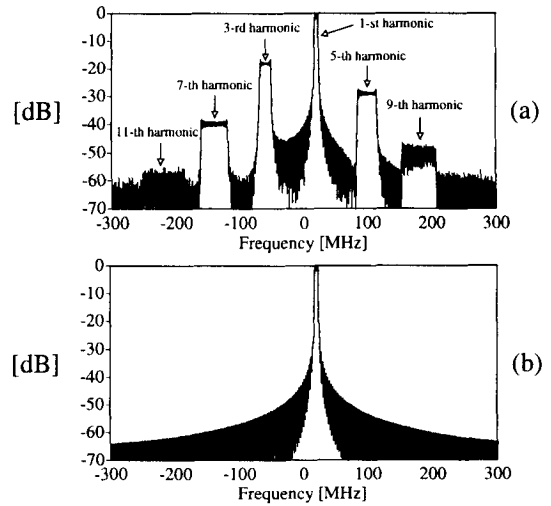


Fig. 8: FT normalized amplitude of a point scatterer response obtained by: (a) SC data; (b) conventionally quantized data

In the practical cases the raw signal is available in a sampled form, then the sampling effect has also to be considered. Sampling at rate  $f_s$  renders in fact the signal spectrum periodic of period  $f_s$ , thus determining aliasing between harmonics.

Very often the SAR raw signals are available in the baseband carrier-quadrature form ( $f_0 = 0$ ). In this case, all the partial spectra, for each  $m$ , are centered on the origin of the Fourier domain, while their bandwidth  $mB$  is still proportional to the order  $m$ . If we choose a sampling frequency  $f_s \geq 2B$ , we can observe (see Fig. 9) that all the harmonics spectra are overlapped each other in the low-frequency part (between  $-B/2$  and  $B/2$ ), but no aliasing between  $v_1 \propto u$  and the replicas of  $v_3$  is present in this range. Note that, in order to obtain such a behaviour, we should sample the signals at a rate at least 2 times larger (along each image dimension) than the Nyquist frequency  $B$ , usually adopted in the conventional case. This leads to an SC data dimension that is almost the same of a 4-bit quantized signal sampled at the proper sampling frequency  $B$ , and that is half respect to a 8-bit quantized signal sampled at  $B$ .

In this the third harmonic can be partially filtered out

by the processing for the SAR image formation. Aliasing effect due to higher order harmonics is very negligible due to their negligible amplitude.

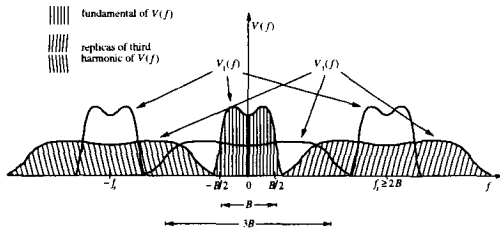


Fig.9: DFT normalized amplitude of a low pass response

### NUMERICAL EXPERIMENTS

To test the performance of the presented methods, a set of SAR raw data of the ERS-1 mission, relative to Fleevoland (The Netherlands) test site, has been considered. The considered data frame is of 2048x4098 samples in the azimuth and range directions respectively.

Different quality parameters have been computed on the SAR images, obtained after the processing of the compressed data. In particular, the most meaningful parameter is the signal to noise ratio (SNR), computed as the reciprocal of the normalized mean square error between the (complex) image obtained by coherently processing conventionally 5-bits quantized data  $y$  and the one obtained by compressed data  $\hat{y}$ . It can then be expressed as:

$$SNR = \frac{\text{SAR image power}}{\text{quantization noise power}} = \frac{\|G(y) - G(\hat{y})\|}{\|y - \hat{y}\|} \quad (6)$$

where  $G$  is the operator performing the SAR image formation.

It has to be noted that the SNR computed on the focused images is certainly higher of the one computed on the raw data, due to SAR processing that processes coherently the useful signal and incoherently the quantization noise.

Other quality parameters are the integrated side lobe ratio (ISLR), and the image dynamic range, which is strictly related to the radiometric resolution [7].

The results obtained by using the BAQ Lloyd Max compression technique are summarized in Table 1.

In Table 2 are reported the results obtained by using the compression technique using a complete 3 levels wavelet packet decomposition (or uniform wavelet

decomposition), and the bit allocation given by (4).

As far as SC techniques is concerned, we first consider the images obtained starting from SC data sampled at a rate tailored on the conventional signals, i.e., we do not neither oversample nor interpolate the involved signals. Then, we consider 2:1 oversampled SC data (i.e., using a double sampling frequency along azimuth and range directions), providing improved quality images. The obtained binary data frames are run length encoded and entropy encoded. Obtained results are shown in Table 3. It can be noted that the performance of the method is not very satisfactory from the point of view of the achieved data rate reduction for a fixed SNR value. However it has to be considered that its main advantage is the possibility of performing real time processing using a very simple hardware [8]. Moreover, better results can be achieved if more efficient compression techniques, exploiting the higher correlation introduced by oversampling, are used for coding the 2:1 oversampled data frame. Then an improvement is expected by applying one of the several techniques developed for fingerprints compression [13], and by using iterative algorithms for a bandpass signal reconstruction from zero crossings by projections on convex sets [14]. These last points need to be further explored in future work.

bps (b/s)	SNR (dB)	ISLR range (dB)	ISLR azimuth (dB)	Dynamic Range (dB)	Rad. res. (dB)
Ref. 4.82		-22.53	-17.59	57.43	21.73
2	11.11	-22.56	-17.61	54.95	20.84
1.5	8.86	-22.51	-17.63	53.90	20.47
1.	5.44	-23.42	-17.62	52.13	19.84

Table 1: Quality parameters computed on the images (after SAR processing) obtained by BAQ Lloyd Max compressed raw data.

bps (b/s)	SNR (dB)	ISLR range (dB)	ISLR azimuth (dB)	Dynamic Range (dB)	Rad. res. (dB)
Ref. 4.82		-22.53	-17.59	57.43	21.73
2.05	11.46	-22.31	-17.44	54.19	20.57
1.51	8.82	-22.77	-17.79	54.68	20.74
1.02	5.43	-23.16	-16.98	54.77	20.77

Table 2: Quality parameters computed on images (after SAR processing) obtained by wavelet packets coded raw data.

bps (b/s)	SNR (dB)	ISLR range (dB)	ISLR azimuth (dB)	Dynami c Range (dB)	Rad. res. (dB)
Ref. 4.82		-22.53	-17.59	57.43	21.73
1.	5.27	-21.76	-17.09	53.36	20.28
2.6	8.44	-21.93	-17.15	57.18	21.64

Table 3: Quality parameters computed on images (after SAR processing) obtained by SC coded and SC coded upsampled data.

#### REFERENCES

- [1] R. Kwok, W. T. K. Jhonson, "Block Adaptive Quantization of Magellan SAR Data", *IEEE Trans. Geosci. Remote Sensing*, GE-27, pp. 375-383, 1989.
- [2] U. Benz, K. Strodl, A. Moreira, "A Comparison of Several Algorithms for SAR Raw Data Compression", *IEEE Trans. Geosci. Remote Sensing*, GE-33, pp. 1266-1276, 1995.
- [3] J. M. Moureaux, P. Gauthier, M. Barlaud, P. Bellemain, "Raw SAR Data Compression Using Vector Quantization", *International Journal of Remote Sensing*, 16, n. 16, 1995.
- [4] P. Bellemain, D. Lebedeff, P. Mathieu, M. Barlaud, C. Lambert-Nebout, "Raw SAR Data Compression", *EUSAR 96*, pp. 281-284, Konigswinter, Germany, 1996.
- [5] J. W. Owens, M. W. Marcellin, B. R. Hunt, M. Kleine, "Compression of Synthetic Aperture Radar Video Phase History Data Using Trellis-Coded Quantization Techniques", *IEEE Trans. on Geosci. Remote Sensing*, pp. 1080-1085, GE-37, 1999.
- [6] N. J. Jayant, P. Noll, "Digital Coding of Waveforms", Englewood Cliffs, NJ: Prentice Hall Inc. 1984.
- [7] V. Pascazio, G. Schirinzi, "Synthetic Aperture Radar Imaging By One Bit Coded Signals", *IEE Electron. & Commun. Eng. Journal*, 10, pp. 17-28, 1998.
- [8] G. Cappuccino, G. Cocorullo, P. Corsonello, G. Schirinzi, "Design and Demonstration of a Real-Time Processor for One Bit Coded SAR Signals", *IEE Proc. Radar, Sonar and Navigation*, 143, pp. 261-274, 1996.
- [9] S. G. Mallat, "A Theory of multiresolution signal decomposition", *IEEE Trans. Pattern. Anal. Machine Intell.*, 11, pp. 674-693, 1989.
- [10] T. W. Ryan, L. D. Sanders, H. D. Fisher, A. E. Iverson, "Image Compression by texture modeling in the Wavelet Domain", *IEEE Trans. On Image Proc*, 5, pp.26-36, 1996.
- [11] S. Mallat, F. Falzon, "Analysis of Low Bit Rate Image Transform Coding", *IEEE Trans. Signal Processing*, SP-46, pp.1027-1042, 1998.
- [12] R. R. Coifman, M. V. Wickerhouser, "Entropy-Based Algorithms for Best Basis Selection", *IEEE Trans. Inform. Theory*, 38, pp. 713-718, 1992.
- [13] M. D. Swanson, A. H. Tewfik, "A Binary Wavelet Decomposition of Binary Images". *IEEE Trans. on Image Processing*, 5, n. 12, 1996.
- [14] N. E. Hurt, "Phase retrieval and Zero Crossings", Kluwer Academic Publishers, Dodrecht (NL), 1989.

## Compression of Temporal Series of Registered SAR Images

Grégoire Mercier<sup>(†)</sup>, Joseph Mvogo<sup>(††)</sup>,  
Marie-Catherine Mouchot<sup>(†)</sup>, Guy Cazuguel<sup>(†)</sup> and Jean-Paul Rudant<sup>(‡)</sup>

(†) École Nationale Supérieure des Télécommunications de Bretagne, Dépt. ITI.  
Technopôle de Brest-Iroise – BP 832 – 29285 Brest Cédex – France  
Tel: +33 2 98 00 10 57; fax: +33 2 98 00 10 98  
e-mail: gregoire.mercier@enst-bretagne.fr

(††) IUT de Douala, BP 8698 Douala. Cameroun.  
Fax: +237 40 24 82,  
e-mail: mvogo@hotmail.com

(‡) Institut Francilien des Géosciences, Université de Marne-la-Vallée,  
5 bd Descartes, 77 454 Marne la Vallée Cedex 2, France.  
Tel: +33 1 49 32 90 71; fax: +33 1 49 32 91 37  
e-mail: rudant@univ-mlv.fr

### ABSTRACT

In this paper, a new method for compressing with loss temporal series of SAR images is proposed. The aim of this compression strategy is to compress images as and when acquired. Then, a reference image is used as an input in the compression process and all the images of the scene have to be co-registered. Then, the image acquired at time  $t_0 - 1$  is used as reference for compressing the image acquired at time  $t_0$ , and so on. The compression is achieved through affine transformations, comparable to the ones used in fractal coding, but applied in a non-convergent way. Blocks in the image to be compressed are defined by a non-overlapping recursive partition. Those blocks are replaced by blocks taken from the reference image at the same location, on which affine transformations, containing isometries and grey level adjustments, have been applied. In order to avoid inherent low-pass effect and texture restitution bias of compression algorithm, grey level adjustment have been calculated to minimize  $\mathcal{L}^1$ -based error criteria. This algorithm is very powerful and outperforms classical compression algorithms (such as JPEG or wavelet-based compression methods) at high compression ratio with poor loss of information. Moreover, the compressed code can be viewed as a description process which points out evolution between the image to be compressed and the reference image. Some results are presented with ERS images of French Guyana, which can be compressed at 40 : 1 while still remaining of sufficient quality for land use monitoring.

### INTRODUCTION

Images are of interest for a large number of applications. In teleconferencing, compression allows two simple PC to communicate through telephonic support. In medical imaging, it is possible, thanks to adapted compression to share results of examinations between doctors to help non-specialists into their diagnostic. To perform environment monitoring, compression is to be considered to manage a large amount of data and to perform multi-temporal analysis.

Nevertheless, the main core of image compression technology consists of 3 processing steps: pixel transforms (such as DCT or DWT), quantization (scalar or vectorial) and entropy coding (as the arithmetic encoding or LZW does) [1]. The next section will focus on problems yielded by such a low-pass filtering-based compression. Then, it is proposed, in the case where a set of co-registered SAR images has to be compressed, to adopt a multi-temporal point of view. This knowledge based strategy allows to compress images as and when acquired and may be viewed as a lossy description process between an image acquired at time  $t_0 - 1$  and the image to be compressed, acquired at time  $t_0$ .

### COMMON COMPRESSION PROBLEMS

Most of the lossy image compression algorithms achieves compression through a low-pass filtering strategy. Orthogonal transforms present information in a frequency point of view, and most of the quantization and bit al-

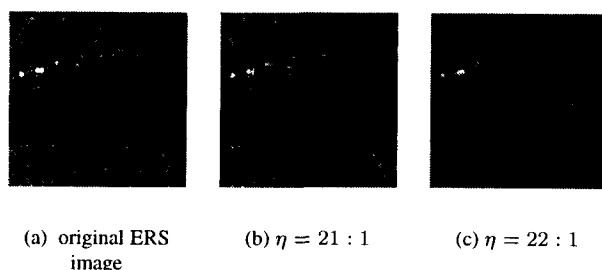


Fig. 1: Example of compression of ERS image: JPEG compression (b), Davis's SQS compression (c). SAR ERS images ©ESA.

location techniques are based on Human Visual System (HVS) which acts as a low-pass filter. Moreover, high frequencies are often considered as noise signatures that may be filtered. The quantization table that is in use for compressing grey level images with the JPEG standard is more selective for high frequency DCT coefficients than for the lowest frequency coefficients (99 for the highest DC coefficient while 11 for the lowest DC coefficient of the  $8 \times 8$  DCT blocks) [2]. In [3], Antonini & al. apply a bit allocation technique to perform the wavelet-based compression. 0.5 bpp are allocated for finest scale wavelet coefficients (high frequency equivalent) while 2 bpp are dedicated to the coarse scale (low frequency equivalent). Efficient wavelet-based compression algorithms, that use efficient partitioning of coefficients, such as the Zerotree concept [4], SPIHT [5] or the SFQ [6], are based on an efficient encoding strategy of zero-value (or insignificant) coefficients.

Fig. 1 shows an example of a compression at  $\eta \approx 20 : 1$  of ERS-1 rice cultures image acquired over French Guyana. This acquisition is dedicated to monitor agriculture activities and extensions. Then, it is necessary to distinguish forest areas and cultivated fields. This point is achieved by a texture analysis. Moreover, field extension may be characterized by structure analysis of the speckled image. It is shown that the JPEG compression does not fit remote sensing problems. On image (b), rice field surface estimation would be achieved with a dramatic bias that is appalling. Also, the image (c) does not suffer from blocky effects. Nevertheless, the smoothing effect that is yielded with the strong quantization of significant wavelet coefficients does not allow any texture analysis that may distinguish forest and fallow fields.

## MULTI-TEMPORAL COMPRESSION

The multi-temporal point of view for compressing a set of images that have the same location and have been acquired at different dates, may be used efficiently to avoid the low-pass effect of strong compression. In order to

compress a set of images as and when acquired, a reference image is used as a blockwise basis and the image to be compressed is describe with the knowledge of the reference image. The strategy is closed to the Vector Quantization (VQ) strategy except that in the case of the use of a reference image, blocks may be considered as truth samples as they have been acquired by a given captor. The basic skim of mutli-temporal compression of co-registered images is shown on fig. 2, and points out concepts of recursive partition, block transformation and error criteria.

## Recursive partition

Blocks of the image to be compressed and blocks of the reference image are defined by a recursive partition. The partition is very similar to the quadtree partition, but has been upgraded with new shapes such as triangles and rhombs [7]. During the compression step, large blocks are considered to be substituted by blocks of the reference image. According to an error criteria, if the substitution between two blocks is too erroneous, the current block is decomposed in order to yield the most homogeneous sub-blocks, choosing between the quadtree way (*i.e.* four smaller blocks) or some triangles. The substitution process continues with the smaller blocks until limited error or one of those smaller blocks reaches the smaller size (fig. 2).

## Block transformation

Each blocks of the reference image is transformed with an affine transformation that fit the template (1) :

$$w \begin{pmatrix} x \\ y \\ z \end{pmatrix} = \begin{pmatrix} a & b & 0 \\ c & d & 0 \\ 0 & 0 & s \end{pmatrix} \begin{pmatrix} x \\ y \\ z \end{pmatrix} + \begin{pmatrix} t_x \\ t_y \\ o \end{pmatrix} \quad (1)$$

Affine transforms are compactly encoded if the  $([a \ b] [c \ d])$  matrix, that characterizes geometric transformation, is limited to height possibilities (Identity, rotations of  $\pi/2$ ,  $\pi$  and  $3\pi/2$ , and horizontal, vertical and

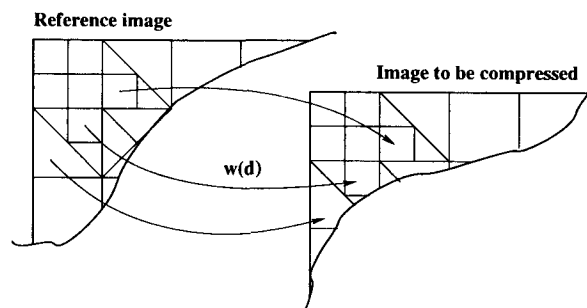


Fig. 2: General skim of co-registered image compression.

diagonal symmetries). Massic transformation, as written with the scale factor  $s$  and the offset  $o$ , has to be scalar quantized. The translation  $(t_x, t_y)$  is to be applied to the block of the reference image (denoted  $d$ , as inspired by the *domain blocks* concept of fractal encoding) to fit current location of the block to be substituted (denoted  $r$ , for *range block*).

### Error Criteria

Given a block  $r$  to be substituted by  $d$  for encoding, an affine transform  $w$  have to be found in order to minimize the distance between  $r$  and  $w(d)$ . The minimization is achieved in two steps: first, find the best isometry (geometric transformation) so that the structural properties of the two blocks  $r$  and  $d$  may match each other. Then, find the massic transformation  $(s, o)$  in order to minimize the MSE.

The isometry to be applied to  $d$  may be easily found thanks to a pre-classification step that was proposed by Fisher [8] for a quadtree-based fractal encoding. This attempts to find an isometry  $iso$  to each block in order to classify the block in to one of the 3 templates that orders grey levels means of each sub-blocks of size  $B/2 \times B/2$  if  $d$  is of size  $B \times B$ .

Then, if  $iso_d$  (respectively  $iso_r$ ) is the isometry to be applied in order to classify  $d$  (resp.  $r$ ) into one of the 3 classes, then  $iso_r^{-1} \circ iso_d$  is the isometry to be applied to  $d$  in order to fit  $r$ . Latter, pixels of the isometrically transformed block  $d$  will be indexed  $d_{iso(i)}$  instead of the original  $d_i$ .

Then, the massic transformation parameters  $(s, o)$  can be estimated directly in order to minimize the Mean Absolute Error (MAE), which is an  $\mathcal{L}^1$ -based error criteria that fit textured images:

$$E_{MAE} = \frac{1}{N} \sum_{i=1}^N |s d_{iso(i)} + o - r_i|. \quad (2)$$

where  $N$  is the number of pixels in  $r$  (typically  $B \times B$  for square blocks).

Optimal parameters may be estimated through a minimization problem. Let's consider a random variable  $X$  which has an expectation  $E[X]$ . The expression  $E[|X - a|]$  is minimum when  $a$  is the median of  $X$ .

Re-writing (2) as  $E[|(R - sD) - o|]$ ,  $o$  can be found to minimize MAE calculating the median of the random variable  $R - sD$ . Even if  $o$  may minimize exactly MAE, the evaluation of  $s$  is more difficult. Knowing that  $|s d_{iso(i)} + o - r_i| \leq |s d_{iso(i)} - r_i| + |o|$ , MAE can then be upper-bounded when  $s$  be the median of the random variable  $R/D$  (talking into consideration pixels  $d_{iso(i)}$  — realizations of  $D$  — not null).

Even if the algorithm finds the optimal affine transform, to fit the current range block, the error of the block matching may remain too high (over a threshold). In that case,

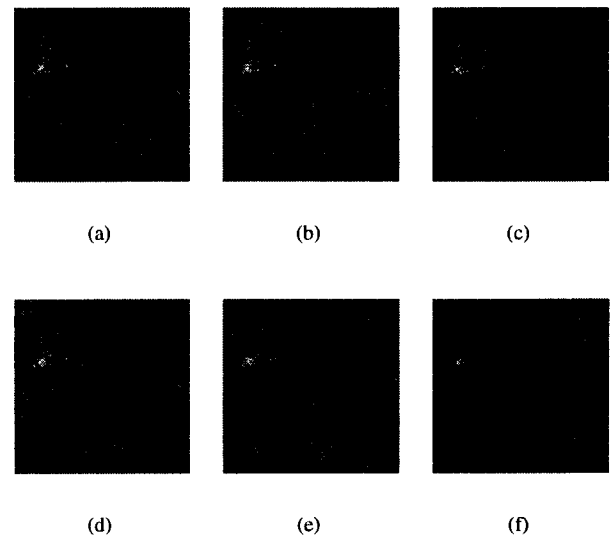


Fig. 3: Multi-temporal registered image compression. Original set (a, b, c). Compressed images (d)  $\eta = 36.5 : 1$ , (e)  $\eta = 38.6 : 1$ , (f)  $\eta = 39.4 : 1$ . SAR ERS images ©ESA.

the range block is decomposed, yielding new smaller blocks, and the algorithm continues the block matching with the new ranges (fig. 2).

### APPLICATION TO ERS IMAGES

Fig. 3 shows compressions of ERS-1 rice fields images, acquired over French Guyana. Compressions achieved by the affine transform-based formalism, have been associated with the  $\mathcal{L}^1$ -based error criteria. The aim the compression strategy is to compress images as and when acquired. Thus, a compressed image becomes reference for the next compression.

Then, images have been compressed at a compression ratio varying from 35 : 1 to 40 : 1, that means that the volume of the compressed code is between 35 to 40 times smaller than the volume of the uncompressed one. It is interesting to note that no blocking effect can be distinguished easily, instead of the block-based approach. In fact, the use of MAE allows to reconstitute textures with a better accuracy than the simple MSE so that no smoothing is introduced. Nevertheless, even if structures are well localized, and the visual restitution is much more satisfactory, the pixel to pixel restitution is much more erroneous with the MAE criteria than the standard MSE criteria.

The MAE criteria requires median calculations to evaluate  $(s, o)$  parameters and to decide the decomposition of the recursive partition. Then, MAE complexity may be considered as appalling. Nevertheless, the co-registered image compression is based on a domain-range substitu-

tion with blocks that have the same location. Finally, less a minute is required for compressing  $1024 \times 1024$  16 bit images.

### ANALYSING THE COMPRESSED CODE

Affine transforms achieved a link between domains of the reference image and ranges of the image to be compressed. This link includes scale and offset adjustments that transform  $d$  to fit  $r$  grey level distribution. Then, affine transforms can be viewed as a compact terrain modification description that is observed between the two images. Thus, scale factors may be considered as modification descriptor and time analysis may be investigated directly into the compressed code.

Fig. 4 shows such an analysis of the compressed stream. In the description process between the reference image and the image to be compressed, scale factors of affine transformations have been stressed. Considering values of  $s$  as pixel-values, it is possible to draw an image of time-modification that is registered with the image to be compressed. Image (a) may be interpreted as contrast evolution between images (a) and (b) of fig. 3, and image (b) as the evolution between images (b) and (c) of fig. 3. Then, scale factor images proved to point out ground modification of rice fields, which may be very useful as this underlined is achieved in 40 times smaller memory space than the one required to analyse one of the two images.

### CONCLUSION AND FUTURE WORK

While classical compression techniques are divided in three steps, transformation-quantization-entropy coding, that yield a low-pass effect compression, affine transform-based multi-temporal compression achieves compression of co-registered images through a lossy de-

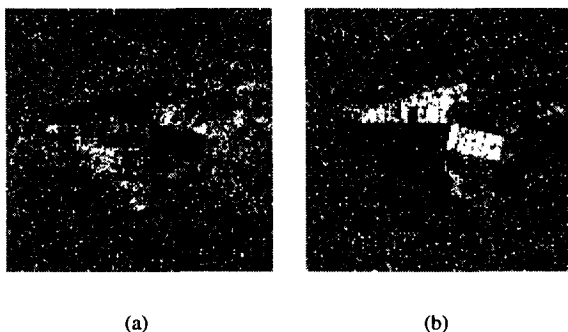


Fig. 4: Ground evolution pointed out into the compressed code. (a) scale factor values of code stream that describe image (b) from (a) of fig. 3. (b) describes the evolution between images (b) and (c) of fig. 3.

scription of structures and textures. Lost may be considered as lack of structural definition (due to the recursive partition that may be too rigid) or as an erroneous texture restitution that fits a  $\mathcal{L}^1$ -based criteria (through the use of the scale factor  $s$ ).

The co-registered multi-temporal compression appears to be a very simple method, even with the use of  $\mathcal{L}^1$ -based distance criteria. This method may attract attention thanks to its power of describing temporal evolution of two successive images into the compressed code.

This algorithm may indeed be upgraded with the use of a Voronoï partition that is much more adaptive than the one used in [7]. In order to move this description-based compression method to an object-based encoder, it should be interesting to select parts of images that may be considered as modified.

### ACKNOWLEDGMENT

The authors would like to thank European Space Agency for the acquisition of ERS images, that has been possible through the project number A03\_160, associated with J-P. Rudant of the university of Marne La Vallée, France.

### REFERENCES

- [1] O. Egger, P. Fleury, T. Ebrahimi, and M. Kunt. High performance compression of visual information—a tutorial review— part I: Still pictures. *Proceedings of the IEEE*, 87(6):976–1011, June 1999.
- [2] W. Pennebacker and J-L. Mitchell. *JPEG Still image compression standard*. Van Nostrand Reinhold, NY, 1993.
- [3] M. Antonini, M. Barlaud, P. Mathieu, and I. Daubechies. Image coding using wavelet transform. *IEEE transactions on image processing*, 1(2):205–220, April 1992.
- [4] J. Shapiro. Embedded image coding using zerotrees of wavelet coefficients. *IEEE transactions on signal processing*, 41(12):3445–3462, december 1993.
- [5] A. Said and W. Pearlman. A New Fast and Efficient Image Codec Based on Set Partitioning in Hierarchical Trees. *IEEE transactions on Circuits and Systems for Video Technology*, 6, June 1996.
- [6] Z. Xiong, K. Ramchandran, and M. Orchard. Wavelet packet image coding using space-frequency quantization. *IEEE transactions on image processing*, 7(6):892–898, June 1998.
- [7] G. Mercier, M-C. Mouchot, and G. Cazuguel. Multitemporal SAR image compression. In *ICIP*, 1998.
- [8] Y. Fisher. *Fractal Image Compression: theory & application*. Springer-Verlag, 1994.



## Wavelet based ScanSAR Image Compression Minimizing Block Effects

Jens V. Fischer, Ursula C. Benz

German Aerospace Center (DLR), Institute of Radio Frequency Technology,  
Oberpfaffenhofen, P.O. Box 11 16, D-82230 Wessling

Phone: (+49) 8153-28-3057, Fax: -1449, Email: jens.fischer@dlr.de

### ABSTRACT

ScanSAR images are important products of modern spaceborne SAR systems. A wide swath is covered during one single data take.

Usual processing of ScanSAR images with a high number of looks not only reduces speckle but also leads to data compression. However, the amount of data can be further reduced, if an appropriate ScanSAR data compression is applied.

In our paper, we propose a new wavelet based compression technique, which adapts to the ac energy distribution in ScanSAR images and minimizes artifacts due to compression. Special attention is paid to reduce block effects.

Our technique is tested on ScanSAR data of RADARSAT and the SIR-C space shuttle mission. Compressing the SIR-C ScanSAR scene of Chickasha/Oklahoma, USA with factor 1:8, we achieve an improvement in the overall signal-to-distorsion-noise ratio (SDNR) from 29.7 dB to 48.03 dB.

### 1. INTRODUCTION

ScanSAR is an important mode of most future spaceborne SAR sensors. Compared to stripmap mode, a much greater coverage of the earth surface can be achieved by mosaicking several sub-swaths. For example, for the ASAR system of ENVISAT a swath width up to 450 km is intended.

SAR images acquired in ScanSAR mode are mainly<sup>1</sup> processed by multi-looking which creates detected images of reduced speckle. Using multi-looking, a certain data compression is automatically performed. The more looks are used the higher is the achieved compression ratio. Furthermore, due to speckle reduction multi-looking increases inter-pixel correlations. Higher correlation between pixels means increase in data redundancy, which provides good precautions for further data compression.

We use ScanSAR images of two different SAR platforms to test our wavelet based data compression technique. The SIR-C image is more difficult to

compress compared to the RADARSAT image due to higher fluctuations in data dynamic. We show that our method overcomes difficulties in both data sets.

Our emphasis in results is not only laid to a high signal-to-distorsion-noise ratio and improved reconstruction of point targets, but also to a scene independent noise to allow proper calibration of SAR products.

### 2. SCANSAR DATA CHARACTERISTICS

The used RADARSAT image in this study has a geometric resolution of 80 meters in both, azimuth and slant range. The scene is of an extent of 355 km in azimuth and 190 km in range. The original data set possesses a sample distance of 100 meters. It is processed with 2 looks in azimuth and 4 looks in range. Filtering has been applied to remove scalloping effects. In this example, we measure no explicit influence of the applied anti-scalloping filter.

The SIR-C data set depicts a scene around Chickasha/Oklahoma, USA [1]. It has 5 azimuth looks and 5.68 looks in range direction. The resolution in ground range deteriorates from 148 meters in far range to 331 meters in near range. The azimuth resolution ranges from 230 meters in near range to 270 meters in far range. Many strong single scatterers such as in the city area cause high fluctuations in data dynamics, which make a dedicated compression technique necessary.

#### *Inter-pixel correlations*

Due to multi-looking, an increase in inter-pixel correlations can be observed in ScanSAR data compared to data acquired in stripmap mode (Fig. 1).

#### *Energy concentration in subbands*

Decreased geometric resolution and reduced speckle in multi-look images enable better energy packing compared to stripmap images if a wavelet transform, for instance as in our approach, is applied. In ScanSAR images, most of the ac energy is concentrated in the LL (low-pass/low-pass) subband which allows a dedicated bit assignment. The ac energy in single-look complex

<sup>1</sup> ScanSAR images can also be complex if interferometric or polarimetric applications are considered.

X-SAR stripmap data is not only concentrated in LL subband, half this amount can be found in the other subbands, too. In Fig. 2, we compare the energy content of the LL subband (100 percent) to energy contained in other subbands. Best energy packing is achieved for ScanSAR images.

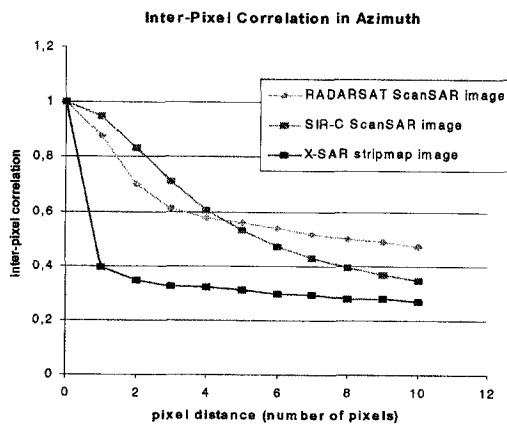


Fig. 1: Inter-pixel correlation in images. The ScanSAR images (RADARSAT and SIR-C) are higher correlated from pixel to pixel compared to a single-look complex X-SAR stripmap image.

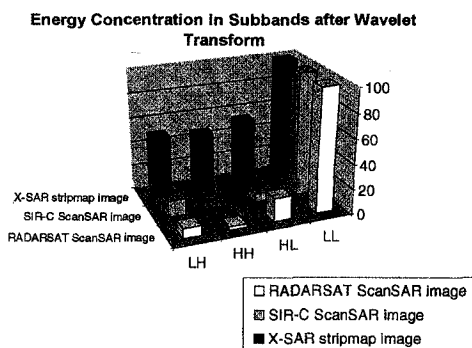


Fig. 2: AC Energy concentration in image subbands. The ScanSAR images (RADARSAT and SIR-C) show better energy packing compared a single-look complex X-SAR stripmap image.

A certain subband can be considered as more important than others if its ac energy is relatively high compared to the other ones. More quantization levels (number of bits) are assigned to those subbands of greater importance. The larger the ratio among the subband energies the more efficient is the bit allocation performed. The used scalar quantization, however, only allows integer number of bits to be assigned. This implies that minor energy ratios between subbands cannot be fully covered.

### 3. COMPRESSION TECHNIQUE

ScanSAR scenes are of large extent. Due to limited memory, it is not possible to hold the entire ScanSAR image in memory and to perform calculations at the same time. The image must therefore be compressed blockwise. We measured no significant influence of the chosen image block size to energy packing and hence to the compression performance. We therefore propose to choose the size of image blocks as large as possible aiming to minimize computation time. Our method is applied to each image block in the following manner.

After transforming the image block into wavelet domain, a quantization of wavelet coefficients is applied to each subband. All coefficients of a certain subband are quantized with the same number of bits by a block adaptive linear quantizer. The number of bits for a subband is read off a table of bit masks.

#### Wavelet transform

We perform a one iteration wavelet transform using a Daubechies-8 wavelet. Other wavelets than the Daubechies are of course imaginable [2]. More than 8 coefficients slightly improve the compression performance [2] but lead to enhanced computational expense. Sufficient energy packing can be reached by only performing one wavelet iteration. In our approach, it is not possible to achieve significant better compression results by iterating the wavelet transform more than once. This is mainly due to the fact that – in case the LL subband is again subdivided into four subsubbands – an even enhanced refinement in bit allocation is necessary to use the additional energy packing. This, however, cannot be done as only integer number of bits can be assigned.

The wavelet transform has to be performed onto overlapped image blocks in order to ensure no invalid pixels<sup>2</sup> within a wavelet transformed image block. An overlap of eight pixels – the number of wavelet coefficients – is sufficient.

#### Quantization

The quantization of a wavelet transformed image block is performed by quantizing each subband separately. A certain subband is quantized by subdividing its coefficients into small quantization blocks, e.g. 8 by 8 coefficients. A subdivision into small blocks is necessary due to the changing data statistic within the subband. The coefficients within each small

<sup>2</sup> A wavelet transform is leads to invalid pixels in marginal areas within the subbands.

quantization block are quantized using a certain number of bits which is read off a bit mask.

#### *Bit mask generation*

To compress a ScanSAR image in wavelet domain, we need an optimal bit mask consisting of four numbers of bits – each for one of the four subbands. The four numbers give a mean number of bits, which – together with the header information – determine the overall compression ratio.

The bit mask is fix for a certain compression ratio; it does not change from image block to image block. We also tested bit masks adapted to each image block. This approach showed no significant improvements.

As a bit mask reflects the typical ac energy packing gained by our wavelet transform, the bit mask can be used for all data of the same SAR platform processed with a certain processing technique, e.g. multi-looking with certain number of looks.

In order to find a suitable bit mask to each data type (SAR platform and processing technique) and each compression ratio, we use a test procedure, which numerically optimizes bit masks by applying test compressions onto small image pieces.

#### 4. MINIMIZING BLOCK EFFECTS

In wavelet domain, the image content is reflected in each subband. And, as described above, each subband is compressed using the same constant number of bits. In case nothing is undertaken to adapt to the changing dynamic within the subbands, those quantization blocks including high dynamic will end up with increased compression noise than others. This finally makes a blocking structure visible indicating the subdivision into quantization blocks. Those block effects can at first be observed in SDNR maps (Fig. 4 and Fig. 12) – a very sensitive measure to show differences between original and reconstructed images. In more severe cases, a high compression ratio for example, the blocking structure even becomes visible in the reconstructed image ruining a homogeneous reconstruction quality across the image.

A simple first approach to minimize block effects is to separate the image content in each subband into 'foreground', i.e. data of high dynamic, and 'background', i.e. data of low dynamic.

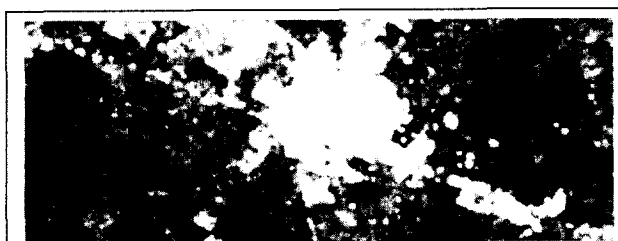
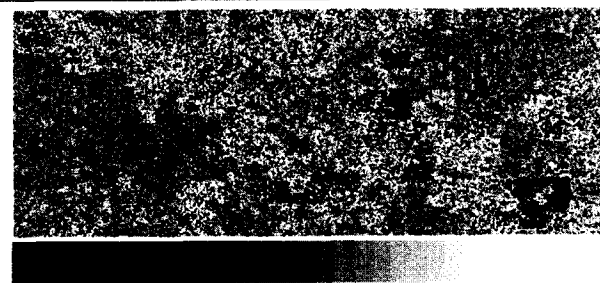


Fig. 3: Detail image in SIR-C ScanSAR image. The city area includes many single scatterers which create high dynamic



$\leq 20$  SDNR [dB]  $\geq 70$

Fig. 4: SDNR map showing sensitively differences between the original (Fig. 3) and the reconstructed image part. Block effects in the environment of high dynamic become visible, compression rate was 1:8.

Normally, those data in SAR images which show very high dynamic compared to their neighborhood make an percentage of far below one percent of the SAR data set. In our first approach for block effect minimizing, we separate in each subband the upper one percent of wavelet coefficients which show highest dynamic in the subband compared to the other coefficients (Fig. 5 to Fig. 8).



Fig. 5: A map corresponding to the detail image (Fig. 3) indicating where high dynamic data are located (high dynamic =1 (white), low dynamic =0 (black)) in the LH subband.

Those coefficients of high dynamic are stored without compression or they are compressed with small compression ratio. As they make up only one percent of the image, the achieved compression ratio is not decreased considerably. For high compression ratios, we recommend to compress also the high dynamic data using a relaxed compression rate in order to avoid an significant deteriorated overall compression ratio.

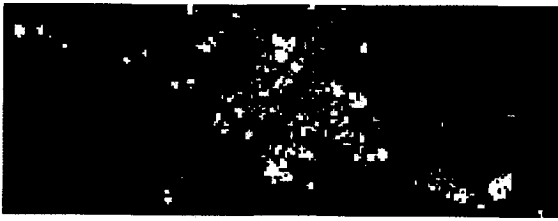


Fig. 6: High dynamic data located in HH subband

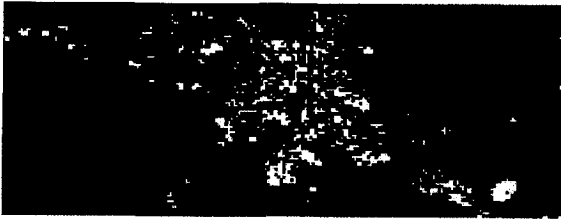


Fig. 7: High dynamic data located in HL subband

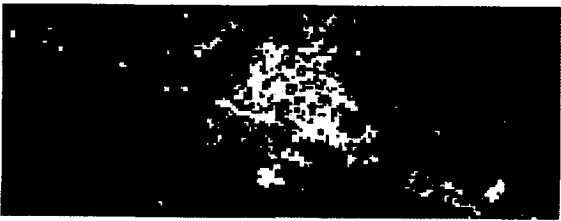


Fig. 8: High dynamic data located in LL subband

The header information is slightly increased by proceeding so, because a binary map indicating the location of high dynamic data by ones and zeros elsewhere has to be added. But due to the high redundancy, this map can be coded easily by using a suitable entropy coder. The slightly increased header information and therefore slightly smaller compression ratio can be accepted since the improved quality in the reconstructed image can make up 20 dB (Fig. 9 and Fig. 10).

Finally, it is to mention that best performance is achieved with approximately the same amount of separated high dynamic data in each subband. In our method, this is assured by the given percentage.

## 5. RESULTS

In our compression technique, there is necessity to introduce two different kinds of blocks. One adapts to limited computer memory, the other adapts to the changing dynamic of image contents. In some cases, e.g. the SIR-C image of this study, the decomposition into quantization blocks can trigger block effects in

reconstructed images due to a rapid change in image dynamic across the scene.

Applying our new technique, we are able to minimize those block effects independent of the data set to compress. Extra treatment of high dynamic data in wavelet domain leads to significant quality improvement in reconstructed images for those ScanSAR scenes depicting many single point targets (see Fig. 9).

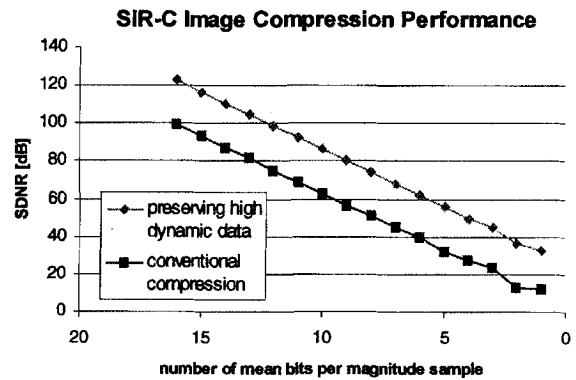


Fig. 9: Compression performance for SIR-C ScanSAR image. Preserving high dynamic data a much better performance is possible.

By proceeding in that way, not only point targets are preserved with excellent quality (infinite SDNR if demanded) but also their environment.

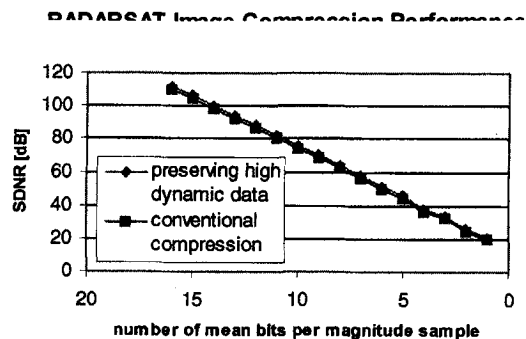


Fig. 10: Compression performance for RADARSAT ScanSAR image. Preserving high dynamic data the performance can not significantly be increased.

Extra treatment of high dynamic data is not necessary for those data sets as the used RADARSAT ScanSAR image in this study. But apart from a minor increase in header information, our method is not disadvantageous

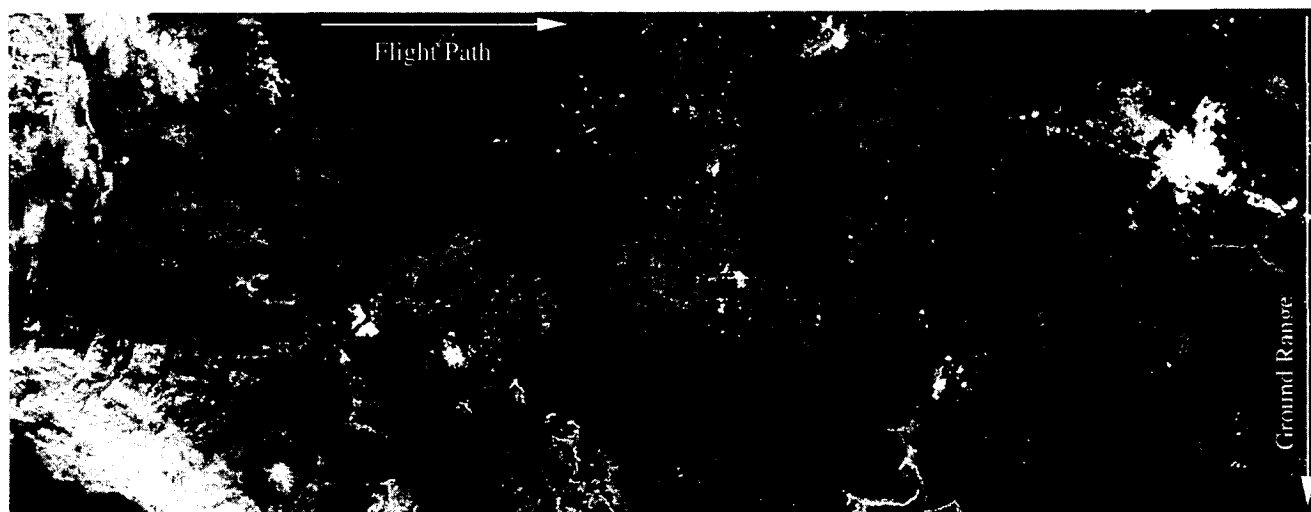


Fig. 11: Part of the original SIR-C ScanSAR image (approx. 200 km x 70 km in azimuth and ground range) depicting an area around Chickasha/Oklahoma, USA.

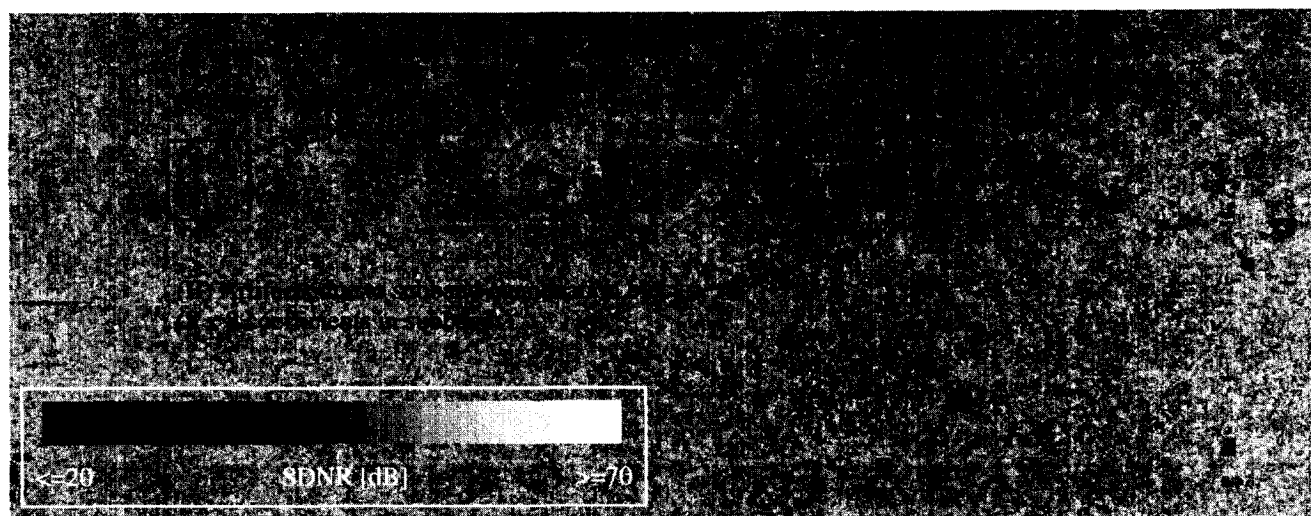


Fig. 12: SDNR map showing block effects due to invalid pixels after wavelet transforming (I) and due to worse SDNR in environments of point targets (II). Image was compressed with factor 1:8. Overall SDNR = 29.71 dB.

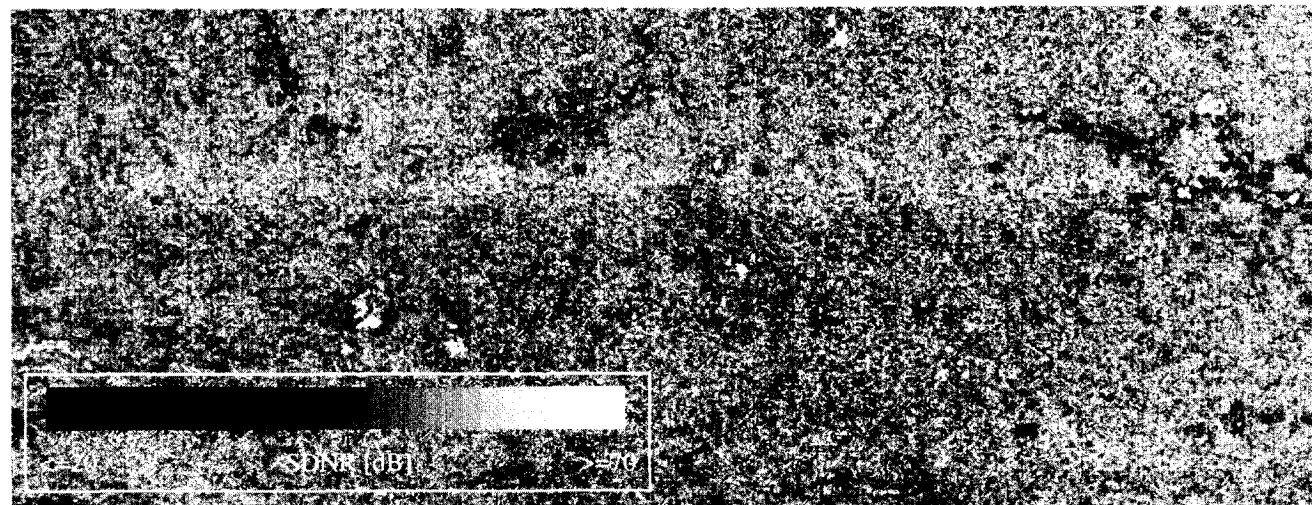


Fig. 13: SDNR map after applying the proposed technique. No block effects visible. Image was compressed with factor 1:8, high dynamic data (approx. one percent) were not compressed. Overall SDNR = 48.03 dB.

for those data sets. It also improves compression performance by small amounts (Fig. 10).

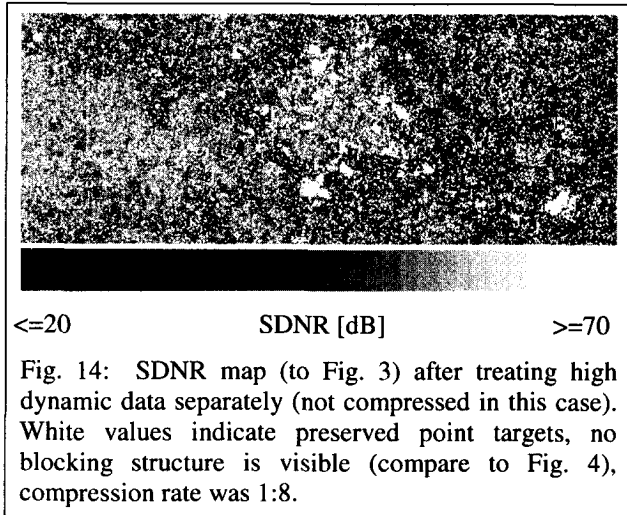


Fig. 14: SDNR map (to Fig. 3) after treating high dynamic data separately (not compressed in this case). White values indicate preserved point targets, no blocking structure is visible (compare to Fig. 4), compression rate was 1:8.

The chosen percentage of separated high dynamic data was approximately one percent for both, the SIR-C and the RADARSAT image. Varying the percentage allows a trade-off between image quality and compression ratio.

Moreover, our intention is not only to reach sufficient overall SDNR but also to achieve a scene independent error distribution. Of course, maps of signal-to-distorsion-noise ratios (SDNR) always show image content but artifacts due to compression should be avoided.

In Fig. 12 and Fig. 13, we compare resulting SDNR maps after decompression of the SIR-C image. Using our technique, we are able to avoid artifacts caused by introduction of necessary blocking in the compression method.

A similar improvement as it is possible for the SIR-C image is not achieved for the RADARSAT image due to the fact that no compression artifacts have to be removed here. We yield an overall SDNR of 36.58 dB after compression with rate 1:8. With extra treatment of 1 percent (high dynamic) data (not compressed), the performance has improved to 38.27 dB. In case an anti-scalloping filter is applied prior to compression the results are 36.81 dB and 38.35 dB, respectively.

## 6. DISCUSSION

In this paper, we only considered *detected* ScanSAR data. But the same procedure as applied to magnitude data can also be applied to both, the real and the

imaginary part of complex ScanSAR data. Proceeding in that way, we still achieve an overall SDNR larger than 30 dB and a standard deviation of phase error<sup>3</sup> below 5° for compression ratios smaller than 1:7.

For compression ratios larger than 1:7, we propose a data format conversion from cartesian to polar format. In this case, the magnitude image is compressed as described in this paper; we recommend for phase compression either no compression or compression by a vector quantizer.

A further refinement of this method can be done. Instead of distinguishing two different types of dynamics in the frequency subbands, more levels of dynamics can be introduced in order to reach a higher adaptability to the reflected image content in subbands.

## REFERENCES

- [1] Alberto Moreira, Josef Mittermayer, Rolf Scheiber, "Extended Chirp Scaling Algorithm for Air- and Spaceborne SAR Data Processing in Stripmap and ScanSAR Imaging Modes", *IEEE. Trans.Geosci.Remote Sensing*, September 1996, vol. 34, pp. 1123-1136.
- [2] Susan A. Werness, Susan C. Wei, and Ronald Carpinella, "Experiments with Wavelets for Compression of SAR Data", *IEEE. Trans.Geosci.Remote Sensing*, January 1994, vol. 32, pp. 197-201.
- [3] Ursula Benz, Jens Fischer, Wolfgang Cöster, Alberto Moreira, "Adaptive Compression of SAR Data", *Proc. of EUSAR'98*, Friedrichshafen, Germany, May 1998, pp. 525-528.

<sup>3</sup> We apply no averaging prior a phase error measurement. Applying a 3x3 averaging window prior to phase error measurement, the standard deviation of phase error decreases from 5° below 2°.

**Sub-session: Post Processing Techniques**





**New Approaches in Speckle Filtering**

Frederic Adragna  
CNES, France

Armand Lopes, Jerome Bruniquel  
CESBIO, France

This paper was not available for publication



## SENSITIVITY OF SAR SPECKLE FILTERING ON THE ASSESSMENT OF SURFACE ROUGHNESS AND SOIL MOISTURE CONTENT

F. ZAGOLSKI<sup>(1)</sup>, S. FOUCHER<sup>(2)(3)</sup>, C. GAILLARD<sup>(2)</sup>

(1) PRIVATEERS N.V., Private Experts in Remote Sensing,  
De Weaver Drive 42, Philipsburg,  
St Maarten - Netherlands Antilles.  
c/o 274 Road 216, Stoke (QC) - CANADA J0B-3G0.

*Phone:* (+1) 819-878-3319

*E-mail:* zagolski@interlinx.qc.ca

*Web-link:* <http://www.treemail.nl/privateers/>

(2) CARTEL, Université de Sherbrooke,  
2500 bd. de l'Université, Sherbrooke (Qc),  
CANADA J1K-2R1.

(3) Technologies SEPIA Incorporation,  
100 Richelieu, suite #200,  
Saint-Jean-sur-Richelieu (Qc), CANADA J3B-6X3.

**ABSTRACT:** The assessment of soil moisture content and surface roughness from remotely sensed data is of primary importance for improving agricultural techniques of conservation farming such as yield forecasts, scheduling irrigations, fertilization. SAR (Synthetic Aperture Radar) remotely sensed data may provide a powerful tool for indirectly retrieving these agricultural surface parameters over large areas with frequent coverage. Nevertheless, one major source of error in the quantitative estimate of such geophysical parameters is the presence of the speckle within the scene. To overcome this difficulty many speckle filtering techniques have been developed for reducing this multiplicative noise. However, up to now, few works analyze the performance of these filters on the retrieval of spatially and physically accurate information useful for the estimates of these soil properties. In this context, this paper outlines the sensitivity of several speckle filtering methods on the assessment of these two agricultural surface parameters. Results stressed that depending on the speckle filtering method used, significant deviations were obtained on the estimates of soil properties.

### INTRODUCTION

Soil moisture content and surface roughness play a critical role in the hydrological processes. They control the distribution of rainfall into runoff, evapotranspiration, and infiltration, which must be considered in water and energy balance [1]. Thus these two soil parameters need to be measured consistently on a spatially distributed basis.

Remotely sensed SAR (Synthetic Aperture Radar) data have the potential to provide spatial and multitemporal estimates of these surface parameters, depending upon the sensor configuration and field condition. Nevertheless, the strong radiometric variability of extended surface targets within the SAR scene make the quantitative estimate of soil properties difficult. This

variability is due to the presence of a signal-dependant multiplicative noise (so-called speckle), and directly results from the coherence of microwave radiations which induce unpredictable interference phenomena within SAR cell resolution.

Many techniques have been developed to attempt to reduce speckle within SAR images. The first category of filters, namely heuristic filters, does not consider the distribution of radar reflectivity within the scene (e.g., median filter) and the second, the adaptive filters, (e.g., Lee filter [2]) incorporate as A Priori knowledge statistical description of the scene and of the speckle. Both methods enhance radiometric resolution at the expense of spatial resolution. Recent more sophisticated filters (e.g., Gamma-MAP filter [3], Wavelet filter [4]) try to preserve pertinent details and spatial resolution keeping a strong speckle reduction in homogenous area.

The Speckle filtering of SAR images is a primordial step in extracting the useful signal (*i.e.*, the underlying scene radar reflectivity or backscattering coefficient,  $\sigma^0$ ) to be inverted for the retrieval of physical properties of the ground target. Although these filtering approaches have been tested with image processing criteria, such as the preservation of edge gradient value and the smoothing degree of homogeneous areas, a main issue is to know how these SAR filters influence spatially and physically the signal useful to the extraction of surface parameters.

In this paper, we attempted to reply to this question for a case study on an agricultural site in Normandy (France). This was conducted using RADARSAT-SGC time-series for which a set of filtering techniques (*i.e.*, 'box' and 'median' filters, and more sophisticated filters using wavelet representation and simulated annealing technique) was applied. Results stressed the significant impact of SAR filtering technique in the assessment of soil moisture content and surface roughness.

## SPECKLE REDUCTION TECHNIQUES

Speckle filtering methods can be separated into two categories: the non-adaptive approaches (box filter, median, *etc.*) and adaptive techniques.

Speckle reduction can be achieved using a simple box filter which enhances radiometric resolution without any consideration on the target nature. Consequently, edges and other significant details are strongly degraded. The median filter allows to better preserve edge properties but with a possible bias in the radar reflectivity estimation.

By using adaptive filters a compromise exists between the radiometric enhancement in the homogeneous areas and the preservation of the spatial resolution within the heterogeneous areas (*i.e.*, the textural area or edges). Depending on the local heterogeneity degree of the target, pixels are weighted with a value ranging from the local mean to the raw intensity values. Filters differ from the local weight determination depending on the *A-Priori* hypothesis applied on the probability density function (pdf) of both speckle and radar reflectivity. Thus, filters can be distinguished by the estimation strategy used such as the Minimum Mean Square Error (MMSE) or the Maximum A Posteriori (MAP). As an example, whereas Lee's filter [2] assumes Gaussian pdf and apply a MMSE criterion, Gamma-MAP filter [3] assumes gamma pdf and uses a local MAP estimation. Oliver proposes a global MAP estimation based on the Metropolis algorithm [5]. Integration of both optimal target and edge detection with an adaptive size of window strategy can improve filtering results [2]. Wavelet filters are based on a multiscale representation of the image where high frequencies (Wavelet coefficients) are denoised using a MAP criterion and gamma pdf assumptions [4].

On the contrary, in the case of an agricultural parcel, a non adaptive filter will be to take the parcel mean as input for the assessment of the soil parameters.

## DATA SET

RADARSAT-SGC time-series (4 dates) were acquired over an experimental agricultural site in Normandy (Blosseville, France) under several incidence angles (standard beam S4, S5, S6 and S7, which correspond to an incidence angle of 37°, 39°, 43.5° and 47°, respectively) during March 1998. These SAR data were over-sampled, reducing the 12.5 m nominal resolution to 25 m, with a number of looks around 4. Moreover, a SPOT-XS image from 1997 completed our remote sensing database.

## METHODOLOGY

### Speckle filtering methods

Five speckle reduction methods were applied on all the calibrated SAR images using the following specifications: (1) box filter (with a window size of

11x11 pixels); (2) median filter (5x5); (3) Gamma-MAP filter (11x11); (4) simulated annealing (ACMAP [5]) using 50 iterations and (5) wavelet filter (3 levels of decomposition) [4].

### Co-registration of SAR images

Standard techniques were employed to extract control points in all images (30 points were found for both optic and SAR data) and, subsequently deduce bilinear polynomial transformations using standard image-processing techniques. Residuals were monitored in the process of selecting the polynomial degree: it was found that simple linear polynomials were sufficient to achieve residual (sub-pixel) levels and that these residuals were independent of the application of higher-order polynomials.

### Parcel sampling

Samples (~300 relatively homogeneous parcels) were selected within the SPOT scene, thus allowing a better control of the sampling quality for the sensitivity study of filtering SAR data in the estimate of physical soil parameters.

### SAR backscattering models

2 SAR backscattering models were used for retrieving surface roughness and soil moisture content over each of all selected parcels.

The first is a semi-empirical model from Dubois [6] which presents some built-in limitations (the imaginary part of the dielectric constant  $\varepsilon$  is not taken into account, no dependence on the surface correlation, *cf.* [7]). Angular dependence of the backscattering coefficient for HH polarization is given by :

$$\sigma_{hh}^o = 10^{-2.75} \frac{\cos^{1.5} \theta}{\sin^5 \theta} \cdot 10^{0.028 \varepsilon \tan \theta} \cdot (k \cdot h) \cdot \sin^{1.4} \theta \cdot \lambda^{0.7} \quad (1)$$

where  $\theta$  is the incidence angle,  $k$  the wave number,  $\varepsilon$  the real part of the dielectric constant,  $h$  the rms height of the surface (cm) and  $\lambda$  the wavelength (cm). The validity domain of this relationship corresponds to rms roughness ( $k \cdot h$ ) values within [0.3 ; 3] and incidence angles between 30° and 65°.

The second is the analytical integral equation model (IEM) specially adapted to roughness values typical of agricultural soil, and convenient for a large range soil status conditions [8]. The SAR backscattering coefficient ( $\sigma^o$ ) is expressed as:

$$\begin{aligned} \sigma_{pp}^o = & \frac{k^2}{2} \cdot |f_{pp}|^2 \cdot \exp(-4 \cdot K_0) \cdot \sum_{n=1}^{+\infty} \frac{(4 \cdot K_0)^n}{n!} \cdot W^{(n)}(2 \cdot k \cdot \sin \theta, 0) \\ & + \frac{k^2}{2} \cdot \text{Re}(f_{pp}^* \cdot F_{pp}) \cdot \exp(-3 \cdot K_0) \cdot \sum_{n=1}^{+\infty} \frac{(2 \cdot K_0)^n}{n!} \cdot W^{(n)}(2 \cdot k \cdot \sin \theta, 0) \\ & + \frac{k^2}{8} \cdot |F_{pp}|^2 \cdot \exp(-2 \cdot K_0) \cdot \sum_{n=1}^{+\infty} \frac{(K_0)^n}{n!} \cdot W^{(n)}(2 \cdot k \cdot \sin \theta, 0) \quad (2) \end{aligned}$$

$$\text{with: } f_{hh} = -\frac{2.R_{\perp}}{\cos\theta} \quad f_{vv} = \frac{2.R_{//}}{\cos\theta} \quad (3)$$

$$F_{hh} = \gamma \cdot [4.R_{\perp} - (1 - \frac{1}{\epsilon_r}) \cdot (1+R_{\perp})^2],$$

$$F_{vv} = \gamma \cdot [(1 - \frac{\epsilon_r \cdot \cos^2\theta}{\mu_r \cdot \epsilon_r - \sin^2\theta}) \cdot (1-R_{//})^2 + (1 - \frac{1}{\epsilon_r}) \cdot (1+R_{//})^2],$$

$$\text{and } K_{\theta} = (k \cdot h)^2 \cdot \cos^2\theta \quad \gamma = 2 \cdot \frac{\sin^2\theta}{\cos\theta}.$$

where  $pp$  stands for  $HH$  or  $VV$  polarization and  $R_{//}$  and  $R_{\perp}$  are the Fresnel reflection coefficients dependent on dielectric constant for vertically and horizontally polarized waves.  $Re$  means the real part of the complex number.  $W^{(n)}(2 \cdot k \cdot \sin\theta, 0)$  characterizes the surface roughness spectrum [9], and is a function of the rms height  $h$  of the surface and of its correlation length  $l$  for a surface with an exponential-distributed roughness values.

For each of all selected samples a least-square fit to (1) was applied on the 4 corresponding angular SAR backscattering coefficients for estimating  $\epsilon$  and  $(k \cdot h)$  values. The SAR multi-angular fit to (2) for retrieving  $(k \cdot h)$ ,  $(k \cdot l)$  and  $\epsilon$  parameters relies on the optimized simplex method [10]. These 2 SAR multi-angular regression methods were performed on a pixel per pixel basis for each set of angular SAR data (*i.e.*,  $\sigma^0$  intensity resulting from parcel averages and  $\sigma^0$  estimated by each of 5 filtering techniques).  $\epsilon$  is converted to volumetric soil moisture  $m$  through empirical curves [11].

Samples with a too small number of pixels ( $n < 200$ ) and for which the number of realistic estimates is lower than 75% were discarded from our analysis. A degree of heterogeneity level for each parcel (sample) was evaluated using the normalized standard deviation coefficient of the underlying radar reflectivity ( $C_R$ ) [5]. The statistical validity of the regression is evaluated using the following probability:

$$P = \int_0^{\chi^2/2} \Gamma\left(\frac{N-2}{2}, x\right) dx \quad (4)$$

where  $\chi^2$  is the fit dispersion and  $N$  the number of observations.  $P > 0.9$  means that the fit should be discarded. This probability will give us a level in confidence in the physical significance of the retrieved parameters.

To analyse the sensitivity of each speckle filtering methods on the assessment of agricultural surface parameters, we defined 2 filter performance indices,  $I_r$  and  $I_h$  for surface roughness and soil moisture content respectively, as follow:

$$I_h = \frac{|h_{filter} - h_{parcel}|}{h_{parcel}} \times \left(1 - \frac{P_{filter}}{P_{parcel}}\right) \quad (5)$$

$$I_r = \frac{|r_{filter} - r_{parcel}|}{r_{parcel}} \times \left(1 - \frac{P_{filter}}{P_{parcel}}\right)$$

where  $h_{filter}$ ,  $r_{filter}$ ,  $h_{parcel}$ ,  $r_{parcel}$  stands for humidity and roughness parameters derived from multi-angular regression on SAR data set filtered with *filter* and *parcel* methods respectively. These indices were computed for each pixel and thresholded in  $[-1; 1]$ . They represent a relative deviation of the estimate on the surface parameter weighted by the relative deviation of the dispersion. If the analyzed filter gives better results on the estimate of the soil parameter than the parcel mean value then the filter performance index value  $I$  for this parameter will be greater than 1, on the contrary if the estimate is degraded then this value will be negative.

## RESULTS

Figure 1 displays the RADARSAT Std Beam S4 image on which were superimposed ~300 field samples used in our SAR multi-angular regression.

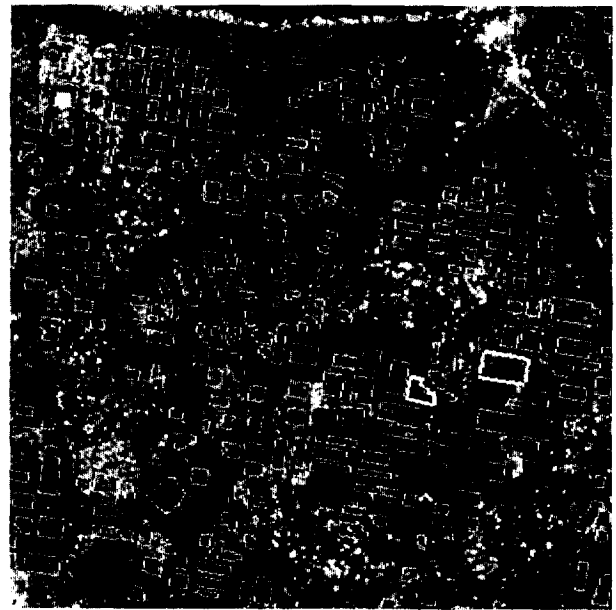


Fig. 1: RADARSAT Std Beam S4 image acquired over Blosseville watershed (Normandy, France) in March 25, 1998. Area shown is 5.6 km x 5.6 km.

Once the 2 statistical criteria (mentioned above) applied to this set of samples, only 100 parcels remained for our filter sensitivity analysis. For each selected parcel and each speckle reduction techniques, 2 performance indices ( $I_h$ ,  $I_r$ ) were then computed for the soil moisture and surface roughness retrievals. Results indicated that 50% of parcels gave a better estimates of soil properties derived from IEM or Dubois' model for each of the 5 local filters (box, median, Gamma-MAP, ACMAP and Wavelet filters) than for the parcel average method. Among this 50%, the large positive values of  $I_h$  and  $I_r$  for heterogeneous parcels stressed the interest of use of

these local filters for retrieving an useful signal to be inverted in a SAR backscattering model. Consequently, this means the parcel average method must be carefully applied even if the parcel seems to be homogeneous.

For a detailed analysis of the performance of these 5 filters two fields are selected within the test site. These two parcels are delimited by a white thick line in the right bottom side of Fig.1. The largest from these two parcels is relatively homogenous with a SAR intensity coefficient variation ( $C_I$ ) of 0.56, and an area of 10 ha. Surface roughness ( $k_h$ ) and soil moisture content ( $m$ ) derived from the parcel average method are 0.42 and 0.53, respectively. The other parcel, with a smaller size (area of 3.5 ha), is heterogeneous ( $C_I=0.61$ ) with an estimated  $k_h$  and  $m$  of 0.15 and 0.56, respectively.

Figure 2 displays  $\langle I \rangle / \sigma_I$  values for each of the 5 speckle filtering methods on the assessment of soil properties for these two selected fields.

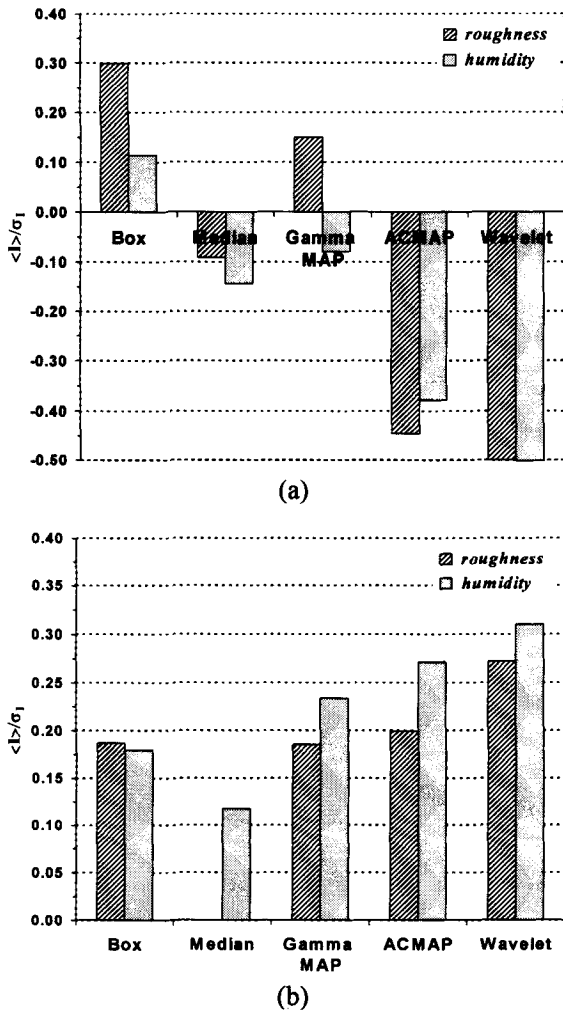


Fig. 2:  $\langle I \rangle / \sigma_I$  values for surface roughness and soil moisture estimates, and for each of 5 speckle filtering methods: (a) homogeneous field, and (b) heterogeneous field.

Results confirm the smoothing filters (Box, Median) are more efficient than the adaptive filters (ACMAP, Wavelet) for the homogeneous parcel (Fig.2a) whereas all the 5 filters are better than the parcel average method for the heterogeneous parcel (Fig.2b). It can be noted that the Gamma-MAP filter realized the best compromise for these two fields.

Figure 3 depicts  $\langle I \rangle / \sigma_I$  values for the 2 soil parameters estimates as function of the window size of the Gamma-MAP filter. For the homogeneous parcel (Fig.3a), it clearly appears an optimal size of windows (*i.e.*, 11x11 pixels) for estimating surface roughness estimates whereas smaller window sizes are better for the case of the heterogeneous parcel (Fig.3b).

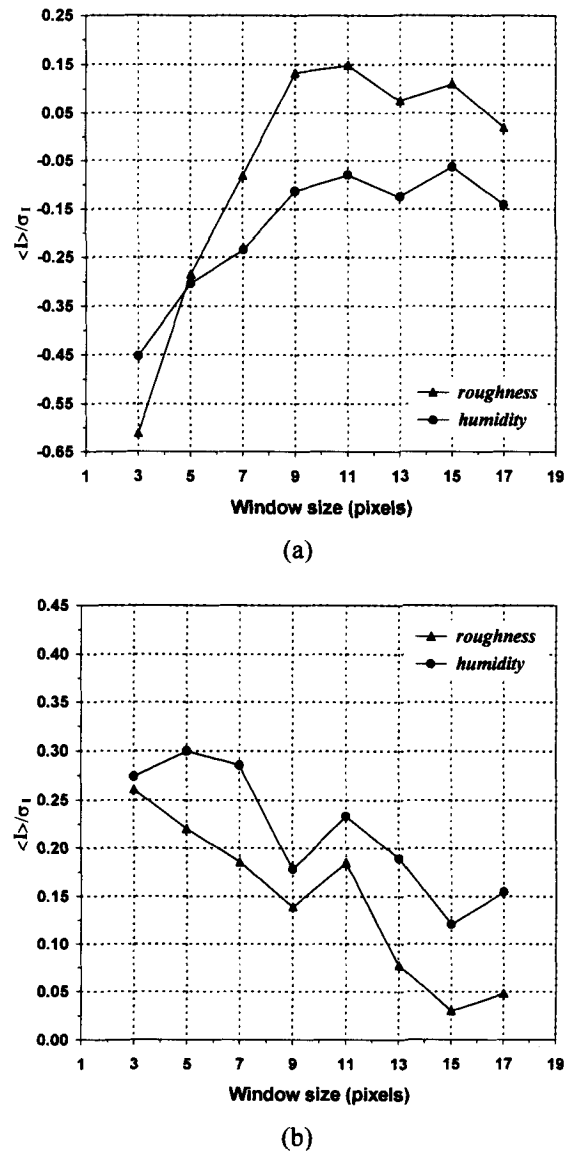


Fig. 3: Variation of  $\langle I \rangle / \sigma_I$  values for surface roughness and soil moisture estimates as function of the window size of the Gamma-MAP filter: (a) homogeneous field, and (b) heterogeneous field.

Figure 4 depicts the spatial variability of the performance indices of the Gamma-MAP filter (Fig.4a & 4b) and the Box filter (Fig.4c & 4b) relative to surface roughness and soil moisture content within the homogeneous field, and the corresponding spatial map for each of two agricultural parameters derived from our multi-angular SAR regression with Dubois' model. Window size of both two filters are 11x11 pixels. This parcel comprises two distinguished areas with different SAR reflectivities (Fig.1). The adaptive filter performs well better than the heuristic approach by preserving this fluctuation. The window size used in speckle filtering appears to be optimal (as observed in Fig.3a), due to the fact that it keeps local statistics unmixed between these two kinds of ground target. For window size larger than 11x11 pixels, we noted a decreasing of the spatial Gamma-MAP performance indices which stresses that many local statistics are not within an homogenous target. This behaviour was observed for the 4 other filters, but also with the soil properties derived from the IEM model.

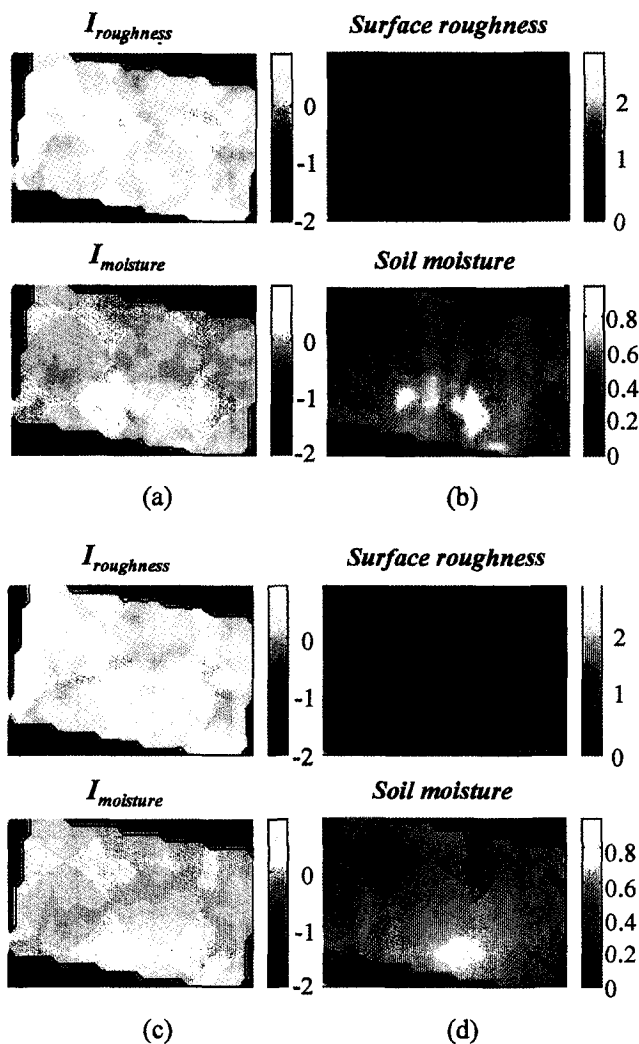


Fig. 4: Filter performance indices relative to 'roughness'

and 'soil moisture' estimates for the homogeneous field, and parameter maps derived from our multi-angular SAR regression with Dubois' model: Gamma-MAP filter (11x11) [a, b], and Box filter (11x11) [c, d].

Figure 5 is similar to Fig.4 but with performance indices of the Gamma-MAP filter 3x3 (Fig.5a, 5b) and the Wavelet filter (Fig.5c, 5d), for the heterogeneous parcel. This is a an illustration case where thin detail preservation strategy of the adaptive filter can improve the performance indices. Gamma-MAP 3x3 and Wavelet filter well perform whereas the Gamma-MAP 17x17 (Fig.6) is inappropriate due to the polluted local statistics.

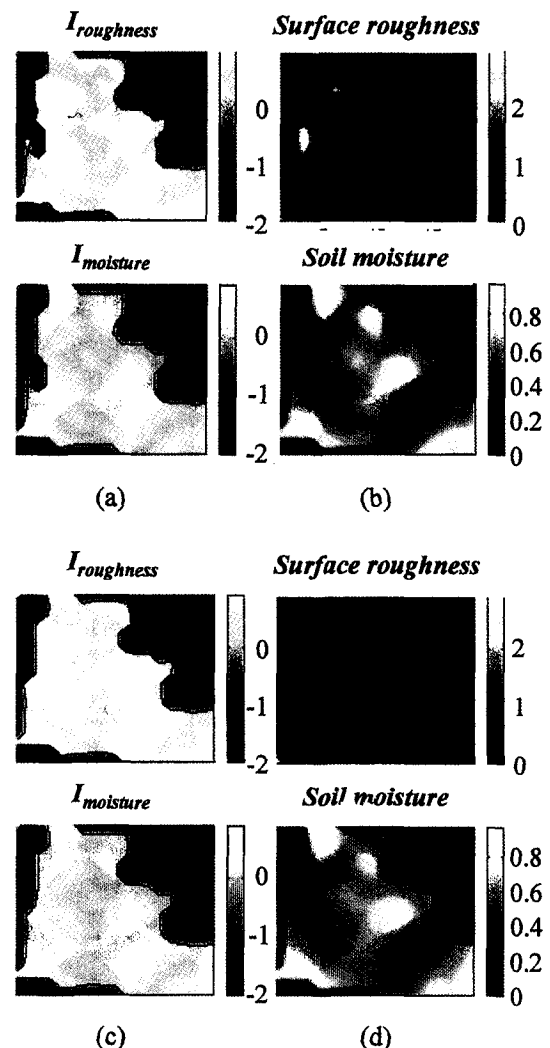


Fig. 5: Filter performance indices relative to 'roughness' and 'soil moisture' estimates for the heterogeneous field, and parameter maps derived from our multi-angular SAR regression with Dubois' model: Gamma-MAP filter(3x3) [a, b], and Wavelet filter [c, d].

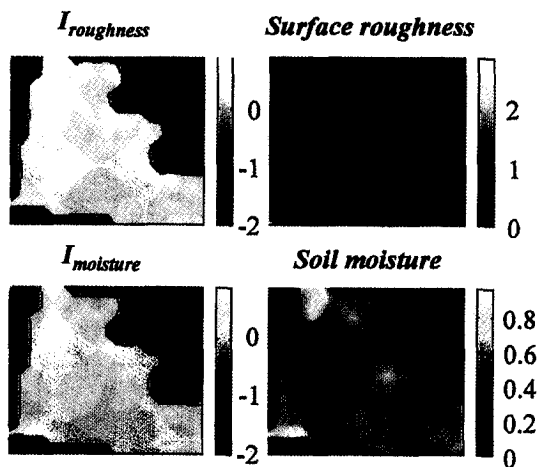


Fig. 6: Same legend as Fig.5 but for Gamma-MAP filter(17x17).

### CONCLUDING REMARKS

Results derived from this study stressed the importance of the choice of the SAR filtering technique for extracting the useful signal to be inverted for accessing information about soil dielectric constant and surface roughness. Depending on the speckle reduction method applied to raw intensity images, significant deviations were obtained on the estimated soil parameters in comparison with the commonly used parcel average method. The soil roughness is much more sensitive to the employed SAR filtering method. In fact, estimates of such a parameter using the parcel average method or non-adaptive filtering approach result from a too large smoothing of SAR intensity fluctuations within the parcel which seems physically significant for soil moisture and surface roughness retrieval.

For a parcel with an uniform radar reflectivity without any discontinuities, a global mean is statistically more efficient than an adaptive filter. However almost all parcels are composed with heterogeneous targets, adaptive local filter seems to be more appropriate because of the visual result they give but also because physical models provide better results. For an heterogeneous parcel, we established that there is an optimal size for the local window which maximized the parameter retrieval. One further step would be to select this window size for each pixel according to the model response.

In short, statistical based filter hypothesis seems to be confirmed by the behavior of the physical models. However, due to the lack of in-situ measurements, we could not validate this result and go thoroughly into the discussion. Consequently, this work needs to be confirmed with another campaign.

### ACKNOWLEDGMENTS

Special thanks to the Canadian Government for the financial support of this research.

### REFERENCES

- [1] M. Benallegue, D. Taconet, D. Vidal-Madjar, and M. Normand, "The use of radar backscattering signals for measuring soil moisture and surface roughness", *Rem. Sens. Env.*, vol.53, pp.61-68, 1995.
- [2] J.S. Lee, "Digital image enhancement and noise filtering by use of local statistics", *I.E.E.E. Trans. On PAMI.*, vol.PAMI-2, pp.165-168, 1980.
- [3] A. Lopes, E. Nezry, R. Touzi, and H. Laur, "Structure detection and statistical adaptive speckle filtering of SAR images", *Int. J. Rem. Sens.*, vol.14, pp.1735-1758, 1993.
- [4] S. Foucher, J.M. Boucher, and G.B. Béné, "Multiscale SAR filtering based on non-Gaussian assumptions", *Proc. IGARSS'98*, Seattle (WA), 1998.
- [5] C. Oliver, and S. Quegan, "Understanding synthetic aperture radar images", *Artech House Eds, Norwood (MA)*, 1998.
- [6] P.C. Dubois, J. van Zyl, and T. Engman, "Measuring soil moisture with imaging radars", *IEEE Trans. on Geosc. & Rem. Sens.*, vol.33, pp.915-926, 1995.
- [7] M.S. Dawson, A.K. Fung, M.T. Manry, "Tools for soil moisture retrieval from radar measurements", *Retrieval from bio- and geophysical parameters from SAR data for land applications*, pp.295-305, Toulouse, 10-13 October, 1995.
- [8] A.K. Fung, and K.S. Chen, "Dependence of the surface backscattering coefficients on roughness, frequency and polarization states", *Int. J. Rem. Sens.*, vol.13, pp.1663-1680, 1991.
- [9] F.T. Ulaby, R.K. Moore, and A.K. Fung, "Microwave remote sensing, active and passive", *vol.III: From Theory to Applications*, *Artech House Eds, Dedham (MA)*, 1986.
- [10] J.A. Nelder, and R. Mead, "A simplex method for function minimization", *Computer Journal*, 7, 308-313, 1965.
- [11] M. Hallikainen, F.T. Ulaby, M.C. Dobson, M.A. El-Rayes, L. Wu, "Microwave dielectric behaviour of wet soil - Part 1: Empirical models and experiment observations", *IEEE Trans. on Geosc. & Rem. Sens.*, vol.23, pp.25-34, 1995.



## A Family of Distribution-Entropy MAP Speckle Filters for Polarimetric SAR Data, and for Single or Multi-Channel Detected and Complex SAR Images

Edmond NEZRY and Francis YAKAM-SIMEN

PRIVATEERS N.V., Private Experts in Remote Sensing  
Great Bay Marina, P.O. Box 190, Philipsburg, Netherlands Antilles  
Phone/Fax: (+33) 5-61545827/61991724; E-mail: 113247.1054@compuserve.com  
Internet: <http://www.treemail.nl/privateers/>

### ABSTRACT

Five new Distribution-Entropy Maximum A Posteriori (DE MAP) speckle filters are established for the following cases: single detected, multilook multi-channel detected, single look complex SAR images, separate complex looks, and fully polarimetric SAR data.

As shown, these new filters are particularly efficient to reduce speckle noise, while preserving textural properties and spatial resolution, especially in strongly textured SAR images.

**Keywords:** Speckle filtering, Maximum Entropy, Maximum A Posteriori filters, Complex SAR images, multi-temporal SAR data, multi-channel SAR data, Polarimetric SAR images.

### 1. DE-MAP SPECKLE FILTERING

In the case of multi-channel detected SAR images, let define the vector quantities of interest:  $I$  is the speckled intensity vector available in the actual SAR data;  $R$  is the radar reflectivity vector which is the quantity we want to restore. The Maximum A Posteriori (MAP) filtering method bases on the famous Bayes' theorem:

$$P(R/I) = P(I/R) \cdot P(R) / P(I) \quad (1)$$

For multi-channel detected SAR images, MAP Filtering is a vector filtering method. For any channel  $i$ , the posterior probability is maximum if the following condition is verified:

$$\frac{\partial \ln(P(I/R))}{\partial R_i} + \frac{\partial \ln(P(R))}{\partial R_i} = 0 \quad \text{for } R_i = R_{i \text{ MAP}} \quad (2)$$

In presence of very strong texture, as it is often the case in SAR images of dense tropical forest, and in the presence of relief, it may be hazardous to make an

assumption about the probability density function of the radar reflectivity.

In this context, the A Priori knowledge with regard to the observed scene can hardly be an analytical first order statistical model. However, we introduce a Maximum Entropy (ME) constraint on texture [1-3]:

$$S(R_i) = - \sum_k [R_{ik} \cdot \log(R_{ik})] \quad \text{for the } i^{\text{th}} \text{ channel} \quad (3)$$

Because the  $R_k$  are non-negative and  $\exp(S(R_i))/Z$  is normalized, it can be treated as a probability density function (pdf) whose entropy is  $S(R_i)$  [1]:

$$P(R_i) = 1/Z \cdot \exp(S(R_i)) = 1/Z \cdot \exp(-\sum_k [R_{ik} \cdot \log(R_{ik})]) \quad (4)$$

To estimate  $P(R_i)$ , the radar reflectivities  $R_{ik}$  are estimated by deconvolution from the SAR impulse response function as described in Nezry *et al.*, 1995 [4].

### 2. DE-MAP FILTERS FOR DETECTED SAR IMAGES

#### Single detected SAR image case:

For a single detected SAR image, the conditional pdf of the speckle can be modelled as a Gamma distribution:

$$P(I/R) = (L/R)^L / \Gamma(L) \cdot \exp(-LI/R) \cdot I^{L-1} \quad (5)$$

With this assumption, the *Gamma/Distribution-Entropy MAP (Gm-DE MAP) filter for single-channel detected SAR images* is the solution of the following equation:

$$L I - LR - R^2 \cdot \sum_k [\log(R_k) - 1/\ln(10)] = 0 \quad (6)$$

Figure 1 and 2 illustrate the application of this speckle filter to a ERS-PRI (3-looks) SAR image. Figure 1 is the original ERS-PRI image, and Figure 2 is its filtered version.

#### Detected multi-channel SAR data case:

For multilook SAR images, the conditional pdf of the speckle  $P(I/R)$  can be modelled as a multivariate Gaussian distribution [5], in the case the speckle is correlated between image channels:

$$P(I/R) = [(2\pi)^N |\text{Cov}_S|]^{-1/2} \cdot \exp[-\frac{1}{2}(I-R) \cdot \text{Cov}_S^{-1} \cdot (I-R)] \quad (7)$$

The ME constraint on texture is introduced as above. With this technique, there is no need to introduce explicit correlation between the diverse texture channels.

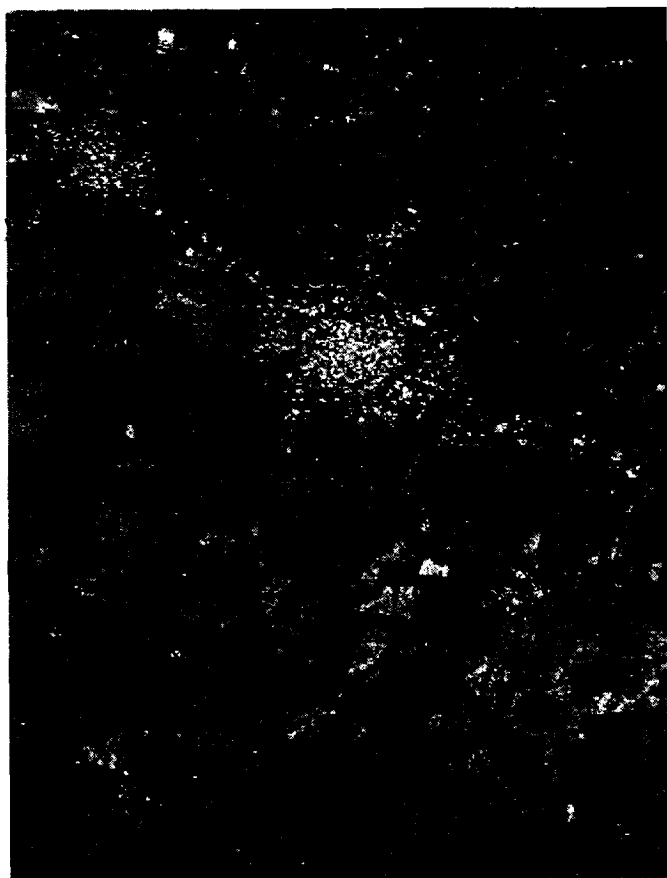


Figure 1: Unfiltered ERS PRI image.

Under these assumptions, the *Gaussian/Distribution-Entropy MAP (Gs-DE MAP) filter for multi-channel multilook detected SAR images* (N channels) comes down to the resolution of a set of N coupled scalar equations of the form:

$$\frac{1}{R_i} \cdot C_S^{-1} \cdot (I-R) + \frac{1}{C_S} \cdot (I-R) \cdot \frac{1}{R_i} - R_i^2 \cdot \sum_k [\log(R_{ik}) - 1/\text{Ln}(10)] = 0 \quad (8)$$

Note that in the case the speckle is not correlated between image channels, the *Gamma/Distribution-Entropy MAP (Gm-DE MAP) filter for multi-channel detected SAR images* (N channels) comes down to the resolution of a set of N independent (uncoupled) scalar equations similar to Equation (6).

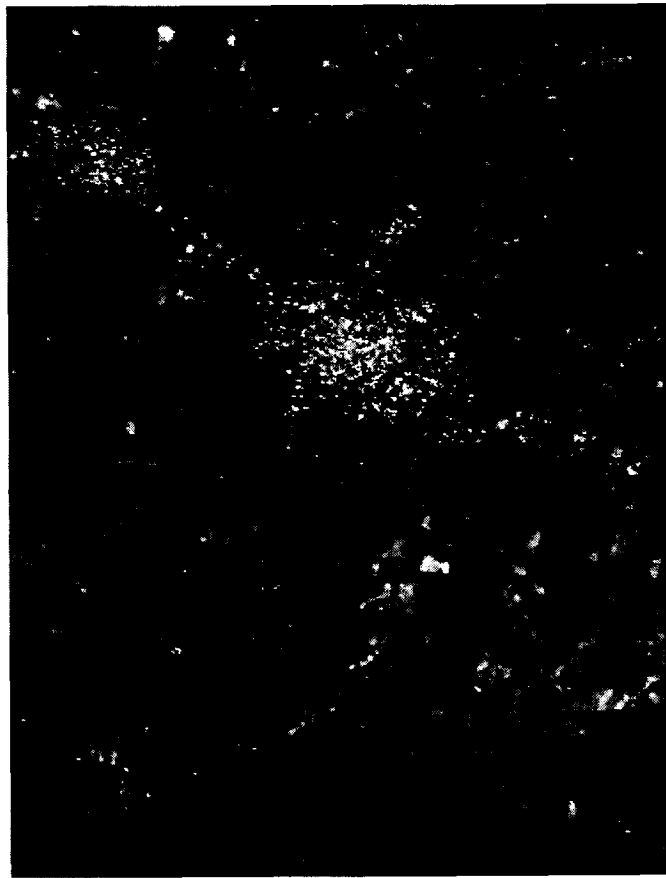


Figure 2: DE-MAP filtered version of the ERS SAR image.

### 3. DE-MAP FILTERS FOR COMPLEX SAR DATA

The  $L$  separate complex looks are usually extracted from the useful Doppler band, at the cost of the azimuth resolution. From the point of view of the speckle-filtering-problem, the case of interferometric complex SAR data sets can be considered in a similar way. The measurement vector for each pixel is  $X=\{y_n\}$ , where  $y_n=i_n+jq_n$ .

When speckle is fully developed, the  $(i_n, q_n)$  are statistically independent random processes. However, the  $y_n$  are correlated complex Gaussian random processes with pdf given by Goodman, 1985 [6]:

$$P(X/C_S) = \exp\{X^* \cdot C_S^{-1} \cdot X\} / (\pi^L |C_S|) \quad (9)$$

#### Separate complex looks case:

In this case, the *Complex-Gaussian/Distribution-Entropy MAP (CGS-DE MAP) filter for separate complex looks* ( $L$  complex looks) is expressed as:

$$X^* \cdot C_S^{-1} \cdot X - LR_i - R_i^2 \cdot \sum_k [\log(R_k) - 1/Ln(10)] = 0 \quad (10)$$

where  $C_S$  is the covariance matrix of the speckle between the complex separate looks [7].

In the case of a series of single-look complex (SLC) images (e.g. interferometric complex SAR data sets),  $C_S$  is the covariance matrix of the speckle between the SLC images, and the same filter can be applied, without loss in the spatial resolution.

#### Single-look complex (SLC) image case:

In this case, the *Complex-Gaussian/Distribution-Entropy MAP (CGS-DE MAP) filter for SLC SAR images* is expressed as follows:

$$1/N \cdot X^* \cdot C_S^{-1} \cdot X - R - R^2 \cdot \sum_k [\log(R_k) - 1/Ln(10)] = 0 \quad (11)$$

where  $C_S$  is the spatial covariance matrix of the complex speckle, and  $N$  is the number of pixels within the processing window.

### 4. DE-MAP FOR POLARIMETRIC SAR DATA

In the case of polarimetric SAR data,  $\Sigma_s$  is the polarimetric covariance matrix, and  $C_s$  is the unspeckled covariance matrix, i.e. the quantity to be restored through speckle filtering.

In the reciprocal case, and for low look correlation, the conditional pdf of  $\Sigma_s$  is a complex Wishart distribution of the form [8]:

$$P(\Sigma_s/C_s) = \frac{(\det \Sigma_s)^{L-3} L^{L-3}}{\pi^3 \Gamma(L) \Gamma(L-1) \Gamma(L-2) (\det C_s)^L} \exp[-\text{Tr}(L C_s^{-1} \Sigma_s)] \quad (12)$$

Using physical backscattering models, assuming (as a rough approximation) that texture is identical in all polarizations, we get the following approximation [8]:

$$C_s = \mu E(C_s) \quad (13)$$

where  $\mu$  is the scalar textural parameter equal to the normalized number of scatterers within the resolution cell, and  $E(C_s)$  is the mean covariance matrix [9].

With this assumption, the ME constraint on texture [1-3] becomes:

$$P(\mu) = 1/\mu \cdot \exp(-\sum_k [\mu_k \log(\mu_k)]) \quad \text{and} \quad E(\mu) = 1 \quad (14)$$

In this case, the *Complex-Wishart/Distribution-Entropy MAP (CW-DE MAP) filter for polarimetric multilook SAR data* is expressed as:

$$L \text{Tr}[E(C_s)^{-1} \Sigma_s] - L\mu - \mu^2 \cdot \sum_k [\log(\mu_k) - 1/Ln(10)] = 0 \quad (15)$$

$E(C_s)$  is obtained using the maximum likelihood estimator described in Lopès *et al.*, 1992 [8].

Figures 3 to 10 illustrate the application of this filter to high resolution P-band 4-look JPL AIRSAR polarimetric data. The restoration of the radar reflectivity is illustrated on Figures 3 and 4. The restoration of the degrees of coherence is illustrated on Figures 5 and 6; the restoration of the phase differences is illustrated on Figures 7 and 8. Figures 9 and 10 allow to appreciate how the CW-DE MAP filter and enhances the P-band polarimetric texture signatures [10] on the textured (forest) area indicated on Figures 3 and 4 (2035 pixels).

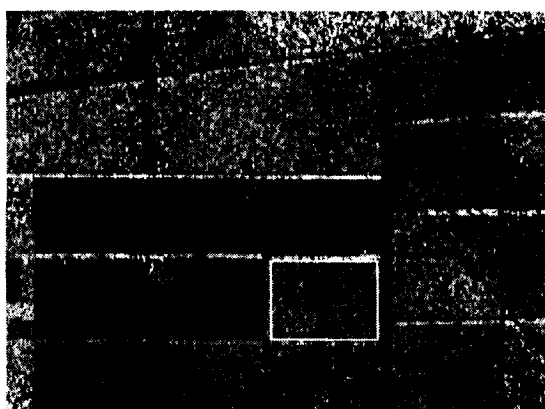


Figure 3: Original 4-look JPL/AIRSAR P-HH image.

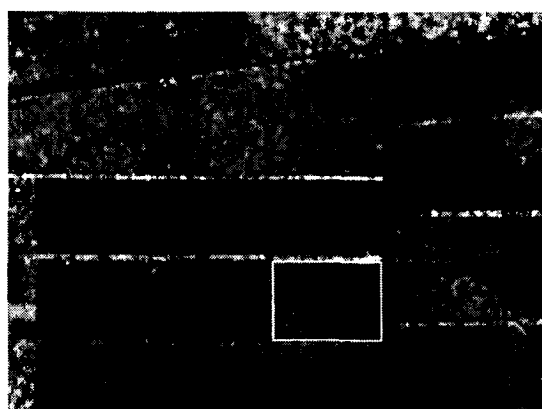


Figure 4: P-HH Pol. after CW-DE MAP filtering.

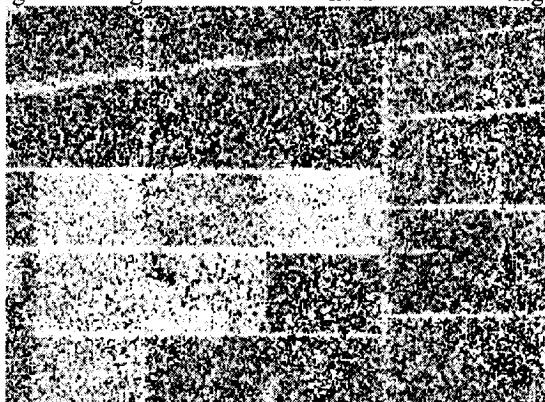


Figure 5: Unfiltered P-HH/VV degree of coherence.

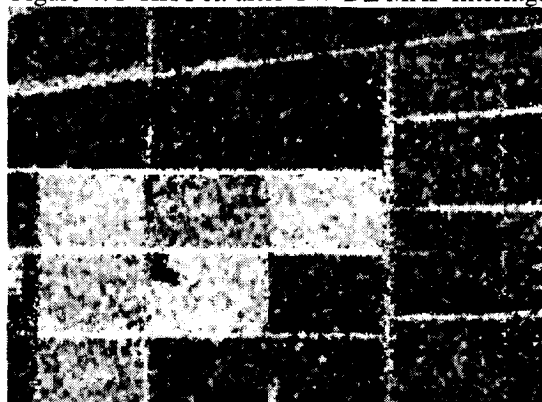


Figure 6: CW-DE MAP filtered degree of coherence.

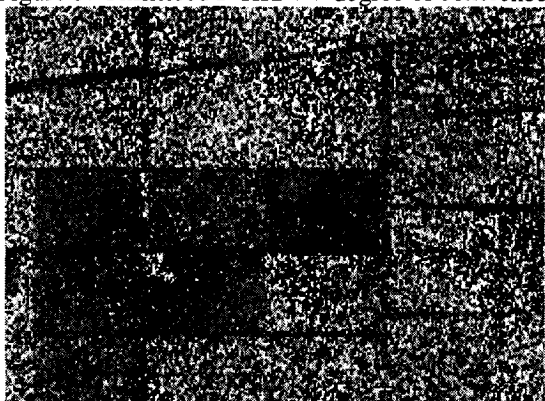


Figure 7: Unfiltered P-HH/VV phase difference



Figure 8: CW-DE MAP filtered HH/VV phase difference.

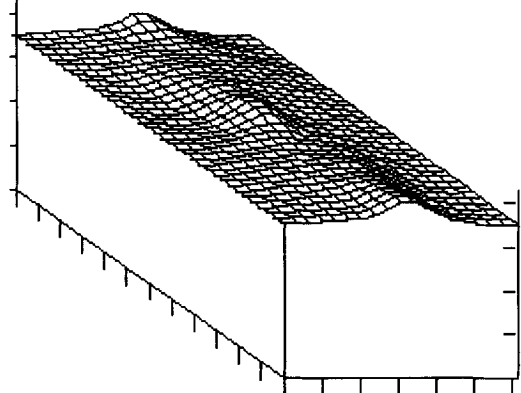


Figure 9: Original polarimetric texture signature.

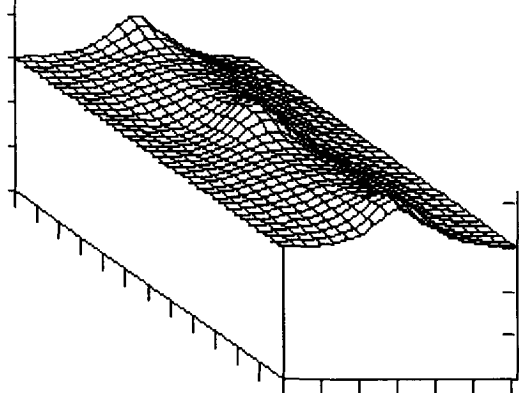


Figure 10: Texture signature after CW-DE MAP filtering.

## 5. CONCLUSION

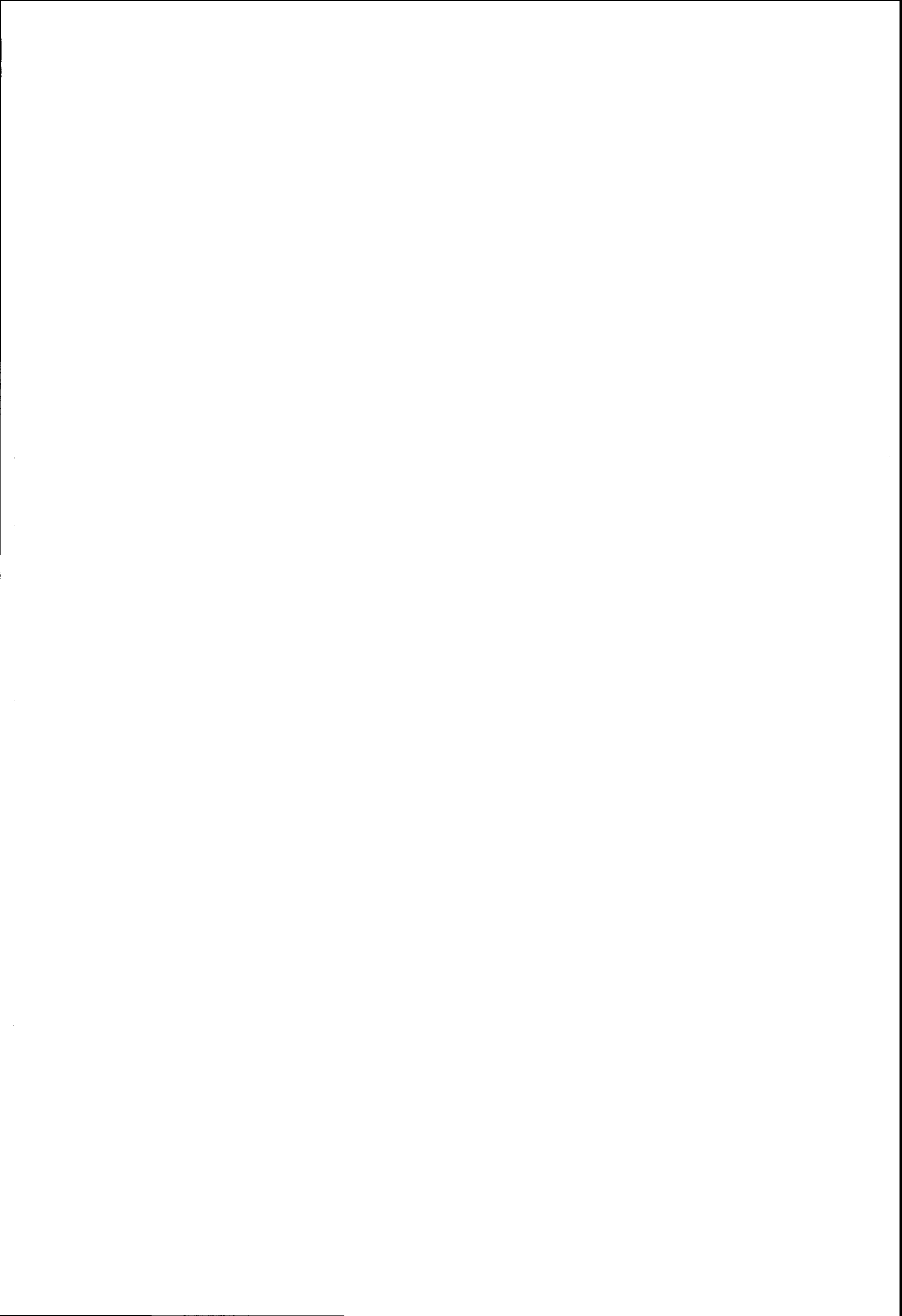
The new DE-MAP filters presented above adapt to a much larger range of textures than the previous MAP filters [7,8,11,12] developed under the assumption of K-distributed SAR intensity. In particular, these filters might be of interest in the case of very high resolution SAR images.

The filtered images shown in Figure 2 and 4 show that performances in terms of speckle reduction, texture restoration (*cf.* [13]), as well as structures and point targets preservation are fully satisfactory. These filters have already proven a remarkable efficiency in operational remote sensing (*cf.* [14,15]).

From the theoretical point of view, it is noteworthy that these filters present the very interesting properties of control systems [12,16].

## 6. REFERENCES

- [1]. A.K. Jain, 1989: "*Fundamentals of digital image processing*", Chapt. 8, pp.316-317, Prentice Hall Ed., Englewood Cliffs (NJ), 1989.
- [2]. M. Datcu and M. Walessa, 1997: "Maximum entropy methods for despeckleling and resampling of synthetic aperture radar images of rough terrain", *Proceedings of SPIE*, Vol.3917, pp.76-83, September 1997.
- [3]. M. Walessa and M. Datcu, 1997: "Bayesian approach to SAR image reconstruction", *Proceedings of IGARSS'97*, Vol.2, pp.767-770, 03-08 August 1997.
- [4]. E. Nezry, M. Leysen and G. De Grandi, 1995: "Speckle and scene spatial statistical estimators for SAR image filtering and texture analysis: some applications to agriculture, forestry, and point targets detection", *Proceedings of SPIE*, Vol.2584, pp.110-120, September 1995.
- [5]. J.S. Lee, 1980: "Digital image enhancement and noise filtering by use of local statistics", *IEEE Transactions on PAMI*, Vol.PAMI-2, n°3, 165-168, March 1980.
- [6]. J.W. Goodman, 1985: "Statistical Optics", J. Wiley & Sons, NY, 1985.
- [7]. A. Lopes, E. Nezry, S. Goze, R. Touzi and G. Aarbakke Solaas, 1992: "Adaptive multilook processing of complex SAR images", *Proceedings of IGARSS'92*, Houston (TX), Vol.2, pp.890-892, 26-29 May 1992.
- [8]. A. Lopès, S. Goze and E. Nezry, 1992: "Polarimetric speckle filters for SAR data", *Proceedings of IGARSS'92*, Houston (TX), Vol.1, pp.80-82, 26-29 May 1992.
- [9]. L.M. Novak and M.C. Burl, 1990: "Optimal speckle reduction in polarimetric SAR imagery", *IEEE Transactions on AES*, Vol.26, pp.293-305, March 1990.
- [10]. G. De Grandi, E. Nezry, J.S. Lee, and D. Schuler, 1997: "Texture and speckle statistics in polarimetric SAR synthesized images", Submitted to *IEEE Transactions on Geoscience and Remote Sensing*.
- [11]. A. Lopès, E. Nezry, R. Touzi and H. Laur, 1993: "Structure detection and statistical adaptive speckle filtering in SAR images", *International Journal of Remote Sensing*, Vol.14, nr.9, pp.1735-1758, June 1993.
- [12]. E. Nezry, F. Zagolski, A. Lopes and F. Yakam-Simen, 1996: "Bayesian filtering of multi-channel SAR images for detection of thin structures and data fusion", *Proceedings of SPIE*, Vol.2958, pp.130-139, September 1996.
- [13]. E. Nezry and F. Yakam-Simen, 1999: "On the preservation of polarimetric signatures and polarimetric texture signatures by fully polarimetric MAP speckle filters", *Proceedings of IGARSS'99*, Vol.3, 3 p., Hamburg (Germany), 28 June-2 July 1999.
- [14]. F. Yakam-Simen, E. Nezry and J. Ewing, 1999: "The legendary lost city 'Ciudad Blanca' found under tropical forest in Honduras, using ERS-2 and JERS-1 SAR imagery", *Proceedings of SPIE*, Vol.3496, pp.21-28, September 1998.
- [15]. F. Yakam-Simen, E. Nezry and J. Ewing, 1999: "The legendary lost city 'Ciudad Blanca' found in the Honduran tropical forest, using ERS-2 and JERS-1 SAR imagery", *Proceedings of IGARSS'99*, Vol.5, 3 p., Hamburg (Germany), 28 June-2 July 1999.
- [16]. E. Nezry, F. Yakam-Simen, F. Zagolski and I. Supit, 1997: "Control systems principles applied to speckle filtering and geophysical information extraction in multi-channel SAR images", *Proceedings of SPIE*, Vol.3917, pp.48-57, September 1997.



# A PROTOCOL FOR SPECKLE FILTERING OF SAR IMAGES

R. Touzi

Canada Centre for Remote Sensing  
588 Booth Street, Ottawa  
Ontario, Canada K1A 0Y7

*Abstract*—Speckle filtering of SAR images that preserves the spatial signal variability (texture and fine structures) remains a challenge. Recently, research activity in this topic has become very active until the appearance of many "new" filters. Filter performance assessment mainly based on visual interpretation, is not effective in revealing hidden limitations of filters. Hence, there is an immediate need for the development of rules which permit more effective assessment. These rules could be also used as the basis for the development of new filters. In this study, a protocol which is based on the state of the art in speckle filtering is introduced. Such protocol, which should not become an obstacle for the advancement of research in speckle filtering, might be updated according to the actual state of the art in the field. Finally, the introduced protocol is used to assess several well-known filters, and to develop a new multi-resolution MMSE (i.e. Minimum Mean Square Error) which is much more effective than the classical MMSE filters.

## I. INTRODUCTION

Speckle filtering of SAR images while preserving the spatial signal variability (texture and fine structures) still remains a challenge. The nonstationary nature of the underlying signal makes adaptive filters more effective than the spatially invariant filters used extensively in digital image processing [4], [13]. The former filters adapt their processing to the nonstationary scene signals by using a spatially moving window of a fixed size. Two speckle-scene models are generally used: the multiplicative model, and the product model. These models yield two families of filters which might be distinguished: filters based on the multiplicative speckle model which do not use explicitly the statistical distribution of the underlying scene such as the Lee and Frost filters [4], [13], and the Bayesian filters [12], [17] based on the product model which requires, in addition, an a priori statistical model for the underlying scene signal. In practice, the two family filters are applied using a moving window of a relatively small size (7x7 window is the mostly used (see [13]) in order to provide a satisfactory compromise between speckle reduction and preservation of small structures within a tolerable computing time.

In the following, the objective of speckle filtering

is considered. In Section III, speckle filtering of nonstationary scene signals is discussed in the context of estimation theory. It is shown that the scene reflectivity can only be retrieved accurately for nonstationary scenes which are locally stationary. Signals which are not locally stationary have to be filtered separately using a priori information. In section IV, the speckle multiplicative noise model, the product model, and the related scene models are analysed with regards to signal nonstationarity. Speckle filtering of locally stationary scenes is discussed in Section V, and the necessity of the use of multi-resolution algorithms for accurate estimation of filter parameters is brought out. Speckle filtering of locally nonstationary scenes is then considered in Section VI. This leads to the introduction of a protocol for speckle filtering in section VII. Finally, the protocol is used to assess theoretically the performance of some well known filters, and to develop a new multi-resolution MMSE filter which is more effective than the classical speckle filters based on the MMSE technique.

## II. OBJECTIVE OF SPECKLE FILTERING

The main objective of speckle filtering is to retrieve the radiometric and spatial scene information "R" from the observed "speckled" SAR measurement "I". "R" is generally the incoherent image of the original scene signal (i.e. scene signal viewed with the incoherent transfer function of the SAR system) [19], [12]. In certain cases, the signal to be retrieved "R" might be the scene signal free from the viewing system transfer function, and the delivered filtered output is named the super resolution image [20]. Deconvolution techniques might be used to reconstruct the scene signal. Such techniques which tend to amplify the high spatial frequency noise are not suitable for the inversion of SAR images of small signal to noise ratios [3]. The scene signal might also be retrieved using the Bayesian inverse problem approach proposed in [2]. Such a technique is very sensitive to the assumed a-priori models, and unrealistic behaviour might be introduced due to an erroneous model [2].

### III. SPECKLE FILTERING IN THE CONTEXT OF ESTIMATION THEORY

In both the two cases mentioned above (i.e. incoherent or super-resolution image), speckle filtering remains mainly an estimation problem, and filter development should be performed with respect to certain rules determined by classical estimation theory. Given one realisation of the stochastic process  $I(t)$  observed during a finite interval of time, the estimation of the random process parameters can lead to meaningful estimates only if  $I(t)$  is ergodic and stationary. Stationarity is required such that the time averages of each process converge to a finite limit. Ergodicity is also required so that the different time averages of each process converge to the same limit: the ensemble average. The process parameters can then be estimated by time (in the image domain spatially) averaging the process over a finite interval of time. In the following, the processes involved in the SAR image modelling are assumed ergodic. Speckle filtering will be discussed in term of signal stationarity-nonstationarity.

Because of the spatial variations of the scene signal, the measured radar signal  $I(t)$  is not generally stationary, and the estimations of the filter parameters (such as the mean and coefficient of variation) lead to meaningless values.

In practice, stationarity in mean (the assumption that the mean  $E(x)$  does not vary) may be relaxed: all that is required is that  $E(x)$  does not change significantly within the observation interval [10]. If such a condition is satisfied by the processes involved in the filtering equation, the nonstationary processes can be considered locally stationary (named "stationary in increments" in [10]), and the parameters required for speckle filtering can be estimated over a moving window in which the processes involved are stationary. This corresponds to the basic idea of the adaptive filtering. The adaptive filter parameters which are estimated locally within a moving window (in which the observed and the scene signals are stationary), vary spatially (with the window position) to cope with the observed and scene signal variations.

### IV. SPECKLE AND SCENE MODELS

#### A. Multiplicative model for speckle

Under the assumption that the terrain reflectivity  $R(t)$  is slowly varying within the resolution cell (i.e. locally stationary within the resolution cell) [29], the multiplicative model states that the observed intensity of the pixel located at  $t=(x,y)$  is given by [4], [13]:  $I(t)=R(t).n(t)$ . The speckle random function  $n(t)$  is assumed to be stationary white unit mean  $\chi^2$  distributed. As we previously mentioned in a study

on speckle filtering of polarimetric data [26], the stationarity assumption for speckle noise is suitable for the following reasons:

- Speckle statistics are constant on the whole scene. They can be accurately estimated, and need to be estimated once for the whole scene.
- The algorithms for filtering of stationary noise are much simpler to implement and less expensive in computing time than the ones developed for nonstationary noise.
- Certain aspects of speckle related to the illuminated scenes (such as the degree of polarization of the scattered wave due [26]) should remain in the filtered image (for a better characterisation of the scene).

#### B. Scene model for stationary speckle noise

For accurate estimation of signal parameters, the observed signal should be locally stationary. Such condition might be satisfied provided that  $R(t)$  is locally stationary (as speckle is stationary). The scene signal and the observed signals are then both stationary in increments, and signal parameters can be estimated accurately within a moving window in which the signals are locally stationary (and ergodic). For a nonstationary scene, signal parameters vary from one window position to another. This leads to parameter estimates which vary spatially with the window position in order to cope properly (and as such to have a better capability of speckle filtering) with the spatial variations of the scene signal. One application of the stationary in increments model is the nonstationary mean nonstationary variance scene model (NMNV) of [12]. It assumes that the scene (and consequently the observed) signals are locally stationary in mean and variance. This model might be presented as the basis of some well known filters such as the Frost and Lee filters whose parameters are mainly the local mean and coefficient of variation estimates.

#### C. Speckle-scene product model

The product model, also called the double stochastic model, was used as the basis of the MAP Bayesian one-level (Gaussian [12], and Gamma [16], [21]), and multi-level([2]) filters. The product model was introduced in ([15], [8], [7]) to express the K-distribution, which fits well ocean backscattering [6], as a function of the Gamma distribution whose statistics are easier to estimate [22], [9]. The spatially varying Rayleigh clutter distribution which is conditioned on its gamma-distributed local mean leads to unconditioned PDF which is K-distributed.

The product model is based on a technique developed for characterising nonstationary functions (see [15] for example). The first-order density function of the nonstationary process is treated as a function of



random key parameters, and is presented in term of conditional probability density function (pdf). The conditional pdf is averaged over the parameter under consideration to yield an unconditional pdf which is stationary in the parameter of integration even though the original (conditional) pdf is not stationary. An equivalent method was proposed in [23] to transform a nonstationary correlation function to a stationary function named the spatially averaged correlation function. This method was used in [28] to justify the use of the adaptive coherence estimate for characterisation of nonstationary coherence signals.

In contrast to the multiplicative model of (IV.A), the product model of (IV.C) assumes that speckle, which is still locally stationary within a resolution cell (i.e. the multiplicative model condition satisfied), is not stationary in mean within the moving processing window. The mean is supposed to vary from one pixel to another according to a given distribution (Gamma for example). Using the product model, the Bayesian filters transform the nonstationary speckled signal ( $I(t)$ ) in a locally stationary signal ( $K$  distribution of stationary mean and variance for example) within the moving processing window. The parameter estimation is applied in two levels: estimation at the pixel level (for each pixel) of the mean of the  $\chi^2$  speckle distribution, and estimation at the window level of the statistics of the mean reflectivity (i.e. the averaged pixel means which corresponds to the Gamma parameter). For meaningful statistical description, the processing window should be large enough to include many samples of the same speckle  $\chi^2$  distribution (for the first-level estimation), and enough samples of the various  $\chi^2$  distribution (for the second-level estimation). Therefore, the filtering window size should be larger than the one which might be used under speckle stationarity assumption of section (IV.A).

The result above concerning the classical product model which is a double stochastic model, might be extended to the multiply stochastic model described in [15], [25]. The multiply stochastic is formed by averaging its mean over a first-level distribution; the latter which might itself have a mean that is subject to uncertainty is then averaged over a second-level distribution of that mean. The process may need to be continued, in principle, until the deepest-level distribution has a mean and other statistical parameters that are truly deterministic. The parameter averaging lead to an unconditional pdf which is stationary in the smeared parameters. The minimum window size required for accurate estimation of these parameters increase with the number of levels of averaging as the complexity of the unconditional pdf tends to rise rapidly with each additional level.

At the deepest level, the a-priori information is

described with a process stationary in mean (or parameters smeared other than the mean). Among the most used a-priori scene models are the Markov Random fields which are expressed in term of Gibbs Random fields under the local stationarity condition [24]. For accurate estimation of the pdf parameters of such process, large neighbour in which the process is stationary, are required. Segmentation and multi-resolution techniques were used for example in [2], [30] to form an image with separate entities in which the process is stationary. If this not done properly, unrealistic behaviour might be introduced in the filtered image.

## V. SPECKLE FILTERING OF STATIONARY INCREMENT SCENES

### A. Adaptive filtering

Many digital filters were developed in the field of communication theory to reduce the transmission channel noise which was generally assumed to be white and additive noise. Some of them were adapted to SAR images to filter the multiplicative speckle noise under the adaptive form which is shown to be suitable for stationary in increment signals. The most well know are based on the Minimum Mean Square Error (MMSE) [4], [13], [12], or the Bayesian [12], [17], [2] techniques. These filters which were originally derived for stationary signals are adapted to slowly varying nonstationary signals. The filters parameters are performed within a moving window in which signals can be assumed to be stationary and ergodic. The filter output is a spatially varying (as a function of the processing window position) scalar (or a vector) which corresponds to an estimate of the nonstationary scene function.

In contrast to speckle filters based on the multiplicative model, the filters based on the product (or the multiply stochastic) model requires a priori models at each level of averaging. Speckle filtering is mainly Bayesian model fitting which optimizes the Maximum a posteriori (MAP) criteria [12], [17], [2]. However, speckle filtering under the multiply stochastic model (like for any inverse problem method) is very sensitive to the assumed a-priori models, and unrealistic behaviour might be introduced due to erroneous models [2]. Consequently, unless the a-priori models fit well the reality, methods based on the simple multiplicative model remains more effective, and more attractive as they are expansive in computing time. A promising solution was proposed in [2] which consists in matching various a-priori models to the scene under study at the expense of large computing time.

### B. Multi-resolution adaptive filtering

The filter parameters are calculated using the observed signal statistics within windows (generally of fixed size) in which the signal is locally stationary. Certain parameters like the second order statistics (the covariance function for example) need large windows for an accurate estimation. Filters based on the product model need larger windows than the ones based on the simple multiplicative model of section IV (A and C). Both models have to be applied within a region where the observed and scene signal are locally stationary. As such, the processing window should be of a limited size such as only a "stationary" portion of the illuminated target is covered. Tests of stationarity should be applied on the observed signal to adapt the size and the shape of processing window to signal nonstationarity. As such, the estimation within the selected window of local stationarity leads to accurate and meaningful parameter estimates. This improves significantly the performance of the classical filters which are blindly applied on a moving window of a fixed size. An example is given in [5] concerning the classical box (average) filter. The Hagg filter which is a multi-resolution box filter is much more effective than the classical box filter of a fixed size. One problem with the Hagg filter is that it is only adapted to areas of constant reflectivity ( $R(t) = \text{constant}$ ). The filter, which is not based on a solid method of signal estimation theory (averaging of homogeneous region), is completely ineffective in textured areas (which might be locally stationary but not necessarily locally homogeneous).

## VI. SPECKLE FILTERING OF LOCALLY NONSTATIONARY SCENES

Scene signals might be nonstationary even within a small region. Nonstationarity might be due to the presence of edges, curvilinear features, or point targets. If the scene signal is varying rapidly within the resolution cell, the multiplicative speckle model (and consequently the product model) cannot even be used. Signal variations from one resolution to another within any small neighbourhood makes statistic estimation meaningless. The solution would be to correlate the observed signal with a replica (noise-free ideal signal) which models local scene nonstationarity. Such correlation would improve the signal to the speckle noise ratio, and as such would enhance the nonstationary feature (the source of nonstationarity). The filter might then adapt the shape of the window to the enhanced feature, and as such use a sufficiently large number of independent samples for an accurate estimation of the unspeckled feature signal. Since the underlying scene signal is not known, various replicas might be tested and the one which

would enhance the best the scene feature might be selected. Multi-resolution processing remains again the best way to increase the signal to noise ratio of the replica-image correlation. The multi-resolution technique first introduced for SAR images in [27], significantly improves the performance of the ratio edge detector in the presence of small edges, and in areas of low contrast (see [27]).

## VII. A PROTOCOL FOR SPECKLE FILTERING

### A. Presentation of the protocol

According to the discussion above, a set of rules (i.e. a protocol) might be set for effective speckle reduction. Filter conception should be done with respect to the protocol presented in Figure 1. This means that any speckle filter should include the following tools:

1. An algorithm which takes into account speckle statistics for speckle reduction of locally stationary areas
2. An algorithm to detect neighbourhood which are not locally stationary,
3. Replicas to match local non-stationarity
4. Algorithm for speckle filtering of locally non-stationary areas as a function of the matched scene replica
5. Multi-resolution algorithms to fit the size and the shape of the neighbour to signal stationarity

### B. Applications of the protocol: filters assessment and development

Such a protocol allows one to assess theoretically the performance of any speckle filter. For example, the following filters suffer of a number of weakness:

- The Hagg filter [5] employs a simple box algorithm for speckle filtering of locally stationary areas. As such, texture cannot be preserved,
- The Kuan and Frost filters do not include tools to detect nonstationarity,
- Application of the Bayesian filters with small windows might lead to erroneous filter parameter estimates.
- Filters based on wavelets [1] can only preserve fine structure. They should be equipped with a speckle model based algorithm for an effective speckle filtering within locally stationary areas.

The protocol above was used to develop an MMSE multi-resolution filter. Figures 2, 3, and 4 present the original image (Radarsat fine mode 1-look), and the images filtered with the enhanced ([18]) MMSE ([13], [11]) filter over 7x7 window, and the multi-resolution MMSE filter. The multi-resolution filter converges to stable values for a 29x29 window size. Obviously, the multi-resolution technique permit better preserving of texture and fine structures with an effective

speckle reduction within homogeneous areas.

### CONCLUSION

Speckle filtering of nonstationary scenes can be performed accurately if the scene signal is stationary in increments. Scenes which are not locally stationary should be filtered separately using a priori replicas of the nonstationary scene feature. The protocol of speckle filtering introduced in this study might be used to assess theoretically the performance of speckle filters. This protocol was used by the author as the basis for the development of a new multi-resolution MMSE filter which is much more effective than the classical MMSE filters. The same multi-resolution technique used here to improve the MMSE filter might be also exploited to improve the performance of other filters such as the Frost [4], Lee [14], and MAP Gamma ([17], [21]) filters.

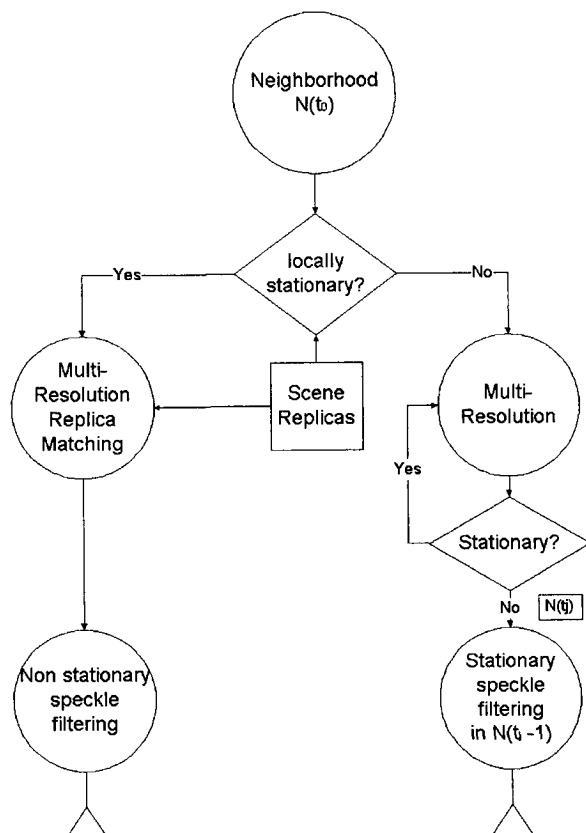


Fig. 1. Flow chart

### REFERENCES

- [1] M. Datcu, D. Luca, and K. Seidel. Multiresolution analysis of SAR images. In *Proc. of EUSAR'96, Germany*, 1996.
- [2] M. Datcu, K. Seidel, and M. Walessa. Spatial information retrieval from remote sensing images. *IEEE Trans. Geo. Rem. Sens.*, 36:1431-1445, 1998.
- [3] V.S. Frost, J.A. Stiles, and J.C. Holtzman. Radar image preprocessing. In *Machine Proc. of Rem. Sensed Data Symp.*, pages 140-147, 1980.
- [4] V.S. Frost, J.A. Stiles, K.S. Shanmugan, and J.C. Holtzman. A model for radar images and its application to adaptive digital filtering of multiplicative noise. *IEEE Trans. Pat. Anal. Mach. Intell.*, 4:157-166, 1982.
- [5] W. Hagg and M. Sties. Efficient speckle filtering of SAR images. In *Proc. IGARSS'97, 08-12 August 1994, Pasadena, USA*, pages 2140-2142, 1994.
- [6] E. Jakeman and P.N. Pusey. A model for non-railigh sea echo. *IEEE Trans. on Antennas and Propagation*, 24:806-814, 1976.
- [7] E. Jakeman and R.A. Tough. Generalized k distribution: a statistical model for weak scattering. *Journal of the Optical Society of America*, 4:1764-1772, 1984.
- [8] J.K. Jao. Amplitude distribution of composite terrain radar clutter and the k-distribution. *IEEE Trans. on Antennas and Propagation*, 32:1049-1062, 1984.
- [9] I.R. Joughin, D.B. Percival, and D.P. Winebrenner. Maximum likelihood estimation of k distribution parameters for sar data. *IEEE Trans. Geo. Rem. Sens.*, 31:989-999, 1993.
- [10] D.L.B. Jupp, A.H. Strahler, and C.E. Woodcock. Autocorrelation and regularization in digital images: basic theory. *IEEE Trans. Geo. Rem. Sens.*, 26:463-473, 1988.
- [11] D.T. Kuan, A.A. Sawchuk, T.C. Strand, and P. Chavel. Adaptive noise smoothing filter for images with signal-dependent noise. *IEEE Trans. Pat. Anal. Mach. Intell.*, 2:165-177, 1985.
- [12] D.T. Kuan, A.A. Sawchuk, T.C. Strand, and P. Chavel. Adaptive restoration of images with speckle. *IEEE Trans. on Acous. Speech and Sig. Proc.*, 35:373-383, 1987.
- [13] J.S. Lee. Digital image enhancement and noise filtering by use of local statistics. *IEEE Trans. Pat. Anal. Mach. Intell.*, 2:165-168, 1980.
- [14] J.S. Lee. Refined filtering of image noise using local statistics. *Computer Graphics and Image Processing*, 15:380-389, 1981.
- [15] D.J. Lewinski. Nonstationary probabilistic target and clutter scattering models. *IEEE Trans. Ant. Propagat.*, 31:490-498, 1983.
- [16] A. Lopes, E. Nezry, R. Touzi, and H. Laur. MAP speckle filtering in SAR images. In *Proc. IGARSS'90, May 1990, Washington*, pages 1683-1686, 1990.
- [17] A. Lopes, E. Nezry, R. Touzi, and H. Laur. Structure detection and statistical adaptive speckle filtering in sar images. *Int. J. Rem. Sens.*, 14:1735-1758, 1993.
- [18] A. Lopes, R. Touzi, and E. Nezry. Adaptive speckle filters ans scene heteogeneity. *IEEE Trans. Geo. Rem. Sens.*, 28:992-1000, 1990.
- [19] S. Lowenthal and H. Arsenault. Image formation for coherent diffuse objects: statistical properties. *Journal of the Optical Society of America*, 60:1478-1483, 1970.
- [20] S.P. Luttrell. The theory of bayesian super-resolution of coherent images: a review. *Int. J. Rem. Sens.*, 2:303-314, 1991.
- [21] C.J. Oliver. Review article: Information from sar images. *J. Phys. D: Appli. Phys.*, 24:1493-1514, 1991.
- [22] C.J. Oliver. Optimum texture estimators for sar clutter. *J. Phys. D: Appli. Phys.*, 26:1824-1835, 1993.
- [23] A. Papoulis. *Probability, Random Variables and Stochastic Processes*. McGraw-Hill, New York, 1965.
- [24] F. Spitzer. Markov random fields and gibbs ensemble. *The American Mathematical Monthly*, 78:142-154, 1971.
- [25] M.C. Teich and P. Diament. Multiply stochastic representations for k distributions and their poisson transforms. *Journal of the Optical Society of America*, 6:80-91, 1989.
- [26] R. Touzi and A. Lopes. The principle of speckle filtering in polarimetric sar imagery. *IEEE Trans. Geo. Rem. Sens.*, 32:1110-1114, 1999.
- [27] R. Touzi, A. Lopes, and P. Bousquet. A statistical and geometrical edge detector for sar images. *IEEE Trans. Geo. Rem. Sens.*, 26:764-773, 1988.
- [28] R. Touzi, A. Lopes, J. Bruniquel, and P. Vachon. Coherence estimation for sar imagery. *IEEE Trans. Geo. Rem. Sens.*, 37:135-149, 1999.

- [29] M. Tur, K.C. Chin, and J.W. Goodman. When is speckle multiplicative? *Appl. Opt.*, 21:1157-1159, 1982.
- [30] M. Walessa and M. Datcu. Texture preserving of SAR images using GMRFs. In *Proc. IGARSS'99, July 1999, Hamburg, Germany*, 1999.

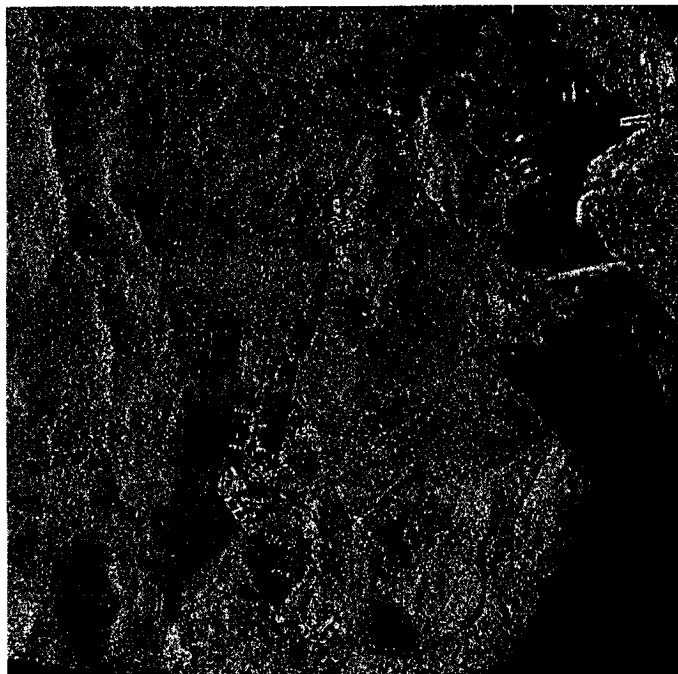


Fig. 2. *Original image*

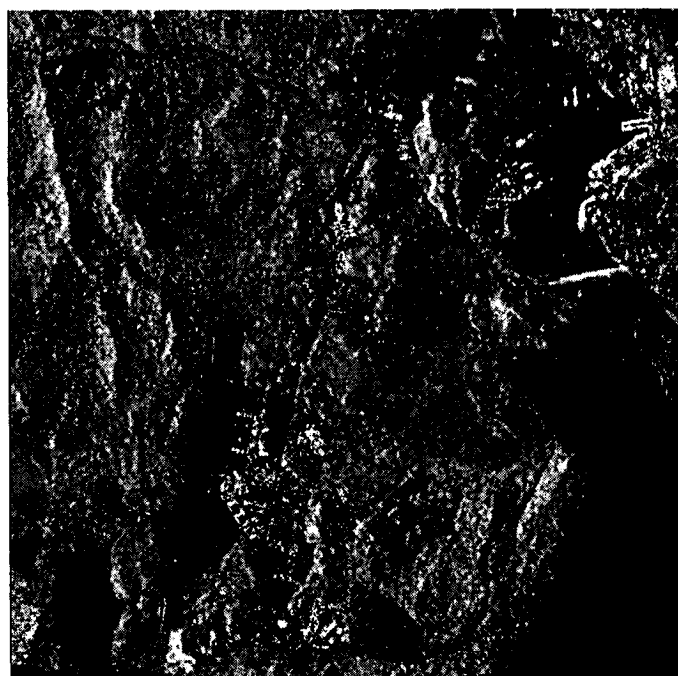


Fig. 3. *Enhanced MMSE filtered image*

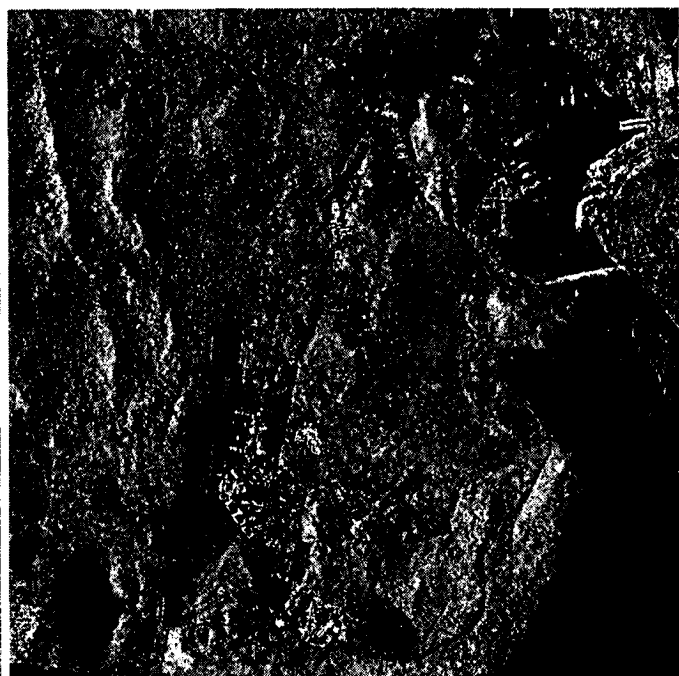


Fig. 4. *Multi-resolution MMSE filtered image*

**Session 6: Instrument Design and New Concepts**



**Space-Borne SAR in Russia: SRIPI's Main Projects**

Ilya Neiman, Sergey Vnotchenko  
Scientific & Research Institute of Precise Instruments, Russia

Alexander Zakharov  
Institute of Radioengineering & Electronics, Russia

Oleg Goriachkin  
Central Specialized Design Bureau, Russia

This paper was not available for publication





## Modular Design of SAR Electronics CEOS SAR Workshop, 26-29 October 1999, Toulouse, France

F.A.Petz, J.Rosello-Guasch, C.Mavrocordatos

TOS-ET, European Space Agency, Keplerlaan 1, NL 2200 AG Noordwijk, The Netherlands

e-mail: (fpetz, jrosello, cmavroco)@estec.esa.nl

Ch.V.Narasimha Rao

MSTD/MSG/SAC, Indian Space Research Organisation, Ahmedabad – 380 053, India

e-mail: cvnrao@hotmail.com

**Abstract --- To achieve better balance between investment and return, the development of more generally applicable technologies (generic, modular, multi-functional) or the application of the proven off-the-shelf technologies are the key issues. Besides cost effective design and manufacturing, the competitiveness can be significantly improved with a wider applicability of the technology. This paper discusses the modular design approach and the implementation related aspects of a multi-frequency, multi-mode, high-resolution SAR system.**

### I. INTRODUCTION

The operational advantages of Synthetic Aperture Radar (SAR) have been clearly shown by ERS1/2 and Radarsat. Excellent images of the Earth can be produced, in all weather conditions, day and night. Considerable progress has been achieved in the interpretation of these images. It is believed that effective cost reduction can be achieved by putting the emphasis on the improvement of SAR technology to attract the commercial market [1].

To achieve better balance between investment and return the development of more generally applicable technologies (generic, modular, multi-functional) is a must. Consequently emphasis has been given to the chirp generation and coherent signal detection. Besides cost effective design and manufacturing, the competitiveness can be significantly improved with a wider applicability of the technology development. Based on the specific features of the basic building blocks, either of frequency independent or of wideband nature as described in this paper, quick radar instrument configuration can be derived from system inputs. Besides the highly accurate performance predictions, specifically for the antenna layout, fairly good estimates of the mass, power and instrument cost can be made.

### II. PRINCIPAL DESIGN APPROACH

From a basic functional point of view the instrument architecture can be subdivided into: RF Front-end (Antenna, Up/Down Conversion) and the Signal Generation / Detection Unit (IF, Tx Chirp Generation, Rx Signal Detection). Furthermore it is very common to distinguish between the Antenna (Radiator, TR module, Subpanel Electronics (SPE), Distribution Network (DNW)) and the Central Electronics (Frequency Converter, LO, IF Signal Handling / Processing Units, Satellite Bus I/F

Electronics). Figure 1 shows the Radar instrument general block diagram.

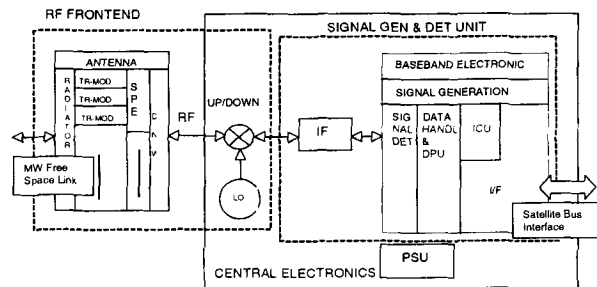


Figure 1 Radar Instrument Block Diagram

### III. RF FRONT-END

Modularity at antenna level should aim for low overall complexity, for easy integration of all modules and units, combined with low weight and temperature insensitivity of electrical antenna performance. Important active array antenna design drivers are in general mass, dc-power consumption and achievable SNR. Obviously good performance will be achieved with a certain number of TR modules. To ensure lowest mass contribution and simultaneously keeping dc-power consumption low, the TR modules must be of lowest possible complexity. Avoiding sophisticated phase, amplitude and thermal control will lower the cost twofold: from hardware implementation as well as from characterisation points of view.

#### A. TR Module

To get low TR module complexity, the minimum number of components required shall be incorporated, which are circulators, limiter, LNA and SSPA. The phase and amplitude control circuitry together with Tx and Rx amplifiers are "centrally" located in the Subpanel Electronics (SPE) avoiding any TCM I/F harness to the individual TR modules, and last but not least to allow this components to be operated in a very tight controlled thermal environment. The only required interface between the TR module and the SPE is a single coaxial cable, which transports the microwave Tx & Rx signals, the SSPA dc power and a 200kHz/2V signal to control the Tx/Rx gating (switching) within the TR module. The TR module hybrid will also employ a suitable simple gain control circuitry to guarantee the gain stability for the LNA, and proper RF drive power for the SSPA versus temperature variations.

Dual polarisation operation is achieved by employing 2 modules, one per polarisation.

Figure 2 shows the architecture of TR module with the proposed concept. The circulator at the antenna radiator I/F separates the Tx and Rx signals. The limiter in front of the LNA prevents passing excessive signal power towards the LNA. The RF signal at the I/F with the SPE is routed via a 2<sup>nd</sup> circulator separating the signals travelling to the SSPA from those coming from the LNA.

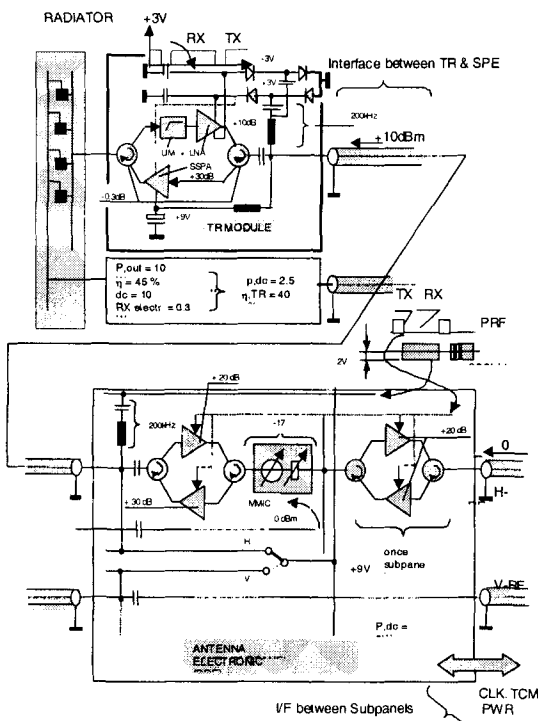


Figure 2 TR Module - Split

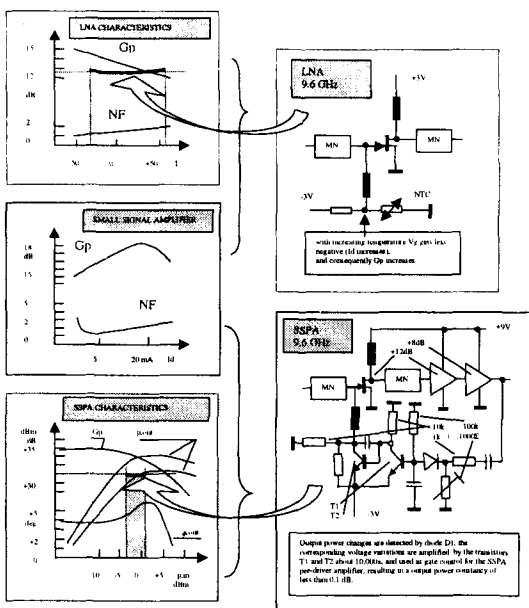


Figure 3 Temperature Stabilised LNA (constant Gain) and SSPA (constant P<sub>out</sub>) [5, 6]

**B. TR Module - Power Supply Unit**

The SPE provides the proper I/F for the TR modules and the CE via the Antenna I/F. This function includes the TCM (phase and amplitude data handling for each TR module, PRF and clock reception) as well as the dc power distribution to the TR modules. As a minimum, this radar frequency independent module contains a Buck Converter for generating the +9V (or any other SSPA voltage) for the SSPA drain supply, the 200kHz/2V signal which serves for the Tx/Rx signal function in the TR module and the +3V generation (LNA voltage supply).

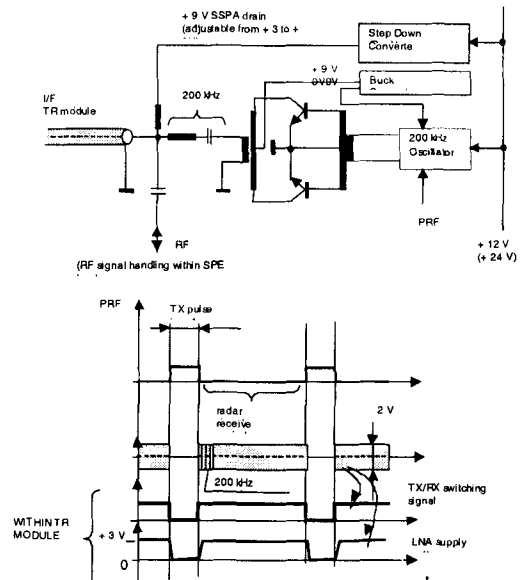


Figure 4 TR Module - Power Supply Unit

**C. TR Module - Phase & Amplitude Control**

The SPE is composed, unlike the TR modules, of frequency dependent and also frequency independent components and units. Highest degree of modularity can be achieved by using a wideband multifunctional GaAs MMIC switch serving all bands and useable for phase and amplitude control, MMIC-external delay lines depending on the frequency bands & a control ASIC which contains the relevant phase and amplitude adjustment look-up tables based on the characterisation of this assembly. The SPE is kept at a constant temperature avoiding the temperature dependent performance drifts.

Figure 5 illustrates the principal switch circuit diagram, and provides an implementation example based on VM function (Vector Modulator function) and switchable delay lines.

**D. Distribution Network**

The Distribution Network (DNW) is split into 3 levels: Subpanel, Antenna and I/F towards Central Electronic (CE). Table I shows details of the distribution network in this approach. Due to the DNW simplicity and hence to the

minimum interconnections at Subpanel level, the bulk of the DNW is concentrated at Antenna level (between the SPEs) and towards the CE.

DNW Type	Subpanel Level	Antenna Level	LF towards CE
Coax Cable (equal length)	RF (TX & RX) +9V dc 200kHz/2V	RF (TX & RX) clk (10MHz)	RF (TX & RX) clk (10MHz)
Twisted Pair	n.a.	TCM (phase, amplitude, mode) PRF	TCM PRF
dc-Power Cable	n.a.	+9V +5V -5V	+12V (+24V)

Table II Active Array Distribution Network

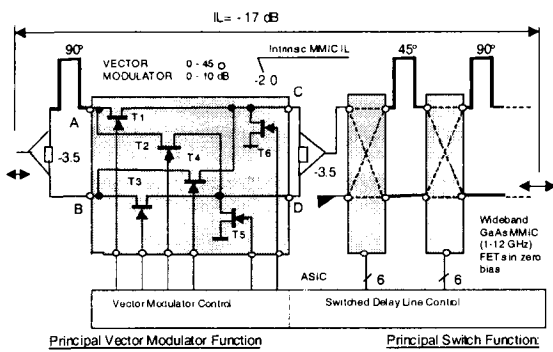


Figure 5 Phase & Amplitude Control

IV. SIGNAL GENERATION & DETECTION

The chosen baseline is modular chirp generation (digitally, at baseband) and modular echo signal detection. The modular blocks (hybrids) are designed for a fixed maximum subband bandwidth  $2\omega_1$ . From a look-up table (chirp memory) a  $2\omega_1$  wide signal is read, D/A converted, lowpass filtered and upconverted to the IF band. After corresponding time  $2t_1$  (subchirp pulse length) the LO switches to a  $2\omega_1$  higher (or lower) frequency and next chirp memory readout over the period of  $2t_1$  takes place, and so on, until the whole chirp of the full bandwidth  $BW = (2N+1).2\omega_1$  and pulse length  $T = (2N+1).2t_1$  is generated. On the detection side functionally a suitable amount of "similar" receive hybrids are operated in parallel, each handling a  $2\omega_1$  subband. Unlike for the signal generation, the LO frequencies are not switched but steadily input to the mixers for basebanding. After lowpass filtering the signal blocks are A/D converted and handed forward to the signal processing / data handling unit.

A. Chirp Hybrid & Receive Hybrids

Full modularity and flexibility is only achievable with a minimum of basic building blocks not requiring additional hardware design efforts [1]. The signal generation / detection is based on 2 building blocks:

- Chirp generation hybrid
- Receive hybrid

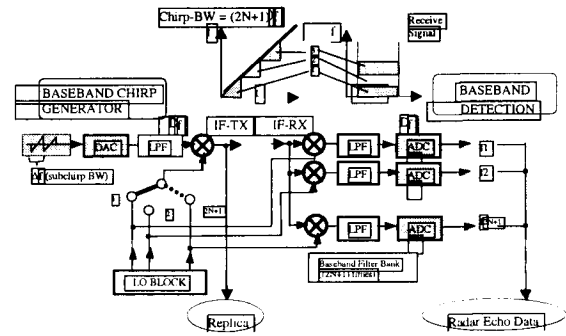


Figure 6 Modular Wideband Chirp Generation/Detection

Both types of hybrids are almost identical from a hardware point of view (and physical hybrid layout!), containing LO-generation, mixers, analog LPFs, DAC or ADC, digital memory or digital LPF. For the sake of flexibility and hardware implementation, the LO block is chosen to be part of the hybrids. Figure 7 shows the architecture of chirp hybrid.

B. I/Q Modulator / Demodulator

For the signal generation and detection, the I/Q modulator/demodulator are preferred to the SSB modulator / Image Reject Mixers respectively, because of the better image rejection performance achievable as the quadrature shifting is required for only for the LO frequency and not over the band of frequencies. Image rejection is a measure of the balances (amplitude & quadrature phase) realised in the chosen configuration. In addition, in the present concept, the quadrature phase shifting network (the delay lines) is kept hybrid external and so delay lines can be designed depending on the position of the hybrid making the modular I/Q networks applicable over wider bandwidths.

C. LO Generator

One mixer block each, out of the required LO frequency generation chain is implemented within a single chirp hybrid. With the final arrangement of all the hybrids, the complete LO frequency chain is automatically installed. Although the prescalers are in principle required only once, nevertheless each hybrid is equipped with one for the sake of full modularity.

D. Phase Bias

To maintain the frequency coherency and phase continuity during the summation process, the LO signals need to be without phase bias at these intersection points (Figure 8). The phase bias at the subchirp summing points, which is due to the quadratic phase variation, can be taken care of by either making it a multiple of  $2\pi$  or by letting consecutive subchirp memories hold the consecutive subsections of whole chirp, but each at baseband (dc to  $2\omega_1$  Hz), and not "individual" chirps having bandwidth of  $2\omega_1$ .

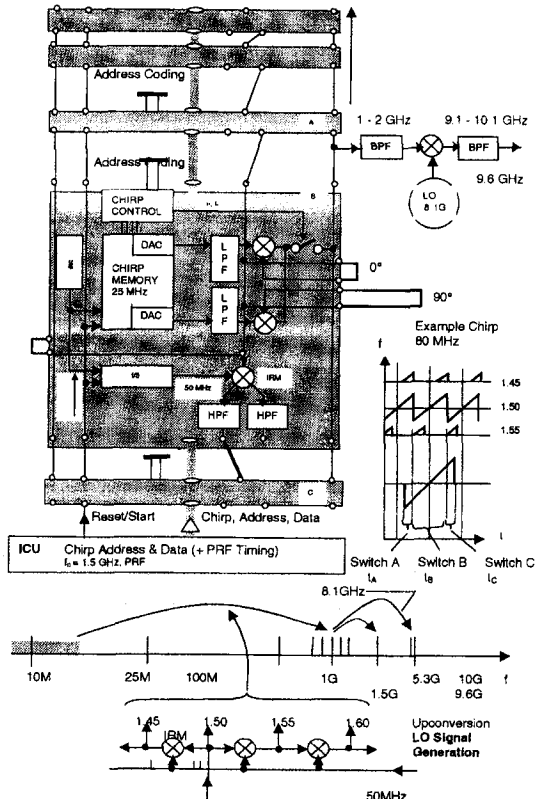


Figure 7 Architecture of Chirp Hybrid

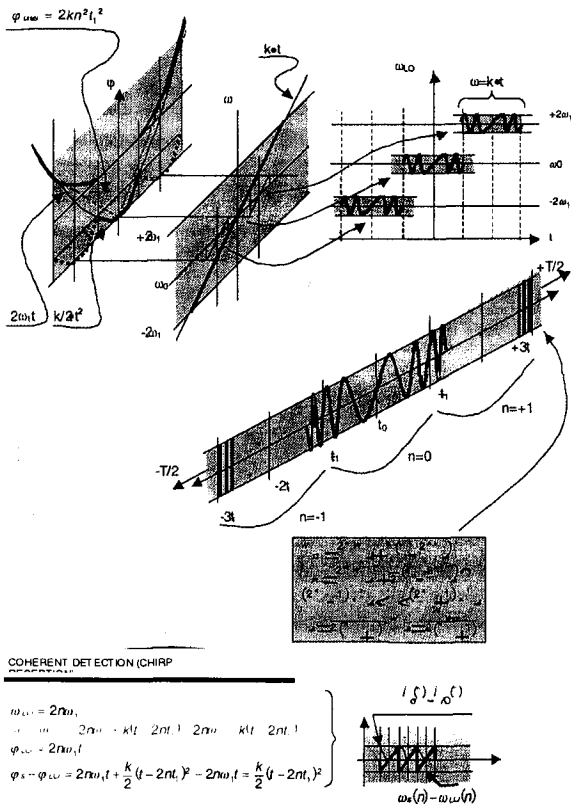


Figure 8 Tx Signal composition

V. MODULAR DATA HANDLING ARCHITECTURE

Figure 9 shows the modular data handling architecture of a multi-mode SAR instrument, whose parameters are given in Table II.

Mode	Azimuth Mode	Subswath (km)	Sampling Frequency (MHz)	samples / echo	Data rate (Mbps)	Pixel size (m)
Very High Resolution	Spotlight	20	>300	20,000	>300	1
High Resolution	Imaging	100	100	25,000	500	4
Medium Resolution	Scan SAR	100	20 to 4	5000 to 1000	100 to 20	20 to 100

Table II Typical Parameters of a Multi-mode SAR Instrument

Each of the modules in Figure 9 comprises of:

- demultiplexing and FIFO buffers in order to distribute the data acquired during the echo window interval all over the Pulse Repetition Interval
- a programmable digital filter in order to introduce further flexibility in the chain.

Each of these modules should be interfaced with:

- Solid State recorders in order to ensure temporary storage on-board and transmission to ground in non-real time (if necessary)
- Instrument Control Unit (ICU), for several operational and monitoring tasks
- And also at least one of the modules should be connected to a Data Processing Unit (DPU) for the on-board processing of low-resolution modes

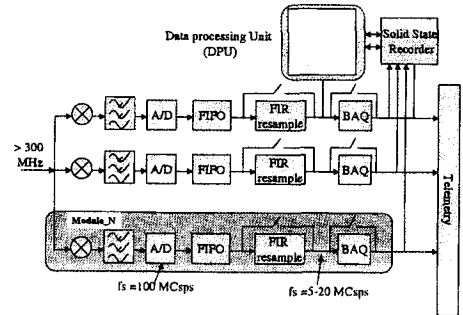


Figure 9 Baseline for a Modular Data Handling Architecture

The subsequent sections deal with processing of raw data for the generation of high-resolution SAR imagery. The following are the major processing stages involved, which could be performed on-ground:

- Combination of data coming from different modules
- Pulse range compression
- Azimuth compression

A. Combination of Data Coming from Different Modules

This problem can be seen from two perspectives: from the time domain and from the frequency domain.

Time Domain Perspective

Every sub-module range line has to be first resampled into the higher resolution and then summed to the other sub-module lines. In practice, this process can be efficiently carried out with decimation and interpolation filters. Figure 10 shows one possible implementation when using the block processing approach with an FFT oriented algorithm.

Frequency Domain Perspective:

In the following paragraphs the decimated data coming from one module or sub-band will be termed 'look'. Figure 13 demonstrates the equivalency between the combination of data from different modules and the so-called multi-look processing in SAR processing terminology. The left-hand side of Figure 11 shows one of the 'looks' in the frequency domain sampled at 'fs' rate. Then, the same signal in the time domain is depicted below with  $T_s = 1 / f_s$ . Its interpolated signal, with the expected high-resolution sampling period  $T_s' = T_s / N$ , requires a new  $f_s' = N \cdot f_s$ . The gaps that appear in the spectrum can be considered as zeros (i.e. the so-called zero padding in the digital domain). Since each look had undergone a different shift in the analog domain in order to bring that to base-band, that shift in frequency has to be corrected to bring back to its original spectral location. In case different looks have overlapping areas of the spectrum, some sort of averaging should be considered. The whole process is depicted on the right hand side of Figure 11. The inconvenience of the frequency domain approach is that it cannot lead to "Perfect Reconstruction" because the equivalent interpolation filter does not depend on the decimation filters. Its advantage however is that it is computationally efficient, especially if it can be combined with the matched filtering (Figure 12) during the pulse range compression.

B. Pulse Range Compression

To generate range compressed data, every raw data echo has to be matched filtered with the transmitted pulse replica of the SAR. This process is outlined in Figure 12 for a full bandwidth range line. Figure 13 shows the similarities between:

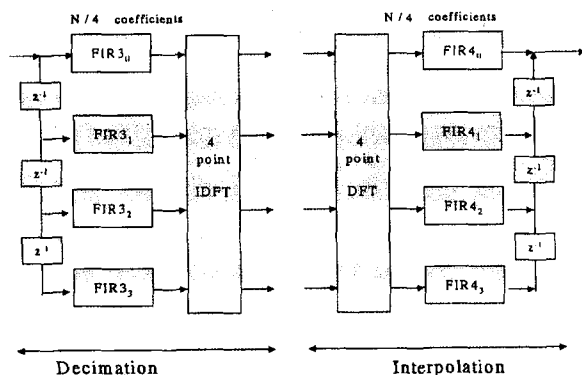


Figure 10 Efficient Interpolation with a 4-band Polyphase Filters

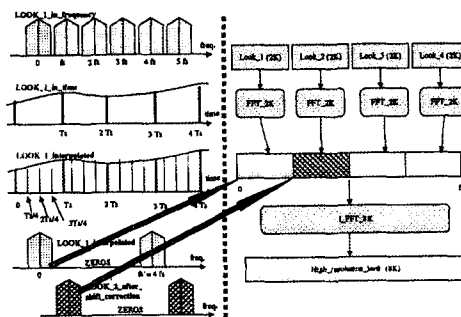


Figure 11 Interpolation and Combination of Looks

- the multi-looking technique, which is used to reduce speckle by summing several lower-resolution images with different spectral contents from higher-resolution raw data,
- and the combination of several lower-resolution modules of raw data, which is then combined to generate a higher-resolution image.

Actually, both processes are simply symmetrically opposed, but they have one common stage: the matched filtering or multiplication in the frequency domain by the conjugate of the spectrum of the SAR pulse replica with the highest resolution. This shows that the modular architecture shown in Figure 9 is equivalent to a set of lower resolution SAR systems with contiguous carrier frequencies. The loss of one of the modules would simply mean a loss in resolution, or a degradation in radiometric resolution (i.e. greater speckle contents) for multi-look processed modules.

C. Azimuth Compression

In order to achieve "almost" square pixels with the same antenna configuration, azimuth processing will vary dramatically from one mode to another. These differences are not explained because they are independent from the modularity principle presented here.

Very high resolution	1	Spot
High resolution	4	Imaging
Medium resolution	20 to 100	SCANSAR

Table III Types of Azimuth Modes

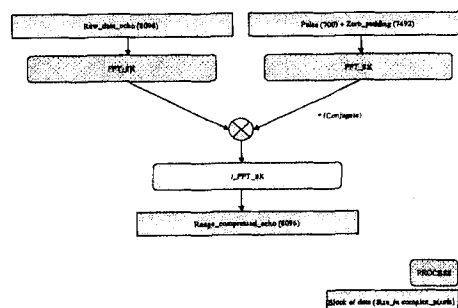


Figure 12 Classical Matched Filter

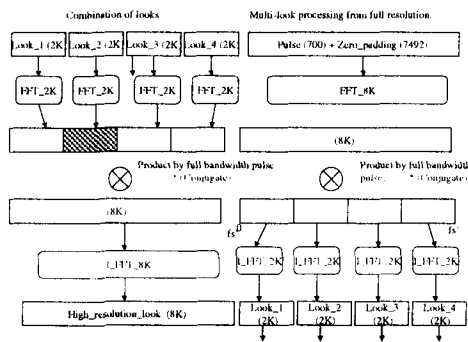


Figure 13 Comparison of Matched Filtering of Modular Data with the Classical Multi-Look Processing

## VI. REDUNDANCY ISSUES

### A. Antenna Level

"Standard" SAR Antenna configurations are usually subdivided into Mechanical Subpanels (of deployable nature) and Electrical Subpanels. Each of these Electrical Subpanels will consist of a certain number of Subarrays, individually connected to dedicated separate TR Modules, which are interconnected to a single Subpanel Electronic on Subpanel Level. The SPE units contain the Phase and Amplitude Control devices as required for flexible antenna beam shaping and steering.

It is obvious when choosing a reasonable high number of Subarrays (e.g. > 500) redundancy on TR Module level is not any longer required as it is understood that up to 10% of the TR Modules can be lost without having significant effect on the antenna performance, provided that the malfunctions occurred are distributed randomly over the whole antenna aperture: this fact is well known as "graceful degradation" in performance.

The TC/TM digital electronics and the TR-PSU and the SPE PSU are in principle required only once per SPE. To avoid loss of a whole Subpanel these circuits are required to be redundant. The DNW is proposed to be of passive nature, so therefore redundancy is not necessarily required. For dual polarisation radars the DNW caused single point failure feature is avoided by the automatically needed 2<sup>nd</sup> DNW.

In-flight Instrument Calibration, specifically for Active Antenna Arrays, has been considered mandatory to ensure the required Instrument Parameter Stability requirements. However for the proposed Modular Instrument Electronic it is believed that the usually performed in-flight Phase and Amplitude characterisation is not any longer required (relying on the assumption that the coaxial cable based DNW is temperature invariant). Nevertheless what might be required is a "Health Check" mechanism (Go-No Go message). Within the TR Module the RF output power detector can provide the necessary information.

### B. Central Electronic Level

As it is a standard practice, Cold Redundancy is the recommended approach for the CE units. Hereby the baseband radar electronic units can be treated in a different way, since it is based on  $(2N+1)$  parallel blocks. And the more blocks are implemented, the less critical is the loss of a single block!

## VII. CONCLUSIONS

This approach is fully in line with the requirements expressed to make radar design commercially self standing, taking full advantage of the synergy with other disciplines (e.g. communication), as well as to establish technology spin-off in any applicable field to ensure highest benefit of R&D investment. Modularity can be fully exploited based on building block implementation. The following are obvious advantages of the approach :

**Technological simplicity:** Each module deals with signals of a reasonable bandwidth (i.e. tens of MHz).

**Scalability:** Larger systems can be built from smaller systems.

**Operational flexibility:** The SAR instrument can be easily operated in several modes, by switching all or just a few modules.

**Reliability:** If some modules fail, it is only necessary to switch on other identical modules, or to accept a minimal degradation in resolution (i.e. less bandwidth).

## ACKNOWLEDGEMENTS

The authors would like to thank Mr.W.Greiner and C.C.Lin for their continuous support and their useful advice.

## REFERENCES

- [1]. SAR Workshop 97 Proceedings, ESTEC October 1997
- [2]. SAR Dossier, ESTEC, March 1998-11-03
- [3]. F.A.Petz: "SAR 2000 Design", ESTEC, November 1989
- [4]. T.Jones, F.A.Petz: "Survey and Review of Active Array System Developments and Applications", ESTEC, October 1994
- [5]. "Extremely Low Noise MESFETs fabricated by Metal-Organic Chemical Vapour Deposition", Electronic Letters, 25<sup>th</sup> June 1981, Vol. 17
- [6]. Franco N.Sechi: "High Efficiency Linear Microwave Amplifiers", IEEE 1980
- [7]. G.Caille, Alcatel Espace: "Antenna Specification Trade-Offs for C-band", RE/89/1058
- [8]. Charles E Cook, Marvin Bernfeld : "Radar Signals - An Introduction to Theory & Applications"
- [9]. Study of Next Generation SAR- Final Report, ESTEC Contract No. 11619/95/NL/PB, Daimler-Benz Aerospace, March 1997, <http://ftp.estec.esa.nl/pub/ws/wsp/tech/notes/>
- [10]. SMCS data sheet [http://www.omimo.be/new/companies/dasa\\_001.htm](http://www.omimo.be/new/companies/dasa_001.htm)
- [11]. "Key payload technologies for future satellite personal communications: a European perspective". J. Ventura-Traveset, I. Stojkovic, F. Coromina, J. Benedetto, F. Petz. International Journal of satellite communications, Vol. 13, 117-135 (1995).
- [12]. "Multirate Digital filters, filter banks, Polyphase networks, and applications: A tutorial", P.P. Vaidyanathan, Proceedings of the IEEE, Vol 78, No 1., January 1990.
- [13]. WAVELETS AND FILTER BANKS. Strang and Nguyen, ISBN 0-9614088-7-1, Wellesley-Cambridge Press, <http://saigon.ece.wisc.edu/~waveweb/Tutorials/book.html>
- [14]. TS8387 ADC from THOMSON-CSF Semiconducteurs Specifiques (TCS), <http://www.tcs.thomson-csf.com/Us/news/comm971017a.html>
- [15]. "On-board SAR Signal conditioner Development": Final Report Phase 2, ESTEC contract Number 10737/94/NL/JG, Saab Ericsson, MDA, SEA, October 1997

## Status of the X-Band SAR Instrument Demonstrator Development

R. Zahn\*, H. Braumann\*\*

Dornier Satellite Systems, D-88039 Friedrichshafen, Germany  
 (\*Telephone: +49-7545-8-4959; \*\*Telephone: +49-7545-8-3996  
 Telefax: +49-7545-8-4177)

### ABSTRACT

The X-Band SAR Instrument Demonstrator (DESA) is the modular part of an envisioned Synthetic Aperture Radar (SAR) instrument with active subarray. This paper describes the technical and programmatic topics of the German development. The technology development started in September 96 and will finish in September 2000. Main goal of the DESA development was the realization of a flight representative panel of a conceivable SAR instrument, which serves as reference and which is addressed in the following. Nevertheless the DESA concept may be also suited to other SAR instrument configurations.

### INTRODUCTION

The X-Band SAR Instrument Demonstrator (DESA) forms the basis for a future Synthetic Aperture Radar (SAR) instrument with active front-end, which is intended to be utilized for earth observation from space. The Demonstrator is a modular part of an envisioned full-size SAR instrument. It embraces the active front-end with its radiators, the transmit/receive modules (T/R modules), the necessary electronics for power supply, control and operation, and the operational software.

In the recent years the DESA technical basis was established starting with the definition on the instrument and some pre-developments of critical parts. Task of the present DESA project phase is the final design and manufacturing of all the hardware. The main emphasis was placed on the development of highly stable X-band T/R modules. Before starting the manufacturing of the T/R modules two representative modules were built and successfully tested under space conditions.

With regard to a future international cooperation for a Multi Frequency/ Multi Polarization (MFMP) mission for earth monitoring from space with a SAR, the relevant X-band antenna technology development is nearly finished in Germany. Such a mission is envisaged for the year 2003.

### SAR SYSTEM REQUIREMENTS

Future spaceborne SAR instruments shall be able to operate in several SAR modes with respect to

coverage and resolution. Only phased arrays with active elements can provide the necessary flexibility.

The present design of the DESA is based on a SAR instrument design which has been taken as reference (SAR-R). This reference SAR has an active antenna of 12m x 0.7m with 30 panels. Details of the system design studies are given in separate IGARSS 97 presentations [Ref. 1, 2, and 4].

The main system requirements for the SAR-R concerning the derived DESA design are listed in table 1:

Center frequency	9.6 GHz
Operational bandwidth	≥ 150 MHz
Polarization	horizontal; vertical
Overall receiving noise figure	< 4.8 dB
Radiated RF-power	> 3,2 kW
Phase stability/accuracy	within ± 10° rms
Receiver gain	15 – 30 dB
RF pulse length	25 – 50µs
Pulse repetition frequency	max. 3000 Hz
Scan capability	± 20° in elevation; ± 0.75 ° in azimuth
Operational temperature range (full performance)	- 20° – +60°C

**Table 1:** Main Requirements for SAR-R

The system shall be capable to change the radar beam within every pulse interval. The SAR performance data result from the technical parameters and is presented in the Ref. 1 and 2.

The radiation pattern will be formed individually in transmit mode (Tx) and in receive mode (Rx) exploiting the full capabilities of active phased array antennas. A fixed amplitude distribution is used for Tx. This scheme has the advantage that in Tx the amplifiers will be operated at the highest efficiency. The sidelobes could be lowered by using T/R modules with different output power in elevation. In Rx the pattern will be formed by phase and amplitude tapering.

**DESA TECHNICAL DESCRIPTION**

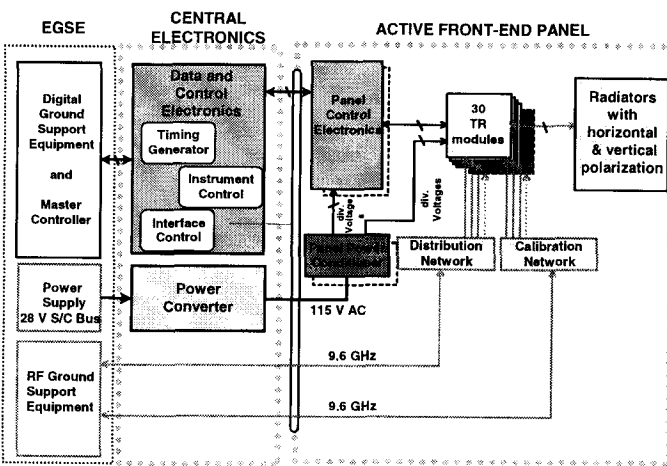
The DESA instrument consists of the elements illustrated in Figure 1. DESA embraces the active front-end panel, the Central Electronics, and the Electrical Ground Support Equipment (EGSE) necessary for operation and testing the active array. For convenience the Central Electronics is merged into the digital part of the EGSE. Another essential part of the EGSE is the RF operation and test equipment (RF-EGSE).

**Mechanical and Thermal Aspects:** In figure 2 the DESA panel is illustrated showing the fundamental parts like

- the row of the T/R modules attached to the radiators,
- the divider /combiner networks for RF-power distribution and calibration,
- the electronic boxes for power conditioning and supply and for digital control.

A compact design is achieved with a panel mass of less than 14 kg and a depth of about 110 mm which is important for the stowage of the active array.

The thermal design of the active front-end for the operation in space is completely passive without any active cooling or heating provisions. The microwave radiator also serves as thermal radiator for the heat generated by the T/R modules. Tests with thermal models of the active subarrays verified the effectiveness of the design. The cooling loop shown in the picture is only required for continuous operation on ground.



**Fig. 1: X-Band SAR Demonstrator Block Diagram**

**Radiators:** The antenna radiator for the DESA panel will be a resonant waveguide type employing the Carbon Fibre Reinforced Plastics (CFRP) technology that was already used in the Space

projects ERS-1, ERS-2 and X-SAR. Essential advantage of this waveguide technology is the thermal stability over the whole temperature range with very good performance. For the multi-polarization capability, two radiators, one for H- and one for V-polarization, are accommodated in the same antenna aperture. Narrow space of these waveguides was the prerequisite to fulfill the scan requirement in elevation. Two waveguides, the assigned T/R module and the thermal provisions form an active subarray as sketched in figure 3. Figure 4 provides the view of the panel on the radiator side.

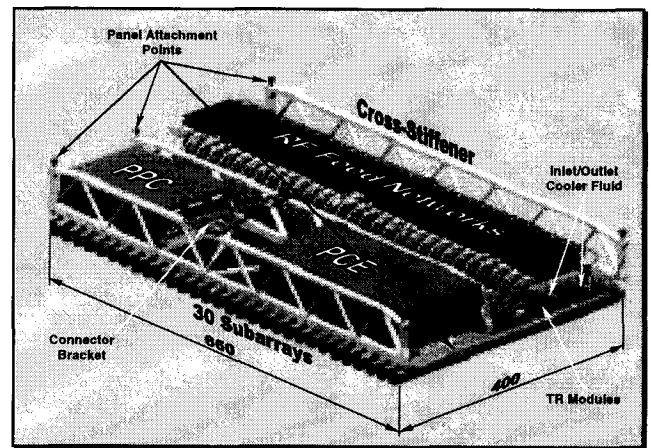
With this configuration the electrical and the thermal performance of a single active subarrays was successfully tested.

**TR Modules:** The TR Modules have been designed and manufactured by DASA/Ulm. The main performance data is listed in the following table 2:

Output power	7 W or 2 W
Noise figure	3.6 dB
Amplitude accuracy	0.5 dB
Phase accuracy	$\pm 6^\circ$

**Table 2: TR Module Performance**

Essential feature of the T/R modules is the active temperature compensation of amplitude and phase over the operational temperature range given above.



**Figure 2: DESA Panel Configuration**

**Digital Control:** The Digital Control Subsystem is split into two parts, the Panel Control Electronics (PCE) and the Digital Control Electronics (DCE). Two redundant PCEs are located on the panel, but only one is active during operation.

The PCE generates the command for the T/R modules on the basis of pre-programmed



configuration tables. 250 entries will cover nearly all conceivable SAR modes. Mode switching by change of the array configuration is possible within every pulse repetition interval.

Furtheron the PCE acquires the housekeeping data of the panel electronics and sends them to the DCE. The DCE would in a full-size SAR be part of the Central Electronics. It corresponds with the PCE (and with all PCEs in a full-size SAR instrument), generates the timing signals for the active array and would in a full-size SAR provide the digital interface to the space craft. In DESA the DCE is part of the Electrical Ground Support Equipment, which is used to operate the active front-end.

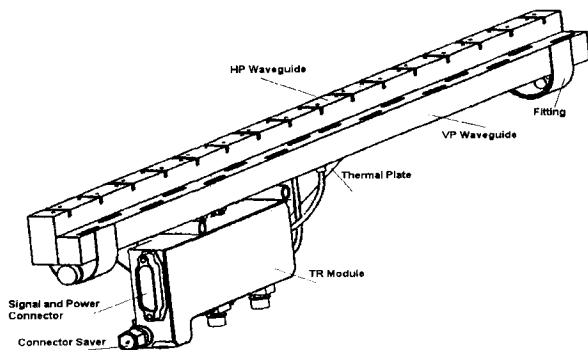


Figure 3: DESA Active Subarray

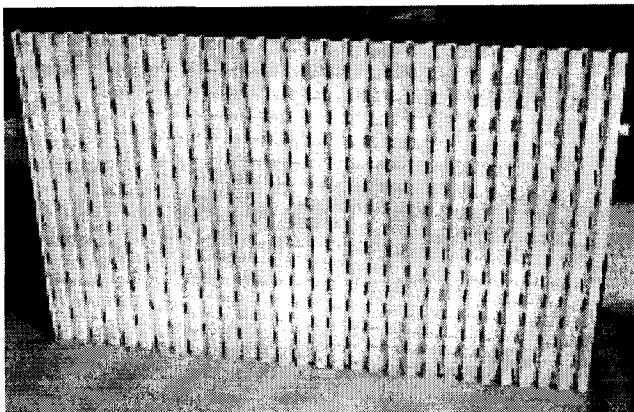


Figure 4: DESA Top View on Radiator Side

**Power Subsystem:** The Power subsystem consists of the Power Converter, which converts the spacecraft voltage (i.g. 28V dc) to 115V ac and supplies the DESA panel (all panels in a full-size SAR instrument). On the DESA panel (later on each panel) the AC-voltage will be conditioned for the panel control electronics and the T/R modules. The

advantage of this system is the high efficiency and the good reliability.

### STATUS AND OUTLOOK

The SAR Demonstrator project is still ongoing with the manufacturing of the complete panel hardware and the EGSE and the development of the software which is intended to be finished at the end of 1999. Afterwards the intergration and test phase will start with the assembly of the DESA panel, while the mechanical and the electrical GSE will be already available. Main task in the next project phase is running a more or less space qualification program with the panel.

This test program includes besides very detailed performance testing the usual tests for space hardware. A thermal test over the whole specified temperature range  $-55^{\circ}$  -  $+70^{\circ}\text{C}$  is planned, where the performance tests are limited to the range in table 1. In a thermal vacuum test the stability of the instrument will be verified. A vibration test shall demonstrate the mechanical integrity of the panel hardware. Finally the the electro-magnetic compatibility with typical spacecraft environment will be tested.

During the manufacturing of the panel hardware investigations will be made to build-up cost effective production lines especially for the T/R modules and the waveguide radiators. The synergies of other radar development and manufacturing programs have to be exploited.

In parallel investigations on SAR data processing are ongoing. Moreover the direct access to SAR data products should be possible by implementation of SAR on-board data processing and compression, which is presently studied within the DARA and ESA technology programs.

### References:

- [1] C. Heer, et. al., "An outlook for European Spaceborne SAR", Proc. IGARSS 97
- [2] E. Velten, C. Heer, "Future Operational Spaceborne SAR System Considerations", Proc. IGARSS 97
- [3] R. Zahn, et. al., "Advanced Antenna Technologies for X-Band SAR", Proc. IGARSS 95
- [4] R. Zahn, "The Design of a Future X-Band SAR", AEÜ, Int. J. Electron. Commun., 50 (1196) No.2, 85-91



## The RADARSAT II Mission: An update towards An End-to-End System Performance

Pierre-Paul Landry  
Systèmes Néotech, 4385 Boyer, Montreal, Canada, H2J 3C9  
Tel: (001) 514-596-0618, E-mail: [neotech@videotron.ca](mailto:neotech@videotron.ca)

Guy Séguin and Ralph Girard, Canadian Space Agency  
6767 route de l'aéroport, St-Hubert, Qc, Canada, J3Y 8Y9  
Tel: (001) 450-926-4637, E-mail: [guy.seguin@space.gc.ca](mailto:guy.seguin@space.gc.ca), [ralph.girard@space.gc.ca](mailto:ralph.girard@space.gc.ca)

### ABSTRACT

In March 1998, the Canadian Space Agency awarded the RADARSAT II contract to MACDONALD DETTWILER ASSOCIATES (MDA). This was a second step, after the creation of RADARSAT INTERNATIONAL (RSI), toward the establishment of a fully commercial Synthetic Aperture Radar (SAR) remote sensing service. The RADARSAT II mission will ensure the continuity of the RADARSAT I data and products and will open new market applications.

The RADARSAT II satellite will carry a C-band SAR offering multiple modes of operation including quad polarization, 3-meter high resolution and right or left looking imaging mode. All RADARSAT I modes will be supported to ensure data continuity. The satellite will be placed on the same orbit than RADARSAT I to ensure data continuity. If RADARSAT I remain in operation for 7.5 years, as it is now projected, there will be a period of time where both satellites will be operated in tandem. Accordingly, the ground infrastructure and data order system must be designed to meet customer requirements in a timely manner. To evaluate the system performance, CSA is developing an analysis tool to simulate the operation of a multi-satellite SAR system. This paper describes the structure of the tool and how it is used to assess the end-to-end performance of the system.

### INTRODUCTION

With RADARSAT II, SAR system design has reached a point where trade-off between the satellite design, the ground infrastructure and the system operation must be taken into account. To get insight into the end-to-end performance of the SAR system, CSA is developing a new software tool that is used to model the complete operation of a SAR system. In this paper, we describe the main features of this tool and explain how it will be used to assess the system performance.

### TECHNICAL CHARACTERISTICS

#### Mission

All the RADARSAT I modes will be supported by RADARSAT II, with most of the image quality parameters met or exceeded. The new modes added on RADARSAT II are dual or quad-polarization on selected beams, 3-meter high-resolution mode and new multi-look 9-meter modes. The RADARSAT II mission modes are shown in Fig.1.

The RADARSAT II orbit will be synchronized with the RADARSAT I orbit, which is a sun-synchronous orbit at an altitude of 797.7 km with a repeat cycle of 24 days. This choice is made to ensure data continuity between the two satellites. In order to use the same TTCS facilities for RADARSAT I and II, the time phasing between the two satellites at the ground station must be of a minimum of 30 minutes to allow for all relevant pre-pass and post-pass activities to complete. The selection of the operating node for RADARSAT II will be dictated by the tandem mission requirements. A twelve-day separation would maximize market access and TTCS operation; a one-day separation may be beneficial for surveillance and calibration.

A capability for quick changes between left and right-looking modes will enable RADARSAT II to support an Antarctic Mapping Mission and result in reduced planning time for imaging requests.

#### Instrument

The RADARSAT II instrument design represents a significant improvement over its predecessor. The new instrument will operate at a center frequency of 5.405 GHz with a signal bandwidth up to 100 MHz. The payload mass budget is 750 kg and power consumption is 685 W.

RADARSAT II will use S band for TTCS up-links and downlinks and X band for data downlinks in two 105

Mbps channels. Therefore, RADARSAT II will be able to operate with the existing network of ground stations. Additional functionality includes a left and right-looking imaging mode, reduced revisit time, encrypted X band down-link and S band up-link, higher down-link power which allows the use of 3-meter dish antenna for ground reception and, finally, on-board solid-state storage.

Interference from mobile communication has forced the migration to a slightly different frequency (RADARSAT I used 5.3 GHz). This is irrelevant for most applications; however, this will preclude interferometry between RADARSAT II and I and necessitate an upgrade of the existing network of active transponders.

### SAR BEAMS

The nominal beams available with RADARSAT II are listed in Table 1. To provide the required coverage, a total of 106 beams are needed per polarization per side. Calibration of the RADARSAT II beams will be a major challenge. The proposed approach at this stage is to fully calibrate a subset of all the required beams and then to rely on antenna modeling to predict the in-flight beams patterns.

The T/R modules that will be employed for RADARSAT II do not have an internal calibration capability. Different schemes are presently being explored to allow for the in-flight calibration of the array. Proposed techniques rely on the use of calibration probes that would be mounted at different locations.

Table 1 Nominal SAR Beams for RADARSAT 2

Beam Type	Mode	# of beams	Min. Elev. (°)	Max. Elev. (°)	Min. Swath (km)
Standard	Standard, Scansar (S5-S7)	7	17.30	42.33	101.7
Wide	Wide, Scansar	3	17.65	38.96	116.5
Extended low	Extended low	1	8.80	20.10	169.6
Extended high	Extended high	6	41.93	50.18	70.18
Extended Fine Low	Fine, Triple Fine	4	26.00	33.42	55
Fine	Fine, Triple Fine	5	32.19	41.07	53
Extended Fine High	Fine, Triple Fine	2	40.08	43.00	55
Quad Pol	Std Quad Pol, Fine Quad Pol	30	17.00	42.00	25
Ultrafine	Ultrafine	48	26.00	50.00	20

The antenna beam synthesis and PRF selection is driven by the ambiguity rejection requirements via the

NESZ. EMS Technologies has completed the synthesis of nearly all the beams required for RADARSAT II.

### GROUND INFRASTRUCTURE

The operation of RADARSAT II will be the responsibility of MDA. Two years after launch, the infrastructure has to be able to handle programming and acquisition of 500 image requests per day and production of 100 RADARSAT II SAR data products. The system shall perform all required activities between the acceptance of a user request and the uplink of the resulting message to the spacecraft in less than 48 hours for routine request, 12 hours for worst-case emergency and 6 hours for best-case emergency.

A complex system of operation will be set up that will ultimately report to the RADARSAT Stakeholders. An Order Handling System will allow customers to access the RADARSAT II system directly, specify their acquisition request and track progress of their orders. Commercial and Government Distributors will be responsible for financial aspects of the transactions with their respective end-users. A simple scheme will be used to prioritize the user requests.

### SAR END-TO-END PERFORMANCE EVALUATION

A common trend for the next generation of SAR systems is that they will be operated on a commercial basis. A key element for the commercial success of a product is quality, ease to order and timely delivery. To measure the end-to-end performance of a SAR system, CSA is building a tool to simulate the operation of the system from the request placement to the delivery of the final product. The simulation is very detailed and includes all significant parameters in the system. The simulation tool is extremely flexible and includes multi-satellites operations, ground stations, processing facilities and sensor state transitions among other features. The structure of the simulation tool is shown in Figure 2. The simulation proceeds in three main steps: Set-Up, Request Scheduling and Analysis.

#### Set-Up

Set-up involves specifying the parameters of the system simulation. All data are structured as records in a Microsoft Access database, which allows a great deal of flexibility in the construction of the various blocks of the simulation. The main simulation blocks are:

- Satellites (Can be any numbers)
- Sensors (Can be more than one sensor per satellite)

- Associated Mission Operation Center
- Associated Ground Stations
- Uplink and Downlink Sub-systems
- Power Supply and Storage
- Image Storage

The parameters for each main module of the system are entered using form sheets similar to what is shown in Fig. 3.

### Request Scheduling

Once the simulation parameters have been entered, one can proceed to the request scheduling, which is the core of the simulation. The system processes a series of user requests, finds appropriate imaging time for the acquisitions (multiple acquisitions are often necessary to fulfill one request) and checks all constraints for the scheduling of the requests.

User requests are entered as a series of records in a database. An interface allows creating tests requests or to import actual requests that have been processed by RADARSAT I Mission Management Office (MMO). A typical user request, from RADARSAT I cycle 21, is shown in Figure 4.

The request date is the date when RADARSAT MMO has received the request. The request consists in a zone to be acquired, an image type for processing, a beam type, a delivery method, a downlink method and a priority. Additional parameters for earliest and latest acquisition dates can also be specified. For example, if the user specifies that the acquisition is to occur at the latest in a week, then this constraint is taken into account in the scheduling.

An orbit propagation module is used to find the access time to stations and acquisition time for the requested area to image as a function of the specified beam. A very fast, variable step, propagation module has been implemented in order to reduce to a minimum the computation time required to find access times to a zone. Typically, all accesses to a  $1^\circ \times 1^\circ$  area over a one-month period are computed in less than 0.5 second on a PC computer.

The basic step in the simulation is the preparation of imaging schedule, which is the program that has to be sent to the satellite, on a daily basis, for its imaging operations. First, the requests are ranked by order of priority. Simulation time is incremented up to the point where the schedule must be frozen for one of the satellites. At that point, the system attempts to schedule all received requests and unscheduled requests on the satellite. It must be noted that the acquisition time itself

may occur much later in the cycle even if the schedule is frozen on a daily basis.

The request placement flow diagram is shown in Fig. 5. First, the program checks if the desired beam and sensor is available on the satellite. Then, the orbit module is used to find the acquisition time. A series of checks are then made for the availability of downlink, data storage and sensor constraints. If all constraints are satisfied, the acquisition is saved in the acquisition database. The process repeats until the total area is covered (margins can be specified). When the requested area is finally covered, the request is returned as successfully scheduled, otherwise, it is returned with a flag explaining why it could not be scheduled.

A typical test case using a RADARSAT I cycle 21 request is shown in Fig. 6. In this case, one acquisition is sufficient to cover the requested area. The acquisition data is returned as a database record. This allows an easy implementation for the system performance analysis tools. In passing, it is worthwhile mentioning that this feature would allow an easy integration of the simulation tool into an operational order handling system.

The simulation tool has been verified by comparing its predictions with RADARSAT I MMO operations. Comparisons made so far are satisfactory and we are moving forward to perform more in-depth simulations. For this purpose, CSA is developing a module to generate synthetic requests with realistic time and geographical distributions to simulate the high throughput expected in RADARSAT II. Main questions to be investigated will be the evaluation of the system performance, phasing between RADARSAT I and II satellites and requirements on optimization.

At present, only a simple optimization scheme based on priority at request time is used. For the RADARSAT I request that have been used for tests, this approach proved sufficient to ensure proper system operation. However, it is anticipated that system performance will decrease for higher throughputs if no optimization is implemented. Implementing different optimization strategies and evaluating their impact on the system performance will test this.

## RADARSAT-2 Beam modes

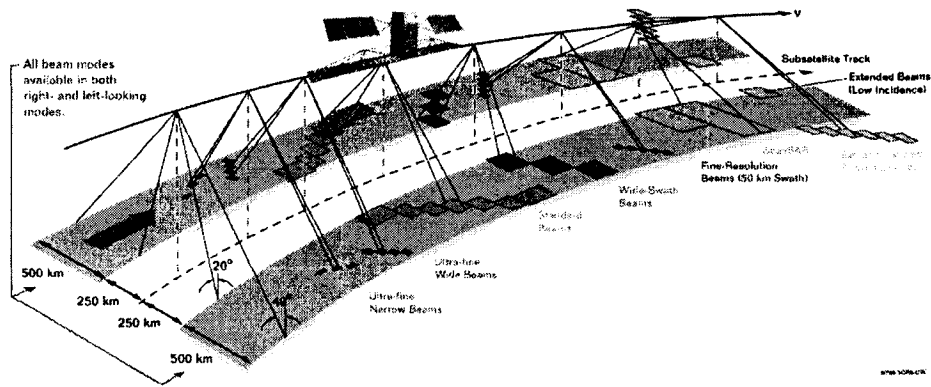


Fig. 1. RADARSAT II Beam Modes.

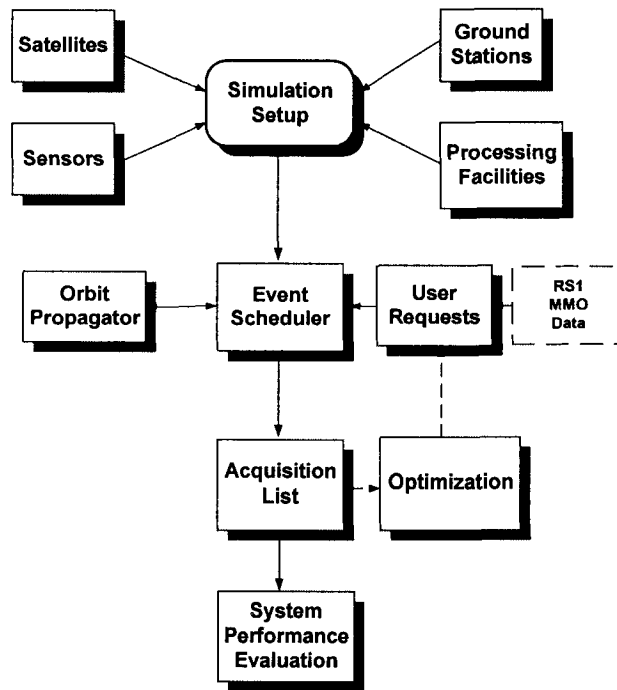


Fig.2. SAR End-To-End Simulation Tool Structure.

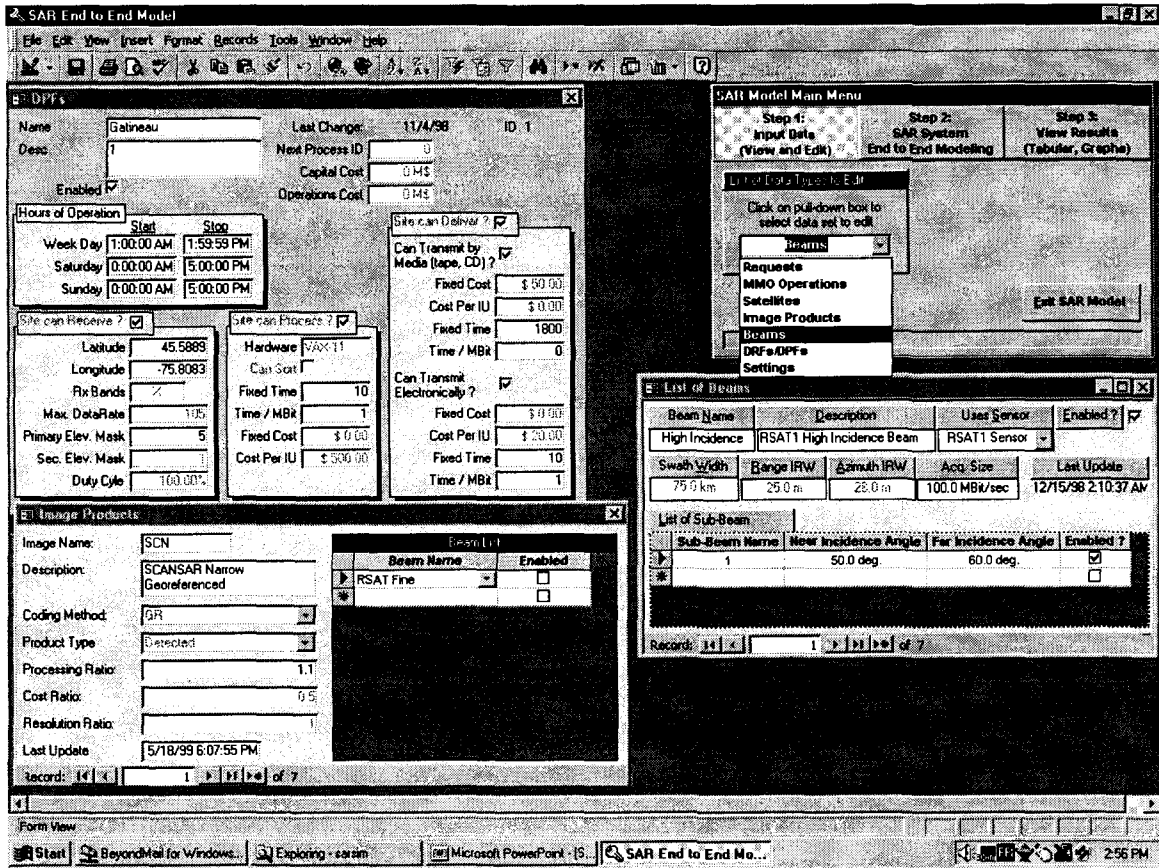


Fig 3. Sub-Menus in SAR End-to-End Simulation Tool. Three sub-menus are shown: DPF, Image Products and Available Beams.

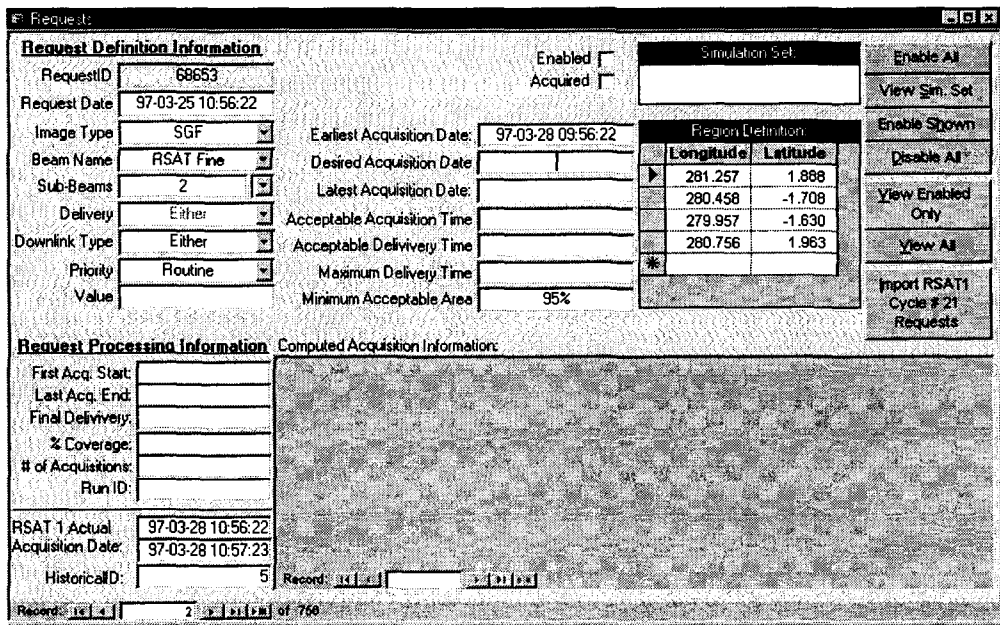


Fig.4. User Request Form extracted from RADARSAT I cycle 21. This acquisition occurred on March the 28<sup>th</sup>, 1997. To avoid providing any commercial information, we have arbitrarily selected the request date to be three days before the actual acquisition.

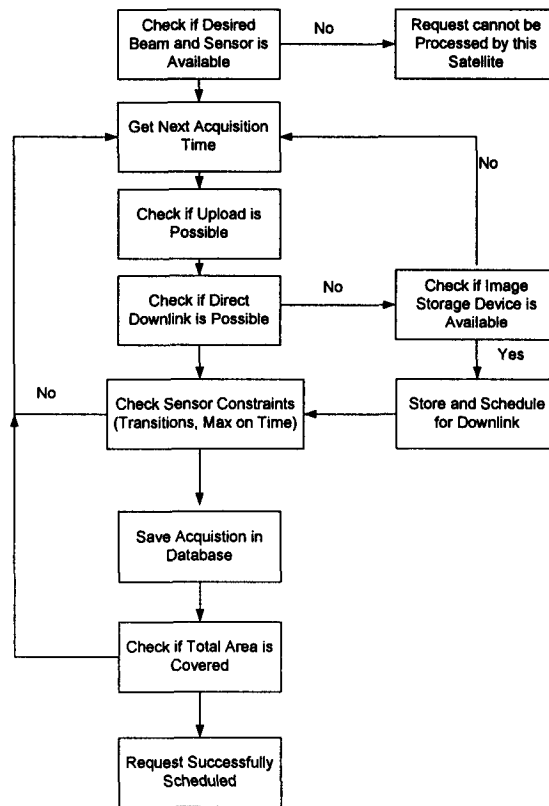


Fig.5. Request Placement Flow Diagram

# Requests

**Request Definition Information**

RequestID: 68656 Enabled  Acquired  Simulation Set

Request Date: 97-03-25 12:23:44

Image Type: SGF Earliest Acquisition Date: 97-03-28 11:23:44

Beam Name: RSAT Standard Desired Acquisition Date:

Sub-Beams: 1 Latest Acquisition Date:

Delivery: Either Acceptable Acquisition Time:

Downlink Type: Either Acceptable Delivery Time:

Priority: Routine Maximum Delivery Time:

Value: Minimum Acceptable Area: 95%

**Region Definition**

Longitude	Latitude
270.632	48.934
269.273	44.639
267.946	44.994
269.200	49.099

**Request Processing Information** Computed Acquisition Information:

AcqID	TStart	TStop	Covered Area
68656	97-03-28 12:23:43	97-03-28 12:24:55	
SatelliteID: RADARSAT 1	DLTStart: 97-03-28 12:23:43	DLTStop: 97-03-28 12:24:55	270.690 48.892
SensorID: 6	DLTStart: 97-03-28 12:23:43	DLTStop: 97-03-28 12:24:55	269.279 44.644
BeamID: RSAT Standard	OPF Proc: 97-03-28 14:25:46	Delivery: 97-03-28 14:55:46	267.863 44.810
DRFID: 1	Delivery: 97-03-28 14:55:46	OutFlag:	269.157 49.068
DownlinkID: 2	OutFlag:	RatioArea: 1.00	
ImageStorageID: 0	RatioArea: 1.00		

First Acq. Start: 97-03-28 12:23:43  
 Last Acq. End: 97-03-28 12:24:55  
 Final Delivery: 97-03-28 14:55:46  
 % Coverage: 100%  
 # of Acquisitions: 1  
 Run ID: Sim01

RSAT 1 Actual Acquisition Date: 97-03-28 12:23:44  
 Acquisition Date: 97-03-28 12:24:54  
 HistoricalID: 8

Record: 14 of 1 (Filtered)

Fig.6. Example of a Request Successfully Placed. The request is returned as a record in a database. The simulation has found the acquisition time that was used in RADARSAT 1.



## CAPABILITIES AND LIMITATIONS OF THE INTERFEROMETRIC CARTWHEEL

D. Massonnet

French Space Agency (CNES)

18, Avenue E. Belin, 31401 CEDEX4, Toulouse, France

Fax : (33) 5 61 27 31 67, E-mail : Didier.Massonnet@cnes.fr

November 1st, 1999

### ABSTRACT

*Almost-simultaneous radar images can be produced by a low cost system using a set of passive receivers onboard a constellation of micro-satellites in a special orbital configuration. The combination of these images can improve the final resolution in range and azimuth and provide a systematic production of across-track and along-track interferometric data. Here we review some of the technical peculiarities of these systems, linked to (1) the system, such as the chronogram, the orbital geometry and the required pointing and positioning, (2) the image quality, such as the ambiguity level, the required clock stability, the processing to higher resolution and the geometric limitations, mainly the behavior of the coherent combinations over high slopes terrains.*

*We illustrate three applications of the concept in cooperation with the radar onboard the Japanese ALOS satellite, the ASAR instrument onboard the European ENVISAT, as well as a study-case for defense applications of the concept.*

### 1 Introduction and background

The interferometric cartwheel [ref.1,2] has been proposed as a cheap solution for implementing some of the possibilities of the coherent combination of radar images. Among these possibilities are the computation of Digital Elevation Models from interferometry using the across-track separation of the data takes [ref.3,4,5], the mapping of ocean currents using along-track interferometry [ref.6] and the super-synthesis in range [ref.7] and azimuth [ref.1,8] using the diversity of point of view within the pixel, expressed in azimuth by the difference in mean Doppler and in range by the slope-dependent spectral shift [ref.9].

The advantages of the concept include the geometric stability of the baselines, both vertically and horizontally, generated by the orbital configuration. Furthermore, the combination of passive images is independent of the emitter, a conventional radar satellite which does not need to care about the passive constellation because it orbits far from it with typical separation of several tens up to more than one hundred kilometers.

Another advantage of the concept is the possibility to split the requirements for global antenna surface, data storage and telemetry between several micro-satellites. For instance, if each micro-satellite

features an easy-to-deploy umbrella of 4 m<sup>2</sup>, 20 Gbits of solid-state memory and a conventional 50 Mbit/s telemetry channel, the coherent association of six of these micro-satellites [ref.1] adds up to a very respectable radar system.

The independance of two images acquired simultaneously from two-point with an along-track separation is characterized by the critical horizontal baseline. It is such that the range difference between the receivers and a given ground target changes by one wavelength from one pulse to the next. For coherent combination of the passive images made by each receiver, the along track separation of the receivers must stay below this critical horizontal baseline. The same way, we define a critical vertical baseline as an adaptation of the traditional orthogonal baseline of active interferometric systems [ref.10,11,12] to passive, vertically-separated systems. It is such that the range difference seen by the second receiver, across the range pixel of the first receiver, differs from the range pixel size by one wavelength. Again, for coherent combination of the passive images made by each receiver, the vertical separation of the receivers must stay below this critical vertical baseline.

We call "interferometric area" [ref.1] the rectangular area in the plane containing the orbit of the satellites, centered on each satellite, and having the critical vertical baseline as a height and the critical horizontal baseline as a length. The resolution of an interferometric product results from the coherent part common to the intersecting "interferometric areas" of the two receivers involved in the combination. It is inversely proportional to the respective sizes of the intersection in azimuth and range. Similarly, the resolution of the combined images of two receivers with intersecting interferometric areas is inversely proportional to the respective sizes of the union of their interferometric areas in azimuth and range. The situation is illustrated by figure 1a and 1b. To summarize, if  $\rho_D$  (resp.  $\rho_A$ ) is the nominal resolution in range (resp. in azimuth) of the emitter, and if  $\alpha_D$  (resp.  $\alpha_A$ ) is the proportion of non-overlapping of the interferometric areas of two receivers in range (resp. in azimuth), with

$0 < \alpha < 1$ , the resulting interferogram will have  $\frac{\rho_D}{(1-\alpha_D)}$

and  $\frac{\rho_A}{(1-\alpha_A)}$  as resolution in range and azimuth, while

we may hope to achieve resolutions of  $\frac{PD}{(1+\alpha_D)}$  and

$\frac{PA}{(1+\alpha_A)}$  as a result of "super-synthesis" in range and

azimuth. As it can be seen on figure 1b, the latter resolutions are not completely right, because the interferometric area explored by the combination is not the stripped rectangle. Two corners of this rectangle are not explored while the common area is explored twice.

Two along-track images sample the same Doppler area with a split second delay. Any moving target will experience a phase shift during this delay. This shift can be used to measure currents [ref.6]. For instance, a one-knot current perpendicular to the satellite track observed under an incidence of  $23^\circ$  during a half-second will generate 10cm worth of displacement, that is 42% of a phase cycle in L-band or almost two cycles in C-band. In the cartwheel configuration, the vertical separation and the horizontal separation will always occur together to some extent. However, we do not expect problems for separating the contributions, because land surfaces will show topography but no slow-moving targets while ocean surfaces might exhibit moving targets, but no topography. The correction for residual orbital fringes will have to be performed in both cases though.

Approximations were proposed [ref.1,2] to compute both the horizontal and the vertical baselines. However, for practical studies, the above definitions are used to determine these parameters numerically, using a straightforward spreadsheet development.

## 2 System aspects

### 2.1 Chronogram

The concept of interferometric cartwheel is an R&D program in CNES, in connection with several projects in cooperation with existing or planned radar instruments, used as emitters for the constellation. The description of the micro-satellite itself and the associated radar payload are not within the scope of this paper [ref.13]. However, we will give a short description of the scenario envisioned for all the missions under study. The micro-satellite spacebus [ref.14] is limited to 100 kg in mass, with a three-axes attitude control capability and a propulsion system capable of delivering a  $\Delta V$  of  $100 \text{ ms}^{-1}$ . Figure 2 gives an artist's impression of the spacecraft. The size of the central cube is 60 cm. In our scheme, the radar payload is not synchronized with the one of the emitter. Its only duty is to point to the area illuminated by the emitter by rotating the whole satellite, to record the data stream continuously over a sufficient bandwidth and to store the results after some data compression. The complexity of the radar payload is thus kept to a minimal. The nominal deployment of the constellation calls for a set of three micro-satellites

orbiting far ahead, or behind, the emitter, on the same orbit. Because of the slight bistatic effect linked to this configuration, the echo of vertical is not a problem in the system chronogram. However, the spillouts of the emitter's antenna combined with the poor diagrams of the antennae of the receivers can create a high level of direct signal. For this reason it is planned to position the constellation at a distance from the emitter such that the direct signal does not arrive to the receivers at the same time than the signal from the main swathwidth. This precaution will be taken at least in the initial phase of the mission. Since the recording is continuous, the direct signal print will be recorded and measured. Besides, it might be used to help accurately position the receivers with respect to the emitter (see section 2.3). If the amplitude of the direct signal is sufficiently low to allow its superposition with the ground signal, the constraint in positioning the constellation will be lifted. Anyway the ambiguous distance is roughly defined by  $\frac{kc}{f_a}$ ,  $k$  being

an integer and  $f_a$  being the pulse repetition frequency of the emitter. For ERS-1 and  $k=1$ , this distance is 175 km.

Since the main mission envisioned for the cartwheel is a global coverage of land surfaces during the lifetime of the receivers, practically limited to two years, the work program of the constellation will be dominated by a very repetitive pattern with three phases during each orbit. Most of the orbit will be spent maintaining the orientation of the small, fixed solar panel toward the Sun. One to three minutes per orbit will be devoted to acquiring radar data after a proper time has been allocated to reorienting the receiver's antennae. Finally, a few minutes will be devoted to downloading the data over one of the several receiving stations of the system, again after the necessary reorientation. Although this has not been yet firmly decided, there is a possibility that the same antenna will be used for data acquisition and data downloading.

Continuous data recording requires a specific resynchronization process on ground. The kind of algorithm which might be used does not make the data processing significantly more complicated [ref.1]. In most implementations of the concept, the data will be sampled on 8 bits (I,Q) and then compressed to 2 bits (I,Q) using a block adaptative quantizer (BAQ).

### 2.2 Orbital cartwheel geometry

Here we recall the geometric configuration of the interferometric cartwheel [ref.1,2]. We consider a nominal orbit with an orbital period  $T$ . For simplicity we assume the nominal orbital to be circular with  $A$  as the value of the semi-major axis. Modifying the eccentricity of the orbit will result in another orbit with the same periodicity, but which describes an ellipse relative to the nominal orbit. The ellipse is included in the plane defined by the direction of the velocity and the vertical

direction. If  $E$  is the additional eccentricity, the relative motion as a function of time is described by :

$$y(t) = 2AE \cos\left(\frac{t}{T} + \phi\right) \quad (\text{vertical direction})$$

$$x(t) = AE \sin\left(\frac{t}{T} + \phi\right) \quad (\text{horizontal direction})$$

where  $\phi$  depends on the position selected for the perigee. Three satellites with the same additional eccentricity but perigees evenly distributed along the orbit lead to the configuration of figure 3, where the satellites follow an elliptical relative trajectory with a constant angular velocity. In figure 3, the perigees are separated by  $120^\circ$ . In a configuration with two satellites (figure 4) they would be separated by  $180^\circ$ . We call  $AE$  the vertical radius of the wheel. Note that the horizontal radius is twice the vertical radius.

If  $V$  is the magnitude of the orbital velocity, the relative velocity reaches  $EV$  (resp.  $-EV$ ) on the upper (resp. lower) part of the elliptical trajectory. For achieving a wheel with a vertical radius of  $AE$  from the nominal orbit, each satellite must expend a  $\Delta V$  totalling  $\frac{EV}{2}$  in two impulses. As a numerical example, creating a vertical radius of 1 km from an ERS-like orbit would typically require  $0.5 \text{ ms}^{-1}$ . The additional velocity along the orbit, with respect to the emitter's trajectory would then be within  $\pm 1 \text{ ms}^{-1}$ .

The advantage brought by the wheel is the stability of the vertical and horizontal baselines. With three satellites, the baseline between the two satellites most separated in the vertical direction changes from a lower limit where two of the three satellites share the same vertical position :

$$\cos\left(\frac{t}{T} + \frac{2\pi}{3}\right) = \cos\left(\frac{t}{T} + \frac{4\pi}{3}\right)$$

leading to  $t = kT$  (with  $k$  integer) and a vertical baseline of :

$$\left(1 - \cos\left(\frac{2\pi}{3}\right)\right) AE = 1.5 AE$$

and an upper limit where two of the three satellites share the same horizontal position :

$$\sin\left(\frac{t}{T} + \frac{2\pi}{3}\right) = \sin\left(\frac{t}{T} + \frac{4\pi}{3}\right)$$

leading to a vertical baseline of :  $2 \sin\left(\frac{\pi}{3}\right) AE = \sqrt{3} AE$

The variation with respect to the average vertical baseline of 1.61  $AE$  is always kept within  $\pm 7.5\%$ , a remarkable stability all along the orbit.

If we consider a wheel with only two satellites phased at  $180^\circ$  (figure 4), the maximum baseline is  $2 AE$  and will remain within 10% of this value when the time to perigee of one of the two satellites is less than 7.2% of the orbital period. The baseline will then remain within 10% of the maximum baseline on two opposite sectors of the orbits (close to apogee and close to perigee) totalling more than 28% of the orbital time. Such a configuration could process all the latitudes in

four different sessions for which the perigees of the two satellites would be shifted by  $90^\circ$ , at the cost of doing and undoing the wheel with appropriate  $\Delta V$ .

More geometric possibilities are brought by an additional change in the relative orbits, for instance a change of the equator crossing time of the satellites. In this case, the plane in which the elliptical relative trajectory is inscribed would not remain vertical, but would "roll" with orbital periodicity. Such a roll could be beneficial as it could allow variable sensitivity to incidence angle. However, this sensitivity would depend on the latitude. The drawback of losing the stability of the parameters along the orbit seems to outweigh any advantage.

### 2.3 Pointing and positioning

A satellite of the constellation does not need accurate pointing nor positioning. There are no severe requirements for calibration of the amplitude signal, so the pointing can be accurate to a fraction of the width of the antenna pattern, itself wider than for a conventional radar satellite. The only requirement is to keep the portion of the terrain illuminated by the emitter within the antenna pattern of the smaller antenna of the receiver. Keeping these low level specifications in mind, we forbid any clever optimization of the sidelobes for reducing the amount of azimuth ambiguity. For instance any "magic", thus unstable, positioning of the sidelobe of the receiver's antenna with respect to the one of the emitter's antenna.

Some specific pointing scheme will also give a limited polarimetric capability to the receivers. By rotating the satellite around the antenna axis, the receiver can be either optimized for the reception of vertical or horizontal polarization. For instance, if each position in the interferometric cartwheel is occupied not by one, but by two identical receivers, with one rotated by  $90^\circ$  along the antenna axis, a full polarimetric AND interferometric signal can be recorded, provided the illuminating satellite emits sequentially in H and V. The cartwheel concept is thus flexible enough to turn a dual-pol satellite into a full polarization satellite, with two restrictions : first, the lower gain will be damaging to the image quality, especially for cross-pol products. Second, given the low specification of antenna design in the cartwheel concept, the result in cross-pol will actually be a mix of cross-pol and direct-pol spillover. This mix will require filtering whom feasibility remains to be demonstrated.

The accurate positioning of the final image products is less straightforward than with conventional radar imaging, because of the bistatic acquisition. If we aim at a typical 20-meter sided cartographic cell, the products should be positioned within ten meters at worst. The emitter's position is assumed to be known with up to date positioning devices which make the error negligible. It is expected to have GPS or DORIS devices

on-board the satellites of the constellation, capable of positioning them within ten or twenty meters (although not in real-time). However, since we are not synchronized with the emitter, knowing the signal range is much less easy than with conventional radar. We will rely on four different means of relocating the imagery : (1) since the signal recording is continuous, we will record the direct pulse from the emitter through the spill-overs of the antennae. Since the constellation is almost motionless with respect to the emitter, we can easily integrate many pulses and resolve the triangle emitter-target-receiver in range, because we can access the pulse rate and we can easily guess the rank of ambiguity being imaged. We can then reconstruct pixel position more or less conventionally. (2) We can use the images from the emitter, which can be conventionally positioned, to derive the actual position of the receiver's images, by correlation. This method is all the more efficient that only two constants are lacking; a range offset and an along-track offset. (3) We can use the topographic product itself to determine the constant offsets with an existing, crude topographic model. The latter will not be accurate (typically 100 m grid), but the large area involved will compensate this drawback. We are interested in a typical 10-meter-class final result. Alternatively (4), if the topography is strong enough, we can use the fake amplitude image generated by shape-form shading to nail one of the receiver's image to the actual landscape. This last procedure has been successfully used on a routine basis during the interferometric case studies that were conducted in CNES using the in-house DIAPASON software, which features this positioning procedure.

Other means for reconstructing range (such as autofocus) lack the necessary accuracy. We cannot claim performances from these various options for positioning before having identified the emitting partner of the wheel. In particular, we need accurate SAR antenna diagram.

### 3 Image quality aspects

#### 3.1 Contribution of the ambiguities

Since the receivers must be placed onboard a small spacebus in order to keep the cost of the cartwheel constellation very low, we must accept the idea that the antenna of the receiver is much smaller than an optimal radar antenna, such as the one of the emitter. In this context, the antenna footprint of the receivers is much larger than the footprint illuminated by the emitter and, depending on the design, the receiver's footprint will collect ambiguous targets from azimuth and possibly range, especially with L-band satellites with large antenna height. Most of the spaceborne radars feature an along-track antenna size on the order of 10 m. Since we do not envision placing an antenna measuring more than

5 m along-track onboard a micro-satellite, we know that the receiver will receive returns from the first ambiguous lobes in azimuth. The two first lobes are much stronger than their followers of higher rank. Thus, we might as well consider that the receiver listens to the first order ambiguous targets in azimuth, without further attenuation that the one they had from the way in, where they are shaped by the antenna of the emitter. As a first approximation, we might then consider that the azimuth ambiguity ratio is, in dB, half the one of the emitter (i.e. 24 dB would become 12 dB). In range, the situation differs because the antenna onboard the microsatellite can match the height of the emitter's antenna, except maybe for L-band systems. Anyway, the ambiguity ratio is degraded in the receiver's image, with respect to the emitter's. However, for coherent combination of several image from the receivers, we will show that the ambiguous targets cannot contribute to the coherent result, and behave as an additional source of noise.

Figure 5 shows symbolically the ambiguous contributions of a nominal target. In addition to the nominal target with the nominal resolution, we have the range ambiguity coming from targets imaged by the previous pulse, located  $\frac{c}{2f_a}$  farther away ( $f_a$  being the pulse repetition frequency). If the geometry of the data takes permits, we might also have the range ambiguity from targets imaged by the next pulse, located  $\frac{c}{2f_a}$  closer. Figure 5 shows range ambiguities elongated along the track, to convey the idea that the offset of  $\frac{c}{2f_a}$

in range creates a severe mismatch of the azimuth reconstruction algorithm, because of a wrong frequency modulation rate. This mismatch is not, however, the reason for which the range ambiguities do not participate to the coherent combination.

If the wheel is tuned to a proportion  $\alpha$  of the critical vertical baseline ( $0 < \alpha < 1$ ), there will be a additional shift of  $\alpha\lambda$  between the images for each range pixel crossing.  $\lambda$  being the radar wavelength. The shift will result in one range pixel shift every  $n$  range pixel with :

$$n = \frac{1}{\alpha} \frac{f_c}{f_d} = \frac{Q}{\alpha}$$

$f_c$  being the carrier frequency,  $f_d$  the range sampling frequency and  $Q$  their ratio. The time between two successive pulses is equivalent to  $m$  range pixels with :

$$m = \frac{f_d}{f_a}$$

The mismatch for the ambiguities, assuming the nominal images are ideally superposed, reaches, expressed in range pixel units :

$$\frac{m}{n} = \alpha \frac{f_d^2}{f_c f_a}$$

The term combining the three frequencies on the right side ranges from 40 (for a typical ERS-1 setting) to 150 (for a typical L-band case). It is then clear that as soon as  $\alpha$  reaches a few percent, the range ambiguities will never be properly superposed for coherent combination (i.e. they will be offset by at least one range pixel).

In Figure 5 the azimuth ambiguities are depicted as targets larger than the nominal targets. This is to convey the idea that azimuth ambiguities are not processed with the correct range migration during radar image reconstruction. To quantify the phenomenon, we assume without loosing the generality that the processing is conducted around zero Doppler in the azimuth frequency band which range from  $-\frac{f_a}{2}$  to  $+\frac{f_a}{2}$ .

This frequency range correspond to a change in distance, with respect to the closest distance of

approach, ranging from zero to  $\beta \frac{f_a^2}{4}$ , where  $\beta$  is a geometric factor depending on the satellite being used, allowing to express the change of distance in units of

range pixels. The expression  $\beta \frac{f_a^2}{4}$  can be equivalently

expressed as  $\frac{N}{8Q}$  where  $N$  is the number of raw data azimuth samples to be processed to achieve full azimuth resolution. The azimuth ambiguity is produced by the same frequency band, but shifted by  $f_a$ . For this target,

the range evolves from  $\beta \frac{f_a^2}{4}$  et  $\beta \frac{9f_a^2}{4}$ , but is compensated as if it were the one of a nominal target

(from  $\beta \frac{f_a^2}{4}$  to zero and then again  $\beta \frac{f_a^2}{4}$ ). Therefore

the ambiguous target is spread in range from 0 to  $2\beta f_a^2$

or, equivalently, from 0 to  $\frac{N}{Q}$ . The range resolution of

the azimuth ambiguous target is not anymore more or less equal to the range pixel size, but to  $\frac{N}{Q}$  range pixels.

As a consequence, the azimuth resolution of the azimuth ambiguous target is not anymore more or less equal to

the azimuth pixel size, but to  $\frac{N}{Q}$  azimuth pixels, because

only a  $\frac{Q}{N}$  fraction of the azimuth bandwidth is processed

at once, due to range spreading. In figure 5, the diameter of the larger circles are therefore  $\frac{N}{Q}$  in units of pixels, in range and in azimuth.

Unlike what happens in range, nothing prevents the azimuth ambiguities to be properly superposed, but their degraded resolution in range practically multiplies  $\alpha$  by  $\frac{N}{Q}$ . As soon as  $\alpha$  exceeds  $\frac{Q}{N}$ , the azimuth ambiguities do not combine coherently anymore. For

ERS-1,  $N$  is typically 1350 and  $Q$  is 280. The azimuth ambiguities become incoherent for a baseline five time shorter than the critical one. For a future L-band satellite such as ALOS [ref.16], the critical baseline for azimuth ambiguities will be 188 times shorter than the nominal one, because we have  $Q = 42.5$  (at 30 MHz) and  $N=8000$ .

### 3.2 Oscillator calibration

In the course of interferometric experiments with ERS-1, we had detected and tentatively explained the effects of a frequency drift of the local oscillator onboard the radar [ref.17]. We assumed the carrier frequency as :

$$f_c = f_0 + t f_b$$

where  $f_b$  is a time-dependent bias of the official frequency  $f_0$ . The bias can create "clock fringes" when the carrier frequency is mixed with a slightly different one when the pulse returns, that is typically after a number  $k$  of inter-pulse periods ( $k$  equals 9 for ESA's ERS satellite). If  $f_a$  is the pulse repetition frequency, the fringe rate, expressed in fringe per second, is :

$$\frac{k f_b}{f_a}$$

If data from ERS-1 and ERS-2 are mixed in an interferogram, only the difference of their frequency biases will contribute to clock fringes. A difference in their  $f_0$  would be cancelled when remixed. The fringe rate would be :

$$\frac{k (f_{b1} - f_{b2})}{f_a}$$

The situation differs when two independent oscillators, the receivers 1 and 2, listen to a third oscillator, the one of the emitter. With obvious notations :

$$f_{c1} = f_{01} + t f_{b1}$$

$$f_{c2} = f_{02} + t f_{b2}$$

$$f_{c3} = f_{03} + t f_{b3}$$

The third term from the emitter has hardly any effect on the receiver's interferogram because the time  $t$  is almost the same when hitting receivers 1 and 2, whose distances to the target differs typically by one kilometer. The resulting  $\Delta t$  is on the order of a few microseconds. After interferogram formation and cancelling  $f_{03}$ , the remaining fringe rate is :

$$f_{01} + t f_{b1} - (f_{02} + t f_{b2}) - \Delta t f_{b3}$$

which will clearly be dominated by the difference between  $f_{01}$  and  $f_{02}$ . If we want less than one clock fringe during a recording session lasting  $T$  seconds, we must have :

$$(f_{01} - f_{02}) T < 1$$

The typical "clock fringes", almost perpendicular to the satellite's track, could be distinguished from the "orbital fringes" resulting from improper knowledge of orbital separation, which are mainly parallel to the track.

### 3.3 Geometric limitations

The level of independence of the images acquired by the cartwheel depends on the local slope of the terrain observed. To quantify these effects, we assume two satellites observing with a difference in point of view expressed by the angle ( $d$ ), as illustrated by figure 6.

The interferometric cartwheel is a passive system and the difference in geometry between images is created only on the return path. However, in order for the reader to remain on familiar grounds, we will develop the following model as if we were in conventional interferometry. We will then link and scale our conclusions to the critical value of the baseline. In doing this our conclusions will remain valid in the passive case, because the definition of the critical baseline takes into account whether the difference is created one-way or two-way.

We first consider the effects of slopes for interferometry, and then for range super-resolution.  $p$  is the size of the resolution cell (a value close to the pixel size in general). We call "orthogonal width" of the pixel the quantity  $L$ , which represents the pixel size once projected on the wavefront. It is such that :

$$L = p \cot(i-a)$$

where ( $i$ ) is the incidence angle and ( $a$ ) the slope. ( $a$ ) can be negative if the slope does not face the radar. The "interferometric limit" [ref.11,12] is reached when the walk difference equals half the wavelength on the one-leg travel. The interferometric domain is such that :

$$L \tan(d) < \frac{\lambda}{2}$$

The angle ( $d$ ), always very small, is close to its tangent. The condition with respect to the pixel size becomes :

$$pd \cot(i-a) < \frac{\lambda}{2}$$

$\frac{2p}{\lambda}$  is the ratio of the radar carrier frequency to its bandwidth, which we assimilate to the range sampling frequency for simplicity and previously designated by  $Q$ . The dimensionless factor equals about 280 for a satellite such as ERS-1. We then have :

$$Qd < \tan(i-a)$$

Or :

$$a < i - \text{Arctg}(Qd)$$

which gives the maximum slope allowed for proper interferometric combination. The formula also gives the limit of flat grounds :

$$i = \text{Arctg}(Qd)$$

hence the maximum difference of point of view, angle ( $d$ ) :

$$d_{\max} = \frac{\tan(i)}{Q}$$

The sensitivity to topography might be expressed by the altitude of ambiguity  $h_a$ , the change in elevation that creates one topographic fringe :

$$h_a = \lambda \frac{\sin(i)}{2d}$$

for  $d_{\max}$ , the altitude of ambiguity equals [ref.12] :

$$\lambda Q \frac{\cos(i)}{2} = p \cos(i)$$

In order to assess the consequences of these relations, let us consider the situations where  $d = 0.3 d_{\max}$  and  $d = 0.7 d_{\max}$  respectively, while the incidence angle is  $45^\circ$ . More generally, we have  $d = \alpha d_{\max}$  where  $\alpha$  ranges from 0 to 1 as the baseline goes from zero to the critical baseline. From our examples, we have :

$$Qd = 0.3 \tan(i) = 0.3 \text{ (resp. } Qd = 0.7)$$

The maximum observable slope is then :

$$i - \text{arctg}(0.3) = 28.3^\circ \text{ (resp. } 10^\circ)$$

From these examples, it is clear that moderate independence between images still allows high slopes to be imaged. If the independence factor is closer to one, the slope condition is more severe. It must be noted, however, that a slope of  $10^\circ$  correspond to what would be called "a 18% slope" on the road network. Such slopes do not exist in practice on these networks. Furthermore the limit applies only if the slope faces the radar and is orthogonal to its track. Nevertheless, these slope limitations are one more reason to work preferably at high incidence.

If we now envision the consequences of slopes on the super-resolution, we consider the resolution  $\rho$  on the slope :

$$\rho = \frac{p}{\sin(i-a)}$$

let us consider a system with  $\alpha$  as the "independence factor". A value  $\alpha_0$  has been selected for  $\alpha$  assuming the surface is flat :

$$Qd = \alpha_0 \tan(i)$$

in the presence of a slope ( $a$ ), we have a local  $\alpha$  such that :

$$Qd = \alpha \tan(i-a)$$

$$\alpha_0 \tan(i) = \alpha \tan(i-a)$$

The size of the super-resolution pixel is, locally :

$$p_s = \frac{p}{(1 + \alpha)}$$

$$p_s = \frac{p}{(1 + \alpha_0 \tan(i) \cot(i-a))}$$

This relation has very interesting consequences. Let us imagine two systems. The first one achieves range resolution in a conventional way, with a range pixel size  $p_1$ . The second achieves resolution using a larger pixel size  $p_2$  but combined in a super-resolution system such that the resolutions of the two systems are the same on flat ground :

$$p_2 = p_1 (1 + \alpha_0)$$

On a slope ( $a$ ), the resolution of the first system is given by :

$$p_1 = \frac{p_1}{\sin(i-a)}$$

and the resolution of the second system by :

$$\rho_2 = \frac{\rho_1 (1+\alpha_0)}{\sin(i-a)(1+\alpha)} = \frac{\rho_1 (1+\alpha_0)}{\sin(i-a)(1+\alpha_0 \tan(i)\cot(i-a))}$$

the ratio of the range resolution is, as long as  $\alpha < 1$  :

$$\tau = \frac{1 + \alpha_0}{(1 + \alpha_0 \tan(i)\cot(i-a))}$$

we then have two situations. 1) as long as  $\alpha$  remains smaller than one, that is if :

$$\alpha_0 \tan(i)\cot(i-a) < 1$$

the resolution of the combined system is less sensitive to slope than the conventional one. 2) When  $\alpha$  grows larger than 1, the super-resolution effect ceases and the resolutions come back to their initial ratio of  $(1 + \alpha_0)$  to the advantage of the conventional system. When the slope is negative, the resolution of both systems improves, but the one of the combined system improves more slowly than the one of the conventional one.

The combined system using super-resolution has a more stable ground resolution than the conventional system to which it is equivalent on flat surfaces. When the slope increases, the independence of the two images of the combined system also increases and compensates some of the slope-related resolution loss. When the slope decreases, the independence of the two images of the combined system decreases and offsets part of the expected resolution improvement.

The critical slope value ( $a$ ) is such that :

$$a = i - \arctan(\alpha_0 \tan(i))$$

when this occurs, the resolution of the conventional system has already been quite degraded by the slope. Figure 7 indicates the resolution as a function of slope for two systems equivalent on flat ground with  $\alpha_0 = 0.5$  and an incidence angle of  $45^\circ$ .

### 3.4 Processing to super-resolution

Assuming an non-overlapping ratio of  $\alpha_A$  in azimuth and  $\alpha_D$  in range, these coefficients ranging from 0 to 1, we might expect to construct interferometric product with resolution  $\frac{\rho_D}{(1-\alpha_D)}$  and  $\frac{\rho_A}{(1-\alpha_A)}$  in range

and azimuth, while we hope to achieve resolutions of  $\frac{\rho_D}{(1+\alpha_D)}$  and  $\frac{\rho_A}{(1+\alpha_A)}$  for the super-resolution products,

where  $\rho$  symbolizes the nominal emitter's resolution. The procedure which will be used is currently being tested. It consists of the following steps : (1) process each image from the receivers in slant-range, up to the maximum resolution in complex format (single-look complex or SLC), (2) project the SLC images one by one onto an oversampled Digital Terrain Model grid with a grid size compatible with the ultimate expected

super-resolution  $\frac{\rho_D}{(1+\alpha_D)}$  or

$\frac{\rho_A}{(1+\alpha_A)}$  (typically two to three meters) . The operation

consists of resampling the SLCs. At the same time, the phase residuals corresponding to the round trip between the point on the ground and the satellite is cancelled. Thus, at this stage, we have three images from the three receivers, each sampled to a high-definition DTM-like grid and each phase compensated. (3) Extracting the difference of phase of any pair of these image results in an interferogram with a resolution degraded by factors  $\frac{1+\alpha_D}{1-\alpha_D}$  and  $\frac{1+\alpha_A}{1-\alpha_A}$  in range and azimuth, with respect to

the desired resolutions. After averaging the phase values by filtering the complex number over the cell size defined by these factors, we have an estimate of the local phase difference between the two images. The phase difference is, hopefully, slowly varying since most of the phase difference has been compensated by the first step. (4) Then we use an oversampled version of the phase difference to correct one of the image of the pair. (5) Finally, we add both images into a super-resolution image.

This way of processing to super-resolution is certainly not unique, but it is the method we currently favor and test. We call it the PHASEMAP architecture. The only threat to this procedure (or any other) is if the phase difference between images varies so fast that the low-resolution image of the phase difference does not reflect the real one. Such a situation may arise when we have obstacles of when the slope reaches its limit (i.e. section 3.3).

## 4 Examples of mission

### 4.1 Example of an L-band mission

Here we present the main features of a cartwheel dedicated to the radar instrument onboard the future ALOS satellite [ref.16]. ALOS features a number of operating modes with variable angles of incidence and range resolution. With a primary mission aimed at producing data for a global DEM, we favor the optimal geometry, that is an incidence angle close to  $45^\circ$ , and the highest range resolution, that is a 28 MHz bandwidth. This does not exclude another operating mode, in particular dedicated to ocean studies, where a lower angle of incidence would be selected for maximizing the gain over water. Considered as a first mission for the concept, a wheel associated to ALOS would have two successive phases. A first phase where the radius of the wheel would be matched to the requirement of covering land surfaces with adequate parameters for optimal DEM computation and a second phase where the wheel could be steered to a radius close

to the maximum in order to test super-resolution. Along the principles of the cartwheel, three micro-satellites would listen simultaneously to the illuminated area, gathering unsynchronized data at a rate of 30 MHz and storing each sample as 2bits (I,Q) samples, which makes  $120 \text{ Mbits}^{-1}$ . At such rate the listening cannot last more than 160 seconds before the 20 Gbit on-board memory is full. We expect the average time of operation to be closer to about one minute per orbit in practice. Although with continuous recording we are not limited to the nominal 75 km swathwidth of ALOS, but rather by the observed signal to noise ratio, we do not expect to cover more than  $30000 \text{ km}^2$  per orbit. One year (5000 orbits) is then a minimum time for a global coverage of the land surfaces.

The features of ALOS imply a minimal altitude of ambiguity of 3.8 m and a nominal pixel surface of  $25 \text{ m}^2$ . The choice of the baseline is influenced by (1) the need to have the contributions of ambiguities made uncoherent (section 3.1), (2) the wish to work with an altitude of ambiguity larger than the average error of the global DEM available at the time of the mission, for automatic unwrapping of the fringes and (3) the goal of topographic sensitivity, which we would like to be around one meter. For these reasons a value of 50 m for the altitude of ambiguity is satisfactory. It represent 8% of the critical baseline; it is compatible with publicly available SRTM results for unwrapping and, as we will see, it is compatible with the required accuracy.

Assuming our micro-satellites are fitted with a circular antenna with a diameter of 2.4 m, the surface ratio with the antenna of ALOS is almost 7. This means a 8 to 9 dB loss in power. In contrast, we are interested in a typical topographic product with a 20 m grid, a surface 16 times larger than the nominal pixel size. Even if the interferometric pixel size (Figure 1a) is slightly larger than the nominal pixel size, this implies a gain of 12 dB due to coherent combination of independent neighbor pixels into the targeted geographic cell. A one meter accuracy in height from an altitude of ambiguity of 50 m means a standard deviation of the phase equal to 2% of a cycle. This is obtained for a signal to noise ratio of 15 dB. Table 1 gives the standard deviation, expressed in percentage of a full phase cycle, as a function of signal to noise ratio. Given the -25 dB noise equivalent target for ALOS, the required ratio of 15 dB and the gain of 3 dB which results from the competition between antenna surfaces and coherent surface integration, a target at -13 dB is seen with a one meter vertical accuracy. From Table 1, we deduce that a target 10 dB weaker (i.e. with a signal of -23 dB) would yield a 3 m accuracy.

The critical vertical baseline of the ALOS wheel is 66 km at  $45^\circ$  incidence. We want an average baseline amounting to 8% of it, or 5 km. This average value is obtained for a vertical radius of the wheel of 3.11 km. At the same time, an average horizontal

baseline of 10 km would be available permanently, creating a difference of time of 1.5 seconds.

Although only the two best positioned micro-satellites are used, whether vertical or horizontal separation is required, the third satellite is not useless. For current mapping, it provides two intermediate differences of time. For topographic mapping, it provides two intermediate values of the altitude of ambiguity, very useful to lower the fringe ranks or to lift ambiguities linked to constructions. For instance, if we have an optimal 50 m topographic sensitivity, if the third satellite is located at 33% of the vertical baseline, it provides additional sensitivities when combined to the two nominal satellites (respectively 150 m and 75 m). A 70-m tall building could be mistaken with a 20-m tall building with the nominal interferogram, but would not be ambiguous anymore with considerations to the two additional interferograms. This possibility is, however, opportunistic rather than systematic.

#### 4.2 Example of a C-band mission

The main features of a cartwheel dedicated to the radar instrument onboard the future ENVISAT satellite [ref.18] would be very similar to the one proposed for ALOS, because the geometric parameters of the wheel can be tuned to mimic the same geometric sensitivity regardless of the wavelength. The difference is with the smaller bandwidth of ENVISAT (16 MHz). With other projects involving a larger bandwidth, such as RADARSAT 2, we should even go beyond the 30 MHz we envision for ALOS.

The wheel could follow ENVISAT as efficiently as ALOS. However, as a case study, we envisioned the use of a wheel configuration for polar research. Using a wheel with two satellites phased at  $180^\circ$ , combined with a wheel vertical radius close to the critical value (for instance 70%), following the ENVISAT satellite, we could attempt to map floating ice thickness in the Arctic and Antarctic regions. The essentially flat landscape allows large area integration and prevents the "high slope limit" despite the high percentage of the critical baseline. The perigee and apogee of the micro-satellites should be positioned at the northern and southern part of the orbits. Figure 4 gives a potential geometric layout. With an altitude of ambiguity of 5 m and a target pixel 200 m by 200 m, 10 cm or less elevation accuracy can theoretically be obtained.

#### 4.3 Example of a military mission

Unlike the previous sections, we will not attempt to describe an actual defense mission but to recall and analyze the advantages of the wheel concept for some of the defense aspects of radar observation.



An advantage of using a synthetic band in azimuth is the possibility to go beyond the bandwidth allocation for any given bandwidth. This advantage is specially true for the wavelengths with the smallest bandwidth allocation. Following a system which uses all the allocated bandwidth, for instance 80 MHz in L-band, with a range super-resolution factor of four (which requires at least six micro-satellites for permanent operations), would create images that literally cannot exist. In particular, very unusual ratio between final range and/or azimuth pixel size and the wavelength would be achieved. The factor Q would be as low as 4 in our example, meaning that phase unwrapping could be achieved by exploiting the results of image correlation. This would also give access to some new textural information and might reverse some of the traditional preference of the military toward shorter wavelengths.

Any system which is not bistatic can be blinded by a passive reflector of sufficient size. Such blinding of ERS-1 occurred accidentally with exceptionally strong or optimally oriented targets. The cartwheel is protected against such a phenomenon. If a corner reflector is strong enough to blind the emitter, it has to be large enough and will therefore be too focussed on the emitter to blind the constellation. Even in L-band, a corner reflector larger than two meter cannot send energy back to the constellation.

Active jamming is more difficult with the constellation because any focussed jammer would be likely to miss the constellation, which remains silent, especially if the jamming devices are automatically triggered by the emitter. Powerful jamming of a large angular sector could damage the observation by the constellation but is more difficult to deploy in the field.

The processing of mobile targets can also be enriched by a wheel system. Of course one could imagine processing the sub-images as independent looks along the track, and use the range displacement between images. This is however, not very different of what can be done directly with sub-aperture. A more specific way to use the wheel is to characterize the variation of azimuth shift between images from receivers with slight difference of distance to the target. The azimuth shift of

a moving target is traditionally  $R \frac{V_t}{V_{sat}}$  where R is the range of observation,  $V_t$  the target own velocity projected on the line-of-sight and  $V_{sat}$  the satellite velocity. Only the fractional part of the shift with respect to the azimuth antenna footprint is observed and it might be difficult to determine the origin, or the real position, of the mobile target. For instance a projection of 5 m/s results in a one-kilometer azimuth shift. More rapid targets quickly become ambiguous in azimuth. Correlating the images of two receivers separated in range by  $\Delta R$  is much more convenient, since the observed shift becomes  $\Delta R \frac{V_t}{V_{sat}}$ , that is typically only

1% of the nominal displacement (or the ratio  $\frac{\Delta R}{R}$ ). The real position of the target in azimuth can be obtained by "undoing" the azimuth shift backwards after multiplication by this ratio. In this scheme, no target is sufficiently rapid to become ambiguous.

Finally, a difference between azimuth super-resolution and SPOTLIGHT acquisition is the time required for gathering the data. The simultaneous along-track acquisition does not change the time that would have been spent for a conventional strip-mode acquisition while multiplying the amount of data. The micro-satellite system is not more sensitive to wind or any other quick changes in the targets than the emitter while a SPOTLIGHT operating mode requires much more stability from the targets. This is in addition to a more straightforward advantage : the increase in azimuth resolution can be obtained for any scene duration while the antenna beam must be steered in azimuth for SPOTLIGHT.

The use of a wheel configuration for dual use with a civilian emitter should not be restricted to configurations with three micro-satellites [ref.1]. The more micro-satellites, the wider the gap between the emitter's initial performance and the final performance

## 5 Conclusion

We described some of the features of passive constellations both in terms of system design and technical limitations and in terms of missions. We believe that such systems are likely to become commonplace in the future and that many of the next generation radar satellites could be followed by these systems for scientific or defense application, implementing dual use at a large scale and generating savings.

These systems create new possibilities of cooperation in space. They are highly dependent of the main radar system they follow while requiring no interface with it. As an illustration, the same radar satellite can be followed by several, independent wheel systems for various purposes. The geometry of these systems would be tuned according to their purposes : emphasis on vertical or horizontal baselines, emphasis of image independence for resolution or image similarity for interferometry, etc...

The data created by these systems can cross-fertilize easily. High resolution DEMs in C-band and L-band can be used for monitoring forest cover and thus become a renewable product.

After the initial concept of super-resolution has been fully tested with simultaneous data acquisitions from space, more ambitious radar systems could be designed, which would rely explicitly on super-resolution in range, azimuth, or both for achieving their basic performances. Such systems could make dual use of civilian emitters, and produce defense-like

resolutions, or they could be considered as add-ons to a military system, in order to boost its performances or improve its anti-jamming or mobile-targets capabilities. Such systems, even if they are based on tens of micro-satellites, are likely to be cheaper than larger ones.

#### ACKNOWLEDGEMENT

The author wishes to thank the team in charge of micro-satellites projects in CNES as well as E. Thouvenot for fruitful discussions on the concept. J. Achache first suggested to apply the cartwheel concept to challenge the performances of a space mission dedicated to polar regions such as CRYOSAT [ref.21].

#### REFERENCE

- [1] Massonnet, D., "The interferometric cartwheel, a constellation of low cost receiving satellites to produce radar images that can be coherently combined", *Int. J. of Remote Sens.*, in press
- [2] Massonnet, D., French Patent n°236910D17306RS "Roue interférométrique", 30 april 1998
- [3] L.C.Graham, "Synthetic interferometer radar for topographic mapping", *Proc. IEEE* vol 62 n° 6 - 1974
- [4] Zebker, H. and Goldstein, R. "Topographic mapping from interferometric SAR observation" *J. Geophys. Res.*, 91, 4993-5001, 1986
- [5] Zebker, H., Wheeler, K., Miller, T., Lou, Y., Alberti, G., Vetrilla, S., and Cucci, A. "The TOPSAR interferometric radar topographic mapping instrument" *IEEE trans. Geosc. and Remote Sens.*, 30, 5, 933-940, 1992
- [6] Goldstein, R. and Zebker, H. "Interferometric radar measurements of ocean surface currents" *Nature*, 328, 707-709, 1987
- [7] Prati, C. and Rocca, F. "Improving slant-range resolution with multiple SAR surveys" *IEEE trans. Aerosp. Elec. Sys.*, 29, 135-43, 1993
- [8] Jakowatz, C., Wahl, D., Eichel, P., Ghiglia, D. and Thompson, P. "Spotlight-Mode SAR: a signal processing approach" Kluwer, Boston, 1996
- [9] Gatelli, F. et al., "The wavenumber shift in SAR interferometry", *IEEE trans. Geosc. and Remote Sensing.*, 32, 855-865, 1994
- [10] Rocca, F., Prati, C. and Monti-Guarnieri, A., "New Algorithms for Processing SAR data", ESA/ESRIN, 1989.
- [11] Zebker, H. and Villasenor, J., "Decorrelation in interferometric radar echoes" *IEEE trans. Geosc. and Remote Sens.*, 30, 950-959, 1992
- [12] Massonnet, D. and Rabaute, T. "Radar interferometry: limits and potential" *IEEE trans. Geosc. and Remote Sensing.*, 31, 455-464, 1993
- [13] Thouvenot, E. et al. "Radar payload and system dedicated to passive radar constellations" in preparation for *IEEE trans. Geosc. & Remote Sens.*
- [14] "Micro-satellites projects in CNES" internal memo.
- [15] Massonnet, D., F. Adragna, and M. Rossi, CNES General-Purpose SAR Correlator. *IEEE Trans. Geoscience & Rem. Sensing*, 1994. 32(3): p. 636-643.
- [15] H. Wakabayashi et al., "A SAR system on the ALOS", *Int. Archives of Photogrammetry and R. Sens.* Vol.31, pp.193-196, 1996.
- [16] Massonnet, D. and H. Vadon, ERS-1 Internal clock drift measured by interferometry. *IEEE Trans. Geoscience & Rem. Sensing*, 1995. 33(2): 7p. 401-408.
- [18] Jordan, R.L. et al., "Shuttle Radar Topography Mapper (SRTM)", *Microwave Sensing and Synthetic Aperture Radar (proc. SPIE)*, pp412-422, 1996.
- [20] Massonnet, D., H. Vadon, and M. Rossi, "Reduction of the Need for Phase Unwrapping in Radar Interferometry". *IEEE Trans. Geoscience & Rem. Sensing*, 1996. 34(2): p. 489-497.

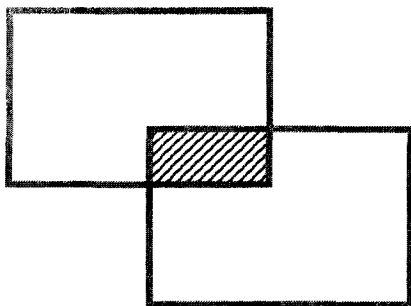


Figure 1A: Resolution of interferometric products

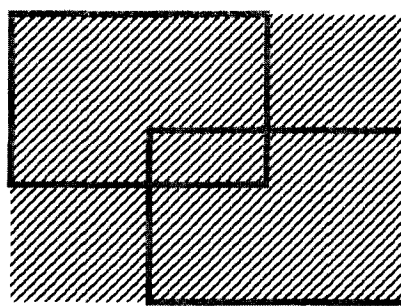


Figure 1B: Resolution of super-synthesis products

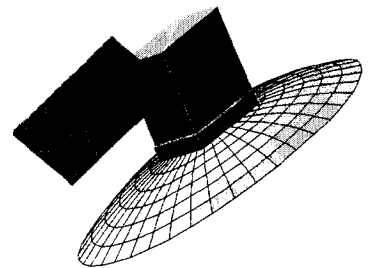


Figure 2

Figure 3: Interferometric Wheel Orbital Configuration

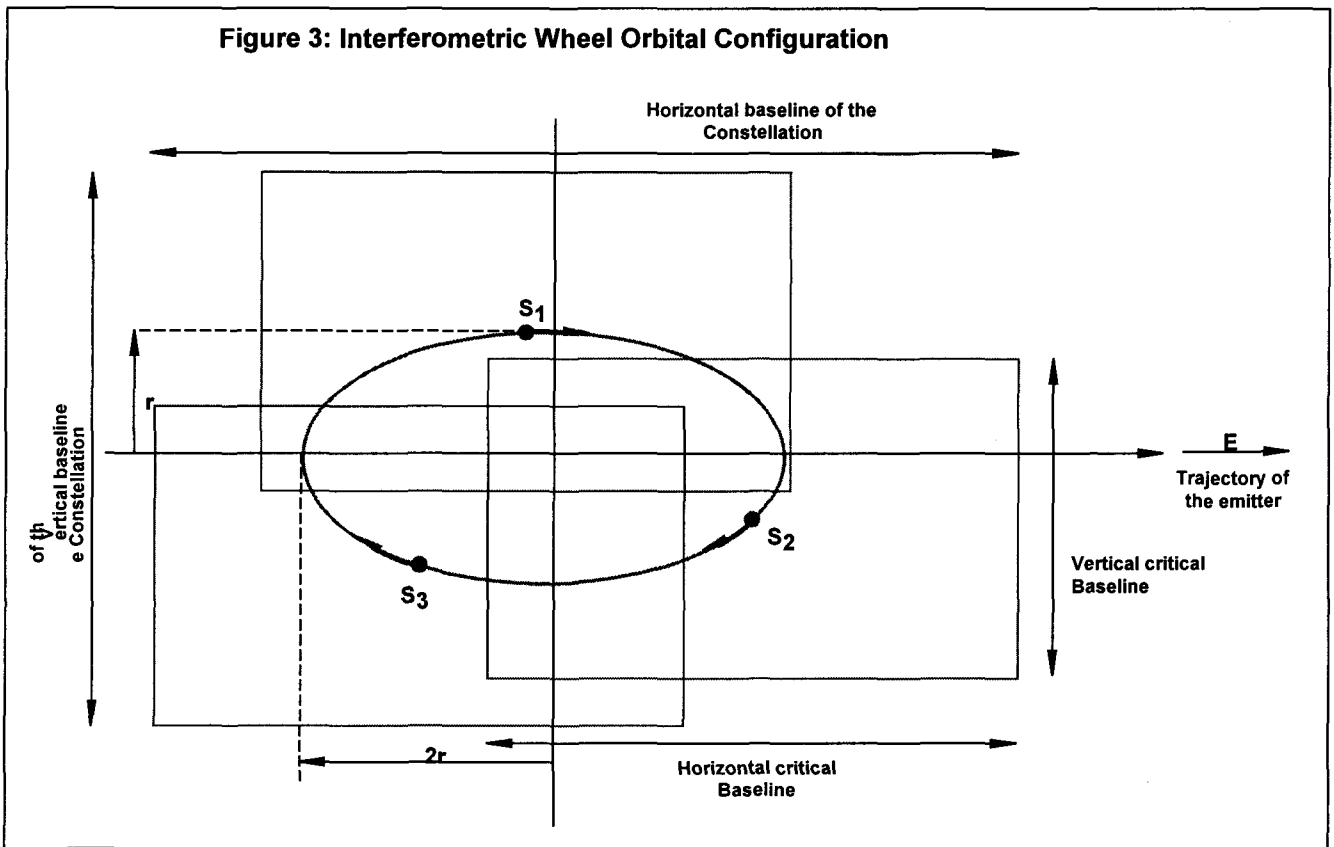
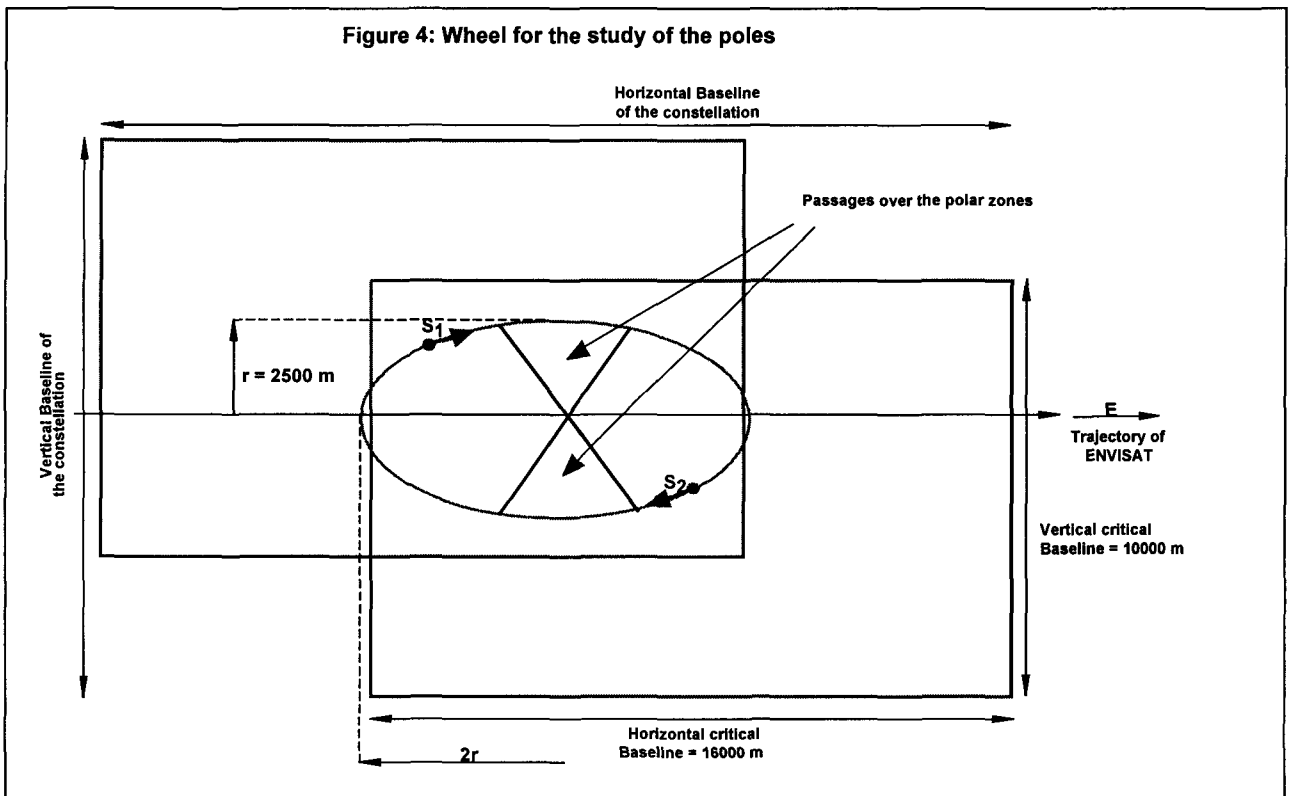
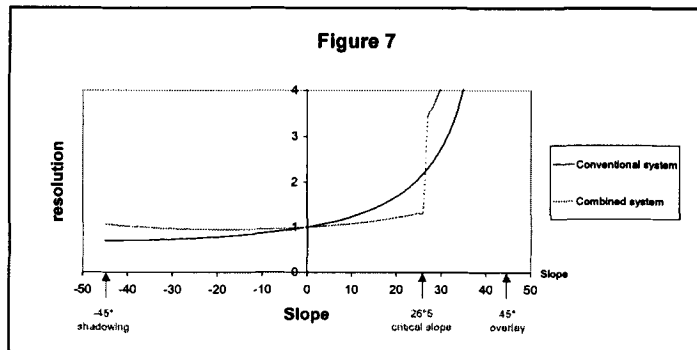
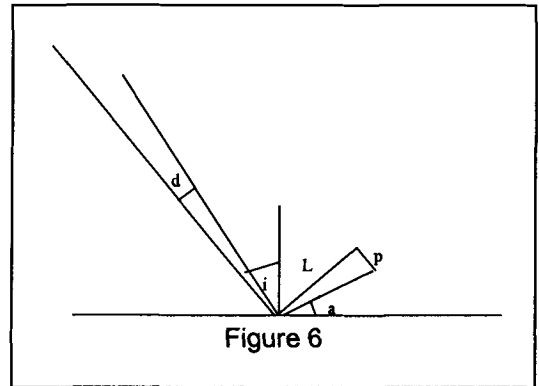
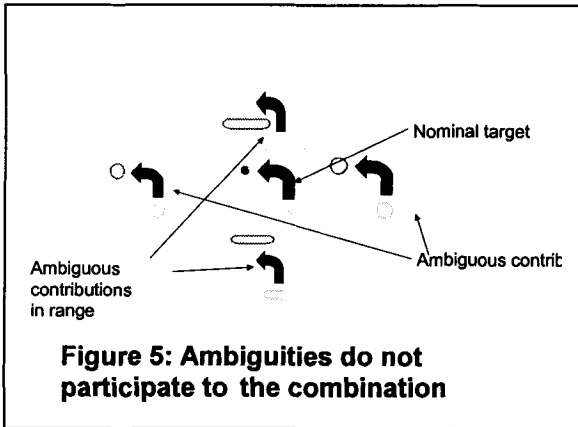


Figure 4: Wheel for the study of the poles





**TABLE 1**

Standard deviation of the phase, in percentage of cycle, as a function of signal to noise ratio, in dB.

0	13,86%	11	3,20%
1	11,60%	12	2,85%
2	9,91%	13	2,54%
3	8,60%	14	2,26%
4	7,52%	15	2,01%
5	6,62%	16	1,79%
6	5,84%	17	1,59%
7	5,16%	18	1,42%
8	4,57%	19	1,26%
9	4,06%	20	1,13%
10	3,61%	21	1,00%

## Prose: A Low Cost P band Transponder Radar Satellite Based on the SAIL concept

Jean Paul AGUTTES, Luc LAPIERRE

CNES (Centre National d'Etudes Spatiales), 31401 TOULOUSE cedex 4, France.

Ph: 33 5 61 27 41 28, Fax: 33 5 61 27 43 59, [jean-paul.aguttes@cnes.fr](mailto:jean-paul.aguttes@cnes.fr)

The SAR (P)ROSE satellite concept is based on the following principles: fixed transmit beam covering a wide elevation range, direct relay to ground of the echoes received by each antenna radiator, narrow receive beam formed on ground in all elevation directions (Digital Beam Forming). It provides a fixed and permanent wide swath (300 to 500 KM) at low or medium resolution ( $> 10$  m) with a very simple communication transponder type payload stripped of signal, diagram control and of ground scheduling. The costs can thus be kept very low.

The concept allows Radar Observation on Systematic (always on, no scheduling) and Economical way (ROSE). It fits applications requiring systematic and frequent (3 to 6 days) acquisition on large area with nevertheless rather good resolution (up to 20 MHz bandwidth) (e.g.: ice and navigation, ships and pollution, hydrology, biomass monitoring).

Such combination of operational performance (huge swath/pixel ratio) and simplicity (transponder) is made possible by the use of the RADAR SAIL original satellite architecture, which, among other things, reduces the number of antenna radiators and thus the number of transponded return channels, and suppresses the nadir echo.

Applied to P band, (P)ROSE becomes even more exciting since for the first time large swath become possible in P band, thanks to the ROSE approach and to the SAIL concept capability for very large antenna (50 to 100 m<sup>2</sup>.) under limited fairing size. This mission opportunity is all the more exciting that it is costly to attain with conventional means and difficult to achieve even with emerging technologies (such as inflatable antennae)..

### 1 SAIL CONCEPT BACKGROUND

#### 1.1 General

RADAR SAIL ([1]) is a SAR satellite concept invented by CNES. The rectangular antenna is lying in the dawn-dusk orbital plane with the length (along speed vector) smaller than the height. This surprising vertical geometry has been proven to work properly for RADAR while enabling a cascade of other innovations converging into a radically new design of the whole satellite for an ultimate goal of simplification and cost reduction.. Such geometry makes it possible to place the solar cells on the back of the antenna, and to use gravity gradient stabilization. Optionally, implementation of a network of GPS antennas on the antenna surface offers an ideal configuration

(multiple path free) for interferometric measurement of the deformations of the antenna and of the absolute attitude of the average antenna plan, for compensation through the phase control of the T/R module. The antenna structure can be relaxed and can be made more easily folded

Such antenna can then almost fly by itself. It is packed for launch inside a cylinder-shaped bus having pyrotechnic doors for the antenna deployment and bearing the rest of the payload and the service equipment (orbit keeping, gravity gradient accompanying with magneto-torquer and magneto-meter).

With respect to the standard design, cost savings come from the bus, whose functions (OACS, power supply) are simplified, from the launch since the mass budget and the stowing configuration become compatible with small or medium size rockets even for very large antenna size (50 m<sup>2</sup>, [1]), and also from the RADAR antenna as shown here after. Moreover, long satellite life can be achieved ( $>10$  years) as result of the simplification of Bus and antenna functions.

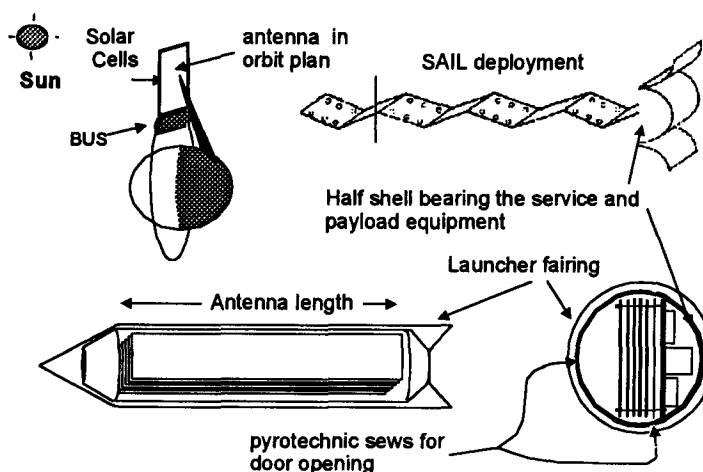


Figure 1: SAIL geometry and layout

#### 1.2 Vertical antenna

**Slight height increase:** For equal performance, the effective antenna height in the target line of sight should be the same for both standard and vertical geometries. There is an antenna height penalty for the new geometry. However, this penalty has to be computed at the high incidence, which dimensions the antenna height (ambiguity issues). For altitude around 550 km, it amounts around to 20% at 60° incidence.

**Great antenna electronic density relaxation:** The new geometry enables the spacing of the elevation antenna control points to be relaxed ( $1.5 \lambda$  or even  $2 \lambda$  instead of  $0.7\lambda$  in the standard tilted case) because the resulting grating lobes are rejected beyond the horizon. The same relaxation applies to the density of the transmit and receive (T/R) electronic and induces great cost and weight saving in spite of the antenna height increase.

**Dual side viewing, nadir echo blocking:** Viewing on both sides of the orbit track can be achieved at the only price of duplicating the radiators on both faces. The vertical antenna geometry allows an obstacle (the bus for instance) to be placed against the nadir echo and beam nulling technique is no longer required. Besides antenna flatness requirement can be relaxed (no more need for low level scattered grating lobes).

## 2 A SAIL AS A MIRROR FOR RADAR SIGNALS

### 2.1 DBF technique (digital beam forming on ground)

All that has been said so far is related to new satellite architecture and leaves the standard working rules of the RADAR unchanged with steerable limited swaths. The SAIL geometry also allows a much simpler RADAR to be designed, reduced to a transponder of signals and offering a fixed, not programmable, wide swath (500 or 1000 Km with moderate resolution  $>10$  m).

Such swath enlargement in spite of the range ambiguity constraints is enabled by the digital beam forming (DBF). All the RADAR echoes received by each radiator of the antenna are sent to the ground, where digital correlation simultaneously reconstitutes, in all the elevation directions, the narrow beam required for removing the ambiguity. Provided that the whole incidence range is illuminated by the transmitted signals, there is no need for beam steering on board, either for transmission or for reception. Since there is no reception during the pulse transmission, the wide image contains blank strips aligned along the speed vector, but this account for only 10 % of the image.

The transmit antenna beam must be broad and the receive one narrow (after DBF), thus the antennas can be distinct with a small (heightwise) transmit one and the overall size being driven only by receive antenna. Providing that there is no azimuth steering (no Spotlight mode), the receive radiators can be combined lengthwise or only one radiator can be used for the whole length. Thus the total number of RADAR echoes to be simultaneously down-linked depends only of the number of receive radiators heightwise. Both transmit and receive antennas can be passive.

### 2.2 Opportunities offered by the SAIL concept

The DBF technique is well known, but the merit of the SAIL concept is to simplify its application. Indeed, the main constraint for DBF implementation comes from the data down-link, whose capacity must be multiplied by the number of radiators. With respect to a conventional steerable RADAR, considering the elevation spacing relaxation ( $2 \lambda$  instead of  $0.7 \lambda$ ) and the slight antenna height increase (20%), the number of radiators is reduced by a factor 2.4 with the SAIL geometry. The high power resource of the SAIL can permanently supply the high power transmitter required for the illumination of a wide area (low antenna gain). The transmit antenna can be implemented on the module's earth face (see figure 2) very close to the amplifier (TWTA) inside the module. Since there is no antenna deployment lengthwise, it is possible to have only one radiator along this direction (possibly slotted wave guide). The nadir echo blocking by the central module avoids another series of blank strips within the image and the RADAR-signals sequencing can be fixed.

Since the receive antenna is passive, the panels can be made rigid through an acceptable mass impact. The miss-alignments between panels along yaw axis cannot be compensated neither on board nor on ground since there is only one radiator lengthwise. But, due to the limited length and the use of the antenna on receive mode only, these miss-alignments can be easily kept under acceptable tolerance. Therefore the only use of GPS is the measurement of panel miss-alignments along roll axis. Of course the compensation is made on ground within the DBF process. The roll miss-alignment between panels can also be directly measured on ground by comparison of ambiguous RADAR images achieved from the different panels before the DBF process on the whole antenna, thus avoiding any need for GPS.

### 2.3 Use of analog downlink (telemetry)

The echoes of each radiator (and the raw GPS signals if any) are directly transponded (after low noise amplifier) in the telemetry band and the whole multiplex is transmitted to ground in analog form. This "analog" approach has two advantages. One is the great efficiency in terms of down-link bandwidth which becomes a key concern when using DBF. One hertz of RADAR occupies one hertz of telemetry as compared with ten or more with digital transmission. The other advantage is simplification. The payload, which was already stripped of any control (none for the antenna, none for the signals sequencing) is now stripped of complex video and digital electronics (ADC, filtering, etc..) and reduced to a communication transponder.

Again because of its large power resources, the SAIL concept facilitates this kind of design. Indeed linearity constraints induce high power requirements for the return down-link transmitters.

## 2.4 ROSE Mission concept

The concept combines unusual simplicity for payload and exploitation (no programming) with equally unusual performance either in terms of image (huge swath to pixel size ratio) or in terms of operational capability: permanent working, earth totally imaged every 3 to 6 days (depending on maximum incidence and side viewing options) with 10 to 20 m resolution.

The concept is well suited to applications requiring systematic and frequent acquisitions on large areas. Ships and pollution, ice and navigation, hydrology and flooding are candidate application domains, among others. Constellations of two or three satellites can do much better than a daily revisit (at least at high latitude).

Such a mission concept does not suffer too much from the absence of on-board recording, which becomes very difficult in analog form. Indeed, the foreseen applications deal with large amount of data and near real time reactions from users not compatible with on-board storage and are better supported by ground antenna (receive only, no uplink since no programming) located near the users.

Two kind of ground reception can be envisaged: Big (5m diameter, working down to 5° elevation) regional receiving station for distribution of selected parts of image to users. Dedicated and local reception for big users located within their monitored area (30° elevation and 2,5 m diameter station).

## 2.5 ROSE design

Figure 2 sketches a generic implementation of the concept, with the basic functions (black) and possible extensions (grey) and table 1 gives rough characteristics of a P band basic implementation. The antenna length (4 m) is driven by the compatibility with small size launcher (SOYUZ, Athena 2). The antenna size (in  $\lambda$ .m unity) drives the maximum available incidence at a given altitude and at given ambiguity protection (-20 dB) whereas the antenna height (in  $\lambda$  unity) is limited by the achievable number of down links and by the total bandwidth.

Considering 10 MHz bandwidth (20 m resolution at 40° mid incidence), the total bandwidth to achieve 55° incidence is 180MHz. The height in P band is rather great (25m) whereas in C band (2 m) it is not sufficient from gravity gradient point of view. That is an opportunity in C band for another antenna (in grey in figure) to provide another polarization. In P band, which does not requires high power and great solar cells area, the opportunity is to implement dual side viewing with same or different polarization. The simultaneous working of these antennas is achieved through Scansar principle (alternate sequences of pulses on each mode) at expense of azimuth resolution degradation ( $\times 3$ ), the down link architecture and bandwidth being unchanged.

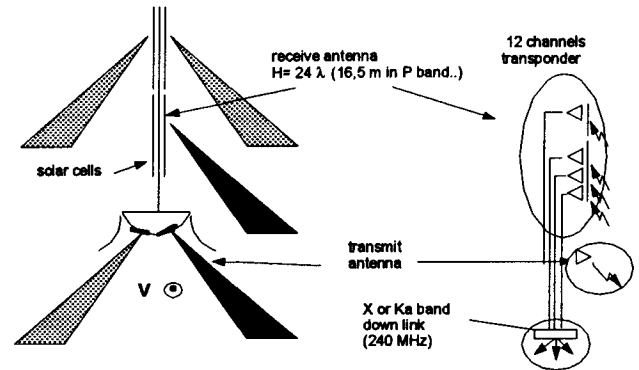


Figure 2: ROSE concept

Swath	Max Incidence Min. = 25°	Antenna H	Number of panels and of downlinks channels ( 2 $\lambda$ each)	BUS diameter	S/C mass
400 km	55	36 $\lambda$ / 25 m	18	1,95 m	1350 Kg
350 km	52,5	32 $\lambda$ / 22,4 m	16	1,85 m	1200 Kg
230 km	45	24 $\lambda$ / 17 m	12	1,75 m	1000 Kg

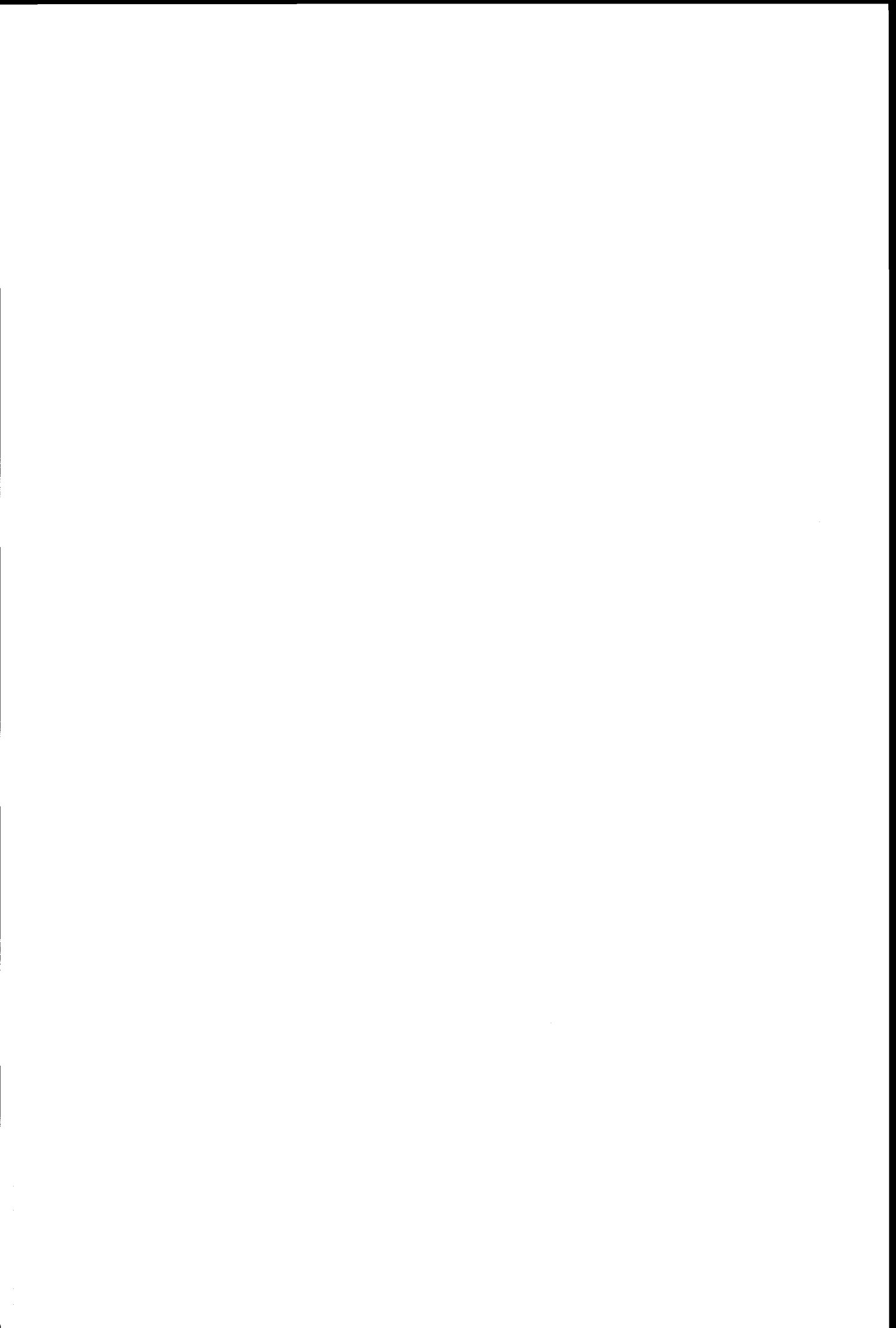
Table 1: PROSE Design (Alt. 500km, 4 m length)

## 3 PROSE: UNIQUE OPPORTUNITY IN P BAND

This concept gets round most of the difficulties of the P band. Large antenna area can be flown without questionable new technologies (inflatable structure). The available illumination and azimuth deviation angle are 10 times greater than that is required by the resolution, that enables to fight against ionospheric effects by auto-focus techniques or by selecting the best azimuth angle. Image formation on ground enables to identify potential jammers (which are likely to be within the great imaging range) and, through the DBF process, to adjust a beam nulling against them. Lastly, the link budget is achieved by the sharp receive which compensates the broad transmit. The transmit power flux density is more than 10 dB lower than with a standard approach, which should help to solve the critical issue of P band frequency allocation for space radar.

## 4 REFERENCES

- [1] J.P.AGUTTES, J. SOMBRIN, E. CONDE, "RADAR SAIL Satellite Concept", ACTA ASTRONAUTICA Volume 39, number 9-12





## Radar penetration in soils : towards a new system for subsurface Earth observation

<sup>1</sup>G. Grandjean, <sup>2</sup>P. Paillou, <sup>3</sup>P. Dreuillet, <sup>4</sup>P. Dubois, <sup>5</sup>J.C. Souyris, <sup>6</sup>N. Baghdadi and <sup>7</sup>J. Achache

<sup>1</sup>BRGM, BP 6009 45060 Oléans, France,  
Tel:(33)2.38.64.34.75, fax:(33)2.38.64.33.61, [g.grandjean@brgm.fr](mailto:g.grandjean@brgm.fr)

<sup>2</sup>Observatoire de Bordeaux, BP 89, 33270 Floirac, France,  
tel :(33)5.57.77.61.26, fax:(33)5.57.77.61.10, [paillou@observ.u-bordeaux.fr](mailto:paillou@observ.u-bordeaux.fr)

<sup>3</sup>ONERA, Chemin de la Hunière, 91761 Palaiseau Cedex, France  
tel:(33)1.69.93.62.65, fax:(33)1.69.93.62.69, [dreuil@onera.fr](mailto:dreuil@onera.fr)

<sup>4</sup>DGA, 16 bis avenue Prieur de la Cote d'Or, 94114 Arcueil Cedex, France  
tel:(33)1.42.31.88.22, fax:(33)1.42.31.99.77, [pascale@ctme.etca.fr](mailto:pascale@ctme.etca.fr)

<sup>5</sup>CNES, 18 av Edouard Belin, 31401 Toulouse, France  
tel:(33)5.61.27.37.98, fax:(33)5.61.27.31.67, [souyris@cnes.fr](mailto:souyris@cnes.fr)

<sup>6</sup>BRGM, BP 6009 45060 Oléans, France,  
tel:(33)2.38.64.34.75, fax:(33)2.38.64.33.61, [n.baghdadi@brgm.fr](mailto:n.baghdadi@brgm.fr)

<sup>7</sup>CNES, 2 place Maurice Quentin, 75036 Paris Cedex 01, France  
tel:(33)1.44.76.78.51, fax:(33)1.44.76.78.33, [Jose.Achache@cnes.fr](mailto:Jose.Achache@cnes.fr)

applications: subsurface imaging, water detection, vegetation and ocean study.

**Keywords:** low frequency radar, penetration, soils, ground-penetrating radar, airborne radar, polarimetry.

### ABSTRACT

The aim of this work was to analyze the penetration capability of microwaves, particularly for L- and P-band systems, and its potential for mapping sub-surface heterogeneities such as lithology variations, water content or sedimentary structures. Our approach consists in using ground-penetrating radar (GPR) sections in as a source for reliable ground truth measurements, and then analyzing the SAR airborne data to understand the backscattering mechanisms and the penetration capabilities. The Pyla dune was chosen as a suitable site for field validations, as it presents a large sandy area of variable thickness for which several radar data sets are available. We present here preliminary results: (1) the characterization (geometric and dielectric) of subsurface structures obtained through GPR imaging analysis; (2) the identification of the scattering mechanisms through polarimetric analysis where the volume scattering contribution appears to be important even at L-band.. These first results stress the potential of longer wave-length imaging and prompted us to propose a new airborne sensor, called Sethi P-band, which will allow both vertical and side looking imagery, and will offer polarimetric capabilities. It is viewed as a tool for the remote sensing community to evaluate the potentials of P-band for various

### INTRODUCTION

In less than 10 years, microwave remote sensing techniques have provided unexpected insights into the Earth surface structure and processes, and triggered the development of entirely new research fields in geodynamics. For instance, spaceborne synthetic aperture radar (SAR) provided measurements of ground geometry and surface displacement with unprecedented accuracy. The characterization of surface parameters using polarimetry is another demonstrative example. With spaceborne SAR (ALMAZ-1, SIR-C/X-SAR, JERS-1, ERS-1/2, RADARSAT), three characteristics of Earth surface can in principle be observed: the slope, i.e. the topography, the surface roughness determined by the geology and erosion processes, and the dielectric properties mainly related to soil moisture. Over arid areas, low frequency SAR allows us to investigate the subsurface down to several meters. So far, this technique has drawn little interest by the radar remote sensing community, despite the fact that low frequency radar systems can achieve penetration capabilities that could be very useful for accurate mapping of subsurface parameters such as soil dielectric parameters, water saturation, or subsurface structures.

The present work describes the first results obtained over our test site, the Pyla dune near Bordeaux, France (cf. Fig. 1), and the preliminary study of a P-band SAR system that will be used for the remote sensing of subsurface humidity and geological mapping. Performance of airborne and spaceborne radar systems, in term of signal penetration depth, is analyzed in the 300-500 MHz frequency. Simulation of such system is performed over known test area for which a thorough dielectric characterization is obtained through GPR measurements and the simulation results are then compared to real data acquisition.

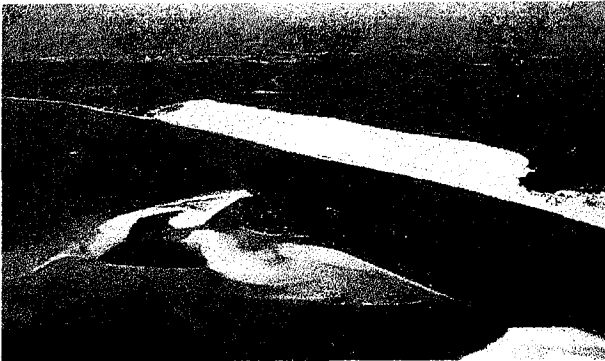


Figure 1: The Pyla dune in France.

The analysis of polarimetric L-band data obtained from two airborne SARs: the French RAMSES system (1.6 GHz) and the US AIRSAR one (1.25 GHz) shows a significant volume scattering component which is coherent with the analysis of subsurface structures detected by GPR. More interesting results should be obtained with lower frequencies (P-band, that is 300-500 MHz frequency range) combined with polarimetric capabilities.

Our first results open the way to new applications of radars for Earth observation, in particular to map the surface and subsurface soil parameters, such as water content, geological layers, buried objects and heterogeneities. A new airborne instrument named SETHI P-band, derived from the RAMSES P-band SAR and combining nadir looking, side looking and polarimetric capabilities, is currently under development at ONERA as an offspring of the RAMSES system. It will offer a new facility to the remote sensing community to evaluate the potential of P-band for various applications: subsurface imaging, water detection, vegetation and ocean study, and archeology in arid regions.

#### FIELD MEASUREMENTS

The studied site is located in the southern part of the Pyla dune, because sedimentary structures become more superficial there. A first field survey, realized in January

99, was devoted to surface roughness measurements and characterization of the spatial distribution of subsurface dielectric structures. This information is needed in order to take into account both surface and volume scattering processes in model validation.

Surface roughness measurements were conducted using a laser profiler developed by ESA [1]. Two roughness profiles of 20 meters long were collected parallel and orthogonal to the coast line direction. A profile is a juxtaposition of five meter long profiles, with a spatial resolution of 5 mm. Once an individual 5 meter sub-profile is acquired, the profiler is displaced exactly by 5 meters and realigned using a theodolite. The two roughness parameters, standard deviation of surface height (S) and correlation length (L), were extracted for profile sections of 1, 2, 4, 5, 6, 10, and 20 meters long. The rms. height (S) is of the order of 5.3 mm in the perpendicular and parallel directions. Fig. 2 illustrates the exponential dependence of the correlation length on profile length. We observe that the correlation length increases as a function of profile length. This increase is very rapid between 1 m and 10 m.

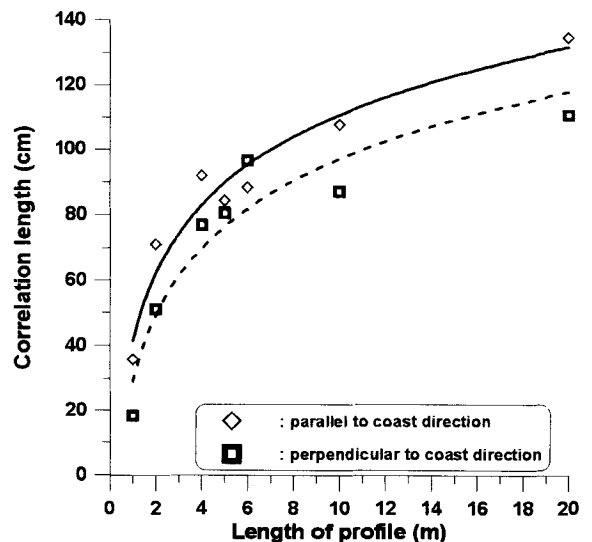


Figure 2: Relationship between the correlation length and the profile length.

Several GPR monostatic profiles were acquired from the shore to the top of the dune, for a total length of 150 m. Frequency range of  $100 \pm 50$  MHz,  $300 \pm 150$  and  $500 \pm 250$  MHz were tested. For each of them, a penetration depth down to 40 m was reached, with a resolution increase with frequency, as expected with this type of instrument [2]. As an example, Fig. 3 shows a depth section of the 100 MHz profile.

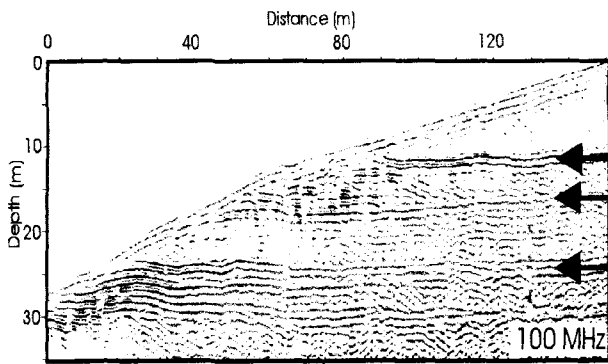


Figure 3: GPR monostatic 100 MHz profile recorded in the southern part of the Pyla dune. Black arrows show the three main reflections related to paleosoils.

In complement, three Common Mid Point (CMP) measurements were recorded to estimate the velocity variation of the radar wave with depth [3]. This velocity law was used for the time to depth conversion of the monostatic profiles. The GPR monostatic profiles analysis coupled to CMPs outlines subsurface structures related to paleosoils, corresponding to subsurface structures with a higher water content, and presenting therefore a higher permittivity.

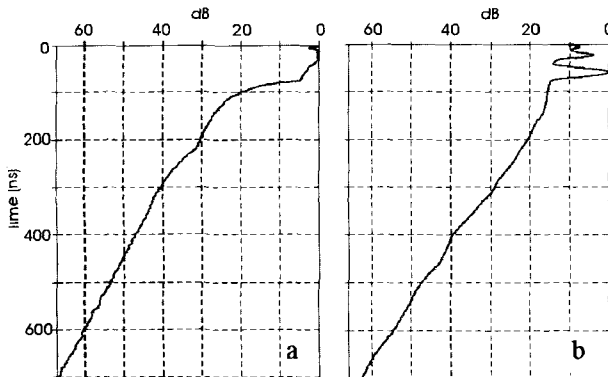


Figure 4: Observed (a) and calculated (b) backscattered power curves.

In addition to this structural study, a GPR modeling procedure [4] was used to estimate the dielectric model providing the best fit to the observed profiles. This was performed by a trial and error approach. The multi-layer dielectric model of the dune presented in Table 1 was validated by comparing the observed backscattered power at the surface to the simulated one (cf Figure 4).

	wet sand	dry sand	paleosoils
$\epsilon_r$	20±10	6±2	8±2
$tg\alpha$	0.01	0.01	0.1
$\mu_r$	1	1	1
$\delta$ (m)	0.005	0.005	0.005

Table 1: Dielectric parameters of the three kind of layers featuring the dune, computed from GPR modeling.  $\epsilon_r$ ,  $tg\alpha$ ,  $\mu_r$  and  $\delta$  are respectively the relative

permittivity, the loss tangent, the relative permeability and the RMS height.

The information concerning the surface (roughness) and subsurface geometry (layering), and the dielectric parameters obtained from GPR modeling, are the basics that will be used to understand low frequency airborne SAR data of the site. This approach is developed in the following to understand how deep the radar waves penetrate into the soil and how subsurface structures are seen by airborne SARs [5].

RADAR PENETRATION PERFORMANCES

Table 2 presents radar penetration depths computed for various frequencies (L and P-bands), using permittivity measurements obtained from GPR and equation:

$$\delta_p = \frac{\ln(J) \lambda}{2\pi} \left\{ \frac{\mu\epsilon'}{2} \left[ \sqrt{1 + \left(\frac{\epsilon''}{\epsilon'}\right)^2} - 1 \right] \right\}^{-1/2}$$

Radar penetration is important for both L (1.5 GHz) and P-bands (500 MHz), of the order of 10 meters in the dry sand that covers the dune. Even wet sand still allows several meters of penetration in L-band. These results already predict that subsurface structures should be seen by L-band airborne SAR (Table 2).

	wet sand	dry sand	paleosoils
1.5 GHz	3.3	6.0	0.5
1.0 GHz	4.9	9.0	0.8
500 MHz	9.8	17.9	1.6
300 MHz	16.4	29.9	2.6

Table 2: Radar penetration depth (in meters) for the various dune layers between 300 MHz and 1.5 GHz.

AIRBORNE SAR DATA

Two airborne L-band SARs were considered: the AIRSAR system developed by JPL/NASA, and the RAMSES system developed by ONERA and DGA. Both provide polarimetric data (HH, HV/VH, and VV polarizations).

AIRSAR

AIRSAR operates C (5 GHz), L (1.25 GHz) and P bands (440 MHz) with a resolution of 3 m in range and 6 m in azimuth. The P-band data could not be used because of strong signal interference caused by a near-military radar, but a polarimetric analysis of the L-band image was performed.

Although full polarimetric imaging radar does provide complex backscattered echoes ( $f_{hh}$ ,  $f_{vv}$ ,  $f_{hv}$ ) the polarimetric information visualization is currently

restricted to the display of intensity backscatter coefficients ( $\sigma_{hh}^0$ ,  $\sigma_{hv}^0$ ,  $\sigma_{vv}^0$ ) on the Red, Green and Blue channels of a color image. Alternative representations consist in mapping parameters derived from the polarimetric analysis (such as the entropy, the dominant or average scattering mechanism, ...). The main issue therefore is to merge all this information, and to identify directly the complementarity (or redundancies) between intensity and phase information.

Using an approach developed in [6], the L band image analysis relies on a synoptic representation of the polarimetric information, in which the output of the polarimetric analysis is overlaid on a 'background' intensity image only when it is expected to hold pertinent information. This occurs when the local backscattered wave is well polarized. The estimation of the local entropy informs us of the state of polarization of the backscattered wave (a low entropy means that the polarized part of the backscattered wave is dominant). In this context, the following approach is proposed : from the eigenvalues and eigenvectors analysis of the local coherency matrix, estimated over a sliding window [7], are derived the local entropy  $H$  (ranging between 0 and 1) and the average backscattering mechanism  $\alpha$  (ranging between 0 and  $\pi/2$ ). Fig.5 displays the entropy map derived from the L band AIRSAR image. The forested part (in the right part of the image) indicates high entropy (presumably due to the predominance of volume scattering), while the low tide water area in the left part of the image indicates low entropy. In between, the entropy in the dune area ranges between low and high values.

In order to achieve the merging between intensity and phase information, the polarimetric information is projected in a Hue-Saturation-Intensity (HSI) system : Hue is controlled by  $\alpha$ , saturation by  $1-H$ , and Intensity by the fusion of  $f_{HH}$ ,  $f_{HV}$  and  $f_{VV}$  using a whitening filter. The meaning of this visualization is the following : First, a 'black and white' intensity image is elaborated. Then we add a local saturation (i.e. a local coloring) which is controlled by  $(1-H)$ . For a low entropy, the image is locally well colored, the color value being fixed by parameter  $\alpha$  that defines the nature of the local backscattering mechanism. Fig.6 displays the L band HSI image representation. The dune indicates two types of behavior : 1) The field backscattered by the colored area is well polarized, the average scattering mechanism being single scattering. In that case, the wave does not penetrate the dune and a surface scattering is observed. 2) Oppositely, the polarized part of the backscattered wave is lost over the dark areas : the wave is attenuated as it is penetrating the dune.

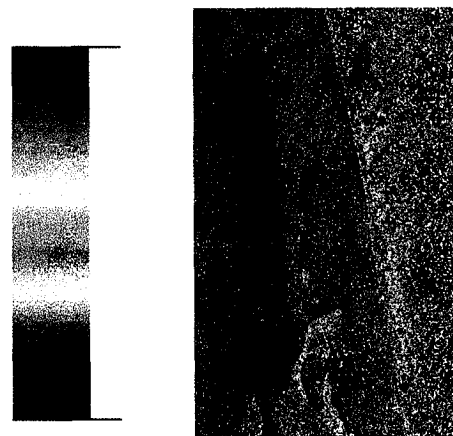


Figure 5: Entropy map of the L band AIRSAR image of the dune du Pyla

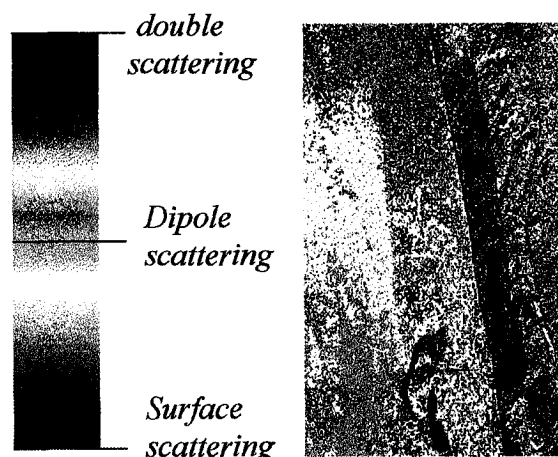


Figure 6: IHS representation of the L band AIRSAR Image of the dune du Pyla

The resolution of AIRSAR is not fine enough to clearly detect subsurface structures related to paleosols, but a polarimetric analysis clearly shows a strong volume scattering component over the sand in L-band data.

#### RAMSES

We dispose of RAMSES L-band scene (1.6 GHz) of the Pyla dune (cf. Fig. 6). It was acquired in June 1998 with an incidence angle of  $45^\circ$  and a track angle of  $20^\circ$ . The resolution is 0.7 m in range and 0.9 m in azimuth. The finer resolution here allows to observe some subsurface structures detected by the GPR (eg. the NE oriented bright line in the southern part of the dune in Fig. 7 - VH polarization).

A polarimetric analysis of RAMSES data was performed to detect regions where volume scattering occurs. Such areas should appear in both HH and VH images, since HH contains both surface and volume components and VH mainly shows volume scattering. Pure volume scattering should also have a VH/HH ratio

of around 1/3 and correspond to a low HH-VV correlation [8]. Combining these two conditions hold the volume scattering map shown in Fig. 8.

The NE oriented bright line at the bottom of the dune in Fig. 8 correspond to a buried paleosoil that was detected during the GPR fieldwork. This shows that subsurface imaging can already be done with L-band sensor, if high resolution is combined to polarimetry. Much more subsurface structures should be seen with a P-band SAR.



Figure 7: RAMSES L-band scene of the Pyla dune. HH polarization (left) and VH polarization (right).



Figure 8: Volume scattering map of the southern part of the Pyla dune (left) and corresponding VH scene.

## A NEW AIRBORNE P-BAND SENSOR

The development of the new airborne sensor SETHI, operating at P-band, should offer interesting perspectives for radar applications with penetration effects. SETHI P-band, derived from the ONERA Airborne facilities (RAMSES), will be implemented on a FOCKER 27 A.R.A.T. of IGN and will provide the possibility to work in both side and nadir looking modes.

The antenna design consists of several patches with high dielectric constant to preserve a relatively small size (80 x 25 cm) and the frequency band (400 - 500 MHz). Antenna will be integrated on a structure located under the Arat fuselage. The design of the receiver is very influenced by the environment of the P band and the polarimetry capabilities. For example, in order to minimize the effect of interferences, the receiver has a high interception point and the multi-channel of the radar can offer the possibility of an antenna processing. The SETHI system is expected to be available in April 2000.

## CONCLUSION AND FUTURE WORK

The objective of this work was to appreciate the capabilities of L and P-band radar systems to penetrate soils in order to obtain information about subsurface structures and related dielectric parameters. The Pyla dune was selected as the first test site to develop a methodology of validation.

GPR was successfully used and confirm it can be an efficient way to map subsurface heterogeneities, and to estimate their dielectric parameters. Even if the dielectric model suggests metric penetration, no quantitative validation is actually established. Evidence of volume scattering was derived from polarimetric analysis of AIRSAR and RAMSES L-band data. The high resolution of RAMSES images allowed to recognize subsurface structures that were previously detected with the GPR. Combining polarimetry and P-band frequency should lead to high performances in subsurface imaging.

Further investigations will be conducted in the future:

- surface and volume scattering model validation (eg. IEM) combining surface roughness measurements, dielectric model estimated with GPR, and airborne polarimetric data, in order to determine which parameters are determinant for radar penetration;
- a SETHI P-band fly by over the Pyla dune with various incidence angles including nadir looking;
- increase of the number of test sites to produce representative results.

## ACKNOWLEDGEMENTS

This work was supported by INSU/PNTS and CNES. BRGM, ONERA and ESA fund respectively the GPR field acquisitions, the implementation of Sethi P-band and the roughness measurements. The authors would like to acknowledge DGA for allowing the use of RAMSES data and JPL/NASA for providing AIRSAR data.

## REFERENCES

- [1] M. Davidson, T. Le Toan, M. Borgeaud, T. Manninen. "Measuring the roughness characteristics of natural surfaces at pixel scales: moving from 1 metre to 25 metre profiles". *Proceedings of IGARSS'98*, July 1998, Seattle, USA, pp. 1200-1202.
- [2] D.G. Smith and H.M. Jol. "Ground-penetrating radar: antenna frequencies and maximum probable depths of penetration in Quaternary sediments." *Applied Geophys.*, vol 33, 1-3, pp. 93-100, January 1995.
- [3] S.Tillard and J.C. Dubois. "Analysis of GPR data: wave propagation velocity determination." *Applied Geophys.*, vol 33, 1-3, pp. 77-92, January 1995.
- [4] A. Bitri and G. Grandjean. "Frequency-wavenumber modeling and migration of 2D GPR data in moderately heterogeneous dispersive media". *Geophys. Prosp.*, 46, pp. 287-301, 1998.
- [5] Ph. Paillou, G. Grandjean, P. Dubois-Fernandez, N. Baghdadi, M. Davidson, G. Claeys. "Arid Sub-Surface Imaging using Radar Techniques", *IGARSS'99*, Hamburg, Germany, June 1999.
- [6] P. Imbo, J.C. Souyris, A. Lopes 'Synoptic representation of the polarimetric information'
- [7] S.R. Cloude, E. Pottier, 'An entropy based classification scheme for land applications of polarimetric SAR', *IEEE Transactions of Geoscience and Remote Sensing*, vol.35, n°1, pp. 68-78, Janvier 1997.
- [8] E. Rignot, "Backscatter model for the unusual radar properties of the Greenland ice sheet", *JGR*, vol 100-E5, pp. 9389-9400, 1995.

## Processing and Calibration of Ultra-Wideband SAR Data from CARABAS-II

L.M.H. Ulander, P.O. Frörlind, and T. Martin

Swedish Defence Research Establishment (FOA)  
Division of Sensor Technology, P.O.Box 1165  
SE-581 11 LINKÖPING, Sweden  
ulander@lin.foa.se

### ABSTRACT

We describe radiometric calibration of ultra-wideband SAR data acquired by the airborne CARABAS-II system. A general system model is derived which is used to compensate the image radiometry so that radar-cross section for each image pixel can be determined. It is shown that corrections for radio-frequency interference (RFI) and ramp filters, as well as antenna response are essential and can be estimated from the response of a large trihedral. Evaluation of the calibration accuracy shows quite good performance, i.e. better than 0.5 dB for incidence angles 30°–60° and 1 dB for incidence angles 20°–70°

### INTRODUCTION

In recent years a new class of synthetic-aperture radar (SAR) systems using ultra-wide bandwidth have emerged. In particular, this has resulted in high-resolution low-frequency SAR systems, e.g. the CARABAS-II system with meter-resolution while operating in the low VHF-band. Behind these developments lie technological advances in digital receiver technology, antenna design as well as signal processing algorithms. As such systems become more commonly available to a broader research community calibration obviously becomes important. The concept of radar calibration, however, has different meanings depending on the application in question. In this paper, we think of a quite general application in which calibration is needed to transform a SAR image to a quantitative measurement of the scattering amplitude (or equivalent parameter) in three-dimensional space and time. In the paper, we give a theoretical framework for calibration of ultra-wideband SAR images and describe a first attempt to calibrate CARABAS-II data.

### CARABAS-II ULTRA-WIDEBAND VHF-SAR

CARABAS-II [1] is an airborne SAR which is designed to operate over an altitude range 3 to 10 km. It transmits a stepped-frequency chirp waveform covering 20-90 MHz. The instantaneous bandwidth is only 2 MHz which facilitates an ultra-linear receiver design with a

spurious-free dynamic range of 88 dB. This is important to accommodate very strong signals due to the nadir echo as well as radio-frequency interference (RFI). The latter frequently occurs in the band due to short-wave communication, low-VHF TV, FM-radio, and numerous mobile communication channels.

The antenna system consists of two push-booms, each containing a biconical wideband antenna of 5-m length. These provide an essentially omni-directional gain pattern and a wide azimuth beamwidth close to 90°. During transmission, a single beam is steered to either side of the aircraft by time-delaying, whereas the received signal from each antenna is digitized in separate receiver channels. Data are stored on tape and image formation is performed off line. The signal processing requires accurate information of the flight track which is measured using phase-differential GPS. The latter results in a positional accuracy of about 0.5 m with an update rate of 1 Hz.

### CALIBRATION PHILOSOPHY

The main objective of SAR calibration is to enable retrieval of radar cross section for each pixel in a SAR image. This implies compensating, as far as possible, for known radar system, processing and image geometry characteristics. Calibration also requires that the measurement uncertainty is assessed.

It is often useful to treat SAR systems as quasi-invariant linear (discrete-time) systems, i.e. the complex image is linearly related to the input ground reflectivity function. This assumes that the overall system is stable and has been designed to minimise non-linear responses which inevitably are present in all electronic systems. The (complex) SAR image is thus modelled as a two-dimensional convolution of the ground reflectivity with a slowly varying impulse response function. Note that the ground reflectivity in this context is the full three-dimensional reflectivity of the ground projected into the two-dimensional representation using the SAR slant range coordinates  $(\rho_0, x_0)$  in Fig. 1.

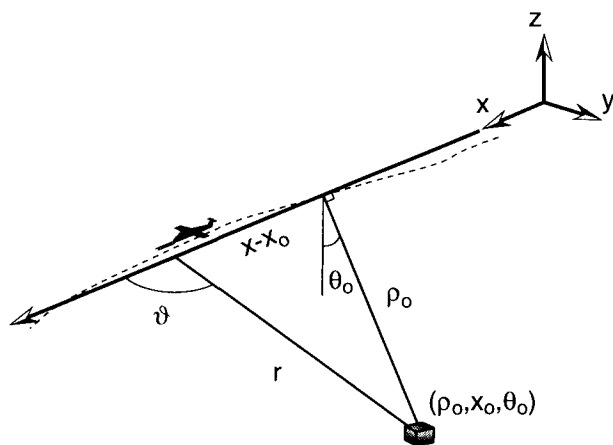


Figure 1. SAR imaging geometry. The antenna phase center ideally moves along the positive  $x$ -axis and the object is imaged in "slant range" co-ordinates  $(\rho_0, x_0)$ . The slant range is  $r$  and the Doppler cone angle is  $\vartheta$ .

There are basically two approaches to SAR calibration, one based on external reference objects and one based on internal reference signals. In practise, all systems need to use a combination of both. The goal is to minimise the need for external reference objects, and a perfectly stable system would only need them once and then all subsequent calibration is based on internal calibration. In practise, however, it is desirable to routinely deploy reference objects for verification purposes. This is particularly important for experimental SAR systems which typically have a large number of system mode settings and are often upgraded.

The choice of external and internal references are essential for the success of the calibration methodology. The external calibration reference should have a large and known RCS to give adequate signal-to-clutter ratio without exceeding the dynamic range of the system. This should be true for all transmit frequencies and Doppler cone angles used by the system. The internal calibration reference should ideally be a signal with the same properties as the transmitted and received signal, only excluding the free-space propagation path and the ground scattering process. In practise, it is not possible to include the antenna system within the calibration loop and thus it is important that the antenna characteristics are stable. Also, in a mono-static radar system it is difficult to include both the transmit and receive paths in the transmit-receive switch unless a long delay line is included to allow for the switching time. An alternative is to assume that the switch is stable and include it in the external calibration.

Based on these considerations, a methodology for calibration of CARABAS-II has been defined which utilises large triangular trihedrals for external calibration as well as an internal calibration measurement. The trihedrals have a short side length of 5.1 m which gives a sufficient (typically  $> 30$  dB) SNR except for the low end of the frequency band ( $< 30$  MHz). The choice of a passive reference object results in a rather large physical structure but with the benefit of being robust and reliable. The internal reference signal is based on the same radar waveform as during normal operation except that the output signal from the switch is attenuated and redirected into the receiver front-end rather than to the antenna feed. This means that all sub-systems except the antenna, transmission line, and the receive path in the switch are included in the internal calibration loop.

## IMAGE FORMATION

We now discuss the process during which a CARABAS-II image is formed. The basic imaging geometry is depicted in Fig. 1 and the different processing stages are summarised in Fig. 2.

A block of radar data is read from tape and decoded to a burst of pulse echoes. Interpolation in "slow time" ( $x$ -axis in Fig. 1) is used to match the pulse echoes to a common time base for all frequency sub-bands. Each sub-band pulse echo is then pulse compressed by matched filtering using a reference function measured during system calibration. In practise, this step is implemented as a multiplication in the frequency domain after a range FFT. The full bandwidth spectrum corresponding to a particular slow time is reconstructed by frequency shifting the individual pulse spectra in accordance with their centre frequencies and summed together. Amplitude calibration to reduce paired-echo sidelobes ends the range compression stage [2].

The range-compressed data includes a significant amount of RFI which needs to be suppressed before azimuth compression. Different methods may be used based on linear filtering and/or interference cancellation. Presently we use a linear filter defined as the inverse of the averaged range spectrum. This is a simple and robust method but has the drawback of distorting the target frequency response which results in increased sidelobe levels and multiplicative noise.

An inverse FFT brings data back to "fast time" domain and azimuth compression is performed using backprojection inversion [3]. The main advantage of the latter is that a well-focused image can be achieved irrespective of the flight track geometry as long as accurate antenna positioning data and a digital elevation model of the ground is available. The main disadvantage is the heavy computational cost, but fast



backprojection algorithms can also be devised which approach FFT-performance.

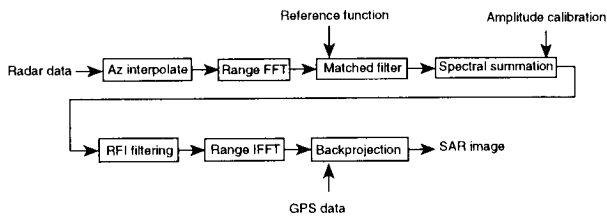


Figure 2. SAR processing chain for CARABAS-II

### ULTRA-WIDEBAND SAR SYSTEM MODEL

In this section we formulate a general system model which is based on the backprojection algorithm. We consider range-compressed data  $g(r, x)$ , acquired along a linear track and from an ideal point target, defined by

$$g(r, x) = \frac{\int A(\vartheta, \theta_o, k_r) P(k_r) \exp[jk_r (r - \sqrt{\rho_o^2 + (x - x_o)^2})] dk_r}{2\pi [\rho_o^2 + (x - x_o)^2]} \quad (1)$$

where  $x$  is the along-track position of the antenna,  $r$  is the slant range from the antenna to the point target,  $k_r$  is the range wavenumber,  $P(k_r)$  is the frequency response corresponding to a radar pulse burst,  $A(\vartheta, \theta_o, k_r)$  is the antenna frequency response, and the point target is located at  $(\rho_o, x_o, \theta_o)$  as in Fig. 1.

The backprojected signal  $h(\rho, x)$  is defined as an integral transformation which in a single pixel position adds all possible contributions in the radar data  $g(r, x)$  originating from this pixel. In the case of a linear flight track this corresponds to a transformation according to

$$h(\rho, x) = \int_{-\infty}^{+\infty} g(\sqrt{\rho^2 + (x' - x)^2}, x') dx' \quad (2)$$

Evaluation of the 2D Fourier transform of  $h(\rho, x)$  gives

$$H(k_\rho, k_x) = 2\pi \int_{-\infty}^{+\infty} \int_{-\infty}^{+\infty} g(r, x) r J_o(r \sqrt{k_\rho^2 + k_x^2}) \exp(-jk_x x) dr dx \quad (3)$$

By inserting (1) in (3), it can be shown that the original reflectivity function can be exactly reconstructed when the pulse and antenna response has constant amplitude for all frequencies and the track is infinite. Approximate evaluation of (3) can also be used when the bandwidth and antenna pattern are finite by using the principle of stationary phase and asymptotic expansions [3]. The

latter results in the following expression for the 2D Fourier transform

$$H(k_\rho, k_x) \approx \frac{2\pi P(\sqrt{k_\rho^2 + k_x^2}) A(\vartheta_s, \theta_o, \sqrt{k_\rho^2 + k_x^2})}{\rho_o \sqrt{k_\rho^2 + k_x^2}} \exp[-j(k_\rho \rho_o + k_x x_o)] \quad (4)$$

where the Doppler cone angle is defined by

$$\tan(\vartheta_s) = \frac{k_x}{k_\rho} \quad (5)$$

We can implicitly include the effect of the RFI filter as part of the pulse spectrum  $P(k_r)$  since it is a function of  $k_r$  only. By 2D inverse Fourier transformation of (4) we obtain a localised response at  $(\rho_o, x_o)$ . The response is not ideal, however, and have been distorted by frequency weighting due to the pulse and antenna responses and spatial weighting as a function of  $\rho_o$ . The system model of the SAR image  $s(\rho, x)$  thus consists of the ground reflectivity function  $f(\rho, x)$  convolved with the impulse response  $h(\rho, x)$  according to

$$s(\rho, x) = f(\rho, x) * h(\rho, x) \quad (6)$$

### CALIBRATION METHODOLOGY

In this section we present results based on calibration corrections using (4). The first effect to compensate is the range-spreading loss, i.e. the  $1/\rho_o$  factor in (4), which simply is an amplitude ramp in the image domain. The second effect to compensate is in two-dimensional frequency domain corresponding to the three other factors in (4). We note that the transfer function in general is space variant since it varies with incidence angle unless the antenna response is perfectly omni-directional. Equally important, however, is that the frequency domain support varies over the image after backprojection due to end effects along the synthetic aperture. To simplify calibration we therefore apply the calibration corrections to the common frequency support area and disregard the rest. We also note that the dominating amplitude distortion is a function of range wavenumber only, i.e. caused by the RFI filter and the  $k_r$  factor ("ramp filter") in the denominator. In this paper we do not attempt to compensate for the Doppler cone angle dependency of the antenna pattern. In fact, it may be difficult to compensate the Doppler dependency since it will increase image noise but this is a topic for future work.

To summarise, we use three steps in the present calibration method based on range and range-frequency corrections ("RFcorr"):

1. Range correction in image domain, i.e. multiplication with the reciprocal of the range-spreading factor in (4).
2. Range-frequency correction in frequency domain, i.e. multiplication with a correction factor determined from analysis of a reference object within or outside the image. Only the common part of the frequency-domain support over the image is extracted and corrected. At present we assume that this correction is spatially invariant and apply a single amplitude correction function which depends on range-frequency only. Although the antenna response in (4) is a function of incidence angle also, it is expected to vary slowly due to the wide beamwidth.
3. The final step is to compute and apply a constant amplitude factor to the data so that the measured image energy equals the average RCS in  $m^2$  (or equivalent parameter). The constant is determined from analysis of the reference object using the integral method to compute the point target energy with background clutter and noise subtracted. The data is scaled so that the magnitude of the complex pixel values equal the RCS on a pixel-by-pixel basis.

#### COMPUTATION OF CALIBRATION FUNCTIONS

Based on the outlined calibration methodology in the previous section, the calibration process can be expressed according to the following equation

$$S_{RFcorr}(k_\rho, k_x) = F^{2D}\{s(\rho, x)\rho\} H_{CAL}(\sqrt{k_\rho^2 + k_x^2}) \quad (7)$$

where  $F^{2D}\{\cdot\}$  denotes the Fourier transform,  $s(\rho, x)$  is the uncalibrated SAR image generated using the backprojection algorithm in (6),  $s_{RFcorr}(\rho, x)$  is the calibrated image,  $h_{CAL}(\rho, x)$  is the calibration filter kernel, and capital letters denote the corresponding Fourier transform.

The calibration kernel is conveniently divided into two factors: one due to the reference object measurement and the other due to the RFI filter. The latter is data-dependent and may therefore vary from one image formation process to the next. This becomes important when the reference object is not located in the image to be calibrated. The calibration kernel is computed according to

$$H_{CAL}(\sqrt{k_\rho^2 + k_x^2}) = \left\langle \frac{S_{RCS}(k_\rho, k_x)}{F^{2D}\{s_{ref}(\rho, x)\rho\}} \frac{H_{RFI,ref}(\sqrt{k_\rho^2 + k_x^2})}{H_{RFI}(\sqrt{k_\rho^2 + k_x^2})} \right\rangle_\theta \quad (8)$$

where  $s_{RCS}(\rho, x)$  and  $s_{ref}(\rho, x)$  are the theoretical scattering amplitude and measured response of the reference object, respectively,  $h_{RFI}(\rho, x)$  and  $h_{RFI,ref}(\rho, x)$  are the RFI filters for the image to be calibrated and the image with the reference object, respectively. The angular brackets indicate a weighted average over Doppler cone angle and a polynomial fit (second order) over range frequency in order to reduce noise effects. Doppler angles close to the antenna broadside direction ( $\vartheta = 70^\circ - 110^\circ$ ) are favoured relative to other angles.

It is not possible to completely remove the effect of the RFI filter during the calibration since this would drastically increase the noise level. It is therefore essential to leave a RFI filter consisting of narrow-band notches in the data for noise suppression but to compensate for the wide-band distortions in the calibration process. We thus define the RFI filter correction according to

$$H_{RFI}(\sqrt{k_\rho^2 + k_x^2}) = \frac{H_{RFI,org}(\sqrt{k_\rho^2 + k_x^2})}{H_{RFI,notch}(\sqrt{k_\rho^2 + k_x^2})} \quad (9)$$

where the subscripts "org" and "notch" denote the original RFI filter and the RFI filter with remaining notches for noise suppression, respectively.

#### RCS OF TRIHEDRAL RCS USING FDTD

The RCS of the trihedral, as required by (8), is computed using the Finite-Difference Time-Domain (FDTD) method [4]. In this method, the Maxwell's equations are discretised in both time and space. The incident plane wave is created within the computational volume by using the equivalence principle, i.e. the fields within a closed volume can be represented by equivalent magnetic and electric surface currents on the volume surface ("Huygens" surface). The technique implies that the total field exists inside a closed volume, whereas only the scattered field exists outside this volume. The computational volume is truncated using a 6-layer PML-boundary condition [5].

For an object in free space, the equivalent currents on the Huygens' surface that create the incident field can be expressed in a relative simple form. The presence of a lossy dielectric halfspace, i.e. the ground, means that the field impinging on the object is composed of both an incident field and a reflected field, which has a complicated time dependence. The incident, reflected and refracted fields are therefore calculated in the frequency domain and then transformed into the time domain using an FFT.

The equivalence principle is also used when transforming the scattered field in the near-zone into the

far-zone. For scattering simulations in free space this is performed by integrating either the surface currents transformed into the frequency domain, multiplied with a free-space Green's function, or the time-domain surface currents convolved with a time-domain form of the free-space Green's function [6]. When a ground is present matters becomes more complicated. The near- to far-zone transformation is performed in the frequency domain and is based on the reciprocity theorem and it has been applied in scattering simulations of triangular trihedrals placed on ground [7,8].

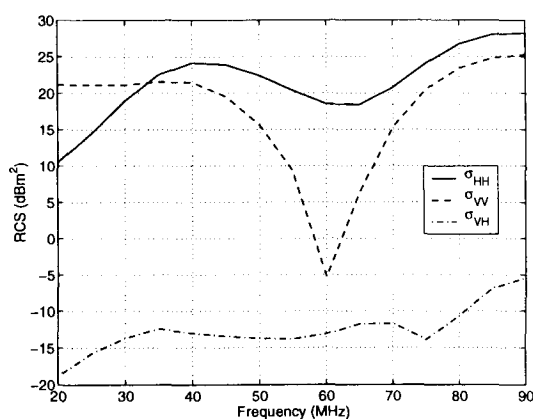


Figure 3. Simulated RCS of a triangular trihedral at Doppler cone angle  $90^\circ$ ,  $\epsilon_r = 10$ ,  $\sigma = 0.01$  S/m.

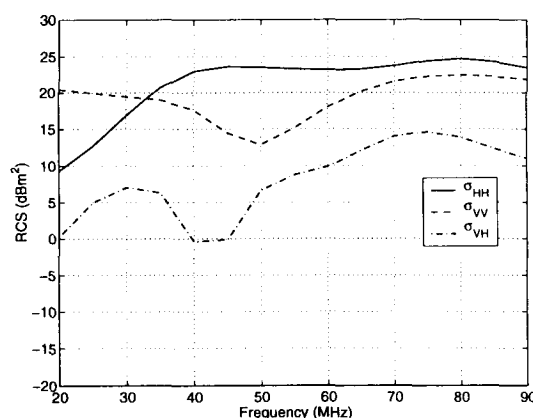


Figure 4. Simulated RCS of a triangular trihedral at Doppler angle  $70^\circ$  or  $110^\circ$ ,  $\epsilon_r = 10$ ,  $\sigma = 0.01$  S/m.

For calibration purposes several flight tracks have been simulated at incidence angles between  $20^\circ$  and  $70^\circ$ . The far-zone scattering amplitude for both vertical and horizontal polarisation was extracted between 20 MHz and 90 MHz, using a frequency step of 5 MHz. The simulated SAR images of the trihedrals on horizontal ground were formed from 11 monostatic scattering

simulations along the flight track for a  $90^\circ$  aperture angle. As an example, the RCS of two such cases are shown in Figs. 3 and 4. The incident angle is  $50^\circ$  in both cases and the results for both polarizations are shown at Doppler cone angles  $90^\circ$  and  $70^\circ$ , respectively. The ground parameters were  $\epsilon_r = 10$  and  $\sigma = 0.01$  S/m. The trihedrals was resolved in the FDTD-grid using a cell-size of 0.1 m.

## CALIBRATION RESULTS

We have applied the calibration methodology to a wide range of imagery produced by CARABAS-II. Normally, only a single or a few trihedrals are deployed to minimise field work. The calibration is then applied across a wider range of incidence angle (typ.  $40^\circ - 70^\circ$ ) without correcting for the incidence-angle dependency of the antenna response. In this section we assess the accuracy which this method gives.

A special calibration experiment was conducted in November 1997 to evaluate the calibration accuracy. Seven 5-m trihedrals were deployed across the swath on the island Visingsö close to Linköping. The incidence angles covered were  $20^\circ - 70^\circ$  in steps of  $10^\circ$ . The seventh trihedral had a slightly different design, i.e. with a 10 m x 10 m ground plane in front of the trihedral, but is not included in the present analysis.

Two images were generated which cover slightly different incidence angles. Both images were calibrated based on the same trihedral at  $50^\circ$  and then the calibration error was assessed by analysing the remaining trihedrals. Note that the two images have a slightly different RFI filter since they are generated from different radar data. The result is shown in Fig. 5. The dual data points at  $50^\circ$  and  $60^\circ$  correspond to the image overlap and thus represent the same trihedrals in the two images.

In general, Fig. 5 shows that the RCS using the present method can be determined with an accuracy of ca. 1 dB over the entire incidence angle range. If we restrict the incidence angle range to  $30^\circ - 60^\circ$  the accuracy improves to ca. 0.5 dB. These results are surprisingly good and show that the CARABAS antenna system is, in fact, quite omni-directional.

The main reason for the incidence-angle dependency is the array factor during transmission when the two elements form a small array using true time-delaying. The distance between the elements is 1.8 m, i.e. about  $2\lambda$  at 90 MHz and  $0.1\lambda$  at 20 MHz. We therefore expect a narrower beam width at the higher frequencies. Other mechanisms also affect the elevation beamwidth, such as mutual coupling between the elements as well as airframe interactions.

A second evaluation has been performed concerning the stability from pass to pass. An example result is shown in Fig. 6. In these cases, the same image has been calibrated based on trihedral measurements from two different imaging passes within about one hour from each other and with the same nominal radar parameters. The pass-to-pass stability is observed to be ca. 0.5 dB, i.e. the system has a good temporal stability.

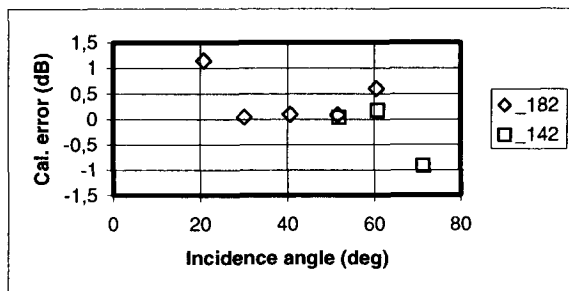


Figure 5. Residual error in dB after radiometric calibration based on a trihedral at incidence angle  $50^\circ$ . The two images (182, 142) are based on the same nominal radar data but are separately generated and have slightly different RFI filters. The frequency support is defined by frequencies 20 – 80 MHz and Doppler cone angles  $\vartheta = 55^\circ - 125^\circ$ .

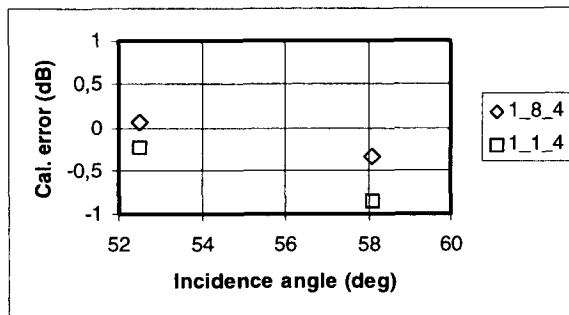


Figure 6. Residual error in dB after radiometric calibration of image 1\_8\_4 based on a trihedral at incidence angle  $52^\circ$ . The points marked 1\_8\_4 used the same image for retrieving the calibration function from the trihedral, whereas the points marked 1\_1\_4 used an image of the trihedral from a different flight track one hour earlier and with the same radar parameters. The frequency support is the same as in Fig. 5.

## CONCLUSIONS

The paper has described radiometric calibration of ultra-wideband SAR data from CARABAS-II. A closed-form system model has been derived which takes into account frequency domain distortions due to pulse burst

response, antenna response, as well as ramp and RFI filters. The system is characterised using the measured response from a 5-m large trihedral compared with a numerically computed RCS signature. Evaluation of the calibration accuracy shows a quite good performance, i.e. better than 0.5 dB for incidence angles  $30^\circ - 60^\circ$  and 1 dB for incidence angles  $20^\circ - 70^\circ$ . Note that these results are obtained without any correction for the incidence angle dependency of the antenna. Pass-to-pass stability is estimated to 0.5 dB. The same general methodology should be applicable also to other ultra-wideband SAR systems with wide beamwidths.

The present investigation is limited to the average radiometric response of the object. We plan to refine the calibration methodology to also facilitate relative calibration over the frequency support region. This will require taking into account the space-variant antenna response, and a trade-off with image noise. Future work will also address frequency-dependent phase calibration.

## REFERENCES

- [1] H. Hellsten, L.M.H. Ulander, A. Gustavsson, and B. Larsson, "Development of VHF CARABAS II SAR", Proc. Radar Sensor Technology, SPIE, vol. 2747, Orlando, FL, 8-9 April, pp. 48-60, 1996
- [2] L.M.H. Ulander, "Performance of Stepped-Frequency Waveform for Ultra-Wideband VHF SAR", Proc. EUSAR'98, Friedrichshafen, GE, 25-27 May, pp. 323-328, 1998
- [3] L.M.H. Ulander, "Approaching the Wavelength Resolution Limit in Ultra-Wideband VHF-SAR", Proc. PIERS workshop on Advances in Radar Methods, Baveno, IT, 20-22 July, pp. 83-85, 1998
- [4] K. S. Yee, "Numerical Solution of Initial Boundary Value Problems Involving Maxwell's Equations in Isotropic Media", IEEE Trans. Antennas and Propagat. vol. 14, no 3, pp. 302-307, 1966.
- [5] J.-P. Berenger, "A perfectly matched layer for the absorption of electromagnetic waves" J. Comp. Physics, vol. 114, pp. 185-200, 1994.
- [6] T. Martin, "An improved Near- to Far-Zone Transformation for the Finite-Difference Time-Domain Method", IEEE Trans. on Antennas and Propag., vol. 46, no. 9, pp 1263-1271, 1998.
- [7] K. Demarest, et. al. "An FDTD Near- to Far-Zone Transformation for Scatterers Buried in Stratified Grounds", IEEE Trans. Antennas and Propag., vol. 44, no. 8, pp. 1150-1157, 1996
- [8] T. Martin and L.M.H. Ulander, "Far-zone transformation in FDTD for VHF-band SAR-image simulations", Proc. of 14th annual review of progress in Applied Computational Electromagnetics, Monterey, CA, 16-20 March, pp. 79-86, 1998

## HSRRA: an advanced radar altimeter for Ocean and Cryosphere monitoring.

L. Phalippou

Alcatel Space Industries

26 avenue Champollion, 31037 Toulouse Cedex, France

Tel: 33 (0) 5 34 35 60 02 / Fax: 33 (0) 5 34 35 61 63 / Email: laurent.phalippou@space.alcatel.fr

D.J. Wingham

University College London

17-19 Gordon Street, London WC1H 0AH, U.K.

Tel: 44 (0) 171 419 3677 / Fax: 44 (0) 171 419 3418 / Email: djw@mssl.ucl.ac.uk

### ABSTRACT

The monitoring of the cryosphere, i.e. mainly ice sheet and sea ice, is of primary importance for climate studies [1]. The required height accuracy is of the order of a few centimetres. Although laser altimeters provide high vertical and horizontal resolutions, the significant advantage of a radar altimeter is its all weather capability, i.e. its relative insensitivity to clouds which are often encountered in polar regions and particularly close to the ice sheet margins.

Current spaceborne radar altimeters are pulse-limited and therefore fail to deliver high accuracy surface height measurements over ice-sheet margins because of pulse spreading and slope induced errors [2]. Moreover, sudden changes in the topography often result in a loss of track. Higher resolution is also desirable in order to distinguish the sea-ice from the ocean surface.

This paper presents the results of a recent feasibility study for a spaceborne high-spatial resolution radar altimeter (HSRRA) performed by Alcatel and the University College of London (UCL) for the European Space Agency (ESA). The concept is based on a Ku-band (13.6 GHz) nadir-looking radar which can be operated in the conventional mode over oceans. Over terrain (ice or land) the "advanced" mode uses Doppler filtering for the enhancement of the along-track resolution. A second antenna mounted on the same satellite provides a second take of the scene which is used for surface height retrieval as it is usually done with SAR interferometry.

An overview of the instrument concept including the processing is given in this paper. The instrument design is briefly described. Some simulation results of the performances over realistic surfaces are also presented and discussed.

This altimeter concept (Doppler filtering and interferometry) has been proposed in the Cryosat mission in response to the Call for ESA Opportunity Missions. This mission has been recently approved for implementation.

### MISSION OBJECTIVES

The science objectives and measurement requirements for high resolution altimetry have been described in the ESA report for the Earth Explorer Topography Mission [3]. The primary mission objectives are related to the cryosphere i.e. land ice (ice sheets of Antarctica and Greenland and glaciers) and sea-ice.

The quantity to be measured is the elevation changes as a function of time and position at different spatial scales. In the case of sea-ice, the lowest spatial scale at which trends may become visible is  $10^5 \text{ km}^2$ . In the case of the ice sheets, there are important scientific questions at regional and large scales i.e. between  $10^4$  and  $13.8 \cdot 10^6 \text{ km}^2$ . The latter area is the total area of the ice sheets.

Arctic Sea-Ice	Ice Sheets	Ice Sheets
$10^5 \text{ km}^2$	$10^4 \text{ km}^2$	$13.8 \cdot 10^6 \text{ km}^2$
1.6 cm/year	3.3 cm/year	0.17 cm/year

### Measurement requirements as a function of spatial scales for ice sheets and sea-ice.

Although the elevation changes to be measured are very small they are obtained by averaging single measurements over large areas such that the short spatial scale noise due to the instrument (e.g. speckle and thermal noise) is considerably reduced, approximately as the square root of the number of measurements.

For the **ice sheet and glaciers** the instrument resolution requirements are driven by the need to obtain adequate

signals in regions with high surface slopes and mission requirements are driven by the capability to monitor changes of the ice sheet margins and smaller ice caps and glacier.

The elevation errors arising over regions with high slopes in normal incidence altimetry are dominated by pulse spreading and loss of signal. Accurate change measurements with pulse limited altimeters become difficult when the surface gradient exceed the antenna beamwidth, e.g.  $0.5^\circ$  for ERS and ENVISAT altimeters. Some 17% of Antarctica and 23% of Greenland exceed this gradient. The need for high spatial resolution arises from mission requirement to provide 98% coverage of the ice sheets. A significant improvement is possible only by an order of magnitude decrease in the horizontal resolution, i.e. about 100-200 m.

In the case of sea-ice, the parameter of interest is the measurement of its thickness. The required instrument resolution is determined by the need to distinguish between ice and open water and the mission requirement are driven by the need to derive thickness and roughness probability density functions. For this application a horizontal resolution of the order of 200 m to 1 km seems adequate.

Although laser altimeters provides high vertical and horizontal resolutions, the significant advantage of a radar altimeter is its all weather capability, i.e. its relative insensitivity to clouds which are often encountered in the polar regions and particularly close to the ice-sheet margins.

## OVERVIEW OF THE CONCEPT

Several techniques have been investigated during the past ten years in order to improve the spatial resolution of radar altimeters and therefore the accuracy of elevation estimates over terrains. Most of these techniques result in a significant increase in cost and complexity compared to a conventional altimeter [4]. This paper presents the results of a recent feasibility study for a spaceborne high-spatial resolution radar altimeter (HSRRA) performed by Alcatel and the University College of London for the European Spatial Agency (ESA).

The concept is based on a Ku-band (13.6 GHz) nadir-looking radar with a 1.2 m antenna diameter which can be operated in the conventional mode over oceans (as TOPEX/Poseidon for instance) and in the high spatial resolution mode over topographic areas such as coastal zones, ice covered or land areas.

The novel feature of HSRRA as compared with conventional altimeters, is the capability to locate a target in the 3 dimensional space. For this, it uses a concept similar to the interferometric SAR technique as shown below :

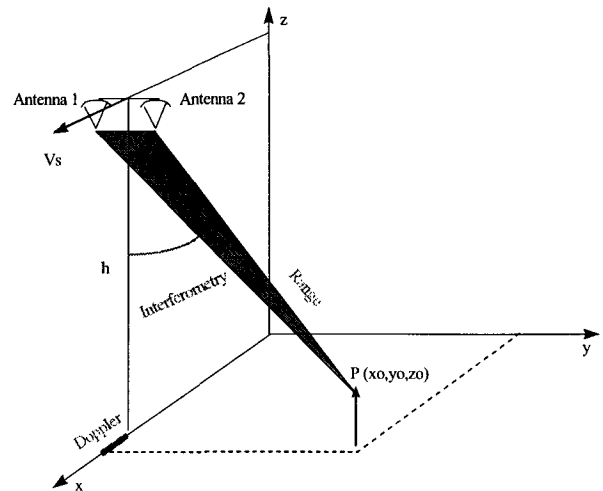


Fig 1 : Measurement principle of HSRRA

A nadir looking radar (off-nadir angle  $\theta=0$ ) has been selected for two reasons:

- i) it is compatible with conventional ocean altimetry
- ii) this configuration allows to minimise the vertical accuracy ( $\sigma_z$ ) of the retrieved surface height as shown by (1) where  $\sigma_h$  is the satellite altitude error,  $\sigma_R$  is the range error,  $R$  is the range, and  $\sigma_\theta$  is the error on the off-nadir angle.

$$\sigma_z^2 = \sigma_h^2 + \sigma_R^2 \cos^2\theta + R^2 \sigma_\theta^2 \sin^2\theta \quad (1)$$

Over terrain (ice or land) the "advanced" mode uses Doppler filtering for the enhancement of the along-track resolution [5]. The antenna half-power beamwidth (HPBW) is  $1^\circ$ . The satellite is at a 800 km altitude in a quasi-circular orbit. The Doppler spectrum is 12.4 KHz and the Pulse Repetition Frequency (PRF) is 13.6 KHz.

A second antenna mounted on the same platform provides a second take of the scene which is used for surface height retrieval (as for SAR interferometry) and quality control of ambiguities due to layover. The interferometric baseline is orthogonal to the satellite velocity and to the nadir direction.

The transmitted chirp bandwidth (320MHz) is equivalent to a vertical resolution of 0.42 m. A 1024 FFT provides a 480 m range window, which corresponds to an average surface slope of 1.9 degrees within the antenna footprint.

As the desired height accuracy is smaller than the vertical resolution some form of model fit to the waveform is necessary at the post-processing level, as it is done for conventional altimetry over ocean.

PROCESSING SCHEME

The processing flow chart is shown in Fig. 2. The radar echoes are first deramped, digitized and stored in a memory. At this stage the range compression is not completed, and range (or delay) has simply be transformed into frequency. For the geometry described above, it has been shown [6] that along track-resolution above 80 meters can be achieved using the Doppler Beam Sharpening (DBS) method. Therefore focusing techniques are not needed as the required along-track resolution for the altimeter is 100m to 250 m. The azimuth impulse response characteristics (PSLR, ISLR) are close to those of an ideal sinc function. Prior to the azimuth FFT a linear phase ramp is used to colocate the looks. The azimuth FFT is then performed on a set of  $N_p$  pulses referred to as a burst. Bursts of 64 and 128 pulses lead respectively to along-track resolution of about 220 m and 110m.

The range curvature during the integration time depends on the relative satellite-target along-track position and on the azimuth resolution. The range curvature is null for a target located at nadir and maximum at the edge of the antenna beam. The maximum range curvature within a burst is about 0.35 m for a 220 m azimuth resolution, i.e. less than the range resolution. In that case range cell migration can be left non-corrected without too big a loss on the performances of the impulse response. However, burst to burst range-migration must be corrected in order to perform multilooking, and we followed the method described in [5]. Note that range walk due to satellite height variation can also be corrected at this stage.

The range compression is completed by taking the inverse Fourier transform (IFFT). The same processing is applied to the echoes received by the second antenna wich provides the second take for the interferogram computation. The multilooked data are then passed to the tracker which command the deramp trigger. The power waveform and the interferogram obtained for successive bursts are multilooked for reducing the speckle.

The resolution cells mapped on a flat earth surface are shown in Fig.2 for a 220 m along-track resolution (64 pulses). Each ring represents iso-range cell and each band represents a Doppler bin (i.e. along track position).

Two timing options have been investigated. The closed burst option is suitable for azimuth resolution above 200 m, and corresponds to the transmission of the complete burst before the return of the first echo. Below 200 m, the open burst option should be used, i.e. an echo is received between two transmitted pulses. Here, the closed burst option is selected as it enables to get longer pulse length and constant PRF.

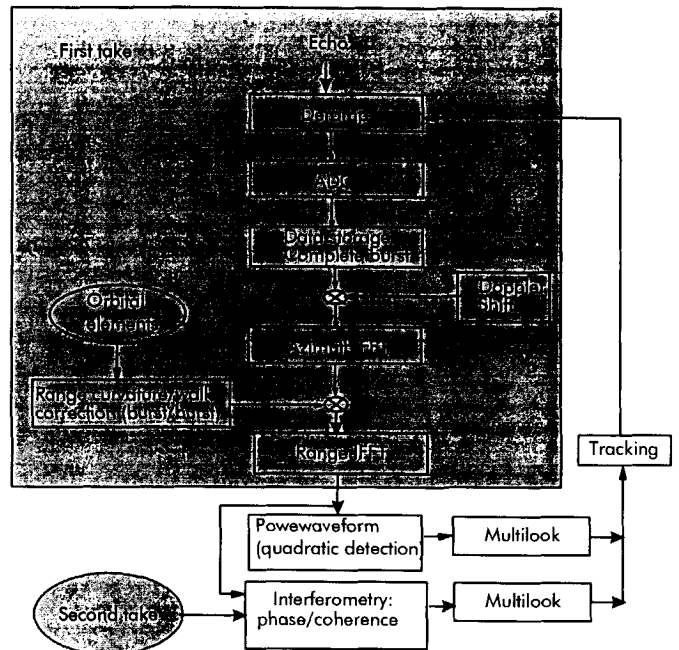


Fig.2: Processing flowchart

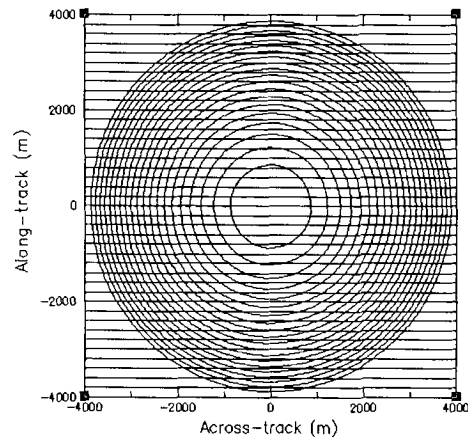


Fig. 3: Resolution cells on a flat surface

POWER WAVEFORM SIMULATION

The mean waveforms (echo power vs range gate) have been simulated for a flat surface with varying along/across-track slopes. An example is given in Fig.4. The waveforms have a peaky shape. The amplitude and the width of the peak depend

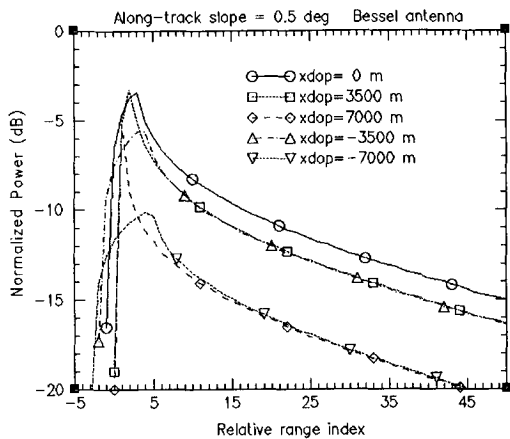


Fig. 4: Power waveform for a 0.5 degree along-track slope. Each curve corresponds to varying Doppler bin identified by their along-track position (xdop) w.r.t. to nadir.

on the Doppler bin and on the surface slope. For slope less than 0.5 degree, the most peaky waveforms correspond to the Doppler bins which span the pulse limited footprint (first-hit of the wavefront on the surface). The results suggest that these most peaky waveforms should be used in the estimation of the elevation. However, when using a limited number of looks, the waveforms would differ from the mean due to speckle and thermal noise. The mean waveform itself depends on the variation of the surface characteristics (roughness and backscattering) in a complicated manner. The number of looks to be used for elevation retrieval is therefore a key issue which is being investigated using a complete simulator including real topography and speckle.

Regarding the transmitted power, for the closed burst option (70µs pulse length) and a 320 MHz bandwidth, 25 W are necessary in order to achieve a 17 dB signal to noise ratio for a -10 dB sigma naught for the first range cell. This SNR corresponds to a thermal noise decorrelation equal to the interferometric baseline decorrelation.

**SURFACE HEIGHT ESTIMATION**

As shown in Fig.3, the nadir looking geometry leads to left-right ambiguities for a flat surface with across-track slopes less than half the antenna HPBW, except for the first return cell. In that case, the altimeter is a profiler, providing non-ambiguous measurement for the leading edge of the waveform only. The ambiguity between elevation and across-track location can be solved by using the across-track interferometry technique. The interferometer baseline must be of the order of the antenna diameter, say 1.2 m in order to avoid phase unwrapping. Such a small baseline would impose stringent constraint on the satellite control if a multi-pass

option were selected. An other drawback of multi-pass interferometry for the altimetry mission would be the temporal decorrelation due to surface changes. For these reasons the single-pass interferometry option is preferred, with two nadir-pointed antennae mounted on the same spacecraft, such that the nominal baseline tilt is orthogonal to the nadir direction.

It can be shown from geometrical considerations, that if the surface slope is constant within the pulse limited footprint, the error in the retrieved surface height for the point of first return depends only on the second order of the phase measurement noise (thermal noise and speckle). This elevation error is shown in Fig.5 for the point of first hit on the surface, as a function of the surface slope. In that case, the fact that the elevation error degrades with off-nadir angle of first hit (i.e. equivalent to the slope over a flat surface) is simply due to the antenna gain weighting.

Note that for across-track slope less than 1 degree, the height errors due to interferometric noise is less than 10 cm for the first return cell and a 0 dB sigma naught, using a 25 W transmitted power and 64 looks.

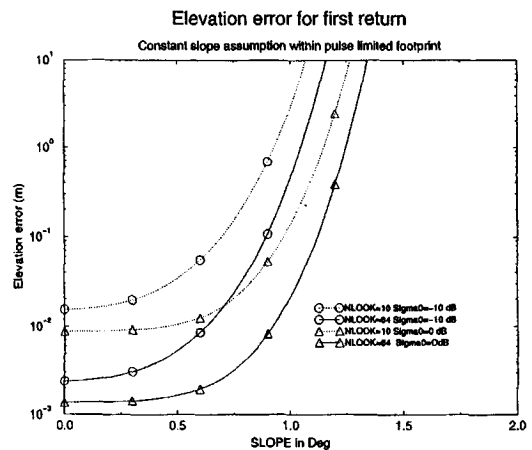


Fig. 5 : Elevation error due to interferometric noise for first return as a function of the surface slope.

Analytical computation [6] also shown that the module of the coherence decays rapidly as a function of range when the across-track surface slope is less than half the HPBW of the antenna. These results suggest that the correlation waveforms could be used alongside the power waveform in order to detect the non-ambiguous cells, and in particular the first return cell.

For large across-track slopes with respect to the antenna beam (say above 0.5 deg), the geometry resembles the side-looking radar geometry, and left/right ambiguities decrease. The SNR is also smaller than for the zero slope case, due to much smaller resolution cells (about a 15 dB loss for a 0.5 degree



across-track slope). This results in a degradation of the interferometric phase accuracy and thus the elevation error increases. However, because of the removal of the ambiguity a swath capability is offered for across-track slope above 0.5 degree. Fig. 6 shows the height error due to interferometric noise (speckle + thermal) as a function of the position of the cell in the across-track direction (off-nadir angle) for a 1 deg. across-track slope, 0 dB sigma naught and a 25 W transmitted power. In that case, a 10 cm vertical repeatability can be achieved over a 7 km swath (+/- 0.25 deg) using 64 looks. Again note that much smaller vertical repeatability can yet be achieved close to the centre of the swath due to the maximum antenna gain and Eq 1.

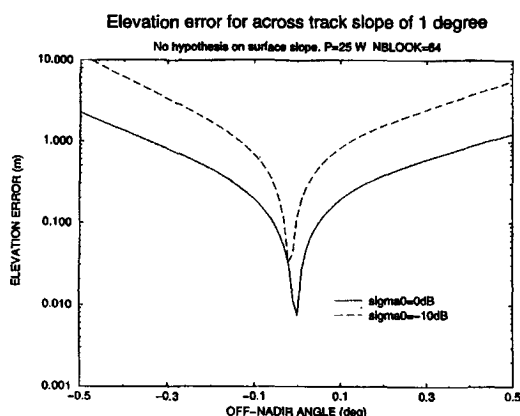


Fig. 6: Height error due to interferometric noise for resolution cells within the antenna beamwidth. The point of first return is in this example is at a 1° off-nadir angle (not shown).

**INSTRUMENT DESIGN**

The altimeter is composed of three subsystems (Fig.7):

- The antenna subsystem
- The RF Unit
- The Processing and Control Unit (PCU)

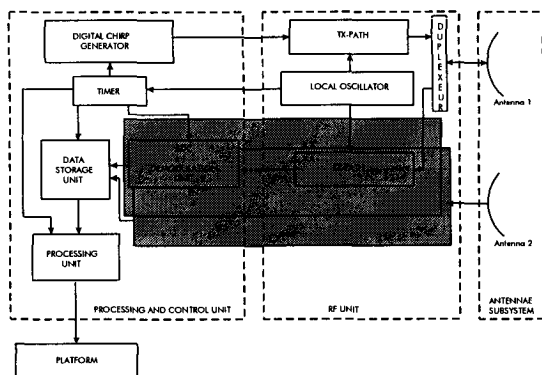


Fig. 7: HSRRA functional block diagram

The antenna subsystem includes two nadir-pointed centred reflectors. Mechanical and thermal decoupling from the platform is ensured by a carbon frame mounted on titanium blades. This is important to guarantee the stability of the baseline length and orientation to the required level.

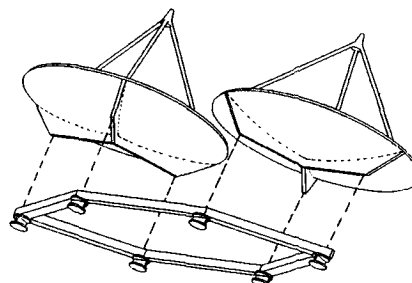


Fig. 8: Antenna interferometric subsystem

The RF power of the HPA is 25W in Ku-band. The output stage of the HPA consists of 4 modules connected in parallel. Each module is composed of two MMIC power chips in PHEMT technology.

To ensure a correct sampling of the Doppler bandwidth the radar operates in burst mode, with a coherent chirp generator, based on the digital generation of a 40 MHz chirp followed by a frequency multiplication.

In order to reduce the downlink data rate, data processing is performed on board by 6 DSPs, providing enough flexibility for eventual modifications of the processing design during the development phase.

A summary of the instrument characteristics is given below.

Altitude	800 km
Frequency	13.575 GHz
Antenna diameter	1.2 m
Interferometer baseline	1.2 m
Chirp bandwidth	320 MHz
FFT length (deramp)	1024
Pulse repetition frequency	13.6 KHz
Pulse length	70 μs
Number of pulses/burst	64
Burst repetition interval	38 10 <sup>-3</sup> s
Transmitted power	25 W
Along-track resolution	220 m
Vertical resolution	0.42 m
Range window	480 m
Number of looks	64
Absolute σ <sub>0</sub> range	-10 to 50 dB
Mass	60 kg
Power consumption*	150 W
Data volume*	2.5 Gbits/orbit
Compatible with intermediate class launcher (ROCKOT, DELTA, PSLV)	

**HSRRA system parameters, performances and interfaces**  
 (\* 32 % of the time in high resolution mode and 68% in ocean mode)

The compatibility of the satellite with a small class launcher was one of the design constraint. Figure 9 shows the proposed implementation of the satellite which is compatible with the Rockot fairing.

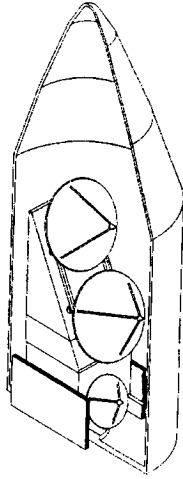


Fig. 9 : HSRRA satellite under Rockot fairing

#### CONCLUSIONS

The computations and performance results for a flat tilted surface presented in this paper have been compared with simulations made by UCL for more complex ice-sheet surfaces [6]. The results shown that they are in agreement with those presented in this paper for simple flat surfaces.

This altimeter concept (Doppler filtering and interferometry) has been proposed in the Cryosat mission (led by Pr. D. Wingham) in response to the Call for ESA Opportunity Missions. This mission has been recently approved for implementation.

#### ACKNOWLEDGEMENT

This work has been performed under ESA/ESTEC contract 12178/96/NL/SB(SC).

#### REFERENCES

- [1] D.J. Wingham: Elevation changes of the Greenland ice-sheet and its measurement with satellite radar altimetry. Phil. Trans. R. Soc. Lond., A, Vol 352, pp335-346, 1995.
- [2] A.C.Brenner, R.A. Bindschadler, R.H. Thomas, H.J. Zwally: Slope-induced errors in radar altimetry over continental ice-sheets. JGR, Vol.88, C3, pp1617-1623, 1983.
- [3] Topography Mission. ESA SP1196(9). April 1996.
- [4] C.G. Rapley, H.D. Griffiths, P.A. Berry: Proceedings of the consultative meeting on imaging altimeter requirements and techniques. ESA ref MSSL/RSG/90.01.
- [5] R.K. Raney: Delay/Doppler compensation: a new concept for radar altimetry. EUROPTO 95, SPIE Vol. 2583, pp412-419.
- [6] L.Philippou: Feasibility study of HSRRA. Final Report. Contract 12178/96/NL/SB(SC).

**Spotlight SAR on Spaceborne Platform**

Tapan Misra, A.M. Jha, D.B. Dave  
Space Application Centre  
ISRO, India

This paper was not available for publication



## HIGH RESOLUTION SAR CONSTELLATION FOR RISK MANAGEMENT

A.HERIQUE, L. PHALIPPOU, S.RAMONGASSIE

Alcatel Space Industries

26 Av. Champollion, BP 1187, 31037 Toulouse Cedex, France

Tel/Fax : (+33) 534 35 36 37/61 63. Email : l.phalippou @space.alcatel.fr

C.C LIN

ESTEC

KEPLERLAAN 1 - Postbus 299 NL 2200 AG NOORDWIJK, The Netherlands

Tel/Fax : (+31)71 565 5813/4696 Email : clin@estec.esa.nl

### ABSTRACT

The management of natural and anthropogenic risks including prevention, crisis and post crisis phases, is characterised by the need for a flexible space system with high resolution instruments, all weather operation, low revisit time and fast information delivery. Spaceborn SAR therefore forms an essential component of the observation system for risk management.

This paper describes the results of the ESA pre-phase A study of a SAR instrument (CZEW : Coastal Zone Earth Watch Mission). The objectives are to design an SAR instrument and satellite constellation for risk management with a cost reduction approach. This study includes mission analysis, instrument definition and space segment preliminary design.

The proposed solution consists of a constellation of 6 SAR associated with a wide range of accessibility, to provide access to any point of the Earth in less than 1 day.

The X band SAR provides high sensitivity and an operating duty cycle of 5-10 minutes per orbit. The main operating mode corresponds to a strip map acquisition in a 20°-53.7° incidence range. This domain is extended at low and high incidences based on platform agility.

In the first part, two instrument concepts are studied based on a parabolic reflector antenna and on an active planar array antenna. The antenna concept has an impact on the whole instrument design, including amplification (High power TWT, T/R modules), on platform accommodation and on the instrument performances.

In the second part, the active array antenna concept is further analysed at sub-system level : antenna architecture, T/R modules design, digital processing and on-board Scansar processing.

Keyword: high resolution SAR, risk management, constellation, active planar array antenna

### RISK MANAGEMENT MISSION

The Risk Management mission will cover a wide range of applications such as resource monitoring (crops, mapping of deforestation, ship routing, geology), assistance for the assessment of the damage to environment, to population and to industries due to pollution and natural hazards (volcanic eruptions, earthquakes, hurricanes, flooding).

The system must be considered as a source of new information which is complementary of other Earth observing system whether space or ground based (such as those providing meteorological data for instance) to be used in a global information system.

The potential users directly involved in the major disasters management are mainly public bodies which may be operational or scientific, national and/or international, namely : civil protections (national level), ministries (environment, defence, planning, fishery...), international organisation (UN, E.U....), non-governmental organisations (red cross...), scientific institutes and universities and specialised centres. There are also potential private users such as insurance, re-insurance companies, industry and services companies in the area of geographical information and communications.

As an example, Table 1 summarises the user needs for risk management which are covered by the different SAR applications.

### SYSTEM SPECIFICATIONS

The proposed Earth observation system designed for risk management must be compatible with the objectives of the Earth Watch Mission ESA program : this means an operational system developed with a cost-effective approach and with a reduced development plan and a limited technological risk.

Information products & model parameters	User major claims & wishes for information and service needs	Contribution of Earth Observation derived products	Main limits of current Earth Observation satellites
Risk maps (hazards & vulnerability maps)	<ul style="list-style-type: none"> <li>All exposed areas not covered</li> <li>Insufficient updating of maps</li> <li>Lack of precision and reliability of current data</li> <li>High cost of data acquisition</li> </ul>	<ul style="list-style-type: none"> <li>Description of the risk areas</li> <li>Evaluation of consequences of land changes in time</li> <li>Updating of topographic maps</li> </ul>	<ul style="list-style-type: none"> <li>Scale : limited the 1:50000</li> <li>but the thematic maps prepared have to be compatible with land and urban planning documents (1:10000 to 1:5000)</li> </ul>
Cartography of risk areas and monitoring	<ul style="list-style-type: none"> <li>Facilitate crisis observation</li> <li>Daily monitoring capability</li> <li>Develop automated monitoring system</li> <li>Near-real time access</li> </ul>	<ul style="list-style-type: none"> <li>Cartography of risk areas</li> <li>Possible monitoring of the evolution of disasters boundaries</li> <li>Update of maps</li> </ul>	<ul style="list-style-type: none"> <li>Revisit capability (days)</li> <li>Probability to access to the requested area</li> <li>Data access and delivery time (days)</li> </ul>
Assessing status of infrastructures and specific damage (at request)	<ul style="list-style-type: none"> <li>Develop observation during and after the crisis</li> </ul>	<ul style="list-style-type: none"> <li>Detailed cartography of damage</li> <li>Comparison with normal situation &amp; production of statistics</li> </ul>	<ul style="list-style-type: none"> <li>Scale too limited</li> <li>Revisit capability (days)</li> </ul>
Input parameters for models	<ul style="list-style-type: none"> <li>Develop the integration of various tools (models, GIS and EO data)</li> </ul>	<ul style="list-style-type: none"> <li>Prepare relevant parameters that make the models easier and cheaper to run and allow them to be used over an entire watershed</li> </ul>	<ul style="list-style-type: none"> <li>Scale not accurate enough (in particular for the DTM and derived products)</li> </ul>

**Table 1 : User needs for Risk Management**

Consequently, the system must be based on a small existing platform which can accommodate the small launcher fairing. In this way the maximum DC power at the instrument level will be around 4 kWatts.

The main requirements of the system concerns the nominal high resolution strip map mode (M1) and are as follows :

- capability for accessing any point of the Earth in 12 hours for crisis management,
- large working time capability (5-10 minutes per orbit and per satellite) in order to provide an operational system for long term monitoring, crisis management and post crisis management,
- wide range of accessibility,
- high resolution (2 m),
- a high sensitivity (-24.7 dB at 53° incidence)
- a 20 km swath width,
- a -20 dB total ambiguity ration
- no drastic constraints for the radiometric accuracy.

The SAR instrument is an X-Band SAR which is compatible with the high resolution requirement and the frequency allocation of ITU. This choice requires a limited antenna size and is consequently is coherent with the small existing platform and small launcher requirement and cost reduction.

To provide the required revisit the proposed system consists in a multi-SAR satellites constellation

associated with a large accessibility domain based on the antenna electronic agility or the mechanical platform agility.

The second main requirement is the sensitivity requirement ( $Ne\sigma_0$ ) which significantly increases with respect to incidence. This increase could be critical at the high incidences considering that the link budget is near constant as a function of the incidence for a constant swath width. It leads to trade-off between power consumption and  $Ne\sigma_0$  requirements.

The performances of the optional modes will be deduced from the instrument optimised for the nominal mode and their specification simply constitutes an objective. These secondary modes are specified hereafter and illustrated on figure 1.

- M2 : The extension of the accessibility domain at low incidence using platform mechanical agility and consequently a progressive degradation of the range resolution due to a constant RF bandwidth,
- M5 : The extension of the accessibility domain at high incidence using platform mechanical agility and consequently a progressive degradation of the total ambiguity ratio and link budget.

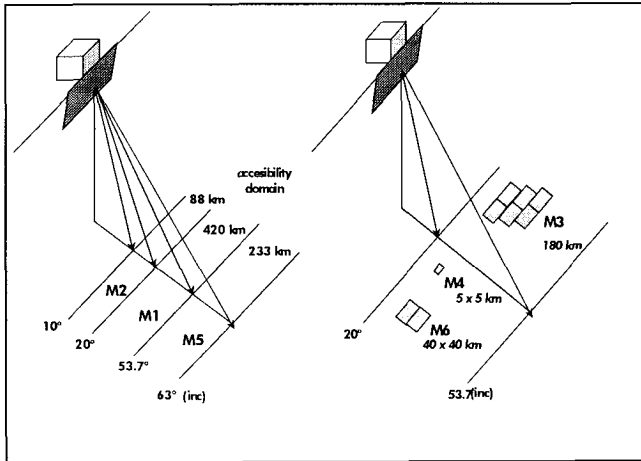


Figure 1 : CZEW modes

- M3 : The Scansar mode in the nominal accessibility domain providing a 25 m resolution for a 180 km total swath width and the same sensibility as the strip map mode
- M4 : The wave mode corresponds to the acquisition of small 5 x 5 km images in the nominal incidence range.
- M6 : The double swath mode corresponds to the acquisition of 40 x 40 km images using antenna electronic agility in both directions while keeping the range and azimuth resolutions equal to that of the strip mode.

MISSION AND CONSTELLATION DESIGN

The revisit performance of the constellations is characterised by the mean and maximum revisit times which correspond to the mean and the maximum intervals between two opportunities to image a given location on the Earth surface. These performances depend on the geographical location (latitude and longitude).

To provide a short revisit time the proposed system consists in a 6 SAR satellites constellation associated with a wide accessibility domain enabled by the antenna electronic agility and the mechanical platform agility. This constellation and this accessibility domain have been optimised in view of the following constraints:

- coverage of the Earth's entire surface except small areas near the poles;
- one or more sun-synchronous orbital planes to simplify the platform thermal design and power management. The sun-synchronous constraint induces a constant local flyby hour and then simplifies control and user ground segment activities.

The optimal constellation is therefore the 510 km altitude walker 6/1/0 constellation. This constellation corresponds to a regular distribution of the 6 satellites on a single orbital plane: Each satellite has a 6-days cycle corresponding to 91 orbits and the constellation has a one day cycle with a circular permutation of the 6 satellites. So the second satellite covers the same area in the same configuration than the first one with a 24 hours delay. The associated incidence range is 20° - 53.7° which corresponds to a complete coverage per cycle (1 day) without gap.

This permutation is a characteristic of the Walker 6/1/0 constellation with this incidence range and this altitude. Other constellation with two orbital planes present a significantly larger maximum revisit time but the mean revisit time is the same because it is independent on the relative position of the satellites.

The 1 day sub-cycle with permutation preserves the whole coverage property during deployment of the constellation and at the end of life when there is a smaller number of active satellites. A redistribution of the satellites on the orbit could therefore be considered to optimise the performances with a limited ergol consumption in case of non-replacement.

This next property of the constellation is to image a point on the Earth's surface with only two incidences: one for ascending orbit, one for descending orbit. This geometry is conducive to multi-image processing such as interferometry, radar-grametry or correlation analysis and offer suitable applications for risk management such as digital elevation model, terrain movement monitoring or damage estimation.

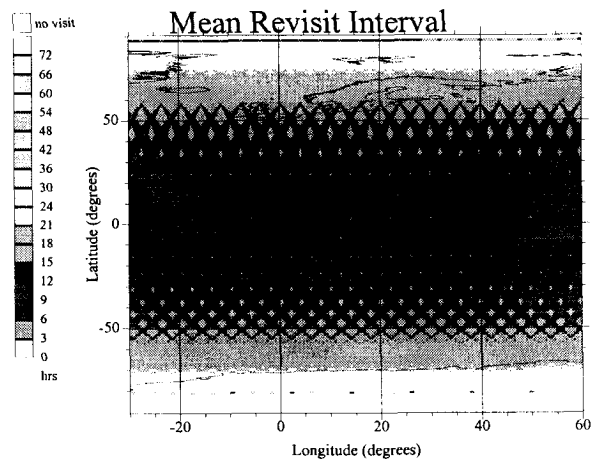


Figure 2 : Mean revisit time with a 20°-53.7° accessibility

The chosen incidence range thus corresponds to a 430 km instantaneous accessibility domain. This domain is completed by an extension at low incidence (10°-20°) and high incidence (53.7°-63°) giving an accessibility

domain of 660 km corresponding to a mean revisit time better than 8 hours (see figure 3).

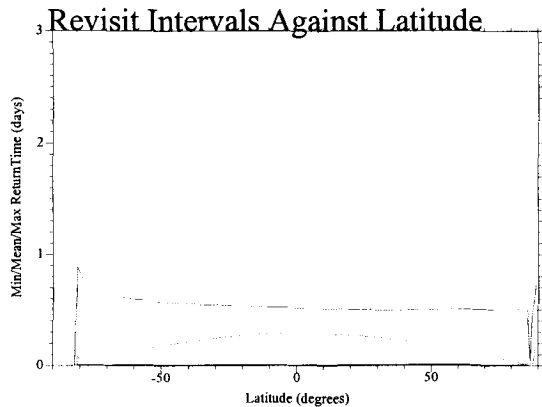


Figure 3 : Mean revisit time with extended accessibility.

**RADAR SYSTEM DESIGN**

A number of instrument concepts has been envisaged during the study as described in the following section. In order to define the instrument parameters, the radar preliminary design is developed on the basis of the most conventional SAR instrument concept which means an instrument based on a planar array antenna with electronic agility in elevation while the impact of the different instrument concepts on the radar parameters is listed below.

As previously explained this design concerns the strip map mode in the 20-53.7° incidence range from the performances of the other modes are deduced from it.

The key goal of the preliminary design is meeting the link budget and the  $N\sigma_0$  requirement. So the instrument has been optimised for this accordingly. The main instrument parameters are summarised in the table 2 including system margins.

The PRF range depends on the antenna concept : only an active antenna one allows nadir null formation in order to reject the nadir return and therefore allows a limited PRF range (200 Hz) while the other antenna concepts without nadir rejection capability require a larger PRF-range.

Without nadir rejection the PRF range depends on system flexibility: 1600 Hz is required to provide complete accessibility where every swath within the nominal swathwidth can be imaged; 1000 Hz for the discrete accessibility where the accessibility domain is just divided in N successive swaths.

At the same time, the fact that the required PRF range is wide at the lower incidences and decreases when the incidence increases, allows the Range Ambiguity Ratio (RAR) to comply with a limited antenna height.

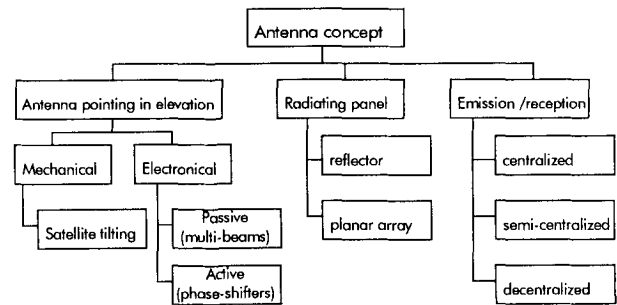
This system parameters are compatible with all the secondary modes. In addition, the double swath mode requires a  $\pm 2.3^\circ$  electronic agility in azimuth.

PRF range with nadir rejection	4550 Hz - 4750 Hz
without nadir rejection (N swaths)	4550 Hz - 5550 Hz
without nadir rejection (full access)	4550 Hz - 6150 Hz
Bandwidth	226 / 45 MHz
Tx duty cycle	16.5%
Rx duty cycle	27 / 90 %
Antenna size	4 x 1.9 m
Beam width in elevation	2.05° / 0.95°
Beam agility in azimuth	+/- 15°

Table 2 : Main instrument parameters

**INSTRUMENT CONCEPT**

The following figure shows the extend of the technical possibilities explored to defined the instrument concepts from the instrument requirements and preliminary design.



The preliminary conclusions are as follows :

- The wide incidence range with a constant swath width requires an beamwidth flexibility in elevation: a unique beamwidth can not be compliant with swathwidth at low incidence and RAR compliant at high incidence. The antenna therefore has to provide a minimum of 3 beamwidths independently of the type of instrument agility.
- For the instrument based on antenna agile in elevation the required de-pointing and the RF bandwidth leads to use Time Delay Lines in the Beam Forming Network. Considering the typical losses of the TDL, this configuration is then incompatible with centralised amplification.
- The operational capacity of a passive antenna based instrument is significantly lower for the risk management mission and in particular the crisis monitoring. In fact, the typical mechanical commutation time between two acquisitions is one



minute (420 km ground displacement) while the electronic commutation time is far below 1 second.

This analyse has therefore given rise to five possible architectures for further investigations:

\* Two concepts are based on reflector antennas :

- a double curved parabolic reflector with few horns as feed to generate few beams with different beam-widths,
- a cylindro parabolic reflector with a linear array of horns given agility in elevation.

\* Three concepts are based on the more conventional planar array antenna :

- an active antenna with agility in both direction,
- a planar array with phase shifter in elevation like Radarsat 1,
- a Blass Matrix antenna with few beams.

These solutions have been evaluated in term of performances, mass and power budget, platform accommodation, flexibility, risk and cost. This evaluation has led to the selection of two instrument architectures : a full-compliant instrument baseline and a low cost instrument baseline which correspond to a simplified design at the expence of a degradation of the performances.

The study of the different sub-system shows the following points:

- centralised amplification requires the development of new TWT in view of the high RF power and raises major problems as regards thermal control and redundancy. Consequently, this RF sub-system architecture appears critical in term of risk, development plan and cost.
- for the reflector antenna based architecture, the novelty of the concept makes it difficult to estimate radar performances at the trade-off study level.

The evaluation of the different candidates is summarised in table 3.

Concerning the secondary modes, all the instrument concepts are compatible with the extended accessibility domain.

The Scansar mode requires antenna electronic agility capabilities in elevation. Nevertheless, the totally passive instrument concepts can allow Scansar acquisition using several beams in fan configuration.

Finally, the double swath mode requires electronic agility capabilities in both azimuth and elevation direction. Thus this mode is compatible with an active antenna which assumes 3 times more modules in azimuth than the strip map mode.

The two solutions selected therefore of the active antenna which appears to be the most flexible with a limited cost considering modern TR modules architecture and the double curved reflector which appears less expensive.

In accordance with the ESA recommendation, the active antenna instrument has been selected as baseline for the second part of the study without the double swath mode.

#### ACTIVE ANTENNA DESIGN

The architecture of CZEW active antenna is shown in figure 5. The main results are summarised below :

- 12 T/R modules in azimuth x 80 modules in range provide the peak power. The proposed technology for 7 Watts HPA is  $\frac{1}{4}$   $\mu$ m PHEMT.
- Five Time Delay Lines are needed due to the large bandwidth to reduce the pointing shift during the chirp, followed by 5 primary amplification modules to compensate RF losses
- The radiating arrays are centre-fed slotted waveguide arrays
- The planned platform allows a non-deployable antenna which facilitates the mechanical design.

The central electronic sub-system was designed as follows :

- The chirp generation is a combined direct/indirect chirp synthesiser based on direct memory generation and up conversion.
- The direct analog quadrature demodulation was selected, followed by an interpolation filter to reduce the sampling frequency.
- Two solutions of data handling architectures are possible depending on the presence of Scansar on-board processing :
  - A router would be the best solution but the actual hardware is incompatible with the required data rate
  - A pipe-line architecture with parallel Scansar processing avoids specific technological development, but interfaces are more complex.

The preliminary power / mass instrument budget leads to 400 kW / 400 kg (with 10% T/R modules redundancy), compatible with the small-satellite class.

CONCLUSION

The mission capabilities of CZEWSAR allows a global coverage and a mean revisited time which are interesting for risk management monitoring.

The design of CZEWSAR instrument is compatible with the philosophy design for Earth Watch mission : an operational system developed in a cost-effective approach (simple and robust architecture, low technological risk, low mass and low power, reduced development plan).

REFERENCES

[1] « Small satellite system for civilian radar imagery application », IGARSS 1998, N. Vincent, D. Gaillard, T. Banos

*This work is based on an ESA contract, with EMS Technologies, SEA (Systems Technologies & Assessment) and COM DEV Europe as sub-contractors of ALCATEL SPACE INDUSTRIES.*

Antenna Concepts	Double curved reflector	cylindro parabolic reflector	Active antenna	Phase shifter antenna	Blas matrix antenna
agility	platform	electronic	electronic	electronic	platform
beam flexibility	Few beams (4)	full	full	full	few beams
amplification	Semi-Centralized	Semi-Centralized	Distributed	Semi-Centralized	Semi-Centralized
performance	3	2	1	1	2
mass	1	2	4	3	3
power	5	4	2	3	1
accommodation	1	4	3	2	2
flexibility	3	2	1	2	4
risk	3	5	1	2	4
cost	1	4	2	2	3

rating : 1 to 5 : best to worst

Table 3 : Antenna candidates for CZEWSAR mission

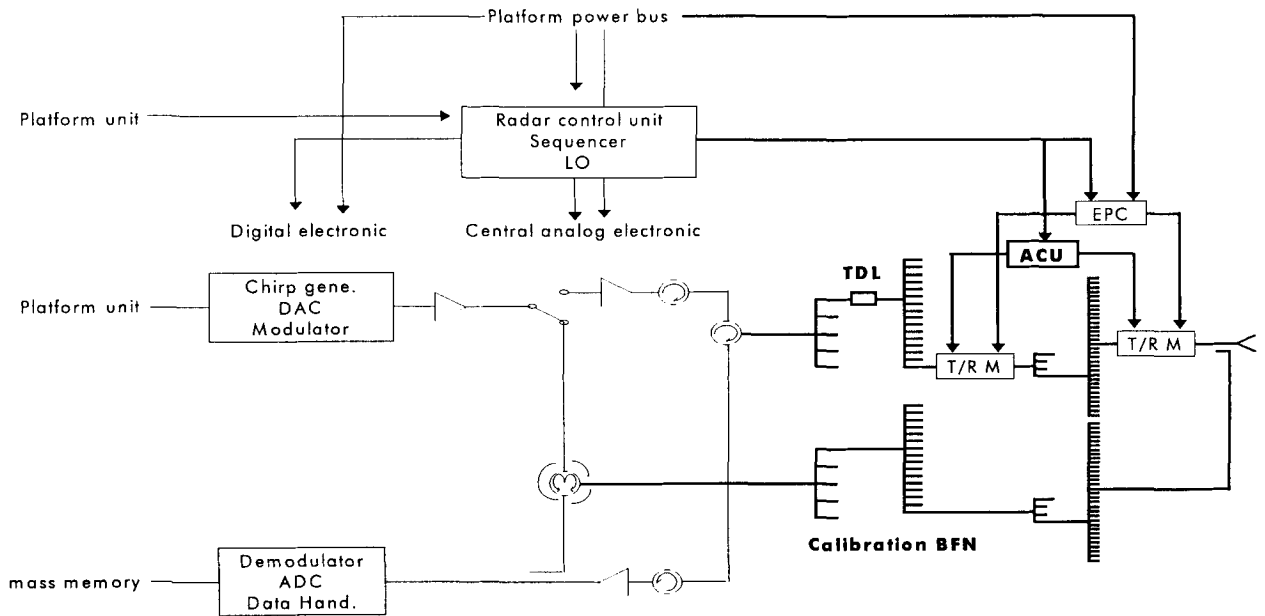


Figure 4 : CZEWSAR Preliminary block diagram

## A Fully Polarimetric L-band Spaceborne SAR Instrument Targeting Land Applications

G T A Burbidge<sup>(1)</sup>, D M Simpson<sup>(2)</sup> & C H Mathew<sup>(3)</sup>

Matra Marconi Space UK

Anchorage Road, Portsmouth, Hampshire PO3 5PU, United Kingdom

+44 (0)239270 5010<sup>(1)</sup>/ 5133<sup>(2)</sup>/ 8612<sup>(3)</sup> (tel) +44 (0)239270 8290 (fax)

geoff.burbidge/david.simpson/colin.mathew @mmsuk.co.uk

### ABSTRACT

An L-band SAR mission is a proposed to meet the requirements of the European Space Agency (ESA) Earth Observation Preparatory Programme (EOPP). The L band SAR instrument (L-SAR) has been studied as part of a pre-phase A contract for ESA (LandSAR). The L-SAR is also one component of the L+X-band TerraSAR system. TerraSAR has been proposed for the overall Earth Watch programme and is also the major asset for data provision to InfoTerra, an initiative being lead by Matra Marconi Space UK (MMS-UK) and Dornier Satellitensysteme (DSS).

This paper describes a fully polarimetric spaceborne L-band SAR instrument currently under development. The instrument architectural definition is summarised, including a synopsis of the major design trade-offs, leading to the selection of an instrument baseline, for which the preliminary design is presented. The satellite-level accommodation aspects of the L-SAR payload are also presented. Both 'conventional' and 'longitudinal diametric' configurations have been examined, and the paper identifies the merits of a solution based on the MMS 'Snapdragon' instrument carrier. The performance and products to be provided are also specified. The basic image products are listed, showing the potential to generate higher level information products and the provide services to a wide range of user communities.

### OVERVIEW

A fully polarimetric L-band spaceborne Synthetic Aperture Radar Instrument (L-SAR) design has been defined as a result of complementary work on a number of study and development programmes involving Matra Marconi Space UK (MMS-UK).

Recent studies have addressed the concept definition, architectural trade-offs and preliminary design definition of the L-SAR. They include the following:

- ❑ LandSAR Study <sup>1</sup> – a pre-phase A study of an L-band SAR instrument, let by ESA/ESTEC;
- ❑ LandSAR follow-on Study – a technology survey and study of the L-SAR on a Snapdragon instrument carrier [1], also let by ESA;
- ❑ TerraSAR Feasibility Study <sup>2</sup> – an industry-lead initiative performed by MMS-UK and Dornier Satellitensysteme (DSS) to define and evaluate the feasibility of an L+X-band SAR system concept;
- ❑ TerraSAR Phase B Study <sup>2</sup> – a programme to design an L+X-band mission, supported by both industry and agencies in the UK and Germany.

A series of hardware development programmes aimed at generic, multi-mission designs have also been in progress over the last 4 years, supported by a combination of company and national funding. Increasing commercial pressures and funding constraints on future Earth observation (EO) missions demands a cost-effective approach to any future L-SAR system implementation. The MMS-UK Common Radar Elements (CORE) programme [2] has yielded a frequency independent CORE Radar Central Electronics Subsystem (CRESS) and generic Front End Subsystem (FESS) architectures which are applicable to the L-SAR. The CORE Front End activities incorporate a Generic Transmit/Receive (T/R) Module programme which is soon to output L-band T/R module prototypes. These existing hardware programmes will therefore contribute substantially to an L-SAR instrument implementation. The completion of the L-SAR system engineering activities within the TerraSAR Phase B, complemented by an L-band Active Array Antenna development, will realise a performant and generically applicable L-SAR Instrument.

<sup>1</sup> also involving DSS, Saab Ericsson Space (SES) and Marconi Research Centre (MRC)

<sup>2</sup> in partnership with DSS

## L-SAR DESIGN DESCRIPTION

### Instrument Requirements

An L-band SAR Instrument design has been derived from a core set of instrument operation, performance and programmatic requirements.

### Frequency and Polarisation

Polarimetric SAR imagery from the SIR-C mission and imagery taken from airborne SAR campaigns show that polarimetric L-band data is very useful in land applications, certain ice applications, and in bathymetry. The need for multi-polarisation L-band information is driven from the intrinsic capability of longer wavelengths to penetrate vegetation, providing an estimate of biomass, measurement of soil moisture, and differentiation/classification of crops. These capabilities to classify land cover makes L-band dual- and quad-polar essential for a land-orientated mission.

### Operation and Performance

A wide variety of end-user applications demands a flexible, multi-mode instrument, allowing product parameters to be optimised. The majority of products are acquired in a Stripmap mode, with extended and wide swaths achieved using a ScanSAR mode. Elevation beam steering in each of these modes is required to enable flexibility in swath selection.

In-orbit selectability of operating polarisations is critical for an L-band sensor that strongly relies on multi-polarisation capabilities. Simultaneous acquisition of all co- and cross-polar information (4 channels, HH+HV, VV+VH) in quad-polarisation operation, or of only co- and cross-polar data for either H or V in dual-polarisation operation (2 channels, HH+HV or VV+VH) provide the main L-SAR modes. Estimates of performance are provided in Table 1.

Table 1: L-SAR Operating Modes/Performance

MODE	RES'N	SWATH	TECHNIQUE	CCESS	POLAR.
Fine - Narrow	9m	40km	Stripmap	15 - 48°	Dual
Fine - Standard	9m	60km	Stripmap	15 - 48°	Dual
Quad - Narrow	15m	40/ 45km	Stripmap	15 - 48°	Quad
Quad - Standard	15m	60 km	Stripmap	15 - 40°	Quad
Extended Swath	30m	100km	ScanSAR	15 - 48°	Dual
Wide Swath	30m	200km	ScanSAR	15 - 48°	Dual

### Programmatic

The technical requirements imposed on the instrument are augmented by a series of programmatic aspects. Generally not supported by military funding due to the resolution constraints, it is realistic to assume that any future L-band SAR mission will be a budget-limited programme demanding a cost-effective solution. Any commercially viable mission can be characterised by:

- a self-sustaining business plan based on generating revenues from acquired data products;
- a technical implementation which is based on a minimum of non-recurring expenditure (NRE).

To secure an effective business plan it is critical that L-SAR products can rapidly establish a solid market. Analysis of market demands suggests that the window for establishing an operational service is early 2004. To minimise NRE it is crucial that existing development programmes are used where possible, and that technology development is minimised.

### Instrument Architecture

#### Trade-Offs

The trade-offs performed on the LandSAR study considered both mission performance aspects and instrument architecture concepts. Options were compared using a set of selection criteria. In addition to the programmatic issues identified above, the following constraints were also considered in the trade-off:

- payload capacity and launch envelope of a medium class launch vehicle (Delta II);
- instrument performance/reliability requirements;
- available instrument power from platform (4kW).

#### a) Chirp Bandwidth

The maximum bandwidth was 55MHz, which is sufficient to fulfil the fine resolution requirements defined in Table 1. The baseline is to match the bandwidth to the resolution for a single look. However the full 55MHz can be used with multiple range looks, at higher incidence angles to provide increased radiometric resolution. Designing a system, which provides the full 85MHz bandwidth allowed by the World Administrative Radio Conference (WARC) will provide enhanced resolution. However, it increases the complexity of the front-end components such as the sub-arrays and T/R modules, as well as the processing and chirp generation chains in the central electronics.

#### b) Antenna Size

This trade-off was driven by the need to meet instrument performance requirements, within the available launcher envelope, and payload mass limit. Antennas from 16m<sup>2</sup> to 48m<sup>2</sup> were considered. An antenna of at least 25m<sup>2</sup> is considered necessary to meet the sensitivity requirements, within the allowable DC budget. The enhanced performance offered by large antennas of up to 48m<sup>2</sup> is debatable given end users' needs (sensitivities of -35dB or even -30dB appear sufficient for many applications).

#### c) Sub-array Dimensions

The sub-array dimensions of a SAR antenna were driven by the need to achieve the required insertion loss and electronic steering requirements. The maximum size was also limited by the need not to exceed the maximum power handling of the antenna technology. Current L-band antenna designs have only been qualified to approximately 60W, and it was considered that the move to a new technology would add significant cost and risk. A spacing of 0.76 wavelengths between antenna rows was chosen to provide the required 30° of elevation steering. The trade-off identified that high bandwidths can be achieved with a longer sub-array providing a co-time or corporate feed is employed. At L-band there is sufficient room on the sub-array to provide this, and this requirement became a secondary consideration.

#### d) Front End Amplification/Beam-steering Control

A critical driver in the Front End design is the need to minimise development costs of a T/R module, which performs the distributed amplification and beam-steering control. On previous projects such as ASAR, the full complement of modules has been the most costly element of the instrument, with development costs running into tens of millions of Euros. The heritage of such a module at L-band is extremely low with, space qualified designs being limited to 10W. Elsewhere, the majority of space qualified amplifiers at L-band come from the communications satellite domain and are also limited to a few tens of watts. This factor became one of the most crucial drivers in considering the Front End amplification and beam-steering control architecture.

Distribution of the T/R module elements in the Front End was considered from row level, down to being fully distributed to the level of individual sub-arrays. Whilst row level distribution, meets the requirements for a low mass antenna, and can fulfil all the beam steering requirements of the proposed L-band mission, it had a significant number of disadvantages, over more distributed schemes. At L-band low loss, high

power handling transmission lines, such as waveguide, become too bulky. Low loss coaxial cable offers the lowest technological risk, alternative. Even so the system losses of row level distribution, on a 25-30m<sup>2</sup> array were over 8dB and prevented the required sensitivity performance being achieved within the allotted power budget. Other disadvantages with row level distribution include the technological risks in designing a highly efficient high power SSPA, in excess of 400W, and the need to provide redundant amplifier units to achieve the required reliability.

Intermediate distribution schemes, from T/R modules driving half a row, down to two sub-arrays per row, reduce DC consumption and design complexity. The fully distributed scheme provided the lowest DC consumption and simplest T/R module design. In addition reliability of the Front End was achieved without the need for T/R module redundancy.

#### e) Central Electronics (CE)

The major trade-off issue for the central electronics was the degree of channelisation, which would be employed for the chirp generation and processing architecture. A multi-channel architecture is implicit to dual- or quad-polarisation operation due to the two receive chains which are required.

The design and testing of the MMS central electronics product, the CRESS, has proved that a similar, channelised approach can be used for the generation of a 'stitched' wideband transmitted chirp and for the segmented processing of echo returns. This offers reduced performance requirements for key components, such as the analogue to digital converters, and digital data compression ASICs, and benefits in hardware modularity. DC consumption can also be reduced, as channels can be switched off if imaging at a lower bandwidth or in single polar mode.

#### *Baseline*

The antenna baseline is a 25 m<sup>2</sup> planar array containing 192 radiating sub-arrays. Amplification, beam-steering phase and gain control functions in the front end, would be fully distributed, with a T/R module driving each sub-array. Beam steering would only be performed in elevation.

The central electronics would be based on the CRESS, with a 55MHz bandwidth limit. The CRESS would have a transmit chain and two receive chains allowing simultaneous reception of H and V polarised echoes.

Table 2 shows a summary of instrument parameters.

Table 2: Major Instrument Performance Parameters

Instrument Mass	760kg
assumes Snapdragon Carrier and 15% margin	
Peak Instrument DC Power	3200W
assumes 25% TR module efficiency, and 20% margin	
Worst Case Data Rate	500Mbps
Antenna Area	25m <sup>2</sup>
Antenna Dimensions	10m x 2.5m
Number of TR Modules	192
Cross Polar Performance	-35dB
Operating Bandwidth	55MHz
2-way System Losses	1.8dB
Receive Noise Figure	2.8dB
Peak RF Power	600W
Duty Cycle	10%

### Subsystem Preliminary Design

#### Front End Definition

The active antenna array is divided into a number of panels with each panel being further divided into a series of sub-panels or tiles. The tile is the smallest repeatable element providing all the functions of the antenna, e.g. T/R modules, power supply, control and RF distribution. A coaxial feed distributes the RF signals from the CRESS to each tile. The feed will be implemented in silicon dioxide, chosen for its low loss, mass and stable electrical performance. Three feeds will provide transmit, receive H-POL and receive V-POL paths. In ASAR a separate calibration feed allowed the routing of calibration pulses in the around the front end, with a centralised switch network in the Central Electronic Sub-assembly (CESA) providing connectivity with the chirp generation and processing paths. Short-comings with this scheme have led to an alternative scheme being recommended for LandSAR, which consists of a distributed calibration network in each T/R module. This scheme allows a 20kg mass reduction for the antenna, and improved reliability.

Beam-steering control is provided by phase and amplitude control in each T/R module. Additionally 2-bits of coarse adjustment are provided with true time delay lines. The extra coarse adjustment is required because of the high percentage bandwidth of the chirp. The phase shifters only produce the exact time delay required at the centre frequency. At the edges of the swath the beam pattern is unacceptably distorted.

A modular solution has been chosen for the T/R module architecture. Two T/R chains provide H and V inputs to the radiating antenna. The design of the basic chain is simpler than for a module containing two receive chains operating simultaneously, easing isolation requirements for example. It also allows

expansion from a single- to a dual-polarised SAR system, such as LandSAR. Receive and transmit chains of each T/R module share a single phase-shifter to reduce component costs. The maximum output power of each amplifier is 40W. The design of the T/R module is underway at MMS-UK with support from ESA. The power amplifier technology is based on a Double diffused Metal Oxide Semiconductor, Field Effect Transistor adapted from a communications application. The target T/R module efficiency including DC-DC conversion is 25%, representing a significant improvement on the current ASAR design.

The antenna trade-offs and design culminated in an aperture coupled radiator element consisting of stacked circular patches. A similar design is proposed and breadboarded for the Global navigation satellite system Receiver for Atmospheric Sounding (GRAS) [3]. This design can achieve 35dB of cross-polar isolation, using mirror cancellation techniques. Each sub-array has four radiating elements. This number was chosen to meet power handling requirements. A co-time feed is proposed to ensure maximum bandwidth is available across the sub-array.

A serial instrument control and monitoring bus will load beam data directly into each T/R module. This can only be done in slow time before imaging due to the limited the capacity of the bus, compared to the amount of data that must be loaded during an multiple beam imaging mode, such as ScanSAR. A second uni-directional high-speed bus, provides a strobe to each T/R module, which selects the beam required during an imaging mode. A further high-speed strobe enables either the transmit or receive chain in the T/R module, when required, to reduce power consumption, and improve isolation between the transmit and receive paths. Each tile requires a control unit that provides buffering of the control and monitoring signals in the front-end. It is also envisaged that some processing capacity will also be provided in this unit to allow temperature compensation by adjusting the T/R module phase and amplitude settings.

The T/R modules will have regulated secondary supplies from separate Power Supply Units on the tile. A non-redundant PSU will supply 2 T/R module pairs. This provides the best compromise between reliability and mass efficiency. The PSUs will be supplied from the primary space craft bus on dedicated power lines, which are centrally switched. This approach was used on ASAR and provides a more reliable solution over a single power ring, and a more manageable harness.

Figure 1 provides a FESS functional block diagram.

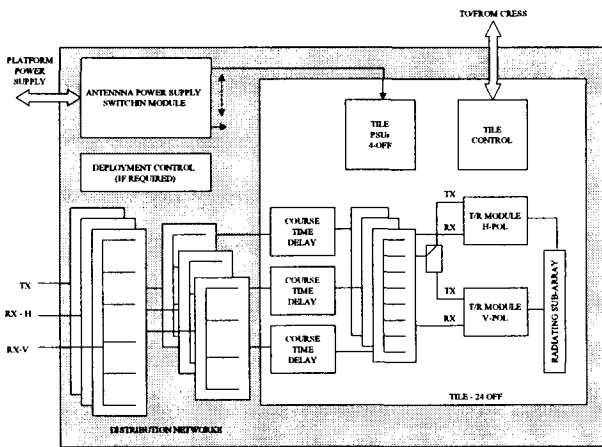


Figure 1: Front End Functional Block Diagram

The FESS mass depends on the stowed and deployed configuration demanded by the platform. However, the non-structural mass density of the FESS is approximately 18kg/m<sup>2</sup>.

*Central Electronics Definition*

The functional block diagram of the CRESS is shown in Figure 2. It comprises a Baseband Equipment (BBE) and an Intermediate Equipment (IFE). The BBE generates the chirp signal to the required bandwidth and modulates to an intermediate frequency (IF). The signal is passed to the IFE, where it is upconverted to L-band and suitably filtered according to mission-specific requirements. The signal is then passed to the front end. The received signal is filtered and downconverted to IF and passed to the BBE, where it is demodulated and converted to digital data. The BBE has a Block Adaptive Quantisation (BAQ) capability that can compress the 8 bit data to 4, 3, 2, or 1 bits. The data is then packetised and passed to the data management and storage system, before being downlinked to a ground station.

The BBE provides the interface between the platform and the instrument. It has a control unit that interprets macrocommands from the platform and passes control signals to the front-end and other units in the CRESS. The IFE contains the reference generator which provides the LO signals required from a master oscillator. The design of the architecture minimises changes to modules in the IFE for different frequency bands, whilst the BBE is frequency independent. The CRESS development is well advanced, having been selected for the C-band Radarsat-2 mission.

A functional block diagram of the CRESS is shown in Figure 2.

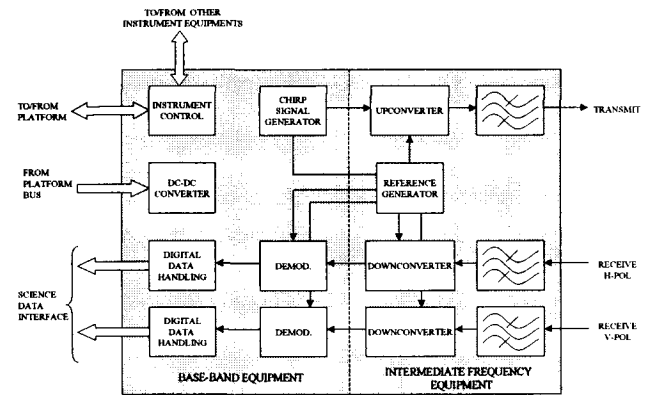


Figure 2: CRESS Functional Block Diagram

Estimates for the CRESS mass and peak power are 45kg and 150W respectively.

L-SAR PRODUCTS AND APPLICATIONS

Addressing the required applications demands that certain key information products are acquired. Core products include the following:

- mapping products at fine spatial resolutions;
- large-area land-cover and geological products;
- agricultural classification products;
- quantitative bio- and geo-physical parameters, including agronomical information.

Imagery that can provide the basis for this range of information products have been identified as 'basic products' and are categorised to include the following:

- Medium-Res-Lq (9m/15m resolution, quad-polar.)
- Medium-Res-Ld (9m/15m resolution, dual-polar.)
- Low-Res-L (30m resolution quad-polar.)

Stereoscopic and interferometric operation is envisaged, realising digital elevation models and coherence maps.

POTENTIAL MISSION CONFIGURATIONS

A number of candidate spacecraft configurations were considered. Conventional box-shaped platforms included Satellite Pour Observation de la Terre (SPOT), MetOp and Earth Observation System (EOS) platforms. The latter two were not compatible with the Delta II envelope or payload mass limit. The SPOT platform would have to fly in a canted attitude to fit a stowed antenna of sufficient size. Previous SPOT platforms flown on the European Remote Sensing missions ERS-1 and 2, flew in a different orientation. Another alternative was to use a SAR specific platform, namely the Snapdragon instrument carrier [1], which MMS-UK has been developing. The stowed and deployed spacecraft is shown in Figure 3.

Both SPOT and Snapdragon configurations have been studied under LandSAR and the follow-on programme. The Snapdragon concept is the preferred platform for a large L-band SAR instrument. The main advantage with this concept is that the spacecraft provides structural support for the antenna and deployment is straightforward, although a greater mass is being deployed. For a conventional platform, a multi-staged deployment of up to 6 panels is necessary. To provide the required deployed stiffness and planarity, a complex deployable truss structure similar to that developed for Radarsat-1 is required. The significant structure to support the individual panels creates a significant mass disadvantage. The conventional SPOT configuration is shown in Figure 4.

It is recognised that the development of a new structure and mechanisms is required for Snapdragon. However, for the conventional platform, substantial modifications would be required due to the increased power requirement of the L-band SAR instrument and the orientation in-orbit. The development of a deployable truss structure and mechanisms is viewed as a task of similar magnitude to development of the Snapdragon platform.

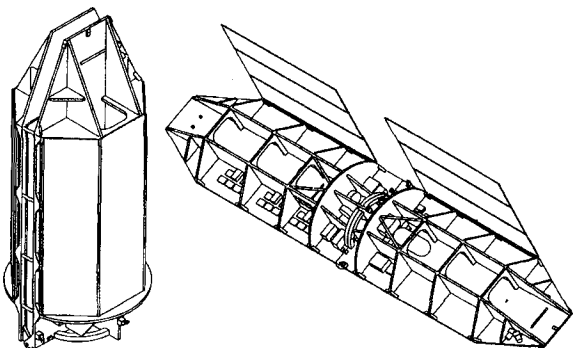


Figure 3: Snapdragon Stowed/Deployed Configuration

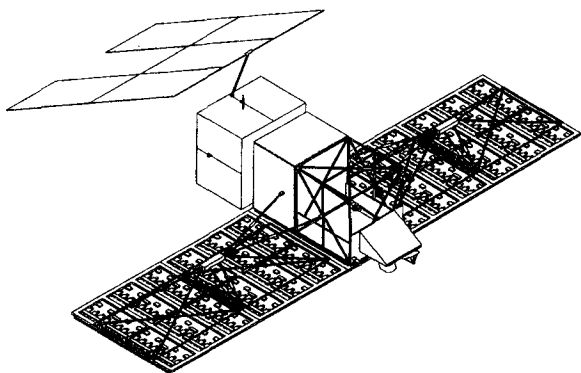


Figure 4: SPOT Deployed Configuration

## L-SAR CONTEXT IN FUTURE PROGRAMMES

The preliminary design of an L-SAR instrument concept has been completed. This has enabled an architectural baseline to be established and those elements of high technical risk to be identified. A land-oriented mission utilising a fully polarimetric L-band SAR sensor has been identified as a highly capable, yet feasible and cost-effective Earth observation asset.

It is also evident through many studies, surveys and imaging campaigns over recent years that multi-frequency information products provide a key means of servicing a growing base of civil and defence-oriented applications. Augmenting the L-SAR with a complementary X-band high-resolution sensor providing increased accuracy of discrimination, expands the product-base to include important cartographic and change detection applications. TerraSAR is designed to target this market niche.

The mitigation of L-SAR technical risks through a suitable demonstrator programme is critical in achieving an efficient and affordable flight programme. This activity is seen as an important development step in advancing critical L-SAR technologies.

## ACKNOWLEDGEMENTS

The authors acknowledge the work of their colleagues at MMS and the other LandSAR team members, DSS, SES and MRC, and the support provided by ESA.

## REFERENCES

- [1] J.D. McCaughey, C.D. Hall, D.M. Simpson, "Instrument Carrier- SAR Specific Polymorphic Configuration", EUSAR98, Friedrichshafen, Germany, pp.167-170, May 1998.
- [2] D.J.Q. Carter, K. Morgan, S. Hartley, "Advanced Multi-use Radar Topography CORE Radar", EUSAR98, Friedrichshafen, Germany, pp.167-170, May 1998.
- [3] A. Carlström, et al, "A suspended Microstrip Technology for Low Loss and Lightweight Printed Antennas", 21<sup>st</sup> ESTEC Antenna Workshop - Array Antenna Technology, pp.179-181.



**A World- Metric- Cartography And Topography Mission**

Frédéric Adragna  
CNES, France

This paper was not available for publication



## **Session 7: Envisat**



## The ENVISAT ASAR Instrument Verification and Characterisation

R. Torres, C. Buck, J. Guijarro, J-L. Suchail and A. Schöenberg  
 ENVISAT Payload Division, ESA-ESTEC  
 Keplerlaan 1, 2200 AG, Noordwijk  
 The Netherlands  
 phone +31 71 5653528, fax +31 71 5653191  
[rtorres@estec.esa.nl](mailto:rtorres@estec.esa.nl)

### ABSTRACT

*The ENVISAT Advanced Synthetic Aperture Radar (ASAR) is a sensor of paramount importance for the remote sensing community. Its enhanced flexibility with respect to the ERS AMI gives a wide combination of different spatial resolutions, incidence angles, swath width sizes and polarisation diversity, which are reflected in an increased number of operational modes for a large set of scientific and operational applications. Its advanced design based on the use of an active antenna, with individual subarray temperature compensation and internal calibration loop, is complex but a breakthrough with respect to the experimented passive antenna design concept. This paper describes the verification and characterisation process of the ASAR instrument from equipment level up to instrument level, the test philosophy throughout the assembly and integration activities, in both aspects: the qualification for the ENVISAT mission and the characterisation to guarantee, as well as enhance, the ASAR instrument performances. A summary of the qualification results and a performance analysis of the characterisation test data is also given.*

### INTRODUCTION AND FUNCTIONAL DESCRIPTION

After the development of the AMI SAR and its successful operation on board ERS-1 and ERS-2, the European Space Agency (ESA) are completing the development of an advanced SAR to be launched with the ENVISAT-1 spacecraft in order to consolidate and enlarge the mission objectives of the previous AMI SARs. The unique capability of imaging a large range of incidence angles with high, medium and low spatial resolutions combined with a multi-polarisation capability and adaptable swath widths will assign to this sensor a role of primary importance among the future microwave imaging sensors. ASAR will exploit its intrinsic design flexibility through five operational modes: The *Image Mode* will generate high spatial resolution data products (30 m) similar to the AMI SAR, imaging one of the seven swaths located over a range of incidence angles spanning from 15° to 45°. The *Wave Mode* will generate vignette sizes of 5 by 5

km spaced 100 km along-track and will be the capable to locate the vignette in any of the seven swaths. The *Wide Swath Mode* and *Global Monitoring Mode* are based on ScanSAR processing of five sub-swaths and will generate wide swath products (400 km) with spatial resolution of 150 m and 1000 m respectively. These four modes will be operated in one of the two copolar polarisations, HH or VV. The *Alternating Polarisation Mode* will provide images from the same area in HH and VV, HH and HV or VV and VH, with the same imaging geometry as the Image Mode and similar high spatial resolution.

The ASAR instrument consists of two main elements: the Central Electronics Sub-Assembly (CESA) and the Antenna Sub-Assembly (ASA) (see figure 1). The active antenna contains 20 Tiles with 16 subarrays each one equipped with a Transmit/Receive (T/R) module. The instrument is driven by the Control Subsystem (CSS), which provides the command and control interface to the spacecraft, maintains the database, manages the distribution of the operation parameters such as transmit pulse characteristics, antenna beam-set, and generates the time-lining of the instrument. The transmit pulse characteristics are set in the Data Subsystem (DSS) the output of which is an up-chirp pulse centred at the IF carrier (124 MHz). In the RF Subsystem (RF S/S) the pulse is up-converted to the RF frequency (5.331 GHz) and amplified. The signal is then passed to the Tile Subsystem (TSS) through a waveguide distribution network (RFPF) and subsequently, within the tile, to each individual T/R module using a microstrip corporate feed. The T/R modules apply phase and gain changes according to the pre-selected beam characteristics, transferred from the Control Subsystem and locally stored the Tile Control Interface Unit (TCIU). In receive the RF-echo signal follows the reciprocal path down to the Data Subsystem where the final science data are generated and provided to the spacecraft interface.

### CENTRAL ELECTRONICS SUBSYSTEM

The CESA is in charge of generating the transmitted chirp, converting echo signal into science data, as well as controlling and monitoring the whole instrument.

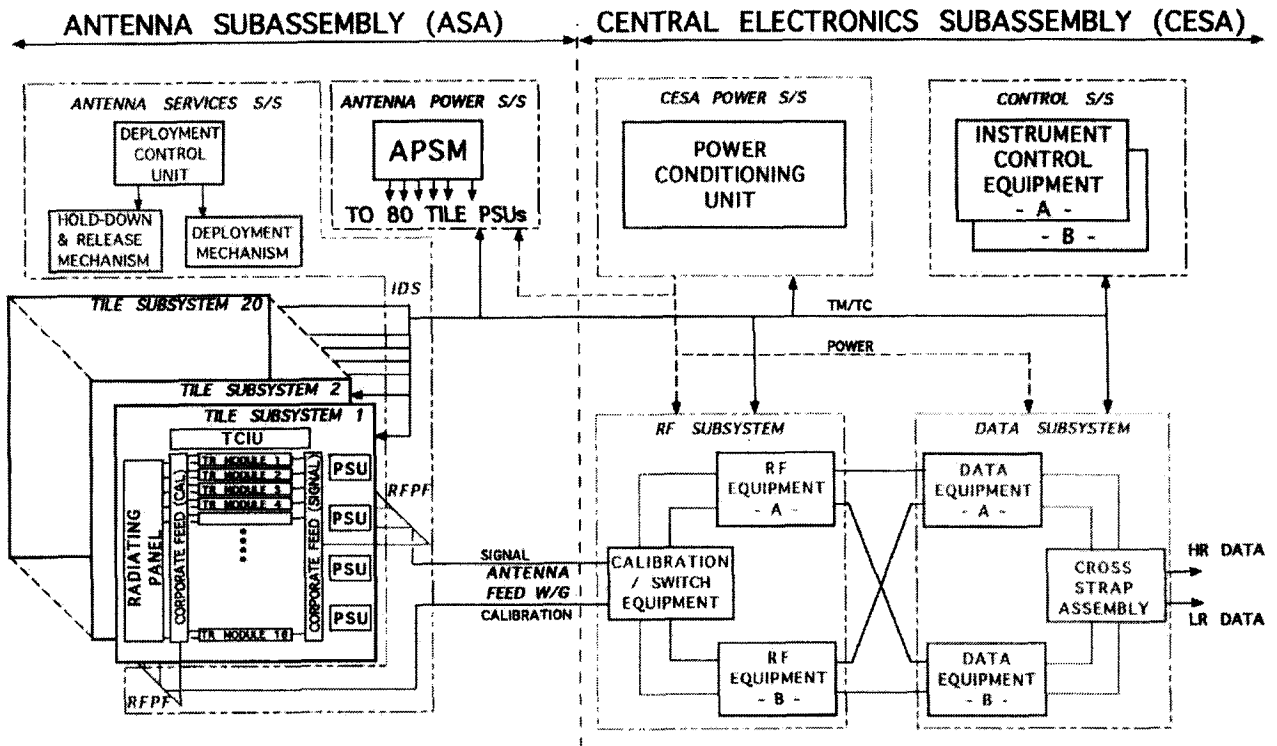


Figure 1 : ASAR Functional Block Diagram

Compared to ERS-1 and ERS-2 which were using SAW devices for analogue chirp generation and On Board Range Compression, ASAR is using more extensively digital technologies for on board chirp generation and data reduction for temporary storage, associated with On Ground Range Compression.

A fundamental advantage of using digital chirp generation is the inherent flexibility of such a design which allows for chirp versatility in terms of pulse duration and bandwidth, thus accommodating efficiently the various requirements associated with the high number of available operational modes and swaths of the instrument.

In the ASAR instrument, the transmit chirp characteristics are set by macrocommand from the Control Subsystem to the Data Subsystem by writing chirp coefficients into the Data Equipment processor. This processor then calculates the In-phase and Quadrature components of the baseband signal to be generated in the form of two digital tables in the Chirp Memory. This memory can store up to 128 chirps of  $2040 \times 8$ -bit samples per I & Q channel each. Once the triggering of the transmit chirp occurs, the contents of the two tables corresponding to the selected chirp are sequentially read and transferred to a pair of low glitch impulse DAC operating with a 38.4 MHz clock in order to generate the baseband I & Q signals. These signals

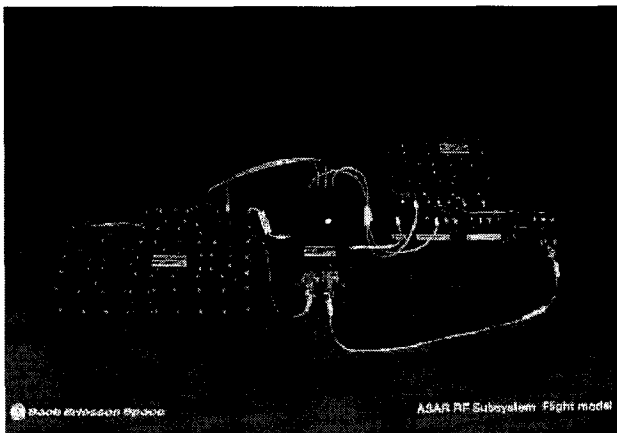


Figure 2: FM RF Subsystem

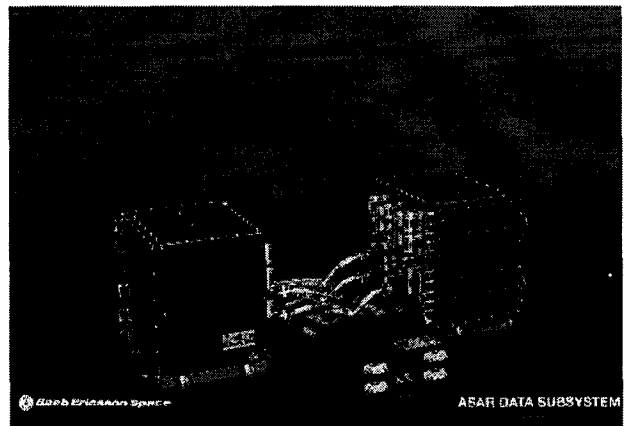


Figure 3: Data Subsystem

are then fed to image rejection mixers for further IF baseband modulation in the Data Subsystem followed by upconversion to C band and amplification in the RF Subsystem.

At reception, the echo signal is first filtered and down-converted to IF in the RF Subsystem, then demodulated into the I & Q components of the carrier. These two signals are then both digitised into 8-bit samples at 19.2 MHz following anti-aliasing filtering. It is then possible to perform some digital decimation of the samples by simply transmitting only one in every N samples, if required, in order to reduce the data stream, such as in Global Monitoring mode where the transmit bandwidth is lower than 1 MHz. Following this decimation, a FBAQ scheme is applied for the echo samples.

The developed FBAQ ASIC can be operated in three main modes: Compression mode according to BAQ algorithm, Bypass mode and Noise mode. In compression mode, each 8-bit sample value is compressed to a selectable 4, 3 or 2-bit sample value. The operation mode of the ASIC can be selected individually in the control register for each data type (echo, calibration and noise). The BAQ Compression mode is selected for echo data, bypass mode (thus

preserving the full 8-bit accuracy) for calibration data and fixed exponent (3-bit magnitude + sign) for noise data.

The Data Equipment also contains a Science Memory where the echo samples are then temporary stored before their transmission to the platform on-board tape recorders in Wave, Global Monitoring and Module Stepping modes (low rate modes). The Science Memory consists of two banks of DRAM memory with  $1\text{M} \times 1$  bit each. It is therefore possible to read from one bank while writing into the other.

#### ACTIVE PHASE ARRAY ANTENNA

The ASAR active antenna is a  $1.3\text{ m} \times 10\text{ m}$  phased array. The antenna consists of five  $1.3\text{ m} \times 2\text{ m}$  panels which are folded over for launch. Each panel is formed by four  $0.65\text{ m} \times 1\text{ m}$  tiles mounted together. Each tile consists of 16 linear subarrays of 24 dual-polarised radiating elements. Each subarray is connected to a T/R module with independent connection for the two polarisations. The Antenna System is broken down in three subsystems: The Antenna Services Subsystem (ASS), the Tile Subsystem (TSS) and the Antenna Power Switching and Monitoring Subsystem (APSM).

##### *Antenna Services Subsystem*

The antenna is based on a mechanical structure consisting of five rigid CFRP frames and a RF distribution network consisting of two similar sets of CFRP waveguides running in parallel along the five panels (RFPF). In launch configuration, the five panels are stowed, folded over a fixed central one, and are held together by eight Hold-Down and Release Mechanisms (HRM) up to a preload of 31 kN. In order to avoid coupling with the launcher, this guarantees the first axial vibration mode frequency to be higher than 42 Hz.

Each HRM consists of a retractable telescopic tube levered by a secondary mechanism based on a non-pyrotechnic device (kevlar cable cut by a redundant thermal knife with a cutting time of less than 120 sec.) derived from well-proven solar array hold-down technology.

After release, the panels are sequentially deployed around four hinge lines by using a stepper motor, each, with 200:1 reduction harmonic drive, thus providing a high motorization margin (approximately 3 times the expected resistive torque). The final latching is performed with the eight built-in latches to achieve the final antenna planarity of  $\pm 4\text{ mm}$  in orbit (this including an apportionment of  $\pm 1.5\text{ mm}$  for the overall thermoelastic effects). Associated to inter-panel

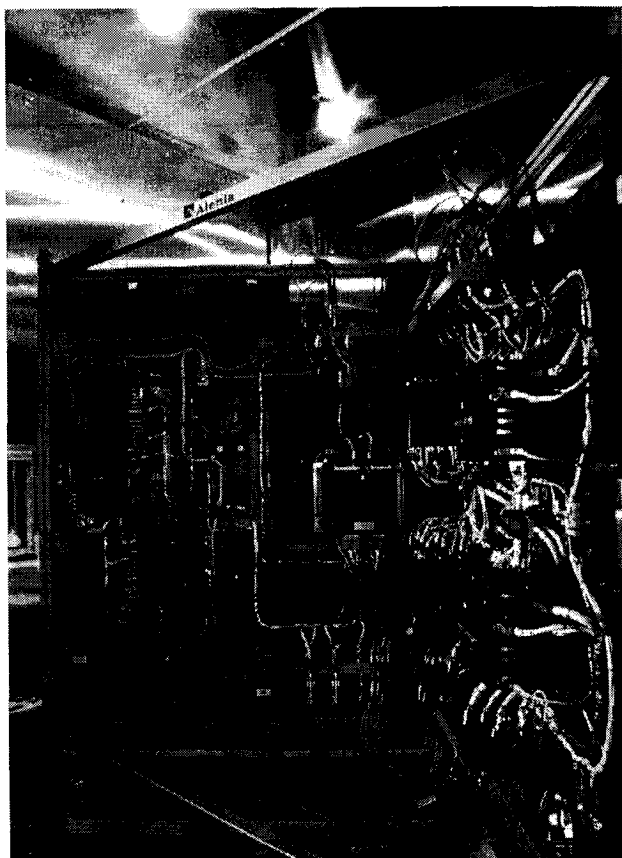


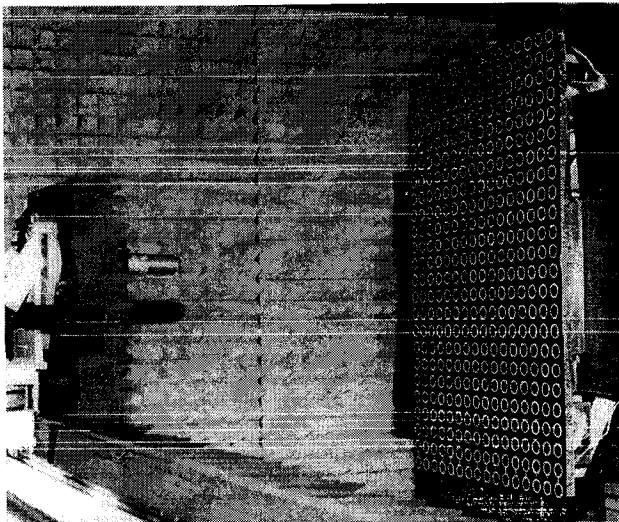
Figure 4: FM CESA during Thermal Tests at ALENIA

contact points, the latches ensure waveguide flange alignment and deployed rigidity of higher than 2.4 Hz to avoid AOCs disturbances. A specific unit (DCU) contains the electronics for driving and controlling the release, deployment and latching operations.

#### *Tile Subsystem*

Each of the twenty tiles is a self-contained full-operating subsystem which contains 4 power units (PSUs), a local control unit (TCIU), 2 RF distribution corporate feeds and 16 subarrays each one fed by a T/R module. The 16 subarrays are mounted together on a panel (*the Radiating Panel*) that provides the structural and thermal integrity to the tile.

The corporate feeds (one for signal distribution and another for calibration) are 1:16 power dividers made in microstrip on Duroid 6002. Each of the four Power Supply Units (PSU) provides power to a group of four T/R Modules and the TCIU. The control functions within the Tile are achieved by a Tile Control Interface Unit (TCIU) which is carrying out local control of the T/R Modules including temperature compensation and beamforming setting, it is transferring data and interfacing to the Control Subsystem. There is one TCIU per Tile using internal duplication for redundancy purposes.

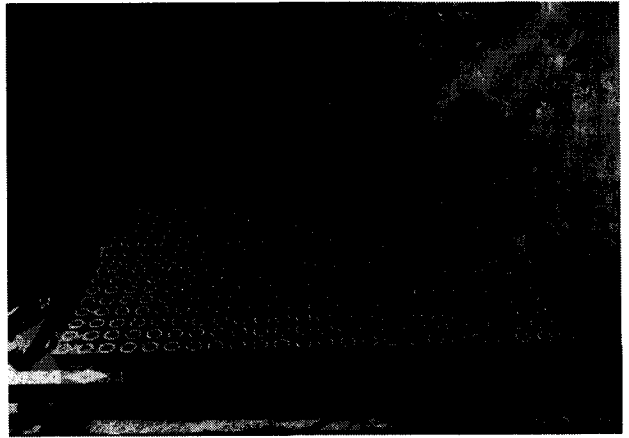


**Figure 6:** FM Tile during radiation tests at ALCATEL.

#### *Radiating Panel*

The subarrays and the modules are mounted on a supporting plate, thermally and mechanically decoupled. The subarrays are formed by 24  $\lambda$ -diameter ring slot radiating elements, electrically coupled to a dual-polarisation low-loss dispersion-free triplate feeding system which provides a constant phase and amplitude illumination.

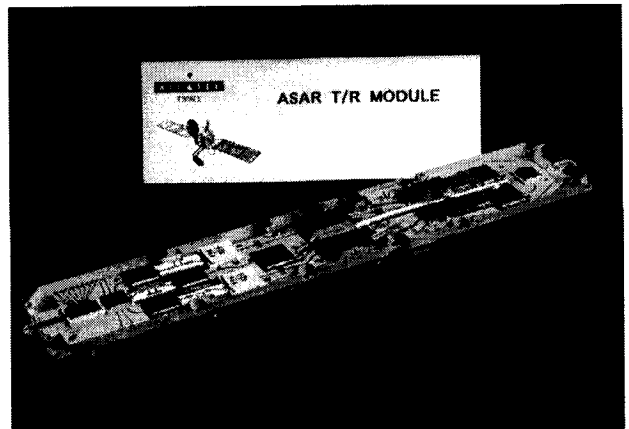
The measured radiating characteristics of the subarrays are showing a gain of 20.5 dB, loss of 1.5 dB, VSWR of -18 dB and a very good crosspolarisation better than -35 dB for both polarisations.



**Figure 5:** FM Radiating Panel

#### *Transmitter/Receiver Module*

Each module consists of two (H/V) transmit and one common receive chains, which amplify and control the signal of each individual subarray, in phase and amplitude. These functions are implemented using MMIC's, glued on etched TMM10i circuits, component interconnections performed by using parallel-gap welding (Au and Ag ribbons).



**Figure 7:** T/R Module

The input Phase Shifter (5 bits) is controlling the Tx/Rx signal, a SP3T switch selects either Tx (H/V) or Rx chains. On the Tx chain a Variable Gain Amplifier (VGA) provides 42 dB of control range, followed by a medium power driver. A Telettra Power Amplifier (SSPA of 10 W at 1 dB compression, 30% efficiency), provides the final output power. The connection to the subarrays is made via a Circulator/Isolator/Passive-Limiter (0.25 dB insertion loss in Tx, 1 dB in Rx, 35





**Figure 8: FM Antenna at MMS, Portsmouth**

dB isolation). On the receive side, a 1.3 dB NF LNA (CFY67 HEMT) is connected to the limiter, a SPDT switches the V/H chain to the common Rx path which includes a third VGA. For Calibration Purposes, a coupler (-24 dB) has been implemented at the output of the module to the antenna. The T/R Module is commanded by a serial link consisting of 3 signals: a data signal, a gated control signal and a strobe signal. The temperature of each T/R Module is monitored and used for correction of amplitude and phase setting.

#### ASAR QUALIFICATION PHILOSOPHY

The overall qualification of the ASAR instrument has been based on three Qualification programmes. The two subassemblies (CESA and ASA) were developed and qualified in parallel following independent qualification and acceptance programmes. They were preceded by a qualification programme which dealt with the new technologies planned to be used in the ASA subassembly.

##### *Qualification of new technologies*

The qualification of new technologies and components has been carried out from the early phases of the development and is, at present, successfully completed:

The GaAs foundry passed the ESA capability approval programme. The Telettra Hybrid Line, in which the Advanced Ceramic Microwave Modules (SSPA) are manufactured, passed the project qualification. TMM10/ACMM gluing, mounting and parallel-gap welding processes were also qualified. Two TRM manufacturing lines were put in operation at ALCATEL and MMS to achieve a production rate of 24 TRM per month. And SSPA, Phase Shifter, SP3T switch and SSPA driver were submitted to Type Approval Test Chart III and Chart IV (Operating Life of 2000 hours at  $T_j$  of 150°C).

##### *Central Electronics Subassembly*

The CESA has followed a standard AIT philosophy (see figure 9). Each equipment has been individually tested electrically. Proto-flight units were vibrated at qualification level and flight units were tested at acceptance levels. Thermal vacuum, EMC and additional electrical test were performed at subsystem level before delivery of the subsystems to CESA AIT.

Due to its large dimensions and based on the fact that the various subsystems had already been extensively tested and that the CESA will undergo thermal vacuum

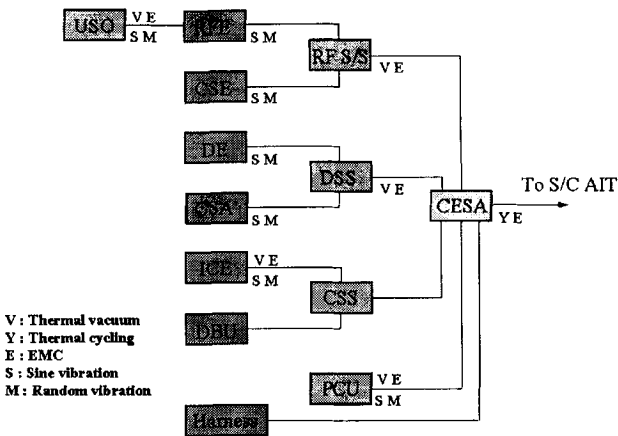


Figure 10: CESA AIT Flow Chart

and vibration tests as part of the spacecraft test campaign, the CESA was only tested at ambient pressure, in a climatic chamber. During CESA tests the overall operation was checked and performance related parameters were measured as part of the characterisation programme.

Since significant margin was demonstrated during the EMC tests on the CESA EM, reduced set of tests were carried out on the flight model. Most of conducted susceptibility tests were skipped because of the risk of over-stressing the flight hardware.

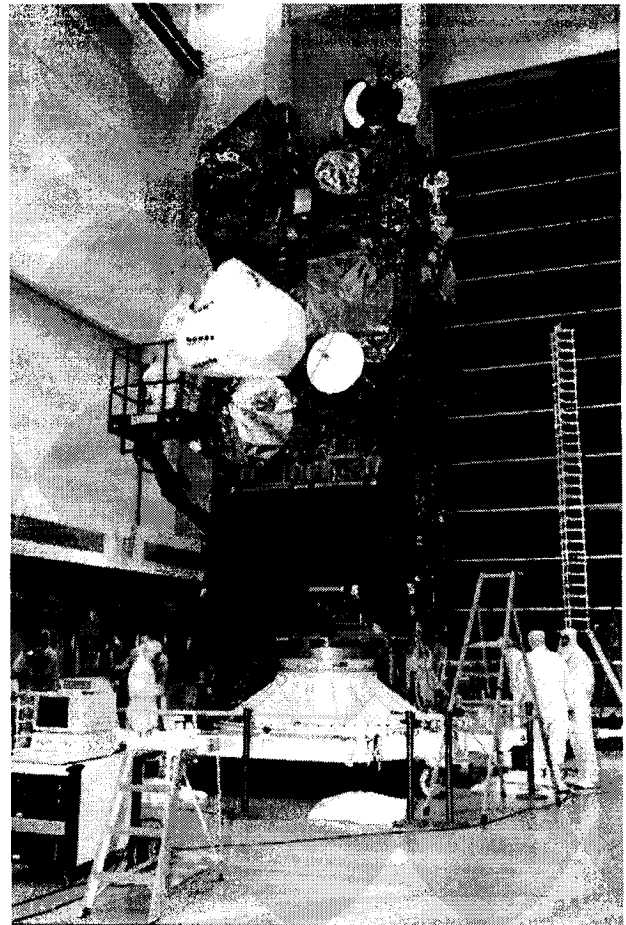


Figure 9: ASA EM and CESA FM on board ENVISAT

Antenna Subassembly

The philosophy and flowchart of the ASA Qualification and Test Programme is summarised in figure 10.

The down breaking of the instrument requirements to those of the two subassemblies, the various subsystems and the components, and the associated testing and qualification at the different levels, has been a complex exercise. The testing and qualification programmes have been balanced between the over-stressing of components and the under-qualification of the equipment.

The Antenna Services Subsystem (ASS) followed a standard Proto-Flight qualification programme. A flight-representative structural model of the Antenna Mounting Structure preceded the P-F Model for an early demonstration of the mechanical properties of the antenna. It has been later used on the Spacecraft Engineering Model during S/C qualification activities. The ASS PFM equipped with the Hold-down and Release mechanisms (HRM), the Deployment mechanisms (DEM), the Waveguide distribution

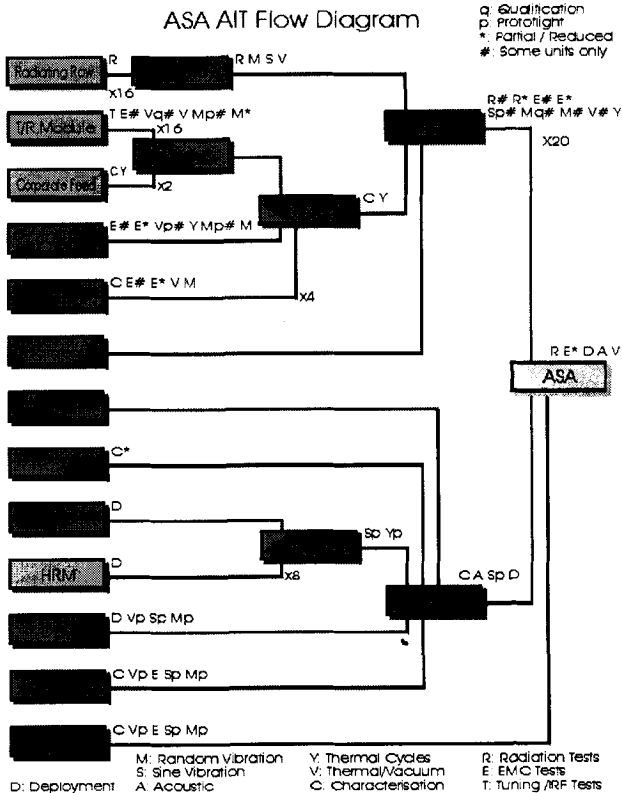


Figure 11: ASA AIT Flow Diagram

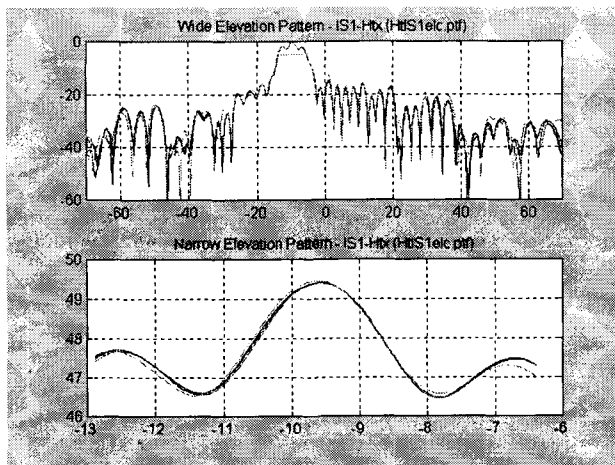


Figure 13: IS1 Tx H-pol Elevation Pattern

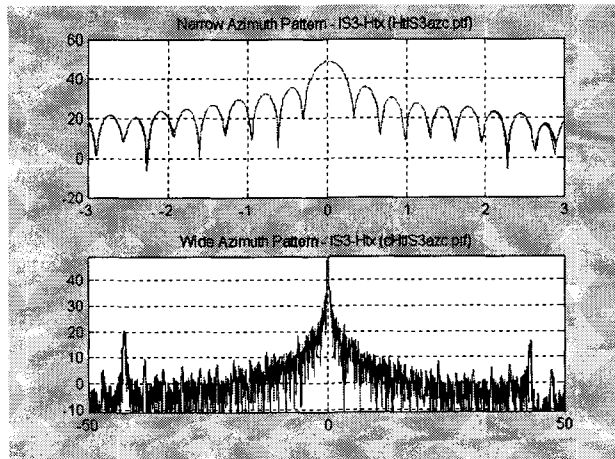


Figure 14: IS3 Tx H-pol Azimuth Pattern

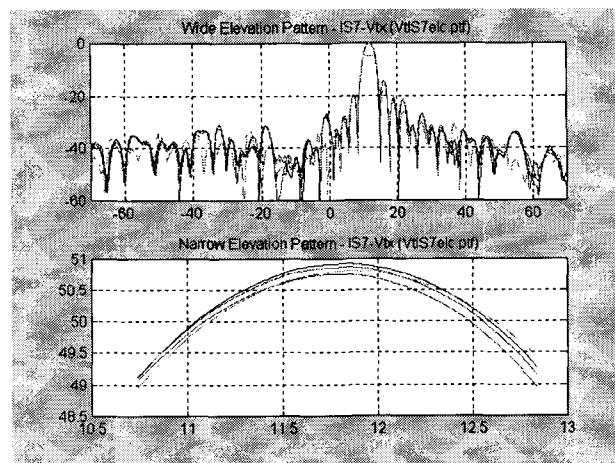


Figure 12: IS7 Tx V-pol Elevation Pattern

network (RFPF) and the Harness was completed with mechanically representative dummy tiles to stand mechanical qualification through vibrations and acoustics. Deployment operation was thoroughly

demonstrated by deployment tests in two antenna configurations: horizontally by the specially designed counter-balance gantry and vertically on the specially designed deployment system on air bearings.

The Tile Subsystem (TSS), comprising 20 Flight Model Tiles and one Flight Spare, followed a pseudo-series-production qualification programme: 4 preliminary Engineering Model Tiles demonstrated the operational requirements, a Qualification Model (EQM), flight-representative which incorporated the modifications from the EM programme, was qualified against standard QM requirements, and, in addition, a Flight Tile was tested to PFM levels to qualify the improvements later implemented. The rest of the FM Tiles followed a reduced acceptance testing.

After the completion of the TSS EM programme at ALCATEL, 3 EM Tiles and the EQM were integrated on the ASA reduced EM (a single panel) for instrument performance testing. The ASA EM has been later used at S/C level for System Tests.

The radiating performances of both antenna models (ASA EM and FM) were measured in the new Large Planar Near Field Range at MMS (Portsmouth). Full characterisation of the FM antenna was performed: 8 beams, two modes (Tx and Rx), two polarisations (V and H), in copolar and crosspolar components. Some patterns are shown in figures 12, 13 and 14. The Range has a scanning capability of  $22 \times 8$  metres, position accuracy of  $\pm 0.1$  mm and planarity of  $\pm 0.4$  mm that guarantees an accuracy of  $\pm 2$  dB at -40 dB relative level.

## PERFORMANCES AND BUDGETS

The inherent principle of the Synthetic Aperture Radar impedes the direct measurement of the ASAR instrument performances on Ground. The selected alternative is the computation of the instrument performance characteristics from measurable lower level parameters throughout the various stages of instrument tests. These parameters are called *Verification Input Parameters (VIPs)*. For most of the VIPs, tests at instrument level are not possible and, in order to measure them with high accuracy, they are measured at subassembly level.

From the VIPs and a certain number of assumptions and physical constraints, the ASAR high level performance parameters, called *Engineering Parameters (EPs)*, are computed by using a *Performance Evaluation and Analysis Software (PEAS)*.

Table 1: ASAR Performance Summary

Parameter	Unit	Image	Alternating Polarisation	Wide Swath	Global Monitoring	Wave
Polarisation		VV or HH	VV/HH, HH/HV, or VV/VH	VV or HH	VV or HH	VV or HH
Spatial resolution (az. x ra.) * except swath IS1	m m	27.5 x 28.1*	28.7 x 29.7*	149 x 145	949 x 977	27.5 x 29.6*
Radiometric Resolution	dB	1.54	2.46 to 2.50	1.45 to 1.72	1.35 to 1.44	1.54
Point Target Ambiguity Ratio						
- azimuth	dB	25.9 to 29.6	19.1 to 28.0	22.3 to 28.6	26.6 to 29.3	27.3 to 29.6
- range	dB	31.6 to 45.8	26.4 to 40.5	25.0 to 33.9	25.0 to 32.2	31.2 to 45.7
Distributed Target Ambiguity Ratio						
- azimuth	dB	22.6 to 24.7	18.1 to 24.5	20.3 to 24.9	24.6 to 27.5	22.6 to 24.7
- range	dB	17.1 to 39.4	17.1 to 39.4	17.1 to 30.8	17.1 to 30.8	21.2 to 47.7
Radiometric Stability ( $1\sigma$ )	dB	0.32 to 0.40	0.50 to 0.55	0.32 to 0.42	0.46 to 0.53	0.55 to 0.60
Radiometric Accuracy ( $3\sigma$ )	dB	1.17 to 1.38	1.62 to 1.81	1.20 to 1.45	1.54 to 1.74	1.80 to 1.94
Noise Equivalent $\sigma_0$	dB	-19.6 to -22.1	-19.4 to -21.9	-20.9 to -26.2	-31.5 to -35.0	-19.8 to -22.4

During the on-Ground test campaign, a certain number of *Characterisation Parameters (CPs)* are also measured or computed from lower level test results. The CPs will be used by the Ground Segment to produce the final data products within the required specifications.

Finally, a limited set of additional parameters will be acquired during the in-Flight external calibration and Characterisation and provided to de Ground Segment.

Based on the VIPs measured at FM subassembly level, the predicted end-of-life performances of the ASAR instrument in terms of Spatial Resolution, Ambiguity Ratios, Noise equivalent  $\sigma_0$  and Radiometric Resolution, Accuracy and Stability are summarised in Table I. They are to be within the agreed specification. In most of cases, they present a large margin with respect to it. Nevertheless, an area of some concern remains in the Distributed Target Range Ambiguity Ratio of IS3 and, to a lesser extent, the farther swath. It should, however, be born in mind that the  $\sigma_0$  model for land and sea/ice used for the computation of the ASAR performances is very severe, making the specification extremely difficult to achieve when Near-in Range Ambiguities are present due to geometry.

The flexibility of the ASAR instrument allows to constantly adjust the power consumption by varying the transmit duty ratio. The current budget on power consumption, compatible with the instrument performances mentioned above, ranges from 1365 W in Image and Alternating Polarisation modes down to

645 W in Wave mode, compared to a Platform Capability Payload Average Power of 1900 W.

The Antenna Mass has been a critical issue from the early phases of the ASAR programme. A significant effort has been done to keep it to a reasonable value of 750 kg. The overall ASAR mass budget estimates 830 kg based on existing hardware (requirement being 850 kg for an overall platform capability of 2145 kg)

#### REFERENCES

- [1] R. Torres, C. Buck, J. Guijarro and J-L. Suchail (ESA-ESTEC, NL). "ESA's Ground Breaking Synthetic Aperture Radar: The ENVISAT-1 ASAR Active Antenna". APS'99.
- [2] J-L. Suchail, C. Buck, J. Guijarro and R. Torres (ESA-ESTEC, NL). "The Development of ENVISAT-1 Advanced Synthetic Aperture Radar". RADAR'99.
- [3] P. Mancini, J-L. Suchail, R. Torres, J. Guijarro and C. Buck (ESA-ESTEC, NL). "The ENVISAT-1 Advanced Synthetic Aperture Radar. The Development Status". CEOS'98.
- [4] J. Guijarro, C. Buck, P. Mancini, J-L. Suchail and R. Torres (ESA-ESTEC, NL). "The Development of the ENVISAT-1 ASAR". IGARSS'96.
- [5] S. Karnevi, Y-L. Desnos, J-L. Suchail (ESA-ESTEC, NL), D. Hurd (Matra-Marconi Space, UK). "The ENVISAT-1 Advanced Synthetic Aperture Radar System Calibration". IGARSS'95. July 10-15, 1995.

## ENVISAT/ASAR Precision Transponders

Harry Jackson (1), Ian Sinclair (2), Sebastian Tam (2)

(1) SerCo Facilities Management BV, under contract to ESTEC  
TOS-ETP, 2200 AG Noordwijk ZH, The Netherlands  
Tel: (31) 71-565-3382, Fax: (31) 71 565 4596  
[hjackson@estec.esa.nl](mailto:hjackson@estec.esa.nl), [www.estec.esa.nl](http://www.estec.esa.nl)

(2) MPB Technologies Inc.  
151 Hymus Boulevard, Pointe Claire, Québec, Canada H9R 1E9  
Tel (1) 514-694-8751, Fax (1) 514-695-7492  
[Ian.Sinclair@mpb-technologies.ca](mailto:Ian.Sinclair@mpb-technologies.ca) and [Sebastian.Tam@mpb-technologies.ca](mailto:Sebastian.Tam@mpb-technologies.ca)  
[www.mpb-technologies.ca](http://www.mpb-technologies.ca)

### ABSTRACT

MPB Technologies Inc. is currently building the Radio Frequency (RF) and control units for a suite of three transponders for the European Space Agency. The transponders are instrumental in the external characterization of the Advanced Synthetic Aperture Radar (ASAR) mounted on board ENVISAT. The prototype transponder was designed and built at ESTEC [1]. This paper presents the operation of the transponders, and describes the final design, integration and testing of the production RF and control transponder units.

Like the earlier ERS-1/2 and RADARSAT-1 transponders [2,3], these units provide a *constant RCS mode*, with constant gain radiometric response, and an *azimuth pattern mode* to allow for amplitude recording of the satellite pass. In the ASAR transponders, two further modes have been added - a *characterization mode* to assist in the commissioning and monitoring of ASAR, and an experimental *phase-stable mode* to provide point target echoes with stabilized phase response.

### WHY TRANSPONDERS?

Transponders form a vital part of the ground segment for satellite-borne SAR. Normally placed on flat, low clutter terrain, these devices offer absolute calibration of the SAR image. They provide a point target of sufficient accuracy for end-end radiometric calibration of ASAR.

The ASAR transponder, at 5.33 GHz, provides a radiometric echo equivalent to a radar cross section (RCS) of about 57 dBsm. In the raw data this is typically 10-20 dB lower than the background response. The post-processing response is typically 40 dB higher than the background and is suitable for calibration and image quality analysis

This design also offers a signal receiver for characterization of active SAR systems. By receiving transmissions from individual rows of the ASAR antenna, they help to verify on-board monitoring of relative phases of the rows. With this information, the ASAR can be tuned to produce an optimal beam shape in elevation. Additionally, the transponder can check the on-board time datation, by recording accurate time with the calibration data

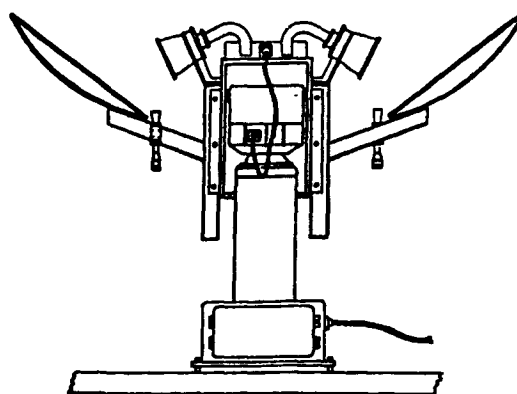


Fig. 1: Transponder RF unit, with pedestal and antennas.

### OVERVIEW OF TRANSPONDER FUNCTIONS

Each ASAR transponder operates in four modes. Two of these allow the device to operate as a point target, with an echo back to the satellite, and two modes permit it to operate as a receiver.

#### Constant RCS Mode

The function of the device in constant RCS mode is to retransmit a signal to the SAR with a calibrated, very stable gain, to allow external calibration of the SAR. While internal calibration is carried on continuously, external calibration is the only way to provide overall end-end calibration.

The transponder gain stability is expected to be 0.15 dB for the ENVISAT/ASAR transponders, necessary to allow ASAR calibration. In the ASAR calibration scheme, the observations of the known target are integrated to provide a calibration-scaling factor. This applies to all imaging modes, and is performed separately for HH, HV, VH and VV polarizations.

The polarization choice drove the design of the ERS-1, Radarsat-1 and ASAR transponders in different ways. ERS-1 was VV, and a single transponder polarization was provided. Radarsat-1 was HH, but there was a desire to see ERS-1 and ERS-2 as well; so a 45° polarization was chosen. For ASAR, separate calibration was demanded for VV, VH, HV and HH, so a dual-polarized horn with switch-selectable polarization was installed.

Phase-stable mode

A phase-stable transponder mode is also provided. This is an experimental mode included for use with differential interferometry. A bright reference target is provided at fixed phase. Such a target could, in principle, allow path differences between the transponder and points in its surrounding area to be known to a high precision, for possible mapping purposes.

Azimuth Pattern Mode

The azimuth pattern mode involves detection and measurement of the amplitudes of received SAR pulses, using a log detector. This confirms the expected along-path beam pattern for the ASAR phased array, as determined by the elements along each row.

Fig. 2 shows a pattern received from ERS-1. This is typical of satellite-borne SAR azimuth patterns. The entire trace is recorded in about five seconds, as the satellite passes the recording site.

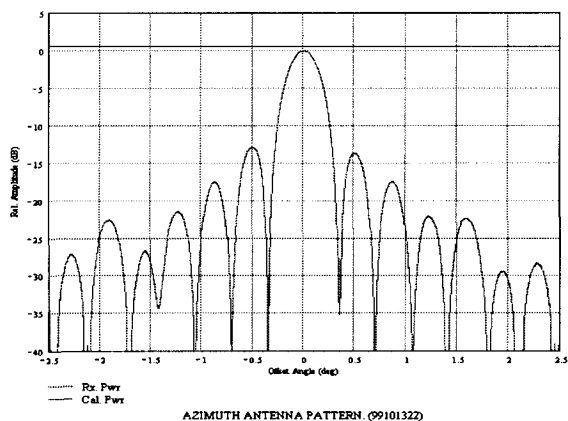


Fig. 2: Recorded azimuthal pattern of ERS-1.

Characterization Mode

Characterization mode is a mode specific to the monitoring of the average amplitude and phase of rows of TR modules in an active SAR array. It involves IQ detection of the received pulses, so that both amplitude and phase are measured and recorded. The characterization measurements are made on five ascending and five descending passes, and involve a pre-defined transmission sequence.

The ASAR antenna (Fig. 3) consists of 320 elements, arranged in a 10 by 32 matrix. There are 32 rows and 10 columns.

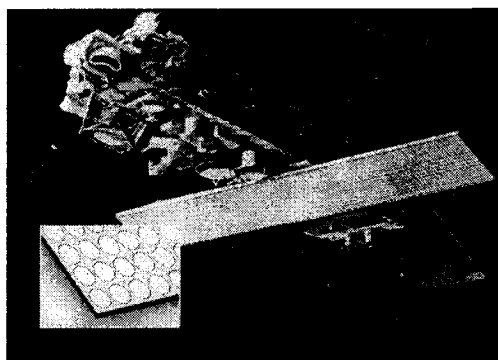


Fig. 3: Concept view of ENVISAT ASAR [Courtesy MMS]

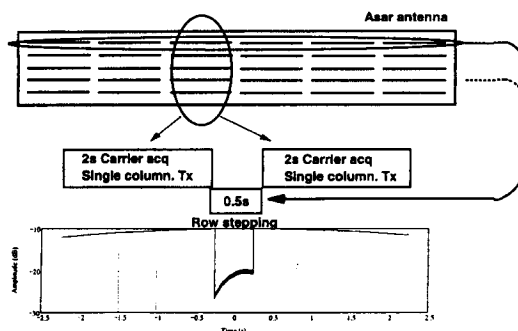


Fig. 4: Time sequence during ASAR characterization.

During the characterization sequence the instrument transmits pulsed CW signals. The frequency of these signals is offset from that of the normal ASAR carrier frequency (CF) by some 750 kHz. A single column of elements is activated for two seconds (Fig. 4). This is followed by a quasi-random row sequence, one pulse per row, for 0.5 seconds. The sequence finishes with another two-second period of single column transmission. The whole event is timed to coincide with alignment of the ASAR antenna with the receiver.

The row signal typically shows a smooth rise and fall in amplitude during the 0.5-second recording interval. It is some 10 dB below the signal due to the column transmission, because of the smaller number of transmitting elements.

The row data contain phase components due to the offset frequency of the carrier, the motion of the satellite and earth rotation. Post-processing fits models to the data, removing these phase components. The row signal can then be used to identify signals emanating from each row in the ASAR antenna. The amplitude and phase of the signals from each row, compared with the onboard measurements of these same signals, allow the phase offset errors of each row to be assessed. By looking at the linear phase component across all 32 rows, the ASAR antenna electrical elevation boresight with respect to the transponder position can be estimated.

During the row transmission time, the 43 pulses emitted from each row are available to be averaged. Tests show errors of only 0.005 dB in amplitude and  $0.06^\circ$  in phase between simulated signals and processed results (Fig. 5).

In addition, all received signals are precisely time-tagged using GPS. In characterisation mode, the transition from single column to row stepping operation is easily detected, and permits verification of the time tagging of onboard data.

#### Operating Sequence

The operation of the transponders is entirely under computer control. When a satellite pass is due, the transponder antennas are pointed toward the expected satellite direction, at the point where the SAR beam is expected to peak. The RF electronics are powered up, and set to the desired operating mode. The equipment locks in about 3 minutes, but is allowed to stabilize

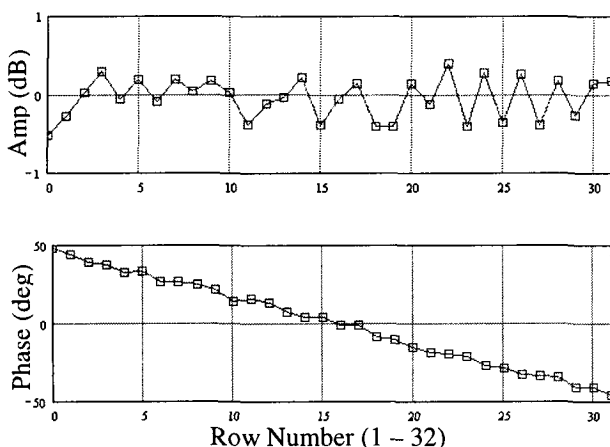


Fig. 5: Residual row errors in test signals

thermally for (1 hour). In order to avoid false triggering, the system only responds to signals of nominal pulse width and PRF. For characterization mode, row phase and amplitude profiles are then processed. Both received and processed data are then transferred to a central site by the public telephone system, and the transponder then goes to sleep (by parking the antennas and powering down the RF electronics).

In radiometric or azimuth pattern modes, the peak signal from the ASAR passes in less than one second, with sidelobes taking up several seconds before and after the main lobe. In characterization mode, the sequence lasts for 4.5 seconds, owing to the broader pattern presented by radiation from a single column.

### TRANSPONDER OPERATION

#### Radiometric Modes

The principle of the radiometric transponder operation is illustrated in Fig. 6. The satellite signal enters the circuit at antenna Rx, follows the route marked by the heavier line, and is retransmitted from antenna Tx. Along the course of this circuit, it is amplified by a net 38 dB, and delayed by 1.5  $\mu\text{sec}$ . After range processing of the ASAR image, the delay gives good separation of the primary transponder response and coherent interference due to residual antenna crosstalk.

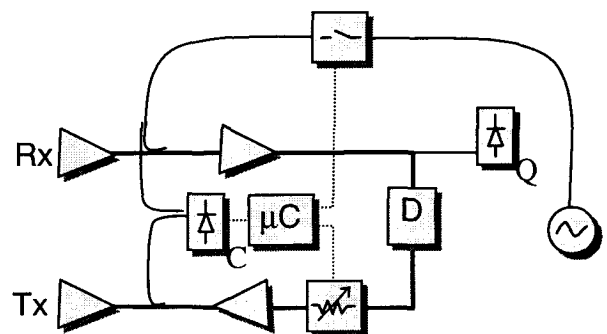


Fig. 6: ASAR radiometric calibration transponder scheme.

The delay also displaces the apparent echo location by several hundred meters. This can have a beneficial affect by displacing the signal away from any buildings near the transponder and onto a low clutter terrain.

In *constant RCS mode*, the gain of the ERS-1 transponder signal is flat to  $\pm 0.1$  dB, with  $\pm 0.1$  dB stability over three years. This gain stability is achieved by a pulse calibration circuit, as depicted by the lighter line in Fig. 6. A series of pulses is fed to the circuit near its input. These go around the main RF circuit, with a 1.5- $\mu\text{sec}$  delay, and are then detected at the internal calibration detector C. The original pulse,

without the delay, is also detected. The amplitudes of the delayed and direct pulse are compared, and any error nulled using the control attenuator in the main RF circuit. The RF unit gain is therefore stabilised and dependent only on the coupling constants between the calibration circuit and the receiver/transmitter chain. Neither the calibration pulse amplitude nor the detector sensitivity affects the stability.

When qualifying pulses from the satellite are detected at the signal-qualifying detector, this calibration sequence is turned off.

ASAR presented some new challenges to the precision transponder designers. This system required measurement of the signals with both amplitude and phase, so an IQ receiver was included in the circuit. There was also an opportunity to create a phase-stable transponder mode for experimental purposes.

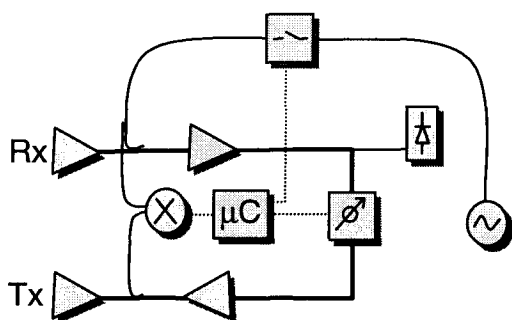


Fig. 7: Phase-stable transponder scheme.

The principle of the *phase-stable mode* is illustrated in Fig. 7. In order to allow for this mode, a variable phase shifter was included in such a way that it could optionally be switched into the circuit in place of the delay line. The pulses travelling around the circuit would then arrive at the location of the internal calibration detector at the same time. (The internal calibration pulse is made longer than the delay time, allowing the signals to overlap for a period of time.) By means of a coupling arrangement, signals are simultaneously routed to a mixer, and the mixer signal is fed into the internal calibration controller. By adjusting the variable phase shifter, this mixer output can be nulled, thereby stabilizing the circuit at a given phase shift.

#### Receiver Modes

The two receiver modes necessitated changes to the detector circuitry from that of the earlier transponders. As illustrated in Fig. 8, the single qualifying detector was augmented by an IQ detector circuit.

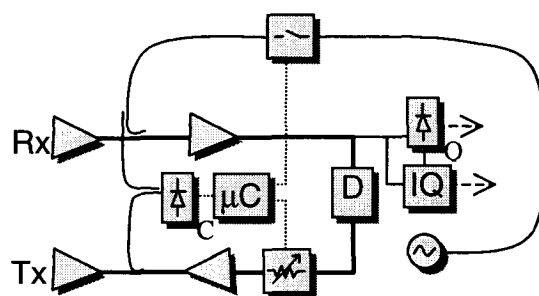


Fig. 8: Schematic showing receiver operation.

In azimuth pattern mode, the signal is received at the qualifying detector Q, then digitized and recorded. The detector is coupled with a log amplifier, to give a dynamic range of 55 dB. Calibration markers may be mixed with the received signal at intervals, to allow off-line calibration of the recorded data (Fig. 9).

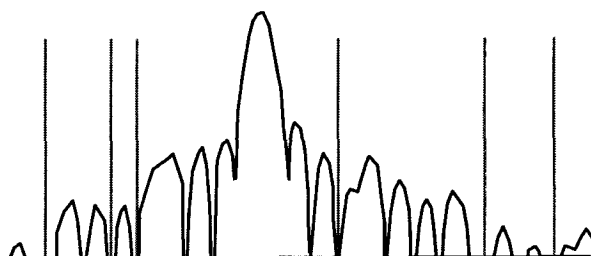


Fig. 9: Received azimuth pattern signal with embedded calibration markers.

In characterization mode, the signal is digitized after being split into I and Q components by a quadrature mixer. These components are produced by mixing the incoming ENVISAT/ASAR signal with a local oscillator signal that is offset by 50 kHz from the characterization carrier frequency. High gain and low gain amplification of the incoming ASAR signal is available in the IQ circuit. For characterization mode, high gain is chosen by optionally switching in an additional amplifier.

The transponder, as designed by ESTEC and altered slightly by MPB Technologies Inc. (MPBT), incorporates these various modes through a series of switches activated in response to commands from a Control Unit. Several Complex Programmable Logic Devices (CPLDs) internal to the RF unit control the operation of the switches, and keep control of the gain and phase calibration loops.



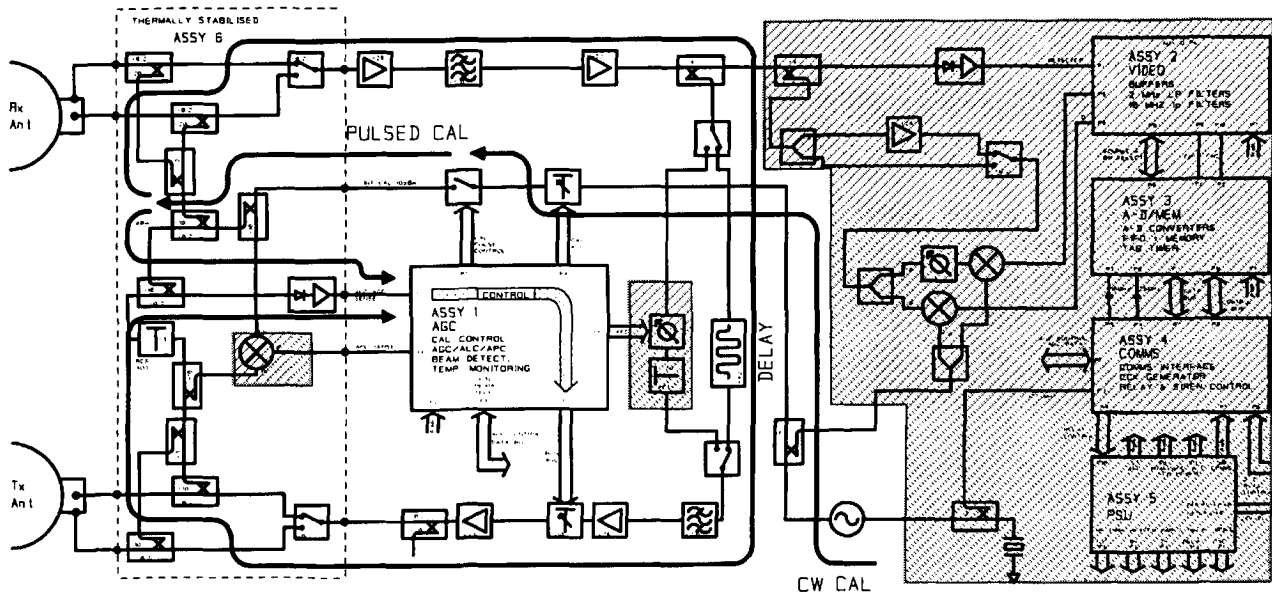


Fig. 10: Constant RCS operation shown against a more complete circuit schematic.

A fuller circuit schematic is shown in Fig. 10. Here, most of the components may be seen in their correct circuit locations, allowing all four operating modes to be invoked in the same device. Fig. 10 illustrates the stabilization phase of the Constant RCS mode. The path of the calibration pulses is shown by the heavier lines; unused portions of the circuit are cross-hatched.

At the baseband end, several printed circuit boards handle the video processing, the analogue to digital conversion, and the onward transmission of these data to the control unit. At the video board, bandwidths of 2 or 20 MHz may be selected. The narrow, 2 MHz bandwidth is selected for the characterization mode (for better signal to noise), while the 20 MHz bandwidth is used for most other operations. (This permits regular ASAR signals to be recorded, with their linear chirped modulation).

#### TRANSPONDER PRODUCTION

MPB Technologies Inc. was contracted by ESA to produce three operational units based on the ESA/ESTEC prototype transponder. The design was first reviewed, and predicted operational signal levels of all RF components were checked. Certain obsolete components were replaced, and the documentation was completed so production could proceed. There were few changes, aside from some packaging modifications. MPBT was pleased to be able to include some more recent computer equipment, to support the control software that had been developed in The Netherlands.

The ESA prototype unit was subjected to temperature testing at MPBT, in order to establish a baseline for the performance of the three MPBT-produced units. One unit has been completed, and has so far met the same standards as the ESA prototype unit in transponder mode at room temperature. Two other units are being wired at this time, and will be ready for testing later this fall.

Thanks to good cooperation between ESA and MPBT, the units are scheduled to be ready some six months ahead of schedule. By working together technically, and by frequent communication by E-mail, we were able to solve problems as they arose.

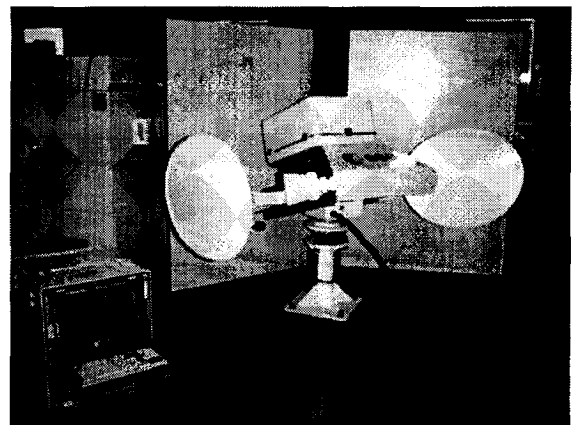


Fig. 11: Prototype Transponder unit at ESTEC

### TRANSPONDER CALIBRATION

When the RF units are installed on the pedestals at ESA and integrated with the antenna units, one more major task will remain before installation in the field. That is to calibrate the transponders themselves, in order to confirm their equivalent radar cross section. These measurements will be performed as they were for the ERS-1 and the Radarsat-1 transponders – a round, flat plate, about 1 meter in diameter, is mounted on top of a building, near an outside corner. This plate is directed at the transponder by the use of a bore-sight telescope.

The calibration makes use of the internal calibration pulses in the transponder. By transmitting these pulses, they may be reflected from the round plate. Because of the 1.5- $\mu$ sec internal delay in the transponder (and with appropriate choice of range), a decaying series of pulses is produced. From this sequence of pulses, and consideration of the radar range equation, the net RCS of the transponder may be determined.

In spite of the low-sidelobe antennas used in the transponder, multipath in the flat-plate calibration is inevitable. Secondary reflections from the vicinity of the flat plate target are a major concern, and are difficult to compensate for. The only practical answer is to find a structure that offers minimal secondary reflections. In addition, a ground reflection is mixed in with the direct signal. This effect is assessed by taking measurements at different positions of the transponder along a path a few meters toward the target. The total signal typically rises and falls sinusoidally with distance, because of the mixing of the direct and ground-reflected signals. The effect of the interfering multipath signal can then be estimated by fitting a model of the multipath effect to derive the direct signal.

### TRANSPONDER POSITIONING

The three transponders are to be located in Flevoland, The Netherlands, arranged on an east-west line. The three devices cover the approximately 100-km wide beam pattern as it sweeps along parallel to the north-south satellite path. At 20 km spacing, the three units provide calibration across the swath, and azimuth beam shape at three points in the elevation pattern. (Fig. 12).

Further, the location was a crossing point for the ascending and descending swaths during the 35 day repeat orbit. ENVISAT has a similar orbit, and so Flevoland remains an optimum location.

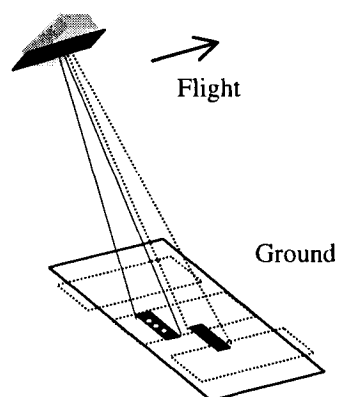


Fig. 12: Three transponders in relation to the ASAR image mode swath pattern. [4]

### FUTURE OF TRANSPONDERS

As satellite-borne SAR gets more sophisticated, we expect that increasingly capable transponders will be required in the future. They are a reliable means of producing external calibration of ASAR systems. Operating both as re-transmitters of the ASAR signal, and as calibrated receivers, they will continue to form a vital part of ASAR calibration schemes.

Some countries are investing significant amounts in ground stations, in order to get a steady and reliable source of SAR images of areas of interest to them. These images could be enhanced with local calibration.

### REFERENCES

- [1] H. Jackson and D. Hannes, "Characterization / calibration for the ENVISAT/ASAR", CEOS SAR Workshop, ESTEC, 3-6 February 1998, p. 247.
- [2] R.K. Hawkins, L.D. Teany, S. Srivastava, S.Y.K. Tam. "Radarsat Precision Transponder". *Adv. Space Res. COSPAR* 19(9), 1997, pp. 1455-1465.
- [3] H. Jackson and A. Woode, "Development of the ERS-1 active radar calibration unit", *IEEE Trans. on Microwave Theory and Techniques*. Vol 40, No. 6, June 1992, pp. 1063-1069.
- [4] A. Woode, Y-L Desnos and H. Jackson, "The development and first results from the Esrec ERS-1 ARC unit", *IEEE Transactions on Geoscience and Remote Sensing*, Vol. 30, No. 6, Nov 1992.

# THE ENVISAT ASAR PROCESSOR AND DATA PRODUCTS

Y-L. DESNOS, H. LAUR\*, J. CLOSA\*, P. MEISL\*\*

ESA - ESTEC - ENVISAT Project - P.O. box 299 - 2200 AG NOORDWIJK, THE NETHERLANDS  
email: ydesnos@estec.esa.nl Tel.: (31) 71 565 4927 Fax: (31) 71 565 3191

\*ESA-ESRIN- ENVISAT Payload Data Segment Team Frascati, ITALY

\*\*MacDonald Dettwiler, Richmond BC, Canada

## ABSTRACT

An Advanced Synthetic Aperture Radar operating at C-band (5.331 GHz) has been selected for the Envisat payload ensuring continuity of ERS SAR and featuring enhanced capability in terms of coverage, range of incidence angles, polarisations, modes of operation. This paper presents the key features of the Envisat ASAR system. The ASAR instrument modes of operation are discussed. The ASAR Ground Processor is presented highlighting the concepts for its development and the performance achieved versus the ESA specifications. The selection of processing algorithm for each product is discussed based on the image quality requirements and the throughput requirements. Finally an ERS processor used for the simulation of ASAR products is introduced.

## INTRODUCTION

The Advanced Synthetic Aperture Radar (ASAR) has been selected for the European Space Agency Envisat payload and features large swath coverage, multiple choice of incidence angles, polarisations and modes of operation.

In section 2 the ENVISAT ASAR System is introduced and the different modes of instrument operation are described. In section 3 the ASAR data collection and processing are presented. In section 4 the processing algorithms are detailed. In section 5 and 6 the ESA ASAR products and their quality are presented. Finally in section 7 is described an ERS processor used for the simulation of ASAR products.

## ASAR SYSTEM OVERVIEW

The ENVISAT ASAR instrument design uses an active array antenna with 320 Transmit Receive modules (T/R) to produce a versatile position of the imaged swath by beam steering in elevation. Additionally, a large swath coverage (400km) is achieved using the SCANSAR technique at medium resolution (150m) or low resolution (1 km). All operating modes feature the possibility to select H or V polarisation on transmit and receive (HH or VV) and the alternating polarisation sub-modes allow to use a combination of both (HH and VV, or HH and HV, or VV and VH). Finally a more

versatile wave measurement mode is offered to the users with 100 km spacing between vignettes and the capability to select the position alternating between 2 positions in any swaths (see figure 1).

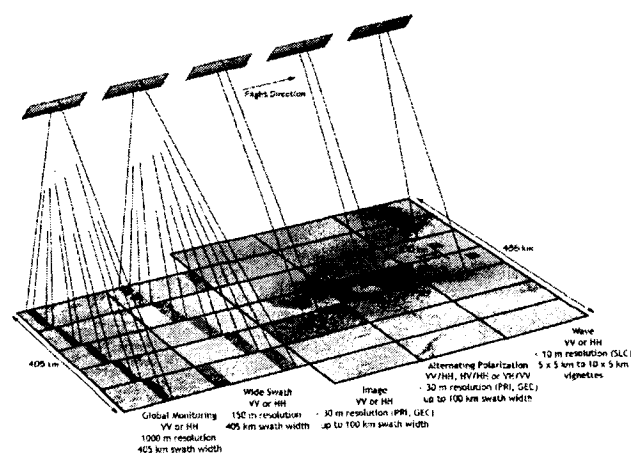


Figure 1: ASAR modes of operation

The ASAR operating modes are mutually exclusive and could be classified in two categories. Low data rate modes for Global Monitoring (GM) and Wave (WV) modes with systematic on-board recording and operation capability up to 100% of the orbit. High data rate modes for Image (IM), Alternating Polarisation (AP) and Wide Swath (WS) with high data rate (100Mbit/s) and operation time up to 30 minutes per orbit (including 10' in eclipse). Data may be transmitted in real time via X band channel to the ground or Ka band channel to the Data Relay Satellite or recorded on-board using the Solid State Recorder for later dump.

More detailed information on the ASAR instrument and calibration is available in the companion papers [5], [6].

## ASAR DATA PROCESSING

The development of the ASAR processor and products is based on three concepts mainly derived from the ERS experience:



*Figure 2: Example of Image Mode Medium Resolution Product (from ERS data) located on the Walgreen Coast in Antarctica.*

- the need for users to have identical products independent of which production facility generate them,
- the preservation of the specifications of the existing ERS SAR high-resolution products (SLC, PRI, GEC) and the introduction of new products (medium resolution and browses)
- the capability to generate a large amount of products in near real time.

Following the above concepts, ESA has developed with Alcatel Space Industries and MDA an ASAR Generic Processor (PF-ASAR) able to process data from all the ASAR modes. PF-ASAR will be installed in the ESA Payload Data Handling Stations (Kiruna and ESRIN-Frascati) and in the ENVISAT Processing and Archiving Centers (PACs) and national stations offering ESA ASAR services. The use of PF-ASAR will insure product compatibility between the different processing centers (same format and processing algorithm) and will simplify product validation.

One of the key features of PF-ASAR is the capability to process acquired data to generate medium resolution products (150 m, example in Figure 2) or low resolution product (1 km) and their corresponding browse images in stripline without geometric or radiometric discontinuity. The stripline image products contain data for an entire acquisition segment up to 10 minutes for Image, Alternating Polarisation or Wide Swath modes and up to a complete orbit for the Global Monitoring mode.

PF-ASAR will be used to insure the systematic processing in near real time of all received high rate data to generate medium resolution and browse products. All Wave mode or Global Monitoring mode data will be also systematically processed in near real time.

Furthermore PF-ASAR will allow to process High Resolution Products from Image or Alternating Polarisation acquisitions (Precision Images, Single Look Complex or Ellipsoid Geocoded products) in near real time or off line depending on user requests. Figure 3 shows an example of Precision Image and Figure 4 an example of Ellipsoid Geocoded Image.

PF-ASAR is targeted to run on an IBM SP-2 parallel computer system and is designed to insure a throughput linearly proportional to the number of processing nodes available in the station.

## ALGORITHMS

The Range Doppler algorithm is used for the image mode precision and geocoded products and for the complex products for both image and alternating polarization mode. Range Doppler is used in order to meet the stringent image quality requirements while still maintaining good throughput.



Figure 3: Example of IMP product of Bathurst Island in Canada (from ERS raw data).

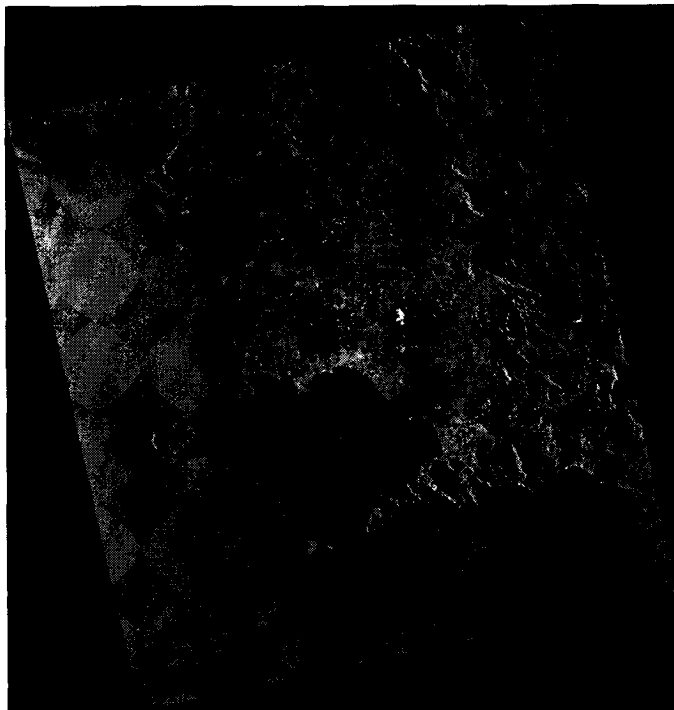


Figure 4: Example of IMG product of the Bay of Naples in Italy (from ERS raw data).

Range Doppler is also used to produce the SLC imagettes for wave mode. These imagettes are used as the input to the wave mode cross spectra algorithm. The cross spectra algorithm was developed by NORUT Information Technology [1]. This algorithm is an improvement over the one used for ERS since it allows the wave direction to be determined with no ambiguity and it compensates for the speckle bias (see example of wave mode products in Figure 5).

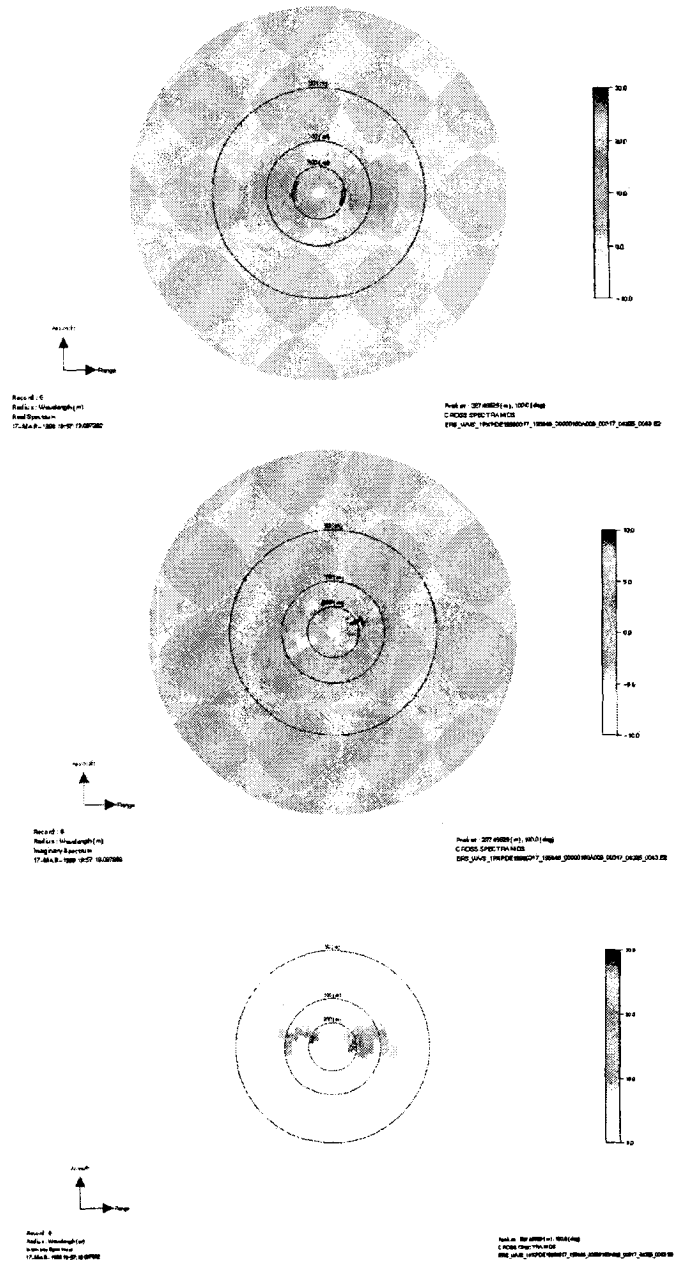


Figure 5: Example of real part (top), imaginary part (mid) and intensity spectra (bottom).

The SPECAN algorithm is well suited to burst-mode data and as a result is used for most AP, WS, and GM mode products. The efficiency advantages of SPECAN are also a reason for its use for all medium resolution (stripline) products. These products are produced systematically and therefore throughput is very important.

A modified version of the Range Doppler algorithm [2] was developed for the AP SLC product. The algorithm was chosen such that the output product would be useful for Interferometric SAR. The algorithm is a modified phase preserving Range Doppler approach. The processed Doppler bandwidth is made equal to four burst bandwidths (multi-burst processing) so as to keep as much of the signal information as possible while maintaining radiometric quality. The resulting product has a modulated impulse response but contains all the necessary information required for Interferometric SAR (InSAR). One method to remove the modulation during InSAR post-processing is to use the short FFT approach [3] to select the common spectra between the two image pairs.

During preprocessing, PF-ASAR performs raw data analysis, noise processing and the processing of the ASAR calibration pulse data. Chirp replicas and antenna pattern gain factors are obtained from the calibration pulse processing. The signal data for all modes is FBAQ decoded prior to processing (from 2, 3 or 4 bits back to 8 bits).

#### ASAR PRODUCTS AND THEIR QUALITY

The complete list of ESA ASAR Products is provided in Table 1 with specific identification (bold) of the products generated on request: PRI, SLC and GEC products of Image and Alternating Polarisation modes. All other products are generated systematically when ASAR is acquiring data in the relevant mode.

Table 1 also identifies the stripline products (italic) which are generated using the stripline capability of the ASAR Generic Processor. The stripline image products contain image data for an entire segment with geometric and radiometric continuity up to a maximum size of 10 minutes for Image Wide Swath and Alternating Polarisation modes and up to a full orbit for the Global Monitoring mode. The optimisation of the product quality has been performed in Wide Swath and Global Monitoring mode by using the inherent flexibility in the instrument setting (e.g. possible transmit chirp bandwidth setting using the digital chirp generator) and the capability in the Generic Processor to generate a desired number of range looks.

#### IMAGE CHARACTERISTICS

The image quality specifications are summarized in Table 2. PF-ASAR meets all of these specifications for all products and modes with the exception of those specifications that cannot be met in GM mode due to the low time-bandwidth-product of the signal. The product quality (equivalent number

of looks) which has been measured during acceptance testing of the ASAR Generic Processor are presented in Table 3.

Table 1 : ASAR Products generated with PF-ASAR

Mode and Product Name	Nominal Resolution (m)	Pixel spacing (m)	Approx Coverage (km)
<b>IM precision IMP</b>	30 x 30	12.5 x 12.5	56-100 x 100
<b>IM single look IMS</b>	9slant x 6	natural	56-100 x 100
<b>IM geocoded IMG</b>	30 x 30	12.5 x 12.5	100 x 100
<i>IM medium resol. IMM</i>	150 x 150	75 x 75	56-100 x 100
<i>IM browse IMB</i>	900 x 900	225 x 225	56-100 x 100
<b>AP precision APP</b>	30 x 30	12.5 x 12.5	56-100 x 100
<b>AP single look APS</b>	9slant x 12	natural	56-100 x 100
<b>AP geocoded APG</b>	30 x 30	12.5 x 12.5	100 x 100
<i>AP medium resol. APM</i>	150 x 150	75 x 75	56-100 x 100
<i>AP browse APB</i>	900 x 900	225 x 225	56-100 x 100
<i>WS medium resol. WSM</i>	150 x 150	75 x 75	400 x 400
<i>WS browse WSB</i>	1800x1800	900 x 900	400 x 400
WV imagette and cross spectra WV1	9slant x 6	natural	5x5 to 10x5
WV cross spectra WVS	-	-	5x5 to 10x5
<b>GM image GM1</b>	1000 x 1000	500 x 500	400 x 400
<b>GM browse GMB</b>	2000 x 2000	1000x1000	400 x 400

Table 2: Image Quality Specification

Parameter	Specification
Range and Azimuth IRF broadening	< 10% of theoretical value
PSLR degradation	< 2 dB
ISLR degradation	< 2dB
Radiometric Error	< 0.1 dB (single beam) < 0.2 dB (scanSAR)
Absolute location accuracy	< 2 pixel
Geometric distortion	< 0.5 pixel

Table 3: Equivalent Number of Looks

Product	IM	AP	WS	GM
PRI	3.9	1.9		
GEC	3.9	1.9		
MR	40	50	12	12
BRW	80	75	57 - 62	18-21

#### PROCESSING ERS DATA with the ASAR PROCESSOR

In order to verify the quality of future ASAR products with large datasets, ESA together with MDA developed a stand-alone ERS processor based on the PF-ASAR system, called PF-ERS. It allows to generate products using the PF-ASAR processing algorithms.

Because its flexibility (e.g. direct interface with ERS raw data), the PF-ERS processor is an excellent tool to provide simulated ASAR products in Image Mode, Wave Mode and soon in Alternating Polarisation Mode (one polarisation only). All the images presented in this paper have been generated with PF-ERS and are identical to ASAR products in terms of format and algorithms (example in Figure 6).

PF-ERS is also an excellent tool to track ASAR products quality problems which could have hardly been detected with the limited test datasets used for the qualification of PF-ASAR. The PF-ERS processor development is also a step in the direction of the full compatibility between ERS and ENVISAT SAR products, i.e. same algorithms, same product specifications and same product formats.

### CONCLUSIONS

The ASAR instrument will offer several improvements compared to the ERS SAR instrument: new modes of operations, increased swath coverage, choice of polarisation and incidence angle. The ASAR Generic Processor which has been successfully completed in November 1997 allows for near real time and off-line processing of all ASAR modes products and for stripline processing of medium and low resolution products and their browse images. The ASAR processor will allow ESA to provide quality products to the appointed distributors and to the several hundreds of selected principal investigators, contributing so to a wider range of scientific and commercial applications for SAR data [4].

### REFERENCES

- [1] G. Engen, H. Johnsen, SAR-Ocean Wave Inversion Using Image Cross Spectra, IEEE, Trans. Geo. Rem. Sensing, Vol.33, No.4, 1047-1056, 1995
- [2] D.Stevens, F. Wong, P. Lim, and Y-L. Desnos, "A Processing Algorithm for the ENVISAT Alternating Polarization Mode Single Look Complex Product," *IGARSS'97*, Singapore, August 1997.
- [3] Frank Wong, David Stevens, and Ian Cumming, "Phase-Preserving Processing of ScanSAR Data with a Modified Range Doppler Algorithm," *IGARSS'97*, Singapore, August 1997.
- [4] ESA, "Envisat ASAR Science and Applications", *ESA SP-1225*, November 1998.
- [5] R. Torres, J-L. Suchail, C. Buck, J. Guijarro, A. Schonenberg, "The Envisat ASAR Instrument Verification and Characterisation", CEOS SAR Workshop, Toulouse, October 1999.
- [6] Y-L Desnos, C. Buck, H. Laur, J-L Suchail, R. Torres, J. Closa, "The Envisat ASAR Calibration and Validation Plan", CEOS SAR Workshop, Toulouse, October 1999.

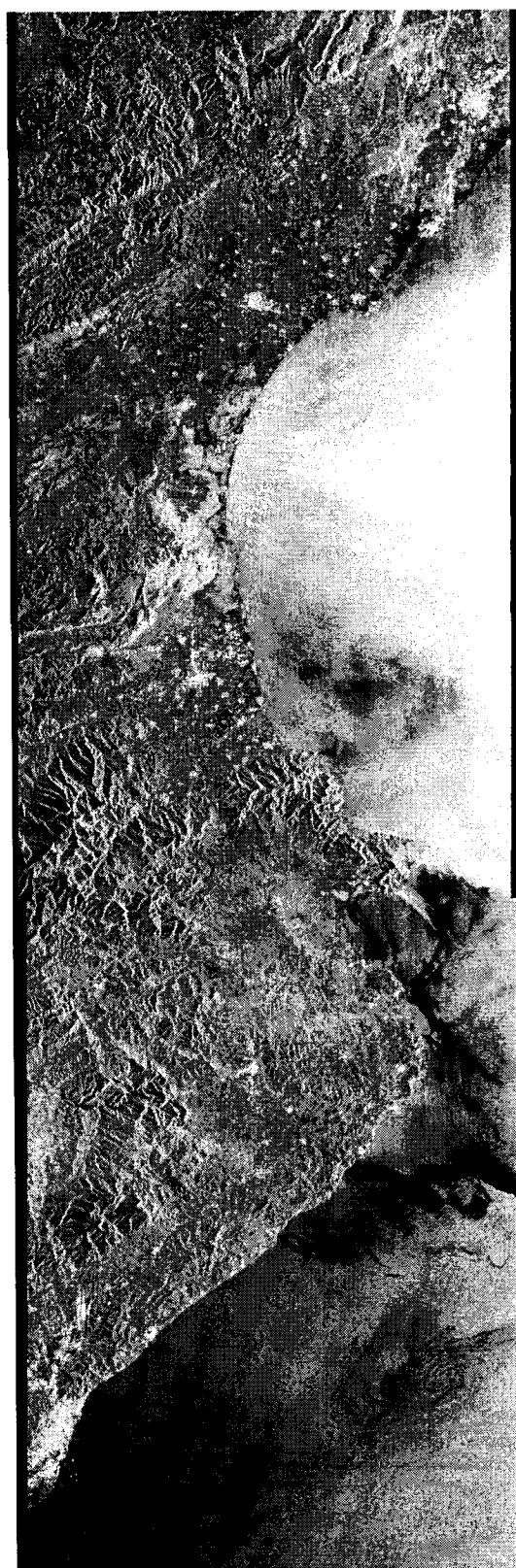


Figure 6: Example of Image Mode medium resolution product (from ERS data) covering the Mediterranean Coast between Montpellier and Barcelona.





## The ENVISAT ASAR Calibration and Validation Plan

Yves-Louis Desnos<sup>1</sup>, Christopher Buck<sup>1</sup>, Henri Laur<sup>2</sup>, Jean-Luc Suchail<sup>1</sup>,  
Ramón Torres<sup>1</sup>, Berthyl Duesmann<sup>1</sup>, Josep Closa<sup>2</sup>

<sup>1</sup>ESA-ESTEC ENVISAT Project, PO Box 299  
2200 AG Noordwijk, The Netherlands  
e-mail: [ydesnos@estec.esa.nl](mailto:ydesnos@estec.esa.nl)

<sup>2</sup>ESA-ESRIN  
Via Galileo Galilei  
Frascati, Italy

### ABSTRACT

This paper presents the approach to the in-flight calibration of the ENVISAT-1 ASAR instrument and the validation of its data products. Particular distinction is made between external calibration and characterization, and internal calibration.

The selection of the various sites for external calibration and in-flight characterization are presented. The techniques and the performance objectives are also reviewed

The instrument calibration activities will be centred around the Instrument Engineering Calibration Facility (IECF), a specially developed facility principally to support the commissioning phase activities.

The organization of the commissioning phase by means of Commissioning Phase Working Groups is addressed. The overall status of the preparatory activities is presented including activities relevant to the validation of ASAR Wave mode products.

### ASAR SYSTEM DESIGN OVERVIEW

#### ASAR System Overview

The ASAR system design has been inherited from ERS which is why the ENVISAT platform is yaw steered and, thanks to the provision of star sensor, the attitude control of the platform is expected to be better than ERS. The ENVISAT ASAR system will benefit from the availability of an on-board Solid State Recorder allowing up to 10 minutes recording of ASAR High Rate modes (100Mbit/s) at any point around the orbit. Finally the DORIS orbit determination system will allow for accurate geolocation of all ASAR products produced in near real time or off-line.

#### ASAR Instrument Overview

The ERS AMI SAR design uses a centralized travelling wave tube amplifier and a passive slotted waveguide array antenna providing imaging in a single fixed position swath and in a single polarization (VV).

The ENVISAT ASAR design uses an active array antenna with 320 Transmit Receive modules (TRM) to produce a versatile position of the imaged swath by beam steering in elevation (see Figure 1). Additionally, a larger swath coverage (400km) is achieved using the ScanSAR technique at medium (150m) or low resolution (1000m).

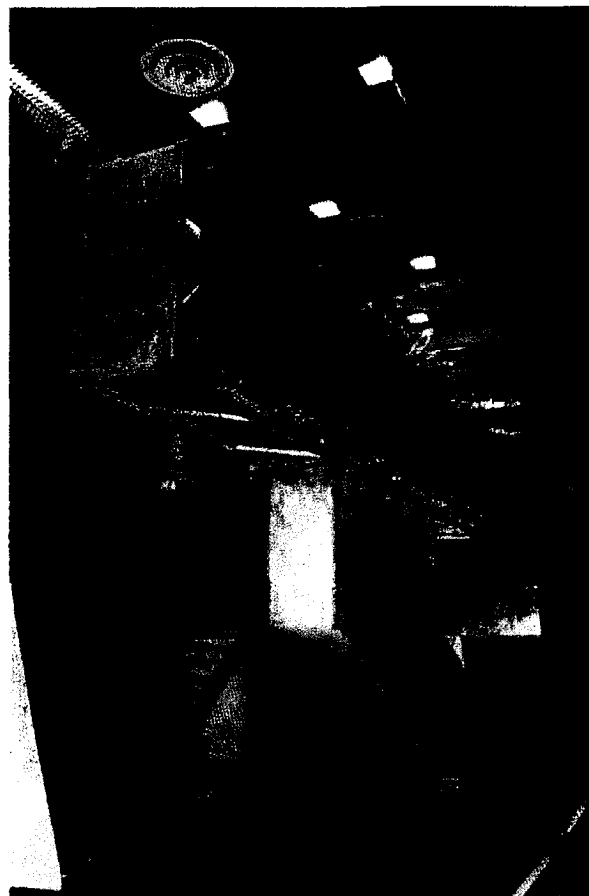
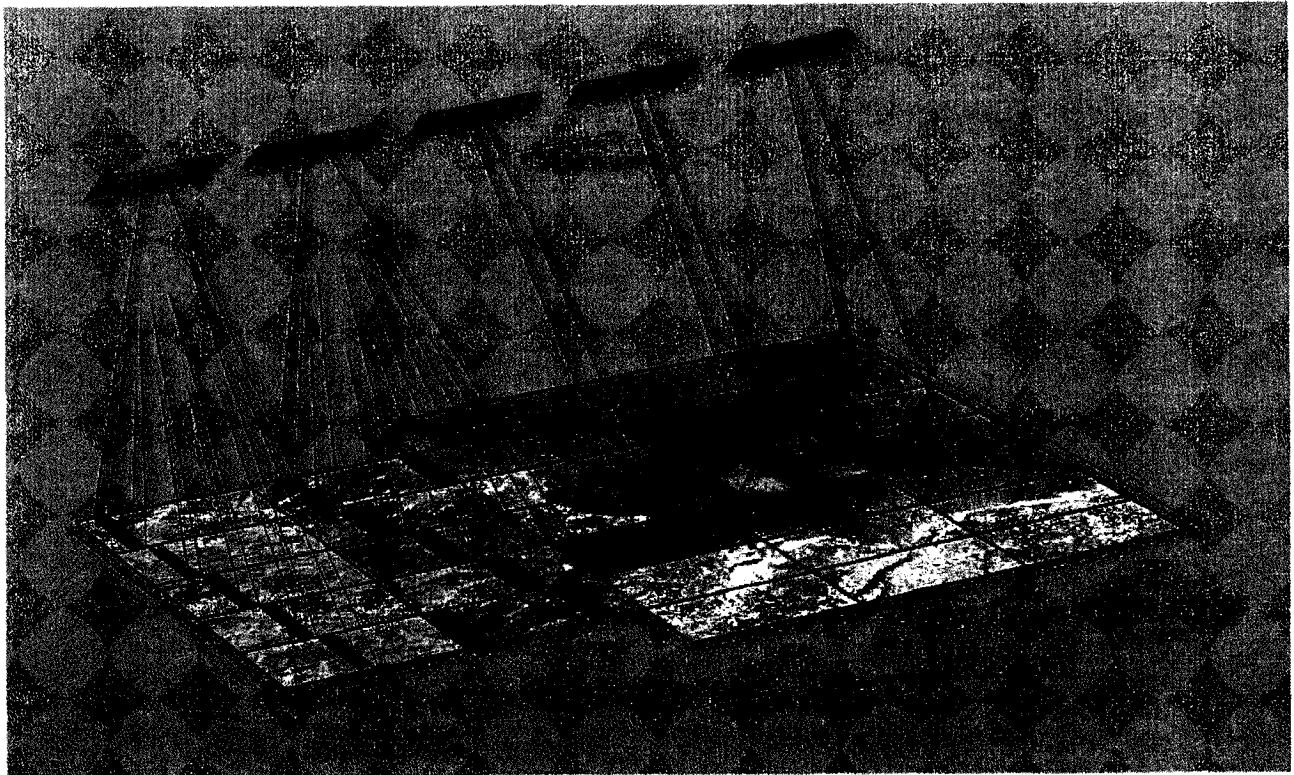


Figure 1 ASAR Flight Model Antenna (courtesy MMS)

All operating modes feature the possibility to select either H or V polarization on transmit and receive (HH or VV) and the alternating ASAR sub-modes allow



**Figure 2: ASAR Operating Modes and Coverage**

the use of a combination of both (HH/VV, HH/HV or VV/VH - see figure 2).

Finally, a more versatile wave measurement mode is offered to the users with 100 km spacing between vignettes and the capability to select the position alternating between two positions in any of the swaths.

Additionally, the ASAR is equipped with a programmable digital waveform generator which will allow the radiometric quality of the product to be optimized. As a further improvement compared to ERS, an eight bit ADC associated with a Flexible Block Adaptive Quantization scheme to be used in 8:4, 8:3 and 8:2 compression ratio will allow a larger dynamic range of the input signals to be sampled within the constraints imposed by the data rate. Finally, the ASAR features a temperature compensation scheme to compensate for drifts observed at transmit/receive module (TRM) level around the orbit.

Furthermore, the instrument frequency stability and datation have been improved to support interferometric applications. A detailed instrument description is provided in a companion paper [1]

#### ASAR OPERATING MODES

The ASAR has five modes of mutually exclusive operation which can be classified in two categories:

- Low data rate modes for Global Monitoring and Wave modes with an operational capability of up

to 100% of the orbit. Both modes are systematically recorded on-board and the on-board recorder is dumped every orbit when visible by an ESA station (Kiruna Station, Sweden or Fucino Station, Italy)

- High data rate modes for Narrow Swath Modes (Image and Alternating Polarization) and Wide Swath with high data rate and operation time up to 30 minutes per orbit (including ten in eclipse). The High Rate mode data are recovered according to one of the following schemes: real transmission via an X-band link to ESA or alternative station or real time transmission via the Ka-band link using Artemis Data Relay Satellite to the ESA ESRIN station in Italy or finally recorded on board the Solid State Recorder and dumped via X- or Ka-band link when in visibility of an ESA station.

#### ASAR PRE-LAUNCH ACTIVITIES

A number of activities have been undertaken in preparation for the launch of Envisat to optimize the instrument programmable settings, to develop the necessary tools and infrastructure in support of calibration and validation such as ground transponders and the Instrument Engineering Calibration facility for the ASAR which will be detailed here.

### Global Monitoring and Wide Swath Mode Settings

Alternative settings for the ASAR Global Monitoring (GM) and Wide Swath (WS) modes have been proposed by ESA and discussed in the ASAR Science Advisory Group (SAG).

A study contract has been awarded to Politecnico di Milano (ITALY) to select from the alternative settings, the optimum setting in terms of performance and product quality.

For GM mode these alternative settings consist of increasing the chirp bandwidth, updating the corresponding re-sampling factors and changing the quantization setting. The results of the study have been discussed in [2] and are summarized in figure 3 in terms of sensitivity versus ENL and FBAQ option. The change from FBAQ 8:4 to 8:2 is the ESA final selection which has been endorsed by the Science Advisory Group presenting the advantage of largest bandwidth giving better ENL, better interferometric performances and allowing simplified processing due to a larger time-bandwidth product. The new instrument settings are detailed in table 1.

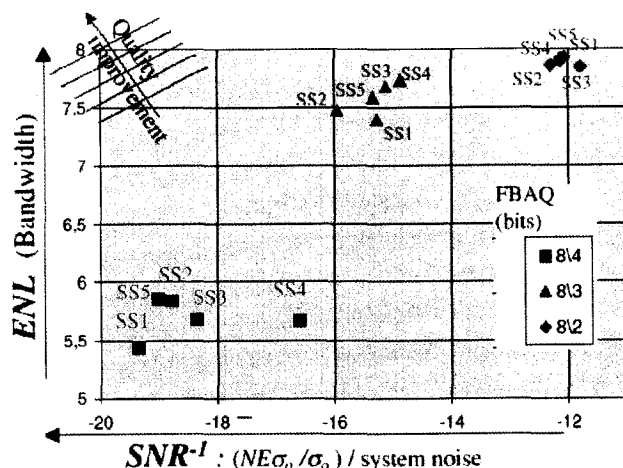
**Table 1 GMM New Instrument Settings**

Swaths	Chirp BW (MHz)	Re-sampling factor	FBAQ Encoding
SS1	1.82	8	8:2
SS2	1.13	14	8:2
SS3	1.00	14	8:2
SS4	0.94	15	8:2
SS5	0.94	15	8:2

For WS mode the alternative settings consist of increasing the chirp bandwidth while accepting a reduction in the corresponding noise equivalent sigma0 for that sub-swath. The benefit is to allow more looks to be processed in range and to increase the ENL in the final product. Furthermore, better interferometric performances can be expected. The new instrument settings are detailed in table 2.

**Table 2 WS instrument setting**

Swath	Chirp BW (MHz)	FBAQ Encoding
SS1	14.31	8:4
SS2	12.05	8:4
SS3	10.04	8:4
SS4	8.85	8:4
SS5	8.03	8:4



**Figure 3: ENL/FBAQ Performance Trade-off**

The new configurations for the GM and WS modes resulting from the optimization study performed by Politecnico di Milano have been successfully tested at Control Electronics Sub-Assembly Flight Model level.

The resulting product quality in WS mode as tested using the ASAR processor is presented in table 3. However an alternative strategy of overlapping looks has been studied and is recommended for the ASAR processor in Wide Swath mode (ref. [2])

**Table 3 PF-ASAR WS product quality**

Swaths	Product ENL	Range Look Bandwidth (MHz)	Range looks
SS1	11.95	4.5	4
SS2	11.87	3.0	4
SS3	11.99	2.55	4
SS4	11.89	2.24	4
SS5	11.89	2.09	4

### Wave Mode Algorithm, Instrument and Processor Settings

The ASAR wave mode level 1b product is derived from the processing of Single Look Complex (SLC) imagettes using the Cross Spectra methodology introduced recently (Engen et al., 1995 and [3]). The derived complex imagette cross spectra are speckle compensated and resolve the propagation ambiguity. The wind speed can be derived either from the backscatter coefficient or from the azimuth cut-off measurement annotated in the product.

In order to adapt existing ERS wave spectra inversion algorithms to the ASAR cross spectra and in view of

the maturity of SAR wind field retrieval algorithms the Agency has decided to initiate the algorithm prototyping for a new level 2 product with NORUT (Norway) and IFREMER (France) which includes the ocean wave spectra together with an ocean surface wind field estimate. The algorithm is now available for implementation at ECMWF and shall be further distributed to other meteorological centres.

ESA convened the algorithm developers and meteorological centre users to review the ENVISAT ASAR algorithm at a Wind and Wave Geophysical Product workshop on 21 and 22 April 1999 [4]. At this workshop experts were invited to discuss the baseline settings for the ASAR instrument Wave mode to be used at the beginning of the commissioning phase.

As a baseline a frog-leg operation was finally recommended with IS2 (similar incidence to ERS-2 vignettes) alternating with IS1 in VV polarization. This would allow continuity with ERS-1/ERS-2 and a comparison with another incidence angles (in IS1).

In addition both VV and HH polarizations should be investigated during the commissioning phase.

Based on validation and assimilation results further recommendations for a definitive wave mode instrument setting will be made during the course of commissioning.

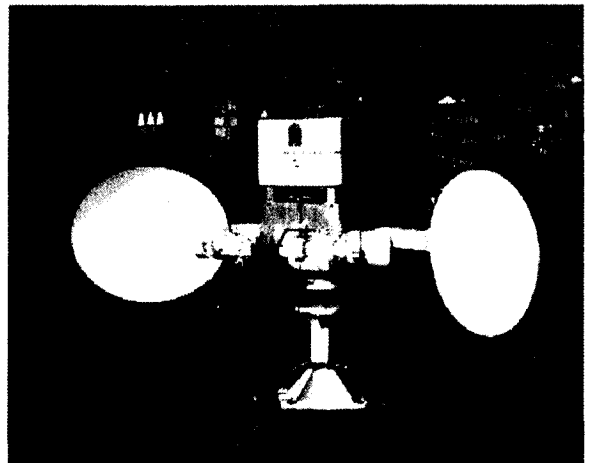
As far as the ASAR processor settings are concerned large data sets of ERS data have been processed by NORUT using the new Wave Mode Cross Spectra algorithm and compared with co-located in-situ measurements. This has allowed to optimize the ASAR processor settings and to validate the Cross Spectra algorithm on large data. The results are that the propagation ambiguity has been resolved in 95% of the cases.

#### *Transponder Development*

The development of three transponder units has been given as result of a competitive tender to MPB (CDN) based on a prototype designed by ESTEC [5] (figure 4).

The ASAR transponders have been designed to support the External Characterization of ASAR and a phase stable mode is also implemented to be used as a reference target for interferometry.

The manufactured units shall be delivered in January 2000 for further integration and later self-calibration. ESA intends to deploy, at yet to be determined fixed locations in the Flevoland polder, the three manufactured units. Additionally the prototype unit will be mounted on a trailer and shall be deployed for specific purposes such as ASAR Wave mode imagette calibration, Alternating Polarization mode calibration, where the availability of four transponders will allow simultaneous calibration of two polarization combinations (HH/VV, HH/HV, VV/VH).



**Figure 4 ASAR Prototype Transponder**

#### *Instrument Engineering Calibration Facility Development*

The calibration activities for the ASAR instrument will be centred around the IECF. The IECF main function specified by ESA are:

- Platform calibration and performance monitoring such as datation, orbit, pointing
- Instrument calibration and performance monitoring such as temperature effects, ageing
- Auxiliary data Products Generation to the Payload Data Segment such as External Characterization mode data file
- Optimization of ASAR Processor set-up parameters
- Instrument Control Table generation such as change of mode setting
- Production of regular reports on instrument status

The acceptance of the IECF is planned for January 2000. The context diagram for the IECF is shown in figure 5. The ENVISAT ground segment consists of the Flight Operation Segment (FOS), the Payload Data Segment (PDS), supported by the Reference Operation Plan Generation Tool (RGT) for planning and operating the ENVISAT mission and the Instrument Engineering and Calibration Facility (IECF) for the characterization and calibration of all on-board instruments.

#### ASAR CALIBRATION

Unlike the passive ERS AMI-SAR, ASAR is an active antenna made up of 320 transmit/receive modules (TRMs). Each TRM has two transmit chains, one for horizontal and one for vertical polarization, and one receive chain. The three chains are independently programmable in amplitude and phase to provide the required elevation beam patterns. Any instabilities in the gain and phase characteristics of the TRMs will distort

## IECF System Context

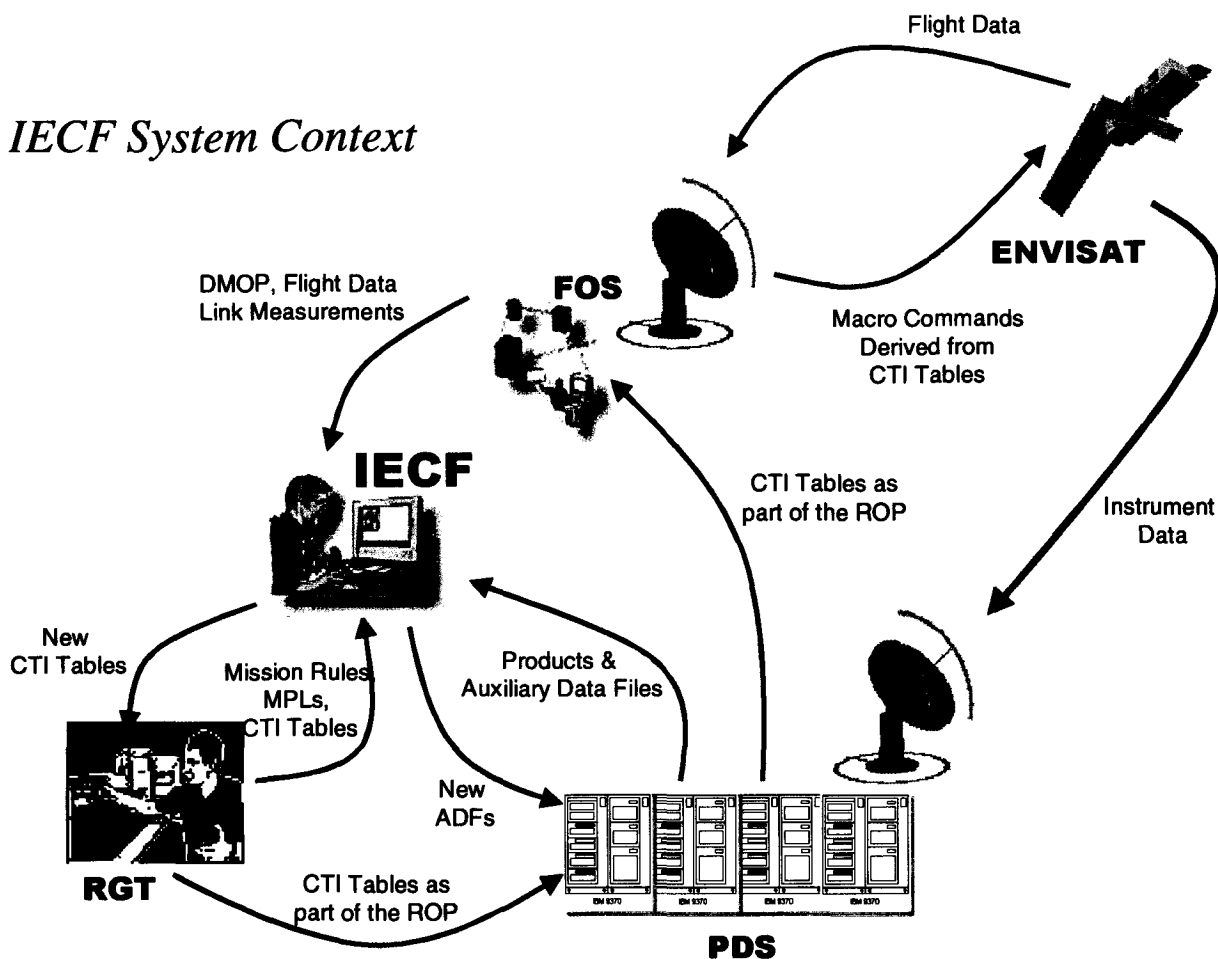


Figure 5: Instrument Engineering Calibration Facility Context Diagram

the beam patterns and can potentially contribute to radiometric errors in the SAR image. For these reasons the ASAR calibration scheme is very different to that used for ERS. The planned radiometric calibration of ASAR is detailed here.

### ASAR Internal Calibration

The objectives of the ASAR instrument internal calibration scheme are to derive the instrument's internal path transfer function and to perform noise calibration. These objectives are realized by dedicated calibration signal paths and special calibration pulses within the instrument for making the required calibration measurements and by using these measurements to perform corrections within the ground processor.

### T/R module Temperature Compensation

The amplitude and phase characteristics of the TRMs will vary principally as a function of temperature. To handle this the instrument includes a scheme to compensate for drifts over temperature. This scheme provides the antenna with a high degree of stability, however it compensates neither for ageing effects nor for eventual TRM failures.

### Calibration Loop

The instrument calibration loop is used to perform three distinct functions. It is used firstly, to characterize the instrument transfer function during the measurement modes, secondly to characterize individual TRMs and thirdly in the special External Characterization mode as described later.

The calibration loop in ASAR is in fact comprised of a distinct calibration path to each of the 320 TRMs. This enables transmit pulses at each TRM output to be sampled and also allows calibration pulses to be injected into the receiver front-end of each TRM. Effectively, the scheme provides a multi-pathed calibration loop that encompasses all the active electronics in the instrument transmit and receive paths. In particular, ageing of TRM characteristics and TRM failure can be detected.

There is no active switching within this network in order to maximize reliability and stability. The calibration distribution network acts as a combiner when the loop is being used to sense TRM transmissions and as a splitter when the loop is being used to inject pulses into the TRM receivers. The antenna calibration port can either be switched to an auxiliary receiver or to an auxiliary transmitter, both of which are located within

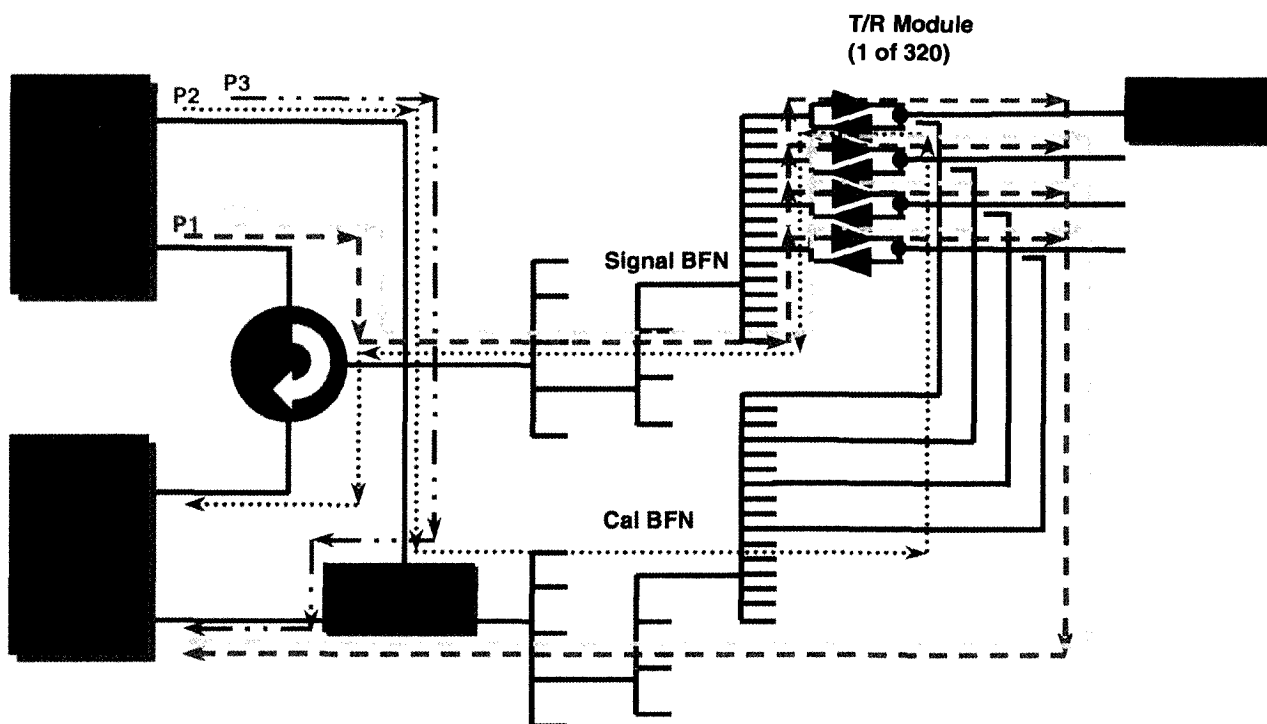


Figure 6: Calibration Pulse Diagram

the instrument central electronics. These elements can be used to detect or inject calibration pulses at the antenna calibration port. The detailed use of the calibration loop is partly controlled by the operating states of the TR modules themselves (i.e. ON/OFF, Tx/Rx, H/V), because there is no switching within the calibration network.

#### Calibration Pulses

During normal operation in any of the ASAR measurement modes, a sequence of calibration pulses is interleaved with the normal radar pulses. These pulses characterize the active array, both on transmit and receive, on a row by row basis (i.e. only ten modules along one row are sensed, while the 310 remaining modules are not sensed). For different pulses within the sequence, different rows are activated. The rationale for row by row characterization is that the ASAR is essentially an elevation plane beam steering instrument. Thus, the amplitude and phase settings applied to the TRMs along a row are nominally uniform and the calibration signals from them are nominally coherent. For each of the 32 rows, the antenna and the central electronics are characterized using three types of pulses (see figure 6 and 7). Pulse P1 is used to characterize the transmit chain of the instrument.

However, since TRMs of the four adjacent rows share the same power supply it is not possible to characterize one row in isolation. Hence the ten modules of the 'wanted' row are set to their nominal phase and amplitude settings for pulse P1, while the phases of the

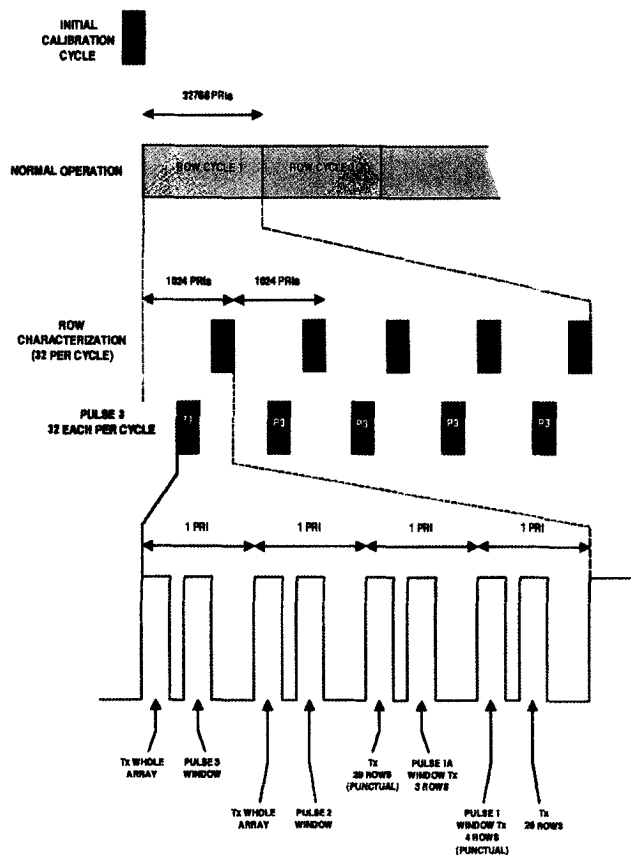
modules of the three 'unwanted' rows are set so that their combined contribution out of the calibration network is nominally zero (each column is 180 degrees out of phase with the next). In this way, their interference to the measurement of the 'wanted' row is minimized. However, to ensure that wanted row has been characterized correctly, a second type of transmit pulse, referred to as pulse P1a, is added, in order to characterize the residual parasitic contribution of the three unwanted rows during P1. During P1a the three unwanted rows are set as for P1 and the previously wanted row is now switched off. Even though the load conditions on power supplies are not exactly representative, the residual error introduced into the estimation of P1a can be considered sufficiently small as to be negligible. The receive path of the instrument is then characterized by pulse P2, but in the receive path, no variation is expected from power supply load variations, and direct row by row characterization is possible.

The central electronics transmit and receive paths are included in both P1/P1a and P2 characterizations. It is therefore necessary to characterize the central electronics independently by the use of the internal pulse P3.

#### Internal Calibration Processing

One consequence of row by row characterization is that the instrument transfer function cannot be simply calculated from a few pulses, as was the case with the AMI SAR. Instead, the ground processor must utilize

the calibration pulses from a complete cycle through the 32 rows in order to estimate the transfer function. In addition, a replica pulse for the instrument must be reconstructed from a complete row cycle.



**Figure 7: Calibration Pulses - Image Mode Normal Operation**

As well as providing internal calibration during the measurement modes, the ASAR includes a special module stepping mode, in which individual TRM characteristics can be measured. This mode can be used to investigate TRM failures and ageing effects. In this mode, only one module is activated at a time, in either transmit or receive.

The internal calibration scheme also includes measurements of the instrument noise level. The measurements are taken during the initial calibration sequences, at the beginning of a mode. In the modes which have natural gaps in their imaging sequence (i.e. wide swath and global monitoring modes), noise measurements are also made during nominal operation throughout the mode.

**ASAR External Characterization**

The internal calibration scheme monitors drifts in the transfer function of the majority of the instrument with

the exception of the passive part of the antenna, the calibration loop itself and the mechanical pointing of the antenna. As part of the overall calibration strategy to monitor these elements the ASAR has a dedicated External Characterization mode which will be operated nominally every 6 months.

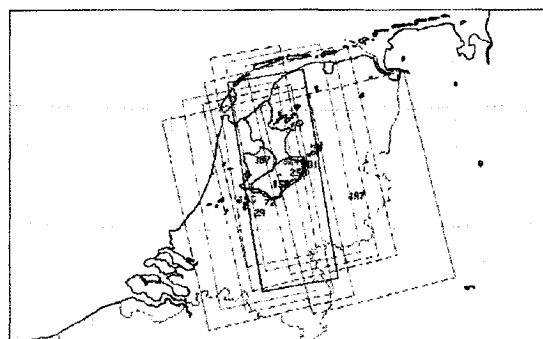
During this mode a sequence of pulses sent by each antenna row in turn is detected by the antenna calibration loop and simultaneously recorded on ground by a special ground receiver built into the ASAR calibration transponder.

The data recorded in the transponder and that down-linked from the instrument are compared in the ground processor to reveal the relative phase and amplitude of the pulse from each row. These relative amplitudes and phases are used to characterize the row of radiating sub-arrays and the calibration path of the row.

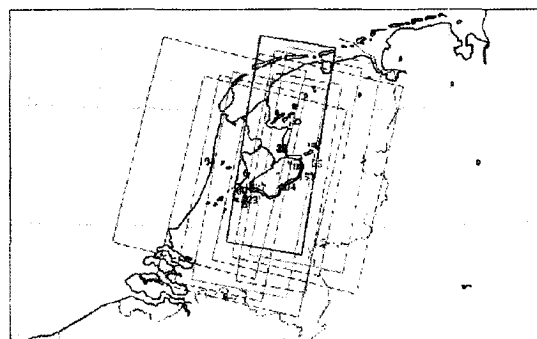
**ASAR External Calibration**

The objective of the external calibration scheme is to derive the overall calibration scaling factor will make use of the successful methodology developed for the narrow swath mode of ERS.

Four specially built high precision transponders with a radar cross section sufficiently high in comparison to the background backscattering coefficient (plus noise) will be deployed across the ASAR swath and observed several times during every orbital cycle of 35 days.



Calibration opportunities for SCANSAR SSI-5 (red, blue, green, purple, black) 35-day repeat cycle (501 orbits); Reference: 0.133500 deg, orbit 1: First orbit 1, Last orbit 501



Calibration opportunities for SCANSAR SSI-5 (red, blue, green, purple, black) 35-day repeat cycle (501 orbits); Reference: 0.133500 deg, orbit 1: First orbit 1, Last orbit 501

**Figure 8: SCANSAR beams ascending/descending**

Images acquired over suitable regions of the Amazonian rainforest will be used to derive the in-flight elevation antenna patterns. Absolute calibration factors derived from transponder measurements and across swath correction derived from the radar equation will be used to calibrate the final image product.

For the wide swath mode using the ScanSAR technique the external calibration approach will be similar to the one used for the narrow swath mode. For Global Monitoring mode, however, the resolution cell size is too large (1000x1000m) in order to be able to distinguish the impulse response function of a  $\sim 60\text{dBm}^2$  transponder from the surrounding clutter. Increasing the radar cross section of the transponder is only likely to saturate the receiver and hence invalidate the calibration. The proposed solution to calibrating global monitoring mode is therefore to make use of a suitable well calibrated, stable distributed target such as the Amazonian rainforest from which backscattering coefficient values will already be known from recent Image or Wide Swath mode passes.

**ASAR Ground Processor Calibration**

As part of the data handling and reformatting of the processor, I/Q science data are decompressed and subject to an I/Q correction (bias, differential gains, non-orthogonality). As with ERS, any necessary corrections

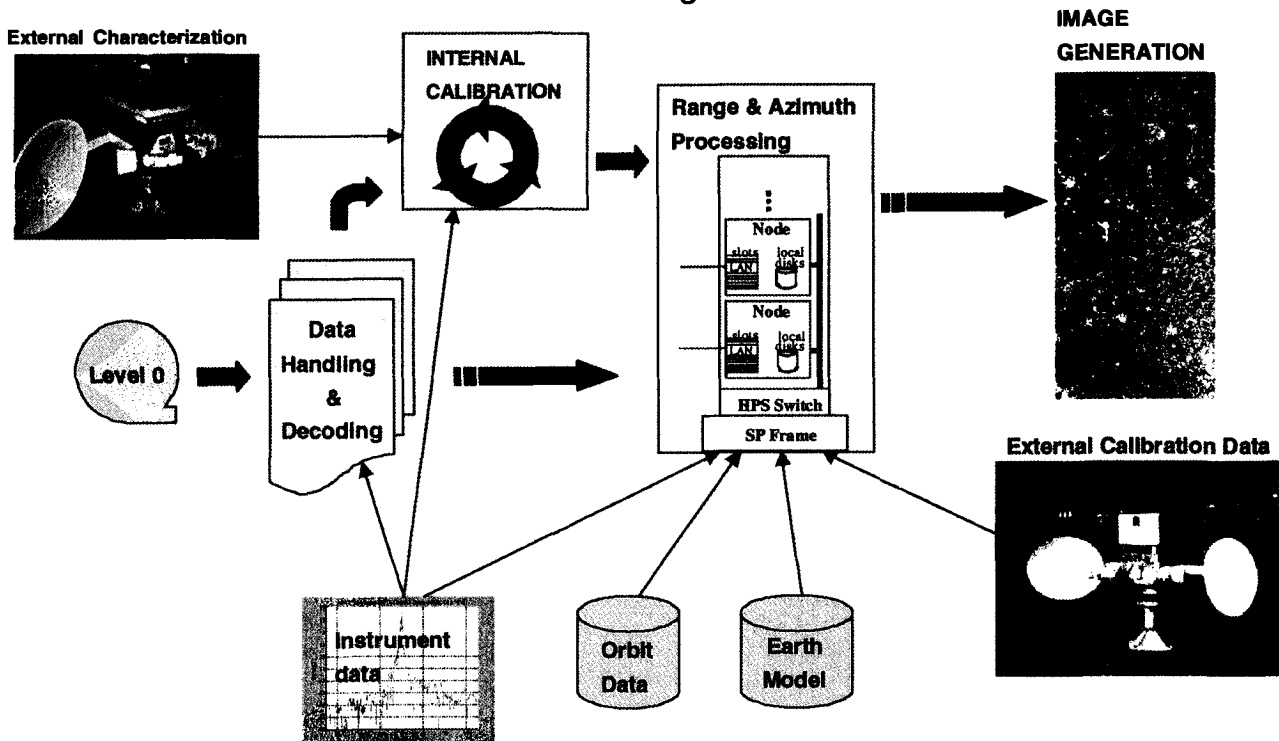
for non-linearity may be applied in the ground processor using pre-launch instrument ADC characterization. As part of the ground processor's internal calibration, the amplitude and phase of calibration pulses (P1, P1a, P2, P3) for each row are used. The amplitude and phase of P2 relative to P3 are calculated and P1a is subtracted vectorially from P1 as discussed earlier.

External characterization data and the derived amplitude and phase values for the 32 rows on transmit and receive are used to measure any deviation of the instrument reference gain pattern from its on-ground characterized value.

The replica of the transmitted pulse is calculated from the P1, P1a, P2 and P3 measurements, the on-ground characterized row patterns and the external characterization data. The constructed replica tracks variations in all the transmit and receive circuits and is used to determine the range reference function for range compression processing.

The ground processor includes a Doppler Centroid Estimator with specified accuracy of 50Hz for image and wave mode like ERS and 25Hz in ScanSAR modes in order to limit radiometric errors in azimuth [6]. The Functional Block Diagram of the ASAR ground processor is outlined in figure 9.

**ASAR Processor Functional Block Diagram**



**Figure 9: ASAR Processor Functional Block Diagram**



## ASAR PRODUCT VALIDATION

The ASAR Products Validation is limited to the Wind/Wave product and will be carried out by:

- ECMWF routinely using the ESA newly developed inversion algorithm developed by NORUT/IFREMER (Envisat AO proposal 270)
- By the Expert Support Laboratory composed of NORUT and IFREMER (AO proposal 799)
- Using existing buoy networks (NOAA and Canadian Marine Environmental Service)

### *Pre-Launch validation using ERS-2 data*

A first meeting of the ASAR Wind and Wave validation team took place during the April workshop at ESTEC reference [4]. A preliminary activity has been decided on and consists in performing a pre-validation of the ASAR Level 1b and Level 2 algorithm products using ERS-2 data.

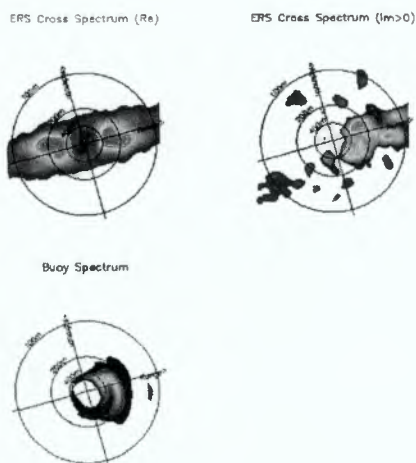
The participants agreed upon two different data sets:

- one month of ERS data over the "Vendee Globe Challenge Race Area" spanning the month of January 1997 for assimilation
- a number of wave imageries collocated with in-situ measurements (e.g. NOAA buoys)

These data are being processed using the ASAR algorithm as part of the validation exercise.

## ORGANIZATION

During commissioning phase the ASAR calibration and validation activities will be under the responsibility of the ASAR Calibration Validation Working Group.



**Figure 10 ERS Cross Spectra vs buoy measurement**

This working group reports to the commissioning phase manager. The group is responsible for the:

- Preparation of the SAR Calibration/Validation Plan
- Execution of the plan
- Organization of the scientific and technical support throughout the commissioning phase
- Preparation of the ASAR commissioning phase report and participation to the ASAR commissioning reviews
- Organization of regular preparation/progress meetings

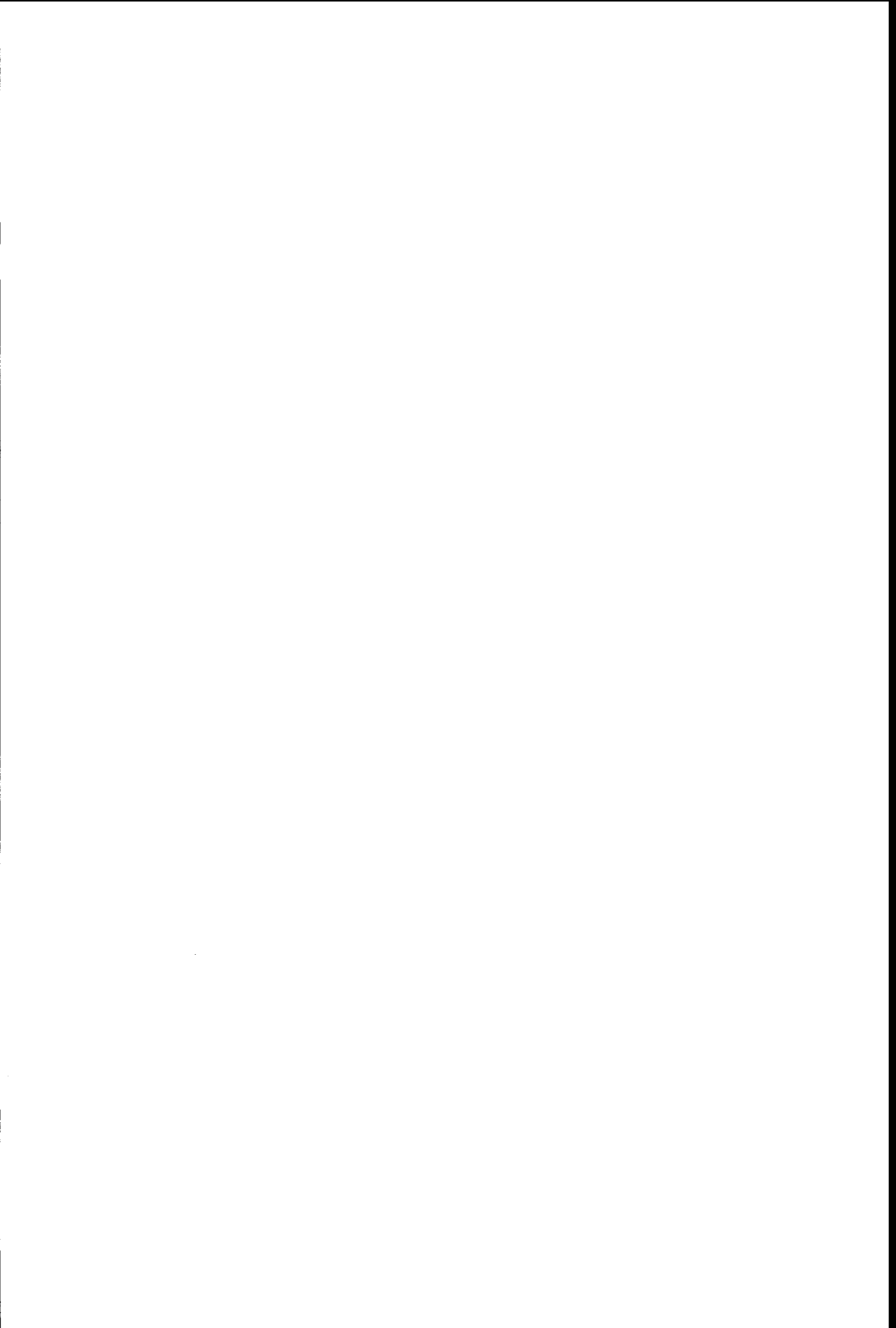
The ACVWG will be composed of ESA staff, instrument experts from industry, External site operators (if applicable for external calibration using foreign sites), members of the ESLs for algorithm and processor validation and finally selected scientists and Announcement of opportunity PIs working on product validation

## CONCLUSIONS

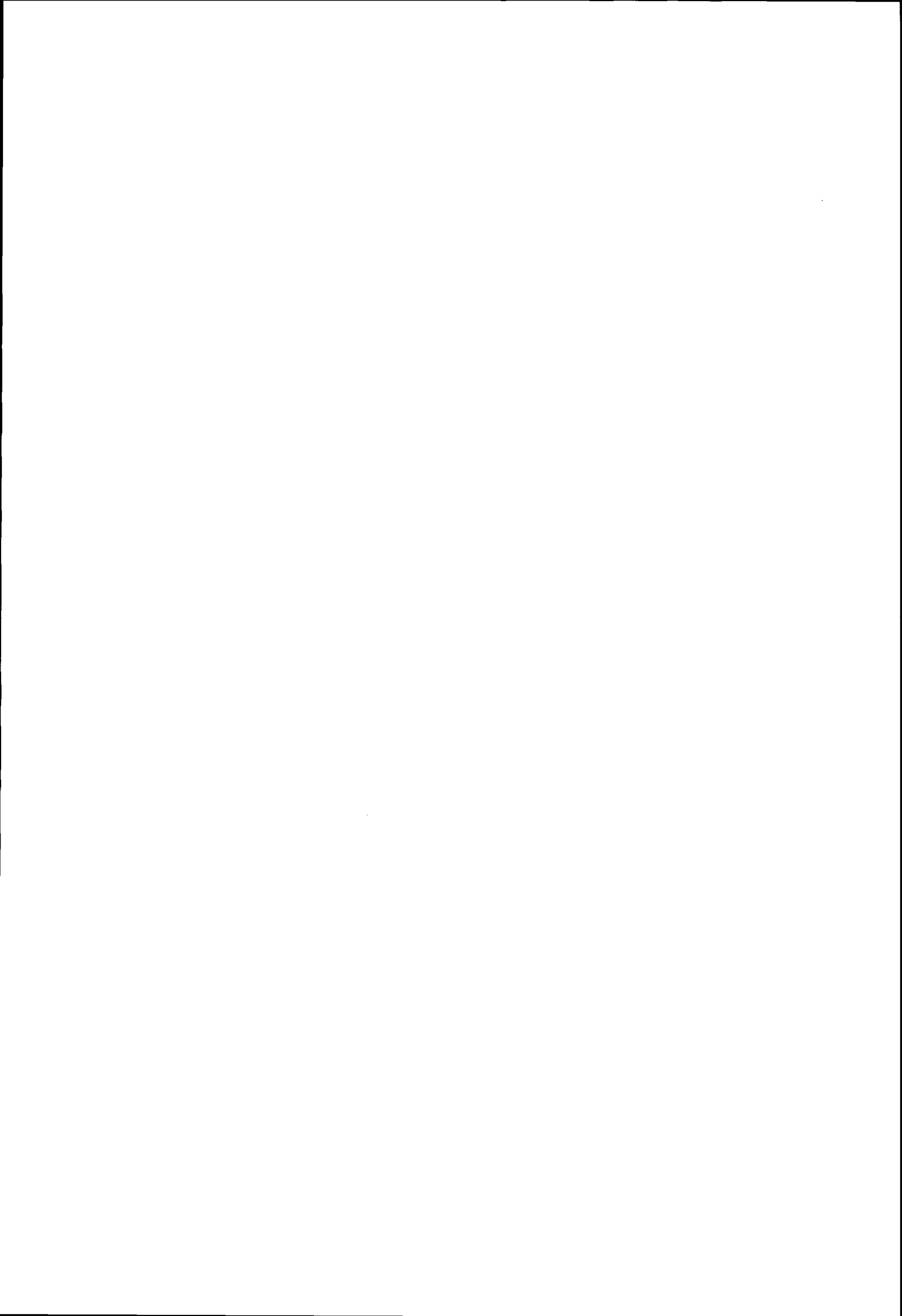
This paper has presented an overview of the main considerations with respect to the calibration and validation of the ASAR instrument to be flown on board ENVISAT. A short summary of the pre-launch activities has been given and the critical areas to be addressed during the commissioning phase have been discussed.

## REFERENCES

- [1] "The ENVISAT ASAR Instrument Verification and Characterization" R. Torres, C. Buck, J. Guijarro, J-L Suchail and A. Schonenberg, ESA, CEOS SAR Workshop 2-29 October 1999, ESA-SP450
- [2] "Optimizing performances of the ENVISAT ScanSAR modes", A.Monti Guarnieri Politecnico Di Milano, Y-L.Desnos ESA, IGARSS'99, Hamburg Germany.
- [3] "The Envisat ASAR Wave mode Cross Spectra Algorithm", H. Johnsen, NORUT IT Norway, CEOS SAR Workshop 3-6 February 1998 ESA-WPP 138
- [4] "Minutes of the first Envisat ASAR Wind/Wave workshop" 21/22 April 1999, ref. PPP/0931/yld
- [5] "ENVISAT ASAR Precision Transponders" H. Jackson ESA/ESTEC, I. Sinclair, S. Tam MPB Technologies Inc., CEOS SAR Workshop 2-29 October 1999, ESA-SP450
- [6] "The Envisat-1 Advanced Synthetic Aperture Radar Processor And Data Products" Y-L. Desnos, ESA-ESTEC, H. Laur ESA-ESRIN, P.Lim & P.Meisl Macdonald Dettwiler, T.Gach Alcatel Space Industries, in proceedings IGARSS'99, Hamburg, Germany



## **Session 8: Polarimetry/Interferometry**



APPLICATION OF THE «  $H / A / \alpha$  » POLARIMETRIC DECOMPOSITION THEOREM FOR  
UNSUPERVISED CLASSIFICATION OF FULLY POLARIMETRIC SAR DATA BASED ON THE  
WISHART DISTRIBUTION.

E. POTTIER<sup>(1)</sup>, J.S. LEE<sup>(2)</sup>

- (1) Laboratoire Antennes et Télécommunications, UPRES-A CNRS 6075 *Structures Rayonnantes*  
Université de Rennes I, Campus de Beaulieu Bât 22, 263 Avenue Général Leclerc, CS 74205,  
35042 Rennes Cedex email : eric.pottier@univ-rennes1.fr  
(2) Remote Sensing Division, Naval Research Laboratory, Washington,  
DC 20375-5351, USA, email : lee@ccf.nrl.navy.mil

**ABSTRACT**

Classification of Earth terrain components using a fully polarimetric SAR image is one of the most important applications of Radar Polarimetry in Remote Sensing.

In this paper, we propose to extend and complement the unsupervised combined Wishart classifier, originally developed by *J.S. Lee et al. (1998)*, with the introduction of the anisotropy information.

The analysis of the final cluster centers in the  $H / A / \alpha$  classification space is useful for class identification of the different scattering mechanisms which occur in the classified SAR image. The introduction of the anisotropy information allows the improvement of the capability to distinguish between different classes whose cluster centers end in the same entropy ( $H$ ) - alpha ( $\alpha$ ) zone.

This new unsupervised combined Wishart classifier is applied to the polarimetric SAR image of San Francisco Bay from the NASA/JPL AIRSAR data base (1988) for segmentation and clustering of different Earth terrain components.

**INTRODUCTION.**

Classification of Earth terrain components using a fully polarimetric SAR (POLARSAR) image is one of the many important applications of Radar Polarimetry. In this paper we consider the use of POLARSAR data for quantitative remote sensing applications.

There is currently a great deal of interest in the use of polarimetry for radar remote sensing. In this context, an important objective is to extract physical information from the observed scattering of microwaves by surface and volume structures.

The most important observable measured by such radar systems is the  $3 \times 3$  coherency matrix  $[T]$ . This matrix accounts for local variations in the scattering matrix and is the lowest order operator suitable to extract polarimetric parameters for distributed scatterers in the presence of additive (system) and/or multiplicative (speckle) noise.

In 1997, *S.R. Cloude* and *E. Pottier* proposed a method for extracting average parameters from experimental data using a smoothing algorithm based

on second order statistics [1]. This original method, based on an eigenvalue analysis of the coherency matrix, employs a 3-level Bernoulli statistical model to generate estimates of the average target scattering matrix parameters.

An unsupervised classification scheme has been introduced [1], based on the use of the two-dimensional  $H / \alpha$  classification plane, where all random scattering mechanisms can be represented.

In 1994, *J.S. Lee et al. [2]* developed a supervised algorithm based on the complex Wishart distribution for the polarimetric covariance matrix.

In 1998, *J.S. Lee et al. [3]* proposed an unsupervised classification method that uses the  $H / \alpha$  classification plane to initially classify the polarimetric SAR image. It has been shown in [3] that during the classification, the cluster centers in the  $H / \alpha$  plane can move out of their zones, or several clusters may end in the same zone.

In order to improve the capability to distinguish between different classes whose cluster centers end in the same zone, we propose in this paper to extend and complement the combined Wishart classifier with the introduction of the anisotropy ( $A$ ) information.

The combined classification procedure presented and discussed in this paper, is applied to POLARSAR images of San Francisco Bay from the NASA/JPL AIRSAR data base (1988) for segmentation and clustering of different Earth terrain components. It is a L band image (1.225 GHz), 4 look averaged Stokes matrix format with a pixel resolution of 10m x 10m. Fig. 1 shows the « *Target Generators* » color coded image of the San Francisco bay.

**THE  $H / A / \alpha$  TARGET POLARIMETRIC DECOMPOSITION THEOREM**

An important development in our understanding of how to best extract physical information from the classical  $2 \times 2$  coherent backscattering matrix  $[S]$  has been achieved through the construction of system vectors [4]. We represent this vectorization of a matrix by the vector  $V(\cdot)$  built as follows:



Fig. 1 : Target Generators color coded image of the San Francisco Bay.

$$\underline{k} = V([S]) = \frac{1}{2} \text{Trace}([S][\psi]) \quad (1)$$

where  $\text{Trace}([A])$  is the sum of the diagonal elements of matrix  $[A]$  and  $[\psi]$  is the set of  $2 \times 2$  complex Pauli basis matrices. The target vector  $\underline{k}$  has the explicit form shown in (2).

$$\underline{k} = \frac{1}{\sqrt{2}} [S_{XX} + S_{YY} \quad S_{XX} - S_{YY} \quad 2S_{XY}]^T \quad (2)$$

In the analysis of experimental POLSAR data, we generally have access either to complete coherent scattering matrix data, or multi-look averaged Stokes matrix data. In either case, the local estimates of the coherency matrix can be formed using pixel averaging, as :

$$\langle [T] \rangle = \frac{1}{N} \sum_{i=1}^N \underline{k}_i \cdot \underline{k}_i^{*T} = \frac{1}{N} \sum_{i=1}^N [T_i] \quad (3)$$

From this estimate, the eigenvectors and eigenvalues of the  $3 \times 3$  hermitian coherency matrix  $\langle [T] \rangle$  can be calculated to generate a diagonal form of the coherency matrix which can be physically interpreted as statistical independence between a set of target vectors [4]. The coherency matrix  $\langle [T] \rangle$  can be written in the form of:

$$\langle [T] \rangle = [U_3][\Sigma][U_3]^{-1} = \sum_{i=1}^{i=3} \lambda_i \underline{u}_i \underline{u}_i^{*T} \quad (4)$$

where  $[\Sigma]$  is a  $3 \times 3$  diagonal matrix with nonnegative real elements, and  $[U_3] = [\underline{u}_1 \quad \underline{u}_2 \quad \underline{u}_3]$  is a unitary matrix of the  $SU(3)$  group, where  $\underline{u}_1$ ,  $\underline{u}_2$ , and  $\underline{u}_3$  are the three unit orthogonal eigenvectors.

To introduce the degree of statistical disorder of each target, the entropy ( $H$ ) is defined, in the Von Neumann sense, from the logarithmic sum of eigenvalues of  $\langle [T] \rangle$  [1][4] :

$$H = - \sum_{i=1}^{i=3} P_i \log_3(P_i) \quad (5)$$

where  $P_i$  are the probabilities obtained from the eigenvalues  $\lambda_i$  of  $\langle [T] \rangle$  with:

$$P_i = \lambda_i / \sum_{j=1}^{j=3} \lambda_j \quad (6)$$

If the entropy  $H$  is low then the system may be considered as weakly depolarizing. If the entropy  $H$  is high then the target is depolarizing. Further, as the entropy  $H$  increases, the number of distinguishable classes identifiable from polarimetric observations is reduced. In the limit case, when  $H=1$ , the polarization information becomes zero and the target scattering is truly a random noise process.

While the entropy is a useful scalar descriptor of the randomness of the scattering problem, it is not a unique function of the eigenvalue ratios. Hence, another eigenvalue parameter defined as the anisotropy  $A$  can be introduced, with :

$$A = \frac{\lambda_2 - \lambda_3}{\lambda_2 + \lambda_3} \quad (7)$$

When  $A=0$  the second and third eigenvalues are equal. The anisotropy may reach this value for a dominant scattering mechanism, where the second and third eigenvalues are close to zero, or for the case of a random scattering type where the three eigenvalues are equal.

In previous publications [1] a parameterisation of the eigenvectors of the  $3 \times 3$  coherency matrix  $[T]$  has been introduced, and under the form :

$$\underline{u} = \begin{bmatrix} \cos \alpha & \sin \alpha \cos \beta e^{j\delta} & \sin \alpha \sin \beta e^{j\gamma} \end{bmatrix}^T \quad (8)$$

A statistical model of the scatterer is considered which is a 3 symbol Bernoulli process i.e. the target is modeled as a sum of three  $[S]$  matrices, represented by the columns of  $[U_3]$ , occurring with probabilities  $P_i$  [1].

In this way, the mean parameters of the dominant scattering mechanism are extracted from the  $3 \times 3$  coherency matrix as a mean target vector  $\underline{u}_0$ , such that:

$$\underline{u}_0 = \begin{bmatrix} \cos \underline{\alpha} & \sin \underline{\alpha} \cos \underline{\beta} e^{j\underline{\delta}} & \sin \underline{\alpha} \sin \underline{\beta} e^{j\underline{\gamma}} \end{bmatrix}^T \quad (9)$$

where the best estimate of each parameter  $\underline{\alpha}$   $\underline{\beta}$   $\underline{\delta}$  and  $\underline{\gamma}$  is easily evaluated as

$$\underline{\alpha} = P_1 \alpha_1 + P_2 \alpha_2 + P_3 \alpha_3 \quad (10)$$

One of the most important property in Radar Polarimetry concerns the roll invariance. The effect of rotation around the radar line of sight [4] can be generated as:

$$\langle [T(\theta)] \rangle = [U_3^R] \langle [T] \rangle [U_3^R]^{-1} \quad (11)$$

where  $[U_3^R]$  is the unitary similarity rotation matrix.

According to the eigenvector-based decomposition approach, the coherency matrix can be written in the form of:

$$\langle [T(\theta)] \rangle = [U_3^R] [U_3] [\Sigma] [U_3]^{*T} [U_3^R]^{-1} = [U_3'] [\Sigma] [U_3']^{*T} \quad (12)$$

where  $[\Sigma]$  is the same 3x3 diagonal matrix with nonnegative real elements.  $[U'_3] = [\underline{v}_1 \ \underline{v}_2 \ \underline{v}_3]$  is the new 3x3 unitary matrix of the SU(3) group, where  $\underline{v}_1$ ,  $\underline{v}_2$ , and  $\underline{v}_3$  are the new three unit orthogonal eigenvectors.

Following the parameterisation of the 3x3 unitary matrix  $[U'_3]$ , it can be seen that the three parameters  $\alpha_1$ ,  $\alpha_2$  and  $\alpha_3$  remain invariant, as the three eigenvalues  $(\lambda_1 \ \lambda_2 \ \lambda_3)$ .

It follows that the mean parameter  $\underline{\alpha}$ , directly related to the underlying average physical scattering mechanism, and the two important scalar functions of the eigenvalues, the entropy  $H$  and the anisotropy  $A$ , are three roll-invariant parameters.

In previous publication [1], an unsupervised classification scheme has been introduced, based on the use of the two-dimensional  $H / \underline{\alpha}$  classification plane, where all random scattering mechanisms can be represented. The  $H / \underline{\alpha}$  classification plane is subdivided into nine basic zones characteristic of classes of different scattering behavior, in order to separate the data into basic scattering mechanisms, as shown on Fig. 2 Complete details of the physical scattering characteristics of each of the nine zones can be found in [1][3].

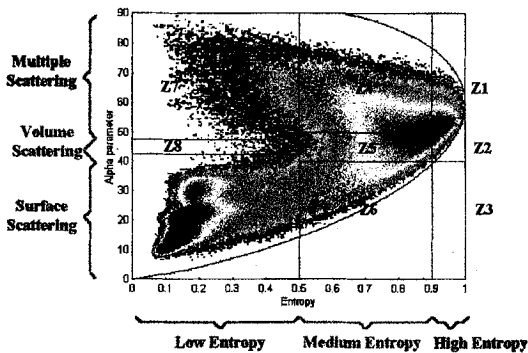


Fig. 2 : PolSAR data distribution in the two-dimensional  $H / \underline{\alpha}$  classification plane

Inherent of the spatial averaging, the entropy  $H$  may increase, and the number of distinguishable classes identifiable from polarimetric observations is reduced. For example, the feasible region of the  $H / \underline{\alpha}$  classification plane is rapidly shrinking for high values of entropy ( $H=0.9$ ), where  $\underline{\alpha}$  parameter reaches the limit value of  $60^\circ$ .

A high entropy,  $H=0.9$ , may correspond to two limit types of scattering process with associated eigenvalues spectra given, for example, by :  $\lambda_1=1, \lambda_2=0.4, \lambda_3=0.4$  or by :  $\lambda_1=1, \lambda_2=1, \lambda_3=0.3$ .

To distinguish between these two different types of scattering process, it is necessary to introduce the anisotropy information, which takes the corresponding

values  $A=0$  and  $A=0.54$  for the two previous examples.

In order to extend the classification scheme and to improve the capability to distinguish different types of scattering process, it is proposed to use some combinations between entropy and anisotropy information, as shown on Fig. 3 The  $\cdot^*$  operation represents the element by element multiplication of two matrices.

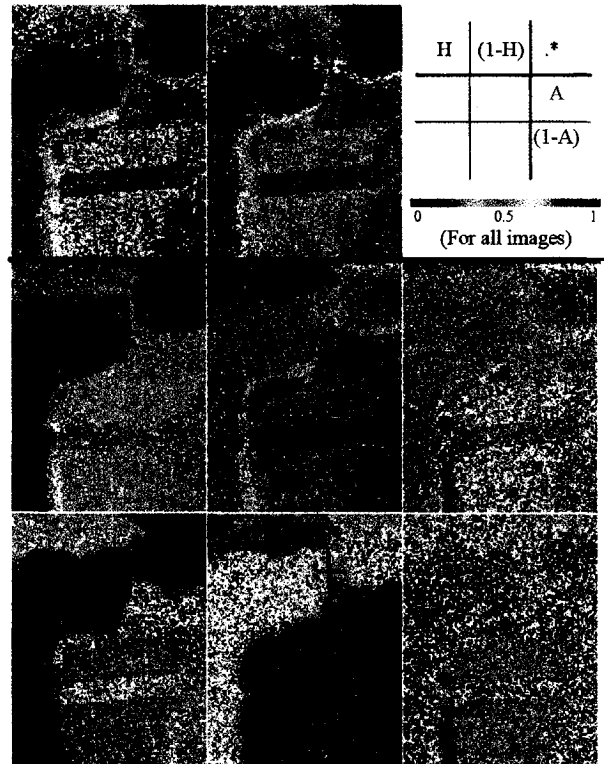


Fig. 3 : Combinations between entropy and anisotropy images.

The examination of the different figures corresponding to the different combinations between entropy and anisotropy images leads to the following remarks :

- 1) - The  $(1-H)(1-A)$  image corresponds to the presence of a single dominant scattering process (low entropy and low anisotropy with  $\lambda_2 \approx \lambda_3 \approx 0$ ).
- 2) - The  $H(1-A)$  image characterizes a random scattering process (high entropy and low anisotropy with  $\lambda_2 \approx \lambda_3 \approx \lambda_1$ )
- 3) - The  $HA$  image relates the presence of two scattering mechanisms with the same probability (high entropy and high anisotropy with  $\lambda_3 \approx 0$ ).
- 4) - The  $(1-H)A$  image corresponds to the presence of two scattering mechanisms with a dominant process (low to medium entropy) and a second one with medium probability (high anisotropy with  $\lambda_3 \approx 0$ ).

These remarks are confirmed by the analysis of the distribution of the San-Francisco bay POLSAR data in the extended and complemented three-dimensional  $H / A / \underline{\alpha}$  classification space, as shown on Fig. 4 This

representation shows that it is possible to discriminate new classes using the anisotropy value.

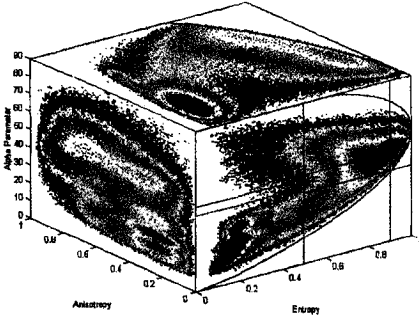


Fig. 4 : Polsar data distribution in the three dimensional  $H / A / \alpha$  classification space

For example, it is now possible to notice that there exists in the « Low Entropy Surface Scattering » area (Z9) a second class associated with a high anisotropy value and which corresponds to the presence of a second physical mechanism which is not negligible.

Identical remarks can be made concerning the « Medium Entropy Vegetation Scattering » area (Z5) and the « Medium Entropy Multiple Scattering » area (Z4). Due to the spread of the POLSAR data along the anisotropy axis, it is now possible to improve the capability to distinguish different types of scattering process which have quite the same high entropy value:

- High entropy and low anisotropy correspond to random scattering.
- High entropy and high anisotropy correspond to the presence of two scattering mechanisms with the same probability.

From the analysis of the different images shown on Fig. 3. and from the distribution of the San-Francisco bay POLSAR data in the  $H / A / \alpha$  classification space shown on Fig. 4, we can conclude that the anisotropy has to be considered now as a key parameter in the polarimetric analysis and/or inversion of POLSAR data.

The information contained in these three roll-invariant parameters extracted from the local estimate of the  $3 \times 3$  hermitian coherency matrix  $\langle [T] \rangle$ , corresponds to the type of scattering process which occurs within the pixel to be classified (combination of entropy  $H$  and anisotropy  $A$ ) and to the corresponding physical scattering mechanism ( $\alpha$  parameter).

### THE COMBINED WISHART CLASSIFIER

A polarimetric radar measures the complete scattering matrix  $[S]$  of a medium at a given incidence angle. Polarimetric SAR data are frequently multi-look processed for speckle reduction, or data compression. The relative polarimetric information is thus contained in the expected value of the coherency matrix  $\langle [T] \rangle$ .

It has been shown in [2][3] that the averaged coherency matrix  $\langle [T] \rangle$  has a complex Wishart distribution. The probability density function is given by :

$$P(\langle [T] \rangle / [T_m]) = \frac{L^L \langle [T] \rangle^{L-p} e^{-L \text{Tr}([T_m]^{-1} \langle [T] \rangle)}}{\pi^{\frac{p(p-1)}{2}} \Gamma(L) \dots \Gamma(L-p+1) \langle [T_m] \rangle^L} \quad (13)$$

where  $L$  is the number of look and  $p$  the dimension of the target vector  $\underline{k}$ , with  $p=3$  for the reciprocal case ( $S_{HV}=S_{VH}$ ) and  $p=4$  for the non-reciprocal case.  $[T_m]$  is the feature coherency matrix of the  $m^{\text{th}}$  class.

This supervised algorithm, is a maximum likelihood classifier based on the complex Wishart distribution for the polarimetric coherency matrix.

Each class is characterized by its own feature coherency matrix  $[T_m]$  which is estimated using training samples from the  $m^{\text{th}}$  class :  $\omega_m$ . According to the Bayes maximum likelihood classification procedure [2][3], an averaged coherency matrix  $\langle [T] \rangle$  is assigned to the class  $\omega_m$ , if :

$$\langle [T] \rangle \in [T_m] \text{ if } d_m(\langle [T] \rangle) < d_j(\langle [T] \rangle) \quad \forall j \neq m \quad (14)$$

with :

$$d_m(\langle [T] \rangle) = \text{Tr}([T_m]^{-1} \langle [T] \rangle) + \ln(\langle [T_m] \rangle) \quad (15)$$

Usually, to implement the classification, the coherency matrix  $[T_m]$  is estimated using pixels within different selected areas of the  $m^{\text{th}}$  class, and data is then classified pixel by pixel. These different training sets have to be selected in advance. For each pixel, represented by the averaged coherency matrix  $\langle [T] \rangle$ , the distance  $d_m(\langle [T] \rangle)$  is computed for each class, and the class associated to the minimum distance is assigned to the pixel. During the procedure, each feature coherency matrix  $[T_m]$  is iteratively updated from the initial estimate. This iterative procedure based on a distance measure, similar to the k-mean method [2][3], is simple and easy to apply. In addition, this algorithm based on the Wishart distribution, uses the full polarimetric information.

As mentioned in the previous part, the supervised algorithm based on the complex Wishart distribution needs different training sets to initialize the procedure. These training sets, selected in advance, require from the user an a priori knowledge of the different significative Earth terrain components which can be found in the POLSAR image.

Lee et al. [3] propose a combined unsupervised classification that uses the polarimetric  $H / \alpha$  decomposition and the supervised Wishart classifier. The polarimetric  $H / \alpha$  decomposition is used to initially classify the POLSAR image. This segmented image is used, then, as training sets for the initialization of the supervised Wishart classifier. The cluster centers of the coherency matrices,  $[T_m]$ , is computed for each zone, with :



$$[T_m] = \frac{1}{N_m} \sum_{k=1}^{k=N_m} ([T])_k \quad (16)$$

where  $N_m$  is the number of pixels in the a priori class  $\omega_m$ . Each pixel in the whole image is then reclassified by applying the distance measure procedure. The reclassified image is then used to update the  $[T_m]$ , and the image is then again classified by applying the same distance measure procedure. The classification procedure stops when a termination criterion, defined by the user, is met. The termination criterion we used is the number of iterations, and is here equal to 4. In this case, the ratio of pixels switching class with respect to the total pixel number is smaller than 10%. The fourth iteration result is shown on Fig. 5 and the initial color coded distribution of the data in the two-dimensional  $H/\alpha$  plane is shown on Fig. 6.



Fig. 5 : Classification result after 4 iterations

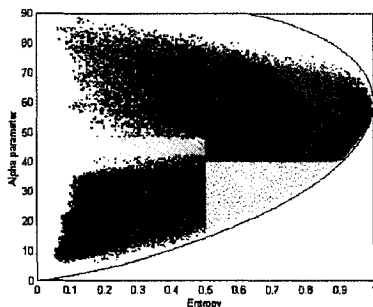


Fig. 6 : Initial color coded distribution of the data in the two-dimensional  $H/\alpha$  plane.

The entire original unsupervised Wishart classification procedure, proposed by J.S. Lee et al., and discussion about the improvement in classification can be found in [3].

The identification of the terrain type directly from the analysis of the classified image may cause some confusion, due to the color scheme [3]. Indeed, during the classification, the cluster centers in the two-

dimensional  $H/\alpha$  plane can move out of their zones, or several clusters may end in the same zone [3]. This is due to the fact that the zone boundaries were set somewhat arbitrarily as mentioned previously. A typical example is given by the coastal ocean, the gulf course or the polo field areas which are classified with a color corresponding to a random process scattering mechanism (zone Z1). It is thus necessary to study the final  $H/\alpha$  location of each class to identify the terrain type and to interpret the scattering mechanisms.

### THE PROPOSED NEW METHOD

In order to improve the capability to distinguish between different classes whose cluster centers end in the same zone, the combined Wishart classifier is extended and complemented with the introduction of the anisotropy ( $A$ ) information.

The proposed method expands the number of class from 8 to 16 by including the anisotropy. Each zone (or class) in  $H/\alpha$  plane is further divided into two classes by its pixels' anisotropy values being greater than 0.5 or less than 0.5. This procedure leads to the definition of an « equivalent » projection of the three-dimensional  $H/A/\alpha$  space in two complemented  $H/\alpha$  planes, as shown on Fig. 7 of the San Francisco bay. The color coding associated to the first 8 classes is retained and 8 new colors are introduced.

From the analysis of these two complemented  $H/\alpha$  planes, it is thus possible to define four main areas in the  $H/A$  plane ( $A1$ ,  $A2$ ,  $A3$ , and  $A4$ ), each of them gathering several zones ( $Z_i$ ), leading to the following interpretation :

- 1) - Area 1 ( $A1$ ) corresponds to the zones where occurs one single scattering mechanism. This is equivalent to the  $(1-H)(1-A)$  image.
- 2) - Area 2 ( $A2$ ) corresponds to the zones where occurs three scattering mechanisms. This is equivalent to the  $H(1-A)$  image.
- 3) - Area 3 ( $A3$ ) and Area 4 ( $A4$ ) correspond to the zones where occur two scattering mechanisms. These are equivalent respectively to the  $(1-H)A$  and  $HA$  images.

Among the different approaches tested, the best way to introduce the anisotropy information in the classification procedure consists in implementing two successive combined Wishart classifiers. The first one is identical to the previous one. Once the first classification procedure has met its termination criterion, the anisotropy comparison for all the pixels, is then introduced, which leads to the definition of 16 new training sets used for the initialization of the second Wishart classifier.

To compare with the previous procedure, we kept the same termination criterion. The fourth iteration result is shown on Fig. 8

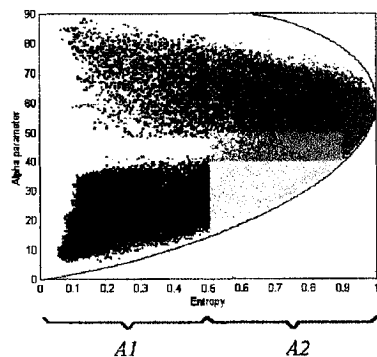


Fig. 7a : Distribution of the San-Francisco bay POLSAR data in the two-dimensional  $H/\alpha$  plane corresponding to  $A < 1/2$

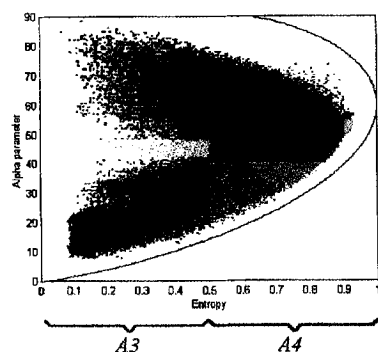


Fig. 7b : Distribution of the San-Francisco bay POLSAR data in the two-dimensional  $H/\alpha$  plane corresponding to  $A > 1/2$ .



Fig. 8 : Classification result after 4 iterations

Improvements in classification and details are observed. Grass fields are much better defined, and more details are shown both in city blocks and in ocean. Some classes, indistinguishable in the classification based on entropy ( $H$ ) and alpha angle ( $\alpha$ ) are now clearly visible with the introduction of the

anisotropy information. For example, it is now possible to clearly distinguish the coastal ocean, the gulf course and the polo field from the vegetated and park areas. It is also possible to discriminate different ocean areas, belonging to the same surface type (same entropy  $H$  and alpha angle) but differentiated with the associated anisotropy information which is there significant of the presence of several scattering mechanism types. The analysis of the final cluster centers in the three-dimensional  $H/A/\alpha$  classification space will provide a more precise interpretation of the different classes of terrain types.

## CONCLUSION

We have proposed to extend and complement the unsupervised combined Wishart classifier, originally developed by *J.S. Lee et al.* with the introduction of the polarimetric anisotropy ( $A$ ) information. The analysis of the final cluster centers in the  $H/A/\alpha$  classification space is useful for class identification of the different scattering mechanisms which occur in the classified SAR image. The introduction of the anisotropy information improves the capability to distinguish between different classes whose cluster centers end in the same entropy ( $H$ ) - alpha ( $\alpha$ ) zone.

## ACKNOWLEDGMENT

The authors wish to acknowledge the support of the ONR- NICOP program for international collaboration.

## REFERENCES

- [1] S. R. Cloude, E. Pottier « An Entropy Based Classification Scheme for Land Applications of Polarimetric SAR », *IEEE TGRS*, vol. 35, n°1, pp 68-78, January 1997.
- [2] J.S. Lee, M.R. Grunes, R. Kwok « Classification of multi-look polarimetric SAR imagery based on the complex Wishart distribution » *International Journal of Remote Sensing*, vol. 15, No. 11, pp 2299-2311, 1994.
- [3] J.S. Lee M.R. Grunes, T.L. Ainsworth, L. Du, D.L. Schuler, S.R. Cloude, « Unsupervised Classification of Polarimetric SAR Images by Applying Target Decomposition and Complex Wishart Distribution » *PIERS 1998*, Nantes, France, 13-17 July 1998, also *IEEE TGRS*, vol. 37, no.5, pp2249-2258, Sept. 1999.
- [4] S. R. Cloude, E. Pottier « A Review of Target Decomposition Theorems in Radar Polarimetry », *IEEE TGRS*, vol. 34, n°2, pp 498-518, Sept. 1995.

# Synoptic representation of the polarimetric information

P. Imbo<sup>1,3</sup> - J-C. Souyris<sup>2</sup> - A. Lopes<sup>1</sup> - Ph. Marthon<sup>3</sup>

<sup>1</sup> : Centre d'Etudes Spatiales de la Biosphère – Institut National Polytechnique de Toulouse  
18, Avenue Edouard Belin, 31401, Toulouse Cedex 4, France  
Tel : +33-(0)5-61-27-47-33 Fax : +33-(0)5-61-55-85-00 E-mail : [imbo@cesbio.cnes.fr](mailto:imbo@cesbio.cnes.fr)

<sup>2</sup> : Centre National d'Etudes Spatiales (CNES) / Département Systèmes Radar  
18, Avenue Edouard Belin, 31401, Toulouse Cedex 4, France E-mail : [souyris@cnes.fr](mailto:souyris@cnes.fr)

<sup>3</sup> : Institut National Polytechnique de Toulouse - ENSEEIHT  
2, Rue Camichel, 31071, Toulouse, France  
E-mail : [marthon@enseeiht.fr](mailto:marthon@enseeiht.fr)

## Abstract.

The purpose of this study is to build up a synoptic representation of the polarimetric information, by overlaying the output of the polarimetric analysis on a 'background' intensity image, only if it is expected to hold a pertinent additional information relatively to the intensity image. For this, we use an *Hue-Saturation-Intensity* representation of the image, Hue and Saturation being controlled by the polarimetric analysis outputs, in particular the average backscattering mechanism  $\bar{\alpha}$  and the entropy  $H$ , derived from the coherency matrix decomposition. Moreover, we present some of the preliminary results regarding the assessment of *partial polarimetry* architectures capabilities, in comparison with *full polarimetry*.

## I. Introduction.

A full polarimetric measurement is defined by the complex scattering matrix  $\overline{[S]}$ , which is constituted by the complex  $pq$  scattering coefficients, where  $p$  (resp.  $q$ ) is the transmitting (resp. receiving) polarization (1).

In the monostatic case, in virtue of the reciprocity theorem ( $f_{HV} = f_{VH}$ ), the single-look polarimetric information is fully defined by 3 intensity backscatter coefficients ( $\sigma_{HH}^0$ ,  $\sigma_{HV}^0$ ,  $\sigma_{VV}^0$ ), and two differential phases ( $\varphi_{VV} - \varphi_{HH}$ ) and ( $\varphi_{HV} - \varphi_{HH}$ ).

Full polarimetry subsequently permits:

- To apply decomposition algorithms that provide information about the dominant and average backscattering mechanisms. In many cases, this type of information is helpful for identification of the targets under observation.
- To apply the principle of polarization synthesis, which consists in deriving a target response for any set of transmitting and receiving polarization. Using this principle, a collection of images corresponding to varying polarization states can be generated and compared. The tuning of polarization is helpful in maximizing/minimizing the sensitivity of the radar measurement to bio-geophysical parameters of interest. The investigation of polarization synthesis capabilities is not further considered in the frame of this study, but remains an open subject for future studies.

The overall objective of this study is to compare *full polarimetry* and *partial polarimetry* capabilities in the context of space-borne studies. The approach consists in primarily assessing the capabilities of full polarimetry, and in further evaluating the deterioration induced by a partial acquisition of the polarimetric information. In this general context, this article is dedicated to the visualization aspect of the polarimetric information (be it full or partial), the purpose being to propose a synoptic representation of it, based on a merging of intensity and phase information.

$$\overline{[S]} = \begin{pmatrix} f_{HH} & f_{VH} \\ f_{HV} & f_{VV} \end{pmatrix} = \exp[j \cdot \varphi_{HH}] \cdot \begin{pmatrix} \sqrt{\sigma_{HH}} & \sqrt{\sigma_{VH}} \cdot \exp[j \cdot (\varphi_{VH} - \varphi_{HH})] \\ \sqrt{\sigma_{HV}} \cdot \exp[j \cdot (\varphi_{HV} - \varphi_{HH})] & \sqrt{\sigma_{VV}} \cdot \exp[j \cdot (\varphi_{VV} - \varphi_{HH})] \end{pmatrix} \quad (1)$$

$$\left[ \overline{\overline{T}} \right] = \langle \overline{\overline{k}}_p \cdot \overline{\overline{k}}_p^{*T} \rangle = \frac{1}{2} \cdot \begin{bmatrix} \langle (f_{hh} + f_{vv}) \cdot (f_{hh} + f_{vv})^* \rangle & \langle (f_{hh} + f_{vv}) \cdot (f_{hh} - f_{vv})^* \rangle & 2 \cdot \langle (f_{hh} + f_{vv}) \cdot f_{hv}^* \rangle \\ \langle (f_{hh} - f_{vv}) \cdot (f_{hh} + f_{vv})^* \rangle & \langle (f_{hh} - f_{vv}) \cdot (f_{hh} - f_{vv})^* \rangle & 2 \cdot \langle (f_{hh} - f_{vv}) \cdot f_{hv}^* \rangle \\ 2 \cdot \langle f_{hv} \cdot (f_{hh} + f_{vv})^* \rangle & 2 \cdot \langle f_{hv} \cdot (f_{hh} - f_{vv})^* \rangle & 4 \cdot \langle f_{hv} \cdot f_{hv}^* \rangle \end{bmatrix} \quad (2)$$

## I. Decomposition schemes based on full polarimetry.

From the single-look complex polarimetric image (i.e. each pixel characterized by the  $\left[ \overline{\overline{S}} \right]$  matrix), the spatial averaging of the polarimetric information relies on the second-order statistics of the backscattered field. For this, the coherency matrix [1] is defined (2) from the target vector

$$\overline{\overline{k}}_p = \frac{1}{\sqrt{2}} \cdot [f_{hh} + f_{vv} \quad f_{hh} - f_{vv} \quad 2 \cdot f_{hv}]^T;$$

$$\left[ \overline{\overline{T}} \right] = \langle \overline{\overline{k}}_p \cdot \overline{\overline{k}}_p^{*T} \rangle$$

Equivalently, the target vector  $\overline{\overline{k}}_L = [f_{hh} \quad \sqrt{2} f_{hv} \quad f_{vv}]^T$  leads to the covariance matrix  $\left[ \overline{\overline{C}} \right]$ . The average operator  $\langle \cdot \rangle$  represents a spatial averaging over neighboring pixels, using a sliding window (in this study, the window size is assigned to  $7 \times 7$ ).

The principle underlying the polarimetric analysis is the decomposition of the coherency matrix into elementary mechanisms (i.e. single, double and volume scattering). The coherency matrix being hermitian, it can be diagonalized when expressed in the basis of its eigenvectors.

### II.1 : The average scattering mechanism $\overline{\alpha}$ :

If we denote  $\overline{\overline{k}}_1, \overline{\overline{k}}_2, \overline{\overline{k}}_3$  the eigenvectors of  $\left[ \overline{\overline{T}} \right]$ , and  $\lambda_i$  its eigenvalues, it can be subsequently expressed as :  $\left[ \overline{\overline{T}} \right] = \lambda_1 \cdot \overline{\overline{k}}_1 \cdot \overline{\overline{k}}_1^H + \lambda_2 \cdot \overline{\overline{k}}_2 \cdot \overline{\overline{k}}_2^H + \lambda_3 \cdot \overline{\overline{k}}_3 \cdot \overline{\overline{k}}_3^H$ , suggesting that the backscattering mechanism can be interpreted as the incoherent sum of three elementary fully polarized backscattering mechanisms. Cloude et al. propose to parametrize  $\overline{\overline{k}}_i$  as follows :

$$\overline{\overline{k}}_i = [\cos \alpha_i, \quad \sin \alpha_i \cdot \cos \beta_i \cdot e^{j\delta_i}, \quad \sin \alpha_i \cdot \sin \beta_i \cdot e^{j\gamma_i}]^T$$

where  $\alpha_i, \beta_i, \delta_i, \gamma_i$  along with  $\lambda_i$  represent a set of five independent parameters characterizing the full polarized backscattered field. The mean parameter  $\overline{\alpha}$  (in the sense of Bernouilli) is defined by :

$$\overline{\alpha} = P_1 \alpha_1 + P_2 \alpha_2 + P_3 \alpha_3$$

where  $P_i$  are the normalized eigenvalues

$$P_i = \frac{\lambda_i}{\lambda_1 + \lambda_2 + \lambda_3}$$

$\overline{\alpha}$  is included in the range  $[0, \pi/2]$ .  $\overline{\alpha} \approx 0$  indicates an average single scattering mechanism,  $\overline{\alpha} \approx \pi/4$  an average dipole-like mechanism, and  $\overline{\alpha} \approx \pi/2$  an average double-bounce mechanism. The information content of other parameters is not considered here. However, preliminary analyses have indicated a much weaker information content than for  $\overline{\alpha}$ .

### II.2. The entropy $H$ :

It is defined by  $H = -\sum_{i=1}^3 P_i \cdot \log_3(P_i)$ . Let us consider two extreme examples : For a target which does not depolarize the impinging wave (e.g. a man-made point target), two eigenvalues among three are null, and consequently  $H=0$ . On the other hand, a truly random target has degenerated eigenvalues ( $\lambda_1 = \lambda_2 = \lambda_3$ ), and  $H=1$ .  $H$  consequently appears to be an indicator of the relative contributions of the polarized and depolarized parts of the backscattered wave.

We assume here that the complete polarimetric analysis (i.e. the use of the phase information in complement to intensity information) is useless when the entropy is high. This assumption will be refined in future studies, especially by introducing the concept of anisotropy (related to the two lowest eigenvalues  $\lambda_2$  and  $\lambda_3$ ) proposed by Pottier et al.[3] When  $H \rightarrow 1$ ,  $\overline{\alpha}$  goes to an attractor value (around  $66^\circ$ ) of doubtful significance. Hence, it is aimless to locally use  $\overline{\alpha}$  in this particular case. On the contrary, for low entropy ( $H \rightarrow 0$ ), the backscattered wave is mainly polarized, and the phase information is potentially significant.

## III. Set-up of the synoptic representation of the polarimetric information.

### III.1. Traditional approach :

The visualization of the polarimetric information is currently restricted to the display of intensity backscatter coefficients ( $\sigma_{hh}^0, \sigma_{hv}^0, \sigma_{vv}^0$ ), displayed on the Red, Green and Blue channels of a color image. Based on this choice, Fig. 1 displays a  $5m$  resolution  $L$  band airborne image (ONERA/RAMSES system) acquired over an airport environment in France (Red is  $\sigma_{hh}^0$ , Green  $\sigma_{hv}^0$ , Blue  $\sigma_{vv}^0$ ). The coloring of the image indicates the complementarity between information acquired under varying polarization conditions. This type of representation has two main drawbacks :

- 1) The use of polarimetric information is only partial (the phase is not considered).
- 2) Although we generally get a 'pretty' colored image, its interpretation is not as obvious as it would seem. In particular, the polarization state of the backscattered wave (relatively to its degree of polarization) does not appear.



**Fig. 1:** L-band airborne image (ONERA/RAMSES system) acquired over an airport environment, France. (Resolution : 5m). Red :  $\sigma_{hh}^0$ , Green :  $\sigma_{hv}^0$ , Blue :  $\sigma_{vv}^0$

As a complement to the intensity image, a collection of polarimetric parameters (requiring the phase information) can be mapped from the local estimation of  $\left[\overline{T}\right]$ . As an example, Fig. 2-a and 2-b display the entropy map and the  $\overline{\alpha}$  map of the RAMSES image. The runway indicates a low entropy (Fig.2-a), whereas the surrounding clutter is generally characterized by a higher entropy. The average backscattering mechanism (Fig.2-b) of the runway is single scattering. Moreover, we can locate on the  $\overline{\alpha}$  map black dots corresponding to trihedrals locations.

The purpose of the next section is to merge the whole polarimetric information into a single synoptic product that can make its interpretation easier.



**Fig. 2-a:** L-band 5m RAMSES image : Entropy map (window 7x7).

**Fig. 2-b:** L-band 5m RAMSES image : Average backscattering mechanism  $\overline{\alpha}$  (window 7x7).

### III.2. Synoptic representation :

The main purpose of this section is to build up a synoptic representation of the polarimetric information, by overlaying the output of the polarimetric analysis on a 'background' intensity image, only in the case where the polarimetric analysis is expected to hold an additional information relatively to the intensity image. We assume that this is the case only when the local polarimetric entropy is low. Under this assumption, the polarimetric information is visualized using an *Hue-Saturation-Intensity* representation [Fig.3]

> The *Intensity* channel can be fed either by an incoherent or a coherent sum of the complex backscattering coefficients  $f_{HH}, f_{VV}, f_{HV}$ .

- 1) The incoherent sum leads to the span operator :

$$I_{SPAN} = \sigma_{hhhh} + 2 \cdot \sigma_{hvhv} + \sigma_{vvvv}$$

$$\text{where : } \sigma_{ijij} = |f_{ij}|^2$$

- 2) The span operator not being optimal for speckle minimization, an alternate method is to use the Polarimetric Whitening Filter (PWF) introduced by [Burl et al., 1990]. The speckle reduction becomes optimal thanks to the coherent aspect of the summation. Using the covariance matrix

formalism, the intensity estimated with the PWF is given by :

$$I_{WF} = \bar{k}_L'^H \cdot \bar{k}_L'$$

with :  $\bar{k}_L' = \left[ \frac{\bar{C}}{\bar{C}} \right]^{-1/2} \cdot \bar{k}_L$

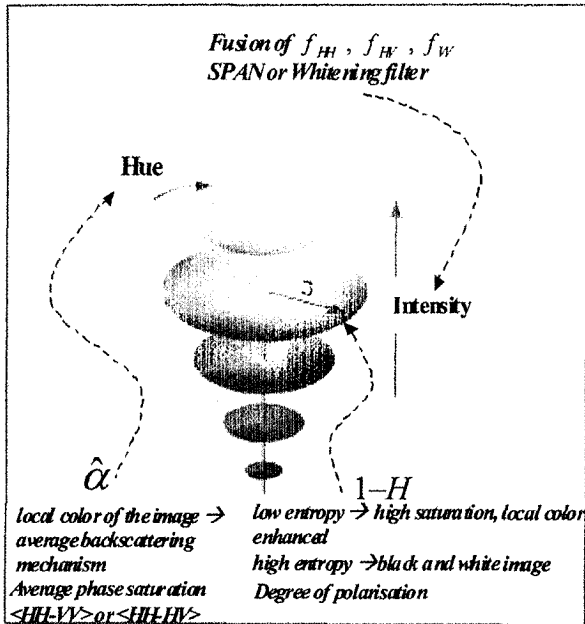


Fig. 3 : Hue-Saturation-Intensity color system

➤ The Saturation channel gives a measure of the degree to which a pure color is diluted by white light. A locally large saturation produces a coloring effect of the image. At the other end, a low saturation filters out the color component of the image and restricts the visualization to the black-and-white intensity image. In our representation, the saturation is controlled by  $(1-H)$ . For a high value of  $H$ , the local representation of the polarimetric information is limited to the intensity channel. For a low value of  $H$ , the image is locally colored. In that case, the Hue is subsequently used to define the color value.

➤ Finally, the Hue channel is the local color attribute of the image. It will be all the more visible that the level of saturation increases. The Hue is controlled by  $\bar{\alpha}$ .

Remark : An alternative representation would be to substitute the degree of polarization of the wave to  $H$ , and the average phase difference between  $HH$  and  $VV$  signals  $(\phi_{hh} - \phi_{vv})$  to  $\bar{\alpha}$ .

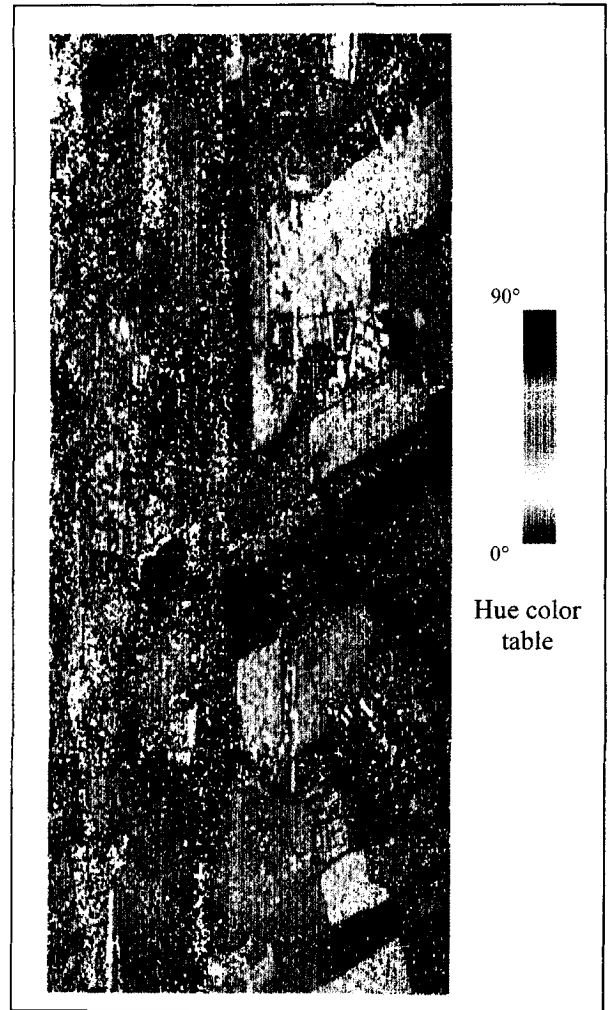


Fig. 4 : Hue-Saturation-Intensity representation of the L-band 5m RAMSES image.

Fig.4 displays the Hue-Saturation-Intensity representation of the L band RAMSES image. We mainly observe a background speckle-reduced intensity image over which colored areas (preserving the polarized structure of the backscattered wave) have been overlaid. The runway shows up in red (domination of a well-polarized single scattering effect). A break is observed on the right of its oblique part, which cannot be seen on the intensity image (see the comparison between Fig.1 and Fig.4). The greenish agricultural areas characterize structured vegetation. Finally, blue dots and lines indicate double-bounce polarized effects, presumably due to the presence of buildings parallel to the SAR trajectory. Moreover, the HSI representation highlights a range effect. The near range area (left part of the image) indicates a predominant polarized effect. Depolarizing effects naturally increase as the incidence increases. Fig. 5 displays a zoom of a 1.5 m resolution X-band image acquired by the RAMSES system over the same area.

In comparison with the previous case, two main features have changed : the frequency increased from  $L$  to  $X$ -band (expected enhancement of the depolarization effect), and the resolution moved from  $5\text{ m}$  to  $1.5\text{ m}$  (expected enhancement of the polarized part of the backscattered wave). The overall result indicates a 'cleaner' image over which the deterministic targets can be better localized. This is the case regarding a set of corner reflectors that were deployed along the runway, the red dots corresponding to trihedral and the blue ones to dihedral corner reflectors.

The purpose of the next section is to investigate the potentialities of partial polarimetric architectures regarding the visualization aspect of the information.

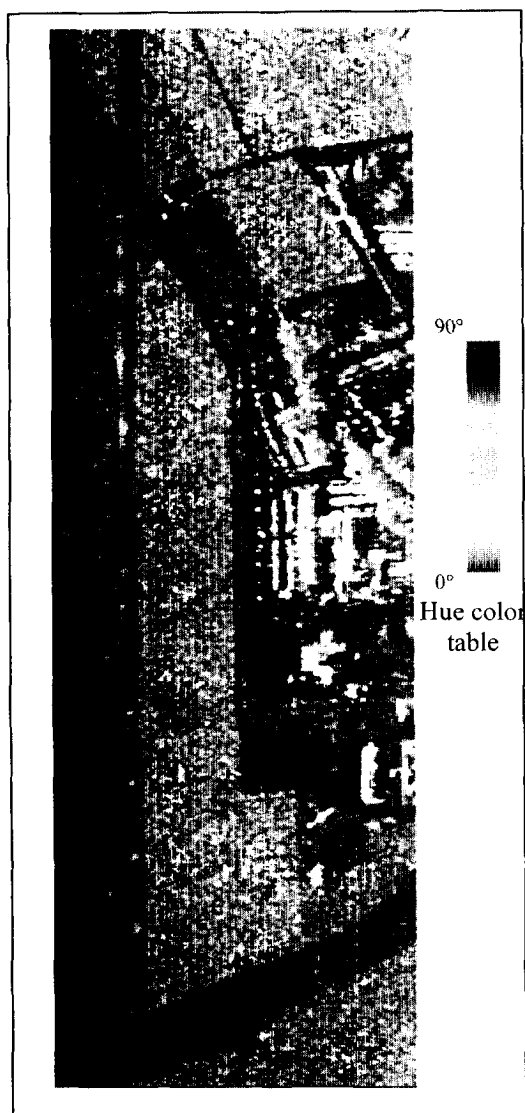


Fig. 5: Detail of the *Hue-Saturation-Intensity* representation of the  $X$  band  $1.5\text{m}$  RAMSES image.

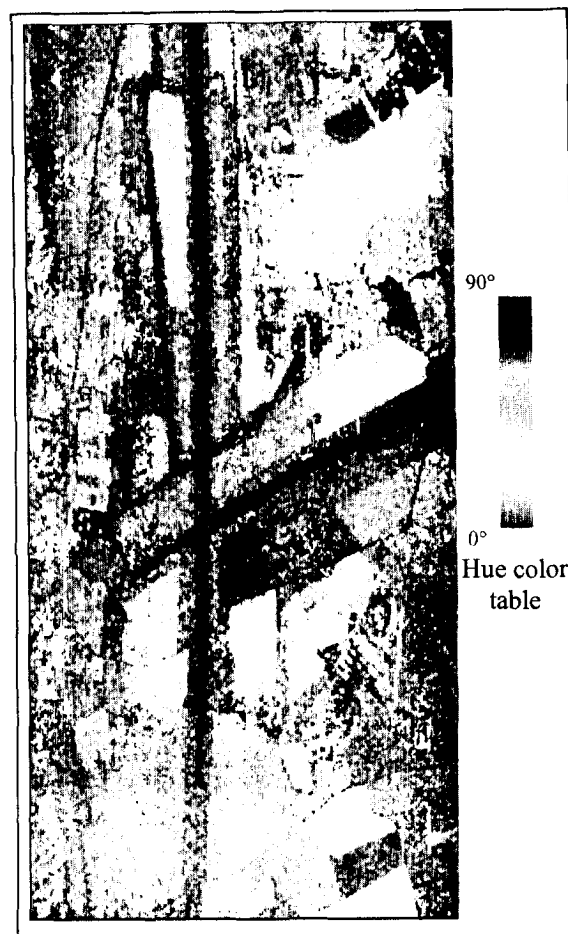


Fig. 6 : *Hue-Saturation-Intensity* representation of the  $L$  band  $5\text{m}$  image in the case of a partial polarimetry acquisition (type 1).

#### IV. Partial polarimetry architectures :

The purpose of this section is to present some of the preliminary results regarding the assessment of *partial polarimetry* architectures that can preserve a correct level of information. Beyond the multi-polarisation case, that consist in acquiring incoherently multi-amplitude data:  $\sigma_{hh}^0$ ,  $\sigma_{hv}^0$ ,  $\sigma_{vv}^0$ , such as the coming ASAR/ENVISAT in the dual-pol mode, two types of architectures were investigated :

- 1) The measurement is restricted to a coherent co-polarized information that allows to relax the power budget (no cross-polarization measurement) :  $\sigma_{hh}^0$ ,  $\sigma_{vv}^0$ , and of the degree coherence between  $HH$  and  $VV$  polarization

$$\rho = \frac{\langle f_{hh} \cdot f_{vv}^* \rangle}{\sqrt{\langle f_{hh} \cdot f_{hh}^* \rangle \cdot \langle f_{vv} \cdot f_{vv}^* \rangle}} \text{ are available.}$$

- 2) Only one transmission channel is available (e.g.H). The measurement is made of  $\sigma_{hh}^0$ ,  $\sigma_{hv}^0$ , and

$$\eta = \frac{\langle f_{hh} \cdot f_{hv}^* \rangle}{\sqrt{\langle f_{hh} \cdot f_{hh}^* \rangle \cdot \langle f_{hv} \cdot f_{hv}^* \rangle}}$$

Until now, using the *L*-band 5m resolution image, the architecture of Type 1 led to the best results in terms of visualization. Fig. 6 displays the *Hue-Saturation-Intensity* representation of the *L* band 5m image when the *Intensity* is chosen to be  $I_{SPAN} = \sigma_{hhhh} + \sigma_{vvvv}$ , the *Saturation* is controlled by  $|\rho|$ , and the *Hue* by  $|\varphi_{VV} - \varphi_{HH}|$ . When  $|\rho|$  is high the phase distribution is narrowed around its mean value. In this case, the phase difference magnitude (ranging between 0 for single scattering to  $\pi$  for double-bounce scattering) controls the Hue. Quantitatively, the comparison between Fig.4 and Fig.6 indicates similar results. The question of how much information is lost when the polarimetric acquisition is only partial remains open.

### V. Conclusion.

The investigation and the use of full polarimetry capabilities look today to be confined to a restricted community of people. Several possible reasons can be put forward : 1) The current operational spaceborne SAR systems (ERS, RADARSAT) are single-polarized. 2) The mathematical developments underlying a polarimetric analysis appear often to be complicated for people who are not familiar with them. In particular, it is difficult to have an overall idea of the polarimetric measurement considered as a whole (intensity + phase). For this reason, we proposed (almost for educational purposes ...) the synoptic representation of the polarimetric information (be it full or partial). 3) The quantitative improvement offered by polarimetry in comparison with partial polarimetry architectures, and the way these performances are corrupted by a partial acquisition of the polarimetric information (for a collection of applications) have not been extensively assessed, especially in the context of medium-resolution ( $\sim 10-20$  m), medium-frequency (*C* band) systems.

The last reason is certainly the most important one. In the context of airborne campaigns, polarimetric systems have been proven to be worthwhile. It is all the more true as the frequency (*P* or *L* band) and the resolutions ( $<5$ m) are low. The merging of polarimetric and interferometric technique is also a promising area of investigation. In the space-borne case however, the implementation of full polarimetry can be critical for several reasons. In the context of low-cost spaceborne SAR studies, it will be important to quantify in the future the increase in value offered by

polarimetry, and to consider the trade-off between polarimetry and resolution for given swath, data storage volume, and telemetry capabilities. In that context, as suggested by Professor W.M. Boerner during last CEOS SAR workshop, the comparison of multi-amplitude versus fully polarimetric (well calibrated scattering matrix) SAR image information is a subject of most importance.

### Acknowledgment.

The authors wish to acknowledge the DSP/STTC/DA/DE and ONERA/DEMR for providing us with airborne RAMSES L and C bands images.

### References.

- [1] S.R. Cloude, E. Pottier. "An Entropy Based Classification Scheme for Land Applications of Polarimetric SAR." *IEEE Trans. Geoscience and Remote Sensing*, Vol. 35, no. 1, pp 68-78, January 1997.
- [2] L.M. Novak, M.C. Burl. "Optimal speckle reduction in polarimetric SAR imagery." *IEEE Trans. On Aerospace and electronic systems*, Vol.26, no. 2, March 1999.
- [3] E.Pottier. "Application of the H/A/ $\alpha$  polarimetric decomposition theorem for unsupervised classification of fully polarimetric SAR data based on the Wishart distribution." *CEOS SAR Workshop*, Toulouse, France, October 26<sup>th</sup>-29<sup>th</sup> 1999.



## Vegetation and Ground Parameter Estimation using Polarimetric Interferometry Part I: The Role of Polarisation

K.P. Papathanassiou<sup>1</sup>, A. Reigber<sup>2</sup> and S.R. Cloude<sup>1</sup>

1: Applied Electromagnetics

83 Market Street, St. Andrews Fife, KY16 9NX, U.K. Tel./Fax. ++44-(0)1334-477598/475570

Email: ael@fges.demon.co.uk

2: Deutsches Zentrum für Luft- und Raumfahrt e.V., (DLR)

P.O. Box 11 16, D-82230 Oberpfaffenhofen, Germany. Tel/Fax: +49-8153-28-2367/-1135

Email: andreas.reigber@dlr.de

**Abstract** - - In this paper, the application of polarimetric interferometry to remote sensing and measurement of vegetation structure is further examined. In the first part, we investigate the influence of polarisation on the interferometric coherence. We analyse multibaseline fully-polarimetric interferometric L-band data and use a coherent scattering model for vegetation cover for the interpretation of the data. In the second part, we propose an inversion algorithm which allows the estimation of vegetation height and extinction using single baseline polarimetric interferometric data. Further, we investigate the physical interpretation of optimum coherence polarisations and their significance for the inversion algorithm.

### INTRODUCTION

SAR polarimetry is a well established technique, which allows the identification and separation of scattering mechanisms of natural media employing differences in the polarisation signature for purposes of classification and parameter estimation. In SAR interferometry the height of a scatterer is determined through the phase difference in images acquired from spatially separated locations. In polarimetric interferometry both techniques are used to provide combined sensitivity to the vertical distribution of scattering mechanisms. Hence it becomes possible to investigate the 3-D structure of vegetation cover using only a single frequency polarimetric radar sensor [1],[2],[3].

The development of an inversion algorithm for the estimation of forest parameters from polarimetric interferometric SAR data requires the understanding of the influence of polarisation on the interferometric observables over forested areas. Up to now, this understanding was limited because of the lack of fully polarimetric interferometric data sets. In the following, based on a simple coherent scattering model, we analyse for the first time available multibaseline fully-polarimetric interferometric SAR and investigate

the influence of polarisation on the interferometric phase and coherence.

### POLARIMETRIC INTERFEROMETRY

A monostatic, fully-polarimetric interferometric system measures for each resolution element in the scene, from two slightly different look angles, two scattering matrices,  $[S_1]$  and  $[S_2]$ . Assuming reciprocal scattering, the three-dimensional Pauli-scattering vectors  $\vec{k}_1$  and  $\vec{k}_2$  are given by [4]

$$\vec{k}_1 = \frac{1}{\sqrt{2}} [S_{1HH} + S_{1VV}, S_{1HH} - S_{1VV}, 2S_{1HV}]^T \quad (1)$$

$$\vec{k}_2 = \frac{1}{\sqrt{2}} [S_{2HH} + S_{2VV}, S_{2HH} - S_{2VV}, 2S_{2HV}]^T \quad (2)$$

The complete information measured by the SAR system can be represented in form of three  $3 \times 3$  complex block matrices  $[T_{11}]$ ,  $[T_{22}]$ , and  $[\Omega_{12}]$  formed using the outer products of  $\vec{k}_1$  and  $\vec{k}_2$

$$[T_{11}] := \langle \vec{k}_1, \vec{k}_1^\dagger \rangle, [T_{22}] := \langle \vec{k}_2, \vec{k}_2^\dagger \rangle, [\Omega_{12}] := \langle \vec{k}_1, \vec{k}_2^\dagger \rangle \quad (3)$$

$[T_{11}]$  and  $[T_{22}]$  are the conventional hermitian coherence matrices [4], which describe the polarimetric properties for each image separately, while  $[\Omega_{12}]$  is a new  $3 \times 3$  non-hermitian complex matrix which contains polarimetric and interferometric information.

Introducing two unitary complex vectors  $\vec{w}_1$  and  $\vec{w}_2$ , which may be interpreted as generalised scattering mechanisms, we are able to generate two complex scalars images  $i_1$  and  $i_2$  as the projections of the scattering vectors  $\vec{k}_1$  and  $\vec{k}_2$  onto the vectors  $\vec{w}_1$  and  $\vec{w}_2$ , respectively

$$i_1 = \vec{w}_1^\dagger \cdot \vec{k}_1 \quad \text{and} \quad i_2 = \vec{w}_2^\dagger \cdot \vec{k}_2 \quad (4)$$

The interferogram related to the scattering mechanisms described by  $\vec{w}_1$  and  $\vec{w}_2$  is given by

$$i_1 i_2^* = (\vec{w}_1^\dagger \cdot \vec{k}_1) (\vec{w}_2^\dagger \cdot \vec{k}_2)^\dagger = \vec{w}_1^\dagger [\Omega_{12}] \vec{w}_2 \quad (5)$$

and the corresponding interferometric phase follows as

$$\phi = \arg \{i_1 i_2^*\} = \arg \{ \vec{w}_1^\dagger [ \Omega_{12} ] \vec{w}_2 \} \quad (6)$$

Finally, using Eqs.(4-5) we derive the generalised vectorial expression for the interferometric coherence [1]

$$\gamma = \frac{|\langle \vec{w}_1^\dagger [ \Omega_{12} ] \vec{w}_2 \rangle|}{\sqrt{\langle \vec{w}_1^\dagger [ T_{11} ] \vec{w}_1 \rangle \langle \vec{w}_2^\dagger [ T_{22} ] \vec{w}_2 \rangle}} \quad (7)$$

with  $0 \leq \gamma \leq 1$ . For example, the  $S_{1HH} S_{2HH}^*$  interferogram may be considered to be formed according Eqs.(4-5) by using  $\vec{w}_1 = \vec{w}_2 = [ 1/\sqrt{2}, 1/\sqrt{2}, 0 ]^T$ , the  $S_{1HV} S_{2HV}^*$  interferogram by using  $\vec{w}_1 = \vec{w}_2 = [ 0, 0, 1 ]^T$ , and the  $S_{1VV} S_{2VV}^*$  interferogram by using  $\vec{w}_1 = \vec{w}_2 = [ 1/\sqrt{2}, -1/\sqrt{2}, 0 ]^T$ .

### SCATTERING MODEL

For the extraction of physical parameters from interferometric data a coherent model of the scattering process which relates the measurables to the desired parameters is required [5],[6]. In the case of vegetation at L-band an appropriate model has to consider both, vegetation and ground scattering. In a simple way the vegetation layer can be modelled as a volume with randomly oriented particles of unknown thickness  $h_V$  with scattering amplitude  $m_V$ , as shown schematically in Fig.1. The volume is located over a ground positioned at  $z = z_0$  with scattering amplitude  $m_G$ . The ground is seen through the vegetation layer employing a radar interferometer operating at wavelength  $\lambda$  with physical baseline  $B$  under a mean incident angle  $\theta_0$  at range  $R$ . In this case, the range spectral filtered complex interferometric coherence, (expressing amplitude and interferometric phase),  $\tilde{\gamma}$  may be written as [6],[7]

$$\tilde{\gamma} = \exp(i\phi_0) \frac{\tilde{\gamma}_V + m}{1 + m} \quad (8)$$

where  $\phi_0 = (4\pi/\lambda)R_0$  is the phase related to the ground topography and  $m$  the effective ground-to-volume amplitude ratio

$$m = \frac{m_G}{m_V} \exp\left(-\frac{2\sigma z'}{\cos\theta_0}\right) \quad (9)$$

$\tilde{\gamma}_V$  denotes the complex coherence for the volume alone, which depends on the extinction coefficient  $\sigma$  for the random volume, and its height  $h_V$  as

$$\tilde{\gamma}_V = \frac{I}{I_0} \left\{ \begin{array}{l} I = \int_0^{h_V} \exp\left(\frac{2\sigma z'}{\cos\theta_0}\right) \exp(i\kappa_z z') dz' \\ I_0 = \int_0^{h_V} \exp\left(\frac{2\sigma z'}{\cos\theta_0}\right) dz' \end{array} \right. \quad (10)$$

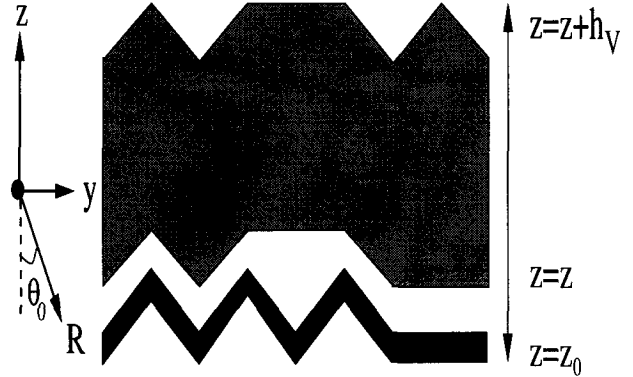


Figure 1: Schematic representation of scattering model.

The extinction coefficient  $\sigma$  corresponds to a mean extinction value for the vegetation layer, and is a function of the density of scatterers in the volume and their dielectric constant.  $\kappa_z$  is the effective vertical interferometric wavenumber after range spectral filtering, which depends on the imaging geometry and the radar wavelength

$$\kappa_z = \frac{\kappa B \cos\theta_0}{R \sin\theta_0} \quad (11)$$

According to Eq.(8), the effective scattering center is located above the ground at a height which depends on the ground-to-volume amplitude ratio  $m$  as well as the attenuation length of the vegetation layer.

Eqs.(8-11) address the coherent random volume over a ground scattering problem as a four parameter problem regarding: 1) the volume thickness  $h_V$  (in meters), 2) the volume extinction coefficient  $\sigma$  (in dB/m), 3) the effective ground-to-volume amplitude ratio  $m$ , and, 4) the phase of the underlying topography  $\phi_0$ . Thus, it cannot be resolved using a single interferometric observation, which provides only two independent measurables, namely the interferometric phase and coherence, in form of the complex coherence coefficient  $\tilde{\gamma}$ .

Fig. 2 shows the dependency of the interferometric coherence of the volume  $|\tilde{\gamma}_V|$  on the extinction coefficient  $\sigma$  and the height  $h_V$  according to Eq.(10), for the case of an L-band interferometric system ( $\lambda = 0.24\text{m}$ ) operating at a height of 3220m with a baseline of  $B = 25\text{m}$  and incident angle  $\theta_0 = 30^\circ$ . It demonstrates clearly the height/extinction ambiguity in the evaluation of the interferometric coherence: high vegetation with a high extinction coefficient may be characterised by the same coherence as a lower vegetation with a lower extinction coefficient [8],[5].

In contrast to the volume scatterer, where the phase centers of the volume particles are distributed over

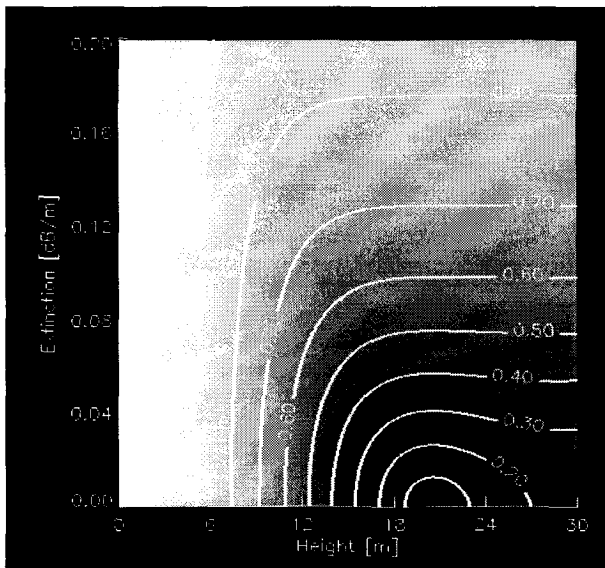


Figure 2:  $|\tilde{\gamma}|$  as a function of  $h_V$  and  $\sigma$ .

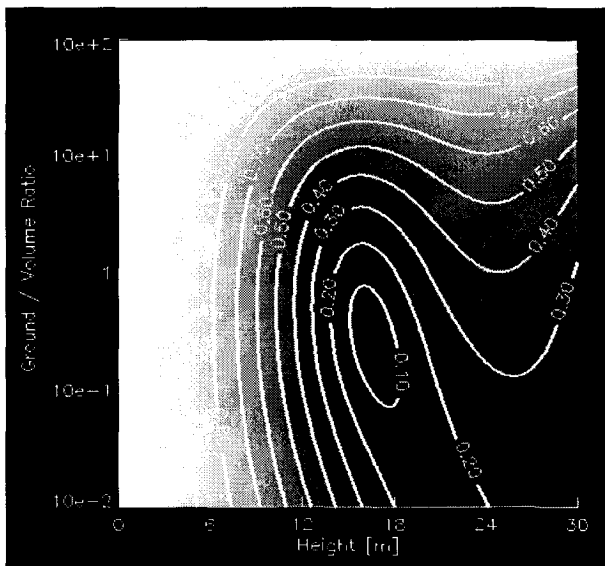


Figure 3:  $|\tilde{\gamma}|$  as a function of  $h_V$  and  $m$  for  $\sigma=0.02\text{dB/m}$ .

the height  $h_V$ , the ground is characterised by a fixed scattering phase center. Therefore it has a strong effect on the interferometric coherence even if its scattering amplitude is relatively small compared to the scattering amplitude of the volume. Figs. 3 and 4 demonstrate the influence of the ground scattering on the interferometric coherence  $|\tilde{\gamma}|$  in terms of Eq(8): Fig.3 shows the variation of  $|\tilde{\gamma}|$  as a function of the ground-to-volume amplitude ratio  $m$  and the height  $h_V$  for a fixed extinction  $\sigma=0.02\text{dB/m}$ , while Fig.4 shows the variation of  $|\tilde{\gamma}|$  as a function of  $m$  and  $\sigma$  for a fixed height  $h_V=20\text{m}$ . In both cases the same imaging geometry as for Fig.2. is used. As the ground component increases from zero, it increases the effective height distribution of the scatterers and the interferometric coherence reduces. However, as

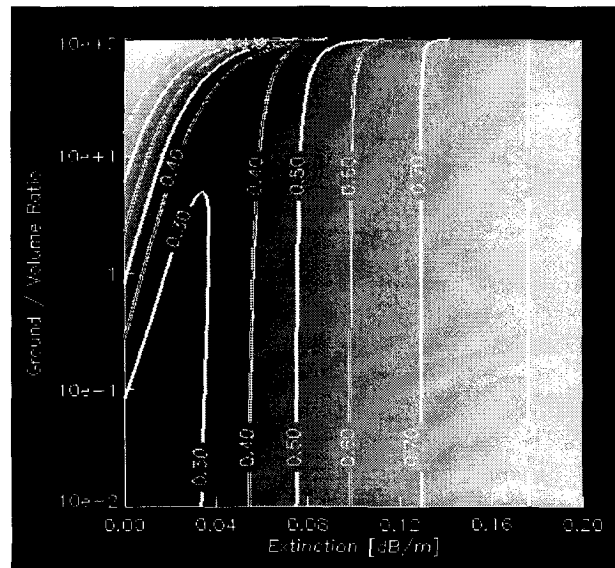


Figure 4:  $|\tilde{\gamma}|$  as a function of  $\sigma$  and  $m$  for  $h_V=20\text{m}$ .

the ground component becomes on the order of the volume scattering component the interferometric coherence increases with increasing ground component in consequence of the presence of a localised scattering center. As one can see in Figs. 3 and 4, the influence of the ground is especially critical for  $10^{-1} < m < 1$  where an increase of  $m$  of the order of few percent can occasionally (depending on the actual  $h_V$  and  $\sigma$  values) increase or decrease considerable the interferometric coherence, leading to a biased estimation of  $h_V$  and  $\sigma$ . Therefore, the accurate estimation of the ground-to-volume amplitude ratio is a key element in the inversion of  $h_V$  and  $\sigma$  from interferometric data especially at frequencies or polarisations characterised by a low ground-to-volume amplitude ratio.

#### EFFECTS OF POLARISATION

In this section, we examine the influence of polarisation on the interferometric coherence  $\tilde{\gamma}$  and investigate the potential of the random volume over a ground scattering model for the interpretation of polarimetric interferometric data. For this we use fully polarimetric repeat-pass interferometric data L-band of the Oberpfaffenhofen test site, acquired by DLR's airborne experimental SAR system in the frame of a multi-baseline experiment in May 1998.

First we consider the case of an isolated random volume. Random volumes are characterised by a diagonal coherency matrix, where the diagonal terms depend only on the shape and dielectric constant of the particles in the volume [9]. Furthermore, propagation through a random volume is polarisation independent. Therefore, polarisation has no influence on the interferometric coherence  $\tilde{\gamma}$  apart from the

amount of backscattered intensity. Assuming a sufficient high backscattered signal, all polarisations lead to interferograms with the same coherence given by  $\tilde{\gamma}_V$ . In this special case the interferometric coherence, for a given  $h_V$  and  $\sigma$ , depends only on the vertical wavenumber  $\kappa_z$ . Polarimetric interferometry does not provide any additional information over single channel interferometry and single polarisation multibaseline approaches may be used for the estimation of  $h_V$  and  $\sigma$  utilising its dependency on  $\kappa_z$  [5],[6].

The situation changes dramatically with the introduction of the ground in the scattering scenario. The fact that the ground has a strongly polarisation dependent behaviour combined with the gained cognition that even small ground scattering contributions affect significantly the interferometric coherence make polarimetric interferometry a challenge.

The scattering model as given in Eqs.(8-10) can be used straightforwardly for the qualitative interpretation of the data. The only note of caution is required on the constitution of the assumptions about the ground scattering process. In conventional polarimetric vegetation modelling the ground is usually assumed as a single component non-depolarising scattering process. In interferometric modelling the sensitivity of the interferometric coherence to any ground component constrains the consideration of a multi-component depolarising ground. The different ground scattering contributions in the different polarisations forces the interferometric coherence to be a function of polarisation.

The influence of polarisation on the interferometric coherence is demonstrated in Fig.5 where the coherence maps of interferograms formed using different polarisations for two baselines  $B = 15\text{m}$ , and  $B = 25\text{m}$  are shown. The scaling from white to black corresponds to the coherence range from 1 to 0. The high coherence ( $|\tilde{\gamma}| \approx 1$ ) of a zero baseline interferogram, formed using one image acquired at the begin and one at the end of the experiment, allows us to neglect the effect of temporal decorrelation in the interpretation of the data [10]. According to the considerations above, the polarisation dependency of the coherence values over the forested areas validates the presence of ground scattering. Further, the appearance of three discriminated coherence values, indicates different ground-to-volume amplitude ratios in the different polarisations. This confirm the hypothesis of a multi-component ground scattering process. To illustrate the amount of volume scattering component the difference between the coherence values for the two baselines,  $\Delta\gamma = \gamma_{B1} - \gamma_{B2}$  is shown in Fig.5. As

the coherence of the ground scattering is independent of baseline because of the fixed scattering center, any baseline variation of the observed coherence is induced by a volume scattering component. One can see that not only the  $S_{HV}$  channel but also the  $S_{HH}$  and  $S_{VV}$  channels are affected by significant volume scattering contributions. The existence of volume scattering in all three orthogonal polarisations confirms the assumption of a random volume.

The only alternative scenario, apart from a random volume over a depolarising ground, which leads to three different coherence values in the three orthogonal polarisations is the presence of orientation effects in the volume [11],[7]. Because of the vertical orientation of the trees, the eigenpolarisations of the oriented volume are expected to be given by the  $S_{HH}$  and  $S_{VV}$  polarisations. In this case the  $S_{1VV}S_{2VV}^*$  interferogram will have the highest coherence, while the  $S_{1HH}S_{2HH}^*$  interferogram will have a lower coherence than the  $S_{1HV}S_{2HV}^*$  interferogram in consequence of a larger volume component. The fact that the  $S_{1HH}S_{2HH}^*$  interferogram shows a higher coherence and has a smaller volume component than the  $S_{1HV}S_{2HV}^*$  interferogram denies volume orientation effects in the interpretation of this data.

## CONCLUSIONS

In the first part of this two-part paper a qualitative analysis of polarisation effects on the interferometric coherence based on multibaseline polarimetric interferometric SAR data and a two stage scattering model for vegetation was performed.

One of the central conclusions is the fundamental importance of the ground scattering: on the one hand, any ground scattering component affects strongly the interferometric coherence. This makes the parameter inversion from interferometric observables not possible without an accurate estimation of the amount of ground scattering. On the other hand, the appearance of the ground forces the interferometric coherence to be polarisation dependent. As polarimetry can be used, directly or indirectly, for the estimation of the ground scattering component, polarimetric interferometry becomes a potential technique for vegetation parameter estimation.

The analysis of the experimental data indicates the presence of a multi-component depolarising ground. This, combined with a random vegetation layer, leads to a second important conclusion: there is no polarisation without both volume and ground scattering contribution. Therefore, a straightforward

estimation of forest height in terms of the phase difference of scattering centers at different polarisations is in general not possible. A more sophisticated inversion technique, which has to take into account the interferometric phase as well as the interferometric coherence at different polarisations is necessary for the extraction of vegetation height and extinction from fully polarimetric interferometric SAR data.

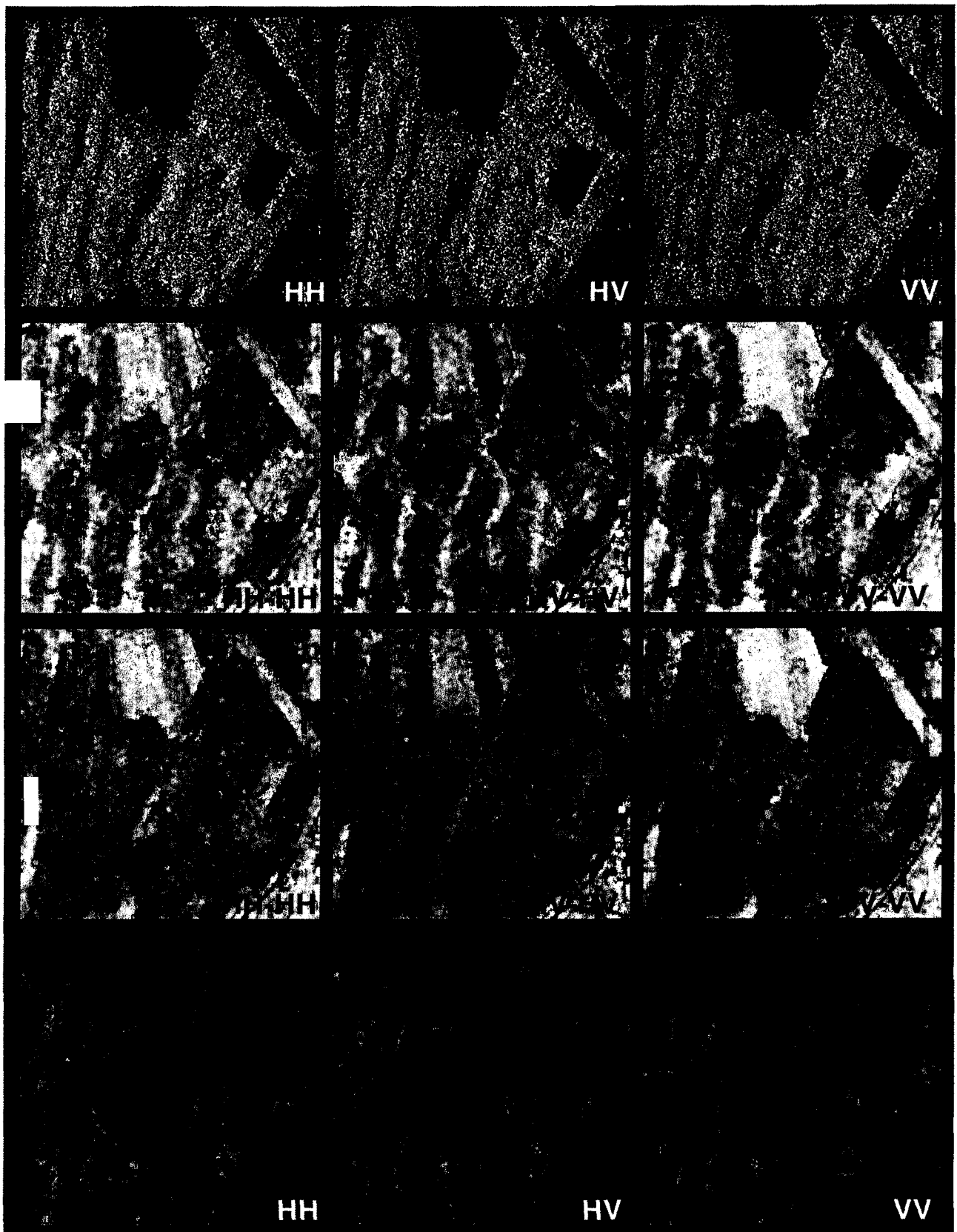
Finally, the random volume over ground scattering model, despite its simplicity, seems to have enough physical structure for the interpretation of the experimental data sets in L-band. This is important because allows, as will be demonstrated in the second part of this paper, the inversion of vegetation parameters from single baseline polarimetric interferometric data. A more extended vegetation scattering model would introduce additional parameters which can no longer be estimated without the need for a priori information or other assumptions.

#### ACKNOWLEDGEMENTS

This work was carried out in the frame of EC-TMR and ONR-NICOP projects. The authors would like to thank R. Treuhaft from JPL, and W-M. Boerner from UIC, for many constructive discussions.

#### REFERENCES

- [1] S.R. Cloude, and K.P. Papathanassiou, "Polarimetric SAR Interferometry", *IEEE Transactions on Geoscience and Remote Sensing*, vol. 36, no. 5, pp. 1551-1565, 1998.
- [2] K.P. Papathanassiou, and S.R. Cloude, "Phase Decomposition in Polarimetric SAR Interferometry", *Proceedings IGARSS'98*, pp. 2184-2186, Seattle, 3-8 August 1998.
- [3] K.P. Papathanassiou, A. Reigber, R. Scheiber, R. Horn, A. Moreira, and S.R. Cloude, "Airborne Polarimetric SAR Interferometry", *Proceedings IGARSS'98*, pp. 1901-1904, Seattle, 3-8 August 1998.
- [4] W.M. Boerner *et al.*, "Polarimetry in Radar Remote Sensing: Basic and Applied Concepts", Chapter 5 in F.M. Henderson, and A.J. Lewis, (ed.), "Principles and Applications of Imaging Radar", vol. 2 of *Manual of Remote Sensing*, (ed. R.A. Reyerson), Third Edition, John Wiley & Sons, New York, 1998.
- [5] R.N. Treuhaft, S.N. Madsen, M. Moghaddam, and J.J. van Zyl, "Vegetation Characteristics and Underlying Topography from Interferometric Data", *Radio Science*, vol. 31, pp. 1449-1495, 1996.
- [6] R.N. Treuhaft, and P.R. Siqueira, "The Vertical Structure of Vegetated Land Surfaces from Interferometric and Polarimetric Radar", to be published in *Radio Science*.
- [7] S.R. Cloude, and K.P. Papathanassiou, "Polarimetric Interferometry for Vegetation Parameter Inversion", in preparation.
- [8] J. Askne, P.B. Dammert, L.M. Ulander, and G. Smith, "C-Band Repeat-Pass Interferometric SAR Observations of the Forest", *IEEE Transactions on Geoscience and Remote Sensing*, vol. 35, no. 1, pp. 25-35, 1997.
- [9] S.R. Cloude, J. Fortuny, J.M. Lopez, and A.J. Sieber, "Wide Band Polarimetric Radar Inversion Studies for Vegetation Layers", *IEEE Transactions on Geoscience and Remote Sensing*, vol. 37, no. 5, pp. 2430-2442, 1999.
- [10] A. Reigber and A. Moreira, "First Demonstration of Airborne SAR Tomography using Multibaseline L-Band Data", submitted to *IEEE Transactions on Geoscience and Remote Sensing*.
- [11] R.N. Treuhaft, and S.R. Cloude, "The Structure of Oriented Vegetation from Polarimetric Interferometry", *IEEE Transactions on Geoscience and Remote Sensing*, vol. 37, no. 5, pp. 2620-2625, 1999.



**Figure 5:** First Line:  $S_{HH}$ ,  $S_{HV}$ , and  $S_{VV}$  images. Second Line:  $S_{1HH}S_{2HH}^*$ ,  $S_{1HV}S_{2HV}^*$ , and  $S_{1VV}S_{2VV}^*$  coherence maps for  $B=15\text{m}$ . Third Line:  $S_{1HH}S_{2HH}^*$ ,  $S_{1HV}S_{2HV}^*$ , and  $S_{1VV}S_{2VV}^*$  coherence maps for  $B=25\text{m}$ . Fourth Line: Baseline induced coherence differences in HH, HV and VV polarisations.

## Vegetation and Ground Parameter Estimation using Polarimetric Interferometry Part II: Parameter Inversion and Optimal Polarisation

K.P. Papathanassiou<sup>1</sup>, A. Reigber<sup>2</sup> and S.R. Cloude<sup>1</sup>

1: Applied Electromagnetics

83 Market Street, St. Andrews Fife, KY16 9NX, U.K. Tel./Fax. ++44-(0)1334-477598/475570

Email: ael@fges.demon.co.uk

2: Deutsches Zentrum für Luft- und Raumfahrt e.V., (DLR)

P.O. Box 11 16, D-82230 Oberpfaffenhofen, Germany. Tel/Fax: +49-8153-28-2367/-1135

Email: andreas.reigber@dlr.de

**Abstract** - - In this two part paper, the application of polarimetric interferometry to remote sensing and measurement of vegetation structure is further examined. In the second part here, we propose an inversion algorithm which allows the estimation of vegetation height and extinction using single baseline polarimetric interferometric data. Further, we investigate the physical interpretation of optimum coherence polarisations and their significance for the inversion algorithm.

### INTRODUCTION

Polarimetric SAR interferometry is a new technique which combines polarimetric and interferometric information for the evaluation of the 3-D structure of scattering processes [1]. In [1] we have demonstrated this potential using the phase difference between interferograms formed using optimal polarisations to resolve the location of the effective scattering center of different vegetation scattering mechanisms. However, as shown in the first part, in the case of a random vegetation layer over a rough depolarising surface, all polarisations are affected by both volume and ground scattering. Hence, the estimation of forest height in terms of the phase difference of scattering centers at different polarisations is, in general, not possible. In the following, we propose a new inversion algorithm which utilises both, interferometric phase and coherence and allows the extraction of vegetation parameters from single baseline fully polarimetric interferometric data.

### INVERSION ALGORITHM

As discussed in the first part, the coherent random volume over a ground scattering scenario can be addressed for a single polarisation in terms of four parameters: the volume thickness  $h_V$ , the volume extinction coefficient  $\sigma$ , the effective ground-to-volume amplitude ratio  $m$ , and the phase  $\phi_0$  related to the underlying topography. Therefore, single polarisation single baseline interferometry which provides only two

interferometric observables (the interferometric phase and coherence) is not able to resolve the problem. The use of an additional polarisation channel increases the number of observables by two, but at the same time, as the ground scattering is present in different amounts in all polarisations, introduces one additional unknown parameter: the ground-to-volume amplitude ratio of the new polarisation. Consequently, for the inversion of the random volume over a ground scattering scenario at least three polarisations, and therefore, fully polarimetric interferometric data are required.

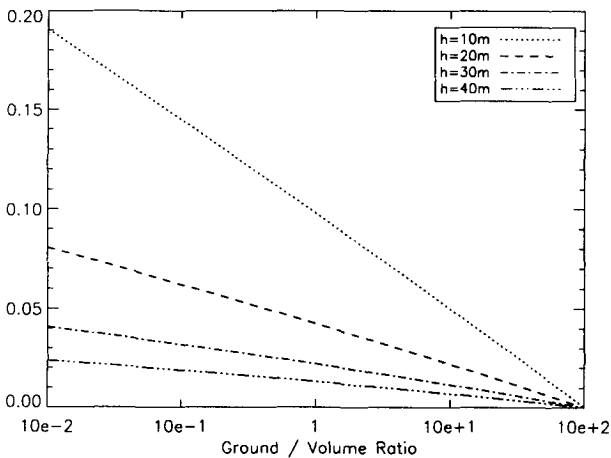
With  $\tilde{\gamma}_1$ ,  $\tilde{\gamma}_2$ , and,  $\tilde{\gamma}_3$  defined to be three complex coherence values at different polarisations the inversion algorithm can be formulated as

$$\begin{bmatrix} h_V \\ \exp(i\phi_0) \\ \sigma \\ m_1 \\ m_2 \\ m_3 \end{bmatrix} = [\mathcal{M}]^{-1} \begin{bmatrix} \tilde{\gamma}_1 \\ \tilde{\gamma}_2 \\ \tilde{\gamma}_3 \end{bmatrix} \quad (1)$$

where the operator  $[\mathcal{M}]$  represents the physical scattering model, as given in Eqs.(8-11) in the first part, which relates the measurables to the physical parameters of the scattering process [2]. As the unknown parameters are coupled, Eq.(1) becomes a non-linear parameter optimisation problem

$$\min \left( \left\| \begin{bmatrix} \tilde{\gamma}_1 \\ \tilde{\gamma}_2 \\ \tilde{\gamma}_3 \end{bmatrix} - [\mathcal{M}] \begin{bmatrix} h_V \\ \exp(i\phi_0) \\ \sigma \\ m_1 \\ m_2 \\ m_3 \end{bmatrix} \right\| \right) \quad (2)$$

$\|\dots\|$  indicates the Euclidean vector norm. Note that it is important to estimate the underlying topographic phase in the complex domain in order to preserve the phase variations over more than one  $2\pi$  cycle

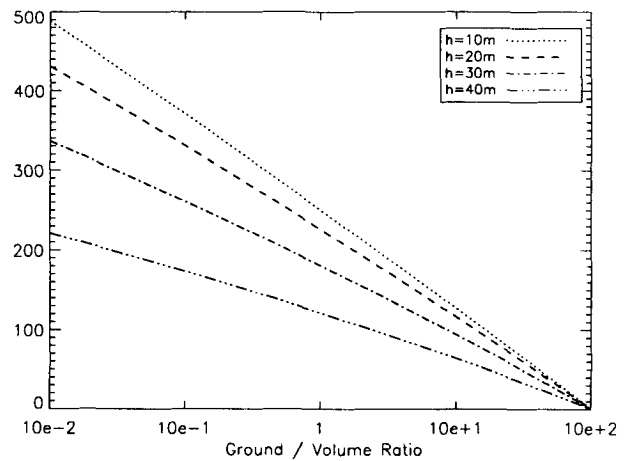


**Figure 1:**  $\partial|\tilde{\gamma}|/\partial h_V$  as a function of the effective ground-to-volume amplitude ratio  $m$ .

as is the case in the presence of topography and/or uncompensated range variation.

The performance of the inversion algorithm depends on the choice of the three polarisations used corresponding to  $\tilde{\gamma}_1$ ,  $\tilde{\gamma}_2$ , and,  $\tilde{\gamma}_3$ . On the other hand, the availability of the complete scattering matrix allows the formation of interferograms in all possible polarisation combinations [1]. To achieve a high estimation accuracy, sensitivity of the coherences  $\tilde{\gamma}_1$ ,  $\tilde{\gamma}_2$ , and,  $\tilde{\gamma}_3$  to all six parameters is required [2]. However, sensitivity is not the central criterion for accurate parameter estimation. The key point is the conditioning of the inversion problem. It can be expressed in terms of the independence of the derivatives of the observables with respect to the parameters. In other words, the more different the influence of the variation of one parameter on the measurables becomes, the higher is the estimation accuracy. In the limit where the variation of one parameter affects only one measurable, the parameter can be estimated directly.

Fig. 1 shows the coherence sensitivity with respect to height  $h_V$  (i.e.,  $\partial|\tilde{\gamma}|/\partial h_V$ ) as a function of the effective ground-to-volume amplitude ratio  $m$  for different heights  $h$ . It shows that as the difference between ground-to-volume ratios in two polarisation states increases, the difference of their coherence sensitivity to height variations increases. Analogously, Fig. 2 shows the coherence sensitivity with respect to the extinction  $\sigma$  (i.e.,  $\partial|\tilde{\gamma}|/\partial\sigma$ ) as a function of the effective ground-to-volume amplitude ratio  $m$ . Also here, the difference in the coherence sensitivity to extinction variations increases with increasing difference in  $m$ . Consequently, the conditioning of the inversion problem depends directly on the difference of the ground-to-volume ratios of the used



**Figure 2:**  $\partial|\tilde{\gamma}|/\partial\sigma$  as a function of the effective ground-to-volume amplitude ratio  $m$ .

polarisations. The use of polarisations with very different ground contributions improves therefore the estimation accuracy, while the use of polarisations with similar ground contributions leads to a poor parameter estimation. We will show that the coherence optimisation algorithm proposed in [1] presents the best possible condition.

Finally, as the proposed inversion algorithm uses the interferometric phase information of the individual polarisations, its performance is sensitive to the phase noise of the interferograms. Thus in general, polarisations with a high interferometric coherence are preferred. However, a loss in coherence can be compensated by spatial averaging taking into account the reduction of spatial resolution.

## POLARIMETRIC COHERENCE OPTIMISATION

The presence of multiple ground scattering components forces the interferometric coherence to be a function of polarisation. The evaluation of the polarisation states which provide the highest possible interferometric coherence leads to two  $3 \times 3$  complex eigenvalue problems with common eigenvalues  $\nu_j$  [1]

$$[T_{22}]^{-1}[\Omega_{12}]^\dagger [T_{11}]^{-1}[\Omega_{12}]\vec{w}_2 = \nu_j \vec{w}_2, \quad (3)$$

$$[T_{11}]^{-1}[\Omega_{12}][T_{22}]^{-1}[\Omega_{12}]^\dagger \vec{w}_1 = \nu_j \vec{w}_1, \quad (4)$$

Eqs.(3-4) yield three pairs (one for each image) of eigenvectors  $\{\vec{w}_1, \vec{w}_2\}$ , with  $j = 1, 2, 3$ , representing the optimum scattering mechanisms. The projection of the scattering vectors  $\vec{k}_1$  and  $\vec{k}_2$  onto  $\vec{w}_1$  and  $\vec{w}_2$ , leads to the two optimised scalar complex images  $i_1$  and  $i_2$ , which are used for the interferogram formation

$$i_{11}i_{21}^* = (\vec{w}_1^\dagger \cdot \vec{k}_1)(\vec{w}_2^\dagger \cdot \vec{k}_2)^\dagger = \vec{w}_1^\dagger [\Omega_{12}] \vec{w}_2, \quad (5)$$



$$i_{1_2} i_{2_2}^* = (\vec{w}_{1_2}^\dagger \cdot \vec{k}_1)(\vec{w}_{2_2}^\dagger \cdot \vec{k}_2)^\dagger = \vec{w}_{1_2}^\dagger [\Omega_{12}] \vec{w}_{2_2} \quad (6)$$

$$i_{1_3} i_{2_3}^* = (\vec{w}_{1_3}^\dagger \cdot \vec{k}_1)(\vec{w}_{2_3}^\dagger \cdot \vec{k}_2)^\dagger = \vec{w}_{1_3}^\dagger [\Omega_{12}] \vec{w}_{2_3} \quad (7)$$

The three real eigenvalues  $\nu_j$  of Eq.(1-2) are related to the corresponding coherence values as

$$\gamma_1 = \sqrt{\nu_1}, \quad \gamma_2 = \sqrt{\nu_2}, \quad \text{and} \quad \gamma_3 = \sqrt{\nu_3} \quad (8)$$

To avoid any confusion, in the following we distinguish between the conventional coherence value  $\gamma$  and the complex coherence value  $\tilde{\gamma} = \gamma \exp i\phi$  which includes additionally the interferometric phase.

In the extreme case of no ground contribution,  $m_1, m_2$  and  $m_3 \mapsto 0$  and the interferometric coherence becomes independent of polarisation. In this case, the coherence optimisation algorithm performs a pure signal-to-noise optimisation. All optimum polarisations have the same scattering center, which location depends on the volume height and extinction, and assuming a sufficiently high signal-to-noise ratio equal coherence values

$$\gamma_1 = \gamma_2 = \gamma_3 = |\tilde{\gamma}_V| < 1 \quad (9)$$

$\tilde{\gamma}_V$  denotes the coherence for the isolated volume. At the other extreme, where only ground scattering occurs,  $m_1, m_2$  and  $m_3 \mapsto \infty$  and  $\gamma \mapsto 1$  independent of polarisation (irrespective of polarimetric signal-to-noise effects) and baseline. The scattering center for all polarisations is located on the ground. In general, the situation will be between these two extremes.

In a simplified interpretation, for the case of a random vegetation layer over a multi-component ground scatterer, the coherence optimisation algorithm is trying to select the ground which gives the inherently highest coherence. But, in the case of a random volume of non-spherical particles it is not possible to remove totally the coherence reducing volume contribution. In order to maximise the interferometric coherence, the algorithm compromises between maximising the ground return and minimising the volume contribution. Thus, it identifies as optimal the polarisation in which the effective ground-to-volume amplitude ratio  $m$  is maximised. The second optimum coherence value corresponds to a ground-to-volume amplitude maximisation performed in a two-dimensional subspace orthogonal to the first solution. Finally the third optimum coherence value represents the maximisation of  $m$  in the one dimensional subspace orthogonal to the first and second solutions. In the case of two orthogonal ground scattering components, (for example direct surface scattering and dihedral ground-trunk interaction) this third optimum coherence value equals the volume coherence  $\tilde{\gamma}_V$ , since the ground components lie in the orthogonal subspace defined by the first two

solutions. However, in the presence of a three component ground, even the third optimum coherence value is affected by a ground scattering component which has to be accounted for. Thus, the optimisation algorithm determines three different coherence values corresponding to different ground to volume amplitude ratios  $m_1 > m_2 > m_3$

$$1 > \gamma_1 > \gamma_2 > \gamma_3 \quad (10)$$

with

$$\gamma_1 = \left| \frac{\tilde{\gamma}_V + m_1}{1 + m_1} \right|, \gamma_2 = \left| \frac{\tilde{\gamma}_V + m_2}{1 + m_2} \right|, \gamma_3 = \left| \frac{\tilde{\gamma}_V + m_3}{1 + m_3} \right| \quad (11)$$

where  $\tilde{\gamma}_V$  denotes the complex coherence for the volume alone. The location of the effective scattering center for each optimum scattering mechanism depends on the corresponding ground-to-volume amplitudes and the attenuation length in the volume. The residual volume component forces all three coherence values to be baseline dependent to a degree dependent on the amount of the individual ground component.

We obtain the complex coherence values using the square roots of the real eigenvalues of Eqs.(1-2) and the phase of the interferogram formed using the projections of the optimum scattering mechanisms onto the corresponding scattering vectors

$$\tilde{\gamma}_1 = \sqrt{\nu_1} \exp(-i \arg\{(\vec{w}_{1_1}^\dagger \cdot \vec{k}_1)(\vec{k}_2^\dagger \cdot \vec{w}_{2_1})\}) \quad (12)$$

$$\tilde{\gamma}_2 = \sqrt{\nu_2} \exp(-i \arg\{(\vec{w}_{1_2}^\dagger \cdot \vec{k}_1)(\vec{k}_2^\dagger \cdot \vec{w}_{2_2})\}) \quad (13)$$

$$\tilde{\gamma}_3 = \sqrt{\nu_3} \exp(-i \arg\{(\vec{w}_{1_3}^\dagger \cdot \vec{k}_1)(\vec{k}_2^\dagger \cdot \vec{w}_{2_3})\}) \quad (14)$$

Fig.3 shows the  $S_{1_{HH}} S_{2_{HH}}^*$ ,  $S_{1_{HV}} S_{2_{HV}}^*$ ,  $S_{1_{VV}} S_{2_{VV}}^*$  coherence maps in comparison to the three optimum coherence images for a baseline of  $B = 25\text{m}$ . The scaling from white to black corresponds to the coherence range from 1 to 0. The first optimum coherence is significantly higher than  $S_{1_{VV}} S_{2_{VV}}^*$  indicating a higher ground scattering component. On the other hand, the  $S_{1_{HV}} S_{2_{HV}}^*$  coherence is higher than the third optimum coherence indicating the presence of a cross-polarising ground component. This underlines the assumption of a three-component ground. As expected, the optimum coherence values becomes 1 on the fields but drops down in the forested areas, because of the residual volume component.

## EXPERIMENTAL RESULTS

In the sense of parameter inversion, the coherence optimisation algorithm as it is trying either to identify the ground (forcing as much as possible  $m \mapsto \infty$ ), or to isolate the volume (forcing  $m \mapsto 0$ ), may

be interpreted as a data adaptive pre-conditioning procedure for the inversion problem. The optimum polarisations are characterised by the widest possible ground-to-volume amplitude ratio spectrum, and therefore lead to the best possible conditioning of the inversion problem. Fig 4. shows the estimated ground-to-volume amplitude ratios for the  $S_{VV}$ ,  $S_{HH}$ , and  $S_{HV}$  in comparison to those of the optimal polarisations, and demonstrates in a direct way two central points of this paper: the ground scattering is present in all polarisations, and the optimum polarisations represent the maximum possible decomposition of volume and ground scattering. In the ideal case of three orthogonal scattering mechanisms, (two on the ground and one in the vegetation layer),  $m_1 = m_2 = \infty$  while  $m_3 = 0$ . The volume scattering is orthogonal to the ground scattering, and the inversion problem becomes decoupled. The observables then are directly related to single parameters: The interferometric phase of the first and second optimum polarisations represents the ground topography while that of the third one the effective vegetation height. Thus, in this case the phase difference between the corresponding interferograms leads directly to the effective vegetation height, as stated in [1]. The proposed algorithm represents an important generalisation of this result.

Fig. 5 shows the extracted forest height and mean vegetation extinction values corresponding to the marked profile, and Fig. 6 shows a 3D perspective view of the estimated forest height. The mean heights are of the order of 20-25m and the mean extinction is about 0.02dB/m in the forested areas. The height variation over homogeneous forest areas and over clear fields is about 1-3m. The lack of accurate ground data makes a large scale validation problematic. However, the vegetation height results are in accordance with the limited ground data available, and with the results obtained in the frame of a tomographic SAR experiment [3]. Further, the inversion of the second baseline ( $B = 15\text{m}$ ) leads to similar results (less than 2m standard variation between the two independent estimations) and verifying the efficiency of the proposed algorithm in terms of a second independent observation.

One of the advantages of the proposed inversion is that, as the case of surface scattering is included in the model as a limiting case, there is no need in general for pre-processing the data for the identification of the forested areas. The inversion algorithm is flexible enough to handle transitions from forested to open terrain. The only case where special attention must be given, is the case of smooth surface scatterers with low backscatter intensity. Because of signal noise

induced decorrelation, these fields show a similar coherence behaviour  $1 > \gamma_1 \gg \gamma_2 \approx \gamma_3$  as sparse or low altitude forest areas (see Fig.3).

## CONCLUSIONS

In this second part of a two part paper, we demonstrate that the random volume over a ground scattering problem can be solved with single baseline polarimetric interferometry without any a priori information. Because in general the forest parameters cannot be decoupled, the proposed inversion algorithm uses the interferometric coherence and phase information in three polarisations to estimate forest height, average forest extinction coefficient and underlying topography. Therefore fully polarimetric interferometric data are needed. Single or even dual polarisation single baseline interferometric data does not provide sufficient observables for the solution of the inversion problem, and thus cannot be used for parameter estimation without assumptions about the scattering process or additional information.

Further, we have evaluated the physical interpretation of the coherence optimisation for the case of random volume over a depolarising ground scattering scenario. Based on this, we propose the use of the optimum polarisations for the solution of the inversion problem. The advantage of using the coherence optimisation lies in the fact that it provides a data adaptive choice of independent polarisations which leads to the best possible conditioning of the problem. In this way the highest parameter estimation accuracy can be achieved.

## ACKNOWLEDGEMENTS

This work was carried out in the frame of EC-TMR and ONR-NICOP projects. The authors would like to thank R. Treuhaft from JPL, and W-M. Boerner from UIC, for many constructive discussions.

## REFERENCES

- [1] S.R. Cloude, and K.P. Papathanassiou, "Polarimetric SAR Interferometry", *IEEE Transactions on Geoscience and Remote Sensing*, vol. 36, no. 5, pp. 1551-1565, 1998.
- [2] R.N. Treuhaft, and P.R. Siqueira, "The Vertical Structure of Vegetated Land Surfaces from Interferometric and Polarimetric Radar", to be published in *Radio Science*.
- [3] A. Reigber and A. Moreira, "First Demonstration of Airborne SAR Tomography using Multibaseline L-Band Data", submitted to *IEEE Transactions on Geoscience and Remote Sensing*.

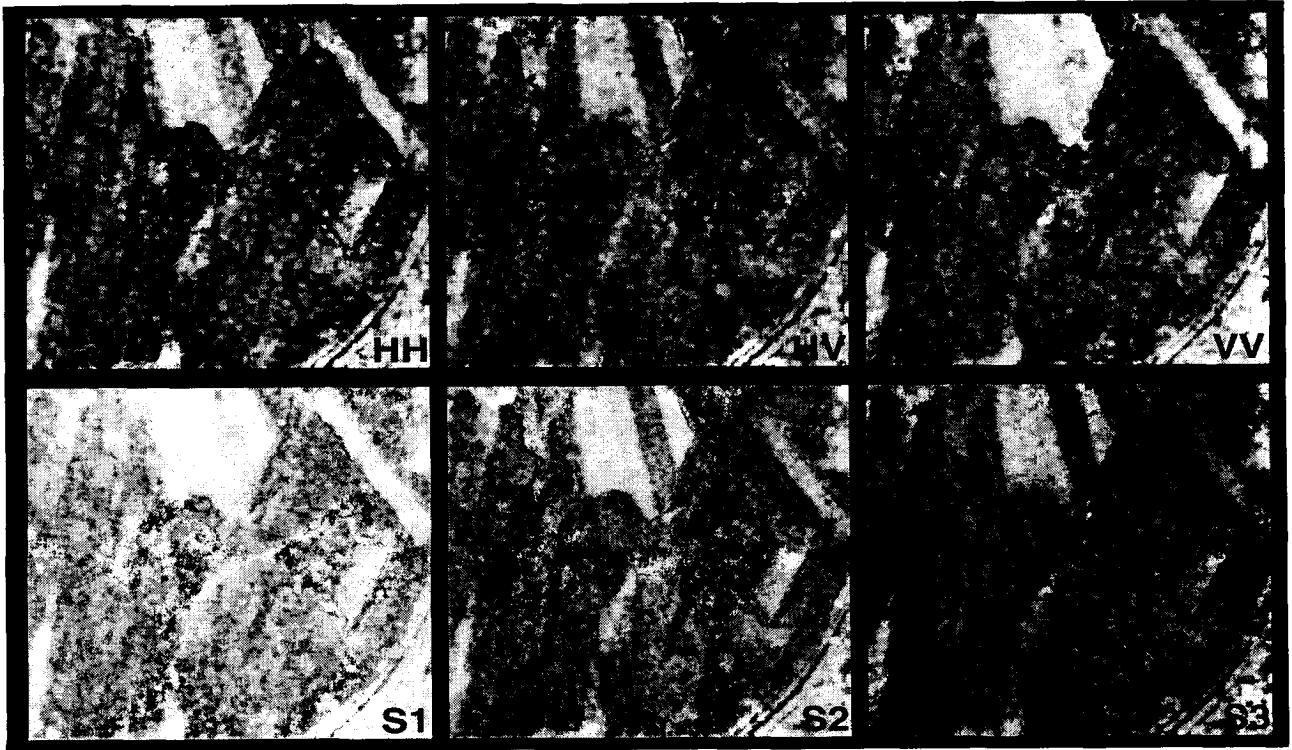


Figure 3: Top:  $S_{1HH} S_{2HH}^*$ ,  $S_{1HV} S_{2HV}^*$ , and  $S_{1VV} S_{2VV}^*$  coherence maps. Bottom: Optimum coherence maps.

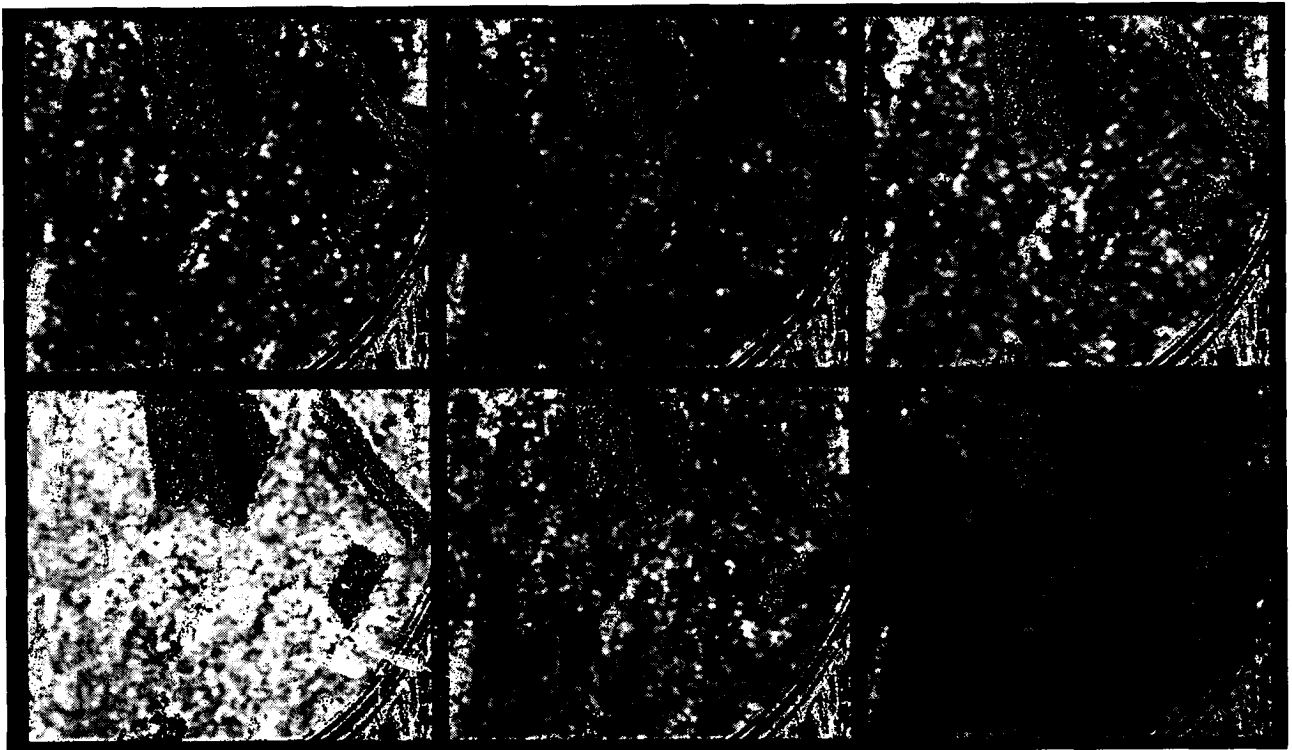


Figure 4: Estimated effective ground to volume amplitude ratio. Top: For  $S_{HH}$ ,  $S_{HV}$  and  $S_{VV}$ . Bottom: For the optimum polarisation states.

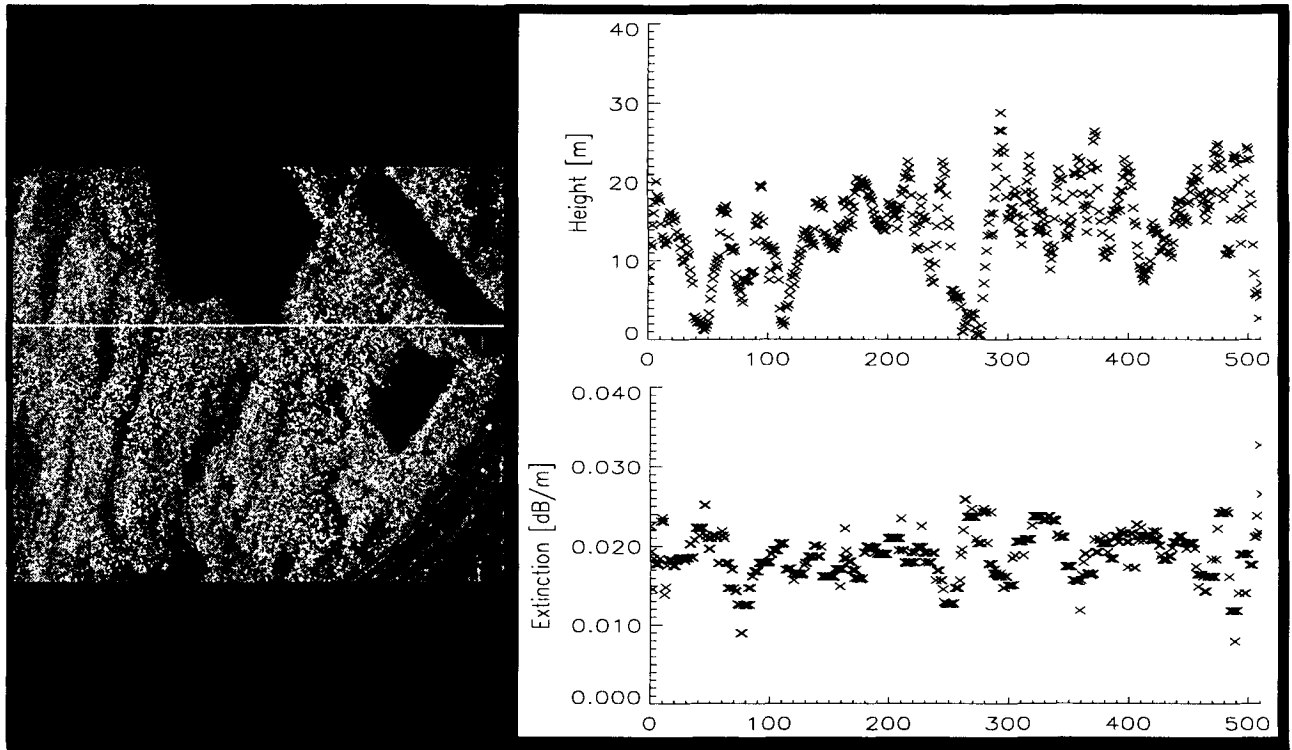
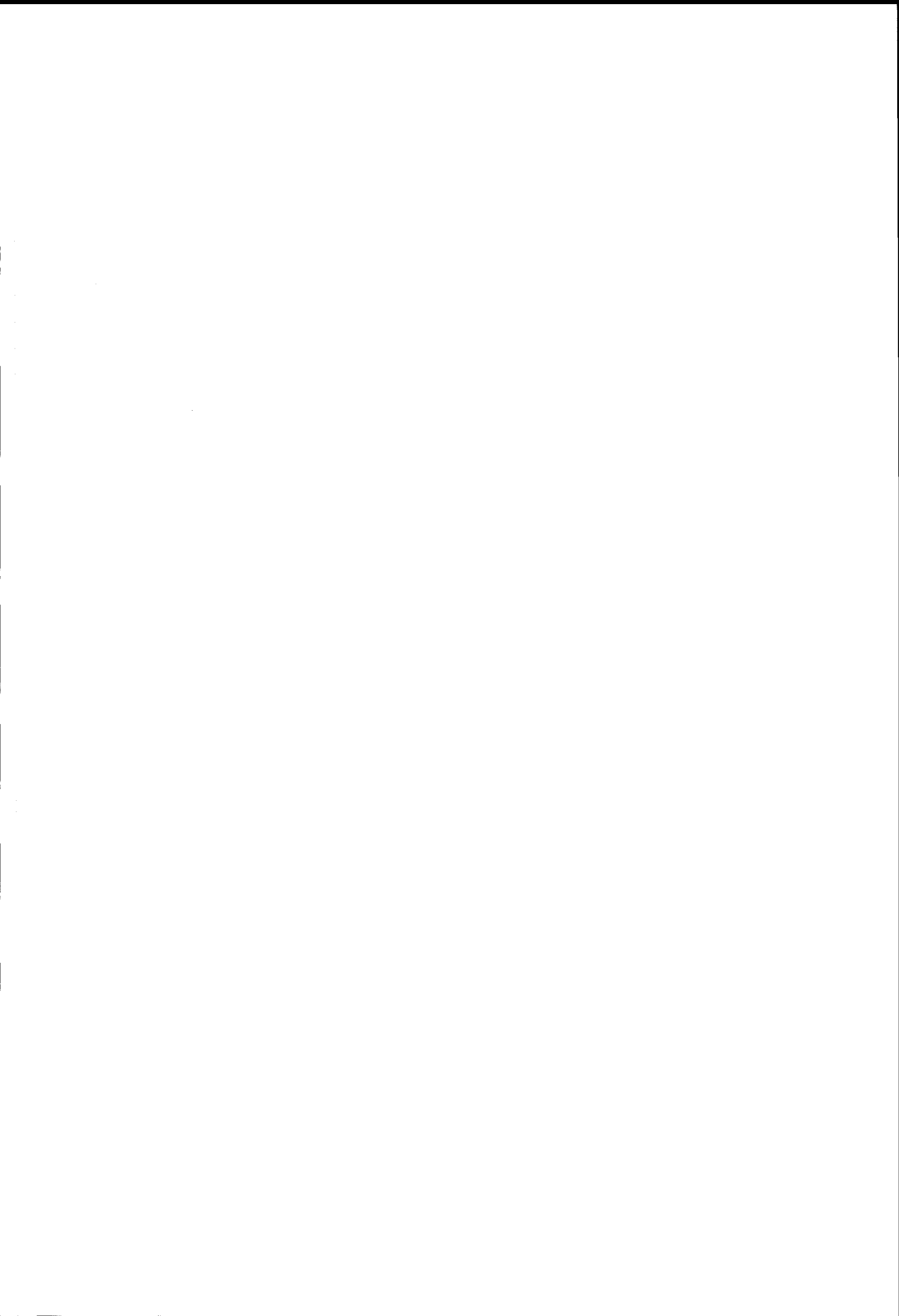


Figure 5: Estimated forest height and extinction coefficient corresponding to the marked profile.



Figure 6: 3D perspective view of the test site.

**Sub session: Interferometry**



## The Shuttle Radar Topography Mission

Tom G. Farr, Scott Hensley, Ernesto Rodriguez, Jan Martin, Mike Kobrick  
 Jet Propulsion Laboratory  
 California Institute of Technology  
 Pasadena, CA USA  
 tom.farr@jpl.nasa.gov

*Abstract*— The Shuttle Radar Topography Mission (SRTM), is a cooperative project between NASA and the National Imagery and Mapping Agency. The mission is designed to use a single-pass radar interferometer to produce a digital elevation model of the Earth's land surface between about 60 degrees north and south latitude. The DEM will have 30 m pixel spacing and about 15 m vertical errors. A rectified C-band radar image mosaic is also planned to be produced.

SRTM will use the same radar instrument that comprised the Spaceborne Imaging Radar-C/X-band Synthetic Aperture Radar (SIR-C/X-SAR) that flew twice on the Shuttle Endeavour in 1994. To collect the interferometric data, a 60 m mast, additional C-band antenna, and improved tracking and navigation devices will be added. A second X-band antenna will also be added by the German Space Agency, which will produce higher resolution topographic measurements in strips nested within the full, C-band coverage.

The SRTM flight is currently manifested for January 2000; data processing will take approximately 2 years.

Digital topographic data are critical for a variety of civilian, commercial, and military applications. Scientists use Digital Elevation Models (DEM) to map drainage patterns and ecosystems, and to monitor land surface changes over time. The mountain-building effects of tectonics and the climatic effects of erosion can also be modeled with DEMs. The data's military applications include mission planning and rehearsal, modeling and simulation. Commercial applications include determining locations for cellular phone towers, enhanced ground proximity warning systems for aircraft, and improved maps for backpackers.

The Shuttle Radar Topography Mission (SRTM) (Fig. 1), is a cooperative project between NASA and the National Imagery and Mapping Agency (NIMA) of the U.S. Department of Defense. The mission is designed to use a single-pass radar interferometer to produce a digital elevation model of the Earth's land surface between about 60 degrees north and south latitude. The DEM will have 30 m pixel spacing and about 15 m vertical errors.

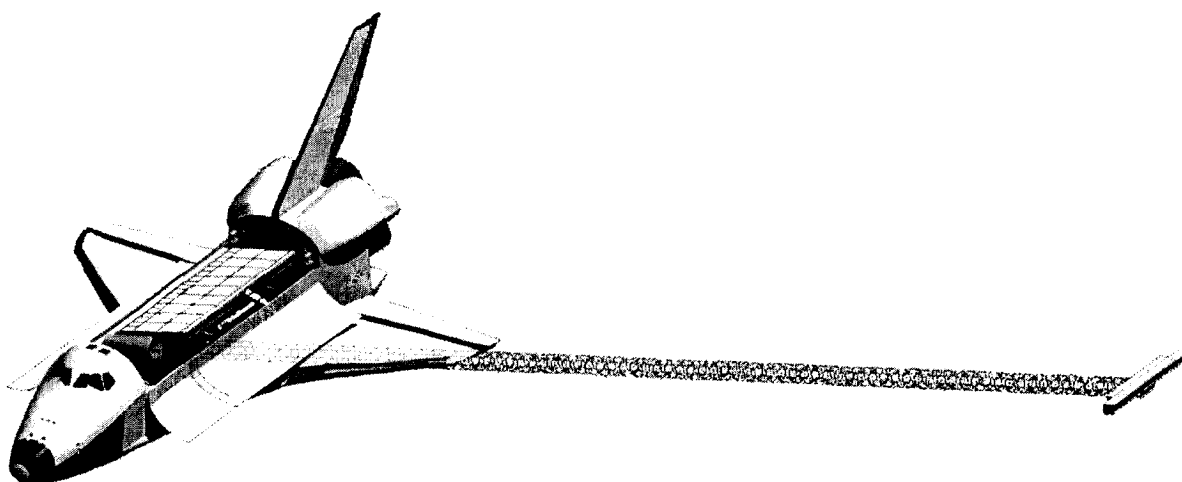


Figure 1. The SRTM payload in the Space Shuttle. The main antenna is seen in the payload bay and the outboard antennas are at the end of a 60 m mast.

The technique to acquire this data set has been used for over a decade to produce accurate topographic and topographic change maps. Radar interferometry uses the fact that the sensor is phase-coherent, so that if two images are acquired at two slightly different locations, a phase-difference image can be produced that contains

information on the topography. The two images can be obtained simultaneously, as with most airborne systems, or at different times, which is the case with all current spaceborne systems. The main drawbacks to the repeat-pass mode are the need to know the baseline separation of the two images to the mm level, and

changes in the atmosphere and surface can occur between the two passes. The baseline can be determined by obtaining a few ground control points, however the other effects are much more difficult to alleviate. Water vapor in the troposphere adds a significant phase delay, which, if different at the two times of image acquisition, will cause large errors in the topographic map produced. Surface changes that degrade the interferometric measurement include incoherent sub-pixel motion such as the waving of leaves and branches on trees. This decreases the amount of correlation between the two images, increasing the error of the phase measurement. In extreme cases, complete decorrelation results in loss of the phase information. These effects have been noted by many investigators; the only feasible way to counteract them is to acquire many pairs of images and search for the best pairs.

To avoid the problems with repeat-pass interferometry, SRTM will acquire its two images simultaneously. SRTM will use the same radar instrument that comprised the Spaceborne Imaging Radar-C/X-band Synthetic Aperture Radar (SIR-C/X-SAR) that flew twice on the Shuttle Endeavour in 1994. SIR-C/X-

SAR was a cooperative project between NASA and the German and Italian Space Agencies and obtained data for over 50 science investigations. To collect the interferometric data, a 60 m mast, additional C-band antenna, and improved tracking and navigation devices have been added. A second X-band antenna, added by the German Space Agency, will produce higher resolution topographic measurements in strips nested within the full, C-band coverage.

The major part of the SRTM hardware will reside in the payload bay of the Space Shuttle (Fig. 2). This will include the main structure, supporting the L, C and X-band antennas, the mast canister, and the Attitude and Orbit Determination Avionics (AODA). The C-band system will be operated in a 4-beam scanSAR mode to acquire a 225 km swath, allowing complete coverage with a small overlap at the equator. Owing to the nature of the original SIR-C/X-SAR digital data handling system, the scanSAR system will operate in a dual-polarization mode: two beams will be HH polarization and two will be VV. The X-band system will operate in VV polarization, as in 1994. In order to save weight, most of the L-band antenna panels were removed, so that system will not be used.

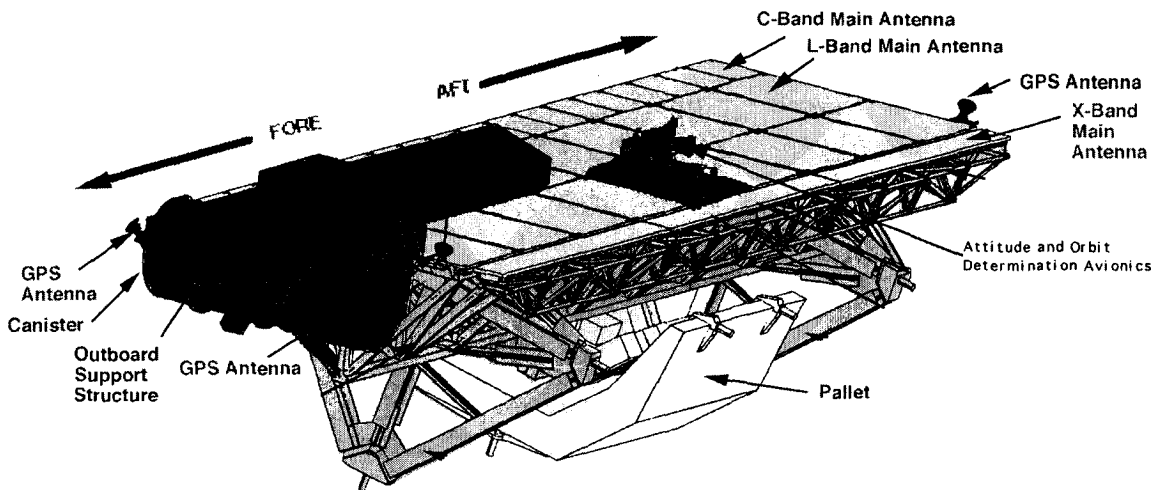


Figure 2. A detailed view of the SRTM hardware in the Space Shuttle payload bay. The 60 m mast is in its stowed configuration with the outboard antennas folded back on top of the main antenna.

The 60 m mast was produced by AEC-Able, based on designs for the International Space Station. It consists of carbon-fiber longerons forming cubes, or bays, with titanium wires under tension as cross-braces. There are 87 bays, each about 70x80 cm making up the full 60 m length. The mast is stored as a collapsed spiral in a canister 2.9 m in length. When deployed, the Shuttle with the mast will be the largest structure ever flown in space.

An important addition to the original SIR-C/X-SAR hardware is the AODA. This system is required to obtain continuous data on the length and orientation of the mast and the location and orientation of the Shuttle

in earth-centered inertial coordinates. These factors are critical to the creation of an accurate digital topographic map automatically without the necessity of ground control points. AODA occupies the place of one of the L-band panels on the face of the main antenna (Fig. 2). It consists of an Astro Target Tracker, Electronic Distance Meter, Star Tracker, GPS receivers, and Inertial Reference Unit. The Astro Target Tracker will track a set of LEDs mounted on the outboard antenna structure, recording data on the motion of the outboard antenna relative to the main antenna. The Electronic Distance Meter will measure the length of the mast to better than 3 mm. The Star Tracker will compare the passing star field with an internal star catalog, to



determine the position and attitude of the Shuttle. The GPS receivers will handle signals from antennas on the outboard antenna structure, providing additional information on the position of the Shuttle. AODA data will be stored on the Shuttle as well as sent to the ground for incorporation into the processing stream of the interferometric data.

Another important addition to the SRTM hardware is the presence of several laptop computers in the mid-deck of the Shuttle. These will perform two functions: Monitor and archive AODA data, and control the Payload High Rate Recorders. AODA data will be sent to one set of laptops so that the Shuttle crew can monitor mast motions. This will also aid in the initial alignment of the two antennas. The recorders are the same as flew on the SIR-C/X-SAR missions, but due to a desire to more efficiently pack data onto a limited number of tapes and the fact that some data takes will be longer than a single tape, a more sophisticated controller was needed. The laptops controlling the recorders will sense the approaching end of a tape, start the next recorder to produce overlapped data, and then hand over to the second recorder. These laptops will also be used to control playback of some of the SRTM data to the ground for quality checks and for processing into DEMs during the flight.

The SRTM flight is currently scheduled for January 2000; flight hardware has been integrated into the Space Shuttle Endeavour and is awaiting launch. The flight is planned for 11 days at 233 km and 57 degrees inclination, which gives a 10 day exact-repeat period. Upon landing, the data tapes will be transferred to JPL for copying and processing. After a checkout and calibration period of a few months, full data processing will take approximately 2 years. The strip data will be compiled into mosaics on a continent basis, allowing block adjustments on that scale. Mosaics will be delivered to NIMA, where validation of the data set will be done. NIMA will deliver data to the civilian archive at the US Geological Survey's EROS Data Center.

An extensive program for calibration and verification of the SRTM data will be undertaken. The calibration of the interferometer will allow fully automatic processing of the data to calibrated DEMs. In addition to the measurements made by AODA, radar path delays will be monitored by a phase-locked optically coupled calibration tone injected at the input to the receiver chains. These systems provide accurate relative calibration over short (less than the orbit period) time scales. Absolute calibration will be carried out through measurements at two ground control sites as well as of the ocean surface before and after every coast crossing, along with a few long deep-ocean passes.

Verification of the interferometric data and the DEMs will be accomplished through the use of 3 major test sites containing high-resolution DEMs and ground control points, some of which will be recognizable in the image data. In addition, a globally distributed set of small, high-resolution DEMs, ground control points, and kinematic GPS surveys will be used in order to evaluate long-period errors in the final DEM mosaics.

More information about the Shuttle Radar Topography Mission can be found at the SRTM Web site: <http://www.jpl.nasa.gov/srtm/>

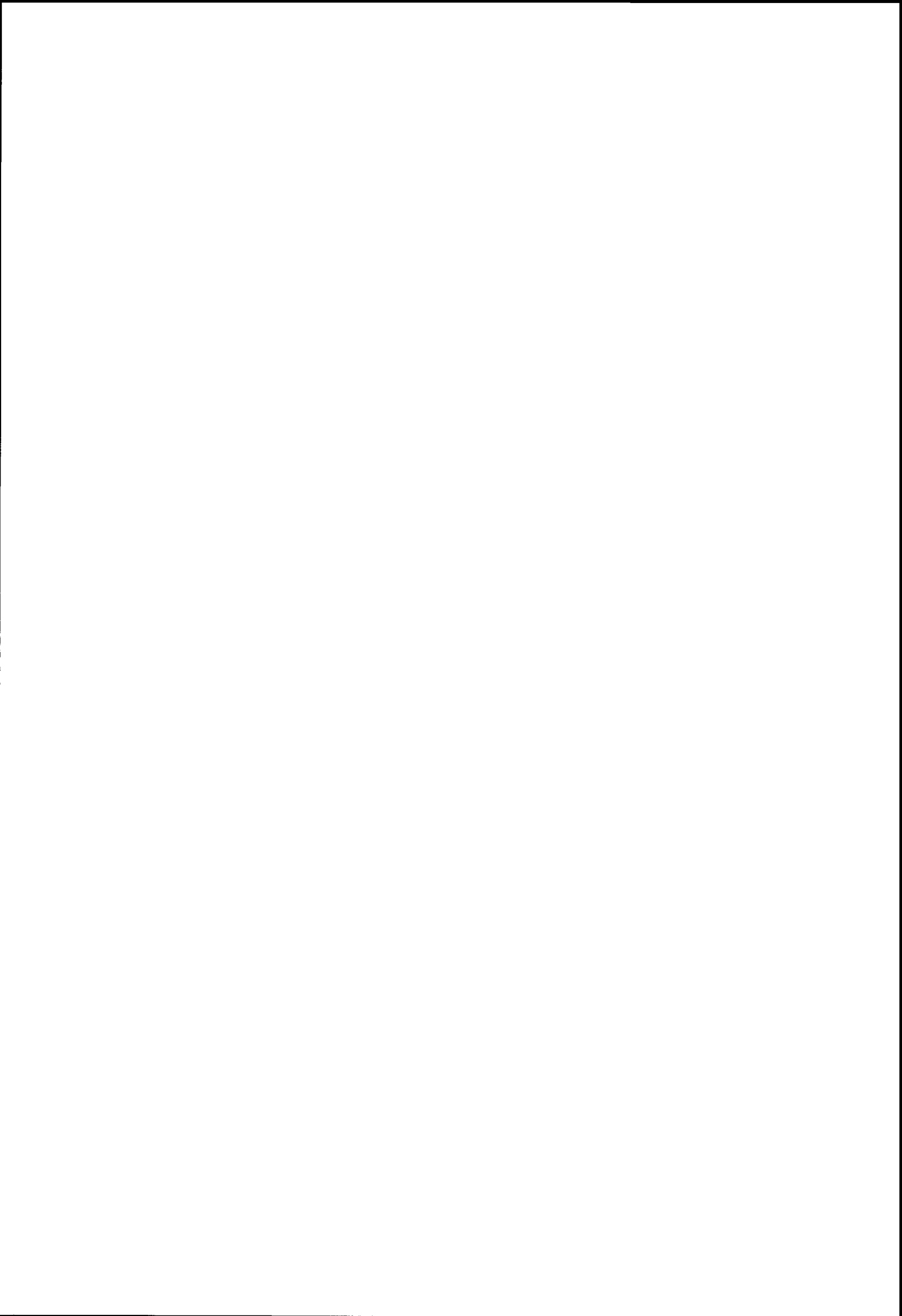
\* Work performed under contract to NASA.



**Interferometric Repeat-Pass SCANSAR Data Processing**

Richard Bamler, Alberto Moreira, Josef Mittermayer  
DLR, Germany

This paper was not available for publication



## Radargrammetry and SAR interferometry for DEM generation: validation and data fusion

Michele Crosetto <sup>(1)</sup>, Fernando Pérez Aragues <sup>(2)</sup>

(1) DIIAR - Sez. Rilevamento, Politecnico di Milano  
P. Leonardo Da Vinci 32, 20133 Milan, Italy  
Tel: ++39-02-2399-6503 E-mail: miche@ipmtf4.topo.polimi.it

(2) ICC - Institut Cartografic de Catalunya  
Parc de Montjuic, E-08038 Barcelona, Spain  
Tel: ++34-93-425-2900 E-mail: fernandop@icc.es

### ABSTRACT

This paper describes the generation of digital elevation models (DEMs) with the radargrammetric and interferometric techniques. In the first part, the main characteristics of the two procedures implemented at ICC and Polytechnic of Milan are presented. Particular emphasis is given to the geometric aspects of the two procedures, which allow achieving an accurate geolocation of the generated DEMs. In the second part, the results obtained processing ERS-1 and Radarsat images are analysed. The generated DEMs were validated over a test area using a suited reference DEM. In this way it was possible to compare the performances of the two procedures and to investigate their complementarity. In the last part of the paper, an example of interferometric and radargrammetric data fusion for the compensation of the atmospheric artefacts that affect the InSAR DEMs is presented.

### 1. INTRODUCTION

Since the advent of the first spaceborne systems, DEM generation has been mainly based on optical imagery and photogrammetric techniques. SAR images are recently gaining importance thanks both to the large availability of spaceborne SAR data and the development of different techniques to exploit them. Starting from SAR images, DEMs can be generated exploiting either the amplitude (radargrammetry or shape from shading techniques) or the phase of the radar signal (interferometric techniques). In this paper only radargrammetry and interferometry are considered.

Radargrammetry works with amplitude SAR images utilising the same approach that photogrammetry uses with optical images. This technique is usually employed with stereoscopic pairs acquired from the same side but with different incidence angles. Its importance has increased in the last years, especially since the launch in November 1995 of Radarsat, the first commercial system that allows acquiring SAR stereo pairs with a large range of incidence angles. Radargrammetry can be

implemented using an interactive approach or an automated one. In the interactive one, based on analytical or digital photogrammetric systems adapted to SAR images, the operator must capture the data manually [1], [2]. In the second kind of approach, based on image correlation algorithms suited to extract pairs of homologous points (matching), the operator becomes a supervisor of an automatic (or semi-automatic) measurement process [3], [4]. In the following sections, only the automated approach is addressed.

Interferometric SAR (InSAR) is based on the processing of complex SAR images acquired from slightly different points of view. InSAR was proposed by Graham in 1974 and applied for the first time at JPL (Jet Propulsion Laboratories) in 1986 using airborne data [5]. Today, a large number of research groups are working on DEM generation with InSAR data coming from different airborne and spaceborne systems. The importance of InSAR is related to its high spatial resolution and good potential precision and to the highly automated DEM generation capabilities.

In the following sections, the main characteristics of the radargrammetric and InSAR procedures implemented at ICC and Polytechnic of Milan respectively are described. Particular emphasis is given to the geometric aspects of the two procedures.

### 2. A RADARGRAMMETRIC PROCEDURE

The radargrammetric procedure implemented at ICC allows generating DEMs in a fully automatic way. The entire process consists of three main stages:

- First, the accurate geometric correspondence between image space and object space must be established.
- Then, solving an inverse trisection problem we obtain the coordinates  $(X, Y, Z)$  of each terrain point whose image coordinates  $(col_1, lin_1)$  and  $(col_2, lin_2)$  are found via a correlation process.

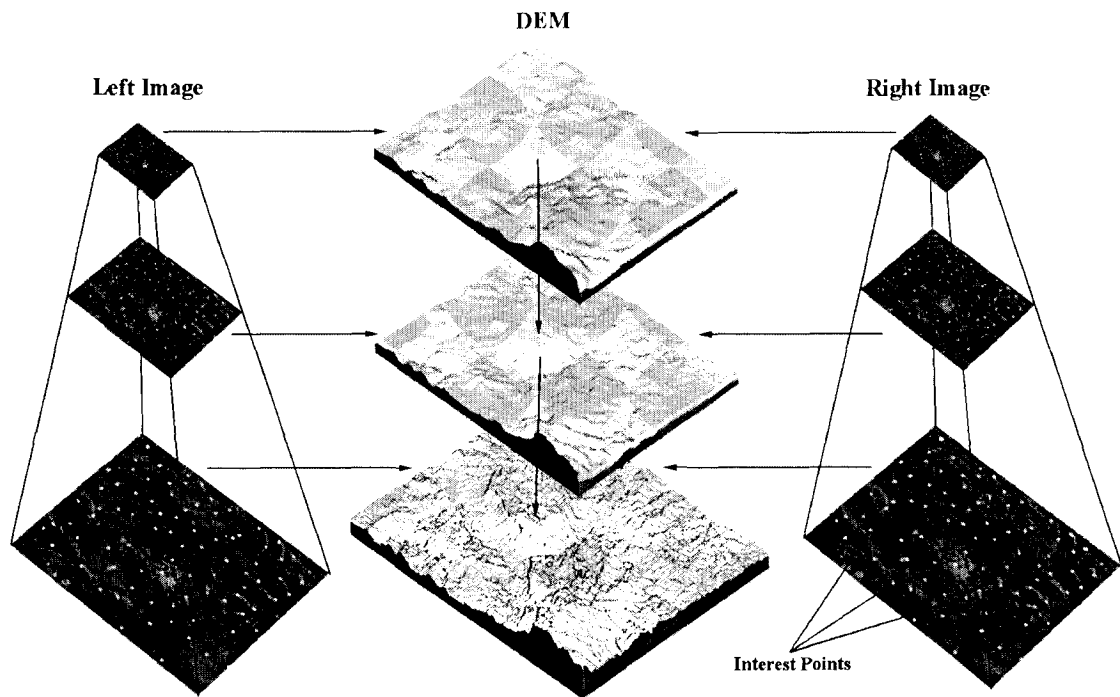


Fig. 1: Image pyramids and interest points

- The huge number of points obtained enter a finite-element adjustment where the whole DEM area is divided in tiles and continuity constraints between tiles are imposed. In this way we eliminate blunders and wrong matches and we get the final raster DEM (regular grid).

In order to establish the image to object space correspondence, a rigorous SAR image formation model (SIFM) must be defined. Furthermore, the model parameters, often known with inadequate accuracy, have to be refined through a calibration procedure based on the measurement of tie points and ground control points (GCPs). The SIFM and the calibration are described in detail in the following sections.

The image correlation algorithms suited to radargrammetry have to take into account the geometric peculiarities of SAR images. The correlation procedure employed at ICC, developed for optical stereo pairs (SPOT) and then adapted to SAR images, uses an area-based matching applied to a pyramid of images where some outstanding features have been found. Firstly, a pyramid of images is created starting from the original images, where the pixel size on each step doubles the size of the proceeding one. Then, the Förstner algorithm [6] is applied to each image level to obtain a set of points that are good candidates for image correlation (interest points, see Fig. 1). Each point is matched with its homologous on the other image shifting up and down the

terrain height until optimum correlation is obtained. A subsequent adjustment on the correlation value permits further refinement in this level. The upper the pyramid level, the coarser the obtained DEM grid and the larger the height shifts. Hence, descending through the pyramid, we obtain a finer and finer DEM ensuring at the same time continuity and stability to the process.

### 2.1. SAR Image Formation Model

An important step in the implementation of a radargrammetric process is the definition of a rigorous SIFM. The one adopted at ICC is based on the two basic SAR mapping equations, namely the range and the Doppler equations:

$$R_S = \left| (\vec{P} - \vec{S}) \right| = SP \quad (1)$$

$$f_D = -\frac{2 \cdot \vec{SP} \cdot \vec{V}_S}{\lambda \cdot SP} \quad (2)$$

where  $\vec{P} = (X_P, Y_P, Z_P)$  is the location of the target point on the ground,  $\vec{S} = (X_S, Y_S, Z_S)$  is the satellite position,  $\vec{V}_S$  is the satellite velocity vector,  $R_S$  is the slant range distance,  $f_D$  is the Doppler centroid frequency and  $\lambda$  is the radar wavelength. The SIFM includes different groups of parameters: orbital parameters, sensor parameters and SAR processing parameters. Working

usually over relatively small areas, we use a polynomial model for orbit description:

$$\begin{aligned} X_S &= a_0 + a_1 \cdot t_R + a_2 \cdot t_R^2 + a_3 \cdot t_R^3 \\ Y_S &= b_0 + b_1 \cdot t_R + b_2 \cdot t_R^2 + b_3 \cdot t_R^3 \\ Z_S &= c_0 + c_1 \cdot t_R + c_2 \cdot t_R^2 + c_3 \cdot t_R^3 \end{aligned} \quad (3)$$

where  $t_R = t - t_0$ ,  $t$  is the time parameter,  $t_0$  is the acquisition time of the first image line and  $(X_S, Y_S, Z_S)$  are the satellite coordinates. The coefficients of the polynomials  $(a_i, b_i, c_i)$  are estimated by least squares (LS) adjustment using few orbital points whose coordinates are available in the image header or in the precise orbit products which can be purchased through the image providers. For a given target point, the acquisition time  $t$  is related to the azimuth coordinate ( $lin$ ) of the SAR image through:

$$t = t_0 + \Delta t \cdot (lin - 1) \quad (4)$$

where  $\Delta t$  is related to the pixel size in azimuth direction. The slant range distance  $R_S$  is related to the slant range coordinate ( $col_S$ ) through:

$$R_S = R_{S0} + \Delta R \cdot (col_S - 1) \quad (5)$$

where  $R_{S0}$  is the near slant range and  $\Delta R$  is the pixel size in range. Working with images given in ground range geometry, we have to include in the SIFM the equation which connects slant range ( $col_S$ ) and ground range ( $col_G$ ) coordinates:

$$col_G = g_0 + g_1 \cdot col_S + g_2 \cdot col_S^2 + g_3 \cdot col_S^3 \quad (6)$$

This equation is omitted when working with slant range images.

## 2.2. Model Parameter Refinement

Some of the model parameters are known with inadequate accuracy. In order to obtain an accurate geolocation, these parameters have to be refined by a LS calibration based on the measure of GCPs and tie points. Working with a stereo pair of SAR images, these are the model parameters treated as unknowns in the calibration: the near slant range  $R_{S0}$ , the acquisition time of the first image line  $t_0$ , the pixel size in azimuth direction  $\Delta t$  and the coefficients of the orbit polynomials. The parameters  $R_{S0}$ ,  $t_0$  and  $\Delta t$  are considered constant within a SAR scene. The polynomial coefficients are refined in case the given orbits are not accurate enough (e.g. when only preliminary orbits are available). In this case a suited weighting of the coefficients has to be performed.

It is important to underline that the calibration can be used to simultaneously refine the parameters of different stereo SAR image pairs. The joint calibration of multiple

pairs can be accomplished measuring both GCPs and tie points. The great advantage of such a calibration is the determination of a unique set of geometrically consistent SIFMs suited to obtain an accurate geolocation of the generated DEMs (i.e. a good DEM merging). The identification and measurement of GCPs on the images is performed manually. For tie points to be collected in same-side image pairs an automatic measurement is employed, while a manual one is used in opposite-side image pairs. Once GCPs and tie points are measured, the joint calibration allows to simultaneously estimating all SIFM parameters of the given SAR image set (block adjustment). The adjustment is carried out with a LS iterative procedure. For a good convergence, a suited weighting of the observations is needed. The weight selection, the initial parameter values and the quality of GCPs and tie points determine the convergence rate of the process.

## 3. AN InSAR PROCEDURE

The InSAR procedure implemented at DIAR-Polytechnic of Milan includes several processing stages namely the image registration, the interferogram calculation and filtering, the image coherence calculation, the phase unwrapping, the generation of the irregular grid of 3D points and the interpolation of the final regular grid. The first three processing stages are based on the ISAR-Interferogram Generator software (distributed, free of charges, by ESA-ESRIN), an effective tool to obtain good filtered interferograms and the related coherence images [7]. The phase unwrapping is based on the "branch cuts" approach [8]. The most original parts of the procedure are the rigorous model for the conversion from interferometric phases to terrain heights and the calibration of the InSAR geometry based on GCPs. Both the InSAR model and the calibration are described in next section. An important aspect of InSAR is the influence of atmospheric distortions on the quality of the generated DEMs. The characteristics of such distortions and a strategy to compensate them using low-resolution auxiliary data are described in section 3.2.

### 3.1 InSAR Model and Geometry Refinement

For the transformation from interferometric phases to terrain heights we adopt a rigorous model that connects the image space (azimuth, slant range and interferometric phase) to the object space (usually a geocentric Cartesian system). The procedure works pixelwise: for each pixel of the interferogram, we derive the object space coordinates of the pixel footprint  $P(X, Y, Z)$  using the slant range (1), the Doppler (2) and the interferometric equations.

For each interferogram pixel we derive the acquisition time  $t$  (4) and the slant range distance  $R_S$  (5). Then, we

calculate positions (3) and velocities of the master  $M$  and slave  $S$  satellites.  $M$ ,  $S$  and the pixel footprint  $P$  are assumed to lie in the same plane (the Doppler centroid plane or antenna mid-plane that goes through  $M$ ). We look for the position  $S$  of the slave satellite that fulfils the following equation:

$$\overrightarrow{MS} \cdot \vec{V}_M = -\lambda \cdot MS \cdot \frac{f_D}{2} \quad (7)$$

where  $\overrightarrow{MS}$  is the baseline vector,  $\vec{V}_M$  is the master velocity vector and  $MS$  is the slave-to-master distance (baseline length). The object space coordinates of the pixel footprint  $P(X,Y,Z)$  are estimated using the two basic SAR mapping equations (1) and (2), and the interferometric equation:

$$SP = MP + D_{IC} + \frac{\Phi_U \cdot \lambda}{4 \cdot \pi} \quad (8)$$

where  $MP$  and  $SP$  are the master and slave slant range distances,  $\Phi_U$  is the unwrapped phase, and  $D_{IC}$  is the interferometric constant. Repeating the procedure for all the pixels of the unwrapped interferogram, an irregular grid of 3D points is generated. Point coordinates refer to the geocentric Cartesian system used for the orbits, thus a transformation to a cartographic system and to orthometric heights is usually performed. Finally does the resampling to get the final regular geocoded grid follow.

As described above for the radargrammetric procedure, some of the model parameters used in the InSAR DEM generation have to be refined by a LS calibration. These are the model parameters treated as unknowns in the calibration: the near slant range  $R_{S0}$ , the pixel size in range direction  $\Delta R$ , the acquisition time of the first image line  $t_0$ , the pixel size in azimuth direction  $\Delta t$ , the Doppler centroid frequency  $f_D$  and the interferometric constant  $D_{IC}$ . The parameters  $R_{S0}$ ,  $\Delta R$ ,  $t_0$  and  $\Delta t$  are considered constant within a SAR scene. For the Doppler centroid frequency a bilinear variation over the SAR image is considered:

$$f_D = f_{D0} + f_{D1} \cdot \text{lin} + f_{D2} \cdot \text{col} + f_{D3} \cdot \text{lin} \cdot \text{col} \quad (9)$$

where  $f_{D0}$ ,  $f_{D1}$ ,  $f_{D2}$ , and  $f_{D3}$  have to be estimated in the adjustment. The parametrization of  $D_{IC}$  is of the form:

$$D_{IC} = d_0 + d_1 \cdot \text{lin} + d_2 \cdot \text{col} + d_3 \cdot \text{lin} \cdot \text{col} \quad (10)$$

where the coefficients  $d_i$  have to be estimated in the adjustment. This kind of parametrization allows taking into account the phase unwrapping integration constant, the effect of orbit errors on the interferometric distance ( $SP-MP$ ), and the linear atmospheric effects on the interferometric phase. There is a single unwrapping constant for the entire scene only if one integration zone

is created during the unwrapping. Otherwise, for each zone a different constant has to be estimated.

The model parameters are refined by LS adjustment using GCPs. Recovering the GCPs necessary for the calibration of each pair is often hard and time consuming. The procedure we implemented allows fusing height data coming from multiple InSAR pairs (e.g. ascending and descending pairs). A joint calibration of all pairs, based on the measure of tie points, can be performed. It allows obtaining an accurate geolocation of the generated DEMs with a reduced number of GCPs.

### 3.2 Atmospheric Artefacts and Data Fusion

In InSAR DEM generation, signal propagation in a medium with constant refractive index is assumed. Indeed, changes in the refractive index between two image acquisitions may happen, causing distortions in the interferometric phase. These changes are mainly due to variations of atmospheric relative humidity [9]. Atmospheric variability results in artefacts (e.g. depressions) interpreted as terrain relief. A single pair can not check the presence of such artefacts, and this represents a very important limit of the InSAR technique.

A reduction of atmospheric artefacts can be obtained combining the information coming from multiple interferograms. We propose a strategy based on the use of auxiliary height data. We assume to use low-resolution data (e.g. with a resolution 10 times lower the one of the InSAR DEMs). Firstly, the InSAR and auxiliary data are accurately geolocated with respect to the same reference system. The fusion procedure employs a multiresolution data analysis in the space domain. We adopt two resolution levels: the first one corresponds to the high frequency components of the terrain topography contained in the InSAR data and the second one corresponds to the low frequency components contained in the auxiliary data. The output DEM contains the high frequency components of the original InSAR DEM and the low frequency components (not affected by atmospheric effects) of the auxiliary data. The proposed procedure represents a deterministic approach to the atmospheric artefact compensation: the low spatial frequencies of the corrected DEM are only estimated with the auxiliary data. A more rigorous approach should estimate the low frequency components of the DEM taking into account the precision of the fused data. An example of data fusion is described in section 4.3.

## 4. VALIDATION OF THE TECHNIQUES

In the last three years the authors were involved in a European Union Concerted Action called ORFEAS (Optical-Radar Sensor Fusion for Environmental Applications), joining five research groups (University of



Thessaloniki, ICC - Cartographic Institute of Catalonia, ETH Zurich, Technical University of Graz and Polytechnic of Milan). A comprehensive data set, covering South Catalonia (Spain), has been made available to ORFEAS participants by ICC. The above described procedures were validated using a suited reference DEM (coming from aerial photogrammetry) whose precision is one order of magnitude better than that obtainable by radargrammetry and InSAR DEMs. The covered area (approx. 25 by 35 km) includes the flat plain crossed by the Ebro river and a set of mountain chains (the maximum height difference is about 1150 m). This area includes many portions affected by foreshortening, layover and even shadow.

#### 4.1 Radargrammetry Results

The ORFEAS data set includes four Radarsat images, grouped in an ascending pair (ASC) and a descending one (DESC). Each image was captured in a different satellite configuration. Some GCPs were found on the images and their coordinates measured (see Tab. 1). Besides GCPs, a set of tie points between each image pair was obtained in an automatic manner. Moreover, some tie points were manually measured between the ASC and the DESC pairs in order to obtain a geometrically consistent image set. Some of the GCPs were used as control points (check points). A simultaneous bundle adjustment of both pairs was performed using the remaining GCPs and tie points. After eliminating few erroneous points, the refined model parameters were obtained, achieving RMS errors (in the image space) over the check points of 1.54 and 1.35 pixels in azimuth and in range respectively. These values confirm the effectiveness of the model parameter refinement to get an accurate global positioning of the generated grid.

Two DEMs (ASC and DESC) with mesh size of 90 m were generated. The quite large mesh size reflects the poor spatial resolution of the matched points (approx. 1 point per 100 by 100 m). The DEMs were compared with the reference one considering three types of areas: the entire covered area, the flat or hilly portions and the mountainous ones (see Tab. 2). Both ASC and DESC DEMs are unbiased (the global constant bias is 0.08 and 0.11 m respectively), i.e. the generated grids are globally well geo-located. Furthermore, the errors are evenly distributed in the entire scene, i.e. they do not show systematic trends. These characteristics make the data fusion for atmospheric artefact compensation possible.

In Tab. 2, one may notice an important difference in the standard deviations of the hilly/flat and mountainous areas. In the latter ones, the SAR geometric distortions (e.g. foreshortening) are more pronounced and affect the image matching.

Image	Mode	Inclination Angle	# GCPs
ASC_1	SB7	40°.16	12
ASC_2	SB2	24°.46	8
DESC_1	SB1	20°.41	11
DESC_2	SB6	38°.04	16

Table 1: Radarsat images of the ORFEAS data set

The ASC DEM is sensibly better than the DESC one, especially in the mountainous areas. This can partially be explained by the ASC geometric configuration, which has bigger inclination angles and hence is less sensitive to SAR geometric distortions.

The grids coming from the matching of the ASC and DESC pairs were fused in order to estimate a new DEM (named ASC/DESC in Tab. 2). Compared with the previous DEMs, the quality of the new DEM improves sensibly. However, the important difference in the precision over the hilly/flat and mountainous areas (the standard deviation is 21.7 and 30.9 m respectively) still remain.

#### 4.2 InSAR Results

Two ascending ERS-1 images of the ORFEAS data set were chosen for the processing. From the original images two sub-images of 1500 pixels in range by 5000 pixels in azimuth were extracted and processed with the ISAR software. The baseline length is 161.5 m and the mean coherence of the filtered images equals 0.57. The unwrapping generated four major zones of integration. The zones were manually "welded" and the unwrapped phases were checked and corrected for aliasing errors. These operations were very time-consuming (about 12 hours). The InSAR parameters were refined using 14 GCPs. With the unwrapped phases and the refined parameter an irregular grid of 3D points was generated.

DEM type / terrain type	Mean Error [m]	Standard Deviation [m]
ASC - hilly/flat	- 0.23	22.92
ASC - mountainous	0.85	32.84
<b>ASC - entire area</b>	<b>0.08</b>	<b>26.25</b>
DESC - hilly/flat	0.76	25.54
DESC - mountainous	- 1.49	37.32
<b>DESC - entire area</b>	<b>0.11</b>	<b>29.53</b>
ASC/DESC - hilly/flat	- 0.39	21.73
ASC/DESC - mountainous	0.01	30.86
<b>ASC/DESC - entire area</b>	<b>- 0.27</b>	<b>24.78</b>

Table 2: Radargrammetry Results - (90 m mesh size)

DEM type / terrain type	Mean Error [m]	Standard Deviation [m]
Before atmo. correction – hilly/flat	0.25	15.18
Before atmo. correction – mount.	- 4.41	22.71
Before atmo. correction – <b>entire area</b>	<b>- 1.21</b>	<b>18.14</b>
After atmo. correction – hilly/flat	0.29	10.84
After atmo. correction – mountainous	1.08	18.47
After atmo. correction – <b>entire area</b>	<b>0.54</b>	<b>13.75</b>

Table 3: InSAR Results – (30 m mesh size)

The irregular grid of 3D points was interpolated in order to derive a regular one with 30 m spacing. The interpolated grid was compared with the reference DEM (before atmo. correction in Tab. 3). The global (constant) bias of the grid can be considered satisfactory, i.e. the calibration resolves quite well the geo-location of the generated 3D grid. One may notice an important decrease of the DEM precision over mountainous areas (where unwrapping errors occur). The InSAR DEM shows important systematic errors with low spatial frequency characteristics. These errors, due to atmospheric effects, have magnitude up to 30+35 m. We computed the autocovariance function of the errors: the correlation length is 505 m and the correlation decreases to zero very slowly, i.e. the errors are spatially highly correlated.

#### 4.3 Radargrammetry and InSAR Data Fusion

It is interesting to assess the potential precision of the interferometric DEM not affected by atmospheric distortions. To this purpose, we adopted the strategy described in section 3.2. We used as auxiliary data the ASC DEM coming from radargrammetry: it is less precise than the InSAR DEM, it is much less dense, but it is not affected by systematic errors. From the irregular ASC grid, a 250 m spacing grid was interpolated and fused with the InSAR one, obtaining a new DEM (after atmo. correction in Tab. 3). Most of the systematic effects on the InSAR DEM were removed through the data fusion (except for the mountainous areas where the radargrammetry DEM has bigger errors). One may notice an important improvement of the DEM precision. The correlation length of the errors is 105 m, which confirms the effectiveness of the artefact correction. In fact, the errors of the new DEM are almost spatially decorrelated because the systematic errors caused by atmospheric heterogeneity were properly removed.

#### 5. CONCLUSIONS

Two new procedures (radargrammetric and InSAR approaches) for DEM generation have been described. Their most original parts are the rigorous geometric models used in the DEM generation and the refinement

of the model parameters (calibration). The procedures were validated employing a suite reference one. Over the considered test area, radargrammetry generated in a fully automatic way DEMs with a quite good global accuracy. However, an important degradation of the DEM quality in mountain areas occurred. Compared with InSAR, radargrammetry DEMs have poorer resolution, are less precise but their quality is independent of atmospheric conditions during image acquisition. InSAR DEMs have high spatial resolution and good precision over hilly/flat terrain. Their precision is quite degraded in mountain areas and can be affected by atmospheric artefacts. A strategy to reduce such artefacts using auxiliary low-resolution data has been proposed. Employing a radargrammetry grid as auxiliary data, the data fusion increased considerably the InSAR DEM precision.

#### ACKNOWLEDGEMENTS

The authors thank Dr. Paolo Pasquali (now at RSL, University of Zurich) and Prof. Claudio Prati (from DEI, Polytechnic of Milan) for kindly providing the software for phase unwrapping.

#### REFERENCES

- [1] B. Mercer, et al, "Relief restitution by radargrammetry". Proc. of the Second ERS Applications Workshop, London, 6-8 December, pp. 277-281, 1986.
- [2] T. Toutin, "Generating DEM from stereo images with a photogrammetric approach: Examples with VIR and SAR data". EARSeL Journal Advances in Remote Sensing, vol. 4, no. 2, pp. 110-117, 1995.
- [3] H. Ramapryyan, "Automated matching of pairs of SIR-B images for elevation mapping". IEEE Transaction on Geosciences and Remote Sensing, vol. 24, no. 4, pp. 462-471, 1986.
- [4] L. Marinelli and L. Laurore, "Relief restitution by radargrammetry". Proc. of 2<sup>nd</sup> ERS Applications Workshop, London, pp. 277-281, 1996.
- [5] H.A. Zebker and R.M. Goldstein, "Topographic Mapping from Interferometric SAR Observations". Journal of Geophysical Research, Vol. 91, No. B5, pp.4993-4999,1986.
- [6] W. Förstner, E. Gülch, "A fast operator for detection and precise location of distinct points, corners and centers of circular features". Proceedings of the Conference on Fast Processing of Photogrammetric Data, Interlaken (CH), pp. 281-305, 1987.
- [7] J. Koskinen, "The ISAR-Interferogram Generator Manual". ESA/ESRIN, Frascati, Italy, 1995.
- [8] R.M. Goldstein and H.A. Zebker, "Two-dimensional Phase Unwrapping". Radio Science, Vol. 23, No. 4, pp.713-720, 1988.
- [9] R. Hanssen, "Atmospheric heterogeneities in ERS tandem SAR interferometry". DEOS Report, No. 98.1, Delft University Press, Delft, 1998.

## **Accuracy Assessment of IINSAR Topographic Mapping**

Pierre Defourny, Xavier Blaes, Cozmin Lucau  
Université Catholique de Louvain, Belgium

This paper was not available for publication



## Calibration of the X-SAR System on SRTM

Manfred Zink and Dirk Geudtner  
 German Aerospace Center, DLR  
 Institute of Radio Frequency Technology  
 82230 Oberpfaffenhofen, Germany, P.O. Box 1116  
 Phone/Fax: +49-8153-28-2386/-1449, Email: Manfred.Zink@dlr.de

**Abstract** – We present the interferometric calibration of the X-SAR system on SRTM. From a height sensitivity analysis we identify key system parameters influencing the height reconstruction performance. Possible error sources in the radar instrument and the geometry determination are discussed. We outline the methods for calibrating the electronics and the geometric parameters and present first results of simulations.

*Keywords: Shuttle Radar Topography Mission, X-SAR, Interferometric Calibration*

### INTRODUCTION

The third SIR-C/X-SAR flight (scheduled for January 2000) will be a mission dedicated to topographic mapping of the entire land mass between latitudes  $\pm 60^\circ$ : the Shuttle Radar Topography Mission (SRTM). Both SIR-C and X-SAR are modified to operate as fixed-baseline interferometers. The outboard receive C- and X-band antennas are mounted on a 60 m deployable mast structure forming the interferometric baseline.

In this paper, we consider the interferometric calibration of the X-SAR system. Absolute radiometric calibration will only be performed on the primary channel according to the previous SRL-1/2 calibration [1].

The objective of the X-SAR interferometric calibration is to correct systematic errors, which significantly affect the height accuracy. Systematic errors may be caused by remaining phase offsets in the instrument electronics and by biasing in measurements of the Attitude and Orbit Determination Avionics system (AODA). Calibration of these errors will improve the overall performance of the DEM products and will reduce the necessity and the effort for tie-point acquisition and measurement.

We first review briefly the theory of the interferometric height reconstruction. Then, based on a height sensitivity analysis we identify the key parameters, which require calibration. Biases in AODA measurements are discussed with respect to their contribution to errors in baseline length and baseline tilt angle. We consider instrument phase errors and discuss the instrument phase calibration strategy. Simulation results are discussed using a Maximum a Posteriori Estimator (MAP).

### INTERFEROMETRIC HEIGHT RECONSTRUCTION

The computation of the terrain height is based on the calculation of the target position vector  $\vec{P}$  using knowledge of the platform position vectors  $\vec{S}_{1,2}$ , baseline vector  $\vec{b}$ , and the unwrapped interferometric phase  $\varphi$ .

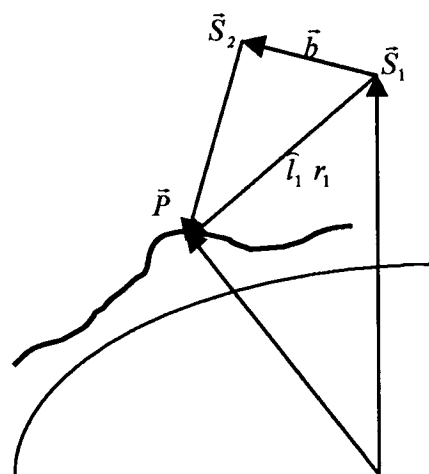


Fig. 1: Simplified 2D InSAR imaging geometry

Fig. 1 shows the simplified, left-looking SRTM/X-SAR InSAR imaging geometry. Basically, the radar measures the slant range  $r_1$ , and assuming a known platform position vector  $\vec{S}_1$  the target position vector  $\vec{P}$  can be written as:

$$\vec{P} = \vec{S}_1 + r_1 \hat{l}_1 \quad (1)$$

The unit vector in the line-of-sight direction  $\hat{l}_1$  can be derived from the interferometric phase  $\varphi$ :

$$\varphi = \frac{2\pi}{\lambda}(r_2 - r_1) = \frac{2\pi}{\lambda} r_1 \left[ \left( 1 - \frac{2(\hat{l}_1 \cdot \vec{b}_p)}{r_1} + \left( \frac{\vec{b}_p}{r_1} \right)^2 \right)^{1/2} - 1 \right] \quad (2)$$

where  $\vec{b}_p$  is the projection of the mechanical baseline  $\vec{b}$  into the plane perpendicular to the direction of the platform velocity. In deriving (2) we assumed zero-Doppler processing and partially linear and parallel orbit tracks.

## SENSITIVITY ANALYSIS

We analyzed the height sensitivity to the various parameters used either explicitly or implicitly in (1). The calculations are based on a complete simulation of the full 3D-X-SAR interferometric imaging and ellipsoidal earth geometry, including the use of nominal orbit state vectors and nominal X-SAR system parameters.

Fig. 2 shows plots of the height sensitivity as a function of ground range for the SRTM swath. It includes only those InSAR parameters, which have a significant impact on the height reconstruction: baseline length, baseline tilt angle, phase, slant range, and platform position. The high sensitivity of the InSAR height on baseline length, baseline tilt angle and phase puts extremely high requirements on the knowledge of these parameters. Note also the different behavior versus range of e.g. the baseline length sensitivity and the phase sensitivity. To achieve highly accurate calibration across the swath it is therefore necessary to estimate biases for all parameters individually instead of cumulating the correction in only one parameter (e.g. phase).

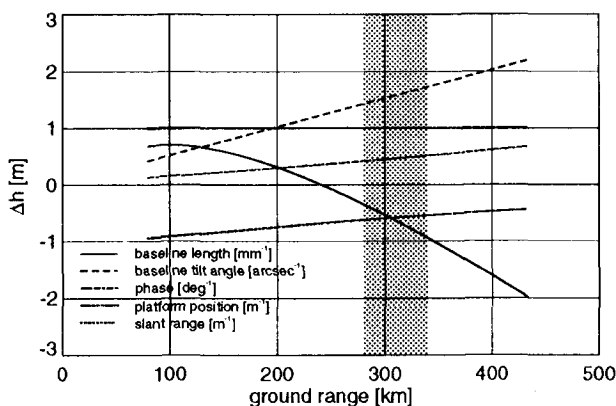


Fig. 2: Height sensitivity as a function of ground range of the SRTM swath. The vertical gray strip marks the X-SAR swath width.

### BASELINE MEASUREMENT

The shuttle's boom structure provides a mechanical fixed baseline that will enable an interferometric imaging from parallel orbits. On the other hand, possible mast dynamics, caused by the shuttle's orbit maintenance maneuvers, gravitational effects, and mast twisting due to thermal effects may cause changes in position and alignment of the outboard antenna with respect to the inboard antenna. As a result, the length and orientation (i.e. tilt angle) of the baseline may vary over time. The use of the AODA system that includes GPS receivers, a star tracker, a inertial reference unit, an optical tracking array, and electronic distance meters, will al-

low an accurate measurement of the mechanical baseline vector [2].

However, AODA measurements may be affected by different error contributions. We distinguish between long term and short term errors, which can be grouped in bias errors and stability/noise errors, respectively. The bias in AODA measurements comprises of mechanical location and alignment errors resulting from pre-launch mounting and surveying inaccuracies. Systematic errors in system parameters of the AODA instruments may cause additional bias effects. Stability/noise errors result from instrument measurement noise, structural and thermal distortions, and estimator noise.

Bias in location and alignment between inboard and outboard antennas contribute directly to errors in the estimation of the baseline vector measured in the inboard antenna coordinate system (ICS). Alignment bias between ICS and the WGS84 coordinate system causes an error in the baseline tilt angle and, therefore, transforms to an additional error in the baseline vector given in WGS84 coordinates.

### INSTRUMENT PHASE ERRORS AND CORRECTIONS

The primary transmit/receive X-SAR channel is the existing X-SAR instrument with a 12m-antenna. The secondary channel uses a receive-only antenna of 6m length, which in addition to the wider azimuth beam width will be electronically steerable in the along track direction to enable alignment of the primary and secondary antenna beams. The received signals are combined and down-converted and run at 135MHz through the boom cable of approximately 100m length [2].

The most critical parts of the X-SAR electronics are the boom cables, where we expect high temperature variations between  $-50^{\circ}\text{C}$  and  $-10^{\circ}\text{C}$ . Both the down-converted receive signal and the reference signal (263 MHz) used for down-conversion at the outboard structure run over these cables and experience phase variations corresponding to the above temperature range. Measurements on the boom cables indicated a phase variation of  $\pm 2^{\circ}$  at 135MHz. The 263MHz local oscillator frequency is multiplied by 36 in the down-conversion as is the phase variation over the boom cables. Corresponding phase errors could reach up to  $140^{\circ}$ .

A further problematic section is the path from the six antenna panels to the combiner box including the phase shifters for the beam steering. Electronic steering effectively tilts the antenna aperture and results in a shift of the phase center. Corrections require a precise knowledge of the behavior of these phase shifters.

Instrument phase monitoring is performed using two calibration signals:

- i) The 263MHz signal is directly sent back via the receive signal cable and its phase is compared with the outgoing signal in a phase detector.
- ii) A so-called calibration tone (cw-signal within the radar signal bandwidth) is used to monitor the LNA's, cables and phase shifters on the outboard structure and to record changing instrument phase differences between the two channels.

With this monitoring loops it is possible to cover most of the electronics. Remaining parts have been characterized during integration and testing in the laboratory. The interferometric phase can then be calculated from the interferogram phase by applying corrections for the cal-tone estimates, the boom cable phase and the pre-flight characterization measurements.

## CALIBRATION OF KEY INSAR PARAMETERS

### Timing Errors

Possible common range delay and time tag errors may occur as image shifts in slant range and azimuth direction, respectively. These error contributions can be estimated by analyzing point target responses in the image to sub-pixel accuracy. For SRTM, there will be deployment of corner reflectors at three calibration test sites: California, Australia, and Oberpfaffenhofen.

### Ocean Calibration

Two long mid-ocean data takes and ocean data takes acquired approximately 15s before and after each land/ocean crossing may provide independent measurements to calibrate the bias in AODA measurements and the remaining phase offset.

#### *InSAR observation model*

The interferometrically derived height  $h_{InSAR}$  can be conceptionally written as:

$$h_{InSAR} = H(\vec{x}) + n \quad (3)$$

where  $H$  is a non-linear operator describing the interferometric height reconstruction, and  $n$  stands for noise.  $\vec{x} = \vec{x}_0 + \Delta\vec{x}$  is the vector containing the nominal InSAR parameters derived from corresponding instantaneous measurements.  $\vec{x}_0$  contains the wanted unbiased key parameters and  $\Delta\vec{x}$  the bias in these parameters.

The non-linear observation process may be linearised by using a Taylor expansion. Thus, equation (3) can be written as:

$$h_{InSAR} = H(\vec{x}_0) + \frac{\partial H}{\partial \vec{x}} \Big|_{\vec{x}_0} \Delta\vec{x} + n \quad (4)$$

where  $H(\vec{x}_0)$  is the correct ellipsoidal height (reference height) of the earth surface calculated from the unbiased InSAR parameters  $\vec{x}_0$ . As reference height we use a sea surface height model that is based on radar altimeter measurements.

$$h_{alti} = H(\vec{x}_0) \quad (5)$$

Forming the difference between the measured and the reference height allows to linearise the estimation problem:

$$h_{InSAR} - h_{alti} = \Delta h = \frac{\partial H}{\partial \vec{x}} \Big|_{\vec{x}_0} \Delta\vec{x} + n \quad (6)$$

We use  $\vec{x}$  instead of  $\vec{x}_0$  as start value and a priori knowledge of biases in baseline length  $b$ , baseline tilt angle  $\alpha$ , and instrument phase  $\phi$  in a Maximum a Posteriori (MAP) estimation process to solve for  $\Delta\vec{x}$ . Finally this provides the calibrated parameters.

#### *Simulation*

We have simulated the 3D interferometric imaging geometry in the zero Doppler plane for the entire swath considering nominal X-SAR system parameters and actual orbit state vectors. For an array of points at a given reference height  $h_{alti}$  we calculated the interferometric phase from the slant range difference. Offsets and noise are introduced on the baseline length, baseline tilt angle and phase to simulate the interferometrically derived heights  $h_{InSAR}$ . According to equation (6) the MAP-estimates of the offsets are computed.

First results of our simulation are summarized in Table 1. We obtained best results for estimating the bias in baseline length and baseline tilt angle. The estimates of phase offsets are less accurate. This is most likely due to the similarity of the height sensitivity with respect to phase and baseline tilt angle errors. Further improvements are being investigated.

	b [mm]	$\alpha$ [arcsec]	$\phi$ [deg]
input bias	-30.00	-60.00	+30.00
estim. bias	-29.66	-64.95	11.17
input bias	0.00	0.00	0.0
estim. bias	-0.64	-0.39	0.06
input bias	30.00	60.00	-30.00
estim. bias	28.37	64.15	-11.02

Table 1: Simulation results of the ocean calibration

## REFERENCES

- [1] M. Zink and R. Bamler, "X-SAR Radiometric Calibration and Data Quality," IEEE-TGARS, Vol. 33, No. 4, pp. 840-847, July 1995.
- [2] M. Zink and D. Geudtner, "Shuttle Radar Topography Mission: X-SAR Calibration and Validation Concept," Proc. EUSAR '98, Friedrichshafen, Germany, pp. 195-198, 25.-27. May 1998.





## RECENT ADVANCES IN POLARIMETRIC- INTERFEROMETRIC SAR THEORY & TECHNOLOGY AND ITS APPLICATION

### Wolfgang-Martin Boerner

University of Illinois at Chicago, Communications,  
Sensing & Navigation Laboratory, UIC-EECS/CSN,  
m/c 154, 900 W. Taylor St, SEL-W-4210, CHICAGO,  
IL/USA 60607-7018, T/F: +[1] (312) 996-5480/413-  
0024, e-m: wolfgang.m.boerner@uic.edu

### James Salvatore Verdi

Naval Air Warfare Center, Aircraft Division, So. Eng.  
Center, AVIONICS: RF-Sensors: SAR Operations,  
48110 Shaw Rd., Bldg. 2187, Ste 2190, PATUXENT  
RIVER, MD/USA 20670-1906, T/F: +[1](301)342-  
0048/0121, em:verdijs@navair.navy.mil

### ABSTRACT

The development of *Radar Polarimetry* and *Radar Interferometry* is advancing rapidly. Whereas with *radar polarimetry* the textural fine-structure, target orientation, symmetries and material constituents can be recovered with considerable improvement above that of standard 'amplitude-only' radar; with *radar interferometry* the spatial (in depth) structure can be explored. In '*Polarimetric Interferometric Synthetic Aperture Radar (POL-IN-SAR) Imaging*' it is possible to recover such co-registered textural and spatial information from *POL-IN-SAR digital image data sets* simultaneously, including the extraction of *Digital Elevation Maps (DEM)* from either *Polarimetric (scattering matrix) or Interferometric (dual antenna) SAR systems*. Simultaneous *Polarimetric-plus-Interferometric SAR* offers the additional benefit of obtaining co-registered textural-plus-spatial three-dimensional *POL-IN-DEM information*, which when applied to Repeat-Pass Image-Overlay Interferometry provides differential background validation, stress assessment and environmental stress-change information with high accuracies. Then, by either designing '*Multiple Dual-Polarization Antenna POL-IN-SAR*' systems or by applying advanced *POL-IN-SAR image compression techniques* will result in '*POL-arimetric TOMO-graphic*' (*Multi-Interferometric SAR*) or '*POL-TOMO-SAR Imaging*'. This is of direct relevance to wide-area, dynamic battle-space surveillance and local-to-global environmental background validation, stress assessment and stress-change monitoring of the terrestrial and planetary covers.

### 1. INTRODUCTION

Both Optical [026, 047, 088, 068, 134] and Radar [007-016] Imaging have matured considerably, and the benefits of using one imaging modality over the other are discussed frequently [047, 116, 102, 103, 073, 035]. For example, '*Hyper-spectral Optical (FIR-VIS-FUV) Radiometric Imaging*' [044, 047, 072, 080] is considered to become the exclusive remote sensing system of the 21st century, and thought to be superior to 'Ultra-wide-band Microwave (HF-UHF-SHF-EHF) SAR Imaging' [020,

021, 073]. Even, it was argued that *UWB-SAR Imaging* is superfluous and could be scrapped altogether because of the exorbitant costs in developing this abstract rather '*invisible*' Remote Sensing technology? [012]. In either case, the inherent electromagnetic vector wave interaction processes are subjected to Maxwell's equations; and constrained by the carrier frequency and bandwidth, the amplitude, phase and polarization [070, 001, 165, 028, 074, 110, 112, 107, 144, 011, 101, 054]; the dispersive and polarization-dependent material constituents of the propagation medium as well as of the illuminated scattering surface, its geometry and structure, and its voluminous vegetative over-burden as well as its composite geological under-burden. However, in order to identify parameters describing voluminous scattering scenarios beyond the skin depth of the vegetation canopy, the entire amenable air/space-borne frequency regime from MF (100 KHz) to FUV (10 PHz) needs to be implemented [041, 026, 057-067] in remote sensing. This implies that we require both radar and optical imaging together with full scattering matrix acquisition capabilities - in order to recover fully the intricate scattering mechanisms [028-033, 052, 057-066, 145-149, 045, 133] and bio-mass assessment tasks - as will be discussed in the following; and maybe assessed by visiting the web-sites collected in chapter 15, specifically [w-01 to w-12].

### 2. EWB-HYPER-SPECTRAL (SPECTROMETRIC) OPTICAL IMAGING (URLs: u-01 to u-10)

Thus, whereas '*hyper-spectral optical radiometry*' will provide high resolution characterization of scattering surface parameters - subject to the skin depth - with appreciable penetration only for a rather limited number of transparent media [002, 025, 057-066, 080, 116, 153]; it lacks manageable coherent phase information and strongly depends on the heterogeneous and dispersive propagation medium such as non-transparent meteorological scatter, smoke and other atmospheric pollution. So, it [044, 047, 068, 067, 116, 130-132, 153] provides very useful direct '*hyper-spectral*' indicators of the vegetative cover and of surface chemical pollutants. However, '*hyper-spectrally extended*

optical (FIR-VIS-FUV) sensing' does not increase the received radiance, but it just divides the overall observation band in order to collect specific wavelength-dependent spectroscopic information in each of the "hyperfine sub-bands" [047, 057-066, 067, 133]. Whereas, hitherto in most of the hyper-spectral optical remote sensing techniques polarization effects were in general totally neglected, it needs to be strongly emphasized that 'Hyper-spectral Optical Radiometry', and especially 'LIDAR/LADAR', is subjected to the 'Arago Sphere' axioms of light scattering [154, 155, 016, 102, 103] in dependence of relative sensor versus scatterer versus source (sun) position. This seems to have been either forgotten or been disregarded altogether [012, 013, 016, 134]. This 'Arago Sphere' dependence [154, 155] also applies throughout the optical (FUV-VIS-FIR) down to the millimeter wavelength region within which atmospheric particle scattering is effective [052, 073]. Complete polarimetric sensor and transceiver technology must be incorporated into future designs [026, 047]. Therefore, any non-polarimetric 'Scalar (amplitude only) Hyper-spectral Radiometric Imagery' must be interpreted with great caution; and, some of the highly overrated attributes for the exclusive use of EO hyper-spectral information are at their best rather misplaced [016, 057-066] unless full polarimetric sensor design is being rapidly developed also for the extended optical spectral regime. This implies the instantaneous acquisition - not the consecutive time-consuming *ellipsometric measurements* - of the Stokes parameters for the instantaneous reconstruction of the 'Stokes Reflection' or the 'Kennaugh Back-scattering' matrix [011, 150, 166, 140, 157].

And, "all-weather, day and night" sensing and imaging is a capability which only 'radar' can provide [134, 101, 070, 054] and not "Hyper-spectral FIR-VIS-FUV Radiometric Imagery" [067, 068, 080]; hence, full attention is paid in the following to 'EWB (HF-VHF-UHF-SHF-EHF) POL-IN/TOMO-SAR' sensing and imaging [016, 033, 108, 114, 151, 117-120].

### 3. HF - EHF RADAR AND SAR POLARIMETRY AND INTERFEROMETRY (URLs: v-01 to v-18)

With increasing wavelength from the EHF (sub-millimeter) via UHF (cm/m) to HF (deca-meter) regimes, the radar imaging process becomes less dependent on the meteorological propagation parameters but more so on parametric target orientation/fine structure/resonance effects [054, 070, 169, 001, 074, 028, 089, 090, 107, 146]; and it possesses increasing polarization dependent penetration capabilities into semi-transparent volumetric under-burden with associated decreasing image resolution [052, 057-066]. With the recent advances made in modern radar electronics device and systems technology, not only the design of 'Scalar (amplitude only) Multi-Polarization Synthetic Aperture Radar (SAR)' [151, 169, 055] but of more sophisticated coherent and fully polarimetric

(scattering matrix) POL-SAR [016] as well as fully coherent Interferometric (dual coherent sensor pair) IN-SAR (or IF-SAR) systems have become feasible [004, 093, 094]. In fact, it is safe to state that '*Non-polarimetric and Non-interferometric SAR Imaging*' is on its way out, and that the IN-SAR Systems are also becoming fully polarimetric *POL-IN-SAR Imaging Systems* [107-109, 114, 115].

#### 3.1 Classical Amplitude-Only Radar and SAR, and "Scalar" IN-SAR Imaging

In classical radar, i.e. "amplitude-only radar" [134], mainly the energy of the returned pulse is utilized; and in basic imaging radar, it is the Doppler phase information in addition. Interferometric SAR (IN-SAR) exploits fully the phase and Doppler information [113, 004], but not the polarization information of the electromagnetic vector wave - scatterer interrogation process [007, 008, 031, 016, 099]; and especially the coherent phase difference of at least two complex-valued SAR images acquired from two different flight-pass/orbit positions and/or at different times are utilized [114, 115]. Provided that coherent two-dimensional complex-valued phase-unwrapping can fully be achieved [004, 094], the IN-SAR information, derived from such interferometric complex image data sets [071, 107, 114], can be used to measure several geophysical quantities such as topography, tectonic surface deformation, bulging and subsidence (earthquakes, volcanoes, geo-thermal fields and artesian irrigation, ice fields), glacial flows, snow avalanches and mud flows, ocean currents, vegetative growth patterns and environmental stress assessment, etc. [052]. Thus, the amplitude and coherent phase information that electromagnetic wave interrogation can recover, is fully utilized in IN-SAR imaging, but not its intrinsic polarization information [004, 093, 094].

#### 3.2 Optical Ellipsometry versus Radar Polarimetry and Polarimetric (Scattering Matrix) SAR Imaging

Polarimetry deals with the full vector nature of polarized (vector) electromagnetic waves throughout the frequency spectrum from Ultra-Low-Frequencies (ULF) to above the Far-Ultra-Violet (FUV) [012, 013, 016]. Where there are abrupt, or gradual changes in the index of refraction (or permittivity, magnetic permeability, and conductivity), the polarization state of a narrow-band (single-frequency) wave is transformed, and the electromagnetic "vector wave" is re-polarized. When the wave passes through a medium of changing index of refraction, or when it strikes an object such as a radar target and/or a scattering surface and it is reflected; then, characteristic information about the reflectivity, shape and orientation of the reflecting body can be obtained by implementing 'polarization control' [070, 054, 016, 150, 101]. The complex direction of the electric field vector, in general describing an ellipse, in a plane transverse to propagation, plays an essential role in the interaction of electromagnetic

'vector' waves with material bodies, and the propagation medium [001, 169, 074-079, 036-039]. Whereas, this polarization transformation behavior, expressed in terms of the "polarization ellipse" is named "*Ellipsometry*" in Optical Sensing and Imaging [026, 028, 047, 091, 136], it is denoted as "*Polarimetry*" in Radar, Lidar/Ladar and SAR Sensing and Imaging [070, 054, 001, 101-103] - using the ancient Greek meaning of "*measuring orientation and object shape*". Thus, *ellipsometry* and *polarimetry* are concerned with the control of the coherent polarization properties of the optical and radio waves, respectively [070, 136]. With the advent of optical and radar polarization phase control devices, *ellipsometry* advanced rapidly during the Forties (Mueller and Land [136]) with the associated development of mathematical *ellipsometry*, i.e., the introduction of '*the 2 x 2 coherent Jones forward scattering (propagation) and the associated 4 x 4 average power density Mueller (Stokes) propagation matrices*'; and *polarimetry* developed independently in the late Forties with the introduction of dual polarized antenna technology (Sinclair, Kennaugh, et al. [070, 101, 016]), and the sub-sequent formulation of '*the 2 x 2 coherent Sinclair radar back-scattering matrix and the associated 4 x 4 Kennaugh radar back-scattering power density matrix*', as summarized in detail in Boerner et. al. [016]. Since then, *ellipsometry* and *polarimetry* have enjoyed steep advances; and, a mathematically coherent polarization matrix formalism is in the process of being introduced - of which the lexicographic covariance matrix presentations [029, 030, 089-093, 105, 106] play an equally important role in *ellipsometry* as well as *polarimetry* [026, 047, 088]. Based on Kennaugh's original pioneering work [070], Huynen [054] developed a "*Phenomenological Approach to Radar Polarimetry*", which had a subtle impact on the steady advancement of *polarimetry* [117-120] as well as *ellipsometry* by developing the "*orthogonal (group theoretic) target scattering matrix decomposition*" [054, 029, 070, 078, 112] and characteristic optimal polarization state concepts, which lead to the formulation of the '*Huynen Polarization Fork*' in '*Radar Polarimetry*' [054, 157, 001, 036-039, 161-163]. Here, we emphasize that for treating the general bistatic (asymmetric) scattering matrix cases, a more general formulation of fundamental *Ellipsometry* and *Polarimetry* in terms of a spinorial group-theoretic approach is strictly required [005, 096, 036-039].

In *ellipsometry*, the Jones and Mueller matrix decompositions rely on a product decomposition of relevant optical measurement/transformation quantities such as di-attenuation, retardance, depolarization, birefringence, etc., [026, 032, 047, 123] measured in a '*chain matrix arrangement, i.e., multiplicatively placing one optical decomposition device after the other*'. In *polarimetry*, the Sinclair, the Kennaugh, as well as the covariance matrix decompositions [011, 028-032, 144, 089,

111] are based on a group-theoretic series expansion in terms of the principal orthogonal radar calibration targets such as the sphere or flat plate, the linear dipole and/or circular helical scatterers, the dihedral and trihedral corner reflectors - - observed in a linearly superimposed aggregate measurement arrangement [074-079]; leading to various canonical target feature mapping [076-079, 029, 030, 082-086] and sorting as well as scatter-characteristic decomposition theories [110, 112, 089-092]. In addition, polarization-dependent speckle and noise reduction play an important role in both *ellipsometry* and *polarimetry* [076-079, 082-086, 138-143]. The implementation of all of these novel methods will fail unless one is given fully calibrated scattering matrix information which applies to each element of the Jones and Sinclair matrices; and the realistic requirements on the calibration of the polarimetric radar data takes at the order of about 0.1 dB in amplitude and 1° in phase must be accepted [138-143, 016].

Very remarkable improvements above classical "non-polarimetric" radar target detection, recognition and discrimination, and identification were made especially with the introduction of the covariance matrix optimization procedures of Tragl [144], Novak et al. [105, 106] Lüneburg [089, 083], Cloude [028], and of Cloude and Pottier [029, 030, 110-112]. Special attention must be placed on the Cloude-Pottier Polarimetric Entropy (H) [030, 111], Anisotropy (A), Feature-Angle ( $\alpha$ ) parametric decomposition because it allows for unsupervised target feature interpretation [111, 086]. Using the various fully polarimetric (scattering matrix) target feature synthesis [110-112, 143, 074-079, 055, 167, 161], polarization contrast optimization, [011, 101-103, 163] and polarimetric entropy/anisotropy classifiers, very considerable progress was made in interpreting and analyzing POL-SAR image features. This includes the reconstruction of 'Digital Elevation Maps (DEMs)' directly from '*POL-SAR Covariance-Matrix Image Data Takes*' [124-127, 112, 016] next to the familiar method of DEM reconstruction from IN-SAR Image data takes. In all of these techniques well calibrated scattering matrix data takes are becoming an essential pre-requisite without which little can be achieved. In most cases the '*multi-look SAR Image data take formatting*' suffices also for completely polarized SAR image algorithm implementation. However, in the sub-aperture polarimetric studies, in '*Polarimetric SAR Image Data Take Calibration*', and in '*POL-IN-SAR Imaging*', the '*SLC (Single Look Complex) SAR Image Data Take Formatting*' becomes an absolute '*MUST*' [016]. Of course, for SLC-formatted Image data, in particular, speckle filtering must be applied always. Implementation of the '*Lee Filter*' for speckle reduction in polarimetric SAR image reconstruction, and of the Wishart distribution for improving image feature characterization have further contributed toward enhancing the interpretation and display of high quality SAR Imagery [081-086, 087], again requiring fully

calibrated *SLC formatted POL-IN-SAR Image data takes*. This distinguishes the limited use of a '**Multi-Amplitude-Polarization SAR**' from a '**Fully Polarimetric, Well-calibrated Scattering-Matrix-SAR**'. Using poorly or badly calibrated POL/IN-SAR Image data takes is also not sufficient and strongly detracts from recognizing the truly superior performance of '**fully polarimetric POL-IN-SAR Imaging**' [138-143, 107-109].

The fully polarimetric (scattering matrix) POL-SAR and its UWB-POL-SAR Imaging applications [003, 017-019, 043, 045, 053, 075-079, 082-086, 087, 095, 098, 100, 135, 128, 168, 170-172] are described in the proceedings of various recent '**Polarimetric Radar Workshops**' [009-012, 026, 102, 103, 117-120, w-01 to w-12]; and, especially in **Chapter 5 on "Polarimetry in Radar Remote Sensing: Basic and Applied Concepts"** [016] of Volume 2, '**Principles and Applications of Imaging Radar**' [052] in the Third Edition of the *Manual of Remote Sensing* [116].

### 3.3 SAR Polarimetry Versus SAR Interferometry

Whereas with '*Radar Polarimetry*' textural fine-structure, *target orientation*, symmetries, and material constituents can be recovered with considerable improvement above that of standard '*Amplitude-Only Radar*' [134, 150, 151]; with standard (scalar) '*Radar Interferometry*' the spatial (range/in depth) structure may be resolved, from which '*Digital Elevation Maps*' can be reconstructed [004, 093, 094]. However, neither method is complete in that POL-SAR by itself does not provide spatial information; and IN-SAR or military (non-polarimetric) air-borne imaging radar cannot provide textural fine-structure information [057-066, 145-149]. Although, IN-SAR enables the recovery of '*Digital Elevation Maps (DEMs)*'; without polarimetry [094], it will be difficult to discern - in all cases - the source orientation/location of the scattering mechanisms [031, 107, 109, 124-127]. Without the full implementation of POL-IN/TOMO-SAR imagery [114, 115], it will be difficult or close to impossible to discern the tree-top canopy from that of the thicket underburden or of the layered soil and sub-surface underburden [145-149]. Many more additional studies of the kind executed by Treuhft, Cloude, et al., as reported in [145-149], are required to establish fully the capabilities of one method as compared to the other, and to their integral POL-IN-SAR implementations. So, speaking strictly in terms of Maxwell's equations, '*amplitude-only SAR*' and '*Scalar IN-SAR*' can only apply to the either the TM (magnetic field parallel to surface) or TE (electric field parallel to surface) incidence on a perfectly conducting two-dimensional surface, by also neglecting the inherent TE-TM hybrid shadowing and front-porching (fore-shortening or overlaying) effects [016]. In order to satisfy the correct implementation of Maxwell's equations fully [007-010], it is necessary - in all cases - to incorporate fully coherent polarimetric (scattering matrix) POL-SAR [016, 070, 117, 120] and especially '*Polarimetric-Interferometric Synthetic*

*Aperture Radar (POL-IN-SAR)*' imaging methods [031, 107-109, 114, 115, 099].

## 4. POLARIMETRIC SAR INTERFEROMETRY

In POL-IN-SAR imaging, it is then possible to associate textural/orientational finestructure directly and simultaneously with spatial information; and to extract the interrelation via the application of novel '*Polarimetric-Interferometric Phase Optimization*' procedures [031,107-109]. This novel optimization procedure requires the acquisition of *highly accurate, well calibrated, fully polarimetric (scattering matrix), SLC-formatted POL-IN-SAR image data sets*. In addition, several different complementing DEM extraction methods can be developed which make possible the precise determination of the source-location of the pertinent scattering centers. Thus, in addition to the standard interferometric "scalar" DEM [004, 093, 094] - derived from IN-SAR, it is possible to generate two DEMs [124-127] directly from the 3x3 covariance matrices of the two separate fully polarimetric sensor data sets as well as various additional ones from the 6x6 POL-IN-SAR correlation matrix optimization procedure [018, 019] for the reciprocal 3x3 symmetric scattering matrix cases. Even better so, from multi-band POL-IN-SAR imaging systems, one can extract directly and simultaneously '*Polarimetric + Interferometric SAR Information*' by implementing the Cloude-Papathanassiou '*POL-IN-SAR Optimization*' procedure developed for a fully polarimetric twin-SAR-interferometer [031, 056, 071, 109]. This provides the additional benefit of obtaining '*co-registered textural/orientational + spatial three-dimensional POL-IN-DEM information*'. Applying this POL-IN-SAR mode of operation to '*REPEAT-PASS Image Overlay Interferometry*' makes possible the '*Differential Environmental Background Validation, Stress Assessment and Stress-Change Monitoring*' with hitherto unknown accuracy and repeatability [031, 016, 109, 113, 114]. The full verification and testing of these highly promising imaging technologies requires first of all that *well-calibrated, fully polarimetric EWB-POL-IN/TOMO-SAR Imaging data takes* become available; and its development has only just begun [109, 114, 115]. There exists a wide range of hitherto unforeseen surveillance and environmental monitoring applications, which require extensive additional analytical investigations next to the acquisition of the well calibrated and ground-truth validated *EWB-POL-D-IN-SAR Image data takes* [107, 122, 018, 019].

For example, more in-depth analyses are required to assess whether *non-polarimetric IN-SAR* alone could in some, but may not in all cases, separate ground scattering mechanisms from those of volumetric scattering layers [145-149, 057-066] by utilizing simultaneously the '*canopy-gap scaling method*', first

introduced in *Optical Hyper-spectral Mapping* [002, 025, 080, 104, 130-132]. Indeed, '*POL-SAR Interferometry*' opened a huge treasure chest of novel modeling methods for an unforeseen large number of hitherto unapproachable problems of environmental stress-change measurement and interpretation. [028-033, 110-112, 107, 108, 114, 115]

## 5. EWB (HYPER-BAND) POL-IN-SAR IMAGING

Depending on the dispersive material and structural properties of the scattering surface, the vegetative overburden and/or geological underburden, a careful choice of the appropriate frequency bands - matched to each specific environmental scenario - must be made [016, 057-066]. This is strictly required in order to recover - next to material bio-mass parameters - canopy versus sub-canopy versus ground-surface versus sub-surface DEM + STRUCTURE information. With increasing complexity of the environmental multi-layered scattering scenario, the implementation of increasing numbers of scenario-matched frequency bands - in the limit - contiguous EWB (HYPER-BAND and ULTRA-WIDE-BAND) POL-IN-SAR becomes all the more necessary and essential [021]. For example, in order to assess - as accurately as ever possible - the bio-mass of specific types of forested regions - - such as *boreal tundra shrubbery*, versus *boreal taiga*, versus *temperate-zone rain-forests*, versus *sparsely vegetated savannahs*, versus *dense sub-tropical to equatorial jungle-forests* - - requires in each case [057-066] a different choice of multiple-to-wide-band POL-IN-SAR imaging platforms, not necessarily operated at one and the same band and altitude, for optimal performance within the HF/VHF{(10)100 MHz} to EHF {100 GHz} regime [016]. For most semi-dense to dense forests of the temperate zones, the EWB VHF/UHF/SHF (600 - 5000 MHz) regime may be optimal [054-066]. Whereas, for a dense virgin equatorial rain forest with huge trees of highly conductive hard-wood, the UWB (100 - 1000 MHz) regime is required, etc. [066]. Thus, the current choice of frequency bands for bio-mass determination is indeed very poor and insufficient in that the L/S/C/X-Bands all lie well above the upper saturation curve; and, the nominal P-Band (420 MHz) well below the lower saturation curve of the bio-mass hysteresis - - for most types of forested regions within the temperate climatic zones [150, 151]. Similarly, in order to recover the three-dimensional sub-surface image information of dry to wet soils including its soil moisture properties, the optimal EWB HF/VHF-regime [152] lies below the nominal P-Band (420 MHz) to well below 10 MHz. Thus, adaptive EWB-POL-IN-SAR modes of operation become a stringent requirement for three-dimensional environmental background validation, stress assessment, and stress-change monitoring. In addition, next to the UHF/SHF (300 MHz - 30 GHz) regime, the EHF (30 - 300 GHz) spectral regime becomes important for the detection of

man-made structures - - such as telephone and electric power-lines - - embedded in forests, shrubbery, thickets, grasslands; and - in addition - for vegetative canopy plus rugged terrain as well as for atmospheric scatter analyses [104, 105].

Therefore, every possible effort must be made to expand and to extend but not to give up the existing, highly insufficient availability of free scientific '*remote sensing spectral windows*', which must absolutely be spread with '*deca-logarithmic periodicity*' throughout the pertinent frequency bands of about 1 MHz to 300 GHz.

## 6. ALLOCATION OF ADDITIONAL SAR IMAGING FREQUENCY BANDS

In order to secure the required frequency windows within the ELF (HF/VHF) to (UHF-SHF) EHF regime for environmental remote sensing, we must place our requests - at once - to the '*World Radio Frequency Conference (WRC'03, Sept./Oct., Geneva, Switzerland)*' via the pertinent *National Research Councils (NRC), Committees on Radio Frequencies (CoRF)* in a unified, concerted effort [034]. The pertinent frequency bands between HF to EHF are already over-crowded; but with the rapidly accelerating conversion to digital communications and worldwide digital video transfer, etc.; we had better wake up. The "*Remote Sensing Community*" must relentlessly request that the rights to operate in periodically spaced "*deca-logarithmic (octave) windows*", extending from below the HF to beyond the EHF bands, be granted.

This indeed represents a very serious, major problem for all of military surveillance and environmental stress-change monitoring [008-013, 057-066, 128]. It is indeed one of the most pressing issues that could reach catastrophic proportions within the near future unless we act immediately. The commercial '*Mobile Radio Communications, Telephone and Video Transmission*' industry has already initiated a fierce battle for acquiring various frequency bands hitherto allocated exclusively for military radar, and for radar sensing and imaging [016]. It is '*densely over-packing*' the "*commercially appropriated frequency windows*" plus '*encroaching into neighboring scientific bands*'.

We must follow the successful example of the '*International Radio Astronomic Research Community*' [034], who had to address a similar problem a few decades ago - - in the early Fifties - - in order to ensure that far-distant Radio-Stars could be detected without interference by radio communications clutter - - for then a still relatively "*sparsely occupied*" VHF, UHF, SHF frequency region. Now, with the imminent threat of the ever accelerating "*Digital Communications Frequency Band Cluttering, Mobile Communications Pollution, and 'www' Propagation Space Contamination*", we - - '*the International Remote Sensing Research Community*' - - are called to duty;

and, we must take the helm - once held by the 'Radio Astronomic Research Community' - in forcing a visionary solution on behalf of future generations to ensure that environmental background validation, stress assessment and stress-change monitoring of the terrestrial and planetary covers - - under the relentless onslaught of an un-abating population explosion and with it the quest for higher standards of living and quality of life - - can be carried out also in the future.

## 7. POLARIMETRIC SAR TOMOGRAPHY

Because the 'twin-antenna-interferometer POL-D-IN-SAR optimization method' [041, 031, 107, 108, 145-149] at narrow band operation allows formally the delineation only of three spatially - in vertical extent - separated scattering surfaces, characterized by polarimetrically unique scattering mechanisms [107, 108, 145-149], it is of high priority to accelerate the development of not only twin-antenna-interferometers but of multi-antenna-interferometers - all being completely coherent POL-IN-SAR IMAGING systems. Furthermore, by stacking the Polarimeters on top of one another (cross-range) and in series next to each other (along-track and cross-track) results in a Polarimetric Tomographic SAR Imaging system with Moving Target Imaging (MTIm), so that a 'POL-TOMO-SAR' imaging system can be synthesized [097, 019, 114, 115] which might also be used for ocean current environmental monitoring and assessment. In addition, using extra-wide-band multiple Repeat-Pass Over-flight operations, at precisely stacked differential altitudes and/or vertically displaced flight-lines, will result - - in the limit - - into a Polarimetric Holographic SAR imaging system, a 'POL-HOLO-SAR' imaging system. This will allow the separation not only of layered but also of isolated closed ("point") scattering structures, occluded under heterogeneous clutter canopies; and embedded in inhomogeneous layered under-burden. This represents a good example on what we cannot achieve merely by implementing 'EO-Hyper-spectral Imagery' [145-149].

The extension from 'narrow-band to wide-band POL-IN-SAR to POL-TOMO-SAR to POL-HOLO-SAR imaging systems' is feasible, and will then enable the realization of true 'Wide-band Vector-Electromagnetic Inverse Scattering' [009-011, 016, 033, 128, 135, 087], i.e., the full recovery of three-dimensional bodies embedded in heterogeneous, multi-layered scattering scenarios [087, 135, 128]. This implies that fully polarimetric multi-baseline interferometry and tomography may obviate the need for introducing constraining assumptions on the models used for estimating polarimetric scattering parameters [145-149]. Full polarimetric multi-baseline, multi-sensor interferometry (POL-IN/TOMO-SAR) - which can now be synthesized by air-borne multi-altitudinal polarimetric interferometry [114, 115] - will result in improved accuracy. It will allow the treatment of more

complicated realistic inverse scattering models than the fundamental "stripped-down" analytic models, which must currently be implemented for non-polarimetric and also for most of POL-SAR twin-interferometric sensing and imaging [016]. The development of these modes of high resolution, fine-structure stress-change imaging and 3-D DEM mapping techniques are of direct and immediate relevance to wide-area, dynamic battle-space surveillance as well as to local-to-global environmental background measurement and validation, stress assessment, and stress-change monitoring of the terrestrial covers [012, 013]. The price to be paid is *high* in that the POL-IN-SAR systems must satisfy stringent performance standards (40 dB channel isolation, high side-lobe suppression of about 35 dB) with calibration sensitivity of 0.1 dB in amplitude and 1\* in polarimetric phase. They must become extra-wide-band, covering the HF to EHF frequency regime, and they must be fully coherent 'Polarimetric (coherent scattering matrix) SAR Multi-Interferometers', which in the limit approach the tomo/holo-graphic imaging capabilities [004, 009, 010, 031, 107, 108, 114, 115]. Yet, in retrospect, the exorbitant costs are justifiable because of the immense gains made. Similar to the early negative predictions of the MRI technology, the cost per Imaging Platform will steadily decrease - opening up never anticipated additional fields of applications.

## 8. LARGE DENSITY DATA BASES AND ULTRA-HIGH SPEED DIGITAL PROCESSING

Since the advent of digital SAR technology in the late seventies, digital image processing, storage and high-density memory device technology has advanced phenomenally; and there exists every reason to be confident that this accelerated advancement will continue [129, 132]. Only two decades ago, the realization of fully polarimetric radar and especially POL-SAR imaging was set in doubt; mainly because of the exorbitantly large digital memory data space required, the insufficient high speed digital processing capacities available in the late seventies and early eighties. However, we have advanced dramatically with the introduction of optical memory devices and high-speed parallel processing technology, now reaching at - 10 Tera-Bytes - another temporary threshold level that cannot easily be overcome without the advent of entirely new device technologies. Such a timely turn of events has occurred in that 'Acousto-Optic Analog Processor (AOAP)' technology has experienced a similar dramatic advancement like digital 'UWB-POL-IN-SAR Repeat-Pass' technology. This makes possible an entirely novel approach to both 'Wide-band Range-Doppler Imaging (WRDI)' plus 'UWB-POL-IN-SAR Image Acquisition, High-Speed Processing' with the potential for considerable image data compression. This new hybrid acousto-optic analog-digital conversion, electro-optic digital data

compression, and exceedingly light-weight, electronic-processor size-reduction technology should strongly contribute to overcoming the problem. Real-time airborne as well as space-borne implementation of Repeat-Pass UWB-POL-D-IN-SAR environmental stress change monitoring can then be realized within the foreseeable future [046] by accommodating the entire set of extra-wide-band sensors with processors on one and the same air-borne or space-borne platform. A processor currently under development, the ESSEX High Performance Optoelectronic (HPO) Processor (also known as ImSyn), demonstrates this potential. The ImSyn HPOP captures the best advantages of digital and optical processing technologies to provide data handling and processing performance which, when completed, promises to eclipse digital-only performance for imaging applications while also having significant size, weight, and power advantages [173].

The advantage of returning to acousto-optical device technology is that the first function to be performed in the "vector signal acquisition and processing chain of events" in radar as well as in SAR - - amplitude-only or polarimetric - - is to correlate the returned signal with the transmitted signal which in the case of fully polarimetric SAR are complex and vector in nature. In 'Modern Optics' [022, 023, 048] this has become a straightforward functional task to be performed with the aid of a 'Fourier Lens'; whereas in the 'Digital World' [129, 132] - - as is currently still being applied without exception - - one needs to A/D-convert the return signal first. This approach is sufficient as long as one is dealing with a LFM waveform, but there are severe problems with the conversion of all data points that need to be processed especially in the case of fully polarimetric-interferometric UWB SAR systems. For digital processing this equates to memory, storage and speed of the devices. Optical processing takes advantage of analog processing in that the signal is converted from electrical to a laser medium (vertical cavity matrix laser), and it is then processed 'almost instantaneously' through acousto-optic Bragg cell and Fourier Optical (FO) processors which at the current state of the art already can handle huge image data blocks as encountered in UWB-POL-IN-SAR image acquisition, processing and storage. We are thus dealing with a 'Hybrid FO-DIG Processor' which performs the correlation functional process in the optical domain; the signal/image analysis, identification, classification - - that follows next - - in the digital domain; and the SAR or POL-IN-SAR processing again in another set of hybrid acousto-optical/digital processor chains. There would be two major 'Hybrid Fourier-Optical-Digital Processor Chains' required - - one for the signal acquisition/detection/identification and a second set for the SAR processing. Although, not yet fully realized, this novel hybrid vector-signal/tensor-image processing concept would, in the end, reduce the exorbitant

processing workload by taking advantage of the true merits of both acousto-optical and digital processing modalities, as for example discussed in [046, 173]. Thus, the symbiotic fusion of Modern Optics with advanced Digital Image Processing will pave the path to follow [047, 129], bringing a realistic solution for the full implementation of UWB-POL-D-IN/TOMO-SAR Repeat-Pass imaging in sight.

## 9. PRESERVATION OF DIGITAL SAR IMAGE INFORMATION (URLs: t-01 to t-03)

One of the major shortcomings of the "Digital Communications Age" is that it does not provide the means of long-term information storage and preservation, in spite of its enormous benefits for immediate and global direct information exchanges at all levels [024]. Of course, the instantaneous dissemination and interactive flow of huge data files presents indeed an enormous benefit to trade, commerce, transportation, global banking and also to accelerating the advancement of science and technology in all fields of human endeavor. However, we are accumulating meta (mega of mega) data banks at a mind-boggling pace, we find no time nor resources for screening the amassing information, but even worse than that, we do not seem to possess the high-density storage and information media guaranteeing long-lasting information preservation. For example, the transition from the 'HARD-COPY BOOK LIBRARY' to the 'FLOATING DIGITAL LIBRARY - - THE TERRA DIGITALIS' [021] cannot yet and must not yet be realized in that we are indeed still missing two major essential components for realizing this dream. For one important basic requirement may not be able to be fulfilled for a long time to come, namely that of developing and manufacturing permanent high-density digital information storage devices. The magnetic tape drives and discs possess a rather limited life-span of only a few years, and need to be replaced at exorbitant costs periodically every five, and definitely by at least every ten years. Its current replacement by EO-CD ceramic/glass compact discs are also not fulfilling the once sought solution of replacing the magnetic disk drives, in that those not only seem to be, but truly are vulnerable to cosmic ray and neutrino bombardment; against which there does not exist a foreseeable cure. This places additional constraints on the SAR Image data refreshment tasks, which have not yet been fully recognized. Furthermore, the extremely rapid pace of digital computer operating systems advancements make the newest operating systems obsolete as soon as those appear on the market, requiring perpetual time-consuming updating, too often every year, at exorbitant costs, with older versions becoming unsupported in some cases. At the same time, the computer programming languages are being upgraded even at a higher pace so that within only a short period of time of a few years major blocks of valuable information may

be lost for ever unless con-current information screening and transfer to the latest computer software package has been maintained. But, who possesses the time and resources to do so? Transfer of most invaluable information onto acid-free paper storage has become exceedingly difficult and expensive in case laser-writing techniques are to be implemented. In retrospect, we must ask ourselves whether we might be creating an insurmountable 'Digital Tower of Babel'; and at the end very little is gained in extracting useful knowledge, and a lot of most valuable information may be lost for posterity in perpetuity [024].

All of these digital information storage and preservation problems are compounded in the case of 'EWB-POL-D-IN-SAR and EO-Hyper-spectral Remote Sensing', because of the rapidly accumulating Exa-Byte, DLTs, and other current mass storage media, once thought to be the answer for years to come. Well, the years *have* come and we need to develop most rapidly highly improved super-high-density information preservation and not only storage media as well as supra-high-speed digital image processing operating-systems which are independent of the past, current and future computer operating and software systems. The ongoing development from UNIX to JAVA must be accelerated with JAVA still required to becoming much more universal and much, much faster. Furthermore, the electronic-chip manufacturing industry must adopt a much more universal far-reaching and visionary approach of accelerating the development of long-lasting digital information storage media so that we may be able to preserve vital 'EWB-POL-D-IN-SAR and EO-Hyper-spectral Information' on the 'Local and Global Terra Digitalis Meta (mega of mega) Information Bases' in perpetuity for posterity. Thus, before we really have become aware of the severity of the serious calamity so created, we have created a historical void - 'the Digital Tower of Babel' - of most valuable knowledge preservation, which commenced - during the Eighties - with the advent of the digital age, and valuable information may be lost irretrievably for ever.

## 10. JOINT RF & OPTICAL REPEAT-PASS SAR OPERATIONS

Furthermore, whereas most 'Hyper-spectral Optical Radiometers' and "Microwave Multi-band Radioaltimeters" operate in a down-look Nadir mode, and the 'UWB-POL-IN/TOMO-SAR Imaging Sensors' in left/right-side-looking operation, inducing shadowing and 'front-porching (fore-shortening or overlay)', the simultaneous implementation and operation of three imaging platforms - - flying side-by-side, and being fully equipped with Microwave Multi-band (polarimetric) Radioaltimeters and Hyper-spectral Optical plus UWB-POL-IN/TOMO-SAR systems - - is strictly required. For example, for the environmental stress-change monitoring within the *Baikal Lake Basin*,

*Siberia* [069, 017-019, 042, 156] or of the multitude of pertinent Pacific Rim (PACRIM) regions, monitored by the SIR-C/X-SAR Mission-2 as well as the PACRIM-AIRSAR-1/2 measurement campaigns [017, 018], such simultaneous triple platform imaging modes of operation may be ideal. By implementing Differential GPS, the three platforms must be flown side-by-side with perfectly overlapping foot prints, and by executing contiguously spaced, parallel repeat-pass flight operations so that the complete wide-band microwave radioaltimeters plus hyper-spectral optical down-look image information can properly be overlaid on top of the strip images produced by the two left/right side-looking UWB-POL-IN/TOMO-SAR platforms. In addition, it is most desirable and necessary for testing newly to be developed 'EWB-POL-D (RP) -IN-SAR Image Processing Algorithms' to execute with highest possible precision, 'Square-Loop - parallel (0), orthogonal (90), anti-parallel (180), and cross-orthogonal (270) Flight-Line Repeat-Pass Operations' over carefully selected, most diverse geo-environmental calibration test and ground-truth validation sites. The execution of such demanding flight operations has - in principle - been realized, is no longer a distant dream, and can be implemented now and immediately thanks to the accelerated advancement of Differential High Precision GPS electronic real-time navigation [099, 097, 122, 114, 115]. In addition, due to the rapidly developing "Terra Digitalis" - - which is to preserve detailed environmental mapping information even of the most distant, hidden, corners of our terrestrial and also planetary covers for posterity - - we should be able to collect a long-lasting complete geo-environmental data base which can be updated continuously.

## 11. DESIGN OF MISSION-ORIENTED MULTI-SENSOR IMAGING PLATFORMS

However, in order to realize the implementation of such highly demanding multi-sensor technologies, it will at the same time be necessary to develop a strategy for the design and manufacture of air-borne sensor platforms which are mission-oriented specifically for the joint 'Extended Radio-Frequency EWB-POL-D-IN/TOMO-SAR' plus 'Extended Optical Hyper-Spectral FIR-VIS-FUV' Repeat-Pass modes of operation. Also, considering that there exist currently efforts to perfect Forward-Looking POL-IN-SAR technology, it is necessary to design platforms with minimal structural interference obstructions, so that the entire frequency regime from at least VHF, if not even HF, up to EHF plus the extended Optical (FIR-VIS-FUV) Regime can be accommodated. Considering that there was no truly mission-oriented new 'Multi-purpose IMAGING AIRCRAFT PLATFORM' designed since that of the P-3 Orion sub-marine hunting platforms of the late Fifties, it is a timely and highly justifiable request to our forward looking, visionary Planning Offices of DOD, NASA (HQT.-JPL), DOC (USGS+NOAA), NATO,



ESA, NASDA, etc., to place top priority on this long overdue demand of having access to the 'ideal imaging platforms' required to execute both the military wide area surveillance as well as the environmental background validation, stress assessment and stress-change monitoring missions - world-wide [016-019]. Just to make use of existing air-borne platforms of opportunity; e.g., the B-707 for the non-polarimetric AWACS, the carrier-based E-2C Hawkeye for the non-polarimetric APS-145, the P-3 Orion for the NAWC UWB-POL-IN-SAR [152], the DC-8 for the AIR/TOP-SAR, etc., is no longer sufficient [099, 128, 134, 135]; because EWB/UWB fully polarimetric POL-SAR Multi-SAR-Interferometers cannot tolerate any multi-path scattering obstructions unavoidably encountered with all of these "polarimetrically clumsy", venerated platform designs. Platforms that could utilize such improvements are among others, also future JSTARS class platforms, plus Predator (UAV), and Global Hawk (UAV) types of aircraft, etc.. Thus, instead of expending any more dead-end efforts on the elimination of platform interference effects of existing imaging platforms for the purpose of developing hyper-fine image processing algorithms in the high-resolution imaging and target detection programs; why not directly and without any further ado aggressively attack the planning and design of the "Ultimate POL-IN/TOMO-SAR Platforms", varying in size according to application and mission performance, required already now, and immediately! Specifically, we require to develop the ideal set of low/medium/high-altitude versus small/medium/large-sized imaging platforms.

## 12. NEED FOR SUB-AQUATIC MULTI-SENSOR (SAS) STRESS-CHANGE MONITORING

In concluding this overview, here we need to pay attention also to another related, most serious environmental stress change monitoring problem dealing with the detection of the rapid destruction of our sub-aquatic flora and fauna in our rivers, ponds, lakes, coastal surf-zones and the shallow to deep ocean environments - - which has assumed absolutely catastrophic almost irreversible conditions. A solution may be in sight, and can be achieved by incorporating multi-sensor high resolution magneto-metric, various forward/side/bottom-scanning sonars, EO sub-aquatic polarimetric high-resolution imaging, 'chemical trace element sniffing' [040, 081] as well as Synthetic Aperture Sonar (SAS) multi-sensor technology [051] into the 'Sub-aquatic Environmental Stress Change Monitoring' operations - - over land including lakes, rivers and ponds; aquifers below land; and in the deep ocean water environment [040, 049-051]. Because of the close relations among image digital and analytical processing techniques for UWB SAR [049, 050] and Wide-band SAS, Polarimetric Magneto-Metric Wide-Area Imaging and POL-SAR Imaging, more attention needs to be paid by the "UWB-POL-D-IN/TOMO-SAR" [050] research

community toward the accelerated co-development of UWB-IN-SAS technology. In addition, it will become necessary to combine directly various - if not all - all of these multi-sensor technologies for the increasingly more complex problems of environmental stress-change monitoring in the littoral coastal surf zones, of the continental wetlands [016, 069], and of the receding glacial ice fields.

## 13. CONCLUSIONS

A succinct summary on the current state of development of Polarimetric and Interferometric Synthetic Aperture Radar theory, technology and applications is provided with a view towards the expected rapid developments of fully integrated "Polarimetric SAR Interferometry" and its extension to 'POL-IN/TOMO-SAR Repeat-Pass' environmental stress-change monitoring. The underlying basic systems analysis of these POL-IN-SAR to POL-TOM-SAR algorithms need to be complemented with recent POL-IN-SAR to POL-TOM-SAR images obtained with air/space-borne NASA-JPL, NASDA, NAWC-AD and DLR imaging platforms; and those of high resolution SAS multi-sensor monitoring platforms using the NCSC-MUDSS systems. With the choice of associated examples provided in the pertinent URLs, we will - at the same time - be able to assess the current 'State-of-the-Art in UWB-POL-IN-SAR and UWB-SAS Technology'; and to identify the current associated inadequate sensor platform availability, the introduction of hybrid acousto-optical/digital processing technology as well as the threat imposed by densely packed worldwide digital communications and video image data transfer. Finally, we will conclude that in order to utilize fully the sensing and imaging capabilities in optical as well as radar vector-electromagnetic surveillance and monitoring, in addition to all the timely and urgent requests made in Sections 6, 8 and 10, 11, 12; more emphasis must be placed on the accelerated development of 'International Collaboratories', such as the 'ONR-EUR-NICOP-WIPSS Collaboratory', for the advancement of pertinent Vector-Electromagnetic Modeling (Inverse Scattering), Image Processing and Interpretation tools for UWB-POL-IN-SAR Image Data Sets, the associated algorithm hardening, and implementation in practice. In summary, we require to develop the "Collaboratorium Terra Digitalis" as proposed in [021], and for Baikal Lake, Siberia, the "Collaboratorium Terra Digitalis Baikalum [021], respectively [t-01 to t-03].

The ESA-CEOS-MRS'99 SAR-CAL/VAL Workshop [w-11] provided another valuable modicum of close international cooperation for the steady accelerated advancement of EWB-POL-D-IN-SAR principals and technology - - - and, at the current pace of development there just cannot be enough of these highly productive Workshops as well as Collaboratories - - like the

"CEOS Collaboratory" - - as summarized in the 'Report on Polarimetric & Interferometric Polarimetry of Friday, 1999 October 25.

#### 14. ACKNOWLEDGMENTS

The Author (WMB) wishes to express his sincere gratitude to Otto Kessler and his co-author (JSV) for their continued support of this research effort; to Dr. William J. Stachnik for sustaining support towards strengthening the *ONR-NICOP-WIPSS Program [w-01, w-02]*, and to its international member teams for their harmonious collaboration which all contributed integrally to this paper. Also, the Author thanks Drs. Yves-Louis Desnos, Maurice Borgeaud, and Evert Attema of ESA-ESTEC, Noordwijk, Netherlands; Dr. Henri Laur, ESA-ESRIN, Frascati, Italy; and Dr. Jean-Cloude Souyris, CNES-RSD, Toulouse, France for inviting us to prepare this *Tutorial Overview* as well as to participate actively in this most thought-provoking, research-inspiring *ESA-CEOS-MRS'99 SAR-CAL/VAL Workshop [w-11]* in the beautiful historical city of Toulouse. Similarly, sincere thanks are extended to several colleagues - - Drs. Eric Pottier, Jong-Sen Lee, Ernst Krogager, Harold Mott, Ernst Lüneburg, Ridha Touzi, Jakob van Zyl, and Wolfgang Keydel - - for their critical assessments of various drafts and/or for providing useful references and constructive comments.

#### 15. REFERENCES

- [001] Agrawal, A. P., "A Polarimetric Rain Back-scattering Model Developed for Coherent Polarization Diversity Radar Applications", Ph.D. thesis, UIC-GC, University of Illinois, Chicago, IL, December 1986.
- [002] Andrieu, B., Sohbi, Y. and Ivanov, N., "A direct method to measure bi-directional gap fraction in vegetation canopies", *Remote Sens. Environment*, Vol.50: 61-66, 1994
- [003] Armand, N.A., A.M.Volkov, A.I.Zakharov, et al, "Prospective spaceborne SAR systems in Russia", *Radiotekhnika i Elektronika*, 1999, v44, n4, pp. 442-447., in Russian.
- [004] Bamler, R. and P. Hartl, "Synthetic Aperture Radar Interferometry", *State of the Art Review, Inverse Problems*, Vol. 14, pp. R1-R54, IOC Publications, Bristol, UK, 1998.
- [005] Bebbington, DH O, "The Expression of Reciprocity in Polarimetric Algebras", *Progress in Electromagnetics Research Symposium (PIERS98)* published in *Proceedings of the 4<sup>th</sup> International Workshop on Radar Polarimetry (JIPR98)* pp 9-18, IRESTE, Nantes, July 1998.
- [006] Bedard, A.J. Jr., "Infrasonic and Near Infrasonic Atmospheric Sounding and Imaging", <http://www4.etl.noaa.gov/infra/infrasonic.html>, September 1999
- [007] Boerner, W-M., et al., (Guest Eds.), *IEEE Transactions on the Antennas & Propagation Society*, Vol. 29(2), Special Issue, *Inverse Methods in Electromagnetics*, (417 pages) 1980-81(1981a).
- [008] Boerner, W-M., "Use of Polarization in Electromagnetic Inverse Scattering", *Radio Science*, Vol. 16(6) (Special Issue: 1980 Munich Symposium on EM Waves), pp. 1037-1045, Nov./Dec. (1981b).
- [009] Boerner, W-M. et al. (eds), "Inverse Methods in Electromagnetic Imaging", *Proceedings of the NATO-Advanced Research Workshop*, (18-24 Sept. 1983, Bad Windsheim, FR Germany), Parts 1&2, NATO-ASI C-143, (1500 pages), D. Reidel Publ. Co., Jan. 1985.
- [010] Boerner, W-M. et al. (eds.), "Direct and Inverse Methods in Radar Polarimetry", *NATO- ARW*, Sept. 18-24, 1988, Proc., Chief Editor, 1987-1991, (1,938 pages), NATO-ASI Series C: Math & Phys. Sciences, Vol. C-350, Parts 1&2, D. Reidel Publ. Co., Kluwer Academic Publ., Dordrecht, NL, 1992 Feb. 15.
- [011] Boerner, W.-M., C. L. Liu, and Zhang, "Comparison of Optimization Processing for 2x2 Sinclair, 2x2 Graves, 3x3 Covariance, and 4x4 Mueller (Symmetric) Matrices in Coherent Radar Polarimetry and its Application to Target Versus Background Discrimination in Microwave Remote Sensing", *EARSel Advances in Remote Sensing*, Vol. 2(1), pp. 55-82, 1993.
- [012] Boerner, W-M., Keynote Address on "Polarimetry in Ultrawideband Interferometric Sensing and Imaging", in H. Anderson and R.A. Chipman, *Proceedings on the Fourth US Army MI-LAB Polarimetry Workshop. Sparkman Auditorium, Redstone Arsenal, AL*, pp. 289-378, 1995a (dedicated to L.W. Root and W-M Boerner).
- [013] Boerner, W.-M., "Polarimetry in Remote Sensing and Imaging of Terrestrial and Planetary Environments", *Proceedings of Third International Workshop on Radar Polarimetry (JIPR-3,95)*, IRESTE, Univ-Nantes, France, pp. 1-38, 1995b.
- [014] Boerner, W-M., Invited Review on "Introduction to Radar Polarimetry - with Assessment of the Historical Development and of the Current State-of-the-Art", pp. 139-214, in A. Guran, R. Mittra and P.J. Moser, eds., *Electromagnetic Wave Interaction - Selected Reviews: the Herbert Überall Sixty-Fifth Birthday-Emeritation Lecture Series at the Catholic University of America*, 1995 June 03, World Scientific Publish. Co., Singapore, 1996: 407 p.
- [015] Boerner, W-M., W-L. Yan, A-Q. Xi and Y. Yamaguchi, "On the Principles of Radar Polarimetry (Invited Review): The Target Characteristic Polarization State theory of Kennaugh, Huynen's Polarization Fork Concept,

- and Its Extension to the Partially Polarized Case", IEEE Proc., Special Issue on Electromagnetic Theory, Vol. 79(10), pp. 1538-1550, Oct. 1991.
- [016] Boerner, W.M., H. Mott, E. Lüneburg, C. Livingston, B. Brisco, R. J. Brown and J. S. Paterson with contributions by S.R. Cloude, E. Krogager, J. S. Lee, D. L. Schuler, J. J. van Zyl, D. Randall P. Budkewitsch and E. Pottier, "Polarimetry in Radar Remote Sensing: Basic and Applied Concepts", Chapter 5 in F.M. Henderson, and A.J. Lewis, (eds.), Principles and Applications of Imaging Radar, vol. 2 of Manual of Remote Sensing, (ed. R.A. Reyerson), Third Edition, John Willey & Sons, New York, 1998.
- [017] Boerner, W-M. et al., "Polarimetry and Polarimetric Interferometry for the Remote Sensing of the Selenga Delta Region of SE Baikal in Buriatia, SE Siberia, Russia", Proc. NASA-JPL AIR-SAR Workshop 1999-02-11/12, Pasadena, CA., in print (15 p.)(1999a)
- [018] Boerner, W., Dhiantravan, Y., Mott, H. Miller, V., Cloude, S., Papathanassiou, K., Treuhaft, R., Kim, Y., Imel, D., O'Leary, E., VanZyl, J., Schmullius, C., Gabriel, J., Moreira, A., Reigber, K., Darizhapov, D., Suchkov, V., Tatkov, G., Bulgakov, S., Tsybjitov, T., 'Air/Space-Borne Repeat-Pass Pol-D-In-SAR image overlay interferometry & its application to geo-ecologic stress-change monitoring within the Selenga Delta, Kudara Polygon, SE Baikal, Buriatia using SIR-C/X-SAR Mission 2', NASA-JPL 8 AIRSAR W'shp. 98-01-15/16, PASADENA, CA, 1-11, 1998
- [019] Boerner, M-W., V. A. Miller, W. K. Volkert, H. Mott, O. Kessler, J.S. Verdi, D. D. Darizhapov, B. Ch. Dorjiev, T. Kh. Tsybjitov, V. M. Korsumow, G. I. Tachkov, Y. Bh. Bashkuyev, C. K. Schmullius, K. P. Papathanassiou, S. R. Cloude, E. Pottier, E. Krogager, J-S. Lee, T. L. Ainsworth, D. L. Schuler, G. de Grandi, P. A. Rosen, R. N. Treuhaft, J. J. van Zyl, "Air/Space-borne, Repeat-Pass Polarimetric Synthetic Aperture Radar Imaging and its Application to Environmental Stress Change-Monitoring of the Baikal Basin World Heritage Site, BINS-RAS-SD, Ulan-Ude, Buryatia, S.E. Siberia, Russia", International Conference on "Baikal as a World Natural Heritage Protection Site", Round-Table I Monitoring of the Lake Baikal ecosystem and International Environmental Standards, Remote Sensing of the Earth's Surface by Aerospace Methods, Ulan-Ude, Buryatia, S.E. Siberia, 1998 Sept 9-(11)-12.
- [020] Boerner, W-M. and H. Überall, SOC-MOT (NATO), "Advanced Research Short Course, Vector Inverse Methods in Radar Target/Clutter Imaging", Co-Ed., Proceedings ARSC, Ecole Supérieur d'Electricité, Gif-sur-Yvette, France, 1986 Sept. 1-4, Springer-Verlag, Heidelberg, 1995, 428p. (ISBN3-540-57791-2).
- [021] Boerner, W-M., O. Kessler, and J. S. Verdi. "Consolidation of Multi-Sensor, Extra-Wide-Band Synthetic Aperture Signal/Image Fusion for Integrating Environmental Stress-Change Monitoring with Dynamic Battle-space Surveillance: paving the way towards creating the 'global digital imaging and mapping laboratories: Terra Digitalis'", Proc. PIERS-WARM (A. Franchois ed) Baveno, It, 1998 July 20 - 22, EC-JRC (also see: 'The Development of the "Collaboratorium Terra Digitalis Baikalum", Int'l. UNESCO/INTAS Conf. on 'Baikal as a World Natural Heritage Protectorate', Ulan-Ude, Buriatia, SE Siberia, Ru., 1999 Sept. 05-12).
- [022] Bracewell, R. N., The Fourier Transform and its Applications, Sec. Rev. Ed., McGraw Hill, New York, 1986 (Third Revised Edition: 1999).
- [023] Bracewell, R. N., Two-Dimensional Imaging, Prentice Hall, Englewood Cliffs, NJ, 1995
- [024] Brand, S., *The CLOCK of the LONG NOW - - eternal time and responsibility*, Basic Books, New York, 1999
- [025] Chen, J-M., Rich, P. M., Gower, S. T., Norman, J. M. and Plummer, S., "Leaf area index of boreal forests: theory, techniques, and measurements", J. Geophysical Research, vol. 102, D24, pp. 29429-29443, 1997
- [026] Chipman, R. A., and J. W. Morris, eds. , "Polarimetry: Radar, Infrared, Visible, Ultraviolet, X-Ray", Proc. SPIE-1317, 1990 ( also see SPIE Proc. 891, 1166, 1746, 1988, 1989, and 3121).
- [027] Clarke, J. E. H., K. A. W. Crook, D. E. Montgomery, K-Y. Lu, G. P. Whitmore, and D. P. Johnson, Combining AIRSAR Data of Huon Peninsula and Hawaii MR1 Data of Huon Golf, Papua New Guinea, for Tectonic and Sedimentary Processes, Marine Geodesy, 212: 111 - 128, 1998 (1998 Taylor & Francis 0149-0419/98)
- [028] Cloude, S. R., Polarimetry: The Characterization of Polarimetric Effects in EM Scattering, Ph.D. thesis, University of Birmingham, Fac. of Eng., UK, Oct. 1986.
- [029] Cloude, S. R. and E. Pottier, "A review of target decomposition theorems in radar polarimetry", IEEE Trans. GRS, vol. 34(2), pp. 498-518, Mar. 1996.
- [030] Cloude S.R. and E. Pottier, "An Entropy-Based Classification Scheme for Land Applications of Polarimetric SAR", IEEE Trans GRS-35(1), 68-78, 1997
- [031] Cloude, S. and K. Papathanassiou, "Polarimetric SAR Interferometry", IEEE Trans. Geosci. Remote Sensing, vol. 36, pp. 1551-1565, Sep. 1998.

- [032] S R Cloude, "Polarimetry in Wave Scattering Applications", Chapter 1.6.2 in SCATTERING, Eds R Pike, P Sabatier, Academic Press, to be published December 1999
- [033] S R Cloude, J Fortuny, J M Lopez, A J Sieber, "Wide Band Polarimetric Radar Inversion Studies for Vegetation Layers", IEEE Transactions on Geoscience and Remote Sensing, Vol 37/2 No 5, pp 2430-2442, September 1999
- [034] CRAF Handbook for Radio Astronomy, 2<sup>nd</sup> Ed., Published by the Committee on Radio Astronomy Frequencies (CRAF), Secretariat, the Netherlands Foundation for Radio Astronomy, PO-2, NL-7990 Dwingelo, Netherlands, 1997 (ISBN: 2-903148-94-5) .
- [035] Curlander, J.C. and R.N. McDonough, Synthetic Aperture Radar: Systems and Signal Theory, John Willey & Sons, New York, 1991.
- [036] Czyz, Z.H., "Advances in the Theory of Radar Polarimetry," Prace PIT, No.117, Vol.XLVI, 1996, Warsaw, Poland, pp.21-28. (In English).
- [037] Czyz, Z.H., "Fundamental Properties of the Polarimetric Two-Ports," Prace PIT, No.119, 1997, Warsaw, Poland, pp.25-37. (In Polish).
- [038] Czyz, Z.H., "Basic Theory of Radar Polarimetry - An Engineering Approach", Prace PIT, No.119, 1997, Warsaw, Poland , pp.15-24. (In English).
- [039] Czyz, Z.H., "Analysis of the Cascade Connection of the Polarimetric Two-Ports", Prace PIT, No.122, 1998, Warsaw, Poland, pp.6-22. (In Polish).
- [040] Darrach, M. and A. Chutjian, Trace Explosives Signatures from Unexploded Under-Sea Ordnance -- using the READ (Reversal Electron Attachment Detector) System, NASA-JPL Report (Prepared for NSWC-DD-CSS, Panama City, FL), June 1997
- [041] Das, Y. and Boerner, W-M., "On Radar Target Estimation Using Algorithms for Reconstruction from Projections", IEEE Trans. APS-26(2), pp. 274-279, 1978
- [042] Diamond, J., '*Guns, Germs, and Steel: the development of human societies*', Norton, New York, 1997
- [043] Dubois, P.C. and J.J. van Zyl, "An Empirical Soil Moisture Estimation Algorithm Using Imaging Radar", IEEE Trans. GRS-33(4), pp. 915-926, 1995.
- [044] Fitzgerald, M., "the NASA-ARC Air-borne MASTER (MODIS + ASTER: 460 - 1263 nm) Simulator", Proceedings of the US-AU PACRIM Significant Results Workshop, MHPCC, Kihei, Maui, HI, 1999 August 24 - 26 (10 pages)
- [045] Freeman, A. and S.T. Durden, "A Three-Component Scattering Model for Polarimetric SAR Data", IEEE Trans. GRS, Vol. 36(3), pp. 963-973, 1998.
- [046] Frampton, K. R., D. A. Coon and M. J. Dorsett, "Acousto-Optic Range Doppler Processor for Target Discrimination", in Proc. SPIE Vol.3462, Radar/Ladar Processing and Applications, pp. 320 - 331, 1998
- [047] Goldstein, D.H. and R.A. Chipman, "Optical Polarization: Measurement, Analysis, and Remote Sensing", Proc. SPIE-3121, 1997 ( see Proc. SPIE 891, 1166, 1317, 1746, 1988, 1989, dealing with OPT-POL).
- [048] Goodman, J. W., Introduction To Fourier Optics, 2nd Revised Edition, McGraw Hill, New York, 1996
- [049] Gough, P. T & D. W Hawkins, "Unified Framework for Modern Synthetic Aperture Imaging Algorithms", Journal of Imaging Systems and Technology (John Wiley & Sons, Inc.), Vol. 8, pp. 343 - 358, 1997
- [050] Gough, P. T. and D. W. Hawkins, "Imaging algorithms for a strip-map synthetic aperture sonar: minimizing the effects of aperture errors and aperture under-sampling", IEEE Journal of Ocean Engineering, Vol. 22(1), pp. 27-39, Jan 1997
- [051] Hawkins, D. W. Synthetic Aperture Imaging Algorithms: with applications to wide bandwidth sonar, Ph. D. thesis, School of Graduate Studies (ECE), The University of Canterbury, Christchurch, N Z, 1995.
- [052] Henderson, F. M. and A. J. Lewis, guest editors, Principles and Applications of Imaging Radar, Manual of Remote Sensing, Third Edition, Volume 2, John Wiley & Sons, Inc., New York, July 1998 (940p.), see: Ch. 5: "Polarimetry in Radar Remote Sensing: Basic and Applied Concepts" (Wolfgang-M. Boerner, Harold Mott, Ernst Lüneburg, Charles Livingstone, Brian Brisco, Ronald J. Brown and J. Scott Patterson -- with contributions by S. R Schuler, J. J. van Zyl, D. Randell, P. Budkewitsch and E. Pottier), 98 p.
- [053] Hensley, S., "Interferometric Studies in Queensland Australia", Proceedings of the US-AU PACRIM Significant Results Workshop, MHPCC, Kihei, Maui, HI, 1999 August 24 - 26 (10 pages)
- [054] Huynen, J. R., Phenomenological Theory of Radar Targets, PhD. thesis, University of Technology, Delft, The Netherlands, December 1970.
- [055] Imbo, P., J.C. Souyris, A. Lopes, Ph. Marthon, Synoptic presentation of the polarimetric information. Proceedings of the ESA-CEOS-MRS'99 SAR-CAL/VAL Workshop, CNES, Toulouse, France, 1999 October 25-29 (6 pages)
- [056] Imel, D. A., "AIRSAR Along-track Interferometry Data", Proceedings of the US-AU PACRIM Significant Results Workshop, MHPCC, Kihei, Maui, HI, 1999 August 24 - 26 (10 pages).

- [057] Imhoff, M. L., "Radar backscatter/biomass saturation: Observations and implications for global bio-mass assessment", International Geoscience and Remote Sensing Symposium (IGARSS'93), Tokyo, Japan Aug. 18-21, 1993
- [058] Imhoff, M. L., "Mapping human impacts on the global biosphere", *Bioscience* Vol. 44 No. 9 p598. (1995)
- [059] Imhoff, M. L., "A theoretical analysis of the affect forest structure on synthetic aperture radar backscatter and the remote sensing of biomass", *IEEE Transactions on Geoscience and Remote Sensing*, Vol. 33, No.2 March 1995, pp 341-352.
- [060] Imhoff, M. L., "Radar backscatter and biomass saturation: ramifications for global biomass inventory", *IEEE Transactions on Geoscience and Remote Sensing*, Vol. 33, No. 2 March 1995, pp. 510-518.
- [061] Imhoff, M. L., "Mapping Vegetation Structure in Kakadu National Park: An AIRSAR and GIS Application in Conservation", Proceedings of the US-AU PACRIM Significant Results Workshop, MHPCC, Kihei, Maui, HI, 1999 August 24 - 26 (10 pages)
- [062] Imhoff, M. L., T.D. Sisk, A. Milne, G. Morgan, and T. Orr, "Remotely sensed indicators of habitat herogeneity: Use of synthetic arpeture radar in mapping vegetation structure and bird habitat", *Remote Sensing of Environment Journal*, Vol. 60, pp. 217-227, 1997
- [063] Imhoff, M. L., W.T. Lawrence, C. Elridge, T. Paul, E. Levine, M. Prevalsky, and V. Brown, Using nighttime DMSP/OLS images of city lights to estimate the impact of urban land use on soil resources in the U.S.", *Remote Sensing of Environment Journal*, Vol. 59, pp. 105-117, 1997
- [064] Imhoff, M. L., W. T. Lawrence, D.C. Stutzer, and C.D. Elvidge, "A technique for using composite DMSP/OLS 'citylights' satellite data to accurately map urban areas", *Remote Sensing of Environment Journal*, Vol. 61, pp. 361-370, 1997
- [065] Imhoff, M. L., S. Carson, and P. Johnson, "A low frequency radar sensor for vegetation biomass measurement", *IEEE Transactions on Geoscience and Remote Sensing*, Vol. 36, No. 6, 1998
- [066] Imhoff, M. L., P. Johnson, W. Holford, J. Hyer, L. May, W. Lawrence, and P. Harcombe, "An Inexpensive Airborne VHF Multi-band SAR System for Vegetation Biomass Measurement", *IEEE Transactions on Geoscience and Remote Sensing*, Vol. 33 No. 6, November 1999
- [067] International Symposia on Spectral Sensing Research (ISSSR), Nov 92, July 94, Nov 95, July 97, Nov 99 (<http://www.tec.army.mil>)
- [068] Jacobs, P.A., "Thermal Infrared Characterization of Ground Targets and Backgrounds", SPIE, Tutorial Texts in Optical Engineering, SPIE Vol. TT-26, 1996
- [069] Valentin A. Koptug, editor, The Present and Future State of the Baikal Lake Region - - Part 1, INFOLIO, Novosibirsk, Siberia/RF (ISBN 5-85826-017-9), 1996
- [070] Kennaugh, E. M., Polarization Properties of Radar Reflections, MSc Thesis, Ohio State University, Columbus, March 1952.
- [071] Kim Y-J, "Polarimetric Interferometry", Proceedings of the US-AU PACRIM Significant Results Workshop, MHPCC, Kihei, Maui, HI, 1999 August 24 - 26 (10 pages)
- [072] Klein, L.A., MM-Wave - IR Multi-sensor Design & Signal Processing, Artech House, Inc., Boston, 1977
- [073] Kramer, H. J. , Observation of the Earth and its Environment - Survey of Missions and Sensors, Springer Verlag, Heidelberg-New York, 1996
- [074] Krogager, E., Aspects of Polarimetric Radar Imaging, Ph.D. thesis, Techn. Uni. of Denmark, Electromagnetics Institute, Lyngby, DK, March 1993.
- [075] Krogager, E., W.-M. Boerner, S. N. Madsen; "Feature-Motivated Sinclair Matrix (sphere/diplane/helix) Decomposition and Its Application to Target Sorting For Land Feature Classification," SPIE-3120, 144-154, 1997.
- [076] Krogager, E., and Z.H. Czyz, "Properties of the Sphere, Diplane and Helix Decomposition" Proc. of 3rd International Workshop on Radar Polarimetry, IRESTE, University of Nantes, France, pp. 106-114, April 1995.
- [077] Krogager, E, and W.M. Boerner, "On the Importance of Utilizing Polarimetric Information in Radar Imaging Classification", AGARD Proc. 582-17, 1-13, April 1996
- [078] Krogager, E., Comparison of Various POL-RAD and POL-SAR Image Feature Sorting and Classification Algorithms, Journées Internationales de la Polarimétrie Radar, Proc. JIPR'98, pp. 77-86, Nantes, France, 13-17 July, 1998.
- [079] Krogager, E., S.R. Cloude, J.-S. Lee, T.L. Ainsworth, and W.-M. Boerner, Interpretation of high resolution polarimetric SAR data, Journées Internationales de la Polarimétrie Radar, Proc. JIPR'98, pp. 165-170, Nantes, France, 13-17 July, 1998.
- [080] Kucharik, C. J., Norman, J. M., Murdock, L. M. and. Gower, S. T, "Characterizing canopy non-randomness with a multi-band vegetation imager (MVI)", *J. Geophysical Research*, vol. 102, no. D24, pp. 29455-29473, 1997
- [081] Lathrop, J. D, J. F. McCormick, P. J. Bernstein, J. T. Bruno, D. J. Overway, G. S. Sammelmann, T. -H. Chao, K. C. Scott, "Mobile Underwater Debris (SAS) Survey System (MUDSS) -- A Feasibility Demo.", Proc. UXO Forum 1996

- March 26-28, Williamsburg, VA, pp. 427-435, US Army Environmental Center, Env.Tech.Div. Attn: USAEC/ETD, SFM-AEC-ETP, Aberdeen Proving Grounds, MD/USA, 1996
- [082] Lee, J.S., "Speckle suppression and analysis for synthetic aperture radar images", SPIE Optical Engineering, Vol. 25 No. 5, pp. 636-643, May 1986.
- [083] Lee, J.S., M.R. Grunes and W.M. Boerner, "Polarimetric Property Preserving in SAR Speckle Filtering," Proceedings of SPIE, Vol. 3120, 236-242, San Diego, 1997.
- [084] Lee, J.S. and M. R. Grunes, Polarimetric SAR Speckle Filtering and Terrain Classification-An Overview 26p., Book Ch. in XX, World Sci.Publ., Singapore, 1999
- [085] Lee, J.S., K.P. Papathanassiou, T.L. Ainsworth, M.R. Grunes and A. Reigber, "A New Technique for Noise Filtering of Sar Interferometric Phase Images", IEEE Trans. GRS Vol. 36 , No.5 pp. 1456-1465.
- [086] Lee, J. S, M R Grunes, T L Ainsworth, L J Du, D L Schuler, S R Cloude, "Unsupervised Classification using Polarimetric Decomposition and the Complex Wishart Distribution", IEEE Transactions Geoscience and Remote Sensing, Vol 37/1, No. 5, p 2249-2259, September 1999
- [087] Lee, R. L., J. Teti, F. Gambucci, S. Krasznay, J. Verdi, A. Rouan, Polarimetric Techniques for Enhancing P-3 SAR Imagery, NAWCAD Code 4.5.5.5, Patuxent River, MD, Fin-Rep./ONR-313,1996-03-20.
- [088] Lu, S-Y L and R. A. Chipman, "Interpretation of Mueller Matrices - in the optical domain - based on polarimetric decomposition", JOSAA-A, Vol. 13(5), pp. 1106 - 1113, May 19
- [089] Lüneburg, E., V. Ziegler, A. Schroth, and K. Tragl, "Polarimetric Covariance Matrix Analysis of Random Radar Targets", pp.27.1 - 27.12, in Proc. NATO-AGARD-EPP Symposium on Target and Clutter Scattering and Their Effects on Military Radar Performance, Ottawa.Canada,1991 May 6 - 10.
- [090] Lüneburg, E., "Principles of Radar Polarimetry", Proceedings of the IEICE Trans. on the Electronic Theory, Vol. E78-C, no. 10, pp. 1339-1345, 1995.
- [091] Lüneburg, E., Radar polarimetry: A revision of basic concepts, in "Direct and Inverse Electromagnetic Scattering", H. Serbest and S. Cloude, eds., Pitman Research Notes in Mathematics Series 361, Addison Wesley Longman, Harlow, U.K., 1996, pp. 257 - 275.
- [092] Lüneburg, E., Comments on "The Specular Null Polarization Theory" IEEE Trans. Geoscience and Remote Sensing, Vol. 35, 1997, pp. 1070 - 1071.
- [093] Madsen, S. N., and H. A. Zebker, "Imaging Radar Interferometry", Chapter 6 in F.M. Henderson, and A.J. Lewis, (ed.), Principles and Applications of Imaging Radar, vol. 2 of Manual of Remote Sensing, (ed. R.A. Reyerson), Third Edition, John Willey & Sons, New York, 1998.
- [094] Massonet D. and K.L. Feigl, "Radar Interferometry and its Application to Displaying Stress-Changes in the Earth's Crust", Review of Geophysics, Vol. 36(4), 1998 Nov, pp. 441-500.
- [095] Milne, T., "Estimating Bio-Mass and Vegetation Structure in Semi-Arid Woodlands of the NWT, Australia using AIRSAR and JERS-1 Data - - - a synergetic approach", Proceedings of the US-AU PACRIM Significant Results Workshop, MHPCC, Kihei, Maui, HI, 1999 August 24 - 26 (10 pages)
- [096] Misner, C.W., K.S. Thorne and A Wheeler, "Gravitation", W.H. Freeman & Co., New York, 1970 (twentieth printing: 1997)
- [097] Mittermayer, Josef, Alberto Moreira and Otmar Lofeld. "The Frequency Scaling Algorithm for Spotlight SAR Data Processing". IEEE Trans. on Geoscience and Remote Sensing, Vol. 37, No. 5, September 1999, pp 2198-2214.
- [098] Moore, E., "Angkor AIRSAR Water control and conservation at Angkor", Proceedings of the US-AU PACRIM Significant Results Workshop, MHPCC, Kihei, Maui, HI, 1999 August 24 - 26 (10 pages)
- [099] Moreira, A., "Synthetic Aperture Radar", Chapter in Book Radar mit realer und synthetischer Apertur. Oldenburg Verlag, Munich 1999, p.88. (also see: Moreira, A., "E-SAR System: Specification of a high resolution Multi-Look Real-Time Azimuth Processor. DLR International Report R-551-11-11/88", Radar Group, 04 November 1988.)
- [100] Moriyama, Toshifumi, Masafumi Nakamura, Yoshio Yamaguchi, Hiroyoshi Yamada, Wolfgang -M. Boerner, Classification of target buried in the underground by radar polarimetry, J-IEICE Trans. Commun., vol.E82-B, no.6, pp.951-957, June 1999
- [101] Mott, H., Antennas for Radar and Communications, A Polarimetric Approach, John Wiley & Sons, New York, 1992, 521 p.
- [102] Mott, H. and W-M. Boerner, editors, "Radar Polarimetry, SPIE's Annual Mtg., Polarimetry Conference Series", 1992 July 23 - 24, San Diego Convention Center, SPIE Conf. Proc. Vol. 1748, 1992
- [103] Mott, H. and W-M. Boerner, editors, "Wideband Interferometric Sensing and Imaging Polarimetry", SPIE's Annual Mtg., Polarimetry and Spectrometry in Remote Sensing Conference Series, 1997 July 27- Aug 01, San Diego Convention Center, SPIE Conf. Proc. Vol. 3120, 1997.

- [104] Nilson, T., "A theoretical analysis of the frequency of gaps in plant stands", *Agric. Meteorol.* 8, 25-38, 1971.
- [105] Novak, L.M., and M.C. Burl, "Optimal Speckle Reduction in Polarimetric SAR Imagery" *IEEE Trans. AES*, Vol. 26, no.2, pp. 293-305, 1990
- [106] Novak L.M., S. D. Halversen, G. J. Owirka, M. Hiett, "Effects of Polarization and Resolution on SAR ATR," *IEEE Trans. AES*, Vol. 33(1), pp. 102-116, Jan. 1997.
- [107] Papathanassiou, K. P., *Polarimetric SAR Interferometry*, Ph. D. Thesis, Tech. Univ. Graz, 1999.
- [108] Papathanassiou, K. P. and S. Cloude, "Phase Decomposition in Polarimetric SAR Interferometry", *Proc. IEEE IGARSS'98*, pp. 2184-2186, Seattle, 3-8 Aug. 1998.
- [109] Papathanassiou, K. P., A. Reigber, R. Scheiber, R., Horn, A. Moreira, S. Cloude, "Airborne Polarimetric SAR Inter-ferometry," *Proc. IEEE IGARSS'98*, pp. 1901-1904, 1998
- [110] Pottier, E., *Contribution de la Polarimétrie dans la Discrimination de Cibles Radar, Application à l'Imagerie Electromagnétique haute Resolution*, Ph.D. thesis, IRESTE, Nantes, France, December 1990.
- [111] Pottier, E., *Unsupervised Classification Scheme and Topology Derivation of POLSAR Digital Image Data Based on the (H/A/ $\alpha$ ) Polarimetric Decomposition Theorems*, *Proc. JIPR-4*, U. Nantes/IRESTE, Nantes, Bretagne, 98 July 13-17, pp. 535-548.
- [112] Pottier, E., *Contribution à la Polarimétrie Radar: de l'approche fondamentale aux applications, Habilitation a Diriger des Recherches; Dr. Ing. habil., Ecole Doctorale Sciences pour l'Ingenieur de Nantes, Université de Nantes, l'IRESTE, La Chantrerie, Rue Pauc, BP 60601, F-44306 NANTES CED-3*, 98-11-12
- [113] Raney, R. K., "Processing Synthetic Aperture Radar Data", *Int'l JRS*, Vol. 3(3), pp. 243-257, 1982.
- [114] Reigber, A., A. Moreira and K. Papathanassiou, "First Demonstration of Airborne SAR Tomography Using Multi-Baseline Data". *Proc. IGARSS-99 (06-28\_07-02)*, A03\_10:50, Hamburg, Germany.
- [115] Reigber, A., A. Moreira: *First Demonstration of SAR Tomography using Polarimetric Airborne SAR Data*. Submitted to *IEEE Transactions on Geoscience and Remote Sensing*, 1999
- [116] Ryerson, R. A., Editor-in-Chief, *MANUAL OF REMOTE SENSING - Third Revised Edition: Vol. 1, Earth Observing Platforms & Sensors* (edited by S. A. Morain and A. M. Budge); *Vol. 2, Principles and Applications of Imaging Radar* (edited by F. M. Henderson and A. J. Lewis); *Vol.3, Remote Sensing for the Earth Sciences* (edited by A. Rencz), Published in cooperation with ASPRS - the American Society for Photogrammetry and Remote Sensing, John Wiley & Sons, Inc., New York, 1998.
- [117] Saillard, J., F.A. Molinet and W-M. Boerner, eds., "Proc. : Int'l Workshop on Radar Polarimetry", *JIPR-1*, 1990 March 20- 23, University of Nantes, IRESTE-S2HF, LeChantrerie, Nantes, France, March 1990.
- [118] Saillard, J., E. Pottier and W-M. Boerner, eds., "Proceedings: International Workshop on Radar Polarimetry", *JIPR-2*, 1992 Sept. 8-10: University of Nantes, IRESTIE-S2HF, Nantes, 1992
- [119] Saillard, J., E. Pottier and S. R. Cloude, eds., "Proceedings: International Workshop on Radar Polarimetry", *JIPR-3*, 95-03-20\_23 (dedicated: WMB)
- [120] Saillard, J., E. Pottier & W-M Boerner, eds, "Proc. Int'l Radar Polarimetry W'shop", *JIPR-4*, 98-07-13\_16
- [121] Sato, Motoyuki, Editor, *Proc. of 6<sup>th</sup> Intern. Conf.on Ground Penetrating Radar (GPR)*, Tohoku University, Aoba Campus, 1996 Sept. 30 - Oct. 03, Sendai, Japan
- [122] Scheiber, R., A. Reigber, A. Ulbricht, K. Papathanassiou, R. Horn, St. Buckreuss and A. Moreira: "Overview of Interferometric Data Acquisition and Processing Modes of the Experimental Airborne E-SAR System of DLR". *Proc. IGARSS-99 (06-28\_07-02)*, A03\_08:30, Hamburg, Germany.
- [123] Schott, J.R., "Remote Sensing -- The Image Chain Approach", Oxford Univ. Pres., New York, 1997.
- [124] Schuler, D.L., J-S. Lee and G. De Grandi, "Measurement of Topography using Polarimetric SAR-Images", *IEEE Trans. GRS-34(5)*, 1210-1221, Sept. 96.
- [125] Schuler, D.L, J.S. Lee, and T.L. Ainsworth, "Topographic Mapping using Polarimetric SAR Data", *International Journal of Remote Sensing*, vol. 19, no.1, pp 141-160, 1998.
- [126] Schuler, D.L., J.S. Lee, and T.L. Ainsworth, "Terrain Topography Measurement using Multi-Pass Polarimetric SAR Data", submitted for review, *Radio Science*, September, 1999.
- [127] Schuler, D.L., J.S. Lee, and T.L. Ainsworth, "Compensation of Terrain Azimuthal Slope Effects in Geophysical Parameter Studies using Polarimetric SAR Data", *Remote Sensing of Environment*, vol. 69/2, pp 139-155, July, 1999.
- [128] Sheen, D. R, C. M. Strawitch, T. B. Lewis, "UHF Wideband SAR Design and Preliminary Results (NAWC ERIM P-3 QuadSAR)", *Proc. IGARSS'94*, Vol. 1, pp. 289-291, Pasadena, CA, August 1994.
- [129] Smarr, L., Guest Editor, Special Issue on "Computational Infrastructure: Toward the Twenty-first Century", *Communications of the*

- ACM (Association for Computing Machinery) Vol. 40(11), November 1997
- [130] Smith, J. A., and S. M. Goltz, "A Thermal Exitance and Energy Balance Model for Forest Canopies", IEEE Trans. GRS Vol 32(5), pp. 1060-1066, Sept. 1994
- [131] Smith, J.A., J.R. Ballard, Jr., J.A. Pedelty, "Effect of Three-Dim. Canopy Architecture on Thermal Infrared Existence", OPT. ENG.-36(1), pp. 3039-3100, Nov. 97
- [132] Smith, P. H and J. van Rosendale, Guest Editors, Data and Visualization Corridors - report on the 1998 DVC Workshop Series, CAL-TECH Inst. Press, 1998.
- [133] SPIE Conferences on Imaging Spectrometry : "I Orlando Apr 95", "II Denver Aug 96", "III San Diego Jul 97", "IV San Diego Jul 98" (<http://www.spie.org>)
- [134] Stimson, G.W., Introduction to Airborne Radar - 2nd Rev. Ed., SciTech Publ., Inc., Medham N.J, 1998
- [135] Sullivan, R A. Nichols, R. Rawson, C. Haney, F. Darreff and J. Schanne Jr., "Polarimetric X/C/L-Band SAR", Proceedings of the 1988 IEEE National Radar Conference, Ann Arbor, MI, pp. 9-14, 1988.
- [136] Swindell, W., Polarized Light, Halsted Press (John Wiley & Sons), Stroudsburg, PA: 423 p., 1975
- [137] Tapley, I., "Using Radar Polarimetry for Mapping for Regolith Geology in Australia", Proceedings of the US-AU PACRIM Significant Results Workshop, MHPCC, Kihei, Maui, HI, 1999 August 24 - 26 (10 pages)
- [138] Touzi R., R. St-Jean, and Y. Crevier, Taking the speckle out of SAR: the Gamma filter, Remote Sensing in Canada, Vol. 23, No. 3, Dec. 1995.
- [139] Touzi R. and A. Lopes, Analysis of Speckle Filtering in Polarimetric SAR Imagery, IEEE Trans. Geoscience Rem. Sens., Vol. 32, No. 5, pp. Sep. 1994
- [140] Touzi R. and A. Lopes, Statistics of the Stokes parameters and of the complex coherence parameters in one-look and multi-look speckle fields, IEEE Trans. Geoscience Rem. Sens., Vol. 34, No. 2, pp. 519-531, March 1996
- [141] Touzi R., A. Lopes, J. Bruniquel, and P. Vachon, "Unbiased estimation of the coherence for SAR Imagery", IEEE Trans. Geoscience Rem. Sens., Vol. 37, No. 1, jan. 1999
- [142] Touzi R., "On the use of polarimetric SAR data for ship detection", Proc. of the IGARSS'99 Symp., pp. 812-814, Hamburg, Germany, July 1999.
- [143] Touzi R., A. Lopes, J. Bruniquel, and P. Vachon, "Unbiased estimation of the coherence for SAR Imagery", IEEE Trans. Geoscience Rem. Sens., Vol. 37, No. 1, jan. 1999
- [144] Tragl, K. "Polarimetric Radar Back-scattering from Reciprocal Random Targets", IEEE Trans. GRS-28(5), pp. 856 - 864, Sept. 1990 (see Dr. - Ing. Thesis, 1989).
- [145] Treuhaft, R. N and P. R. Sequeira, "The Vertical Structure of Vegetated Land Surfaces from Interferometric and Polarimetric Radar", Radio Science, Vol.xx(y), 1999/2000(?), accepted for publication.
- [146] Treuhaft, R N, S R Cloude, "The Structure of Oriented Vegetation from Polarimetric Interferometry", IEEE Transactions Geoscience and Remote Sensing, Vol 37/2, No. 5, p 2620, September 1999
- [147] Treuhaft, R. N., S. N. Madsen, M. Moghaddam, and J. J. van Zyl, "Vegetation Characteristics and Surface Topography from Interferometric Radar," Radio Science, 31, p. 1449-1485, 1996.
- [148] Treuhaft, R. N., "Estimating Vegetation Parameters from Interferometric and Polarimetric Radar Using Physical Scattering Models," URSI General Assembly, Toronto, August 1999 (invited)
- [149] Treuhaft, R. N., S. Hensley, B. E. Law, P. R. Siqueira, "Estimating Forest Vertical Structure from Multialtitude, Fixed-Baseline Radar Interferometric and Polarimetric Data," IGARSS99, Hamburg, July 1999 (invited)
- [150] Ulaby, F. T. and C. Elachi, Editors, Radio Polarimetry for Geo-science Applications, Artech House, Inc., Norwood, MA, 1990, 364p.
- [151] Ulaby, F. T., R. K. Moore, and A. K. Fung, Microwave Remote Sensing, Vols. 1- 3, Addison Wesley, Reading, MA, 1981, 2184p
- [152] Verdi, J.S., R. Lee, P.R. Kersten, S.K Krasznay, D.R. Statter, and W-M. Boerner, Comparative Analysis of Polarimetric SAR Image Exploitation Algorithms For Environmental Stress-Change Monitoring, Proc. IGARSS-99 (06-28\_07-02), E05\_5, Hamburg, Germany, July, 1999
- [153] Waring, R.H. and S.W. Running, Forest Ecosystems - Analysis and Multiple Scales, Acad. Press, 2<sup>nd</sup> Ed., Harcourt Brace & Co., San Diego CA, 1998
- [154] Waterman, T. H., Polarization Sensitivity by {Marine Animals}, pp. 281-469, Chap. 3, in H. Autrum, ed., Comparative Physiology and Evolution of Vision in Invertebrates, Part B: Invertebrate Visual Centers and Behavior I, Springer Verlag, NY, 1981, 469p.
- [155] Waterman, T. H., 'Navigational Potential of E-Vector Pol-Sensing by Marine Animals', Keynote Paper, Radar Polarimetry, Proc. SPIE-1748, pp. 2 - 10, 1993
- [156] Wilson E.O., 'The Diversity of Life', Norton, New York, 1999
- [157] Xi, A-Q and W-M. Boerner, "Determination of the Characteristic Polarization States of the



- target scattering matrix [S(AB)] for the coherent Monostatic and Reciprocal Propagation Space Using the Polarization Transformation Ratio Formulation", *JOSA-A/2*, 9(3), pp. 437-455, 1992.
- [158] Yamaguchi, Y., T. Nishikawa, M. Sengoku, W-M. Boerner and H.J. Eom, "Fundamental Study on Synthetic Aperture FM-CW Radar Polarimetry", *IEEE Trans. Comm.*, vol. S77-B, no. 1, pp. 73-80, January 1994
- [159] Yamaguchi, Y., T. Nishikawa, M. Sengoku and W-M. Boerner, "Two-Dimensional and Full Polarimetric Imaging by a Synthetic Aperture FM-CW Radar", *IEEE Trans. GRS*, Vol. 33, no. 2, pp. 421-427, March 1995
- [160] Yamaguchi, Y., Y. Takayanagi, W-M. Boerner, H.J. Eom and M. Sengoku, "Polarimetric Enhancement in Radar Channel Imagery", *IEICE Trans. Communications*, vol. E78-B, no. 1, pp. 45-51, Jan 1996
- [161] Yang, J., Y. Yamaguchi, H. Yamada, M. Sengoku, S. Lin, "Stable Decomposition of Mueller Matrix", *IEICE Trans. Comm.*, vol. E81-B(6), pp. 1261-1268, June 1998
- [162] Yang, J., Yoshio Yamaguchi, Hiroyoshi Yamada, "Co-null of targets and co-null Abelian group," *Electronics Letters*, vol.35, no.12, pp.1017-1019, June 1999.
- [163] Yang, J., Yoshio Yamaguchi, Hiroyoshi Yamada, Masakazu Sengoku, Shi -Ming Lin, Optimal problem for contrast enhancement in polarimetric radar remote sensing, *J-IEICE Trans. Commun.*, vol.E82-B, no.1, pp.174-183, Jan. 1999
- [164] Zebker, H.A, and R.M. Goldstein, "Topographic Mapping from Interferometric Synthetic Aperture Radar Observations", *J. Geo. Res.*, Vol. 91, pp. 4993-4999, 1986.
- [165] van Zyl, J.J. On the Importance of Polarization in Radar Scattering Problems, Ph.D. thesis, California Institute of Technology, Pasadena, CA, December 1985.
- [166] van Zyl, J.J., H. Zebker, and C. Elachi, "Imaging Radar Polarization Signatures: Theory and Application", *Radio Science*, vol. 22, no. 4, pp. 529-543, 1987.
- [167] van Zyl, J.J. "Application of Cloude's Target Decomposition Theorem to Polarimetric Imaging Radar Data", *SPIE Proceedings* (H. Mott, W-M Boerner eds.), Vol. 1748, San Diego, CA, 23-24 July 1992.
- [168] van Zyl, J.J., and J.S. Hjelmstad, 'Interferometry in Remote Sensing', State of the Art Review (1996 - 1999), *Proceedings of the URSI-GA-99*, Toronto, Ontario, Canada, Special Issue, *Radio Science*, Vol. 35, 2000, 12 p.
- [169] van Zyl, J.J., "An Overview of the Analysis of Multi-frequency Polarimetric SAR Data", *Proceedings of the US-AU PACRIM Significant Results Workshop*, MHPCC, Kihei, Maui, HI, 1999 August 24 - 26 (10 pages)
- [170] Zakharov, A.I., L.E.Nazarov, "Classification of the forests types based on the textural analysis of SIR-C SAR images", *Earth Research from Space*, 1998, n2, pp. 102-109., in Russian
- [171] Zakharov, A.I., P.V.Tugarinov, "Research of the dynamics of the sea ice covers near Antarctic coast based on the ALMAZ-1 SAR data", *Radiotekhnika*, 1998, n12, pp.63-67., in Russian
- [172] Zakharov A.I., Kucheryavenkova I.L, "On the quality of forest types classification using SIR-C/X SAR polarimetric data at various observation angles", *Proceedings of CEOS SAR Workshop*, Netherlands, 1998, WPP-138, pp. 97-100.
- [173] Turpin, T. M, P. Woodford, C. Price, J. L. Lafuse, S. M. Evanko, and L. C. Phillips, "ImSyn: Optoelectronic Product for Image Synthesis and Correlation," *Proc. SPIE-XXXX*, pp. uvw - xyz, Lake Tahoe CA, March 1997

**16. PERTINENT WEB SITES: (<http://.....>)  
POL-SAR-Imaging (see Kramer : [44] & [71, Vol. 1] )**

- [w-01] ONR-IFO-NICOP: <http://www.ehis.navy.mil/>
- [w-02] EU-TMR-RP:<http://www.dlr.de/ne-hf/projects/TMR>, e-m: [tmr-network@dlr.de](mailto:tmr-network@dlr.de)
- [w-03] IGARSS-99: <http://www.igarss.org>
- [w-04] ERIM-IARSCE:[http://www.erim-int.com/CONF/4th airborne/intro.html](http://www.erim-int.com/CONF/4th_airborne/intro.html)
- [w-05] RADAR-99: <http://www-rad99.enst-bretagne.fr> or e-m: [s.e.e@wanadoo.fr](mailto:s.e.e@wanadoo.fr)
- [w-06] IEEE-AESS-Radar Systems Panel: <http://www.aeroconf.org>
- [w-07] SPIE-AM&E: <http://www.spie.org/web/oer/september/sep99/spiescene.html>
- [w-08] URSI-GA-99: <http://www.nrc.cal/confserv/ursi99/welcome.html>
- [w-09] NASA-JPL AIRSAR: <http://airsar.jpl.nasa.gov> or <http://southport.jpl.nasa.gov>
- [w-10] USA-A&S-MI-LAB/RDECHSMSMMS: <http://smaplaboratory.uah.edu/HMSM>
- [w-11] ESA-CEOS: <http://www.estec.esa.nl/CONFANNOUN/99b02>
- [w-12] EU-SAR: <http://www.dlr.de/ne-hf/eusar2000/>

**POL-IN-SAR IMAGING PLATFORMS**

- [v-01] GEOSAR: [southport.jpl.nasa.gov](http://southport.jpl.nasa.gov)
- [v-02] AIR-SAR: [airsar.jpl.nasa.gov](http://airsar.jpl.nasa.gov)

- [v-03] ERIM-SARS: [www.erin-int.com](http://www.erin-int.com)
- [v-04] ESAR: [www.dlr.de/NE-HF/projects/ESAR](http://www.dlr.de/NE-HF/projects/ESAR) ,  
AEROSENSING:  
<http://www.op.dlr.de/aerosensing>
- [v-05] PI-SAR: [www.crl.go.jp](http://www.crl.go.jp)
- [v-06] EMISAR: [www.dcrs.dk/DCRS](http://www.dcrs.dk/DCRS)
- [v-07] RAMSES: [www.onera.fr/english.html](http://www.onera.fr/english.html)
- [v-08] CARABAS: [www.foa.se/eng/carabas.html](http://www.foa.se/eng/carabas.html)
- [v-09] PHARUS: [neonet.nlr.nl/tno-fel](http://neonet.nlr.nl/tno-fel)
- [v-10] HUTRAD: [www.space.hut.fi](http://www.space.hut.fi)
- [v-11] SRTM:[www-  
radar.jpl.nasa.gov/srtm/index.html](http://www-radar.jpl.nasa.gov/srtm/index.html)
- [v-12] SRTM-  
DLR:[www.dlr.de/NEHF/projects/SRTM](http://www.dlr.de/NEHF/projects/SRTM)
- [v-13] RADARSAT: [www.ccrs.nrcan.gc.ca/globesar2](http://www.ccrs.nrcan.gc.ca/globesar2)
- [v-14] ERS-1/2: [earth1.esrin.esa.it/ERS/](http://earth1.esrin.esa.it/ERS/)
- [v-15] JERS-1: [www.eoc.nasda.go.jp](http://www.eoc.nasda.go.jp)
- [v-16] ENVISAT-1: [envisat.estec.esa.nl/](http://envisat.estec.esa.nl/)
- [v-17] ADEOS: [www.nasda.go.jp/index\\_e.html](http://www.nasda.go.jp/index_e.html)
- [v-18] COMMERCIAL: [www.spaceimaging.com](http://www.spaceimaging.com)

#### **HYPERSPECTRAL OPTICAL IMAGING PLATFORMS**

- [u-01] JPL AVIRIS: [makalu.jpl.nasa.gov/aviris.html](http://makalu.jpl.nasa.gov/aviris.html)
- [u-02] GSFC:  
[ltpwww.gsfc.nasa.gov/ltp/ltp\\_projects.html](http://www.gsfc.nasa.gov/ltp/ltp_projects.html)
- [u-03] VCL: [essp.gsfc.nasa.gov/vcl/](http://essp.gsfc.nasa.gov/vcl/)
- [u-04] SLICER:  
[ltpwww.gsfc.nasa.gov/eib/slicer.html](http://www.gsfc.nasa.gov/eib/slicer.html)
- [u-05] EO-1: [eol.gsfc.nasa.gov/](http://eol.gsfc.nasa.gov/)
- [u-06] ASAS: [asas.gsfc.nasa.gov/asashome.html](http://asas.gsfc.nasa.gov/asashome.html)
- [u-07] NASA-MASTER:  
<http://masterweb.jpl.nasa.gov>
- [u-08] NASA-MODIS&ASTER:  
<http://ltpwww.gsfc.nasa.gov/MODIS/MAS>
- [u-09] USA-AS-MI-LAB, REDSTONE ARSENAL:  
<http://www.tec.army.mil>

#### **COLLABORATORIUM TERRA DIGITALIS**

- [t-01] TERRA-DIGITALIS:  
<http://www.digitalearth.net.cn/de99.htm>
- [t-02] T-D-B, TERRA-DIGITALIS BAIKALUM:  
<http://pipeline.swan.ac.uk/siberia>

## **Seed Questions**



## Seed Questions

### A Land Applications:

- 1) At the information product level (e.g. biomass, soil moisture, etc..), do we have a good understanding of the requirements on accuracy, temporal sampling, and spatial resolution?
- 2) At the instrument level, is current research and applications demonstration giving us clearer views on the radar system parameters (e.g. wavelengths, polarisations, resolutions, ...) that are required? Can we say what radar parameters are acceptable (even though not necessarily optimum)?
- 3) What are the key deficiencies in current SAR sensors that limit the scientific or commercial value of the information which can be extracted?
- 4) Can we quantify the tradeoffs between multi-parameter radar imaging and multi-temporal imaging with simple radar systems?
- 5) How well are SAR data being integrated with other data (e.g. DEM, meteo, optical, ...) for the derivation of truly high-level products (e.g. crop yield, water runoff, ...)?

*Please try to answer these questions by keeping in mind the differences between the application(s) you are expert in, and the more general case of the use of SAR data for land applications.*

### B Ocean Applications:

- 1) What are the key requirements to help integrate SAR data with other available sources of information (*in situ*, scatterometers, altimeters, radiometers, ...) and model outputs to derive high level products for scientific and/or commercial applications?
- 2) Are the current research efforts sufficient to give us a clear understanding of the use of specific ASAR modes (incidence angle, spatial resolution, polarisation, ...) for scientific and/or commercial applications ? If not, what should be done?
- 3) Are the current retrieval algorithms (wave, wind, ...) sufficiently robust for global applications, or are regional derivatives necessary? What is the ASAR engineering performance requirement for wave and wind retrieval in terms of radiometric accuracy and spatial resolution?

### C Geometry/radiometry/calibration:

- 1) Is the methodology for phase and amplitude calibration of space and airborne systems mature?
  - a) What issues remain open?
  - b) What role do distributed targets play in the calibration of S/B radars?
  - c) How should these be attacked?
  - d) Is there a need for white papers on this subject?
  - e) There are a number of techniques available for the absolute calibration of SARs (e.g. using transponders, corner reflectors etc) - is there an optimum technique or are they complementary?
- 2) What are the driving requirements for users of SAR data in terms of calibration?
  - a) Is accessibility of data properties an issue?
  - b) How can users be assured about the quality standard of the products disseminated to them?

- c) Do users need to deploy their own calibration devices?
- 3) Has the gap between point target calibration measurements and instrument performance been adequately addressed?
- 4) What system information would aid in improving the characterisation or accuracy of future systems?
- 5) How do we make products that reflect the potential localisation accuracy available from ephemeris data?
- 6) What are the data product dissemination media and formats of the future?
- 7) For RADARSAT-1, what is the influence of attitude and beam displacement on the calibration and image quality of RADARSAT Products?
  - a) How accurately can RADARSAT attitude be measured and under what conditions?
  - b) What is the observed stability and variability of the RADARSAT attitude?
- 8) How can the beam azimuth offset be taken into account within a SAR processor and how can the model for this effect be improved?

#### **D SAR processing:**

- 1) SAR processing:
  - a) What is the most robust algorithm for estimating the Doppler centre frequency?
  - b) Is the chirp replica necessary in SAR processing? If so, what is the required accuracy of the chirp replica?
  - c) Is using the same number of bits as in the raw data accurate enough for correlating the SAR data? What about the frequency?
- 2) Auxiliary data:
  - a) Should we use the digital elevation model to generate the high quality image (antenna pattern correction using the DEM)? If so, what DEM accuracy is needed in terms of height accuracy and spacing?
  - b) Are the "Ortho-photo" SAR data products requested as often from the SAR data users when compared with the Ortho-photo in the case of Optical data users ?
  - c) What is the accuracy requirement of the orbit data (position and velocity) as well as the attitude data?
- 3) Mosaicing:
  - a) Co-registration of the image scenes is a concern on the generation of the mosaics. De-stripping is one of the important steps in generating a good mosaic image. What is the best method to do this?

#### **D Antenna synthesis:**

- 1) Has the ultimate antenna elevation gain pattern synthesis tool been developed? i.e. is there a preferred synthesis technique?
- 2) How can we be sure that the maximum possible performance is being obtained from an antenna?
  - a) Are there other suggestions or recommendations for driving parameters?
- 3) What is the best way to deal with modelling phase/amplitude setting errors and/or TRM failures?
  - a) In including errors in the analysis, the ASAR approach is to increase the sidelobe levels. This removes any trade-off capability between Tx and Rx to offset a sidelobe in one pattern by a null in the other. Is this reasonable?
- 4) How should we assess the overall performance of the instrument with regard to errors?
  - a) What (if any) aspects of antenna pattern synthesis are not included in present-day synthesis techniques?

- 5) Can we recommend a *sigma nought* model which should always be used, in order to be able to compare the performance of different SARs? The performance of the synthesis process is ultimately based on the performance algorithms. This is influenced heavily, however, by the radar cross-section model adopted. How may we combine different models to produce a definitive case (e.g. the ASAR land/sea combined model)? Should we instead adopt an approach using mean levels from models (e.g. RADARSAT)?

#### **E Data compression:**

- 1) Raw Data Compression
  - a) necessity of on-board vs. ground-based compression?
  - b) need for application-based quality criteria for compression evaluation, e.g. interferometry, wave mode spectra?
  - c) with block-based methods, how do you choose the best block size?
  - d) are wavelet-based methods applicable when there is little data redundancy (i.e. data is not oversampled)?
- 2) Image Data Compression
  - a) compare wavelet based methods with conventional methods (e.g. Chen & Smith JPEG)
  - b) can one effectively combine speckle reduction with data compression?
  - c) what criteria do you use to evaluate the quality of reconstructed images?

#### **F Post processing techniques:**

- 1) Is the field of speckle filtering for a single polarisation SAR image mature enough? Should more research be encouraged?
- 2) How can speckle filtering techniques be generalised and applied to multi-temporal SAR images, polarimetric SAR images and interferometric phase images?
- 3) SAR and polarimetric SAR image texture remains a difficult parameter to define. What is the best method for texture extraction? Could it be Markov random field, Wavelet transform, K-statistics, standard deviation to mean ratio, etc.?
- 4) Is the field of SAR and polarimetric SAR image classification (or segmentation) mature enough?
  - a) What is the effect of speckle filtering and texture analysis on the classification accuracy?
  - b) How can terrain types can be identified, when unsupervised techniques are applied?

#### **G Instrument design and new concepts:**

- 1) Do we correctly exploit lessons from previous programmes( ERS, Radarsat..) for designing and reducing the cost of new ones, particularly for ambiguity and noise level which drive antenna size and power? This is even more important at low frequency (L and P bands) where ambiguity requirement could block access to low cost solution (the power demand is less of a constraint). Why do all previous and current designs use roughly the same figure (-20 dB az+range scattered target protection)? The user does not directly need ambiguity protection, he does however need a radiometric quality which involves also the whole scene radiometric context as seen from space. The ambiguity requirement should be based on real measurements from space, on a theme per theme basis (geology, vegetation, etc). It seems that after ERS, J-ERS and Radarsat, which have produced a large number of images for a wide range of users, we are still specifying

ambiguity requirement as we did 20 years ago when we had no way to get a wide statistical radiometric knowledge.

- 2) What is the rationale for a -35 dB requirement for NeSigma0 (as envisaged in L-band) if the ambiguity requirement is still -20 dB (impossible to reach -35 dB anyway)?

## **H Envisat:**

- 1) Recommendations regarding the collection of strategic data sets (SDS). SDS are to be acquired by ASAR for general scientific and application demonstration purposes in addition to the data requested by individual users. The following SDS have been proposed:
- a) During the commissioning phase:
    - Full European ASAR coverage in ERS like mode
    - ASAR coverage of selected sites distributed worldwide with different combinations of polarisation and incidence angles
    - Full global ASAR coverage in Wide Swath mode
    - ASAR Wave Mode over oceans
    - ASAR Global Monitoring Mode over any land and ice surface
    - ASAR Wide Swath over European Coastal Zones
  - b) During the operational phase:
    - Data sets to support the action of participating countries
    - Data sets to support the action of commercial distributors
    - Coverage of areas poorly covered by ERS (ERS like mode and as interferometric pairs in ERS like mode)
    - Collection of coherent representative data sets(e.g. full global coverage in ERS like mode, different combinations of polarisation and incidence angles over selected sites, full global interferometric coverage)
    - ASAR Wave Mode over oceans and large seas
    - Global Monitoring Mode over land, ice and sea-ice surfaces
- 2) What is the usefulness for science and operational applications of the new ASAR mode and products as compared to ERS?
- a) Near Real Time stripline products (Image Mode, Alternating Polarisation,
  - b) Medium Resolution, Wide Swath, Global Monitoring Mode)
  - c) Alternating Polarisation products HH/VV or HH/HV or VV/VH (PRI,GEC, SLC, Medium Resolution)
  - d) ASAR Global Monitoring Mode(1 km resolution, HH or VV, products per orbit, Global coverage in 6 days)
  - e) Selectable Polarisation and Incidence angle High Resolution Products in Image mode
- 3) What is the potential of the Newly developed ASAR Wind Wave algorithm and product? Should it be extended to Alternating Polarisation?



## **I Polarimetry:**

Radar Polarimetry, Radar Interferometry and Polarimetric SAR Interferometry represent the current peak of 'Microwave Remote Sensing' technology, but we still need to progress very considerably in order to reach the limits of physical realisability. It is the ultimate goal of this endeavour to eventually realise air-borne and space-borne 'Geo-Environmental Background Validation, Stress Assessment, and Stress-Change Monitoring'. Keeping this goal in mind, a set of topics for discussion and meditation was selected for the Round Table. The selected topics are collected in three groups, dealing with:

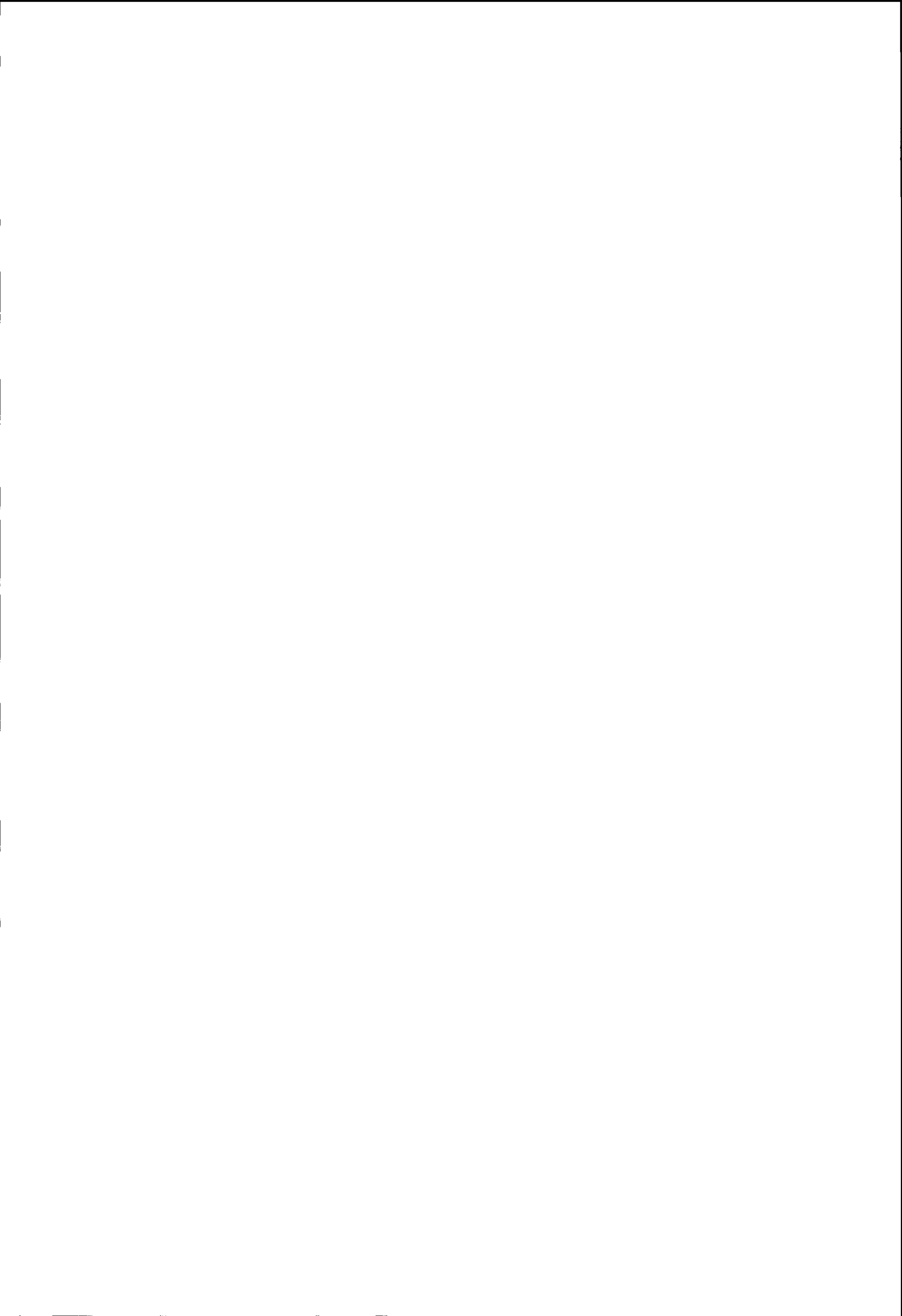
- 1) Development of the underlying basic theory of Polarimetry, Interferometry, Polarimetric SAR Interferometry, and of the associated EWB-D-POL-IN-SAR' ALGORITHMS.
- 2) Polarimetric SAR Interferometry data formatting and standardisation (SLC, MLC ...), systems calibration procedures, and ground truth validation (permanent test site ...).
- 3) Polarimetric SAR Interferometry imaging systems and platform improvements (Polarisation Purity and Channel, Narrow-Band Antenna-Array Systems Performance versus Side-lobe Reduction ...) plus standardisation.

## **J Interferometry:**

- 1) What is the reliability of unwrapped phases without independent data (i.e. multibaseline, multifrequency)?
- 2) What is the optimum baseline to get minimum elevation deviation (apart from phase unwrapping)?
- 3) What is the status of the design of stable and unobtrusive reflectors (dihedral and trihedral reflectors, lenses, multi polarisation resonating surfaces?) for DINSAR applications.
- 4) What is the status of *meteo* effect compensation?
- 5) Future missions dedicated to InSAR/DinSAR? Military or civilian?



## **Session Syntheses and Recommendations**



# 1. Land applications

Chairman: T. Le Toan (CESBIO)

Co-chairman / Report: M. Borgeaud (ESA)

## 1.1. Session highlights:

- 6 oral papers presented.
  - For applications requirements, NASA 'Experimental SAR' mission to meet three science goals: cold regions, vegetation recovery, and global topography for which mission requirements are well-defined (L+X-band)
  - In the field of terrain deformations, permanent scatterers were identified in urban areas from long temporal series of interferograms to remove atmospheric effects. Used to detect vertical motion with < 1m accuracy
  - In snow monitoring, use of SAR polarimetric data for classification. Mapping of wet snow versus bare ground best done at high incidence angle
  - In Forestry, vegetation cycle of deciduous forest can not be measured by one-day repeat SAR interferometry coherence
  - Extensive project to map (forest/non-forest) part of Siberia using JERS SAR data
- 19 posters presented.
  - Use of SAR data for land-cover mapping in Guyana, Germany, France with ERS, Radarsat and airborne polarimetric SAR data
  - SAR interferometry used to retrieve crop parameters and to assess flood damage
  - Requirements on Sigma0 for soil moisture and snow-covered areas
  - Sigma0 database derived from ERS scatterometer data over land
  - Coupling of crop growth models with SAR data
  - Combined use of SAR and optical data for land-use in India and Nepal, and Ghana
  - Extensive use of SAR data for monitoring purposes (Amazon and urban areas)
  - Joint use of ERS and JERS SAR data for forest mapping of Siberia
  - Integration of SAR data in GIS

## 1.2. Seed questions:

- 1) At the information product level (e.g. biomass, soil moisture, etc..), do we have a good understanding of the requirements on accuracy, temporal sampling, and spatial resolutions?
  - Cannot answer this question in a general manner; depends heavily on the application and the product considered
  - However, requirements are well-known for LightSAR mission, and for some limited applications (e.g. rice maps, topography, snow-melt runoff)
  - Real problem is not on SAR data but more on the availability of in-situ data
- 2) At the instrument level, is current research and applications demonstration giving us clearer views on the radar system parameters (e.g. wavelengths, polarisations, resolutions, etc... ) that are required? Can we say what radar parameters are acceptable (and not necessary optimum)?
  - Depends again on the application considered
  - Very difficult to draw conclusions since good-quality experimental data (e.g. in-situ data) is still missing
  - Clear case on topography → add X-band on NASA "Experimental SAR"

- 3) What are the key deficiencies in current SAR sensors that limit the scientific or commercial value of the information which can be extracted?
  - Same answers as in 2); depends again on the application considered
  - Some applications for which volume scattering is important would be best satisfied with a depolarisation channel (HV)
- 4) Can we quantify the tradeoffs between multi-parameter radar imaging and multi-temporal imaging with simple radar systems?
  - Depends on application considered
  - A good understanding on the physics (scattering mechanisms) is first needed to define the application requirements, then the property of the SAR data (polarisation, frequency, temporal sampling) can be addressed
  - Trade-off for multi-mode SAR (which mode to use) should not be neglected
- 5) How well is SAR data being integrated with other data (e.g. DEM, meteo, optical, etc...) for the derivation of truly high-level products (e.g. crop yield, water runoff, etc...)?
  - Depends on the application
  - Necessary to identify a clear application/goal and to see then how radar data can contribute and which other types of data are required
  - For topography, more auxiliary data (weather, temperature) is needed to correct for atmospheric effects

### **1.3. Conclusions:**

- Distinction to be made between science requirements (How SAR data can be useful to help solving a complex environmental problem, e.g. forest monitoring), and commercial requirements (SAR data can be directly used to create a product, e.g. rice maps using SAR data)
- Start with a well-defined science/applications requirements and then to investigate how SAR data can contribute
- Difficult to generalise the SAR requirements for land applications since they strongly depends on each individual applications
- More in-situ data required to test/validate algorithms proposed by the user community
- Lots of partial results which needs to be validated on a more general case

### **1.4. Recommendations:**

- Previous years of spaceborne SAR data archived should be opened to the user/scientific community
- Identify feasible important problems for which a SAR may contribute. Then only use the SAR data and not the reverse
- Still missing good quality *in-situ* data to test latest keys development in SAR technique
- More then 20% of the papers presented at CEOS'99 deal with land applications. Future meetings should maybe keep only the ones addressing real SAR requirements and cal/val issues
- Include seed questions when the call-for-papers is published, to make sure that abstracts submitted address these issues

## 2. Ocean applications

*Chairman: B. Chapron (IFREMER)*

*Co-chairman / Report: E. Attema (ESA)*

### **2.1. Session Highlights:**

- New SAR wind/wave products with or without a priori knowledge, applied/tested with ERS and RADARSAT, prepared for ASAR
- Sea ice thickness product
- Coastal monitoring applications

### **2.2. Seed questions:**

- 1) Data Integration:
  - ERS Wave mode could be scatterometer quality flag
  - Synergy with altimeters for ocean currents
  - Synergy with ocean salinity missions
  - Assimilation in numerical weather prediction models (NWP)
- 2) Research Requirements:
  - Regarding ENVISAT no specific recommendations were made for pre-launch research other than the preparation of the calibration and validation
  - Validation should be prepared at selected instrumented sites and high resolution SAR modes should be used initially
  - After launch new research will start in many areas. It was noted that ASAR would be ideal for the derivation of an HH version of CMOD4
- 3) Algorithms:
  - After the successful completion of the development of the new SAR wind/wave products new initiatives are solicited
  - It was noted that ASAR HH modes would be a good choice for vessel detection applications

### **2.3. Recommendations:**

- The general recommendation was made for (continued) co-ordination between Agencies to optimise spatial and temporal SAR coverage for ocean/ice applications
- Key requirements for Arctic basin-scale science application are:
  - Routine and reliable repeat (3-day) wide swath high-resolution (150 m) coverage of the Arctic Ocean at VV
  - Geometric fidelity (absolute geo-location: 100 m; relative location: 50 m). This is critical for the calculation of ice cover deformation
  - Radiometric calibration (absolute ~ 1-2 dB) for monitoring backscatter history over the season
  - Dual polarisation is an added bonus for identification of areas of open water and thin ice

### 3. Geometry/radiometry/calibration

Chairman: R.K. Hawkins (CCRS)

Co-chairman / Report: G. Keyte (DERA)

#### 3.1. Session highlights:

- 6 oral papers presented dealing with the following aspects:
  - Updates on two marvellous SAR systems: ERS-2 and RADARSAT
  - Overview and plans for RADARSAT-2 and its calibration
  - Reports on two advanced A/B SAR systems and their calibration
  - Stability of Amazon rainforest at C-band: ERS SAR, Scatt, RADARSAT
  - Use of calibrated ocean spectral widths as a globally available cal reference
  - InSAR phase for co-registration of ERS SAR and SPOT
  - Localisation using ERS for Mapping
  - Study on the accuracy of S/C attitude estimation from Doppler Tracking

Key results are:

- Both ERS and RADARSAT rely on precision ARCs for absolute calibration and Amazon for Antenna pattern
- Use of ARCs for calibration of RADARSAT-2 is being questioned partly on the grounds of cost
- For RADARSAT-2, antenna model parameters will be tuned from Amazon measurements of a subset of the beams will be used to quickly generate the others
- Requirement for ARCs was questioned in another paper which proposed ocean spectra be used as an economical way of proceeding. The method has the advantage of being applied around the orbit; however it was pointed out that true costing involves operational issues as well as initial capital investment
- The stability of the rainforest at C-band has been compared using measurement from ERS and RADARSAT and its characteristic as a distributed target standard studied. This appears to be approximately  $0.6 \text{ dB RMS}$  and this is the range of typical existing SAR accuracies
- S/C attitude information and beam pointing accuracy was shown to be a very sensitive driver for Doppler centroid estimates and a formalism for determining pitch and yaw from Doppler results has been presented. A deficiency in the RADARSAT system appears to be a good knowledge of the static offset in azimuth as a function of beam elevation

Other papers discussed specific problems with airborne SAR calibration and showed that in some respects radiometric accuracy is more difficult to achieve than for satellite systems. Little was said about geometrical calibration, but two papers described how space SAR was used to register other data. In one case, in-SAR was used to provide Ground Control Points for SPOT data. A systematic timing bias was identified in ERS and later corroborated from the audience

#### 3.2. Seed questions:

Round table discussion explored the question of whether calibration "had been solved" and whether users were confident with calibration data provided. It was clear that data providers needed to provide the means for accurate radiometric calibration



### **3.3. Conclusions / Recommendations:**

There will continue to be a need for some system of manmade targets to provide an absolute references

There may be a need for an international QA authority which would validate calibration processes set up by data providers, and provide a system of man made targets as an international reference. This function is one which could perhaps be undertaken by CEOS

Within existing measurement accuracies, rainforest appears to be sufficiently stable to be used for both relative and absolute reference. It is suggested that this topic be explored more formally as a specific task on CEOS

Data formats appear to be emerging and will probably depart significantly from CEOS format. Data providers appear to be making this seamless by providing freeware

It was clear that there are many possibilities of combining existing and emerging methods for calibration. The tradeoffs in developing a comprehensive strategy for a particular instrument involve costs (capital and operational) and need to be considered carefully. Given the benchmarks set by existing satellite SARs, the standards are high

## 4. SAR Processing

Chairman: *F. Adragna (CNES)*

Co-chairman / Report: *M. Shimada (NASDA)*

### 4.1. Session highlights:

- 9 oral papers presented, dealing with various techniques, the application fields being very large and papers not controversial:
  - 4 papers were dedicated to 'New Processing': ScanSAR (DLR), SpotLight (Alcatel), phase corrections for interferometric processing (JPL GEOSAR and DLR X-SAR/SRTM). The case of GEOSAR was dedicated to multi-path correction. It seems that each problem can find a solution (multi-path, Doppler, ScanSar, SpotLight, etc...). No 'blocking point' was encountered
  - 2 papers were dedicated to Radargrammetry: in the case of Radarsat (medium resolution) the technique has been already used operationally. Works are going on to improve the 'correlation' step (direct use of the SAR signal?) and the architecture of the whole processing chain. In the case of airborne SAR (high resolution), the goal is to first extract the linear structures from the two images and then to compare them. Process are not operational for the moment
  - A very good and 'synthetic' paper on 'Doppler estimation algorithms' was presented by Ian Cumming. Different techniques or algorithms (MLCC, MLBF, ...) are compared. The behavior on discontinuities is discussed. The best estimation seems to be reached with a phase based estimator, computed on blocks. The accuracy can be as good as 5 to 10 Hz (1% bandwidth)
- 2 papers dealt with Localisation, Geometry and Mosaïcking. This topics led to a lot of discussions and most of them were transcribed into recommendations

### 4.2. Recommendations:

- To develop Phase Preserving Processed Products (SLC) for the SCANSAR modes of operations of existing or future SAR systems (to support Interferometric applications)
- Referring to 'Orbital Data' useful for geometry accuracy and applications (which are usually provided by Space Agencies), reconstituted orbits (as well as predicted ones) should be available on the web.
- For interferometric pairs selection (and/or acquisition programming), precise orbits should be made available more quickly than at present time (e.g. 3 days after the satellite pass)
- The format of orbital data should be the same (or close) for all satellites:
  - Fixed Earth coordinate system
  - 60 s. sampling
  - Continuity at the equator
- The along track accuracy should be much more precise than at present time. It is possible (an useful) to reach 10 or 1m accuracy, which corresponds to 1 or 0.1 ms in time. GPS system could be used as time reference for both platform and payload ...

## 5. Antenna Synthesis / Data Compression / Post-Processing Techniques

---

### 5.1. Antenna synthesis sub-session

*Chairman and report: M. Brown (Marconi)*

#### 5.1.1. Session highlights:

The session Papers presented performance-based synthesis and a potential ASAR beam re-optimisation following Transmit Receive module failure. The questions raised were:

- 1) Does the synthesis software handle polarimetric modes?
  - Yes, current synthesis tool can handle stripmap and ScanSAR modes and polarisation selections from single channel through dual to quad
- 2) Does your software optimise the beam using the full 2d pattern?
  - No, as this would be exceptionally computationally expensive. The assumption that the 2d pattern can be decomposed into an azimuth and a range cut is valid so long as the level of failures is small
- 3) Can we recommend a sigma nought model which should always be used in order to be able to compare the performance of different SARs?
  - Although some doubt whether it is desirable to compare different SARs, for two SARs operating in a very similar manner such as ASAR HH polarisation and RADARSAT-1 it is very useful to be able to compare performances directly. Nevertheless, we should still design any SAR using sigma nought models which reflect the demands of the intended applications
- 4) A suggestion was made that the ambiguity suppression required for polarimetric modes was in excess of  $35dB$ 
  - Although ambiguity suppression of this level may be desirable for certain applications, in general we would suggest that such performance may only be achievable for a fully functioning antenna (i.e. without TRM failures). In practice we suggest that ambiguity suppression of the order of  $20dB$  should be sufficient for most current applications and a realistic level for end-of-life performance
- 5) What does the phase pattern look like following successful synthesis, i.e. is it flat in the main beam?
  - Normally we do not look at the phase pattern but successful synthesis will mean that the phase will be flat in the main beam
- 6) Do you take quantisation into account during synthesis?
  - Yes, we can impose quantisation constraints on both phase and amplitude. ASAR has 6 bits each for phase and amplitude
- 7) How are different TRM failure scenarios catered for?
  - The baseline for ASAR is to assume an end-of-life failure of 6% of TRMs which is modelled at the 90% confidence level. This allows for some clustering of failures
- 8) What is the strategy for re-optimising ASAR following module failure?
  - Provided the failure level remains within the 6% end-of-life limit and the distribution is essentially random across the antenna, then no re-optimisation is foreseen. However, should an entire tile fail (5%) or other serious clustering of failures occur then re-optimisation may prove inevitable

## 9) Have you tested an antenna with failed modules?

- No since we have yet to fly an active SAR antenna we have no first-hand experience of the effect of failures on the beams. It would, of course, be possible to test the ASAR in the range with any number of TRMs switched off

**5.1.2. Recommendations :**

For different SAR systems operating in very similar modes (specifically frequency and polarisation) and being used for a particular application it is desirable to be able to compare their performances on an equal footing. To this end the use of standardised radar cross section models is recommended

**5.2. Data Compression sub-session**

*Chairman and report: I. Cumming (UBC)*

**5.2.1. Session highlights:**

- **On Raw data compression:**

- Useful when data oversampled
  - Take FFT of raw data
  - Filter noise from unused frequencies
  - Compress and transmit in frequency domain
  - Use more bits in strong part of spectrum
  - Higher compression than BAQ when data are oversampled
- ***ENVISAT/RADARSAT 2 Raw Data Compression Summary:***
- 8, 4, 3, 2 bit FBAQ
  - 8 bit uncompressed best suited for high precision, calibration but very narrow swath due to data rate constraint
  - 4 bit main ENVISAT operating mode: provides excellent image quality and a small phase error for INSAR applications ( $<10^\circ$ )
  - 3 bit preserve Sigma0: good compromise for general wide swath use (use of this compression ratio not planned)
  - 2 bit for low bit rate modes, and very wide swath applications (e.g. wave mode and global monitoring mode of ASAR)
- ***Application based requirements:***
- Space Agencies selects compression levels based on system and product quality trade-offs
  - Users must evaluate their requirements for raw data compression
  - Does raw data compression affects calibration? (e.g. 2 bit case)

- **On SAR Image Compression:**

- Scansar image compression
- Multilooking gives more data redundancy
- High energy compaction in wavelet LL band: often only one level of decomposition necessary
- Use mask to allocate bits in each band : apply more bits in high dynamic areas, apply block adaptive linear quantiser
- Compression of multitemporal images: use first image to optimise selection of blocks, apply to subsequent registered images
- Compression of multipolarisation images: statistical properties of channels allow higher compression ratios

- ***SAR image compression Summary:***

- Wavelet techniques:

- Provide higher compression ratios
- Preserve edges and point targets well
- Preserve mean/sigma and texture well
- For complex data, polar format compression preserves phase better (use vector quantisation for phase information)

- Can we combine speckle reduction with compression?

- Despeckled images have lower entropy
- Wavelets can combine despeckling and compression

### **5.2.2. Recommendations:**

- Need for CEOS Standards for SAR image compression:
- Many new methods being developed
- Time to get consensus on best methods/standards/formats
- ESA has test data sets available

## **5.3. Post-Processing Techniques**

*Chairman and report J.S. Lee (NRL)*

### **5.3.1. Session highlights:**

- 6 oral papers presented and one poster.
  - The paper 'New approaches in Speckle filtering' was discussed. The claim of not using the Hamming aperture weighting in multi-look processing to reduce speckle level has to be further assessed. In addition, the author's proposition to organise an evaluation of many speckle filtering algorithms is delicate and has to be conducted carefully. Many algorithms have parameters that require fine tuning. Programming errors and simplification may produce erroneous results.
  - The other oral papers are related to speckle filtering of a single or polarimetric SAR images. The last paper by Touzi emphasised that locally stationary and locally non-stationary scene signals have to be treated separately.
  - The poster paper is about edge detection accuracy in SAR images.

- This sub-session was running more than an hour late in the late afternoon. Many experts in post processing techniques have left for the day including some of the authors. Consequently, few questions were asked for the last two presentations and discussions on seed questions were lacking from remaining attendees.

### **5.3.2. Seed questions:**

- 1) Is the field of speckle filtering for a single polarisation SAR image mature enough? Should more research be encouraged?
  - During the last twenty years, many good speckle filtering algorithms for a single SAR image have been developed. We believe that it has matured, and is ready for applications.
  - However, we should not shut the door completely, because new signal processing techniques may appear on the horizon, and could produce better filters.
  
- 2) How can speckle filtering techniques be generalised and applied to multi-temporal SAR images, polarimetric SAR images and interferometric phase images?
  - Speckle filtering techniques have been extended to multi-temporal SAR images with reasonable good results. Adding incoherently many ERS-1 images, for example, could produce erroneous results, because the physical information might change from one date to others dates.
  - The polarimetric SAR speckle filter has been around for almost ten years, but the preservation of polarimetric property and the problem of introducing cross-talk are the main issues. The adoption of speckle filtering techniques to filter interferometric phase noise is still at its early stage.
  
- 3) SAR and polarimetric SAR image texture remains a difficult parameter to be defined. What is the best method for texture extraction? Could it be Markov random field, Wavelet transform, K-statistics, stand deviation to mean ratio, etc.?
  - Texture information has been underutilized in SAR applications, because texture is a parameter difficult to be defined. There is a lot to be done in this field concerning the most suitable parameters for textural characterisation. The most frequently used techniques are the standard deviation to mean ratio and the K-statistics (the product model) for wide stationary texture. The correlations between neighbouring pixels that forms texture patterns were not being used in these two techniques. Markov random field presented with the Gibbs distribution and wavelet transform show some promise, and need to be explored further.
  
- 4) Is the field of SAR and polarimetric SAR image classification (or segmentation) mature enough? What is the effect of speckle filtering and texture analysis on the classification accuracy? How terrain types can be identified, when unsupervised techniques are applied?
  - Supervised classification for polarimetric SAR imagery is mature enough, but unsupervised techniques need further development. Unsupervised classification techniques can be divided into two categories: (1) based on scattering mechanism, and (2) based on statistical characteristics. How to combine these two categories of techniques needs further research.
  - It is well-known that speckle filtering improves classification accuracy for polarimetric SAR images. Texture is often ignored in the classification due to polarimetric data often contains enough information for classification. The inclusion of texture may not improve accuracy significantly. For single SAR image, however, the texture should play an important role.
  - The advantage of fully polarimetric data over a single or multi-polarisation data is in its capability in identifying the inherent scattering mechanism that provide information for terrain type identification, and geophysical parameter estimation.

## 6. Instrument Design and New Concepts

Chairman: J.P. Aguttes (CNES)

Co-chairman / Report: L. Ulander (SDRE)

### 6.1. Session Highlights:

- During the session were presented:
  - New ideas on low frequency (20 MHz to 450 MHz) and topography missions. Both require innovative approaches deviating from conventional design
  - Concerning future 'operational / commercial' missions a rationale is emerging towards X band high resolution, mainly because of expected dual use, and L band, even if it appears more challenging because of large antenna size and remaining technology development.

### 6.2. Seed questions:

- 1) Do we correctly exploit lessons from previous programmes (ERS, JERS, Radarsat) for design of new ones, in particular concerning ambiguity protection requirement?
  - It is recognised that there is a lack of formal feedback from past space missions on ambiguity requirement although it actually drives the antenna size and thus the cost of future missions. It is difficult to say where in the overall system design process, from the end user to the requirement, there is a lack of feedback. This question will however become more critical for future missions with focussed applications and commercial prospects. For these missions the ambiguity requirement needs to be properly revised.
- 2) Do we have adequate methodology to calibrate in a timely fashion the very large number of beam modes in future systems like ASAR and Radarsat-2?
  - Consensus in the audience was that it is a challenging task but that methods exist and provide satisfactory results.
- 3) Should we make a concerted action to obtain frequency allocation in the 10-1000 MHz?
  - Recommendation has in fact already been made by CEOS, but it only considered a particular frequency (7 MHz around 450 MHz) and was not successful. The matter has been postponed to the WARC conference 2006. Both the usefulness and system feasibility has to be demonstrated, or if this is already done it should be properly communicated into a dossier. It is recognised that the national representatives play a key role and have to be addressed by CEOS, national space and environment agencies, as well as international bodies. Presently, it is crucial to investigate and identify what is the best compromise (usefulness / feasibility) in the frequency range 10 to 1000 MHz. Maybe 450 MHz is not sufficient to fulfil the need for global environmental observation. The analysis should therefore also consider the complementarity of airborne and spaceborne platforms. It is also recognised that there is a real commercial potential provided that much greater bandwidth is used.

### **5.3.3. Recommendations:**

- Techniques of speckle filtering for single polarisation SAR images has matured sufficiently and are ready for applications.
- Further research on multi-temporal speckle filtering, and multi-polarisation and polarimetric SAR speckle filtering should be encouraged.
- SAR image texture is difficult to be properly extracted. The inclusion of texture in classification, identification and geophysical parameter extractions needs further research.
- For ENVISAT ASAR, it is desirable to select the optimal combination of polarisation channels based on quantitative evaluation of classification accuracy for various applications.



### **6.3. Recommendations:**

- For future missions, with focussed applications and commercial prospects, SAR image ambiguity requirement needs to be properly assessed.
- For low-frequency SAR (*10-1000 MHz*), the usefulness and system feasibility has to be demonstrated and properly communicated into a dossier. The best compromise (usefulness/feasibility) in this frequency range needs to be identified, considering also the complementarity of airborne and spaceborne platforms.
- For wide-band low-frequency SAR:
  - To demonstrate coexisting capabilities with users of the same frequency band
  - To improve the methods for analysing compatibility between systems

## 7. ENVISAT

*Chairman: Y.L. Desnos (ESA)*

*Co-chairman: S. Srivavasta (CSA)*

*Report: H. Laur (ESA)*

### **7.1. Session Highlights:**

- The presentations were covering a large span of ESA/ASAR activities, from instrument characterisation to on-ground processing, including the calibration aspects.
- Because ASAR uses an active antenna, the presentations insisted on the complexity of the above activities, in particular with the instrument qualification and calibration. ESA confirmed that transponders will be the prime tool to check the radiometric stability of ASAR.
- The presentations highlighted the instrument flexibility of various modes and sub-modes of operations. At the same time the effort of standardisation of the ESA products in the different processing centers was stressed: the generic processor approach (same processor, same algorithm, same output format).
- Note was taken that spaceborne SAR missions would face a maximum solar activity in the year 2001 so more frequent orbit manoeuvres will be required to keep the same orbital accuracy.,

### **7.2. Recommendations:**

- To provide users with the necessary tools in case of calibration problems with archived products
- To develop / provide tools allowing predicted orbit baseline knowledge few days before acquisition relative to already acquired and archived data. Such a tool shall allow for best selection of mode and swath for the new acquisition relative to the application objective.
- To use the Alternating Polarisation of ASAR in HV polarisation
- ASAR strategic data sets:
  - Wide Swath: global land coverage on a bi-yearly basis to allow interferometry with narrow swath (image mode) and coverage of coastal areas
  - Wave mode: close to the coasts
  - Wide swath over Antarctica
  - INSAR coverage outside the SRTM coverage for DEM generation, but valuable data sets already exist with ERS tandem data in those regions

## 8. Polarimetry / Interferometry

*Polarimetry: Chairman: E. Pottier, U. Rennes, Co-chairman; W. Boerner, U. Illinois.*

*Interferometry Chairman: D. Massonnet, CNES, Co-chairman: C. Prati, PoliMi*

### 8.1. Session summary:

The 'Combination of Radar Polarimetry with Interferometry' has proved to show considerable new potential applications in quantitative 'Remote Sensing'. This Double Session on 'Polarimetry versus Interferometry', and with the subsequent insertion of 'Polarimetric SAR Interferometry' was opened with an introductory overview on 'Unsupervised SAR Image Feature Sorting and Characterisation' in coherent (fully polarimetric: complex 2x2 scattering matrix) POL-SAR Imaging; followed by a 'Synoptic Assessment' of the 'Polarimetric Information Content of Partially versus Fully Polarimetric SAR Imagery'. This main 'Polarimetry Session' was crowned by two visionary pivotal reports on most recent advances in 'Multi-Baseline Polarimetric SAR Interferometry', and how 'Topographic Estimations' can be extracted more accurately from POL-IN-SAR Image data sets. In addition, four Poster displays on the subject matter deserve careful attention; and, the poster on the 'Extraction of Surface Parameters in Polarimetric SAR' was a highly praised, truly interactive display event.

The 'Second Sub-Session' dealt with 'Scalar (non-polarimetric) SAR Interferometry', tailored around the SIR-C/X-SAR MISSION-3: SRTM - with several papers sandwiched in between on rather pertinent issues of 'Interferometric Repeat-Pass Scan-SAR, Radargrammetry', plus an assessment of the related accuracy of 'IN-SAR Topographic Mapping'. These in parts well presented papers were supplemented by nine Poster displays - being in parts also highly interactive. It was felt that the highly 'Interactive Poster Displays' contributed profoundly to the success of this Workshop, and that those ought to be amplified in similar future events; and become a permanent integral component of future CEOS-SAR-CAL/VAL Workshops.

The combination of these two sub-sessions provided a good starting point for a sobering 'Round-Table Discussion' it was concluded that the SAR Polarimetry and the SAR Interferometry experts should be combining their research efforts in digital image processing. This is justified because of the decisive advances made in Polarimetric SAR Interferometry proving that both techniques need to be fully integrated, so culminating in the optimal utilisation of SAR Imagery.

### 8.2. Seed questions on interferometry:

#### 1) What is the optimum baseline for minimum elevation error?

In case of ERS-1 and ERS-2 Tandem acquisitions it can be shown that a baseline larger than the present average value (100-200) meters should be adopted to optimise the elevation accuracy. The optimum baseline ( $B$ ) setting should reconcile opposite requirements:

The baseline should be kept as large as possible to maximise the elevation to phase noise ratio as suggested by the phase ( $\varphi$ ) to elevation ( $h$ ) conversion equation,

$$\sigma_h = \sigma_\varphi \frac{R\lambda \sin\theta}{4\pi B}$$

where  $R$  is the sensor target distance, and  $\theta$  the incidence angle

On the other hand, the geometric decorrelation increases with the baseline, leading to a coherence loss  $\gamma = \left(1 - \frac{B}{B_c}\right)$ , where  $B_c$  is the critical baseline (1200 m in the ERS case for horizontal terrain).

However, if the baseline is kept shorter than the critical one, this decorrelation term can be almost completely removed by means of the so-called 'common band filtering' technique.

Nonetheless, the number of independent samples ( $NB$ ) used in the average (band-pass filtering of the interferogram) is still dependent on the number of resolution cells involved in the average and on the ratio between the actual baseline and the critical one:  $N_B = N \left(1 - \frac{B}{B_c}\right)$

It should be pointed out that the critical baseline shrinks with smaller incidence angles (i.e. positive terrain slopes). Nonetheless positive terrain slopes are foreshortened in SAR images and they cover a small percentage of the imaged area (that is why both ascending and descending satellite passes should be exploited).

In conclusion, if we combine the previous equations with the relation between coherence and phase dispersion:

$$\sigma_\varphi = \frac{1}{\sqrt{2N_B}} \frac{\sqrt{1-\gamma^2}}{\gamma}$$

we get that  $B = 2/3B_c = 800$  m is the optimum theoretical baseline for ERS that, without volume scattering and having removed the geometrical decorrelation term ( $\gamma$  accounts for the temporal decorrelation only), minimises the elevation dispersion:

$$\sigma_h = \frac{1}{\sqrt{2N \left(1 - \frac{B}{B_c}\right)}} \frac{\sqrt{1-\gamma^2}}{\gamma} \frac{R\lambda \sin\theta}{4\pi B}$$

This is just an **upper theoretical limit for ERS** over which there is no gain in the achievable elevation accuracy:

$$[\sigma_h]_{MIN} \approx 3.2 \sqrt{\frac{1-\gamma^2}{N \gamma^2}}$$

It should be pointed out that this value changes if no common band filtering is carried out. The expression of the elevation dispersion becomes (accordingly to Rodriguez and Martin 'Theory and design of interferometric synthetic aperture radars' IEE Proceedings-F, Vol 139, No. 2, April 1992, pp. 147-159):

$$\sigma_h = \frac{1}{\sqrt{2N \left(1 - \frac{B}{B_c}\right)}} \frac{\sqrt{1 - \left(1 - \frac{B}{B_c}\right)^2} \gamma^2}{\gamma \left(1 - \frac{B}{B_c}\right)} \frac{R\lambda \sin\theta}{4\pi B}$$

The minimum is now found at  $B = 460$  m for  $\gamma = 0.5$  (now the optimum baseline changes  $\pm 30$  m depending on the temporal coherence) and it is about 3 times larger than that found with the common band filtering.

However, there are at least three good reasons that push toward shorter baselines:

1. Phase unwrapping would be very very difficult
2. Space variant common band filtering would be problematic
3. Phase dispersion due to large volume scattering would be dominant.

The first two points lead to a reduction of the baseline to say *350-450 m*: phase unwrapping and common band filtering problems would be further simplified thanks to the large collection of *100-200 m* baseline pairs already available. A moderate increase of the elevation dispersion (say *50%*) ensues.

As far as volume scattering is concerned, its contribution to coherence losses can be approximated assuming that the scatterers are randomly distributed within a box of height  $\Delta$  :

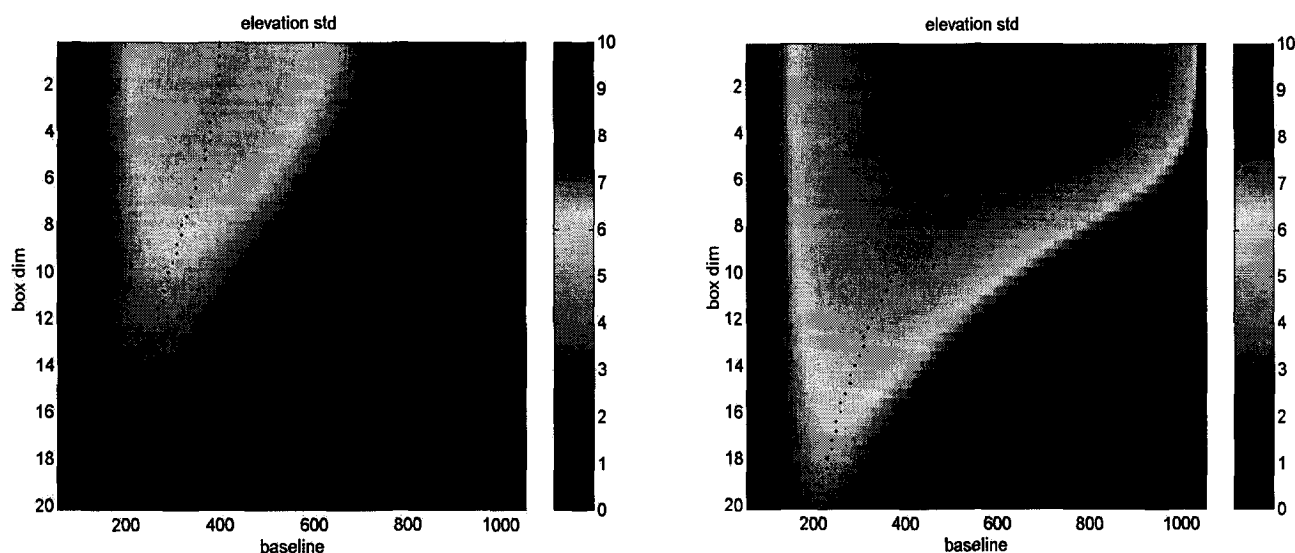
$$\gamma_v = \text{sinc} \left( \frac{\Delta}{h_{2\pi}} \right) = \text{sinc} \left( \frac{2B\Delta}{\lambda R \sin \vartheta} \right)$$

$h_{2\pi}$ : elevation of ambiguity.

Figure 1 shows the theoretical STD of the elevation error as a function of the baseline (perpendicular projection) and volume height for two distinct processing strategies: with and without common band filtering. The ultimate limit of  $2/3Bc$  is reached for  $\Delta=0$ ; increasing  $\Delta$ , the optimal baseline decreases. From the image on the right (common band filtering) *350-450 m* baseline is seen to minimise the elevation dispersion in correspondence to a volume height of *7-11 m*: a large enough value to cover most of the actual scenarios.

Our conclusion is thus the following:

**The baseline of the ERS tandem mission most suitable for DEM generation is about 400 metres**



**Figure 1 – Left:** Standard deviation (in metres) of the theoretical elevation error as a function of the perpendicular baseline and volume height. No common band filtering has been included.  $N=5$  resolution cell averaging (getting a  $\sim 25 \times 25$  m sampling) and a temporal coherence of  $0.5$  have been used. The dotted line shows the minimum STD. **Right:** Same as left image with common band filtering included. It should be noted that for volume height in the range *7-11 m*, the minimum of STD (*3-5 m*) is reached for baselines in the range *350-450 m*.

## **2) Do we have stable and unobtrusive reflectors?**

Not yet. Corner reflectors are still the most robust solution thanks to their wide aperture. Of course the smallest possible corners should be adopted to gain stability and to have unobtrusive objects to be left on the terrain for long time periods. In the case of ERS, a  $1500\text{ m}^2$  RCS seems to be the lower limit. This means that corner reflectors with at least  $1\text{ m}$  side should be exploited. Nonetheless if repeated ERS images are available, they could be stacked in order to identify corner reflectors with a smaller side.

Other wide aperture solutions (e.g. dielectric lenses) do not offer real advantages with respect to corner reflectors. An interesting alternative might be that of the resonant reflectors. Their aperture is very narrow and they should be positioned very accurately, but they can be done flat and placed in a stable way on the terrain. Moreover, they could be painted on existing stable monuments (e.g. properly oriented walls) thus resulting absolutely unobtrusive. This solution could be adopted in fault/earthquake monitoring where long observation time and high stability are needed.

## **3) What is the status of meteo effect compensation?**

Presently only multi image processing can be exploited to get an operational solution to the elimination of low spatial frequency contribution from the atmosphere.

## **8.3. Recommendations:**

### **• On Polarimetry and Polarimetry-Interferometry:**

- Encourage continuation of Fundamental Studies on the underlying 'Theory of Radar Polarimetry and Radar Interferometry' coupled with that of 'Polarimetric Radar/SAR Interferometry'. A separate 'CEOS Modelling And Inverse Scattering Working Group' is desirable for identifying serious shortcomings and/or major problems in the existing 'Polarimetric Radar Theory' relevant to the development of POL-IN-SAR Imaging Algorithms.
- Assessment of partially versus fully polarimetric SAR Image data takes, including rigorous comparisons of multi-polarisation with fully polarimetric information, together with the establishment of realistic calibration requirements ( $0.1\text{ dB}$  polarimetric amplitude,  $1$  polarimetric phase). The response to this pragmatic question is dictated by the '*Space-borne SAR Systems Design Industry*', in context to the design of '*Low Cost*' space-borne SAR implementation: we need to quantify the anticipated increase in imaging value by partially versus fully polarimetric imaging systems - and to estimate the trade-off between '*Polarimetric (Interferometric) SAR*' and resolution for given swath width, data storage volume, and telemetry capabilities.
- Establishment of a task force for POL-INSAR image data formatting. New constraints arise from the emerging POL-INSAR techniques: the highly calibration sensitive '*Single Look Complex (SLC) SAR Image Data Take Formatting*' becomes an absolute '*MUST*' because absolute polarimetric phase information is required!
- Permanent '*Calibration and Ground-truth Validation Test Sites*' need to be established worldwide. This demand should be realised within the first decade of the next millennium, and CEOS ought to assume a leadership function.
- Polarisation Purity and Channel Isolation must be improved: polarimetric amplitude isolation of better than  $40\text{ dB}$  with amplitude precision calibration of better than  $1\text{ dB}$  (desirable  $0.1\text{ dB}$ ) and relative as well as absolute polarimetric phase calibration of better than  $5^\circ$  (desirable  $1^\circ$ )
- Recommendation to explore systematically the quantitative benefits of higher resolution versus fully polarimetric and partially polarimetric (interferometric) imaging

- Recommendation to compare the DEM recovery procedures from IN-SAR, POL-SAR, and POL-IN-SAR Image data takes and its rigorous interpretation (subgroup on Terrain Mapping?)
- **On scalar Interferometry:**
  - The baseline of the ERS tandem mission most suitable for DEM generation is about 400 metres (see details in section 8.2.)





## **Workshop Recommendations**



## Summary and Conclusions

The chairman opened a forum to discuss suggestions for enhancing interaction and information exchange of future CEOS SAR subgroup meetings. The consensus was that for future meetings, there should not be any overlapping sessions, and this was endorsed.

A proposal was put forward that the 'Sessions' should consist of a 30 minute 'Tutorial Address' on the identification of unresolved topics, followed by a 10 minute 'Succinct Report', highlighting specific issues identified in the 'Tutorial Address'. This proposal was debated but the general opinion was that equal opportunity and time be given to all presenters.

The length of the 'Sessions' needs to be reduced somewhat so that lively 'Interactive Poster Display Sessions' can be arranged and this was endorsed. Each principal poster author shall present a 5 minute comprehensive outline (not paper) of the salient features presented in the poster. The 'Topical Interactive Poster Display Sessions' could be 'paralleled'.

It was proposed that the Polarimetry and Interferometry Sessions be combined into a "Polarimetric SAR Interferometry" Session and this was endorsed. It was agreed that more emphasis and time be dedicated to the Round Tables although the Chairman noted that some 10 hours of Round Table discussions had already been organised during this workshop.

A 'CEOS Workshop Bookshelf', including display material and most up-to-date research books and reports pertinent to the workshop, should be organised. This was endorsed.

### Next Meetings

During the Workshop, a number of agencies (NASDA, DLR, CSA) proposed to host the next meeting; a good measure of the success of the present meeting. The proposals to host the CEOS SAR subgroup meetings have all been welcomed and the following order was endorsed: no meeting is foreseen in 2000 because of other important SAR related meetings throughout this year (i.e. May, July and October 2000). The next SAR subgroup meeting will take place in Japan and will be hosted by NASDA in Spring 2001. A firm offer stands from DLR (Germany) to host the 2002 meeting. The offer from CSA (Canada) will have to be reconfirmed closer to the meeting date.

### Chairman's Concluding Remarks

The 1999 CEOS SAR subgroup workshop was extremely successful, thanks to the joint efforts of the organising and scientific committee, the session chairmen and staff from CNES and ESA Conference bureaus and last but not least, all the participants. I would specially like to acknowledge the work of our workshop local organiser Jean-Claude Souyris, our CEOS SAR workshop webmaster Maurice Borgeaud, and finally our editor Bob Harris.

The CEOS SAR workshop is now more than ever THE FORUM for information exchange in the SAR System Engineering field. We have been able to discover the latest technical developments and application of SAR data, to discuss key technical issues to be resolved and to address requirements for Data Product Calibration and Validation.

This workshop has enabled us to make a significant number of recommendations and has confirmed that various issues remain to be solved. The SAR subgroup will continue to meet every year to address these issues. I would like to take this opportunity to thank all attendees for their efforts in contributing to the lively discussions at the workshop. I look forward to seeing all of you at our next CEOS SAR Workshop in Japan!.

Yves-Louis DESNOS  
Chair CEOS WGCV SAR Subgroup  
and Head User Support Section , Earth Observation Applications Department, ESA/ESRIN

## **Poster Session**



## Geographic data base enriching from ERS SAR scenes : examples in French Guiana

<sup>1</sup>Nicolas Classeau, <sup>1</sup>Jean-Paul Rudant, <sup>2</sup>Hervé Trebossen, <sup>3</sup>Isabelle Jeanne, <sup>4</sup>Patrick Guillopé.

<sup>1</sup>Laboratoire de Géomatériaux / Institut Francilien de Géomatériaux - Université de Marne la Vallée 5 Bd Descartes  
77454 Marne La Vallée - France - tél 01 49 32 90 71 - fax 01 49 32 91 37 - mail classeau@univ-mlv.fr.

<sup>2</sup>Section de Géodésie Géophysique - Service Hydrographique et Océanographique de la Marine. 13 rue du Chatelier BP  
426 29275 Brest Cedex. - tel 02 98 22 17 98 - fax 02 98 22 08 99 - mail trebosse@shom.fr.

<sup>3</sup>Institut Pasteur de Madagascar - BP 1274 - Antananarivo 101 - Madagascar - mail : ijeanne@pasteur.mg

<sup>4</sup>C.E.T.E Normandie Centre - Chemin de la Poudrière - BP 245 - 76121 Le Grand Quevilly Cedex - France -  
Fax : +33 02 35 68 19

### ABSTRACT

Geographic information system accessibility and popularity play an important role in spatial and temporal analysis of anthropic and natural activities. Optical images are not efficient for geographic data base on the French Guiana because of its characteristics (cloud cover, dense forest cover).

A series of applications have been integrated in a G.I.S. on French Guiana. SAR ERS data are used as cartographic resource when available ones are obsolete, as environmental data source, and also to enrich and bring up to date available vector layers (by classification process or photo-interpretation).

We have a global ERS SAR PRI cover of the territory at our disposal and multi-temporal sequences on the coastal plain. Because of the effect of speckle, isolated scenes are, in general cases, only useful for small scale map (about 1 : 200 000). But this scale is not proportional with available vector layers. SAR sequences are filtered with a multi temporal filter so as to increase the image quality by reducing the variance of the speckle. The average scenes are used for applications that require larger scale map (1 : 50 000).

The capacity of ERS SAR sensor to enrich geographic data bases is valorized by some application examples : developments, health (malaria zones), natural cover and deforestation , coastal cartography.

### CONTEXT

French Guiana, a French overseas 'Département', covers an area of 90 000 km<sup>2</sup>. Some 90% of the country is covered by dense tropical forests. The first complete coverage of the country by satellite imagery required 18 images gathered by ESA's ERS1 satellite [1]. We also have at our disposal a G.I.S on the French Guiana, it contains a series of ERS clipping, extract from the mosaic, and a vector layer jointly realized by photo-interpretation of ERS SAR data and from I.G.N (French Geographic Institute) data. Following applications have been integrated in the geographic data base : coastal cartography <sup>1</sup> (collaboration with Service Hydrographique et Océanographique de

la Marine), development<sup>2</sup> (collaboration with Centre d'Etude Technique de l'Équipement), health<sup>3</sup> (collaboration with Institut Pasteur), deforestation<sup>4</sup> (collaboration with D.A.F and Ecole Nationale du Génie Rural et Forestier), relief information<sup>5</sup>. Numbers refer to the studies location as shown on Figure 1.

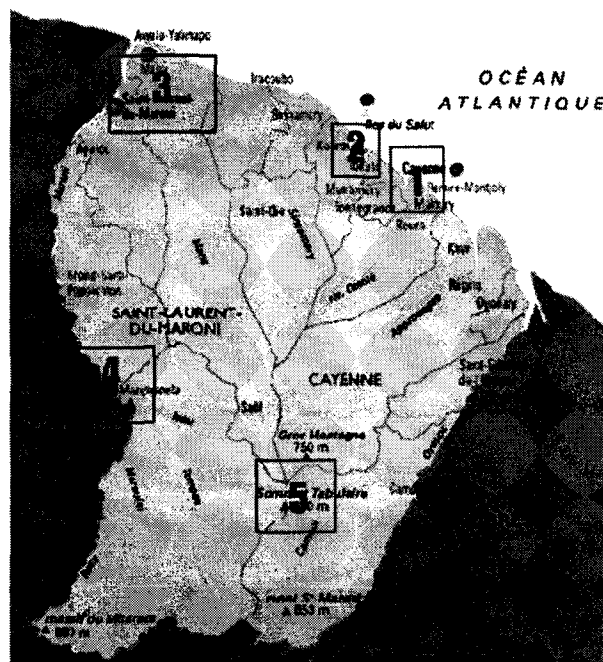


Figure 1 : application location.

### DATAS

We have a global ERS SAR PRI cover of the territory at our disposal and multi-temporal sequences on the coastal plain. We use for this study a geocoded mosaic (it is precisely located and rectified onto a map projection, as well as corrected for terrain distortion [2] (DGA-IGN-UPMC product) as geometric reference, at best taking into account available relief information.

For deforestation applications, we use the IGN vector layer, and airborne SAR images. ERS data have been used for health application.

Data processing :

Multi-temporal filters have been applied on the multi-temporal sequences on the coastal plain in order to increase the restitution scale.

For development and deforestation application, we used markovian based classifications.

Data volume :

The mosaic assembled represents about 1 Giga bytes, after 16 bit 8 bit conversion. Conservation of the original pixel size is not necessary on the global territory but only on interested areas.

Multi-scale approach for geographic data base is possible using reduced pixel size images for a global view of the territory and higher resolution SAR images (multidate average, high resolution sensor) for interested areas.

Data volume troubleshooting could be resolved by cutting the data base in different geographic areas pieces or applications theme.

APPLICATIONS AND RESULTS

1 Coastal dynamics

From the Oyapock river, in the East, to the Maroni, to the West, the french Guiana Coastline is 320 km length. The entire coast is strongly affected by the load dispersal system associated with the Amazon river. This results in significant changes in the coastline. While silt accumulates in some areas, it is eroded in others. Overall, the serial of 5 major mud-banks currently established along the French Guiana coast migrates westward at an average rate of around 1 km/ year (Figure 2). The coastal G.I.S. is useful to follow this coastal evolution and for bringing nautical map up to date [3]. This data base constitutes information for inland navigation and allow to apprehend the mouth of river silt up.

2 Development

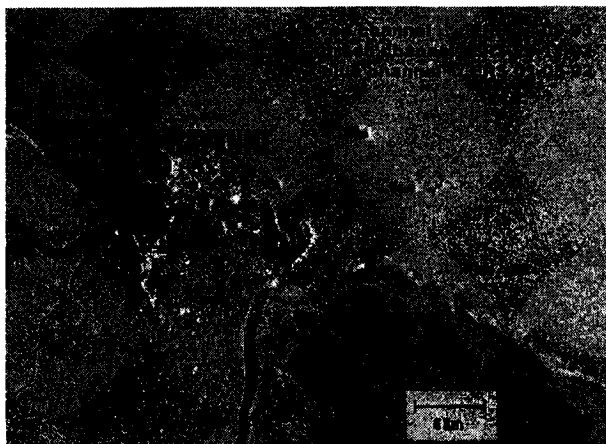


Figure 2 : mudbank displacement.

The site, located near Kourou in Northern French Guiana (5°10 N, 52°40 W), is a 140 Ha savanna on the coastal plain. This savanna, cut in two parts by a road which connects Kourou with Cayenne, is flooded in rain season (April and May), and partially emerged in dry season.

The previous method is applied to estimate the dike effect tied of a road route. Markovian classifications are calculated using 2 center classes : flooded vegetation and all other land cover (Figure 3).

Table 2 presents the wet variation between the East and the West part of the road.

Table 2 : flooded surface variation compared with season

	East	West
Dry season	9.69 Ha	1.45 Ha
Rain season	45.8 Ha	23.23 Ha
% dried up surface	78.8 %	93.47 %

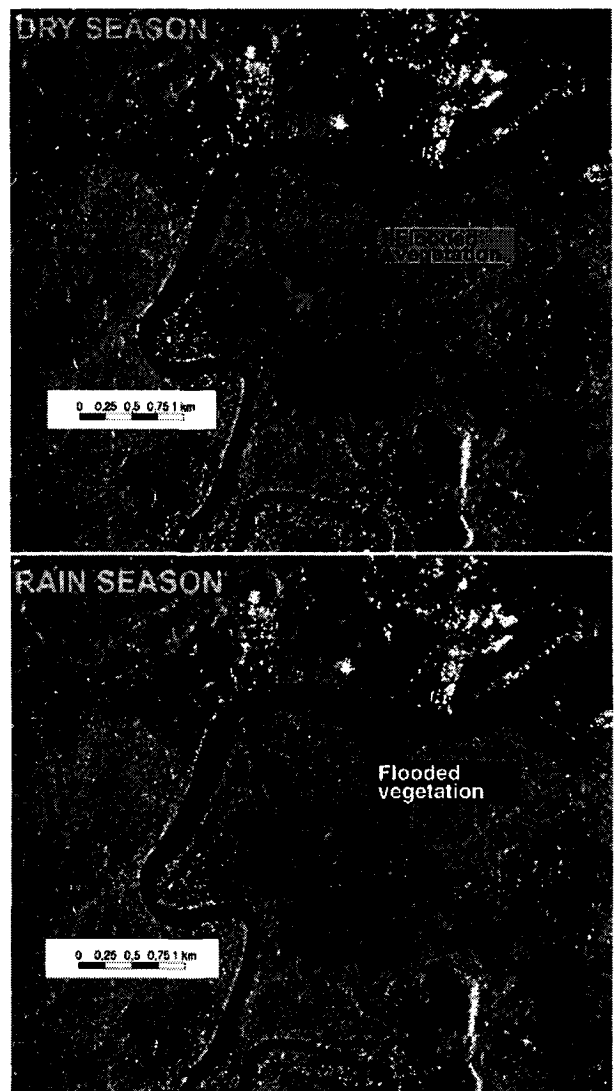
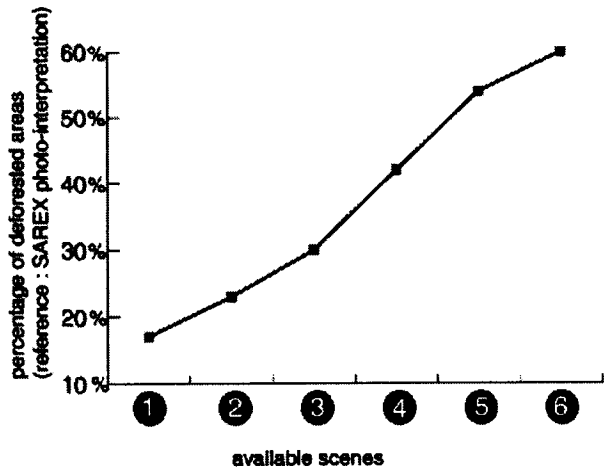


Figure 3 : results of classification during rain and wet season



### 3 Monitoring of Deforestation

The regular repeat cycle of the ERS SAR makes it a potentially valuable data source for monitoring the deforestation. In addition to that, the fusion of multiple scene on the same area increases the restitution scale. The test site stretches out the district of Saint-Laurent du Maroni in the Western French Guiana), along road axes. We use a photo-interpretation of airborne SAR data as reference. Multitemporal SAR data can be used to track deforested small area (1,5 Ha) due to the extreme variation in backscatter for a new parcel : limits between deforested areas and forest are visible after multi-date ave-



Graphic 4 : percentage of deforested areas detected / available scenes.

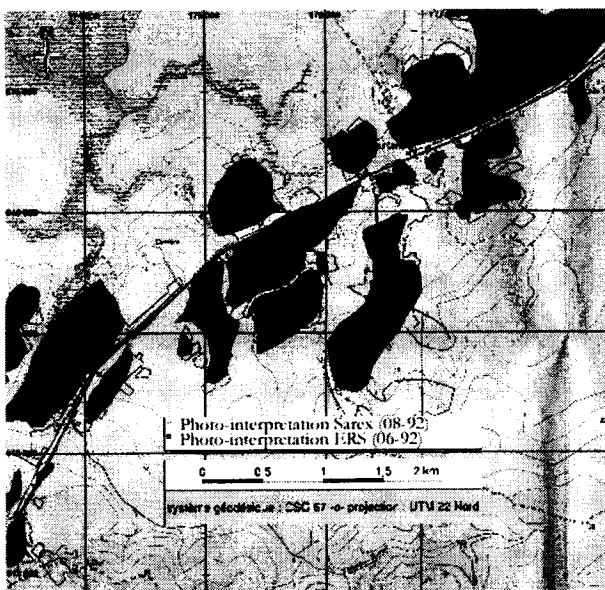


Figure 4 : Result of photo interpretation

rage [4]. Graphic 4 shows us that 60 % of the deforested areas (or non-forest one such as savanna) are visible on ERS SAR images after multi-date average (6 images in this case).

Integration of those information in a deforestation data base is usable on one hand for the monitoring of the new deforestation areas, on the other hand to evaluate the deforestation potential of areas, according to development (road axes, town ...).

### 4 Health

The study area is located near the Maroni river. We have at our disposal ERS and JERS SAR data, and entomological data which result from missions realized by the Pasteur Institute.

The flooded and shaded off forest areas are less protected from the sun light than the dense forest. Those areas constituted favorable zones for the malaria vector.

On a JERS scene acquired during rain season we can observe some high radiometric areas in the river's borders. That could be interpreted as deforested areas or as flooded areas. We can observe those areas especially on JERS scenes because of the L Band penetration power in the canopy.

A comparison realized between JERS scene acquired during dry season shows us that the high radiometric areas have disappeared[6]. Figure 6 present an extract of G.I.S on the Maroni river.

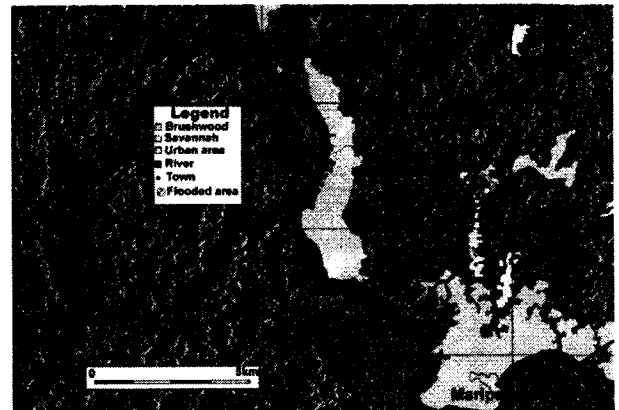


Figure 5 : Flooded areas on the Maroni river.

### 5 Topography

The southern part of French Guiana is probably the least well mapped of any French territory. Relief information on this area are often poor and partially inexact.

With the exception of few areas (urban, savanna), we are able to check test site and show that radiometric variation

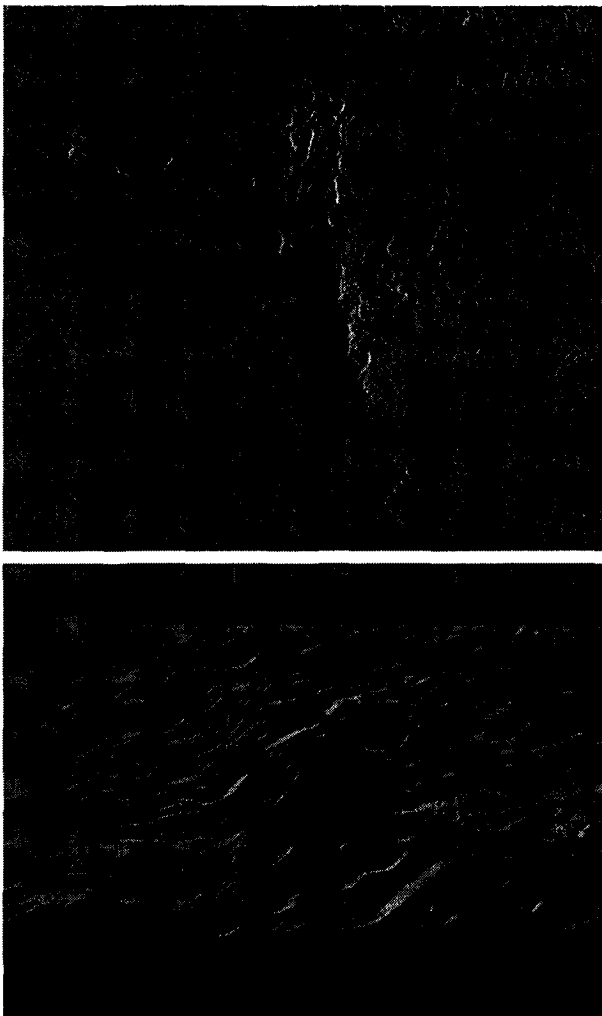


Figure 6 : Radarclimetry on the Inini camopi Mount (600 m).

can be transform into slope effect (figure 6) .

Radiometric variation can be used to determine the terrain elevation using the basic principles of the radarclimometer method [7].

#### CONCLUSION

SAR images constituted an important raster layer in tropical environment. The SAR images background replace the cartographic background when this one is obsolete

(particularly in the south).

Classification results calculated and interpretation on SAR images could enriched geographic data base vector layers (health, development, deforestation, coastal environment). The access to sensor that offer different spatial resolution allow multi-scale SAR images use.

#### ACKNOWLEDGMENT

Authors thank ESA for the ERS SAR data supplied. We also grateful to the DGA.

#### REFERENCES

- [1] Rudant, J.P., et al., 1996, "Apport des images radar satellitaires ERS1 et JERS1 dans le domaine de la cartographie générale et thématique en contexte tropical humide", S.F.P.T., N° 142, pp. 371-376.
- [2] Cantou, J.P., Tonon, M., 1997, "Cartographie radar de la Guyane : vers une chaîne de production opérationnelle des spatiocartes", bull. SFPT N°148, pp36-43.
- [3] Trebossen, H., Rudant, J.P., Fruneau, B., Classeau, N., 1999, "Contribution of RADAR SAR imagery for mapping coastal areas: examples of French Guyana and Mauritania", proceedings of CEOS, Toulouse, France.
- [4] Classeau, N., Mvogo, J., Onana, V.-Paul, Guillope, P., Rudant, J.P., 1999, " SAR scene potential for the monitoring of anthropic activities (deforestation, development) through markovian segmentation techniques and tree-structured wavelets based segmentation algorithms ", Proceedings of IGARRS, Hambourg, Allemagne, IEEE.
- [5] Jeanne, I., 1998, " Apport de la télédétection et des Systèmes d'Information Géographique dans l'étude épidémiologique de la bilharziose à Shirtsosoma dans la région de Ihoy, Madagascar ", Colloque " Santé et développement ", Nov. 98, Antsirabe, Madagascar.
- [6] Rudant, J.P., Guillope, P., 1997, " Apport de l'imagerie radar pour l'appréciation des surfaces inondées sous couvert forestier en contexte tropical humide (Guyane) ", Octobre 97, Rapport interne, C.E.T.E Normandie Centre.
- [7] Paquerault, S., Maître, H., 1997, " Radarclimetry ", French Society in Photogrammetry and in Remote Sensing Congress, bulletin (SFPT) number 148, December 1997, pp 20-30.

## Contribution of RADAR SAR imagery for mapping coastal's areas: examples of sedimentation and erosion zones in French Guyana, Mauritania.

Hervé TREBOSEN(1) + (2), Jean Paul RUDANT(1), Bénédicte FRUNEAU(1), Nicolas CLASSEAU(1).

(1)Laboratoire de Géomatériaux / Institut Francilien de Géomatériaux  
 Université de Marne la Vallée 5 Bd Descartes 77454 Marne La Vallée  
 tel 01 49 32 90 71 - fax 01 49 32 91 37 - mail trebosse@dedale.univ-mlv.fr.

(2)Section de Géodésie Géophysique  
 Service Hydrographique et Océanographique de la Marine.  
 13 rue du Chatelier BP 426 29275 Brest Cedex.  
 tel 02 98 22 17 98 - fax 02 98 22 08 99 - mail trebosse@shom.fr.

### ABSTRACT

**Keywords:** RADAR SAR, Cartography, coastline, bathymetry, interferometry, flooding zones, RADAR SAR images geometry, coastal evolution.

In this communication we propose to study coastline evolutions and possibilities for nautical charts update with the examples of French Guyana and Mauritania.

This study is a collaboration between Marne La Vallée University, Hydrographic and Oceanographic service of the French navy (SHOM) and Digital Mapping Studies Service of the French army (CEGN).

RADAR SAR imagery provides satellite images under any climate conditions. The coastline evolution, in French Guyana, is characterised by displacement of mud banks along the coast (among 1km per year). These mud banks are quite recognisable and can be followed on RADAR SAR images. A comparison between ERS1-2, JERS1, RADARSAT data, old optical images and nautical charts shows coastline evolutions as large as 10 km over 50 years and demonstrates important changes in coastal bathymetry. The objective on this site is to accumulate data RADAR SAR and in situ measurements to modelize coastline evolution.

In Mauritania, presence of a harbour dyke causes erosion and sedimentation zones. Erosion of the offshore bar can cause flooding of depression zones. The contribution of RADAR SAR imagery on this site is the monitoring of coastline evolution and detection of depression zones by RADAR SAR interferometry.

### 1. INTRODUCTION

Optical images are commonly used to nautical chart for coastal bathymetry, coastline and topography. Particularly, for several years, French hydrographic survey updates nautical charts in French polynesian atolls, African coasts and French territories, it represents among one hundred re-actualisation with spot images.

Under tropical humid climates sites, bad quality of this sort of images leads to study RADAR SAR imagery potentials for coastal mapping.

So objective of this study is to demonstrate the properties of RADAR SAR for mapping coastal's zone with the examples of erosion and sedimentation areas of French Guyana, Mauritania.

We will accentuate our effort in the follow of the coastal area evolution by studying complementarities between Radar SAR sensors (Ers1 and 2, JERS 1), old optical images (SPOT and Landsat), two centuries of nautical cartography in French navy and in-situ measurements, by implementing tools for coastline's detection on numerical images and RADAR images segmentation, testing interferometry for coastal topography. All these results will be carefully and precisely geographically localised.

Results will permit operational nautical cartography re-actualisation in respect with SHOM attributes, in fact French hydrographic service is responsible for mapping and sea-navigation on French and some African coasts.

### 2. COASTAL EVOLUTION IN FRENCH GUYANA

#### 2.1. French Guyana coastal context

Morphological changes of the French Guyana's coastline are striking and rapid, directly linked with the Amazon discharge. Under the influence of the Guyana current, the suspended matter moves north-westward (among  $2 \cdot 10^9$  tons per year) and creates along the coast, mud-banks [1]. The displacement of these mud-banks is evaluated of about 1 km per year [3]. This migration takes place between December and February when the sea is rough and trade-wind speed are higher and the North Brazil Current flows closer along the coast. The great consequence of all this sedimentation is the fast evolution of the coastline and the bathymetry by weak deep. Two types of zones can be distinguished: erosion and sedimentation zones: Erosion coastal's zones are exposed to ocean waves. These waves destroy vegetation, which grows on a

weakly soil. On the contrary, sedimentation zones are coastal's zone where a mud bank stays, then waves are broken and will not disturb vegetation grows. In this part of the communication we will study the coastal region near Kourou, European Launch Space center.

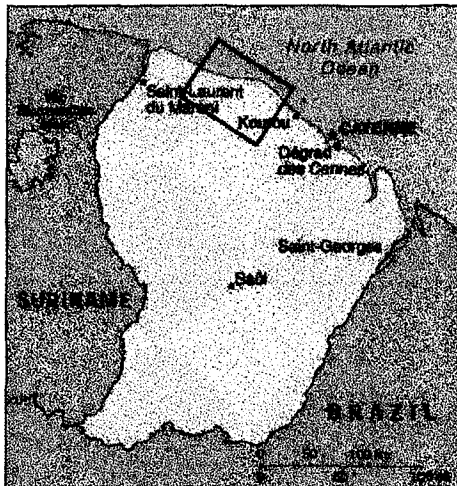


Figure 1 : Study geographic situation.

2.2. Data used

We used for Sinnamary site a lot of spatial images and in situ measurements acquired during two missions in French Guyana.

N°	Sensor	Dates	Orbit	frame	Tidal level ©(m)
1	ERS1	17/04/92	3948(*)	3501	0.58
2	ERS1	22/05/92	4449(*)	3501	1.78
3	ERS1	18/12/92	7455(*)	3501	2.28
4	ERS1	16/07/93	10461(*)	3501	1.16
5	ERS1	09/07/95	20825(*)	3501	1.35
6	ERS2	15/04/96	5160(*)	3501	0.93
7	ERS2	12/10/98	18186(*)	3501	2.58
8	ERS2	05/11/98	18523(**)	0099	0.65
9	ERS2	16/11/98	18687(*)	3501	1.55
10	SPOT	26/10/86			1.85
11	Land-sat TM	08/08/76			0.43

Table 1 : data on French Guyana

All ERS images issued from ESA AO3 160

© SHOM Tidal level software.

\* Downward mode

\*\* Upward mode

All data are PRI product except image number 6 (ESA SLC product).

All nautical charts from French Navy Hydrographic Survey have been used and especially Global Nautical chart of French Guyana (1953) 1/500,000.

A dozen of precise GPS points (submetric precision) were acquired during october - december 1998 mission on SHOM d'Entrecasteaux hydrographic vessel.

According to the lack of precisely positioning points in French Guyana on RADAR SAR images, we decided to acquire GPS trajectography data by helicopter flights. All these measures were corrected by GPS acquisition on geodetic point during flights. Considering elevation of helicopter, we evaluate precision of this flight of about +/- 30 meters across coastline. This lack of precision was counterbalanced by an acquisition time of 0.6 sec.

2.3. Image processing

The single SLC product we have was transformed from slant range geometry to ground range by an internal imagery tool considering incidence and azimuth angle after extraction of module part of terrestrial reflection wave to obtain an image superimposable on PRI.

The images were also filtered by a multitemporal filter to eliminate speckle in RADAR SAR images. Speckle is a random noise caused by micro-relief reflections. This filter is based on comparison between images on the same site. Speckle won't appear in the same conditions in these images. A coefficient permit to keep the original information contained in reference scene [4].

2.4. Results

GPS points and trajectography allow us to test the georeferenced RADAR product used in French Guyana. Static points were acquired on bridges along coastal road and trajectography on non movable coastlines. Figure 2 represents GPS trajectography measures (white curve) comparing to RADAR SAR images dated from 1992 to 1998 along western guyana s border (Maroni river).

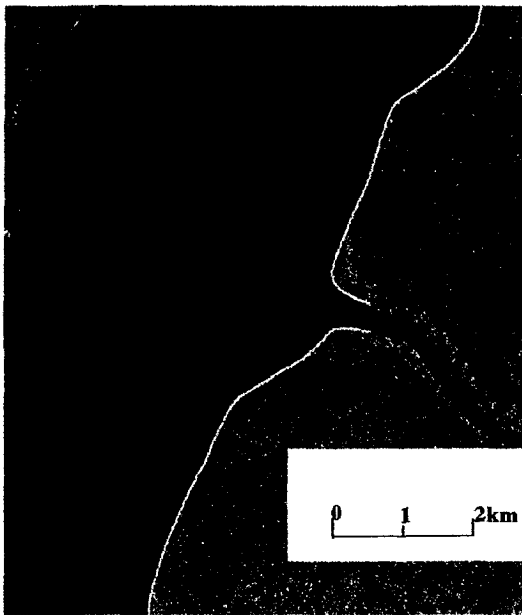


Figure 2 : Georeferencement verification.

In figure 3, we can interpret texture on ERS images. We observe with a low radiometry mud banks at low tide (region 1), mud banks reflect with its smooth surface RADAR waves and can be easily delimited with ocean which has a rough surface caused by swells on ERS images (5.6 cm wave length). On JERS images (20 cm wave length) contrary to ERS there is no contrasts mud banks - oceans, sea appears like a smoothly surface . Vegetation along coast is constituted by mangrove (region 2) in a homogenous texture on RADAR SAR ERS images, it represents a coastal band large as 1 km to 10 and 0 to 5 meters high. Trunks laid out on mud banks at the limit of mangrove vegetation present an high radiometry caused by waves retro-reflection after reflection on mud. South to this zone the quaternary off shore bar (region 4) limits savannah vegetation and higher elevated regions.

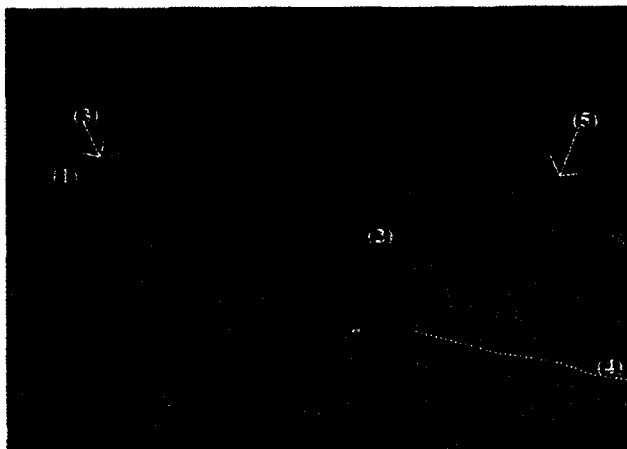


Figure 3 : ERS images interpretation.

Interpretation of coastline on spatial images and nautical charts shows mud banks displacement and coastline evolution by erosion and sedimentation between 1953 and 1998 [5]. It appears that coastal area of this site is submitted by alternatively erosion and sedimentation periodicity. We measured coastline evolution in Iracoubo site (region 5, figure 3). Figure 4 shows different coastlines and evolutions between 1953 to 1998.

N°	Dates	Differences (m)
1	17/04/92	<b>référence</b>
2	22/05/92	<b>25</b>
3	18/12/92	<b>50</b>
4	16/07/93	<b>50</b>
5	09/07/95	<b>950</b>
7	12/10/98	<b>2000</b>
8	05/11/98	<b>2000</b>
9	16/11/98	<b>2000</b>
	chart 1953	<b>-6000</b>

Table 2 : Metric coastline evolution.

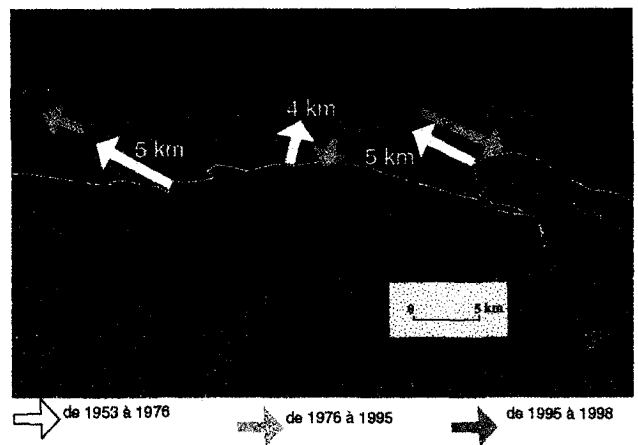


Figure 5 : coastline movements on Sinnamary site

Coastline evolution and mud banks displacement give problems for nautical charts re-actualisation to sailors safe. Actually a first map, scale 1/50 000, around Cayenne (figure 5) has been re-actualised by RADAR SAR ERS images for coastline and intertidal zone. For futur umber of ERS 1 and 2 images from east to west Guyana will allow us to participate of Global nautical chart elaboration.

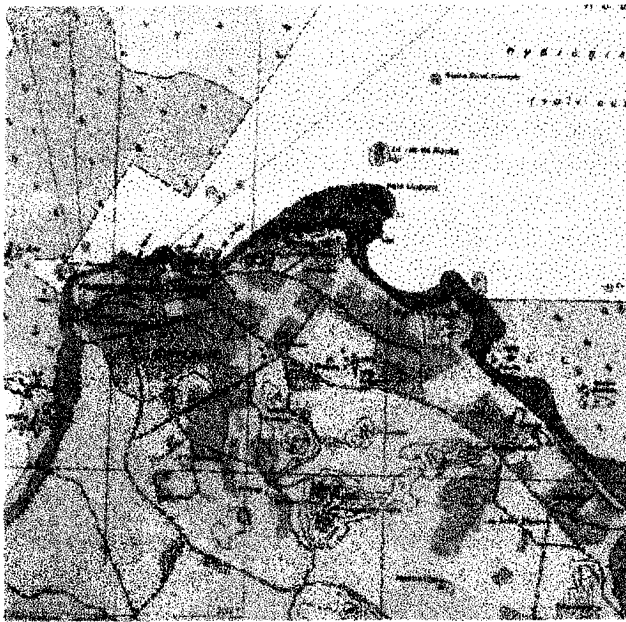


Figure 5 : Extract from SHOM nautical chart N 7379 re-actualized by ERS images / september 1999.

### 3. COHERENCE AND INTERFEROGRAMS FOR COASTAL MAPPING.

#### 3.1. Context

In Mauritania, a sea wall was built perpendicular to the coast for Nouakchott's harbour, we observed in the north of the dyke: sedimentation and a coastline's retreat in the south. These phenomena produce first a silting up of the seaport and a high risk of inundation with seasonal storms for depression zones situated back the off shore bar. These depression zones and globally Mauritania's coastal area are interesting for RADAR SAR interferometry applications for comparing coastline evolution and localised depression regions. So RADAR coherence images will be used for coastline expression while interferograms will permit to study morphology of coast plain [6].

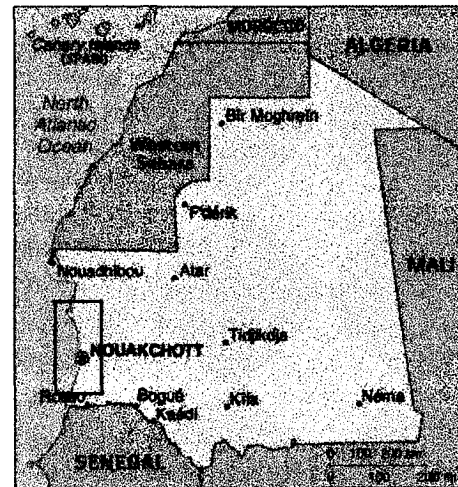


Figure 6 : Study geographic situation.

#### 3.2. Data.

Six ERS1-2 SLC were acquired in tandem mode in the same Orbit segment. Tandem mode significate that ERS2 aquisition follow ERS1 24 hours after. For comparison we own topographic maps on Mauritania's coast.

#### 3.3. Image processing

All images were processed by CNES interferometry software DIAPASON. This software permit to obtain amplitude images (resolution approximately 20\*20 meters), coherence images, by extracting modulus of correlation between two acquisitions, and interferograms.

Interferometry is based on phase study of the returned RADAR signal. Then we can link phase differences and ground elevation. We need that the acquisition orbits are closed ( $< 1$  km).

On amplitude and coherence images we used to detect coastline edge detection and classification tools.

The edge detection tool is a program based on Derriche filter with a threshold to eliminate unwanted edges[7].

Classification is made by an iterative program based on markovian field theory [8].

#### 3.4. Results.

On amplitude images, we observe with a quite good contrast coastal zone. Ocean appears with an high radiometry while terrestrial regions are with a weak one. Nouakchott's urban and harbour structures are easily recognisable.

Of course on coherence images sea has always a low coherence. On terrestrial regions, we observe many inhomogenous zones. It implies several considerations :

First, for regions which have a good coherence, there is

here no real surface changes between the two acquisition of the satellite.

Secondly, regions with low coherence caused by a low radiometry on amplitude images with a low signal/noise ratio.

Third, regions with low radiometry caused by terrestrial geometric effects and differences between orbits. The second region is interesting for our research, it represents for us humid and argilous depression zones, they are easily suitable on coherence images. On figure 7, we observe in Red and Blue channel amplitude image, in Green coherence one. Good contrast ocean - land permits an easier interpretation than in amplitude image only. Land appears in green because coherence is elevated, but depression zones appear in black and urban structures in red and blue.

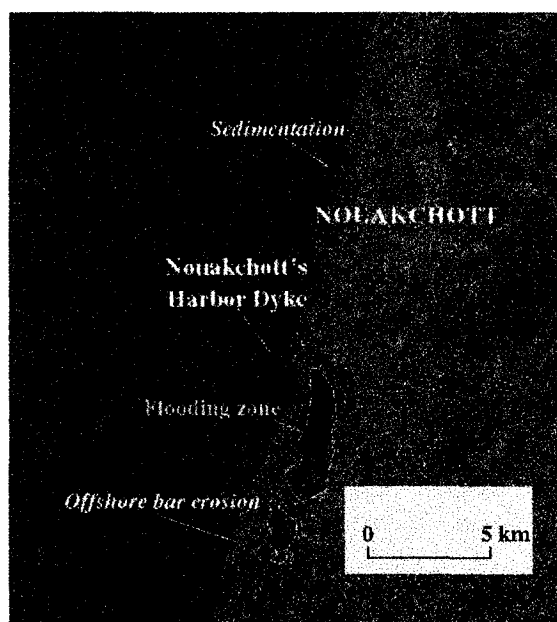


Figure 7 amplitude (red+blue channel) and coherence (green) image.

For coastline extraction, we obtain good results with markovian field classification program on amplitude and coherence images consecutively to last considerations. We have compared human coastline interpretation and extraction tools results. On coherence images, automatic coastline is the same that interpretation (figure 8). The same comparison shows artifacts on amplitude images (figure 9). Coastline interpretation is not exactly identical between coherence and amplitude.

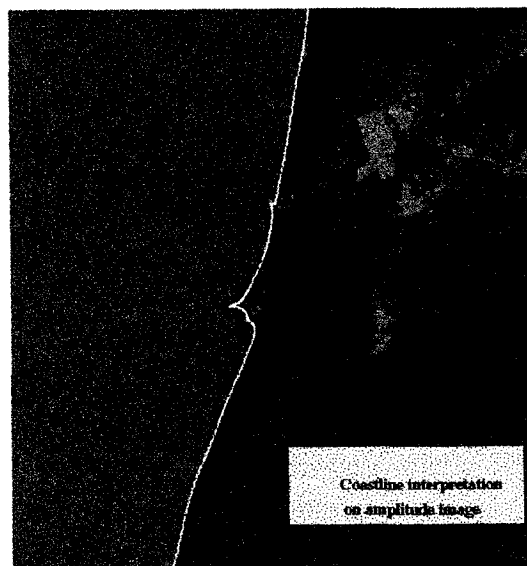


Figure 8 : Classification on coherence image.

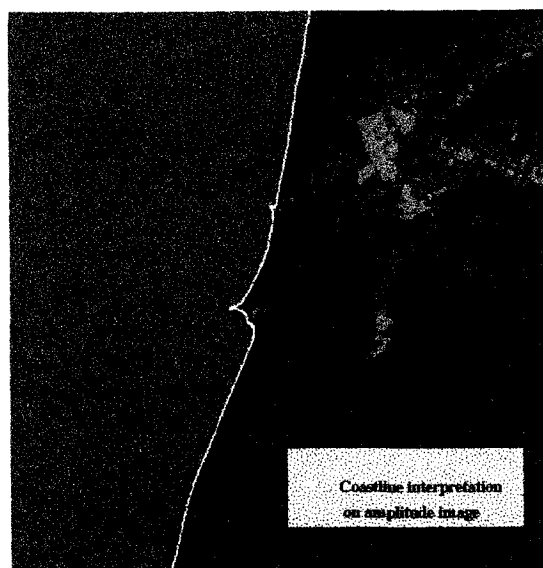


Figure 9 : Classification on amplitude image.

At last, interferogram obtained shows us, coastal topography. This site is not hilly : from -5 to 30 meters high. But we retrieve in figure 10, topographic elements contained in figure 11. We recognize offshore bar along sea and northeastward topographic formation. Regions presenting inhomogeneous phase represents zones with low coherence.



Figure 10 : interferogramm



Figure 11 : topographic map.

#### 4. CONCLUSIONS

This communication demonstrates RADAR SAR potential for coastal mapping in some applications in french Guyana and in Mauritania. Contribution of first nautical chart elaboration has been facilitate by a lot of RADAR SAR images integrated in a geographic database on

French Guyana (GPS points, tidal levels, measures, georeferenced products [9]). In Mauritania, original complementarities between interpretation of amplitude images and interferometry processing had permitted comprehension of this coastal phenomena.

#### 5. ACKNOWLEDGEMENTS

Special thanks to ESA for its support to announcements AO3-160 and AO3-119 where issued french Guyana and Mauritania ERS1-2 images

#### 6. REFERENCES

- [1] JM Froidefond, M Pujos, X André. Migration of mud banks and changing coastline in french Guiana. *Marine Geology*.(84) pp 1-12, 1988.
- [2] JM Pujos, JM Froidefond. Water masses and suspended matter circulation on the french Guiana continental shelf. *Continental Shelf Research*. pp 1-10, 1994.
- [3] P. Rudant, F. Baltzer, J.P. Deroin, M. Lointier, H. Maître, C. Penicand, M.T. Prost, D. Sabatier. Possibilités cartographiques offertes par ESR1 en contexte tropical humide, exemple en Guyane française, apports spécifiques des séquences multitemporelles. *Workshop Tolède*, pp 371-376, 1994.
- [4] W. Stroobans, C. Ledez, C. Penicand, J.P. Rudant, P. Vallet. Une approche pragmatique de la fusion multitemporelle des image ERS1. *Fusion of Earth Data*, Cannes, pp 131-142, 1996.
- [5] MT Prost, F Baltzer, JP Rudant, M Dechambre. Using Sarex and Erasme imagery for coastal studies in French Guyana : Example of the Kaw Swamp.
- [6] G. Tulliez. Apport des données de télédétection dans la compréhension de deux systèmes littoraux : le littoral de la région de Nouakchott et la baie du Mont St Michel. Rapport de soutenance de thèse, EPHE, 1998.
- [7] Ph. Paillou, "Detecting Step Edges in Noisy SAR Images: A New Linear Operator", *IEEE Transactions on Geoscience and Remote Sensing*, 35(1), pp. 191-196, 1997.
- [8] M. Moctezuma. Analyse de séquences d'images satellitaires et détermination des modifications géographiques des paysages. *Rapport de soutenance de thèse, ENSTP*, 1995.
- [9] Nicolas Classeau , Geographic database enriching with ERS scenes : example of french Guyan, CEOS october 1999, Toulouse.



## Crop parameters retrieval by SAR Phasimetry

Xavier Blaes and Pierre Defourny

Department of Land Use Planning, College of Agriculture, Université Catholique de Louvain  
Place Croix du Sud, 2/16 - 1348 Louvain-la-Neuve, Belgium

Tel: +32 10/ 47 81 92, Fax: +32 10/ 47 88 98, email: [blaes@biom.ucl.ac.be](mailto:blaes@biom.ucl.ac.be), <http://www.agro.ucl.ac.be/biom/>

**Abstract** - This paper concludes to the great interest of the 1-day interval coherence images derived from pairs of SAR tandem acquisitions for the agricultural applications. Coherence images have been analysed with regards to a synchronous field campaign including 4 crops, i.e. winter wheat, sugar beet, potato and maize. First the high sensitivity of the coherence to the plant height and the canopy cover is statistically demonstrated. A prediction model of the wheat height has been computed and the mean absolute error of about 7 cm seems compatible with the information requirements for a crop monitoring systems. The shape of these relationships varies according to the crop structure and their respective development type.

**Index Terms** -Phasymetry, radar, crop parameters retrieval.

### I. INTRODUCTION

The phase information of the backscattered signal have been investigated using InSAR techniques for various applications. In the agricultural case, a strong linear relationship between interferometric coherence at one day and potato, sugar beet and winter wheat height was established in [1]. Unfortunately the relationship could not be established between the measured crop height and the coherence value of the same year. From the interferometric correlation it was possible to estimate the canopy cover fraction for rape seed fields and canopy height for lucerne fields [2] and [3] and similar relationship are expected for other crops. The present paper investigate the relationship between the crop height and the coherence in the sugar beet, potato, maize and winter wheat cases using fields and SAR data acquired simultaneously. A winter wheat height prediction model is developed and his accuracy is analysed. A classification of the wheat fields following the crop height retrieved by the model inversion is also assessed. The mean coherence value per fields is also analysed with respect to the canopy cover rate.

All of the results describe in this paper were obtained in the framework of the ERS Tandem Project B302 of the European Spatial Agency [4] and [5]. The CSL (Centre Spatial de Liège) has developed a complete InSAR processor for producing the interferometric products to be used by the co-investigators [6]. The field measurements were carried out jointly by the Department of Environmental Sciences and Land Use Planning of the UCL, the Facultés Universitaires des Sciences Agronomiques de Gembloux (FSAGx) and the Centre de Recherches Agronomiques de Gembloux (CRAGx).

The specific objective of the data analysis is to document the relationships between the interferometric

coherence and crop variables, i.e. canopy cover and crop height, for 4 different crops.

In the following sections, the coherence ( $\gamma$ ) always refers to the interferometric coherence which is a quantitative measure of the amount of noise present in the SAR interferogram. In this study this interferometric coherence is always derived from a tandem pair with 2 satellite acquisitions within 24 hours. The interferometric baseline measures the distance between the antenna positions at the time of the acquisitions. The crop canopy cover or cover fraction used in this study is defined by the proportion of the soil surface covered by the vertical projection of the crop canopy.

### II. DATA

#### A. SAR Data

Six tandem pairs of SAR images were acquired over the study area in 1996. The 6 coherence images and the 12 corresponding images of the backscattering signal intensity, called module image, have been used for the interpretation. The pixel resolution of these images is 40 by 40 meters. In order to keep the full information content of these images, they were neither resampled nor geometrically corrected but only co-registered in 2 separate data sets corresponding to the two different tracks, i.e. track 151 and track 423.

#### B. Meteorological Data

The daily rainfall data were provided by the Royal Meteorological Institute (Belgium) for the station of Ernage located in the centre of our study area.

#### C. Field Data

The study area is located in an intensive agriculture region of Belgium (Figure 1). During the 1996 growing season, 24 agricultural fields cultivated with 4 different crops were selected for the ground monitoring: 7 parcels of winter wheat, 5 of maize, 6 of potato and 6 of sugar beet. The size of these fields is greater than 3 hectares in order to get a representative average signal for each field.

This set of fields was more or less systematically visited at each overpass of the satellites. For each field, the ground survey records the canopy height, the description of the phenological stage (number of leaves per plant), and the soil moisture measured by a gravimetric method using 6 samples per field.

Vertical colour photographs (Figure 2) of the crop were regularly taken using a 50-mm camera hold at 4-m high. These pictures correspond to the same spot for

each field over the whole season and so allow an accurate measurement of the crop canopy cover for each acquisition date. This canopy cover measurement was completed by visual interpretation based on a 350-dot random sample.

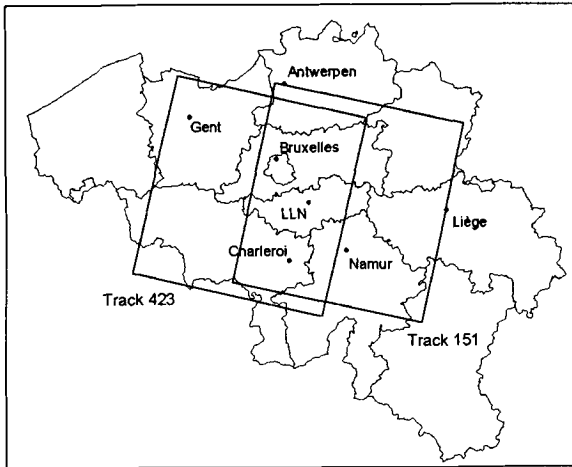


Figure 1: Localisation of the two set of images over the study area.



Figure 2: Potato field as viewed from 4-m high on the day 165.

The Figure 3 and Figure 4 show the temporal evolution of the crop canopy cover fraction and the crop height as measured during the 1996 growth period.

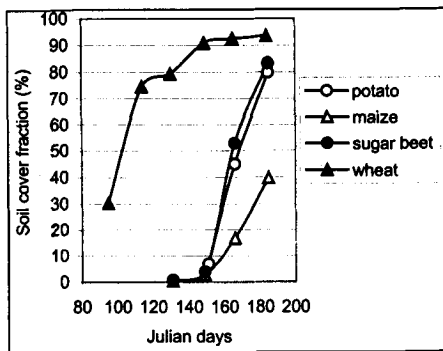


Figure 3: Temporal evolution of the canopy cover fraction of the 4 studied crops measured on the vertical photographs.

The selected fields have been located on a digital ortho-photography with 1-m resolution and then digitised twice for both times series corresponding to the tracks 151 and 423.

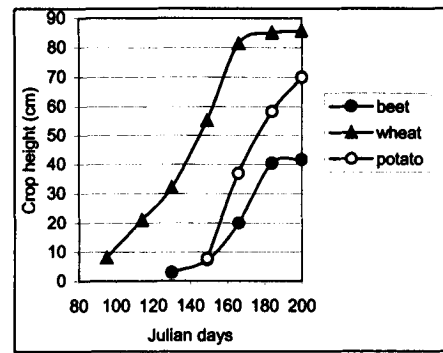


Figure 4: Height evolution of the sugar beet, the wheat and the potato crops during the growing period.

### III. CROP MONITORING

#### A. Wheat

For each of the tandem satellite overpasses between the days 95 and 185, the crop height of 7 wheat fields was measured. Figure 5 presents the relationship between the wheat height and the interferometric tandem coherence averaged for each field. A very strong linear relationship is observed between these two variables with more than 90 % of the coherence variability explained by the crop height.

The Figure 6, on the opposite, shows a non linear relationships between the canopy cover and the tandem coherence. The coherence remains constant at the beginning of the growth and sharply decreases when the wheat plants are 60 cm high. This late sensitivity will be discussed further with respect to the results obtained for the sugar beet.

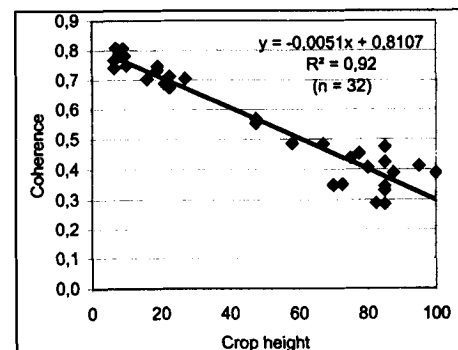


Figure 5: relationship between the tandem coherence and the winter wheat height.

It is important to point out however that the 32 points used to calculate the regression are not independent. In this case, as in most of the literature, it is not statistically correct to consider the samples as independent because the same 7 parcels were visited and measured 5 times during the growth period.

A set of relationships using strictly independent samples randomly selected from the available data set has been computed to address this dependence issue. The number of points available for the regression is 7 since each parcel is considered only once for each relationship. The four linear regressions computed from

independent points still confirm the strong relationships between the crop height and the coherence. In spite of the number of points, the coefficient of determination remains as high as before:  $R^2 = 0.95$  (with  $n = 7$ ),  $R^2 = 0.87$  ( $n = 7$ ),  $R^2 = 0.95$  ( $n = 7$ ) and  $R^2 = 0.94$  ( $n = 7$ ).

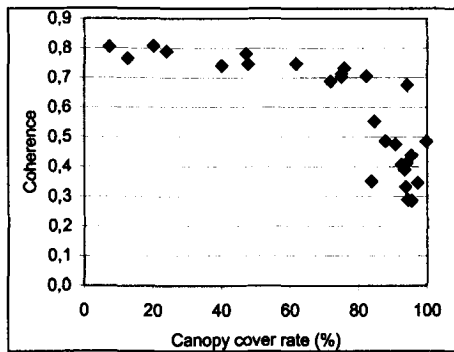


Figure 6: Relationship between the tandem coherence and the canopy cover of 28 winter wheat fields.

This analysis highlights the robustness of the relationships which is neither related to the dependence between the samples nor very sensitive to the number of points. The inversion of such relationships can then be investigated with respect to potential agricultural applications.

**B. Wheat Height Estimation Model**

In order to balance statistical requirements related to both the sample independence and size, 16 samples have been selected in such a way that each parcel was included only 2 or 3 times in the model calibration set. The so called 'jack-knife' procedure can then be applied: a set of observations serves for the calibration while the remaining observations are set aside for model validation.

The empirical model computed from the calibration set is a linear relationship predicting the crop height from the coherence value and is as follows:

$$H = -185.13 * \gamma + 153.63 \quad R^2 = 0.92$$

with  $\gamma$  is the tandem interferometric coherence and  $H$  is the crop height.

This relationship is then used to estimate the crop height for the 16 remaining observations in order to document the prediction accuracy. The difference between the estimated value and the measured value of the crop corresponds to the model error. As shown in Figure 7, there is no bias but the model accuracy decreases as the height to be estimated increases.

75% of the points present an error value varying between -8 cm and +4 cm. Moreover, the model has a slight tendency to underestimate the crop height values because 56% of the points underestimate while 44% of the points overestimate the height values.

The mean of the absolute error value calculated from the 16 validation points is 6.9 cm. The absolute error is smaller for small values of the measured height than for high values. The difference between estimated and

measured height increases with plant height. This corresponds to a relative error which is constant and independent from the plant height (except for the height lower than 10 cm). The average relative error values computed from the validation set is equal to 22 %.

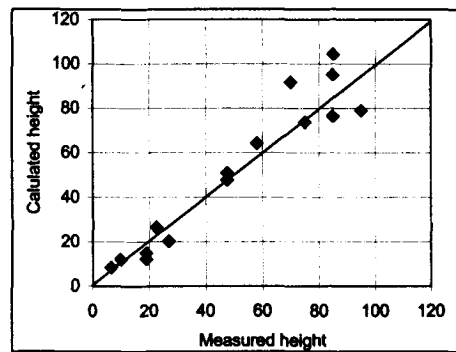


Figure 7: Validation of the wheat height prediction model: differences between measured and estimated value.

To be relevant to crop monitoring applications, the model performances must be compatible with the information requirement. For instance, the main issue is not really to detect that the wheat grew from 20 cm to 55 cm from one date to another but more to discriminate the differences in height between parcels at a given time. Figure 8 shows the measured crop height for the 16 validation samples at the different dates and the corresponding estimation of the crop height for the same 16 samples.

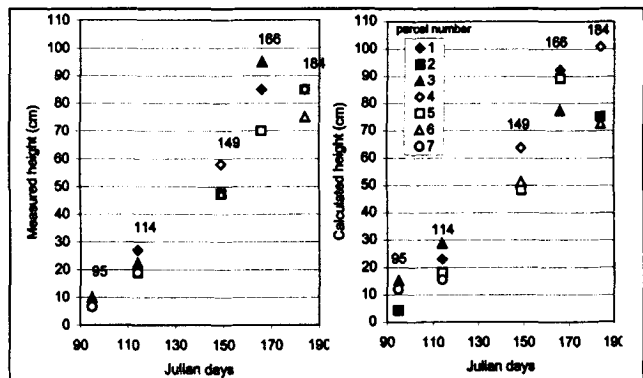


Figure 8: Comparison between (a) the measured crop height for 16 winter wheat fields at different dates and (b) the calculated crop height for the same fields at the same date.

At the beginning of the growth season, the measured height of the different parcels is very similar and the estimated height does not present significant differences between parcels. On the 149<sup>th</sup> day, the predicted crop height allows the distinction of 2 classes of height: the first one corresponds to parcels 5 and 6 and second one to parcel 4. This discrimination concords with the actual observations. On the other hand, the results of the days 166 and 184 do not allow to confirm further the usefulness of the model for agricultural monitoring. Indeed, the number of observations used here for the discrimination between height classes is really too small to provide any positive or negative answer with respect to the operational usefulness of the coherence image for

crop monitoring. It is however very clear that this approach must be further investigated on a larger scale basis and should also include other sources of variability such as topography and row orientation.

C. Potato

A similar analysis has been carried out for the potato crop. Linear relationships have been established between the potato plant variables and the field coherence average. These include all the available data: 6 parcels visited at 3 different dates during the growth season (days 149, 166, and 184) which correspond to the last 3 available tandem pairs. Figure 9 and Figure 10 show strong linear relationships between the crop measurements and the coherence values.

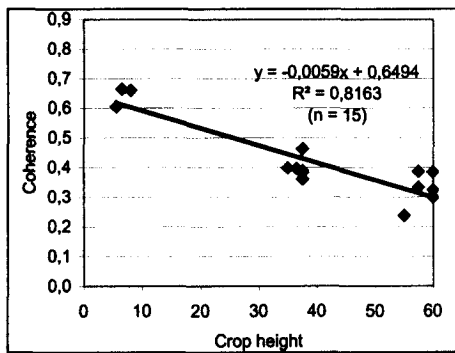


Figure 9: Linear regression between the tandem coherence and the potato height.

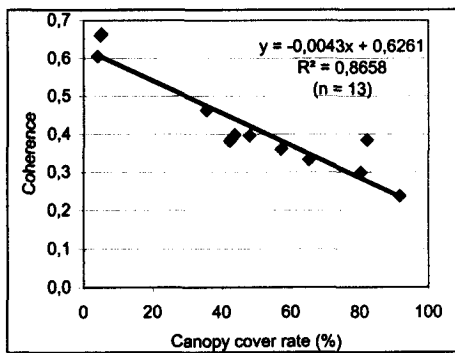


Figure 10: Relationship "Tandem coherence - soil cover fraction" for potato fields.

The regression between the crop height and the coherence plotted in Figure 9 is driven by three crop height clusters. This irregular height distribution corresponds to three different dates of field survey. This indicates that the growth of the potato plant was very high, i.e. from 8 to 58 cm, and very similar in the 6 parcels.

The relationship between the canopy cover and the coherence values seems slightly stronger than the previous one ( $R^2 = 0.87$  versus 0.82). The residues distribution is also slightly better thanks to a more regular distribution of the crop cover values.

Of course, the plant height for the potato fields is directly related to the soil cover fraction as shown in Figure 11. Unlike the other crops, the correlation

between these 2 variables is quite high and the relationships are linear.

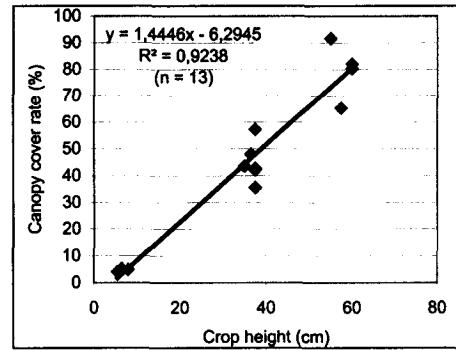


Figure 11: Relationship between the canopy cover fraction and the plant height for the potato fields.

Thus, both variables, i.e. canopy cover and crop height, can probably be estimated from the interferometric coherence values. However, the number of observations available does not allow to investigate further the accuracy of the estimation model which can be derived from such results.

D. Sugar Beet

The mean coherence has been extracted for 6 sugar beet fields at 3 different dates which correspond to the ground measurements taken during the growth season.

A linear relationship between the crop height and the coherence is presented in Figure 12. The coefficient of determination is smaller than those obtained previously. There is a sharp drop in the coherence value at the beginning of the growth when the plant height is lower than 25 cm. Then, only a slight decrease of the coherence occurs with the height increase. At this stage, the relationship can be linearised by a power function which improves significantly the determination coefficient. This aspect will be discussed further in the next paragraphs.

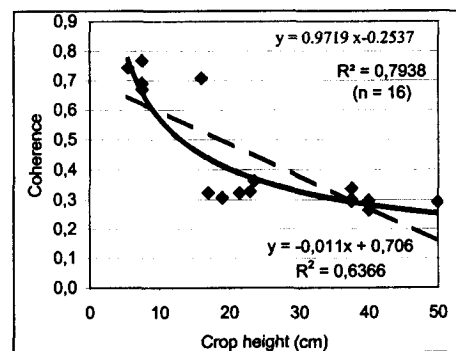


Figure 12: Relationship between the tandem coherence and the sugar beet height; linear regression and power regression.

Figure 13 shows the relationship between the canopy cover and the coherence. The  $R^2$  coefficient obtained for a linear regression is equal to 0.72 versus 0.64 for the crop height - coherence relationship.

The relationship between the plant height and the canopy cover of the sugar beet shows that the young

sugar beet leaves first cover the soil before they grow in height. The relationship between the plant height and the canopy cover is slightly lower than in the potato case ( $R^2=0.92$  for the potato versus 0.86 for the sugar beet). This is the reason why the linear relationship between the canopy cover and the coherence is stronger than the one between the crop height and the coherence (0.72 versus 0.64).

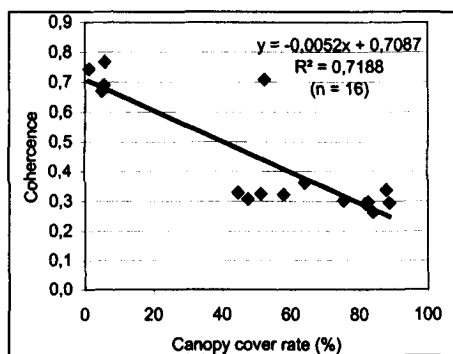


Figure 13: Relationship between the coherence and the canopy cover fraction for sugar beet fields.

#### E. Maize

Figure 14 shows the coherence as a function of the canopy cover for maize fields. The intensity of the relationship seems weaker than for the other crops ( $R^2 = 0.64$ ). However a similar linear decrease in the coherence value occurs with the vegetation growth in spite of the limited number of observations.

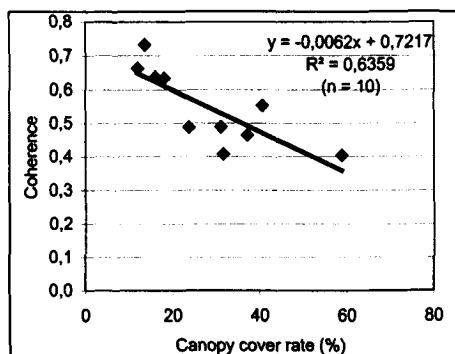


Figure 14: Relationship between the coherence and the canopy cover for the 10 maize fields.

#### F. Discussion

These results call for a complementary study in order to investigate further the observed relationships and their diversity. However the comparison of the results for the 4 species and for the 2 plant variables suggest some preliminary explanations. Besides some similarities, the shape of the various relationships between the plant variables and the coherence values varies according to each crop. The signal coherence is probably influenced by two types of scattering: the volume scattering and the surface scattering. The latter provides a more coherent signal as far as the soil is concerned. Its moisture and

roughness can be considered as stable for a 1-day interval.

Hereafter the shape of the relationships are split into three different phases which are discussed successively.

At the earlier stage, the coherence values for any crop (smaller than 10 cm high) varies between 0.7 and 0.8, except for the potato fields. The soil surface scattering dominates the signal and provides a very high and similar coherence for all the crops at this stage. For the potato, the very specific soil preparation producing a low-frequency roughness could explained the difference.

As the canopy cover increases for the 4 crops, a decrease in the coherence is observed, except for wheat. For instance, a canopy cover of 40 % corresponds to coherence value of around 0.4 for the sugar beet and the potato, around 0.5 for the maize and around 0.7 for the wheat. These differences can be related to the different types of plant structure and crop development. In particular, the leaves size and the plant height-canopy cover relationships varies significantly from one species to another.

The sugar beet shows the sharpest drop (0.4 unit) because of the large thick leaves with regards to the C-band wavelength. The surface scattering is probably the main source of signal but a main part of it comes from the crop leaves which are unstable scatterers (wind, water stress). This would be the reason why a rather low canopy cover affects so much the signal coherence.

At the opposite, the wheat plant seems transparent to the microwave signal in spite of high canopy cover (up to 70 %). The development phase of the plant structure for the wheat is illustrated in Figure 15: first the young plant increases its canopy cover and then it grows in height. This is the tillering stage. However, the wheat leaves are very small with regard to the C-band wavelength. It is expected that the only backscattering effect comes from the soil background which provides very high coherence values.

The potato case shows a intermediary effect with a coherence drop of 0.2 unit which could also be related to the plant development. Along with its growth in height the potato plant covers progressively the soil background with medium-size leaves.

In the last phase of development all the crops grow in height, their canopy cover reaches at least 80 % and all 1-day interval coherence values are as low as 0.3. This could be explained by the more important contribution of the vegetation in the signal backscattering relatively to the soil surface scattering. The vegetation contribution can probably be related to volume and/or surface scattering depending on the crop type.

For the wheat, the volume scattering seems the key factor because only dense canopy with longer leaves and higher stalks can significantly affect the signal coherence. Furthermore the canopy volume increase which is directly proportional to the height evolution is linearly correlated to the coherence decrease.

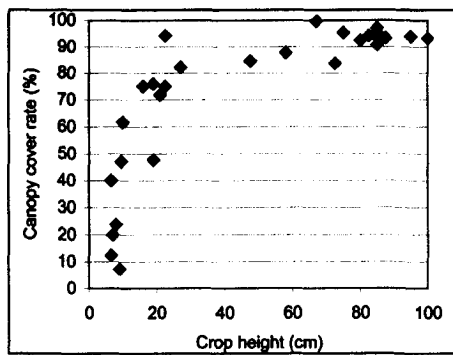


Figure 15: Relationship between the canopy cover rate and the crop height for 28 winter wheat fields.

For the sugar beet, the coherence values decrease only slightly during this last phase of plant development. This contrast between the first high drop and then this little change could indicate that the signal coherence is still mainly driven by the surface scattering which has almost saturated the coherence reduction since the earlier stage. This is confirmed by the rather curvilinear relationship between the crop height and the canopy cover as shown in the Figure 16.

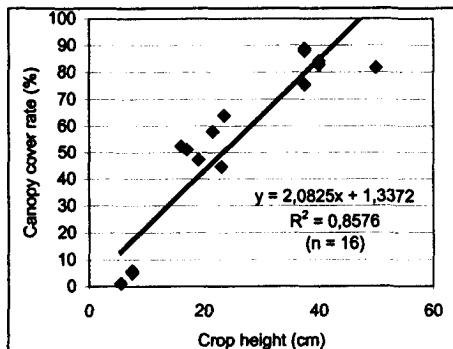


Figure 16: Relationship between the canopy cover rate and the height for 16 sugar beet fields.

The potato plant could be interpreted as an intermediary case combining volume and surface scatterings. The coherence reduction is not saturated by the first step of crop development and still sensitive to the further development where canopy volume and cover increase together.

#### IV. CONCLUSIONS

This paper confirms and documents in details the great interest of the coherence images derived from interferometric pairs for the agricultural applications. Six pairs of SAR tandem acquisitions and the corresponding 1-day interval coherence images have been analysed with regards to a synchronous field campaign including 24 fields distributed between 4 crops, i.e. winter wheat, sugar beet, potato and maize.

First the high sensitivity of the coherence to the plant height and the canopy cover is statistically demonstrated. Strong relationships between the plant height and the coherence are observed for the 4 crops. A prediction model of the wheat height has been computed and the mean absolute error of about 7 cm seems

compatible with the information requirements for a crop monitoring systems. The shape of these relationships varies according to the crop structure and their respective development type. These differences are discussed with regards to the correlation obtained between the canopy cover and the coherence.

Further understanding would definitively confirm the great potential exploitation and the operational limits of the interferometric coherence as a key source of information for crop monitoring. An other important conclusion of this study is the fact that a single source of data, i.e. a few tandem pairs, may provide relevant information for at least 4 crops unlike most of the other sources of information. The diversity in the plant structure of the crop selected for this study leads to expect similar results for most of the main European crops.

#### V. REFERENCE

- [1] E. Engdahl and M. Borgeaud, "ERS-1/2 Tandem Interferometric Coherence and Agricultural Crop Height", in *Proc. on Second International Workshop on Retrieval of Bio- and Geo-physical Parameters from SAR data for Land Applications, ESTEC, Noordwijk, The Netherlands, 1998*, p. 121.
- [2] U. Wegmüller and C. Werner, "Retrieval of Vegetation Parameters with SAR Interferometry", *IEEE Trans. on Geosci. Remote Sensing*, vol. 35, pp. 18-24, Jan. 1997.
- [3] U. Wegmüller, T. Strozzi, T. Weise and C. L. Werner, "ERS SAR Interferometry for Land Applications", Gamma Remote Sensing AG, Switzerland, Final Report ESTEC/Contract 11740/95/NL/PB(SC), Feb. 1997.
- [4] C. Barbier, P. Defourny, S. Dautrebande, J. Guiot and A. Ozer, "An Assessment of SAR Phasimetry by Case Studies in Tectonics and Agronomy", Centre Spatial de Liège, Liège, Belgium, Proposal in Announcement of Opportunity for the Scientific Exploitation of the ERS Tandem Mission, May 1996.
- [5] X. Blaes, E. Auquièrre and P. Defourny, "An assessment of SAR Phasimetry by case studies in tectonics and agronomy", UCL-Department of Environmental Sciences and Land Use Planning, Louvain-la-Neuve, Belgium, Final Report-UCL part, ERS Tandem Project B302, Jan 1999.
- [6] D. Derauw, *Phasimétrie par Radar à Synthèse d'Ouverture; théorie et applications*, Thèse de doctorat, Faculté des Sciences, Université de Liège, Liège, Belgium, 1999.

## Geometric and Physical Constraints on Recovering Snow Covered Area from SAR

R Caves<sup>1</sup>, S Quegan<sup>1</sup> and T Nagler<sup>2</sup>

<sup>1</sup>Sheffield Centre for Earth Observation Science,  
Hicks Building, University of Sheffield, Sheffield S3 7RH, UK.

<sup>2</sup>Institute for Meteorology and Geophysics,  
University of Innsbruck, Innrain 52, A-6020 Innsbruck, AUSTRIA.  
Tel: +44 114 222 3778, Fax: +44 114 222 3809, Email: S.Quegan@sheffield.ac.uk

### ABSTRACT

Snow covered area is an important variable in snowmelt runoff modelling. SAR can supply information on this parameter by detecting the decrease in the backscattering coefficient which occurs when the snowpack becomes wet. However, the method is subject to several geometric, geophysical and logistical constraints which limit its general applicability. These include missing coverage due to relief, reference image availability, inferring dry snow cover, validation and the sampling and time requirements for runoff modelling and forecasting. These are reviewed in this paper and where available, solutions are outlined along with their limits of applicability. Many of the topics discussed have relevance to other SAR applications.

### INTRODUCTION

Wet snow cover can be detected using spaceborne C-band (wavelength 5.7 cm) synthetic aperture radar (SAR) such as ERS and Radarsat [1]. SAR derived estimates of wet snow covered area (SCA), and hence inferred estimates of dry and total SCA, are of interest to various applications including snowmelt runoff modelling [2]. As part of a broader project promoting the use of EO data in snowmelt hydrology, SAR wet snow mapping has been demonstrated over a variety of geographical regions including the Zillertal basin in the Austrian Alps, the Tjaktjajaure basin in northern Sweden and the Spey basin in the Scottish Highlands [3-8]. This work has revealed a number of geometric, geophysical and logistical constraints to general application of the method. These are each discussed below. However, the SAR wet snow mapping method is first briefly described.

### SAR WET SNOW MAPPING

#### Theoretical Basis

At C-band, the penetration depth of dry snow is of the order of tens of metres and the backscatter mainly comes from the underlying surface [1,9]. In contrast, even 1% liquid water by volume reduces the penetration depth to tens of centimetres. As most losses

in the wet snow are due to absorption rather than volume scattering, the backscattering coefficient is substantially reduced [1]. Wet snow can therefore be detected by comparing calibrated backscatter values with those in a reference image from a period of no or dry snow cover.

#### Methodology

In order to ensure that the snow and reference images have the same imaging geometry, they are taken from the same repeat pass. Wet snow is detected by calibrating and registering both images, filtering each image to reduce speckle and then applying a threshold to their intensity ratio. Wet snow is detected if this is less than -3 dB. Relative calibration to radar brightness is sufficient for purposes of image ratioing [10] and registration of repeat pass images requires only translation. The ratioing cancels backscatter variations due to the local incidence angle. A transform for geocoding ratio images is defined by matching the reference image to a SAR image simulated from a DEM [11]; layover features are used as ground control points. A fuller description of the SAR wet snow detection method can be found in [1,4,6-8]

### GEOMETRIC CONSTRAINTS

The primary constraint arising from the SAR image geometry is missing coverage. Specific constraints also apply to large basins.

#### Missing Coverage Induced by Relief

The geographic coverage provided by SAR is appreciably reduced by even moderate relief. Missing coverage arises where relief causes the local incidence angle ( $\theta$ ) to be particularly low or high. As a result wet snow detection is limited to local incidence angles between 17° and 78° [1]. This is due to foreshortening and specular effects at low angles, and the poor signal to noise ratio at grazing angles. Foreshortening and grazing are themselves limited by local incidence angle ( $\theta \leq 0^\circ$  and  $\theta \geq 90^\circ$  respectively). Beyond this additional problems of missing coverage arise due to layover and radar shadow [12].

Some control over the local incidence angles within a scene is available through the choice of imaging geometry, namely the look angle (the angle subtended at the antenna between the radar beam and nadir). At steep look angles layover and foreshortening are the primary sources of missing coverage. As the look angle increases, layover and foreshortening decrease while radar shadow and grazing increase. Amongst current spaceborne SAR systems, the mid-beam look angle ( $\alpha$ ) of ERS is fixed at  $20^\circ$  while Radarsat offers a mid-beam look angle of between  $20^\circ$  and  $40^\circ$ . For three basins of differing relief and mid-beam look angles of  $20^\circ$  and  $40^\circ$ , Table 1 lists the percentage area of each basin affected by missing coverage and the breakdown into layover, radar shadow, foreshortening and grazing (note: layover and foreshortening can overlap). DEMs of the basins were used to identify areas of layover and radar shadow [10] and to calculate local incidence angles [11]. All of these calculations were based on orbit parameters for actual ERS and Radarsat frames. The basins include a high relief alpine basin (the Zillertal in Austria, elevation range 560 to 3503 m), and two higher latitude basins of more moderate relief, the Tjaktjajaure basin in Northern Sweden (450 to 2044 m), and the Spey basin in Scotland (198 to 1284 m). The elevation ranges are listed to give a rough indication of the amount of relief.

Table 1. The effect of look angle  $\alpha$  on the percentage area of missing coverage in three basins of differing relief, including the breakdown into layover, radar shadow, foreshortening and grazing [3,6,8].

Basin	$\alpha$	Tot.	Lay.	Sha.	For.	Gra.
Zill.	$20^\circ$	38.8	34.9	< 1	3.9	NA
Zill.	$40^\circ$	10.6	0.9	0.4	9.3	NA
Tjak.	$20^\circ$	12.0	6.0	0.08	8.0	0.01
Tjak.	$40^\circ$	2.1	0.4	0.9	0.3	0.7
Spey	$20^\circ$	21.8	7.4	0.06	18.6	0.003
Spey	$40^\circ$	1.7	0.56	0.29	0.91	0.2

At the steeper,  $20^\circ$ , look angle (ERS or Radarsat), missing coverage affects a large part (38.8 %) of the Zillertal basin, most of which is layover. Missing coverage is considerably less (12 to 21.8 %) in the more moderate relief basins, but is still appreciable. Here, foreshortening rather than layover is the dominant cause. In all three basins radar shadow and grazing are comparatively insignificant.

Because the look angle varies across the image swath, the amount of missing coverage also depends on the range position of each basin within the swath. This effect can be observed in the results for the Tjaktjajaure

and Spey basins. Based on the elevation range, the Tjaktjajaure basin would be expected to be worse affected than the Spey basin. However, the contrary is true due to the range positions the basins were imaged at, in these examples. Tjaktjajaure was imaged at far range, hence layover and foreshortening were reduced relative to mid-swath. The opposite occurs with the Spey which was imaged at near range. On adjacent passes to those used here, the basins will be imaged at a more/less distant range and hence will exhibit slightly less/more missing coverage.

At the shallower,  $40^\circ$ , look angle (Radarsat only) missing coverage is markedly lower in all three basins. This is due to the reduction in layover being much greater than the increase in radar shadow and grazing. While the Tjaktjajaure and Spey basins show a decrease in foreshortening the Zillertal basin shows an increase. This is due to part of the area that was previously affected by layover now being affected by foreshortening. Foreshortening is now the dominant source of missing cover in the Zillertal and Spey basins while radar shadow is the dominant source in the Tjaktjajaure basin. The differences between the Spey and Tjaktjajaure basins can once again be explained by their relative range positions.

The above examples illustrate that at steep look angles missing coverage can be a severe constraint to estimating wet SCA over regions of even moderate relief (1000 m variation in elevation). At shallower look angles, the problem is greatly reduced but can still exceed 10 % of the image in regions of high relief. Finally, it should be noted that steeper slopes, and hence missing coverage, more often occur at mid to higher elevations where snow cover is more likely [3].

Two approaches have been developed to reduce the effects of missing coverage:

- Image combination;
- Inferring wet snow cover in areas of missing coverage.

#### *Image Combination*

Missing coverage can be reduced appreciably by combining images taken from different viewing directions, such as the ascending and descending passes of a spaceborne SAR [1]. For example, the combination of ERS passes reduces missing coverage over the Spey and Zillertal basins to less than 1 % and 6 % respectively [3,6].



The usefulness of this approach is limited by the temporal lag between the ascending and descending passes which is latitude dependent. Wet snow detection requires both images to be taken close together in time during a period of little change in snow conditions. In the Alps ( $\sim 47^\circ$  N), where the wet snow detection method was originally developed, the lag between the two passes is only half a day [1]. However, at most other latitudes the lag is a day or more longer. For example, for the Spey and Tjaktjajaure basins the time lags are 1.5 and 6.5 days respectively. While snow conditions may remain stable over such intervals during a cold period of no snow melt, this is unlikely during melting periods. Hence, inferences on wet SCA based on image combination are unlikely to be valid in these basins.

#### *Inferring Wet Snow Cover in Missing Coverage*

A statistical method for inferring wet snow in areas of missing cover has been developed, based on zones of similar aspect and elevation [4,5]. It uses the following steps:

1. The image is classified into zones defined by elevation and aspect.
2. The area of wet snow,  $A_i$ , and other surfaces (excluding missing cover),  $B_i$ , is calculated for each zone  $i$ , and the proportion of wet snow cover for that zone is calculated as  $P_i = A_i/(A_i+B_i)$ .
3. If  $P_i > T$  all areas of missing cover within that zone are classified as wet snow.

The use of a hard threshold causes wet SCA to be over/under-estimated within some zones. However, for an appropriate choice of threshold these errors will balance out in the total wet SCA. A value of  $T = 50\%$  has been used. This is suitable when the area of zones has a symmetric distribution with respect to  $P$ . Since this is not always the case a more optimal method is needed to select the threshold. An alternative would be to apply a fuzzy rather than a binary classification. Pixels in missing cover would be assigned their corresponding  $P_i$  value. Elsewhere, wet snow pixels would be assigned the value 1 and all other pixels the value 0. The total wet SCA could then be estimated by simply summing pixel values in the fuzzy classification.

The method needs at least part of any given aspect-elevation zone to be unaffected by missing cover and this determines how finely aspect and elevation are partitioned. In Tjaktjajaure, where the method has been

applied over several melt seasons,  $15^\circ$  aspect zones and 100 m elevation zones were found to be adequate.

#### *Spatial Coverage over Large Basins*

The scan SAR and wide beam modes available with Radarsat enhance SAR capability for wide area coverage ( $> 100$  km) by a single image. However, where two or more images are still required to cover a basin two constraints apply. The first is purely geometric while the second introduces a problem of geophysical interpretation.

- Where the basin just extends over consecutive frames in the azimuth direction the reference and snow frames need to be accurately mosaicked prior to ratioing. If mosaicking is left to after ratioing gaps can arise due to slight differences in the start and end times of repeat frames.
- Where it is not possible to cover the basin within the image swath, images from two or more distinct times will be needed to provide coverage. Hence, the problems of geophysical interpretation of snow maps from different dates, already noted earlier with respect to image combination, will apply. This problem can be circumvented by splitting the basin into smaller sub-basins each of which can be covered by a single swath.

#### **GEOPHYSICAL CONSTRAINTS**

The SAR snow mapping method is subject to a variety of geophysical constraints including reference image choice, other types of backscatter change, wet snow detection in forest, dry snow inferences and validation.

#### *Choice of Reference Images*

Images from cold winter periods with only dry or no snow cover give the best reference for detecting backscatter change due to wet snow. However, such conditions can be infrequent in temperate maritime basins having seasonal but generally wet snow cover, e.g. basins in the Scottish Highlands. Opportunities for acquiring suitable winter reference images will then be rare. In such cases reference images should be selected from long dry periods during the summer.

The dependence of reference images on specific surface conditions and speckle can be reduced by averaging multiple reference images, if available.

### Other Types of Backscatter Change

Wet snow detection is based on backscatter change which can also arise from other causes, such as agricultural activity, flooding and wind roughening of open water. Land cover and elevation information can be used to mask out areas likely to be affected. However, mis-classification will occur where other change cannot be predicted.

### Wet Snow Mapping in Forest

Mapping snow cover under forest is difficult with both SAR and optical sensors. It has been shown that wet snow can be detected by C-band SAR in sparse forests [13] but not in thicker forest [14]. Hence, land cover information should be used to mask out forested areas.

### Inferring Dry Snow Cover

Following wet snow detection, dry snow cover must be inferred. If it is assumed that snow cover patterns remain similar from year to year, a map of dry snow cover can be built up from wet snow maps from later periods in previous melt seasons [7]. This requires an archive of SAR-derived wet snow maps from previous years. Where archive data is unavailable a "hill climbing" approach which classifies pixels lying above wet snow as dry snow, can be adopted [4,5].

The hill climbing approach assumes that snow cover is complete at higher elevations, but this is often not the case; for example, exposed ridges are often snow free. Hence, this approach tends to overestimate SCA. By contrast the archived data approach distinguishes between snow-covered and snow-free areas at higher elevations and is the preferred method if sufficient data is available.

### Geophysical Validation

To check the accuracy of SAR derived (wet+dry) snow cover maps, they have been compared with snow cover maps derived from near coincident high resolution optical data.

In the Zillertal basin good agreement was found between snow maps derived from ERS and Landsat TM (7 day gap, 86.4 % agreement) and Radarsat and Landsat TM (2 day gap, 82.8 % agreement) [6-8]. In both cases SAR was observed to underestimate snow cover relative to TM.

By comparison, in the Tjaktjajaure basin marked differences were found between snow maps derived

from ERS and Landsat TM (2 day gap) [4,15]. Overall the SAR SCA is 15 % less than the TM SCA but the differences are elevation dependent (Fig. 1).

- Above 1500 m, the SAR SCA is near 100 % and is considerably greater than the TM SCA. This is probably because of overestimation by the hill climbing approach used to infer dry snow cover, as noted above. The TM+SAR common SCA is also coincident with the TM SCA indicating all snow cover detected by TM is also detected by SAR.
- Between 1200 m and 1500 m, the TM SCA changes to being greater than the SAR SCA with the maximum SAR and TM SCA occurring at around 1400 m, although the SAR maximum is slightly greater and at a higher elevation than the TM maximum. Confusion between the SAR and TM SCA is indicated by the common SCA being less than either.
- Below 1200 m, SCA is significantly underestimated by SAR relative to TM and the common SCA is coincident with the SAR SCA indicating that all the snow cover detected by SAR is also detected by TM. Analysis of the TM image reveals that snow cover is increasingly patchy at these lower elevations. It is suspected that this patchiness reduces the backscatter change due to wet snow to below the -3 dB detection threshold. Such a reduction in backscatter change has been observed in areas of patchy wet snow elsewhere in Scandinavia [16] and in the Spey basin in the Scottish Highlands [3].

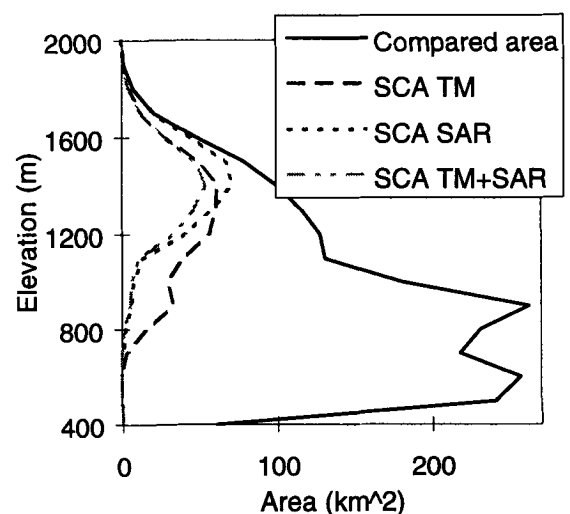


Fig. 1. Tjaktjajaure: elevation plots of the basin area, the SCA derived from Landsat TM (25/06/92) and ERS SAR (23/06/92) and the SCA common to both sensors.

If patchy snow cover is the cause of SAR underestimating SCA at lower elevations in higher latitude basins, similar effects might be expected in alpine basins. However, due to the greater relief in alpine basins, slopes are steeper and the transition zone from full to no snow cover is much narrower.

The SCA differences observed in the Tjaktjajaure basin need to be resolved before SAR derived SCA can be reliably used in snowmelt forecasting in similar basins, particularly if SCA estimates derived from SAR and optical EO are to be used together.

### LOGISTICAL CONSTRAINTS

Snowmelt runoff modelling requires weekly estimates of SCA [17]. Also for near real-time forecasting of snowmelt runoff, SAR derived estimates of SCA must be available within a day of data acquisition. Below we discuss how these conditions can be met using current spaceborne SARs.

#### Temporal Coverage

Over most basins of interest four images can be acquired by ERS within its 35 day repeat cycle (i.e. using adjacent ascending and descending passes from the 16 day sub-cycle). This gives an average of one image every 8.25 days, just outside the one week requirement. However, the temporal pattern of coverage is latitude dependent due to the lag between ascending and descending passes, which was discussed earlier under image combination. In terms of even spacing of temporal coverage short lags are disadvantageous. For example, over Zillertal the interval between passes ranges from 0.5 to 18.5 days, while over Tjaktjajaure the interval between passes ranges from 6.5 to 12.5 days.

The shorter 24 day repeat cycle of Radarsat combined with a steerable beam means that basins of interest can be imaged more frequently than with ERS. The pattern of temporal coverage will still be determined by latitude. Radarsat and ERS temporal coverage will of course be reduced if other applications impose data acquisition conflicts.

#### Near Real Time Transfer of Data

During 1999, ERS data were used to derive snow cover maps for forecasting snowmelt runoff in Tjaktjajaure and Zillertal. While the required timescale was 24 hours, normal delivery of ERS PRI data takes two weeks. However, cooperation by ESA and D-PAF allowed a special fast data delivery chain to be formed.

The raw SAR data was downloaded to the Neustrelitz receiving station and processed by DFD within 1.5 to 6.5 hours of data acquisition. Data transfer (130 Mbytes) to the customers in Austria and the UK then took between 5 and 20 minutes. Finally, geocoding and classification by the customer took under 2½ hours. This delivery chain permitted snow maps to be derived from descending (morning) passes within 6 hours. Ascending (evening) passes took longer due to data transfer not taking place until the following morning. However, snow maps were still derived well within 24 hours.

### CONCLUSIONS

- While it has been clearly demonstrated that C-band SAR can be used to estimate snow covered area, general application of the method is constrained by the factors reviewed in this paper. Where available, possible solutions have been indicated.
- In regions of moderate to high relief geographic coverage can be constrained by missing coverage. This can be substantially reduced by using shallow incidence angles, such as are available from Radarsat (and will be available from Envisat). This approach is preferable to image combination, which is latitude dependent, and inferences based on aspect and elevation.
- Large basins introduce specific problems of image mosaicking and geophysical interpretation.
- SAR wet snow mapping is dependent on the availability of suitable reference images. These are more easily obtained under dry continental climates than wet maritime climates.
- The wet snow classification has to make allowance for other types of backscatter change and lack of snow detection in forest.
- For inferring dry snow cover from SAR images, use of an archived data approach is preferred to the hill climbing approach, again subject to suitable data availability.
- While snow maps derived from SAR and high resolution optical data show good agreement in an alpine basin, large elevation-dependent differences are observed in a higher latitude basin. At higher elevations the difference is due to incorrect inferences on dry snow cover. At lower elevations it

is suspected that the difference is due to patchy snow cover being underestimated by SAR.

- Snowmelt runoff modelling requires weekly estimates of SCA. Of current spaceborne SARs Radarsat can meet this requirement while ERS can provide near weekly coverage, dependent on latitude.
- Data transfer and processing facilities are sufficiently fast for providing data for use in near real time forecasting of snowmelt runoff.
- While this paper is written in the context of snow mapping, many of the constraints equally apply to other SAR applications involving change detection and time series analysis. The problem of missing coverage needs to be addressed in any area of moderate to high relief. While the geophysical constraints are mainly application specific, the logistical constraints will be of concern to any applications requiring regular repeat coverage and near real-time data access.

#### ACKNOWLEDGEMENTS

This work was conducted as part of HYDALP (Hydrology of Alpine and High Latitude Basins) which is a CEO Shared Cost Action Project of the European Union DGXII 4th Specific Programme for Climate and Environment (Contract number ENV4-CT96-0364).

#### REFERENCES

- [1] T. Nagler, *Methods and analysis of synthetic aperture radar data from ERS-1 and X-SAR for snow and glacier applications*, PhD Thesis, University of Innsbruck, 1996.
- [2] A. Rango, Spaceborne remote sensing for snow hydrology applications, *Hydrological Sciences Journal*, vol. 41 no. 4, pp. 477-494, 1996.
- [3] R. Caves, et al, Field verification of SAR wet snow mapping in a non-Alpine environment. In Proc. *2nd International Workshop on Retrieval of Bio- and Geo-physical Parameters from SAR Data for Land Applications*, ESA SP-441, pp. 519-526, 1998.
- [4] R. Caves, et al, The use of Earth Observation for monitoring snowmelt runoff from non-alpine basins. In Proc. *EARSel Symp.*, 1999.
- [5] R. Caves, et al, Improvements in snowmelt runoff modelling and forecasting using EO data. In Proc. *Remote Sensing Society Conf.*, pp. 525-533, 1999.
- [6] T. Nagler and H. Rott, 1998. SAR tools for snowmelt modelling in the project HYDALP, In Proc. *IGARSS'98*, pp. 1521-1523, IEEE.
- [7] T. Nagler, H. Rott and G. Glendinning, SAR-based snow cover retrieval for runoff modelling, Proc. of *2nd Int. Workshop on Retrieval of Bio- and Geo-physical Parameters from SAR data for Land Applications*, ESA SP-441, pp. 511-517, 1998.
- [8] T. Nagler, H. Rott and G. Glendinning, Snowmelt modelling using Radarsat data, In Proc. *ADRO Final Symp.*, 1998.
- [9] C. Mätzler, Applications of the interaction of microwaves with the natural snow cover, *Remote Sensing Rev*, vol. 2, pp. 259-387, 1987.
- [10] H. Laur, et al, *Derivation of the backscattering coefficient in ESA ERS SAR PRI products*, ESA Document No: ES-TN-RS-PM-HL09, Issue 2, Rev. 4, 1997.
- [11] B. Guindon and M. Adair, Analytic formulation of spaceborne SAR image geocoding and value-added product generation procedures using digital elevation data, *Canadian Journal of Remote Sensing*, vol. 18, no. 1, pp. 2-12, 1992.
- [12] G. Schreier, Geometrical properties of SAR Images, In, G. Schreier (Ed.), *SAR Geocoding: Data and Systems*, pp. 103-134, Wichmann, 1993.
- [13] J.T. Koskinen, J.T. Pulliainen and M.T. Hallikainen, The use of ERS SAR data for snow melt monitoring, *IEEE Trans. Geoscience and Remote Sensing*, vol. 35, no. 3, pp. 601-610, 1997.
- [14] N. Baghdadi, Y. Gauthier and M. Bernier, Capability of multitemporal ERS-1 SAR data for wet snow mapping, *Remote Sensing of the Environment*, vol. 60, pp. 174-186, 1997.
- [15] R. Caves, et al, Comparison of snow covered area derived from different satellite sensors: implications for hydrological modelling. In Proc. *Remote Sensing Society Conf.*, pp. 545-552, 1999.
- [16] T. Guneriusson, Backscattering properties of a wet snow cover derived from DEM corrected ERS-1 SAR data, *International Journal of Remote Sensing*, vol. 18, no. 2, pp. 375-392, 1997.
- [17] A. Rango, Snow hydrology processes and remote sensing, *Hydrological Processes*, vol. 7, pp. 121-138, 1993.

Assessment of multi-temporal products for multi-thematic applications with ERS SAR Data  
 J. Bruniquel<sup>(1)</sup>, H. Sassier<sup>(1)</sup>, S. Péraudeau<sup>(1)</sup>, L. Rognant<sup>(1)</sup>, S. Goze<sup>(1)</sup>, G. Chust<sup>(2)</sup>, D. Ducrot<sup>(2)</sup>, K. Fellah<sup>(3)</sup> and H. Laur<sup>(4)</sup>

- (1) : ALCATEL SPACE INDUSTRIES (DI/IS/ISR), 2, av. J.F. Champollion, BP 1187, 31037 Toulouse Cedex, France  
 Phone : +33-5-3435-4710 ; Fax : +33-5-3435-6163 ; Email : Jerome.Bruniquel@space.alcatel.fr  
 (2) : CESBIO (CNES/CNRS/UPS), 18 avenue E. Belin, BP 2108, 31401 Toulouse Cedex 4, France  
 (3) : SERTIT, boulevard S. Brandt, 67400 Illkirch, France  
 (4) : ESA/ESRIN, via G. Galilei, Casella Postale 64, 00044 Frascati, Italy

### ABSTRACT

The diversity of information is highly desirable to monitor land surface processes with SAR and is often obtained through temporal acquisition. However, large temporal sets are difficult to interpret and the extraction of information is often performed on an image per image basis. In this study, we focus our work on the optimal use of a temporal set of images. Precise change detection techniques as well as land use classification have been performed and a visualisation combining cartographic map and information of temporal change is proposed.

### INTRODUCTION

The diversity of information is highly desirable to monitor land surface processes with Synthetic Aperture Radar (SAR). The current available civil sensors can be considered to be poor in terms of diversity of acquisition : ERS-1/2 can only provide multi-temporal channels, RadarSat-1 combines temporal and incidence angle acquisitions. Therefore, for numerous applications, the lack of diversity must be overcome by a greater amount of data than it would have been necessary otherwise. ERS sensors offer the possibility to obtain sufficient data within a year (at least one per month, two in case of tandem pairs). In that case, the only possible characterisation of the land surface is done by studying the temporal variations. However, large temporal sets (say more than 3 images) are difficult to interpret and the extraction of information is often performed on an image per image basis.

In this study, we focus our work on the optimal use of a temporal set of images. The images were provided by ESA<sup>®</sup>, in the frame of the third *Announcement of Opportunities* AO3-405, and were acquired over three test sites

- the Grand Morin, located in the south-east of Paris. The set is composed of 8 Single Look Complex (SLC) images, both from ERS-1 and ERS-2 ;
- the Minorca island whose temporal set is composed of 12 images ;
- the Mulhouse site where 9 images are available.

Ground truth and/or optical image are also available for these sites to assess some quantitative results. Only

works achieved on the first test site are presented in this paper.

Various existing tools are used to extract the temporal information and to derive land use map. Image processing tools like filtering and/or segmentation enhance the statistical accuracy of some features permitting to give indication on the type of terrain (variation of radiometry and correlation) while more sophisticated tools like classification allow to go deeper to the establishment of thematic products.

### DATA SET

The agricultural « Grand Morin Basin » test site is located in East of Paris (3°14'East, 48°35'North). Eight ERS images are available on the test site. Two tandem data couples were acquired on 24-Dec-95/25-Dec-95 and 03-Mar-96/04-Mar-96 respectively. The 4 last images are spread over the year 97 depending on the crop cycle : 24-Mar-97, 28-Apr-97, 07-Jul-97 and 11-Aug-97. It must be added that this test site has been already under consideration in the frame of an ADRO project where 4 Radarsat images in the F1 mode were acquired on 1997 [1]. The landscape is mainly composed of agricultural parcels : maize, corn, barley, sugar beet, pea, colza, forest, grass, bare soil and urban. To assess the various results mainly concerning the classification process, a ground truth collection was performed by SOGREAH Ingénierie and CGE (Compagnie Générale des Eaux) on 10-Jul-1997 in order to identify the land cover and the various parcels. Radiometric variations as well as classification tools will be studied with the 1997 data while coherence will be more particularly studied with tandem data.

### PRE-PROCESSING STEPS

#### Co-Registration

The first step of this work consists in co-registering the images in the same geometry. For ERS data, distortion is generally not severe, nevertheless the offset in azimuth and range may vary within the swath. The co-registering process is based on the correlation between two images and is performed over SLC data to take into account the Mean Doppler Centroid.

### Speckle Filtering

Because of speckle interferences and inferred granularity, the visual interpretation is difficult and the statistical estimation is not accurate enough. In the later case, filtering processes are necessary to really exploit the microwave information. Following our experience gained in this field, the best result is obtained by combining multi-temporal summation with a spatial filter. This combination leads to a better trade-off between spatial degradation and speckle reduction than with a single spatial filter. All the steps necessary to achieve the required speckle reduction are summarised in [2].

In our case, the filtering process is mainly applied to enhance the statistical estimation of various variables that are used hereafter. Consequently, a possible slight degradation of the spatial resolution can be allowed since it is more important to well smooth the images than to perfectly preserve all the thin structures. Following these steps of radiometric improvement, it is possible to produce various indexes map with a high level of confidence such as map of radiometric variation or map of correlation, ...

### Segmentation map

All the tools that are adaptive are applied through a sliding window whose drawback is to degrade strongly the spatial resolution. Some improvements have been proposed in the past. One possible technique is to refine the local window so as to exclude detected edges, lines or strong scatterer. The window is split into two parts and the ratio of intensity of each sub-area is compared to a fixed threshold (depending on the desired false alarm rate) [2]. This approach works well to preserve most of thin structures. However, the number of samples used in each sliding window is reduced and then the speckle reduction achieved with a structural detection process is lower than with a full window.

It is possible to overcome this drawback by segmenting the image. This step aims at decomposing an image in non-overlapping regions characterised by constant reflectivity [3]. This approach is particularly well adapted to agricultural landscape and we used it for the Grand Morin test site.

## CHANGE DETECTION

### Radiometric Variation

The follow-on of the mean radiometry through a temporal set is *a priori* a simple way to discriminate land surfaces. Agricultural land surfaces are able to vary much more (depending on the type of crops and human intervention) than forest or urban areas. Mean radiometry ratio between each image indicates change that

occurred date after date. This ratio of mean radiometry is expressed as below with a logarithm scale

$$\forall i \neq j \in [1, N], \Delta\sigma_{ij} = 10 \log(\bar{I}_i / \bar{I}_j) \quad (1)$$

where  $i$  and  $j$  refer to different dates and  $N$  is the number of images. There are  $N(N-1)/2$  possible couples to study. Hence, the number of combination raises up significantly when the number of images increases. Consequently, the temporal signatures analysis is not so easy and it is of interest to reduce the number of indexes.

One possible technique consists in performing Principal Component Analysis (PCA) on the original images (or rather on the filtered images, PCA being definitively not adapted to data corrupted by a multiplicative noise) or on various indexes such as the radiometric ratio [3].

The different change detection indexes calculated for each couple can be simplified by a simpler but more consistent description. For instance, a very relevant approach is to take the maximum among all the indexes expressed in (1)

$$\forall i \neq j, \max\_var = \max|\Delta\sigma_{ij}| \quad (2)$$

Equation (2) is actually expressing the amplitude of variation within the temporal set and allows the discrimination of surfaces submitted to numerous changes (such as agricultural land) with those which are more stable (forest for instance).

### Coherence Change

The coherence is sensitive to changes that occur within the resolution cell. It is well known that the modulus of coherence drops if the position of the scatterers inside the cell is slightly different from one acquisition to another. Hence, it is mainly sensible to very small movements of about half-wave range and the physical meaning of such change is sometime not so easy to interpret. Another difficulty concerns the estimation of the coherence, specially when the number of samples is low which implies a bias coupled with a high variance. In our case, with a sliding window approach, we used large window (15x5) and performed the estimation over the SLC images. Then, the coherence map has been shrunk so as to be in a square geometry. This approach is compatible to the one that has been presented by Touzi *et al.* [5]. Of course, the segmentation pre-process step permits the use of a higher number of samples and is therefore particularly benefit for the coherence estimation.

### Visualisation of the Results

It is always possible to display every index map (coherence map for instance) on its own. Nevertheless, we find more comfortable to associate the thematic information with the SAR image of the area. Hence, the

recognition of the main landscape structures is easier. The SAR image which is used as a background is the temporal mean of the 8 images acquired over the site, presented with a spatial filtering process to enhance the interpretation. The colour information corresponding to the thematic information content is added as a new layer over the background image. It must be noted that this background image could be obtained by another sensor (e.g. panchromatic image), the thematic information being extracted by the SAR acquisitions.

The temporal mean image is presented in fig. 1. Fig. 2 displays the grey-level background image and the colour information is obtained from the amplitude of variation index expressed in (2) calculated with a sliding window. Fig. 3 shows the same index except that it has been estimated with a region approach. The correlation calculated with the second tandem pair is displayed on fig. 4.

### CLASSIFICATION TOOLS

#### Description of the Methods

For the classification, two main methods can be applied to minimise the inter-class confusion caused by the speckle noise: (1) pixel-by-pixel basis classification which requires a preliminary spatial or temporal speckle filtering, (2) contextual method based on sliding windows or regions obtained by a preliminary segmentation [7]. Several tests [1] have shown that best results are obtained with contextual methods (and without filtering pre-processing). The contextual methods consist in classifying pixels of a same region (segmentation process) or to consider the pixel neighbourhood (window analysis). The statistical properties of the radar distribution are taken into account. The Gauss-Wishart maximum likelihood is applied for supervised classification.

#### Results

Classification has been performed with a varying number of images (from one date to the full set) so as to evaluate the required number of images that leads to acceptable classification rate. The results are analysed with the proportion of Pixel Correctly Classified (PCC) of each class i.e. the percentage of well classified pixels for each class. It allows to assess the classification accuracy.

The temporal contribution is important. The mean of PCC on the classes is between 30% and 48% with one

date according to the chosen dates (winter, spring or summer dates), 43%-53% with two dates, 52%-70% with three dates and 57%-72% with four dates, about 72% with five dates and 82% with seven dates. The eighth date does not bring any additional information and thus any improvement. Visualisation of classification performed with the full set is presented in fig. 5.

### CONCLUSION

This study has highlighted the utility of temporal SAR acquisitions through the ERS sensors. It has been shown in particular that 6 dates lead to a very acceptable classification rate, actually close to the one that can be obtained with optical data (but with a fewer number of dates).

Further investigations will be carried out to see how the indexes proposed in the first part are useful for thematic interpretation of a SAR temporal set and for classification process.

### REFERENCES

- [1] D. Ducrot *et al.*, « Contextual methods for multi-source land cover classification with application to RADARSAT and SPOT data », *Proceedings of SPIE Europto'98*, Barcelona, Spain, 1998.
- [2] J. Bruniquel and A. Lopès, « Multi-variate optimal speckle reduction in SAR imagery », *Int. J. Remote Sensing*, Vol. 18, No. 3, pp. 603-627, 1997.
- [3] R. Fjørtoft *et al.* « An optimal multiedge detector for SAR image segmentation », *IEEE Trans. Geoscience and Remote Sensing*, Vol. 36, No. 3, pp. 793-802, May 1998.
- [4] R. Touzi, A. Lopès and P. Bousquet, « A statistical and geometrical edge detector for SAR images », *IEEE Trans. Geoscience and Remote Sensing*, Vol. 26, No. 6, pp. 764-773, November 1988.
- [5] Y. Moisan, M. Bernier and J.-M. Dubois, « Détection des changements dans une série d'images ERS-1 multitudes à l'aide de l'analyse en composantes principales », *Int. J. Remote Sensing*, Vol. 20, No. 6, pp. 1149-1167, 1999.
- [6] R. Touzi *et al.*, « Coherence estimation for SAR imagery », *IEEE Trans. On Geoscience and Remote Sensing*, Vol. 37, No. 1, pp. 135-149, 1999.
- [7] F. Sery *et al.*, « Multisource classification of SAR images with the use of segmentation, polarimetry, texture and multitemporal data », *Proceedings of SPIE Europto'96*, Taormina, Italia, Sep. 1996.

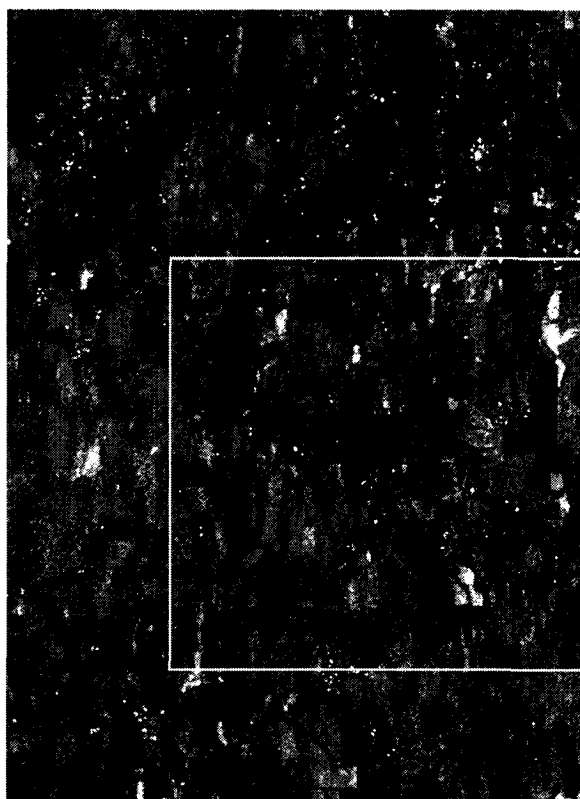


Figure 1 – Temporal mean image of the test site – the frame indicates the restricted area

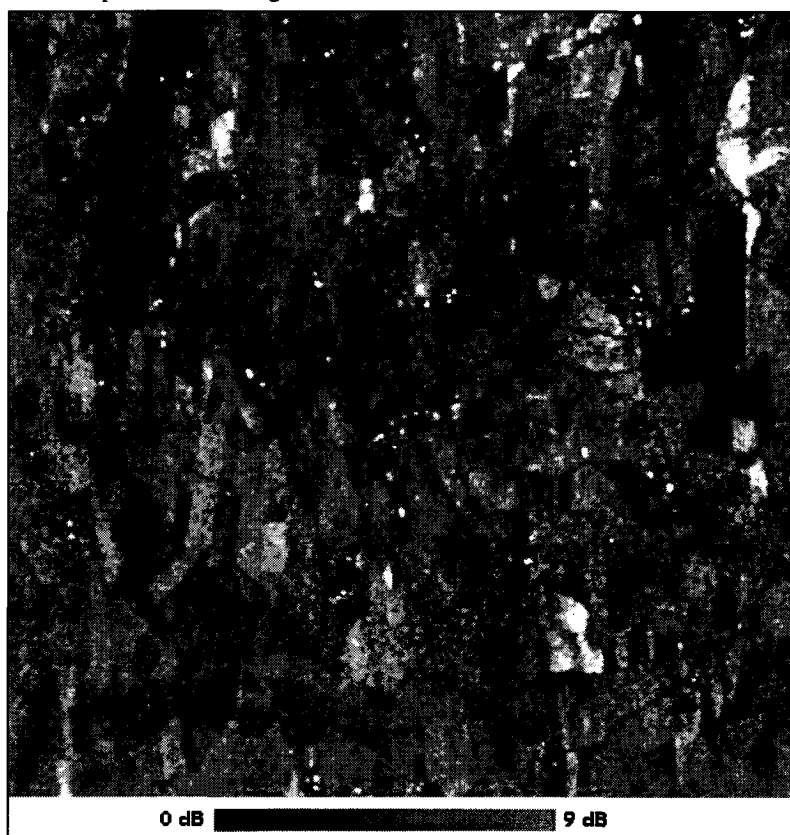


Figure 2 – Background image whose colour information represents the maximum amplitude of the radiometric variation estimated over a sliding window



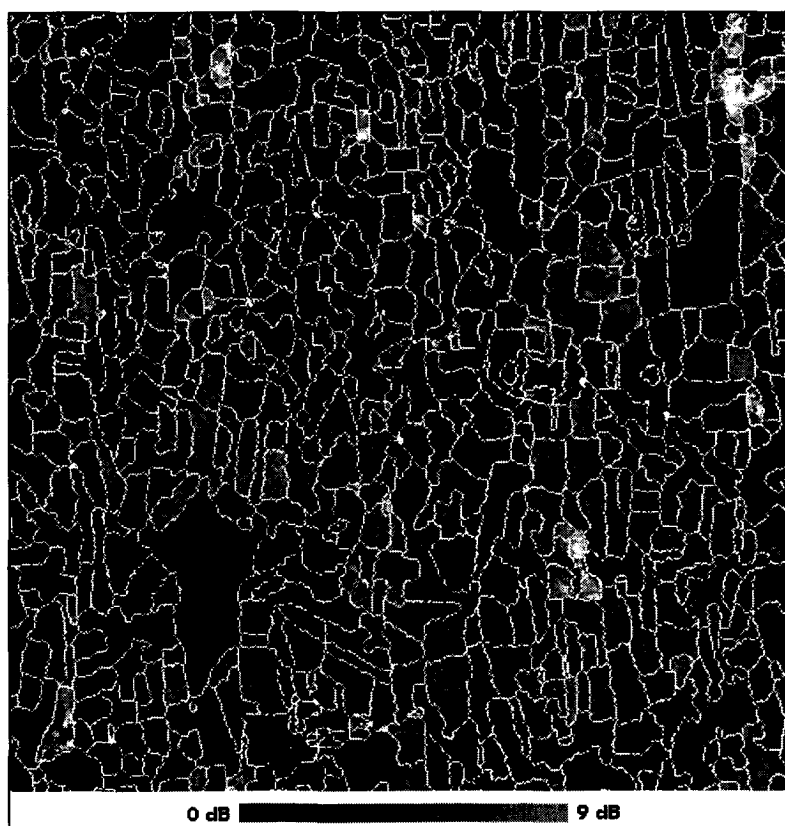


Figure 3 – Background image whose colour information represents the maximum amplitude of the radiometric variation estimated over a segmentation map

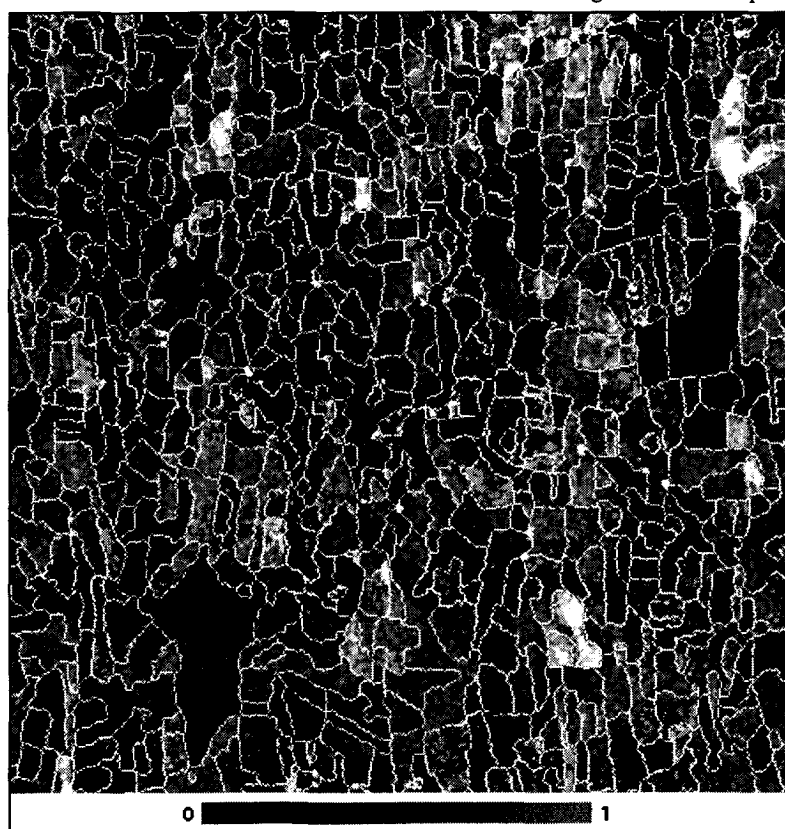


Figure 4 – Background image whose colour information represents the correlation estimated over a segmentation map



Figure 5 – Supervised Classification map obtained with 8 ERS dates

## A Global NRCS Database Derived from ERS Scatterometer Data

C.C. Lin<sup>1</sup> and V. Wismann<sup>2</sup>

- 1) ESTEC (APP-FPE), PO Box 299, 2200 AG Noordwijk, The Netherlands  
T: +31-71-5655813; F: +31-71-5654696; E: clin@estec.esa.nl
- 2) Institute for Applied Remote Sensing, Klarastrasse 81, 79106 Freiburg, Germany  
T: +49-761-2851717; F: +49-761-2851719; E: wismann@ifars.de

### ABSTRACT

A database containing the information of nearly seven years of ERS Scatterometer data has been set-up for global statistical analysis of the C-band radar backscatter over land and ice surfaces. The data were re-sampled onto a Goode Homolosine map projection with a grid spacing of 50 km and incidence angles bins of 5 degrees. For 3-month intervals histograms of the measured NRCS were stored for each incidence angle bin and grid point in this database. A graphical user interface offers various tools for statistical analyses and manipulations of the data, which can be selected interactively based on temporal and spatial windows or classification constraints. The classifications provided within the databases are based on radar data, e.g., mean NRCS and mean incidence angle dependence and also comprise the Matthews vegetation types and the Leemans' Holdridge Life Zones classification. The open architecture of the database and the GUI allows continuous updating as well as integrating any other user defined classification scheme or data analysis tools. The database together with the GUI can be obtained free of charge on CD-ROM from the European Space Agency.

### INTRODUCTION

The Windscatterometers (AMI-Wind) of the European Remote Sensing Satellites ERS-1 and ERS-2 provide global measurements of the normalized radar cross section (NRCS) at C-Band (5.3 GHz) and vertical polarization (VV) of the Earth's surface since August 1991 [1]. The excellent calibration and maintenance of the instruments guarantee high quality data, which allow a precise evaluation of the spatial and temporal variability of the NRCS of the Earth's surface. A glance of the quality of the ERS Scatterometer data is shown in Fig. 1, depicting a time series of the C-Band NRCS for a location in Central Greenland. The measured seasonal variability of 0.6 dB indicates the relative accuracy and radiometric resolution of the instrument while the overall temporal stability reflects the excellent maintenance of both Windscatterometers. Note that the switch-over from ERS-1 to ERS-2 in May 1996 is not visible in the data, indicating the precise inter-calibration of both systems. Table 1 summarizes the

operational phases of the ERS-1 and ERS-2 satellites which data were used for this database.

Time Period	Orbit	Start Orbit	End Orbit	Satellite
28.07.91 - 10.12.91	3-day Commissioning Phase A	126	2103	ERS-1
28.12.91 - 30.03.92	3-day Ice Phase B	2354	3695	ERS-1
14.04.92 - 20.12.93	35-day Multidisciplinary Phase C	3901	12707	ERS-1
23.12.93 - 10.04.94	3-day Ice Phase D	12754	14300	ERS-1
10.04.94 - 27.09.94	168-day Geodetic Phase E	14302	16745	ERS-1
28.09.94 - 21.03.95	168-day Geodetic Phase F	16747	19247	ERS-1
21.03.95 - 25.05.96	35-day Multidisciplinary Phase G	19248	25426	ERS-1
19.03.96 - 25.05.96	Tandem	4765	25426	ERS-2 / ERS-1
25.05.96 - 22.05.98	35-day Multidisciplinary	4766	16246	ERS-2

Table 1: ERS-1/2 Orbit Characteristics

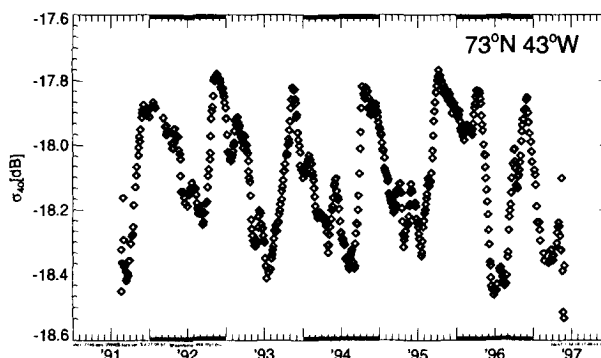


Fig. 1: Time series of the C-Band NRCS for a location in Greenland. The measured seasonal variability of 0.6 dB indicates the accuracy of the instrument while the overall temporal stability reflects the excellence of both Windscatterometers.

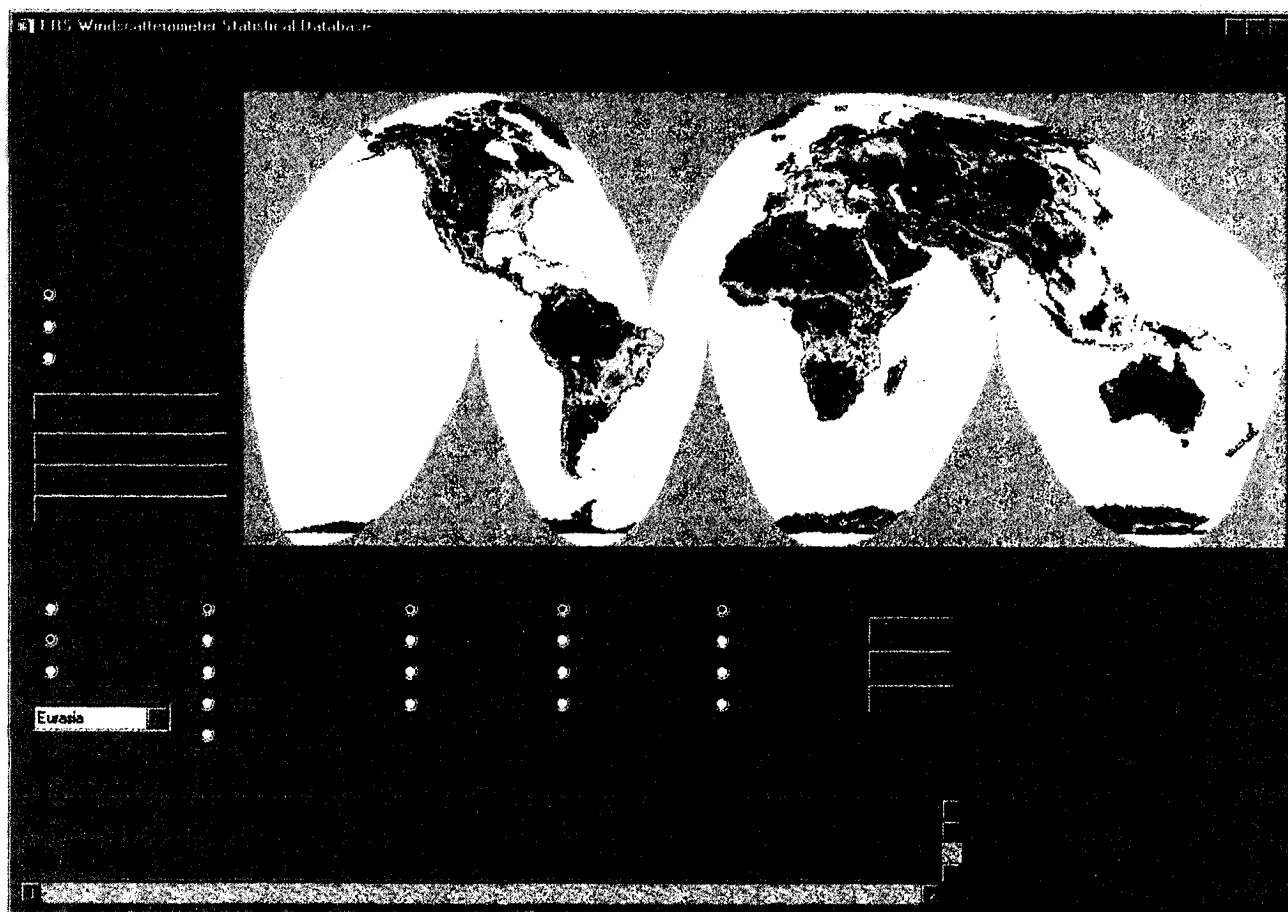


Fig. 2: A sample view of the Graphical User Interface to the database.

#### DATABASE CONTENT

The ERS Scatterometer data were extracted from the ERS WNF CD-ROM supplied by the French Archiving and Processing Facility CERSAT (F-PAF). This data set amounts to 107 CD-ROMs (August 1991 to May 1998), each containing approximately 3 weeks of Scatterometer data organised in orbit files. The goal was to compress the ERS data set to a volume that can be stored on a single CD-ROM for convenient use and distribution, whereby spatial, temporal, and radar parameter information should be preserved as much as possible [2].

The NRCS data are stored as histograms for 3-month intervals and for incidence angle bins of 5 degrees for each grid point of the Goode Homolosine map projection [3] with a grid spacing of 50 km. In order to achieve very compact data representation, the histograms have a fixed number of 20 bins. The bin size is adjusted according to the width of the histogram to be represented, and the 20 bins are centred on the mean value of the histogram.

The width of the bins is kept constant for a grid point with time, but varies spatially in order to account for different seasonal variability of the NRCS. The respective mean and bin size values are stored with the histogram. Table 2 summarizes the specification of the database content.

In general, the 3-month histograms provide sufficient number of measurements per incidence bin and grid point for a statistical analysis. However, information in the temporal variation might be smoothed out. As an addition to the database, 1-month mean data for the NRCS at 40 degrees of incidence angle, the slope, and the standard deviation are provided. Time series plots for single grid points can be obtained through the GUI.

The open concept of the database format assures a maximum of flexibility. The database files are accessible from virtually any programming language and under various platforms due to the use of Network Common Data Format (NetCDF) files.

Dimension	Extent	Resolution	Comment
Spatial coverage	Global	50km × 50km	Goode Homolosine projection
Time coverage	04.08.91 - 22.05.98	3 months	Dec.-Feb., Mar.-May, June-Aug., Sep.-Nov.
Incidence angle	17° ~ 57°	5°	
Histogram	$\sigma_{\min}^o - \sigma_{\max}^o$	$\frac{\sigma_{\max}^o - \sigma_{\min}^o}{20}$	$\sigma_{\min}^o$ and $\sigma_{\max}^o$ derived from the entire period

Table 2: Organisation of the NRCS samples into a multi-dimensional array

### DATABASE ACCESS

The front end to the database in form of a graphical user interface (GUI) was developed using the Interactive Data Language (IDL) [2]. This GUI allows a non-expert user to quickly visualize and print the requested information [4]. The GUI comprises menus, a status field and a display window as depicted in Fig. 2. Additional windows are used for the selection of statistical parameters and data ranges, and a display window highlights the grid points that meet the selected criteria before starting the data analysis. Different possibilities are provided to select a subset of the database for evaluation.

Predefined areas may be selected or interactively chosen with the computer mouse on the display between a single grid point and the entire globe. To assist the interactive selection of a region of interest, the following global maps can be displayed and zoomed:

- Mean NRCS (40 deg. of incidence angle)
- Standard deviation of the NRCS
- Seasonal variation of the NRCS
- Month of maximum NRCS
- Interannual variation of the NRCS
- Mean slope (incidence angle dependence of the NRCS)
- Seasonal variation of slope
- Month of maximum slope
- Anisotropy of the NRCS

The spatial selection can be further confined by applying classifications based on radar parameters (mean NRCS, slope, and standard deviation) or different land cover/vegetation type and climate zone classifications. These are Matthews Vegetation Types [5] consisting of 33 categories and Leemans' Holdridge Life Zones Classification [6] comprising in its original form 40 categories and 15 in its aggregated form.

The temporal range of the data to be evaluated can be chosen freely. Here the GUI offers easy access to a specific year or season.

### RESULTS

The following radar parameters can be selected for evaluation:

- NRCS
- Slope (incidence angle dependence)
- Standard deviation of the NRCS
- Availability of measurements

For the parameters NRCS, standard deviation and availability any range or combination of incidence angles can be chosen. Four types of output are provided by the GUI for the radar parameter chosen :

1. A cumulative histogram (probability density function) is computed and displayed including a Gaussian fit to the data and the probability distribution curve (see Fig. 3).
2. A time series plot of the mean value together with an indication of the standard deviation is displayed and a linear trend analysis as well as a seasonal sine-fit is computed and plotted (see Fig. 4).
3. If spatial data were selected, the result can be displayed as a map. The region of interest is shown on a global map. A zoom function is available as well as a print option.
4. The dynamic range function displays the NRCS probability distribution as a function of incidence angle. Isolines are plotted every 5% (see Fig. 5).

A PostScript print option as well as a data export function is available. The selection criteria and the fit parameters can be stored in an ASCII info-file.

### CONCLUSION

A nearly seven years of ERS Scatterometer data over land and sea-ice have been compiled into a statistical database. Many application possibilities are offered by such a database. For Earth scientists, global change observations and processes studies on global scale are the main areas of applications. From an engineering point of view, it is a useful tool for defining gain settings of airborne or spaceborne radar sensors, for calibrating those sensors or for deriving instrument specifications for new radar sensors. It is planned to regularly update the database in order to add new data, extending the time coverage up to the end of the ERS operation.

The database together with the GUI can be obtained free of charge on CD-ROM from the European Space Agency (see the points of contact in Table 3). The CD-ROM also contains the IDL source files as well as the user's manual. For further details see also: <http://www.ifars.de>.

REFERENCES

[1] ESA, ERS-1 System, ESA Publications Division ESTEC Noordwijk, The Netherlands, ESA SP-1146, 1992.  
 [2] V. Wismann and K. Boehnke, Global C-Band NRCS Statistics for Land Surfaces and Sea Ice using ERS Windscatterometer Data and Creation of a Database, *Final Report to the European Space Agency, Contract 12587/97/NL/RE*, 1998.

[3] J.P. Goode, "The Homolosine projection: a new device for portraying the Earth's entire surface," *Association of American Geographers, Annals*, 15, pp.119-125, 1925.  
 [4] V. Wismann, Database of Global C-Band Radarbackscatter, *User Manual to the European Space Agency, Contract 12587/97/NL/RE*, 1998. (see also <http://www.ifars.de>)  
 [5] E. Matthews, "Global vegetation and land use: new high resolution data bases for climate studies," *Journal of Climate and Applied Meteorology*, volume 22, pp.474-487, 1983.  
 [6] Rik Leemans, "Global data sets collected and compiled by the Biosphere Project," *Working Paper*, IIASA-Laxenburg, Austria, 1990.

	ERS Help Desk	ESTEC	CERSAT	ifars
Telephone	+39 06 94180-666/777	+31 (0)71-5655813	+33 (0)2-98224492	+49 (0)761-285 1717
Fax	+39 06 94180-272	+31 (0)71-5654696	+33 (0)2-98224533	+49 (0)761-285-1719
E-mail	eohelp@esrin.esa.it	clin@estec.esa.nl	fpaf@ifremer.fr	helpdesk@ifars.de

Table 3: Points of contact for ordering the database

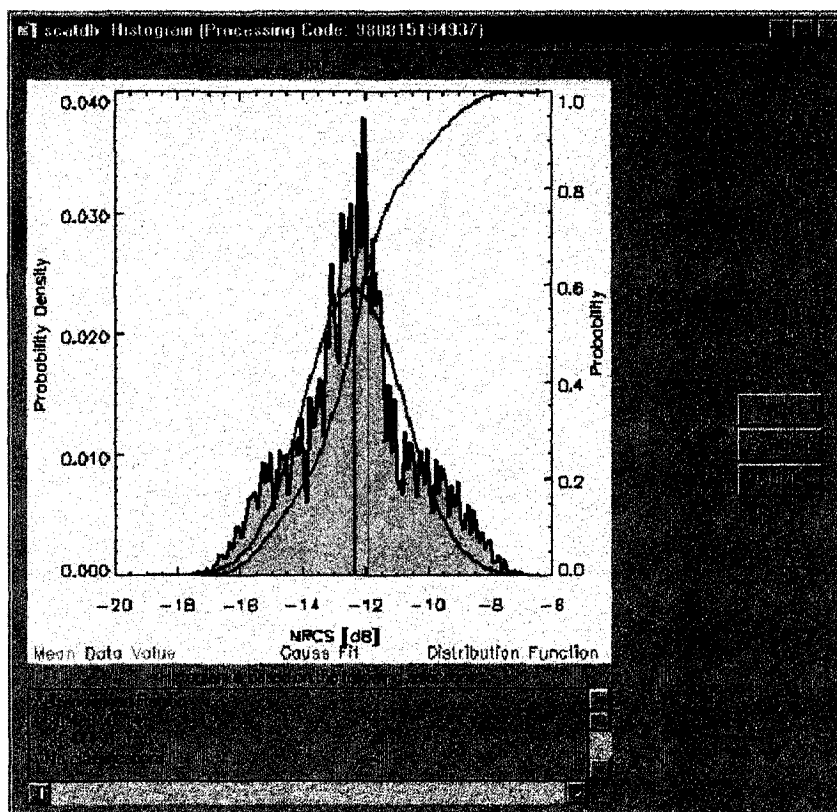


Fig. 3: Example of a histogram

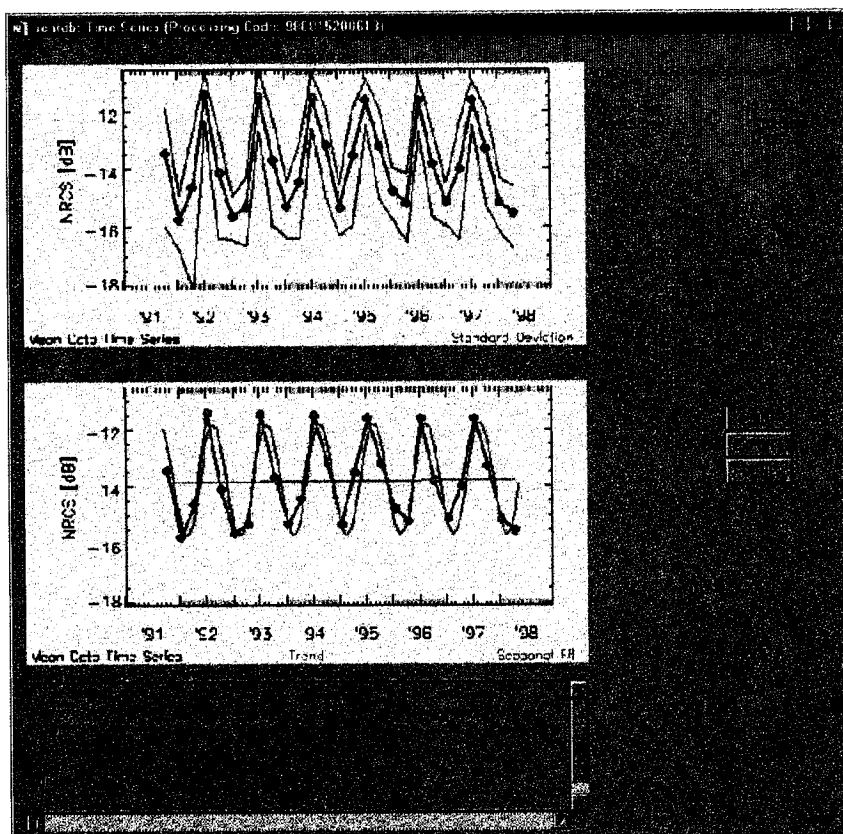


Fig. 4: Example of a time series

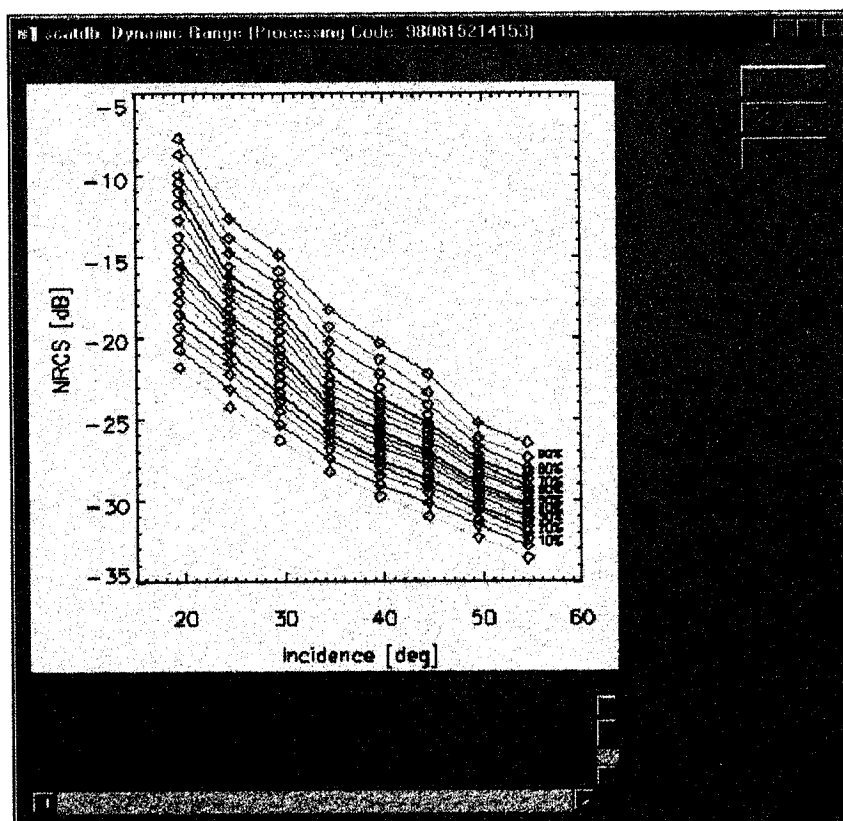
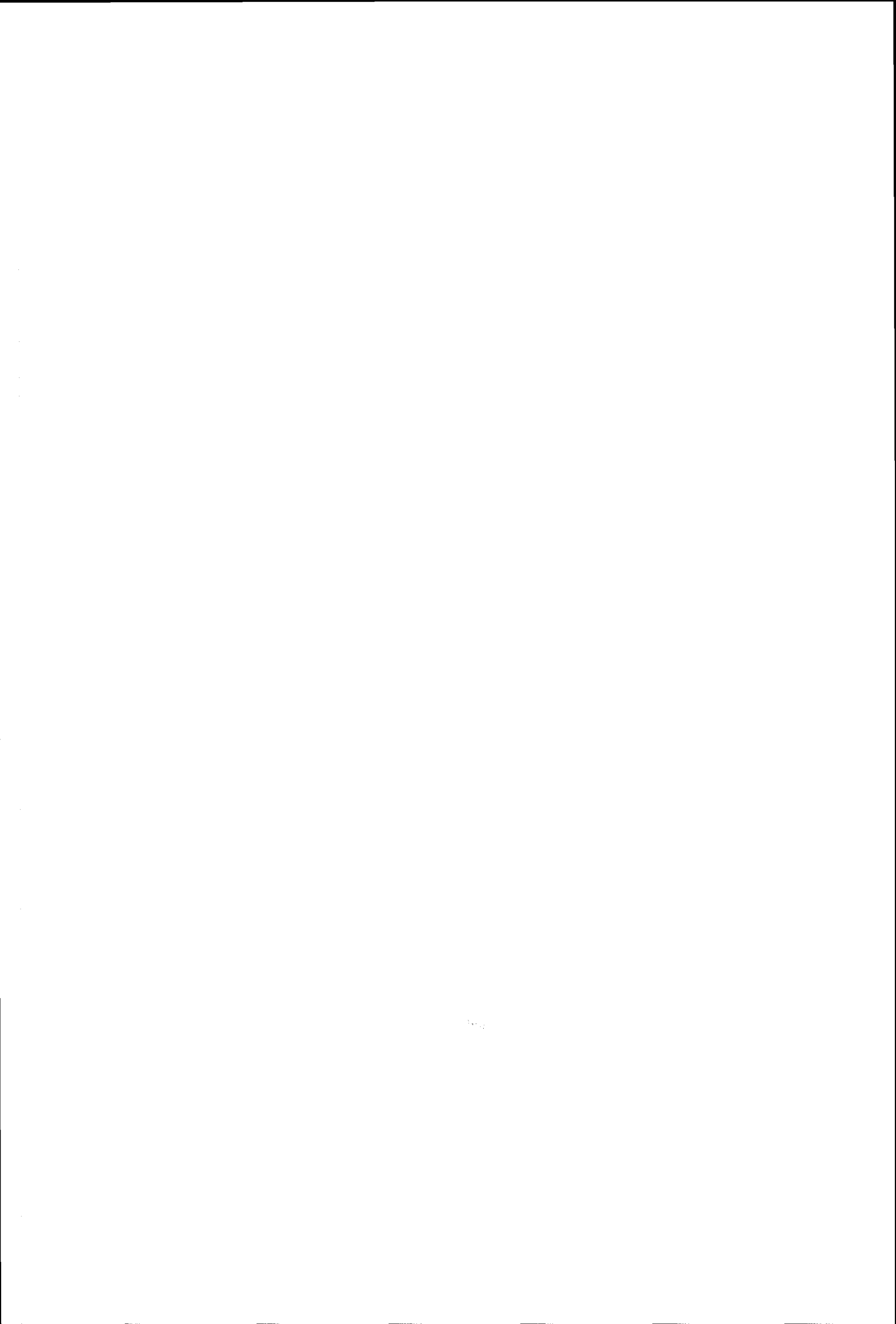


Fig. 5: Example of a dynamic range plot





## On the impact of C-band SAR calibration errors on soil moisture retrieval

G. Satalino <sup>(1)</sup>, F. Mattia <sup>(2)</sup>, T. Le Toan <sup>(3)</sup>, M. Davidson <sup>(3)</sup>,  
G. De Carolis <sup>(2)</sup>, G. Pasquariello <sup>(1)</sup>, M. Borgeaud <sup>(4)</sup>

(1) IESI-CNR, via Amendola 166/5 - 70126 Bari (Italy);

tel. +39 080 5481612, fax. +39 080 5484311, e-mail: satalino@iesi.ba.cnr.it

(2) ITIS-CNR, c/o CGS-ASI Loc. Terlecchia - I 75100 Matera (Italy);

e-mail: mattia@asimt0.mt.asi.it

(3) CESBIO, 18 av. Edouard Belin bpi 2801 - 31401 Toulouse Cedex 4 (France);

e-mail: letoan@cesbio.cnes.fr

(4) ESA, ESTEC, TOS-EEP, P.O. Box 299, 2200 AG Noordwijk (The Netherlands);

e-mail: maurice@xe.estec.esa.nl

### ABSTRACT

The objective of the paper is to assess the feasibility of retrieving soil moisture content over bare fields using SAR data at C-band. In particular, we consider SAR data which is currently available on a continuous basis, such as ERS data, or will be available in the near future, in this case the ASAR system on ENVISAT. The retrieval algorithm is based on the inversion of theoretical direct scattering models. The inversion task is achieved by means of an appropriately trained Neural Network. In the analysis an emphasis is put on assessing the impact of SAR calibration and model errors on the accuracy of the retrieved soil moisture content. The algorithm performances are assessed using both simulated and experimental data.

### INTRODUCTION

In the past, the sensitivity of SAR data to soil moisture content has been widely demonstrated. However empirical soil moisture retrieval approaches based on the statistical relationships between soil moisture content and backscattering value have been found to be site and time dependent and therefore of little general validity. This is mainly because surface backscattering is determined to a greater extent by surface roughness conditions than by soil moisture content. Consequently, a robust soil moisture retrieval algorithm needs to account for both roughness and moisture properties of soils. In this respect, only theoretical scattering models based on fundamental physical laws provide the flexible mathematical tools which can easily be adapted to very different surface conditions.

The objective of the paper is to assess the feasibility of separating three moisture classes over bare fields using SAR data currently or in the near future available on a continuous basis, i.e. ERS, RADARSAT, and the forthcoming ASAR on board ENVISAT. For this reason, different SAR configurations in terms of polarisation and

incident angle are investigated. The developed retrieval algorithm is based on the inversion of the IEM model [1] using appropriately trained Neural Networks. The IEM model assumes that surface roughness can be well represented by a single scale stationary Gaussian process. However, recent experimental works (see for example [2]) have shown that rough soils are often better described by multi-scale than by single-scale random processes. For this reason, in [3] the IEM model has been adapted to a multi-scale roughness description developing a multi-scale IEM version (MLS-IEM). In this paper, in order to assess the impact of a multi-scale modelling on the retrieval problem, both traditional IEM and MLS-IEM version are used to train different NN sets. In addition, in assessing the performances of the developed soil moisture retrieval algorithm, an emphasis is put on investigating the impact of calibration and model errors on the total error budget. In the analysis, both simulated and experimental data are exploited.

In the next paragraph, the inversion method is introduced. Subsequently, the characteristics of the simulated and experimental data sets used in the work are illustrated. Then, the algorithm performances, measured in terms of the attainable accuracy in the retrieved soil moisture content, are assessed as a function of the different SAR configurations. Finally, concluding remarks are given.

### INVERSION METHOD

A soil moisture retrieval algorithm may be regarded as a black box, accepting as input data SAR measurements and producing as output data, the related soil moisture estimates. In the case of single specification SAR data, like ERS SAR data, the soil moisture retrieval problem is "ill posed experimentally" because several surface parameters concur to determine the surface backscattering whereas the input information is limited only to one channel, i.e. one frequency, one polarisation and one incident angle. Consequently, there is not as much information in the experimental data as needed to retrieve

the parameter we are interested in. Such a kind of problem can be solved either by using *a priori* information about surface parameters or by adding more SAR channels.

In this paper, the range of surface roughness conditions are constrained in order to reduce the ambiguity in the retrieval problem. In particular, the work focuses on assessing the feasibility of retrieving moisture content over *smooth surfaces* for which the low frequency approximation of the IEM model holds (i.e.  $ks < 1.5$ , where  $s$  is the profile rms and  $k$  is the wave number of the impinging electromagnetic wave). Within this overall constraint a wide variety of moisture and roughness conditions are investigated. In particular, the effect of single-scale and multi-scale surfaces is studied.

The inversion method consists of training a set of Neural Networks (NNs) using simulated data produced by the direct IEM and MLS-IEM models. The NN architecture used in this application is the Multi Layer Perceptron (MLP) trained by the Back Propagation (BP) learning rule [4]. The actual used MLP NN has one hidden layer with 15 nodes and a non linear activation function, i.e. a sigmoid activation function.

The goal is then to obtain a relationship between the backscattering coefficient and the soil moisture content. This task can be regarded as an optimisation problem such as the minimisation of the differences between the measured backscattering values ( $Y_i$ ) and those ( $T_i$ ) predicted by the direct forward model  $M(p)$  where  $p$  are the geophysical parameters to be retrieved. In other words, the set of parameters to be estimated  $p$ , can be obtained by minimising the cost function:

$$C(p) = \|Y_i - T_i(M, p)\|$$

Such an inversion technique has been selected because the NN serves as a general and robust inversion method which can be easily extended to the cases of multi-specification SAR data. Moreover, the technique easily allows one to separately assess the impact of different error sources.

For the inversion study three main sources of errors affecting the performance of the retrieval algorithm need to be considered: the *inversion-error*, the *calibration-error* and the *model-error*. The *inversion-error* is determined by the amount of input information with respect to the complexity of the direct model to be inverted. More precisely, in the ideal case where the measurements are not affected by errors and the model exactly predicts the experimental data, the accuracy of the retrieved soil moisture will depend on the amount of input SAR information, on the number of free parameters contained in the model, on their range of variability and

on the method used to perform the inversion task. As an example we note that in the case of single specification ERS SAR data, the same value of backscattering coefficient may be produced by many different combinations of surface parameters. Consequently, the *inversion-error* quantifies the variation in the soil moisture estimate due to the variation in the surface roughness parameters for constant values of the input SAR data. In order to reduce the *inversion-error*, the range of variation of surface roughness parameters has to be reduced which implies adding *a priori* information about the possible ranges which soil roughness parameters can take on. The second source of error, referred to as *calibration-error*, is related to the measurements techniques and, more precisely, to the error affecting the measurements. The third source of error, referred to as *model-error*, is related to the errors always present in the direct forward modelling. The *calibration* and *model errors* add to the *inversion-error* and may be more or less important depending on the characteristic of the SAR configuration.

## DATA SETS

### *Simulated Data Set*

The use of a NN requires a training phase and a test phase which is performed on an independent data set. Here, two independent data sets have been obtained by exploiting the two direct forward IEM models. The roughness input parameters required by IEM are: the profile rms ( $s$ ), the profile autocorrelation function (ACF) and the associated correlation length ( $l$ ). For the MLS-IEM on the other hand, the roughness input parameters are [3,5]: the inner spatial scale ( $b$ ), the number of scales ( $P$ ) characterising the surface, a parameter  $\gamma_0$  proportional to the value of the profile rms ( $s$ ), and, a parameter  $\nu$  related to the profile fractal dimension  $D$ .

The ranges of the input parameters have been selected on the basis of a multi-site database of roughness measurements described in [2] and represent the variability found on experimental data for profile lengths of 3 to 5 m. For IEM, the parameter ranges are:  $s = [0.6 \text{ cm}; 1.6 \text{ cm}]$ ; Exponential ACF with  $l = [6 \text{ cm}; 24 \text{ cm}]$ ; whereas for MLS-IEM are:  $b = 1 \text{ cm}$ ;  $P = 8$ ;  $\gamma_0 = [0.4 \text{ cm}; 0.7 \text{ cm}]$  roughly corresponding to  $s = [0.6 \text{ cm}; 1.6 \text{ cm}]$ ;  $\nu = [1.2; 1.74]$ .

Both for IEM and MLS-IEM, the range for the input dielectric constant is  $\epsilon^f = [3.0+j0.1; 20.0+j5.0]$ . This  $\epsilon^f$  range corresponds approximately to a volumetric moisture content range of  $M\nu = [3\%; 40\%]$ . The correspondence between soil moisture and dielectric constant in this case is obtained by means of a semiempirical polynomial expression described in [6].

In order to separate three moisture classes with  $M\nu$  ranging between 3% and 38%, the upper bound for the

error on the retrieved  $M_v$  values is of the order of  $\pm 4\%$ . In this case, the three classes might be, for instance:  $3\% \leq M_v \leq 10\%$  dry soils;  $10\% < M_v < 20\%$  medium wet soils;  $20\% \leq M_v \leq 38\%$  wet soils.

The simulated SAR sensor configurations are summarised in Tab. 1. Two different incident angles and the two co-polarised channels are combined. Using the backscattering coefficients obtained from IEM and MLS-IEM models for each configuration, different NNs have been trained. The fit between the NN outputs and the expected values is evaluated by means of the normalised root mean square error (rms).

Tab. 1: Simulated SAR sensor configurations

Configuration	Polarisation	Angle
[1p:23]	VV	23
[1p:45]	VV	45
[2p:23]	HH,VV	23
[2p:45]	HH,VV	45
[4p:23:45]	HH,VV	23, 45

#### Experimental Data Set

The experimental data set used in the paper concerns ERS data collected during three different ground campaigns conducted over European sites. Data have been acquired over the sites of Middle Zeeland (The Netherlands); Marestaing (France) and Matera (Italy). Ground measurements consist of both roughness profiles measured by laser profiler and moisture data. Soils presented different roughness as well as moisture conditions.

## RESULTS

#### ERS Case: Simulated Data

As a first step in assessing the feasibility of retrieving soil moisture content using ERS SAR data (i.e. one frequency of 5.3 GHz, one incidence angle of  $23^\circ$  and one polarisation: VV) the NN outputs versus the input  $\sigma_0$  values for MLS-IEM model are plotted in Fig. 1. The figure shows the volumetric soil moisture content values derived from the NN outputs versus the  $\sigma_0$  input values. The original  $M_v$  values used to test the NN are also plotted. It can be clearly seen that those values are denser in the region of large values than in the region of small values. This is due to the fact that the training data set has been produced by uniformly sampling the  $e^f$  space, not the  $M_v$  space. Moreover, it is worth noting that many different  $M_v$  values can be associated with a given backscattering coefficient. Consequently, the output given by the trained NN is the mean among all possible values as required to minimise the cost function  $C(p)$ , and the rms error between the retrieved and the expected soil

moisture content constitutes the *inversion-error* described previously. The corresponding plot for the NN trained by the conventional single-scale IEM model is similar to that of Fig. 1. The overall rms errors  $\Delta M_v$  affecting the volumetric moisture content percentage when using the NN trained by IEM and MLS-IEM data were found to be 5.48 and 5.46, respectively.

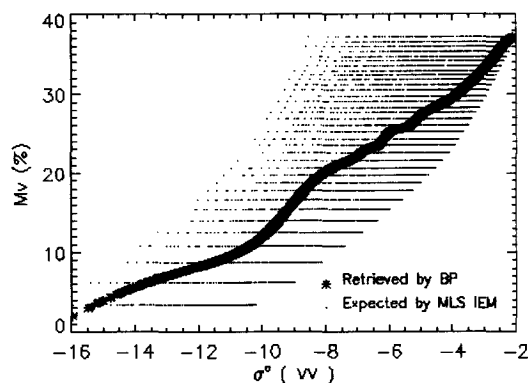


Fig. 1: ERS configuration, output of NN trained by MLS-IEM data vs  $\sigma_0$  input

Since, the *inversion-error* constitutes a lower bound for the total budget of soil moisture rms error, which also includes calibration and *model-errors*, a first conclusion, stemming from the inversion error analysis, is that the goal of separating three moisture classes cannot be achieved in a general way by using ERS SAR data, even when only *smooth surfaces* (i.e.  $ks < 1.5$ ) are considered. At the same time, since the inversion results show that there are no significant differences in the *inversion-error* using either multi-scale or single-scale direct scattering modelling, at least in the ERS configuration, a second preliminary conclusion is that the overall mathematical complexity of the direct model does not change between IEM and MLS IEM.

As a second step, the effect of the *calibration-error* on the  $M_v$  estimation has been investigated. To do so, the IEM and MLS-IEM data used to train and test NNs have been perturbed by a zero-mean Gaussian random noise. The rms errors for the retrieved  $M_v\%$  obtained using perturbation levels of  $\pm 0.5/\pm 1.0$  dB and for NNs trained using IEM and MLS IEM were found to be 5.71/6.12 and 5.68/6.13, respectively. These results indicate that both NN algorithms possess a good robustness with respect to *calibration-errors* since the errors levels in retrieved  $M_v$  are of the same order as those obtained for the case in which only *inversion-errors* were taken into account. To further assess the impact of the *model-error* on the soil moisture retrieval, the NN trained with IEM data has been tested using an independent simulated data set obtained from the MLS-IEM. In this way there is a bias between the two data sets which may be greater than 2 dB. The

errors due to such a bias may be ascribed to the single-scale model errors since the former does not take into account the multi-scale nature of natural surfaces. The rms error estimated on the retrieved Mv% using this approach is 5.57.

A summary of the individual sources of inversion error and total error budget affecting the Mv estimates is given in Tab. 2. The *inversion, calibration and model-errors* for the different cases are reported for both the SLS and MLS IEM models. As can be seen, the two trained NNs show more or less the same performance. Moreover, *the inversion-error is by far the most important source of error for the ERS case*. This implies that the limiting factor in retrieving soil moisture from ERS SAR data is the reduced amount of input information with respect to the complexity of the direct model to be inverted. In this case, improvements in calibration or in direct model reliability only marginally contribute to improve the overall algorithm performances. It is thus not feasible to retrieve three moisture classes by using ERS SAR data collected over smooth surfaces, unless the roughness characteristics of the observed surfaces are restricted further. At the same time, the results of Tab. 2 indicate that it is feasible to separate two classes, i.e. dry and wet soils, and that the algorithm, although inaccurate, is robust with respect to both calibration and model errors.

Tab. 2: The rms error budget affecting the Mv % using the NN trained by IEM and MLS-IEM data, respectively

ERS case rms error on Mv %	NN trained by IEM	NN trained by MLS-IEM
<i>Inversion-error</i>	5.48	5.46
<i>Inversion and calibration-errors (<math>\pm 0.5/\pm 1.0</math> dB)</i>	5.71/6.12	5.68/6.13
<i>Inversion and Model-errors</i>	5.57	-

*ERS Case: Experimental Data*

In this section, the developed retrieval algorithms are applied to the ERS data set collected over the Middle Zeeland, Marestaing and Matera sites and their performance are evaluated. Fig. 2 shows the correspondence between the volumetric soil moisture (Mv%) values retrieved directly from ERS measurements using a NN trained by MLS-IEM data and those recorded in-situ during the ground truth campaigns.

Similar results are obtained if a NN trained by IEM data is considered. For both the inversion algorithms there is a good overall agreement between retrieved and measured data. The two wet and dry soil moisture classes present within the ground data sets are clearly identified using both inversion algorithms. At the same time, however, the sensitivity within each moisture class to soil moisture variations is low and, in the case of the dry soil class, the moisture content is generally overestimated.

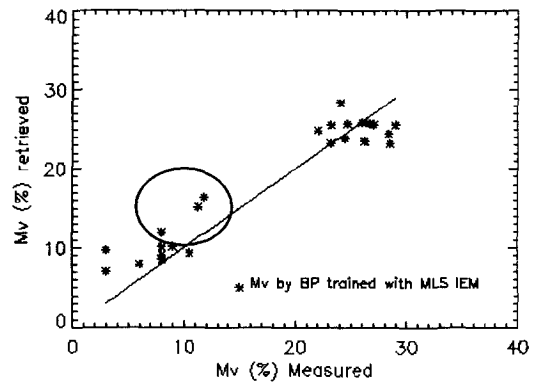


Fig. 2: Experimental ERS data: retrieved vs. measured Mv values obtained from the NN trained by MLS-IEM data

A difference can be seen when comparing the results of the two different retrieval algorithms. An advantage of the MLS approach is that the results are less sensitive to errors in surface roughness status. This can be seen by comparing IEM results with MLS-IEM results for the three cases circled in the figures. These three points correspond to soil moisture values recorded over Matera fields whose rms height was approximately equal to 2 cm and therefore lies outside the roughness range used to train the two NN. In this respect, the results show that the NN trained by MLS-IEM data is less sensitive to inaccurate surface information than the NN trained by IEM data and thus more robust.

Tab. 3 summarises the rms errors on Mv% obtained for the experimental data using the different retrieval approaches. It is interesting to note that the errors in the inversion of experimental data are significantly smaller than those obtained when testing the algorithms performances with simulated data. As pointed out previously, this is due to the limited range of experimental conditions (roughness, humidity) covered by the data set, which may be regarded as a subset of the conditions tested using simulated data.

Tab. 3: Experimental ERS data: retrieval error on Mv%

ERS case	rms error on Mv %
<i>NN trained by IEM data</i>	3.14
<i>NN trained by MLS-IEM data</i>	3.04

*Future C-Band SAR Configuration: Simulated Data*

In this section, the potential of soil moisture retrieval algorithms in the case of different C-band SAR configurations is examined. As for the ERS analysis, the contribution of *inversion, calibration and model-errors* to

the total error budget of the soil moisture procedure is quantified and the possibility of distinguishing among three moisture classes using C-band multi-specification SAR data is discussed.

The data set to train and test NNs was simulated by using both IEM and MLS-IEM models, considering the SAR data configuration as shown in Tab. 1. In a similar fashion to the approach followed in the case of ERS configuration, *inversion-errors* are obtained by testing the NN performances with the appropriately simulated independent IEM data sets. To estimate *calibration-errors*, the IEM and MLS-IEM training and testing data sets have been randomly perturbed by a zero mean Gaussian noise with a rms of  $\pm 0.5$  and  $\pm 1.0$  dB, for each SAR configuration. Whereas, to estimate *model-errors*, the testing data sets generated by using the MLS-IEM have been fed to the NN trained by IEM data. Errors are reported in Tab. 4 in the case of *inversion-error*, Tab. 5 in the case of *inversion plus calibration-errors* and in Tab. 6 for *inversion and model-errors*. For the sake of comparison the ERS configuration results are also included.

Overall the results indicate that, for single incidence angle SAR systems, the ability to retrieve soil moisture using the NN is generally insensitive with respect to the incidence angle. However significant improvements are obtained when a second polarisation and a second incident angle are added. Also the performances of NNs trained by IEM data and those trained by the MLS-IEM data are almost the same. This implies that the mathematical complexity between the two IEM model versions is not changed. Adding more input SAR information in each case decreases the *inversion-error* which become negligible when a 4 polarisation 2 incidence angle system is considered.

An important difference between the inversion results for single-parameter SAR systems and multi-parameter SAR systems is that in the case of multi-parameter SAR data, the *inversion-error* no longer determines the total error budget. Instead, it is the calibration and to a greater extent the *model-error* which play the most important role in determining the overall accuracy in the soil moisture retrieval. This can be seen when comparing the results shown in Tab. 4 (*inversion-error*) with those in Tab. 5 (*calibration-error*) and, more evidently, with those in Tab. 6 (*model-error*). For instance for the 4 polarisation 2 incidence angle configuration for which the extra information captured by the system makes the *inversion-error* very small, the presence of *calibration-errors* raises the rms error on the volumetric moisture content Mv% to approximately 4 (see Tab. 5). However, it is the *model-error* which may completely destroy the algorithm performances (see Tab. 6). In this respect, using a C-band SAR system equipped with HH and VV channels and

imaging at two incidence angles (i.e. configuration [4p:23:45]), the retrieval of three moisture classes may be feasible provided an accurate direct model is used.

Tab. 4: C-band multi-specification simulated SAR data: *inversion-error*

<i>Inversion-error</i> (rms error on Mv%)	NN trained by IEM	NN trained by MLS-IEM
[1p:23]	5.48	5.46
[1p:45]	6.19	6.53
[2p:23]	3.30	3.53
[2p:45]	3.87	3.01
[4p:23:45]	0.38	0.14

Tab. 5: C-band multi-specification simulated SAR data: *calibration-error* ( $\pm 0.5/\pm 1.0$  dB)

<i>Inversion and calibration-errors</i> (rms error on Mv%)	NN trained by IEM	NN trained by MLS-IEM
[1p:23]	5.71/6.12	5.68/6.13
[1p:45]	6.28/6.48	6.60/6.83
[2p:23]	5.17/6.03	5.43/6.10
[2p:45]	4.56/5.60	4.34/5.78
[4p:23:45]	3.34/4.54	3.25/4.65

Tab. 6: C-band multi-specification simulated SAR data: *model-error*

<i>Inversion and Model-errors</i> (rms error on Mv%)	NN trained by IEM
[1p:23]	5.57
[1p:45]	6.50
[2p:23]	3.96
[2p:45]	4.13
[4p:23:45]	Too big

## CONCLUSIONS

In this work, the feasibility of retrieving soil moisture from ERS SAR data and future multi-parameter SAR systems such as ENVISAT ASAR has been investigated. The focus was on developing general model-based retrieval algorithms which are applicable to a diversity of situations and are not time or site dependent. If we restrict ourselves to the validity domain of the IEM model ( $ks < 1.5$ ) then the main results of the study can be summarised as follows.

For the ERS-1/2 configuration the attainable accuracy, quantified by the overall rms in the retrieved volumetric soil moisture content, is of the order  $\Delta Mv\% = \pm 6$ . The

uncertainties in  $M_v$  are due almost exclusively to variations in roughness conditions which influence the relationship between soil moisture-radar backscattering coefficient. Moreover, it might be possible to retrieve soil moisture locally with a higher accuracy as long as the range of roughness parameters typical of the area has been determined previously.

For a sensor configuration using two co-polarisation at the same time, the overall error (assuming a calibration error of  $\pm 0.5$  dB and an accurate direct model) in the retrieved soil moisture is reduced to  $\Delta M_v\% = \pm 5.2$  at  $23^\circ$  of incidence angle.

For a sensor imaging simultaneously at two polarisation and two incidence angles (e.g.  $23^\circ$  and  $45^\circ$ ) the best accuracy is attained. In this case, still under the hypothesis of  $\pm 0.5$  dB of calibration error and an accurate direct model, results show that soil moisture can be retrieved with an accuracy of  $\Delta M_v\% = \pm 3.3$ .

An important result of the study was to show that modelling errors influence to a great extent the accuracy of soil moisture retrieval using multi-parameter SAR. This was seen in the results obtained when inverting MLS-IEM data using a NN trained with IEM data.

As a consequence it would appear that forward models better adapted to the modelling of backscatter from natural surfaces such as MLS-IEM could play a crucial role in the development of retrieval algorithms for future multi-parameter systems. If these model errors can be reduced than the results show that three moisture classes may be realistically separated using multi-specification C-

band SAR data provided that the calibration errors remain within 0.5 dB.

#### ACKNOWLEDGMENTS

This work has been supported by ESA-ESTEC under contract n. 12008/96/ND/NB.

#### REFERENCES

- [1] A.K. Fung, *Microwave Scattering and Emission Models and their Applications*, Norwood, MA: Artech House, 1994.
- [2] M. Davidson, T. Le Toan, F. Mattia, G. Satalino, T. Manninen, M. Borgeaud, "On the characterization of agricultural soil roughness for radar remote sensing studies," accepted for publication on *Trans. on Geoscience and Remote Sensing*, March 2000.
- [3] F. Mattia, T. Le Toan, "Backscattering Properties of Multi Scale Rough Surfaces," *Journal of Electromagnetic Waves and Applications*, Vol. 13, No. 4, 1999.
- [4] J. A. Hertz, A. Krogh, and R. G. Palmer, *Introduction to the Theory of Neural Computation*, Redwood City, CA: Addison Wesley, 1991.
- [5] F. Mattia, T. Le Toan, M. Davidson, P. Borderies, E. Bachelier, M. Borgeaud, "On the effect of multi-scale surface roughness on SAR data," *proceedings of CEOS Workshop*, 26-29 October 1999.
- [6] M. T. Hallikainen, F. T. Ulaby, M. C. Dobson, M. A. El-Rayas, L. Wu, "Microwave dielectric behaviour of wet soil - Part I: Empirical models and experimental observations," *IEEE Trans. Geosc. Remote Sensing*, Vol. Ge23, pp. 25-34, Jan 1985.

## Application of SAR Interferometry to Flood Damage Assessment

C H Buck, S Monni

ESA/ESTEC  
TOS-ETP, Keplerlaan 1, Postbus 299  
2200 AG Noordwijk, The Netherlands  
e-mail: [cbuck@estec.esa.nl](mailto:cbuck@estec.esa.nl)

### ABSTRACT

Multi-temporal SAR intensity images have been successfully used to demonstrate various changes in a scene including seasonal changes, ice floes, landslides, earthquake damage and flooding. This paper examines the possible benefits of using SAR interferometry to map flood damage.

As a test case the Yangtze river flooding of summer 1998 was chosen. The interferometric coherence was obtained using ERS-1 and -2 images from during the height of the flooding and compared with references from a tandem pair dating from December 1995 and an ERS-1 pair from summer 1993. The additional information provided by the absence of coherence over water allows for more confident assessment of the flooded areas compared to simply relying on the backscatter intensity.

This paper compares the two techniques of multi-temporal intensity analysis to multi-temporal coherence analysis and demonstrates the added advantage of using interferometric SAR for flood damage assessment.

### INTRODUCTION

Floods world-wide, beyond loss of life, also cause many millions of dollars worth of damage each year to crops and property. Understanding exactly which regions have been affected by a flood is of vital importance for the relief effort and in order to put into place measures to limit the effects of a flood in the future.

Spaceborne sensors have great potential to provide this information and multi-temporal SAR in particular has been used in recent years to significant effect due to the SAR's ability to observe through the cloud which is inevitable if flooding is taking place.

Normally speaking SAR interferometry and water coverage would be considered to be mutually exclusive due to the lack of interferometric coherence obtained over rivers, lakes, seas and inundated areas. However, it is precisely the lack of this parameter which can make it useful in identifying otherwise ambiguous regions which are in fact flooded.

### BACKGROUND

The interferometric correlation or coherence is a parameter which is generally used to give an indication of the quality of an interferogram. Its magnitude,  $\gamma$ , is computed from two registered complex SAR images,  $A_1$  and  $A_2$ , so:

$$\gamma = \frac{E[A_1 A_2^*]}{\sqrt{E[|A_1|^2] E[|A_2|^2]}}$$

Equation 1

Where  $E[\ ]$  is the expectation value. In practice the expectation value is approximated by performing a summation over an area centred on each pixel in the image in turn.

Beyond its use as a measure of interferogram quality however, the coherence can be useful as a parameter in its own right [ref. 1]. For example, at C-band the coherence is generally high for sparsely vegetated areas and low for forested regions. Over water it is always very low because either there is no wind (or it does not flow quickly) causing a very smooth surface and resulting in specular reflection and so there is no backscatter to the SAR, or the wind is causing capillary waves to form on the surface of the water in which case there is backscatter, but it cannot be coherent with images acquired on a different date since the capillary waves effectively appear and move randomly.



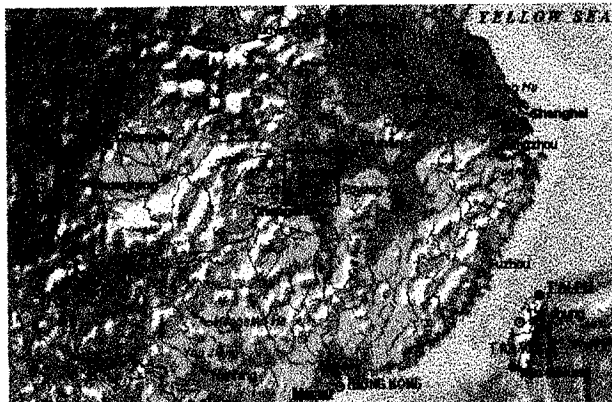
Figure 1: Oxbow lake seen to "disappear" due to windy conditions

The same is of course not true for the sigma zero. In the case of no wind, the sigma zero of a still lake approaches the noise figure of the instrument known as the noise equivalent sigma zero. In windy conditions or with fast moving water, the measured sigma zero can be very high. This can result in the "disappearing lake" phenomenon whereby under certain conditions a body of water can be seen to blend with its surroundings and no longer be distinguishable in a SAR image (see figure 1).

This property of the coherence of water in SAR interferograms can allow it to be unambiguously detected in multi-temporal SAR imagery.

**YANGTZE RIVER**

In order to test the idea of using interferometric correlation to assist in the detection of water under flood conditions, a recent flood event was selected. In the summer of 1998 the Yangtze River region of the Republic of China suffered one of its worst floods in decades. Many people were killed and countless more made homeless. The flooding was caused by torrential rains in the centre of China around the end of July. New rains during the first week of August in central Hubei and Hunan provinces pushing the water levels on the upper reaches of the Yangtze to a flood peak. Flood waters washed away a 3000m section of newly constructed dikes in Hunan's Huarong county and opened a 600m crack in the embankment surrounding Caisang Lake, both near Yueyang (ref. [2]).



**Figure 2: Map of Yangtze River region showing area of acquisitions**

Due to the long duration of the event, this was considered to be a good test for the theory proposed since it should be possible to find ERS tandem images acquired both before the flood and during it. In fact three apparently suitable pairs of acquisitions centred on 112°E, 29°N (track 261, frame 3015 - see figure 2) were found, two tandem pairs from 1995 and 1998 and a reference ERS-1 35-day repeat pair from 1993. This is summarized in table 1.

Mission	Date	B//	B⊥
ERS-1	930714	85m	226m
ERS-1	930818		
ERS-1	951229	113m	295m
ERS-2	951230		
ERS-1	980731	214m	547m
ERS-2	980801		

**Table 1: ERS Acquisitions over Yangtze River**

**DATA ANALYSIS**

The selected frames were provided by ESRIN in SLCI format as part of a mini-project. The images were 4900 pixels in range and ~26700 pixels in azimuth. Each complex pair was registered using the Gamma Interferometric SAR Processor and re-processed to 20 looks (two in range and ten in azimuth). Having registered them, the phase difference image or interferogram was generated. Based on the orbital information given in the headers, the geometry was calculated and the so-called "flat earth" interferometric fringes removed from the raw interferograms to leave only the height related phase difference. From this flattened interferogram, the interferometric coherence was calculated based on a 5x5 matrix with linear weighting as given in table 2 and pictured in figure 3.

0.057	0.255	0.333	0.255	0.057
0.255	0.529	0.667	0.529	0.255
0.333	0.667	1.000	0.667	0.333
0.255	0.529	0.667	0.529	0.255
0.057	0.255	0.333	0.255	0.057

**Table 2: Coherence Matrix Weighting**

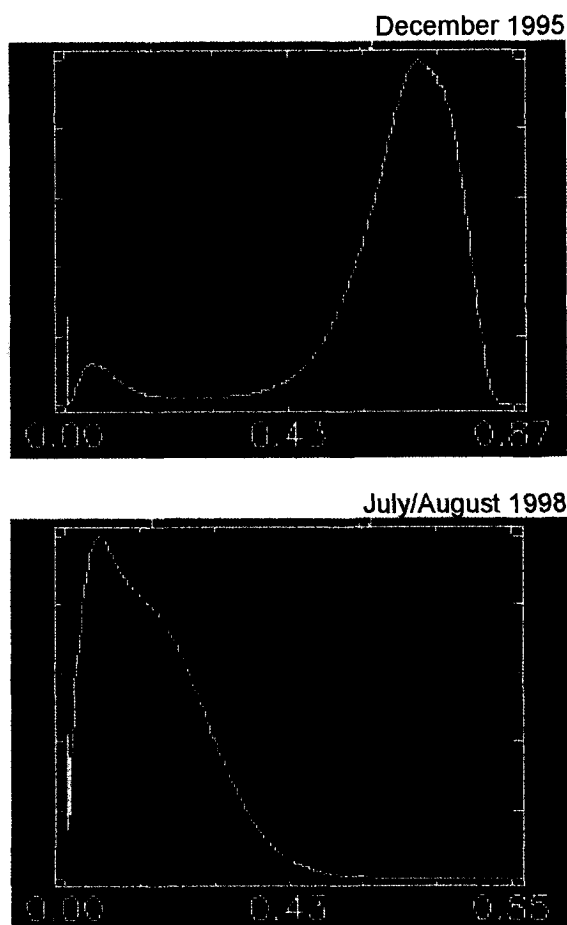
Ideally the analysis would have concentrated on the acquisitions from the summers of 1993 and 1998 since they should be most comparable in terms of the prevailing weather conditions and growing season. Un-



**Figure 3: Graph of Pixel Weighting**



fortunately, despite the favourable short baseline, the coherence obtained for the 1993 images after a 35 day acquisition interval, was very poor. The value obtained even over urban areas was around 0.3 and so this pair of images could not be used as part of this study although the July image was used together with the 1998 July image to create a standard multi-temporal image of the flooding.

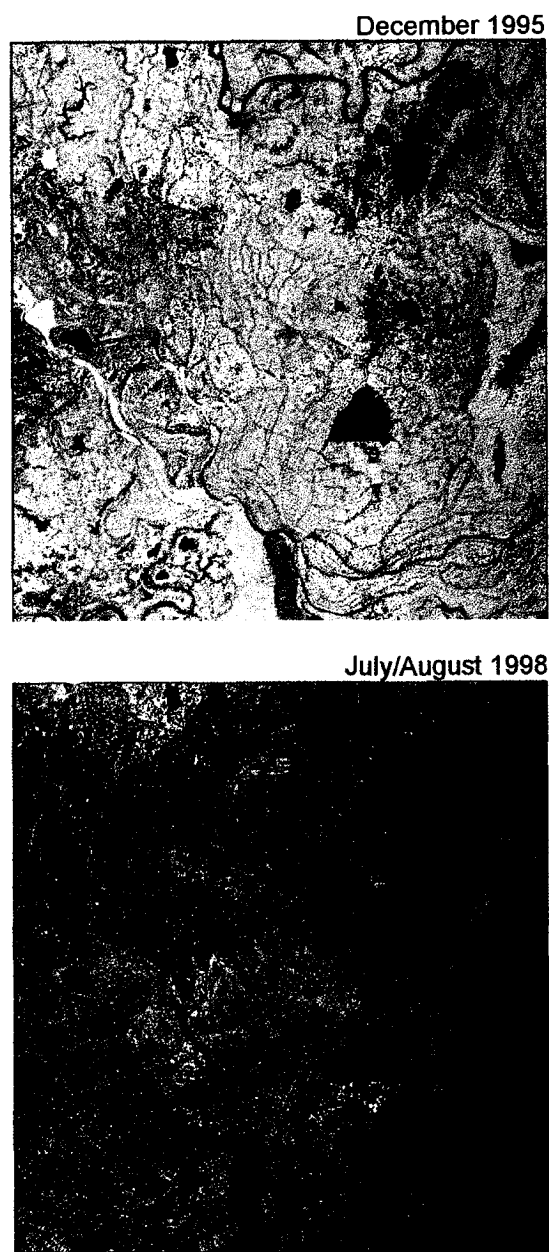


**Figure 4: Histograms of Coherence**

The coherence of the 1998 image pair is also quite low but still useful. This, apart from the large baseline, is probably also due to the extreme rainfall at the time of acquisition. The coherence of the 1995 image pair is extremely high. It would appear that this area of China is very much drier in December than in July/August and this improves the interferometric correlation. The relative histograms of the coherence are given in figure 4.

The actual coherence images are shown in figure 5. From these images it is immediately apparent that there is higher coherence in the 1995 pair than in the 1998 pair due to the general bright appearance of the former compared to the latter. Easily discernible in both pictures are the bodies of water, notably the river in the

top right (approximately north-east) of each image and the triangular shaped lake just south-east of centre. Less obvious is the forested region in the major bend of the river (Yangtze) again in the north-east and why the obvious river that runs from the west to the south is white in 1995 and black in 1998.



**Figure 5: Coherence Images**

#### LAND CLASSIFICATION

In ref. [1] a method is described whereby SAR image intensity, difference in intensity and coherence for an interferometric pair can be combined into a single image to produce a land classification map. According to this method of classification, the coherence is assigned

linearly to the red channel, the green to the square root of the intensity and the blue channel is used to display the difference in intensity in dB.

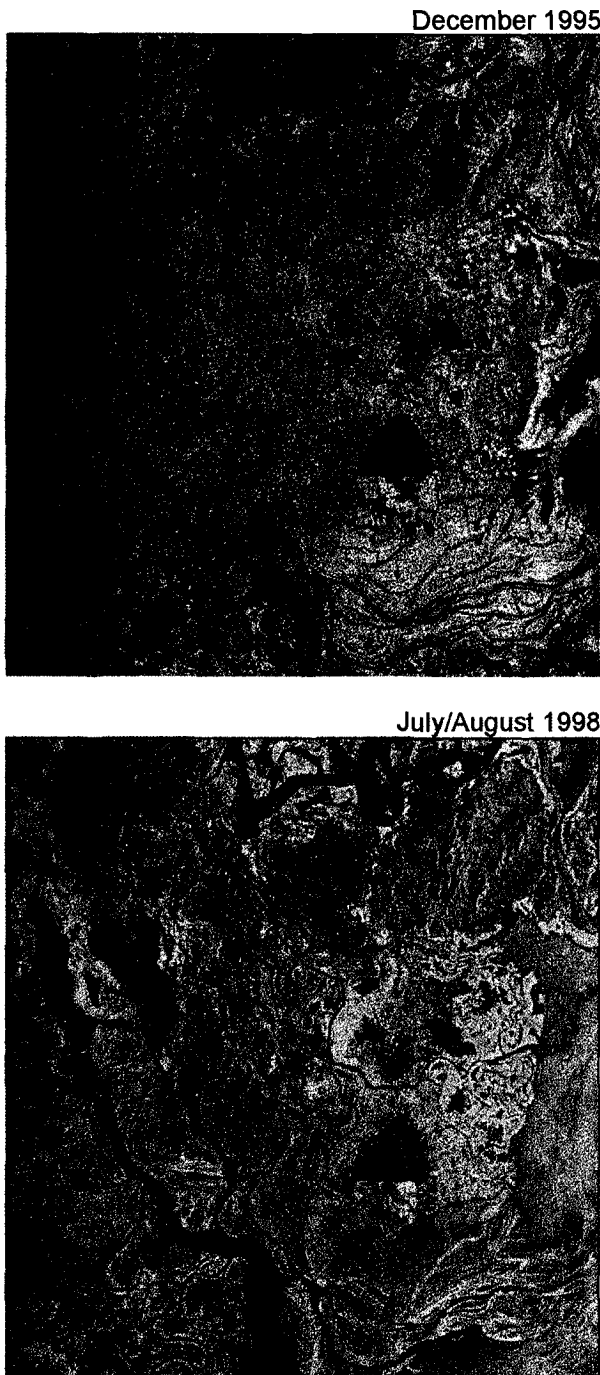


Figure 6: Land Classification Images

However, for the purposes of this research, although the coherence is in red, the intensity in green and the difference in intensity is in blue, each channel has been subjected to a histogram equalization, in order to be better able to compare the two scenes. This is because, as demonstrated by the histograms (figure 4), coher-

ence is not an absolute quantity. Using the ref. [1] technique reveals a 1995 image dominated by the red coherence channel making it almost entirely orange/red, while the resulting 1998 image is dominated by the green intensity channel.

Figure 6 shows the results of the modified land classification technique and makes interpretation very simple. Water in general appears black for low wind conditions at the time of both acquisitions, blue when windy during one take and not during the other or green if it was windy on both occasions. In particular the Yangtze river is a very vivid blue in the 1995 scene. Vegetated areas appear green due to the relatively high backscatter and low coherence. Areas of high coherence and low backscatter such as sand and rock are picked out in red. It is now very easy to see why the white "river" of 1995 in figure 4 turns black in 1998. This is because in December 1995 the water level is very low, exposing the sand, mud and rocks on the river bed whilst in 1998 the river is bursting its banks, completely covering all the high coherence materials. Flooded regions can be seen around the banks of the river in the north and large areas have been inundated in the west of the scene.

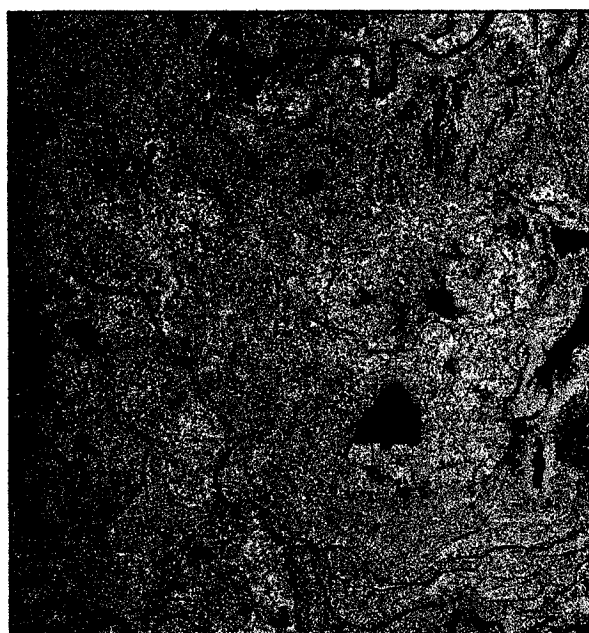
These land classification images already show the potential for using interferometric coherence to assist in flood damage assessment. The problem now is how to combine usefully coherence information together with the intensity images to produce a single image depicting inundated regions.

#### MULTI-TEMPORAL INTENSITY

First it is worthwhile to look at the traditional use of multi-temporal images to show major changes such as result following a flood event.

Normally this is done by taking two intensity images, registering them and then producing a colour image with two of the colour channels (red, green or blue) for each of the registered intensity images and the third one for the difference in intensity between the two dates.

The result of this process for the ERS-1 images of December 1995 and July 1998 is shown in figure 7. Here, the 1998 intensity image is displayed in red, the 1995 intensity image in green and their difference in blue. In general it can be expected that flooded areas will show up in blue since the change in backscatter for these areas should be high (=blue channel). Certainly this is the case for the river which runs from the west to the south of the image and the inundated areas in the west. These are highly visible in bright blue. However, what is less clear is why the large lake in the east of the scene which has filled up in between the two acquisitions appears not blue at all, but red and yellow indicating no change and hence no flooding.



**Figure 7: Multi-temporal ERS-1 Image (Red: 98, Green: 95, Blue: 95-98)**

Going back to the land classification images in figure 6 it can be seen that the backscatter intensity of most of the lake (in green) changed little between the two dates due to the presence of wind over the lakes in the 1998 image and hence the blue component is very low. This of course can lead to mistakes being made when interpreting SAR imagery of flood events. A method which makes use of the interferometric correlation will not be fooled so easily since the coherence over the water will be low whether or not there was wind over the lake at the time.

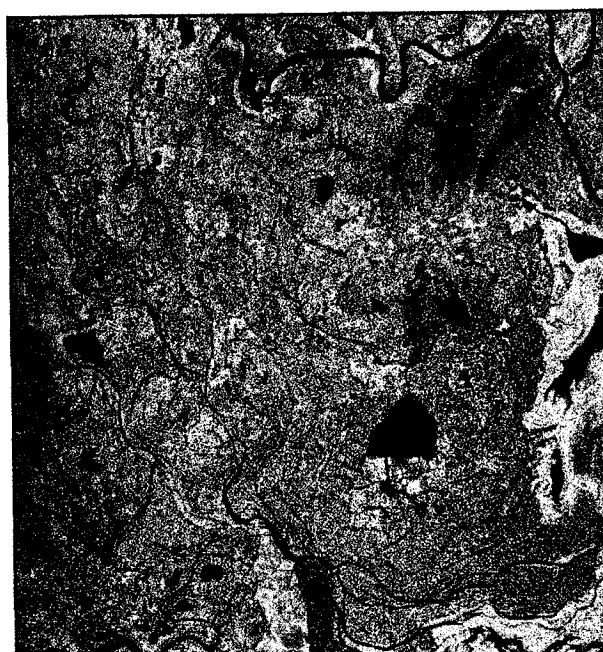
#### MULTI-TEMPORAL COHERENCE

As suggested earlier, the difficulty in making use of the multi-temporal coherence as a parameter is how to incorporate it together with other parameters such as intensity and intensity difference to make a single image which will unambiguously highlight the inundated areas.

After much experimentation the best combination of parameters appears to be in red, the coherence during the flood event, in green, the intensity of one of the images from before the flood and in blue, the difference in coherence from during the flood to before it.

Using this arrangement of parameters and colour channels, the image shown in figure 8 was generated. Now, the flooded lake is very clearly visible since the relatively high coherence from when it was empty in 1995 to the almost total lack of coherence when filled in 1998 turns it entirely blue. The river which runs from west to south also appears blue as does most of the south eastern corner. Less visible, but still generally

blue are some of the inundated areas in the west of the scene. There is a good reason for this. Looking closely at the regions square structures or partitions can be seen. These are presumably a network of dikes as they give points of high coherence even in the 1998 scene. Due to the poor spatial resolution resulting from the 20 looks (~60x60m ground range) and the large mask (5x5 see table 2) used to compute the coherence, this is spread over the region to some degree. Processing with fewer looks and/or a smaller mask should further improve the definition in this region and show the flooding even more clearly.



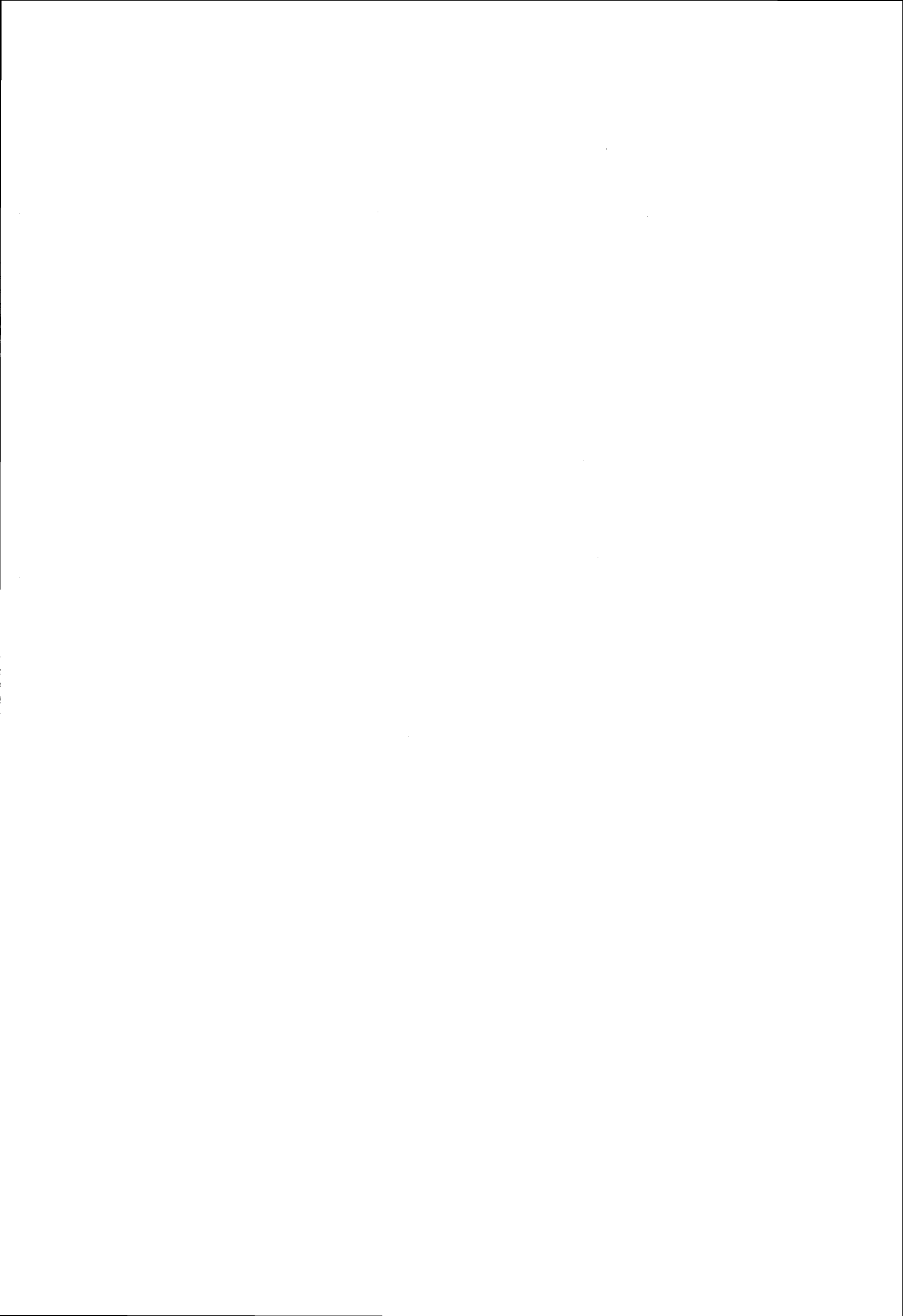
**Figure 8: Multi-Temporal Intensity/Coherence**

#### CONCLUSIONS

Assessing a region for flood damage using multi-temporal SAR imagery has the advantage over optical imagery that it is not necessary to wait for a cloudless day. However, this does not mean that flooded areas can be unambiguously detected in all cases if only the backscatter intensity is taken into consideration. Incorporating the coherence into the analysis can be of great benefit in reducing the ambiguity and giving increased confidence in the flood damage assessment made.

#### REFERENCES

1. ERS SAR Interferometry for Land Applications, ESA Contract 11740/95/NL/PB(SC), U Wegmüller, T Strozzi, T Weise, C Werner
2. <http://www.dfd.dlr/de/app/land/flood/China/index.html.de>
3. [http://earth1.esrin.esa.it/ew/china\\_f.htm](http://earth1.esrin.esa.it/ew/china_f.htm)



## Potentiel de Détection des Traits Structuraux d'un Territoire Semi-Désertique sur des Images RADARSAT : Le cas du Macizo del Deseado, Argentina.

Daniela Marchionni<sup>(1)</sup>, François Cavayas<sup>(2)</sup> et Edgardo Roller<sup>(1)</sup>

<sup>(1)</sup>INREMI Universidad Nacional de La Plata. Calle 47 N° 522, La Plata 1900, Bs. As., Argentina  
Télé/Fax : 54-221-4225648, Email : dmarchi@museo.fcnym.unlp.edu.ar

<sup>(2)</sup>Département de géographie, Université de Montréal, C.P. 6128, Succ. Centre-Ville, Montréal, Québec, H3C 3J7,  
Canada, Télé : 1-514-3438016, Fax : 1-514-3438008 Email : francois.cavayas@umontreal.ca

### RÉSUMÉ

Le but de cet article est de discuter le potentiel de détection des linéaments sur des images SAR de RADARSAT d'une zone de la Patagonie argentine caractérisée par un événement volcanique très étendu lors du Jurassique. Différents types de filtres de détection d'arêtes et de lignes dans le domaine spatial et spectral (Fourier) ont été testés à cet effet. Dans le domaine spatial tous les filtres détectent plus ou moins bien les linéaments dans les endroits avec un fort pattern structural, dépendant de la direction d'illumination du radar. La situation est différente dans les zones qui ont été couvertes par des basaltes postérieurs où les filtres de détection des lignes se sont avérés les plus efficaces pour localiser des linéaments avec une faible expression topographique. Le domaine spectral présente un grand intérêt car il permet de différencier les morphologies associées aux traits structuraux à différentes échelles avec des filtres passe-bande. La validation des résultats des analyses à partir des documents existants a démontré que les images RADARSAT ont un fort potentiel pour la cartographie structurale dans un territoire avec des patterns complexes. De plus des linéaments qui pourraient avoir une grande importance géologique et dont la présence n'a été jamais signalée auparavant, ont pu être détectés.

### INTRODUCTION

Dans le cadre du programme canadien d'échanges avec l'Amérique du sud, GlobeSar2, un projet de recherche a été initié en 1998 entre l'Université de La Plata (Argentine) et l'Université de Montréal (Canada) portant sur l'application des images RADARSAT pour la cartographie géologique-structurale du Macizo del Deseado (Province de Santa Cruz). Cette unité morphostructurale est étudiée depuis plusieurs années par l'INREMI afin de localiser de concentrations minérales quartz-aurifères, associées spatialement et temporellement au volcanisme jurassique [1], [2]. La plupart des minéralisations déjà localisées sont liées à des fractures préexistantes qui ont facilité la circulation

et précipitation des fluides hydrothermales [3], [4]. La connaissance des différents systèmes de fractures du secteur et leur chronologie devient donc importante pour la prospection géologique.

Ce territoire très étendu géographiquement (environ 10000 km<sup>2</sup>) n'a été cependant cartographié à un niveau détaillé que très partiellement, pendant des travaux de recherche minière réalisés sur le terrain et à l'aide des photos aériennes. Afin d'étendre cette cartographie dans l'ensemble du territoire, des images RADARSAT, ERS et TM-LANDSAT ont été utilisées. Le but de cet article est de présenter et discuter les résultats des analyses pour la détection des traits structuraux uniquement à partir des images RADARSAT. Les résultats déjà obtenus à l'aide des autres images satellites [5], [6] sont utilisés à titre de comparaison.

### CARACTÉRISTIQUES MORPHOSTRUCTURALES DU TERRITOIRE

Le territoire d'étude se trouve dans la portion centre sud de la Patagonie argentine (centre à 48°00'S et 69°45'W) et fait partie du secteur central du Macizo del Deseado (Fig. 1). Ce secteur, avec une altitude moyenne entre 300 et 1000 mètres a.n.m, présente un climat continental rigoureux et une pauvre couverture végétale de type arbustif. Il s'agit d'un plateau où l'on peut différencier trois environnements morphologiques a) des collines douces formées principalement par des coulées d'ignimbrites d'âge jurassique qui représentent plus de 50% des affleurements, b) des plateaux basaltiques étendus à deux niveaux différents (tertiaire et quaternaire), et c) des dépressions avec de remplissage moderne (Fig. 2). Les processus qui modèlent le paysage sont de type éolien et fluvial.

Le cadre stratigraphique du massif commence dans le Paléozoïque (?), par des métamorphites, couvertes pendant le Jurassique moyen par l'effusion de basaltes et andésites qui se présentent dans des petits affleurements isolés (Fm. Bajo Pobre), [7]. Pendant le Jurassique moyen et tardif s'est produit un événement

effusive d'une grande ampleur spatiale (Gr. Bahía Laura) [8]. Il est constitué essentiellement par des coulées d'ignimbrites de nature plutôt acide (Fm. Chon Aike) et des tufs stratifiés (Fm. La Matilde). On trouve aussi des laves et des dômes subordonnés. Ce volcanisme est l'événement géologique le plus important de la région et il est aussi le principal porteur des minéralisations. Dans le Crétacé une importante tectonique de failles s'est produite avec l'évolution des petites bassins, particulièrement à l'est de la région, où des sédiments continentaux et pyroclastiques se sont déposés. À la fin du Crétacé se produisent les premières effusions de basaltes qui suivent en intermittence dans le Tertiaire (Éocène, Oligocène, Miocène, Mio-Pliocène et Pléistocène sup.), alternant avec des dépôts sédimentaires continentaux à l'ouest et marins et continentaux à l'est. Pendant le Tertiaire sup. et le Quaternaire des mouvements d'ascension ont engendré la formation d'atterrissements. Ce cadre géologique fini par des dépôts fluviaux et alluviaux modernes.

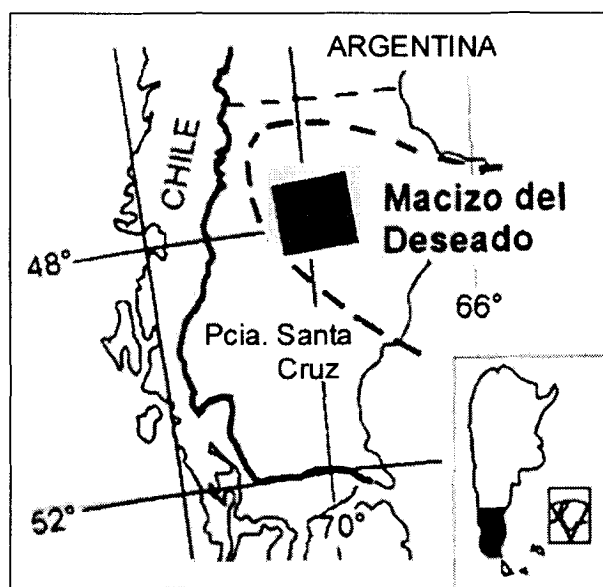


Fig. 1: Localisation de la zone d'étude et couverture des images RADARSAT utilisées

La structure de la région est la conséquence de l'action de plusieurs phases diastrophiques dominées par des failles avec des plissements très subordonnés. Les principaux systèmes de fracturation présents [9], [10] sont : le système El Tranquilo (Jurassique sup.), avec une direction principale N 25-35°W et conjuguée N 50-60°E, et le système Bajo Grande (Crétacé inf.), avec une direction principale N 50-65°W et conjuguée N 25-35°E. Un troisième système identifié, de type direct et plus récent qu'aux deux autres, a une direction N 80-100° W.

## DONNÉES ET MÉTHODES

Les images SAR-RADARSAT analysées comprennent une paire stéréoscopique des scènes ascendantes prises au mois d'août 1998 avec 20 jours de différence. Les images sont en mode standard S2 (24-31°) et S6 (41-46°) avec une résolution nominale de 25 m. La Fig. 2 montre l'image S2. Les autres images utilisées afin de valider les résultats incluent : a) une mosaïque de deux images SAR ERS-2 acquises en orbite descendante en février 1996, et b) une mosaïque de deux images TM-LANDSAT5 acquises en janvier 1986, couvrant le même territoire.

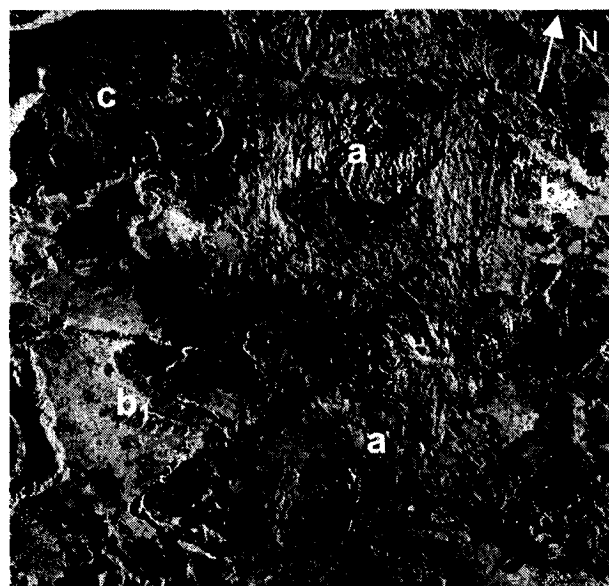


Fig. 2: Image RADARSAT (S2) : affleurements d'ignimbrites (a), basaltes tertiaires (b<sub>1</sub>), basaltes quaternaires (b<sub>2</sub>) et remplissage moderne (c).

Les images RADARSAT stéréoscopiques ont été traitées par le Centre Canadien de Télédétection pour créer un modèle numérique d'élévation (MNÉ). Afin d'étudier les effets des angles de visée sur la détection des linéaments et pour pouvoir comparer les résultats des analyses avec ceux obtenus à partir des autres images, les images RADARSAT ont été orthorectifiées à l'aide du logiciel PCI et du MNÉ. Les images LANDSAT et ERS ont été corrigées géométriquement à l'aide des transformations polynomiales.

La méthodologie suivie pour analyser le potentiel des images RADARSAT comprenait les étapes suivantes :

- 1) Sélection des sous-scènes couvrant des unités morphostructurales différentes et lissage du bruit de chatoiement,
- 2) Analyse du spectre de fréquences spatiales et établissement des filtres adaptés aux caractéristiques structurales du territoire,

- 3) Application des filtres de détection d'arêtes et des lignes et identification de ceux qui optimisent la détection des linéaments et des traits structuraux dans les différentes unités,
- 4) Application des différents filtres sélectionnés à une sous-scène représentative de l'ensemble du territoire et validation des résultats.

La sélection des filtres a été réalisée en fonction des résultats obtenus sur un ensemble de douze imassettes de 256x256 pixels. La sous-scène de validation quant à elle a été de 1024 x 1024 pixels et couvre plusieurs unités. Pour réduire le chatoiement toutes les images RADARSAT ont été lissées avec un filtre moyen 3x3.

**Filtrage des Fréquences Spatiales :**

Selon Daily [11], le spectre de Fourier des images radar est caractérisé par trois composantes principales (Fig. 3) : a) les basses fréquences spatiales dues aux variations spatiales « lentes » des teintes de gris reliées souvent à la lithologie; b) les hautes fréquences dues à la topographie et la rugosité de la surface; et c) une composante qui correspond au bruit de chatoiement. Le point de transition entre les hautes et basses fréquences ( $f_c$ , Fig. 3) varie selon la morphologie dominante du territoire.

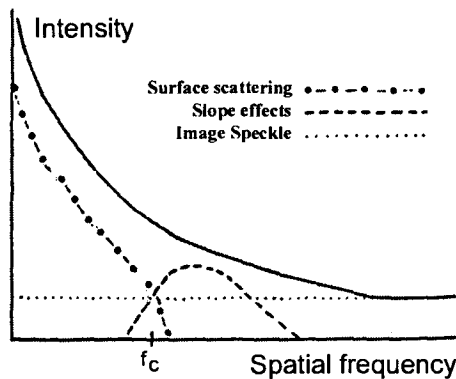


Fig. 3. Composantes du spectre de puissance d'une image radar (selon [11]).

Pour localiser cette fréquence dans notre cas, différents filtres circulaires passe-bas, passe-haut et passe-bande ont été appliqués sur la transformée de Fourier de chacune des imassettes. Les images résultantes de la transformée inverse de Fourier ont été par la suite analysées visuellement, afin d'observer les traits qui ressortaient le mieux dans chaque cas.

**Filtrage Spatiale (lignes et arêtes) :**

Les filtres spatiales de détection d'arêtes sont appliqués couramment pour l'identification les traits linéaires de signification géologique [12], [13]. Dans notre cas nous

nous sommes limités à des filtres de Sobel directionnels ainsi qu'à des filtres de Laplace. Puisque certains linéaments géologiques (ex. filons de quartz) peuvent présenter des variations de brillance qui s'apparentent à des lignes (une ligne étant composée de deux arêtes à grande proximité spatiale), des filtres directionnels de détection de lignes ont aussi appliqués sur chacune des imassettes. Deux exemples des filtres appliqués sont montrés dans la Fig. 4. Dans certaines cas un seuillage a suivi le filtrage numérique des images.

$$\begin{matrix}
 \begin{bmatrix} -1 & -1 & -1 & 6 & -1 & -1 & -1 \\ -1 & -1 & -1 & 6 & -1 & -1 & -1 \\ -1 & -1 & -1 & 6 & -1 & -1 & -1 \\ -1 & -1 & -1 & 6 & -1 & -1 & -1 \\ -1 & -1 & -1 & 6 & -1 & -1 & -1 \\ -1 & -1 & -1 & 6 & -1 & -1 & -1 \\ -1 & -1 & -1 & 6 & -1 & -1 & -1 \end{bmatrix} & 
 \begin{bmatrix} 0 & 1 & 1 & 1 & 1 & 1 & 2 \\ -1 & 0 & 1 & 1 & 1 & 2 & 1 \\ -1 & -1 & 0 & 1 & 2 & 1 & 1 \\ -1 & -1 & -1 & 0 & 1 & 1 & 1 \\ -1 & -1 & 2 & -1 & 0 & 1 & 1 \\ -1 & 2 & -1 & -1 & -1 & 0 & 1 \\ 2 & -1 & -1 & -1 & -1 & -1 & 0 \end{bmatrix} \\
 \text{N-S} & \text{NW-SE}
 \end{matrix}$$

Fig. 4. Exemples des filtres directionnels utilisés pour la détection de lignes (gauche) et arêtes (droite).

**ANALYSE ET RÉSULTATS**

Dans le cas de l'analyse des fréquences spatiales, trouver la fréquence de coupure pour séparer la lithologie de la morphologie devient facile si la topographie n'est pas très accidentée (plateaux de basaltes, dépôts alluvionnaires). Lorsque l'image est dominée par une topographie abrupte avec des alternances fréquentes des versants éclairés et ombragés (coulées d'ignimbrites) cette tâche devient plus délicate.

La Fig. 5 illustre certains exemples de filtrage dans l'espace de Fourier des imassettes des différentes unités. La première série de figures (5a-5d) montre un plateau basaltique où seule la lithologie domine. On peut observer également les résultats de coupure des hautes fréquences (5b), de coupure des basses fréquences (5d) et celle des fréquences moyennes (filtre passe-bande) (5c). Les arêtes ici sont liées à la rugosité des matériaux de surface.

Les autres séries de figures montrent des paysages avec une topographie plus ou moins abrupte. Les Fig. 5e et 5i montrent des unités sédimentaires et pyroclastiques respectivement où le réseau de drainage domine. Les Fig. 5g et 5l montrent les résultats de coupure des basses fréquences tandis que la Fig. 5k montre le résultat de coupure des hautes fréquences dans le cas des roches pyroclastiques. On peut observer que les arêtes du réseau de drainage sont présentes dans les hautes et les moyennes fréquences. Il n'est pas donc facile de les isoler (p.ex. par seuillage) sans les

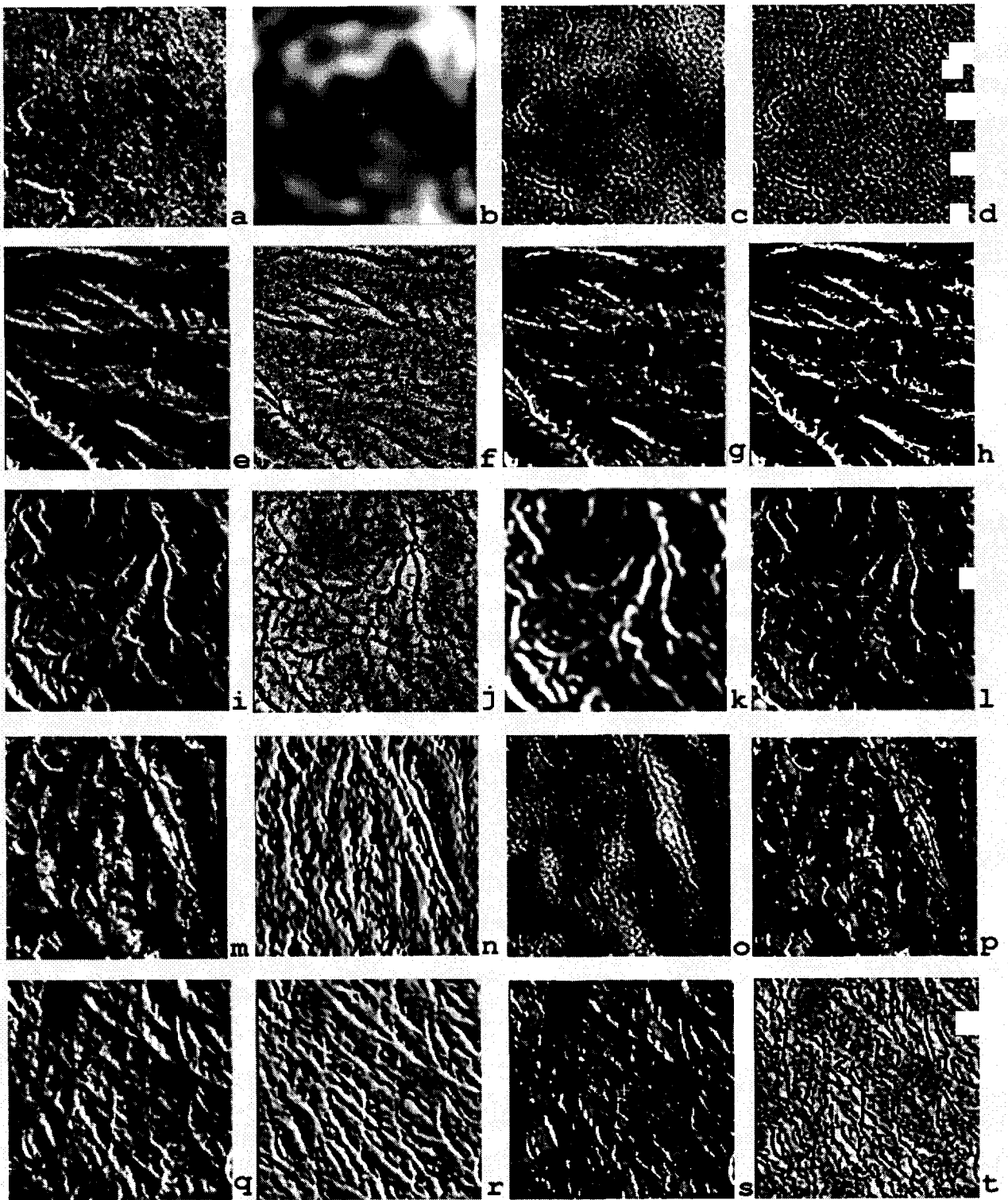


Fig. 5. Quelques exemples des résultats de l'application des filtres sur l'image RADARSAT S2 pour la détection des traits morphostructuraux dans différentes unités géologiques du Macizo del Deseado (voir texte).



fragmenter (5h). Les Fig. 5m et 5q montrent des unités d'ignimbrites avec une topographie très fracturée. Les arêtes sont ici un indicateur important des structures géologiques en place. Les Fig. 5p et 5s montrent les résultats de coupure des basses fréquences tandis que la Fig. 5o montre le résultat de la coupure des moyennes fréquences. Pour ces unités d'ignimbrites nous avons pu constater que les variations des teintes sur les images reliées à l'alternance des versants ombragés et éclairés correspondent à des fréquences moyennes entre 0,0013 et 0,002 cycles  $m^{-1}$ . En soustrayant donc ces fréquences de l'image originale il est beaucoup plus facile d'isoler les arêtes liées à la fracturation. La Fig. 5t montre l'exemple d'un filtre de Laplace appliqué sur une telle image.

Dans le cas des filtrages spatiaux, le filtre de Laplace a donné un bon résultat pour faire ressortir le réseau de drainage. Une fenêtre de 11x11 était bien adaptée pour le réseau plus dense (Fig. 5j) tandis que une fenêtre de 21x21 pour le moins dense (Fig. 5f). Les filtres de type Sobel avec une fenêtre 7x7 étaient plus adaptés à la détection des arêtes reliées à des failles et des diaclases sur les ignimbrites (Fig. 5n et 5r). Il faut mentionner cependant que les arêtes détectées avec des filtres de gradient sont décalées par rapport à la position exacte des linéaments sur le terrain, effet qui devient plus important quand on utilise des fenêtres plus grandes. Les filtres de détection ont donné des résultats équivalents avec les filtres de détection d'arêtes sauf dans les plateaux basaltiques comme l'on verra dans la prochaine section.

#### Validation des Résultats:

La Fig. 6 montre les spectres de Fourier obtenus sur les différentes images de validation. La présence d'une orientation dominante du nuage de points reflète un phénomène périodique.

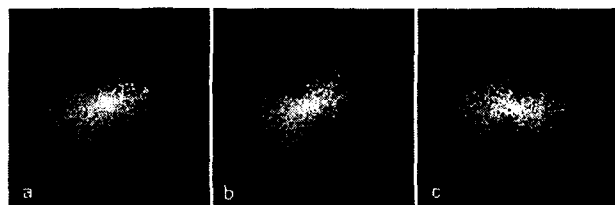


Fig. 6. Spectres de Fourier de l'image de validation pour S6 (a), S2 (b) et ERS (c).

On peut noter que, entre les images RADARSAT, l'angle de visée a une conséquence sur la présence d'une telle orientation : dans le mode S2 (Fig. 6b) les directions préférentielles sont plus nettes que dans le mode S6, où cette direction est moins évidente (Fig. 6a). La comparaison avec le spectre de l'image ERS-2 en orbite descendante (Fig. 6c) met en évidence les

problèmes de visibilité des linéaments liés à la direction d'illumination radar: les directions détectées ont une orientation opposée à celle du RADARSAT (orbite ascendante) avec un angle de visée comparable (mode S2).

L'interprétation des images résultantes de l'application des différents filtres déjà essayés sur les imagerie, nous a permis de reconnaître les directions structurales décrites dans la bibliographie et observées sur le terrain ou sur les images ERS [5], [6], [9], [10]. Cette analyse a aussi permis de mettre en évidence sur les basaltes tertiaires et quaternaires des linéaments très subtiles, d'une faible expression topographique mais d'une grande continuité (Fig. 7). Ces linéaments étaient mieux visibles sur des images obtenues par filtrage de détection de lignes avec une fenêtre de 7x7.

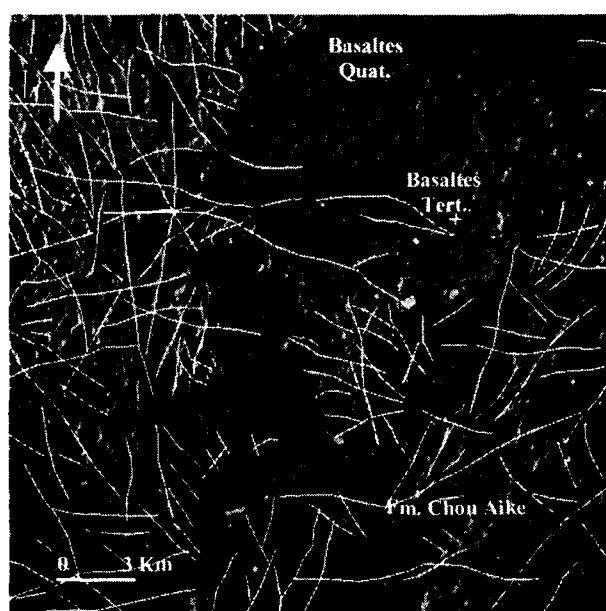


Fig. 7. Schéma géologique-structurale réalisé à partir de la sous-scène de validation en synthétisant les résultats des différents filtrages.

#### DISCUSSION ET CONCLUSION

La reconnaissance des linéaments et des traits structuraux en général (failles et diaclases) est facilitée sur les images satellitales lorsque des indicateurs indirects reliés à la morphologie et la rugosité des surfaces naturelles sont visibles: escarpements et vallées, contrôle du réseau de drainage, etc. Ces caractéristiques se manifestent dans des images satellitales par les limites entre zones de texture ou de tonalité différentes, la linéarité ou l'alternance de tonalité, etc. Les changements de pentes associés à la morphologie des zones de faille sont mis en évidence par la géométrie d'observation du radar: les versants qui sont orientés vers le radar ont une plus grande

rétrodiffusion que les autres. La continuité des versants, qui se montre dans les images, comme une ligne ou frange d'une même tonalité, peut donc, dans certains cas, nous indiquer la présence d'une zone de faille ou d'une fracture importante à proximité. Il faut quand même mentionner la perte d'informations à cause du phénomène de repliement des pentes faisant face au faisceau radar. Comme nous l'avons montré, l'application des filtres, que ce soit dans le domaine des fréquences ou dans le domaine spatial, nous aide à mieux distinguer la morphologie associée aux traits structuraux et non pas le « tracé » de la structure même sauf exception. Le recours à l'image originale est donc important afin de bien interpréter les images filtrées.

L'application des filtres de détection des lignes et des arêtes dans les domaines spatiale et spectral constituent un outil valide pour la cartographie des structures géologiques sur les images RADARSAT. La performance de ces traitements numériques dépend du type de données, des caractéristiques des surfaces et des algorithmes utilisés. Il faut remarquer que, pour une cartographie plus complète, il est nécessaire d'avoir des images dans les deux directions d'illumination possibles (orbites ascendante et descendante) et bien choisir l'angle de vise du radar. Les angles d'incidence les plus faibles ont montré un plus fort potentiel de détection des traits structuraux. La sélection de la taille des masques, dans le cas de Fourier, et de la fenêtre des filtres, dans le cas des filtrages numériques, a une incidence très grande dans la détection de ces traits. Mais avant toute opération il faut bien comprendre les caractéristiques spatiales du territoire à étudier : traits morphologiques, complexité des patterns, rugosité du relief, etc. L'analyse de Fourier est un bon moyen pour en arriver afin d'exploiter au maximum le fort potentiel des images RADARSAT.

#### REMERCIEMENTS

Les auteurs tiennent à remercier les responsables du programme GlobeSAR2 du Centre Canadien de Télédétection dont l'appui nous a permis de réaliser ce projet, ainsi que RADARSAT Int. qui nous a fourni les images RADARSAT. Nous tenons à remercier tout spécialement Mme Lyuan Wu (CCT) de sa collaboration.

#### RÉFÉRENCES

- [1] M. Del Blanco et al. "Estancia La Josefina, un nuevo prospecto aurífero en el Macizo del Deseado, provincia de Santa Cruz, Argentina" *Encuentro Internacional de Minería, Secretaría de Minería de la Nación*, Actas, pp. 93-99, Buenos Aires, 1994.
- [2] I. Schalamuk, R. Fernández et R. Etcheverry "Gold-silver epithermal veins in the Macizo del Deseado, Argentina" *Mineral Deposits, The Third Biennial SGA Meeting, Proc.*, pp. 385-388, Prague, 1995.
- [3] R. Fernández et al. "Control volcánico y tectónico de la mineralización epitermal del área La Josefina, Macizo del Deseado, Santa Cruz, Argentina" *XIII Congreso Geológico Argentino*, Actas III, pp. 41-54, Buenos Aires, 1996.
- [4] M. Tessone, M. Del Blanco et D. Marchionni "Mineralización epitermal de Veta Speme, Macizo del Deseado, Provincia de Santa Cruz" *III Reunión de Mineralogía y Metalogéneis*, INREMI, Publicación N° 5, Actas, pp. 231-235, 1996, La Plata.
- [5] D. Marchionni et al. "Aportes de la información de ERS-1 en el reconocimiento de rasgos estructurales del sector central del Macizo del Deseado, provincia de Santa Cruz, Argentina. Su implicancia metalogénica" *International Seminar on The Use and Applications of ERS in Latin America, Proc.*, pp. 133-141, Chile, 1996.
- [6] D. Marchionni et al. "Patrones estructurales y morfológicos reconocidos sobre las imágenes SAR de ERS-1 y ERS-2 y vinculados a mineralizaciones hidrotermales, Macizo del Deseado, Provincia de Santa Cruz, Argentina", *Jornadas Argentinas de Teleobservación*, Actas, pp. 1, Buenos Aires, 1998.
- [7] P. Lesta et R. Ferello "Región extraandina de Chubut y norte de Santa Cruz" *Geología Regional Argentina*, pp : 601-653, 1972.
- [8] P. Stipanovic et A. Reig "El Complejo Porfirico de la Patagonia Extraandina y su fauna de anuros" *Acta Geológica Lilloana*, Vol. I, pp. 185-297, 1957.
- [9] J. L. Panza, "Descripción geológica de las Hojas 53e Gobernador Moyano y 54e Cerro Vanguardia", Inédito, *Servicio Geológico Nacional. Buenos Aires*, 1982.
- [10] J. L. Panza, "Descripción geológica de la Hoja 54d La Manchuria" Inédito, *Servicio Geológico Nacional. Buenos Aires*, 1986.
- [11] M. Daily "Hue-Saturation-Intensity Split-Spectrum Processing of Seasat Radar Imagery" *Photogrammetric Engineering and Remote Sensing*, Vol. 49, No. 3, pp. 349-355, March 1983.
- [12] S. Deslandes, et Q. Gwyn, "Evaluation de SPOT et SEASAT pour la cartographie des linéaments: comparaison basée sur l'analyse de spectres de Fourier" *Canadian Journal of Remote Sensing*, Vol. 17, No. 2, pp. 98-110, April 1991.
- [13] P. Budkewitsch, G. Newton et A. Hynes, "Characterization and extraction of linear features from digital images" *Canadian Journal of Remote Sensing*, Vol. 20, No. 3, pp. 268-279, September 1994.

## Assimilation of ERS and RadarSat SAR observations within the STICS crop growth model.

Chauki H.(1), Prévot L. (1), Troufleau D. (1), Brisson N. (1), Olioso A. (1), Baret F. (1), Guérif M.(2).

(1) INRA - Bioclimatologie, Domaine St Paul, Site AGROPARC, 84940 AVIGNON Cedex 9, France.

(2) INRA - Agronomie, 02007 LAON Cedex, France.

tel: +33 4 32 72 20 00 Poste 24 07

fax: +33 4 32 72 23 62

e-mail: [habiba@avignon.inra.fr](mailto:habiba@avignon.inra.fr)

### ABSTRACT

Crop models are useful for monitoring crop production at a local scale. Their application to larger areas is difficult because some of their parameters may greatly differ from field to field. Remote sensing data can be helpful in solving out this problem.

In the present work, we describe a feasibility study for assimilating radar data into a crop model. The CLOUD radar model [5] was linked to the STICS [6] crop growth model to simulate time series of observed ERS and RadarSat SAR data over wheat crops. STICS is used to simulate the amount of water in the canopy and the soil moisture, which both serve as driving variables for calculating the radar backscatter through the CLOUD model. The comparison of the combined STICS+CLOUD model outputs with actual ERS and RadarSat SAR observations allows to estimate new values for some key parameters of the STICS model.

This methodology was applied at a local scale for wheat canopies, focusing on the parameters describing initial conditions such as the sowing date, the soil dry bulk density, the initial soil moisture and the initial amount of nitrogen in soil. Correcting these initial conditions was performed by minimising the difference between observed and simulated radar backscattered coefficients.

The simulated canopy biomass and leaf area index obtained after correction of initial conditions were then compared with the values simulated with standard initial conditions, as well as with those measured over six fields in the same year and same location (Alpilles-ReSeDA campaign 1996-1997, [7]). The results indicate that radar data improve the accuracy of STICS predictions.

### INTRODUCTION

In agriculture, monitoring of the crop growth and development, and estimation of yield components are of general interest, both at local and regional scale. However, over large areas, this objective is limited by the difficulty in obtaining information about field

conditions or crop properties at any given point. Combining remote sensing data with a crop growth model allows to estimate these information, and hence permits a spatial calibration of the model. Assuming that remote sensing data provide a quantification of the actual state of crops through one or more biophysical variables, the crop growth model is constrained to simulate these state variables at the time of remote sensing acquisitions. In other words, comparing the biophysical variables derived from the crop growth model with those derived from remote sensing permits to adjust the crop growth model by re-estimating values for some growth parameters, chosen by sensitivity analysis. This approach has been developed by several authors [1,2,3,4]. The chosen parameters are generally the sowing date, the growth rate and the light use efficiency [3].

In this paper a methodology for integrating remote sensing data within a crop growth model is presented. The remote sensing model is the CLOUD model [5]. It is not analytically inverted, but used in direct mode, giving radar backscattering coefficients in C-band (5.7 cm wavelength). The crop growth model is STICS [6] (Simulateur multiDisciplinaire pour les Cultures Standard). The methodology was tested against the data obtained over six fields of durum wheat, during the same year and on the same location.

### MATERIALS AND METHODS

#### The Alpilles-ReSeDA site

The test site is an agricultural area whose dimension are 4 km x 5 km, located in the Rhône Valley, near Avignon, France (N43°47', E4°45'). This area was the study site of the Alpilles-ReSeDA project [7]. This project was conducted from October 96 to November 97 and was aimed at improving methods for monitoring of agricultural areas by assimilation of remote sensing data into canopy functioning models and soil-vegetation-atmosphere transfer models. The area is homogeneous in climate conditions and soil properties.

The main crops were wheat, sunflower, corn, alfalfa and grass.

### SAR data

During the Alpillles-ReSeDA experiment, 20 SAR images were collected: 8 ERS images and 12 RADARSAT images. The ERS and RADARSAT SAR operates in C-band (5.3 GHz). The ERS SAR were obtained with an incidence angle of 23° in VV polarisation, while six RadarSat images were obtained at 23.3° incidence angle and the six others at 38.4° incidence angle, both in HH polarisation. In this paper, we only use the field averages of radar backscattered signals, extracted from six wheat fields.

### Ground data

The meteorological data required by the crop growth model were acquired close to the center of the site. Frequent biological measurements were performed during the crop cycle on the six wheat fields, including the fresh and dry total biomass, the fresh and dry organ biomass, the canopy height, the leaf area index and the yield components. Measurements of the surface soil moisture were performed concurrently to each radar acquisition, using gravimetric samples or TDR probes installed at 2.5 cm depth. The soil dry bulk density was measured on each field, in order to compute the volumetric soil moisture from gravimetric measurements.

The six wheat fields were used at two levels [7]:

- field 101 was used to *calibrate* the whole model (STICS+CLOUD);
- the five other fields (*calibration* fields 120, 208, 210, 214 and 300) were used to test and to evaluate the performance of the method (assimilation approach).

### The CLOUD model

The radar signal backscattered by the canopy  $\sigma^\circ$  is represented by a simplified one-layer CLOUD model [5] adapted to wheat [8] :

$$\sigma^\circ = -2B w_c / \cos\theta + C(\theta) + D m_v \quad (1)$$

where  $\sigma^\circ$  is expressed in dB,  $\theta$  is the incidence angle,  $w_c$  is the canopy water content (in kg/m<sup>2</sup>) and  $m_v$  is the volumetric surface soil moisture (in m<sup>3</sup>/m<sup>3</sup>). In this expression, the signal backscattered by the soil surface is given by  $C(\theta) + D m_v$  and its attenuation by the vegetation is given by  $-2B w_c / \cos\theta$ . The effect of the soil surface roughness on the angular variations of the backscattered signal is represented by the angular dependence of the parameter  $C(\theta)$ . The parameters B, C and D are derived by fitting eq. (1) to the observed radar data. The fitting procedure was twofold [8]. In a

first step, the sensitivity to soil moisture, given by parameter D, was estimated using RadarSat data at 23°. In a second step, the parameters B and C were estimated for each SAR configuration, using the data obtained on two fields (fields 101 and 120). This constitutes the calibration phase of the CLOUD model. Calibration results in terms of the B, C and D are given in table 1.

SAR	B	C 23° (range)	C 38° (range)	D	rmse (dB)
ERS	0.358	-10.04 -11.37		15.13	1.83
RadarSat	0.138	-9.30 -9.38	-13.36 -13.38	15.13	1.01

Table 1: Parameter values of the CLOUD model (Eq. (1), [8])

### STICS: the crop growth model

STICS [6] is a dynamic simulation model that calculates the growth and development of crops as well as the water and nitrogenous balance of the soil-crop system, at a daily time step. It is a generic model that can be easily adapted to various kinds of plants. The various formalisms involved within STICS were chosen for their generic nature: only a few parameters and some functions describing yield elaboration require to be adapted to various species. Model inputs account for the climate (solar radiation, minimum and maximum air temperature, precipitation, reference evapotranspiration, wind speed and relative moisture), the soil properties and the crop management. The main outputs of the model are the production (amount and quality) and the environment. The crop is globally characterised by its total above-ground biomass (carbon and nitrogen), leaf area index and the number and biomass of harvested crop organs. In its original version, STICS does not account for the water content of the canopy, nor for the partitioning of the vegetative biomass between organs (leaves, stems). So the STICS model was extended by including a parameterisation of the fraction of total above ground biomass allocated to each type of organs (leaves, stems, ears), and a parameterisation of their water content. Both parameterisations are expressed as functions of the development stage. This allows to calculate the canopy water content needed as input by the CLOUD model [9].

### SAR data assimilation approach

Temporal radar backscatter of wheat crops was predicted from a combination of modelling of radar backscatter and modelling of crop growth. The CLOUD

model was used to predict radar backscatter of crops over time. Driving variables of the CLOUD model are the canopy water content and the surface soil moisture. The time courses of both these variables are simulated by the crop growth model STICS using default values for its parameters. To improve the accuracy of the crop growth model, crop simulation are fitted to the radar backscatter by adjusting one or several initial conditions and crop growth model parameters. These adjusted values were iteratively moved from their initial values (standard values) to optimised values, which should be closer to the actual values. The minimisation criterion was the sum of the squares of the differences between simulated and measured backscattering coefficients.

The parameters and initials conditions to be adjusted were carefully selected by a sensitivity analysis. They correspond to those parameters having the largest effect on the simulated radar backscatter or on the state variables of interest [3,10].

#### Sensitivity analysis of the coupled STICS+CLOUD model

Sensitivity analysis is highly dependant on the combination of parameter values. In addition to the problem of the computation time, variance diagnostic and regression analysis give better results when the simulation experiment is well designed. Experimental design consists in a collection of runs of the model, for various values of the input parameters.

In this study, the full factorial design at three levels was chosen. This experimental design is accomplished by using each combination of the level of each factor.

As variable response to analyse, we have focused on ERS and RadarSat signals, total dry biomass, leaf area index at six phenological stages (emergence, floral satge, maximum of leaf area index, beginning of senescence, beginning of grain filling and physiological maturity).

For each variable response, there were a large number of parameters to be tested (more than 35). Generating designs for so many factors was impossible with the software used in this study. It also required too many simulations to get an efficient design in terms of variability and robustness of the estimations. To solve out this problem, we have first analysed the sensitivity to parameters of particular process of the STICS+CLOUD model, for each variable response. In other words, a process per process sensitivity analysis was conducted in a first step. Once the sensitivity of the parameters was completed for each process, the parameters that appear to be the most important contributors were selected independently for each process. Then, we have realised the sensitivity to this selection of parameters belonging to the whole set of processes, leading to a global sensitivity analysis.

## RESULTS AND DISCUSSION

#### Sensitivity analysis of the coupled STICS+CLOUD model.

Table 2 summarises the parameters found to be the most important for the coupled STICS+CLOUD model in the process per process sensitivity analysis. These parameters, sorted by relative importance, are: *iplt* (sowing date), *density* (number of plants per m<sup>2</sup> of soil after emergence), *extin* (extinction coefficient of photosynthetic active radiation in the canopy), *da* (dry bulk density of the first horizon of soil), *hcc1* (water content at field capacity of the first horizon of soil), *hcc3* (water content at field capacity of the third horizon of soil), *hl* (initial water content of the first horizon of soil) and *N1* (initial nitrogen content of the first horizon of the soil). We note that the radar signals are sensitive to the same parameters, especially those parameters describing the soil properties and driving the surface soil moisture. Among the crop parameters, only the sowing date and the crop density have an important effect on the radar signal.

	Bio-mass	LAI	$\sigma^{\circ}$ ERS	$\sigma^{\circ}$ (23°) Radarsat	$\sigma^{\circ}$ (38°) Radarsat
<i>Iplt</i>	++++	+++	+	+	+
Density	++	++	+	+	+
Extin	+++	+			
Da	++	+	++++	+++++	+++++
Hcc1	++	+	++++	++++	++++
Hcc3	++	+	+++	+++	+++
H1	++	+	+++	+++	+++
N1	++	+	++	++	++

Table 2: Summary of the sensitivity of the different variables to the STICS parameters (sensitivity increases with the number of +).

The result of the global sensitivity analysis is presented in table 3 and for as response radar backscattering ERS at emergence, leaf area index maximum and at physiological maturity. It shows that *da* (dry bulk density of the first horizon of soil) is the main contributor to the variability observed in the response, followed by *hcc1*, *hl* and *iplt*. The coupled STICS+CLOUD model is almost insensitive to the variations of the other parameters.

#### a) Estimated effects for response: $\sigma^{\circ}$ ERS at emergence

R-Squared = 0.847

	Coef	Std Error	t value	Pr(> t )
(Intercept)	-8.11e+00	0.0388	-2.09e+02	<.001
N1	3.84e-02	0.0115	3.34e+00	<.001
da	1.49e+00	0.0115	1.29e+02	<.001
hcc3	5.65e-03	0.0115	4.91e-01	0.624
hcc1	1.22e+00	0.0115	1.06e+02	<.001
hl	2.77e-01	0.0115	2.40e+01	<.001
extin	3.47e-04	0.0115	3.01e-02	0.976
densite	9.22e-04	0.0115	8.01e-02	0.936
iplt	1.94e-01	0.0115	1.68e+01	<.001

b) Estimated effects for response:  $\sigma^{\circ}$ ERS at LAI max  
 R-Squared = 0.909

	Coef	Std Error	t value	Pr(> t )
(Intercept)	-1.09e+01	0.02000	-542.000	<.001
N1	-7.04e-02	0.00595	-11.8000	<.001
da	8.36e-01	0.00595	141.0000	<.001
hcc3	-8.21e-02	0.00595	-13.8000	<.001
hcc1	9.20e-01	0.00595	155.0000	<.001
h1	2.84e-03	0.00595	0.477000	0.633
extin	-8.54e-02	0.00595	-14.4000	<.001
densite	-1.12e-02	0.00595	-1.890	0.059
iplt	5.72e-01	0.00595	96.2000	<.001

c) Estimated effects for response:  $\sigma^{\circ}$ ERS physiological maturity.  
 R-Squared = 0.991

	Coef	Std Error	t value	Pr(> t )
(Intercept)	-8.140000	0.00907	-897.000	<.001
N1	-0.029300	0.00269	-10.900	<.001
da	1.460000	0.00269	540.000	<.001
hcc3	-0.266000	0.00269	-98.900	<.001
hcc1	1.480000	0.00269	549.000	<.001
h1	0.005640	0.00269	2.090	0.036
extin	0.021800	0.00269	8.080	<.001
densite	0.001550	0.00269	0.576	0.564
iplt	-0.566000	0.00269	-210.000	<.001

Table 3: Summary for scaled coefficients of sensitive STICS parameters

**Calibration of coupled STICS+ CLOUD model**

Calibration was conducted on filed 101. Only the parameters describing the duration time of development and the crop management were changed to account for the genotype (cv. Armet) and the agronomic conditions. All other parameters and functions were set to their default values. The 0-10 cm soil moisture simulated by STICS was taken as input to the CLOUD model, as it appeared to be the closest to the soil moisture values measured over the 0-5 cm layer.

The combined model accurately simulates the crop growth (figure 1a). However, it highly overestimates the LAI (figure 1b), probably as result of the important water stress that occurred in 96-97, explaining the very low observed LAI values (maximum 1.5 m<sup>2</sup>/m<sup>2</sup>). [11] showed that for durum wheat, the photosynthetically active plant area is more determined by all organs wheat (leaves, stems and ears) than only by the leaves, specially when the canopy is stressed. Indeed, LAI simulated by STICS was in better agreement when compared to Licor LAI-2000 measurements, which include all organs.

The radar signal simulated by the combined model (figure 1c, 1d and 1e) is accurately simulated. The underestimation observed at the beginning of the crop season is due to a feature of STICS which limits the soil moisture to its value at field capacity. At the beginning of Alpilles-ReSeDA experiment, all the fields were saturated, due to heavy winter rains.

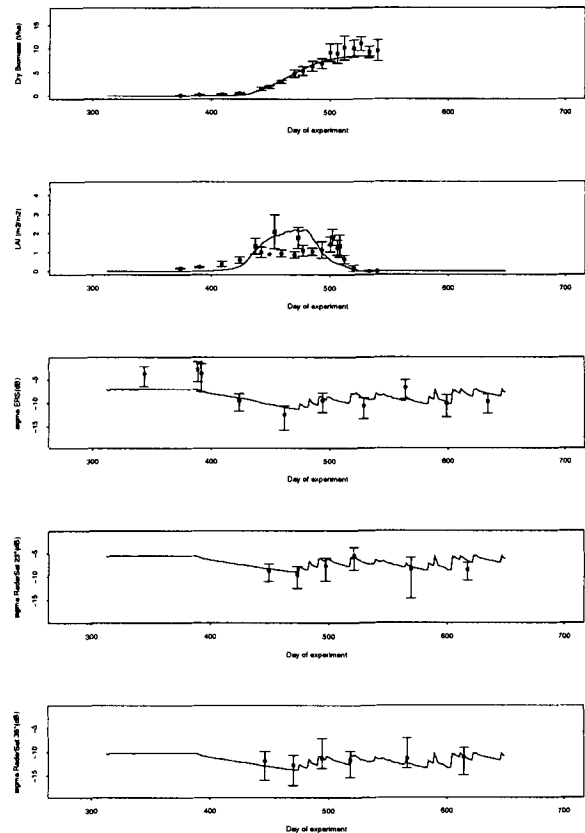
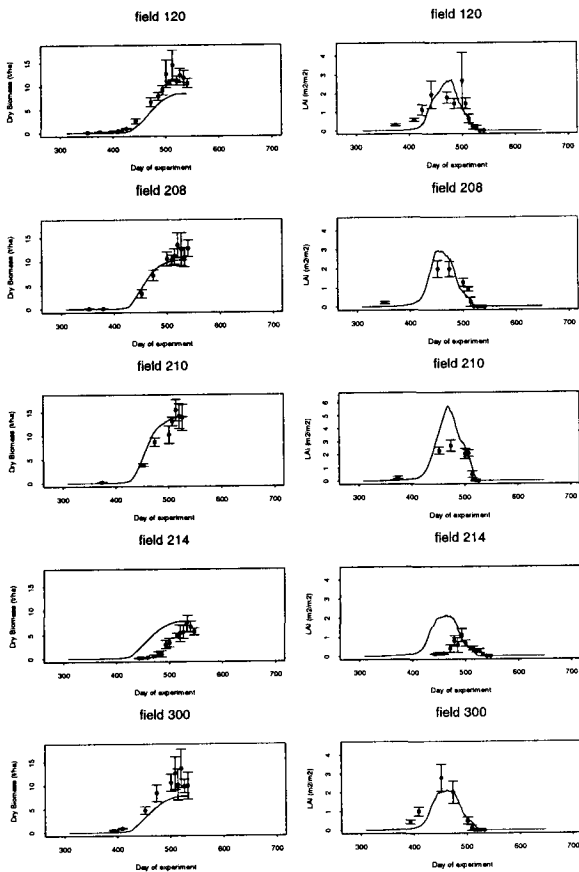


Figure 1: Crop growth and radar signal simulated by the calibrated combined model STICS+ CLOUD, a) Total above ground biomass, b) LAI, c) d) and e) radar signal backsattered respectively ERS, RADARSAT 23° and RADARSAT 38°. [•, measurements (±SD); —, simulation].

**Validation of crop growth simulations using the coupled STICS+ CLOUD model.**

The validation was twofold. In a first step, the parameters obtained in the calibration phase (see above) were used as standard values. Only the time and rate of irrigation and nitrogen applications were adapted for each field. This led to systematic inaccuracies in the STICS+ CLOUD model predictions, as can be seen in figures 2).

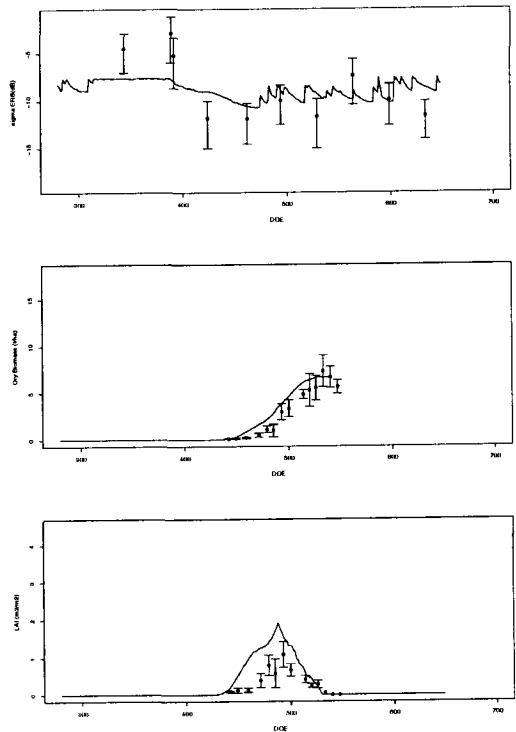


**Figure 2:** Simulation of crop growth under validation conditions by combined model STICS+CLOUD, a) Total above ground biomass, b) leaf area index LAI [•, measurements (±SD); —, simulation].

In a second step, the SAR data obtained over each field were used to optimise the crop model parameters. This was done by minimising the difference between simulated and observed radar signals. The parameters on which the optimisation was performed were those selected in the sensitivity analysis: *da*, *hccl*, *h1*, *ipt* and *density*.

An example of simulated canopy biomass, LAI and radar signals, after optimisation of the STICS+CLOUD model, is given for field 214 in figure 3 and 4. Field 214 was chosen here because it was cultivated with a spring wheat, whereas calibration field 101 was a winter wheat crop. After optimisation on the radar signals (ERS or RadarSat at 23° et 38°), the simulated canopy biomass and LAI overestimated measured values for a large part of the growing season. There was still some differences between the measured and simulated radar signals, especially for ERS. The better agreement was obtained for RadarSat at 23°. However, the accuracy of canopy biomass and LAI simulations was of the same order when optimising with other radar configurations, probably because of a relatively large contribution of the soil background to the radar backscatter. In any cases, the introduction of measured radar values greatly improved the accuracy of the

simulations of LAI and biomass, compared to those obtained with the standard values of the parameters.



**Figure 3:** Simulation of crop growth for field 214 by combined model STICS+CLOUD using ERS radar backscattering observations [•, measurements (±SD); —, simulation].

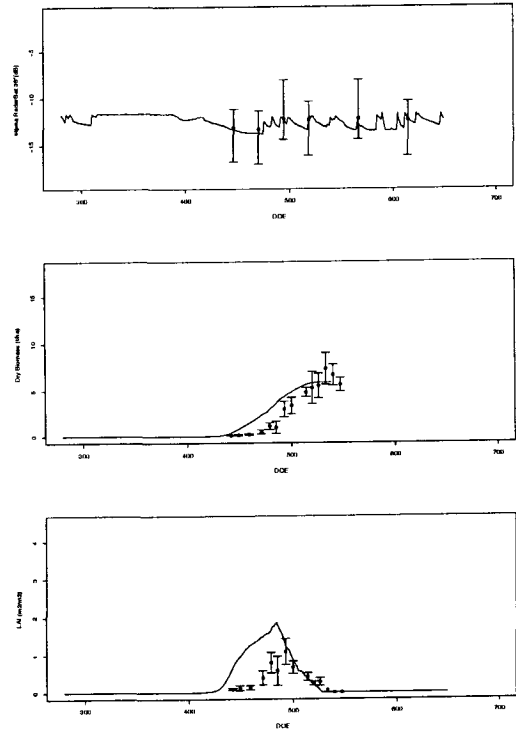


Figure 4: Simulation of crop growth for field 214 by combined model STICS+CLOUD using ERS radar backscattering observations [ $\bullet$ , measurements ( $\pm$ SD); —, simulation].

#### REFERENCES

- [1] S.J. Maas, R. Delécolle, M. Guérif, F. Baret, "Incorporation of remotely-sensed information into agricultural crop growth simulation models", In: Proc. 15<sup>th</sup> Symposium Remote Sensing for Agriculture, Beltsville, 1990/05/16-18, 40p.
- [2] R. Delécolle, S.J. Maas, M. Guérif, F. Baret, "Remote sensing and crop production models: present trends", ISPRS J. Photogramm. Remote sensing (NLD) 47:145-161, 1992.
- [3] B.A.M. Bouman, "Linking physical remote sensing models with crop growth simulation models, applied for sugar beet", International Journal of Remote Sensing, 13(14):2565-2581, 1992.
- [4] H.J.C. van Leeuwen, J.G.P.W. Clevers, "Synergy between optical and microwave remote sensing for crop monitoring", In: 6<sup>th</sup> Symp. ISPRS., Physical Measurements and Signatures in Remote Sensing, Val d'Isère, France, 1994/01/17-21, 1175-1182.
- [5] E. Attema, and Ulaby, F., "Vegetation modelled as a water-cloud", Radio Science, 13:357-364, 1978.
- [6] N. Brisson et al., "STICS: a generic model for the simulation of crops and their water and nitrogen balances. I- Theory and parametrisation applied to wheat and corn". Agronomie, 18:311-346, 1998.
- [7] L. Prévot and 66 co\_authors, "Assimilation of multisensor and multi-temporal remote sensing data to monitor vegetation and soil: the Alpilles-ReSeDA project", IGARSS'98, International Geoscience and Remote Sensing Symposium, Seattle, USA, 1998/07/06-10, 3p.
- [8] L. Prévot and al., "Comparison of ERS and multi-angular RadarSat measurements over agricultural canopies: first results of the Alpilles ReSeDA campaign", 2nd Int. Workshop on Retrieval of Bio- and Geo-physical parameters from SAR data for land Application, Noordwijk, The Netherlands, 1998/10/21-23, 7pp.
- [9] H. Chauki, N. Brisson, L. Prévot, "The meaning of wheat crop water content and its dynamic", unpublished.
- [10] S.J. Maas, "Use of remotely-sensed information in agricultural crop growth models", Ecological Modelling, 41:247-268, 1988.
- [ ] M.L. Casals, "Introduction of mechanisms of drought resistance to phasic and trophic plant functioning within a dynamic growth model", Ph.D thesis, INA-PG, France, January 1996.
- [ ] J.P.C. Kleijnen, "Five-stage procedure for the evaluation of simulations models through statistical techniques", Winter Simulation Conference, California, 1996/12.



## SUIVI DE LA COLONISATION EN AMAZONIE (ETAT D'AMAPA) A PARTIR D'IMAGES ERS

Francois-Michel Le Tourneau

Martine Droulers

Centre de Recherche et de Documentation sur l'Amérique Latine (CREDAL)

28 rue Saint Guillaume

75007 PARIS

francois.michel.le.tourneau@ens.fr

m.droulers@univ-paris3.fr

Jean-Paul Rudant

Laboratoire Géomatériaux

Université de Marne la Vallée

rudant@dedale.univ-mlv.fr

**Résumé :** Nous nous intéressons dans ce travail à l'Etat d'Amapá, situé au Nord du Brésil. Certains signes permettant de penser qu'une nouvelle phase de colonisation agricole pourrait s'y préparer, nous cherchons à faire le point sur la présence ou non de défrichements dans des zones forestières jusqu'ici préservées. Nous utilisons pour ce faire des combinaisons multi-temporelles d'images ERS, qui nous permettent facilement de repérer si des abattis ont été pratiqués dans la forêt.

Constatant peu de traces d'une colonisation agricole à grande échelle, nous nous intéressons alors à la capitale de l'Etat d'Amapá, toujours avec la même méthode de travail. Nous pouvons ainsi observer une importante croissance spatiale de cette dernière. On peut donc penser qu'une grande partie du courant migratoire existant en direction de l'Amapá a pour destination la ville et ses mirages et non les zones rurales.

**Abstract :** A certain number of signs permits to think that a new movement of agricultural colonization is to occur in the state of Amapá, northern Brazil. We thus try to produce an objective constatation on the presence of eventual deforestation zones, using a set of ERS images in multi-temporal combinations. These are actually an effective way of detecting any change in the cover of primary forest.

Not constating any large scale movement of colonization, we then experiment the same method of study on the state capital, the city of Macapá. As we can observe an important growth of the urban area, we can deduce that an important share of the people that are coming to Amapá are attracted by the city more than by rural zones.

Dans une Amazonie brésilienne qui connaît encore une forte déforestation annuelle, l'Etat d'Amapá apparaît comme une île à part. Il n'a en effet presque pas été atteint par les mouvements de colonisation des an-

nées 1970, et est resté jusqu'il y a peu en dehors des grands mouvements de population qui agitent les autres Etats de la région.

Dès lors, l'apparition depuis quelques années d'un courant migratoire important amène à se demander si l'on n'est pas à la veille du déclenchement dans cette zone d'un nouveau mouvement de colonisation de grande ampleur, qui menacerait tout à la fois les zones forestières et la politique de développement durable que tente de mettre en place l'actuel gouverneur.

Pour faire le point sur les mouvements de population et les éventuels défrichements, nous avons mis en place un SIG basé principalement sur l'exploitation d'images ERS, qui nous permet, par l'usage de combinaisons multitemporelles, de rechercher où se trouvent, à l'heure actuelle, les grandes zones de colonisation.

### I Pourquoi étudier la colonisation agricole en Amapá ?

L'Etat d'Amapa est une zone encore préservée en Amazonie, ne comptant que 390 000 habitants pour 143 000 km<sup>2</sup>. La majorité des zones forestières y est encore préservée et les réserves naturelles y occupent 41 000 km<sup>2</sup>. Ainsi, d'après l'IBGE (*Instituto Brasileiro de Geografia e Estatística*) moins de 5 % de la surface forestière de l'Etat sont aujourd'hui détruits. Dans les années 1970 et 1980, contrairement aux autres parties de l'Amazonie et notamment de l'Etat du Pará, la construction de routes (Route Macapá-Oiapoque, tronçon de route Périmétrale Norte) n'a pas provoqué d'afflux massif de colons le long de ces voies de pénétration dans la forêt. Seules quelques centaines de familles venues du Maranhão ont été installées à l'extrémité du tronçon de route Périmétrale Norte, et quelques autres autour du village de Carnot, créé à cette occasion dans le Nord de l'Etat. Les difficultés de communication ont cependant fait que, à la différence des mouvements observés sur plusieurs tronçons de la Transamazonienne, aucune colonisation

spontanée n'a suivi la colonisation officielle. Les effectifs humains très faibles de ces colonies ont donc spontanément limité leur impact sur l'environnement.

Aujourd'hui la situation de l'Amapá a changé. D'un côté les voies de communication avec le reste du pays (bateau ou avion) se sont améliorées, permettant un afflux migratoire d'environ 30 000 personnes par an qui, pour être limité, n'en est pas moins constant. Cet afflux, combiné à un accroissement naturel encore important, donne à l'Amapá l'un des taux de croissance les plus forts du Brésil dans le début des années 1990 : 5 % par an, soit un doublement de la population tous les 15 ans.

Cette croissance de la population se conjugue avec d'autres facteurs pour susciter certaines craintes sur le démarrage en Amapá d'un nouveau front pionnier, ou du moins de celui d'une pression plus importante sur les réserves forestières. En effet, malgré l'opposition du gouvernement actuel de l'Etat, qui cherche à mettre en place une politique de développement durable, le programme «*Brasil em ação*», mené par le gouvernement fédéral, cherche à résoudre la question foncière brésilienne en installant sur de nouvelles terres les paysans déshérités provenant pour nombre d'entre-eux du Nordeste. Il impose donc à l'Amapá de recevoir sur son territoire un certain nombre de projets d'installations consistant généralement en une ouverture de certaines zones forestières pour la pratique d'une petite agriculture basée sur la trilogie riz, maïs, manioc. Il était ainsi prévu d'installer en Amapá 21 projets regroupant 3500 familles, à raison de 20 à 30 hectares par famille.

Or, on sait que souvent l'ouverture de routes et de clairières dans les zones forestières est le point de départ d'une déforestation massive. En effet, les nouvelles facilités de pénétration permettent tout d'abord aux forestiers d'avoir accès à de nouvelles ressources. Elles permettent ensuite l'installation de paysans pratiquant une agriculture sur brûlis et cherchant généralement à se diversifier vers l'élevage bovin, spéculation extrêmement lucrative en Amazonie brésilienne. Le processus s'achève lorsque la plus grande partie des zones de forêt a été transformée en pâturages.

A l'opposé de cette thèse particulièrement sombre, on peut souligner qu'une grande partie de l'immigration dirigée vers l'Etat d'Amapá ne s'achemine pas vers les zones rurales, mais qu'elle reste au contraire concentrée dans la capitale de l'Etat, Macapá, comme c'est actuellement le cas dans toutes les capitales des Etats de l'Amazonie brésilienne. En effet, outre l'attraction de la grande ville, Macapá peut susciter bien des espoirs d'emploi chez les migrants depuis l'ouverture – et le succès – de sa zone de libre commerce, dans laquelle les produits d'importation sont vendus hors taxes.

Faire le point sur les causes et les conséquences de l'immigration en Amapá impliquait donc de pouvoir d'une part observer si des défrichements dans les zones

forestières se produisent et d'autre part se faire une idée la plus précise possible de la croissance spatiale de la capitale de l'Etat. Dans la mesure où une campagne de terrain ne pouvait, pour des raisons évidentes d'accessibilité des zones forestières et de coût, envisager de visiter l'intégralité de l'Etat, nous avons choisi d'étudier un certain nombre de zones stratégiques par imagerie satellitale.

## II Mise en place d'un SIG à partir d'image ERS et sélection des zones de travail

### 1. Mise en place du SIG

L'Amapá se situe à l'embouchure du fleuve Amazone, sur l'équateur, et son climat est de type tropical humide. L'utilisation d'images optique se heurte donc à la très forte nébulosité de cette zone. Par ailleurs, nous souhaitons étudier la dynamique de cet espace, et non seulement la situation à un instant donné. Nous avons donc décidé de nous appuyer sur un jeu d'images radar (en partie obtenu par le laboratoire Géomatériaux dans le cadre du programme AO3-160 «*Environnement littoral et fluvial guyanais*», et en partie acquis par le CREDAL avec un financement du Programme SIG) et en particulier sur des combinaisons multitemporelles permettant de révéler facilement les zones dans lesquelles ont eu lieu des changements importants dans l'état de la surface considérée. Ces changements de l'état de surface peuvent être attribués soit à des phénomènes naturels (marées, inondations, ...), soit à des changements dans l'occupation du sol, une bonne connaissance des milieux naturels des zones d'étude permettant le plus souvent de faire la part des deux types de phénomènes.

Les images acquises, composées de deux séries datant de 1992 et 1996, ont été ensuite introduites dans notre SIG, recalées d'après les orbites précises en ce qui concerne les images de 1992 et sur les images de 1996 pour les données de 1996. Les combinaisons colorées multitemporelles ont alors été constituées, en utilisant les données de 1992 pour le vert et les données de 1996 pour le rouge. Ces combinaisons sont alors aisément interprétables à l'œil nu : les zones teintées en jaune sont celles qui n'ont pas vu de changement notable dans leur état de surface entre les deux dates, les zones en rouge sont celles qui ont vu une forte augmentation de leur rétrodiffusion entre les deux dates, celles en vert, elles, ont vu une forte diminution de leur rétrodiffusion.

Deux types d'évolution sont particulièrement recherchés dans les images. Le premier correspond à la destruction de la forêt sur certaines parcelles et se traduit par une diminution de la rétrodiffusion entre les deux dates. On sait en effet que la forêt primaire possède un coefficient de rétrodiffusion bien supérieur à celui d'un sol de prairie. Comme la transformation d'une parcelle de forêt primaire en pâturage n'est pas effectuée immé-

diatement, mais qu'elle passe par de nombreuses étapes, l'intervalle de temps entre nos deux séries d'images peut être considéré comme optimal. L'autre évolution que l'on recherche est la croissance des zones urbaines, et en particulier de la capitale de l'Etat. Elle se traduit à l'opposé du premier cas par une croissance très fortes de la rétrodiffusion, puisque les zones urbaines ont un coefficient de rétrodiffusion largement supérieur à celui des milieux naturels, tout au moins en plaine.

De nombreuses incertitudes pèsent sur la bonne détection des zones de colonisation agraire, en particulier sur la capacité des images à repérer les parcelles déforestées de petite taille. La précision de l'analyse demandée aux images est donc accordée à ces difficultés : nous ne cherchons pas à établir une cartographie précise des zones défrichées, mais bien plutôt à repérer dans quelle partie du territoire de l'Amapá des signes d'une dynamique de colonisation sont perceptibles. En revanche, nous nous attendons à une bonne validité de la détection des zones urbaines denses et de leur croissance.

## 2. Détermination de zones d'étude

L'Etat d'Amapá est très étendu et remarquablement peu peuplé, puisqu'il rassemble à peine 400 000 habitants sur un territoire grand comme presque cinq fois la Bretagne. C'est dire qu'il est en plus grande partie désert, et qu'il est donc inutile de l'étudier dans son ensemble, au moins pour les questions qui nous intéressent dans la présente étude.

Les fronts de colonisation agricole en Amazonie s'articulent en général autour de routes, qui permettent seules la pénétration dans la forêt. Ils se localisent d'autre part le plus souvent dans des zones dans lesquelles la terre n'a pas de propriétaire, pour des raisons évidentes. Enfin, étant donné le type d'agriculture mis en place, les fronts pionniers amazoniens se situent en général en zone forestière. Ces différents éléments nous permettent donc de sélectionner des zones d'intérêt dans le territoire amapaense.

Nous nous concentrons donc sur deux tronçons routiers s'enfonçant en forêt, le premier au centre de l'Etat, dans la région de Serra do Navio, le second dans le Nord, à la frontière avec la Guyane française. Dans ces deux zones en effet, il existe une route traversant de vastes zones forestières quasiment intactes et peu protégées. A ces deux zones s'ajoute celle de la capitale de l'Etat, Macapá, dans laquelle se concentre probablement une grande partie des immigrants de fraîche date.

### III Résultats de l'étude et perspectives

#### 1. Des zones rurales encore peu affectées

Les combinaisons multitemporelles permettent

de voir que, sur les deux zones rurales étudiées, la croissance des défrichements est faible. Même si des pâturages existent déjà, leur création remonte le plus souvent à la période de la construction des routes. Néanmoins, même faible l'activité de défrichement existe le long des routes. Elle correspond probablement à une volonté des propriétaires des terrains en question de valoriser leur emplacement en bordure des axes de communication. On note par ailleurs une plus grande déforestation à proximité des villes au développement rapide, comme le bourg d'Oiapoque à la frontière avec la Guyane française. On peut supposer qu'en plus des raisons exposées ci-dessus, la demande en produits agricoles et en particulier en viande y est forte, et les approvisionnements extérieurs difficiles à se procurer.

D'après nos analyses, confirmées par une visite de terrain en avril 1999, les zones rurales de l'Amapá n'ont pas vu de grande colonisation agricole jusqu'en 1996. Il semblerait qu'après cette date des mouvements plus sensibles se soient dessinés, notamment à la suite de l'application – contre l'avis du gouvernement local – du programme «Brazil em ação». Nous envisageons donc de poursuivre notre suivi à partir de données plus récentes.

#### 2. Une croissance importante de la capitale de l'Etat

Une visite de terrain dans la ville de Macapá suffit pour voir la dynamique de croissance très importante qui l'anime. De nouveaux quartiers s'adosent ainsi aux anciens, alors que les pauvres ou les spéculateurs envahissent en de nombreux endroits les terrains publics pour essayer de s'approprier un lot de terre et y construire une maison. Ce phénomène de croissance urbaine est bien montré par les images ERS dont nous disposons.

On y distingue en effet quelques quartiers neufs et en particulier le nouveau lotissement «*Pantanal*» dans lequel la municipalité essaie de reloger les habitants des «invasions» les plus insalubres, et qui se situe sur une zone largement inondable. L'analyse des textures des zones urbaines permet d'autre part de mieux cerner la nature des différents quartiers. Le centre-ville, plus ancien et composé de maisons basses, avec des jardins débordant de végétation tranche en effet nettement avec les quartiers neufs, qu'ils soient postérieurs à 1992 ou légèrement antérieurs. Ceux-ci ont une texture beaucoup plus vive et une rétrodiffusion manifestement beaucoup plus importante, sans doute due au fait que la première étape de la création d'un quartier est la destruction de la végétation. Les bâtiments en bois ou en brique, avec leurs toits de tôle ou de fibrociment ont donc une rétrodiffusion forte, qu'aucun arbre ou jardin n'atténue.

Nous pouvons donc suivre l'étirement de la capitale de l'Etat, soit vers le Nord, le long de l'Amazone, soit vers l'Ouest le long de la route principale de l'Etat,

soit enfin vers le Sud, en direction de l'agglomération jumelle de Porto Santana, qui sera sans doute bientôt rejointe. Nous espérons donc là aussi acquérir de nouvelles données, à la fois pour actualiser nos cartes et pour couvrir cette nouvelle zone, elle aussi en pleine ébullition.

### Conclusion :

Si les grandes difficultés à obtenir des données optiques a beaucoup compté dans le choix de données radar pour nourrir une étude des dynamiques de l'Etat d'Amapá, ce choix s'est avéré bien plus riche qu'escompté au départ. Les combinaisons multitemporelles apparaissent en effet comme de très bons révélateurs des changements dans l'occupation du sol, et permettent d'évaluer la dynamique de zones étendues et difficiles d'accès. Par ailleurs, les vérifications effectuées sur le terrain montrent que les erreurs dues aux effets de saison ou au jeu des dynamiques naturelles peuvent être évitées à partir du moment où l'on possède un minimum d'information sur la présence et le fonctionnement des écosystèmes dans la zone d'étude.

En ce qui concerne l'Etat d'Amapá, il reste à ce jour l'une des zones les plus préservées de l'Amazonie, et pourrait conserver cette spécificité durant de longues années si toutefois la politique mise en place par le gouverneur actuel trouve des échos au sein de la population locale. Sur la période 1992-1996, il semble bien que la plus grande partie de l'immigration se soit répartie dans la capitale, posant de nombreux problèmes sur le plan social, mais ne déclenchant pas de grand mouvement de colonisation agricole des zones forestières.

Deux faits peuvent encore peser dans le sens du déclenchement récent d'une nouvelle poussée pionnière. Le premier est la volonté de l'Etat fédéral d'établir de nombreuses installations de paysans sans terre dans le cadre du programme «*Brasil em ação*». Le second est le renforcement de la coopération avec la Guyane française toute proche, qui doit passer principalement par une ouverture de liaisons terrestres entre Cayenne et Macapá, et qui risque donc de peser sur la préservation des zones forestières en accélérant la spéculation sur les terrains proches de la route.

### Bibliographie

- [1] Bonaventura, F.M.C., Narita, C., 1974, Macapá, Folha NA/NB 22, *Projeto RADAM, volume 6*, IBGE, rio de Janeiro  
 [2] Instituto Estadual de Pesquisa do Amapá, *Zoneamento : projeto de gestão ambiental do Amapá*, non-publié  
 [3] Le Tourneau, François-Michel, 1999, *Etude des paysages du littoral amazonien à partir d'images de radar à synthèse d'ouverture*, thèse de doctorat, Université de Marne la Vallée

[4] Masteau, Antoinette, 1997, *La frontière franco-brésilienne de l'Oyapock : essai de géographie culturelle et politique*, Thèse de doctorat, Paris III

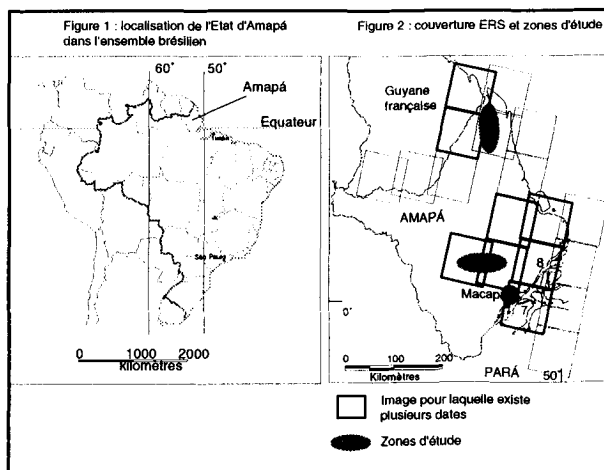
[5] Rudant, Jean-Paul, Pénicand, Claude, Nezry, Emmanuel, 1995, Utilisation opérationnelle d'images de télédétection radar pour la cartographie, *Bulletin de la Société Française de Photogrammétrie et Télédétection*, 137

[6] Stroobans, William, 1999, *Apport des données R.S.O. à la production cartographique en contexte tropical : l'exemple du Sénégal*, thèse de doctorat, Université de Marne la Vallée

[7] Teixeira Guerra, Antonio, 1954, *Estudo geografico do Territorio do Amapá*, Biblioteca geografica brasileira, Rio de Janeiro

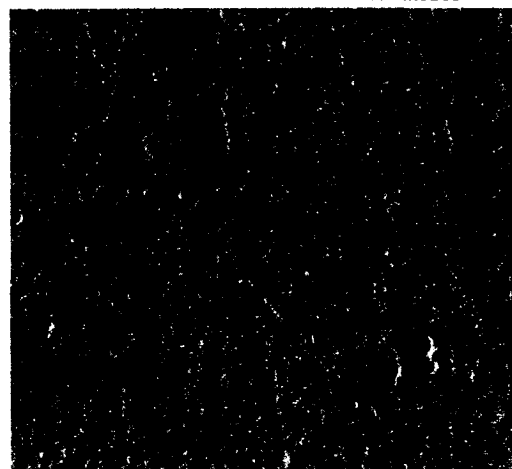
[8] Théry, Hervé, 1997, Des hommes, des femmes, des migrants, *Cahiers des Amériques latines*, 24, pp. 183-193

[9] Théry, Hervé (Dir.), 1997, *Environnement et développement en Amérique Latine*, Belin



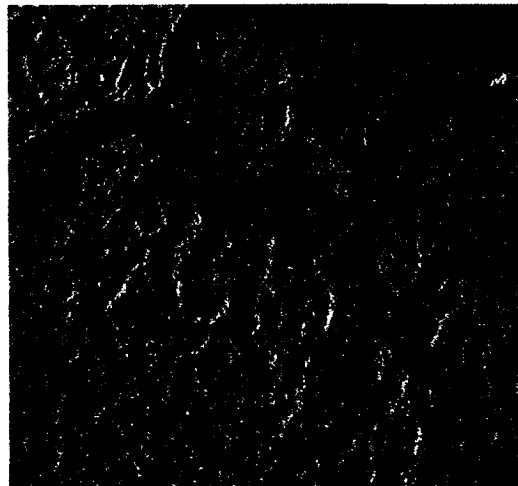
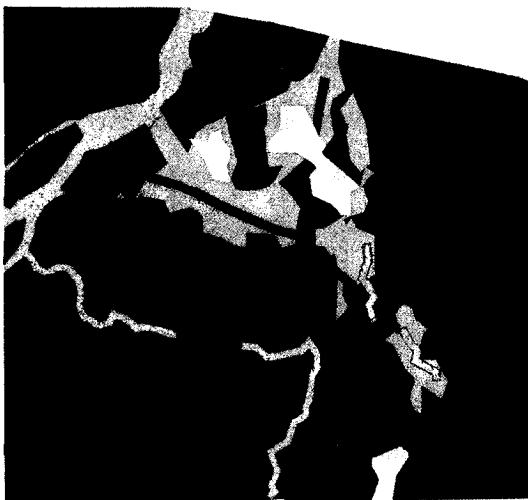
## Evolution des paysages le long de la route Carnot-Oiapoque □□ et autour de la ville d'oiapoque

1. Portion de route entre Carnot et Oiapoque










0 1 2 4  
Kilomètres

2. Alentours de la ville d'Oiapoque



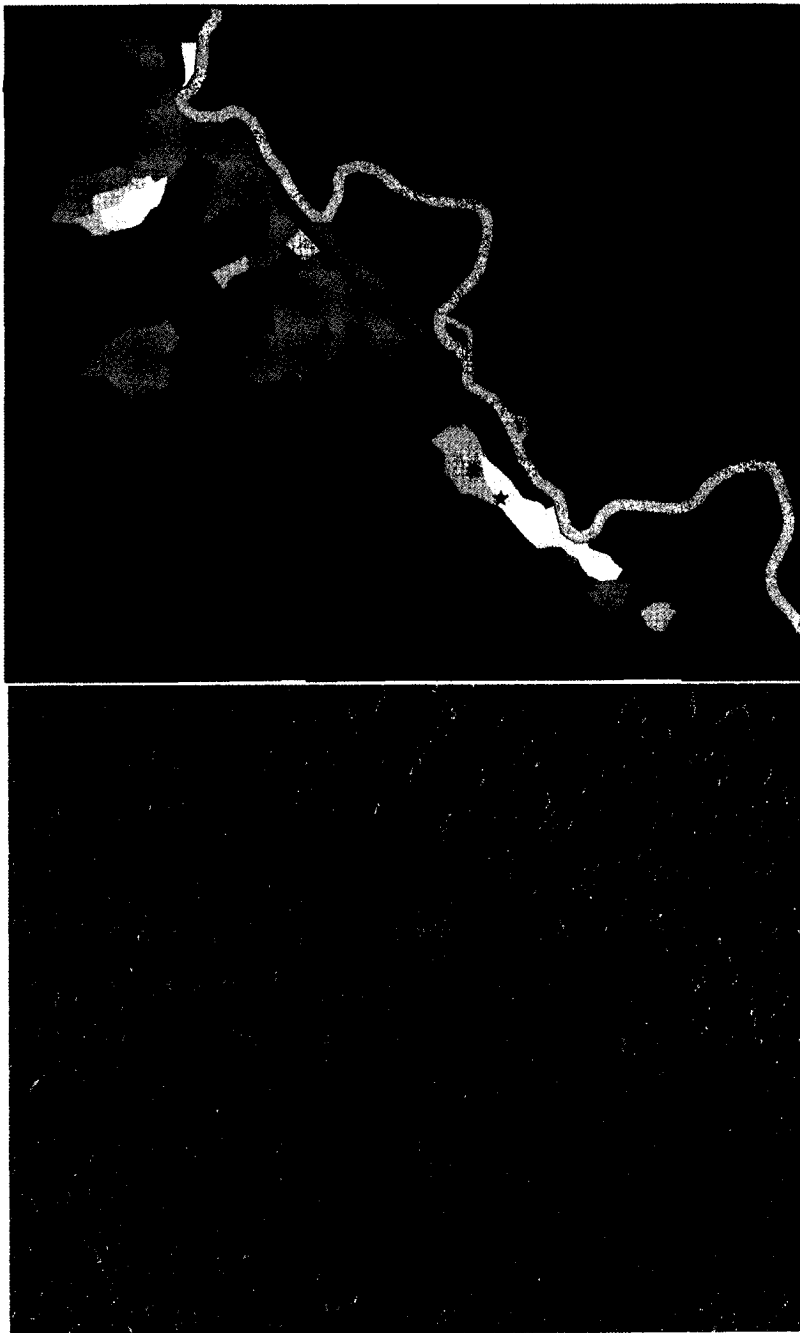
0 1 2 4  
Kilomètres

### Légende des interprétations :

- |   |                                     |   |   |   |   |
|---|-------------------------------------|---|---|---|---|
|  | Forêt sur relief en demi-orange     |  | Zones défrichées (pâturages)                      |  | Points GPS enregistrés lors de la visite de terrain |
|  | Forêt sur sol plat                  |  | Zones modifiées entre 1992 et 1996 (défrichement) |   |   |
|  | Reliefs plus prononcés (Inselbergs) |  | Route ou piste d'aviation                         |   |   |



Les images sont des compositions colorées d'images ERS. Le canal vert correspond à l'image de 1992, le rouge l'image de 1996

**Avancée des pâturages et colonisation agricole dans la zone de Pedra Branca do Amapari**









**Interprétation manuelle des images**

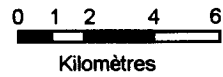
**Zones naturelles**

-  Forêt sur sol plat
-  Forêt sur faible relief

**Zones anthropisées**

-  Pâturages anciens
-  Pâturages apparus en 1996
-  Zones défrichées ou cultures
-  Village
-  Route ou piste
-  Point GPS enregistré lors de la visite de terrain

Composition colorée d'images ERS; en vert image de 1992, en rouge image de 1996



# Monitoring urban areas (Paris) with multitemporal multiincidence ERS images

Alberta BIANCHIN<sup>1</sup>, Henri MAITRE<sup>2</sup>, Jean-Marie NICOLAS<sup>2</sup>, Florence TUPIN<sup>2</sup>

(1) Istituto Universitario di Architettura Venezia  
DAEST, Ca'Tron, Santa Croce 1957, 30135 Venezia, Italia  
e-mail : alberta@iuav.unive.it

(2) ENST Département Traitement du Signal et des Images  
46 rue Barrault 75634 Paris Cedex 13, France  
e-mail : maitre@enst.fr, nicolas@enst.fr, tupin@enst.fr

## ABSTRACT

Urban areas monitoring with SAR data seems to be a rather difficult task. If specificities of urban areas have already been emphasized[1], the exploitation of ERS ESA archives allows the possibility of multitemporal analysis in order to characterize temporal stability or unstability of retrodiffusion parameters. A first interactive visual analysis of such data on Paris yields the constatation that some Paris districts, with specific urban characteristics, seem to have a rather good temporal stability.

ERS PRI images provided by ESA (ERS-AO3 169 "Urban Monitoring by multitemporal multiincidence radar imaging") allow us to illustrate the capabilities of SAR images for urban monitoring. Firstly, a set of 12 PRI scenes, obtained during the C ERS phase with the same incidence angle (descending mode), allows a temporal comparison during 19 months (april 1992 until november 1993). With the help of a 3-D Lee like filter (the whole neighbourhood of each pixel being defined as well on each image - a quincunx neighbourhood - as on temporal dimension : the other images), we can characterize the most stable pixels and the most unstable ones. Then, for the stable pixels, the analysis of 10 images acquired during E and F ERS phases (the geodetic mode) allows the analysis of slight variation of the incidence angle (about 9 values between 20 and 25 degrees). The multiincidence stability is performed with the help of the same 3D Lee like filter.

## A MODEL OF URBAN AREAS

SAR images acquired on urban areas are rather difficult to deal with as reflectivity law is a mixing of fully developed speckle (obtained for instance by rough surface backscattering), isolated targets with specular reflection law and smooth surfaces acting as infinite planes and verifying Snell-Descartes' laws [1]. If speckle

can be rather well described by Goodman model, this phenomenon varies strongly with temporal variations (in urban areas, there are for instance squares with deciduous trees so that images varies strongly between winter and summer). In the case of specular reflections, the backscattering response varies strongly with incidence angle and the geometric configuration of the urban object surfaces with the radar direction.

Moreover in urban studies, the urban areas concept covers a multiplicity of urban structures. Such urban structures are given a) by different organisation of streets, squares and blocks, b) by different built/non built areas ratio, c) by the different sizes of the elements giving shape to the structure. The case of Paris is still more complex as urban areas have been determined by some historical interventions (Haussmann) in which several transformations happened afterwards. The homogeneity of structure is not the only factor intervening in the traditional definition of urban areas.

By this way, it seems impossible to describe urban areas with an oversimple model. Yet, by comparing with fully developed speckle modelling, it is always possible to evaluate the adequation of a zone with the Goodman model of speckle. Indeed, by assuming the pdf (Probability Density Function) of the SAR image verifies the following 2-parameters law :

$$\mathcal{G}(u) [\mu, L] = \frac{2}{\Gamma(L)} \frac{\sqrt{L}}{\mu} \left( \frac{\sqrt{L}u}{\mu} \right)^{2L-1} e^{-\left(\frac{\sqrt{L}u}{\mu}\right)^2} \quad (1)$$

we know that, in the case of fully developed speckle,  $\mu$  depends on the backscattering mean value, and  $L$  corresponds to the number of looks. More, if we estimate these parameters on  $N$  samples for instance by the moment method, it is possible to obtain an approximation of the variance of these estimators. The variance of  $L$ ,

the estimator of  $L$ , can be approximated by [2]

$$\text{Var}(L) = \frac{(3L - \frac{1}{4})L}{N} \quad (2)$$

Knowing the theoretical number of looks  $L_t$ , we can always estimate these two parameters and a strong assumption of a non fully developed speckle area can be done if  $\hat{L} < L_t - \sqrt{\text{Var}(\hat{L})}$ , i.e. if  $\hat{L} < L_t - \frac{\sqrt{3L}}{\sqrt{N}}$ .

#### THE DATA

At ENST, we are in charge of an AO project (AO-163) devoted to the analysis of small incidence angle variations on urban area. In order to cope with this new problem, ESA provided us a lot of data acquired both in C phase (12 data during 1,5 year) and in geodetic phase (E and F, 11 data). The first set of data yields some conclusions on temporal stability, the second set is used in order to analyse the effects of slight variations of incidence angle. A preprocessing step yields a registration of these data.

C Phase : incidence angle constant		
Orbit number	Date	incidence angle
4118	19920429	21°.80
4619	19920603	21°.80
6122	19920916	21°.80
6623	19921021	21°.80
7625	19921230	21°.80
8126	19930203	21°.80
8627	19930310	21°.80
9128	19930414	21°.80
9629	19930519	21°.80
10130	19930623	21°.80
11633	19931006	21°.80
12134	19931110	21°.80
E&F Phase : variations of the incidence angle		
Orbit number	Date	incidence angle
14441	19940420	24°.10
15503	19940703	21°.23
15790	19940723	25°.61
16321	19940829	24°.83
16565	19940915	21°.06
16852	19941005	23°.72
17914	19941218	22°.21
18201	19950107	25°.24
18445	19950124	21°.46
18732	19950213	24°.47
18976	19950302	20°.65

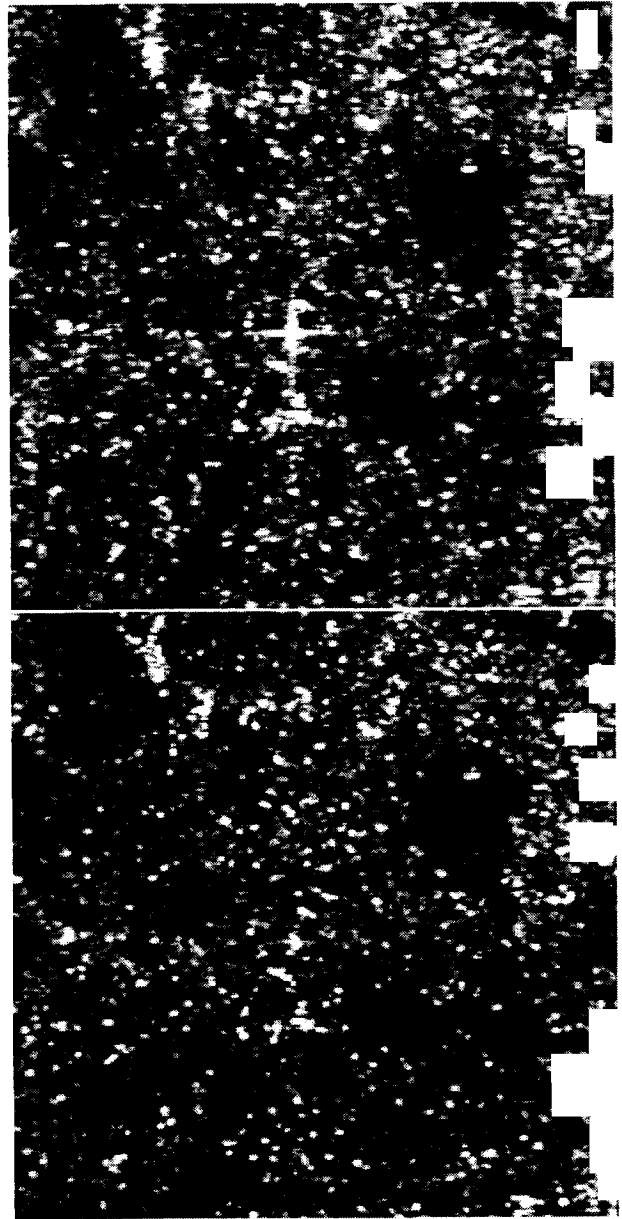


Figure 1: Two images around Montparnasse Station (June and September 1992), ©ESA 1992



In order to analyse temporal stability, we have focused our analysis on a test zone around Montparnasse station. The rectangular aspect of this station is always obtained on the full set of images. Near this station, the Montparnasse Tower can add a "sinc" response on several images.

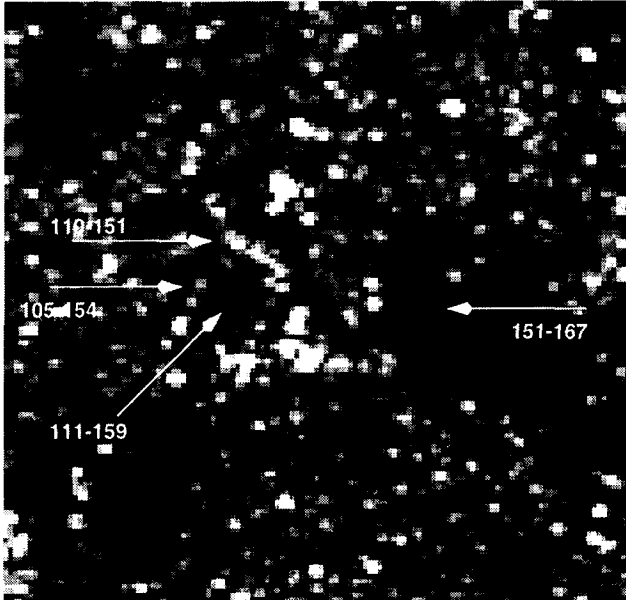


Figure 2: Pixel localisation around Montparnasse Station

- Four typical pixels have been selected :
- a specular-like pixel (110,151)
  - a specular-like pixel (105,154)
  - a speckle-like pixel inside the Montparnasse Station (111,159)
  - a speckle-like pixel inside the Montparnasse graveyard (151,167)

We compare the temporal changes (figure 3) with the incidence variations (figure 4). We can observe that the two first points seems to have a specular behaviour, and the two last points can be good candidates for a Rayleigh law.

It must be noted that such an analysis, aiming to state the variation of the radiometric values of the same pixel in several images, is not an easy task as the target appearance on a SAR image is often ambiguous. Indeed :

- the accuracy of the image registration depends on the stability of the pixel chosen for it. Usually, a visible stable pixel brilliant on the dark background, it is not a single pixel, but a set (5-9) of pixels with a maximum. The maximum is taken within different spatial configuration of the brilliant set, yielding at least a 1-pixel

error.

- the different base values for the orbits joined to the spatial correlation of radar response, can change the distribution of the intensity in the neighbourhood of the pixel considered. By this way, isolated points, as the Senat within the Luxembourg garden, are not easy to track. For it it seemed better to analyse the pixels belonging to a visible structure.

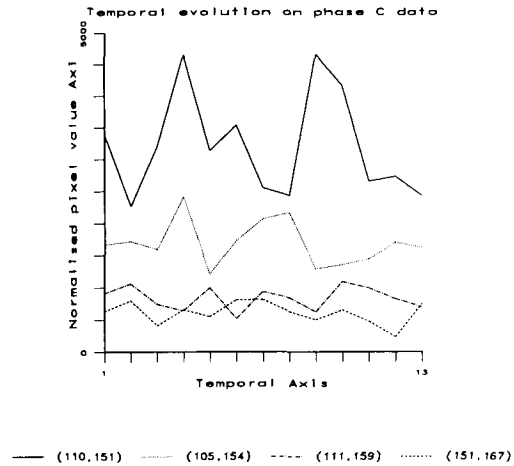


Figure 3: Temporal changes for 4 pixels around Montparnasse Station (from 29/04/1992 to 6/10/1993)

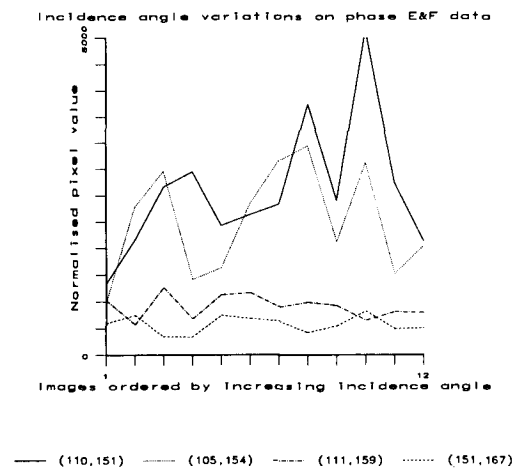


Figure 4: Incidence angle variations for 4 pixels around Montparnasse Station (from 20°.65 to 25°.61 ). The two first pixels correspond to specular-like pixels, the two last ones to speckle like pixels.

### A NEW TEMPORAL FILTER

As each acquisition has its own characteristics, it seems important to deal with a temporal filter taking into account the specific information contained in each image as well as the temporal evolution of the zone (and of the sensor). It is why we have defined a temporal Lee-like filter based on the following consideration :

- if the temporal variations seem to be similar to speckle effects, the temporal mean value is chosen
- if the pixel correspond to isolated target, the pixel value is kept.

Let us consider a pixel with a spatial and temporal neighbourhood. On this neighbourhood, it is possible to estimate the pdf of the pixel values according to the previous Gamma law  $\mathcal{G}(u) [\mu, L]$  (equation 1). If  $\bar{L}$  is near from  $L_t$ , the theoretical number of looks (3 for ERS-1), the value of the pixel is modified and equal to  $\mu$ . If  $L$  is equal or smaller than 1, the initial value remains. Between these two values, a linear law is chosen. In order to avoid interpixel correlations (visible in the case of strong isolated targets), we have defined in each initial image a quincunx neighbourhood :

X		X
	X	
X		X

By this way we obtain  $I_f$ , the filtered value with the help of  $\bar{\mu}$  and  $L$  :

$$\begin{aligned}
 I_f &= I && \text{if } L < 1 \\
 I_f &= \frac{L_t - \bar{L}}{L_t - 1} I + \frac{\bar{L} - 1}{L_t - 1} \mu && \text{if } 1 \leq L \leq L_t \\
 I_f &= \mu && \text{if } L_t < L
 \end{aligned}$$

In the case of phase C images (12 images,  $L_t = 3$ ), and with the quincunx neighbourhood, formula 2 gives  $Var(\bar{L}) < 0.44$ .

Even if this filter is not the best one (with a criterion as the mean squared error), it seems to be a good candidate to deal with urban areas images where speckle is mixed to isolated targets. On the figure 5, we can observe that the "sinc" is well kept on the upper image.

It can be noticed that the 3-D Lee-like filtered image allows to better differentiate three classes corresponding to three types of stable radiometric behavior:

- low values, generally corresponding to zones where speckle is supposed to be fully developed,
- high values corresponding to isolated target points,
- medium values corresponding to a mixed behavior (speckle not fully developed + several targets).

The filtered image, compared to the raw one, improve the detection of the structures of streets, squares and, in general, of non built areas. It is the case of the empty spaces within blocks which come out and can be easily delimited. By comparing with a simple mean filter (figure 6), this filter provides for each image a filtered

one taking into account its own characteristics (for example, the presence of the Montparnasse tower which appears as a sinc on few images and which remains on the mean filtered image).

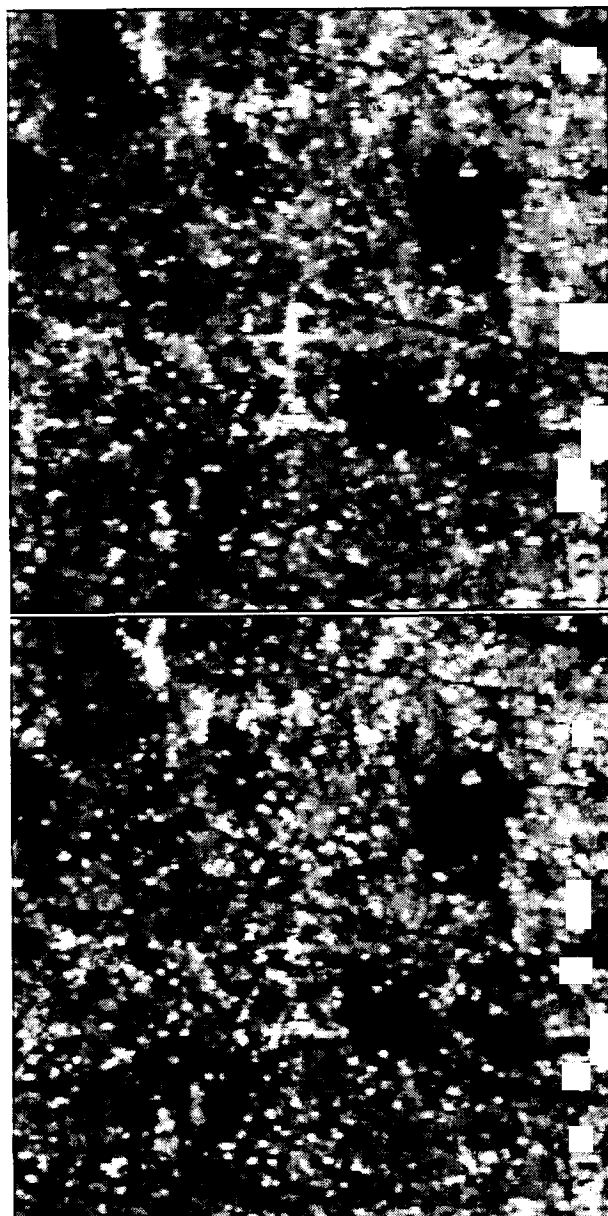


Figure 5: The two previous images around Montparnasse Station filtered by the 3-D Lee-like filter (with the help of 12 C phase images).

### CHARACTERISATION OF URBAN AREAS

The quincunx neighbourhood can provide an other interesting information : the  $\bar{L}$  value for each pixel on



Figure 6: Phase C : the classical mean filter on the full set

the image. By comparing with the theoretical value  $L_t$  and by taking into account the variance of the estimator  $\hat{L}$ , we obtain a classification on the  $\hat{L}$  image by putting a threshold at the value  $L_t - \sqrt{\text{Var}(\hat{L})}$ .

Figure 7 gives the visualisation of  $\hat{L}$  for the C phase data set (upper) and the E-F phase data set (lower), yielding a comparison between C-phase and E-F phase : it seems that, on the C-phase data, there is more areas acting as fully developed speckle. The black areas can be linked either on areas varying strongly with time acquisition (i.e. an isolated target appearing or disappearing), or on areas with backscattering depending on incidence angle (for example, a specular backscattering), or the both (for E-F phase).

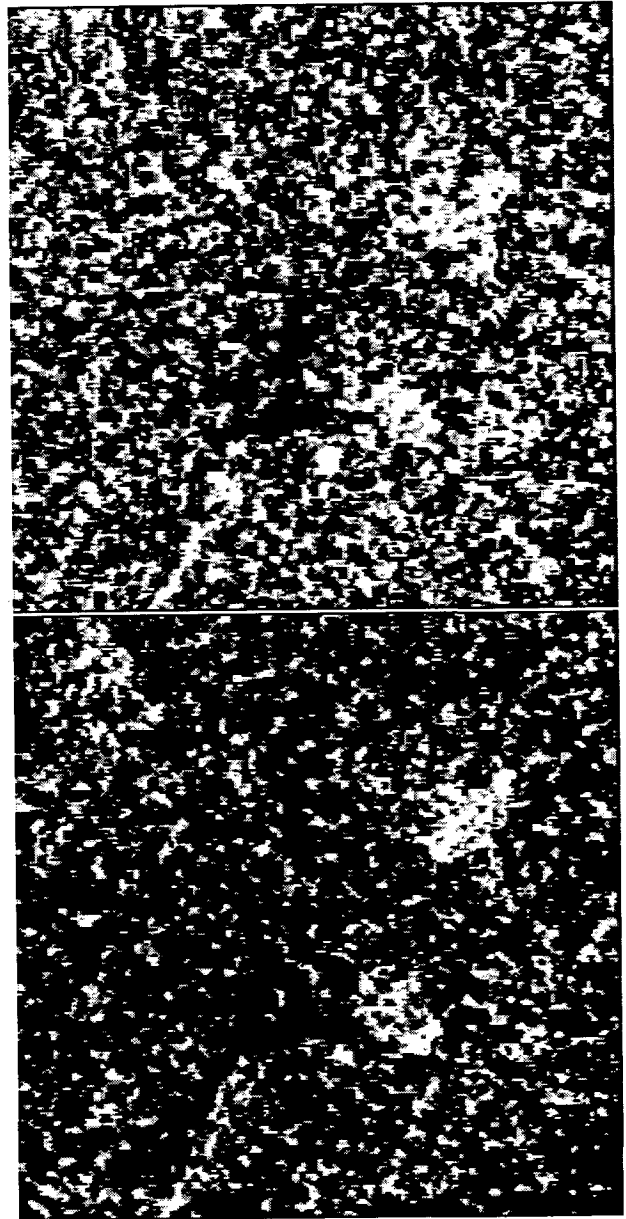


Figure 7: Around Montparnasse Station : the  $L$  value for C phase (up) and E-F phase (down). Threshold has the value  $L_t - \frac{\sqrt{3}L_t}{\sqrt{N}}$ . Black pixels correspond to non fully developed speckle

## CONCLUSIONS

Urban areas monitoring with multitemporal multi-incidence SAR data seems to be a difficult task as the aspect of SAR urban areas depends strongly on target distribution, speckle and incidence angle. A specific tool based on the Gamma law seems to be an interesting way to analyse and characterize stable points. A more complete validation will be done on a complementary set of 15 PRI images.

Yet, the analysis of the ERS data set shows that some clear shapes are always visible on the images : they correspond to urban structures (streets, blocks,...) with specific orientation with regard to the line of sight of the sensor. An interesting deepening would be reachable if other kinds of data, with different line of sight orientation (SIR-X, SIR-X, Almaz, ...), would be analysed on this test zone in order to propose a more general approach of SAR image understanding on urban areas.

## ACKNOWLEDGMENT

The authors wish to acknowledge the support of the European Space Agency in provision of data (AO-3).

## References

- [1] F.Tupin, C.Gouinaud, H.Maitre, JM Nicolas *Potential of ERS-1 images for characterisation and detection of man-made structures : road network and urban areas*. Second ERS Applications Workshop, London 1995.
- [2] JM Nicolas, A. Maruani *Modélisation du chatoiement des images de Radar à Synthèse d'Ouverture* Note technique ENST 99D007

# USING LAYOVERS IN FUSION OF OPTICAL AND SAR DATA : APPLICATION TO MUSTANG LANDSCAPE ANALYSIS

Lionel MERLIN<sup>1</sup>, Jean-Marie NICOLAS<sup>1</sup>, Denis BLAMONT<sup>2</sup>

(1) ENST Département Traitement Du Signal Et Des Images Paris,

46 rue Barrault 75634 Paris Cedex 13, France

e-mail : nicolas@enst.fr

(2) GRTS/LSIIT/ULP, Pôle API,

5 bld. Sébastien Brant, 67400 Illkirch, France

## ABSTRACT

In highly mountainous regions, it is rather impossible to get fusion of SAR and optical data, the geometric bendings on SAR images being too important. When a DEM (Digital Elevation Model) is available, we propose a new method based on the use of layovers to build a relationship between these two kinds of images. The idea is to use the characteristic shapes of layovers to establish a correspondence between a SAR image and a synthetic image obtained with the DEM. If the real image and the synthetic one are similar enough, it is possible to find some points in order to registrate firstly the real SAR image with the synthetic one, and by this way, to registrate the SAR image with the SPOT one (if a good registration between DEM and SPOT image exists already). All the success of the process is based on the quality of the synthetic image obtained. The most important parameters are the slant range  $d$ , obtained by an equation dealing with the local earth radius ( $R_t$ ), the altitude of satellite ( $H_s$ ), the elevation over GRS-80 ( $h$ ) and the elevation angle between platform position and the considered point on the earth surface ( $\theta$ ). Despite a lack of accuracy on the different parameters we could perform a fusion between an ortho SPOT image and a ERS-1 one on area of Mustang in Himalaya.

## INTRODUCTION

The fusion of optical and SAR images remains a difficult problem in mountainous regions. The important geometric bendings on SAR images forbid the use of traditional methods to get the fusion of different captors. In the scope of a landscape analysis of the Mustang region in Himalaya we had to find an other way to get an effective and valuable fusion of SPOT and ERS-1 images. We proposed a new method based on the use of an available DEM of the studied area. The idea is to simulate a SAR image (as in [1])

using the DEM to get a fusion of the synthetic image obtained and the SAR image it represents. The two images being in the same geometry, and thanks to the very important layovers in mountainous areas, we can find similar points on both images, and, consequently, determine a polynomial model from them. Finally, the fusion of a SPOT image and a SAR can be done. In this paper we present the simulation of the SAR image and the fusion of an ortho SPOT and an ERS-1 image. The process of the method is summed up by figure 1.

## Mustang's Landscape

The area of Mustang is very particular. Geologically, it belongs to the Tibetan plateau and its altitude ranges from 2600 to more than 5400 metres. This sink-basin has been filled by sedimentary layers deeply cut by narrow and steep canyons. Its climate is dry, and the vegetation is scarce. It is a steppic area, inhabited by a few thousands people. All the crops have to be irrigated and the cultivated area covers only 0.3% of the total area. Thanks to the numerous pasture lands, below 5000m, animal husbandry amounts for more than 50% of the income of the population. There are no roads, but only tracks, allowing trade with Tibet and India. On ERS-1 and SPOT images the city of Lo-Manthang and the villages of Tsarang, Marang and Ghemi are visible, as well as the Kali-Gandaki river flowing southward (particularly visible on SAR images with its very deep valley).

## SAR Images and Relief

The consequence of the existence of steep slopes is either the weak importance of speckle, or the important number of layovers.

The speckle is a well known phenomenon caused by the use of a coherent enlightenment. In mountainous areas

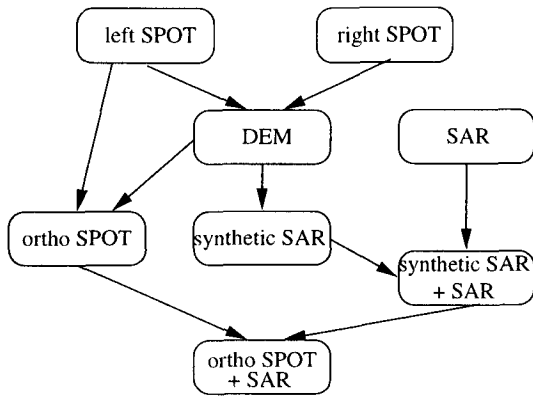


Figure 1: fusion using simulation

the pixel size is determined by the slope. Where slope is near from incidence angle, the pixel radiometry is made from a large area and thus, the speckle has a weak impact on the pixel radiometry. On the contrary, on horizontal areas (such as the plain of Lo-Manthang) the speckle appears again.

Along with the speckle, layovers are considered as the main drawback of SAR images. In mountainous areas, layovers are very important and one could think that the utility of such images is small. Nevertheless, since layovers have a characteristic shape reflecting the nature of the relief, they can be used for our purpose.

Method Used

The method we propose can be divided in the following steps :

- making of the synthetic image
- registration of a polynomial model between the synthetic image and the real one
- fusion of the ortho SPOT and the SAR images

SIMULATING A SAR IMAGE

The making of a synthetic SAR image is the most important step of the process. The image quality will affect the polynomial model and the fusion of the ortho SPOT and the SAR images. Each pixel of the synthetic image represents the area which would be seen by a SAR captor. For each line of the synthetic image we determine the pixels of DEM we used (see figure 2). For each slope we determine the two slant ranges associated with it. From these 2 slant ranges we can obtain the pixel in which the area will be seen in the synthetic image.

All the success of the method is based on the evaluation of the slant range *d* calculated from the following

equation :

$$d = \sqrt{(R_t + H_s)^2 + (R_t + h)^2 - 2 \times (R_t + H_s) \times (R_t + h) \times \cos(\theta)} \quad (1)$$

where *R<sub>t</sub>*, *H<sub>s</sub>*, *h*, *θ* are the parameters described in figure 3.

To simulate a SAR image the parameters are :

- the platform position *θ*
- the track angle *β*
- the local earth radius *R<sub>t</sub>*
- the platform altitude *H<sub>s</sub>*
- the ground elevation *h*

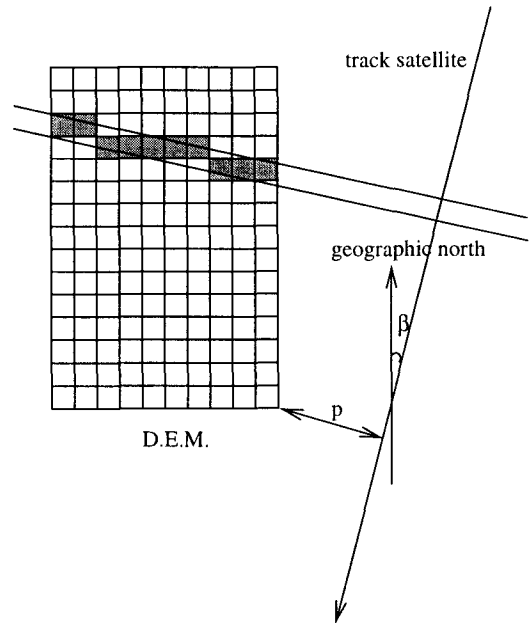


Figure 2: track's satellite

Impact of *R<sub>t</sub>*, *H<sub>s</sub>*, *θ*, *β*

On this section we quickly describe the role of these different parameters on the simulation and the impact of their accuracy on the result.

Earth radius *R<sub>t</sub>*

We can consider on SAR scene (ERS-1) the local earth radius as a constant. The local radius is calculated from the formula :

$$R_t = a \times \sqrt{\frac{((\cos(\phi))^2 + (\frac{b}{a})^4 \times (\sin(\phi))^2)}{((\cos(\phi))^2 + (\frac{b}{a})^2 \times (\sin(\phi))^2)}} \quad (2)$$

Where *a* and *b* are respectively the semi great axis and the semi small axis of the referential ellipsoid, and *φ* the geodetic latitude of the considered point. The latitude of Mustang ranges from 29 to 30 degrees. This leads to a variation of earth radius *R<sub>t</sub>*

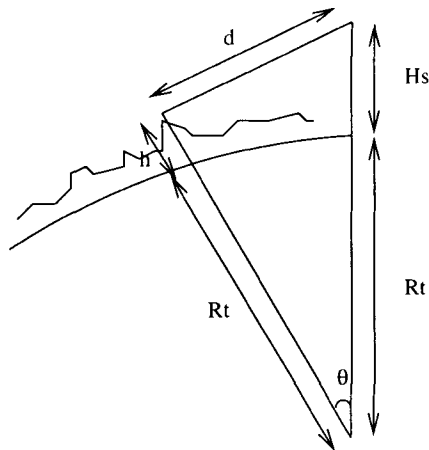


Figure 3: earth radius  $R_t$ , elevation  $h$ , satellite's altitude  $H_s$ ,  $\theta$ , slant range  $d$

of about 300 metres. A variation of 300 metres on  $R_t$  involves a variation of 8 metres on slant range  $d$ . The earth radius has a weak impact on slant range  $d$ .

#### Platform altitude $H_s$

The satellite's altitude can be known using the header parameters of SAR image. But the precision of this data is not sufficient, so we choose to use the data of the University of Delf (<http://deos.lr.tudelft.nl/ers/>), which provides the position of the ERS-1 satellite with a 10 centimetres accuracy. The position is calculated using the GRS-80 reference ellipsoid. The impact of  $H_s$  on slant range  $d$  is,  $\delta d \approx 0.9 \times \delta H_s$ . This leads to an error of 9 centimetres with an accuracy of 10 centimetres on  $H_s$ .

#### Platform position $\theta$

The parameter  $\theta$  is difficult to evaluate. The accuracy of the DEM position and the SAR position does not allow to evaluate the distance between the DEM and the SAR captor. We choose to fix the value of  $\theta$  in using approximately the position of the area on the SAR image. With a 12.5 metres pixel size and roughly counting the pixels number between the edge of the image and the studied area, we got a position of about 273 kilometres. The  $\theta$  parameter is very badly known and is one of the most critical parameters in our experiment. An error on this parameter leads to a translation of the image, and may affect the layovers.

#### Track angle $\beta$

A too important error on the track angle  $\beta$  may alter the quality of the simulation : the variation of the angle leads to a rotation of the simulated scene and the area is seen under a different angle and different

layovers are created, erased or modified. But, in our case,  $\beta$ , evaluated from the header data of the image, is known with a sufficient accuracy.

#### Ground elevation $h$

The different elevations needed to make the simulation are provided by the available DEM. The DEM represents the ground and consequently remains the main factor in order to get a successful fusion. The accuracy of the DEM is very important and must be known to evaluate the possibility to get a good simulation or not.

With an incidence angle of about 23 degrees, layovers appear with a slope of 23 degrees. If we consider two consecutive pixels away from each other by a step  $s$ , there will be a layover if the difference elevation is equal to :

$$\delta h = \tan(\theta) \times \delta s \quad (3)$$

With an incidence angle of 23 degrees (ERS-1) and a DEM with a 20 metres step  $\delta h = 8.48m$ . Consequently, if the available DEM has an accuracy of 10 metres, there is a strong probability to get non-existing layovers. The accuracy of the DEM must be known and compatible with the step according to the incidence angle.

Unfortunately, in our case, the accuracy of the different available DEMs was unknown, and we had to use them carefully. We'll see later on this paper the results obtained with different steps.

#### Sampling in PRI Format

The ERS-1 image is in PRI format with 12.5 metres pixel size. The synthetic image obtained has a pixel size roughly equals to the DEM step. A sampling of lines and columns must be done in order to get the correct SAR pixel and the same scale between the synthetic image and the real one.

#### Examples of Synthetic Image with 10 and 20 metres step DEMs

As we said previously, we didn't know the accuracy of the different available DEMs. Here are the results of the utilisation of a 10 and 20 metres step DEMs. The different parameters used are those of table (1). With the 20 metres step DEM the analogy between the SAR image and the synthetic one seems good, the layovers appear in a very similar way and we can observe the good similarity of details on both images. On flat areas the result is not as good, but, on the whole, is very encouraging. With the 10 metres step, the result is very disappointing. Despite the use of a step twice bigger, many layovers appear on the whole

pulse (m)	7.91
$d_{min}$ (km)	829.7
$p$ (km)	273
$H_s$ (km)	783
$R_t$ (km)	6373
$\beta$ (deg)	9.83
PRI size (m)	12.5

Table 1: Experimental parameters

image. This is the consequence we described in the previous section : the too poor accuracy of the DEM leads to non-existing layovers. Finally, we kept the synthetic image made from the 20 metres step DEM.

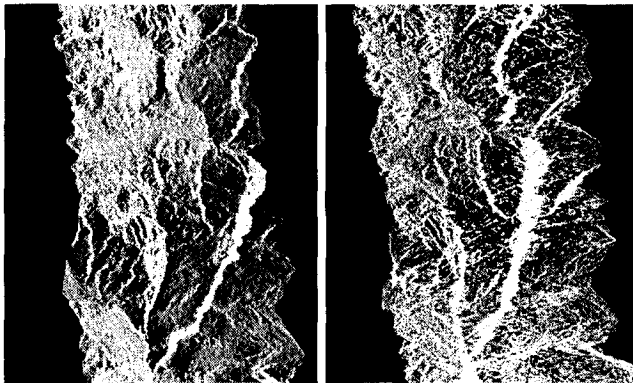


Figure 4: Simulations : 20 and 10 metres step

Comparison between ERS-1 Image and its Synthetic one

The likeness between the two images (figure 5) seems good. The layovers appear in a very similar way on both, and we can observe in more details the good accuracy of different features on layovers. However in less steep areas (like in the south-west of the image where layovers are non-existing) the similarity is more difficult to find. All the success of the simulation is based on the importance of layovers. In this case, we can find registration points on both image in order to get a polynomial model.

### POLYNOMIAL MODEL

Previously, we saw that the layovers play the main role to get registration points. Layovers offer very characteristic shapes which can be found in the synthetic image and in the real one. Now, we must determine a polynomial model. We must respect the following rules :

- the number of registration points must be as important as possible in order to have a representative

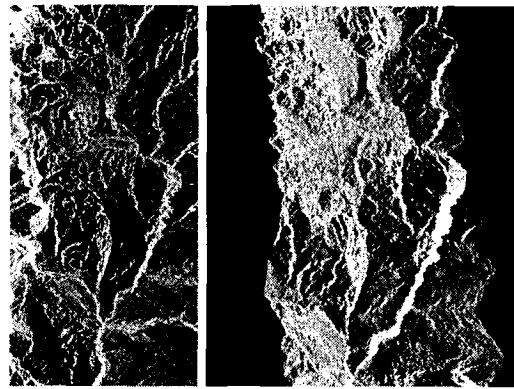


Figure 5: ERS-1 (©ESA) and its corresponding synthetic image

sample.

- the number of registration points must be compatible with the degree of polynomial model. A  $d$  degree polynomial model must have a minimum of  $\frac{(d+1) \times (d+2)}{2}$  points.

- the registration points must be equally distributed on the whole image.

It is at this point that we can appreciate the layovers that allow finding registration points. In areas where the layovers are non-existing it is very difficult (when it is not impossible) to get such points. After several attempts, we get a set of 12 points. All of these points are chosen among layovers, but we can't get points in flat areas. With 12 points we can get a second degree polynomial model (6 were required) in using the traditional method of moindre carre. A third degree polynomial model could be calculated but the numbers of points were not sufficient. On table 6 we can see the  $x$  and  $y$  residuals. There amount about 1 or 2 pixels, this is a good result which shows that the polynomial model obtained is valid. Once a polynomial model was found, we could put the synthetic image in the geometry of the real one. We used a bilinear interpolation and obtained the following image.

### FUSION OF ORTHO SPOT AND SAR

The ortho SPOT can be superimposed on the DEM, and the synthetic image can be put in correspondence with the ortho SPOT. Consequently we can get a fusion of the ortho SPOT with the SAR image. With the polynomial model we determined we could put the ortho SPOT in SAR geometry. The layovers are left blank (it's impossible to associate several pixels with one).

The layovers seems to be at the right place on the SPOT image where there are crest lines. (figure 8).

### CONCLUSION



points	x	y	x residuals	y residuals
1	540	912	1.114	1.122
2	542	774	1.239	1.215
3	940	662	2.529	2.539
4	313	867	0.377	0.374
5	551	1411	0.750	0.762
6	662	363	1.364	1.324
7	564	897	1.558	1.673
8	940	836	1.972	1.927
9	827	109	1.401	1.432
10	564	54	2.082	2.015
11	424	179	1.487	1.469
12	697	570	1.093	1.134

Figure 6: Example of points and their residuals

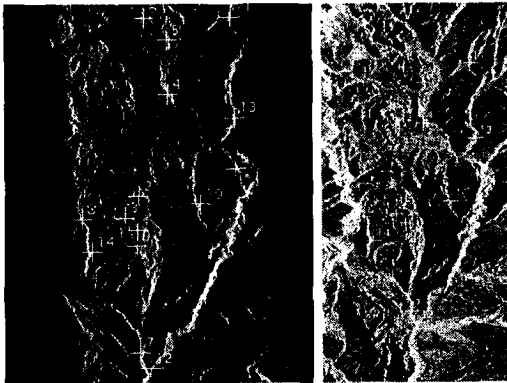


Figure 7: simulation and real images

The results obtained with the ERS-1 and ortho SPOT images are encouraging. Despite the lack of accuracy on different parameters used, we can get a valid polynomial model. The best interest is probably the use of layovers whose shapes are an effective way to get fusion. Other tests must be done to really study the interest of this method.

The simulation is based on 5 parameters :

- earth radius  $R_t$
- satellite's altitude  $H_s$
- platform position  $\theta$
- track angle  $\beta$
- altitude  $h$

$R_t$  and  $H_s$  are well known and do not have a great impact on the result.  $\beta$  and  $\theta$  are not very well known and are the most critical point in the making of the synthetic image altitude  $h$  provided by the available DEM remains the most influent parameter.

On these 3 parameters depends the success or the failure of the method.

Finally, to have the best probability to get an effective fusion, conditions are :

- working in mountainous areas



Figure 8: ortho SPOT in SAR geometry

- using a valuable DEM
- using images in near range to favour layovers, even if this analysis can be surprising.

In order to improve our method, two directions can be explored :

- The use of the method in less mountainous areas
- The use of the method with JERS-1 images

A simulation was made with a 10 metres step DEM in a average mountainous regions. It seems layovers are numerous enough, but unfortunately the speckle was too important on SAR image to find registration points.

Other tests were done on Mustang using JERS-1 images. With a 35 degrees incidence angle, the layovers were less numerous and it was harder to find registration points and the polynomial model was not utilisable.

This work has been supported by the "Programme National de Teledetection Satellitaire" (PNTS-96 and PNTS 98), in a framework of a project driven by GdR ISIS.

## References

- [1] M.Gelautz, H.Frick, J.Raggam, J.Burgstaller, F.Leberl *SAR image simulation and analysis of alpine terrain*. ISPRS Journal of Photogrammetry and Remote Sensing, Vol.53, N° 1, Feb, 1998, pp17-38



## Boreal Forest INSAR Classification Properties

David L.A. Gaveau, Heiko Balzter and Stephen Plummer

Natural Environmental Research Council  
 Centre for Ecology and Hydrology  
 Institute of Terrestrial Ecology, Monks Wood  
 Abbots Ripton, Huntingdon, Cambs, PE17 2LS, UK  
 Tel: +44 (0)1487 773381/Fax: +44 (0)1487 773277/e-mail: [DGAV@wpo.nerc.ac.uk](mailto:DGAV@wpo.nerc.ac.uk)  
<http://www.nmw.ac.uk/ite/>

### ABSTRACT

The EU-project SIBERIA aims at producing a large-scale map of Siberia, a region for which only limited information is currently available. The boreal forests of Central and Western Siberia represent the largest unbroken tracts of forest on Earth, host approximately 22% of the world growing stock and contain 11% of the world's live biomass. These forests are also regarded as a critical stabiliser of the global climate [1]. Forest inventories on this scale can only be carried out efficiently using remote sensing. Radar imagery combined with SAR interferometry lead us to the development of a method for boreal forest classification within the framework of the SIBERIA project.

### INTRODUCTION

The aim of this study was to develop a method for classification of boreal forest by means of SAR interferometry and L- and C-band radar imagery. This was achieved by a two-staged maximum-likelihood based classification algorithm using different combinations of input channels.

Results are presented for an area within the forest district of Ust-Ilimsk (59°N 103°E) in Eastern Siberia.

### DATA CHARACTERISTICS

Data from ERS-1 and ERS-2 from the Tandem Phase, a second ERS-2 image and JERS-1 data are used. Tab. 1 gives an overview of the data sources, sample images are shown in Fig. 1. All backscatter intensities have been corrected for the antenna pattern. The images have been multi-looked 2 by 10 for ERS and 2 by 6 for JERS and resampled to 50 meter pixel spacing.

### CLASSIFICATION METHOD

#### Theoretical Assumptions

Interferometric coherence is linked indirectly to forest biomass. In a low biomass forest the ground contributes

stronger to the backscatter than in a high biomass forest. Since soil is more inert than vegetation the temporal correlation of two SAR signals decreases with increasing biomass. Practically, this indirect relationship is difficult to quantify because of the dependence of coherence on slope, surface roughness, and weather conditions. The effect of these extraneous perturbations remains to be established. Slope and wind are the most problematic parameters in retrieving forest biomass from InSAR coherence.

JERS-1 and ERS-1/2 backscatter intensities are also linked to forest biomass through the same mechanisms as for coherence. The more the radiation interacts directly with the ground the more its reflection is specular. A low backscatter signature is therefore expected from low biomass areas. As vegetation cover increases the multiple interactions of radiation with vegetation elements increase (volume scattering). Up to a certain wavelength-dependent saturation, a higher backscatter signature is therefore expected from high biomass areas [2]. Because of its longer wavelength L-band ( $\lambda = 23 \text{ cm}$ ) is even more linked to forest biomass than C-band ( $\lambda = 5.6 \text{ cm}$ ). Indeed, from the same surface roughness, reflection at L-band is more specular,

Table 1. Characteristics of SAR data and weather conditions in Ust-Ilimsk

	Acquisition date	Orbit	Frame	Weather conditions
ERS-1	23 Sept. 97	32371	2439	no precipitation $T_{mean} \approx 10^\circ \text{ C}$
ERS-2	24 Sept. 97	32371	2439	no precipitation $T_{mean} \approx 10^\circ \text{ C}$
ERS-2	27 May 98	32371	2439	no precipitation $T_{mean} \approx 10^\circ \text{ C}$
JERS-1	04 May 97	28593	201	Probably snow cover
JERS-1	31 July 97	29911	203	no precipitation



Figure 1: SAR images used for classification. From left to right: ERS-1 intensity, ERS-1/2 coherence, JERS-1 intensity.

whereas reflection at C-band is more diffuse. In the case of:

- the ERS satellites,  $\lambda = 5.6 \text{ cm}$ ,  $\theta_i \approx 23^\circ$  the surface roughness maximum height  $\Delta h$  must be smaller than  $0.77 \text{ cm}$  to have perfect specular reflection.
- the JERS satellite,  $\lambda = 23 \text{ cm}$ ,  $\theta_i \approx 37^\circ$ ,  $\Delta h$  must be smaller than  $3.66 \text{ cm}$  to have perfect specular reflection.

JERS-1 L-HH intensity should therefore be a more valuable source of information than ERS-1/2 C-VV intensity for the discrimination of the following 5 land cover classes: low biomass clear-cuts, high biomass clear-cuts (birch regrowth), low biomass forest, high biomass forest, and low/little vegetation areas. It is also an easier parameter to handle than coherence since it varies much less with wind and its dependence on slope is known.

A more consistent analysis of L- and C-band interaction with vegetation canopy is needed to validate the above theoretical assumptions.

#### Classification Procedure

The classification method includes two maximum likelihood classification (MLC) with different SAR input channels, and two processing steps to improve classification accuracy. The Iterated Contextual Probability Classifier (ICP) has been recently developed at the Institute of Terrestrial Ecology. The algorithm iteratively adjusts contextual prior probabilities based on the spatial neighbourhood of each pixel and the posterior probabilities from the last iteration. It is initialised with the posterior probabilities from MLC. In each iteration a weighted combination of the information from the MLC signatures and the spatial contextual prior is calculated.

The classification consists of the following processing steps:

The classification procedure is divided in 5 distinct steps.

- 1) Supervised Gaussian maximum likelihood classification (MLC) for the retrieval of 5 land cover classes:
  - river
  - bog
  - low/little vegetation area (arable land, bare soil, low grassland, very low biomass clear-cut)
  - clear-cut
  - forest

The input data are:

- ERS-1/2 intensity scenes (23 Sept and 27 May)
- ERS one day coherence
- JERS-1 intensity scene (31 July)

The ERS intensity scenes are used to detect boggy areas. Coherence serves as a forest non-forest discriminator. JERS-1 intensity scene is used to detect low/little vegetation areas.

- 2) Iterated Contextual Probability classification (ICP) of (1) with 3 iterations, 5 by 5 window, weight = 2
- 3) MLC for the retrieval of 2 land cover classes:
  - low biomass area
  - high biomass area

The input data are:

- JERS-1 intensity scene (31 July)

classification (3) is performed over the areas that classification (1) defined as clear-cut areas.

- 4) 3 by 3 median filtering of (3)
- 5) Fusion of (2) and (4)

Fig. 2 shows the classification results after step 2, 4 and 5.

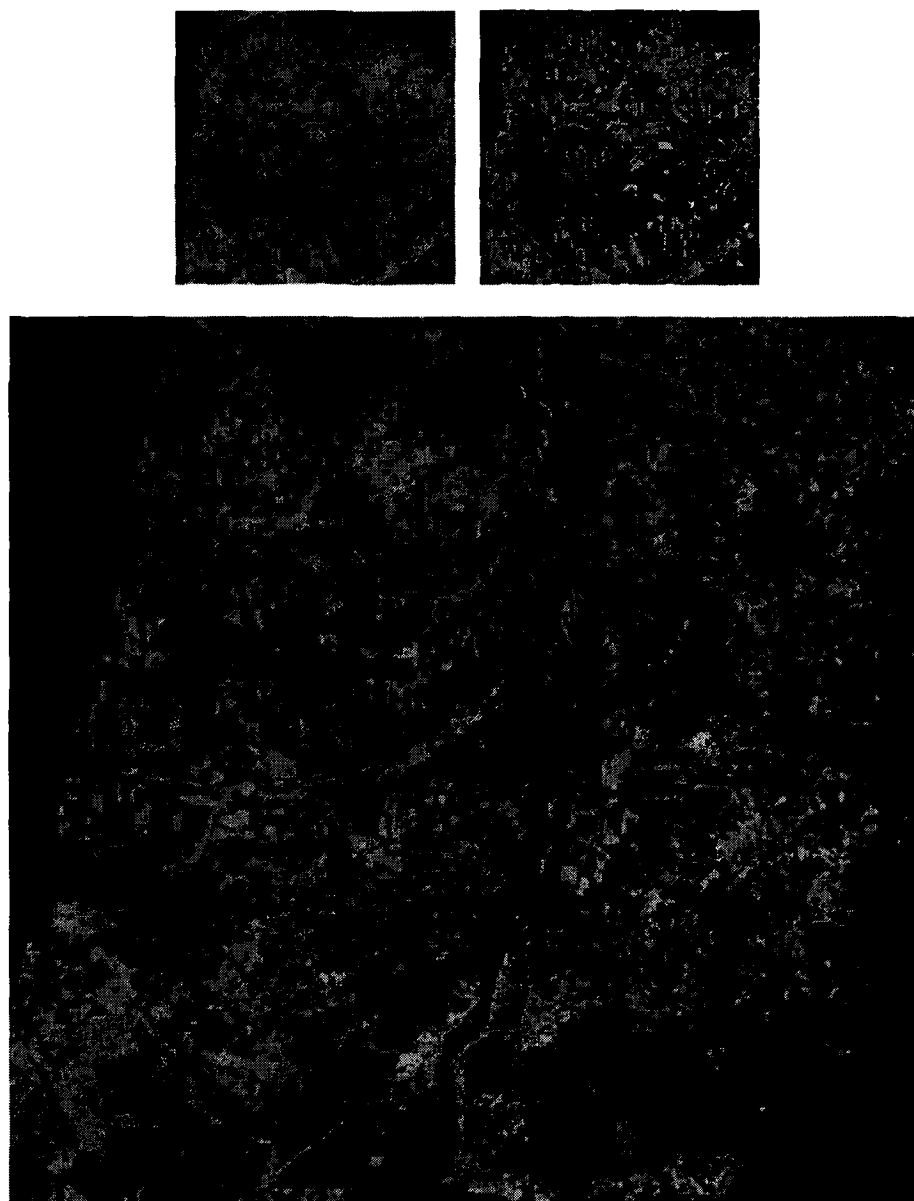


Figure 2: Classification stages. Top left: Result of processing step 2, top right: result of processing step 4, bottom (large image): final result of step 5.

Table 2: Signatures of the land cover classes in the two-staged classification.

classification stage	class	ERS coherence	ERS-1 intensity	ERS-2 intensity	JERS-1 intensity
1	river	0.149	688.95	1151.35	0.0301
1	bog	0.758	14093.87	25103.04	0.2943
1	Low/little vegetation area	0.724	13111.70	11409.99	0.0708
1	forest	0.293	11785.32	16263.56	0.3796
1	clearcut	0.619	8179.76	12311.11	0.1891
2	high biomass area	-	-	-	0.2188
2	low biomass area	-	-	-	0.1156

## RESULTS

ERS one day coherence proves useful as a forest non-forest discriminator. As predicted, low/little vegetation areas (arable land, bare soil, low grassland, recent clearcuts) and low biomass clearcuts have on average a lower backscatter than the surrounding forest in the JERS-1 scene and in the ERS scenes (Tab. 2). A similar characteristic was found for low biomass forest areas.

A comparison of the early spring JERS-1 scene (4 May 1997) with the summer JERS-1 scene (31 July 1997) reveals that the latter detects low/little vegetation areas and clear-cuts more reliably. According to the weather data for 1998 snow cover as late as the 4<sup>th</sup> May is likely. Dry snow cover has a volume backscattering coefficient equal to that of rain for the same precipitation rate [3] so that backscatter from clearcuts covered with dry snow becomes more correlated to that from the surrounding forest.

Therefore, the best scene for forest class discrimination (low and high biomass forest and low and high biomass clear-cut) is the JERS-1 L-HH intensity scene acquired the 31<sup>st</sup> July.

## CONCLUSION

A method for classification of boreal forest by means of SAR interferometry and L- and C-band radar imagery has been presented. It only applies for relatively low moisture content land surfaces. In the future, an accuracy assessment of the map will be done to check the robustness of this method.

## ACKNOWLEDGEMENTS

ERS data pre-processing has been carried out at the German Aerospace Research Institute (DLR). JERS-1 data have been pre-processed by Gamma Remote Sensing. Ground data have been kindly provided by the Russian Forestry Sector through the International Institute of Applied Systems Analysis (IIASA). This work has been funded by the European Commission through the SIBERIA project.

## REFERENCES

- [1] M.C. Dobson et al., "Dependence of Radar Backscatter on coniferous biomass," *IEEE Transactions on Geoscience and Remote Sensing*, vol. 30, pp. 412-415, 1992.
- [2] M.L. Imhoff, "A Theoretical-Analysis of the Effect of Forest Structure On Synthetic-Aperture Radar Backscatter and the Remote Sensing of Biomass", *IEEE Transactions on Geoscience and Remote Sensing*, vol. 33, pp. 341-352, 1995.

- [3] F.T. Ulaby, R.K. Moore and A.K. Fung, "Microwave Remote Sensing", *Addison-Wesley Publishing Co.*, vol I, p. 329, 1981

## Analysis and Prediction of Internal Waves Using SAR image and Non-linear Model

Hafedh HAJJI (1), Stéphane SOLE (1), Alfred RAMAMONJIARISOA (2)

(1) MétéoMer, Quartier Les Barestes, RN7, 83480 Puget/Argens, France

e-mail: [hhajji@meteomer.fr](mailto:hhajji@meteomer.fr)

(2) I.R.P.H.E

Labo I.O.A Case 903, Centre de Luminy 163 Av. De Luminy, 13288 Marseille Cedex, France

e-mail: [fred@pollux.univ-mrs.fr](mailto:fred@pollux.univ-mrs.fr)

### ABSTRACT

It is well known that tidal movement over a significant topography feature creates internal waves of large amplitude. Where there is a sill, the tidal current is, in general, assumed to be alternating and weak on either side of the barrier. During the ebb, a solitary wave is formed. Along its movements, the solitary wave develops into a group of solitons, creating change in the roughness of the sea.

For operational purposes, the French Navy, for instance, needs to simulate temperature and salinity fluctuations which influence underwater sound propagation.

Moreover, many marine operations are perturbed by the presence of internal waves. It was admitted that these waves are generated at the continental shelf by incoming and out-coming tides. To assist these marine operations, MétéoMer is developing an operational system based on Synthetic Aperture Radar (SAR) image analysis and hydrodynamic model for simulating the internal waves generated by barotropic tides on a continental shelf in the presence of stratification.

### INTRODUCTION

Internal solitary waves generated by the non-linear deformation of internal tides are a common feature of density stratified oceans. Most observations of these waves show that they occur particularly near regions of variable bathymetry such as shelf edges, seamounts, and sills, where the tidal flow over the bathymetry forces the pycnocline to oscillate with a tidal frequency, a phenomenon known as the internal tide. Internal waves can also be generated in coastal regions where a strong stratification occurs between Fresh River outflow on top of salt water from the ocean, as occurs in fjords. Examples of areas of strong internal tides are the continental shelf of the UK [1], the Strait of Gibraltar [2], Russian Seas [3], Biscay and Guinea Gulfs [4] Andaman Sea [5] and Sulu Sea [6].

If the internal tide becomes sufficiently large, non-linear and dispersive effects become important, and the wave can transform into a bore or a packet of high frequency, large amplitude internal waves. Ostrovsky and Stepanyants [7] review internal solitary wave observations from the ocean. These non-linear waves are frequently seen in in-situ data as large excursions of the

thermocline, and associated current pulses. Packets of high frequency waves and solitons are frequently observed during analysis of field in-situ measurements made from moored buoys [8]. A consequence of the current pulses is that the waves can be imaged by remotely-sensed SAR and photography, which senses the modulations of the sea-surface waves caused by the convergence and divergence between the pulses [9]. The SAR images show packets of internal waves, many with a radial spreading form, and often separated by distances comparable to the internal tide wavelength [4]. There are a number of theoretical, laboratory and numerical studies of the generation of solitons in the ocean. Lee and Beardsley [10] were first, who applied the Korteweg - de Vries equation (KdV) to modelling the evolution of a shoreward propagating internal tide over the slope and shelf region in the Massachusetts Bay. Then, this equation was used for soliton modelling in the Sulu Sea [11], at the Northwest Shelf of Australia [12], and Alboran Sea [13]. Effect of the Earth rotation was included in numerical model by Gerkema [14]. He has shown that the rotation leads to decreasing of the number of solitons generated at the long tide evolution. This model included only a two-layer model of the density stratification. The main limitation of the previous studies are as following. Usually, for calculations of the coefficients of the KdV equation only a single vertical profile of stratification is used assuming the density to the horizontally uniform. The shelf/slope zone is generally characterised by large bottom slope and large variations in stratification and shear flow, and using the mean stratification can be inaccurate in the calculation of the coefficients of the KdV equation. And second, usually the dissipative effects are parameterised by the turbulent viscosity.

To test the possibility of making accurate predictions of phase speeds and amplitudes from SAR, Small et al. [1] used the KdV equation. Results of their applications were compared to experiment measurements.

The joint analysis of remote and in-situ measurements using moored buoy stations together with modelling provides a good scientific basis for analysis and prediction of internal waves. Thus, in this study we use SAR images as well as hydrodynamic model to analysis these internal waves and we show the possibilities of making predictions of the main characteristics such as wavelength, amplitude, phase speed and associated currents.

## INTERNAL WAVES IN SAR IMAGES

## SAR observation of internal waves

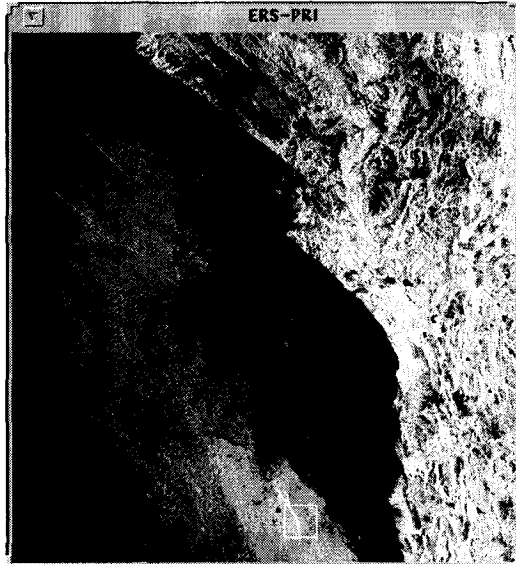


Fig.1: ERS1-SAR image (100kmx100km) acquired on Angola coastal area on the 23 July 1994 at 09H18. Three packets of internal waves are visible on the image. The black area corresponds to calm wind

Internal waves are one of the most interesting features seen by SAR, mainly because their detection was unexpected. Waves longer than several hundred meters are often seen and these large features are commonly attributed to short surface waves interacting with internal waves. The imaging mechanism seems to be well explained by a modulation of surface roughness by current variations often linked to tides. In fact, internal wave motion induces surface currents with horizontal gradients. These gradients modulate the surface wave spectrum above the internal waves, and thus the local intensity of the image in question [9].

## KdV Solitons

As in [1], the observed internal waves in SAR will be modelled in terms of the first order KdV equations. This theory has limitations, in its assumptions that the waves are small amplitude, long wavelength and in shallow water, but it allows a rapid interpretation of SAR signatures.

The steady soliton solutions predicted by KdV are [9]:

$$\eta(x,t) = \eta_0 \operatorname{sech}^2\left(\frac{(x - x_c) - c_1 t}{L}\right) \quad (1)$$

$\eta_0$  is the maximum pycnocline displacement,  $x$  and  $t$  are range and time respectively,  $x_c$  is the soliton central position, and the soliton half width  $L$  and the soliton phase speed  $c_1$  are given by:

$$L^2 = \frac{12\beta}{\eta_0 \alpha} \quad c_1 = c_0 \left(1 + \eta_0 \frac{\alpha}{3c_0}\right) \quad (2)$$

where  $c_0$ ,  $\alpha$  and  $\beta$  are the linear phase speed, and coefficients of non-linearity and dispersion respectively, strongly dependent on the stratification and water depth. These coefficients can be easily estimated from two-layer stratification with density discontinuity  $\Delta\rho$  at the depth  $h$  [15]. In the next section, we will give their expressions for continued stratification.

The internal currents can also be obtained by the approximation to the continuity equation:

$$u = -c_1 \frac{\partial \eta}{\partial x} \quad (3)$$

The surface currents induced by the soliton give rise to the areas of convergence and divergence, which can modulate the surface roughness in the capillary-gravity range, which is imaged by the SAR. Of particular note is the range  $D$  between convergence and divergence, which is suitable circumstance can be measured from the SAR [9]. A fixed relationship between  $D$  and  $L$  is given simply by:

$$D = 1.32L \quad (4)$$

From these equations, one can estimate amplitude and phase speed from the distance  $D$  on the SAR signatures.

## Application

The ERS1-SAR image acquired on the 23/07/94 at 0918 corresponds to a generation area of internal waves on Angola coast (Fig.1). Not far from this area, Sedcoforex platform "Omega" was shifted 4°. Fig. 2a is zoom of the internal waves located southeast and at approximately 200m depth. The imagette was smoothed to filter noise. The cross-section scaled in relative image intensity gives a clear profile of different solitons (Fig.2b).

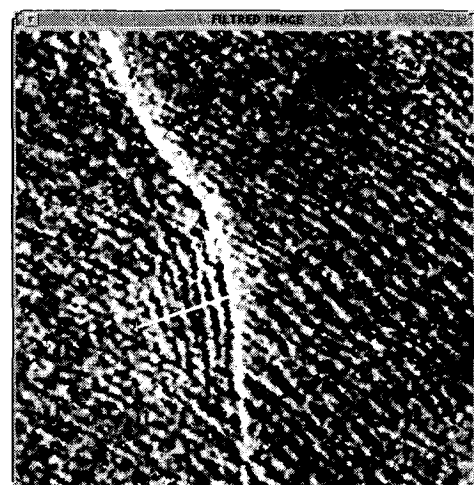


Fig.2a : Filtered imagette (6.4kmx6.4km) showing swell and solitons. The crossed line corresponds to the cross-section given in Fig. 2b.



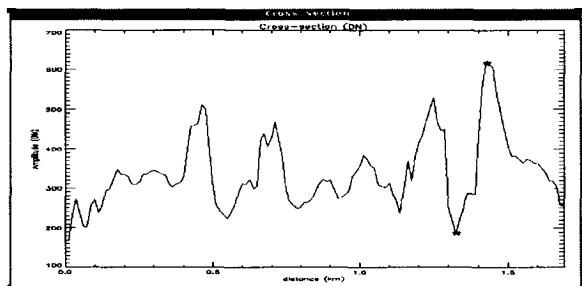


Fig.2b : Relative cross-section. The largest D is estimated at 150m (distance between the two stars)

Fig.3 shows the Brunt-Väisälä frequencies computed from the Levitus atlas [16] at the nearest grid-point to the SAR image location and for different seasons. July-August-September (JAS) was chosen to compute the KdV coefficients. For the four seasons the stratification is characterised by two layers. The depth of the upper layer is 20m.

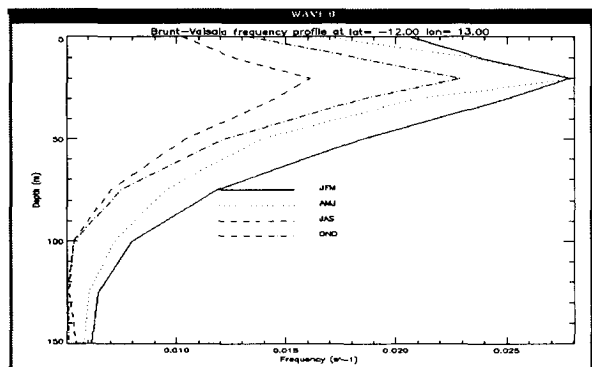


Fig.3: Brunt-Väisälä frequency computed for different seasons using the Levitus data.

Application of KdV solution gives for the heading soliton a pycnocline displacement of 6m, a surface velocity more than 0.4m/s (Fig.4) and a phase speed of 0.4m/s.

Assuming a tide period of 12.42 hours corresponding to M2 tide component, one can estimate the phase speed from measuring the distance between the two packets observed northwest of the image (Fig.1). This will give approximately 0.3m/s.

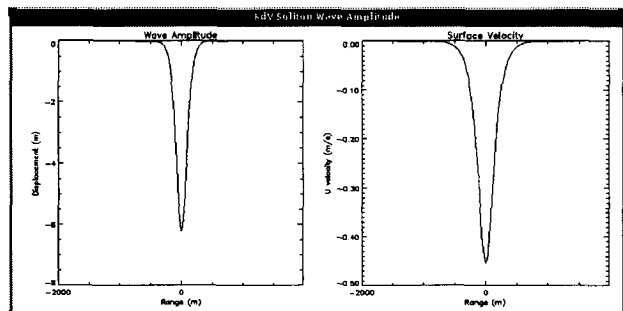


Fig.4 : Pycnocline displacement and surface current associated to the heading soliton (see Fig.2b).

### KDV EQUATION FOR INTERNAL WAVE.

The rotated-extended KdV model

The KdV equation is an appropriate physical model for the description of the non-linear and dispersive properties of an internal wave field. It is derived as a perturbation expansion and is valid to first order in wave amplitude and for long waves; that is, it is assumed that  $H/\lambda \ll 1$  and  $a/H \ll 1$ , where  $H$  is the local water depth,  $\lambda$  is a representative wavelength, and  $a$  is a representative wave amplitude. For arbitrary vertical stratification of ocean density and background shear flow, the rotated modified extended KdV equation

$$\frac{\partial}{\partial x} \left( \frac{\partial \eta}{\partial t} + (c + \alpha \eta + \alpha_1 \eta^2) \frac{\partial \eta}{\partial x} + \beta \frac{\partial^3 \eta}{\partial x^3} \right) = \frac{f^2}{2c} \eta \quad (5)$$

([12], [17], and [18]) is written as

where  $\eta$  is the wave profile corresponding to the vertical isopycnal displacement,  $f=2\Omega \sin \phi$  is the Coriolis parameter ( $\Omega=7.29 \cdot 10^{-5} s^{-1}$ ) and  $\phi$  is latitude.

The phase speed of the linear long wave  $c$  is determined by the eigenvalue problem:

$$\frac{d^2 \Phi}{dz^2} + \frac{N^2(z)}{c^2} \Phi = 0 \quad (6)$$

with boundary conditions  $\Phi(0)=\Phi(H)=0$  and with the normalisation  $\Phi_{max}=1$ .  $N(z)$  is the de Brunt-Väisälä frequency and the coefficients  $\alpha$ ,  $\beta$  and  $\alpha_1$  are [19]:

$$\alpha = \frac{3c}{2} \frac{\int (d\Phi / dz)^3 dz}{2 \int (d\Phi / dz)^2 dz} \quad (7)$$

$$\beta = \frac{c}{2} \frac{\int \Phi^2 dz}{\int (d\Phi / dz)^2 dz} \quad (8)$$

$$\alpha_1 = -\frac{\alpha^2}{c} + 3c \frac{\int ((d\Phi / dz)^4 - (N\Phi / c)^4) dz}{\int (d\Phi / dz)^2 dz} + 3c \quad (9)$$

$$\frac{\int (c(d\Phi / dz)^2 + (N^2\Phi^2 / c) - (2\alpha / 3)(d\Phi / dz))(dT / dz) dz}{\int (d\Phi / dz)^2 dz}$$

where the integration is over the total depth and where  $T(z)$  is the first correction to non-linear wave mode which is a solution of the ordinary differential equation:

$$\frac{d^2 T}{dz^2} + \frac{N^2}{c^2} T = \frac{\alpha N^2}{c^4} \Phi + \frac{dN^2 / dz}{c^3} \Phi^2 \quad (10)$$

with boundary conditions  $T(0)=T(H)=0$  and normalised condition  $T(z_{max})=1$ , where  $\phi(z_{max})=1$ .

The extended KdV "(5)" is valid for a ocean of constant depth when dispersion, non-linearity and rotation are weak. The effects of slowly varying depth can be accounted for by including the weak additional tem ( $Q$ ) in KdV equation, giving:

$$Q = \sqrt{\frac{c_0^3 \int (d\Phi_0 / dz)^2 dz}{c^3 \int (d\Phi / dz)^2 dz}} \quad (11)$$

subscript 'o' are values at some fixed point  $x_0$ . The parameter  $Q$  characterises the amplification of the linear long internal wave.

Introducing a change in variable:

$$\zeta(x, s) = \frac{\eta(x, t)}{Q(x)}, \quad (12)$$

and co-ordinate:

$$s = \int \frac{dx}{c(x)} - t, \quad x = x \quad (13)$$

the KdV "(5)" reduces to:

$$\frac{\partial \zeta}{\partial x} + \left( \frac{\alpha Q}{c^2} \zeta + \frac{\alpha_1 Q^2}{c^2} \zeta^2 \right) \frac{\partial \zeta}{\partial s} + \frac{\beta}{c^4} \frac{\partial^3 \zeta}{\partial s^3} = \frac{f^2}{2c} \int \zeta ds \quad (14)$$

Friction in the bottom boundary layer is also included giving:

$$\frac{\partial \zeta}{\partial x} + \left( \frac{\alpha Q}{c^2} \zeta + \frac{\alpha_1 Q^2}{c^2} \zeta^2 \right) \frac{\partial \zeta}{\partial s} + \frac{\beta}{c^4} \frac{\partial^3 \zeta}{\partial s^3} + \frac{kcQ}{\beta} \zeta |\zeta| = \frac{f^2}{2c} \int \zeta ds \quad (15)$$

where  $k$  is the coefficient of quadratic bottom friction. The "(15)" is solved with a periodic boundary condition:

$$\zeta \left( s + \frac{2\pi}{\omega}, x \right) = \zeta(s, x) \quad (16)$$

corresponding to a periodic internal tide of frequency  $\omega$  and with the "initial" condition [17]:

$$\zeta(s, x_0) = a_0 F(\omega s) \quad (17)$$

where  $F$  is a periodic function, which characterises the form of the initial wave at the origin  $x_0$ . Here, the initial wave is taken as a sinusoidal long wave representing an internal tide and the model is used to study the possible

generation of solitons induced by the non-linear transformation of internal tide.

Moreover, Garreau and Mazé [20] used a non-dimensional parameter indicating non-linearity. This parameter is the ration of the tidal excursion,  $L_M$ , over the horizontal topographic length scale,  $L_T$ . If  $U$  is the current amplitude of the tide, these length scales are therefore defined by:

$$L_M = \frac{U(x)}{\omega} \quad L_T = H(x) / \frac{dH}{dx} \quad (18)$$

Application

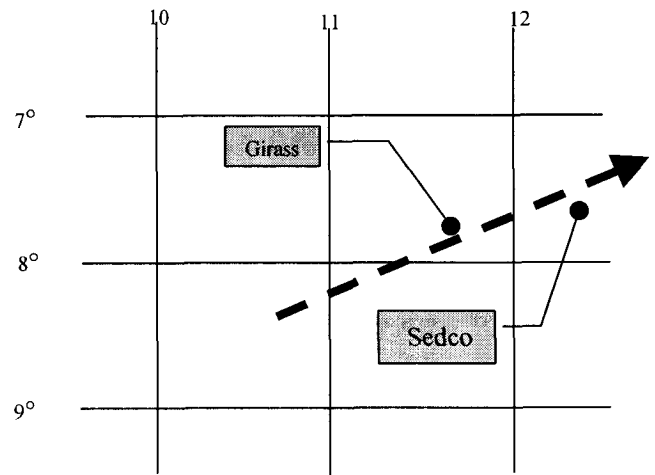


Fig.4: Girassol and Sedcoforex operation sites; The arrow shows the ray where the simulation is conducted.

The model was developed and applied successfully to the West Australian shelf using the KdV coefficients estimated from figures given in [17].

Fig.5 represents the main coefficients of the ReKdV model (Extended KdV model including Rotation effect) computed for the Guinea Gulf (Fig.4) using the world ocean atlas of the NOAA known as Levitus data [16]. This site is closed to the area where Sedcoforex drilling operations were perturbed by solitons. Northwest the GIRASSOL site is located too.

Length scales  $L_M$  and  $L_T$  have been calculated considering a tidal current with an amplitude of 0.20m/s at a depth along the ray. Fig.5a shows the ration of this ratio. The minimum is observed at 195km.

Fig.6 shows the different pycnocline displacements computed from the ReKdV model at different distance starting with an internal tide amplitude of 2 m. The shock associated with the solitons started after a distance of 190 km and development of the undulation group is really clear when the internal tide reach 200km, distance corresponding to minimum value of  $L_M/L_T$ . The influence of rotation was not significant.

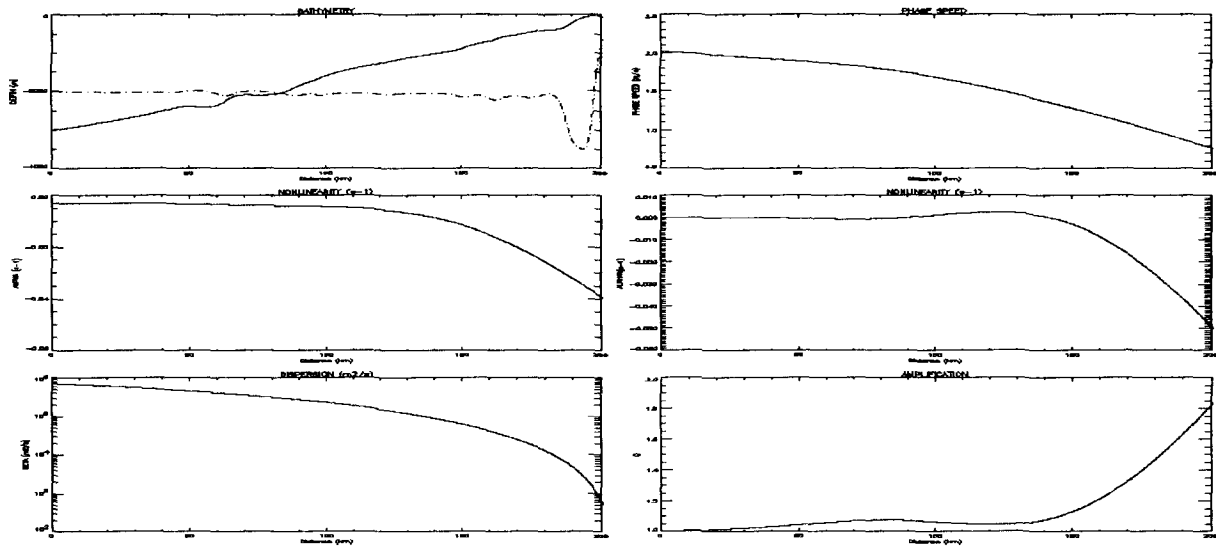


Fig.5 : ReKdV coefficients estimated from the Levitus data. The bathymetry is obtained from the French Navy chart.

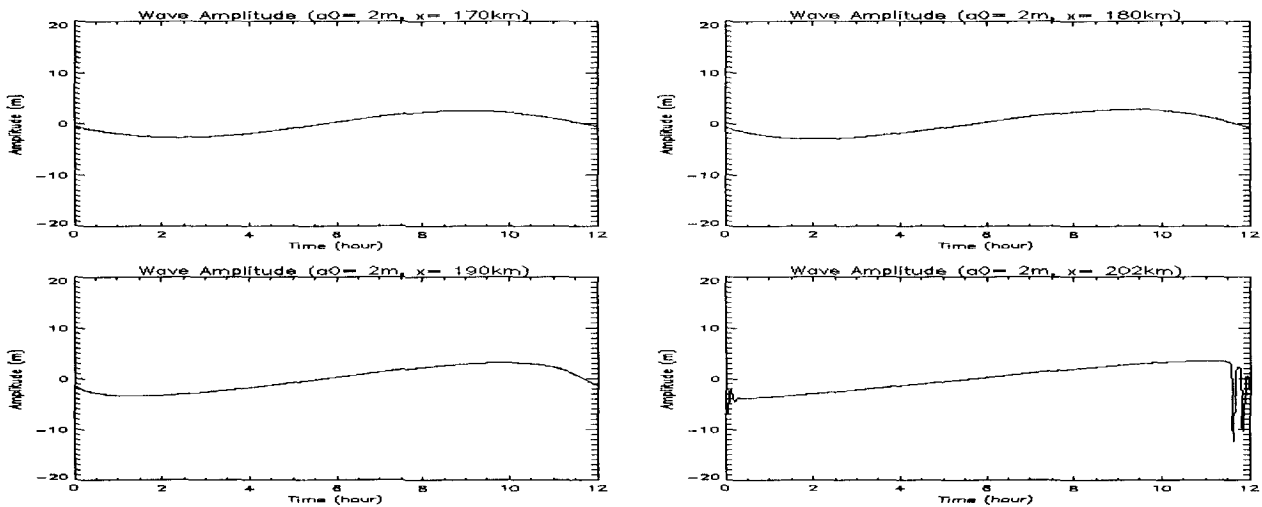


Fig.6 : The pycnocline displacements computed from the ReKdV model and presented for different distances (see Fig.4).

An important parameter for marine operations in real time assistance and for design study is the current velocity. Giving the pycnocline displacement, the horizontal and vertical velocities can be estimated using the streamfunction. Thus, assuming linear wave theory, this can be obtained by:

$$\psi(x, z, t) = c\eta(x, t)\Phi(z) \tag{19}$$

Using “(19)”, current profiles are computed from the maximum extreme pycnocline displacements obtained from the ReKdV model simulation. The horizontal and vertical velocities are shown on Fig.7 and Fig.8.

The surface velocity does not differ from the value computed from the SAR image.

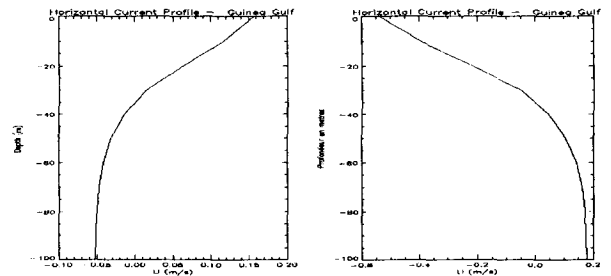


Fig.7 : Horizontal current profiles estimated from the maximum displacement of the pycnocline

If we assume an internal tide wavelength of 10km, distance between the two packets observed by the SAR

image (Fig.1), the vertical velocity is relatively high, giving strong impact on offshore structures.

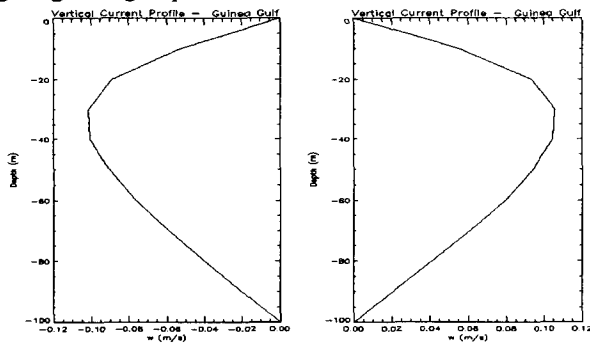


Fig.8: Vertical current profiles estimated from the maximum displacement of the pycnocline

### CONCLUSION

The association of SAR imagery allowed soliton current characterisations. The non-linear model applied for the Guinea Gulf and Andaman Sea (not presented here) is an interesting tool for soliton generation. The association of both SAR imagery and the numerical model can be used for operational studies. When applied in combination, it will be possible to:

- characterise area within risk for offshore operations
- to predict non-linear internal tide
- to define better the in-situ survey campaigns

### ACKNOWLEDGEMENTS

A part of the financial support of ANAIS project is provided by the FSH (French Oil Organism). We thank the ESA for providing the SAR images.

### REFERENCES

- [1] Small, J., Sawyer, T and Scott, J., "Repeated observations of an evolving internal bore at the Malin shelf edge during SESAME 1996," *Submitted to Annales Geophysicae, 1988*
- [2] Rodenas, J.a, and Garello, R., 1998 "A new automatic internal wave detection and characterisation method for SAR images," *Proc., Oceans'98, 613-618, 1998*
- [3] Morozov, E.G, 1995, "Global semidiurnal internal wave field," *Deep Sea Res., 42, 135-148.*
- [4] Hajji, H., Bonicel, D., Ramamonjirisoa, A., Joelson, M., Deveaux, M., Garello, R. and Chapron, B., "Internal waves, topography and Ocean fronts and eddies observed with ERS synthetic Aperture Radar," *Proc., Oceans'98, 898-903, 1998.*
- [5] Osborne, A.R and Burch, T.L, "Internal solitons in the Andaman Sea," *Science, 208, 451, 1980*
- [6] Apel, J.R and Holbrook, J., "Internal solitary waves in the Sulu sea," *Johns Hopkins APL Technical Digest, Vol4, N° 4, 267-275, 1983*
- [7] Ostrovsky, L.A and Stepanyants, Yu.A, "Do internal waves exist in the ocean?," *Review Geophys., 29,293-310, 1989*
- [8] Morozov, E.G, 1985, "Oceanic Internal waves," *Nauka publishers, Moscow, 1985*
- [9] Alpers, W. and Hennings, I., "A theory of the imaging mechanism of underwater bottom topography by real and synthetic Aperture Radar," *J of Geoph research, 89 (6), 10529-10546, 1984*
- [10] Lee, C., and Beardsley, R.C, "The generation of long non-linear internal waves in a weakly stratified shear flow," *J. Geophys. Res, 79, 453-462, 1974*
- [11] Liu, A.K., J.R Holbrook, and J.R Appel, "Non-linear internal wave evolution in the Sulu Sea," *J. Phys. Oceanogr, 15, 1613-1624, 1985.*
- [12] Holloway, P., Pelinovsky, E., Talipova, T., Barnes, B, "A non-linear model of internal tide transformation on the Australian North West Shelf," *J. Phys. Oceanogr., 27, 871-896, 1997*
- [13] Pierni, S., 1989, "A model for the Alboran Sea internal solitary waves," *J. Phys. Oceanogr., 19, 755-772, 1989*
- [14] Gerkema, T., "An unified model for the generation and fission of internal tides in a rotating ocean," *J. Marine Res., 54,421-450,1996.*
- [15] Pelinovsky, E., Stepanyants, Yu.A, Talipova, T., "Simulation of non-linear internal wave propagation in horizontally inhomogeneous ocean," *Phys. Atmos. and Ocean., 77-83,1994.*
- [16] NOAA, "World ocean atlas 1994," *National Oceanography Data Center. US department of commerce, 1994*
- [17] Holloway, P., Pelinovsky, E., Talipova, T., "A general Korteweg-de Vries model of internal tide transformation in the coast zone," *J. Geophys. Res., 1999 (submitted)*
- [18] Talipova, T., Pelinovsky, E., Lamb, K., Grimshaw, R., Holloway, P., "Effects of cubic non-linearity at the internal wave propagation," *Transactions of Russian Academy of Sciences, Earth Section, 1998 (accepted).*
- [19] Lamb, K.G and Yan, L., "The evolution of internal wave undular bores, Comparisons of a fully non-linear numerical model with weakly non-linear theory," *J. Phys. Ocean, 26, 2712-2734, 1996*
- [20] Garreau P. and Mazé, R., "Tidal rectification and Mass transport over a shelf break: A barotropic frictionless model," *J. Phys. Reseach, 22, 719-731, 1992*

## The Impact of RADARSAT ScanSAR Image Quality on Ocean Wind Retrieval

P.W. Vachon, J. Wolfe, R.K. Hawkins  
 Canada Centre for Remote Sensing  
 588 Booth St., Ottawa, Ont. K1A 0Y7 Canada  
 Phone: 613 995-1575 Fax: 613 947-1385  
 E-mail: [paris.vachon@ccrs.nrcan.gc.ca](mailto:paris.vachon@ccrs.nrcan.gc.ca)  
<http://www.ccrs.nrcan.gc.ca>

### ABSTRACT

We compare image quality and radiometric calibration of several RADARSAT ScanSAR processors to assess impact on ocean wind retrieval. To address the relative state of ScanSAR processing, we arranged to have several ocean scenes processed by four different ScanSAR processors. We found some variability in image quality and radiometric calibration. Nevertheless, ScanSAR images should be able to provide useful high-resolution wind field information at near-synoptic scales.

### INTRODUCTION

Ocean surface wind vector retrieval from ScanSAR images is a topic of emerging interest. For example, it has been shown that RADARSAT (C-band HH polarization) ScanSAR images could have a role in hurricane surveillance, polar low monitoring, and operational coastal wind field measurement. It is now well established that, knowing the radar geometry, the wind speed can be estimated from the SAR-observed radar cross section using a suitable wind retrieval model [6]. Hybrid C-band HH polarization models (consisting of a C-band VV polarization ERS scatterometer model such as CMOD\_IFR2 and a suitable C-band polarization ratio) have been successfully demonstrated for use with single beam RADARSAT SAR images [8].

Unfortunately, the calibration of RADARSAT ScanSAR products has proven to be a rather long and difficult process. Complicating factors have included: our rather poor knowledge of the spacecraft's attitude leading to azimuth stripes due to errors in applied elevation antenna patterns; image scalloping that arises from errors in Doppler parameter estimation; the limited available dynamic range of ScanSAR image products; and the occurrence of analogue-to-digital converter (ADC) saturation.

The latter problem is now well understood. When ADC saturation occurs, a loss in signal power and a consequent underestimation of the radar cross section results. RADARSAT's automatic gain control (AGC) is essentially driven by only the contents of the near-half sub-swath [7]. Two acquisition strategies have been proposed to address this AGC problem. First, dynamic gain acquisitions can lead to saturation-induced dark

bands over land and possible underflow over water. For this approach, it is recommended that the ocean target of interest be maintained in the near-half swath. Second, fixed gain acquisitions require an *a priori* decision by the user to supply a suitable gain setting. Of course, the appropriate gain for the ocean is wind speed dependent. For each strategy, the occurrence of saturation can be monitored in the signal data and calibration correction factors can be estimated by assuming a Gaussian signal data distribution.

We have obtained ScanSAR products from four RADARSAT processors: the Canadian Data Processing Facility (CDPF), the Tromsø Satellite Station (TSS), the Alaska SAR Facility (ASF), and *IOSAT's* SentrySAR processor. In this paper, we present our understanding of the calibration status of these ScanSAR processors and we intercompare some derived data profiles. The comparisons are based on StormWatch data [2] acquired over a buoy near the Hibernia oil production platform (N46:45 W48:47) on the Grand Banks of Newfoundland during winter '97/'98 (Fig. 1), and a ScanSAR image of Hurricane *Danielle* (Fig. 2) acquired in August 1998 off the US East Coast, as summarized in Table 1. The high resolution (*i.e.*, 100's of meters) with which we can see the wind field's imprint on the ocean surface across the nearly 500 km swath of these images illustrates why RADARSAT ScanSAR images are of interest for high resolution (compared to scatterometry's 25 to 50 km resolution) wind field retrieval at near-synoptic scales.

### CALIBRATION REQUIREMENT

We first consider the requirement on radiometric calibration for wind speed estimation from SAR images. In Fig. 3, we have plotted the wind speed error that would be expected for a given error in normalized radar cross section  $\sigma^0$  at a particular incidence angle and for a known wind direction. From the plot, we see that in order to retrieve wind speeds to an accuracy of better

Table 1: Summary of ScanSAR data sets considered.

Data Set	Date/Time [UTC]	Pass	Wind
StormWatch	25-Nov-97 21:06	Asc.	18 m/s, 317°
StormWatch	19-Dec-97 21:06	Asc.	9 m/s, 304°
StormWatch	12-Jan-98 21:06	Asc.	n/a
StormWatch	01-Mar-98 21:06	Asc.	7 m/s, 19°
<i>Danielle</i>	31-Aug-98 10:51	Desc.	n/a

Table 2: Summary of ScanSAR processors considered.

Processor	Data Orientation	DN format	Output dynamic range control	ADC saturation compensation	Radiometric Calibration
CDPF	Zero Doppler	8-bit integer	output LUT, linear in $\beta^\circ$	No	$\pm 1.35$ dB (more for scallops) [5]
ASF	Beam Centre	8-bit integer	-25.5 dB to 0 dB, logarithmic in $\sigma^\circ$	No	$\pm 0.2$ dB SCWB only [4]
TSS [3]	Beam Centre	8/16-bit integer	-30.1 dB to 22.5 dB, logarithmic in $\beta^\circ$	Yes	No
SentrySAR	Beam Centre	8/16-bit integer or float	output LUT, linear in $\beta^\circ$	Yes	Yes, error bar unknown

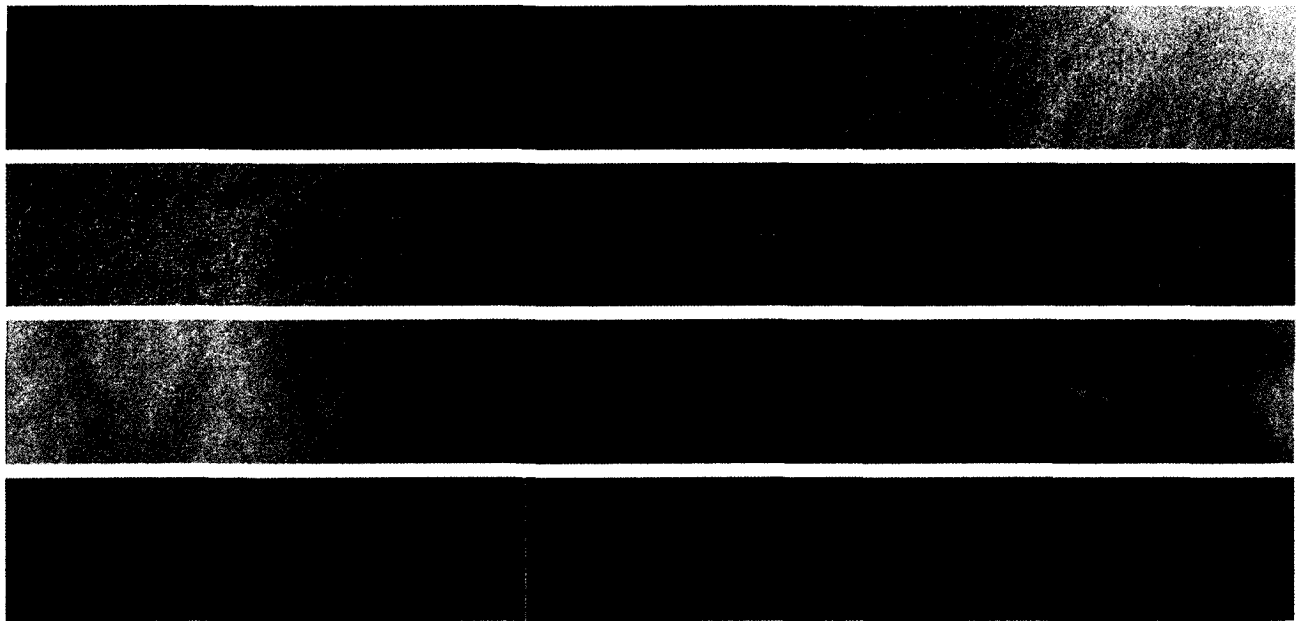


Fig. 1: RADARSAT ScanSAR Wide B images (CDPF) of Hibernia (right of centre) acquired during StormWatch: full swath, near edge to the left, sequenced as in Table 1. The line is nadir ambiguity. (© CSA 1997 and 1998)

than 2 m/s, in general, we may need to achieve calibration that is much better than 1 dB, absolute, especially for the higher wind speeds that are of greater interest. This calibration tolerance assumes that the wind direction is known. The required tolerance on radar cross section is even smaller if the wind direction is also to be estimated from the SAR image since a wind direction error can also contribute to the error in the retrieved wind speed.

### THE PROCESSORS

The salient details of the products from the available ScanSAR processors are summarized in Table 2. In each case, the SPECAN processing algorithm is used, so well known ScanSAR image quality problems, such as image scalloping, can arise in the event of errors in the estimated Doppler centroid. The image products are provided in varying geometries and with various radiometric calibration statuses, as noted. We only considered 8-bit image products. The TSS ScanSAR products are not radiometrically calibrated. For the TSS

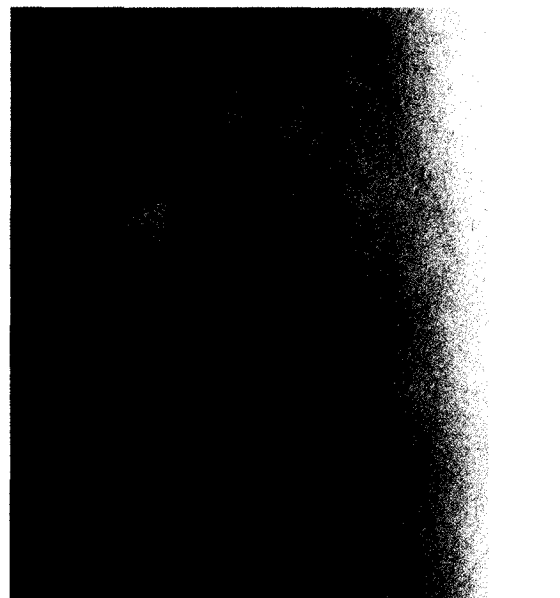


Fig. 2: RADARSAT ScanSAR Wide B image (SentrySAR) of Hurricane *Danielle*: full swath, near edge to the right. (©CSA 1998)

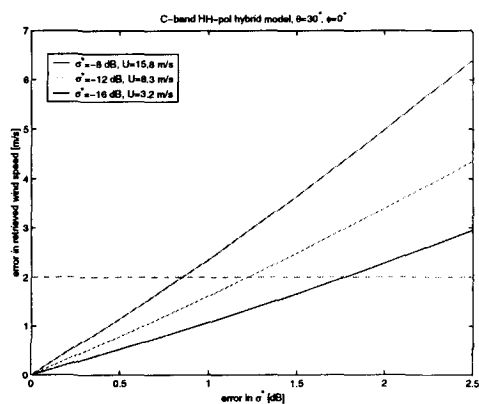


Fig. 3: Error in retrieved wind speed for a given error in  $\sigma^0$  for a hybrid C-band HH polarization model at  $30^\circ$  incidence angle for the wind blowing towards the radar. We assumed that the wind direction is known.

products, we have subtracted 46 dB from the  $\beta^\circ$  values interpreted from the digital numbers (DNs). While this is certainly not a robust calibration, this does serve to nominally align the TSS data with the data from other calibrated processors.

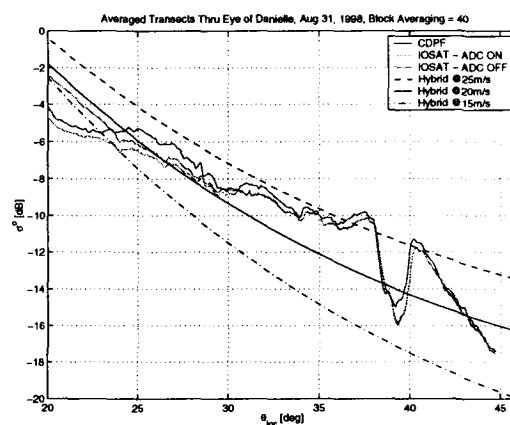


Fig. 4:  $\sigma^0$  transect through the eye of Hurricane *Danielle* showing ADC saturation power loss compensation with the SentrySAR processor (labelled IOSAT - ADC on). The correction is important at the near edge of the scene.

The TSS and SentrySAR processors can operationally carry out ADC saturation analysis and compensation. The impact of this correction for a fixed gain acquisition over a hurricane is illustrated by the radar cross section

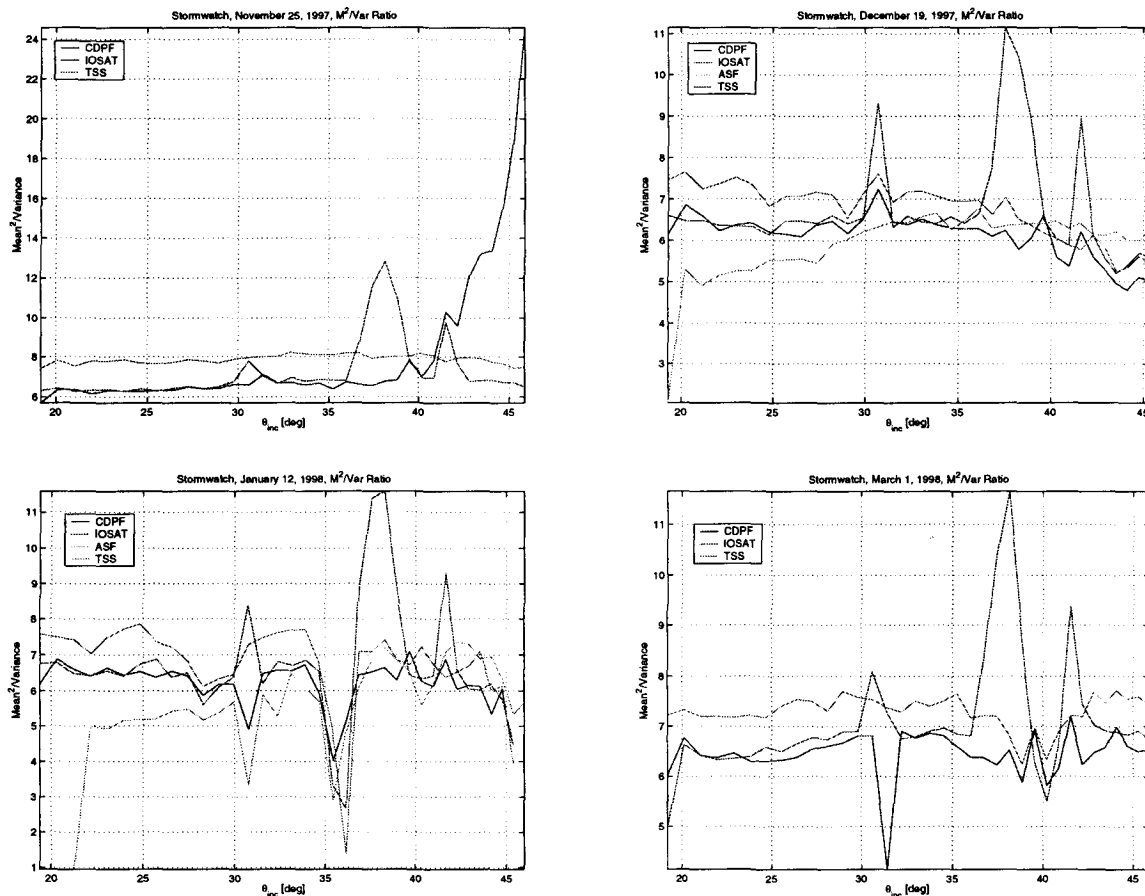


Fig. 5: MSVR as a function of local incidence angle for the StormWatch scenes, as available for each processor.

profiles shown in Fig. 4. The CDPF and ASF products tend to underestimate the radar cross section by up to 2 dB, especially for smaller incidence angles. In general, ADC saturation could arise for fixed gain acquisitions. It would become worse for higher wind speed situations, especially in the vicinity of the elevation antenna pattern maxima of each beam that makes up the ScanSAR image swath.

### IMAGE QUALITY

As a check on image quality, we have inspected the images for obvious problems such as scalloping and inter-beam seams. Although these artifacts are not rare, none of the images that we worked with had dramatic problems in this regard. The worst case of scalloping was measured at about 0.7 dB peak-to-peak. The SentrySAR processor carries out platform orientation estimation in order to refine the Doppler centroid, and dynamically updates the orientation parameters within a scene [1]. The products from this processor had essentially immeasurable scalloping for the cases that we examined in this study.

As a quantitative check on image quality, we plotted the mean-squared-to-variance ratio (MSVR) as a function of local incidence angle through the Hibernia location for each of the StormWatch scenes (Fig. 5). We see that each processor has generated products with nominally 7 statistically independent looks. The local reduction in MSVR for all processors near 36° on Jan 12 is due to a local loss of the backscattered signal.

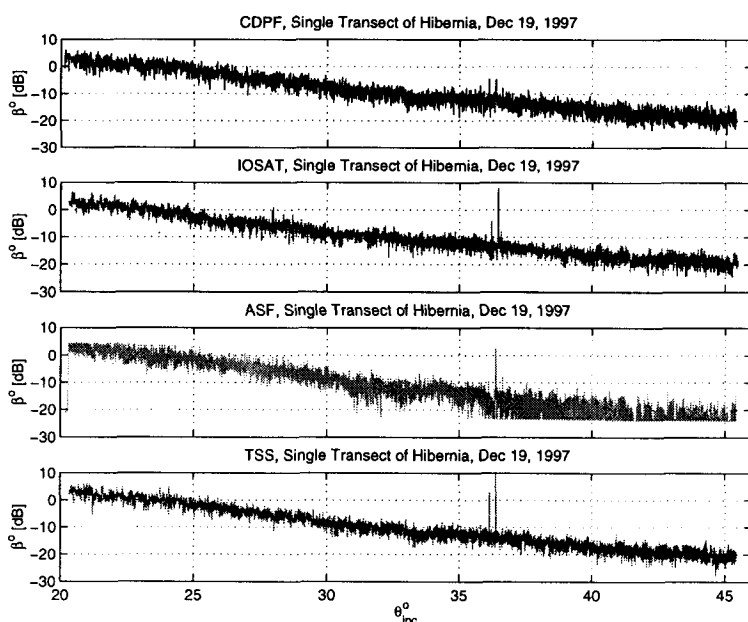


Fig. 6: A single transect of  $\beta^\circ$  as a function of incidence angle for one StormWatch image.

The increase in MSVR at the far edge of the Nov. 25 CDPF product is attributed to overflow of the 8-bit DN's in the image product (*i.e.*, the output LUT was inappropriately large in this case). The ASF products show a roll-off in MSVR at the near edge. The reason for this is not so far understood.

For the SentrySAR products, and some of the others to a lesser extent, there is a local increase in MSVR in the vicinity of the interbeam seams. Presumably, this is caused by the SentrySAR blending the data in the entire beam overlap region, effectively increasing the local number of statistically independent looks. Furthermore, some of the processors show an increase in MSVR while others show a decrease in the vicinity of the W1 nadir ambiguity (near 31°, see the Jan. 12 transect, in particular). Again, we presume that the various processors treat the nadir ambiguity in different ways. The nadir ambiguity is most visible in the CDPF and ASF products. In Fig. 6 we show a single range  $\beta^\circ$  transect for each processor through the Hibernia location. We see the effects of DN underflow and overflow, particularly for the ASF product. There is also some DN truncation for the CDPF product, but it is less obvious due to use of an output LUT to scale  $\beta^\circ$  into an image DN.

### RADIOMETRIC CALIBRATION

In Fig. 7, we show range transects of the mean normalized radar cross section  $\sigma^\circ$  through the Hibernia location from each of the processors for which we have data available. The TSS and SentrySAR processors each used ADC saturation power loss compensation, although these scenes were actually acquired using dynamic gain.

We have also plotted, for reference, some model transects of radar cross section based upon a hybrid C-band HH polarization wind scatterometry model that is composed of CMOD\_IFR2 and a polarization ratio based on Kirchhoff scattering [8]. The central model curve is based on the *in situ* measured wind vector that is assumed to apply across the entire swath (except for the 12 Jan. '98 case, for which an *in situ* wind vector was not available). The other two model curves correspond to the measured wind speed plus or minus 2 m/s. If the



radiometric calibration is satisfactory, we would expect that the SAR-observed radar cross section profiles should agree with the model in the vicinity of the Hibernia platform (near  $36^\circ$  local incidence angle), while the slope of observed profiles should agree with the model slope, at least in the vicinity of the wind vector measurement.

We see that, in general, the transects from the various processors agree with each other to within several dB. The exception is that the ASF data show smaller radar cross sections, compared to the other processors for the two available cases, at least for larger incidence angles. We also see reasonable agreement with the model curves, particularly in the vicinity of the *in situ* measurement. The variability in radar cross section as a function of incidence angle is a measure of the variability in local wind speed across the nearly 500 km image swath. However, radar cross section discrepancies at these scales suggest that the calibration of certain of these processors is not accurate enough to support wind field estimation to within 2 m/s. At this point, we do not know which processor has provided

data with the best calibration.

For completeness, in Fig. 8 we show a normalized radar cross section transect in azimuth through one of the StormWatch scenes. We do not see any systematic differences among the available data sets in the azimuth direction, aside from the smaller radar cross sections from the ASF product that were noted earlier.

## CONCLUSIONS

We have compared RADARSAT ScanSAR ocean images processed on 4 different ScanSAR processors with the ocean wind retrieval application in mind. In general, we found comparable image quality among the processors. The occurrence of inter-beam seams and the degree of scalloping tended to be small for these open ocean images. Such images do not have large backscatter changes over small distances in azimuth, making Doppler centroid estimation straightforward.

In some cases, underflow and overflow of the digital numbers in the image products caused problems with

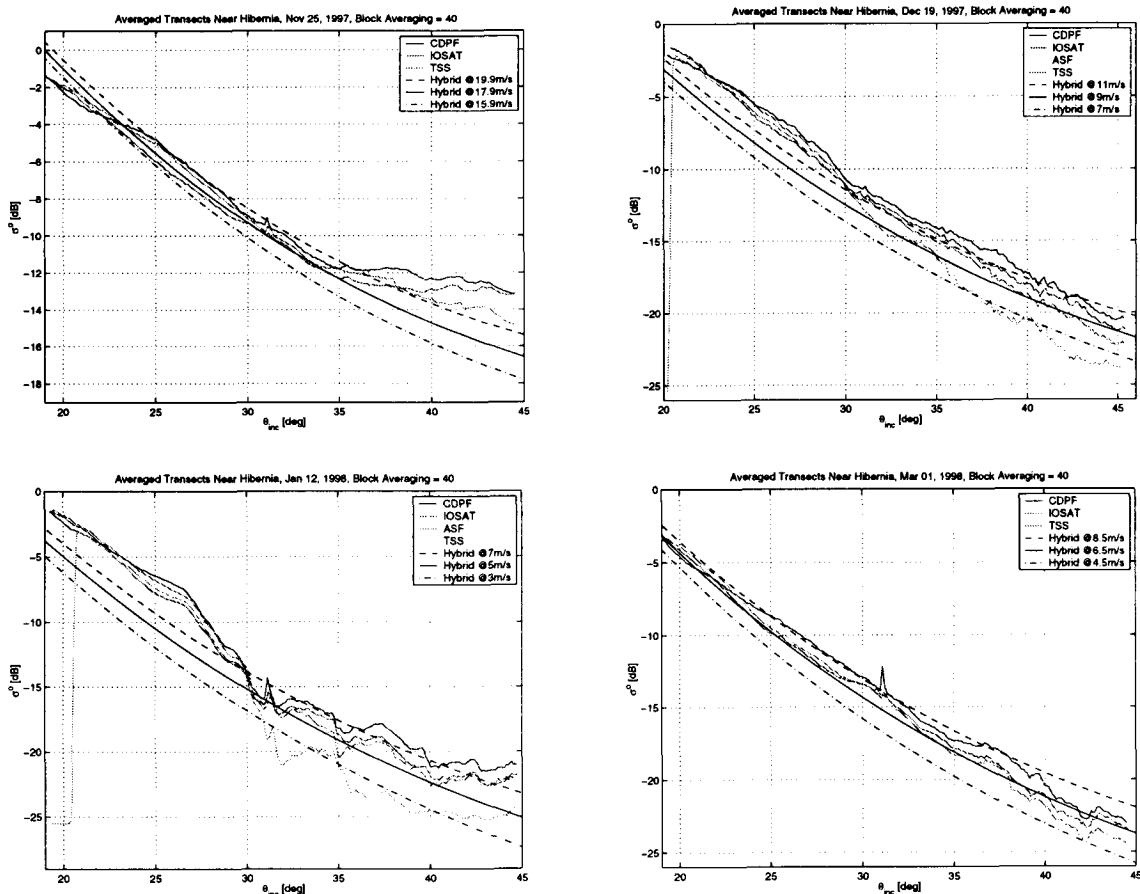


Fig. 7:  $\sigma^0$  as a function of local incidence angle for the StormWatch scenes, as available for each processor. Also plotted are hybrid C-band HH polarization model cross sections for the wind speed and direction (if available) measured at Hibernia and that speed  $\pm 2$  m/s.

image quality and calibration. Digital number overflow can be a problem for higher wind speeds.

Each processor had a similar MSVR for open ocean regions with measurable backscattered power, in spite of differences in the way the DNs are coded and scaled in the image products. Evidently, some of the processors treat the beam overlap region in different ways.

ADC saturation power loss could be a problem under some circumstances. It is recommended that a correction based on signal data saturation analysis is applied routinely to all images. This saturation problem becomes more severe for larger wind speeds if the image was acquired with a fixed gain. Unfortunately, there may be little evidence in the image for this saturation, and the product does not provide information on the gain settings that were actually used.

The radiometric calibration agreed to within several dB among the processors considered. Exceptions were when ADC saturation power loss occurred and was not compensated, and the ASF products that indicated lower radar cross sections at larger incidence angles.

It appears that the radiometric calibration of RADARSAT ScanSAR images could support the ocean wind retrieval application. The caveats are that the raw digital numbers in the images should be examined for overflow, ADC saturation power loss, if present, should be compensated, and that radiometric problems could arise locally if image scalloping occurs. However, at this point, further analysis is required to understand the noted discrepancies in normalized radar cross section. Analysis of Amazon rainforest and (adequately sampled) calibration transponder images could provide new insight in this regard.

#### ACKNOWLEDGEMENTS

We thank Tony Bauna (TSS) and Marina Dragošević (IOSAT) for helpful discussion, supplying image products and information on their processors, and for their interest in this project. The ASF data were obtained through PWV's participation in the Alaska SAR Facility User Working Group (ASFUWG). Fred Dobson (BIO) supplied the Hibernia wind measurements.

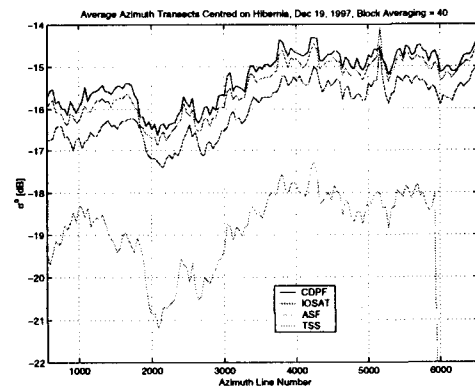


Fig. 8:  $\sigma^\circ$  as a function of azimuth position for the various processors, as available, for one of the StormWatch scenes.

#### REFERENCES

- [1] Dragošević, M.V., "On accuracy of attitude estimation and Doppler tracking", these proceedings.
- [2] <http://fermi.jhuapl.edu/sar/stormwatch/index.html>
- [3] Kongsberg Spacetec, "MEOS, SAR Satellite Instrument Processor, Product Description", SIP-PD-SPT-SY-0001, 8 October 1999
- [4] Martyn, P., *et al.*, "Calibration of the RADARSAT SWB processor at the Alaska SAR Facility", Proc. IGARSS'99, 28 June to 2 July 1999, Hamburg, Germany.
- [5] Srivastava, S.K., *et al.*, "Maintaining image quality and calibration of RADARSAT-1 CDPF products", Proc. IGARSS'99, 28 June to 2 July 1999, Hamburg, Germany.
- [6] Vachon, P.W., and F.W. Dobson, "Validation of wind vector retrieval from ERS-1 SAR images over the ocean", *The Global Atmosphere and Ocean System*, Vol. 5, pp 177-187, 1996.
- [7] Vachon, P.W., *et al.*, "Adaptive compensation of RADARSAT SAR analogue-to-digital converter saturation power loss", Geomatics in the ERA of RADARSAT (GER'97), CD-ROM Proceedings, 27-30 May 1997, Ottawa, Ont., Canada.
- [8] Vachon, P.W., and F.W. Dobson, "Wind retrieval from RADARSAT SAR images: Selection of a suitable C-band HH polarization wind retrieval model", to appear, *Can. J. Rem. Sens.*, 2000.

## The use of Ground Receiving Stations for ERS SAR Quality Assessment

P.J. Meadows

Marconi Research Centre, West Hanningfield Road,  
Chelmsford, Essex, CM2 8HN, United Kingdom.  
Email: peter.meadows@gecm.com

### ABSTRACT

At the 1998 CEOS SAR workshop Evert Attema (ESA/ESTEC) asked whether ground receiving stations act as stable point targets – this paper helps to answer that question.

### INTRODUCTION

The quality assessment and calibration of the ERS-1 and ERS-2 SARs has been performed using the three ESA transponders deployed in the Netherlands [1, 2]. With the single 100km swath ERS SAR instrument, the ESA transponders can be imaged up to 6 times per 35 day repeat period. The forthcoming ESA Envisat ASAR instrument has a large number of swaths and modes of operation which means that the quality assessment and calibration task will be much more onerous than for the ERS SARs. This task can be made easier by increasing the number of suitable targets.

One source of additional point targets is ground receiving stations. As these are used to acquire data in real time, they will be pointing towards the satellite while acquiring the data and thus could be a stable point target. If the ground stations prove to be suitable as secondary calibration sources, then the number of suitable point targets that could be used for Envisat ASAR calibration is increased in number. In addition, the spatial distribution of suitable point targets could be substantially increased.

This paper examines the image quality, stability and localisation aspects of two ground stations: the ESA ground station at Salmijaervi, Kiruna, Sweden and the German national station at Neustrelitz.

### THE GROUND STATIONS

The majority of the ERS SAR data archived at the UK-PAF has been acquired by the ESA ground station at Kiruna, Sweden. Within the footprint of this ground station there are three national ground stations receiving ERS SAR data: at Neustrelitz, Germany, at Tromsø, Norway and at West Freugh, Scotland. All four ground stations have been examined for suitability to derive image quality and stability measurements:

- The Kiruna ground station has an extremely saturated impulse response function (IRF) – its radar cross-section is estimated at  $71\text{dBm}^2$  (cf.  $57\text{dBm}^2$  for the ESA transponders). However, the ground station azimuth ambiguities are sufficiently strong to enable some IRF parameters to be measured. Fig 1(a) shows the ground station IRF and azimuth ambiguities (top and bottom). Fig 1(b) shows in more detail an azimuth ambiguity and an ESA transponder. Although the ambiguities have a radar cross-section of approximately  $47.5\text{dBm}^2$  (a 2.5m corner reflector), no sidelobe structure is visible.

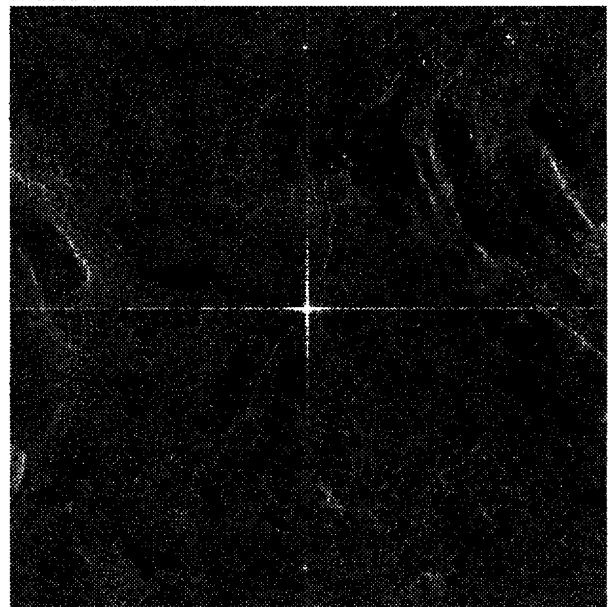


Fig.1(a): Kiruna ground station from ERS-2 orbit 13317, frame 2223, 30<sup>th</sup> November 1997 (the image size is 12.5km by 12.5km).

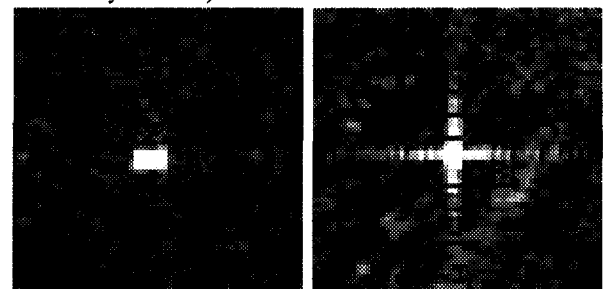


Fig 1(b): An azimuth ambiguity (left) from ERS-2 orbit 13317, frame 2223, 30<sup>th</sup> November 1997 and an ESA transponder (right) from ERS-2 orbit 22550, frame 2547, 13<sup>th</sup> August 1999 (image size is 750m by 750m).

- The Neustrelitz ground station is not saturated in three-look detected PRI products and so can be used to derive all IRF parameters. Fig 2 shows the ground station IRF.

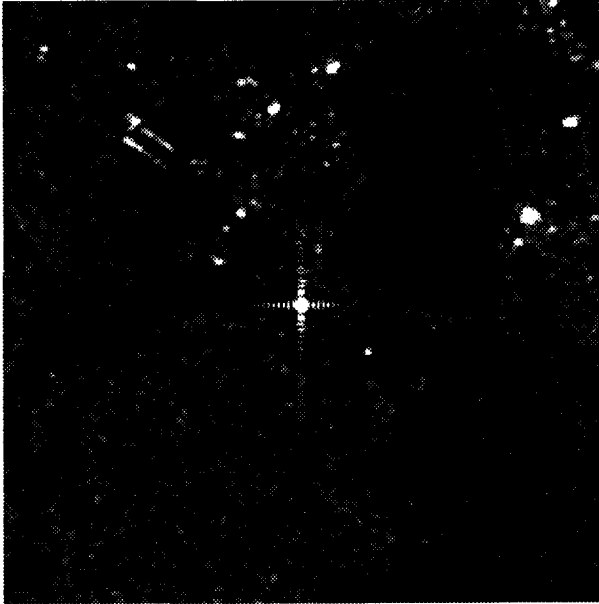


Fig. 2: Neustrelitz ground station from ERS-2 orbit 22442, frame 1066, 5<sup>th</sup> August 1999 (the image size is 3.0km by 3.0km).

- The Tromsø ground station is just saturated in the PRI product and is thus unsuitable for any IRF parameter estimation (the azimuth ambiguities are far too weak to be of use).
- The West Freugh ground station is also just saturated in the PRI product and is thus unsuitable.

Thus, of the four ERS SAR ground stations within the Kiruna footprint, only two are suitable for analysis: Kiruna and Neustrelitz. Of these only the Neustrelitz ground station is suitable for image quality and stability assessment while both can be used for stability and localisation assessment.

#### IMAGE QUALITY ASSESSMENT

The image quality measurements include the azimuth and range spatial resolutions, peak sidelobe ratio and integrated sidelobe ratio (see [1] for definitions). Table 1 gives values for these parameters derived using PRI products. The Kiruna results are for ERS-1 and ERS-2 SARs while the Neustrelitz results are for the ERS-2 SAR. In addition, Figs 3 and 4 shows the azimuth resolution as a function of acquisition date and range resolution as a function of incidence angle. The solid line and curve show the theoretical resolutions.

Parameter	ERS-1	ERS-2
Azimuth resolution (m)	22.77±0.53	22.80±0.97
Peak sidelobe ratio (dB)	-8.37±1.17	-8.09±1.34
Integrated sidelobe ratio	-4.09±0.82	-4.19±0.97

Table 1(a): Kiruna ERS-1 and ERS-2 SAR PRI image quality (based on 37 images for ERS-1 and 34 images for ERS-2).

Parameter	ERS-2
Azimuth resolution (m)	22.29±0.90
Peak sidelobe ratio (dB)	-16.1±1.0
Integrated sidelobe ratio	-13.8±1.1

Table 1(b): Neustrelitz ERS-2 SAR PRI image quality (based on 61 images acquired since April 1996).

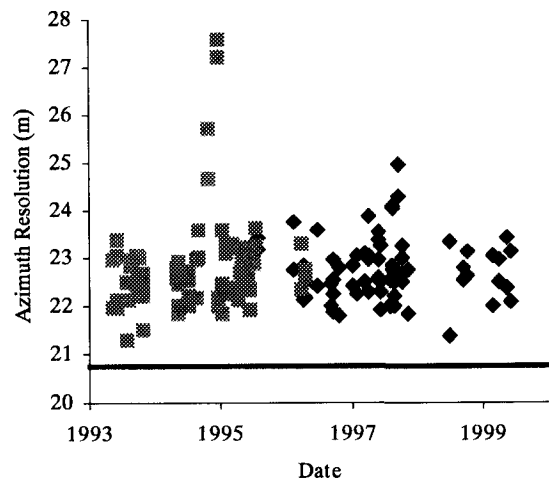


Fig 3(a): Kiruna ERS-1 and ERS-2.SAR.PRI azimuth resolution – squares for ERS-1 and diamonds for ERS-2 (the line is the theoretical azimuth resolution).

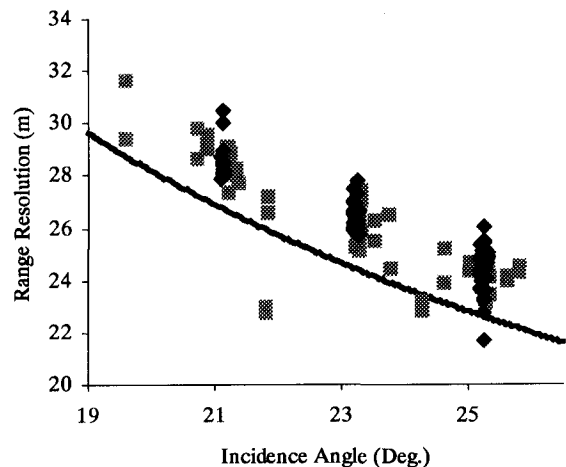


Fig 3(b): Kiruna ERS-1 and ERS-2.SAR.PRI range resolution – squares for ERS-1 and diamonds for ERS-2 (the curve is the theoretical range resolution).

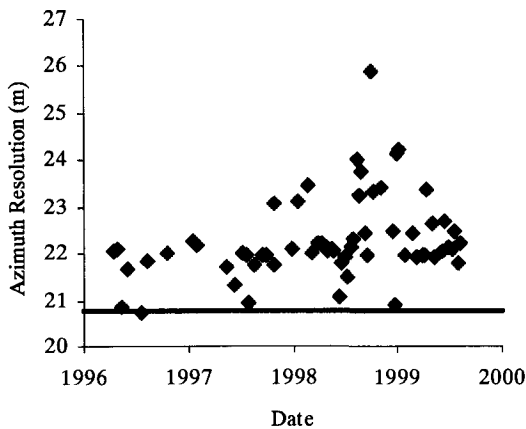


Fig 4(a): Neustrelitz ERS-2.SAR.PRI azimuth resolution (the line is the theoretical azimuth resolution).

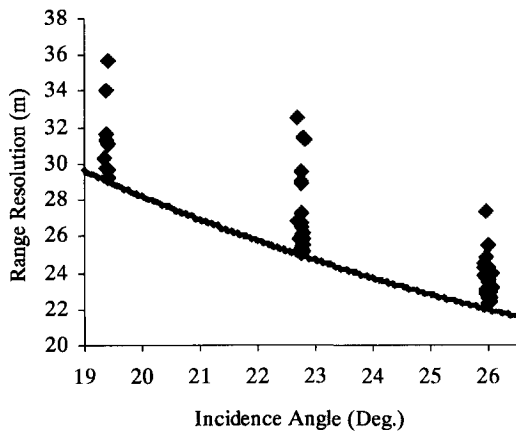


Fig 4(b): Neustrelitz ERS-2.SAR.PRI range resolution (the curve is the theoretical range resolution).

Table 1 shows acceptable mean values for the Kiruna azimuth resolution and for all the Neustrelitz IRF parameters. As the Kiruna azimuth ambiguities show very little sidelobe structure, the peak and integrated sidelobe parameters are much worse than those measured using the Neustrelitz ground station. The main difference between these results and those derived using the ESA transponders [2] is that the spread of values is greater. For example, the range resolution results (Fig 3(b) & 4(b)) shows a much greater range of values than for the ESA transponders although there are some measurements which are close to the theoretical range resolution curve. This indicates that provided a sufficient number of measurements are made, the Neustrelitz ground station gives acceptable IRF values.

## RADIOMETRIC STABILITY

The measured radar cross-section (RCS) of the Kiruna ground station azimuth ambiguities and the Neustrelitz ground station have been used to derive the stability of the ERS-1 and ERS-2 SARs (the standard deviation of the RCS measurements). For the Kiruna results, the average of the both ambiguities is derived for each image. The use of the azimuth ambiguities assumes that the ERS SAR azimuth antenna pattern is constant.

Table 2 gives the mean radar cross-section, stability and peak to peak RCS values of the Kiruna ambiguities. Figure 5 shows the ERS-1 and ERS-2 Kiruna ambiguity radar cross-section relative to their mean values as a function of date and incidence angle. The results for ERS-1 are higher than those derived using the ESA transponders (c.f. 0.24dB stability and 1.42dB peak to peak) while those for the ERS-2 SAR are comparable with the transponder results (c.f. 0.27dB for stability and 1.23dB for peak to peak) (see [2]). Note also that the mean ambiguity radar cross-section derived using ERS-1 and ERS-2 imagery is similar (given the standard deviation of each measurement) thus giving good relative radiometric calibration between the two instruments. Figure 5 shows the ERS-1 and ERS-2 Kiruna ambiguity radar cross-section relative to their mean values as a function of date and incidence angle. There is no obvious radar cross-section trend with incidence angle.

Parameter	ERS-1	ERS-2
Mean RCS ( $\text{dBm}^2$ )	47.36	47.67
Radiometric Stability (dB)	0.44	0.25
Peak to Peak RCS (dB)	1.81	1.03

Table 2: Kiruna ERS-1 and ERS-2 SAR radiometric stability results.

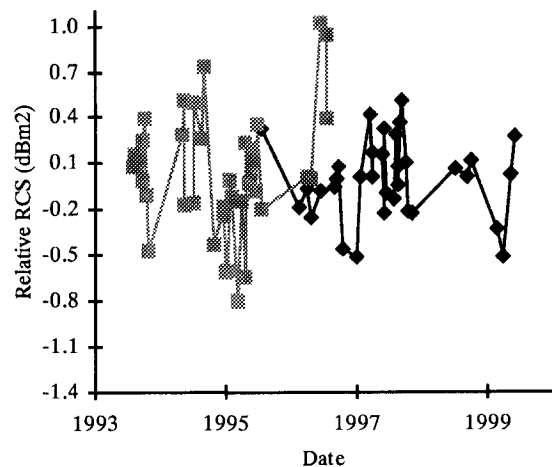


Fig. 5(a): Kiruna azimuth ambiguity relative radar cross-section (squares for ERS-1 and diamonds for ERS-2).

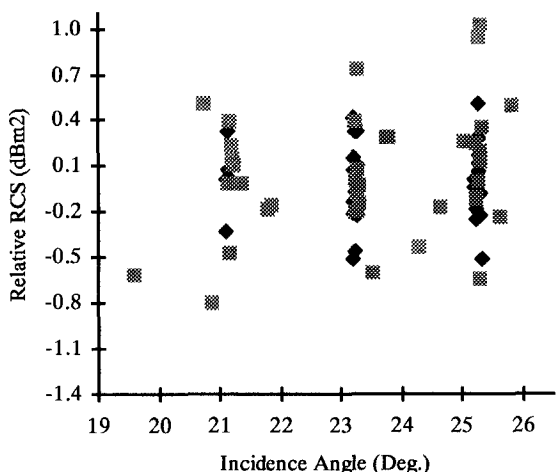


Fig. 5(b): Kiruna azimuth ambiguity relative radar cross-section as a function of incidence angle (squares for ERS-1 and diamonds for ERS-2).

Table 3 gives the mean radar cross-section, stability and peak to peak RCS values for the Neustrelitz ground station. Figure 6 shows the ERS-2 Neustrelitz radar cross-section relative to its mean values as a function of date and incidence angle. The radiometric stability and peak to peak RCS results are slightly higher than for the ESA transponder and for ERS-2 Kiruna results. Examination of Fig 6(b) shows there are several radar cross-section measurements that are significantly lower than the majority. These occur when the ground station IRF is at extreme low and high incidence angles. The fact that there are other higher radar cross-section measurements at low and high incidence angles suggests that the ground station itself is contributing to the larger than expected radar cross-section variations.

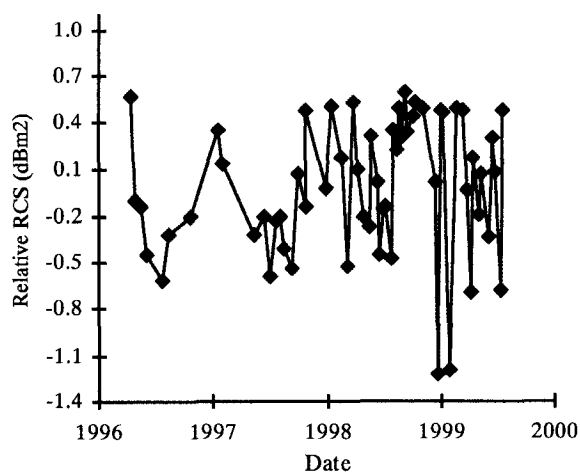


Fig. 6(a): Neustrelitz ERS-2 relative radar cross-section.

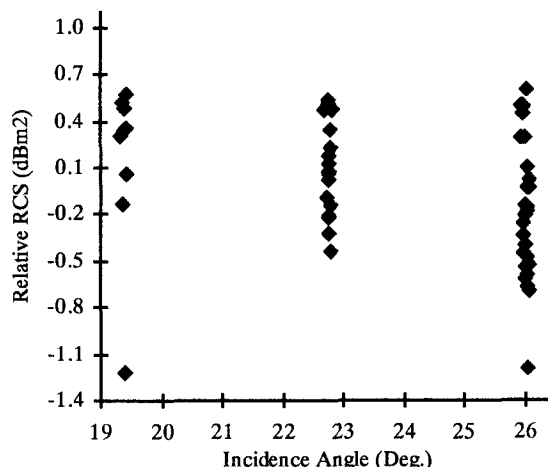


Fig. 6(b): Neustrelitz ERS-2 relative radar cross-section as a function of incidence angle.

Parameter	ERS-2
Mean RCS (dBm <sup>2</sup> )	58.89
Radiometric Stability (dB)	0.43
Peak to Peak RCS (dB)	1.82

Table 3: Neustrelitz ERS-2 SAR radiometric stability results.

Overall, the radiometric stability results using the Kiruna and Neustrelitz give results that are, at worst, only a factor of 2 higher than derived using the ESA transponders.

### IMAGE LOCALISATION

The measured pixel coordinates of the ground stations can be used to assess image localisation. This is achieved by converting the image corner latitude and longitudes to cartographic coordinates using a UTM map projection. Then a bilinear fit using the corner cartographic coordinates and the corresponding pixel coordinates is used to determine the cartographic coordinates of the ground station. These can then be used to determine the image localisation.

Fig 7(a) shows the location of the Kiruna ground station itself, in cartographic coordinates, relative to the mean cartographic location of the ground station in ERS-2.SAR.PRI images. Notice the separation between the ground station acquired during ascending passes and descending passes – the difference of the average ascending pass location and average descending pass location is 1340m. The displacement between the passes is a consequence of the VMP SAR processor used at the ESA PAFs assuming that the surface being imaged is located on the surface of an ellipsoid. If the terrain being imaged is located above this ellipsoid, then

a displacement towards near range will occur. For ascending passes, this displacement is mainly towards smaller cartographic coordinates, while for descending passes it is mainly towards larger cartographic coordinates. The displacement will also be a function of incidence angle as is shown in Fig 7(b).

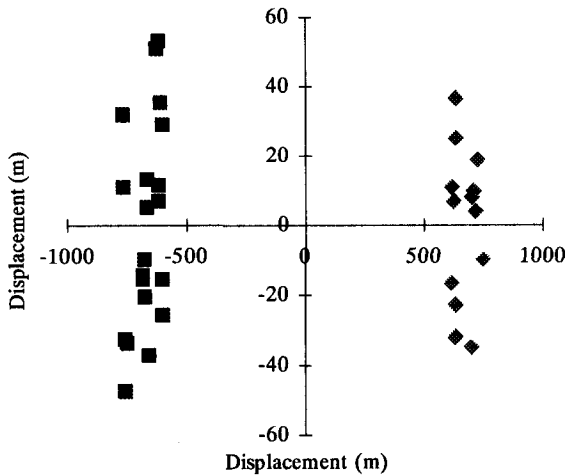


Fig. 7(a): Kiruna ground station cartographic coordinate displacements (m) for ascending passes (squares) and descending passes (diamonds).

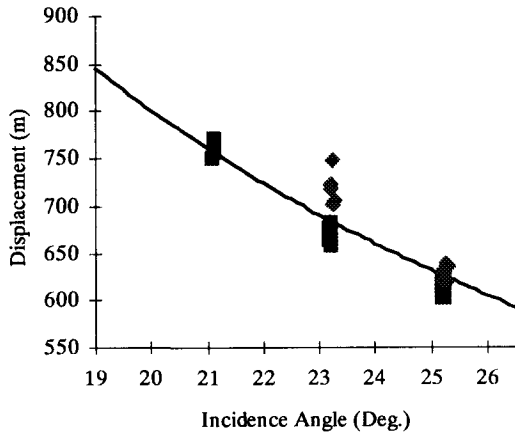


Fig. 7(b): Kiruna ground station displacement as a function of incidence angle. The solid curve is for a terrain height of 288m.

The curve shown in Fig 7(b) shows the displacement variation with incidence angle for a terrain height above the ellipsoid of 288m. This height occurs when the difference between the displacement measurements and the curve is a minimum – i.e. the image localisation after correcting for terrain height. Fig 7(c) shows the image localisation - the mean displacement is  $29.7 \pm 14.2m$ .

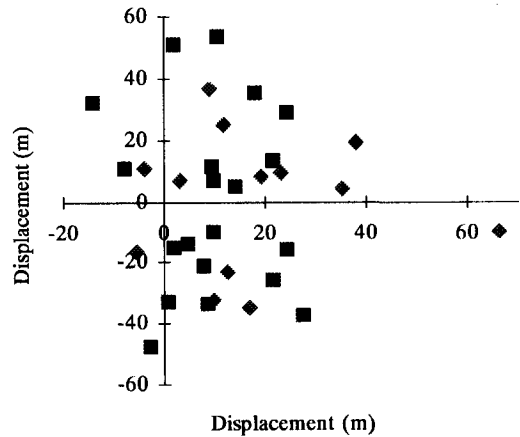
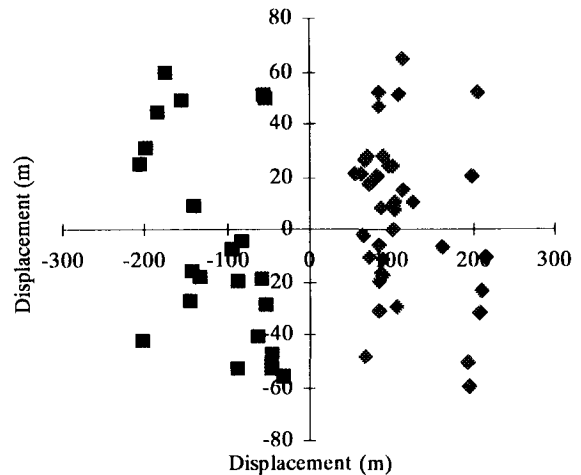


Fig. 7(c): Kiruna ground station localisation after correcting for a terrain height of 288m.

In Fig 8(a) the location of the Neustrelitz ground station, in cartographic coordinates, relative to the mean cartographic location of the ground station in ERS-2.SAR.PRI images is shown. The difference of the average ascending pass location and average descending pass location is 230m. The displacement as a function of incidence angle is shown in Fig 8(b) - the curve shows the displacement variation for a terrain height above the ellipsoid of 42m. Fig 8(c) shows the image localisation - the mean displacement is  $51.8 \pm 33.3m$ . This localisation is higher than that derived using the



ESA transponders [2] and the Kiruna ground station.

Fig. 8(a): Neustrelitz ground station cartographic coordinate displacements (m) for ascending passes (squares) and descending passes (diamonds).

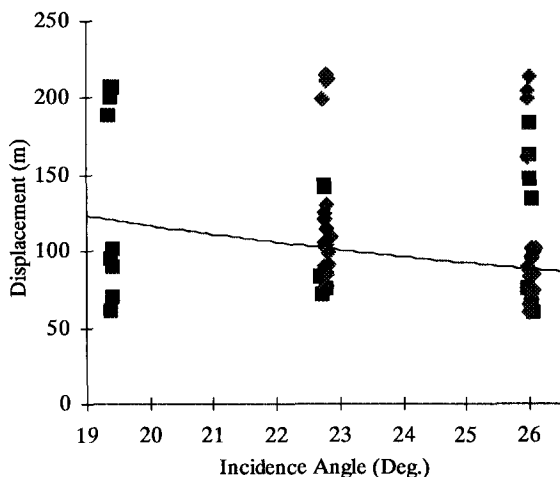


Fig. 8(b): Neustrelitz ground station displacement as a function of incidence angle. The solid curve is for a terrain height of 42m.

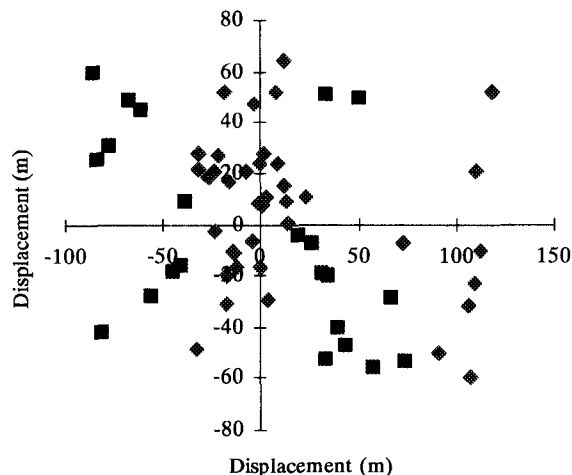


Fig. 8(c): Neustrelitz ground station localisation after correcting for a terrain height of 42m.

The Kiruna and Neustrelitz ground stations have shown that the displacement between ascending and descending passes is significant in ERS.SAR.PRI products. Fig 9 shows the displacement as a function of terrain height at near, mid and far incidence angles. This shows that the highest parts of the earth's surface will have displacements in excess of 10 km. Thus, users of ERS.SAR.PRI products should be aware of this displacement when using imagery to derive the location of a feature using the latitude and longitude information provided with the product. The ellipsoid corrected product, ERS.SAR.GEC, also processed at the PAFs have a mean terrain height correction already included and so the ascending/descending pass displacements are much smaller.

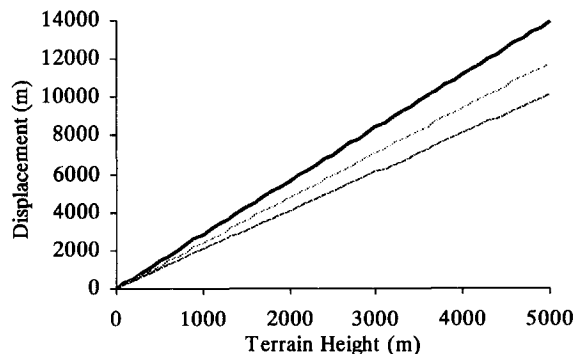


Fig. 9: Ascending/descending displacement as a function of terrain height above the ERS.SAR.PRI processed ellipsoid at near (top line), mid (middle line) and far (bottom line) incidence angles.

## CONCLUSIONS

This paper has shown that image quality assessment mean values using ground stations are only slightly greater than those derived with the ESA transponders although the spread of measurements is larger. Sidelobe parameters could not be measured using the Kiruna ground station azimuth ambiguities. Radiometric stability results are comparable to or, at worse twice of those derived using the transponders. Unlike the ESA transponders, the Kiruna and Neustrelitz ground stations are not at a terrain height close to the ellipsoid used during processing of the ERS.SAR.PRI products. This has meant that there is a significant displacement in the location of the ground stations between ascending and descending passes. After correction for terrain height, the localisation of the PRI product is comparable to, or at worst twice that derived using the transponders.

The results presented here show that ground receiving stations can be used a useful secondary calibration sources and it recommended that they be used as part of the Envisat ASAR commissioning phase where many suitable point targets will be required to assess the performance of this instrument.

## REFERENCES

- [1] Meadows, P.J., Laur, H., Sánchez, J.I. & Schättler, B., 'The ERS SAR Performances', Proceedings of the CEOS SAR Workshop, 3-6 February 1998, ESTEC, Noordwijk, The Netherlands, ESA WPP-138.
- [2] Meadows, P.J., Esteban Fernández, D. & Mancini, P., 'The ERS SAR Performances: An Update', Proceedings of the CEOS SAR Workshop, 26-29 October 1999, Toulouse, France.



## Maintenance of Radiometric Calibration Performance of RADARSAT-1

B.T. Banik, M. Adamovic<sup>1</sup>, S.K. Srivastava

Satellite Operations, Canadian Space Agency

6767 Route de l'aéroport, Saint Hubert, Quebec, Canada J3Y 8Y9

Tel: (450) 926-5134 Fax: (450) 926-4433 E-Mail: [bob.banik@space.gc.ca](mailto:bob.banik@space.gc.ca)

R.K. Hawkins, K.P. Murnaghan<sup>2</sup>

Canada Centre for Remote Sensing

588 Booth Street, Ottawa, Ontario, Canada K1A 0Y7

Tel: (613) 995-1067 Fax: (613) 947-1383 E-Mail: [Robert.Hawkins@CCRS.NRCan.gc.ca](mailto:Robert.Hawkins@CCRS.NRCan.gc.ca)

### ABSTRACT

RADARSAT-1, the first Canadian SAR remote sensing satellite, was launched on November 4, 1995. After commissioning, it was put into routine operations on April 1, 1996. Significant effort has been expended in the provision of geometrically and radiometrically calibrated products to users. After calibration, the beams are monitored routinely as part of the Maintenance Phase for image quality. Radiometric accuracy performance is monitored through periodic measurements of the elevation beam pattern of single beams using images of the Amazon rainforest. For some beams, pattern changes have occurred after calibration, but compensation has been made in the processor by recalibrating these beams. This paper describes the overall process of data acquisition, data analysis and recalibration for maintaining calibration accuracy within the *design goal limits* [1].

### INTRODUCTION

RADARSAT-1, the first Canadian radar remote sensing earth observation satellite, was launched into orbit on November 4, 1995. Since then, an extensive effort was spent on calibrating the imagery produced by the Synthetic Aperture Radar (SAR) processor which is located at the Canadian Data Processing

Facility (CDPF) receiving station near Ottawa. An important requirement of the RADARSAT-1 program was to provide users with radiometrically calibrated imagery. This means that users should be able to extract values of the radar brightness parameter from imagery which are calibrated to within 1 dB across the swath regardless of the terrain imaged. Radiometric calibration of the elevation beam patterns is required in order to achieve the required accuracy.

To achieve the initial calibration of the beams, numerous images were acquired over active transponder sites and over the Amazon rainforest region. The latter set of measurements are routinely used for monitoring the elevation beam pattern measurements. The calibration performance of the RADARSAT-1 system has been reported elsewhere [2]. This paper focuses on the process of maintaining the radiometric calibration performance of the RADARSAT-1 system and describes tools that were developed for such purposes.

### APPROACH

The approach used for maintaining radiometric calibration of the RADARSAT-1 system is comprised of the following steps which are depicted in the flowchart given Fig. 1.

<sup>1</sup> On contract from *Lockheed-Martin Canada*.

<sup>2</sup> On contract from *Isosceles Information Solutions Inc.*

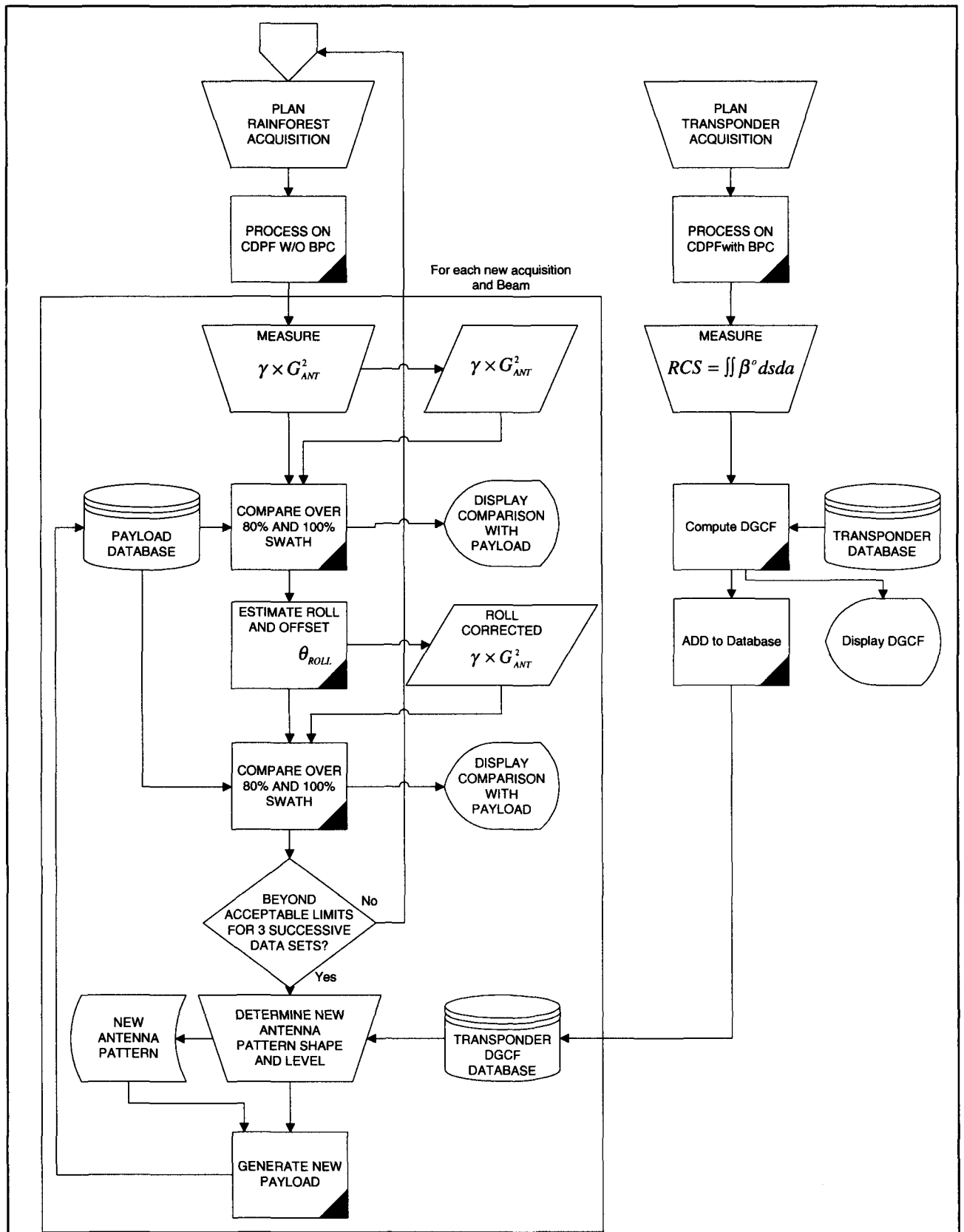


Fig. 1: Flowchart illustrating the steps taken in maintaining radiometric calibration of RADARSAT-1

There are broadly speaking eight steps to maintaining the radiometric calibration of RADARSAT-1 as follows:

1. Acquire raw Amazon data for measurement of Elevation Beam Pattern (EBP).
2. Process Amazon Data without Elevation Beam Pattern Correction (EBPC).
3. Measure EBP from processed image
4. Compute difference pattern without removal of spacecraft roll.
5. Compute difference pattern with removal of spacecraft roll.
6. If necessary, recalibrate the current EBP stored in the processor.
7. Test recalibrated EBP confirming radiometric improvement
8. Replace EBP in payload database with recalibrated EBP.

The following paragraphs briefly describe the steps involved in maintaining radiometric calibration performance of RADARSAT-1.

#### **Step 1: Acquire Raw Amazon Data**

The first step is to gather raw data in the Amazon rainforest region, which is noted for its roughly homogeneous radar backscatter properties [3]. In the Maintenance Phase of the RADARSAT-1 program, Amazon data are collected roughly once every two months for all 26 beams. In practice, the data collection process is limited by imaging opportunities of the Amazon region with the spacecraft due to orbital constraints. Typically, imaging opportunities are once every two to three days by any beam. If we are interested in only one particular beam, the opportunities are further reduced, and especially in the case of some narrow fine beams where imaging opportunities may be restricted to roughly once per month.

Acquisitions are routinely scheduled for all calibrated beams to enable identification of those beams which might be experiencing pattern changes due to possible aging effects (e.g. variable phase shifters). Once the problematic beams have been identified, additional acquisitions may be scheduled to confirm changes in the beam pattern. If consistent pattern changes are evident, recalibration of the elevation beam pattern is required to be performed (step 6).

#### **Step 2: Process Amazon data without EPBC**

The second step is to process the raw Amazon data as an SGF product without beam pattern correction. This is to

enable the beam pattern to be measured from the image product. Processing is performed by the CDPF and the products are copied to exabyte tape for off-line pattern measurement.

#### **Step 3. Measure EBP from Processed Image**

The third step is to measure the elevation beam pattern from Amazon scene products. The beam pattern measurement method for scene products has been described elsewhere [4]. Once measured, the test pattern is stored for off-line analysis.

#### **Step 4. Compute Difference Pattern Without Removal of Spacecraft Roll.**

In this step, the calibrated and test patterns are compared by computing the difference pattern without removal of spacecraft (S/C) roll. This is to quantify the level of radiometric errors which can be expected from products processed with the current Payload Parameters File (PPR). The calibrated pattern for the desired beam is obtained from the PPR file. The test pattern is obtained from the beam pattern measurement in step 2. The difference function is computed over two regions: the whole beam and the central 80%. Normally the outer edges of the scene are more sensitive to roll variations in the S/C and the two comparisons allow a rough assessment of whether the differences are caused by pattern change or by S/C roll.

In a perfect match, we expect to find a constant difference and the Peak to Peak (P-P) excursion of the curve (difference of the maximum and minimum) is used as a measure of the match of both pattern and S/C roll.

#### **Step 5. Compute Difference Pattern With Removal of Spacecraft Roll.**

This step is similar to the previous one except it to compute the difference pattern with removal of spacecraft roll. This is useful to identify any possible pattern changes, either in the electronic boresight and/or the shape when the effect of spacecraft roll is removed. If changes in pattern shape are noticed, more data is acquired and the process is repeated (steps 1-5).

The computation of the optimal roll offset is initiated by a coarse grid search followed by a correlation technique. Typical values for the grid search range from  $\pm 0.3$  degrees.

When the excursion of the measured antenna pattern from the payload reference pattern is more than 1 dB, for 3 or more consecutive data takes, a new pattern is

determined. Otherwise monitoring beam performance continues.

#### Step 6. If necessary, Recalibrate the Current EBP

When it has been determined that the elevation beam requires recalibration (step 5), it is necessary to identify the approximate date at which the pattern shape changes began to occur. This information is obtained by noting the P-P excursion and central 80% swath deviations in the difference pattern computed without removal of S/C roll determined at step 4. This is taken as the validity date of the updated payload file.

The new antenna pattern calibration is established in two substeps:

- At least three test antenna pattern measurements,  $\{\gamma \times G_{ANT}^2\}$ , are combined to a single smoothed pattern using a tool developed and implemented in MATLAB™. The pattern combination algorithm has been described elsewhere [5].
- The freshly determined smooth pattern is then fitted using least squares analysis [6] to precision transponder measurements taken since the first detected occurrence of pattern departure from specification. This gives the absolute level of the calibration.

#### Step 7. Test Recalibrated EBP

Repeat the antenna pattern measurement on those Amazon products for which the radiometry was degraded. Using the recalibrated pattern as the reference, repeat steps 2 through 5 comparing the test pattern. The results of the P-P deviations are stored for comparison with the original values.

The difference pattern without removal of spacecraft roll is verified to be less than about 0.3 dB peak-to-peak deviation across the swath. This confirms that radiometry has indeed improved when comparing the shifted test pattern with the recalibrated pattern.

#### Step 8. Replace EBP in Processor with Updated EBP.

Issue an updated PPR file containing the recalibrated elevation beam pattern for use by all processing facilities.

#### EXAMPLE

An illustrative example of the above technique is provided for recalibration of Standard Beam 3 (S3). The software tools have been developed in the IDL 3.6 programming language running under the Sun Solaris 2.6 operating system.

Fig. 2 shows a summary plot of the difference patterns without S/C roll for beam S3 acquired before and after recalibration. Updated results of the P-P deviations ( $\Delta P_{100}$  and  $\Delta P_{80}$ ) versus time for calibrated beams are reported elsewhere [2].

Fig. 3 shows the pattern analysis results for a product acquired on March 6, 1999 where the radiometry is degraded with PPR file #19. Fig. 4 shows the same product after recalibration. Identified on each plot are the calibrated and original test patterns, the shifted test pattern and the original and shifted difference patterns (upper curves), the spacecraft roll, and the P-P swath deviations for the original and shifted difference patterns.

Comparing Fig. 3 and 4, the improvement is self-evident between the degree to which the shifted test pattern matches the calibrated pattern. The same technique is repeated for other products where radiometry was degraded and radiometry was found to improve, indicating a successful beam recalibration. The payload parameters file was updated to PPR #20 with the recalibrated S3 pattern on April 21, 1999.

Table 1 provides a summary of the PPR files which have been used to date since launch. It is noted that the three most recent PPR files (#19,#20,#21) resulted from recalibration of beams W1, F4, S3, S6 and S1 based on the tools and techniques described here.

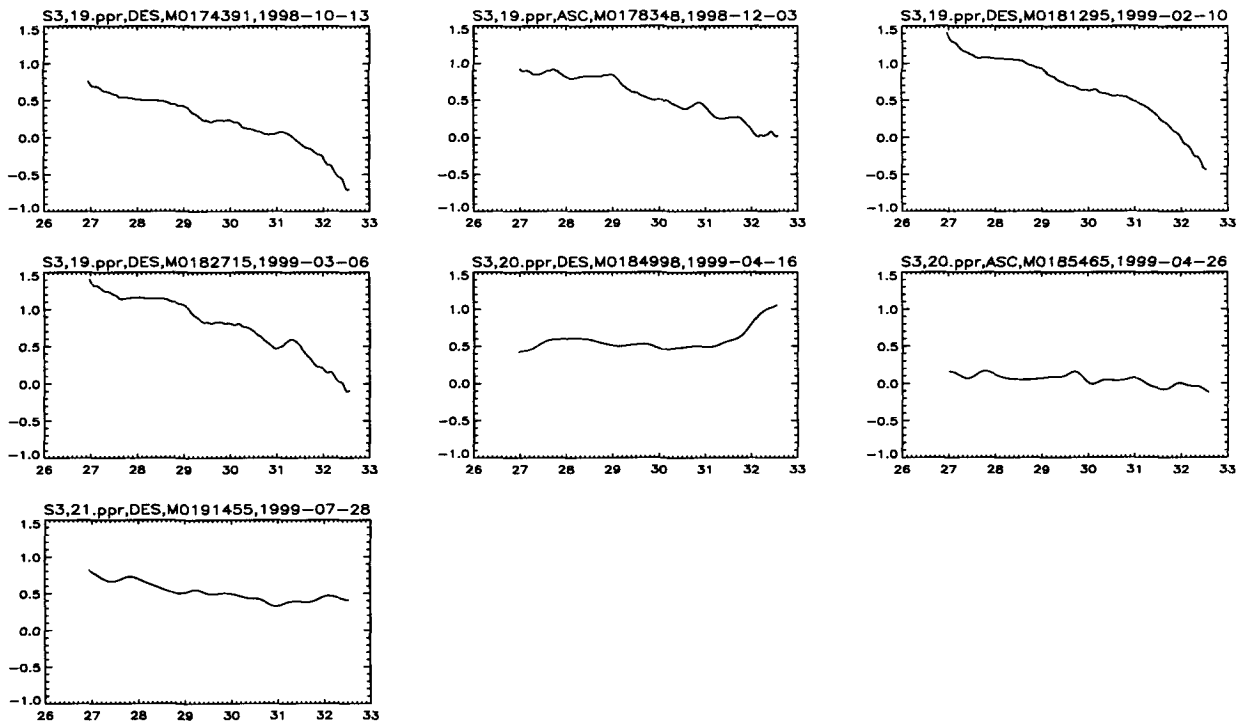


Fig. 2: Two-way difference patterns versus elevation angle without removal of spacecraft roll for beam S3. Amazon data were acquired between October 13, 1998 and July 28, 1999. Beam S3 was recalibrated on April 21, 1999.

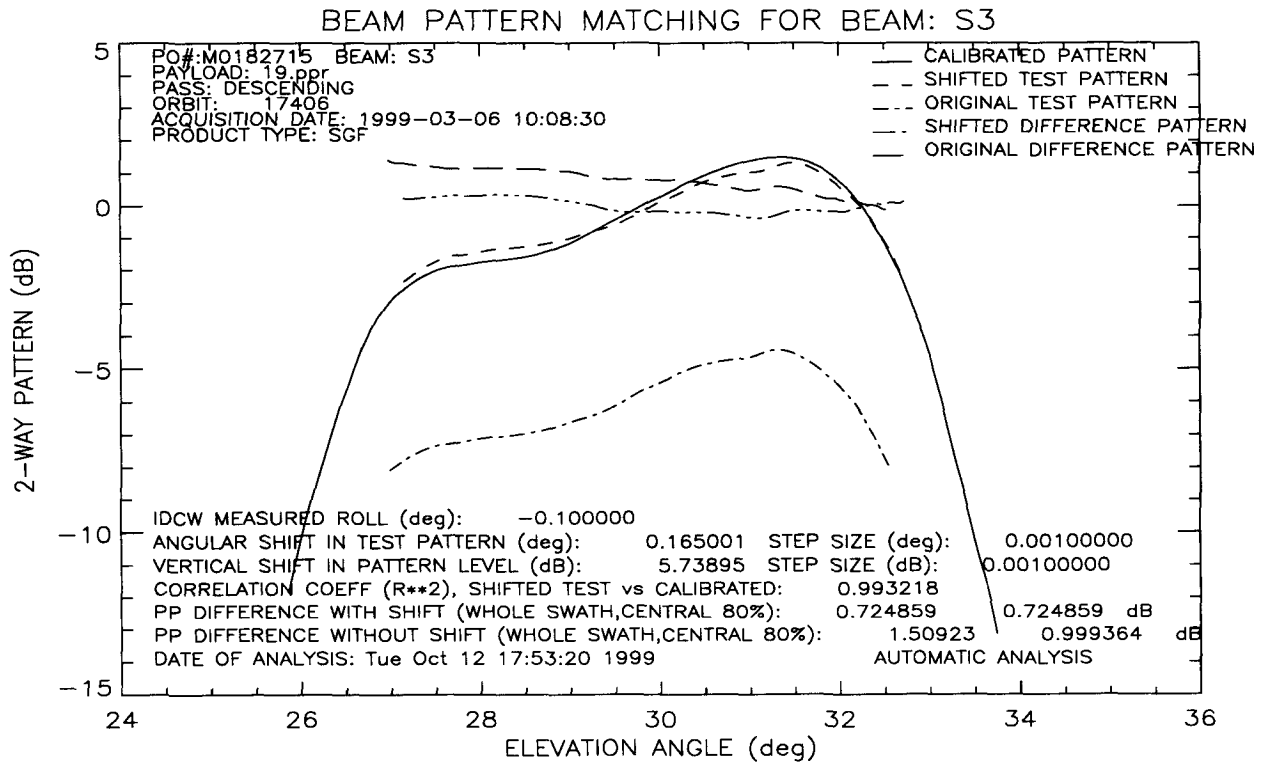


Fig. 3: Beam pattern matching results for beam S3, product M0182715, before recalibration.

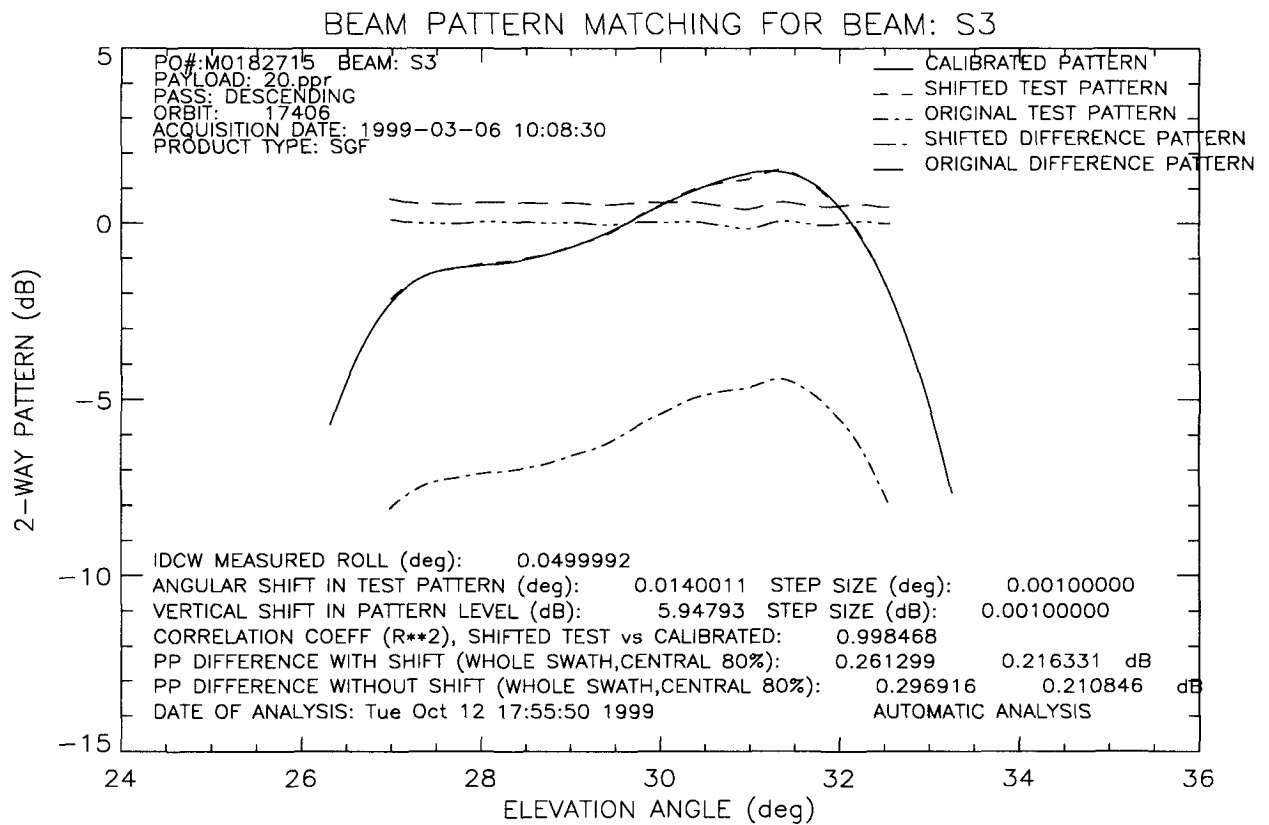


Fig. 4. Beam pattern matching results for beam S3, product M0182715, after recalibration.

### DISCUSSION

Caution must be exercised to check that the pattern matching achieved at the edges is good, i.e., the beam edges of the shifted test pattern and the calibrated pattern should overlap each other. When there is a large pattern change even with removal of S/C roll, it may be concluded that the beam recalibration is required. In the recent example of beam S3, the P-P deviations in the roll corrected difference pattern (0.7 dB) were indicative of the comparable elevation pattern shape. The contribution of the S/C roll in the whole swath P-P deviation is the difference with and with out roll correction ( $1.5 - 0.7 = 0.8$  dB). After recalibration, the deviations in the difference are significantly reduced (0.2 dB).

### CONCLUSION

The pattern matching technique has been used to detect small changes in the elevation beam pattern of all calibrated beams of the RADARSAT-1 system, which are routinely monitored as part of the Maintenance Phase. Tools have been developed for monitoring and evaluating the pattern shape changes and for generating

an updated calibrated beam pattern which is used for pattern correction by the SAR processor. The tools and techniques described here can be easily adapted to future Earth Observation Systems designed to produce radiometrically calibrated products for the user community.

### REFERENCES

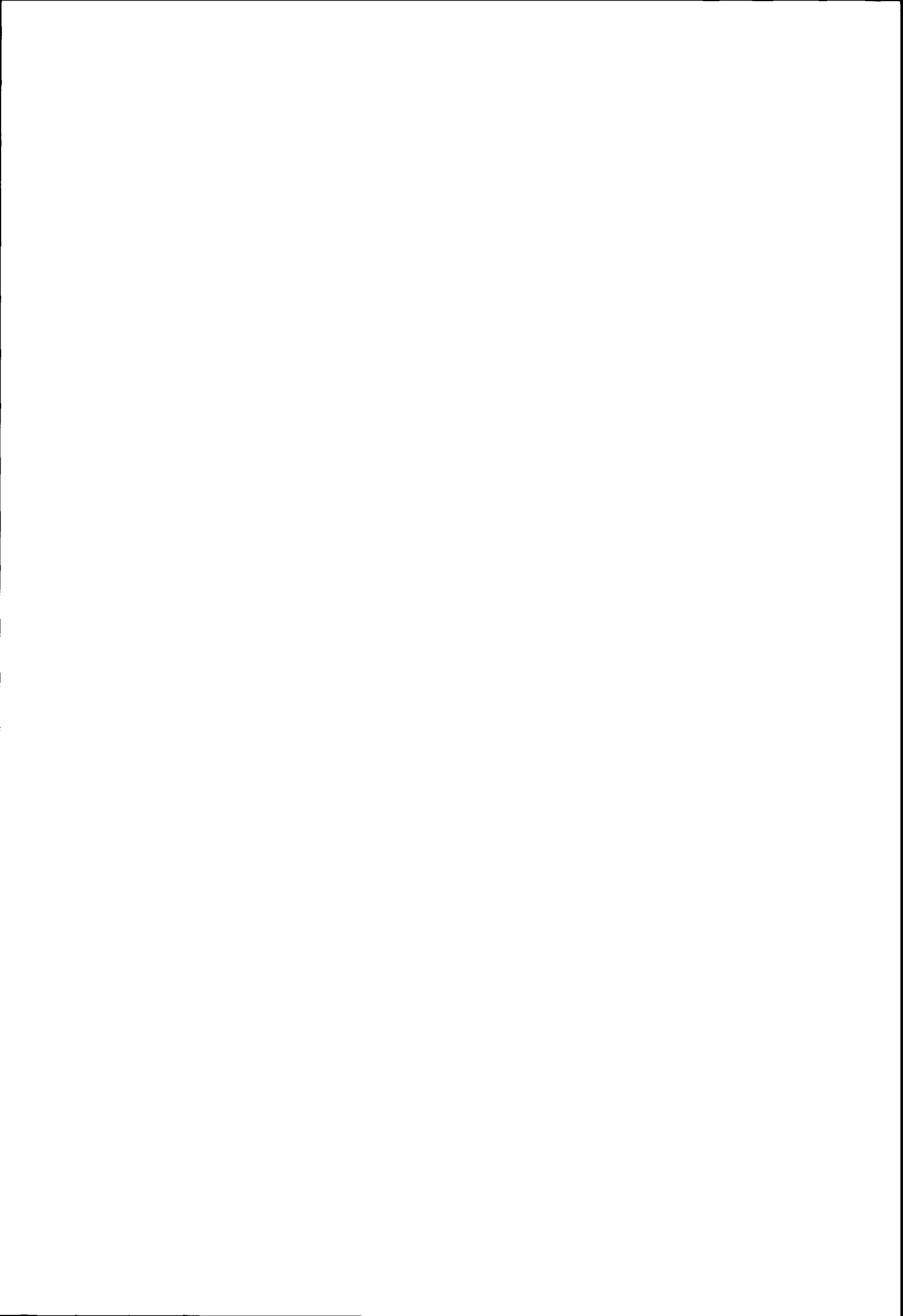
- [1] "RADARSAT System Specification", CSA Document RSCSA-SP0002, Rev.C, 1996.
- [2] S.K. Srivastava, *et al.*, "RADARSAT Image Quality Update," this proceedings.
- [3] R.K. Hawkins, *et al.*, "Stability of Amazon Backscatter at C-Band: Spaceborne SAR Results from ERS-2 and RADARSAT-1", this proceedings.
- [4] T.I. Lukowski, *et al.*, "RADARSAT Elevation Antenna Pattern Determination," *Proc. IGARSS '97*, vol. 3, Singapore, pp. 1382-1384, 1997.

[5] K.P. Murnaghan, R.K. Hawkins, and T.I. Lukowski, "Combination Procedure for RADARSAT Antenna Pattern Determination," *Proc. Canadian Symposium on Remote Sensing*, Calgary, 1998.

[6] R.K. Hawkins and S.K. Srivastava, "The Radiometric Error Budget of RADARSAT-1", this proceedings.

RADARSAT PAYLOAD FILES				
Payload #	Submitted	Valid Start Time	Valid End Time	Comments
05	28-Nov-95	1995-12-28 23:24:28	1996-02-28 21:03:41	
06	28-Feb-96	1996-02-28 21:03:41	1996-05-21 21:36:00	Revised replica_phase_coeff
07	21-May-96	1996-05-21 21:36:00	1996-06-14 15:34:53	New beam table load
08	14-Jun-96	1996-06-14 15:34:53	1996-07-23 20:06:25	New beam patterns for S1-7, W1-3, F1-5
09	23-Jul-96	1996-07-23 20:06:25	1996-09-25 21:13:05	Refinement of elevation beam patterns and GCF
10	25-Sep-96	1996-09-25 21:13:05	1996-11-27 19:39:39	Beam slot changes for extended high beams
11	27-Nov-96	1996-11-27 19:39:39	1997-01-21 14:35:58	Calibration of beams S1, S2, S3, S4 of CDPF products
12	21-Jan-97	1997-01-21 14:35:58	1997-02-14 17:12:08	EL1 Beam replacing EH1 beam
13	14-Feb-97	1997-02-14 17:12:08	1997-06-02 16:39:46	S5-S7, W1-W3 calibrated, S1, S2, S4 and GCFs upgraded
14	02-Jun-97	1997-06-02 16:39:46	1997-08-12 15:35:51	F1-F5 calibrated, GCFs and TRNLs updated, Relative beam gains adjusted
15	12-Aug-97	1997-08-12 15:35:51	1997-09-08 07:00:00	Calibration upgrade to Beam EL1
16	08-Sep-97	1997-09-08 07:00:00	1997-09-09 07:00:00	Beam EL1 calibrated
17	8-May-98	1997-09-09 07:00:00	1997-10-20 19:00:00	Beam S4 Calibrated for Left-Looking Mode (Antarctic Mapping Mission)
18	8-May-98	1997-10-20 19:00:00	1998-04-21 21:12:32	Copy of Payload 16 with an update of TNRL
19	23-Dec-98	1998-04-21 21:12:32	1998-10-13 20:57:17	Beams F4 and W1 recalibrated
20	21-Apr-99	1998-10-13 20:57:17	1998-12-10 20:57:17	Beams S3 and S6 recalibrated
21	17-Jun-99	1998-12-10 20:57:17	2014-07-23 00:00:00	Beams S1 recalibrated and TNRL updated

Table 1. Radarsat-1 Payload Parameters Files Used Since Launch.





## The Radiometric Calibration Budget of RADARSAT-1

RK Hawkins<sup>†</sup> and SK Srivastava<sup>‡</sup>

<sup>†</sup>Canada Centre for Remote Sensing, 588 Booth St, Ottawa, K1A 0Y7, Canada;  
Email: robert.hawkins@ccrs.nrcan.gc.ca; http://www.ccrs.nrcan.gc.ca

<sup>‡</sup>Canadian Space Agency, 6767 Route de l'aéroport, Saint Hubert, Québec, J3Y 8Y9, Canada  
Email: satish.srivastava@space.gc.ca; http://www.space.gc.ca

### ABSTRACT

This paper reviews the radiometric calibration budget of RADARSAT-1 using a model for the estimation of parameters used to set the calibration. The model involves all of the externally determined quantities used in the calibration together with their statistical variation including: antenna pattern determination, replica energy variation, absolute calibration using reference targets, and spacecraft attitude stability. Results from the modelling are applied to the case of standard beam S3 which may be extended to other beams without losing generality are consistent with previously reported uncertainty estimates.

### INTRODUCTION

Since its launch in November 1995, RADARSAT-1 has undergone a number of stages including commissioning, qualification, calibration and maintenance phases. It was declared fully operational on April 1, 1996 and its beams have gradually been calibrated and sometimes recalibrated [1], [2], [3], [4]. During the process of estimating the RADARSAT-1 beam patterns, there is an opportunity [5] to estimate the associated radiometric errors in products generated from the Canadian Data Processing Facilities (CDPF). In this paper, we clarify the procedure and express the assumptions and limitations of that process. The absolute calibration of RADARSAT-1 is implemented in the CDPF as a product of several factors.

$$\beta^o = \frac{\sigma^o}{\sin \theta} \propto P_r \frac{G_{CF}^2 \times G_{overall}}{G_{ant}^2} \quad (1)$$

Here,  $\beta^o$  is the scattering brightness,  $\sigma^o$  is the normalized radar backscattering coefficient,  $P_r$  is the received power,  $G_{CF}$  is the Gain Correction Factor (GCF),  $G_{overall}$  is the overall gain factor determined

from pulse replica power, and  $G_{ant}^2$  is the two-way antenna pattern shape as we shall see below. The antenna shapes and the GCFs come to the CDPF through the Payload Parameter File which is updated as necessary to maintain an overall calibration accuracy.

There are four principle sources of error associated with the calibration of any product outlined and described in the subsections below. Briefly, these include antenna pattern shape and mask overlay, pulse replica power determination, external target radar cross section (RCS) and extraction of impulse response measurements from point targets, and overall system gain variation.

In addition, there are factors which relate to processor normalization and we assume that these are well understood and do not play a significant role here. In the next section, we provide a theoretical framework for the main sources of uncertainty and then go on to provide an example of overall uncertainty before drawing some conclusions.

### THE APPLICATION OF THE ANTENNA PATTERN

The factor  $G_{ant}^2$  in (1) represents the two-way relative gain of the RADARSAT-1 beam. In the current configuration of the CDPF it is placed over the image swath assuming a nominal geometry for both single beams and for ScanSAR since any attitude changes are unaccounted. Uncertainties associated with the antenna pattern can therefore be attributed to two sources: the shape of the pattern and its placement over the image. More discussion on these aspects are given in the subsections below.

### The Shape of the Antenna Pattern

The antenna pattern is determined from a small set (at least 3) of Amazon rainforest measurements [6]. These are combined and contain statistical variations. Some of these are textural in nature, and some due to other causes like drainage fields and atmospheric effects. We assume that although the shape of the pattern may be

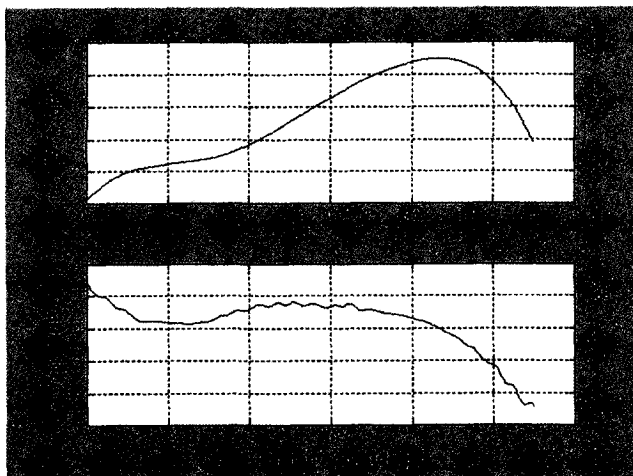


Fig 1: Roll dependence of radiometric calibration from beam S3

stable, there may be overall gain variations (either due to the instruments on the satellite or variation in the backscatter of the rainforest) and spacecraft roll variations. These allow us to displace the individual patterns that make up the final shape both in gain and in angle in order to obtain the best overall fit [7].

The error in estimating the shape itself is found from the spread in the amalgamated and shifted data from the smooth profile fitted through it and is our estimate of the uncertainty in the fitting process itself. We quantify this as  $\Delta\beta_{G_{ant}}$  and it is a direct output of the antenna amalgamation software as the standard deviation of the smoothed pattern and the amalgamated data.

### The Roll Variation of the Satellite

In the process of determining the amalgamated antenna pattern, the beams are shifted along the angular axis and this is attributed to roll variations in the satellite. One beam is taken as reference and the others are shifted to form the best match. The amount of the horizontal shifting is the estimated roll.

The radiometric uncertainty associated with roll is a function of the size of the roll variation encountered and the shape of the antenna pattern itself through the relation:

$$\Delta\beta_{roll}^o \approx -\frac{dG_{ant}^2}{d\vartheta_e} \Delta\vartheta_e \quad (2)$$

In this equation,  $\Delta\beta_{roll}^o$  is the change in the apparent normalized radar cross section due to an error  $\Delta\vartheta_e$  in the roll angle which couples directly into the beam elevation angle associated with the two-way gain  $G_{ant}^2$ . When the antenna pattern is determined in dB, the relation provides uncertainty in dB provided the excursions are small. Fig. 1 shows the beam pattern for beam S3 from payload 16 and the derivative of the two-way pattern below it. In this figure, the effect of a  $1^\circ$  roll on the radiometric accuracy is shown. Note that the overall variation in each case is about 6 dB. Within the first phase of calibration for RADARSAT, the roll error in the satellite was less than  $0.3^\circ$  in the worst case. Nevertheless errors from roll uncertainty can be significant. Most transponder data takes will be in the region of the middle of the beam where the slope is approximately 1.5 dB/deg and typical roll variations are about  $0.1^\circ$ . From this figure, we see that the expected errors from this source will vary from approximately 0.2 dB to  $-0.4$  dB for this beam, presuming that roll variations are approximately 0.1 degrees. In estimating uncertainty from this source, we assume that the uncertainty of the roll is the standard deviation of the roll estimates from the antenna amalgamation process.

### THE DETERMINATION OF THE REPLICA POWER

The overall gain, as it is reported in the .PRC (Processing Report Card) files from the CDPF processor [8] is determined from integration over the pulse replica and is reasonably stable. It includes any changes in the transmitted pulse energy and most of the receive path excluding the antenna and the limiter/LNA. Its function is to monitor transmitted power and any attendant receiver gains but because it does not include all parts of the link budget, we prefer to call this source of uncertainty as  $\Delta\beta_{rep}$ . We determine it as the standard deviation of the replica pulse energy determinations for the scene. It is listed in the standard .PRC analysis done by CCRS as illustrated in Fig. 2. In the CDPF, a single overall gain factor is determined from the average of the replica energies as follows.

$$G_{overall}^2 = \frac{10^{6.5}}{\langle E \rangle} \quad (3)$$

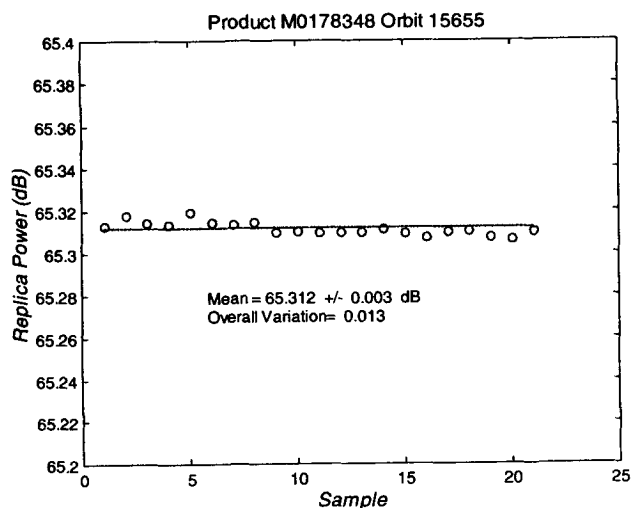


Fig. 2: Pulse replica energy from processing a scene

Here,  $\langle E \rangle$  is the average of the 21 replica energies normally used in the scene. The exponent of 6.5 comes from an early normalization for replica energy and which sets the reference energy as 65 dB.

There are small variations observed in the individual estimates of the replica power used in the processor and reported in the .PRC files. We use the standard deviation of this value for  $\Delta\beta_{rep}$ .

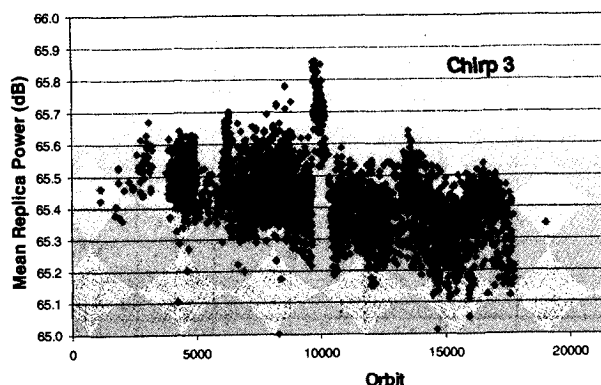


Fig. 3: Evolution of RADARSAT-1 chirp 3 energy

Fig. 3 shows the overall variation from the ensemble of chirp 3 (11.73 MHz) replica means determined since launch. We see that this systematic correction can be as much as 0.6 dB and is therefore an important systematic correction. The jump in the data near orbit 10000 relates to the Antarctic Mapping Mission in which the spacecraft was rotated to look left instead of its normal look-right geometry.

## THE ESTIMATE OF THE RCS OF THE EXTERNAL CALIBRATORS

In the method used to determine absolute calibration, precision transponders [9] with known RCS are imaged and used as calibration references. Associated with this process are three related sources of uncertainty: RCS for the precision targets, impulse integrated response, and fitting error in the process of matching the target responses to the antenna pattern.

The manufacturer's specification on this was  $\Delta\beta_{RCS} = \pm 0.25$  dB. It is expected that this estimate is actually low [10]; however, in this report, we shall assume the number is valid.

An important source of uncertainty here is fading between the clutter and the replica of the transponder return characterized by the set of Impulse Response Measurements (IRM). For the products analysed for RADARSAT-1 transponder response, the following relation can be derived [5] for the linear variance of the integrated response,  $\epsilon_I^2$ , using the integrated signal-to-clutter ratio computed by the Image Analysis Workstation (IAW),  $\left(\frac{S}{C}\right)_{iaw}$ .

$$\Delta\beta_{IRM}^o = 10 \log_{10}(1 \pm \epsilon_I) \quad (4)$$

$$\epsilon_I^2 = \left[ \left(\frac{S}{C}\right)_{iaw}^{-2} + 2 \left(\frac{S}{C}\right)_{iaw}^{-1} \right] \times \frac{2}{76} \quad (5)$$

Typically  $\left(\frac{S}{C}\right)_{iaw}$  is in the range of 15 to 22 dB and  $\Delta\beta_{IRM} \approx .12$  dB.

## UNCERTAINTY MATCHING POINT TARGET AND ANTENNA PATTERN

Fig. 4 is an example of the results of a fitting process between the smoothed antenna shape and the integrated response from the precision targets for a set of data for the recalibration of beam S3. The line is the smoothed antenna pattern with its associated shape uncertainty as described above. The error bars are the estimated RCS uncertainties and do not include the contribution of the measurement of the integrated response described by (5) nor the uncertainty in the antenna pattern shape imposed on the measurements (quite apart from our determination of it) nor the uncertainty of the placement of the antenna mask at the acquisition time of the transponder data points; nor the replica power estimate. These factors *all* contribute to the scatter of the points

and reflect the overall uncertainty in the region of the transponder measurements. As part of the process, three quantities are determined: the average displacement of the curve and the transponder points,  $\langle d \rangle$ ; the standard deviation of the displacement mean,  $\sigma_{\langle d \rangle}^{\mu}$ ; and, the standard deviation of the displacement,  $\Delta\beta_{\langle d \rangle} = \sigma_{\langle d \rangle}$ . The line has been displaced by all processor gains, by the expected backscatter of the Amazon (-6.5 dB) and finally adjusted by a least squares process to make a best fit with the point target results. The value of D represents this final displacement. The points represent the point target results from the five acquisitions over the RADARSAT-1 precision transponders. Their error bars are the nominal spec. on the transponder absolute accuracy of  $\pm 0.25$  dB.

From the discussion above, we can estimate the contribution from unknown sources associated with the fitting,  $\Delta\beta_{\langle d \rangle}$ , by the relation which follows.

$$\Delta\beta_{fit}^2 = \Delta\beta_{\langle d \rangle}^2 - \Delta\beta_{rep}^2 - \Delta\beta_{IRM}^2 - \Delta\beta_{RCS}^2 - 2\Delta\beta_{G_{ant}}^2 - \Delta\beta_{roll}^2 \quad (6)$$

Here,  $\Delta\beta_{fit}$  is an unknown gain outside the mechanisms so far discussed. The antenna gain uncertainty (shape) is included twice because it appears both in the shape being fitted and the transponder data because we assume that these are approximately the same size. In the next section, we relate this to a measure of overall gain variation. Here, each of the subtracted components are evaluated in the region of the image near the IRMs. In using this relation, it is assumed that the variations are all smaller than the fitted transponder data. If this is not

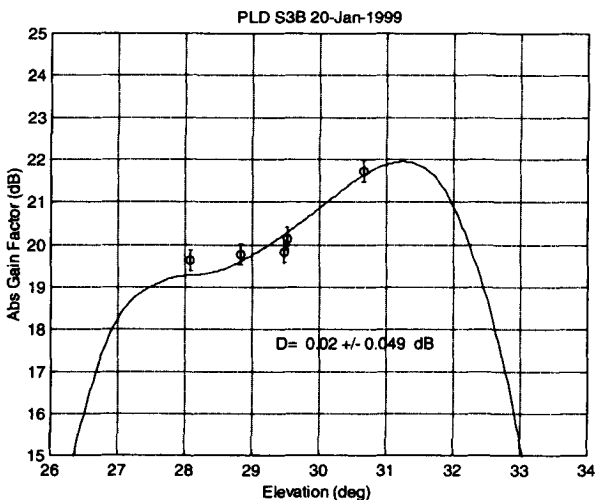


Fig. 4: Absolute recalibration of beam S3

the case, any gain variations may be assumed to be small.

OVERALL SYSTEM GAIN VARIATION.

In evaluating the calibration, there are several stages which the data passes through including the transmitter/receiver chain and the antenna as well as the processor before IAW work is performed. Several factors do however point to the possibility of RADARSAT-1 system gain changes:

- o In reviewing the data from the Amazon rainforest [11] it is clear that there is pass to pass variation in the overall gain of the scene which does not appear to affect the shape of the extracted antenna pattern. We have no *a priori* means of telling whether this source of change is due to geophysical phenomena or gain changes in the RADARSAT-1 system.
- o In some cases, similar size variations also occur in the precision transponder data that appear to be beyond the manufacturer's specification on uncertainty and again the separation of target and system is not intrinsically possible.

If we assume that both observed variations have the same system gain source and that they are random, there is an additional overall uncertainty in the absolute gain of RADARSAT-1 which can be addressed from the calibration data itself.

$\Delta\beta_{fit}$  Estimation from Precision Transponder Data

In the calibration of RADARSAT-1, we view the precision transponders as the calibration standard and the rainforest as an unknown error source. In this scenario, provided that other known sources of uncertainty are sufficiently small, we can estimate a system gain contribution.

The uncertainty in gain can then be determined from the RMS variation of the transponder integrated response fits taking into account the already included uncertainty: replica power, IRM error, antenna pattern and mask placement, and RCS uncertainties. If we assume these are in turn independent, the component associated with unaccounted overall gain variations can be determined from  $\Delta\sigma_{gain} = \Delta\beta_{fit}$  using (6) to obtain  $\Delta\beta_{fit}$ .

Table 1 is an example of this calculation for the beam S3 recalibration. In this case, the total systematic error before inclusion of the possible gain variation exceeds  $\Delta\sigma_{\langle d \rangle}$ . This means that we cannot find any new

variation from this data set and there are no unaccounted gain variations observed in RADARSAT-1.

Table 1: Systematic error estimates from point targets

Quantity	Standard Deviation		Variance
	(dB)	linear	linear
$\Delta\beta_{rep}$	0.003	0.00	0.0000
$\Delta\beta_{IRM}$	0.12	0.03	0.0007
$\Delta\beta_{RCS}$	0.25	0.06	0.0035
$\Delta\beta_{G_{ant}}$	0.18	0.04	0.0018
$\Delta\beta_{roll}$	0.15	0.04	0.0012
Systematic total	0.39	0.10	0.01
$\Delta\beta_{<d>}$	0.25	0.06	0.0035

A similar analysis [5] carried out using the rainforest as a distributed target source leads to the same conclusion.

#### AMALGAMATION OF ERRORS

Each of the errors indicated in the preceding sections are statistically independent. In the RADARSAT-1 calibration, it has been traditional to talk about uncertainties in terms of three aspects:

1. The central 80% of the beam where the edges of the elevation pattern are not apparent and the slopes are more gradual.
2. The whole beam including the skirts of the beams.
3. Typical and worst case scenarios.

Returning to (1), we see that the overall uncertainty in calibrating a scene can be found from the relation

$$\Delta\beta_T = \sqrt{\Delta\beta_{G_{ant}}^2 + \Delta\beta_{<d>}^2 + \Delta\beta_{rep}^2 + \Delta\beta_{roll}^2} \quad (7)$$

Estimates for various error sources are indicated as per the formulae above. These results are compatible with those presented in previous summaries [4] and consistent with the Mission Requirements Document for RADARSAT-1.

#### Extension to More Global Statistics

The data presented so far are from a particular example for the determination of the beam pattern for beam S3. The extension to the global set of data for RADARSAT-1 will involve bringing in the larger set of data from all beams. This should provide better estimates for such quantities as the attitude variations, replica energies, rainforest variations, *et cetera*. There are no reasons in principle why these could not be jointly evaluated. Where it may not make sense to amalgamate data would be in the error due to antenna pattern roll variation which are highly dependent on the shape of the pattern itself and individual beams for this reason may have more intrinsic variation. In general, however, RADARSAT-1 calibration accuracy has been quoted globally and this would be one way of determining these statistics.

#### CONCLUSIONS AND RECOMMENDATIONS

In this report, we have discussed the error sources associated with the RADARSAT-1 calibration and have estimated typical and worst case overall calibration accuracy. Example data are given using recent data from the recalibration of beam S3. From these data, we conclude the errors found in the example are in line with previous estimations and appear to be fully accounted for by known systematic errors in both the transponder and rainforest data. It should be noted that all of the analysis is based on the assumption of sea level featureless terrain.

It is recommended that a full set of statistics be assembled for data from all sources to see how this analysis applies globally.

#### ACKNOWLEDGEMENTS

The authors would like to thank the members of the RADARSAT Image Quality Working Group for their support in this work. In particular, we would like to thank Tony Luscombe of MDA for his comments and the RSI operations team for supplying data to the CSA IQ group. We also thank Andrew Wind and Tom Lukowski for reviewing the manuscript.

Table 2: Summary of Uncertainties from S3 Recalibration

Aspect	Typical				Worst Case			
	Central 80%		Whole Image		Central 80%		Whole Image	
	dB	linear	dB	linear	dB	linear	dB	linear
$\Delta\sigma_{G_{ant}}$	0.18	0.04	0.12	0.03	0.54	0.13	0.36	0.09
Roll Variation (deg)	0.07		0.15					
$\Delta\sigma_{roll}$	0.14	0.03	0.60	0.15	0.42	0.10	1.8	0.51
$\Delta\sigma_{rep}$	0.03	0.01	0.05	0.01	0.09	0.02	0.15	0.04
$\Delta\sigma_{<d>}$	0.25	0.06	0.25	0.06	0.747	0.19	0.747	0.19
Total	0.33	0.08	0.65	0.16	0.98	0.25	1.92	0.55
$\Delta\sigma_{RCS}$	0.25	0.06	0.25	0.06	0.75	0.19	0.75	0.19
$\Delta\sigma_{IRM}$	0.12	0.03	0.17	0.04	0.36	0.09	0.516	0.13
$\Delta\sigma_{roll}$	0.07	0.02	0.15	0.04	0.21	0.05	0.45	0.11
$\Delta\sigma_{gain}$ from Transponders	0.00	0.00	0.00	0.00	0	0.00	0	0.00
$\Delta\sigma_f$	0.1	0.02	0.1	0.02	0.3	0.07	0.3	0.07
$\Delta\sigma_{offset}$	0.09	0.02	0.34	0.08	0.27	0.06	1.02	0.26

## REFERENCES

- 1 Proceedings of Committee on Earth Observations Satellites (CEOS) Workshop on RADARSAT Data Quality, Canadian Space Agency, St Hubert, Québec. Feb. 4-6, 1997.
- 2 RK Hawkins, BT Banik and SK Srivastava, "Evolution of RADARSAT Calibration to Date," Proceedings of CEOS SAR Workshop, Noodwijk, the Netherlands, ESA Publication, WPP-138, 1998, pp. 187-197.
- 3 SK Srivastava *et al.*, "RADARSAT Image quality and calibration performance," *ibid*, 1998, pp. 169-175.
- 4 SK Srivastava *et al.*, "Maintaining image quality and calibration of RADARSAT-1 CDPF products," *Proc. IGARSS'99*, vol. 1, 1999, pp. 443-445.
- 5 RK Hawkins, "Radiometric error estimation from RADARSAT beam pattern determination," CCRS internal Tech. Note CCRS-TN-1999-03, 1999, 16p.
- 6 BT Banik *et al.*, "Maintenance of radiometric calibration performance of RADARSAT-1," this proceedings.
- 7 KP Murnaghan, RK Hawkins, and TI Lukowski, 1998, "Combination procedure for RADARSAT antenna pattern generation", *Proceedings of the 20<sup>th</sup> Canadian Symposium on Remote Sensing*, Calgary, Alberta, pp. 85-90.
- 8 MacDonald Dettwiler and Associates, "RADARSAT CDPF system specification," Document RZ-SY-50-4381, 1994, ~100p.
- 9 RK Hawkins, LD Teany, and SK Srivastava, "Radarsat precision transponder," *Advances in Space Technology*, vol. 19, no. 9, 1997, pp. 1455-1465.
- 10 RK Hawkins and LD Ikkers, CCRS Tech. Note in progress, 1999.
- 11 RK Hawkins *et al.*, "Stability of Amazon backscatter at C-band: Spaceborne results from ERS-1/2 and RADARSAT-1," this proceedings.

# Roll Angle Measurement and Compensation Strategy for RADARSAT ScanSAR

Marina V. Dragošević and Glenn E. Davidson

IOSAT Inc. Richmond Terminal, Pier 9 Halifax, NS, Canada B3K 5V8

Tel: 1 902 492-4780 Fax: 1 902 492-4781

marina.dragosevic@satlantic.com; glenn.davidson@satlantic.com

## Abstract

One of the main challenges in ScanSAR processing is to suppress radiometric artifacts which stem from the burst nature of the ScanSAR systems. Cross-track radiometric uniformity of the RADARSAT ScanSAR imagery critically depends on the accuracy of the antenna elevation beam patterns and the accuracy of the spacecraft roll angle. Beam calibration has been done in single beam mode for various RADARSAT beams independently and at different times. Such measurements are sensitive to roll instability. Thus relative beam boresight pointing and relative peak gains of the beams used in ScanSAR remain an issue, as well as time variations of the satellite attitude. This paper deals with practical issues of roll estimation in: i) ScanSAR processor calibration and ii) ScanSAR processor production.

## INTRODUCTION

Radiometric distortions across track depend on two factors. The first one is due to the sensor to target distance, or slant range, and the second reflects the elevation beam patterns. The latter is more difficult to correct because it depends on the unknown roll angle. Therefore spacecraft roll has to be estimated and tracked during processing. ScanSAR systems [2] provide a unique opportunity to extract roll information from the overlap regions between two beams. On a logarithmic scale, the difference between the intensities of the same target in two beams should, on average, be equal to the difference in the elevation gains of those beams at the target position. Any mismatch between these two differences can be attributed to the sensor's roll angle, but also to other imperfections in the system, as

will be discussed in the following sections. The main idea is to estimate roll by minimizing a quadratic criterion based on these mismatches. The proposed algorithm is similar to Jin's range centroid estimation method [3]. The principal difference is that roll will be estimated directly and all beam overlaps are used at once. This procedure will succeed only if the beams are well calibrated, if the processor is well calibrated and if along track radiometric artifacts are minimized.

## ROLL ESTIMATION IN PROCESSOR CALIBRATION

One way to calibrate a processor is to use a distributed target of uniform, steady and known  $\gamma_0$ , the Amazon rain forest. The main objective is to determine the calibration constant  $A$ , but in order to do that, the roll angle  $\phi$  has to be matched to the antenna beam pattern.

The main assumption is that the antenna gain pattern  $w(\gamma)$  is known for a set of elevation angles  $\gamma \in \Gamma_W \subseteq R$  and that the measurements of the range profiles  $s(\gamma)$  are available for a subset  $\gamma \in \Gamma_S \subset \Gamma_W \subseteq R$ . We will define the window function

$$u(\gamma) = \begin{cases} 1 & \gamma \in \Gamma_S \\ 0 & \gamma \notin \Gamma_S \end{cases} \quad (1)$$

Now, fitting of both  $A$  and  $\phi$  can be defined by

$$\begin{bmatrix} A \\ \phi \end{bmatrix} = \arg \min_{(A, \phi) \in R^2} (\| (As(\gamma) - w(\gamma - \phi))u(\gamma) \|^2) \quad (2)$$

The solution is

$$A(\phi) = \frac{\sum_{\gamma} w(\gamma - \phi)s(\gamma)}{\sum_{\gamma} s(\gamma)^2} \quad (3)$$

$$\phi = \arg \min_{\phi \in R} \sum_{\gamma} \left( w(\gamma - \phi)^2 - \frac{(\sum_{\gamma} w(\gamma - \phi)s(\gamma))^2}{\sum_{\gamma} s(\gamma)^2} \right) \quad (4)$$

This is essentially a correlation method. It is sensitive to nonuniformities in the scene. We have assumed that intensity and beam patterns are expressed on a linear scale. The correlation algorithm will perform better for additive noise.

## IMAGE INTENSITY IN BEAM OVERLAPS

A commonly used model for the image intensity  $s_i$  of a radar target located at the slant range  $r$  in the field of view of beam  $i$  is

$$s_i = g_i(r) + \sigma - 4r + e_i \quad (5)$$

where  $g_i(r)$  is the sensor gain,  $\sigma$  is the target back scattering,  $e_i$  is a speckle noise term. It is multiplicative on the linear scale. All values are assumed to be normalized to some suitably chosen reference and expressed in  $dB$  units, i.e. on a logarithmic scale. If the same target is also in the field of view of beam  $i+1$ , a similar expression can be written, and the difference  $s_i - s_{i+1}$  will only depend on  $g_i(r) - g_{i+1}(r)$ . The same can be said after averaging the image intensities in the along track direction, over several bursts or, in other words, over several kilometers. Within such limits of averaging, the lines of constant slant range are approximately also the lines of constant elevation angles, constant ground range and constant sensor gain. Thus, for the values averaged along the ground lines of constant sensor gain, one can write

$$\bar{s}_i - \bar{s}_{i+1} = g_i(r) - g_{i+1}(r) + \epsilon_i \quad (6)$$

where  $\epsilon_i$  is a combined noise term.

The difference between the sensor gains in (6) will be modelled as

$$g_i(r) - g_{i+1}(r) = w_i(\gamma + \phi) - w_{i+1}(\gamma + \phi) + h_i \quad (7)$$

where  $\gamma$  is the elevation angle corresponding to slant range  $r$ ,  $\phi$  is the unknown roll angle,  $w_i(\gamma)$  is the known beam pattern of beam  $i$ , and  $h_i$  is an unknown constant. The motivation for introducing a constant gain offset between two beams is practical. There are several sources that can contribute to

this gain offset. First,  $h_i$  may include a term caused by relative miscalibration of the beam  $i$  and beam  $i+1$  antenna gains. Another discrepancy between beam gains may be due to a possible difference in the replica energies in the two beams. The ScanSAR processor should internally compensate for any such difference in the transmitted energy of different beams. However, if the replica energies are not known precisely, or have to be estimated from the downlink sampled data, as is the case with RADARSAT, a slight error may occur. ADC (analog to digital converter) saturation can also cause a gain offset. Finally, a processor error in azimuth antenna pattern compensation, due to inaccurate Doppler centroid estimation, will result in an approximately constant gain offset between beams. This property will be explained in some more details.

To illustrate the influence of Doppler centroid errors, we will assume that a target is located at a distance  $x_i$  along track from the azimuth antenna beam center in beam  $i$ . Then, the same target is located at a different distance  $x_{i+1}$  from the azimuth antenna beam center in beam  $i+1$ . The difference  $\Delta x_i = x_i - x_{i+1}$  is a function of the satellite velocity relative to the target and the timing of the two beams. It is referred to as the along track beam offset. For RADARSAT it is a few hundred meters. For simplicity, the azimuth antenna pattern will be modelled as an even polynomial function  $a(x) = a_0 + a_2x^2 + a_4x^4 + \dots$  with dominant low order terms. If the applied correction is dislocated along track by  $d$ , caused by a small Doppler centroid estimation error, then the image intensity distortion along track will be  $a(x) - a(x-d)$ . This is known as the along track intensity modulation or scalloping effect. For the same target, the difference between the intensity distortions in the two adjacent beams would amount to

$$(a(x_i) - a(x_i - d)) - (a(x_{i+1}) - a(x_{i+1} - d)) \approx 2a_2d\Delta x_i \quad (8)$$

where the higher order terms in  $d$  have been neglected. In other words, by subtracting the beam intensities, the scalloping variations are largely cancelled and the residual beam-to-beam difference is directly proportional to the Doppler centroid error and the along track offset of the two beams.

Some RADARSAT beams suffer from strong nadir returns in the overlap region. This effect violates the above model. It is beneficial to apply median filtering to the estimated intensities to mitigate the



influence of the strong nadir reflections.

### MATRIX NOTATION FOR BEAM OVERLAPS

Assuming that  $b$  beams are sorted in the increasing order of elevation angles, expressions of the type (6) and (7) can be written for all  $n = \sum_{i=1}^{b-1} n_i$  averaged ground pixels that fall in any of the beam overlap regions,  $n_i$  being the number of ground range pixels between beams  $i$  and  $i + 1$ . To do this, some basic matrix notation will be introduced, starting with the definition of the following vectors for the far overlap of the beam  $i$  (overlap with beam  $i + 1$ ):

$$\begin{aligned} \mathbf{S}_i^{far} &\in \mathbb{R}^{n_i} && \text{intensities } \bar{s}_i \\ \mathbf{W}_i^{far}(\phi) &\in \mathbb{R}^{n_i} && \text{antenna gains } w_i(\gamma + \phi) \\ \mathbf{E}_i &\in \mathbb{R}^{n_i} && \text{noise terms } \epsilon_i \end{aligned}$$

Similar definitions are introduced for the near overlap (overlap with beam  $i - 1$ ):

$$\begin{aligned} \mathbf{S}_i^{near} &\in \mathbb{R}^{n_{i-1}} && \text{intensities } \bar{s}_i \\ \mathbf{W}_i^{near}(\phi) &\in \mathbb{R}^{n_{i-1}} && \text{antenna gains } w_i(\gamma + \phi) \end{aligned}$$

Additionally, the following vectors are introduced:

$$\begin{aligned} \mathbf{H} &\in \mathbb{R}^{b-1} && \text{beam to beam gain offsets } h_i \\ \mathbf{1}_m &\in \{1\}^m && \text{each element is 1} \\ \mathbf{0}_m &\in \{0\}^m && \text{each element is 0} \\ \bar{\mathbf{X}} &= \frac{1}{m} \mathbf{1}_m \mathbf{1}_m^T \mathbf{X} && \text{each element is mean of } \mathbf{X} \end{aligned}$$

Derived from the above are:

$$\begin{aligned} \mathbf{D}_i^{far}(\phi) &= \frac{\partial}{\partial \phi} \mathbf{W}_i^{far}(\phi) \\ \mathbf{D}_i^{near}(\phi) &= \frac{\partial}{\partial \phi} \mathbf{W}_i^{near}(\phi) \\ \mathbf{S}_i &= \mathbf{S}_i^{far} - \mathbf{S}_{i+1}^{near} \\ \mathbf{W}_i(\phi) &= \mathbf{W}_i^{far}(\phi) - \mathbf{W}_{i+1}^{near}(\phi) \\ \mathbf{D}_i(\phi) &= \mathbf{D}_i^{far}(\phi) - \mathbf{D}_{i+1}^{near}(\phi) \\ \mathbf{S} &= \begin{bmatrix} \mathbf{S}_1 \\ \vdots \\ \mathbf{S}_{b-1} \end{bmatrix} \\ \mathbf{W}(\phi) &= \begin{bmatrix} \mathbf{W}_1(\phi) \\ \vdots \\ \mathbf{W}_{b-1}(\phi) \end{bmatrix} \end{aligned}$$

$$\begin{aligned} \mathbf{D}(\phi) &= \begin{bmatrix} \mathbf{D}_1(\phi) \\ \vdots \\ \mathbf{D}_{b-1}(\phi) \end{bmatrix} \\ \mathbf{E} &= \begin{bmatrix} \mathbf{E}_1 \\ \vdots \\ \mathbf{E}_{b-1} \end{bmatrix} \\ \mathbf{M} &= \begin{bmatrix} \mathbf{1}_{n_1} & \cdots & \mathbf{0}_{n_1} \\ \vdots & \ddots & \vdots \\ \mathbf{0}_{n_{b-1}} & \cdots & \mathbf{1}_{n_{b-1}} \end{bmatrix} \end{aligned}$$

Combining all overlaps together, one can write in a condensed form

$$\mathbf{S} = \mathbf{W}(\phi) + \mathbf{M}\mathbf{H} + \mathbf{E} \quad (9)$$

In this system of  $n$  equations the unknown parameters are: the roll angle  $\phi$  and the  $b - 1$  elements of  $\mathbf{H}$ . The model (9) is linear in  $h_i$ , but nonlinear in  $\phi$ . Starting from an initial estimate, e.g.  $\hat{\phi}^{(0)} = 0$ , we shall linearize the model in the neighbourhood of  $\phi$ , and develop an iterative algorithm for refined estimates  $\hat{\phi}^{(k)}$ ,  $k \in \{1, 2, \dots\}$ , as well as  $\hat{\mathbf{H}}^{(k)}$ . The linearized model is

$$\mathbf{S} - \mathbf{W}(\hat{\phi}^{(k)}) = \begin{bmatrix} \mathbf{D}(\hat{\phi}^{(k)}) & \mathbf{M} \end{bmatrix} \begin{bmatrix} \Delta\phi \\ \mathbf{H} \end{bmatrix} + \mathbf{E} \quad (10)$$

The desired estimates are the LMS solution to this overdetermined system of equations. The solution is an iterative procedure which takes into account all beam overlaps simultaneously.

### ALGORITHM A

If zero gain offset is assumed, only roll has to be estimated and the following iterative solution applies:

$$\hat{\Delta\phi}^{(k+1)} = \frac{\sum_{i=1}^b \mathbf{D}_i(\hat{\phi}^{(k)})^T (\mathbf{S}_i - \mathbf{W}_i(\hat{\phi}^{(k)}))}{\sum_{i=1}^b \mathbf{D}_i(\hat{\phi}^{(k)})^T \mathbf{D}_i(\hat{\phi}^{(k)})} \quad (11)$$

### ALGORITHM B

If both roll and offsets are estimated, the solution is as follows:

$$\hat{\Delta\phi}^{(k+1)} = \frac{\sum_{i=1}^b \Delta\mathbf{D}_i(\hat{\phi}^{(k)})^T (\Delta\mathbf{S}_i - \Delta\mathbf{W}_i(\hat{\phi}^{(k)}))}{\sum_{i=1}^b \Delta\mathbf{D}_i(\hat{\phi}^{(k)})^T \Delta\mathbf{D}_i(\hat{\phi}^{(k)})} \quad (12)$$

where the mean is subtracted from all the relevant vectors

$$\Delta \mathbf{D}_i(\hat{\phi}^{(k)}) = \mathbf{D}_i(\hat{\phi}^{(k)}) - \bar{\mathbf{D}}_i(\hat{\phi}^{(k)}) \quad (13)$$

$$\Delta \mathbf{W}_i(\hat{\phi}^{(k)}) = \mathbf{W}_i(\hat{\phi}^{(k)}) - \bar{\mathbf{W}}_i(\hat{\phi}^{(k)}) \quad (14)$$

$$\Delta \mathbf{S}_i(\hat{\phi}^{(k)}) = \mathbf{S}_i(\hat{\phi}^{(k)}) - \bar{\mathbf{S}}_i(\hat{\phi}^{(k)}) \quad (15)$$

and the gain offset estimates are

$$\hat{h}_i^{(k+1)} \mathbf{1}_n = \mathbf{S}_i - \bar{\mathbf{D}}_i(\hat{\phi}^{(k)}) \hat{\Delta} \phi^{(k+1)} \quad (16)$$

The above expressions show that this algorithm can not be applied in all cases. If the beam pattern differences in the overlap happen to be linear functions of the elevation angle, then the derivatives  $\mathbf{D}(\phi)$  are flat and equal to the mean  $\bar{\mathbf{D}}(\phi)$ . The roll adjustment becomes undetermined and so do the gain adjustments. This is the case with ScanSAR A types, SCWA and SCNA. The B modes, SCWB and SCNB can use the algorithm B. This is owing to the fact that the W2/S5 pattern difference is a nonmonotonous function of the elevation angle in the overlap region.

## COMPARISON OF FITTING RESULTS

The following table summarizes some results obtained for three data sets over the Amazon rain forest.

Orbit Orientation Type	8930 dsc. SCNB	8880 asc. SCWB	9173 dsc. SCWB
W1 fit		0.0421	0.1179
W2 fit	0.1600	0.0084	0.0926
S5 fit	0.1347	0.0337	0.0926
S6 fit	0.0926	0.0168	0.0758
mean	0.1291	0.0025	0.0947
Algorithm B	0.1319	0.0033	0.0967
tracking rms	0.0082	0.0168	0.0087

The top part of the table specifies the data sets used. All processing was done with IOSAT's SentrySAR processor with compensation for possible ADC saturation [4]. However, no steps were taken to exclude areas with rivers. Instead, the entire files were used and averaging was applied. The middle section of the table shows the results of the independent beam fitting via the correlation method as a part of

the processor calibration procedure. Results for different beams within the same dataset differ slightly. The difference may come from a relative roll between beams which could not be determined during the beam calibration since only single beam modes were used. An other source of error may be the roll variability within the scene under consideration. The mean value of roll over all beams is also shown. Two data sets are rolled roughly by 0.1 degree and one is not. The last section of the table shows the results of the tracking algorithm B applied to the beam overlaps during processing. Along track averaged value is shown, along with the tracking root mean square variability. The results of the two completely different approaches are in good accordance.

The above results also indicate that the S5 fit results in larger roll estimates than the S6 fit and W1 fit yields larger roll than S5. Nothing conclusive can be said for some other beam pairs, especially regarding W2. It is interesting to note that the W2 fit was overall the worst one (measured by the fitting r.m.s. error).

## SUMMARY OF ROLL ESTIMATION

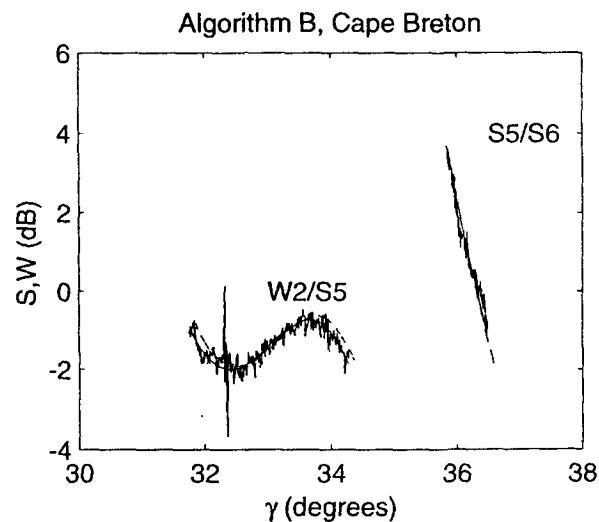
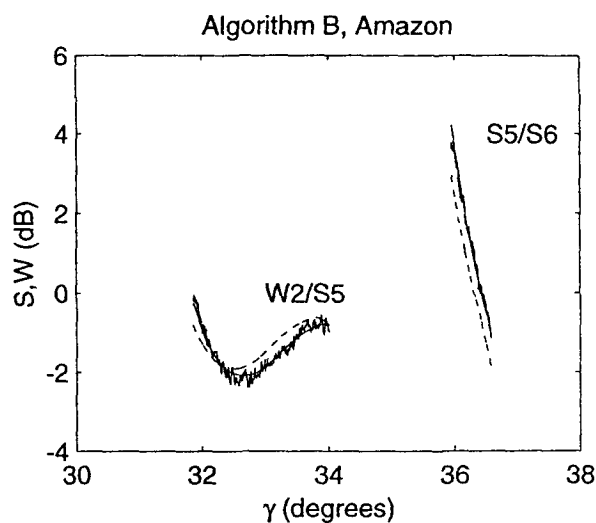
- Roll estimation is very sensitive to many factors: the beam patterns and their calibration, ADC saturation and proper normalization by replica power.
- Roll estimation is very sensitive to the internal geometric calculations performed in the processor, for example mapping from slant range to elevation angle, mapping from slant range to ground range, pixel registration and overlaying of the overlapping areas.
- Roll estimation is sensitive to along-track intensity modulation (scaloping).
- The correlation method (used in processor calibration) is very sensitive to scene content, but the operational roll tracking algorithms are not.
- The described algorithms are not sensitive to nadir interference, which is filtered out by median or other forms of rank statistics filtering.
- The tracking algorithms are designed to work on all overlap data at once to estimate a common roll. If there is any systematic relative roll

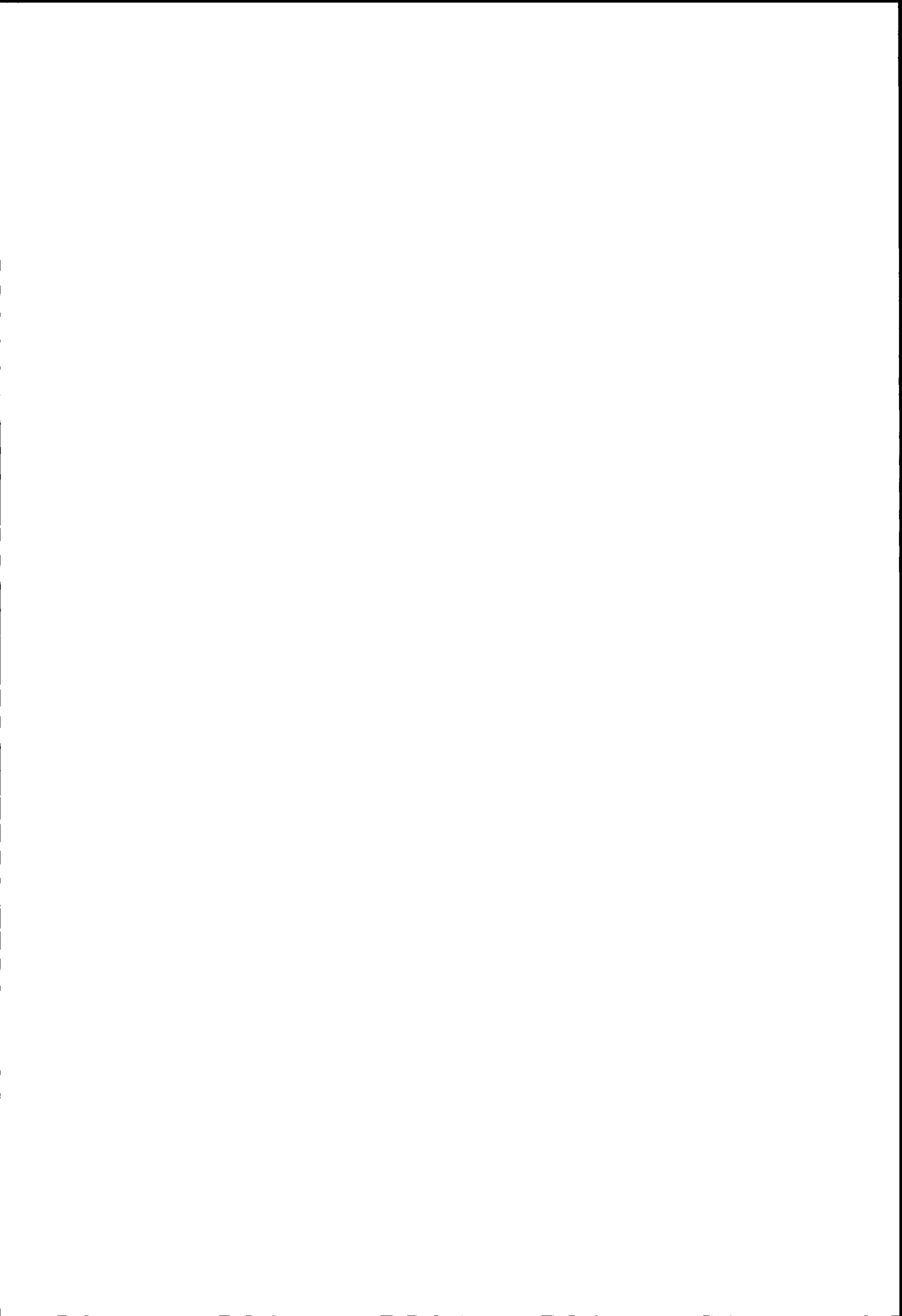
offset between the beams, it has to be determined (via correlation methods) and compensated for.

- Algorithm A is more suitable for SCNA and SCWA, since overlap pattern differences have almost constant slope. Therefore, this method is even more sensitive to all sources of gain mismatch between the beams.
- Algorithm B is more suitable for SCNB and SCWB, since W2/S5 overlap "locks" to both roll and gain offset (see the figure).
- The roll estimates can be block-to-block averaged or smoothed. To do this in an optimal way, one would have to gain more insight into the actual roll variability and rate of change.
- Besides roll tracking for the purpose of image formation, algorithms A and B can also be used to verify relative beam calibration.

## References

- [1] R. K. Raney, A. P. Luscombe, E. J. Langham and S. Ahmed, "RADARSAT", *Proc. IEEE*, vol. 79, pp. 839-849, June 1991.
- [2] A. P. Luscombe, "Taking a Broader View: RADARSAT Adds ScanSAR to its Operation", *Proc. IGARSS'88*, Edinburgh, Scotland, pp. 1027-1032, Sept. 1988.
- [3] M. Y. Jin, "Optimal Range and Doppler Centroid Estimation for a ScanSAR System", *IEEE Trans. on GE*, vol. 34, pp. 479-488, March 1996.
- [4] P.W. Vachon, A.L. Gray, C.E. Livingstone, "Adaptive compensation of RADARSAT SAR analogue-to-digital converter power loss", *Geomatics in the ERA of RADARSAT, GER'97 CD-ROM Proceedings*, Ottawa, Ont., Canada, 27-30 May 1997.





## MODELLING OF ELECTROMAGNETIC WAVES INTERACTION WITH FOREST CANOPIES.

C. Ruiz<sup>(1,2)</sup>, P. Borderies<sup>1</sup>, I. Chênerie<sup>2</sup>, E. Mougin<sup>3</sup>, C. Proisy<sup>3</sup>

<sup>1</sup> ONERA/CERT/DEMR, 2 Av. E. Belin, BP 4025, 31055 Toulouse Cedex, France  
Ph : 33 05 62 25 27 18 e-mail : [ruiz@oncert.fr](mailto:ruiz@oncert.fr), [borderies@oncert.fr](mailto:borderies@oncert.fr)

<sup>2</sup> AD2M Université Paul Sabatier, 118 Route de Narbonne, 31062 Toulouse Cedex, France  
Ph : 33 05 62 25 27 14 e-mail : [chenerie@cict.fr](mailto:chenerie@cict.fr)

<sup>3</sup> Centre D'Etudes Spatiales De La Biosphère, 18 Avenue E. Belin, BPI 2801, 31401 Toulouse Cedex 4, France  
e-mail: [proisy@cesbio.cnes.fr](mailto:proisy@cesbio.cnes.fr), [mougin@cesbio.cnes.fr](mailto:mougin@cesbio.cnes.fr)

### ABSTRACT

Forests constitute complex, multi-scale media whose characteristics may be very different according to the sensor configuration: frequency, polarisation, and incidence. In order to improve the extraction of parameters, which take profit from the potentiality of SAR data, it is important to understand and interpret the mechanisms of interaction between electromagnetic waves and forested areas. For this purpose we need accurate modelling of SAR backscattering, the aim being at last to help in defining and optimising future SAR systems. In this paper we concentrate on some topics related to interferometry over forested areas. We present a polarimetric scattering model that can be used for both purposes. Using this coherent multi-scattering model, based on a Monte Carlo technique, we are able to investigate the influence of the physical properties of the scatterers on polarimetric and interferometric observables. We will limit here to simulation results for volume scattering only, which can be simulated by generating a canopy of randomly oriented anisotropic particles. A parametric study of penetration depth will be shown. Interferometric coherence on the repeat-pass mode is investigated based on the volume decorrelation induced by the canopy height. The influence of temporal changes with a random variation in scatterer orientation between two data acquisitions is also studied.

### 1/ INTRODUCTION

Microwave remote sensing from spaceborne and airborne platforms has received considerable interest in the past two decades. Many systems have been set up to perform various experiments, such as sensing of the land and sea surfaces. Data collected from such experiments have been extensively used in the frame of the monitoring of the earth resources. Particularly forested areas are important from a remote sensing point of view as they cover large parts of the earth, and are important for environment and economy. Spaceborne microwave remote sensing has been

widely used for attempting to retrieve global forest cover and biomass [1][2].

Most of observations of forest properties have been based on the radar backscattered intensity, using the ERS-1 satellite C-band SAR. The information content from spaceborne SAR was shown recently to be increased by including repeat-pass interferometric SAR (INSAR) observations. As a matter of fact coherency shows a significant advantage over intensity for classification between forest and non-forest areas. Coherency measurements over forested areas is related, first to volume decorrelation due to the geometry, and further, with the repeat-pass mode, to temporal decorrelation resulting from displacements or changes in the properties of the scatterers involved. Consequently the volume of interaction between the incident electromagnetic wave and the canopy has to be studied through the penetration depth.

Measurement campaigns are expensive and time-consuming. Thus theoretical models are useful for interpreting the measured data, and for understanding the mechanisms of interaction between electromagnetic waves and natural media. Parametric studies can then be conducted and significant features obtained. This paper is about modelling of phenomena related to interferometry over forested areas. The models can be extended to a full representation of the forest, but here it is limited to the upper layer mainly composed of leaves and small branches, which is realistic at a relatively high frequency band.

In section II we present an incoherent multiple scattering model for deriving the backscattering coefficient and attenuation constant from a vegetative layered medium. This model will provide penetration sensibility to multiple scattering effect and to frequency band. The effect of the mean orientation of the scatterers on the penetration capabilities will also be studied. In section III we adapt this incoherent model to a coherent one for the interferometric simulation and present results on the influence of the

volume height and temporal variation of the coherency between the two images pair [8][9][10].

## II/ INCOHERENT MODEL

Various scattering theories have been developed to model microwave backscattering and propagation of vegetative media. Most of these scattering models solve the problem using radiative transfer theory. Recently a model based on the Monte Carlo technique has been developed by Chuah and Tan [3] to study microwave backscatter from random scattering centers in the vegetative medium. We focused our simulation on this method because it looked much more appropriate to be adapted to coherence evaluation, as will be described in section III.

The incident beam is considered to be a flux of photons that is progressively scattered by the particles in the medium. The approach characterises each scattering by the probability function for the photon to be scattered or absorbed, as well for its being scattered into a certain direction. This process is tracked until the photon is finally absorbed or scattered toward the receiver. Variance reduction techniques are introduced to reduce the computation time required for acceptable ensemble averages of the backscattering cross section. Ellipsoidal dielectric scatterers are used to model circular disk-shaped and needle-shaped leaves [7] which are randomly distributed in a layer (see Fig 1).

The advantage of this statistical approach is that multiple scattering can be treated in a straightforward way, since only a single scattering probability function is required.

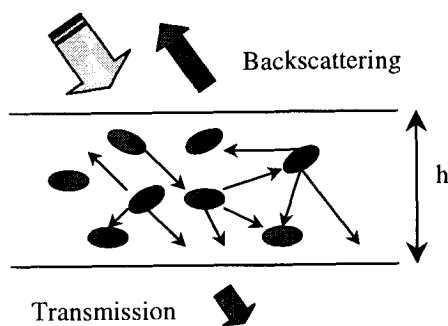


Fig 1: Canopy model for backscattering and transmission calculations

### Formulation

At each scattering event, we account for the probability for:

- 1- the photon to be scattered or absorbed,

- 2- the scatterer to be described by a certain orientation with given Eulerian angles  $(\alpha, \beta, \gamma)$ ,
- 3- the photon incident from direction  $r'$  to be scattered into a new direction  $r$ .

The intensity  $I$  after one interaction is then obtained from the incident intensity  $I'$  by

$$I = PWI' \quad (1)$$

where  $I$  and  $I'$  are the modified Stoke's vector,  $P$  the phase matrix of the scatterer encountered, and  $W$  the weight matrix as biasing function of variance reduction technique.  $W$  takes into account the extinction coefficient of the medium since the distance travelled by the photon is deduced from the mean free path length. This last parameter depends on the concentration of the scatterers and on extinction coefficient calculated by averaging over orientation distribution. Detailed description of this method is given in [3]. For multiple scattering, the process described by equation (1) is repeated to give

$$I_n(r) = [P(r_{n-1}, r_n)W_n][P(r_{n-2}, r_{n-1})W_{n-1}] \dots [P(r_1, r_0)W_0]I_0 \quad (2)$$

where  $I_n$  is the Stoke's vector of a particular photon that has reached the receiver in the  $r$  direction after undergoing  $n$  collisions. Finally the Stoke's vector of the scattered wave is given by

$$I(r) = \frac{1}{k} \sum_k \sum_n I_{k,n}(r) \quad (3)$$

where  $k$  is the number of photons trajectories.

### Application to a vegetative medium

The vegetation medium is modelled as a layer of discrete scatterers embedded in a background of air (see Fig 1). Since leaves constitute the major part of a vegetation canopy the scatterers used in this article have been limited to disks and thin needles. Phase matrices functions are calculated using the generalised Rayleigh-Gans approximation for disc- or needle-shaped leaves, assuming that one of the dimension of the scatterer is very small compared to the incident wavelength. The relative permittivities  $\epsilon_r$  of the scatterers is estimated with the dual-dispersion model given by Ulaby and El-Rayes [6]. Preferential orientation of the leaves can be stressed by simulating different possible distribution functions of Eulerian angles.

### Backscattering

Relation (3) is used to calculate radar backscattering cross sections from a canopy layer. It is defined as [3]

$$\sigma_{pq}(\theta) = \frac{4\pi \cos(\theta) I_{sq}(\theta)}{I_{ip}(\theta)} \quad (4)$$

where  $p, q$  are either vertical (V) or horizontal (H) polarisation state.  $\theta$  is the angle of observation,  $I_{ip}$  is the incident intensity with  $p$ -polarisation and  $I_{sq}$  the backscattered intensity with  $q$ -polarisation.

### Attenuation

The effective attenuation coefficient with  $p$  polarisation,  $\kappa_p$ , in  $r$  direction, can be calculated as follow [5][4]:

$$\kappa_p(r) = \frac{\ln\left(\frac{I_{ip}(r)}{I_{ip}(0)}\right)}{h} \cdot \cos(\theta) \quad (5)$$

where  $I_{ip}$  and  $I_{ip}$  are the incident intensity and the transmitted intensity with  $p$  polarisation respectively,  $h$  is the height of the layer and  $\theta$  the incidence angle. Penetration depth corresponds to an attenuation of about  $1/e$ .

## SIMULATIONS

### Backscattering

For backscattering, considering only single scattering of photons we obtain excellent agreement with results based on the first-order solutions of the radiative transfer, like Chuah [3]. This confirms the agreement of the Monte Carlo method compared with the radiative transfer theory.

### Attenuation

It is well known that the transmissivity of a vegetation layer as a function of incidence angle, depends on shape, orientation and size of the layer's scattering elements relative to wavelength [11]. If scatterers are randomly oriented the transmissivity shows a decreasing trend in  $1/\cos \theta$ . In general, even though the individual vegetation element may have polarisation-dependent transmission and scattering properties, the transmissivity, i.e. penetration depth, of a layer may exhibit a weak dependence on polarisation when the elements are randomly distributed in both orientation and space within the layer. In contrast, for a layer consisting of elements with a specific orientation, such as a layer of vertical stalks or of predominantly vertical wheat heads, penetration depth may exhibit a strong angular dependence and a pronounced polarisation dependence. Penetration depth has been

computed with the Monte Carlo model on a layer of disk (see Fig 2a) and needle-shaped (see Fig 2b) leaves at 5.3 GHz. Note the sensibility of the polarisation with increasing incidence angle.

We can also have a regard on the dependence of a layer transmissivity on frequency and on moisture content of the leaves. Figure 3 shows the penetration results obtained for different frequencies and moisture contents. Note the decay of penetration depth with increasing frequency and moisture.

### Effect of multiple scattering on attenuation coefficient

As frequency increases the effect of multiple scattering becomes important. It is then necessary to use a multiple scattering model for better estimate the canopy attenuation. For this purpose the effective attenuation coefficient  $\kappa_v$  and  $\kappa_h$  have been calculated at 8 GHz versus incidence angle (see Fig 4).

The attenuation coefficients calculated from the Monte Carlo multi-order model (4<sup>th</sup> order) are smaller compared to the values estimated for the zero-order approximation (Fig 5). This is due to the fact that multiple scattering is no more neglectable and contributes significantly to the transmitted power. Figure 5 shows an increase of 30 % of the penetration depth for incidence angles close to nadir.

## III/ COHERENT MODEL

This coherent model is derived with the incoherent model presented above and associates a precise description of the geometry. Each pixel is a realisation of the process. For computing its contribution, the previous approach is kept but the complex echo of each series of interactions is computed and saved, and at last summed up coherently.

Then at each scattering event, instead of working with the 4x4 Phase matrix which represent only magnitude of the scattering with no phase preserving, we use the complex scattering coefficients of the 2x2 scattering matrix [S]. For a given statistical description of the vegetative medium (density of scatterers, spatial and orientation distribution, etc.) and for a given radar parameter system (frequency, incidence angle, polarisation) the free path length  $l_p$  calculation in the canopy is derived [3]. It is initialised from the top of the vegetation layer in downward incident direction and represents the distance between the upper limit and the scattering event occurring inside the medium. It depends on density  $N$  and on the averaged extinction coefficient  $\sigma_{ext}$  of the scatterer over the orientation distribution:

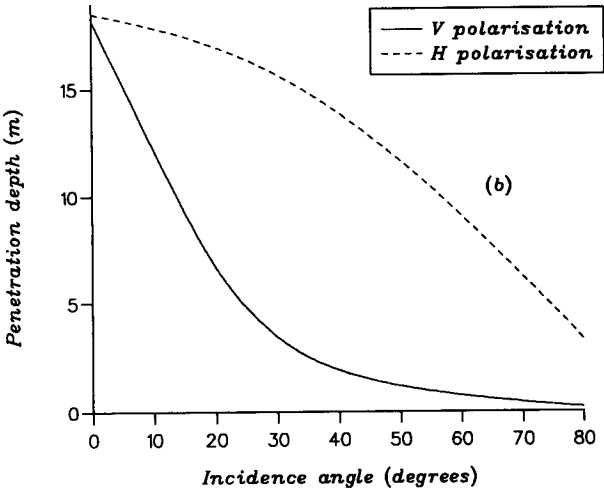
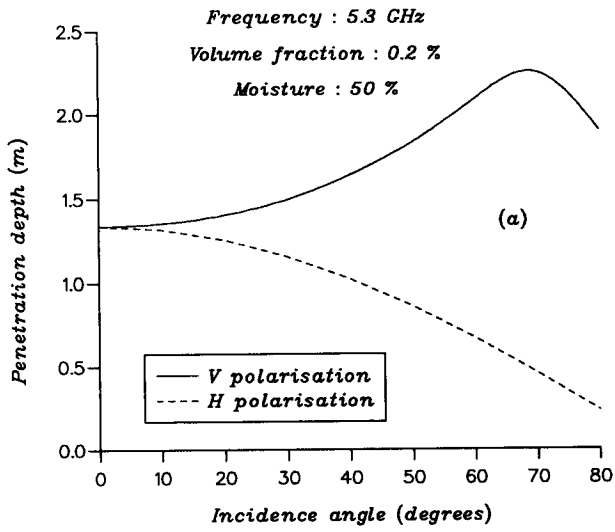


Fig 2 : Penetration depth versus incidence angle with (a) horizontal orientation distribution of disk-shaped leaves ( $a=b=2.5$  cm,  $c=0.1$  mm) and (b) vertical orientation distribution of needle-shaped leaves ( $a=b=1.2$  mm  $c=5$  cm)

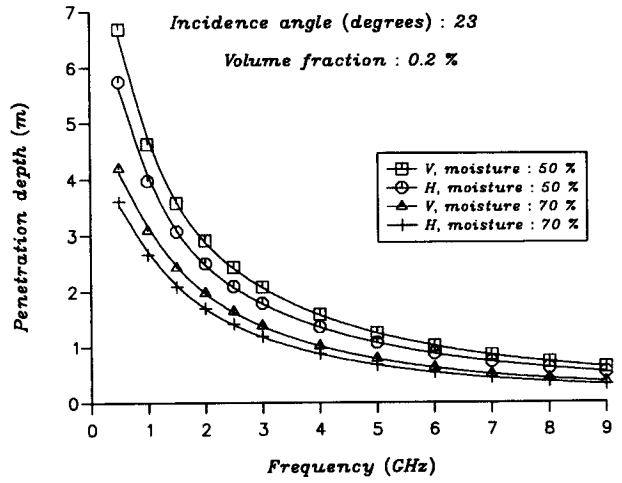


Fig 3 : Penetration depth versus frequency. Horizontal orientation distribution of disk-shaped leaves (disk dimensions,  $a=b=2.5$  cm,  $c=0.1$  mm)

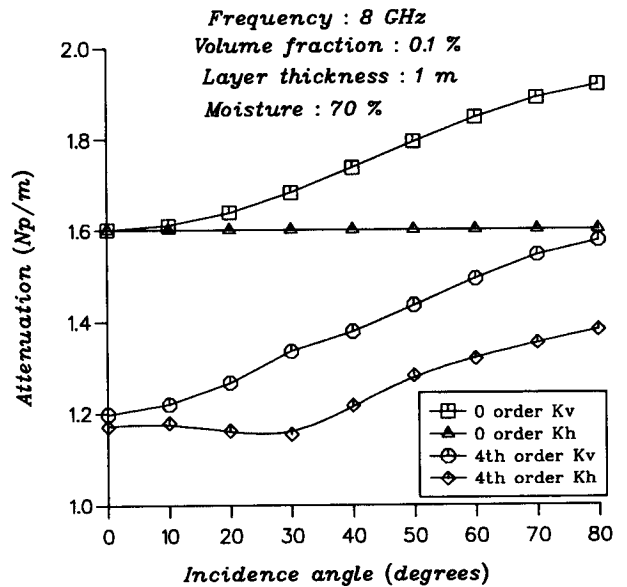


Fig 4 : Multiple scattering effect on the attenuation coefficient of a layer of circular disks with a uniform random distribution in orientation (disk dimensions,  $a=b=2.5$  cm,  $c=0.1$  mm)



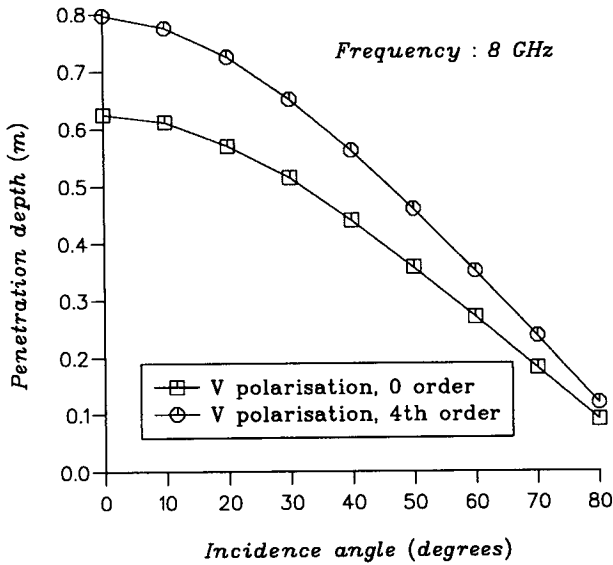


Fig 5 : Multiple scattering effect on the penetration depth at 8 GHz. Uniform random distribution in orientation of disk-shaped leaves (disk dimensions,  $a=b=2.5$  cm,  $c=0.1$  mm)

$$l_p = \frac{-\ln(rnd)}{N \cdot \sigma_{ext \text{ averaged}}} \quad (6)$$

where  $rnd$  is a random variable uniformly distributed on the  $[0,1]$  interval.  $\sigma_{ext}$  may differ by changing the incidence angle. The free path length  $l_p$  is then considered in the propagation phase term as it is added to the distance separating the radar and the top of the canopy (see Fig 6).

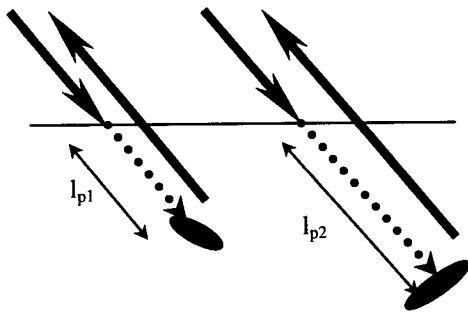


Fig 6 : Free path length modifying propagation phase term at each scattering event

**SIMULATIONS**

Let us consider the geometry associated with the interferometric technique on three resolution cells in the across-track direction (see Fig 7). For ERS-1/2 satellites each resolution element is about 20 meters in ground-

range direction and 5 meters in azimuth direction. The scattering of vegetative medium is related to the active volume interacting with the incident wave. This active volume, which is determined by the penetration depth, introduces volume decorrelation.

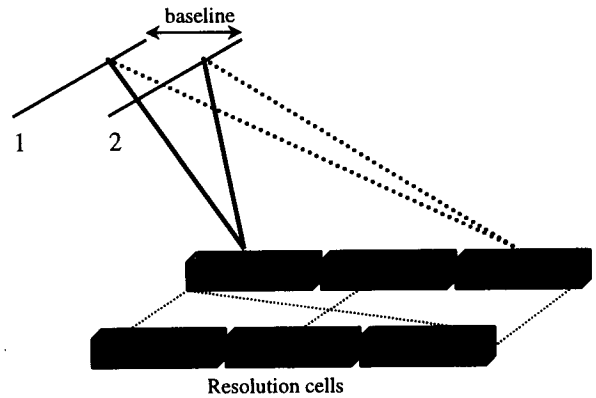


Fig 7 : Geometric configuration for INSAR simulation

If the two image acquisitions are separated in time, which is the case of ERS-1/2 (repeat pass interferometry), for short times scales, we may add the temporal decorrelation due to motion of the scatterers caused by the wind. In the next section simulations volume and temporal effects on coherency coefficient are investigated.

**Volume decorrelation**

We have first considered only volume decorrelation without temporal changes. The effect of volume scattering on a distributed scattering layer of thickness  $h$  has been computed when increasing baseline (see Fig 8). The coherence calculation have been done with a  $3 \times 15$  window as used typically with ERS-1 configuration (5.3 GHz,  $\theta=23^\circ$ , VV polarisation, 780 km altitude). Scatterers were uniformly oriented disk-shaped leaves with a moisture content of 50 % and volume fraction of 0.1 %.

**Temporal decorrelation**

Temporal decorrelation between two acquisitions on forested areas is more complex because decorrelation exists at various time scales. At short time scale motion due to the effect of wind is the most important, acting on time scales of few seconds. At longer time scale dielectrics changes can affect the scatterers due to seasonal variations. Only effects related to leaves motion will be shown in the following, as the wind mostly affects the top of the trees in dense forest. Here we have limited the motion to a simple rotation. Figure 9 shows decorrelation effect due to rotation as the number of rotating scatterers increases. The higher is

the magnitude of the rotation, the faster the decay of coherency.

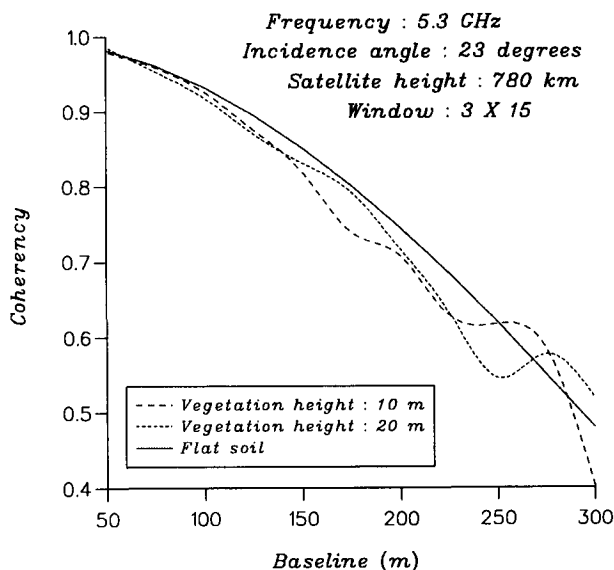


Fig 8 : Volume decorrelation effect on coherency when increasing baseline

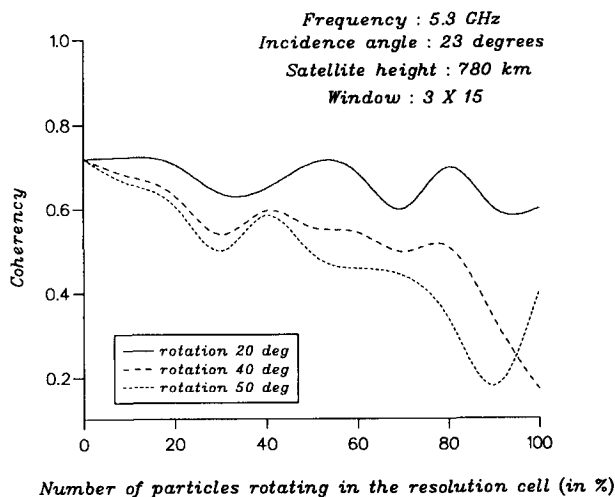


Fig 9 : Temporal decorrelation between two image acquisitions as increasing the number of rotating scatterers (200 m baseline)

## DISCUSSION/CONCLUSION

We have described a model for attenuation evaluation and interferometric observation of forests. With the help of this model it is possible to simulate extinction effects, polarisation dependent propagation and coherence. Temporal and volume decorrelation have been studied regarding the influence of the physical properties of the scatterers. Rotational movement was studied also. The

follow-up will concern a systematic parametric study with this model to investigate which parameter, of the system as well as of the observed scene, play a significant role on coherency over forested areas.

## REFERENCES

- [1] E. Mougin and C. Proisy, "Radar Remote Sensing of a Mixed Deciduous Temperate forest Results and Perspectives", *Proceedings of the 2<sup>nd</sup> International Workshop on Retrieval of Bio- & Geo-physical Parameters from SAR Data for Land Applications*, ESA SP-441, pp. 285-292, 1998.
- [2] G. Smith and P. B. G. Dammert, "Biomass Retrieval in Boreal Forest Using ERS and JERS SAR", *Proceedings of the 2<sup>nd</sup> International Workshop on Retrieval of Bio- & Geo-physical Parameters from SAR Data for Land Applications*, ESA SP-441, pp. 293-300, 1998.
- [3] H. T. Chuah and H. S. Tan, "A Monte Carlo method for radar backscatter from a half-space random medium", *IEEE Transactions on Geoscience and Remote Sensing*, vol. 27 (1), pp. 86-93, 1989.
- [4] H. T. Chuah and H. S. Tan, "A Multiconstituent and Multilayer Microwave Backscatter Model for a Vegetative Medium", *IEEE Transactions on Remote Sensing and Environment*, vol. 31, pp.137-153, 1990.
- [5] H. T. Chuah and W. L. Kung, "A Microwave Propagation model for Estimation of Effective Attenuation Coefficients in a Vegetation Canopy", *IEEE Transactions on Remote Sensing and Environment*, vol. 50, pp. 212-220, 1994.
- [6] F. T. Ulaby and M. A. El-Rayes, "Microwave Dielectric Spectrum of Vegetation - II: Dual-Dispersion Model", *IEEE Transactions on Geoscience and Remote Sensing*, vol. GE, pp. 550-557, 1987.
- [7] M. A. Karam and A. K. Fung, "Leaf-Shape Effects in Electromagnetic Wave Scattering From Vegetation", *IEEE Transactions on Geoscience and Remote Sensing*, vol. 27 (6), pp. 687-697, 1989.
- [8] J. I. H. Askne, and P. B. G. Dammert, "C-Band Repeat-Pass Interferometric SAR Observations of Forest", *IEEE Transactions on Geoscience and Remote Sensing*, vol. 35 (1), pp. 25-35, 1989.
- [9] U. Wegmuller and C. L. Werner, "SAR Interferometric Signatures of Forest", *IEEE Transactions on Geoscience and Remote Sensing*, vol. 33 (5), pp. 1153-1161, 1995.
- [10] P. B. G. Dammert, L. M. H. Ulander and J. Askne, "SAR Interferometry for Detecting Forest Stands and Tree Heights", *Proceedings of SPIE - The International Society for Optical Engineering*, vol. 2584, pp. 384-390, 1995.
- [11] F. T. Ulaby, R. K. Moore and A. K. Fung, "Microwave Remote Sensing, Active and Passive", Textbook, vol. III, pp-1868-1872 Artech House, 1986.

## The Technology Development of a Spaceborne On-Board SAR-Processor and Storage Demonstrator

Martin Suess<sup>(1)</sup>, Christoph Schaefer<sup>(2)</sup>, Rolf Zahn<sup>(3)</sup>

Dornier Satellite Systems

88039 Friedrichshafen, Germany

Tel.: ++49-7545-8 3728<sup>(1)</sup>, ++49-7545-8 5550<sup>(2)</sup>, ++49-7545-8 4959<sup>(3)</sup>

e-mail: [martin.suess@dss.dornier.dasa.de](mailto:martin.suess@dss.dornier.dasa.de),

[christoph.schaefer@dss.dornier.dasa.de](mailto:christoph.schaefer@dss.dornier.dasa.de),

[rudolf.zahn@dss.dornier.dasa.de](mailto:rudolf.zahn@dss.dornier.dasa.de)

### ABSTRACT

SAR instruments in general generate a huge amount of measured data. This is especially true for missions with a global coverage at low resolution, and for very high resolution SAR systems. An efficient SAR data compression processing on board the satellite is therefore mandatory for these mission profiles. This paper describes the newest German efforts in the development of on-board processing technology for SAR. A Project for the *Technology Development of a Spaceborne On-Board SAR Processor and Storage Demonstrator* called **TOPAS** was initiated by the German Space Agency, DLR, in June 1999 and is scheduled for two years. After the introduction the benefits of on-board processing are discussed. The important requirements and system parameters of the reference mission on which the **TOPAS** demonstrator is based are presented. The applied generic and scalable SAR processor architecture and the underlying processing strategy are shown. Finally the expected performance are discussed.

### INTRODUCTION

In the recent years airborne and space borne Synthetic Aperture Radars (SAR) have shown their relevance for a large number of applications. Scientists from various disciplines as well as ecologists show great interest in remote sensing data of the earth. Moreover, high resolution remote sensing data gain more and more commercial importance as raw material for the upcoming global information society. In many areas of the globe only radar instruments can guarantee continuous observation, since only radar is capable to penetrate clouds. Other advantages are the day and night

#### Acknowledgement:

*The Technology Development of a Spaceborne On-Board SAR Processor and Storage Demonstrator is initiated and financed by the German Space Agency, DLR*

capability, and at low frequency bands radar can even penetrate into the soil.

The image formation from the radar echo of the SAR instrument involves a highly sophisticated processing effort. In the early times of SAR imaging, processing was done by analogue optical focussing of the SAR raw data. In the early 1970's the digital processing started which forms the basis of today's highly flexible, accurate and error compensating SAR image formation. For all satellite SAR instruments up to now this image generation takes place off line in a ground based facility. The SAR raw data are stored on the satellite, transmitted to the ground station with only low or no compression and are then transferred to the processing facility. After processing these data have to be distributed to the customers and the interpreting organisations. This time consuming process cannot fulfil the customer's need for instant and easy information access.

The introduction of SAR image processing on board of the satellite can bring the earth observation system operationally closer to the user.

### ADVANTAGES OF ON-BOARD PROCESSING

The integration of the processing capability into the SAR instrument shows a number of advantages discussed in the following. This is especially true for missions with a global coverage at low resolution and for very high resolution SAR systems. In the scope of the **TOPAS** project the attention is focused on the high resolution case.

- In the project, a future spaceborne, high-resolution SAR instruments with a signal bandwidth of 150 MHz in X-band is taken as reference. This bandwidth corresponds to a ground range resolution between 3.0 and 1.5 meters depending on the incidence angle. The SAR generates a huge amount of data at a very high data rate (~2880 Mbps in the bursts). The processing can lead to a drastic reduction of the amount of raw data to be stored in

the satellite memory and to be transmitted to the ground.

- Up to now the Block Adaptive Quantiser (BAQ) algorithm is the state of the art method for SAR raw data compression on-board. Publications [ 1 ], [ 2 ] suggest that this easy-to-implement algorithm can compress SAR raw data by a factor of 2 (from 8 to 4 bits per real sample) without a significant loss of data quality. Our preliminary investigation indicates that by applying a more involved raw data compression algorithm a compression factor of 4 (effective 2 bit per real sample) and similar data quality can be achieved.
- The processing of SAR images allows to achieve much higher compression ratios than with the raw data compression. From the available image compression algorithms the wavelet based image compression shows the most promising results [ 3 ]. It is already being implemented into hardware for space application [ 4 ]. Additionally, multi-looking can be applied on image data if needed.
- In the case of the raw data compression as well as the wavelet based image compression the data compression ratio can be adapted to the customer's needs. This allows a trade-off between the costly system resources and the data quality requirements of the applications.
- A state of the art SAR instrument can operate in many different modes. The SAR signal bandwidth is adapted to provide a constant ground range resolution over the access region and to provide a homogeneous SAR data quality. A digital filter which can be integrated into the raw data compression always provides the adequate signal sampling.
- A smaller number of ground stations is required as more data can be stored in the limited on-board memory before a transmission to ground is required. This especially eases the problem of successive blind orbits without down-link opportunity.
- Easy, direct and fast access to the SAR image data by the customer becomes possible. They can be served directly from the satellite as highly compressed data can be transmitted with less energy and be received with small antennas without the need of sophisticated processing afterwards.
- As a long term goal, on-board feature and information extraction can be envisaged. The highest data compression can be achieved by transmitting the information wanted (e.g. position and velocity of ships on the ocean) rather than the whole image.

The major disadvantages of the introduction of on-board processing to a spaceborne SAR system are the additional mass, power dissipation, complexity and cost. These disadvantages are being more and more reduced

by the ongoing development and the resulting performance increase of the integrated components for such a SAR processor. We are convinced that the benefits and additional flexibility will win the trade-off with the listed disadvantages in the future. On-board SAR processing will then become an important and integrated part of the future SAR instrument.

### THE REFERENCE MISSION

The envisaged concept for the On-Board SAR Processor and Storage Demonstrator is generic and fully scalable. It can provide a solution for a large variety of different SAR systems and performance requirements by adapting the memory size and the number of processing elements. The processing software which runs on each processing element is identical and generic, so that only minor modifications will be needed when changing the performance requirements.

For the derivation of the requirements for the demonstrator project, a reference mission and a reference instrument are defined. This reference is called SmartSAR in the following. SmartSAR is a high resolution SAR system with a modern active phased array SAR instrument [ 5 ]. A number of reasonable assumptions of the different SAR system and instrument parameters are listed. They represent the target system for the technology development and will be used to measure the performance of the demonstrator. The results from the demonstrator performance test will be applied to develop a performance model of the on-board processor. With this model the performance of a scaled processor system and the processor performance for modified SAR system parameters can be predicted.

### REQUIREMENTS FROM THE REFERENCE MISSION

The requirements for the SmartSAR instrument are derived from the requirements on the image products. The key parameters are the geometric resolution, the radiometric resolution and the scene size.

	Range Resolution	Azimuth Resolution	Range Size	Azimuth Size
Product 1	2.6 m	2.6 m	>20km	>20km
Product 2	8 m	8 m	>40km	>40km
Product 3	3m..1.5m	1 m	>10km	>5 km

Tab. 1: SmartSAR Image Products

The noise equivalent sigma zero (NESZ) and the integrated ambiguity ratio shall be better than  $-21$  dB. The image product 1 shall be realised as a conventional strip map SAR, image product 2 shall be realised with a strip map SAR with 3 look in range and in azimuth, and the image product 3 shall be realised with a spotlight mode.

## ORBIT PARAMETERS

The system reaction or information access time depends on the number of satellites, the access area of the SAR instrument in cross track direction and on the orbit parameters. Assuming one satellite the preferred orbit parameters are as follows in Tab. 2.

Parameter	Unit	Value
Orbit height	h km	660
Orbit type		polar
Inclination angle	degree	98.0
Max. orbit duty cycle	%	10
Expected average orbit duty cycle	%	<5

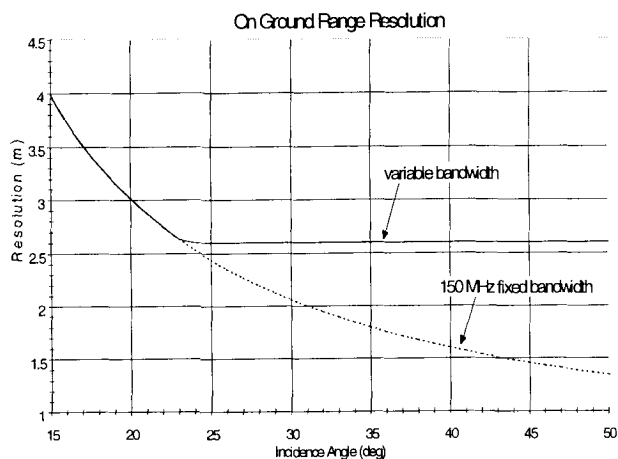
Tab. 2: Satellite Orbit Parameters for SmartSAR

The parameters of this platform play an important role for the complexity of the SAR image processing. The expected average duty cycle for operation of the SAR instrument is *less than 5%* of the orbit time. This is an important fact when determining the actual processing power which needs to be installed on-board the satellite.

## REQUIREMENTS OF THE INSTRUMENT

In order to fulfil the SAR system requirements, the corresponding requirements for the SAR instrument are established. They result in a number of parameters describing the SmartSAR instrument design. In Tab. 3 the mode-independent, key instrument parameters for the processing are listed.

In some of the instrument modes a constant ground range resolution is required. In reality the ground range resolution is a function of the incidence angle as shown in Fig. 1. The dashed curve gives the resolution for a fixed chirp bandwidth of 150 MHz. The solid line assumes that the chirp bandwidth is set such that the



required ground resolution of 2.6 m is achieved. The

Fig. 1: On Ground Range Resolution

reduction of the bandwidth for larger incidence angles has two effects. First the noise energy is reduced so that the sensitivity of the SAR is improved for higher slant ranges. Secondly the average receive data rate is reduced with a benefit for the requirements of the mass memory size and the down link capability, if the receive signal can be sampled according to its bandwidth. On very flexible way to realise this is to apply a down-sampling filter to the raw data.

Parameter	Unit	Value
Antenna height	m	1.4
Antenna width	m	4.8
Azimuth scan angle range	degree	+/- 0.4
T/R module duty cycle	%	10
Average RF output power	W	530
Frequency band		X-Band
Max. transmit bandwidth	B MHz	150
Max. incidence angle	degree	50
Min. incidence angle	degree	15
Max. PRF	PRF Hz	8000

Tab. 3: General SAR Instrument Parameters

## FUNCTIONS OF THE PROCESSING AND STORAGE SUBSYSTEM

In the following the functions of the on-board processing and storage subsystem (P&S) are listed.

1. Buffering of the SAR raw data stream in real-time
2. Off-line image processing and compression of the buffered SAR data
3. Mass memory data management and organisation
4. Reformatting and output of compressed data at down link rate

### Raw Data Buffering

The digital input data stream from the analogue to digital converter in the data and control subsystem to the processing and storage subsystem will have a peak data rate of 2.88 Gbps for the SmartSAR system with 150 MHz bandwidth. This is the maximum data rate which must be handled by the input of the subsystem. The input data come in bursts, which correspond to the receive echoes of the radar system. The maximum receive duty cycle of the instrument is required to be up to 70%. The continuous data stream after the range extension buffer, which is realised in the data sorter, is up to 2.016 Gbps in the worse case. This is the rate of data which is required to be written into the solid state mass memory continuously. The solid state mass memory is organised in memory modules. The necessary number of memory modules is determined by the maximum input data rate of

each memory module and by the required total mass memory capacity.

### Off-line SAR Data Compression

The average orbit duty cycle for the SAR instrument is specified to be less than 5%. This means that the instrument is switched off 90% of the time if another maximum 5% is reserved for the down-link of the data. The off-line SAR data compression or processing shall be completed during this time, when the instrument is switched off. It is required to realise three different types of data compression.

#### - Data volume reduction of the oversampled data

As described before, the SAR instrument is required to operate with a bandwidth adjusted to the range resolution. This compression operates lossless and reduces the data volume according to the actual useful data rate.

#### - Raw data compression with a BAQ type algorithm

The total dynamic range of SAR data is target dependent and very high. Compared to this, the instantaneous dynamic range is considerably less. This effect is used for lossy data reduction. If this technique is used on data in a transform domain, the properties of the instrument and the SAR processor can be used to achieve even better compression ratios. This technique can be combined with the data volume reduction of the oversampled data.

#### - SAR image processing and compression

The highest compression of SAR data can be achieved when they are processed to SAR images. Multi-looking and very efficient conventional image compression processes (e.g. Wavelet compression) can be applied.

### Mass Memory Data Management and Organisation

The allocation of the SAR data resulting from the different data takes and the header data for each data set has to be managed.

### Reformatting and Output of Compressed Data at Down Link Rate

The SAR raw data and the SAR header data have to be read out from the mass memory, encrypted, packetised and transferred to the data transmission subsystem.

## GENERIC P&S ARCHITECTURE

In this section, the concept of the generic P&S subsystem architecture realised in TOPAS is presented. This architecture may be scaled to meet variable processing requirements. In the following section, a particular instantiation of the generic architecture is generated which comply with the SmartSAR requirements. We shall therefore distinguish between the *generic architecture* and the *TOPAS architecture*.

Fig. 2 depicts a block diagram of a generic P&S architecture at a coarse level. It will be described briefly in this section. In the figure, the digitised, raw data enters the subsystem from the left. The data is assumed to consist of 16 bit complex samples, sampled at a rate which is 20% higher than the chirp bandwidth. Hence it is assumed that basebanding, demodulation, and digitisation have taken place externally to this subsystem. (Digital demodulation could also be performed within the subsystem. In this case, the input would consist of 8 bit real samples, with twice the sampling rate as before.) In the figure, the compressed output exits the subsystem at the right, through a number of  $t$  parallel channels ( $t \leq p$ ).

Architecture scaling parameters:

$p$  = number of input channels

$q$  = number of processing elements in the 1<sup>st</sup> MPS

$r$  = number of processing elements in the 2<sup>nd</sup> MPS

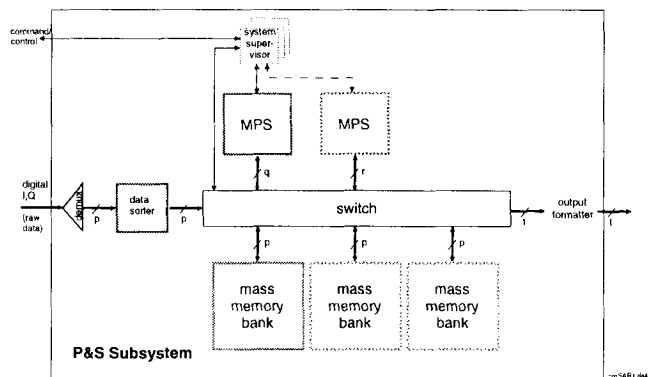


Fig. 2: Generic architecture for P&S subsystem

At the centre of the diagram is located a switch which connects either the input data lines or one of the agents, located above the switch, with one of the mass memory banks, located below the switch. The agents generally are multi-processor systems (MPS) whose function is the execution of compression algorithms. One MPS is baseline, shown as the left-most agent, additional MPS are optional. Additional MPS are employed when the processing power of the subsystem is to be upscaled. One bank of mass memory is baseline, others are optional. They may be implemented in the event that the memory capacity of the system is to be upscaled.

During Input Mode, the input data channel - consisting of  $p$  parallel subchannels - is connected to one of the memory banks Fig. 3, top left). Each memory bank has  $p$  input ports which are used simultaneously.

During Processing Mode, each agent is connected to either one or two memory banks. (Examples are furnished by Fig. 3, top right and bottom left). More specifically, an agent can be connected to one memory bank for data input and to another - or the same - for (simultaneous) data output. If multiple agents and multiple mass memories are present, the agents may process their respective data simultaneously.

During Output Mode, the output formatter is connected to one of the memory banks (Fig. 3, bottom right). The function of the output formatter is to read data (which has been compressed) from memory, to generate source packets of the required format, and to output these packets over  $t$  parallel lines. If  $p$  is a multiple of  $t$ ,  $p = kt$ , the  $t$  channels of the output formatter are reconnected to the  $p$  channels of a memory bank  $k$  times. This is done in such a way that each memory port is connected to one of the output lines once and only once.

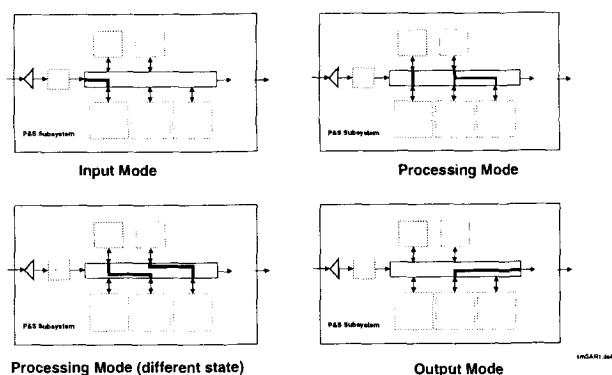


Fig. 3: Switch states corresponding to different operational modes of P&S architecture

Most of the modules in this architecture are easily scalable with respect to different values of  $p$ ,  $q$ ,  $r$ , ..., i.e. a new architecture with different values of these parameters can be built without redesign of these modules. A more detailed description of this architecture can be found in [6].

#### ARCHITECTURE SCALED FOR TOPAS

The architecture is scaled for TOPAS for 150 MHz chirp bandwidth as shown in Fig. 4. The following scaling factors have been used:

- Parallelisation factor  $p=12$
- number of agents =2
- number of memory banks =1
- number of processing elements in MPS  $q=4$
- number of processing elements in CWIC  $r=1$

The second agent is a Constant-rate Wavelet-based Image Compressor (CWIC). This application specific hardware unit is employed to compress processed SAR images at high data rates. The compression ratio is user specified. Due to the high throughput of this unit, only one module of CWIC ( $r=1$ ) is required.

In a more powerful version of the TOPAS architecture for a 150 MHz chirp bandwidth, the MPS can be scaled to include  $q=6$  or  $q=12$  processing elements, increasing the processing speed of the system accordingly.

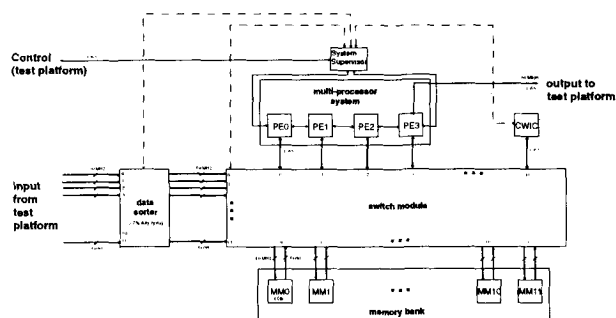


Fig. 4: Architecture Scaled as realised in TOPAS

Each memory module in the demonstrator will have a capacity of 4 Gbits (as opposed to the 32 Gbits of the operational architecture). This corresponds to about 24 seconds of raw data intake time which is sufficient for demonstration purposes.

#### EXPECTED PROCESSING PERFORMANCE

The processing system performance parameters are the processor dependent common image quality parameters, the compression ratio to be achieved and the processing speed. The expected performance of the different parameters is listed in the following.

##### Processor Quality

The quality of a SAR image processor is verified by analyzing the point target response.

- The deviation of the point target resolution from the theoretical value shall be  $< 3\%$

The integrated sidelobe ratio (ISLR), the peak sidelobe ratio (PSLR) and the spurious sidelobe ratio (SSLR) are other parameters commonly used for describing the point target performance.

	Azimuth	Range
Resolution	2.6 m (single look)	2.6 m (inc. angle $> 25^\circ$ )
ISLR	-14.2 dB	-15.8 dB
PSLR	-18.6 dB	-21.2 dB
SSLR	-32.9 dB	-33.9 dB

Tab. 4: Expected Point Target Performance

##### Compression Ratio

Two types of compression ratios have to be distinguished. First the compression ratio achieved on SAR raw data:

- Our preliminary investigation suggests that by applying a more involved raw data compression algorithm a compression factor of 4 can be achieved at similar data quality as with the common BAQ algorithm.

Second the compression ratio achieved by applying a wavelet compression on a processed SAR image:

- It is expected that a compression ratio  $>40$  can be reached for a wavelet compressed 4 look SAR image in stripmap mode.

### Processing Speed

The system requirements indicate that 90% of the orbit time are available for processing the SAR data.

- All image processing and compression functions are realized in less than 18 times the data acquisition time.

The demonstrator has 4 Processing Elements which work in parallel. It is expected that 6 or 12 Processing Elements are required to fulfil the SmartSAR processing speed requirement.

The determination of the number of Processing Elements required and the development of a model for the performance prediction of a scale architecture will be one very important outcome of the TOPAS project

### CONCLUSIONS

In recent years many of the technologically critical elements, which allow the realisation of such a powerful computer in space, have been elaborated in various technology programs of DLR, ESA and the European Union. The demonstrator will fully benefit from these technologies like the digital signal processor for space application (Mosaic020 DSP board with TSC21020 [ 7 ]), the very efficient FFT co-processor [ 8 ], the solid state mass memory [ 9 ] and the wavelet image compressor [ 4 ] developments. Therefore the demonstrator developments can concentrate on the remaining technologically critical elements and on the overall system.

With this solid foundation the near term goal of implementing efficient SAR data compression on board of the satellite can be reached in the framework of TOPAS project presented in this paper.

The far term goals of direct distribution of the image products and the automatic classification of SAR images on-board are beyond the scope of this project and require further development.

### REFERENCES

- [ 1 ] U. Benz, K. Strodl, A. Moreira, *A Comparison of several Algorithms for SAR Raw Data Compression*, IEEE Transactions on Geoscience and Remote Sensing, Vol. 33, No. 5, Sept. 1995, pp. 1266-1276
- [ 2 ] J. C. Curlander and R. N. McDonough, *Synthetic Aperture Radar Systems and Signal Processing*, New York: Wiley, 1991
- [ 3 ] W. Gasti, S. Martinez Aragonés, J. Rosello Guasch, *SAR Image Compression for Progressive Transmission*, CEOS 98, Feb. 3-6, 1998
- [ 4 ] C. Schaefer, E. Krahn, *Constant-Rate Wavelet-Based Image Compressor (CWIC)*, IEEE 1999 International Geoscience and Remote Sensing Symposium (IGARSS'99), Hamburg, Germany, July 1999
- [ 5 ] R. Zahn, H. Braumann, *Status of the X-Band SAR Instrument Demonstrator Development*, CEOS 99, Toulouse, August 1999, this volume
- [ 6 ] C. Schaefer, E. Krahn, *Processing and Storage Subsystem for High-Resolution SAR Instruments*, DASIA'99, Conference on 'Data Systems in Aerospace', Lisboa, Portugal, July 1999, pp. 625-630
- [ 7 ] A. Christen, K.-P. Förster, P. Armbruster, *An Architecture for Heterogeneous Multiprocessor Systems and its Implementation*, 6<sup>th</sup> international Workshop on Digital Signal Processing Techniques for Space Applications (DSP'98), ESTEC, Noordwijk, The Netherlands, Sept. 1998, p. 14
- [ 8 ] H. Zwartenkot, M. Boerrigter, L. Bierens, J. Smit, E. Deprettere, *A Single Chip Implementation for Fast Convolution of Long Sequences*, Proceedings RISC/IEEE-Benelux Workshop on Circuits, Systems and Signal Processing, Nov. 1996, pp. 1-4
- [ 9 ] F. Rombeck, E. Weih, *Ultra High Speed & Large Capacity Solid State Mass Memories*, Proceedings of the DASIA'99 Conference on 'Data Systems in Aerospace', Lisboa, Portugal, July 1999



## Simulator of Ocean Scenes Observed by Polarimetric SAR

Christian COCHIN<sup>(1)</sup>, Thierry LANDEAU<sup>(2)</sup>, Gérard DELHOMMEAU<sup>(3)</sup> and Bertrand ALESSANDRINI<sup>(3)</sup>

(1) DGA/Direction des Centres d'Expertise et d'essais, CELAR/Division Guerre Electronique Observation et Signatures, BP 7419, 35174 BRUZ CEDEX, France, Cochin@celar.fr

(2) IRESTE/Laboratoire Systèmes Electroniques et Informatiques - EP CNRS 2018, Rue C. Pauc, BP 60601, 44306 NANTES CEDEX 3, France, Thierry.Landeau@ireste.fr, www.ireste.fr/Sei

(3) ECN/Laboratoire de Mécanique des Fluides/URA 1217 CNRS, 1 rue Noë, 44300 NANTES, France, Gerard.Delhommeau@ec-nantes.fr

### ABSTRACT

This paper presents an operational and easy-to-use simulator, developed for the CELAR (French Defence Electronics Centre). Two Research Laboratories also participated in this project (IRESTE/Electronic Systems and Computer Engineering & ECN/Fluids Mechanisms), each contributing within its specialist field.

The aim of this simulator is to generate ocean scene images, illustrating what would be observed by an airborne or spaceborne SAR, within the 1-18 GHz frequency bandwidth and for spatial resolutions between 1 and 10 m.

It thus provides a fully controlled and realistic radar signal enabling the simulation of different sea states, ships and observation configurations.

### 1. INTRODUCTION

The principle of SAR imagery requires the received radar signal to be synthesised during an "integration period" which increases as resolution is improved. When observing maritime scenes, the sea surface changes during this time and ships are affected by complex motions. This disrupts and complicates the SAR synthesis and affects image quality [1] [2]. As with an optical system, a compromise must be sought between magnification (resolution) and the stability (integration time) that is needed for the image to be usable.

To address this problem, the aim of the simulator is to generate a radar signal (raw radar) that is representative and fully controlled, derived from:

- sea states (function of wind and swell),
- ships (signatures, associated wake movement),
- observation characteristics (frequency, incidence, direction).

This therefore provides a tool enabling the study of various SAR synthesis processes or SAR image processing algorithms, their analysis, parameterisation

and adaptation to the specific nature of maritime scenes.

This simulator was funded by the DGA (French General Armament Delegation) to meet CELAR requirements. It is the fruit of collaboration between CELAR, IRESTE and ECN, each making its contribution within its specialist field:

- CELAR/GEOS: definition of requirement and architecture, SAR expertise, co-ordination of activity,
- IRESTE/SEI: development of signal processing modules, calculation of polarimetric RCS of the sea, calculation of polarimetric radar signal and SAR processing,
- ECN/MF: hydrodynamic modelling, hull and inertial motion modelling, wakes and multi-dimensional sea spectra, water particle and ship dynamics.

The originality of this work lies in the use of high levels of synergy to reveal the specificities of the polarimetric SAR radar and hydrodynamic problems, and the development of a coherent advanced signal processing suite able to carry out parametric sweeps.

### 2. DESCRIPTION OF THE SIMULATOR

Fig.1 shows the modular architecture of the simulator.

#### 2.1 MONITORING MODULE

This module controls the entire processing sequence. The input parameters are high level thereby enabling operation by a non-specialist.

These parameters are classified under three categories: scenario, weather and radar. This module generates about fifty low-level parameters that are used by the various modules and ensure their coherence. The specialist can adjust these calculated parameters.

#### 2.2 FREE SURFACE CALCULATION MODULE

This module calculates temporal/spatial examples of the sea using 3D FFT. The spatial generation is

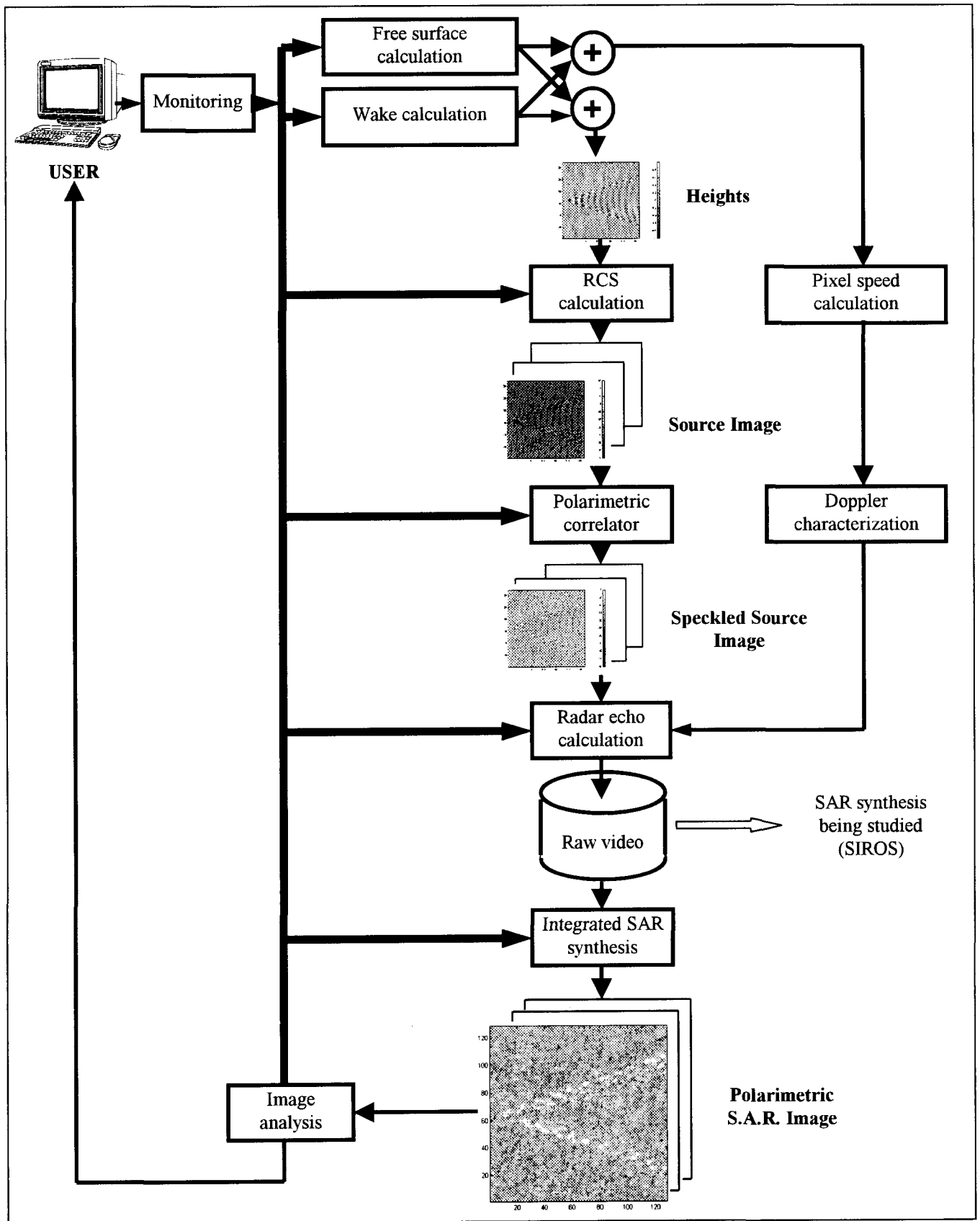


Fig.1. Modular simulator architecture.

obtained by filtering of a Gaussian white noise [3]. The spectrum used is of the Pierson-Moskowitz type [4] (1) for gravity values and of the ISSC type for the swell (2). These two spectra are superimposed and made directional using a distribution function  $S_r$ , [5] (3). The temporal evolution of the surface is obtained using a spectral ergodicity principle [6].

$$S_g(\omega) = \frac{0.008 \cdot g^2}{\omega^5} \cdot \exp\left[-0.74 \cdot \left(\frac{g}{\omega \cdot U}\right)^4\right] \quad (1)$$

where:  $g = 9.81 \text{ m/s}^2$ ;  $U$  is the wind speed (m/s) at 19.5 m altitude.

$$S_h(\omega) = \frac{124.025 \cdot H^2}{T^4 \cdot \omega^5} \cdot \exp\left[-\frac{496.1}{(T \cdot \omega)^4}\right] \quad (2)$$

where:  $H$  is the significant swell height;  $T$  is the peak period.

$$S_r(\phi) = \frac{4}{\pi} \cdot \cos^2(2 \cdot \phi) \quad (3)$$

where:  $\phi$  is the wind direction, respecting  $|\phi| < \pi/4$ .

Fig.2 is an example of superimposition of two spectra along the principle wind direction ( $\phi = 0$ ) and fig.3 is an example of the final result.

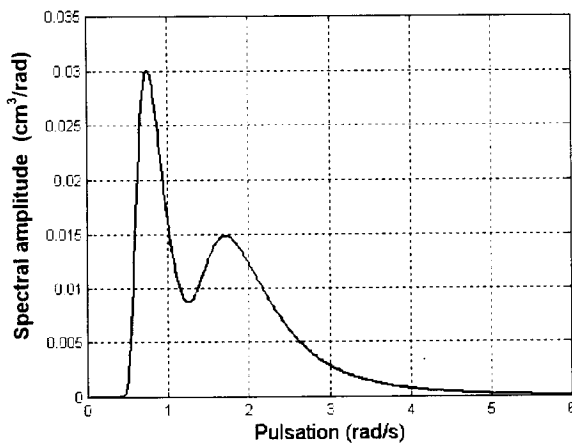


Fig.2. Example of sea spectrum: the gravity waves are obtained for  $U = 4.9 \text{ m/s}$  and the swell is defined by  $T = 6 \text{ s}$  and  $H = 0.5 \text{ m}$  (sea state 2).

Respect of sampling criteria for the spectra used gives typical resolutions of 1 m in spatial and 0.5 s in temporal (the maximum pulsation is 6 rad/s for the lowest sea state). 3D FFT processing enables images with  $512 \times 512$  points at 128 time points to be obtained in a few tens of seconds. Spatial sampling is then carried out as a function of the desired resolutions. The symmetry properties of the FFT then enable this image to be used as a pattern and to duplicate it to obtain images of significantly greater sizes.

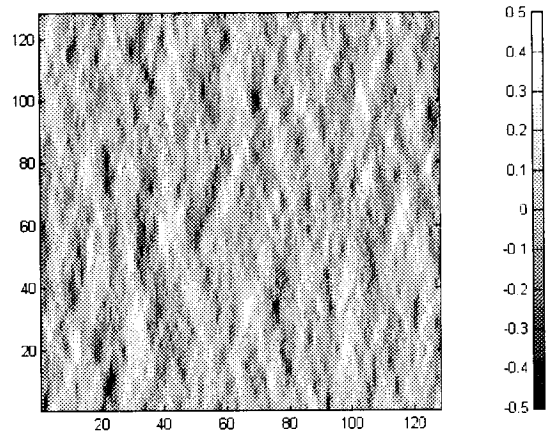


Fig.3. Example surface obtained using the parameters from fig 2 (X, Y and Z in m).

This module also produces:

- point histories enabling, using filtering, the calculation of ships' motions (roll, pitch, yaw),
- the velocities of free surface particles (orbital motion) [7], which cause the Doppler effect which affects the SAR synthesis [8].

### 2.3 WAKE CALCULATION MODULE

In this version of the simulator, we have limited ourselves to generating Kelvin-type wakes [9]. This type of wake corresponds to that generated by a ship with a narrow hull. If the ship is affected by uniform rectilinear motion in a deep sea of infinite extent, it will therefore generate a wave field which can be defined by the following expressions [10].

$$\begin{cases} X = A \cdot \cos \theta \cdot \left(1 - \frac{1}{2} \cdot \cos^2 \theta\right) \\ Y = \frac{A}{2} \cdot \sin \theta \cdot \cos^2 \theta \end{cases} \quad (4)$$

The properties of this wave field are as follows:

- this field is confined to a part of the free surface such that the waves are behind the ship and contained within a semi-angle of approximately  $19.5^\circ$ ,
- in this zone, two wave systems can be identified: transverse waves whose peaks and troughs are essentially perpendicular to the ship's axis and divergent waves whose crest lines appear to originate from the ship, as shown in fig.4.

Using this module [11], the operator may place the ship at the relevant co-ordinates, with the desired heading and speed. The image is generated directly at the final size and at the requested pitches. We have various standard hulls, ranging from trawlers to aircraft carriers.

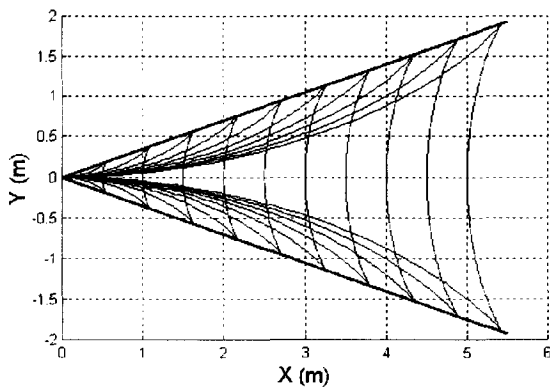


Fig.4. Representation of Kelvin wake heights for  $A$  varying between 1 and 10, with the ship moving towards negative values of  $X$ .

Fig.5 shows an example of a trawler sailing at 5 m/s on the surface generated at Fig.3.

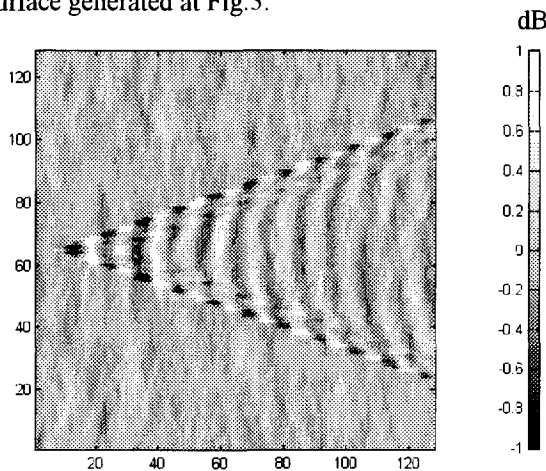


Fig.5. Example of scene (Cf. fig.3) where a trawler is sailing at 5 m/s ( $X$ ,  $Y$  and  $Z$  in m).

### 2.4 RCS CALCULATION MODULE

The energy scattered by a sea surface and observed by a SAR results mainly from capillary waves [12]. For the development of this module we have therefore applied the two scale composite model theory [13] [14]. This enables the estimation of polarimetric backscattering ( $\sigma_o$  and covariances), by starting from the principle that the large scale slopes (induced by gravity waves) modulate the small scale ones (themselves induced by the capillary waves).

The effect of the latter is obtained by the small perturbation method, which enables calculation of the field diffused by a rough surface whose irregularities are small compared with the wave length  $\lambda$ , in other words which respect:  $k \cdot \sigma < 0.3$ ; where  $\sigma$  is the

standard deviation of wave heights and  $k = 2 \cdot \pi / \lambda$ .

The backscatter coefficients for the polarisation  $pq$  of a facet are obtained from: (5)

$$\sigma_{pq}^f = 8\sigma \cdot k^4 \cdot \cos^4 \theta \cdot |\alpha_{pq}|^2 \cdot S_c(2 \cdot k \cdot \sin \theta) \cdot S_d(\phi)$$

where:  $\{p, q\} = \{h, v\}$ ;  $\theta$  is the local incident angle expressed in the earth reference frame; the terms  $\alpha_{pq}$  are linked to the Fresnel reflection and transmission coefficients [13];  $S_c$  is the capillary wave spectrum, as defined by [4]:

$$S_c(\omega) = \frac{0.875}{2 \cdot \pi} \cdot \left( \frac{2 \cdot \pi}{\omega} \right)^{5 - \log U'} \quad (6)$$

where:  $U'$  is the friction wind speed (cm/s).

$$S_d(\phi) = \frac{1}{2 \cdot \pi} + \frac{(1 - R)/(1 + R)}{\pi} \cdot \cos(2 \cdot \phi) \quad (7)$$

where:  $R$  is a function of the wind speed [4].

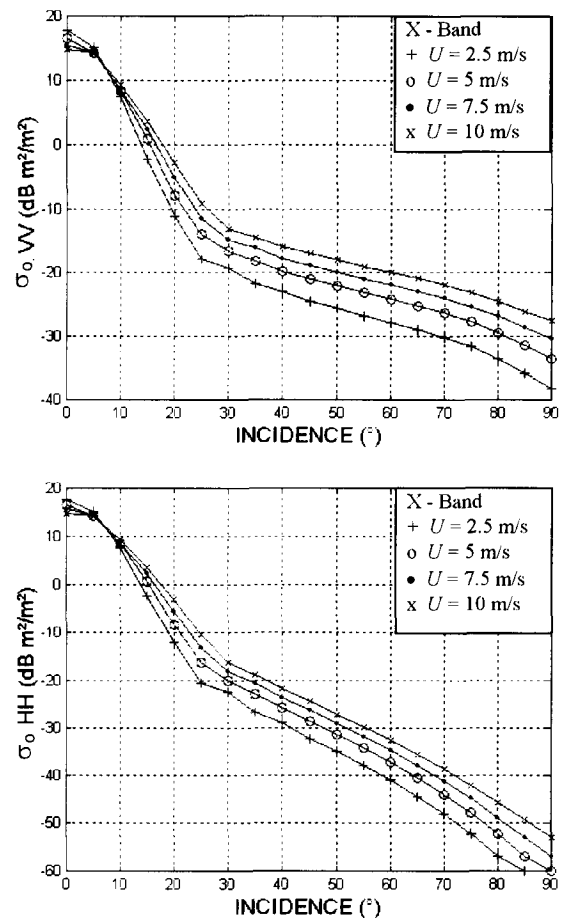


Fig.6. Reflectivity for VV and HH polarisation as a function of incidence  $\theta$  and wind speed  $U$ .

To obtain reflectivity throughout the scene, integrals along the slopes  $p_x$  and  $p_y$  are applied as follows [4]:

$$\sigma_{pq}^o = \iint \sigma_{pq}^f \cdot P_\theta(p_x, p_y) \cdot dp_x \cdot dp_y \quad (8)$$

where:  $P_\theta(p_x, p_y)$  is the density probability of the

slopes, a function of the slopes, wind direction and also wind speed.

Fig.6 shows examples of variations in reflectivity as a function of incidence  $\theta$  and wind speed  $U$ , for the components VV and HH. Note in particular:

- the increase in RCS with wind speed,
- the superiority of component VV over HH from a value of  $\theta = 20^\circ$ .

At the output from this module, the source image is calculated in covariance matrices  $[\Sigma]$ .

Fig.7 shows the HV component of the matrix  $[\Sigma]$  calculated from the scene slopes in fig.5. This illustrates the depolarisation resulting from the wake.

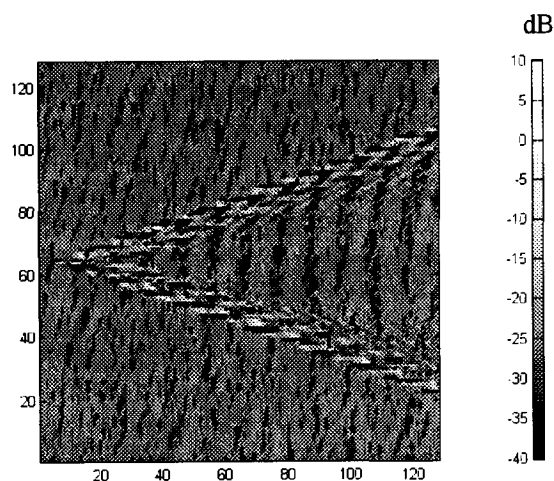


Fig.7. HV component of the matrix  $[\Sigma]$  calculated from the scene in fig.5 ( $\theta = 45^\circ$ , X-band).

## 2.5 POLARIMETRIC CORRELATION MODULE

This module [15] enables backscatter matrices  $[S]$  to be obtained from matrices  $[\Sigma]$  to which speckle has been introduced. This follows a Rayleigh law if the sea is calm and a more heterogeneous law (type K) if it is rough. Several other laws are available: lognormal, Weibull,  $\text{Khi}^2$ , Gamma, Beta.

Fig.8 shows the HV component of the speckled matrix  $[S]$  calculated from the scene in fig.5.

## 2.6 RADAR ECHO CALCULATION MODULE

This module calculates the raw video [16] taking account of the Doppler from the sea surface calculated upstream. Thus, for integration times of less than 0.5 s (temporal sampling limitations), the gravity waves are considered as being of constant speed, inducing a central Doppler frequency and a Doppler slope (first order). The capillary waves are characterised by a standard deviation in speed, inducing a second order Doppler effect, phenomenon that has been ignored in this first version of the simulator [17]. It must be

remembered that a Doppler shift primarily induces a change in position of the synthesised SAR image and that a change in Doppler slope creates a defocusing.

For integration times greater than 0.5 s, the computation of the raw video is achieved by summing the sub-looks with duration of 0.5 s.

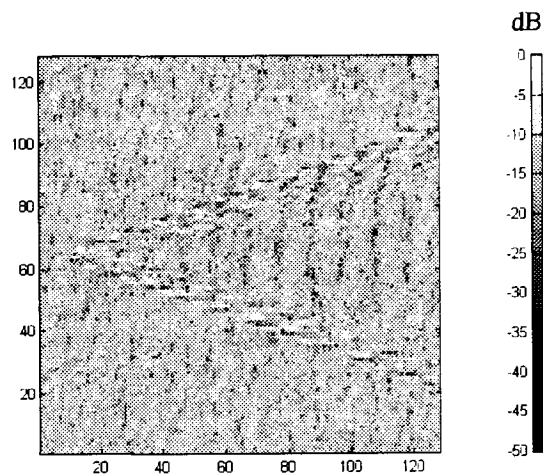


Fig.8. HV component of the matrix  $[S]$  calculated from the scene in fig.5.

## 2.7 SAR SYNTHESISING MODULE

In this first version, to provide a tool that can be totally autonomous, the simulator contains a basic SAR synthesis module that carries out:

- SAR synthesis (strip mode) taking account of several typical parameters,
- mono or multi-polarimetric processing,
- mono or multilook processing.

This module facilitates validation and offers immediate image generation. Availability of the raw video signal enables an interface with CELAR's SIROS simulator [18] for evaluations of synthetic SAR algorithms or more advanced image analysis.

Fig.9 shows the HV response of the scene from fig.5 observed by a SAR at 1m resolution, in X-band, with DCS (ERIM) sensor characteristics [19].

## 2.8 IMAGE ANALYSIS MODULE

This module analyses the images produced to characterise the ship/sea and wake/ocean contrasts and to generate statistics associated with parametric sweeping. This module could also be used on available measured images for validation purposes.

This module is limited in this simulator, but will enable an assessment of analysis algorithms adapted to different civil or military requirements, such as fishing activities or the detection of wakes.

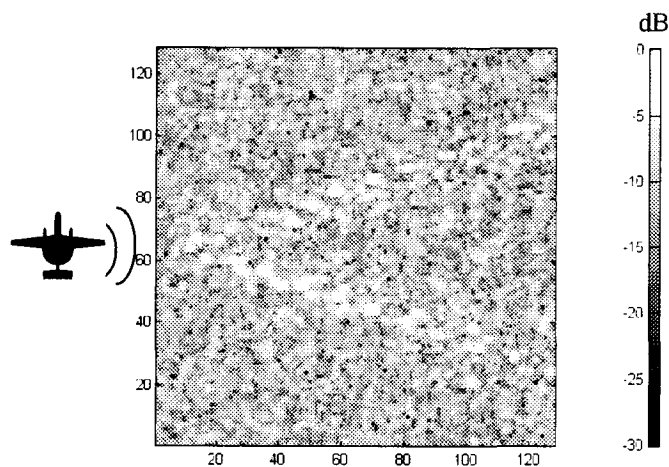


Fig.9. HV SAR Image of the scene from fig.5 (the radar is moving towards positive values of Y and is illuminating towards positive values of X). The ship's echo is not presented here.

### 3. CONCLUSION AND PROSPECTS

With this simulator, CELAR has a tool with sufficient capability to enable operation using parametric sweeping, as the calculation of each image lasts only a few minutes.

This tool, which is easy to use, enables among other things, the representation of various intermediate results, especially the source image. This gives an "idealised" image of the scene (radar with an infinite number of looks, zero integration time, no speckle, etc.) enabling distortions specific to the radar acquisition and degradations introduced by the SAR sensor to be identified.

We are currently working on the finalisation of this initial version of the simulator, which will include:

- the ship's signature (computer calculation of RCS) and the taking into account of inertial movements of the ship on the radar signal [11],
- sea/ship interactions which introduce a bistatic reflection module on the sea close to the ship [20].

### 4. REFERENCES

- [1] R.A. Shuchman and J.S. Zelenka, 'Processing of ocean wave data from a SAR', *Boundary-Layer Meteorology*, Vol.13, pp.181-191, 1978.
- [2] J.F. Vesecky and R.H. Stewart, 'The observation of ocean phenomena using imagery from the SEASAT SAR - An assessment', *Jour. Geophys. Res.*, Vol.87, No.C5, pp.3397-3430, 1982.
- [3] G.A. Mastin et al., 'Fourier synthesis of ocean scenes', *IEEE Comp. Graphics and Appl. Mag.*, pp.16-23, 1987.
- [4] A.K. Fung and K.K. Lee, 'A semi-empirical sea-spectrum model for scattering coefficient estimation', *IEEE Jour. Oceanic Engineering*, Vol.7, No.4, pp.166-176, 1982.
- [5] H.T. Wang, 'Temporal and spatial simulations of random ocean waves', *Proc. of the Fourth Offshore Mechanics and Arctic Engineering Symp.*, ASME, Vol.1, pp.72-80, 1985.
- [6] W.G. Price and R.E.D. Bishop, *Probabilistic theory of ship dynamics*, Ed. Chapman and Hall, London, 1974.
- [7] J.V. Wehausen and E. Laitone, *Surface waves*, Handbuch der Physik, Vol.IX, 1960.
- [8] W.R. Alpers and C.L. Rufenach, 'The orbital motions on SAR imagery of ocean waves', *IEEE Trans. on Antennas and Propagation*, Vol.27, No.5, pp.685-690, 1979.
- [9] W.H. Munk, 'Ships from space' A412, 231-254, *Proc. Royal Soc.*, 1988.
- [10] M.J. Lighthill, *Waves in fluids*, Ed. Cambridge University Press, 1979.
- [11] G. Delhommeau et al., 'Calculation and measurements of forces on a high speed vehicle in forced pitch and heave' *Applied Ocean Res.*, Vol.14, pp.119-126, 1992.
- [12] R.A. Schuchman et al., 'Static and dynamic modeling of a SAR imaged ocean scene', *IEEE Jour. Oceanic Eng.*, Vol.6, No.2, pp.41-49, 1981.
- [13] F.T. Ulaby, R.K. Moore and A.K. Fung, *Microwave remote sensing - Active and passive*, Vol.2, Ed. Addison-Wesley Pub. Comp., 1982.
- [14] K. Oumansour et al., 'Multifrequency SAR observation of a ship wake', *IEE Proc. on Radar and Sonar Navigation*, Vol.143, No.4, pp.275-280, 1996.
- [15] C. Cochin et al., 'Operational polarimetric scene generator for a SAR radar simulator', *Third Int. Workshop on Radar Polarimetry*, Nantes, pp.667-673, 1995.
- [16] J.C. Curlander and R.N. McDonough, *SAR - Systems and signal processing*, Ed. Wiley, New York, 1991.
- [17] M.J. Tucker, 'The imaging of waves by satellite borne SAR - The effects of sea-surface motion', *Int. Jour. Remote Sensing*, Vol.6, No.7, pp.1059-1074, 1985.
- [18] M. Busson, 'SIROS : un simulateur pour la conception d'un système d'observation spatiale par radar', *Colloque SEE 'Imagerie à vision latérale'*, Gif-sur-Yvette, 1988.
- [19] H.J. Kramer, *Observation of the Earth and its environment - Survey of missions and sensors*, Ed. Springer, Germany, 1996.
- [20] A. Khenchaf et al., 'Bistatic polarized scattering by rough surfaces', *Third Int. Workshop on Radar Polarimetry*, Nantes, pp.175-186, 1995.

## On the effect of multi scale surface roughness on SAR data

Francesco Mattia (1),  
Thuy Le Toan (2), Malcolm Davidson (2)  
Pierre Borderies (3), Elodie Bachelier (3)  
Maurice Borgeaud (4)

- (1) ITIS-CNR, c/o CGS-ASI Loc. Terlecchia, Matera (Italy), e-mail: Mattia@itis.mt.cnr.it  
(2) CESBIO, 18 av. Edouard Belin bpi 2801, Toulouse Cedex, France, e-mail: LeToan@cesbio.cnes.fr  
(3) ONERA-DEMUR, 2 Av. E. Belin, BP 4025, Toulouse Cedex, France, e-mail: Borderies@oncert.fr  
(4) ESA, ESTEC, TOS-EEP, P.O. Box 299, Noordwijk, The Netherlands, e-mail: Maurice@xe.estec.esa.nl

### ABSTRACT

The overall objective of this paper is to investigate the backscattering from multi-scale soil surfaces. Two separate aspects are investigated. The first concerns a comparison between the integral equation model (IEM) and a novel recently-developed version of the IEM specifically tailored to deal with backscattering from multi-scale surfaces (MLS IEM). The aim in this case is to investigate and assess the sensitivity of the radar backscatter to the multi-scale roughness properties. In a second step a comparison is made between the MLS IEM analytical model predictions and numerical computations. The results from two Monte Carlo numerical approaches, namely the Method of Moments (MoM) and the finite difference time domain (FDTD) are used in this respect. The numerical results are then compared to those obtained by using the IEM and the novel MLS IEM models.

### INTRODUCTION

In the context of SAR applications, surface roughness has been usually modelled as a bidimensional single scale Gaussian process. The physical assumption underlying this approach is that, although natural surfaces clearly show large scale components at topographic level, at the level of SAR resolution cell roughness behaviour may be well described as a single scale stationary Gaussian process. Besides, this assumption greatly simplify the application of electromagnetic theory to model the scattering from rough surfaces.

However, recent experimental studies [1] have shown that, even within the typical dimension of a SAR resolution cell, soil roughness is often better described as a superposition of many scales. Consequently, it is of interest to investigate the scattering properties of multi scale surfaces in order to better understand the electromagnetic scattering from natural bare soils.

Some work has already been done in this respect. In a previous study [2], surface roughness has been modelled as a band limited fractal random process and such a description has been matched to available

asymptotic direct forward scattering models such as the Integral Equation Method (IEM) [3]. A feature of this novel multi scale IEM version (MLS IEM) is that it no longer depends on conventional surface roughness parameters, namely the profile rms height ( $s$ ) and the profile correlation length ( $l$ ), but instead requires a new set of parameters which are related to the multi scale surface properties. Initial results based on the MLS IEM model, in the case based on experimental data collected over several smooth soils monitored during spring 1998 over the Marestaing site located near Toulouse, France, have shown that the MLS IEM shows a better agreement with ERS data than IEM [4]. This then motivates a further investigation into the sensitivity of the model to it's parameters and as well as it's validation.

The objective of this paper is accordingly, first to contribute at numerically assessing the scattering properties of multi-scale rough surfaces and secondly to validate the MLS IEM by comparing its prediction with numerical results.

To do so, a numerical study, including both Monte Carlo MoM and FDTD approaches, has been conducted in order to obtain reference  $\sigma_0$  values for 1-dimensional (1-D) multi scale surfaces. The MoM approach has been used to study the backscattering properties of perfectly conducting 1-dim. surfaces for an incidence angle ranging between  $0^\circ$  and  $60^\circ$  and at a frequency of 5.3GHz. On the contrary, the FDTD approach has been applied to investigate, for a given incident angle, the backscattering response of 1-D dielectric surfaces for impinging electromagnetic waves with frequencies within the interval 3.3-6.3 GHz.

In the next section the basic properties of multi-scale processes are introduced and some experimental results concerning the analysis of long roughness profiles recently collected are summarised. Subsequently, the modified multi-scale IEM version is briefly introduced. Then the numerical study is presented and its results are compared to the IEM and MLS IEM predictions. Finally concluding remarks are given.

MULTI-SCALE PROCESSES

Landscapes at scales of tens of metres to more than 10 km have been often modelled by self-similar random processes, i.e. random fractals [5]. The statistical properties of these processes are invariant to spatial scale transformations (i.e. multi-scale random processes) and possess a power spectrum  $S(f)$  given by

$$S(f_x) = \frac{c_x^2}{f_x^\nu} \tag{1}$$

where  $\nu$  is related to the surface fractal dimension by the simple relationship

$$\nu = (5 - 2D) \tag{2}$$

Due to eq. (1) random fractals are also called  $1/f$  random processes.

The most well known example of a  $1/f$  process is the Gaussian fractional Brownian motion ( $fBm$ ) process characterised by stationary increments [6].

In Fig. 1 an example of  $fBm$  with  $\nu=2$  is shown. As can be seen, it displays roughness features over different spatial scales. The  $fBm$  profiles have been simulated by using the Successive Random Addition algorithm which is an improved version of the Midpoint Displacement Algorithm suggested by Voss [7].

For  $fBm$  processes traditional roughness parameters, namely the profile height rms ( $s$ ) and profile correlation length ( $l$ ) are not intrinsic properties of the surface, but, depend on the bandwidth of the measurement process. In other words, any measurement technique is characterised through a bandwidth smaller than the bandwidth of the fractal process and, as a consequence, the  $s$ ,  $l$  parameters depend on the measured profile length  $L$  [8]. More precisely, Church derived the following relationships between the traditional roughness parameters  $s$ ,  $l$  estimated over  $fBm$  profiles of length  $L$ :

$$\begin{cases} s^2 = c_\nu \frac{L^{\nu-1}}{\nu-1} \\ l = \frac{(\nu-1)^2 L}{2(2\nu-1)} \end{cases} \tag{3}$$

The equations in (3) suggest a convenient way for experimentally assessing whether or not a set of measured profiles possess multi-scale features. It consists of estimating the  $s$ ,  $l$  roughness parameters over increasing profile lengths and then studying the trend of their mean values. If they show an overall increasing trend the surfaces should be better described by multi-scale processes than by single-scale processes. On the contrary, if  $s$  and  $l$  estimated over increasing

profile lengths show a converging trend then the surfaces should be better described by single-scale processes.

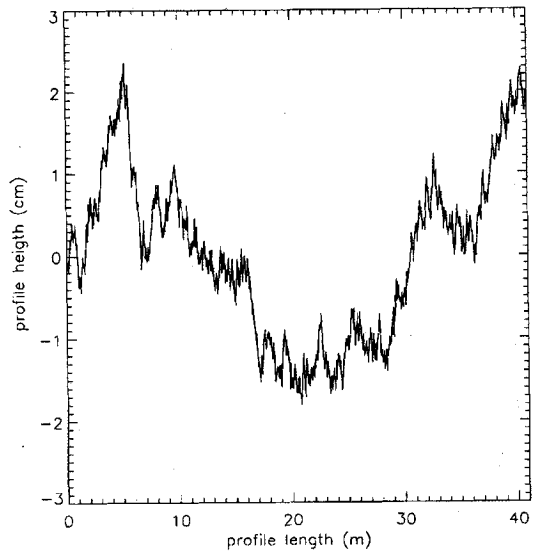


Fig. 1 Simulated Gaussian  $fBm$  process  $\nu=2.0$ .

For instance, Fig. 2 shows  $l$  estimated over increasing portions of simulated  $fBm$  roughness profiles with  $\nu=2$ . More precisely, 10 profiles 40.96m long (spacing of 0.005m) were simulated and correlation lengths values over increasing profile lengths were estimated.

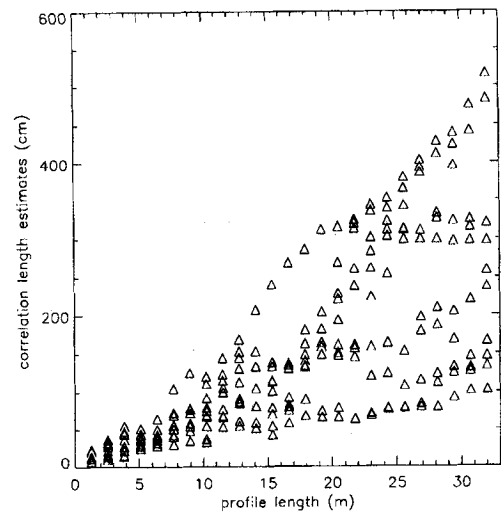


Fig. 2 Simulated Gaussian  $fBm$  process with  $\nu=2.0$ . Estimates of the profile correlation length as a function of profile length

Starting from the above considerations, a set of 25m long roughness measurements collected over the agricultural sites of Marestaing, France, and Matera, located in the south Italy, during Spring and Autumn 1998, respectively, has been analysed in order to ascertain to what extent the multi-scale statistics can apply to the case of scales ranging from tens of millimetres to 10m. The experiment and the complete



data set analysis is reported in [1]. As a main result, the analysis has shown that ploughed soils, i.e. very rough surfaces, are usually better represented by single-scale processes. On the contrary, seed bed soils, i.e. very smooth surfaces, are often better described by multi scale processes, whereas, harrowed soils, i.e. smooth-medium rough surfaces, are an intermediate case probably better described by a superposition of single and multi scale processes.

In this respect, the assessment of scattering properties of multi-scale surfaces may play an important role in order to better understand the scattering from, at least a certain type of, bare soils.

MLS IEM

In order to investigate the backscattering response of multi-scale random surfaces, an approach to match the multi-scale statistics with the requirements of the IEM surface scattering model was developed in [2]. In that work, natural roughness is assumed to be a isotropic multi-scale random process having a power spectrum  $S(f) \propto 1/f^\nu$  over a finite range of spatial scales going from a inner spatial scale ( $b$ ) of a few millimetres to a outer spatial scale ( $B$ ) of several meters. Its one dimensional expression, obtained by exploiting a Karhunen-Loève expansion of  $1/f$  processes in terms of orthonormal wavelet bases [9], is:

$$z_p(x) = \sum_{m=0}^P \sum_{n=-\infty}^{+\infty} z_n^m \Psi_n^m(x/B) \tag{4}$$

where  $z_n^m$  are a collection of uncorrelated zero mean Gaussian random variables with  $\text{var}(z_n^m) = \gamma_0^2 2^{-m\nu}$ ,  $B = 2^P b$  and  $\Psi_n^m(\cdot)$  are a collection of  $R$ -th order regular orthonormal wavelet basis. It can be easily shown that  $z_p(x)$  is a zero mean Gaussian cyclostationary process with period  $B$ .

In other words,  $z_p(x)$  is a superposition of  $P$  Gaussian random processes each one characterised by an increasing spatial scale. The resulting process is not a stationary process, i.e. the ACF associated to (4)

$$\rho(x, x') = \langle z_p(x) z_p(x') \rangle \tag{5}$$

depends both on  $x$  and on the spatial lag  $\xi = x' - x$ . However, the dependence on  $x$  is periodic with period  $B$ . As a consequence, it can be shown that the stationary part associated to (5) is given by:

$$r_0(\xi) = \frac{1}{B} \int_0^B \rho(x, x + \xi) dx =$$

$$= \gamma_0^2 \sum_{m=0}^P 2^{-m(\nu-1)} R_m(\xi) \tag{6}$$

where

$$R_m(\xi) = \int_{-\infty}^{+\infty} \Psi(\alpha) \Psi\left(\alpha + \frac{2^m \xi}{B}\right) d\alpha \tag{7}$$

is the wavelet mother function ACF. The mean variance of  $z_p(x)$  is:

$$s^2 = r_0(0) = \gamma_0^2 \frac{1 - 2^{-P(\nu-1)}}{1 - 2^{-(\nu-1)}} \tag{8}$$

The ACF function  $\frac{r_0(\xi)}{r_0(0)}$  representing the mean correlation properties of  $z_p(x)$  will be referred to as the multi-scale ACF (MLS ACF). According to such a surface description, relevant roughness parameters are:  $b, B, \gamma_0, \nu$ . The parameters  $b$  and  $B = 2^P b$  are the inner and outer spatial scales characterising the surface, respectively. The  $\gamma_0$  parameter is proportional to the value of the profile height rms and therefore it is related to the  $z_p(x)$  vertical roughness properties, whereas the  $\nu$  parameter is simply related to the fractal dimension  $D$ , see eq. (2).

In Fig. 3a and Fig. 3b, the MLS ACF is displayed in the case of  $\nu=2$ ,  $b=1cm$  and for two values of  $B$ ,  $B=256cm$  (i.e.  $P=8$ ) and  $B=1024cm$  (i.e.  $P=10$ ). Exponential trends are also superposed. As can be seen, the MLS ACF close to the origin follows an exponential trend. However, away from the origin, the two trends are quite different. The MLS ACF oscillations indicate the presence of more than one spatial scale interacting over longer distances. The effect of including two more spatial scales in the roughness description is to increase the correlation length value. In fact, it increases linearly with the outer scale  $B$  (see eq. 3). The wavelet basis used is the 4<sup>th</sup>-order Daubechies wavelet basis.

In [2], it has been furthermore shown that under appropriate hypothesis of "smoothness" for the surfaces, i.e.  $k\gamma_0 < 0.7$ , the canonical expressions of IEM for co-polarised backscattering coefficients apply also to the case of multi-scale surfaces. In this case, the roughness spectrum is numerically obtained using the MLS ACF.

In order to better understand under which conditions it is relevant to take into account the effect of multi-scale roughness on backscattering coefficients, a comparison between IEM (using an exponential ACF) and MLS IEM has been carried out. Since the study is restricted to studying the effects of surface roughness on co-polarised backscattering coefficients, the comparison

has been limited to the case of perfectly conducting 1-dimensional surfaces.

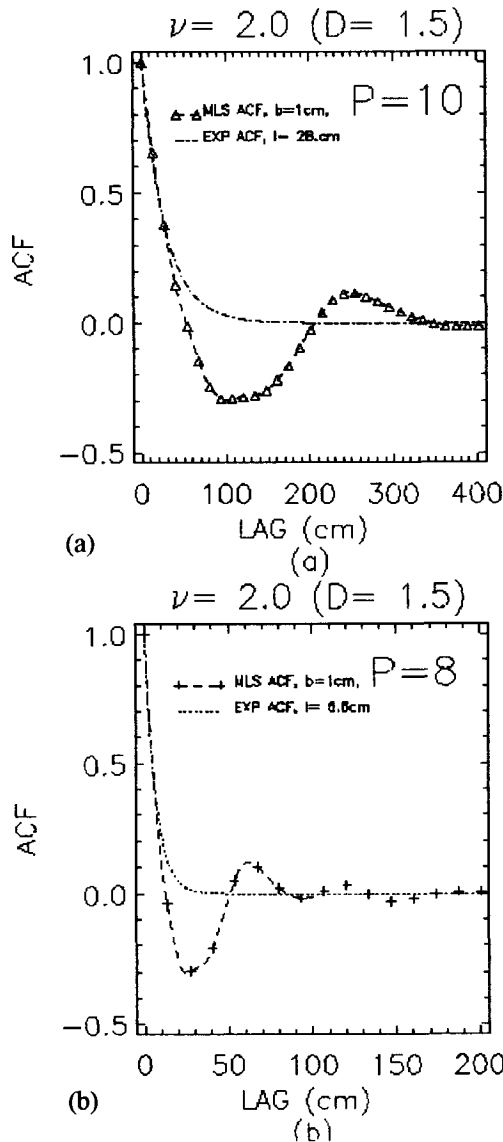


Fig. 3 MLS ACF at two different outer scales:  $B=1024$  cm (i.e.  $P=10$ ) (a) and  $B=256$  cm (i.e.  $P=8$ ) (b). Exponential trends are also superposed.

The set of multi-scale parameters investigated includes:  $\nu$  ranging between 1.3 and 2.2 and the outer spatial scale  $B$  ranging between approximately  $45\lambda$  and  $730\lambda$  (corresponding to  $P$  ranging between 8 and 12 with the inner spatial scale  $b$  constant and equal to  $\lambda/5.6$ ). The  $\gamma_0$  parameter has been kept constant to  $\lambda/10$ . For each combination of these parameters, the MLS ACF expression has been used to obtain the corresponding traditional roughness parameters, namely  $s$  and  $l$ . It is worth noting that the estimated correlation lengths are always found much larger than the impinging  $\lambda$ .

The results for both IEM and MLS IEM models are summarised in the Fig. 4. For an incidence angle of

$30^\circ$ , the IEM results at V polarisation are plotted versus those of MLS IEM.

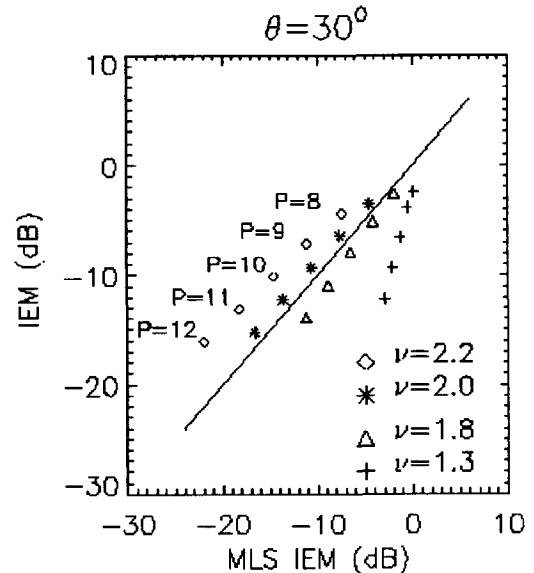


Fig. 4 IEM vs MLS IEM, 1 dim., V pol., backscattering coefficients.

As can be seen, for  $\nu=2$ , IEM and MLS IEM yield almost the identical results irrespective of the incidence angle or the outer spatial scale used. When  $\nu$  is lower than 2, IEM tends to underestimate the MLS values, whereas when  $\nu$  is greater than 2 it tends to overestimate the MLS IEM predictions. Such a behaviour can be interpreted in terms of the single and multi-scale roughness spectra [4].

The outer scale parameter also plays an important role in the comparison. We note that decreasing the outer scale reduces the differences between IEM and MLS IEM results. When the number of scales decreases it is reasonable to have a convergent behaviour between MLS and SLS models.

## NUMERICAL STUDY

In order to obtain reference  $\sigma_0$  values to compare with the MLS IEM predictions, a numerical study has been conducted. Two numerical approaches have been applied: the Monte Carlo MoM and the FDTD methods. In the following the results are summarised, respectively.

### The MoM approach

Four sets of 1-dim.  $fBm$  surfaces having increasing values of  $\nu$ , namely  $\nu=1.3$ , 1.8, 2., 2.2, have been simulated. Each set consisted of 50 profiles.

The Monte Carlo MoM approach has been widely exploited in literature to compute the backscattering response of rough surfaces. Here the study has been conducted over the 1-dim.  $fBm$  perfectly conducting surfaces for a range of incidence angles going from  $0^\circ$

to  $60^\circ$ . Moreover, both TE (V) and TM (H) polarisation have been investigated. The actual ratio between the impinging wavelength and the profile length  $L$  is  $L \approx 90\lambda$  and the profile was generated with a spacing ( $d$ ) corresponding to  $\lambda/d \approx 11$ .

The MoM code has been preliminary tested over deterministic classical targets and over single-scale random rough surfaces Gaussian and exponentially correlated.

A synthetic view of the comparison between IEM and MoM and between MLS IEM and MoM is shown in Fig. 5 and Fig. 6, respectively. The incidence angle is equal to  $30^\circ$ , however, an analogous trend holds over the entire range of incidence angles [4].

As can be seen, numerical trends confirm the analytical results illustrated in the previous section. In particular, surfaces with small  $\nu$  lead to an underestimation of the true backscattering coefficient by the IEM, whereas surfaces with large  $\nu$  values produce the opposite effect. On the contrary, the MLS IEM shows an overall better agreement with the MoM reference values. The surface input parameters  $s$  and  $l$  used to run the IEM model have been measured over the total profile length  $L$ . The ACF actually used is the exponential ACF.

To run the MLS IEM the  $\gamma_0$  parameter has been estimated using the expression in eq. 8, whereas the inner and outer spatial scales have been fixed according to the following considerations. The inner spatial scale  $b$  should be equal to the profile spacing  $d$ . However, it has been set constant to  $\approx \lambda/6$ .

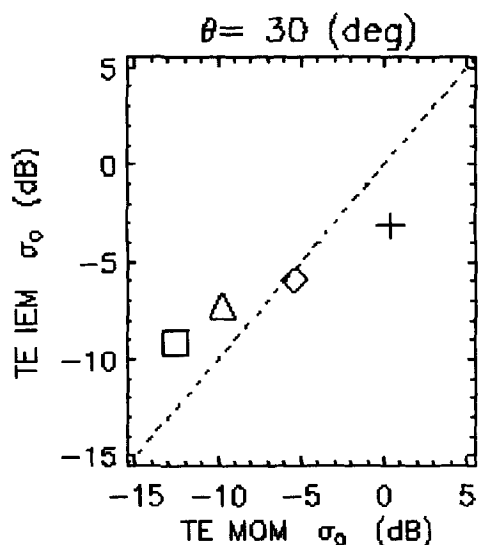


Fig. 5 IEM versus MOM  $\sigma_0$ . Symbols for the  $\nu$  values are:  $\square$   $\nu=2.2$ ;  $\Delta$   $\nu=2.0$ ;  $\diamond$   $\nu=1.8$ ;  $+$   $\nu=1.3$ .

This is because, firstly, the MLS IEM is not critically sensitive to  $b$  (particularly for  $\nu \approx 2$ ) and, secondly, a value for this parameter larger than  $d$  significantly speed up the numerical calculation of the MLS ACF spectrum which enters the MLS IEM expression. The outer spatial scale ( $B$ ) on the other hand is fixed by the profile length.

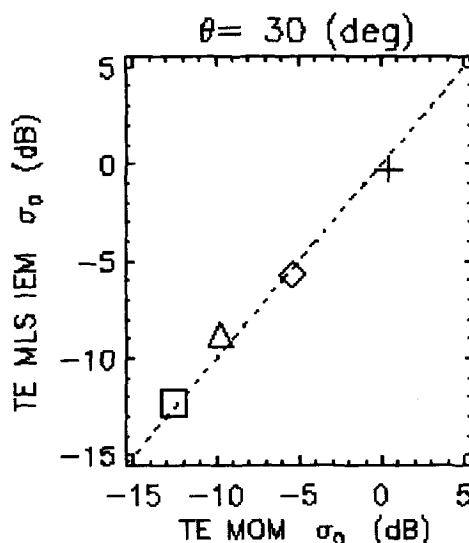


Fig. 6 MLS IEM versus MOM  $\sigma_0$ . Symbols for the  $\nu$  values are:  $\square$   $\nu=2.2$ ;  $\Delta$   $\nu=2.0$ ;  $\diamond$   $\nu=1.8$ ;  $+$   $\nu=1.3$ .

More precisely, if the profile length is  $L$  then  $B=L/2$  because, when computing the ACF of profiles having a finite length  $L$ , spatial scales up to a maximum of  $L/2$  can be displayed, implying that the following relationship connecting  $B$  with  $L$ ,  $P$  and  $b$  holds:

$$B = \frac{L}{2} = 2^P b \quad (9)$$

#### The FDTD approach

The FDTD method is based on a finite difference approximation of order 2 both in space and time of Maxwell's equations which are explicitly solved in the time domain. The FDTD main advantage with respect to the MoM approach is that the former can be easily applied to non-homogeneous objects having any dielectric constant and an arbitrary shape. Moreover, since the FDTD results are obtained in the time domain, they can predict both the transient as well as the steady state. The application of the FDTD approach to study the scattering from rough surfaces has been previously described in [10].

In this study, only 1-dim. homogeneous dielectric surfaces imaged at a constant incident angle of  $20^\circ$  are considered. Three frequencies have been investigated: 3.3, 5.3 and 6.3 GHz.

In order to estimate the surface backscattering a study on the convergence rate of  $\sigma_0$  as a function of the number of averaged field estimates has been preliminarily conducted at a frequency of 5.3 GHz. Overall this part of the study, concerned with the trade-off between accuracy and computation time, led to a total profile length of  $L \approx 90\lambda$ , spacing size  $d \approx \lambda/50$  and backscatter coefficients estimated over 50 profile realisations as reference values. In order to compare the

FDTD results with the MLS IEM predictions, a set of 50 1-dim.  $fBm$  profiles with  $\nu=2$ , total length  $L$  and spacing  $d$  were generated. Fig. 7 shows a comparison between the FDTD reference values and the MLS IEM predictions in the case of two different complex relative dielectric constant, namely  $\epsilon' = 10 + j3$  and  $\epsilon' = 16 + j5$ .

We can observe that there is a good overall agreement (within  $\pm 1$  dB) all over the frequency range for both the investigated dielectric surfaces.

#### Multiscale IEM and FDTD Comparisor

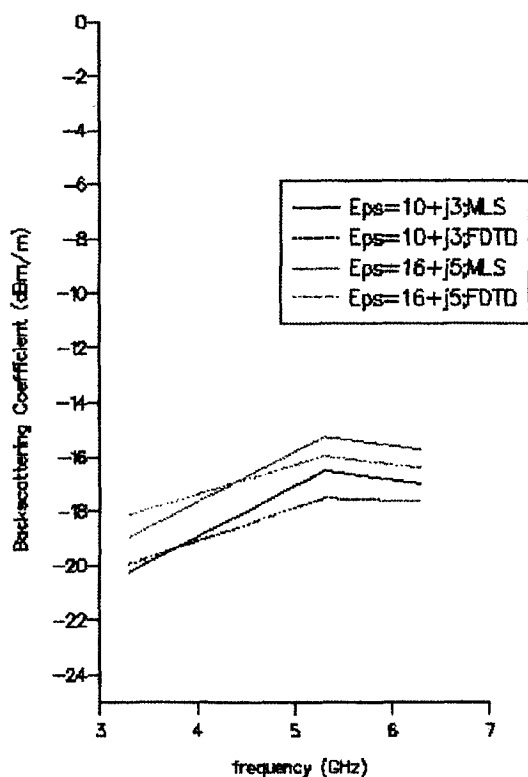


Fig. 7 FDTD and MLS IEM comparison.

#### CONCLUSIONS

In this paper, an analytical and numerical study on the backscattering properties of multi-scale random surfaces has been carried out. In a first instance this was done by exploiting the IEM model in its conventional single-scale version and in a novel version (MLS IEM) specifically tailored to tackle with scattering from fractal surfaces [2]. Significant differences between the predictions of both models were observed.

In a second step different sets of 1-dim. fractal surfaces, both perfectly conducting and dielectric, have been numerically investigated by using Monte Carlo MoM and FDTD approaches, respectively. The

numerical results have been compared to the IEM direct forward model. As a general result, multi-scale fractal surfaces are found to be not well described by the conventional single-scale IEM. The disagreement is more important at high incidence angles and at V polarisation. On the contrary, the MLS IEM has shown a good overall agreement with numerical data.

The results of this study raise some interesting questions for remote sensing applications. A number of studies have shown, for instance, that natural surfaces are better described by multi-scale processes than by traditional single-scale processes. In particular, recent accurate measurements of very long surface profiles have shown that even within the typical dimension of a SAR system, surface roughness is often better represented by fractal processes [1]. Given the sensitivity of radar backscatter to the multi-scale roughness characteristics of surfaces, the quantification of these effects of the radar backscatter signatures is a prerequisite for the development of physical based inversion algorithms for an effective use of SAR data.

#### ACKNOWLEDGMENTS

This work has been supported by ESA-ESTEC under contract n. I2008/96/ND/NB.

#### REFERENCES

- [1] Davidson, M., T. Le Toan, F. Mattia, G. Satalino, T. Manninen, M. Borgeaud M., "On the characterisation of agricultural soil roughness for radar sensing studies", accepted for publication on IEEE TGARSS;
- [2] Mattia, F., T. Le Toan, "Backscattering properties of multi-scale rough surfaces", Journal of Electromagnetic Waves and Applications, vol.13, 1999;
- [3] Fung, A.K., Microwave scattering and emission models and their applications, Artech House, 1994;
- [4] Mattia, F., T. Le Toan, M. Davidson, "An analytical, numerical and experimental study on scattering from multi-scale rough surfaces", submitted;
- [5] Burrough P.A., Fractal dimensions of landscapes and other environmental data, Nature, vol. 294, 19 November 1981
- [6] Mandelbrot, B.B., Van Ness, J.W., "Fractional Brownian motions, fractional noises and applications", siam Rev., 10, 1968;
- [7] Voss, R.F., Random fractals forgeries; in Fundamental algorithms in computer graphics (editor);
- [8] Church, L.E., Fractal surface finish, Applied Optics, vol.27, n.8, April 1988;
- [9] Wornell, G.W., Signal Processing with Fractals: a wavelet-based approach, Prentice Hall, 1996;
- [10] Fung, A.K., M.R. Shah, S. Tjuatja, "Numerical Simulation of Scattering from Three-Dimensional Randomly Rough Surfaces", IEEE TGARS, vol.32, n.5

## Stereo vision measurements of soil surface characteristics and their use in model validation

A J MCDONALD, S CROSSLEY, J C BENNETT, S C M BROWN,  
G COOKMARTIN, K MORRISON and S QUEGAN  
Sheffield Centre for Earth Observation Science (SCEOS), The University of Sheffield,  
Hicks Building, Hounsfield Road, Sheffield S3 7RH, UK.  
Phone: +44 (114) 2223749  
Fax: +44 (114) 2223809  
Email: A.J.Mcdonald@shef.ac.uk

### ABSTRACT

Examination of extant microwave backscattering models indicates that one of the critical constraints on predicting the microwave returns from soils quantitatively is the measurement of the statistical roughness characteristics of the surface. This work examines the capability of a stereo vision system in determining both the single-scale (correlation length and rms height) and multi-scale (fractal dimension) roughness characteristics of a soil surface. The measured profile of a soil surface derived using the stereo vision apparatus is first compared with that produced using a pin-board device to show the validity of the method. The resultant comparison shows that the two profiles are in good agreement when experimental constraints are taken into account. Statistically well-defined simulated surfaces are then used to assess the likely accuracy of the values, derived by the stereo vision system, of the correlation length, rms height and fractal dimension. Initial measurements from the stereo vision are then qualitatively compared with measurements of the microwave backscatter from the prepared surface using the ground-based synthetic aperture radar (GB-SAR) at Sheffield University. Finally, the possibilities of using this stereo vision system in conjunction with the GB-SAR apparatus for the development of the next generation of models are discussed.

### INTRODUCTION

Many studies have suggested that SAR observations are potentially useful in the remote determination of soil biophysical variables. One of the restrictions on understanding the microwave returns from soils quantitatively is the measurement of the soil surface roughness. This follows from the fact that the extant models of microwave backscatter from soil require detailed information on the statistical characteristics of the surface [1-6]. The most usual statistical measures of a soil surface are the rms height and the correlation length, however recent work has also begun to examine the utility of multi-scale measures such as the fractal dimension. Fig. 1 shows the effect on the microwave

backscatter observed when the correlation length and rms height of a surface are varied by 10% from their mean values of 4cm and 1cm, respectively, these quantities being representative of these variables. The values of the parameters used in the IEM model are shown in Table 1. Examination of Fig. 1 indicates that the difference between the backscattered power associated with the changes in rms height and correlation length is as large as 5dB, these differences being particularly clear at high and low incidence angles. Therefore to validate microwave backscatter models precisely it is obviously necessary to determine the statistical properties of the surface accurately. Examination of the current literature indicates that techniques for the measurement of bare soil surfaces using pin-board devices [7] and laser profilometers are well-developed [8-9]. However, these systems measurements are relatively time-consuming for the amount of data necessary to derive correlation length and rms height accurately [10-11]. Thus, a stereo vision system has been developed to measure the structure of soil surfaces.

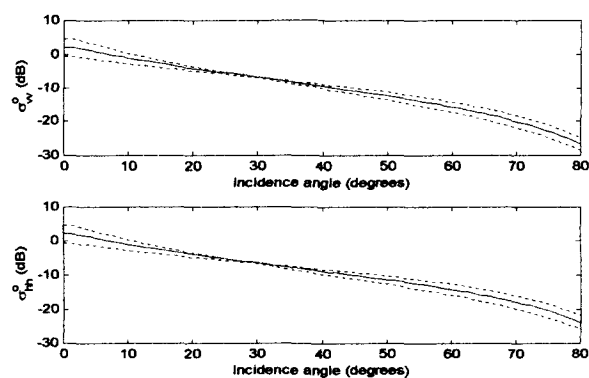


Fig. 1: Derived values of the microwave backscattering coefficient, using the IEM model [1], at VV (upper) and HH (lower) polarisations. The full line shows the backscatter for the mean values described in Table 1. The dotted lines show the maximum and minimum values derived when the correlation length and rms height are varied by 10% of the mean value (see Table 1)

Parameter	Mean value	Variation
Wavelength (m)	0.06	0.0
Rms height (m)	0.01	±0.001
Correlation length (m)	0.04	±0.004
Volumetric moisture (m <sup>3</sup> /m <sup>3</sup> )	0.3	0.0
Complex dielectric constant	15.99 + i3.28	0.0+i0.0

Table 1: The values used in the IEM simulations the results of which are shown in Fig. 1.

This paper first describes the stereo vision methods and the apparatus used. Initial measurements showing the ability of the system are then discussed. The results of several sets of Monte-carlo simulations are described later, these data being produced to examine the ability of the stereo vision apparatus to determine statistical parameters associated with the surface roughness (correlation length, rms height, and fractal dimension). Comparisons between a radar image produced using the GB-SAR facility at Sheffield University and stereo vision measurements are then made. Finally, the conclusions drawn from this study are described and possible areas of further work are discussed.

#### STEREO VISION MEASUREMENTS

The experimental stereo vision system is comprised of two CCD cameras, a mount, and a frame grabber connected to a PC. By placing a calibration tile (a small white board with 16 black squares arranged in a grid) in the field of view (FOV) of both cameras and then focusing the cameras on the object it is possible to measure the structure. It should be noted that at present this system can only be used under laboratory conditions. The procedure used is to record the images from the two cameras simultaneously using the TINA software tool [12]. The acquired images are then examined to determine the position of the edges in the two photographs using an edge detection algorithm described in Canny [13]. The detected edges in each image are then examined separately to define the 64 corners of the 16 black squares on the calibration tile. This information is used in the calibration procedure described in Tsai [14] which allows each camera's viewing geometry relative to the calibration tile and its focal length to be derived. This calibration process basically yields 64 constraints on the 7 camera parameters (translation vector, three angles of rotation and the focal length) which are used to optimise these values. The relative geometry of the cameras can then be derived by using each camera's position relative to the calibration tile. To ensure that the minimisation procedure has worked efficiently the parameters are further optimised by ensuring that the derived co-ordinates of the calibration tile are in a plane.

The calibration tile is replaced by the object of interest in the FOV of both cameras, the acquired

images are then examined to determine the position of the edges in the two new images using the edge detection algorithm [13]. The software uses this information along with the camera parameters previously derived to rectify the stereo images to a parallel camera configuration. The edge features in the rectified images are then correlated to determine the relative positions of the pixels in each image [15]. The positions of the correlated pairs of pixels in the rectified image are then triangulated to determine the position of particular points on the soil surface with reference to the position of the left camera. The parameters necessary to determine the real world co-ordinates of an object are now all defined, with the addition of user information on the physical size of each pixel the structure of the object can be derived.

It was determined that the best way to measure a soil surface was to take several sets of stereo images offset by a known amount, a mosaic of these images could then be used to produce useful measurements of the soil profile at the required resolution. To aid the correlation procedure, which can become confused when noisy images are used, a laser stripe generator (a laser diode with an elliptical lens attached which forms a stripe) was used to produce one distinct line in the pair of images. Because a number of surface profiles need to be measured to obtain information over the relevant scales (metres) and these need to be lined up accurately. The movement of the cameras and the laser line source should be constrained to one dimension. The simplest solution to this problem is to mount the CCD cameras and laser diode on a linear scanner. A mosaic of stereo images is produced by imaging the laser stripe on the soil surface, moving the supporting frame a known amount (this movement being regulated by a computer-controlled stepper motor) then repeating this procedure over the length of the linear scanner (3m). Information stored on the relative positions of each image pair can then be used to correct each component surface profile in order to produce a composite surface profile over the length of the linear scanner. The accuracy of the positional information is thus dependent on the resolution of the CCD camera and the integrity of the reference and the soil images, and the alignment and the positional accuracy of the linear scanner. Fig. 2 shows a diagram of the soil-profiler system used.

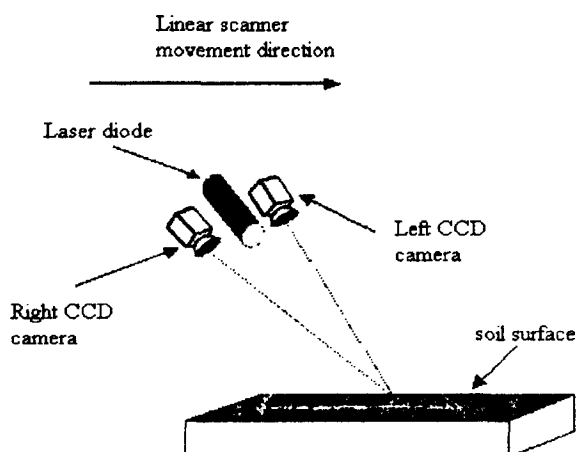


Fig. 2: A schematic of the stereo vision soil profile measurement system. Note that both the CCD cameras and the laser line generator are mounted on a linear scanner which is not shown in this diagram.

## RESULTS

### Initial Measurements

Initial results comparing the measured profile of a soil surface derived using the stereo vision apparatus with that produced using a pin-board device are shown in Fig. 3. The stereo vision measurements are made up of a mosaic of several pairs of images. The pairs of images used were made to overlap significantly in order to reduce areas of missing data (produced when one or other of the cameras is occluded) to a minimum. The difficulty in trying to find the components due to separate stereo vision pairs in the figure indicates that the image registration in this experiment was excellent. The two profiles in Fig. 3 are in relatively good agreement when experimental constraints are taken into account. It is likely that a closer connection between the two sets of data would result if a more accurate correspondence between the stereo vision apparatus's co-ordinate system and the pin-board systems co-ordinate system had been made. It should also be noted that the soil surface was significantly disturbed in the process of making the pin-board measurements. Indeed some of the pins were observed to enter the soil surface by 10mm in places, this large impact on the soil surface occurred because the soil was dry and inadequately packed down in the seed tray. Thus, the correspondence is considered to be excellent under these experimental conditions. The relatively large variance of the stereo vision measurements is due to the fact that the edge detection algorithm finds an edge on both sides of the laser stripe and thus two separate profiles approximately 2mm apart are actually measured.

Unfortunately, the very small horizontal resolution measurements possible with the stereo vision system (approximately 0.2mm horizontal resolution for cameras with focal lengths 25mm and CCD chips with 640 by 480 pixel arrays) must be degraded by averaging to remove the small gaps observed in the stereo vision data. These gaps occur where the laser stripe on the surface is not in one camera's field of view because of obstructions. Therefore to derive the autocorrelation function of the surface from the stereo vision data, individual values must be averaged and larger gaps must be interpolated over using a polynomial interpolation routine [16]. The autocorrelation function of the soil surface may then be derived from this processed data using a fourier method described in Press et al. [16]. Fig. 4 shows the autocorrelation function of a single profile from a prepared soil surface, the length of profile used was approximately 1.8m and the horizontal resolution was reduced to 5mm in this case. The values of the rms height and correlation length, assuming a gaussian and an exponential model, derived from this surface and shown in Fig. 4 are 0.8cm, 4.2cm and 4.5cm, respectively. It is interesting to note that the autocorrelation function is closer to the exponential model than the gaussian model. This is particularly interesting because the vast majority of previous soil surface measurements made under field conditions suggest that most surfaces' autocorrelation functions are modelled more accurately by the exponential model. Thus, this suggests that the procedure used to simulate a soil surface in the laboratory has been successful.

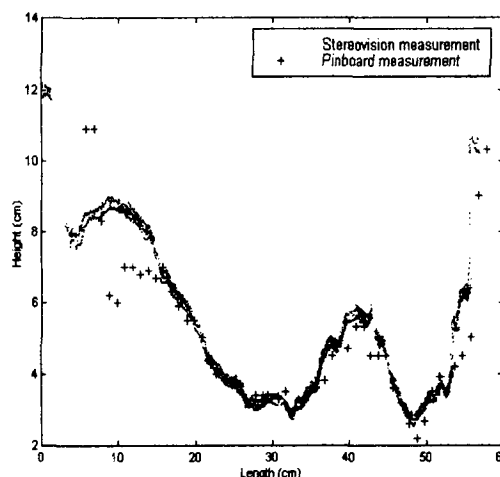


Fig. 3: Comparison of the measurements derived using the stereo vision technique and those measured using the pin-board device. It is important to remember at this point that the stereo vision measurements are made up of a mosaic of 7 images.

### Monte-carlo Simulations

To examine the ability of the stereo vision system simulations similar to those described in Ogilvy and Foster [10] and Oh and Kay [11] were performed. In this study, over 200 random profiles with statistics represented by the exponential autocorrelation function model have been synthesised. Each of these surfaces has been produced to have a correlation length of 4cm and a rms height of 1cm. The histograms below show the values of the correlation length derived for profiles of length 5m and horizontal resolutions of 1mm. However, the histogram on the left has been derived by averaging data and interpolating over large gaps to a horizontal resolution of 1mm from data with an initial resolution of 0.2mm with a high proportion of missing data (20%), this being produced to represent the stereo system. A comparison of the two histograms will allow us to examine whether any bias or increased error in the data results from the processing used on the stereo data.

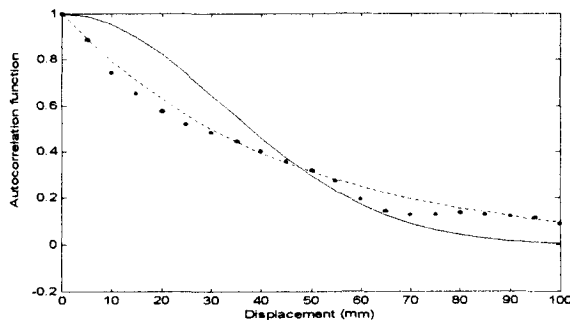


Fig. 4: Autocorrelation function of a measured soil surface (dotted line) and the form of the exponential (dashed line) and gaussian (full line) models fitted to the measured values.

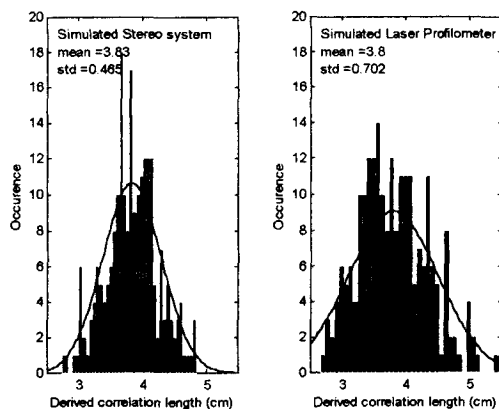


Fig. 5: Histograms of the derived correlation length derived from processed (left) and unprocessed (right) measurements using a profile length of 5m and a horizontal resolution of 1mm. Actual value of the correlation length is 0.04m.

Comparison of these histograms suggests that no obvious bias has been introduced by the manipulation of the stereo data, but both derived values are slightly smaller than expected (0.0383 and 0.0381 for the averaged and unaveraged data, respectively). It is suggested that this unexpected bias may be associated with variations in the simulation of the surface structure using the procedures described in Oh and Kay [10]. It is also noticeable that the standard deviation on the stereo systems simulations have been reduced which suggests that this system is potentially more accurate than the laser profilometer system over the same profile length. Measurements of the rms height derived using the two different systems showed no significant differences. Therefore, the stereo system seems to be able to derive the correlation length and rms height of soil surfaces well enough to validate single-scale microwave models.

A second set of simulated surfaces based on fractional brownian motion multi-scale surfaces described in Falconer [17] have been produced. Over 200 random profiles with statistics represented by the fractional brownian motion model have been synthesised, each of these surfaces has been produced to have a fractal dimension of 1.5. The fractal dimension of each of these surfaces has then been derived by examining the gradient of the power spectra of these surfaces. Discussions on the relative merits of different methods for determining the fractal dimension can be found in Constantine and Hall [18] and Davies and Hall [19].

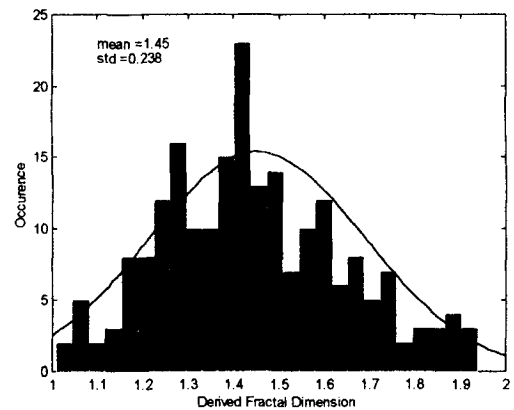


Fig. 6: Histogram of the derived fractal dimension using a profile length of 5m and a horizontal resolution of 1mm.

Initial estimates of the surfaces fractal dimension, using the power spectrums gradient, proved very poor and showed a noticeable bias towards very low fractal dimension (1.0-1.1). After some analysis it became clear that this was associated with always using the same range of wavelengths over which the least-squares fit was made. Thus, after experimentation a number of



least-squares regressions over a number of regions were performed. The best gradient was then selected by using the gradient with the smallest uncertainty. Fig. 6 shows the histogram of the fractal dimension derived from processed measurements using a profile length of 5m and a horizontal resolution of 1mm, the actual value of the fractal dimension in this case being 1.5.

The fractal dimension shows a mean value of 1.45 and a standard deviation of 0.23 when a gaussian model is fit to the data. This result suggests that profiles lengths of 5m are not long enough to determine the fractal dimension accurately. Especially, when the fact that for a profile the range of the fractal dimension is limited to between 1 and 2. Thus, it seems that a laboratory environment is not suitable to examine multi-scale electromagnetic models which incorporate the fractal dimension. The possibility of examining the multi-scale model described in Mannien [4] needs to be examined. This model relies upon deriving the correlation length at a number of scales to be able to determine characteristic multi-scale surface roughness parameters.

#### Combined SAR and Stereo Vision Measurements

In addition to the system's ability to measure surface profiles, and thereby the surfaces statistical properties, it is a relatively simple procedure to measure 2-D areas of soil surfaces by mounting the cameras and the laser diode perpendicular to the direction of motion of the linear scanner. Fig. 6 compares the results of measuring a section of a soil, using the stereo vision system, with a SAR image of the entire soil surface using the microwave system available at the ground-based Synthetic Aperture Radar (GB-SAR) facility. The microwave measurements displayed were taken at X-band with a HH polarisation and at an incidence angle of 55 degrees. Details of the GB-SAR facility and the SAR imaging procedure used to produce the microwave image are described in Morrison et al. [20]. Inspection shows that the three furrows on the soil surface observed by the stereo vision system correspond to areas of strong microwave backscatter. Analysis suggests that these enhancements are likely to be associated with the back faces of the furrows, where the local incidence angles relative to the relative to the tangent of the surface are near normal incidence. The last area of enhanced backscatter in the diagram (at  $\approx 150\text{cm}$ ) is associated with the back surface and is thus likely to be associated with a double bounce scattering mechanism. Thus, using the stereo vision system in conjunction with the GB-SAR apparatus may be of significant use in the testing and development of models of microwave backscatter from soil surfaces.

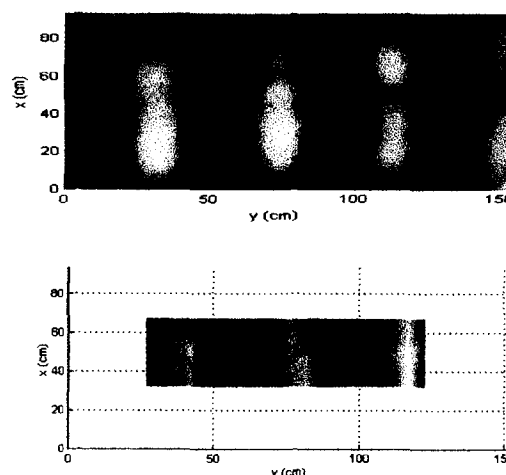


Fig. 7: A comparison of the SAR image of the microwave backscatter at HH polarisation over the soil surface (top) and the stereo vision measurement of a section of the same surface (bottom).

#### CONCLUSIONS AND FURTHER WORK

The use of stereo vision techniques in conjunction with a linear scanner is shown to be capable of measuring soil surface profiles relatively accurately in a laboratory environment. Simulations suggest that the correlation length and rms height can also be precisely determined using this system, thus, making it possible to truly validate single-scale soil surface models. Simulations also suggest that the fractal dimension can not be adequately determined using short profile lengths. Thus, the electromagnetic models which use fractal dimension can not be validated in a laboratory environment for the conditions specified in the simulations. This analysis needs to be extended to examine whether this system is capable of measuring other statistical parameters which characterise multi-scale soil surfaces. For example, those used in the multi-scale model described in Mannien [4]. The use of GB-SAR measurements of the microwave backscatter could then be compared with models to ascertain whether these simulations are valid.

The stereo vision measurements of a 2-D area of a surface show a clear correspondence with a SAR image. This indicates another potential way of utilising this technique in the testing and development of models of microwave backscatter from soil surfaces. At present this system only works in a laboratory environment because of constraints associated with the portability of the linear scanner, however the next phase of this work is to construct a portable field-based system.

## REFERENCES

- [1] A. K. Fung, Z. Li, and K. S. Chen, "Backscattering from a randomly rough dielectric surface," *IEEE Trans. Geosci. Remote Sens.*, vol. 30, pp. 356-369, 1992.
- [2] A. K. Fung, M. R. Shah, and S. Tjuatja, "Numerical simulation of scattering from three-dimensional randomly rough surfaces," *IEEE Trans. Geosci. Remote Sens.*, vol. 32, pp. 986-994, 1994.
- [3] D. L. Jordan, and F. Moreno, "Enhanced backscattering and cross depolarization from multiscale surfaces," *J. Opt. Soc. America A*, vol. 10, pp. 1989-1995, 1993.
- [4] T. Manninen, "Multiscale surface roughness and backscattering," *Prog. Electromag. Res.*, vol. 16, pp. 173-201, 1997.
- [5] Y. Oh, K. M. Sarabandi, and F. T. Ulaby, "An empirical model and an inversion technique for radar scattering from bare soil surfaces," *IEEE Trans. Geosci. Remote Sens.*, vol. 30, pp. 370-381, 1992.
- [6] R. L. Wagner, J. Song, and W. C. Chew, "Monte Carlo simulation of electromagnetic scattering from two-dimensional random rough surfaces," *IEEE Trans. Antennas Propagat.*, vol. 45, pp. 235-245, 1997.
- [7] N. H. Cremers, P. M. van Dijk, A. P. de Roo, and M. A. Verzaandvoort, "Spatial and temporal variability of soil surface roughness and the application in hydrological and soil erosion modelling," *Hydrological Processes*, vol. 10, pp. 1035-1047, 1996.
- [8] C. Huang, and J. M. Bradford, "Portable laser scanner for measuring soil surface roughness," *Soil Sci. Soc. America J.*, vol. 54, pp. 1402-1406, 1990.
- [9] C. Huang, C., and J. M. Bradford, "Applications of a laser scanner to quantify soil microtopography," *Soil Sci. Soc. America J.*, vol. 56, pp. 14-21, 1992.
- [10] J. A. Ogilvy, and J. M. Foster, "Rough surfaces: gaussian or exponential statistics?," *J. Phys. D: Appl. Phys.*, vol. 22, pp. 1243-1251, 1989.
- [11] Y. Oh, and Y. C. Kay, "Condition for precise measurement of soil surface roughness," *IEEE Trans. Geosci. Remote Sens.*, vol. 36, pp. 691-695, 1998.
- [12] S. B. Pollard, T. P. Pridmore, J. Porril, J. E. W. Mayhew, and J. P. Frisby, "Geometrical modelling from multiple stereo views," *Int. J. Robot. Res.*, vol. 8, pp. 3-32, 1989.
- [13] J. Canny, "A computational approach to edge detection," *IEEE Trans. Patt. Anal. Machine Intelli.*, vol. 8, pp. 679-698, 1986.
- [14] R. Y. Tsai, "An efficient and accurate calibration technique for 3D machine vision," In *Proceedings of IEEE Conference on computer vision and pattern recognition* (IEEE Publications), pp. 364-374, 1986.
- [15] R. A. Lane, N. A. Thacker, and N. L. Seed, "Stretch-correlation as a real-time alternative to feature-based stereo matching algorithms," *Image Vision Comput.*, vol. 12, pp. 203-212, 1994.
- [16] W. H. Press, B. P. Flannery, S. A. Teukolsky, and W. T. Vetterling, *Numerical Recipes in C*: Cambridge University Press, 1990.
- [17] K. Falconer, *Fractal Geometry: Mathematical foundations and applications*: John Wiley and Sons Ltd, 1990.
- [18] A. G. Constantine, and P. Hall, "Characterizing surface smoothness via estimation of effective fractal dimension," *J. Roy. Statist. Soc. B*, vol. 56, pp. 97-113, 1994.
- [19] S. Davies, and P. Hall, "Fractal analysis of surface roughness by using spatial data," *J. Roy. Statist. Soc. B*, vol. 61, pp. 3-37, 1999.
- [20] K. Morrison, J. C. Bennett, G. Cookmartin, A. J. McDonald, and S. Quegan, "Very high resolution microwave measurements of the scattering from vegetation," In *Proceedings of IEEE International geoscience and remote sensing symposium* (IEEE Publications), 1999.

## An Accurate Geometrical Error Model for Airborne SAR : A Design Example

Hubert CANTALLOUBE

ONERA, Chemin de la Hunière, 91761 PALAISEAU Cedex, France.

Phone: (33) 1 69 93 62 14, Fax: (33) 1 69 93 62 69, E-mail: cantallo@onera.fr

### ABSTRACT

Many applications of SAR imaging and in particular those involving a registration or a geo-coding step, require an accurate knowledge of the geometry of the image. Furthermore, in the airborne SAR context, irregularities in aircraft motion due to air turbulence, introduce severe distortions in the images.

We have implemented a Geometrical Error Model for our generic off-line BID SAR processor. The GEM provides an image distortion map together with some derivatives with respect to errors in radar parameters and errors in aircraft trajectory measurements (velocity, altitude, oscillations). It allows an efficient estimation of the errors from distortion measurements (tiepoints).

### 1. GEOMETRY OF THE SAR PROCESSOR

The geometry of a SAR image depends on the SAR processor itself. For our BID SAR processor (implemented in the PAMELA software presented on Fig. 9), the images are calculated with a constant squint angle with respect to the nominal trajectory. The nominal trajectory is defined as the linear non-uniform projection of the trajectory to its chord.

This convention is chosen, quite arbitrarily, in order to facilitate the projection of an image without model error. The choice of a constant squint angle versus a constant Doppler frequency is a less questionable choice, since otherwise, in case of strong trajectory non-linearities, a given point on the ground might appear at several different positions in the image. The corresponding focusing point on the ground of a given pixel on the image, is obtained as displayed on Fig. 1. Suppose the pixel lies on the line of which the integration time is centred at T. Then denote N the projection of T on the nominal trajectory. Calculate the intersection between the cone of angle  $\delta$ , the sphere of radius R centred at N and the ground plane.

### 2. SAR IMAGE DISTORTIONS

Depending on the SAR-processor conventions, a given pixel of the SAR (slant range, azimuth) image could be easily mapped to its corresponding point in some

geographic coordinate system. Either the terrain may be assumed "flat" with height the average flight altitude, or a Digital Elevation Model (DEM) may be considered. But the main difficulty is to retrieve the accurate antenna position during the integration time. Also, the estimation of the phase of the signal should be sufficiently precise to avoid ruining the signal samples addition. If, for example, we assume that the phase should not vary more than  $45^\circ$ , it means that the error on antenna position should be below  $\lambda/8$ .

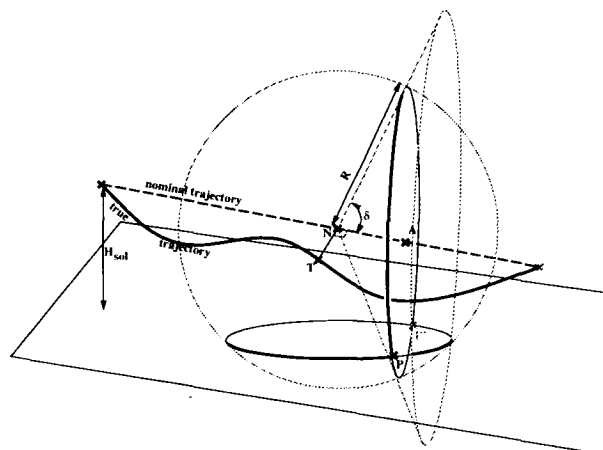


Fig. 1: Geometry of a SAR image for our BID processor

This results comes from the formula linking the phase rotation  $\Omega$  in terms of the wavelength  $\lambda$  of the radar to the difference between the assumed antenna range R and its real value D:

$$\Omega = 4\pi(R-D)/\lambda$$

Typically, for S-band or X-band SAR images, the integration times are approximately 3 seconds and 1 s respectively. Knowing that the aircraft speed is about 80 m/s, this implies that the aircraft position should be estimated with an accuracy of 12.5 mm along a trajectory segment of 240 m for the S-band and 3.75 mm along a path of 80 m for the X-band. The relative precision approximates 1/20 000!

Of course, such a precision on the carrier trajectory is impossible to achieve. However, remark that a global translation error on the trajectory results mostly in a

translation of the image with respect to the ground, provided focusing is tuned to a "flat" terrain. If the focusing exploits the DEM, it will obviously be altered since the elevation is incorrect. That is the reason why DEM focusing requires a pre-registration, at least to an accuracy comparable with that of the DEM.

Another difficulty may come from a slight error on the carrier velocity estimation. At the first order, it leads to a geometrical distortion of the image. Blurring is in fact a second order effect.

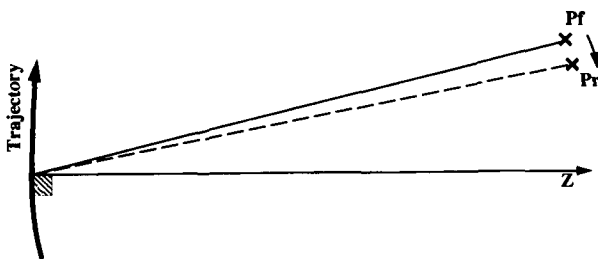


Fig. 2 : First order effect of an underestimation of carrier velocity. The phase correction corresponds to a true point  $P_T$  closer to the zero-Doppler direction  $Z$  than the target point  $P_r$  we are focusing at.

In order to understand this, assume that we underestimate the aircraft velocity. When we correct the phase for a target point (any pixel centre in the image), we underestimate the phase rotation to compensate, meaning that we compensate for a point closer to the sphere centre than the target point "aimed at". This means that the "effectively compensated" point will appear in the resulting image at the "target" pixel position. In other words, the image will be distorted in such a way that offset between the instantaneous flight direction and the direction of the tangent sphere centre (also called the "zero Doppler" direction since, at first order, distance is constant there) is amplified.

The geometrical effect of any low frequency trajectory error can be derived from this principle: The point effectively focused is the point at the same distance to the antenna, having the same radial velocity as the aimpoint was assumed to have with the erroneous trajectory during the image synthesis.

Notice that geometrical distortions of a SAR image may also come from errors in the radar parameters themselves. For example, with the ONERA airborne radar RAMSES, unmodelled delays in the demodulation circuits may introduce a bias on the wavelength  $\lambda$ , which would yield the same kind of distortion than a velocity bias. Clock trigger unmodelled delays may

also introduce a bias in the range measurements, shifting the whole image along the range axis.

### 3. GEOMETRICAL ERROR MODEL

A Geometrical Error Model (GEM) is a routine that establishes both the direct coordinate transform rule from a geographical referential to the image coordinates, and the inverse coordinate transform rule from the image coordinates to a geographical referential. Those transforms should involve an error parameter vector, modelling the low frequencies trajectory errors and some radar parameters errors.

In order to increase the numerical efficiency of the routine, the GEM also provides the derivatives of the transforms as well as their partial derivatives with respect to error parameters.

### 4. AN EXAMPLE OF GEM DESIGN

First of all, in order to create a GEM, one must choose an error parameter vector structure. For the applications illustrating reference [1], we suggested two radar parameter errors: a bias on the radar frequency  $c/\lambda$  and a bias on the near range (range of the first echo sample). This choice was motivated by the waveform type (linear chirp with deramp) and the radar electronics, since those errors can originate from unmodelled time delays in the circuits.

Concerning the trajectory errors, there were used a bias on the initial position (longitude, latitude and altitude), a bias on the heading, a bias on velocity along flight direction, a bias on slope and a set of oscillation terms along the vertical, longitudinal and transversal axes. The number of oscillation terms is "user selectable" depending on the required accuracy of the model. In fact any type of low frequency modelling (such as polynomial expansion, Chebycheff polynomials, Fourier terms...) of the errors could have been used.

Once the error parameters structure is established, computer subroutines for direct and inverse coordinate transformations together with their derivatives, must be provided. It was in fact easier to start with inverse transforms:

We recall that the designed SAR-processor uses constant squint angle with respect to the nominal trajectory, range also measured with respect to the nominal trajectory, cross-range axis as time and, optionally, DEM elevation data. According to those conventions, for a pixel of given coordinates in the image, the

corresponding focusing point on the ground was computed as explained in Section 1. With the focusing point coordinate on the ground and the time from the cross-range image coordinate, its nominal range and radial velocity can be calculated. Thus, from the error-free trajectory, its phase rotation speed is deduced. Thereafter the range and phase are modified according to radar parameter error values, in order to obtain effective range and radial velocity.

Using the corrected trajectory, the point on the ground at a given elevation is determined that has this range and radial velocity with respect to the erroneous trajectory. In fact there are two solutions, one at each side of the aircraft, but only one is on the "imaging side".

Thus at this stage, we have designed the procedure (inverse transform) which computes latitude and longitude as a function of the image coordinates, the altitude and the error parameters.

It was relatively easy, by formal derivation of each program line, to get from this procedure another one giving the derivatives of the inverse transform.

The direct transform is slightly more difficult to compute, since given geographical coordinates and an altitude, the erroneous trajectory allows to deduce at each time, range and radial velocity of the point. SAR-processor design choices (and parameters such as the squint angle value of the single-look) allow to find the time (at mid-integration) when the point was focused, by means of a bracketing iteration which is slow. In practice, the iterative search can be initialised from the solution for a close point, thus accelerating considerably the process when we call the function successively for all the pixels of an image.

The formal computation of the derivatives is however not feasible. The solution was to use the image coordinates from the direct transform and invert the Jacobian matrix of the inverse transform in order to obtain the derivative of the direct transform. In a similar manner, the partial derivatives of the direct

transform are obtained from the partial derivatives of the inverse transform.

Fig.3 to 6 show an application example of the GEM. Two looks had been synthesised in X band with a trajectory from hybridisation of inertial unit and differential GPS (Fig 3). Their squint angles were respectively  $-0.4^\circ$  and  $+5.6^\circ$ . We distorted these looks with the GEM by adding a longitudinal oscillation of 30 meters amplitude to the trajectory (Fig 4). This error induces a mismatch between the two looks, clearly visible on Fig 5 which shows the difference of the two single looks images. To confirm the validity of the model, we synthesised the same single looks from the raw radar signal and the erroneous trajectory of Fig 4. The resulting difference image (Fig 6) shows the same positional error. Observe, however, that the focusing of the image is also impaired, and that the average illumination level is uneven. The reason of the latter fact is the miscorrection of the antenna lobe pattern on the ground, since the true trajectory was that of Fig 3.

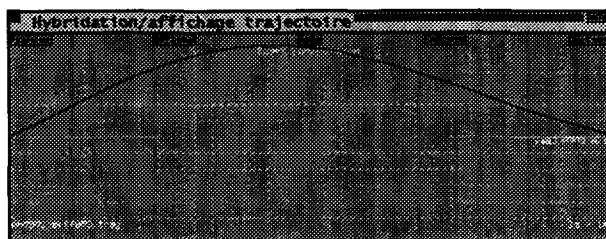


Fig 3 : Example of a real acquisition trajectory (one minute). Deviations from the linear uniform trajectory along the longitudinal axis (amplitude  $\approx 6$  m).

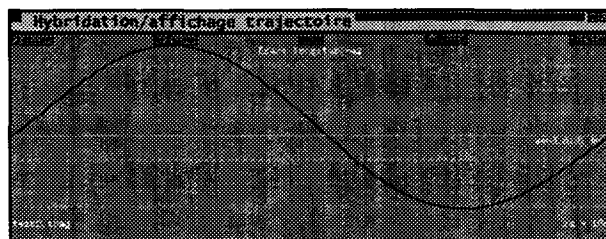


Fig 4 : The trajectory of Fig 3 with a 30-meter wide longitudinal oscillation added.

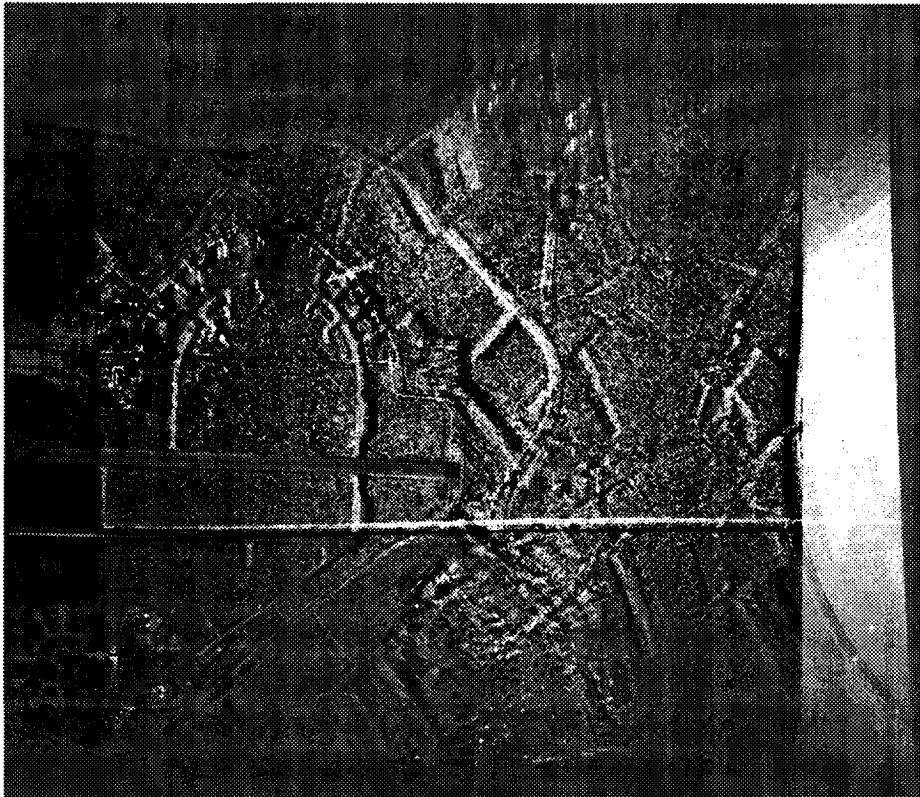


Fig 5 : Misregistration of two single-looks modelled for a 30-meter wide longitudinal oscillation.

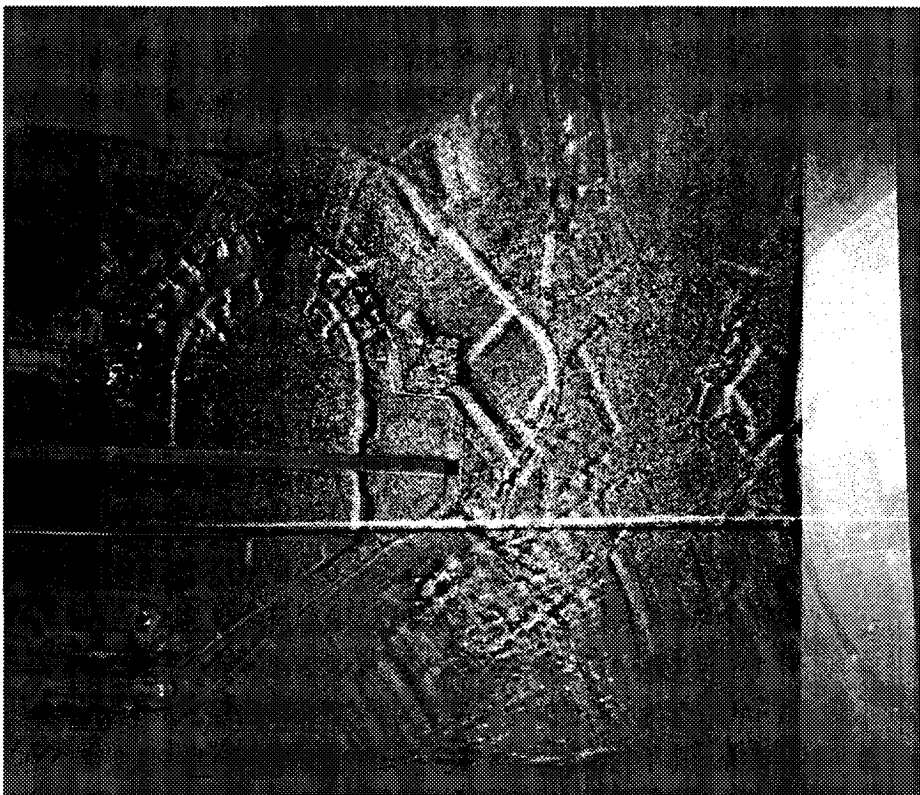


Fig 6 : Misregistration of the same single-looks synthesised with the altered trajectory of Fig 4. Note the unfocusing and the uneven illumination due to erroneous antenna lobe positioning.

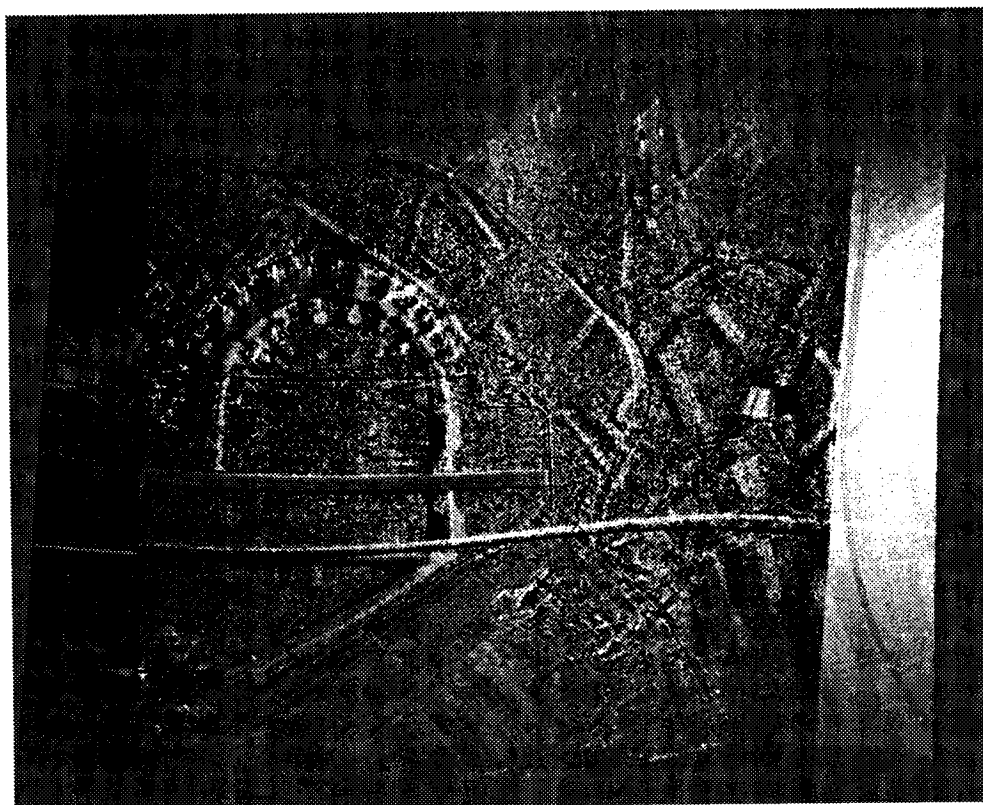


Fig 7 : Misregistration of the two original single-looks modelled for a 30-meter wide transversal oscillation.

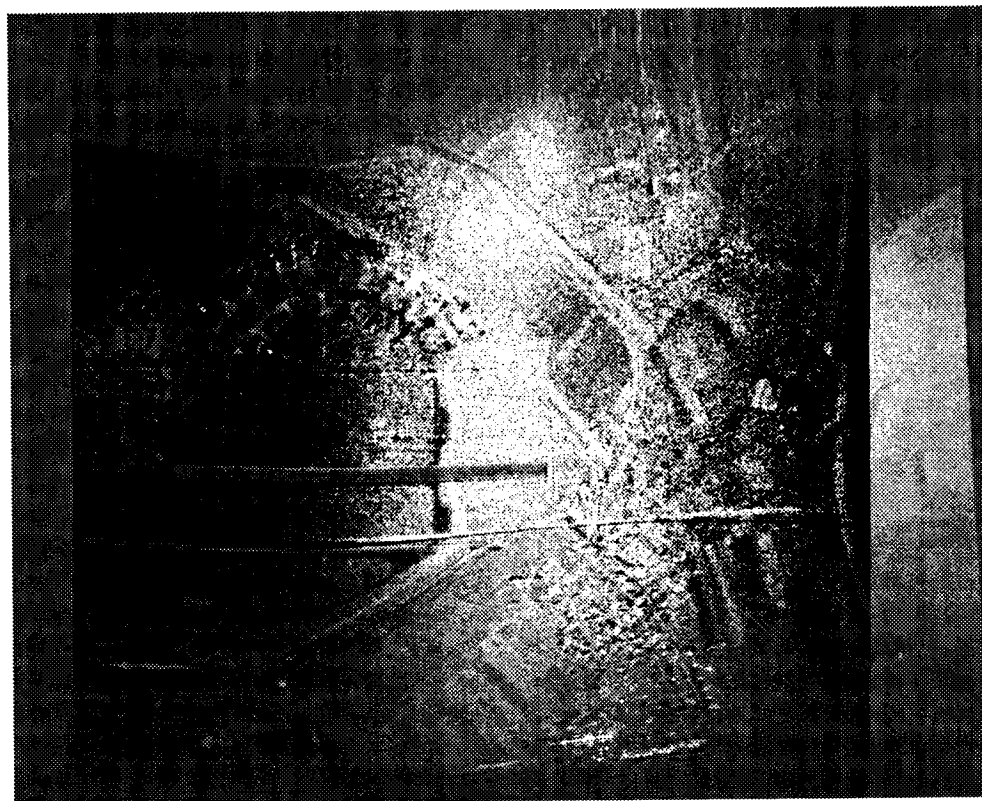


Fig 8 : Misregistration of the single-looks synthesised from the radar signal, with the trajectory altered by the transversal oscillation. The unfocusing and the unevenness of the illumination is even worse than on Fig6.

## 5. CONCLUSION

Because of the high resolution of the airborne SAR images and the irregularities of the aircraft trajectory which may distort them, a Geometrical Error Model (GEM) must be defined.

The GEM gives the transformation from image position to geographical coordinates together with the inverse transformation and the derivatives with respect to some error parameters.

Some illustrations are given in [1]. The images were obtained by the SAR RAMSES designed and operated at ONERA. Among the studied applications of a GEM, multi-look processing, elevation dependent motion compensation, combination of images, repeat-pass interferometry and change detection have been addressed.

## BIBLIOGRAPHY

- [1] Cantalloube H. Some Applications of an Accurate Geometrical Error Model for Airborne SAR, CEOS 99

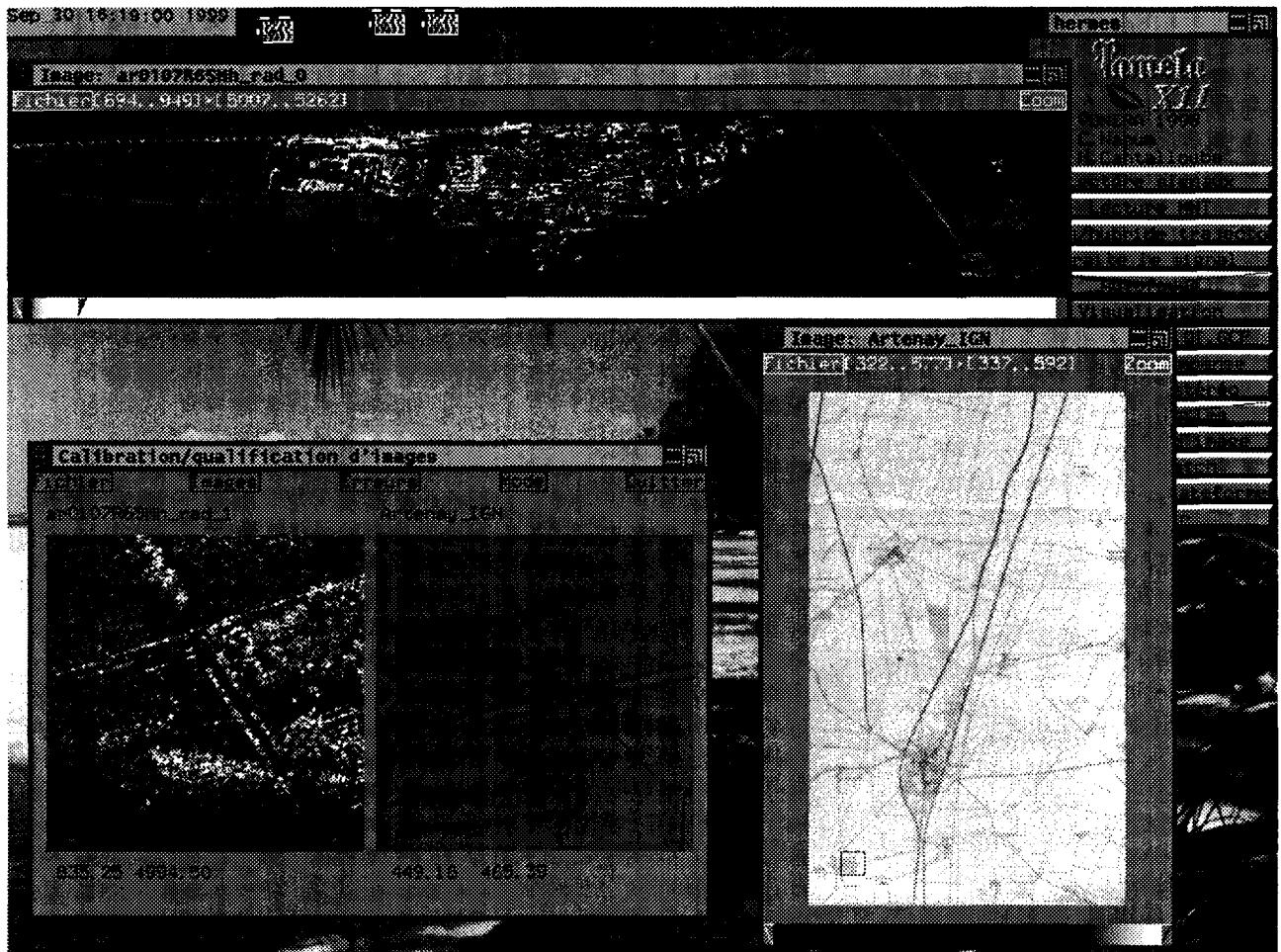


Fig. 9 : General Presentation of the Pamela Interactive Software. This tool developed at ONERA offers several functions such as Synthesis of SAR images, Hybridisation of trajectories, Visualisation, Quality assessment and calibration, Autofocusing, Geocoding, Registration and Combination of images, interferometry etc...



## Airborne Imaging Radar Simulation in Realistic Environment Using Shooting and Bouncing Ray Technique

H.J. MAMETSA<sup>1</sup>, T. CATHALA<sup>2</sup>, A. BERGES<sup>1</sup>, J. LATGER<sup>2</sup>

1: ONERA-CERT/DEMR

2, av. E. Belin, BP 4025 31055 Toulouse Cedex France  
Phone: 33 5 62 25 27 07 email: [mametsa@oncert.fr](mailto:mametsa@oncert.fr)

2: Société OKTAL

2, rue Boudeville 31100 Toulouse France  
Phone: 33 5 62 11 50 25 email: [cathala@oktal.fr](mailto:cathala@oktal.fr)

### ABSTRACT

This imaging radar simulation concept was developed as part of a joint project between the Electromagnetism and Radar Department of ONERA and the OKTAL Company. This paper sets out a specification of the principles. Imagery output from the simulations illustrates the effectiveness of the tool.

### INTRODUCTION

A 3-D realistic radar simulation package applied to multisensor scenarios was developed as a project between the Electromagnetism and Radar Department of ONERA and the OKTAL Company. This partnership respectively associates the expertise of ONERA in radar phenomenology, millimetre wave interaction with targets and clutter, with that of OKTAL in the generation and management of realistic scene databases in the infrared and optical domain using advanced Shooting and Bouncing Rays (SBR) techniques [1, 2, 3]. The objective of this program is to develop simulation tools capable to predict the behaviour of sensors in a realistic environment. This is achieved by coupling terrain database completed by multispectral features and a fast SBR algorithm. For example, a specific purpose is to simulate the response of airborne multisensor equipment to determine the operational contribution of millimetre wave radar coupled with infrared and optical sensors according to a particular scenario. Applications include development and evaluation of new detection and signal processing algorithms and indeed to carry out ergonomic study. Simulation parameters take into account equipment potentialities, the sensitivity to meteorological effects and moving or non-moving target discrimination.

### PURPOSE

Multitude of applications could be treated from the basic principles investigated in this project. This paper deals with the possibility of calculating a radar image comparable with the same one obtained by a specific Synthetic Antenna Radar (SAR) imaging. This paper sets out a specification of the airborne imaging radar principles and examines the results of the first simulations in realistic environment. Operational simulation of the millimetre wave sensor permits us to specify, to evaluate, to qualify and to test the performances and limits of such future systems. Simulation parameters take into account the sensitivity to meteorological effects. To illustrate the effectiveness of the tool for performing research in this field, imagery output from the simulations will be shown.

### TECHNICAL FEATURES

#### Geometrical Realistic Database

Simulations are achieved using geometrical database which represents a numerical model of terrain, relatively undulating, rich in woodlands vegetation, and separated trees (see figure 1). The database is composed of a very accurate high-resolution central area and a surrounding area at a lower resolution. This central area represents a 5 km x 7 km rectangular terrain, containing plane surfaces (crop fields, meadows, forests, lake), linear elements (roads, river) and punctual items (trees, man-made constructions, bridge, pylons with electrical wires). 200,000 faces describe it. The central area is enclosed by a 20 km x 20 km surrounding domain, which is made up of fields, a lake and a river. 7,000 faces describe this environment. Interesting faceted targets, fixed or in motion, land or airborne can be positioned in this scene.

## Features

Specific features and textures related to infrared, optics and radar are provided for each face of the database and the targets. For radar analysis, two classes of materials can be defined: the metallic materials and the environmental clutter with respectively, predominance of specular and scattering effects. Each category of clutter is characterised by its backscattering coefficient average  $\sigma_0$ , which depends on the incidence angle and polarisation components (HH, VV, VH, and HV). Metallic materials (steel, aluminium) follows the Fresnel reflection coefficients  $R_{\perp}$  and  $R_{\parallel}$  (respectively equal to  $-1$  and  $+1$  for the electric field). The plane wave and clutter or target (composed essentially of metallic structure) interaction is specified below.

## Shooting and bouncing rays technique

The shooting ray technique is well adapted to our purpose. A set of rays representing the incident plane wave is shot toward the observed area composed by target and clutter. More specifically, from an emission point, this area is included in a cone in which elementary tubes of four rays are launched. Every tube is defined so that their intersection with the target (respectively the environmental clutter) constitutes a planar surface (respectively the same category of clutter). When in [4], a dense grid of geometrical optics rays (10 rays per wavelength) is shot; our shooting ray number is improved thanks to this planar or homogeneous criterion of intercepted surfaces. A fast Radar Cross Section (RCS) analysis of complex 3-D perfectly conducting targets was carried out using this approach [5].

## Plane wave and clutter interaction

Each category of clutter is characterised by its backscattering coefficient average  $\sigma_0$ , which depends on the incidence angle and polarisation components (HH, VV, VH, and HV). But real simulation values for  $\sigma$  are obtained by including statistical fluctuations (for speckle effects) using an exponential probability density function coupled with a uniform probability density function for the phase of backscattered field. Data on backscattering coefficients are extracted from (sparse) measurement campaigns published in literatures and F.T. Ulaby and M.C. Dobson's works [6].

An important synthesis task was performed in order to take into account frequency bands diversity and polarisation information. Contributions from all rays are summed up at a far-field observation point to obtain the final backscattered field from a definite area.

## Plane wave and target interaction

High frequency asymptotic techniques and shooting rays technique were coupled in order to predict the RCS of complex target [5]. To evaluate the multiple interactions, each ray is followed from one part of the target to another one. For large targets (according to the wavelength), the main contributions come from specular points at surfaces or edges. Second order effects are usually ignored. Thus, the RCS of complex targets can be predicted using the high frequency asymptotic approximations. Now, for faceted targets, three principal methods are applied: Physical Optics (PO) for surface scattering [4, 5, 7] Method of Equivalent Currents (MEC) for edge of finite length diffraction [5, 8] and Geometrical Optics (GO) coupled with both previous methods to take into account multiple interactions. The shooting and bouncing rays technique performs very well in processing these interactions which have not to be neglected because of their high return in wide aspect angle. So, the scattering of intercepted surfaces throughout the multiple bounces, the edge diffraction, the reflection(s)-diffraction and/or diffraction-reflection(s) coupling are considered. Again, contributions from all rays are summed up at a far-field observation point to calculate the final backscattered field, eventually leading to the RCS of the target. We test this method using examples of complex vehicles such as jeep or tank and then, illustrate the necessity to take into account the multi-bounce effects in backscattering prediction.

## Propagation

Attenuation due to vegetation and meteorological parameters has been taken into account. Both effects are predicted by applying the recommendations in 1986 and 1992 of the CCIR (Comité Consultatif International des Radiotélécommunications) in Geneva respectively. The vegetation model was improved after a comparison with a database of measurements for the cases of vegetation with and without leaves [10]. The atmospheric effects cover oxygen and water vapour absorption; and clouds, haze, fog, and different intensities of rain attenuation.

## Radar

The principles used in the radar sensor modelling are flexible and thus preserve the evolutionary concept. This modelling transforms the field in front of the antenna into parameters such as range, radial velocity and angles. Then, this domain is processed according to specific procedures and operating modes. The performed simulation is developed from the matched filter theory and the associated ambiguity function. This approach based on energetic concepts (maximising signal-to-noise ratio for a known signal) is applied on all standard radar systems and remains quite general.

## Antenna

Various antenna models are under consideration according to specific objectives, practical applications and aspect angle coverage requirements.

## Exploitation – Utilisation

Generally, imagery sequences generated by the radar transfer function are visualised using 2-D or 3-D visualisation tools. The visualised output data are voxels, which contain information about backscattering strength and velocity.

In this particular case of SAR simulation, the illustrated calculations (figures 2 and 3) have been conducted using the following parameters:

- flight altitude of the carrier: 2 000 m
- image area: around 2 km x 2 km
- synthetic antenna beamwidth:  $0.032^\circ$
- elevation beamwidth:  $13^\circ$
- incidence angle:  $63^\circ$

1024 range gates of 2 m (i.e. range resolution) were used to calculate the image on figure 2.

They were chosen in order to achieve the same resolution both in cross range and along range. For each resolution cell or pixel, coherent summation of the different contributions from clutter and targets were performed according to the principles described above.

## Summary and prospects

The simulation tool provides realistic RCS and 2-D SAR image calculation for complex geometry or database. The future prospects intend to take into account target description by parametric surfaces, dielectric layers on or material loading in the targets and roughness of the target surfaces. Moreover research is ongoing on strong coupling between target and its immediate environment for other potential applications on radar imagery.

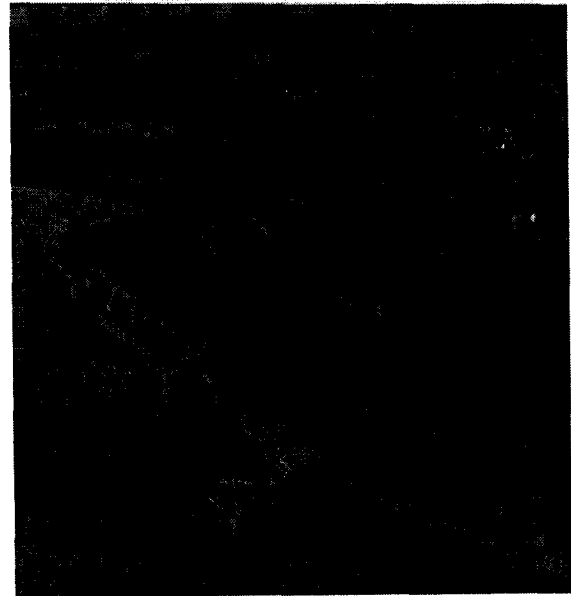


Figure 1: part of a scene from the database in optical domain



Figure 2: specific area from database in optical domain.



Figure 3: radar imaging simulation of the scene.

## References

- [1] P. Pitot, "The Voxar Project",  
IEEE Comp. Graph. Appl., January 1993, pp.27-33.
- [2] J. Latger, J.F. Talaron, "A useful kernel to  
make realistic infrared simulation",  
ITEC'98.
- [3] J. Latger, J.F. Talaron, "ONDE, a numerical tool  
for describing environment",  
Defence and Optronics symposium'96.
- [4] H. Ling, R.C. Chou, S.W. Lee "Shooting and  
Bouncing Rays: Calculating the RCS of an  
Arbitrarily Shaped Cavity"  
IEEE Trans. Ant. Prop., Vol. 37, N°2, Feb. 1989,  
pp. 194-205.
- [5] G. Ramière, P. Pitot, P.F. Combes, H.J. Mametsa  
"Shooting Ray and Multiple Interaction Coupling for  
Complex 3-D Radar Cross Section Predictions"  
Radar 99 Conference, Brest (France), May 99.
- [6] F.T. Ulaby, M.C. Dobson "Handbook of Radar  
Scattering Statistics for Terrain"  
Artech House 1989
- [7] G.T. Ruck, D.E. Barrick, W.D. Stuart, C.K.  
Krichbaum "Radar Cross Section Handbook"  
Plenum Press, New York – London 1970
- [8] A. Michaeli, "Elimination of infinities in  
equivalent edge currents, Part I: Fringe currents  
components", IEEE Trans. Antennas and  
Propagation, Vol. AP-34, 1986, pp. 912-918.
- [10] A. Seville "Vegetation Attenuation: Modelling  
and Measurements at Millimetric Frequencies"  
10<sup>th</sup> International Conference on Antenna and  
Propagation, 14-17 April 1997.

## A new interferogram simulator : 2SIR. Study of coherence losses for tortured reliefs.

D. PETIT<sup>(1)</sup>, F. ADRAGNA<sup>(2)</sup>.

<sup>(1)</sup> Institut de Recherche en Informatique de Toulouse (IRIT)  
 TCI, Université Paul Sabatier, 118 route de Narbonne 31062 Toulouse Cedex, France  
 Ph: +33 5 61 55 63 20 Fax: +33 5 61 55 62 58 email: [petit@irit.fr](mailto:petit@irit.fr)

<sup>(2)</sup> Centre National d'Etudes Spatiales (CNES)  
 QTIS/SR, 18 Avenue Edouard Belin, Bpi 811 31401 Toulouse France  
 email: [frederic.adragna@cnes.fr](mailto:frederic.adragna@cnes.fr)

### ABSTRACT

Recent developments in interferometric radar technique largely highlighted potentialities of radar interferometry for the generation of high resolution DEM (Digital Elevation Models). Nevertheless, the performances of this almost automatic process are strongly degraded for tortured reliefs and for vegetation areas. A research in progress with the CNES (Centre National d'Etudes Spatiales), CSSI (Communication & System, group "Systeme d'Information") and the IRIT (Institut de Recherche en Informatique de Toulouse) proposes to approach these phenomena by the means of simulation. So a new simulator, called 2SIR (Simulateur d'Images Radar & Simulateur d'Interférogrammes Radar), has been developed in which complex scenes can be described. As a first application, this simulator is used to reproduce and study coherence losses for tortured reliefs and the appropriateness of classical coherence to characterize interferograms quality is also discussed.

### INTRODUCTION

SAR interferometric techniques have been already used for several years for the generation of Digital Elevation Model (DEM) [9][10][...]. Whereas processes are well known for ground with small slopes and for homogeneous or sporadic vegetation; on the other hand, in urban areas, or in any situations with involved interactions, these procedures are not adapted or accurate. In spite of its limitations, simulation is a very practical tool to approach complex cases, since ground measurements are not always available or easy to exploit.

Many simulators already make it possible to generate interferometric radar images, starting from DEM [8][11]; however, those are generally not adapted to the context of the high resolution in urban areas, or in vegetal domains, but are to the characteristics of bare soils. Indeed, it is often difficult to take into account the dielectric specificities of each surface element, to

modelize vertical planes or overhang, and especially to simulate volumic interactions.

Therefore, the feature of the new simulator called 2SIR (Simulateur d'Images Radar & Simulateur d'Interférogrammes Radar) is to overcome the deficiencies of DEM by allowing complex situations to be described with the help of simple models. In this aim, it exploits 3 data bases which contain the "3D" information and the dielectric properties of the scene, and it can produce 4 types of images (see Fig 4). As its purpose is to simulate a realistic interferogram, it has been first tested on tortured reliefs to verify its capacity to reproduce coherence losses.

### TECHNICAL FEATURES OF THE SIMULATOR

#### Data Bases

##### *The Materials Data Base*

In this data base, each type of material is characterized by 8 parameters for each type of polarization. The 3 parameters  $\rho_s$ ,  $\kappa$ ,  $\rho_0$  quantify the backscattering coefficient  $\sigma$  (1), which has two components (2):

- A specular part, characterized by  $\rho_s$ , which specifies the specular contribution when then local angle of incidence  $\theta'$  is null (Fig 3). The coefficient  $\kappa$  is a roughness parameter that reduces the width of the specular part.

- A scattering component characterized by  $\rho_0$ .

$$\sigma = 10 \log(\rho) \quad (1)$$

$$\rho = \rho_s \exp(-\sin(\theta')/\kappa) + \rho_0 \cos(\theta') \quad (2)$$

These three parameters are computed by fitting data extracted from the Handbook of F. T. Ulaby and M. C.

Dobson [1]. An example of such a modelization is given in Fig. 1.

A fourth parameter defines the density of targets that will be randomly distributed on a surface or in a volume and a fifth one characterizes the vanishing coefficient for volumic interactions. Additional Red, Green and Blue parameters allow color of the material to be defined in the optical representation (merely to get a better representation rather than to simulate the material response in the optical domain)

*An Objects Data Base*

In order to describe the scene more easily, a few basic objects are provided. Examples are given in Fig. 2. The circles represent randomly distributed targets, which means that speckle would be modeled by a well-known Rayleigh distribution [2].

*A Terrain Object Models Data Base*

The scene is described in a Terrain Object Models Data Base (TOMDB  $\supset$  DEM), by basic objects defined in the Object Data Base (ODB) with some properties specified in the Materials Data Base (MDB). Each element of the TOMDB consists also in 2 links with the 2 other Databases, and an object descriptor that specifies the localization and the sizes of the object.

**Images Generator**

The images are computed in 2 steps (Fig. 3). First of all, targets are randomly distributed within objects, then returned echoes are added to simulate the radar response in an intermediate angular image. The aim of this preprocessing is to manage masked echoes (with the technique called z-buffering) and transparency, effects which can't be ignored with tortured reliefs. The second step consists of a summation of echoes registered at the same range gate to generate the final radar image. As an intermediate angular image is computed, it allows an optical view to be processed (according to geometrical considerations).

Therefore, this application provides 4 types of images, such as the bare example of a kind of building as shown in Fig. 4. Anaglyph grants a quick and practical perception of puzzling "3D" scenes.

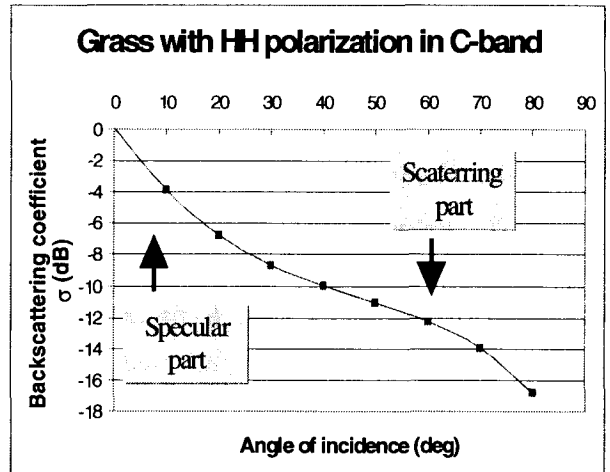


Fig 1: A modeled backscattering coefficient

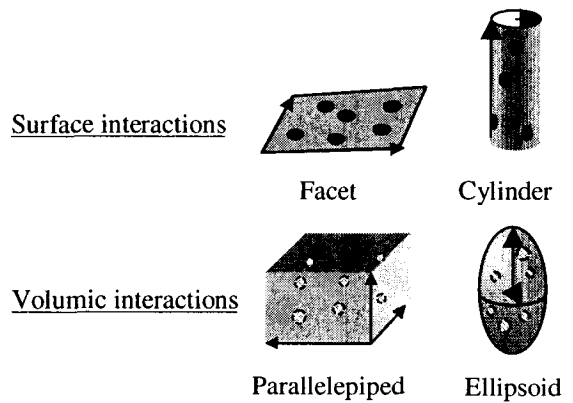


Fig 2: Examples of objects.

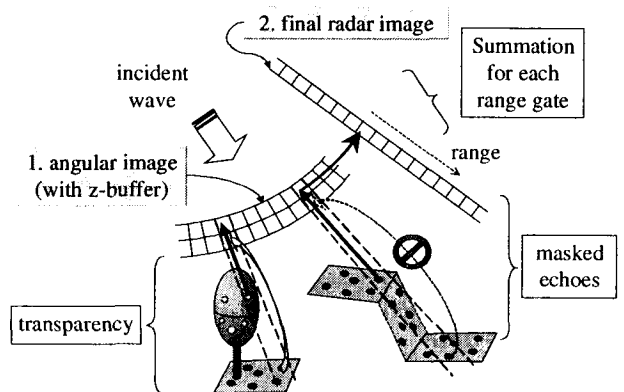


Fig 3: The 2 steps of the image generator.

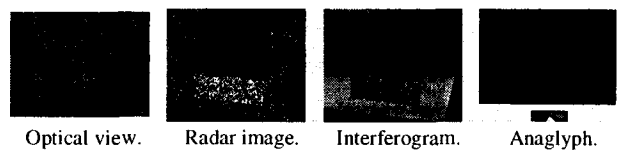


Fig. 4: Types of images produced by 2SIR.

COHERENCE LOSSES

Theoretical Definition

The classical definition of the coherence  $\gamma$  is (3), where  $x_1$  and  $x_2$  are complex images, the function  $E(\ )$  represents the expectation function; and the operator  $*$  is the complex conjugate associated to a complex value.

$$\gamma = \frac{E(x_1 \cdot x_2^*)}{\sqrt{E(x_1 \cdot x_1^*) E(x_2 \cdot x_2^*)}} \quad (3)$$

This function is often used to characterize the quality of interferograms, however it is a little bit risky to use it. Indeed, in practice, only (4) can be computed. Signals are supposed to be ergodic and locally spatially stationary, thus the expectation function is replaced by a local mean  $\langle \ \rangle$ .

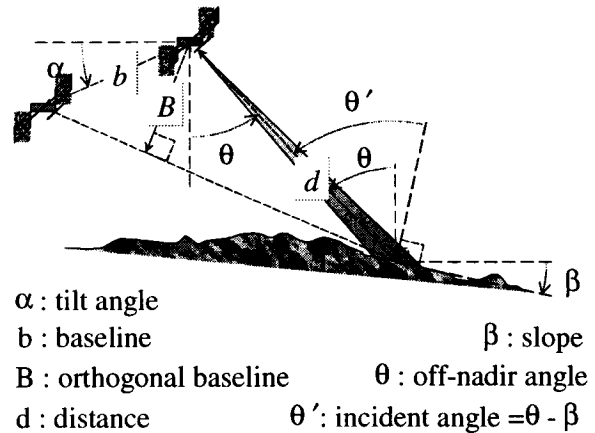
$$\tilde{\gamma} = \frac{\langle x_1 \cdot x_2^* \rangle}{\sqrt{\langle x_1 \cdot x_1^* \rangle \langle x_2 \cdot x_2^* \rangle}} \quad (4)$$

Therefore this estimator is maximal when the phase difference is constant, that is, when there are no fringes. Therefore, the more fringes there are, the lower  $\tilde{\gamma}$  is. In fact,  $\tilde{\gamma}$  evaluates correctly the interferometric noise only if the phase difference is stationary. Besides, the window size (within which the mean operator  $\langle \ \rangle$  is computed) affects the quality of the coherence estimator. With small sizes, this estimator is biased [3][7]. With large windows even though the scene is stationary [4][7],  $\tilde{\gamma}$  falls off since the phase difference turns if there are fringes (and that is what is expected). Thus the classical coherence as defined in (4) do not well estimate interferograms quality.

Theoretical Effects of Slope and Baseline

Under certain conditions (simultaneous survey or negligible terrain decorrelation and atmospheric effects), the phase difference  $\Delta\phi$  between pixels of the two images correctly coregistered can be approximated by (5). This function depends on geometrical parameters described in Fig. 5, and on the wavelength  $\lambda$  and the coefficient  $k$  which worths 1 in bistatic case, and 2 in monostatic case.

$$\Delta\phi = \frac{2\pi}{\lambda} \cdot k \cdot b \cdot \sin(\theta - \alpha) \quad (5)$$



- $\alpha$  : tilt angle
- $b$  : baseline
- $B$  : orthogonal baseline
- $d$  : distance
- $\beta$  : slope
- $\theta$  : off-nadir angle
- $\theta'$  : incident angle =  $\theta - \beta$

Fig 5: Geometry of acquisitions.

For a little variation of  $\theta$ , the phase difference  $\delta\Delta\phi$  follows variation of  $d$  as (6). This formula is equivalent to a frequency shift defined in (7) (where  $f_0$  is the central frequency) [5].

$$\delta\Delta\phi = -\frac{2\pi}{\lambda} k \frac{b \cos(\theta - \alpha)}{d \tan(\theta')} \delta d \quad (6)$$

$$\Delta f = -k \cdot f_0 \frac{B}{d \cdot \tan(\theta')} \quad (7)$$

Practical Definition

Coherence becomes a good estimator of interferograms quality if fringes can be subtracted [6]. Nevertheless, those are usually unknown, since this is what we want to study. In (8), a phase function  $\Phi$  has been introduced to describe fringes that we want to remove [6][7]. Without this knowledge, orbital fringes defined in (9) can at least be deduced, which are fringes due to the baseline on a flat ground. In this case, the slope is null, then  $\theta'$  equals  $\theta$ . The coefficient  $R_d$  is the slant range resolution, and  $n$  is the index in range of the pixel. However, if the local slope is known, or a local gradient of fringes can be computed like in (10), it may be subtracted to improve the accuracy of coherence.

$$\tilde{\gamma} = \frac{\langle x_1 \cdot x_2^* \cdot \exp(-i\Phi) \rangle}{\sqrt{\langle x_1 \cdot x_1^* \rangle \langle x_2 \cdot x_2^* \rangle}} \quad (8)$$

$$\Phi_{orbital} = -\frac{2\pi}{\lambda} k \frac{b \cos(\theta - \alpha)}{d \tan(\theta)} R_d \cdot n \quad (9)$$

$$\Phi_{slope} = \left\langle \nabla Phase \left( \frac{x_1 \cdot x_2^*}{\sqrt{x_1 \cdot x_1 \cdot x_2 \cdot x_2^*}} \right) \right\rangle \quad (10)$$

## APPLICATION

## Simulation

The simulations have been defined so that the produced images are representative scenes as we could observe with the ERS system on soil and rock surfaces. In order to compute coherence, one or two facets in the case of layover have been placed according to the geometrical conditions of acquisition. The specific parameters of simulations are fixed in Table 1.

Parameters:	Nominal values
Wavelength $\lambda$	0.056 meters
Polarization	VV
Material type	Soil & rock
Slant range resolution $R_d$	7.9 meters
Azimuthal resolution $R_a$	3.9 meters
Window size in range	4 pixels
Window size in azimuth	100 pixels
Mean range of the facet	850 000 meters
Tilt angle $\alpha$	0 degrees
Local incident angle $\theta'$ (for layover only)	23 degrees
Orthogonal baseline $B$ (for layover only)	250 meters

Table 1: The default values.

In each case, two interferometric radar images are generated, then (8) is computed. The function  $\Phi$  can be (9) or (10) when the slope is known. Each coherence value is reported in graphs such as in Fig. 6. So as to give the best general survey, each value appears twice, first in a surface representation which gives us an idea of the absolute value, and also in a gray-level image which provides us with an easy way to examine relative variations.

Therefore, in each graph  $2 \times 100 \times 100$  images are produced. We must notice that when  $\theta'$  is close to 0 degree or 90 degrees (for a difference lower than approximately 5 degrees), the simulation may be corrupted. The waves, which appear on the edges in Fig. 7 are a good example. This is not a serious weakness because in the cases it happens, the coherence is low.

## Simulated Effects of Slope and Baseline

In Fig. 6, we remark the expected coherence losses due to a large baseline and a slope. The Fig. 7 tends to prove that coherence loss is almost due to how coherence is computed. Coherence is much better when the local phase gradient has been previously subtracted, since it is

nearly constant and it worths 1. This means that the effect of the phase rotation within pixels is negligible, contrary to the effect of the size of the evaluation window, which is the main cause of coherence loss.

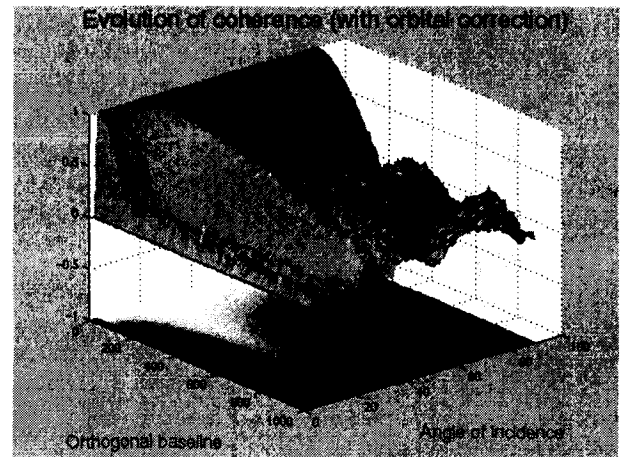


Fig 6: Effects of slope and baseline in the case (9).

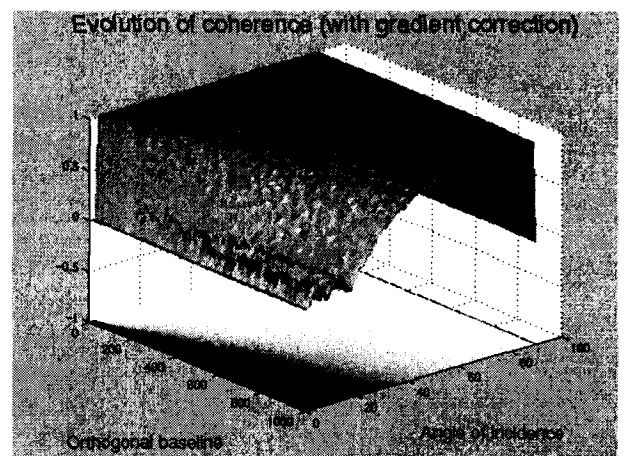


Fig 7: Effects of slope and baseline in the case (10).

## Layover

A priori, two types of layover cases can be distinguished. The case of Fig. 8, in which one facet faces the other one, has been named the "positive layover" case. In this occurrence, multi-paths are allowed, and cases of double or triple bounce may be likely, however those phenomena are ignored in this first approach. Moreover, those effects are actually negligible on natural surfaces, which are too rough to admit of coherent effects.

The second case, shown in Fig. 9, can be found on the top of mountains, hills or buildings, and has been called the "negative layover" case. Obviously, it is hardly to be expected that it can be observed without a "positive layover" unless the radar (for example if it is masked)



does not lighten the surface in front of the relief. However, it is interesting to separate the two effects.

The function  $\Phi$  used in the computation of the coherence is (9). Therefore, Fig. 10 and Fig. 11 show that coherence is even better since each facet is horizontal (*i.e.* there is no residual fringes due to the slope); and because one of them is parallel to the incident wave (*i.e.* little energy is back scattered by the surface, thus only the other one contributes to the signal). On the other hand, coherence is worse when one of the facets is perpendicular to the incident wave. Since the slant range resolution is low, it means that the phase rotation within pixels becomes significant, thus coherence falls off.

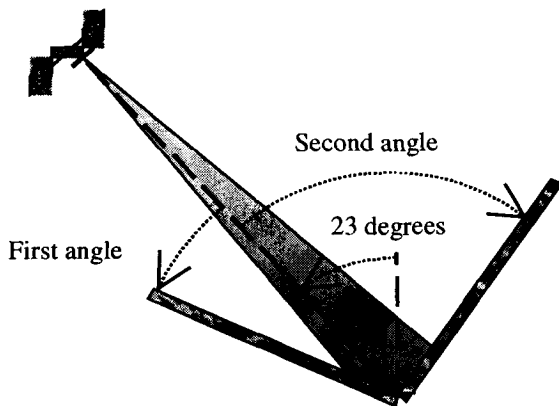


Fig 8: Geometry in the case of the "positive layover".

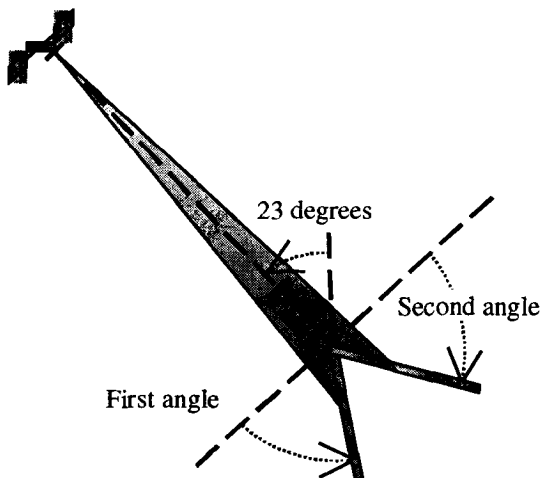


Fig 9: Geometry in the case of the negative layover

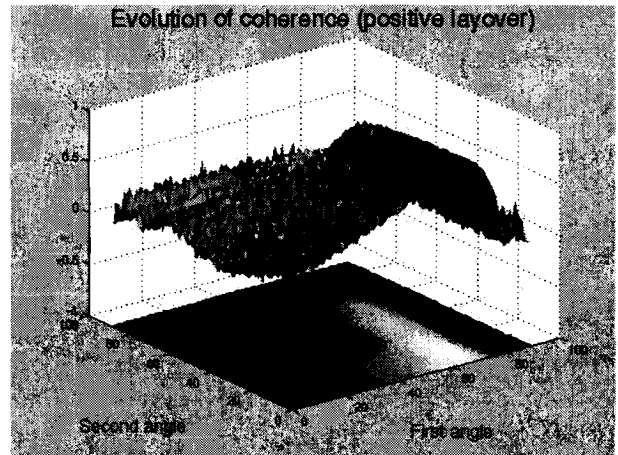


Fig 10: Coherence in the case of the "positive layover".

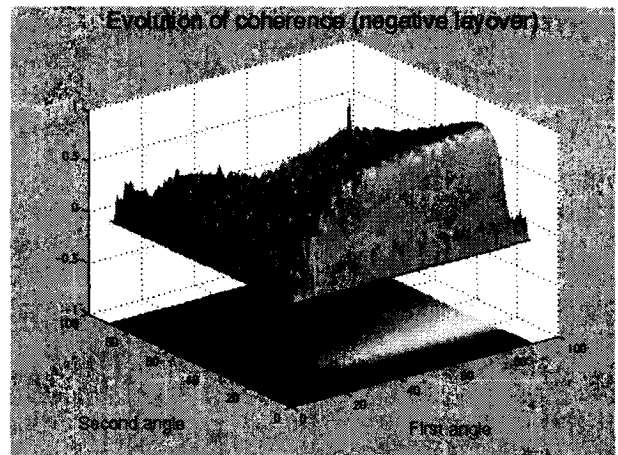


Fig 11: Coherence in the case of "negative layover".

## CONCLUSION

Therefore, all the tests done so far (a great number of not yet published tries on fractal relief and other surfaces, has been made) seem to provide realistic simulations. Owing to the great number of parameters available in 2SIR (material, polarization, angles, shape of the objects, ...) a perfect validation of the simulator is difficult moreover this is not required for our future studies.

However, the next step will be to make tests on the volumic interactions, then to introduce a management of multiple bounces particularly in urban areas.

## ACKNOWLEDGEMENTS

We must express our appreciation to J.D. Durou of the IRIT, L. Neuville and all people who helped us in this task, for giving us their time.

## REFERENCES

- [1] F. T. Ulaby, M. C. Dobson, "Handbook of radar scattering for terrain", Artech House editor.
- [2] T. F. Bush, F. T. Ulaby, "Fading characteristics of panchromatic radar backscatter from selected agricultural targets", *IEEE Trans. On Geosci. Electronics*, vol. GE-13, no 4, pp. 149-157, october 1975.
- [3] R. Touzi, A. Lopes, J. Bruniquel, P. Vachon, "Unbiased estimation of the coherence from multi-look SAR data", *IGARSS' 96, Remote Sensing for a Sustainable Future*, Lincoln, Nebraska, IEEE, vol. 1, pp. 662-664.
- [4] R. Touzi, "Estimation of stationary and nonstationary coherence in SAR imagery", *IGARSS' 98, Sensing and Managing the Environment*, Seattle, Washington, IEEE proceedings, vol. 5, pp. 2659-2661.
- [5] F. Gatelli, A. Monti Guarnieri, F. Parizzi, P. Pasquali, and C. Prati, "The wavenumber shift in SAR Interferometry", *IEEE Transac. on Geosci. and Remote Sensing*, vol. 32, no. 4, pp. 855-865, July 1994.
- [6] A. Monti Guarnieri, and C. Prati, "SAR interferometry : A 'quick and dirty' coherence estimator for data browsing", *IEEE Transac. On Geosci. and Remote Sensing*, vol. 35, no. 3, pp. 660-669, May 1997.
- [7] R. Touzi, A. Lopes, J. Bruniquel, P.W. Vachon, "Coherence estimation for SAR imagery", *IEEE Transac. On Geosci. and Remote Sensing*, vol. 37, no. 1, pp. 135-149, January 1999.
- [8] S. Dupont, F. Perlant, M. Berthod, "SAMI: an InSAR simulator to improve SAR calibration", *IGARSS' 95, Florence, Italy, Quantitative Remote Sensing for Science and Applications*, vol. 1, pp. 559-561.
- [9] S. N. Madsen, A. Zebker, and J. Martin, "Topographic mapping using radar interferometry : processing techniques", *IEEE Transac. On Geosci. and Remote Sensing*, vol. 31, no. 1, pp. 246-256, January 1993.
- [10] S. N. Madsen, N. Skou, K. Woelders, and J. Granholm, "EMISAR single pass topographic SAR interferometer modes", *IGARSS' 96, Remote Sensing for a Sustainable Future*, Lincoln, Nebraska, IEEE, vol. 1, pp. 674-676.
- [11] G. Franceschetti, A. Iodice, M. Migliaccio, D. Riccio, "A novel across-track SAR interferometry simulator", *IEEE Transac. On Geosci. and Remote Sensing*, vol. 36, no. 3, pp. 950-962, May 98.

## ERS attitude errors and its impact on the processing of SAR data

D. Esteban Fernández<sup>1</sup>, P.J. Meadows<sup>2</sup>, B. Schättler<sup>3</sup>, P. Mancini<sup>4</sup>

<sup>1</sup>GAEL Consultant, Cité Descartes, 18 rue Albert Einstein,  
77420 Champs-sur-Marne, France.  
E-mail: [desteban@esrin.esa.it](mailto:desteban@esrin.esa.it)

<sup>2</sup>Marconi Research Centre, West Hanningfield Road,  
Chelmsford, Essex, CM2 8HN, United Kingdom.

<sup>3</sup>German Aerospace Center, German Remote Sensing Data Center,  
Algorithms and Processors, DLR Oberpfaffenhofen 82234 Wessling, Germany.

<sup>4</sup>European Space Agency, Directorate of Application Programmes,  
ESRIN, 00044 Frascati, Italy.

### ABSTRACT

The attitude accuracy of both ERS satellites may deteriorate due to either the failure of some of the available on-board gyros, or because of new AOCS (Attitude and Orbital Control Subsystem) configurations capable of reducing the number of simultaneous working gyros, might lead to inaccurate satellite pointing. This will directly impact on the quality of the acquired SAR data as well as its processing. In this paper, the results of an end-to-end simulation of the ERS SAR instrument performances which takes into account the foreseen attitude inaccuracies will be presented. An analysis on the robustness of the algorithms implemented in ESA's reference SAR processors (i.e. VMP and W-K) when dealing with critical attitude configurations is also presented in order to ensure their suitability in generating data of high image quality. Some examples of scenes acquired during manoeuvres and some nominal products properly modified to include the attitude inaccuracies and processed with the VMP will be analysed in order to verify the theoretical simulation performed.

### INTRODUCTION

A spacecraft is subjected to small but continuous disturbance torques, which can impact either cyclically (i.e. as a stationary random process along the orbit) or secularly (i.e. growing with time) [13]. The ERS Attitude and Orbital Control Subsystem (AOCS) tries to stabilise the vehicle by using spinning bodies called *gyroscopes* (momentum wheels). The attitude reference for a spacecraft is typically obtained for pitch and roll from infrared sensors pointed to the Earth horizon, and for yaw from narrow

field sun sensors aligned to the sun as the satellite crosses the day/night boundary.

Some of the original ERS on-board gyroscopes are not available anymore, and strategies have been already presented [12] in order to extend the lifetime of the remaining ones. Because of new AOCS configurations or gyroscopes failure, the ERS attitude accuracy can be expected to deteriorate.

### ERS ATTITUDE ACCURACY

The loss in attitude accuracy suffered by a spacecraft can be directly modelled [1][2] by means of a squint angle  $\psi$ , defined as the antenna pointing angle offset from the Zero Doppler direction. It is usually found in the literature [1][2] to use instead deviation angles from each one of the axes that constitute the satellite's co-ordinates system. In this sense, the spacecraft may *yaw*, *pitch* and/or *roll* from its nominal attitude thus inducing an error in the SAR antenna beam pointing.

To a first approximation roll has no influence on squint because is similar to an altitude variation, and thus does not affect the synthetic-aperture processing. However, this is only true when the roll is small enough so that the change in illumination of the imaged points on the ground can be neglected. For the ERS case, if this error is of the order of fraction of degree, it can be easily enclosed in the antenna elevation beam synthesis. Otherwise, similar techniques as those used for correcting the earth oblateness (i.e. steering of the sampling window, or modifying the PRF if the steering of the sampling window starts to impact the transmitted pulse position) could be used. On the other hand, range

ambiguities are also impacted by relatively large roll angles; for the SEASAT SAR case a roll error of 0.5 degree would induce an increase of the range ambiguity ratio of around 7 dB (at maximum orbit latitude). An increase of around 3 dB can be thus extrapolated for the ERS SAR, as the 3 dB elevation beamwidth is halve and the PRF is similar to the SEASAT SAR. Nevertheless, even with such a relatively large deviation, the range ambiguity ratio for SEASAT in the useful swath would not rise above -20 dB. For the ERS case, range ambiguities are not considered of great concern due to the lack of ambiguities at closer range and large sigma zero values.

Yaw and pitch errors introduce a squint angle as given by the following expressions [1]:

$$\tan(\psi) = \cos(\theta_0) \tan(\alpha_p) \quad (1)$$

$$\tan(\psi) = -\sin(\theta_0) \tan(\alpha_y) \quad (2)$$

where  $\theta_0$  is the elevation angle at mid-swath,  $\alpha_p$  is the pitch error angle and  $\alpha_y$  is the yaw error angle. For the ERS case, and in the assumption of earth rotation compensation, the sensor attitude is directly related to the Doppler Centroid frequency  $f_{DC}$  by the following relationship [3]:

$$f_{DC} = \frac{-2V_s}{\lambda} \sin \psi \cdot \cos \alpha \cdot \left[ 1 - \left( \frac{\omega_{earth}}{\omega_{satellite}} \right) (\cos \beta \cdot \sin \zeta \cdot \tan \alpha + \cos \zeta) \right] \approx \frac{-2V_s}{\lambda} \sin \psi \quad (3)$$

where  $V_s$  is the spacecraft velocity,  $\omega_{satellite}$  is the satellite orbital rotation rate,  $\omega_{earth}$  is the Earth rotation rate,  $\alpha$  is the angle between the range elevation plane and the spacecraft orbital plane,  $\beta$  is the latitude of the sensor (the angle between the ascending node and the satellite position from the centre of the Earth) and  $\zeta$  is the spacecraft orbit inclination measured from the Earth spin vector to the orbit rate vector. Therefore, assuming both pitch and yaw can be combined linearly we found:

$$f_{DC} = \frac{-2V_s}{\lambda} \left[ \sin(\tan^{-1}(\cos \theta_0 \tan \alpha_p - \sin \theta_0 \tan \alpha_y)) \right] \quad (4)$$

Thus, any pitch or yaw variation generates a Doppler Centroid shift from that expected (i.e. theoretically zero offset for the ERS case if no relative motion between the target and the spacecraft is considered). Furthermore, as a pitch error can be seen as a yaw error for our present

purpose, it is possible to consider only the yaw error when performing an analysis of the consequences of introducing a Doppler offset into a SAR processor.

The performances of a SAR system relies on accurate determination of the Doppler Centroid and the Doppler frequency rate for the matched filter processing in the azimuth dimension. Relatively small Doppler Centroid errors will impact on the signal-to-noise ratio (SNR), the azimuth ambiguity ratio and the point target Impulse Response Function (IRF). Moreover, errors in the Doppler frequency rate  $f_{FM}$  will lead to significant blurring (i.e. defocusing) of the processed image because of a high mismatch in the matched filtering [15]. However, the FM rate is usually not sensitive to spacecraft attitude, due to the fact that the FM rate can be approximated by [3]:

$$f_{FM} \approx -2|V_s| |V_g| / \lambda R \quad (5)$$

at a particular range distance  $R$ , where  $V_g$  is the observed scatterer velocity, and where the acceleration term has been neglected. In fact, for SEASAT, with a FM rate of about -530 Hz/s, the variation is less than 0.5 Hz for a 1 deg pitch and yaw error [9].

If it is assumed that the SAR processor has a robust Doppler Centroid estimator then, to first order, there will be no other impact on the SAR than the geometrical one due to the different perspective of the scene seen by the sensor.

However, both the spacecraft and the target seen on the Earth are in motion. If we take the orbital plane as fixed in space, the targets on the Earth's surface move with respect to the orbit plane with a linear velocity dependant on their latitude  $\beta$  as  $V \approx 460 \cos(\beta)$  [11]; this means that the velocity is maximum at equator (since  $\beta = 0$ ) and minimum at the poles. The consequence of this motion is very similar to a yaw angle: to add an additional Doppler shift. This effect is partially corrected in ERS (usually about an 80%) by means of the *yaw steering*, which tries to compensate the yaw error by adjusting the sensor's yaw in the opposite direction. Another possible way to achieve the same result is by means of modifying the local oscillator frequency or addressing the problem directly in

the SAR processing. If yaw steering is used, the angle  $\rho$  needed to correct this effect is given by [3]:

$$\rho = \text{atan} \left( \frac{\omega_{\text{satellite}} - \cos \zeta}{\omega_{\text{earth}} (\cos \beta \sin \zeta)} \right) \quad (6)$$

Thus, yaw compensation is obviously dependant on the spacecraft latitude  $\beta$ . However, because of orbit perturbations, there is a further Doppler offset which cannot be removed by the yaw steering and that cannot be always neglected, as it can be as high as 4 KHz (worst case), which clearly can result in the Doppler Centroid being in the second azimuth ambiguity window. One consequence of this is that the Doppler Centroid has always had relatively large offsets (although not as large as those of SIR-C, for which up to 8 ambiguities could be expected in the worst case, or up to 15 ambiguities for X-SAR [14]). This situation has forced the ERS SAR processors to always perform an azimuth ambiguity removal before fine estimating the Doppler Centroid.

Some ERS data has been already acquired during critical attitude configurations; for instance, data acquired during out-of-plane manoeuvres, as in the example presented in Fig 1, where the Doppler Centroid is located up to the second azimuth ambiguity. It is possible to determine the platform attitude for this manoeuvre by using expression (4) and taking a measurement of the Doppler centre frequency at the near and far ranges of the swath. Thus, we obtain a linear system of equations that we can solve for the yaw and pitch angles [2]:

$$y = \frac{\lambda}{2V_s \sin \xi} (f_{DC2} \cos \theta_{\text{near}} - f_{DC1} \cos \theta_{\text{far}}) \quad (7a)$$

$$p = \frac{\lambda}{2V_s \sin \xi} (f_{DC2} \sin \theta_{\text{near}} - f_{DC1} \sin \theta_{\text{far}}) \quad (7b)$$

where  $\xi$  is the range beamwidth and  $\theta_{\text{near}}$  and  $\theta_{\text{far}}$  are the near and far swath look angle, respectively. This gives for frame 2709, with a Doppler Centroid of 3399 Hz, a pitch error of  $-0.994$  degree and a yaw error of  $0.468$  degree. For this scene, processed with the VMP ESA ERS SAR processor, the Doppler Centroid has been correctly estimated resulting in a scene of good image quality, as shown in Fig 2. ESA's reference ERS SAR processors robustness to perform the fine Doppler Centroid estimation and azimuth ambiguity removal will be addressed shortly.

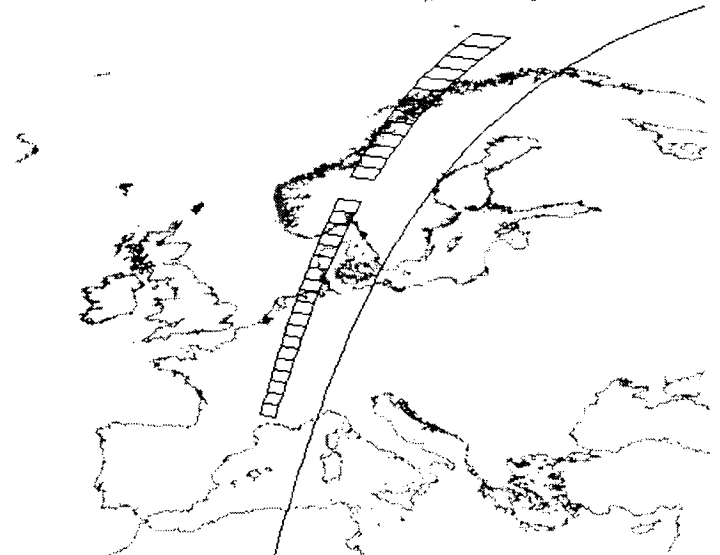
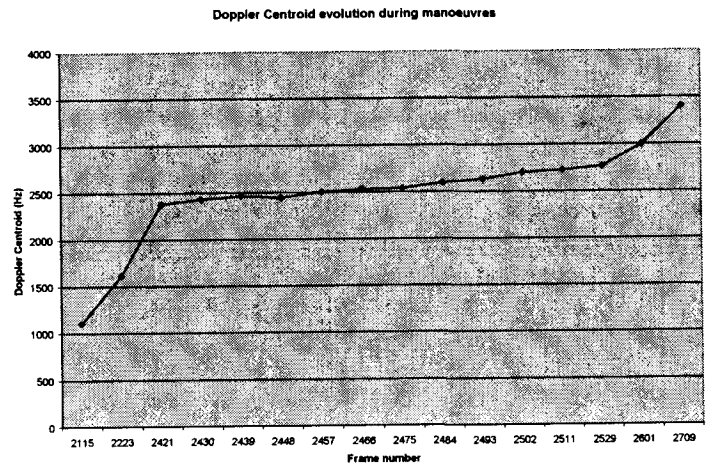


Fig. 1: Doppler Centroid evolution and map location for some frames of ERS-2 descending orbit 10483, acquired during out-of-plane manoeuvres.

## 1. ERS END-TO-END ANALYSIS

Two different situations have been taken into account for the ERS End-To-End analysis performed in order to foresee the impact of critical attitude configurations into the acquired data as well as into the processing and the resulting image quality of the processed products:

- i. The simulation of introducing different small yaw angles in the spacecraft which, as explained above, lead to a Doppler frequency offset. In this part of the analysis, the yaw angles introduced are small enough so that the Doppler offset is kept within the baseband (i.e. Doppler offsets less than half the PRF). The important quality parameters of the processed scene have been obtained as if these offsets were not correctly estimated

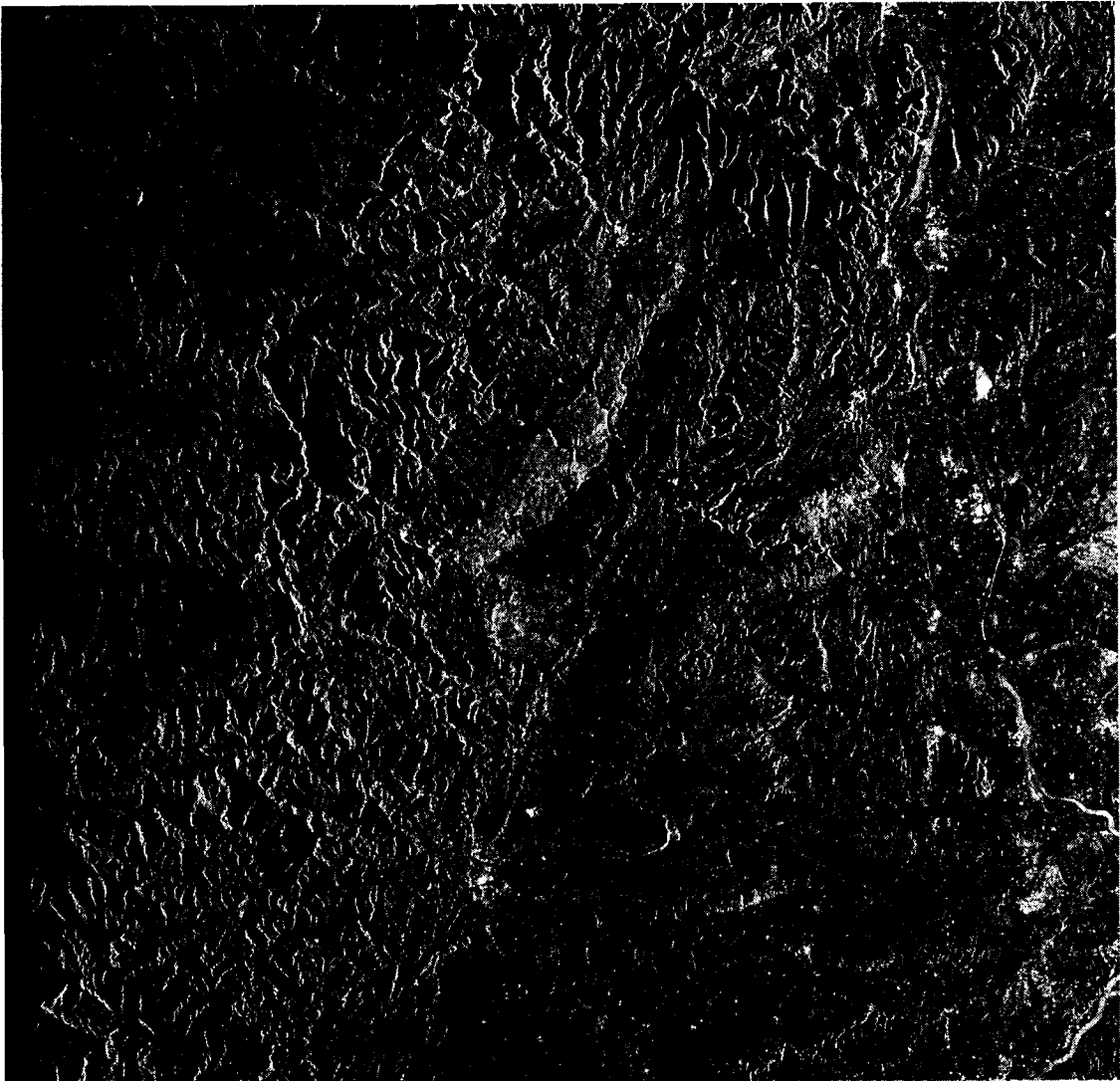
(i.e. the SAR processor assumes that the Doppler Centroid is located under a 50 Hz window).

- ii. The simulation of relatively large yaw angles (compared to the 3 dB antenna azimuth beamwidth, which is around 0.32 degree for the ERS case), which forces the Doppler Centroid to fall either into the first or the second azimuth ambiguity. In this situation it is clear that the problem can arise because of a failure in the processor's azimuth ambiguity removal algorithm. If the estimation is correct, and the fine Doppler Centroid estimation is also successfully performed, no impact on the image quality should appear. It is precisely the purpose of this analysis to tackle the case in which the wrong ambiguity

is selected to process the data, i.e. the case in which the scene is focused in the wrong PRF alias tone. The essential quality parameters have also been derived under this circumstance.

#### Wrong estimation of the Doppler Centroid

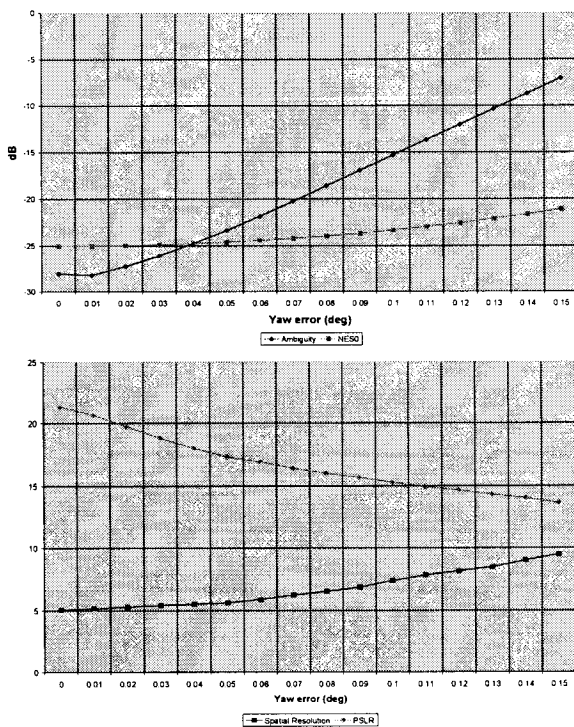
The tolerance of a SAR to attitude errors is primarily determined by the azimuth antenna beamwidth (and, therefore, by the radar wavelength and the azimuth antenna length); for a given aperture size, the antenna pattern beamwidth decreases linearly with the wavelength; for example SEASAT, had an antenna azimuth 3 dB beamwidth of around 1.26 degree, which made it not very sensitive to yaw variations of the order of 0.2 degree (which



**Fig. 2:** ERS-2 orbit 10483 frame 2709 processed into PRI with the VMP ESA reference SAR processor. The acquired zone, located at Besseges (France) and acquired during out-of-plane manoeuvres, exhibits a Doppler Centroid of 3399 Hz, which corresponds to a yaw error of 0.468 degree and a pitch error of 0.994 degree.

would have introduced a 200 Hz Doppler offset and would have worsened the azimuth ambiguity ratio by about 5 dB [9]). For ERS the same yaw error would introduce a Doppler offset of about 900 Hz and would worsen the azimuth ambiguity ratio by more than 20 dB (always assuming the Doppler Centroid is never correctly estimated). For the Shuttle, the Attitude Control System allows a variation of the pitch, roll and yaw up to 1.5 degree. Thus, because the azimuth beamwidth for X-SAR is around 0.15 degree (i.e. ten times smaller than the allowed attitude variation), robust techniques need to be applied when performing the Doppler Centroid estimation.

In this first part of the simulation the final goal is to retrieve the main azimuth Impulse Response Function parameters (i.e. azimuth spatial resolution and the peak sidelobe ratio (PSLR)), radiometric parameters such as the radiometric stability, the radiometric resolution, the Noise Equivalent Sigma Zero ( $NE\sigma_0$ ), and the distributed-target azimuth ambiguity ratio for yaw errors ranging from 0 degree (the perfect side-looking situation) up to 0.15 degree (which corresponds to half the 3 dB azimuth antenna beamwidth). A PRF of 1700 Hz and a flat sigma zero curve of -18 dB have been used for the present purpose. The results are presented in Table 1.



**Fig. 3:** Distrib. target azimuth ambiguity ratio (in dB), Noise Equivalent Sigma Zero (in dB), azimuth spatial resolution (in m) and PSLR (in dB) deterioration as yaw error increases.

Fig 3 presents the losses in distributed target azimuth ambiguity,  $NE\sigma_0$ , spatial resolution and PSLR as the yaw error increases. This is to be expected as ambiguity noise leaks into the processed useful bandwidth every time the yaw error increases. Of particular concern is the situation above 0.07 degree from which the azimuth ambiguity becomes worse than -20 dB. On the other hand, the image quality is not noticeably deteriorated when the Doppler tracker has accuracy better than 50 Hz.

Under critical attitude configurations, an increase of the PRF would provide a slight improvement; if the PRF were increased to 1900 Hz, the  $NE\sigma_0$  would improve by 0.75 dB and the azimuth ambiguity ratio would improve by more than 5 dB in the 0.15 degree yaw error case. The range ambiguities would not suffer from this increase in PRF as they remain always below -50 dB.

<b>YAW error (degree)</b>	<b>0</b>	<b>0.01</b>	<b>0.02</b>	<b>0.03</b>
Doppler offset (Hz)	0	43.87	87.74	131.6
Spatial resolution (m)	5.07	5.16	5.28	5.41
PSLR (dB)	21.35	20.67	19.73	18.81
Rad. Stability (dB)	0.24	0.24	0.24	0.26
Rad. Resolution (dB)	3.36	3.36	3.36	3.38
$NE\sigma_0$	-25.04	-25.02	-24.97	-24.76
Azimuth ambiguity (dB)	-28.05	-28.17	-27.22	-26.08
<b>YAW error (degree)</b>	<b>0.04</b>	<b>0.05</b>	<b>0.06</b>	<b>0.07</b>
Doppler offset (Hz)	175.5	219.4	263.2	307.1
Spatial resolution (m)	5.52	5.63	5.88	6.25
PSLR (dB)	18.01	17.34	16.93	16.41
Rad. Stability (dB)	0.26	0.28	0.32	0.39
Rad. Resolution (dB)	3.38	3.39	3.41	3.43
$NE\sigma_0$	-24.76	-24.61	-24.42	-24.20
Azimuth ambiguity (dB)	-24.78	-23.34	-21.82	-20.23
<b>YAW error (degree)</b>	<b>0.08</b>	<b>0.09</b>	<b>0.1</b>	<b>0.11</b>
Doppler offset (Hz)	351.0	394.8	438.7	482.6
Spatial resolution (m)	6.53	6.85	7.39	7.83
PSLR (dB)	16.01	15.67	15.28	14.95
Rad. Stability (dB)	0.47	0.58	0.71	0.86
Rad. Resolution (dB)	3.46	3.49	3.53	3.58
$NE\sigma_0$	-23.95	-23.64	-23.31	-22.93
Azimuth ambiguity (dB)	-18.6	-16.95	-15.29	-13.63
<b>YAW error (degree)</b>	<b>0.12</b>	<b>0.13</b>	<b>0.14</b>	<b>0.15</b>
Doppler offset (Hz)	526.4	570.3	614.2	658.1
Spatial resolution (m)	8.16	8.47	9.01	9.48
PSLR (dB)	14.67	14.34	14.02	13.64
Rad. Stability (dB)	1.05	1.26	1.51	1.80
Rad. Resolution (dB)	3.64	3.71	3.79	3.89
$NE\sigma_0$	-22.53	-22.08	-21.6	-21.08
Azimuth ambiguity (dB)	-11.97	-10.33	-8.685	-7.06

**Table 1.** Resulting ERS performances for yaw errors ranging from 0 to 0.15 degree.

### Wrong estimation of the azimuth ambiguity number

When the attitude error introduces a yaw angle greater than the 3 dB antenna azimuth beamwidth, the Doppler frequency rate remains almost the same because the slant range is the same, but the Doppler Centroid will differ by a multiple of the PRF, leading to a Doppler ambiguity that must be resolved by the SAR processor. In case the processor fails to match the correct baseband Doppler window (and under the assumption of correct Doppler Centroid estimation), the consequences are:

- i. The acquired image will be displaced from its true location [6], due to the Doppler Centroid offset of the order of  $n$  PRFs (see table 2).
- ii. There will be an additional range migration [6] due to the change in the phase history of every target which will lead to a broadening of the impulse response and, consequently, to a dispersion of the target (see table 2).

Azimuth ambiguity number	1	2
Range displacement (m)	41	82
Azimuth displacement (m)	5862	11724
Additional range dispersion (m)	33	66
Additional range dispersion (range cells)	1.14	2.28

**Table 2. Displacements and additional range migration when focusing at the wrong PRF alias tone.**

Because the radar wavelength is relatively small, the influence of choosing the wrong ambiguity can seem to be less problematic when compared to other SARs (as JERS or SEASAT, which are L-Band radars), where the displacement can be of the order of 23 Km. However, because the azimuth ambiguity number estimation is usually performed upon the estimation of the range migration, there is a real problem for the case of low additional range dispersion (compared to the more than 10 range cells of additional range dispersion with SEASAT), which can make difficult to resolve the PRF alias tone. In the ERS case, the dispersion of the ambiguity would also imply a decrease in peak signal of 0.57 dB for the first ambiguity case and 3.58 dB when wrongly processing in the second ambiguity.

### 2. IMPACT ON ESA's REFERENCE ERS SAR PROCESSORS

As already demonstrated, it is of fundamental importance to perform a very accurate estimation of the Doppler Centroid. The attitude control of a spacecraft allows residual attitude errors that the usual techniques to perform the estimation (namely, Clutter Locking or Doppler Tracking) [8][9] must be based on the raw data provided that the Doppler bandwidth shape coincides with the 3 dB azimuth antenna pattern and its maximum corresponds to the Doppler Centroid. Due to the fact that this technique has difficulties when processing scenes with large variations in sigma zero (e.g., a land-water boundary), a usual modification is to average two or more spectrums shifted in time. This method provides mean accuracy of the order of 5 Hz in the best case (uniformity) and of 30 Hz with large variation in sigma zero.

From the previous analysis, it is evident that a first estimation of the azimuth ambiguity number is strictly necessary with ERS SAR data. Many SAR processors use range cell migration (RCM) techniques because the amount of RCM is directly related to the ambiguity number (as discussed above). This is the approach followed by the VMP, which measures the range walk between two outer looks. However, because this method operates with detected data, it requires image contrast, and may fail only when this requirement is not satisfied in the imaged scene [4][5]. Moreover, this technique provides better results with low frequency SARs (such as L-band) because the registration error is of the order of several pixels. Another technique [5], which works by means of the linear dependence between the Doppler Centroid and the transmitted radar frequency for a given antenna squint angle, allows to obtain the necessary accuracy on low-contrast data.

The W-K SAR processor, on the other hand, computes the Doppler ambiguity number just by obtaining the Doppler Centroid from ephemeris data, which is not accurate enough to obtain fine Doppler Centroid estimate but it is capable to solve the ambiguity number under nominal attitude conditions. However, this technique can be much less robust under the described severe attitude conditions. Once the azimuth ambiguity has been estimated, the fine Doppler Centroid estimation is performed. The VMP uses spectrum estimation techniques, which are always very sensitive to the available SNR, but will often provide the accuracy needed (less that



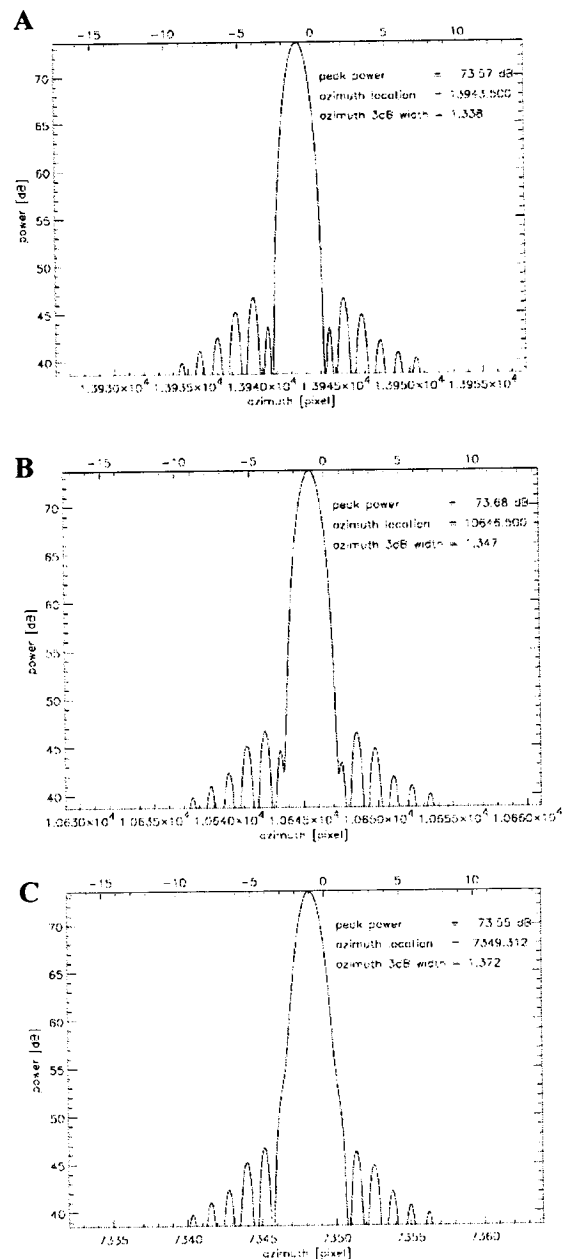
50 Hz). The W-K has two different methods to estimate the Doppler Centroid: either by Clutterlock or in time domain with the Sign-Doppler Estimator algorithm. The last one is more robust and is the one used by default for the standard production of ERS products.

Even if a precise enough Doppler centroid as well as ambiguity estimation is most important for the processing of data acquired under deteriorated attitude situations, the correct focussing capability of a SAR processor in high Doppler frequency situations is also indispensable. Approximations of the azimuth matched filter function (either in the time or in the frequency domain) used in a SAR processor might be limited in their accuracy to low Doppler frequency offsets. Furthermore, Doppler frequency variations over range exceeding one PRF band (variations of about 1 kHz are observed in SAR data acquired in ERS manoeuvre situations) must be handled properly.

Therefore, a variety of ERS raw data products containing point targets for different Doppler situations are simulated and processed with the VMP and - for cross-comparison reasons - with the DLR BSAR processor [17]. The processing of 3 different scenes showing a constant Doppler frequency offset for all point targets of 0 Hz, 4 kHz and 8 kHz shows, that the VMP azimuth resolution suffers an increasing azimuth broadening with increasing Doppler frequency offset, whereas the BSAR maintains the same good image quality under all tested Doppler conditions [16].

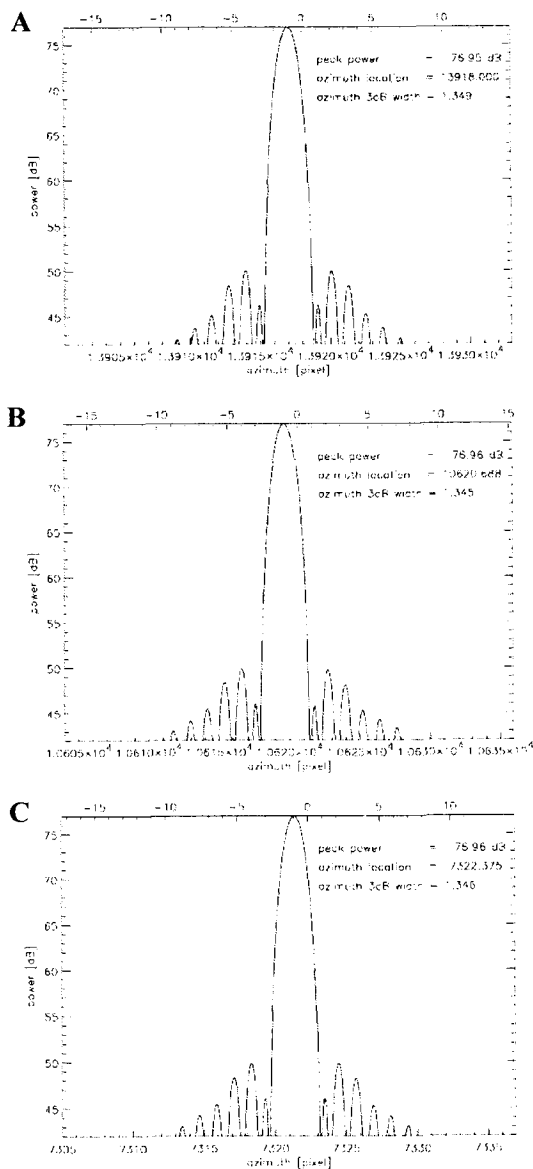
Fig 4 shows the azimuth cut through the VMP point target impulse response function. The first sidelobes start to 'migrate' into the main lobe for the 4 kHz case and are part of the mainlobe in the 8 kHz case. Even if the VMP azimuth broadening is clearly to be seen in the plots, it is only measured to be about 2.2 % in the 8 kHz case. Nevertheless, it is assumed that a more careful azimuth matched filter generation (involving higher order terms) inside the VMP would suppress this artifact completely.

The BSAR proves to be very robust with respect to high Doppler frequency offsets and shows no artefact at all (Fig 5). Note that BSAR is a multi-sensor SAR processor being especially the basis for the operational DLR SRTM/X-SAR processor and thus necessarily has to accommodate large Doppler offsets and variations.



**Fig. 4:** Azimuth cut through of the VMP point target IRF for a constant Doppler frequency offset of: (a) 0 Hz, (b) 4 KHz and (c) 8 KHz.

In a next test series, different Doppler variations over range (up to 2 kHz, including especially PRF boundary crossings) are simulated. The azimuth spectrum of the processed point targets are checked for their correct location with respect to the underlying Doppler frequency to test if the processors follow the Doppler behaviour correctly. No artefacts are observed under the test conditions.



**Fig. 5:** Azimuth cut through of the BSAR point target IRF for a constant Doppler frequency offset of: (a) 0 Hz, (b) 4 KHz and (c) 8 KHz.

It is also worth to note that applications such as interferometry would suffer rather seriously, not only because of possible errors in the SAR processing, but directly by the attitude situation. This is due to the fact that the illuminated area of interest in the along track direction may not have enough overlapping bandwidth between the passes, thus directly impacting on the coherence. The worst case is given by a total loss of coherence, just as the case of two azimuth looks (as a rule of thumb, at least one third of the bandwidth should overlap to allow enough S/N and averaging, although this depends on the scene decorrelation). Thus, as the processed

azimuth beamwidth is around 0.2 degree, it is evident that the critical attitude situations will deteriorate the coherence. On the other hand, in range direction there will also be a coherence loss due to speckle decorrelation, but this is a second order issue when compared to the azimuth impact previously described.

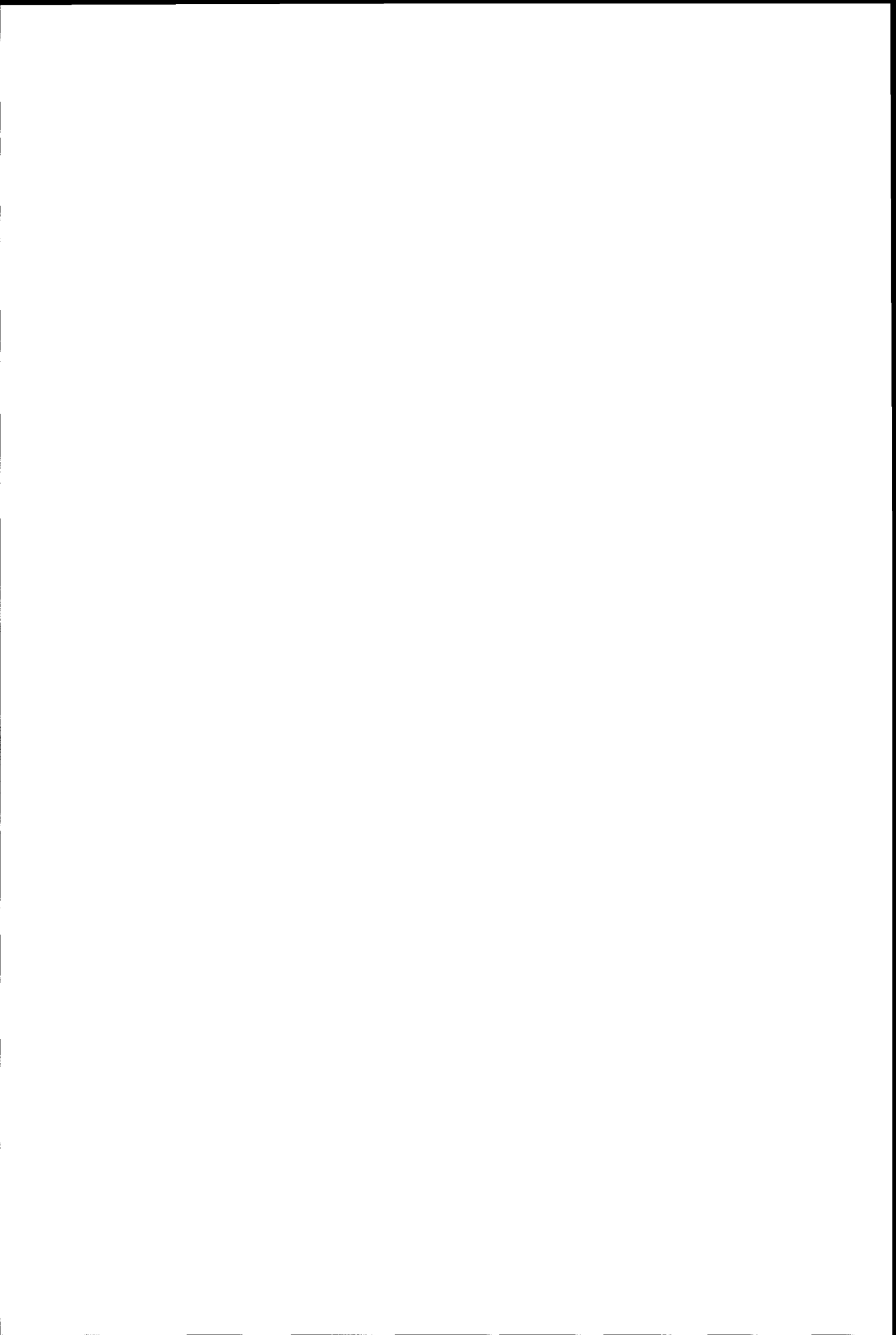
### 3. CONCLUSIONS

This paper has shown how ERS attitude errors impact on the quality of the acquired SAR data through an End-To-End simulation of the ERS SAR performances, as well as its processing with ESA's reference SAR processors. The analysis show that the basic quality parameters can be very impacted even with relatively small attitude errors above 0.07 degrees provided the SAR processor cannot correctly estimate the Doppler Centroid; much more greater attitude errors force the SAR processor to perform a correct estimation of the azimuth ambiguity number. With respect to the Doppler Centroid estimation, the VMP and W-K SAR processors can provide the necessary accuracy. The VMP's ambiguity removal algorithm is robust in front of scenes provided a certain image contrast; W-K's ambiguity removal has been proven to be less robust under severe attitude conditions.

### REFERENCES

- [1] Gunter Schreier (Ed.), *SAR Geocoding: Data and Systems*. Wichmann, 1993.
- [2] C. Wu, J.C. Curlander, A. Di Cenzo. *Determination of spacecraft attitude using synthetic aperture radar data*. The AIAA Sensor Systems for the 80's Conference. CO, Dec. 2-4, 1980.
- [3] R.K. Raney, *Doppler properties of radars in circular orbits*, Int. Journal Remote Sensing, 1986, Vol. 7, No. 9, 1153-1162.
- [4] I.G. Cumming, P.F. Kavanagh, *Resolving the Doppler ambiguity for spaceborne synthetic aperture radar*, Proceedings of IGARS' 86, Zürich, 8-11 Sept. 1986
- [5] R. Bamler, H. Runge, *PRF-Ambiguity Resolving by Wavelength Diversity*, IEEE Transactions on Geoscience and Remote Sensing, Vol.29, No. 6, November 1991.
- [6] F.K. Li, W.T.K. Johnson, *Ambiguities in Spaceborne Synthetic Aperture Radar Systems*, IEEE Transactions on Aerospace and Electronics Systems, Vol. AES-19, No. 3, May 1983.
- [7] Ulaby, F.T., Moore R.K., 1982, *Microwave Remote Sensing*, Vol II, Addison-Wesley.
- [8] S. Norvang Madsen, *Estimating the Doppler Centroid of SAR Data*, IEEE Transactions

- on Aerospace and Electronic Systems, Vol. AES-25, No. 2, March 1989.
- [9] F.K. Li, D. N. Held, J. Curlander, C. Wu, *Doppler Parameters Estimation for Spaceborne Synthetic-Aperture Radars*, IEEE Transactions on Geoscience and Remote Sensing, Vol. GE-23, No. 1, January 1985.
- [10] R.K. Raney, J. Princz, *Reconsiderations of azimuth ambiguities in SAR*. Proceedings of IGARS'86, Zürich, 8-11 Sept. 1986.
- [11] Elachi, C., *Spaceborne Radar Remote Sensing*, 1988, IEEE Press.
- [12] *AOCS Study using 1 or 2 gyros. Final Activity report*, ESA Ref. SOE. E2. CR. 0048. MT, 15/02/1999.
- [13] Wiley J. Larson, James R. Wertz, *Space Mission Analysis and design*, Space Technology Series, Kluwer Academic Publishers.
- [14] C.Y.Chang, J.C.Curlander, *Applications of the Multiple PRF technique to resolve Doppler Centroid estimation ambiguity for spaceborne SAR*, Transactions on Geoscience and Remote Sensing, Vol. 30 No.5, September 1992.
- [15] M. Bernfeld, C. E. Cook, J. Paolillo, C. A. Palmieri, *Matched filtering, pulse compression and Waveform design*, The Microwave Journal, October 1964, pp. 57-64.
- [16] B. Schätler, *ERS Point Target Simulation and Processing with Varying Doppler Frequency Offsets using the DLR Point Target Simulator and the MDA VMP and DLR BSAR Processors*. Technical Note, Version 1.0, September 1999 Deutsches Zentrum für Luft-und Raumfahrt, Oberpfaffenhofen
- [17] H. Breit, B. Schätler, U. Steinbrecher, *A High Precision Workstation-Based Chirp Scaling SAR Processor*, Proc. IEEE Geoscience and Remote Sensing Symposium IGARSS'97, Singapore, pp. 465-467, 1997



## Mosaic Generation using ERS SAR Imagery

P.J. Meadows & P.A. Wright

Marconi Research Centre, West Hanningfield Road,  
Chelmsford, Essex, CM2 8HN, United Kingdom.  
Email: peter.meadows@gecm.com, patricia.wright@gecm.com

### ABSTRACT

This paper gives detail of how mosaics using ERS SAR have been generated for the British Isles, Iceland and Denmark. For the latter two regions, multi-temporal mosaics have been created. These mosaics enable large scale land features and temporal change to be visualised and show potential for land use monitoring on a Europe wide scale.

### INTRODUCTION

The ERS-1 and ERS-2 Synthetic Aperture Radars (SARs) have been acquiring calibrated imagery since September 1991 and July 1995 respectively. During that time, both SARs have acquired large quantities of data [1] over large areas of the Earth's surface. Indeed many areas have been imaged at frequent intervals and some even once per repeat period<sup>1</sup>. With such large quantities of acquired data, there are opportunities for SAR images over large areas covering short periods of time to be available.

ERS SAR swaths are 100km wide, which limits the coverage of large scale land features. In addition, the orientation of SAR swaths is determined by instrument and orbit factors. The generation of SAR mosaics serves two purposes: to convert the location of images to a common map projection and to combine images from different swaths. With the ERS 35 day repeat period, adjacent swaths can, at mid latitudes, be acquired only 3 days apart. At higher latitudes the time separation is shorter.

ERS SAR data has also been used to generate mosaics of French Guyana [2], Germany [3] and Central Africa [4].

### MOSAIC GENERATION

<sup>1</sup> During 1991 and the first 3 months of 1993, ERS-1 was placed in a 3 day repeat period; during the 12 months from April 1994 it was in a 168 day repeat period while at all other times it has been in a 35 day repeat period. ERS-2 has always been in a 35 day repeat period.

To generate a mosaic using ERS SAR PRI imagery several problems have to be overcome. These include the removal of across-track image intensity variations due to the changing radar cross-section of land surfaces across the SAR swath and the masking out of ocean regions. The various steps to generate a SAR mosaic are now described:

- Image selection. Images used for a mosaic should be selected so that the time interval to cover a particular region is as short as possible. In addition, all images should be from either ascending or descending passes - this simplifies the procedure of combining images to form the mosaic. As more descending ERS SAR data has been acquired than ascending data, all three mosaics presented here were generated using descending pass data. For the multi-temporal mosaics, it is necessary to ensure that the time span between the individual mosaics is sufficient to show changes in radar backscatter.
- Image spatial averaging. In order to reduce the computational time plus disk space required to generate the mosaic, individual ERS PRI images are spatially averaged. A root mean square (RMS) pixel block averaging is carried out. The PRI images used for all the mosaics presented here were averaged to give 100m pixels (i.e. using 8 by 8 pixel blocks).
- Geocoding. The geocoding process converts the spatially averaged PRI image, which is supplied in instrument coordinates, into a suitable map projection - here the Universal Transverse Mercator (UTM) map projection has been used. The image latitude and longitude information within the ERS SAR PRI products was found to be adequate for registration of images within the mosaic. The PRI image corner latitude and longitudes were used for the transformation into the UTM map projection. For simplicity ellipsoid geocoding (i.e. with no terrain correction) has been used. The mosaics have an output pixel size of 500m, 300m and 200m for the British Isles, Iceland and Denmark respectively.

- **Across-track radar cross-section variation removal.** ERS SAR scenes exhibit a variation in radar cross-section from near to far across-track positions. This variation needs to be removed to avoid any discontinuity between adjacent swaths. This has been carried out by fitting a straight line to the average range profile of several sample images from the mosaic (those that do not contain any ocean). The fitting uses a least squares technique and was applied to the amplitude version of the PRI imagery. Once an across-track profile was derived, it was removed from all the PRI images prior to geocoding. Where there were significant changes in terrain, another range profile was derived.
- **Swath overlaps.** Adjacent swaths of the mosaic overlap. Where possible, the swaths are selected to ensure a small as possible overlap; this requires that all swaths are either ascending or descending. Two approaches were used for overlapping swaths: intensity averaging of the overlap and using the most recent image. The first of these calculates the intensity average of the pixels in the overlap while the second places the image most recently geocoded on top of an earlier geocoded image. In mountainous regions, the second of these methods is preferable. This is because the location of a mountain top is a function of range position and so any averaging will lead to a blurring of the mountains. The first approach was used for the British Isles mosaic while the second approach was used for the Iceland and Denmark mosaics.
- **Coastline mask.** The visual appearance of a mosaic with any coastal regions is spoiled by the changing radar cross-section of the ocean (not only across-track but also from swath to swath). This can be avoided by the generation of a coastline mask. The mask relies on having suitable coastline data available. This data needs to have a spatial accuracy similar to or better than the mosaic. To generate the mask, the coastline data are geocoded and an ocean mask produced where the ocean is assigned a value of zero and the land is assigned a value of one.
- **Multi-temporal mosaic generation.** As the three mosaics used to produce a multi-temporal mosaic have been generated in exactly the same way, the only task to be performed is to assign the red, green and blue colours to each mosaic. This assignment is selected to give a visually satisfying image.

## THE MOSAICS

Fig 1 shows a mosaic of the British Isles. This was generated using 95 ERS-2 PRI images. The majority of these were acquired between October 1996 and January 1997. The mosaic shows significant radar cross-section differences between, for example, the mainly agricultural regions of England and the more mountainous regions of Wales and Scotland. Within Scotland, there are differences in radar cross-section between the lowland where Edinburgh and Glasgow are located and the adjacent highlands. In Ireland, a high backscatter region can be seen in the west. The major cities such as London, Birmingham, Glasgow and Dublin are clearly seen.

Fig 2 shows three mosaics of Iceland while Fig 3 shows these combined into a multi-temporal mosaic. Each mosaic was acquired during a period of only 34 days and used 36 ERS-2 PRI images. Fig 2 (left) was acquired during late winter. Figs 2 (middle) and (right) were both acquired during mid summer and are just one repeat period apart. The dominant features in these mosaics are the glaciers. In the winter mosaic they have a high radar cross-section while in the summer they have a very low radar cross-section. Changes in these regions can even be seen between the two summer mosaics whereby the size of low backscatter regions have reduced slightly in the later of the summer mosaics. More details of the changes in radar backscatter can be found in [5].

Fig 4 shows the multi-temporal mosaic of Denmark and surrounding countries - Norway to the upper left, Sweden to the upper right, and Germany at the bottom. Each of the three mosaics comprised 32 ERS-2 PRI images. Each mosaic was acquired over a period of 15 days in April 1997, July/August 1997 and November 1997 (i.e. in spring, summer and early winter). The combination of colours for the three mosaics was chosen to give a pseudo true colour image where agricultural areas are mainly green. As with the British Isles mosaic, the major cities are clearly visible: Copenhagen, Denmark, Hamburg, Germany and Gothenburg, Sweden as well as many towns. The majority of Sweden and the part of Norway shown in the mosaic had a similar radar backscatter over the three mosaics as indicated by the grey/purple colour - this is for forested regions. The southern coastal region of Sweden shows much greater change in backscatter as indicated by the green/blue colours - for agricultural regions. The majority of Denmark and Germany is also green/blue indicating



Fig 1: British Isles mosaic generated from ERS-2.SAR.PRIs acquired between October 1996 and January 1997.

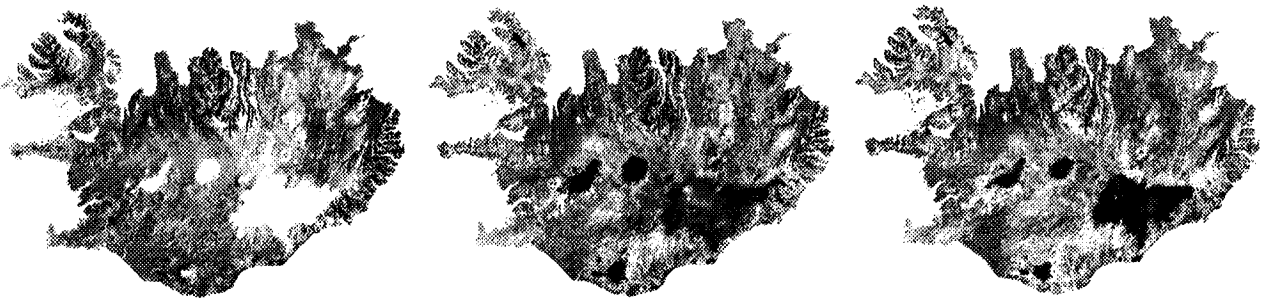


Fig 2: Iceland Mosaic generated from ERS-2.SAR.PRI images acquired between 1<sup>st</sup> February and 6<sup>th</sup> March 1996 (left), 5<sup>th</sup> June and 9<sup>th</sup> July 1997 (middle) and 10<sup>th</sup> July and 13<sup>th</sup> August 1997 (right).

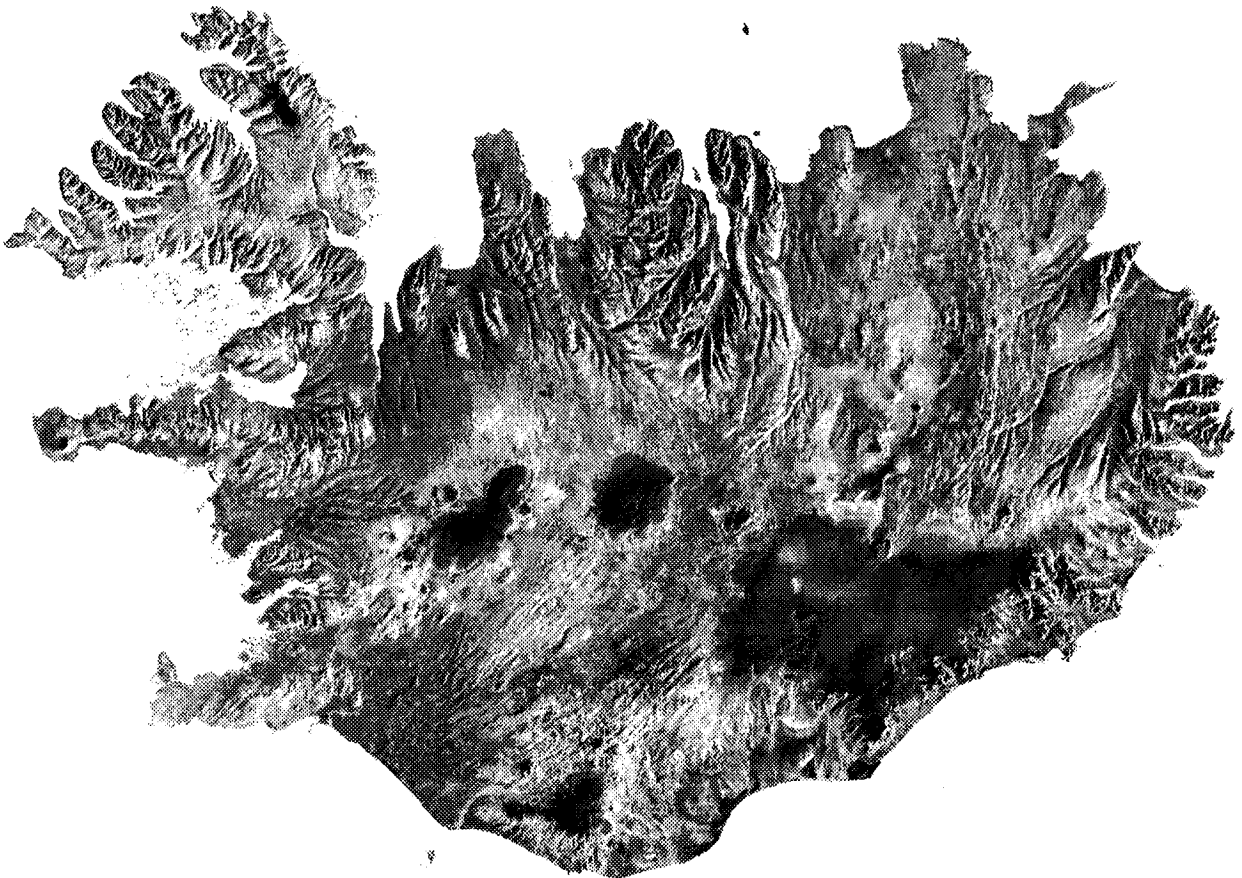


Fig 3: ERS-2 SAR multi-temporal mosaic of Iceland.





Fig 4: ERS-2 SAR multi-temporal mosaic of Denmark.

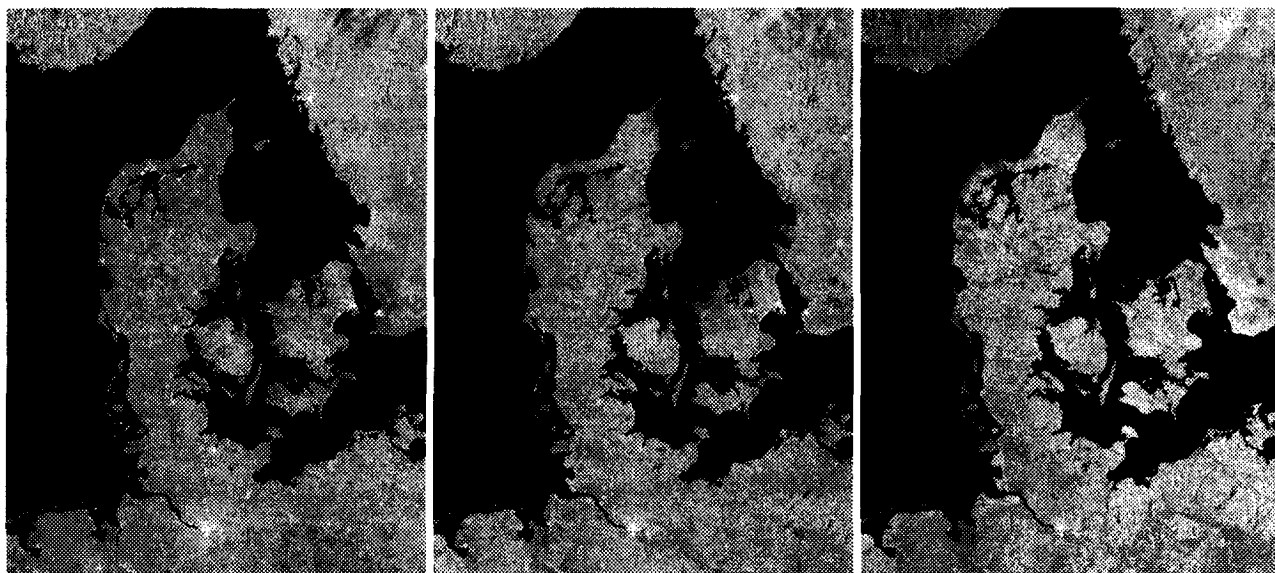


Fig 5: Denmark Mosaic generated from ERS-2.SAR.PRI images acquired between 10<sup>th</sup> April and 25<sup>th</sup> April 1997 (left), 24<sup>th</sup> July and 8<sup>th</sup> August 1997 (middle) and 6<sup>th</sup> November and 21<sup>st</sup> November 1997 (right).

agricultural regions. Many lakes within Sweden and eastern Germany are clearly visible - fortuitously the majority of these have appeared blue. Fig 5 shows the three individual Denmark mosaics. The change in radar backscatter between these three mosaics is much smaller than for the Iceland mosaics. Nevertheless changes can be seen, especially between the November mosaic and the others - the agricultural regions have a higher radar backscatter. There are also obvious changes in the north eastern part of Sweden and for the part of Norway shown in the mosaics.

#### CONCLUSIONS

The mosaics of the British Isles, Iceland and Denmark presented in this paper clearly show that large area land features can be visualised using this technique. As the mosaics are presented in a standard map projection, additional data from other sources can be used to complement the SAR data. The British Isles mosaic shows differences in radar backscatter over large areas while the Iceland mosaics show that large area changes in radar backscatter occur as a function of season. As the three mosaics used to generate the Denmark mosaic were acquired over three seasons, there are sufficient changes in radar backscatter for agricultural regions to clearly show distinction with the forested regions of Sweden and Norway.

Wide swath products from the forthcoming ENVISAT ASAR instrument will enable mosaics, including multi-temporal mosaics, to be generated more easily than has been possible with ERS SAR products.

#### REFERENCES

- [1] D'Elia, S. & Jutz, S., 'SAR Mission Planning for ERS-1 and ERS-2', *ESA Bulletin*, 90, pp 62-70, 1997.
- [2] J.-P. Rudant, 'The 'Petit Saut' Dam in French Guiana seen by ERS-1 and JERS-1', *Earth Observation Quarterly*, No 54, December 1996.
- [3] DLR/German Aerospace Centre, 'Radarmap Germany', [http://isis.dlr.de.services/radarmap\\_en/index.html](http://isis.dlr.de.services/radarmap_en/index.html)
- [4] De Grandi, F., Malingreau, J.P., Leysen, M., Rauste, Y., Simard, M. & Mayaux, P., 'Wither Radar Global Mapping of the Tropical Forest: New Avenues from the TREES ERS-1 Central Africa Mosaic, Proceedings of the Third ERS Symposium on Space at the Service of our Environment, ESA SP-414, Florence, Italy, 14-21 March 1997.
- [5] Meadows, P.J. & Rott, H., 'ERS SAR multi-temporal mosaic of Iceland', *Earth Observation Quarterly*, No 61, February 1999.

## Location accuracy of edge detectors for SAR images

Olivier Germain and Philippe Réfrégier

Laboratoire Signal et Image, École Nationale Supérieure de Physique de Marseille,  
 Domaine universitaire de Saint-Jérôme, 13397 Marseille cedex 20, France.  
 Tel: 33 4 91 28 88 09, Fax: 33 4 91 28 82 01, Email: germain@lsi.u-3mrs.fr

### ABSTRACT

We here study the spatial accuracy of well-known edge detectors for Synthetic Aperture Radar (SAR) images. The likelihood ratio (LR) edge detector is first considered. We show that this detector provides biased location of the edge, if it is not a perfect step edge of known orientation or if the speckle is correlated. A simple model enables us to interpret this observation and to evaluate the bias. Finally, a similar study is addressed for the maximum likelihood (ML) estimation of the edge position.

### I. INTRODUCTION

Segmentation of SAR images has been a subject of intensive research, leading, in particular to various speckle-dedicated edge detectors [1]-[4]. In 1995, Oliver *et al.* proposed a two-stage algorithm which first detects edges optimally using the LR operator and then determines more accurately the edge position with ML estimation [3]. Actually, both stages use the same radiometric criterion but with different analyzing window configuration. This algorithm was designed for ideal, straight, step edges, of known orientation. We first show that the location of non perfect edges (like sinuous edge, edge corrupted by correlated speckle or with an orientation different from the assumed one) with the LR method is systematically biased. A simple model enables one to interpret this observation and yields an approximated expression of the bias. We then study the location of non perfect edges with the ML method.

### II. EDGE DETECTION METHODS

In this section, we present more precisely the two edge detectors, namely the LR and the ML methods [3]. The LR method uses a Scanning-Window Central-Edge (SWCE) configuration (cf. fig. 1). The image is thus scanned with a window split in two equal parts. For each position of the window in the image, the presence of an edge is tested using the Neyman-Pearson strategy. For this purpose, one estimates the log-ratio of the likelihoods of two hypoth-

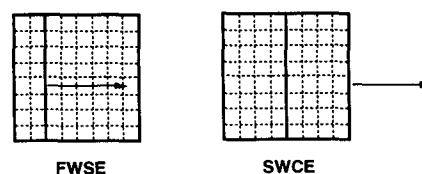


Fig. 1. Two different window configurations for edge detection. Fixed-Window Scanning-Edge is used for the ML algorithm while Scanning-Window Central-Edge corresponds to the LR algorithm.

esis ( $\mathcal{H}_1$ : an edge is present,  $\mathcal{H}_0$ : no edge is present). Assuming a white gamma model for the speckled image intensity distribution finally yields the following expression:

$$D = n \left( \log \frac{m_1 + m_2}{2} - \frac{\log m_1 + \log m_2}{2} \right), \quad (1)$$

where  $m_1$  and  $m_2$  are the empirical means estimated in the two sub-regions and  $n$  is the total size of the window. The window position that maximizes  $D$  is then the LR estimate of the edge position. The LR detector is optimal for edge detection since it gives the best trade-off between probability of detection and probability of false alarm. Edge location is a different issue, related to estimation and not decision. However, the LR filter is practically used to perform edge location when edges are extracted as maxima of the edge strength map. This latter image  $\mathcal{D}(x, y)$ , is obtained by computing  $D$  for each position  $(x, y)$  of the SWCE (see [5] for example).

The ML method relies on a Fixed-Window Scanning-Edge (FWSE) configuration (cf. fig. 1). Here, an edge is assumed to be present in the fixed window and the aim is to determine its most probable location. For that purpose, we assume that the window is composed of two sub-windows in which, the intensities follow white gamma laws of different means. We test for each possible position of the edge within the window and retain the one that maximizes the likelihood of the scene, relatively to this model. The ML estimation of the edge position is the one

that minimizes the following expression:

$$L = n_1 \log(m_1) + n_2 \log(m_2), \quad (2)$$

where  $m_1$  and  $m_2$  are the empirical means estimated in the two sub-regions and  $n_1$  and  $n_2$  are the size of the two sub-regions.

### III. EDGE LOCATION WITH THE LR DETECTOR

#### A. Experimental observation of the bias

In this section, we provide examples which reveal that edge location with the LR filter is biased in some situations. For this purpose, we synthesized speckled edge images and processed them with the LR filter, using a vertical,  $10 \times 10$  window (fig. 5). Edges were extracted with a constrained watershed algorithm.

When the edge is an "ideal" step (fig. 5, line 1), the LR filter yields a correct location. On the other hand, for different types of "non-ideal" edges, we observe a bias towards the darker side. In the first example, the step edge was tilted so that the orientation of the window is no longer adapted (fig. 5, line 2). This case was already studied in [6]. In the second example, the edge is not a straight line but a sinuous frontier (fig. 5, line 3). The third example (fig. 5, line 4) shows the location bias when the ideal reflectivity image is blurred by the point spread function (psf) of the instrument, thus leading to correlated speckle.

One can notice that the occurrence of the bias depends on whether the edge is "ideal" (the edge is a step, vertically oriented) or not. We conjecture that when a "non ideal" edge is filtered, the estimation of the means nearby the frontier is somehow degraded, yielding a false location of the edge. We explore more precisely this conjecture in the next section.

#### B. A phenomenological model to evaluate the bias

We propose a simple phenomenological model to interpret the results observed in the previous section and to give an approximated expression of the bias.

If the window is shifted along the  $X$  axis (axis of equation  $y = 0$ ) across the edge, then the edge position estimate  $\hat{x}$  is the one that maximizes the LR response along this axis:

$$\hat{x} = \underset{x}{\operatorname{argmax}} \mathcal{D}(x, 0). \quad (3)$$

The bias  $\delta$  is then defined as the expectation of the difference between the estimated edge position and the real edge position (say  $x = 0$ ):  $\delta = \langle \hat{x} \rangle$ . In our phenomenological model, we consider that the bias can be approximated by applying the LR filter on the

speckle-free image, that is to say an image made of two domains of constant intensities  $\mu_1$  and  $\mu_2$ . Let  $M_1(x)$  and  $M_2(x)$  be the means estimated on the speckle-free image, within the two regions when the window is at the position  $x$  on the  $X$  axis. We then propose to do the following approximation :

$$\delta \simeq \underset{x}{\operatorname{argmax}} \phi(x), \text{ with :}$$

$$\phi(x) = \left[ \log \frac{M_1(x) + M_2(x)}{2} - \frac{\log M_1(x) + \log M_2(x)}{2} \right]. \quad (4)$$

Let us analyse the behaviour of the plots  $M_1(x)$  and  $M_2(x)$  with the help of figures 2 and 3. On these

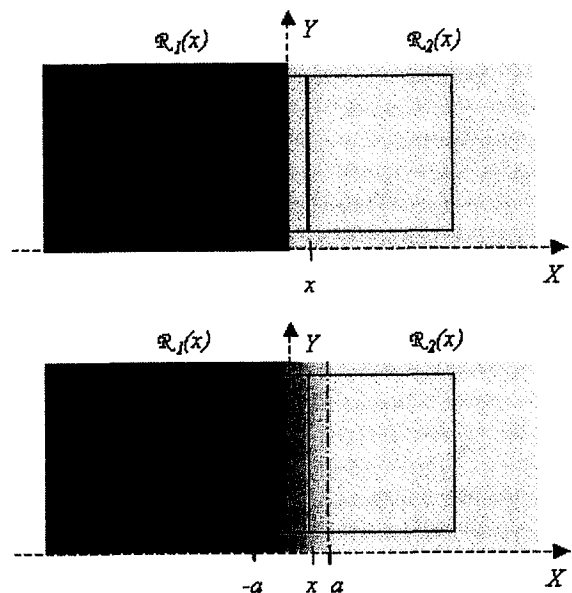


Fig. 2. Top: "Ideal" edge. Bottom: "Non ideal" edge with a "mixture zone" of length  $2a$ .

figures, we have set  $\mu_2 > \mu_1$  and we have introduced a phenomenological positive parameter  $a$  that gives the size of the "mixture zone". In the case of an "ideal" edge,  $M_1(x)$  is constant ( $M_1(x) = \mu_1$ ) for any  $x \leq 0$  and increases linearly with  $x$  (until it reaches  $\mu_2$ ). Similarly,  $M_2(x)$  is constant ( $M_2(x) = \mu_2$ ) for any  $x \geq 0$  and decreases linearly (until it reaches  $\mu_1$ ) when  $x$  decreases. Things are slightly different for a "non ideal" edge.  $M_1(x)$  remains constant ( $M_1(x) = \mu_1$ ) as long as  $\mathcal{R}_1(x)$  does not enter the zone containing a mixture of the two intensities  $\mu_1$  and  $\mu_2$ , i.e. for  $x \leq -a$ . Then  $M_1(x)$  increases with  $x$  towards  $\mu_2$  but not in a linear manner. Similarly,  $M_2(x)$  remains constant ( $M_2(x) = \mu_2$ ) as long as  $x \geq a$  and non-linearly decreases towards  $\mu_1$  when

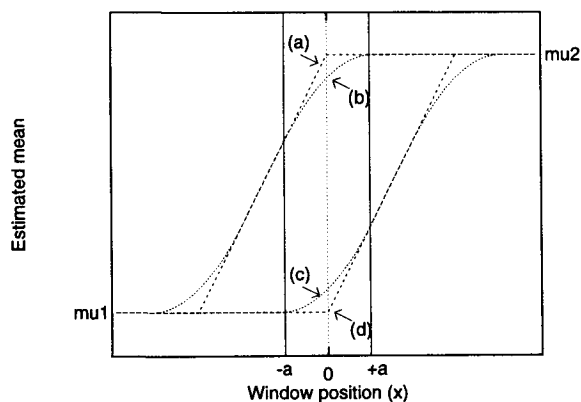


Fig. 3. Typical variation of the estimated means as the window is shifted across the edge. (a)  $M_2(x)$  for an "ideal" edge. (b)  $M_2(x)$  for a "non ideal" edge. (c)  $M_1(x)$  for a "non ideal" edge. (d)  $M_1(x)$  for an "ideal" edge. The means are computed on the speckle-free images.

$x$  decreases. We propose to model the behaviour of  $M_1(x)$  and  $M_2(x)$  in the interval  $x \in [-a, a]$ . As mentioned above, this behaviour is not necessarily linear and we therefore use quadratic expansions:

$$\begin{aligned} M_1(x) &\simeq \mu_1 + k(x+a)^2 \Theta(x+a), & (5) \\ M_2(x) &\simeq \mu_2 - k(x-a)^2 \Theta(-x+a). \end{aligned}$$

where  $k$  is a positive constant and  $\Theta$  is the Heaviside function. Combining equations 4 and 5 and expanding the calculation to the second order, one can obtain the following expression:

$$\delta = a \frac{1-\rho}{1+\rho} \quad \text{with: } \rho = \mu_2/\mu_1, \quad (6)$$

which does not depend on  $k$ . Although it is very simple, this model permits to describe three main facts:

- the bias is towards the darker side (see the sign of  $\delta$ ),
- the absolute value of the bias increases with the edge contrast  $\rho$ , (approximately as  $\left| \frac{1-\rho}{1+\rho} \right|$ ),
- the asymptotic value of the bias (as  $\rho \rightarrow \infty$ ) is given by a phenomenological parameter  $a$  which is related to the size of the mixture zone within the sliding window.

The relevance of this model also lies in its generality: it allows the description of several different cases for which biased location occurs. One only needs to determine the size of the mixture zone. Thus, in the case of blurred edge (fig. 5, line 4), the mixture zone size is equal to the psf width  $d$ :  $2a = d$ . If the edge

is tilted by an angle  $\alpha$  with respect to the window (fig. 5, line 2), then it can easily be seen that the mixture zone has a size:  $2a = L_y \tan \alpha$ , where  $L_y$  is the height of the window. For a sinuous edge (fig. 5, line 3),  $a$  is related to the variance of the edge position.

We performed simulations to test the reliability of this model. For that purpose, we used speckled edges, blurred with a circular kernel of diameter  $d$ . (like the one presented on fig. 5, line 4). For a given set  $(\rho, d)$ , 1000 realizations of the edge image are generated to estimate the bias. This estimation is compared to the bias measured on the speckle-free image and to the value given by expression 6. The results are shown on figure 6. Please note that no scaling or free parameter have been adjusted to obtain these plots. There is rather good agreement between the estimation of the true value of the bias and the measurement on the speckle-free image: this shows that the phenomenological model we considered is a good way of evaluating the bias. On the other hand, the expression 6 does not fit very well with the estimations, especially for large  $d$  and small values of  $\rho$ . This is due to the fact that this expression has been obtained with a second-order expansion. However, the general behaviour of the curve remains well described and the asymptotic values of the bias are correctly determined.

#### IV. ML EDGE LOCATION

On fig. 4, we have measured the bias of the edge position ML estimate, as a function of the real position of the edge in the fixed window (which is assessed by the difference of the sizes of each region:  $n_1 - n_2$ ). The simulations were performed for white and correlated speckle (the psf is a circular kernel of 2 pixel diameter), for various edge contrasts and for different window sizes. The darker side of the edge is on the right ( $\mu_1 > \mu_2$ ).

In all cases, we observe a drastical increase of the bias when the edge to be located is not correctly centered in the fixed window (i.e.  $n_1 \neq n_2$ ). Basically, if the real edge is positioned on the extreme left hand side of the window ( $n_1 - n_2 < 0$ ), it is very likely that spurious location occurs on the right of the real edge and therefore a positive bias appears. In the same way, when the edge is positioned on the extreme right hand side, a negative bias is measured. The absolute value of this bias increases when the edge contrast decreases because spurious location is likelier at low edge contrast. Obviously, this bias is introduced by the limited size of the window. If the length of the window is doubled, then the bias is reduced (compare fig. 4b and fig. 4c) since the real edge position no longer corresponds to window ex-

tremities.

Let us now consider the bias measured when the real edge is centered in the window ( $n_1 = n_2$ ). When the speckle is uncorrelated (fig. 4a), the ML edge location is unbiased. When the speckle is correlated (fig. 4b and 4c), the location is biased towards the darker side. We also note that the bias increases with the contrast. The same qualitative behavior is therefore observed for the bias in ML and LR edge location.

This observation led us to compare the value of the bias for each method. We have therefore estimated the bias in edge location for ML and LR strategies. The edges are corrupted by correlated speckle and both windows (FWSE and SWCE) are  $128 \times 128$ . The results are presented on tab. I. Once again, we note that the behaviour of the bias is analogous for both methods: the bias is towards the darker side, increases with the contrast and is bounded by an asymptotic value ( $d/2$  in this case) when  $\rho \rightarrow \infty$ . We note that that the improvement obtained using the ML approach in comparison with LR is more important at low contrast values. Nevertheless, the bias is still important for high contrast values and in this case, both techniques yield approximatively the same bias.

## V. CONCLUSION

In this paper, we pointed out a particular property of the LR edge detector: it gives a biased location of an edge when it is not an "ideal" step edge of known orientation or when the speckle is correlated. We proposed a phenomenological model that is general and allows one to interpret the results for various cases where the bias is observed. It has then been shown that the bias is towards the darker side of the edge, increases with the edge contrast and is limited by an asymptotic value, related to a certain phenomenological parameter  $a$ .

A bias was also observed for edge location with the ML estimate, when the speckle is correlated. The bias is also towards the darker side and increases with the contrast. Find out a model which would interpret the bias in ML location of non ideal edges is presently an open question.

## ACKNOWLEDGEMENTS

This work was supported by the French Space Agency (CNES) and Région Provence Alpes Côte d'Azur.

## REFERENCES

- [1] A. C. Bovik and D. C. Munson, "Optimal detection of object boundaries in uncorrelated speckle", *Optical Engineering*, vol. 25, no. 11, pp. 1246-1252, 1986.
- [2] R. Touzi, A. Lopès, and P. Bousquet, "A statistical and geometrical edge detector for SAR images", *IEEE Transactions on Geoscience and Remote Sensing*, vol. 26, no. 6, pp. 764-773, 1988.
- [3] C. J. Oliver, I. Mc Connell, D. Blacknell, and R. G. White, "Optimum edge detection in SAR", in *Conf. on Satellite Remote Sensing, Paris, France*. SPIE, 1995, vol. 2584, pp. 152-163.
- [4] R. Fjørtoft, A. Lopès, P. Marthon, and E. Cubero-Castan, "An optimum multiedge detector for SAR image segmentation", *IEEE Transactions on Geoscience and Remote Sensing*, vol. 36, no. 3, pp. 793-802, 1998.
- [5] R. Fjørtoft, A. Lopès, J. Bruniquel, and P. Marthon, "Optimal edge detection and localization in complex SAR images with correlated speckle", *IEEE Trans. on Geoscience and Remote Sensing*, vol. 37, no. 5, pp. 2272-2281, 1999.
- [6] O. Germain and Ph. Réfrégier, "Edge detection and localisation in SAR images : a comparative study of global filtering and active contour approaches", in *EurOpto Conf. on Image and Signal Processing for Remote Sensing, Barcelona, Spain*. SPIE, 1998, vol. 3500, pp. 111-121.

		$\rho = 2$	$\rho = 4$	$\rho = 10$	$\rho = 10^3$
$d = 10$	ML	0.4	1.5	2.5	4.5
	LR	1.4	2.3	3.3	5.0
$d = 20$	ML	0.3	2.8	4.9	9.8
	LR	1.8	4.4	6.7	10.0
$d = 30$	ML	0.5	3.6	7.0	14.1
	LR	3.0	6.0	9.7	14.7
$d = 40$	ML	0.4	4.4	8.6	19.1
	LR	3.8	7.7	12.4	19.4

TABLE I

Bias in edge location with ML and LR methods, performed for different contrasts  $\rho$  and different psf (which are circular kernels of diameter  $d$ ). Both windows (FWSE and SWCE) are  $128 \times 128$ .

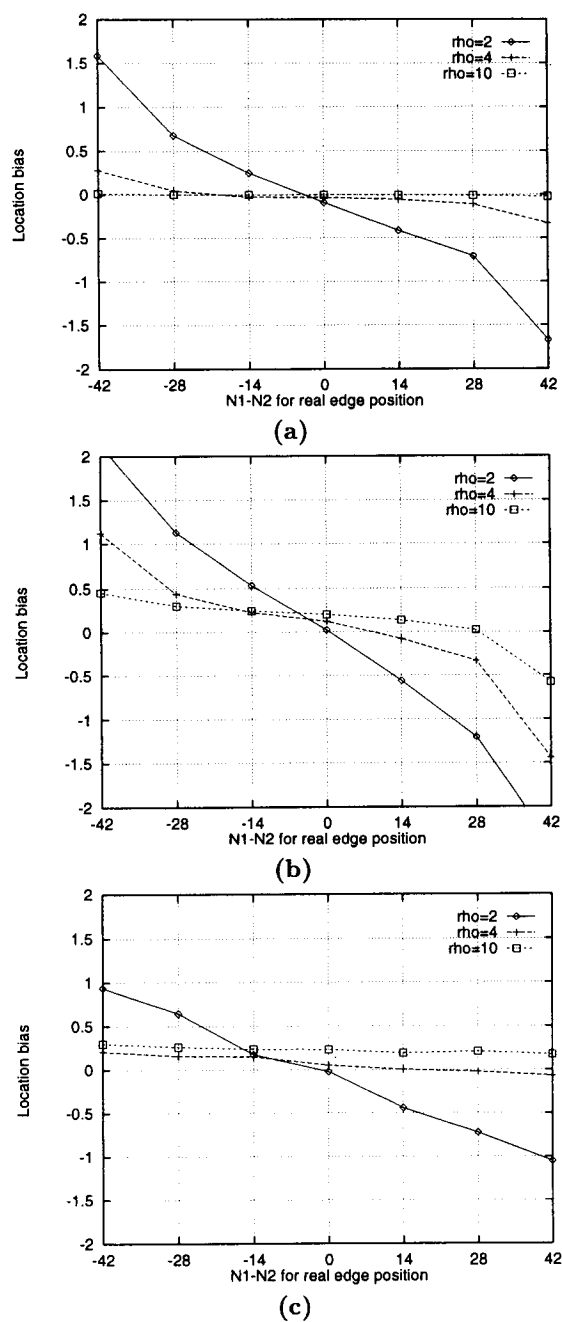


Fig. 4. Bias of the ML estimate of the edge position as a function of the real edge position in the fixed window and for different edge contrasts. (a) Uncorrelated speckle, window  $7 \times 8$  (b) Correlated speckle, window  $7 \times 8$  (c) Correlated speckle, window  $7 \times 16$ .

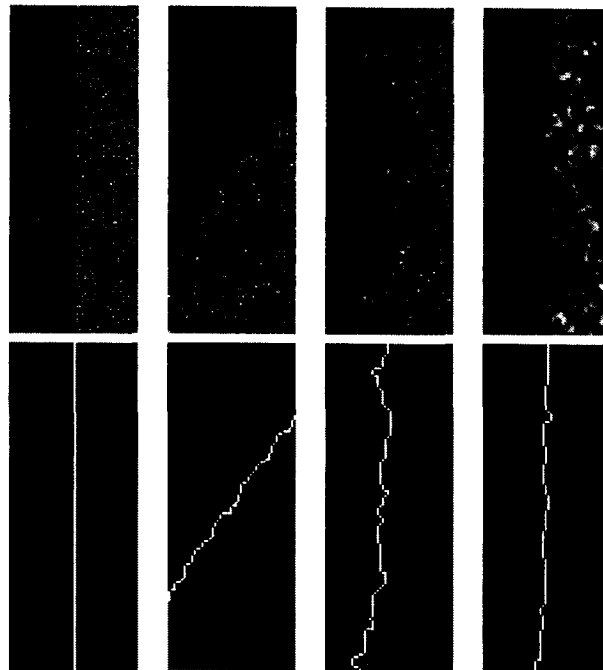


Fig. 5. Edge location for different situations. In all cases, the contrast is  $\rho = 4$ . **First line:** Speckled edges. **Second line:** Edge location performed by LR filtering ( $10 \times 10$  vertical window) followed by an edge extraction step (watershed algorithm). The result is shown on the speckle-free edge. **First column:** Ideal, straight, step edge. **Second column:** Edge tilted by  $35^\circ$ . **Third column:** Sinuous edge. **Fourth column:** Edge corrupted by correlated speckle (the psf is a circular kernel of diameter  $d = 5$ ).

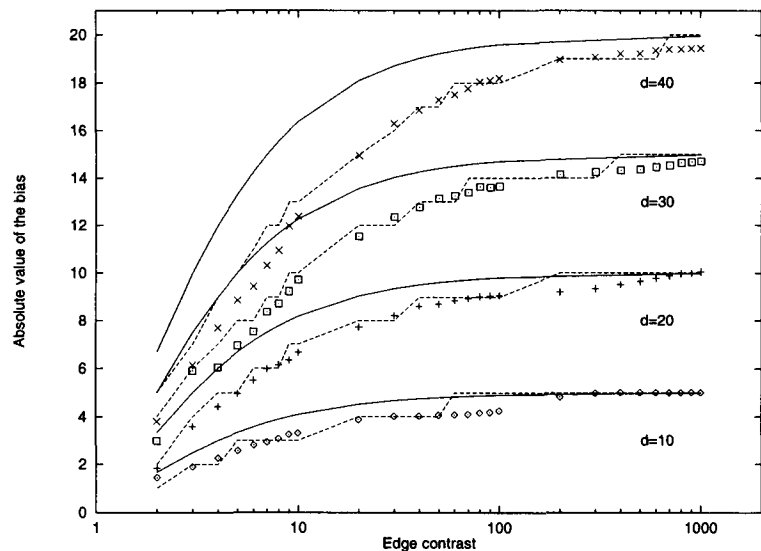


Fig. 6. Bias of the edge position estimate as a function of the edge contrast  $\rho$ , for different size of correlation kernel  $d$ . For each  $d$ , three curves are plotted: bias estimated from 1000 realizations of the speckled image (points), bias measured on the speckle-free image (dashed curve), approximated expression of the bias (solid curve). The sliding window is  $128 \times 128$ .



## ANALYSIS OF COMPLEX SAR RAW DATA COMPRESSION

Svetlana Peskova, Sergey Vnotchenko  
 Microprocessor Systems, Electronic and Electrical Engineering,  
 Tsyolkovsky Russian State Technological University  
 3, Orshanskaya Str.  
 121552 Moscow, Russia  
 E-mail: [ssv1@nym.alias.net](mailto:ssv1@nym.alias.net)

### ABSTRACT

In this paper two format of the complex SAR raw data are applied for compression: representation with real and imaginary parts and polar format with magnitude and phase. In both formats the phase information of the compressed data is preserved to a great extent. A block adaptive Max quantizer was used with 1-5 bit quantization of components. The quality of the reconstructed data is compared in terms of compression ratio and quality parameters: signal to noise ratio, standard deviation of the phase and mean phase error. The parameters are calculated for SAR raw data, complex image data and 8-bit gray scale image. Finally, original and reconstructed gray scale images are presented.

### 1. INTRODUCTION

Transmission and storage of synthetic aperture radar (SAR) data is often possible using data compression only. SAR raw data can be used for various applications including interferometry. In this case, it is necessary to deal with the complex format data and images.

Primarily requirement to compression ratio (*CR*) based on quality gray scale SAR images. While compressing data for interferometry, high phase preservation is required to prevent large errors. Therefore, complex SAR raw data compression makes greater demands on the reconstruction accuracy than in most other compression applications.

Up to now, many algorithms for SAR raw data compression used the block adaptive quantizer (BAQ) or Max quantizer. The BAQ algorithm consists basically of quantizing the raw data with a fewer bits (usually from 1 up to 5 bits). Main procedures of the BAQ are: dividing the SAR raw data into blocks; evaluation of the standard deviation in each block; optimal nonuniform quantizing of data blocks in accordance with statistic distribution. The standard deviation is transmitted as a single value for each data block. During decompression the proper output levels of Max quantizer are multiplied by the block's standard deviation.

In this paper the property of BAQ are studied for the complex SAR raw data compression. Two format of the complex raw data are used for compression:

1. Representation data with real and imaginary parts or inphase and quadrature (I and Q) components. Max quantizer is optimized for normal distribution.
2. Polar format with magnitude and phase. The BAQ is optimized for Relay distribution for magnitude and phase is quantized uniformly.

After defining the SAR data quality parameters (section 2) and considering of the algorithm for transforming the SAR raw data to an image (section 3) in section 4 are presented the results of experiments with data compression.

### 2. SAR DATA QUALITY PARAMETERS

The SAR data quality parameters are used to compare various methods of data compression.

The efficacy of compression procedure is defined by compression ratio (*CR*) or by coding rates in bits per sample (bps).

The most commonly used quality parameter for data compression is the signal to noise ratio (*SNR*). It is defined as the ratio of signal power original data to the difference signal power original and reconstructed data after compression / decompression procedure in dB:

$$SNR = 10 \cdot \lg \left[ \frac{\sum_{m=0}^{M-1} \sum_{n=0}^{N-1} s_{m,n}^2}{\sum_{m=0}^{M-1} \sum_{n=0}^{N-1} (s_{m,n} - u_{m,n})^2} \right], \quad (1)$$

with  $s_{m,n}$  - input (original) data;  $u_{m,n}$  - reconstructed data. The *SNR* is global parameter and allows the comparison of different compression methods. For gray scale SAR images problem is finding the best compromise between *SNR* and *CR*. Interferometry applications require more reconstruction accuracy, because the phase information is important. There are used the standard deviation of the phase (*PSD*)

$$PSD = \sqrt{\frac{1}{M \cdot N - 1} \cdot \sum_{m=0}^{M-1} \sum_{n=0}^{N-1} (\phi_{m,n} - \varphi_{m,n})^2} \quad (2)$$

and the mean phase error

$$MPE = \frac{1}{M \cdot N} \cdot \sum_{m=0}^{M-1} \sum_{n=0}^{N-1} |\phi_{m,n} - \varphi_{m,n}|, \quad (3)$$

with  $\phi_{m,n}$  - original phase;  $\varphi_{m,n}$  - reconstructed phase after compression and decompression procedure. All quality parameters can be applied both on SAR raw data and SAR images.

### 3. SAR IMAGE PROCESSING

The complex SAR data set was taken in X-band by the air-borne SAR "Compact"[1] of SRIPI (Moscow, Russia). The input SAR data are represented with 8-bit for each channel: inphase and quadrature (I and Q). This data set is used for studying all compression methods.

There are following processing steps for transforming SAR raw data to SAR image:

- the matched filtering of chirp signals (range transform) and transposing of matrix complex samples; this range transformed data (RTD) are in floating point format;
- the aperture synthesis (azimuth transform), where output samples (I and Q) are the complex image data in floating point format;
- the forming output elements (pixels) of SAR image  $w_{i,j}$ ; that include: the evaluation of absolute value input samples for each image pixel and the normalization samples  $v_{i,j}$  for deriving a gray scale image with 256 gray levels; it is calculated by

$$w_{i,j} = \text{int} \left\{ 255 \cdot \exp \left[ \frac{1}{(v_{i,j}/k + p)^2} \right] \right\}, \quad (4)$$

with parameters  $k$  and  $p$ , which allows to control image histogram for the best reproduction of all scale intensity.

After the above procedures were fulfilled, we obtain the fragment of the original detail image of countryside near St. Petersburg, shown in a fig. 1 (see end of paper). For the best comparison of the results of the compression and decompression SAR raw data we used BAQ on the same image fragment. Also all algorithms of the image processing and its parameters were the same. Quality parameters were evaluated for SAR raw data set, complex image and gray scale image.

### 4. COMPLEX DATA COMPRESSION

#### Histograms

The histograms of experimental SAR complex samples were estimated. The histograms I and Q components of experimental data shown the good accordance to the normal distribution. So BAQ method optimized for normal distribution was used.

After transformation of complex data in a polar format the statistical properties of amplitude and phase were estimated. The histogram of magnitude shown the very good accordance to the Rayleigh distribution, and the phase was distributed approximately uniform.

#### Data Compression for I and Q Format

The BAQ procedure was used for compression and decompression of complex data with coding rate from 1 bps to 4 bps for each I and Q component.

The quality parameters (1) - (3) were evaluated for raw data, complex image and 8-bit gray scale image for all coding rates. The visual monitoring of gray scale image was carried out also. The results of experiments are given in table 1.

Table 1: Data quality parameters for format with real and imaginary parts

BAQ (bit per sample)	4	3	2	1
Calculated for:	<i>SNR</i> , dB			
- SAR raw data	20.5	14.9	9.5	4.4
- complex image data	22.5	16.9	11.3	5.7
- gray scale image	22.3	16.8	11.8	7.7
Calculated for:	<i>PSD (MPE)</i> , degrees			
- SAR raw data	7.0° (4.5°)	12° (8.4°)	19° (14°)	26° (23°)
- complex image data	15° (7.6°)	26° (14°)	41° (25°)	60° (43°)

The evaluations of *SNR* carried out on SAR raw data (table 1, line 1) are similar to well-known results, for example [2]. For complex image and gray scale image *SNR* values were more approximately on 2 dB. The phase errors *PSD* and *MPE* show good results only for 4 bps quantization ( $CR = 2$ ). After range and azimuth transform (for complex SAR image) phase errors were increased.

The visual monitoring of 256 gray scale image shows, that BAQ with 4 and 3 bps have no difference from original image (fig. 1). The quantization with 2 bps gives weak noise on dark sites (radar shadows) of an

image. At last quantization with 1 bps for each channel noticeable increase the noise over all image (fig. 2).

#### Data Compression for Polar Format

After transformation complex SAR data to a polar format the magnitude and phase are quantized with different coding rate: magnitudes with 1-4 bps and phases with 2-5 bps. The quality parameters *SNR*, *PSD* and *MPE* were evaluated for the SAR raw data and are given in table 2. It must be noted, that phase errors *PSD*, obtained in these experiments, are equal its theoretical values, which defined as  $[360^\circ / (2^k \cdot 12^{1/2})]$ , where *k* - number of bits for uniform quantization.

Table 2: Data quality parameters for polar format calculated for SAR raw data

<i>PSD</i> ( <i>MPE</i> ), degrees	<i>SNR</i> , dB					
	Phase, bps	Magnitude, bps				
		4	3	2	1	0
3.3° (2.8°)	5	23.2	20.4	16.2	11.4	6.5
6.5° (5.7°)	4	18.4	17.3	14.8	10.9	6.3
13° (11°)	3	12.8	12.5	11.5	9.3	5.7
26° (23°)	2	7.0	6.9	6.6	5.9	4.0

The comparison *SNR* of two different formats for complex SAR data: I and Q (table 1) and polar (table 2), shows that if the same coding rates are used in each channel (4+4 bps, 3+3 bps etc.), the polar format gets worse values of *SNR*. But in a polar format there are variants of unequal quantization (magnitude + phase): 3+5 bps, 2+4 bps, 1+3 bits, which for identical *CR* have the same *SNR* as I and Q format. Moreover, these variants enable phase errors twice less due to 1 bit greater for a phase coding.

As well as for I and Q format, *SNR* evaluated for complex image in polar format (table 3), has values approximately on 2 dB larger, than for SAR raw data. The phase errors *PSD* and *MPE* are increased after a data conversion to complex image. *SNR* evaluated for 8-bit gray scale image is given in table 4. The visual monitoring of gray scale image shows good quality of polar format data compression. For example fig. 3 illustrate BAQ with 1+3 bps.

#### Phase Data Compression

The importance of a phase information for SAR is well-known. Therefore attempts of data compression with phase information only [3] are very interesting. We used the following scheme: the phases are coded uniformly (2-5 bps) and the magnitudes are transmitted as single

value for each block. This value is square root from mean power and is constant inside each block during the decompression. *SNR* for phase coding are given in table 2 and 4 (right column).

The visual comparison between a gray scale image with 2 bps phases quantization (fig. 4) and I and Q format compression with 1 bps for each channel (fig. 2) shows, that distribution of brightness on these images noticeably differs. It confirms by difference of their histograms, and shows presence of the significant non-linearity, when only phase information is in use. In spite of both variants provide *CR* = 8, its comparison in term of *SNR* (table 1, 2 and 4) is not correct, since *SNR* in fig. 4 is modified both by compression / decompression and by non-linearity.

Table 3: Quality parameters for polar format calculated for complex image data

<i>SNR</i> , dB				
Phase, bps	Magnitude, bps			
	4	3	2	1
5	25.3	22.5	18.3	13.3
4	20.4	19.3	16.8	12.8
3	14.8	14.5	13.5	11.2
2	8.9	8.8	8.6	7.8
<i>PSD</i> ( <i>MPE</i> ), degrees				
Phase, bps	Magnitude, bps			
	4	3	2	1
5	11.8° (5.6°)	15.5° (7.6°)	22.5° (12.0°)	34.7° (20.7°)
4	18.5° (9.6°)	20.7° (10.9°)	25.8° (14.3°)	36.3° (21.9°)
3	30.9° (17.8°)	31.6° (18.4°)	34.2° (20.3°)	41.2° (25.9°)
2	49.1° (32.5°)	49.5° (32.7°)	50.3° (33.5°)	53.4° (36.3°)

Table 4: *SNR* for polar format compression calculated for 256 gray scale image

<i>SNR</i> , dB					
Phase, bps	Magnitude, bps				
	4	3	2	1	0
5	25.0	22.3	18.1	13.6	9.1
4	20.2	17.3	19.1	13.1	9.0
3	14.8	14.5	13.6	11.7	8.5
2	9.6	9.5	9.3	8.8	7.1

### Compression of Range Transform Data

An analog-to-digital converter on SAR output quantized the signals with sampling rate  $F_q$  and transformed to complex data with  $2 \cdot m_q$  bit per sample. The data rate is  $2 \cdot m_q \cdot F_q$  bit per second. At presence of the buffer RAM the digital samples are writing during time  $t_c$ , and are reading during a pulse repetition period  $T$ . The time interval  $t_c$  consist of two components: one is depended on swath width  $L$  and average incidence angle  $\epsilon$ , and another is transmit pulse rate  $\tau$ . Then output data rate  $W$  defined as:

$$W \approx 2 m_q F_q (2 L \sin \epsilon / c + \tau) / T \quad \text{s} \quad (5)$$

The large transmit pulse rate  $\tau$  is usually used in modern SAR. After range data transform in (5)  $\tau$  is 0, then the data rate  $W$  is reduced. For example, parameters SAR "Severyanin" [4] is:  $L = 50$  km,  $\epsilon = 45^\circ$ ,  $\tau = 60$   $\mu\text{sec}$ . The relative reduction of the data rate is about 1.25 without any losses of information. Therefore total compress ratio may be slightly increased using compression of range transform data. Taking this into account, it is offered to implement the compression of range transformed data for their archival storage.

To confirm a possibility and expediency of such approach, block adaptive quantization on range transformed data in floating point format was carried out. The evaluations for all variants of compression are obtained:

- at a compression in I and Q format the *SNR* parameter decreased on 0,1-0,8 dB relative to table 1 data. The phase errors are slightly decreased (exception makes variant of 1bps quantization, where degradation of all parameters was very significant);
- at a compression in a polar format the *SNR* parameter decreased on 0,1-1,5 dB relative to table 2 and 4 data (large values concern to a complex image). The phase errors practically were the same.

The visual monitoring shows, that low-rate quantization of range transformed data causes noticeably spreading of marks from the brightest objects by azimuth on images. With identical *CR* this spreading is more for I and Q format. For example RTD BAQ with 2+2 bps is shown on fig. 5. However after increasing of coding rate this effect disappears.

For problems of the remote sensing that need good phase information, it is possible to recommend the following quantization parameters: 3 bits for magnitude and 5 bits for a phase. It provides  $CR > 2$  and  $SNR = 20,4$  dB with very good visual quality of reconstructed image (fig. 6).

### 5. CONCLUSION

It is possible to use a polar format for complex data compression using BAQ method. This format gives large number of coding variants and permits to discover the acceptable compromises. For problems requiring better knowledge of phase more bits is selected for phase coding.

In special cases, the quantization of phase information only is possible.

All considered methods of compression are effective for SAR raw data and for range transformed data.

For increasing overall data compression BAQ algorithm can be used in a combination with other methods of data compression.

### ACKNOWLEDGMENTS

We thank SRIPI (Moscow) for supplying the SAR data used in these experiments.

### REFERENCES

- [1] T.G. Moussiniants, I.S. Neiman, "Small-size synthetic aperture radar "Compact", " *Proc. of the Third Int. Airborne Remote Sensing Conf. and Exhib. Copenhagen, Denmark*, vol. II, pp. 158-164, 7-10 July 1997.
- [2] U. Benz, K. Strodl, and A. Moreira, "Improved SAR Raw Data Compression with Adaptive Gain Estimation," *EUSAR'96, Kunigswinter, Germany*, pp. 285-288, March 1996.
- [3] G. Franceschetti, M. Tesauro, "Toward a cheap SAR," *IGARSS'98, Seattle, USA*, pp. 1144-1146, 6-10 July 1998.
- [4] V.I. Koslov, I.S. Neiman, A.V. Shishanov, "Prospective projects of Russian space-borne SARs for Earth remote sensing," *CEOS SAR Workshop, ESTEC, Noordwijk, Netherlands*, pp. 323-326, 3-6 February 1998.



Fig. 1: Original image (8+8 bps)



Fig. 2: BAQ (1+1 bps);  $CR = 8$



Fig. 3: Polar format (1+3 bps);  $CR = 4$



Fig. 4: Only phase coding (2 bps);  $CR = 8$



Fig. 5: BAQ for RTD (2+2 bps);  $CR = 4$



Fig. 6: BAQ for RTD (3+5 bps);  $CR = 2$



## High Resolution Spectral Analysis Applied to SAR Images

Laurent Savy\*, Jean-Guy Planès\*, Christophe Moal\*\*

\*Alcatel Space Industries, 26 avenue J.F. Champollion, BP 1187 Toulouse Cedex, France  
Tel (33) 05.34.35.44.83, Fax (33) 05.34.35.61.63.

\*\*ENSICA (Ecole Nationale Supérieure d'Ingénieurs en Constructions Aéronautiques),  
1 place Emile Blouin, 31056 Toulouse, France. Tel (33) 05.61.61.86.34.  
Email :laurent.savy@space.alcatel.fr, jean-guy.planes@space.alcatel.fr, cmoal@ensica.fr

### ABSTRACT

Classical high resolution (HR) methods become unrealisable when applied to large SAR image, due to memory size and computational time requirements. In this paper, a 2D version of beamspace MUSIC algorithm, called « imagespace MUSIC », is proposed for large image SAR processing. Simulations and real data processing results are provided, and demonstrate resolution improvement as well as « good » behaviour on clutter.

### 1. INTRODUCTION

Spatial resolution of radar images given by synthetic aperture radar (SAR) is typically bounded by both the bandwidth of the emitted signal and the observation time duration. Results in image interpretation (detection, classification) are directly connected with spatial resolution that has a major influence on the cost of the satellite.

Hence, implementation of high resolution (HR) spectral analysis methods, that could be carried out on ground, is of great interest, to reach a given level of performances at lower system cost, or to increase performances of already existing systems

In this paper, a 2D version of beamspace MUSIC algorithm [1], called « imagespace MUSIC », is proposed for large image SAR processing.

In a first section, a parametric signal model will be assumed, well suited to SAR image of human made targets imbedded in clutter and thermal noise.

In a second section, the well known MUSIC spectral analysis will then be reminded. This method works in the wavenumber space (radial frequency, azimuth frequency), also called data space. In practice this method becomes unrealisable when applied to SAR image larger than 32x32, due to memory size and computational time requirements.

In a third section, the paper will then present a 2D HR method, derived from MUSIC algorithm, but which works directly in image space (radial range, azimuth range), also called in [1] beamspace. This method is computationally efficient, as well as adaptative to clutter heterogeneity's, since it works sequentially on small parts of the global image. It also offers amenability to parallel implementation.

In a fourth section, performances in resolution and results on real Radarsat data will then be exposed.

### 2. SIGNAL MODEL IN WAVENUMBER SPACE

Single look complex (SLC) SAR image ( $I_{SLC}$ ) are composed of point like echoes, clutter, and noise. We are interested in HR analysis of point like echoes, which come essentially from human made targets.

So, the signal in the wavenumber space (inverse FFT of  $I_{SLC}$ ) is supposed to satisfy the following equation :

$$x(m,n) = \sum_{k=0}^{K-1} \sum_{l=0}^{L-1} a(k,l) \cdot e^{i2\pi r_1^{(k)} m} e^{i2\pi r_2^{(l)} n} + b(m,n) \quad (1)$$

$x(m,n)$  : SLC SAR data in wavenumber domain  
( $0 \leq m \leq M-1, 0 \leq n \leq N-1$ )

$a(k,l)$  : complex amplitude of point target echo (k,l)  
 $b(m,n)$  : clutter + thermal noise

$r_1^{(k)}$  : normalized radial range of point echo (k,l)  
 $0 \leq r_1^{(k)} \leq 1$

$r_2^{(l)}$  : normalized azimuth range of point echo (k,l)  
 $0 \leq r_2^{(l)} \leq 1$

If  $\delta r_1, \delta r_2$  are respectively the pixel spacing in radial and azimuth range of the SLC SAR image  $I_{SLC}$ , ( $I_{SLC}$  is the Fourier Transform of the data  $x(m,n)$ ), then the real radial and azimuth range of echo (k,l) are respectively  $R_1^{(k)} = r_1^{(k)} M \delta r_1, R_2^{(l)} = r_2^{(l)} N \delta r_2$ .

In vector notation, this becomes :

$$\mathbf{x} = \mathbf{E}\mathbf{a} + \mathbf{b} \quad (2)$$

$$\begin{aligned} \mathbf{E} &= [e(0,0), e(1,0), \dots, e(K-1,0), \dots, e(0,L-1), \dots, e(K-1,L-1)] \\ \mathbf{a} &= [a(0,0), a(1,0), \dots, a(K-1,0), \dots, a(0,L-1), \dots, a(K-1,L-1)] \\ e(k,l) &= [e_0^T \dots e_n^T \dots e_{N-1}^T]^T \\ \mathbf{e}_n &= [e^{i2\pi_2^{(1)}n}, \dots, e^{i2\pi_2^{(1)}n}, e^{i2\pi_1^{(k)}m}, \dots, e^{i2\pi_2^{(1)}n}, e^{i2\pi_1^{(k)}(M-1)}]^T \\ \mathbf{b} &= [b_0^T, \dots, b_{N-1}^T]^T \quad \mathbf{b}_n = [b(0,n), \dots, b(M-1,n)]^T \\ \mathbf{x} &= [x_0^T, \dots, x_{N-1}^T]^T \quad \mathbf{x}_n = [x(0,n), \dots, x(M-1,n)]^T \end{aligned}$$

Vector  $\mathbf{x}$  is the concatenation of all the lines of  $x$ . Vector  $\mathbf{b}$  represent clutter plus noise. It is non white in the general case (clutter can be viewed as a coloured noise). As explained in section (3), this property can lead to spurious peaks when applying classical MUSIC algorithm on non locally white clutter.

As for the one dimension case, we call signal subspace in the following the space spanned by the vectors  $\mathbf{e}(k,l)$ , columns of matrix  $\mathbf{E}$ .

### 3. MUSIC ANALYSIS IN WAVENUMBERSPACE

MUSIC analysis in wavenumberspace is classical MUSIC spectral analysis. Its principle is briefly reminded in this section. It relies on Singular Value Decomposition (SVD) of the signal autocorrelation matrix  $\mathbf{R}$  :

$$\mathbf{R} = E\{\mathbf{x}\mathbf{x}^H\} \quad (3)$$

For K.L source (K.L complex exponential), the subspace spanned by the K.L eigenvectors associated to the K.L strongest eigenvalues is merged with the signal subspace. This properties holds only with vector  $\mathbf{b}(m,n)$  being white noise. As  $\mathbf{R}$  is an autocorrelation matrix, all the eigenvectors are orthogonal.

Let us note  $\pi_b$  the orthogonal projector into the noise subspace. Columns of  $\pi_b$  are composed of the (M.N - K.L) eigenvectors associated to the (M.N - K.L) smallest eigenvalues. The MUSIC 2D spectral density estimate or pseudo 2D MUSIC spectrum, that is to say the HR image, is obtained by plotting :

$$I_{MUSIC}(r_1, r_2) = \frac{\sigma^2}{\mathbf{s}^H(r_1, r_2) \pi_b \mathbf{s}(r_1, r_2)} \quad (4)$$

with

$\sigma^2$ : white noise power.  $\sigma^2 = E\{|b(m,n)|^2\}$

$\mathbf{s}(r_1, r_2)$ : 2D signal replica for a point like echo

$$\mathbf{s}(r_1, r_2) = [s_0^T \dots s_n^T \dots s_{N-1}^T]^T$$

$$\mathbf{s}_n = [e^{i2\pi_2 n}, \dots, e^{i2\pi_2 n}, e^{i2\pi_1 m}, \dots, e^{i2\pi_2 n}, e^{i2\pi_1 (M-1)}]^T$$

$r_1$ : normalized radial range  $0 \leq r_1 \leq 1$

$r_2$ : normalized azimuth range  $0 \leq r_2 \leq 1$

While directly applying MUSIC algorithm to SAR image, the first limitation come from the computation of the SVD of matrix  $\mathbf{R}$  which is typically 1024x1024 for a 32x32 points image. The second limitation comes from the computation of the pseudo MUSIC spectrum which needs over sampling in  $r_1, r_2$ , because of high resolution properties of MUSIC algorithm. The last limitation, but not the least, comes from the necessity for noise  $\mathbf{b}(m,n)$  to be white. For SAR images,  $\mathbf{b}(m,n)$  represents clutter + thermal noise, and clutter is of course non white. The signal subspace is then not merged with the eigenvectors associated to the strongest eigenvalues, which results in spurious peaks.

To overcome this three limitations, a 2D version of beamspace MUSIC algorithm [1], called imagespace MUSIC has been defined, and is presented in the next section.

### 4. MUSIC SPECTRAL ANALYSIS IN IMAGESPACE (BEAMSPACE MUSIC)

#### 4.1 Theory

The major idea to overcome the limitations due to SAR image size is to work directly and locally in image space (that is to say on the Fourier transform of  $x(m,n)$ ), in the same way proposed for MUSIC algorithm for antenna processing [1],[3]. More precisely, the Fourier transform of the data  $\mathbf{x}$  from the wavenumber domain to the image domain can be formalised as :

$$\tilde{\mathbf{x}}_b = \mathbf{H}_b^{(\mu\nu)} \cdot \mathbf{x} \quad (5)$$

$\mathbf{H}_b^{(\mu\nu)}$  is a 2D DFT transformation matrix. Only  $B \times B$  frequencies around the  $\frac{\mu}{M}, \frac{\nu}{N}$  reference frequencies are computed ( $0 \leq \mu \leq M-1, 0 \leq \nu \leq N-1$ ). Size of  $\mathbf{H}_b^{(\mu\nu)}$  is  $B^2 \times (MN)$ . Typically,  $B$  is less than 5 or 7, which results in less computational complexity, and local processing (subimages of size 5x5 or 7x7).



$\tilde{x}_b(i+(j-1)B)$  is the DFT of  $x(m,n)$  at the frequencies  $\frac{k-(B-1)/2+i}{M}, \frac{l-(B-1)/2+j}{N}$ .

As DFT is a unitary transform,  $\mathbf{H}_b^{(\mu\nu)} \mathbf{H}_b^{(\mu\nu)H} = Id_{B^2 \times B^2}$  (white noise is still white noise after DFT), the MUSIC spectral analysis, transposed to imagespace can be written following the same ideas as in section (3). We consider now the autocorrelation matrix  $\tilde{\mathbf{R}}_b$  :

$$\tilde{\mathbf{R}}_b = E \{ \tilde{x}_b \tilde{x}_b^H \} = \mathbf{H}_b^{(\mu\nu)} \mathbf{R} \mathbf{H}_b^{(\mu\nu)H} \quad (6)$$

$\tilde{\mathbf{R}}_b$  is small size,  $B^2 \times B^2$ .

The SVD of  $\tilde{\mathbf{R}}_b$  gives in a similar way as in section (3) the orthogonal projector  $\tilde{\mathcal{P}}_b$  into the noise subspace. The HR 2D spectral estimate with imagespace MUSIC algorithm is then :

$$\tilde{I}_{MUS}(r_1, r_2) = \frac{\sigma^2}{\tilde{s}_b^H(r_1, r_2) \tilde{\mathcal{P}}_b \tilde{s}_b^H(r_1, r_2)} \quad (7)$$

$$\tilde{s}_b(r_1, r_2) = \mathbf{H}_b^{(\mu\nu)} s(r_1, r_2)$$

(note that  $\tilde{s}_b$  is a 2D sinc like function centered in  $r_1, r_2$ )

#### 4.2 Estimation of the noise subspace

To estimate the noise subspace, one have first to compute an estimation of the autocorrelation matrix  $\tilde{\mathbf{R}}_b$ , without using Equation (6) very time and memory consuming.

The first step is then to break the SAR SLC data in the wavenumberspace  $x(m,n)$  into subblocks, each of size  $M/2 \times N/2$  (this size has appeared to be the best compromise between resolution improvement and quality of estimation of  $\tilde{\mathbf{R}}_b$ ). In order to perform a good estimation, the subblocks have to overlap. To get an insight into the necessary value of the overlapping factor it is worth noting that changes on the spectrum of a signal inside a subband  $\Delta B$  can come only from samples with  $1/\Delta B$  spacing on the signal. We guess then, with the notations of section (4.1) that the overlapping factor should be more than  $1-1/B$  in each dimension. In practice, good results were obtained by choosing an overlapping factor of  $1-1/2B$  (increasing more the overlapping factor induces no change onto the estimation of  $\tilde{\mathbf{R}}_b$ ). This choice leads to  $2B \times 2B$  overlapping subblocks.

The second step is now to take the 2D fourier transform on each blocks. This is a fast computation of Equation (5) for all  $(\mu, \nu)$ . From the results for block  $(t)$  it is easy to extract the vector  $\tilde{x}_b^{(t)}$ . In a similar way as described in section (4.1),  $\tilde{x}_b^{(t)}(i+(j-1)B)$  is the DFT of  $x^{(t)}(m,n)$  (subblock  $(t)$  of the data  $x(m,n)$ ) at the frequencies  $\frac{k-(B-1)/2+i}{M/2}, \frac{l-(B-1)/2+j}{N/2}$ . The estimated matrix  $\hat{\tilde{\mathbf{R}}}_b$  is then computed by :

$$\hat{\tilde{\mathbf{R}}}_b = \frac{1}{2B} \sum_{t=1}^{2B} \tilde{x}_b^{(t)} \tilde{x}_b^{(t)H} \quad (8)$$

The third step is now to estimate the noise subspace. We proceed here as described in [4] pp. 193 to 198. Montecarlo simulations on the SVD of  $\hat{\tilde{\mathbf{R}}}_b$  were performed to get the statistics of the noise subspace eigenvalues for all possible dimension of the noise subspace. Relatively to a given level of false alarm on the size of the noise subspace, thresholds are defined on the eigenvalues. An iterative threshold detection procedure can then be applied to the eigenvalues to determine the noise subspace dimension.

Once we get the noise subspace dimension, the estimated pseudo MUSIC spectrum is computed using Equation (7). The noise variance  $\sigma^2$  is simply estimated by averaging all the eigenvalues of the noise subspace.

The whole image can be processed sequentially by computing Equation (7) for all  $(\mu, \nu)$ .

## 5. PERFORMANCES

### 5.1 Synthetic data

Synthetic data composed of two points echoes were used to compute the probability of resolution versus the relative position of the two echoes (measured in DFT bins of the whole image) of the method proposed in section (4). Results for various SNR (on the whole classical FFT image) are plotted on figure (1) and compared to classical FFT Hamming 0.58 weighting image analysis (PSLR = -34dB). Imagespace MUSIC algorithm allows a resolution improvement by a factor greater than 2 for SNR greater than 25dB and a probability of resolution of 0.9. Other simulations have shown that the imagespace MUSIC algorithm already exhibits the same performances in resolution as the wavenumberspace MUSIC algorithm.

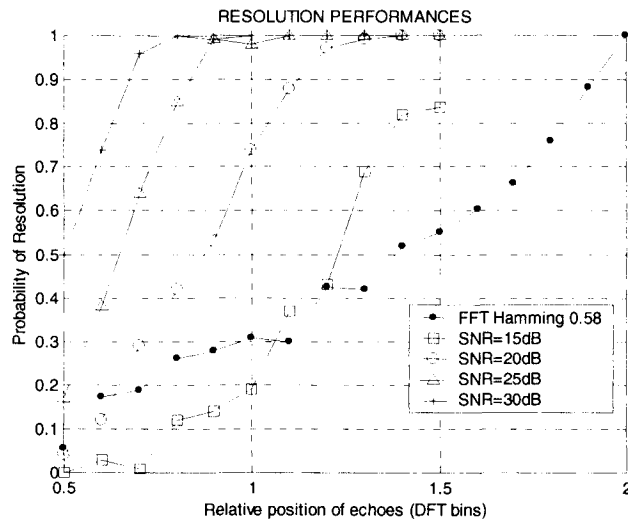


figure 1

## 5.2 Real data

We also applied imagespace MUSIC analysis to real Radarsat image of the bay of Toulon (France). Figure (2) shows the whole image with Hamming 0.58 weighting. Figures (3.1),(4.1), (5.1) are zoom of figure (2) on three ships. Figure (3.2), (4.2), (5.2), show the same ships processed with the imagespace MUSIC algorithm. Clearly, resolution is improved, without spurious peaks on sea clutter. Scatters are more resolved, which should be useful to help classification for example.

## 6. CONCLUSION

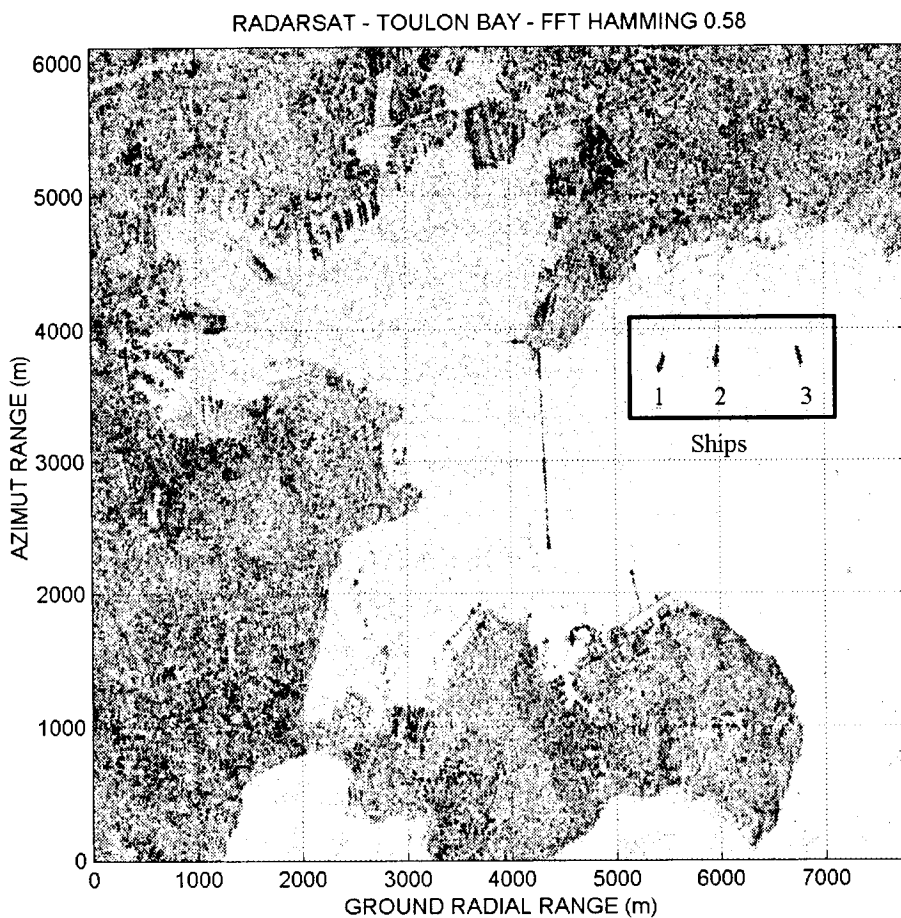
The paper has presented a 2D version of beamspace MUSIC algorithm, called « imagespace MUSIC », able to process large SAR image with « well » behaviour on clutter (no spurious peaks on clutter). This is because the proposed method works locally and directly in the image domain.

Simulations on synthetic data shows a factor greater than 2 in resolution improvement for SNR greater than 25 dB, compared to Hamming 0.58 weighting.

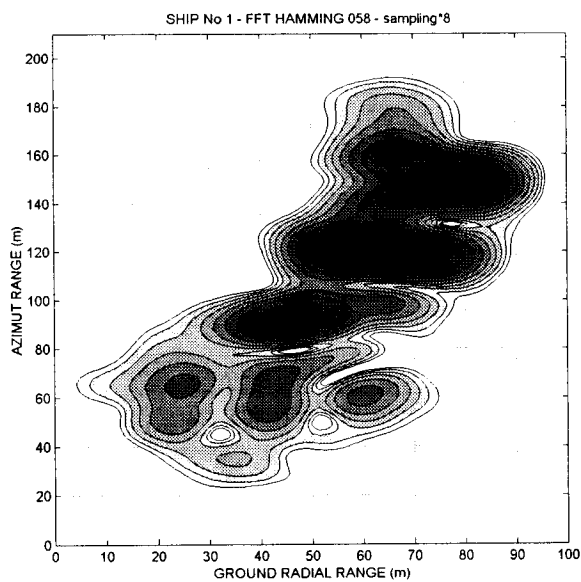
The proposed method also exhibits « well » behaviour and resolution improvement on real Radarsat data.

## REFERENCES

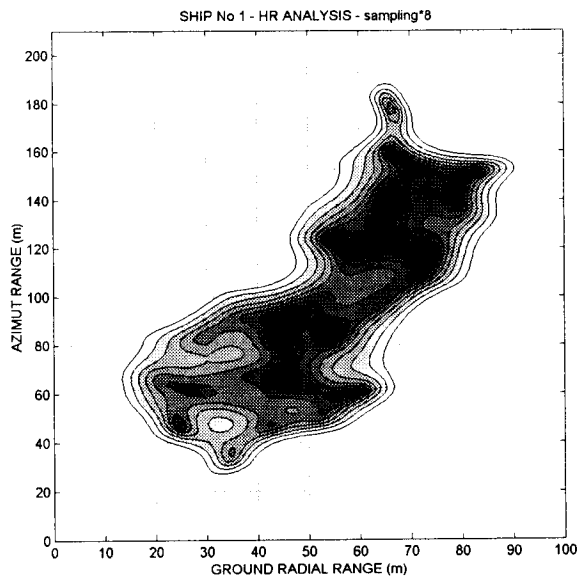
- [1] Michael D. Zoltowski, Gregory M. Kautz, Seth D. Silverstein « Beamspace Root-MUSIC » IEEE Transactions on Signal Processing, Vol. 41, No. 1, January 1993.
- [2] Steven M. Kay « Modern Spectral Estimation » PTR Prentice Hall Signal Processing Series, Alan V. Oppenheim, series editor, 1988.
- [3] Harry B. Lee, Michael S. Wengrovitz, « Resolution Threshold of Beamspace MUSIC for two Closely Spaced Emitters », IEEE Transactions on Acoustic, speech, and Signal Processing, Vol. 38, No. 9, September 1990.
- [4] S.Marcos, « Les Méthodes à Haute Résolution », série Traitement du signal, édition HERMES, Paris, 1998



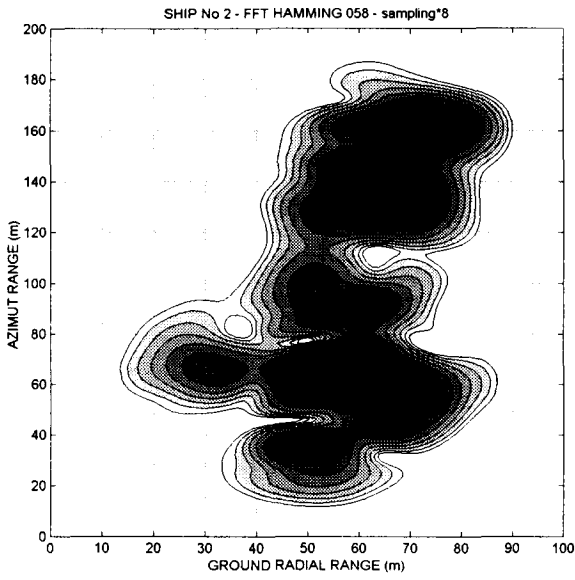
*figure 2*



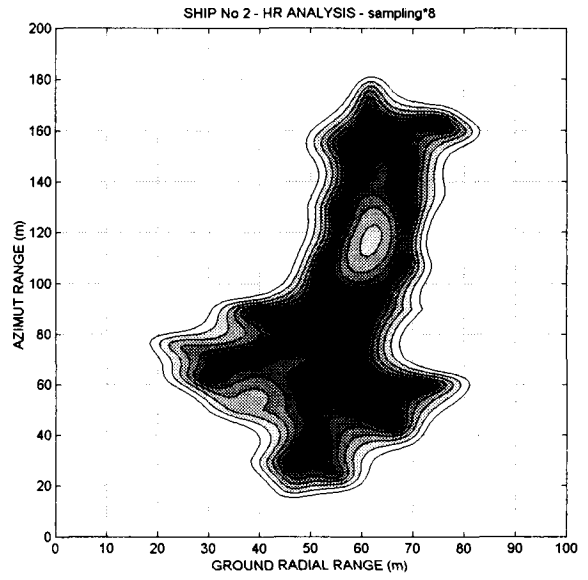
*figure 3.1*



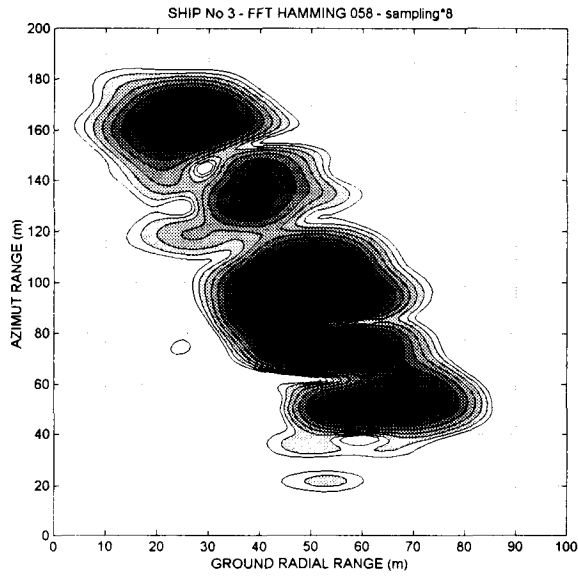
*figure 3.2*



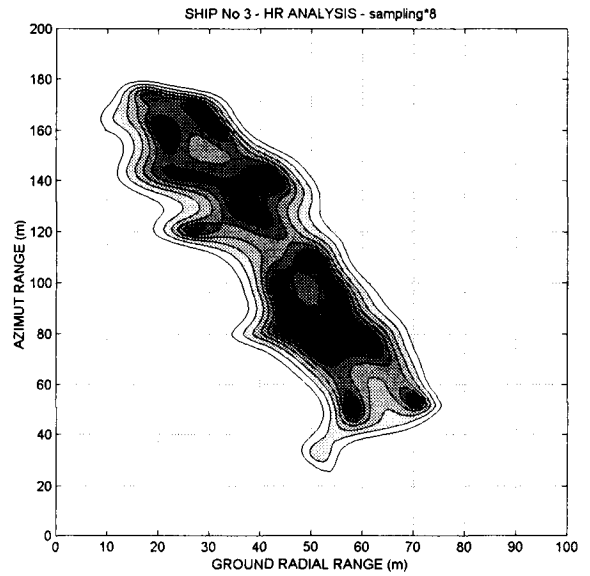
*figure 4.1*



*figure 4.2*



*figure 5.1*



*figure5.2*

## Data compression for transmission of polarimetric SAR signal by vector quantization - Performance evaluation

Nicole de Beaucoudrey<sup>(1)</sup>, Thierry Seren<sup>(1)</sup>, Dominique Barba<sup>(1)</sup>, Xavier Morin<sup>(2)</sup>

(1) IRESTE, Laboratoire SEI, EP CNRS 2018  
Rue Christian Pauc, La Chantrerie, BP 60601  
44306 Nantes Cedex 3, France  
e-mail: ndebeauc@ireste.fr

(2) Institut Francais Pour La Recherche Et La Technologie Polaires  
Technopole Brest-Iroise, BP 75  
29280 Plouzané, France

### ABSTRACT

SAR imaging systems produce by themselves a great amount of raw data, still further increased when multipolarization is considered. As a result, on-board image reconstruction is usually impossible and raw signal must be transmitted to the ground station before processing. Before that, compression of polarimetric SAR raw data becomes necessary, in order to reduce the bit rate for transmission purpose. With the aim of improving compression performances, it is essential to exploit statistical properties of the signal, not only inside every polarized component, but between these different components. The compression in the data representation is based on vector quantization techniques. We present results obtained with different vector organizations. In each case, we compute the data volume expansion due to the use of a full multipolarimetric SAR imaging system compared to the use of a non polarimetric one.

### 1. INTRODUCTION

SAR imaging systems require extensive computation of a great amount of collected data in order to produce images with high spatial resolution. As a result, on-board image reconstruction is usually impossible and raw signal must be transmitted to the ground station before processing. This huge quantity of data is still further increased when multipolarization is considered. Polarimetric radar sensors produce distinct two-dimensional data in up to four channels. Usually, only three channels are considered (HH, VV, HV), consisting in an increase of the number of data by a factor 3. Therefore, it becomes necessary to compress polarimetric SAR data in order to reduce bandwidth requirements of transmission channels, while maintaining an acceptable quality. In order to improve compression performances, we can take into account different statistical properties of the signal. After

presentation of the statistical analysis of the raw SAR signal (section 2) and of the compression algorithm we use (section 3), we compare in section 4 compression results between multi- and mono- polarized data.

### 2. STATISTICAL ANALYSIS OF RAW SIGNAL

A polarimetric radar transmits two orthogonal waves, in either horizontal (H) or vertical (V) polarization, and receive backscattered waves in either H or V polarization, yielding four resultant combinations of complex signals, HH, VV, HV and VH. Polarimetric SAR systems are coherent systems and return complex signals, represented in either cartesian format (with real and imaginary parts) or in polar one (with magnitude and phase). Signal in each polarization channel has two dimensions: radar position, in the azimuthal direction, and emitted signal frequency, in the range direction which is orthogonal to the motion of the radar.

The data we use within this study are recorded in real experiments and supplied by the CELAR organization (Centre Electronique de l'Armement). Two systems (STRADI and SARAPE) are considered, both systems are with lateral sighting and synthetic antenna, quasi-monostatic, multifrequency, multipolarization and high resolution:

- STRADI system [1] consists in a moving gantry with antennas 30 m height and a displacement length of 200 m. Recorded data are responses of 501 discrete frequencies of emitted signal and for every one out of 111 positions. Artificial targets are added for calibration purpose; their radar level of backscattering is higher than the one of surrounding scene and influences noticeably statistical properties of received signals.
- SARAPE[2] is a similar system but with lower geometry (3 m height and 3.5 m displacement). Data

correspond to 500 frequencies out of 120 or 130 positions. No artificial targets are present, but only natural scenes of homogeneous zones, mainly fields, meadows, wasteland.

Statistical dependancy (in term of correlation) between components of the signal can be exploited to increase compression algorithm performances. These correlations are therefore calculated as a function of polarimetric dimension as well as in the frequency or lateral displacement range.

Tables 1 to 4 show the different intercorrelations for the complex data represented in either magnitude and

phase, or real and imaginary parts. Correlation is calculated in two directions, frequency or displacement, and between the 3 polarization components, HH, VV and HV. In each cell of these tables, values of normalized intercorrelations are given with the same frequency (or position) sample of data ( $d = 0$ , for instance  $HH_{f_i}$  and  $VV_{f_i}$ ) and with the next frequency (or position) sample ( $d = 1$ , for instance  $HH_{f_i}$  and  $VV_{f_{i+1}}$ ). In these tables, the values correspond to the average computed on five SAR different records, but correlations are computed independently on each signal.

Table 1 : Intercorrelations for STRADI data, between polarization components for magnitude and phase, as a function of frequency or displacement (average on 5 experiments) - in percentage -

magnitude (displacement)				magnitude (frequency)				phase (displacement)				phase (frequency)							
		HH	VV	HV			HH	VV	HV			HH	VV	HV			HH	VV	HV
HH	d=0	100	-46	13	HH	d=0	100	-46	13	HH	d=0	100	-30	16	HH	d=0	100	-30	16
	d=1	78	-51	13		d=1	36	18	9		d=1	60	-33	16		d=1	11	7	-9
VV	d=0		100	16	VV	d=0		100	16	VV	d=0		100	-2	VV	d=0		100	-2
	d=1		81	14		d=1		35	17		d=1		63	0		d=1		11	-6
HV	d=0			100	HV	d=0			100	HV	d=0			100	HV	d=0			100
	d=1			76		d=1			87		d=1			72		d=1			5

Table 2 : Intercorrelations for STRADI data, between polarization components for real and imaginary parts, as a function of frequency or displacement (average on 5 experiments) - in percentage -

real part (displacement)				real part (frequency)				imagin. part (displacement)				imagin. part (frequency)							
		HH	VV	HV			HH	VV	HV			HH	VV	HV			HH	VV	HV
HH	d=0	100	-54	15	HH	d=0	100	-54	15	HH	d=0	100	-55	15	HH	d=0	100	-55	15
	d=1	81	-62	13		d=1	38	21	0		d=1	81	-63	13		d=1	38	20	0
VV	d=0		100	-17	VV	d=0		100	-17	VV	d=0		100	-17	VV	d=0		100	-17
	d=1		83	-9		d=1		36	-2		d=1		83	-10		d=1		36	-1
HV	d=0			100	HV	d=0			100	HV	d=0			100	HV	d=0			100
	d=1			89		d=1			32		d=1			89		d=1			32

Table 3 : Intercorrelations for SARAPE data, between polarization components for magnitude and phase, as a function of frequency or displacement (average on 5 experiments) - in percentage -

magnitude (displacement)				magnitude (frequency)				phase (displacement)				phase (frequency)							
		HH	VV	HV			HH	VV	HV			HH	VV	HV			HH	VV	HV
HH	d=0	100	24	6	HH	d=0	100	24	6	HH	d=0	100	26	-1	HH	d=0	100	26	-1
	d=1	38	10	5		d=1	66	22	8		d=1	33	13	0		d=1	51	25	-3
VV	d=0		100	6	VV	d=0		100	6	VV	d=0		100	-1	VV	d=0		100	-1
	d=1		40	4		d=1		69	4		d=1		36	0		d=1		51	-1
HV	d=0			100	HV	d=0			100	HV	d=0			100	HV	d=0			100
	d=1			33		d=1			44		d=1			34		d=1			33

Table 4 : Intercorrelations for SARAPE data, between polarization components for real and imaginary parts, as a function of frequency or displacement (average on 5 experiments) - in percentage -

real part (displacement)				real part (frequency)				imagin. part (displacement)				imagin. part (frequency)							
		HH	VV	HV			HH	VV	HV			HH	VV	HV			HH	VV	HV
HH	d=0	100	46	-2	HH	d=0	100	46	-2	HH	d=0	100	46	-1	HH	d=0	100	46	-1
	d=1	57	24	-2		d=1	78	45	-6		d=1	57	25	-1		d=1	78	45	-6
VV	d=0		100	-2	VV	d=0			-2	VV	d=0		100	-1	VV	d=0		100	-1
	d=1		61	-1		d=1			-2		d=1		62	-1		d=1		79	-1
HV	d=0			100	HV	d=0			100	HV	d=0			100	HV	d=0			100
	d=1			57		d=1			51		d=1			57		d=1			51

These tables show that the correlation is higher in the frequency direction than in the azimuthal direction. In the SARAPE system, correlation of real and imaginary parts are very similar and higher than those of magnitude and phase. Intercorrelations are relatively high between direct polarization channels HH and VV, but almost zero between crossed channels, HH-HV or VV-HV. In the STRADI system, intercorrelation exists between crossed channels, mainly because of artificial reflectors.

This statistical analysis will allow us to choose the most suitable way to group the data for vector quantization : 3 polarimetric channels with contiguous samples in frequency direction. For STRADI, complex data will be separated in magnitude and phase, whereas SARAPE data will be divided in real and imaginary parts.

### 3. VECTOR QUANTIZATION

In scalar quantization, each signal sample is represented by the closest value chosen out of a finite set of values. Vector quantization is a generalization of scalar quantization, where several signal samples are grouped together to form blocks of data : the vectors. Due to its ability to take advantage of data redundancy, it has proven its efficiency for data compression [3]. Basically, we use the LBG algorithm [4], which requires to build a dictionary before compression process. So, the algorithm is divided into two steps :

- the design of the dictionary, called "codebook", constituted of a finite set of vector prototypes, the "code-vectors". They are the most representative of the data vectors to encode. This step is performed off-line ;
- The quantization step consists, for each input vector, in searching through the codebook for the best matching code-vector and encoding this input vector by the index of this closest vector. Measure of distance between the input vectors to encode and their corresponding code-vectors is often chosen to be the mean square error and has to be minimized. Only the index of the closest code-vector need to be transmitted for each data vector (its index code in fact).

The code-vector dimension is dependant of the extent of correlations, but it cannot be too large for computation purposes. On the same side, the codebook size is selected in order to have the right trade-off between bit rate and compression quality.

In the codebook design and encoding steps, searching for the closest code-vector is a highly computational process, especially for high dimensional vectors.

Nevertheless, we have shown [5] that this method gives the best performances for polarimetric SAR type data, even at the price of higher complexity.

The process of quantization is applied separately on either magnitude and phase or real and imaginary parts, the choice depending on the statistical properties of the signal, as discussed in section 2.

### 4. RESULTS AND DISCUSSION

As a measure of the extra-cost brought by the full multipolarimetric information to transmit, we calculate the bit rate increasing between the first case of a non polarimetric SAR system (i.e. solely HH channel) and the second one with 3 polarimetric components (HH, VV, HV). Without any specific compression, the polarimetric bit rate will be at a maximum of 3 times the non-polarimetric bit rate. Therefore, the objective of vector quantization is to lower this factor and decrease the extra-cost due to the polarization.

In other words, we compare vector quantization, noted VQ, with vectors having 6 components, corresponding to the 3 polarimetric channels, every one with 2 consecutive samples along the frequency direction  $(HH_{f_i} \ HH_{f_{i+1}} \ VV_{f_i} \ VV_{f_{i+1}} \ HV_{f_i} \ HV_{f_{i+1}})^t$ , to scalar quantization, noted SQ, with a single channel of polarization coding each sample of frequency separately  $(HH_{f_i})$ .

Bit rate is close to entropy, therefore we perform calculation of entropy as a measure of bit rate. The polarimetric cost,  $C$ , is the ratio of entropy corresponding to VQ to entropy corresponding to SQ :

$$C = \frac{E_V}{E_S} = \frac{(E_{V,1} + E_{V,2})}{2(E_{S,1} + E_{S,2})}$$

$E_{V,1}$  and  $E_{V,2}$  (respectively  $E_{S,1}$  and  $E_{S,2}$ ) being the entropies obtained after VQ (respectively SQ), for the two components magnitude and phase, or real and imaginary parts, of the complex signal. The factor 2 in the denominator proceeds from the fact that vector quantization groups two consecutive frequency samples in the same vector, as opposed to scalar quantization where each sample is coded individually.

Table 5 (for STRADI) and table 6 (for SARAPE) give the polarimetric extra-cost,  $C$ , corresponding to several experiments, for a given signal to noise ratio (10 dB), where the considered noise is the quantization noise.

Table 5 : Entropy and polarimetric cost,  $C$ , in STRADI (for SNR = 10 dB)

data file	$E_{S,1}$	$E_{S,2}$	$E_{V,1}$	$E_{V,2}$	$C$
305	1.55	1.65	4.9	4.25	1.43
friche	1.48	1.86	5.3	3.5	1.32
parcelle	1.4	2	5	3.6	1.26
sable	1.26	1.68	4.75	2.8	1.28
toit	1.76	1.89	4.72	3.3	1.1

$E_{S,1}$  ( $E_{S,2}$ ) : entropy of SQ for magnitude (phase) of signal

$E_{V,1}$  ( $E_{V,2}$ ) : entropy of VQ for magnitude (phase) of signal

Table 6 : Entropy and polarimetric cost,  $C$ , in SARAPE (for SNR = 10 dB)

data file	$E_{S,1}$	$E_{S,2}$	$E_{V,1}$	$E_{V,2}$	$C$
08298_05	1.63	1.72	6.5	6.55	1.95
26297_06	1.7	1.41	7.85	7.9	2.53
26297_14	1.8	1.56	8.45	8.45	2.51
29697_08	1.52	1.7	8.4	8.3	2.59
30097_24	1.63	1.55	7.7	7.7	2.42

$E_{S,1}$  ( $E_{S,2}$ ) : entropy of SQ for real (imaginary) part

$E_{V,1}$  ( $E_{V,2}$ ) : entropy of VQ for real (imaginary) part

Results depend on the signal considered : they are much better for STRADI, because the presence of artificial targets increase noticeably the correlations between polarization channels. For SARAPE, if we look at tables 3 and 4, we see that normalized correlations between cross-channels, i.e. HH-HV or VV-HV, are very low and, consequently, do not participate to the advantage potentially brought by the grouping of elements in vectors of vector quantization.

This study reveals the difficulty to test the validity of a method on experimental data representing so extreme situations. We plan now to use simulated data illustrating ocean scenes in various configurations, generated by a simulator of polarimetric SAR [6], in order to be able to tailor existing correlations inside the signals.

## REFERENCES

- [1] J.C. Motet, B. Marechal, "High resolution radar measurement of clutter", Colloque radar 1994, pp. 534-539.
- [2] A. Berges, F. Christophe, SARAPE : "pocket SAR for outdoor RCS analysis", Colloque radar 1994, pp. 523-527.
- [3] A. Gersho, R. Gray, "Vector quantization and signal compression", Kluwer Academic Publishers, 1992, ISBN 0-7923-9181-0.
- [4] Y. Linde, A. Buzo, R. Gray, "An algorithm for vector quantizer design", IEEE Transactions on Communications, Vol. Com-28, 1980, pp. 84-95.
- [5] X. Morin, D. Barba, S. El Assad, "Caractérisation statistique de signaux de type ROS polarimétriques. Application au codage avec compression d'information", GRETSI'97, Grenoble, Sept. 1997, pp. 793-796.
- [6] C. Cochin, T. Landeau et al, "Simulator of ocean scenes observed by polarimetric SAR", CEOS SAR Workshop, Toulouse, Oct. 99, paper 037.



## How to Compute a Multi-Look SAR Image ?

Hubert CANTALLOUBE, Carole NAHUM

ONERA, Chemin de la Hunière, 91761 PALAISEAU Cedex, France.

Phone: (33)1 69 93 62 14, Fax: (33)1 69 93 62 69, E-mail: cantallo@onera.fr nahum@onera.fr

### ABSTRACT

Multi-look processing is known to improve SAR image quality because it reduces the speckle. We develop in this paper the exact linear combination of looks, which provides a least square optimum estimation for the retro-diffusion of a pixel. The algorithm we implement is iterative.

The results are analysed and compared with classical multi-look processing, with some SAR images obtained by the airborne SAR RAMSES.

### 1. MULTI-LOOK PROCESSING

Due to the low directivity of the radar antenna inboard the aircraft, one given point on the ground can be illuminated by the radar during a much longer time than the integration time.

On Fig.1, the point is illuminated from the time it appears under squint1 (on the forward side of the antenna lobe) to the time it appears under squint 2 (on the rear side of the antenna lobe). SAR images can be computed for a same point with different integration intervals as represented on Fig.2 (the two image rows containing the target point for each integration interval, are depicted). Clearly, since the direction of observation is different, the "range axis" in the two images (so called "single-look") do not match as displayed on Fig. 3.

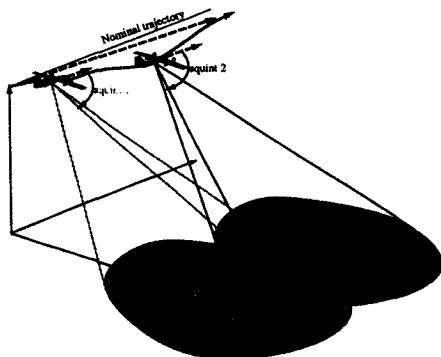


Fig 1 : Principle of multi-look processing.

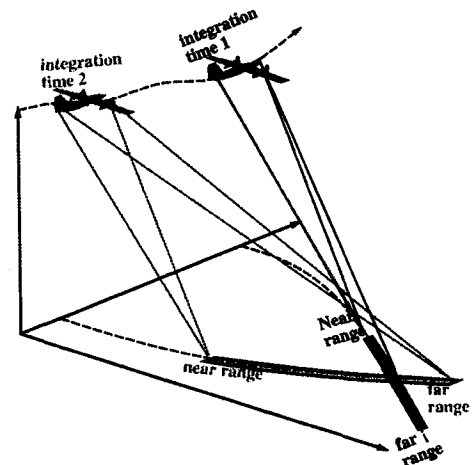


Fig 2 : The same point on the ground may be imaged from separated integration intervals (synthetic antennae).

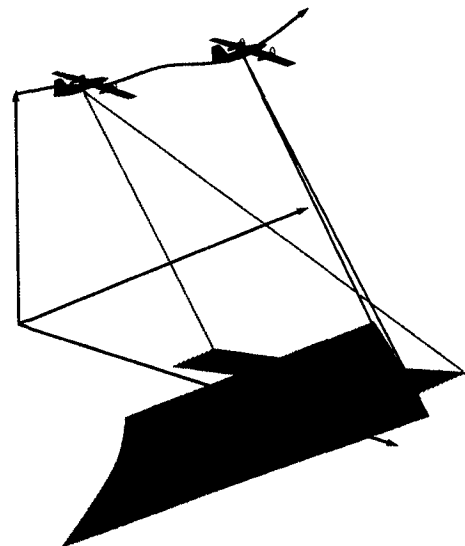


Fig 3 : The corresponding single-look images have their range axis oriented along different squint angles.

The accurate matching of the single-look images require a good geometrical model, especially if the aircraft trajectory is far from linear (in case the trajectory is linear uniform, a simple skewing maps one single-look to the other).

As it is well known, a multi-look combination has the advantage of reducing the speckle of the diffuse reflections on rough surfaces. This graininess is inherent to coherent imaging: holograms obtained by coherent visible light (from a laser) are also "grainy". One of the property of the speckle is that grain locations are independent for single-look images calculated from disjoint integration time intervals, thus averaging several single look images (after co-registration in the same coordinate system) will provide a smoother multi-look image.

This result on "real" rough textures is empirical. In fact, it is related to the statistical characteristics of the texture: Theoretically, a texture with fractal surface (fortunately, unlike any real surface is) would remain grainy whatever the number of looks combined!

### 2. OPTIMAL COMBINATION OF LOOKS

Assume that the exact back-scatter value of a given pixel in the SAR image is  $x$ . On the look number  $n$ , the measured value is  $y_n$ . This value  $y_n$  and  $x$  are related by the following equality, where  $b_n$  stands for the thermal noise amplitude and  $i_n$  the illumination (antenna lobe, propagation...).

$$y_n = x \cdot i_n (\nu_{n,1} + j\nu_{n,2}) + b_n (\nu_{n,3} + j\nu_{n,4}) \tag{1}$$

The  $\nu_{n,k}$  denote independant gaussian noises of mean zero and unit variance.

When performing a linear intensity combination of  $N$  looks, the intensity value of the result pixel becomes:

$$X^2 = \sum_{n=1}^N \lambda_n y_n^2 - \lambda_0 \tag{2}$$

Our aim is to determine the coefficients  $\lambda$  for obtaining an estimate of  $x^2$  with minimum variance. The  $\lambda_0$  term is intended to subtract the average value of the additive noise. This term is optional since it is sometimes unadvisable to have negatives estimates for  $x^2$ .

Expanding (2) provides for the mean of  $X^2$ :

$$x^2 \left( \sum_{n=1}^N 2i_n^2 \lambda_n \right) + \sum_{n=1}^N 2b_n^2 \lambda_n - \lambda_0 \tag{3}$$

and for the variance of  $X^2$ :

$$\begin{aligned} x^4 \left( \sum_{n=1}^N 2i_n^4 \lambda_n^2 \right) + x^2 \left( \sum_{n=1}^N 4i_n^2 b_n^2 \lambda_n^2 \right) + \sum_{n=1}^N 2b_n^4 \lambda_n^2 \\ = 2 \sum_{n=1}^N \lambda_n^2 (x^2 i_n^2 + b_n^2)^2 \end{aligned} \tag{4}$$

The problem is hence to minimise the variance (4) of  $X^2$  under the constraint that (3) equals  $x^2$ . The easiest solution comes from a geometrical viewpoint. Let us rescale the unknown weights  $\lambda_n$  as:

$$\phi_n = \lambda_n (x^2 i_n^2 + b_n^2) \tag{5}$$

The variance (4) becomes the distance to the origine squared. The constraint on  $x^2$  in (3) becomes the equation of a straight line:

$$\sum_{n=1}^N \frac{2i_n^2}{x^2 i_n^2 + b_n^2} \phi_n = 1 \tag{6}$$

Of which the point nearest to origine is:

$$\phi_n = \frac{i_n^2}{(x^2 i_n^2 + b_n^2)} \frac{\sum_{p=1}^N i_p^4}{\sum_{p=1}^N (x^2 i_p^2 + b_p^2)^2} \tag{7}$$

Thus yielding:

$$\lambda_n = \frac{i_n^2}{(x^2 i_n^2 + b_n^2)^2} \frac{\sum_{p=1}^N i_p^4}{\sum_{p=1}^N (x^2 i_p^2 + b_p^2)^2} \tag{8}$$

And the optional noise bias removal term comes from (3) as:

$$\lambda_0 = \sum_{n=1}^N 2b_n^2 \lambda_n \tag{9}$$

Remark that in (9), the weights  $\lambda_n$  are functions of  $x^2$  the value we want to estimate. Which means that the optimal linear combination weights depend on the signal to noise ratio. We hence have to implement an iterative process in order to get the result, starting with an initial guess of  $x^2$  (using the "negligible noise" limit case below). In practice, it seems that four iterations are sufficient and lead to a satisfactory result. This fact will be discussed in the next section where some illustrations are displayed.

The limit cases are interesting: When the amplitude  $b_n$  of the thermal noise becomes negligible with respect to  $x$ , the weights do not depend on the signal level itself.

$$\lambda_n = \frac{1}{N i_n^2} \tag{10}$$

Since  $\gamma_n^2/i_n^2$  is the intensity for the mono-look of which the illumination has been compensated, (10) correspond to the common way of computing a multi-look image.

The opposit limit case, when  $i_n x \ll b_n$ , is the case the thermal noise is dominant and the weights become:

$$\lambda_n = \frac{i_n^2}{b_n^4} \sum_{p=1}^N \frac{i_p^4}{b_p^4} \tag{11}$$

If we denote by  $\hat{y}_n$  the illumination compensated amplitude  $\gamma_n/i_n$ , their weights in the optimal linear combination are expressed in terms of the signal-to-noise ratio  $(S/B)_n = \hat{y}_n/b_n$ :

$$X^2 = \frac{\sum_{n=1}^N S/B_n^4 \hat{y}_n}{\sum_{p=1}^N S/B_p^4} \tag{12}$$

3. ILLUSTRATIONS

The SAR images displayed in this paper, were obtained from acquisitions of the ONERA airborne SAR RAMSES with linear-chirp deramped-on-receive waveforms in S-band. Images are synthesised with the BID SAR-processor, with flat-terrain focusing. Their slant-range resolution is 0.7 m, mid-swath depression is 35° and mid-swath range is 4 km. Trajectories are estimated by an inertial navigation unit with an error of the order of one nautical mile per hour, corrected by frame drift autofocus and registred to a scanned IGN paper map.

Note that (8) and (10) differ only when both the illumination  $i_n$  varies with  $n$  and the thermal noise contribution  $b_n$  is significant with respect to the image level  $y_n$  (hence to  $x^2 i_n^2$ ). The average energy of single-look images from the same signal acquisition varies little with most commonly used RAMSES waveforms (up to 3dB) because of the steep edges of the pre-summing filter applied onboard before digitising. Therefore for illustration purposes, we combined six single-looks images from three separated acquisitions on the same area.

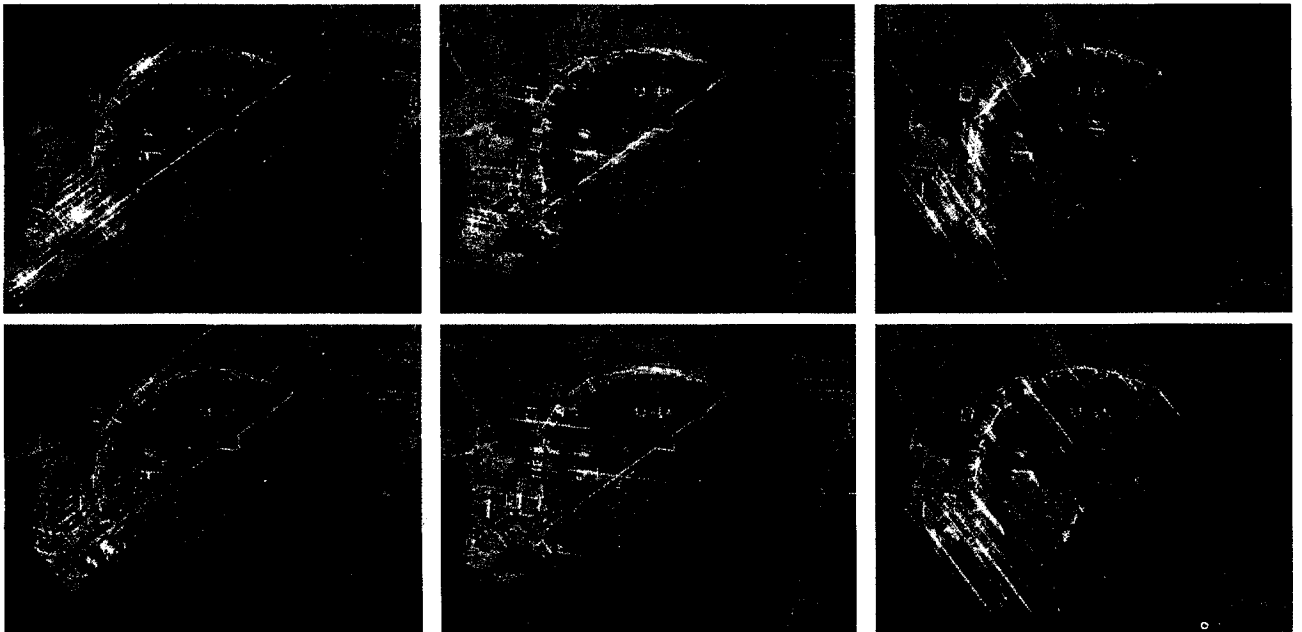


Fig 4: Six single-look band-S images from three acquisition fights (left to righttop), for two squint angles (backwards on the top, forwards on the bottom)

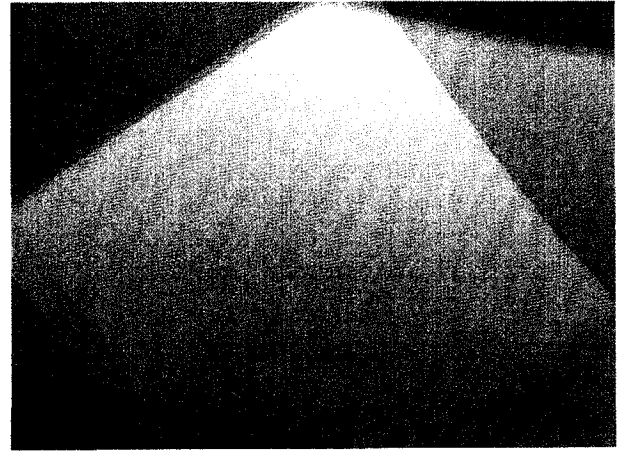


Fig 5 : Multilook image according to optimal or negligible noise laws (left). Corresponding radar illumination (right).

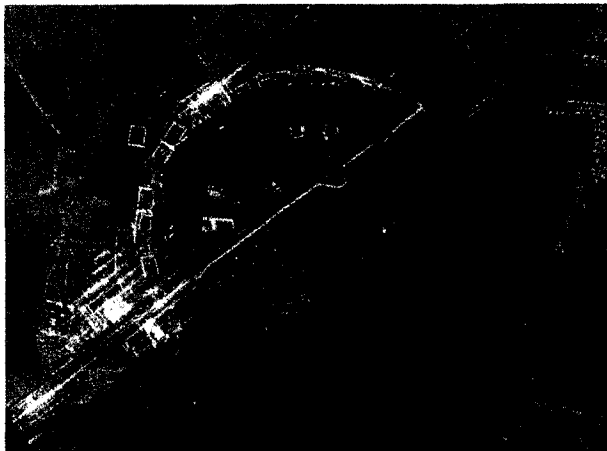


Fig 6 : Multilook image according to dominant noise law.

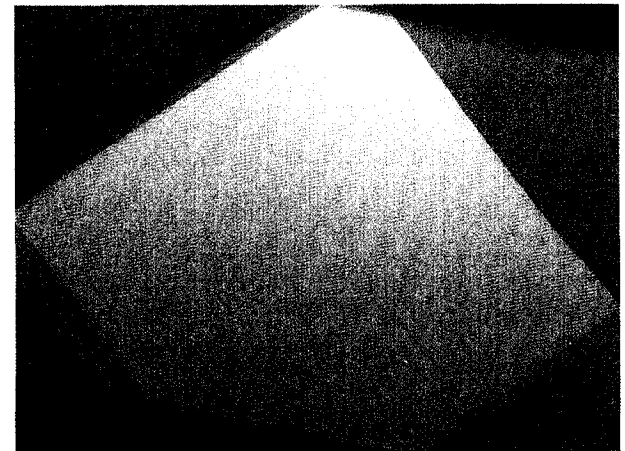
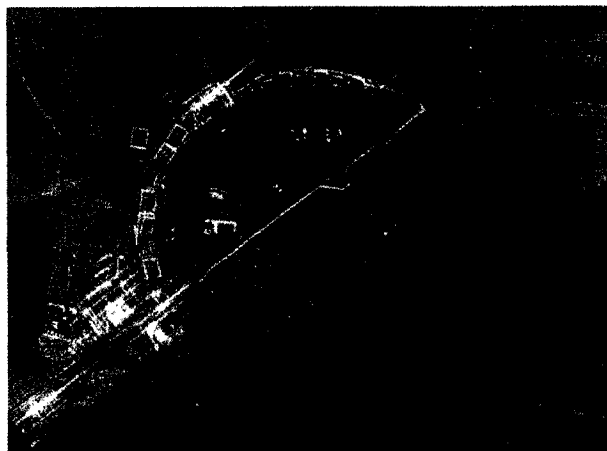
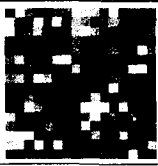

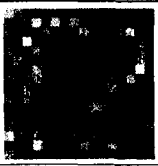
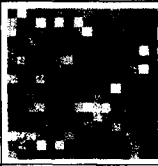
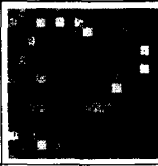


Fig 7 : Multilook image processed as optical image compositing (left) corresponding summed amplitude (right).

Table I: comparison of the composition laws on the images of Fig 4

law	single-look	multi-look	negligible noise	dominant noise	optical
sample					
mean	0.162	0.180	0.180	0.174	0.161
std.deviation	0.859	0.0408	0.0407	0.0545	0.0434
std.dev mean	0.528	0.227	0.226	0.312	0.269

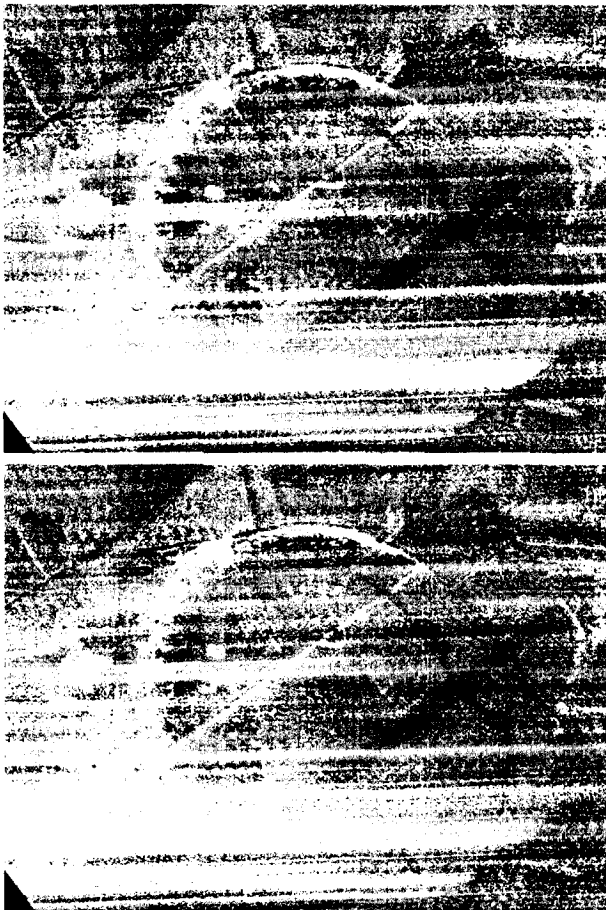


Fig 8 : multi-look images from images of fig 4 with strong noise (signal) injection. multi-look (top left), with negligible noise approximation (top right), dominant noise approximation (bottom left), optical image compositing (bottom right).

Difference between the multi-look composition law and the limit-cases approximations are minute for the images acquired by the RAMSES radar since the thermal noise level is low compared to the image levels ( $NE\sigma_0$  ranges from 20 to 30 dB depending on the squint angle). To emphasize on the difference we should add considerable noise, as we did on fig 9 by letting signal leak inside the image for half the energy. Even there, most of the difference is confined to the range extreme edges of the single-look images where the signal-to-noise ratio varies most between the images.

#### 4. CONCLUSION

We have implemented the optimal multi-look processing and compared the result with the classical version. The comparison shows a difference only if signal-to-noise ratio is low and signal levels varies significantly between the looks. Since generally SAR image noise is dominated by speckle, and the single looks corresponding to a single signal acquisition vary of only a few dB, the quadratic means of the illumination compensated amplitude is practically the optimal linear composition.

Optimal linear combination is only relevant for multi-look images from signal acquisition from different trajectories, in case of high  $NE\sigma_0$ .

## **Get Out of the Black Box: Turn Remote Sensing Data into Useful Information and Knowledge!**

Michel Oddou  
StorageTek SBG Europe  
1, rond point Général Eisenhower  
31000-Toulouse, France  
Phone : +33.5.62.14.32.07  
Email : michel\_oddou@storagetek.com

### ABSTRACT

Remote sensing data storage is coming through its evolution/revolution.

Where yesterday's means of managing archives were quite enough for the then current requirements, today's requirements are quite different.

The purpose of this paper is to show what's new in the domain of remote sensing data and how a storage provider company like StorageTek is offering an answer.

### 1. STORAGETEK

StorageTek is a worldwide company, present within the main countries through subsidiaries, and through distributors for other smaller markets. It has been created 30 years ago, and is headquartered in Boulder, CO.

StorageTek is a worldwide leader for storage solutions, originating from the 'IBM' world, with manufacturing capabilities for disk, tape and network products.

StorageTek is the leader in tape business with around 80% market share in the Plug Comptible Manufacturer (aka PCM) world, and with currently 60% shipment share in the 'open system' world (Unix, NT, and now Linux).

StorageTek is the leader in virtualization (disk, tape) that brings total benefits from their investments to the customers.

And to come with the use of these storage devices, StorageTek is heavily engaged into the move to fiber channel. As an example, StorageTek will be, with its 9840 tape device, the first vendor to market a tape device with native FC attachment.

StorageTek is used to become a new leader in every market it enters: open system libraries, then digital media, then medical. StorageTek is now entering the GIS market with the same ambitions.

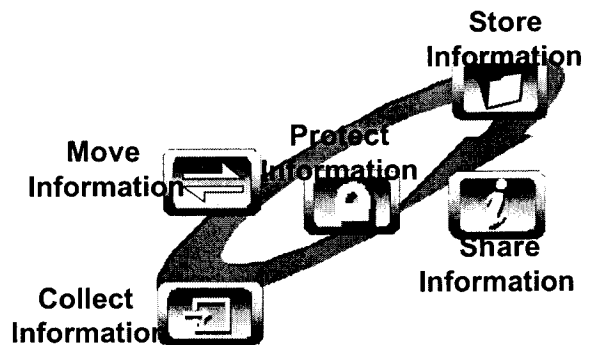
Through the Solutions Business Group, based in Toulouse for its EAME operations, StorageTek intent is

to provide business solutions for vertical markets, and functional solutions for horizontal markets.

With its tape library systems, its offer starts with less than 1 TB for small needs and ends with up to 7.5 PB for very large needs.

StorageTek is a company that masters its business with research and development capabilities and manufacturing plants in the US and in Europe.

When it is needed, it partners with leaders to provide complete solutions.



StorageTek business focuses on the data. From its Collection, through its Moving, up to its Storing, allowing to be Shared, and Protected against loss or illegal access.

Typically a data management project should look at all these aspects.

### 2. WHAT DOES CHARACTERIZE DATA WITHIN THE GIS ENVIRONMENT?

We have seen an ever-increasing resolution from satellites.

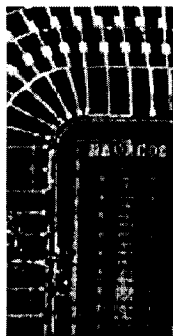
The unit of capture for satellite images is the pixel. One pixel is the size of the very small square that is seen on the PC screen but that may correspond to something very much larger on the earth. It is called the resolution.

The resolution in the early 70's used to be 30m. It was the time of the Landsat satellite. But there still may exist, for more global needs, larger resolution. I should say that it's only with the 30m resolution that problems begin to appear on the storage side! With a 30m resolution, users can start seeing small rivers and lakes, and distinguish urban areas.



The following resolution is the 10m one. It is the current resolution for Spot Image pictures. Streams and ponds can be distinguished. And on the building site, one could distinguish between residential and industrial areas.

The following major step is the 1m resolution. It is currently the finest resolution that can be purchased for commercial use. Satellites bringing such a resolution are for the most of them still to be launched. But they are there waiting on the pads. With 1m resolutions, streets can be detailed, parking lots can be identified, airplane models can be distinguished, and one can see windshields on cars.



The next resolution that can be achieved, and today available only for military and intelligence purposes, is the .3 meter one. With such a resolution, lines can be seen on a tennis court, people can be counted.

This increase in resolution goes with an ever-increasing quality. Where many years ago, only black and white pictures were taken with a limited gray scale, today color is required, and with more information also in the non-visible range. That will translate into the pixel size, as we'll see later.

Another increase that concurs to increase in data storage is the number of satellites. Even is today tens of satellites are already circling the earth, much more are still to come. And the launch planning that can be seen under <http://www.itc.nl/~bakker/launch-table.html> can just confirm this. And that's only the public launches.

Another characteristics for satellite imaging is that, like many other imaging industries (TV medias, medical), it is going from analog to digital. And digital data bring some characteristics of its own: it's never destructed (at

most it is archived) because it may be used or analyzed later, and it is so easily replicated and transported.

Another characteristic for the GIS world is that it is using more and more several types of data. It's quite common now to mix and marry vectors, raster data and images.

And finally, being so easily transportable and so easy to process, there is an ever-increasing need for access.

### 3. HOW DOES THIS TRANSLATE INTO DATA CHARACTERISTICS WITHIN THE GIS ?

As mentioned before a pixel is more and more 'heavy'. Where it was a 8 to 10-bits pixel for black and white pictures, it is now a 24-bits pixel for panchromatic

Image size is with regards to the matrix that can be put on board of the satellites. The most common size is 6000x6000 pixels. This translates into pictures of 60x60 kms for 10m resolution, and 6x6 kms for 1-meter resolution. Each pixel weighting 24-bits, i.e. 3 bytes, that's already more than 100 MB per picture.

Another parameter is the transfer rate that can be obtained from the satellites. Currently it's in the 70 Mb/s range. And this can translate into nothing but nearly 10 GB/day. For one satellite only!

Hopefully, once the data is received it can be compressed. And using the MrSID algorithm, which is very efficient, the storage size can be reduced by a factor of around 30.

### 4. WHICH EVOLUTION HAVE WE SEEN IN THE GIS WORLD ?

On the Collection side, as mentioned before, there has been a move from analog to digital.

Another evolution there is that due to the high-speed process that is collection of this data, the storage tends to be 'on site'. Before anything else is done on the data.

On the Move side, higher speed transmission is required due to the higher 'quality' of the data. This very often requires also a higher speed for the backbone, and obviously for the networks.

As noticed above, the collection point is also a storage point. It is now common to speak of something like a terabyte of storage there. And it's just enough to handle a few weeks of collection.

The phenomena is just more amplified at the central archival (and it often exists) where the units maybe hundreds of terabytes, and even petabytes.



As points of collections are spread around the world, the data is also spread around the world. And as users that require these data are not at all near these points, there is a need to move this data as quickly as possible. Moreover, some users need to get the freshest data that is surely not nearby them.

These data are of a commercial value. And its access through the web does require more security. A web access may be the best but also the worse! And this same commercial value requires more protection against either loss, or non-accessibility.

#### 5. HOW TO GET DATA.... INTO THE BLACK BOX

As mentioned before, it is now necessary to put data capture as close to the antenna as possible.

For current installations this is done through a multi-pass equipment, that prevents from modifying anything in the existing flow.



Through this multi-pass system, a copy of the received data is sent to a Direct Ingest System (DIS).

The role of the DIS is to acquire data, format images for the archives, record data on a temporary file, and provide metadata and quicklooks.

This is really an ingestion system, which includes dedicated software, that is suited to the data flow characteristics of the satellite for which it is working.

The DIS is running continuously, as an autonomous process.

Data comes out of the DIS into the Local Catalog and Archive System (LCAS).

The role of the LCAS is to have an automated ingest of image, metadata and population of index. Then through a hierarchical storage management system (HSM), it optimizes the utilization of storage, that is split between a RAID disk configuration and a tape library. The purpose of this HSM function is to put the most recent data on RAID, and the older data on tape.

Due to the relative limitation in size for this LCAS

(although it is in the terabyte range, it doesn't allow permanent storage for more than a few weeks of ingest), the role of the LCAS is also to create a copy of the data for the Central Archiving System (CAS).

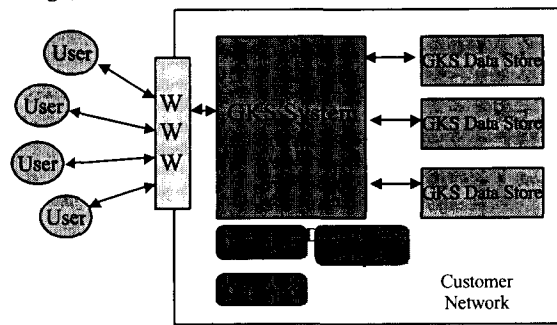
It will not be said more about the CAS, as it is just a bigger and larger LCAS unit, with the same architecture and the same functions.

That ends the process that put data into the black box.

#### 6. HOW TO GET DATA.... OUT OF THE BLACK BOX

The LCAS/CAS is also designed to facilitate access to the data.

It is architected so as to provide a global view of the storage, wherever it is.



All the LCASs and the CAS create a really distributed system, seen by the customer as if it were a unique central large system.

An LCAS system provides customers with a web-based interface to get access into the archives.

This web based interface:

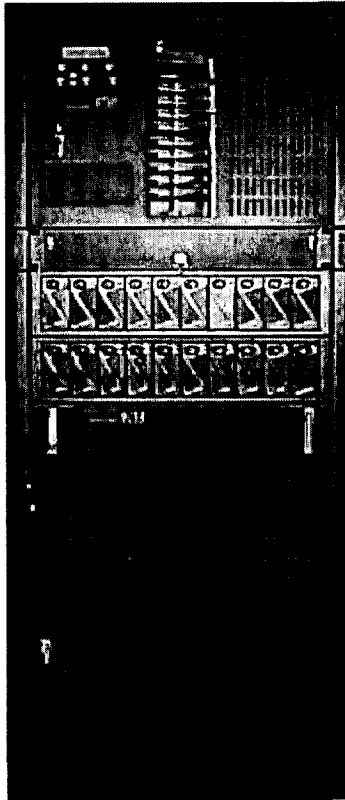
- Allows to get to the desired location, wherever it is in the world, within a few mouse clicks;
- Allows to select the source of the desired data (the many different resolutions that have been mentioned above just reflect the many different level requirements from different users populations);
- Allows to get the desired time of capture (it's obvious to say that that the pictures taken for the Alps aren't quite always revealing the same features);
- Permits a pre-viewing through the use of quicklooks.

Thus, it facilitates identification of data sets and easy ordering through the use of maps and footprint results. Then during this shopping, customer can put orders into a shopping cart.

And finally, distribution of the orders is done overnight.

## 7. A COMPLETE OPERATIONAL RUNNING SYSTEM: GEOSPATIAL KNOWLEDGE SYSTEM, FROM STORAGETEK

Following the architecture that has been described above, StorageTek has created a complete system that is ready to be used. It has been called the Geospatial Knowledge System, or GKS.



*GKS unit for 1TB of managed storage*

This system is built from 'over the shelf' components.

This approach brings the following advantages:

- Lower cost of acquisition
- Easy use of up to date technology
- Minimal learning for use and maintenance

Following these rules, GKS is built using:

- A Sun platform (the minimal configuration is an E450 for the LCAS's) running Solaris
- OpenSystem RAID5 disk and Timberwolf/ Powder-Horn tape libraries from StorageTek, providing from less than 1TB, and up to 7.5 PB
- An Oracle relational data base (optionnal, for very large needs), complemented by its Spatial Data Cartridge
- The ASM hierarchical storage management soft-ware from StorageTek
- The TerraSoar software from Core Software Technology
- Apache as web server
- ImageNet as web distribution vector

and is delivered and put into production with some additional services for StorageTek SBG and/or Core Software Technology.

## 8. CONCLUSIONS

With GKS StorageTek is bringing to the market a solution, not one solution.

The architecture of GKS should allow it to fulfill many other requirements in the domain of geographical information storage.

With some minor modifications that don't apply to its architecture, it could be used to store satellite telemetry, SAR datas...

## REFERENCES

None

## A Spaceborne Ground Penetrating Radar : MIMOSA

A. Herique <sup>(1)</sup>, W. Kofman <sup>(2)</sup>, P. Bäuer <sup>(3)</sup>, F. Remy <sup>(4)</sup>, L. Phalippou <sup>(1)</sup>

(1) ALCATEL SPACE INDUSTRIES, 26 avenue Champollion - BP 1187 - 31037 Toulouse cedex, France

(2) LPG, UJF Bat de physique D, BP 53, 38041 Grenoble cedex 9, France

(3) CNES, 18 avenue Edouard Belin 31401 Toulouse cedex 4, France

(4) LEGOS, 18 avenue Edouard Belin 31401 Toulouse cedex 4, France

The MIMOSA radar is a spaceborne unfocused nadir looking synthetic aperture radar designed to penetrate the Earth superficial layers and proposed in the frame of the Earth Explorer Opportunity Missions (ESA).

This paper reviews all the mission aspects. The scientific objectives are presented: 3D mapping of Antarctic ice sheet, biomass monitoring, and prospective objectives.

The instrument concept is developed. The physics of the measurement is analyzed to show that the expected signal is a mixture of deep echoes and surface clutter. A clutter rejection processing is proposed. Some results of signal simulation are given for typical ice surfaces.

A preliminary instrument design is described, based on the physics analysis and simulations results.

### INTRODUCTION

The MIMOSA radar has been proposed to the European Space Agency in the framework of the Earth Explorer Opportunity Missions.

Remote sensing over continents is generally limited to the thin surface layer, while many issues related to climate or Earth resources require information at some depth. The scientific objectives of the MIMOSA mission are to improve our understanding of the Earth processes involving global scale monitoring of continental ice, vegetation and soil surfaces.

The proposed instrument is a nadir looking P-band Synthetic Aperture Radar to observe the Earth surface at depths beyond the superficial layers, with horizontal resolutions from 1km to few tens of km and monthly temporal coverage. This radar will be complementary to existing and forthcoming spaceborne optical and radar observation systems, which are limited to observations of superficial surfaces.

This exploratory mission should have a two-year duration. The frequency will be ~300 MHz, with a 10 MHz bandwidth. It will be implemented on a small size satellite launched in a true polar orbit at an altitude of 500 km. The temporal repeat cycle is designed to provide a total coverage of Antarctica and Greenland over the two-year mission.

### MIMOSA OBJECTIVES

The main objective of the MIMOSA mission is to map the thickness of the Antarctic ice sheet. The secondary objectives are more prospective : Permafrost mapping, biomass monitoring of forested areas; Hydrogeological surveys.

#### Antarctic Ice Sheet

The Antarctic ice sheet with a volume of 30 million km<sup>3</sup> is the result of the balance between accumulation of snow and losses through, melt and iceberg calving. It constitutes a memory of the few last 100 000 years history of the Earth climate. The exploitation of these archives and the prediction of future evolution requires three-dimensional numerical models, based on observational data, in order to describe the entire regime of the ice sheets.

The existing space borne instruments : microwave radar, altimeter, scatterometer provide information on the surface state. Several airborne ground penetrating radar missions have been performed since the seventy's ([ 1 ], [ 2 ]): a limited part of the Antarctic has been sounded with a horizontal sampling step of about hundreds kilometers, the largest part is unknown.

Only a spaceborne radar can provide a global coverage with a good spatial resolution of the whole Antarctic continent. It is the aim of the MIMOSA proposal to compile the following physical parameters over the entire Antarctic ice sheet with a kilometric horizontal resolution and a 10-meter vertical resolution :

- ice thickness (up to 4500m),
- bedrock topography,
- internal layers (up to -60dB reflection coefficient) and
- ice dielectric properties estimation [ 3 ].

These measurements associated with measurements of the surface parameters will provide an essential information for the knowledge of the ice sheet dynamic and a crucial input for the numerical modeling:

- total ice sheet volume given by the ice thickness,
- estimation of ice flow velocity and direction related to the ice thickness, the bedrock and the internal layers topography (isochrone layers due to volcanic activities)
- history of the ice flow related to the local disruption in layering
- ice physical evolution related to the estimation of the ice dielectric losses.

#### Secondary objectives

The other MIMOSA scientific objectives are prospective: the goal is to cover a large field of application in order to demonstrate the interest and the performances of a P-band spaceborne radar. These applications are related not only to the properties of penetrating waves but also to the compatibility with the instrument design given by the ice mode, in particular the nadir looking configuration.

**Biomass** The interest of the low frequency observation for vegetation monitoring has been demonstrated in the past few years by several airborne missions.

The correlation between radar backscattering coefficient and forest biomass increases significantly as the radar frequency decreases [ 4 ]: the P-band allows to monitor over 200 tons per hectare at oblique incidence versus 100 tons/ha for the L-band.

The Nadir looking measurement associated with a 15-m resolution allows to penetrate into the vegetation layers and to obtain a vertical structure of the forest [ 5 ].

The measurement of biomass and forest structure provides the global monitoring of natural and anthropogenic evolution of the forest and its impact on the carbon and water cycles.

**Other applications** The P-Band allows to monitor the dielectric properties of such soil in the nadir looking geometry. This technique makes possible the mapping of large areas and the monitoring of ground properties evolution.

The prospective fields of applications are huge and concern:

- the permafrost mapping and monitoring which are related to the carbon cycle and the climate evolution,
- the desert areas sounding which is related to their evolution modeling,
- the water and water table monitoring in semi-arid regions which is related to the natural resources management,
- the water saturation study which is related to the infiltration and water movement comprehension and to the flood risk management.

## PHYSICS OF THE MEASUREMENT AND INSTRUMENT CONCEPTS

The Mimosa instrument is a spaceborne ground penetrating radar primary designed to sound the Antarctic ice. This radar is a unfocused nadir-looking synthetic aperture altimeter : the design and the nominal operating mode, optimized for this primary objective (ice), are also compatible with all the other scientific objectives.

#### Wave propagation in ice

The propagation of electromagnetic waves in ice is determined by its complex permittivity  $\epsilon = \epsilon' - j\epsilon''$ . The loss tangent,  $\text{tg } \delta$ , is given by  $\text{tg } \delta = \epsilon''/\epsilon'$ .

The real part of the permittivity is essentially constant and equal to 3.2 for the ice in the VHF/UHF band. This real permittivity gives the radiowave velocity  $v = c / \sqrt{\epsilon}$  where  $c$  is the speed of light in vacuum ( $v \cong 1.7 \cdot 10^8 \text{ m.s}^{-1}$ ). This wave velocity is larger in the upper part of the ice sheet of snow which density increases with depth. In the upper 200 m, the permittivity of the ice/air mixture increases from 1.5 at the top to 3.2 [ 1 ], [ 3 ].

In contrast, the loss tangent, from which the dielectric absorption is calculated, depends upon the electromagnetic wave frequency and the ice temperature. Figure 1 shows the dielectric absorption versus frequency and temperature. It clearly exhibits a low absorption coefficient, nearly constant with frequency up to about 300 MHz and strongly temperature dependent. This fact justifies the choice of the baseline frequency: a frequency sufficiently high, so as to limit the physical size of the aeriels, but still located in the low attenuation band. For the Antarctic case, the expected mean attenuation is 3 dB per kilometers.

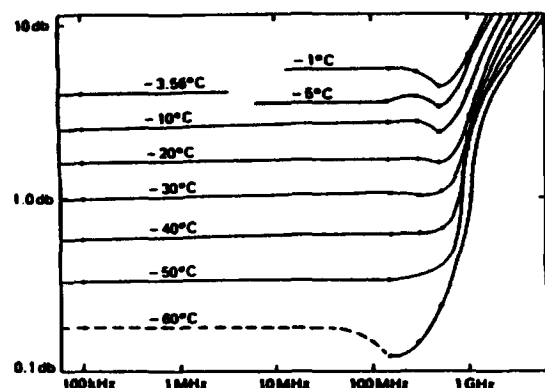


Figure 1 : Dielectric loss coefficient as a function of radar frequency (in dB/100m) at different temperatures [ 6 ]

The mission is faced with a frequency allocation problem: there is, as yet, no allocation in the P-Band for active remote sensing of the Earth. Considering that the primary objective of MIMOSA is the observation of ice caps and other non-populated areas, the possibility of granting a secondary allocation, as is the case for radar altimeters, is regarded as quite feasible. While a frequency of 300 MHz is preferred, the band between 430 and 440 MHz is still acceptable and has been requested by the Space Frequency Co-ordination Group for the purpose of active remote sensing from space.

### Physics of the measurement

Due to the low frequency, the Mimosa radar is a new class of instrument in terms of physics of the measurement itself. The radar return is a mixture of deep echoes and surface echoes (figure 2):

- *The first type of echoes gives (for the case of the ice) the signal of interest.* These coherent echoes correspond to a nadir specular reflection (geometrical optics).

At each interface (surface, ice layer or bedrock) the wave is partially reflected by the first Fresnel zone. The first Fresnel zone has, in the present case, a 1-km radius around the nadir direction which defines the spatial resolution of the Antarctic sounding mode.

The reflected power is given by the Fresnel reflection coefficient (Snell law) which is a function of the permittivity contrast at a given interface. For a realistic physical interface, this power is modified by the surface roughness : the specular reflected power approaches zero when typical height of the random surface approaches the magnitude of the wavelength.

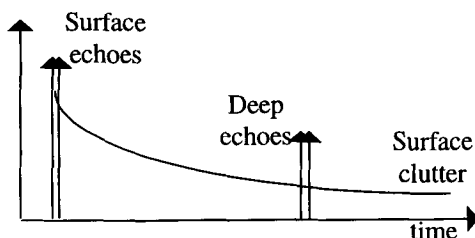
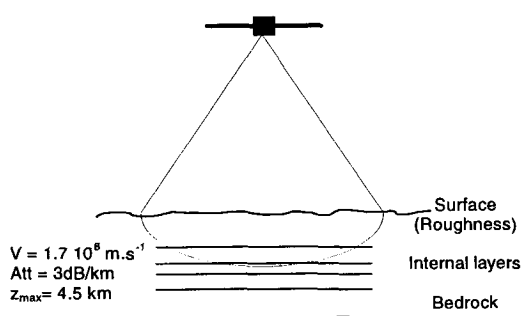


Figure 2 : Wave propagation in ice  
Specular reflection and incoherent scattering

- *The second type of echoes corresponds to unwanted incoherent echoes* coming from surface scattering.

This clutter comes from the whole surface illuminated by the antenna. Due to this phenomenon, ambiguities will arise between expected in-depth echoes and unwanted lateral clutter echoes: indeed, side incoherently backscattered echoes could reach the detector at the same time as wanted coherent echoes coming from a deep interface and, thus, could mask the signal of interest (figure 2).

The power of the clutter echoes is a function of the incoherent backscattering coefficient which depends upon the statistical properties of the surface roughness : the scattering increases with the roughness. The angular distribution of the scattered signals depends upon the horizontal correlation length of the roughness.

### Clutter rejection

The instrument and the processing are designed to maximize the coherent to clutter power ratio and to limit the "blind depth".

In the across track direction, the clutter is only limited by the antenna pattern. This has an impact on the antenna pattern specification and, therefore, on the size of the antenna.

In the along track direction, the clutter is reduced by the processing: to achieve this, a very low antenna directivity is sufficient in the along direction.

The processing is an unfocused synthetic aperture near the vertical based on the localization in the Doppler domain of the signal of interest:

- The signal of interest originates from the direction perpendicular to the imaged interface. It is preserved by Low Pass Doppler filter.

- The clutter, on the contrary, which comes from all directions illuminated by the antenna is eliminated in this process.

Simulations show that this Doppler filtering process is required in order to image -60 dB internal layers. As a consequence, the operating modes and the synthetic aperture length have to be compatible with this filtering constraint.

### Ionospheric effect

At the proposed operating frequency, the main propagation effects are introduced by the presence of the ionospheric layers between the satellite and the ground. These effects are the Faraday rotation and the absolute phase variation. In order to cope with Faraday rotation effects, a circular polarization in transmission and reception has been chosen.

The variation of the phase with respect to propagation in vacuum introduced by the presence of the ionosphere is

$$\Delta\phi = [2\pi / fc] \int f_p^2(z) dz$$

where  $f_p(z)$  is the plasma frequency and  $f_p^2 = K n_e$  ( $n_e$  electron concentration). The phase  $\Delta\phi$  appears to be proportional to the ionospheric total electron content  $TEC = \int n_e(z) dz$  which varies along the satellite track.

For 300MHz and 10 MHz bandwidths, the effect of the constant  $TEC(x_0)$  which produces a about constant time delay in the radar pulse group propagation time, is to introduce a bias in the altimetric measurement but no distortion on the relative positioning of the intermediate layers and of the bedrock with respect to the Antarctic surface.

The horizontal gradient in TEC, however, produces a bending of the radio ray at essentially all points of the orbit. The impact on the SAR imaging resolution is characterized by the following relation:

$$L_s \frac{1}{TEC} \frac{\partial TEC(x)}{\partial x} < 0.44 \frac{R}{H_1} \frac{\lambda}{H_{eq}} \left( \frac{f}{f_{pav}} \right)^2$$

where  $L_s$  is the synthetic antenna length,  $R$  is the satellite altitude,  $H_1$  is the average altitude of the ionospheric layer,  $H_{eq}$  is an equivalent thickness of the ionosphere, and  $f_{pav}$  is an average r.m.s. plasma frequency over this thickness. In practice, this places an upper limit on  $L_s$  for a given ionospheric gradient. The ionospheric total electron content must not change by more than 3.2 % over  $L_s$  where one used the typical values:  $H_{eq} = 100$  km,  $H_1 = 250$  km,  $f_{pav} = 5$  MHz. In general the

variability of the electron content in the ionosphere is at least one order of magnitude less than this value. However in the auroral zone strong irregularities can exist especially during the auroral arcs when the variability of electron content can increase above the indicated limit.

## INSTRUMENT SPECIFICATION

A simulation of the wave propagation has been developed in order to demonstrate the experiment feasibility, to specify the instrument and to guide its design. This simulation has been done by the Laboratoire de Planetologie de Grenoble and by Alcatel Space Industries, Toulouse.

### Measurement simulation

Figure 3 shows the expected power of coherent and incoherent components versus depth or equivalent propagation time. The measurement is simulated for a rough interface modeled by a random Gaussian distribution of heights defined by its height standard deviation ( $\sigma_h$ ) and its slope rms ( $s$ ). The two ice sheet surface statistics correspond to the central part and the coastal zones of the Antarctic.

The simulation includes a complete link budget, the antenna gain and the signal processing (i.e. clutter reduction). All the field components are estimated as a function of time using different theoretical or empirical approaches.

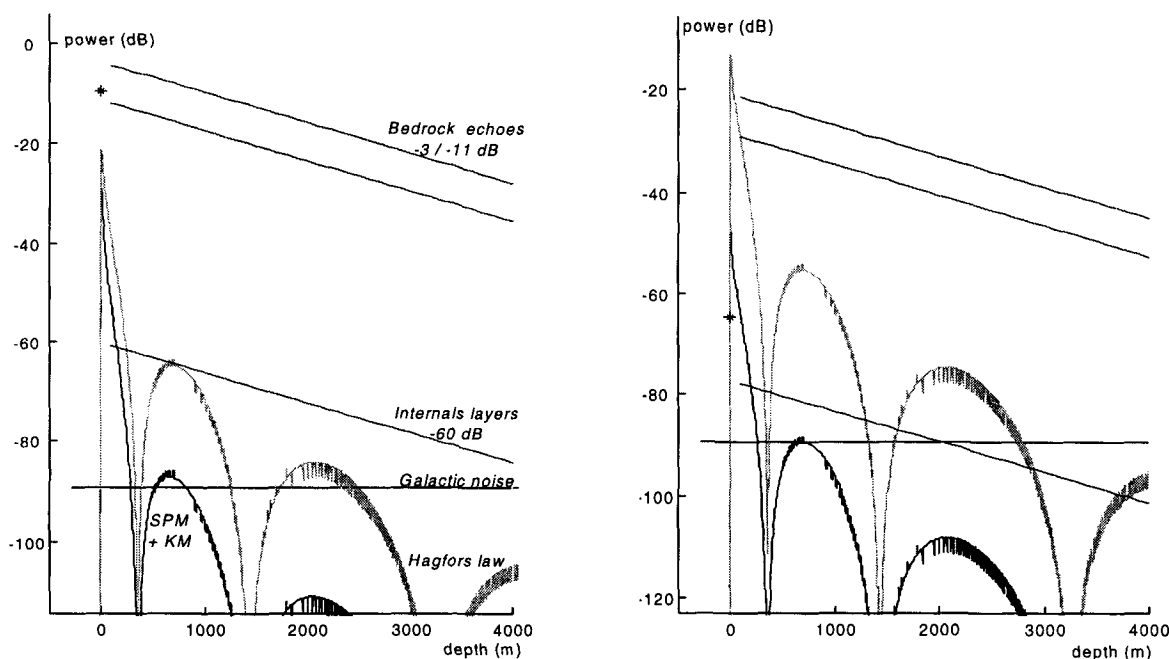


Figure 3 : MIMOSA simulations for surface roughness corresponding to the Antarctic central part (left) and coastal zone (right)

The surface echo coming from the Fresnel zone is the first received signal corresponding to the star at the null depth. It is incoming from the nadir direction which corresponds to maximum antenna gain. This power depends on the Fresnel reflection coefficient modified by the roughness attenuation  $\chi$  ( $0 < \chi < 1$ ). This one is estimated using the classical Kirchoff approximation:

$$\chi = \exp(-2 \sigma_h^2 k^2)$$

where  $k$  is the wave number in vacuum.

The surface backscattering coming from the whole antenna pattern is spread in time and corresponds to the two curved lines in the figure. The backscatter coefficient is estimated for a given surface statistic using two methods:

The lower graph is based on theory [ 7 ]. The backscattering coefficient is then the sum of the Small Perturbation Model and of the Kirchoff First Order Model:

$$\sigma(\theta) = \frac{8 k^4 \sigma_h^3 \cos^4 \theta R^2}{s^2} \exp\left(-\frac{2k^2 \sigma_h^2}{s^2} \sin^2 \theta\right) + \frac{R^2}{2 \cos^4 \theta s^2} \exp\left(\frac{-1}{2s^2} \tan^2 \theta\right)$$

where  $R$  is the reflection coefficient. The Small Perturbation Model is given by an electromagnetic field development at large incidence angles and tends to underestimate the component near nadir. The Kirchoff First Order Model is a classical approximation in the geometrical optics for rough enough surfaces at low incidence angles.

The higher graph is based on an observational law: the backscattering coefficient is given by the semi-empirical Hagfors law [ 8 ]:

$$\sigma(\theta) = \frac{1}{2} R C (\cos^4 \theta + C \sin^2 \theta)^{-\frac{3}{2}}$$

with the following height characteristic function:

$$C = \frac{1}{4 k^2 \sigma_h^2 s^2}$$

The deep echoes coming from internal layers or from the bedrock correspond to the three parallel straight lines. The graphs show the expected power versus depth for three kinds of deep interfaces: an ice / liquid water transition for a bottom lake (reflection coefficient = - 3 dB), an ice / rock transition for the bedrock (-11 dB) and a very low internal transition with a -60dB reflection coefficient.

The estimate of the power includes the roughness effect on both interfaces (in transmission for the surface, in reflection from the deep interface), and the dielectric absorption due to the ice propagation (3dB/km).

The ice / water interface echoes are more powerful than the specular echo coming from the surface. This is due to a low reflection coefficient at the air/ice interface (-10dB).

Simulations show the feasibility of the experiment and the expected performances. For depth larger than 300 m, the radar sensitivity after Doppler processing is larger than -60 dB inside the continent and about -35 dB near the coast. These performances could be increased by an antenna optimization.

Other simulations show that the bedrock is nearly detectable directly from the raw data in the whole range of depths in the central part of the ice sheet.

#### Instrument specifications and performances

##### *Mission requirements*

Duration	2 years in orbit
Orbit	polar
Altitude	500-600 km
Stabilization	3 axes
Altitude knowledge	100 m on board
Antenna pointing	Nadir

##### *Radar system requirement*

Carrier frequency	300 MHz	P band
Bandwidth	10 MHz	
Instantaneous Rx Dyn.	> 60 dB	
radiometric accuracy	3 dB	
radiometric stability	1dB	
antenna aperture		
Across track	5°	
Along track antenna	Large	

##### *Ice mode performances*

Fresnel zone diameter	1 km
Vertical range resolution	8.4 m (ice)
sensitivity	-60 dB (at bedrock level)
Ice sheet thickness	0 - 4 km
Max. integration time	0.5 s

#### PROPOSED IMPLEMENTATION

Figure 4 shows the proposed implementation in flight configuration based on a Proteus platform and Table 1 summarizes the mass and power budgets.

Subsystem	weight	average power
Antenna	2x20 kg	-
Radar Electronic	12 kg	10 W
Data Handling system	13 kg	20 W
Platform	350 kg	300 W
TOTAL	415 kg	330 W

Table 1 : Mimosa power and mass budget

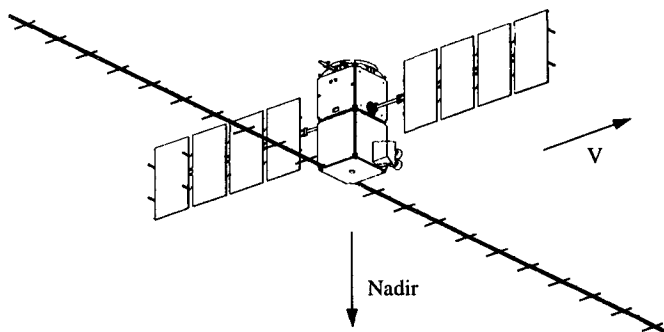


Figure 4: Mimosat flight configuration

**Payload** The MIMOSA payload consists of a radar operating at 300 MHz (P Band) and designed to sound the Antarctic ice. This radar functions as an altimeter with a large receive dynamic range and with an unfocused synthetic aperture which requires pulse to pulse phase coherence. The payload is made up of three parts: the radar antenna, the radar electronics and the payload telemetry (including mass memory).

The antenna directivity requirements induce a large array antenna in the across track direction. The spatialization and deployment of large structures is a problem studied for several projects. The antenna design constitutes a main point of the mission complexity and cost reduction.

The baseline concept is based on two arrays of cross half length dipoles distributed along two deployable masts. The electromagnetic accommodation of the antenna shall be specially studied using the background from the space electronic warfare including VHF/UHF coupling simulations and measurements facilities.

The MIMOSA radar electronic and data handling subsystems do not require particular complexity. They are comparable to SAR and altimeter systems.

**Spacecraft** The proposed mission is compatible with a Proteus platform developed by CNES and Alcatel. Matching a wide range of LEO orbits, the Proteus platform design allows to define the mechanical and thermal environments of the payload, provides the power supply, attitude and orbit control, and the command and control capabilities. Based on a mature concept, this platform enables a cost effective access to space for scientific missions such as MIMOSA.

The preliminary system analysis for the adaptation of the payload on the platform shows that the specifications of the mission fit in the flight envelope of the platform, yielding a robust satellite based on a recurrent design. In particular, the following points have required a particular attention:

- The solar panel orientation cannot be optimized during

all the orbits due to the polar orbit requirements and the antenna across track orientation. This constraint reduces the average power but a large margin has been preserved.

- The attitude and orbit control is a mission difficulty due to the size of the antenna masts and their inertia momentum. The 3D attitude control requires minor modifications of the platform.

**Ground Segment** The proposed system makes great use of existing elements such as the PROTEUS satellite control center and the ENVISAT Payload Data Segment which have been designed to be reused thus allowing for cost reduction, delay minimization and risk reduction mainly at integration and validation levels.

## CONCLUSION

The MIMOSA P-Band radar is a new class of scientific spaceborne radar. It constitutes a major opportunity not only for understanding of the Antarctic ice sheet past and future evolution but also for several prospective applications like biomass and geophysical monitoring.

From the technical point of view, this mission combines technological innovations and heritage of previous missions.

## REFERENCES

- [ 1 ] Bogorodsky, V.V., C. Bentley, P. Gudmandsen, Radioglaciology, 1985, D. Reidel, Germany.
- [ 2 ] Gudmandsen, P., Layer echoes in polar ice sheets, J. Glaciol., 1975, 15, pp95-101.
- [ 3 ] Herique A., W. Kofman, Determination of the ice dielectric permittivity using the data of the test in antarctica of the ground penetrating radar for mars'96. *IEEE GRS*, 1997, n°5. pp 1338-1349.
- [ 4 ] Le Toan T., A. Beaudoin, J. Riou, D. And Guyon, Relating forest biomass to SAR data, *IEEE. GRS*, 1992, Vol 30, N°2, pp 403-411.
- [ 5 ] Bernard R., M.E. Frezal, D. Vidal-Madjar, Nadir looking airborne radar and possible applications to forestry, *Remote Sen. of Env.* 1987, vol 21, p 297-309.
- [ 6 ] Evans S., B.M.E. Smith, A radio equipment for depth sounding in polar ice sheets, *J. of Scientific Instruments*, 1969, vol 2, n°2, pp131-136
- [ 7 ] Ishimaru, A., Wave propagation and scattering in random media, 1978, *Academic Press*, New-York,
- [ 8 ] Hagfors T., Relations between rough surfaces and their scattering properties as applied to radar astronomy in *Radar Astronomy*, 1968, Eds J.V Evans and T.Hagfors, pp. 187-218, McGraw-Hill.



## Phase Unwrapping by Ground Slopes Estimation

Xavier Dupuis, Pierre Mathieu, Michel Barlaud.  
mathieu@i3s.unice.fr

Laboratoire I3S CNRS  
Université de Nice-Sophia Antipolis  
2000, route des Lucioles  
Les Algorithmes / Bât. Euclide, BP 121  
06903 Sophia Antipolis Cedex, France  
Tel. :+33 4 92 94 27 35 Fax :+33 92 94 28 96

### ABSTRACT

This paper deals with synthetic aperture radar interferometry. Our approach is based on gradient components estimation. Indeed we proposed to compute the ground slopes, because there are the gradient components of the observed interferogram without fringe lines due to wrapping. Because of the gradient components high sensitivity to noise level, we propose a three-step phase unwrapping approach. The purpose of preprocessing is to organize the phase in order to improve the estimation of ground slopes. The main process smoothes the phase gradient components while edge preserving. The gradient components are integrated with a locally adapted two-dimensional integrator. We present experimental results for real ERS1 data.

### INTRODUCTION

Synthetic aperture radar (SAR) interferometry is a powerful technique allowing the generation of digital ground models (DGM). In order to get a high quality DGM, we must have a low-noise interferometric image. To unwrap the phase, it is thus necessary to combine two single complex views, obtained from different observation angles, of the same scene. In a low-noise case the unwrapping would be easy; however, local errors due to noise result in global errors due to causal nature of unwrapping. Several methods exist [3] [4] to avoid the propagation of local errors; for example [2], detects fringe lines with edge enhancing and then adds  $2\pi$  whenever the path crosses a fringe line. Efficient Methods are recently developed, which are based on Green's integral formulation [5][6]. These methods lead to heavy algorithms. Our approach consists in a preprocessing that organize data in order to improve the estimation of ground slopes, followed by the main algorithm, which estimates the ground slopes of the unwrapped phase from the gradient components of the wrapped phase. Then, these ground slopes are integrated to obtain the unwrapped phase.

### STATEMENT OF THE PROBLEM

The problem can be defined as following:

$$\psi = \theta + 2k\pi + \eta \quad (1)$$

Where  $\psi$  represents the unwrapped phase,  $\theta$  the observed wrapped noisy phase,  $k$  an integer for unwrapping, and  $\eta$  uniform noise.

The solution, we propose, is based on the slopes of the signal. Indeed, we make the strong assumption that the ground slopes are smooth with ground irregularities. Our unwrapping algorithm works in three steps:

- The first step (preprocessing), is used to get a better estimation of the gradient of the signal i.e. the ground slopes. This algorithm is very simple and fast, it directly works on observed signal  $\theta$ .
- The second step (main processing), and the original contribution of this paper, is to use ground slopes to unwrap and smooth the phase.
- The third step is the two-dimensional integrator that is locally adapted to choose the best integration path in order to avoid global errors.

### MAIN PROCESSING

The main idea is to smooth the ground slopes while preserving edges [5] due to wrapping. We use the assumption that the ground slopes are very smooth. Mathematically, we define:

$$\nabla\psi = \begin{pmatrix} Z_x \\ Z_y \end{pmatrix} = \begin{pmatrix} \frac{\partial}{\partial x}(\theta + 2k\pi + \eta) \\ \frac{\partial}{\partial y}(\theta + 2k\pi + \eta) \end{pmatrix} \quad (2)$$

$$= \begin{pmatrix} D_x(\theta + 2k\pi + \eta) \\ D_y(\theta + 2k\pi + \eta) \end{pmatrix}$$

with  $Z_x$  and  $Z_y$  the components of the ground slope vector, or first order derivative of  $\psi$ .

#### Removing the Peaks Due to Wrapping

The removing of the peaks, due to wrapping, consists to minimize the absolute difference between the observed phase and the observed phase with shifted fringe lines. To shift the fringe lines we add  $\pi$  to the observed interferogram and wrap the result.

So  $\theta_{+\pi}$  is the observed interferogram with shifted fringe lines, and  $Z_{y+\pi}$  are the components of its gradient vector.

To unwrap the phase we estimate four gradient components:  $Z_x$ ,  $Z_y$  and  $Z_{x+\pi}$ ,  $Z_{y+\pi}$ . So we need four criteria but these criteria are the same so we will explain only one of these.

#### Ground slopes estimation:

In order to estimate  $Z_x$  from  $\theta$  while taking into account the assumption of homogeneous ground slopes, we minimize a criterion of the form:

$$J(Z_x) = \int_{\Omega} (Z_x - D_x(\theta + 2k\pi))^2 d\Omega$$

$$+ \lambda_{\varphi} \int_{\Omega} \varphi \left( \frac{|\nabla Z_x|}{\delta} \right) d\Omega \quad (3)$$

Where  $\Omega$  is an open bound of  $\mathbb{R}^2$ ,  $|\nabla Z_x|$  is the modulus of the gradient of  $Z_x$  and  $\lambda_{\varphi}$  represents a regularization parameter that controls the relative weighting between the data term and the regularization term. The potential function  $\varphi$  that is applied on the gradient of the slopes is chosen in such a way to preserve edges [5] and peaks due to wrapping, to low-coherence or due to low-sampling. Consequently, we introduce the program parameter  $\delta$  as a threshold level

from which we decide to preserve or smooth the discontinuities. In order to preserve discontinuities, the  $\varphi$  functions must satisfy several properties [1].

#### Euler-Lagrange's Equation

We use a derivative method to minimize the criterion (3). Consequently, the minimum of  $J(Z_x)$  if it exists, satisfies the following Euler-Lagrange's discrete equation:

$$\frac{\partial J(Z_x)}{\partial Z_x} = 0 \Leftrightarrow (I_d - \lambda_{\varphi} \Delta_{pond}) Z_x = D_x(\theta + 2k\pi) \quad (4)$$

With  $\Delta_{pond}$  as a discrete approximation of weighted laplacian. Indeed, the coefficients of  $\Delta_{pond}$  mapped at location  $(i,j)$  are given by:

$$\begin{pmatrix} 0 & b_{x_{i-1,j}} & 0 \\ b_{x_{i,j-1}} & -S & b_{x_{i,j}} \\ 0 & b_{x_{i,j}} & 0 \end{pmatrix} \quad (5)$$

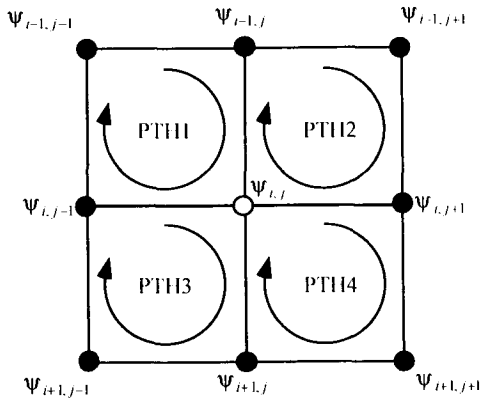
with  $S = b_{x_{i-1,j}} + b_{x_{i,j-1}} + 2b_{x_{i,j}}$

$$b_{x_{i,j}} = \frac{\varphi' \left( \frac{1}{\delta} |\nabla Z_x|_{(i,j)} \right)}{2 \frac{|\nabla Z_x|_{(i,j)}}{\delta}} \quad (6)$$

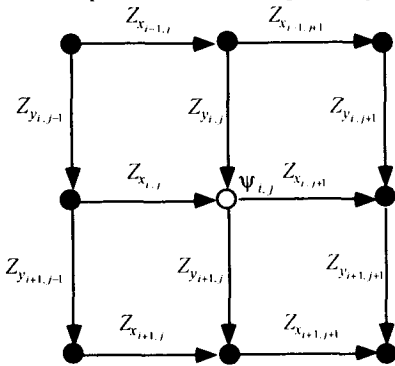
The variable  $b$  is then a map of the edges locations.

#### TWO DIMENSIONAL INTEGRATOR

We locally define the integration paths (PTH1, PTH2, PTH3 and PTH4) and the local components around  $\Psi_{i,j}$  as following:



The components of the integration paths are:



So the value of  $\psi_{i,j}$  depends of the chosen path; the possible values are:

If PTH1 is chosen:

$$\begin{aligned} \psi_{i,j} = \frac{1}{V} & (\psi_{i-1,j-1} + Z_{x_{i-1,j}} + Z_{y_{i,j}} \\ & + \psi_{i-1,j-1} + Z_{y_{i,j-1}} + Z_{x_{i,j}} \\ & + \psi_{i,j-1} + Z_{x_{i,j}} + \psi_{i-1,j} + Z_{y_{i,j}}) \end{aligned} \quad (7)$$

If PTH2 is chosen:

$$\begin{aligned} \psi_{i,j} = \frac{1}{V} & (\psi_{i-1,j+1} - Z_{x_{i-1,j+1}} + Z_{y_{i,j}} \\ & + \psi_{i-1,j+1} + Z_{y_{i,j+1}} - Z_{x_{i,j+1}} \\ & + \psi_{i-1,j} + Z_{y_{i,j}} + \psi_{i,j+1} - Z_{x_{i,j+1}}) \end{aligned} \quad (8)$$

If PTH3 is chosen:

$$\begin{aligned} \psi_{i,j} = \frac{1}{V} & (\psi_{i+1,j-1} + Z_{x_{i+1,j}} - Z_{y_{i+1,j}} \\ & + \psi_{i+1,j-1} - Z_{y_{i+1,j-1}} + Z_{x_{i,j}} \\ & + \psi_{i,j-1} + Z_{x_{i,j}} + \psi_{i+1,j} - Z_{y_{i+1,j}}) \end{aligned} \quad (9)$$

If PTH4 is chosen:

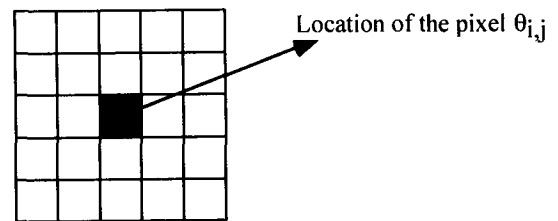
$$\begin{aligned} \psi_{i,j} = \frac{1}{V} & (\psi_{i+1,j+1} - Z_{x_{i+1,j+1}} - Z_{y_{i+1,j}} \\ & + \psi_{i+1,j+1} - Z_{y_{i+1,j+1}} - Z_{x_{i,j+1}} \\ & + \psi_{i,j+1} - Z_{x_{i,j+1}} + \psi_{i+1,j} - Z_{y_{i+1,j}}) \end{aligned} \quad (10)$$

$V$  the normalization coefficient depends on the number of  $\psi$  values known along the integration path.

The choice of the integration path depends of the edge map  $b$ . Indeed we integrate first the homogeneous areas in order to avoid the global errors due to low-coherence. So we integrate first the areas without sharp discontinuities ( $b > 0.1$ ). We loop the integration until the entire image is not integrated. In fact, we decrease the value condition on  $b$ . If the low-coherence areas are too numerous, we can easily use a mask, obtained by the classification of the image of coherence, to avoid the integration in these areas.

### PREPROCESSING

The basic idea is to organize the data such there is no difference between a pixel and its previous neighbors bigger than  $\pi$ . We use the following neighborhood of the scanned pixel:



For a neighborhood of size  $t$ , we estimate the local value of  $k$ :

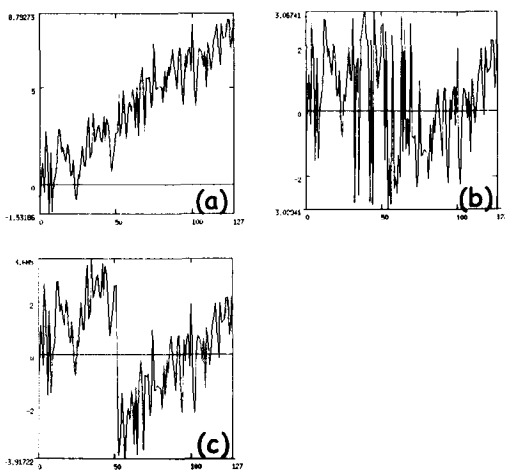
$$k(\theta_{i,j}, t) = \text{nint} \left( \frac{E(t) - \theta_{i,j}}{2\pi} \right) \quad (11)$$

where  $nint$  is the nearest integer and  $E(t)$  is the mean of neighborhood pixels. Notice that  $k$  depends of the neighborhood size ( $t$ ).

Thus, we obtain a filtered interferogram:

$$\theta_{i,j} = \theta_{i,j} + 2\pi.k(\theta_{i,j},t) \quad (12)$$

The figures below illustrate the preprocessing. A noisy line (a) is wrapped (b). The oscillations due to noise prevent the slope estimation. This is the role of our preprocessing to reduce these oscillations (c).



#### ALGORITHM

$\Theta = \text{Preprocessing}(\theta)$ , see § 6.

Repeat

Repeat

Compute  $Z_x$ , solving (4) with a conjugate gradient algorithm.

Compute  $Z_{x+\pi}$ , solving (4).

Compute  $Z_y$ , solving (4).

Compute  $Z_{y+\pi}$ , solving (4).

Compute  $b_x$ , calculating (6).

Compute  $b_{x+\pi}$ , calculating (6).

Compute  $b_y$ , calculating (6).

Compute  $b_{y+\pi}$ , calculating (6).

Until convergence.

Remove peaks:

$$Z_x = \min(\text{fabs}(Z_x), \text{fabs}(Z_{x+\pi}))$$

Remove peaks:

$$Z_y = \min(\text{fabs}(Z_y), \text{fabs}(Z_{y+\pi}))$$

Until convergence.

Compute  $\Psi$ , see § 5.

#### EXPERIMENTAL RESULTS

Experiments on our algorithm were conducted for real ERS1 data. The interferogram of a part of the New Caledonia island (Fig 1). We present:

The interferogram with shifted fringe lines (Fig 2), the ground slopes (Fig 3 and Fig 4), the unwrapped phase (Fig 5) and the its wrapping (Fig 6), to compare with the observed phase, the 3D visualization of the ground (DGM) (Fig 7) and the modulus image of the same area to compare it.

*Acknowledgment: many thanks to the GDR ISIS for providing the ERS1 data<sup>1</sup>.*

#### CONCLUSION

In this paper, we have proposed a new SAR interferometry algorithm for phase unwrapping using ground slopes estimation. The experimental results show the efficiency of our approach and its low sensitivity to peaks on gradient components. Our current work focuses on a faster algorithm. We also seek to improve our method by allowing ground irregularities preservation, and by improving the homogeneous slope model.

#### REFERENCES

- [1] P. CHARBONNIER, L. BLANC-FERRAUD, G. AUBERT, M. BARLAUD, *Deterministic Edge Preserving Regularisation in Computed Imaging*, IEEE Transaction on Image Processing, vol. 6, N. 2, February 97.
- [2] QUIAN LIN, JOHN F. VESECKY, HOWARD A. ZEBKER, *New approaches in Interferometric SAR Data Processing*, IEEE Transaction on Geoscience and Remote Sensing, Vol. 30, no. 3, pp. 560-567, May 1992.
- [3] XU WEI, CUMMING IAN, *A Region Growing Algorithm for InSAR Phase Unwrapping*, Proceedings of the IGARSS'96, pp. 2044-2046.
- [4] S. DUPOND, D. LABROUSSE, M. BERTHOD, *SAR Interferometry : An Application of Simulated Annealing to Phase Unwrapping*, The 9<sup>th</sup> Scandinavian Conference on Image Analysis, Uppsala, Sweden, June 1995.
- [5] G. Fornaro, G. Franceschetti, R. Lanari, E. Sansosti and M. Tesauro. *Finite element method for interferometric SAR phase unwrapping*. EUROPTO'96, Taormina, Italia, September 23-26, 1996.
- [6] I. Lyuboshenko and H. Maître. *Phase unwrapping for interferometric synthetic aperture radar by use of Helmholtz equation eigenfunctions and*

<sup>1</sup> <http://www-isis.enst.fr>

*the first Green's identity*. Opt. Soc. Am. A/Vol. 16, No. 2/October 1999.

- [7] P. MATHIEU, L. DIRAT, X. DUPUIS, M. BARLAUD, *Speckle Reduction With Edge - Preserving*, ICASSP'97, April 21-24 Munich Germany. Vol. 4, pp. 2785.

- [8] X. Dupuis, P. Mathieu and M. Barlaud. *Synthetic aperture radar interferometry using ground slope vector to phase unwrapping*. EUSIPCO'98, pp.: 1129-1132.

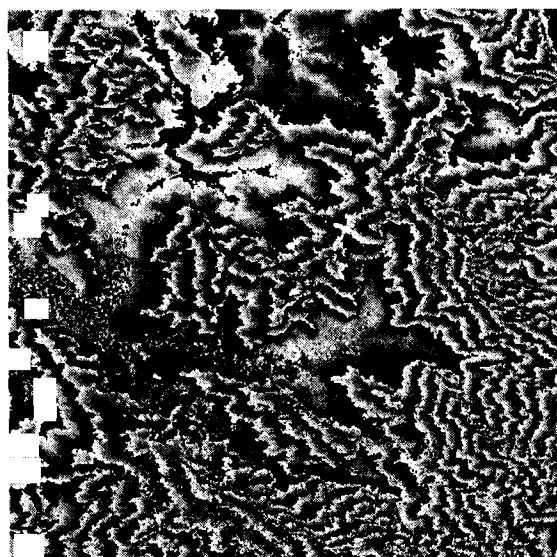


Fig 1: Interferogram of a part of the New Caledonia island ( $\theta$ ).

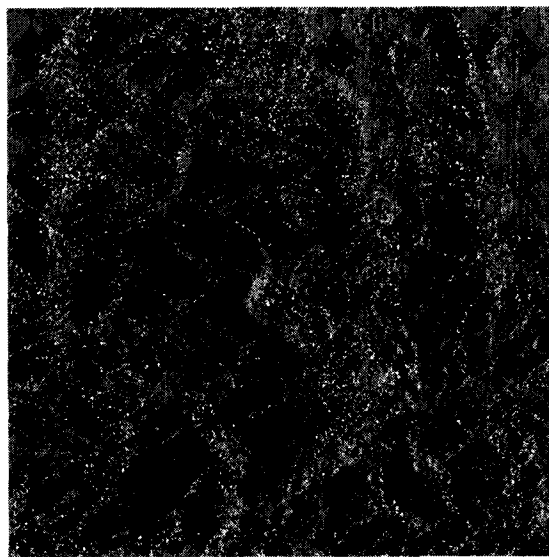


Fig 3: Ground slope component ( $Z_x$ ).

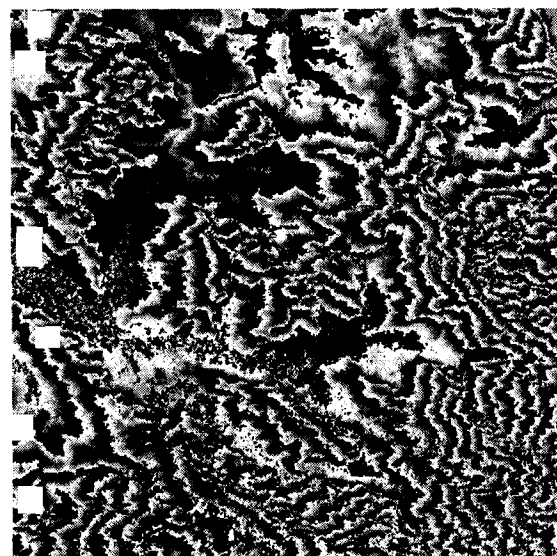


Fig 2: Interferogram of a part of the New Caledonia island where the fringe lines are shifted ( $\theta_{+\pi}$ ).

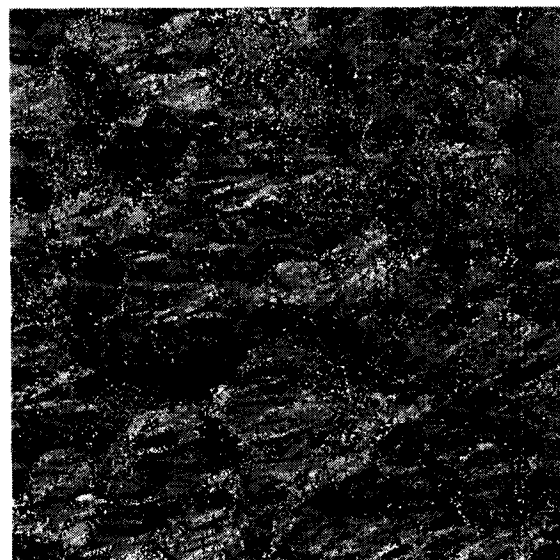
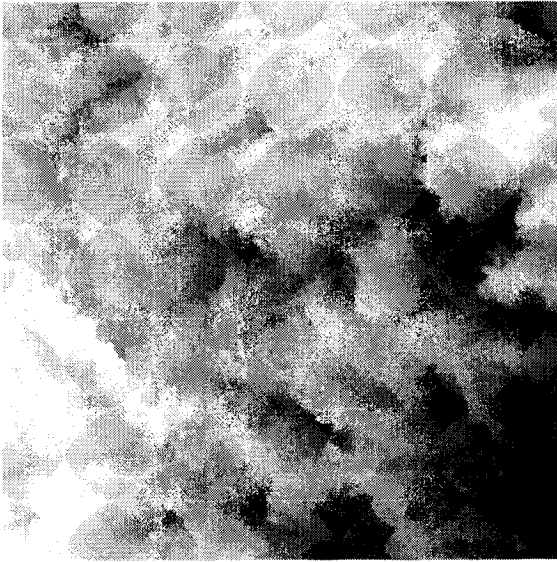
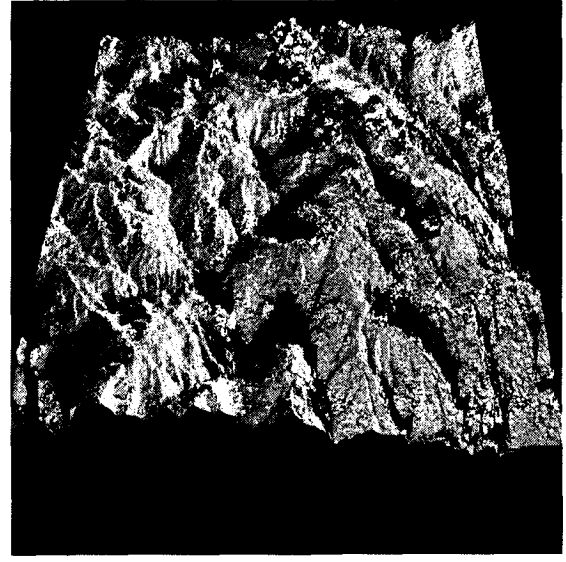


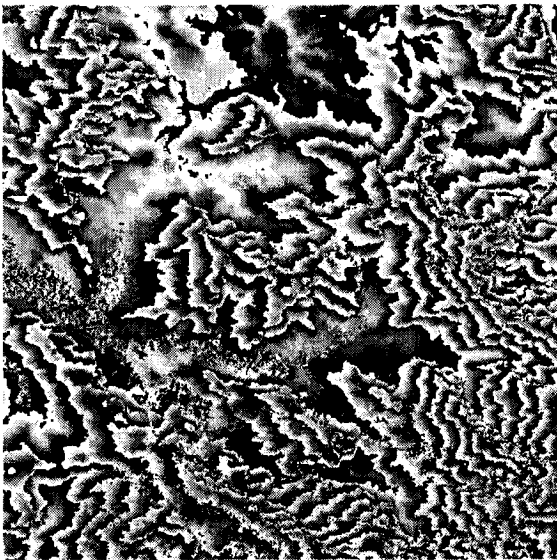
Fig 4: Ground slope component ( $Z_y$ ).



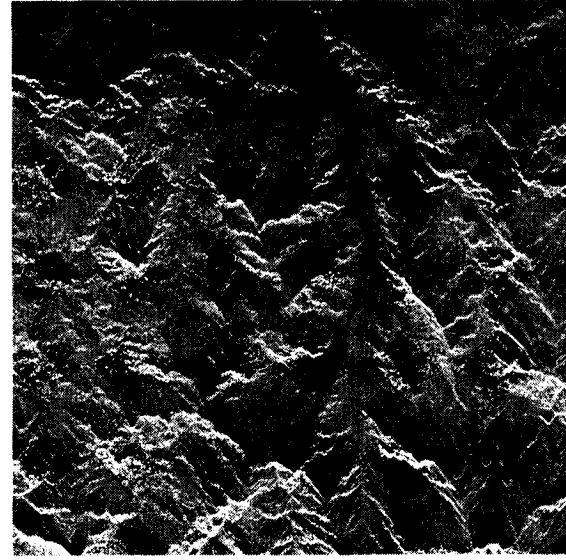
**Fig 5:** The unwrapped phase ( $\Psi$ ).



**Fig 7:** The 3D visualization of ( $\Psi$ ) made with Povray software.



**Fig 6:** The wrapping of the unwrapped phase ( $\Psi$ ) to compare with the observed interferogram ( $\theta$ ).



**Fig 8:** The modulus image of the same part of the New Caledonia area, to compare with the above 3D visualization (Fig 7).

## Operational Interferometric ERS Tandem Data Processing

Birgit Schättler, Michael Eineder, Walter Knöpfle, Michael Hubig

German Aerospace Center (DLR)  
P.O. Box 1116, D-82230 Wessling, Germany  
Phone: +49-8153-28-1353 Fax: +49-8153-28-1420  
e-mail: Birgit.Schättler@dlr.de

### ABSTRACT

From an operational point of view, the interferometric processing of repeat-pass space-borne SAR data is a challenging task. A large amount of data has to be handled and processed in a reasonable time frame. An automated processing without user interaction calls for robust and reliable algorithms, especially with respect to phase unwrapping. The data quality of the generated products is a-priori unknown.

On the other hand, the quality of digital elevation models derived from SAR interferometry is improved, when multiple interferometric data sets of sufficient quality can be used.

Therefore, the German Aerospace Center (DLR) is processing and archiving a large set of interferometric products mainly over Europe, but also over regions in Asia as well as South America and Antarctica covered by DLR ERS ground stations. This enables the browsing through hundreds of interferograms and the pre-selection of products suitable for a specific application, a large scale digital elevation model (DEM) in our case.

This paper presents the processing system and status and describes the generated products as well as the major algorithms they are based on.

### INTRODUCTION

After many years of operational SAR data processing, DLR is now establishing an operational system for the processing of interferometric SAR data, mainly for the generation of a global Digital Elevation Model from the X-band system of the Shuttle Radar Topography Mission (SRTM) to be flown early 2000 [1], [2]. This system is currently used in various research interferometry projects for ERS, Radarsat and J-ERS data as well.

The massive production of interferometric data sets requires fast and robust algorithms which have to give reliable results independently from the region and the current imaging conditions, still a critical and challenging requirement with respect to e.g. phase unwrapping. Another design approach is the elimination of as many operator interactions as possible in the automatic production chain.

From that point of view, only the ERS-1/2 tandem mission provides enough specific characteristics for setting up an operational automated processing chain: 1 day repeat cycle, enormous amount of interferometric data acquired, availability of precise orbit information.

Nevertheless, the commonly known back-striking factors of a repeat-pass interferometer like different atmospheric deteriorations and loss of coherence still may restrict the quality of the derived products like a DEM considerably.

### SYSTEM DESCRIPTION, OPERATIONAL SCENARIO AND PROCESSING STATUS

#### System Overview

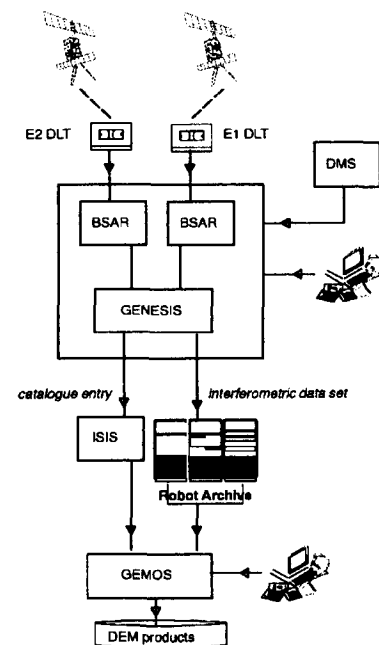


Figure 1: System overview

The following DLR developed processing systems contribute to the overall processing chain:

**BSAR** a phase-preserving high-precision multi-sensor chirp scaling SAR processor used to generate single-look complex data sets [3]

**GENESIS** a flexible multi-sensor InSAR processor used to generate an interferometric data set consisting essentially of the two under-lying amplitude images, the raw interferogram, the unwrapped phase, a regions control mask and a coherence map [4]

*GEMOS* a geocoding and mosaicking system for the conversion of the unwrapped phase information into height information, for the geocoding into various map projections, for the mosaicking of individual scenes into large area DEMs (including the composition of DEM data from a stack of products of the same area) and for the derivation of geocoded coherence maps [5] [6]

Both, BSAR and GENESIS are modular software systems allowing the extension to new sensor configurations essentially by plugging in sensor-specific new input modules. Their multi-threaded scalable architecture guarantees a high throughput on a multi-CPU hardware system, while the same software system can still be used on smaller workstations.

The *Data Management System* DMS, which maintains a catalogue of all available ERS raw data at the German PAF (D-PAF), and the *Intelligent Satellite Information System* ISIS together with the *robot archive*, which hold the catalogue and the physical archive of the generated interferometric data sets, complement the overall system architecture.

#### Operational Scenario

BSAR and GENESIS systematically process all available tandem acquisitions over a pre-selected geographical region. The operator chooses two corresponding ones from the complete tandem acquisition listing in the order tool, retrieves the corresponding DLTs from the raw data archive, feeds a DLT stacker with them and starts the BSAR/GENESIS processing. The acquisitions are automatically split into the ESA defined ERS frames (100 km by 100 km) and processed into an interferometric data set on this frame by frame basis. Since the setup (provision with the appropriate orbit file as well as the time correlation and scene description parameters) and the final cataloguing and archiving step is done automatically, the processing of the two tandem acquisitions runs fully autonomously without any operator interaction in between. Nevertheless, the production run can be stopped any time in between and processing can be resumed at that point, even inside a specific processing system. The generated interferometric product data sets are archived and catalogued. Browse images and annotation parameters of all product components are available on-line and thus are not only the basis for the selection of suitable candidates for further processing through the GEMOS system, but also providing valuable selection criteria for specific interferometric user applications. See the HTML page printout below for an example. Frames 1017 through 855 from the orbits E1 40054 and E2 20381 cover a region from the North Sea down to the Mediterranean Sea crossing the Rhine Valley, the Swiss Alps, the Po River Valley and the Appennines.

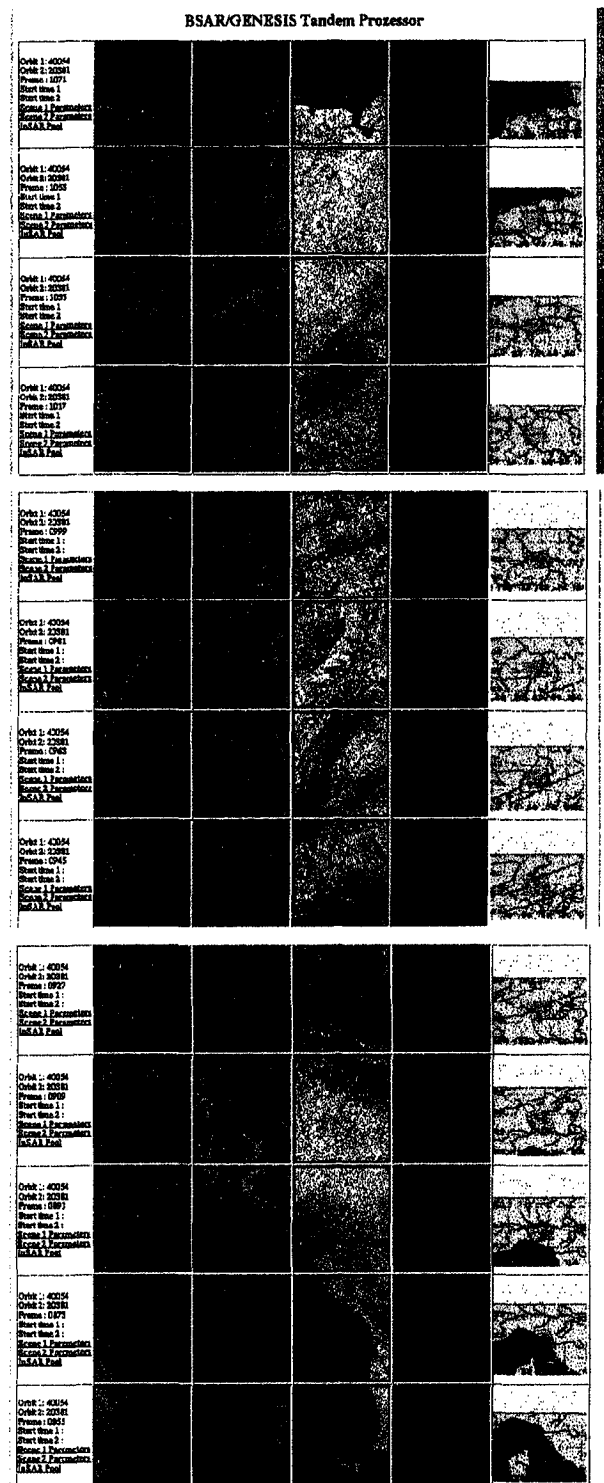


Figure 2: HTML Page with browse images

#### System Throughput and Processing Status

The generation of the raw interferogram of a frame starting from the two raw data sets on DLT takes about one hour on a system with 12 CPUs and 250 MHz



clock rate. The phase unwrapping step may be done in about 30 minutes, but can also take several hours for difficult scenes

The GEMOS processing of one frames takes about 1.5 hours when done in automatic mode with no user interaction, but can also require several hours up to a day of work for difficult scenes, for which an expert operator has to influence manually certain processing steps (e.g. interactive measurement of tie points, repetition of phase unwrapping step).

At time, over 700 interferometric data sets of about 60 tandem orbits are already archived and catalogued. The following figure shows their coverage over Europe.

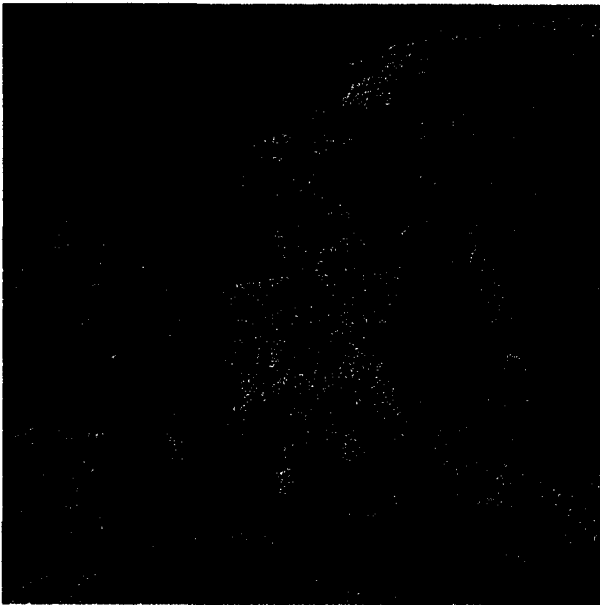


Figure 3: Current product coverage map over Europe

## PRODUCTS AND ALGORITHMS

Due to the modular processing concept, a range of products is generated on the way from the raw data to the final DEM. Some of the products are stored permanently in order to

- a) operationally decouple systems that run autonomously from systems that need operator interactions
- b) generate a database of interferograms for further studies and applications (see also [7])

Other intermediate products are temporary and no more available after completion of the routine processing. This is especially true for the BSAR generated complex images which resemble very much the standard ESA SLCI products. They are represented in the natu-

ral radar time coordinate system and sampled at the PRF (typically 1680 Hz) in azimuth and at 18.96 MHz in range. Actually BSAR proved its interferometric quality in numerous cross comparisons against those SLCIs. Since it takes less than 10 minutes to generate one complex BSAR product, there is no need for a long-term archival.

### *Interferometric Data Set*

All generated products are represented in a simple format. The signal data are stored in an appropriate binary format with a modified 32 byte SUN rasterfile header. Annotation and processing parameters are stored in so-called parameter pools, a structured keyword based ASCII format that is easily human readable.

The InSAR processor GENESIS produces a sandwich of coregistered layers from two input SLCIs. See Table 1 for the structure of such a sandwich.

In order to achieve an almost quadratic ground pixel spacing and a significant phase noise reduction, a pixel averaging process (5 to 1) is applied during the interferogram generation. The geometry, however is left in the radar azimuth / range time coordinate system throughout this processing phase.

Before the interferogram generation, both SLCIs are filtered to eliminate coherence loss due to baseline induced spectral shift and Doppler centroid differences between both acquisitions. The amplitude images however, are generated from unfiltered data to avoid influences of filtering on image calibration. As of today, radiometric antenna correction is not applied.

After coregistration of the two complex images to an accuracy of ca.  $1/10^{\text{th}}$  of a pixel, the complex interferogram is formed. To allow for possible follow-on offline interferometric experiments or investigations, we store the complex interferogram permanently.

From the complex interferogram we derive the filtered phase using an adaptive filter proposed by [8]. This filter is tuned to reduce the phase noise in flat areas considerably on one hand, but to retain terrain details in alpine regions on the other hand.

The unwrapped phase is derived from the filtered phase using a minimum cost flow (MCF) algorithm [9], [10]. After unwrapping, the precise location of every branch-cut can be inspected in the MCF control image. Unlike other algorithms, the MCF method unwraps noisy areas even if the result is questionable. For quality assessment, we therefore generate an additional segmented region mask to identify regions that are most probable consistently unwrapped.

A flattened version of the unwrapped phase is used to calculate the terrain slope corrected coherence image.

By doing this, and using about 100 looks, we reduce the systematic estimation bias and can measure coherence down to 0.1 even in hilly areas.

Finally, for quality control we generate a digital map of the covered area. Using this map the operator or investigator can easily match features on the map with amplitude, phase or coherence image.

Product	data format	Typical size [samples]
Amplitudes	SRF, 16 bit	4900 x 5400
Complex raw interferogram	SRF, complex IEEE float	4900 x 5400
Filtered Phase	SRF, IEEE	4900 x 5400
Unwrapped Phase	SRF, IEEE float	4900 x 5400
MCF Control	SRF, 8 bit	4900 x 5400
Region Mask	SRF, 8 bit int	4900 x 5400
Coherence	SRF, 8 bit	4900 x 5400
Orientation map	SRF, 8 bit	300 x 300
Parameters	"Parameter Pool", ASCII	80 kB

Table 1: Components of an interferometric data sandwich

#### Digital Elevation Model

GEMOS transforms the interferometric sandwich from the radar time coordinate system into a user selectable map coordinate system and resamples the unwrapped phase into a digital elevation model. Typically we use WGS84 as the vertical and horizontal datum, but other user supplied reference systems are possible as well.

Furthermore, a height error map is generated out of the coherence map together with geometrical confidence parameters.

Existing ERS DEM products can be ordered from DLR/DFD.

Product	Data format	Typical Data Size
DEM	DTED format, 16 bit	901 x 901 (15' x 15' tile)
Height Error Map	DTED format, 8 bit	901 x 901

Table 2: DEM products

## SOME ANALYSIS RESULTS

Just by analyzing the processing parameters only of 660 interferograms located mainly over Europe, we can now derive deeper insight into quantitative properties of ERS tandem interferometry. Here are some recent examples:

#### Coherence Distribution of ERS Interferograms

For each interferogram we store the average coherence over the whole scene, which may serve as a quantitative quality indicator without inspecting the coherence image itself. Figure 4 shows the distribution of all our processed interferograms. We can see the lower limit of our coherence estimator (0.1) and that 29 scenes had a high average coherence between 0.8 and 0.9. The maximum average coherence value observed is 0.89.

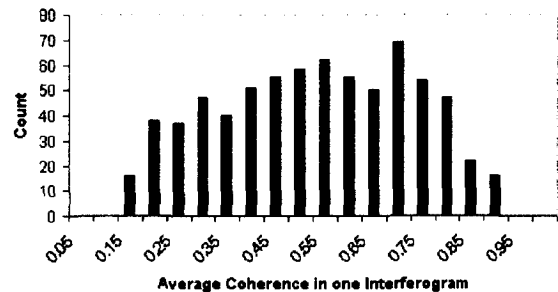


Figure 4: Distribution of average coherence from 660 interferograms mostly over Europe

#### ERS Orbit and Timing Accuracies

ERS precise orbit products are used to coarsely coregister the two SLC images at scene center coordinates on a geometrical basis followed by a fine registration done with image correlation methods. By subtraction the corresponding shift vectors, we obtain the total error with contributions from the image correlation itself, from the both precise orbits and the timing of the two radar instruments. Since we have two instruments and two orbit measurements all the errors should be decorrelated apart from a negligible influence of the common earth gravity model used to model the orbits. Figure 5 shows the distribution of the error derived from 100 high coherent interferograms. We can see, that the azimuth localization error is less than 1 pixel or 4 meters. In range we observe a systematic shift of 0.35 pixels or 2.8 meters between ERS-1 and ERS-2, which is most probably due to a different electronic delay of both instruments. The total error in the range localization is less than 0.2 pixels or 1.6 meters. The results confirm the excellent stability of the ERS instrument and the precision of the ERS/D-PAF provided precise orbit products, specified in the order of tens of centimeters. We believe, that the observed range error is essentially caused by the coregistration

method and the azimuth error by the uncertainty of the time correlation elements between orbit and radar data.

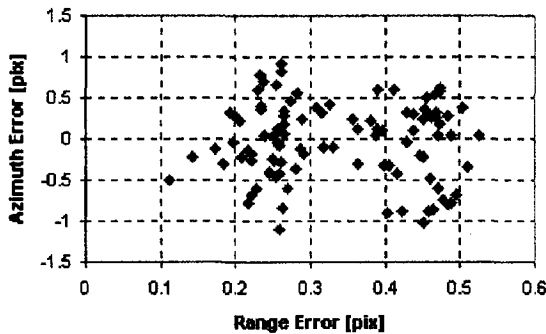


Figure 5: difference between geometric and correlation coregistration of ERS SLCIs

EXPERIENCES WITH DEM GENERATIONS

More than 20 samples out of the 700 archived interferometric data sets and some more using standard SLCI products as input have been recently processed into DEMs, mostly from regions promising spectacular results and coming from our ERS ground stations in Neustrelitz, Antarctica, Kitab and Libreville. For these sample DEMs, which are partly generated automatically, partly with human interaction, the best results are mainly obtained with baselines between 80 and 120 meters. The following table gives the RMS accuracy with respect to GLOBE as the reference DEM.

Number of DEMs	RMS error with respect to GLOBE
1	< 20 m
1	20 m – 30 m
6	30 m – 50 m
8	50 m – 150 m
4	100 m – 500 m
3	> 500

Table 3: RMS error classes of generated DEMs

Furthermore, much effort is spent to generate a high quality, large DEM mosaic (see image on last page) covering the area of Bavaria. 28 underlying complex products (see next figure), mainly processed by the BSAR/GENESIS tandem processor, partly generated by the ESA/D-PAF operational SAR processor VMP, are used.

The obtained height accuracy lies between 15 and 25 meters for regions showing a medium relief and between 25 and 50 meters for high relief areas. The average location accuracy is about 20m. The area covered is 150000 km<sup>2</sup> with a pixel spacing of 25 m.

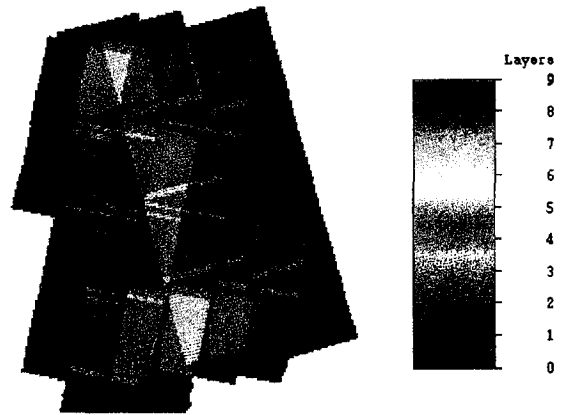


Figure 6: Product layer for Bavaria DEM

CONCLUSIONS

Even if a full automatic generation of DEMs from ERS interferometry data is not achievable due to system and algorithms related reasons, we automated considerable parts of the overall processing chain. The archived interferometric data sets are a valuable basis not only for the DEM candidates selection, but also for other follow-on interferometry investigations.

REFERENCES

[1] R. Bamler, "The SRTM Mission: A World-Wide 30m Resolution DEM from SAR Interferometry in 11 Days", Proc. 47<sup>th</sup> Photogrammetric Week, Stuttgart, 1999

[2] H. Breit, N. Adam, M. Eineder, "The Shuttle Radar Topographic Mission: Processing Techniques and First Results", CEOS SAR Workshop, Toulouse, 1999, to be published

[3] H. Breit, B. Schättler, U. Steinbrecher, "A High-Precision Workstation-Based Chirp Scaling SAR Processor", Proc. IGARSS'97, Singapore, 465-467, 1997.

[4] M. Eineder, N. Adam, "A Flexible System for the Generation of Interferometric SAR Products", IGARSS'97, Singapore, 1341 – 1343, 1997.

[5] A.Roth, W. Knöpfle, B. Rabus, S. Gebhardt, D.Scales, "GEMOS – A System for the Geocoding and Mosaicking of Interferometric Digital Elevation Models", Proc. IGARSS'99, Hamburg, , 1999

[6] W. Knöpfle, G. Strunz, A. Roth, "Mosaicking of Digital Elevation Models derived by SAR Interferometry", International Archives of Photogrammetry and Remote Sensing, Vol. 32, Part 4, pp. 306-313, 1998

[7] N. Walker, S. Mica, H. Laur, "The ERS Interferometric Quick Look Processor: a Powerful System to Assess and Exploit the ERS Tandem Archive for Land-Use Information Retrieval", Proc. 2<sup>nd</sup> Int. Work-

shop on Retrieval of Bio- and Geo-physical Parameters from SAR Data for the Land Applications, pp. 579-583, October 1998, ESTEC, Noordwijk, ESA-SP 441

[8] R. Goldstein, C. Werner: "Radar Ice Motion Interferometry", 3rd ERS Symposium (ESA) 18-21 March 1997, Florence (Italy)

[9] M. Costantini, "A Novel Phase Unwrapping Method Based on Network Programming", IEEE Trans. Geosc. Remote Sensing, Vol. 36, No. 3, pp. 813 - 821, May 1998

[10] M. Eineder, M. Hubig, Björn Milcke, "Unwrapping Large Interferograms Using the Minimum Cost Flow Algorithm", Proc. IGARSS'98, Seattle, 83-87, 1998

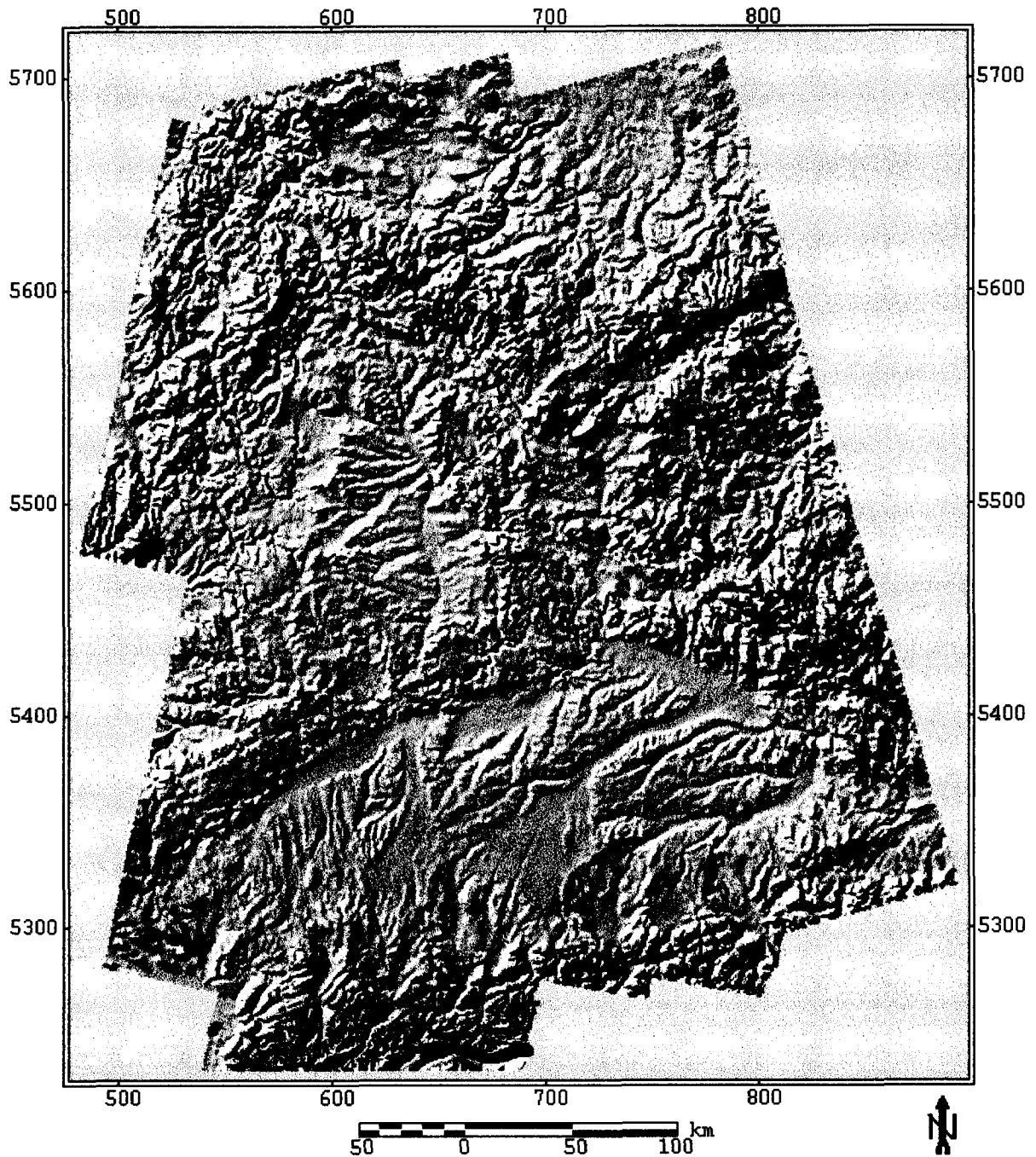


Figure 7 : Bavaria DEM Mosaic

## Insar analysis of the effects of the Izmit earthquake with ERS data

F. Sarti<sup>1</sup>, F. Adragna<sup>1</sup>, N. Pourthié<sup>1</sup>, B. Rosich<sup>2</sup>, A. Arnaud<sup>2</sup>, K. Feigl<sup>3</sup>, M. Rosengren<sup>4</sup>,  
P. Imbo<sup>5</sup>, D. Petit<sup>6</sup>

<sup>1</sup>CNES, QTIS/SR,  
18 avenue Edouard Belin, Bpi 811, 31401 Toulouse, France  
Tel : 33.5.61.28.21.33 / Fax : 33.5.61.31.67 / e-mail: francesco.sarti@cnes.fr

<sup>2</sup>ESA/ESRIN  
Via Galileo Galilei, 0004 Frascati, Italy  
e-mail: brosic@esrin.esa.it

<sup>3</sup>OMP/CNRS  
16 Avenue Edouard Belin, 31401 Toulouse, France  
e-mail: kurt.feigl@cnes.fr

<sup>4</sup>ESA/ESOC  
R. Bosch Str.5, Darmstadt, Germany  
e-mail: mrosengr@esoc.esa.de

<sup>5</sup>CESBIO,  
18 avenue Edouard Belin, Bpi 2801, 31401 Toulouse, France  
e-mail: imbo@cesbio.cnes.fr

<sup>6</sup>IRIT/UPS,  
118 Route de Narbonne, 31062 Toulouse, France  
e-mail: petit@irit.fr

### Abstract

After the 17/08/99 earthquake in Turkey, ESA and CNES decided to coordinate their efforts for the emergency study of the earthquake effects based on satellite observations (ERS, SPOT). In particular, a set of archived ERS acquisitions over the interested sites was promptly provided by ESA, a series of tandem acquisitions were programmed (ERS-1 was switched on over Turkey) and the acquired post-event images were also made available. This allows not only for the study of the first seismic effects, but also for the evaluation and monitoring of the post-seismic deformations. For the particular case of the ERS-1 and ERS-2 orbits 30 and 31 days after the first earthquake, the orbit control strategy could exceptionally take into account InSAR requirements, obtaining minimal orbital baselines between co-seismic interferometric acquisitions over the site of interest.

This paper will present part of the interferometric results obtained at CNES and ESA, using the best available dataset. Several interferograms are compared in order to take into account possible residual topographic effects, and analyse the effect of orbital errors or possible atmospheric artifacts. Further analyses based on different techniques are still ongoing at CNES, such as correlation of optical data and radar multitemporal analysis.

### 1. Introduction

In the last decade the Radar Department of CNES has contributed to several studies for disaster monitoring, including cartography of earthquake and volcano deformations, measurement of ground subsidences and monitoring of natural or industrial risks based on the CNES differential interferometry tool (DIAPASON) using spaceborne SAR data. SAR differential interferometry allows for the determination of ground displacements with a centimeter level accuracy. The feasibility of deformation mapping based on radar interferometric techniques was well demonstrated at CNES in the case of several earthquakes, including Landers (see for example [1], [2], [3], [4], [5], [6]) and Etna eruptions [7] or, more recently, for the Piton de la Fournaise (La Reunion Island) eruption [8].

On 22nd July at the United Nations UNISPACE III conference in Vienna, ESA and CNES pledged to pool their satellite-based resources and provide timely, pertinent information on parts of the Earth struck by natural or man-made disasters. Less than a month after, on 17 August 1999, a strong earthquake (magnitude of 7.8) shook northwestern Turkey. ESA decided then to initiate an ERS1-ERS2 campaign over Izmit area while CNES started a collection and analysis of multisource (radar/optical) data over the same area.

Radar and optical satellites provide images for Turkey disaster relief operations, with different timescale and space resolutions. Images of the earthquake-struck regions of Turkey are being provided by European observation satellites: ESA's ERS satellites and SPOT satellites of the French national space agency CNES. SPOT 4 yielded detailed pictures of the Izmit and Istanbul areas for 9th July and 20th August, while a large dataset of ERS acquisitions on the area was provided by ESA. Several cloud-free acquisitions acquired by VEGETATION (a large field-of-view optical instrument on the SPOT4 platform providing daily revisit at our latitudes) were also available, including an acquisition taken a few hours after the earthquake.

## 2. Overview of the region: the North Anatolian fault

The North Anatolian Fault splays westward into two main branches, 100 km apart. The Northern branch bounds the southern side of the Gulf of Izmit, outlines the Marmara pull apart basin, cuts the Dardanelles structure, and marks the southern side of the Saros Gulf. The Izmit earthquake occurred on that branch, east of Marmara Sea.

Geological studies over a longer time period (holocene) indicate a slip rate of 2.5 cm/year on the North Anatolian Fault (Hubert, 1998). The Izmit earthquake broke a 110 km long section of the North Anatolian fault (Armijo et al., more details on the web : <http://www.ipgp.jussieu.fr/depts/TECTO./IzmitWEB/IzmitUK.html>)

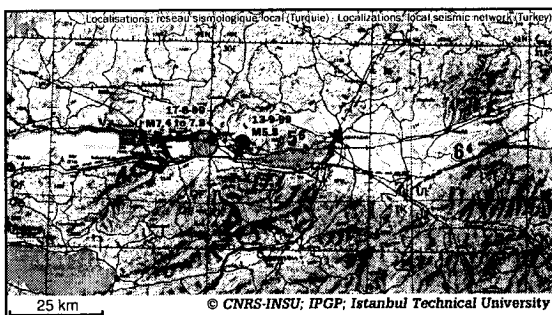


Fig 1: Localization of the local seismic network (Turkey)

## 3. First interferometric result

The first co-seismic interferogram over the Gölcük area could be generated after the ERS-1 acquisition of the 25<sup>th</sup> August 1999. This interferogram was computed at CNES using this ERS-1 acquisition (25<sup>th</sup> August, orbit 42408) and the ERS-2 image acquired on 24 December

1998 (orbit:19228) on an ascending track 336 (Fig.2). This first interferogram was available at the beginning of September. In spite of a baseline favourable to differential interferometry (about 40 m) a poor coherence was obtained because of the 8 month interval.

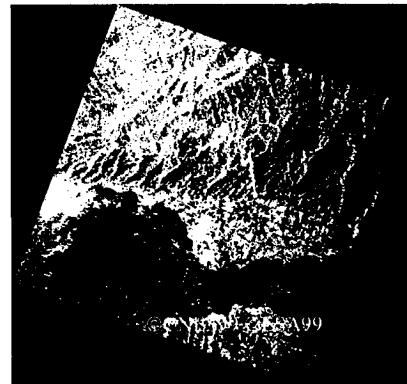


Fig. 2: Extract of the first CNES interferometric result (ERS-2 24/12/98 - ERS-1 25/08/99). It showed poor coherence, limited to the zone northern of Derince.

The next acquisition over the track 336 (26<sup>th</sup> Aug.) had a long baseline with the pre-event acquisitions, resulting in a too large frequency shift in range and in a limited coherency. Following acquisitions (10<sup>th</sup>/11<sup>th</sup> Sept., track 64) had also long baseline with the corresponding pre-earthquake images.

## 4. Orbit control

On factor limiting the accuracy of the interferometric results depends on the separation of the two orbits at the acquisition time: the smaller the separation, the lower the sensitivity to topography and to DEM residual errors. Fig.3 shows the perpendicular baseline between the two ERS-2 orbits computed over the subsatellite point of coordinates 26.54 E (longitude), 40.63 N (latitude). The orbital baseline relative to Izmit was about 18 m, corresponding to 566 m altitude of ambiguity.

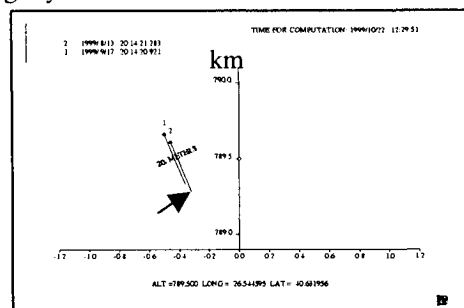


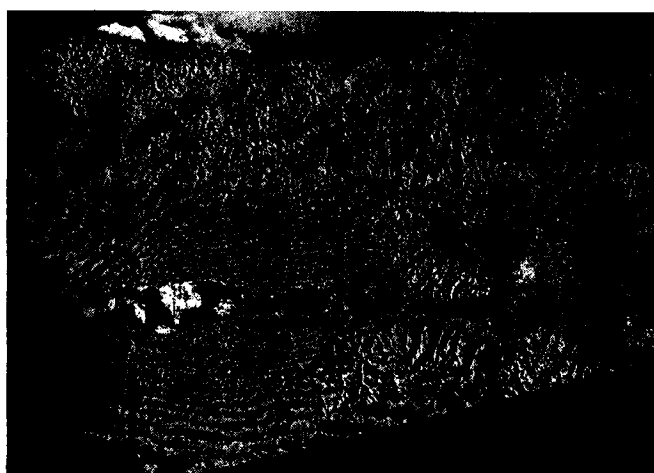
Figure 3: Perpendicular baseline computed by ESA/ESOC between two ERS-2 orbits (22556 and 23057) which allowed high quality interferogram on the Izmit area.

Without adapting the orbital manoeuvre strategy the baseline would have been 40 times larger (800 m) and the high quality interferogram shown on *Fig.4* would not have been possible, because of reduced coherency. These computations allowed ESA to pilot ERS orbits in order to optimize differential interferometry performances, without disturbing other users, for the particular case of the ERS-2 23057 orbit (with ERS-2 22556 as a reference orbit). The main orbit maintenance manoeuvre (that would have been needed anyway) was slightly anticipated to September 14<sup>th</sup>, 1999 with one burn at 3:47 Z and one burn at 4:37 Z. This was a few days earlier than it would have been the case without the "Izmit project" and this time was selected to have a minimal baseline at Izmit. A small "touch-up" manoeuvre had to be executed on September 15<sup>th</sup>, 1999 at 0:51 Z to compensate for the manoeuvre dispersion and two small "touch-up" manoeuvres had to be executed 99/09/16 at 0:51 Z and 23:20 Z to compensate for the unexpected low air-drag (relative to the available air-drag model). If the main orbit maintenance manoeuvre would have been executed 2 days later the Izmit baseline would have been in the order of 700 - 800 m. The orbit control strategy and precise orbit determination were performed at ESA/ESOC, Darmstadt. More details on ERS orbital control at ESOC are available on the web page: <http://nng.esoc.esa.de>

## 5. Best interferometric result

The pair ERS-2 23057-ERS-2 22556, with a 35-days interval, descending track, with a dedicated orbital control strategy allowed for an excellent altitude of ambiguity and a good interferometric coherence. Radar synthesis and interferometric processing were performed by the Radar System Department of CNES, using the Diapason software. ESA restituted orbits were used, and the results were validated using three different DEM with a 100 m grid (the re-sampled GTOPO30, a commercial DEM derived from digitized maps, a tandem interferometric DEM that was kindly made available by the university of Oxford). The large altitude of ambiguity and the almost identical results in the three cases guarantee that the interferogram did not contain residual topographical effects.

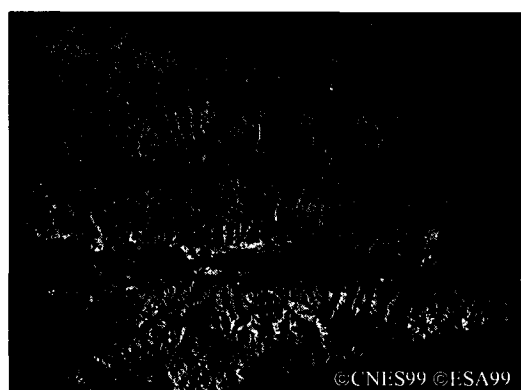
Fig.4 shows ground deformation due to the 17 August 1999 earthquake in the region of Izmit, Turkey. This representation is obtained by super-imposing an ERS radar image (Fig.5) to the image of the measured deformations (Fig.6).



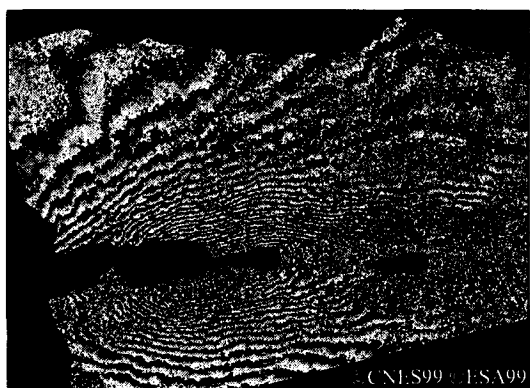
*Fig.4 : superimposition of the amplitude image and the phase interferogram (ERS-2 13/08/99 - ERS-2 17/09/99)*

Each colour cycle corresponds to a 28-mm change in distance between the ground and the satellite. A geophysical deformation model is described in par.7.

Radar image analysis provides an intensity measure as well as a phase information (radar wave travel time) at each point. *Phase* is directly related to the distance between the observed target and the radar. By computing phase differences between two satellite acquisitions, it is possible to measure ground displacement during the time interval elapsed between acquisitions, with a centimeter-level accuracy.



*Fig.5: Mean Amplitude Image (ERS-2 13/08/99 - ERS-2 17/09/99)*



**Fig.6: Phase Interferogram (ERS-2 13/08/99 - ERS-2 17/09/99)**

The first satellite image for this pair was acquired by the ESA satellite ERS-2 over Izmit on 13/08/99, four days before the earthquake, from an altitude of 800 km. The second image was programmed and acquired on 17/09/99, one month after the earthquake. This interferogram was compared to the ERS-1 12/08/99-ERS-1 16/09/99 interferogram (respectively in tandem configuration with the two ERS-2 acquisitions used previously). This ERS-1 interferogram was slightly less coherent than the ERS-2 interferogram shown in Fig. 4, but it allowed to validate this result and to ensure that the observed fringes were free of atmospheric effects.

## 6. Impact of precise orbits

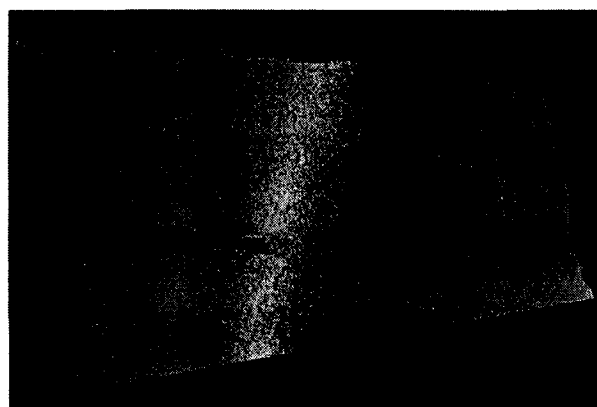
ERS predicted orbits are first estimated at ESOC 6 days before the pass, then 3 days before and finally 1 day before. The accuracy of predicted orbits depends on solar activity, which was very high in '91 and will reach its maximum in 2001. Accuracy in orbit estimation 6 days before the orbital pass can then vary from about 100 m (like in August '96) to 2 km (in a period of high solar activity, like Feb'99). Predicted orbits are used to adjust the orbit control manoeuvres.

The interferogram shown in par.5 was first obtained using the restituted orbits computed by ESOC. These orbits are available at ESOC 1-2 days after the satellite pass. They are estimated to be 1-2 meters rms accurate in cross-track, 2-4 meters rms in along-track about 50 cm rms in the radial component.

ERS precise orbits are estimated at ESOC 7-10 days after the orbit pass and are the result of a least square estimation based on Laser and Radar altimeter data collected over 4 days and including accurate orbital and perturbation models. The accuracy of precise orbit estimation is of the order of 20-30 cm rms (along-track, cross-track components), 10 cm rms (radial component).

Their accuracy is similar to that of precise orbits computed by Delft or by DLR.

The interferogram shown in Fig.4 was recomputed using these precise orbits, and the difference with respect to the previous interferogram is shown in Fig.7.



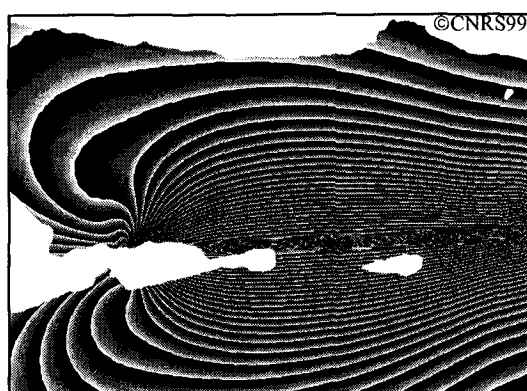
**Fig.7: Residual orbital fringes on the ERS-2 13/08/99 - ERS-2 17/09/99 interferogram when passing from restituted to precise orbits**

Fig.7 shows that the impact of precise orbits versus restituted orbits is minor for the case of the ERS-2 13/08/99 - ERS-2 17/09/99 interferogram (a few fringes in range, in a case where several tens of displacement fringes in azimuth are observed). The availability of precise orbits may nevertheless be important for different cases. More details about ERS orbit determination at ESOC are available on the web page <http://nng.esoc.esa.de>

## 7. Geophysical model and orbital cleaning

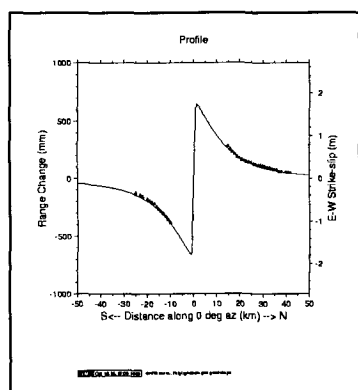
The geometry of the fault rupture and the measured deformations allow the geophysicists to build a theoretical model of the fringe pattern of the seism. Some examples were shown in [9],[10]. One of these geophysical models for Izmit was produced by K.Feigl, OMP/CNRS (Fig.8)





**Fig.8:** A theoretical model simulating the fringe pattern produced

This model is estimated by nonlinear inversion of the manually unwrapped fringes. It was also assumed that the absolute fringe counts on the north and south sides are offset according to the profile of Fig.9. This model assumes 4.3 meters of right-lateral slip on a fault 78 km long and 15 km wide which cuts the surface vertically and strikes at an azimuth of 85 degrees. This is equivalent to magnitude 7.48. The calculation assumes the conventional dislocation in an elastic half space.



**Fig.9:** Profile of the computed model simulating the fringe pattern.

Profile extending from south to north through the maximum number of fringes. To perform the orbital correction, we assumed that the fringe gradient must be symmetric about the fault, located at the origin of this profile (0 km). This assumption is justified by the elastic half space calculation (solid line). We adjust the fringe pattern accordingly by adding a north-south gradient (number of fringes per km), or 10 fringes over the length of the image. The necessity for this assumption would be alleviated by either a longer data acquisition or more precise orbits.

The geophysical interpretation of the observed fringes is that a vertical, east-west trending fault ruptured in with right-lateral strike slip of over 4 meters. Assuming purely horizontal, east-west motion, we find that one fringe of range change implies 66 mm of displacement.

This displacement is eastward north of the fault (and the bay), and westward to the south. The fringes closing near the west edge of the peninsula suggests that the rupture terminates near the triangular delta.

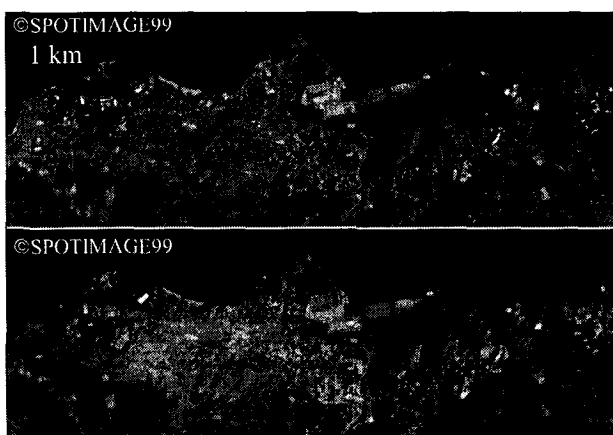
This theoretical model and the orbital cleaning will be improved using in-situ data which are now becoming available, longer data records (orbital fringes in azimuth) and precise orbits (orbital fringes in range)

## 8. Comparison with optical data

ERS interferograms can be combined with optical data such as SPOT multitemporal observations that provide a useful complementary local information. Two days after the earthquake, Spot Image promptly reacted by programming the SPOT satellites over the disaster area. On the 20<sup>th</sup> of August, SPOT 4 acquired the first image that fortunately was cloud-free.

20 images in total were acquired in 23 days by SPOT (16 with SPOT 4). Only 8 acquisitions were exploitable because of the meteorological conditions. Two cloud-free acquisitions of SPOT4, before and after the earthquake, were compared and superimposed, in order to detect variations due to earthquake effects.

Fig.10 shows a zoom of the two acquisitions, close to the harbour of Gölcük. Flooded areas due to earthquake-induced subsidence can be observed.



**Fig.10:** Extracts of SPOT 4 XS acquisitions over Gölcük. Top: 09/07/99 Bottom: 20/08/99

Fig. 11 and 12 are obtained superimposing the acquisition of the 9th of July (before the earthquake) to the one of the 20th of August. This colored composition of multitemporal acquisitions allows for the localisation of visual changes such as fires or areas underwater. Fig.11 shows clearly the subsidence (vertical deformation component) on the area of Gölcük : the two

red areas along the coastline indicate changes due probably to a bradyseism phenomenon. The large red area in Fig.12, on the south of Derince, is due to the smoke plume of a fired refinery.



**Fig.11: Superimposition of two Spot 4 images (before and after the earthquake) over the harbour of Gölcük)**



**Fig.12: Superimposition of two Spot 4 images (09/07/99 and 20/08/99) over the south of Derince. Red is associated to the image acquired after the earthquake is colored in red, Green and Blue to the pre-seismic image.**

Several cloud-free acquisitions taken by VEGETATION (a large field-of-view optical instrument on the SPOT4 platform) were available, including an acquisition taken a few hours after the earthquake was also available. Though with a resolution (1 km) not adapted to the study of the effects of the Izmit earthquake, this instrument shows a good potential for other applications of global monitoring or major floods/fires, because of its daily revisit at our latitudes.

Correlation results using radar intensity images or optical (Spot) data may also give very useful complementary information on the fault rupture, where interferometric fringes become too dense and coherence decreases.

## 9. Conclusions and perspectives

In-situ data are now becoming available and allow for a model validation and improvement. Together with an utilisation of longer data records containing southern frames, they will allow for a more precise correction of orbital effects.

We also envisage to perform a fusion with the results derived from optical analysis, and from radar or optical correlation.

Radar multitemporal analyses are also planned at CNES in order to perform a study of damaged urban areas.

This work is an example of a successful collaboration between several space agencies and research centers, sharing available data, human resources, expertise and processing resources in order to promptly put at the disposal of the scientific community the results of space observations for the monitoring of natural disasters.

## 10. Acknowledgments

We thank ESA/ESRIN for promptly providing the data, ESA/ESOC for the details about orbit determination and control, SPOT IMAGE for the SPOT4 data. We are grateful as well to all the contributors of the multi-disciplinary work described in this paper. Special thanks to J.Dow (ESA/ESOC), P.Durand (CNES/QTIS), E.Fielding (JPL/University of Oxford), D.Massonnet (CNES/QTIS), M.Barbieri, L.Castellano, N.Walker (SERCO), R.Gachet and P.Tissier (CNES/QTIS), H.Joannes and L.Demargne (SPOT Image).

## 11. References

- [1] D. Massonnet, M. Rossi, C. Carmona, F. Adragna, G. Peltzer, K.L. Feigl, and Th. Rabaute, "The displacement field of the Landers earthquake mapped by radar interferometry", *Nature*, vol. 364, pp. 138-142, July 1993
- [2] D. Massonnet, K.L. Feigl, M. Rossi, and F. Adragna "Radar interferometric mapping of deformation in the year after the Landers earthquake", *Nature*, vol. 369, 227-230, 1994a.
- [3] D. Massonnet, K.L. Feigl, H. Vadon, and M. Rossi, "Coseismic deformation field of the M = 6.7 Northridge, California, earthquake of January 17, 1994, recorded by two radar satellites using interferometry", *Geophys. Res. Lett.*, vol. 23, pp. 969-972, 1996a.

- [4] D. Massonnet, W. Thatcher, and H. Vadon, "Detection of postseismic fault zone collapse following the Landers earthquake", *Nature*, vol. 382, pp. 612-616, 1996b.
- [5] B. Meyer, R. Armijo, D. Massonnet, J.B. Chabaliier, C. Delacourt, J.C. Ruegg, J. Achache, P. Briole, and D. Panastassiou, "The 1995 Grevena (northern Greece) earthquake: Fault model constrained with tectonic observations and SAR interferometry", *Geophys. Res. Lett.*, vol. 23, pp. 2677-2680, 1996.
- [6] D. Massonnet, and K.L Feigl, "Satellite radar interferometric map of the coseismic deformation field of the  $M = 6.1$  Eureka Valley, California, earthquake of May 17, 1993", *Geophys. Res. Lett.*, vol. 22, pp. 1541-1544, 1995b.
- [7] D. Massonnet, P. Briole, and A. Arnaud, "Deflation of Mount Etna monitored by spaceborne radar interferometry", *Nature*, vol. 375, pp. 567-570, June 1995.
- [8] F. Sigmundsson, Ph. Durand, and D. Massonnet, "Opening of an eruptive fissure and seaward displacement at Piton de la Fournaise volcano measured by RADARSAT satellite radar interferometry", *Geophys. Res. Lett.*, vol. 26-5, pp. 533-536, March 1999.
- [9] K.L. Feigl, A. Sergent, and D. Jacq, "Estimation of an earthquake focal mechanism from a satellite radar interferogram: Application to the December 4, 1992, Landers after-shock", *Geophys. Res. Lett.*, vol 22, pp. 1037-1048, 1995.
- [10] D. Massonnet, and K. Feigl, "Discrimination of geophysical phenomena in satellite radar interferograms", *Geophys. Res. Lett.*, vol. 22, pp. 1537-1540, 1995.



## The Spot Image Coherence Product and Dimap : A new format for a new product

Philippe Bally, Christophe Angleraud, Yves Somer  
Spot Image

[philippe.bally@spotimage.fr](mailto:philippe.bally@spotimage.fr), [christophe.angleraud@spotimage.fr](mailto:christophe.angleraud@spotimage.fr), [yves.somer@spotimage.fr](mailto:yves.somer@spotimage.fr)

Tel +33 5 62 19 40 40 / Fax +33 5 62 19 40 53 / <http://www.spotimage.fr>

### ABSTRACT

Spot Image is about to release a new standard ERS value added Coherence product. This product provides two images packaged together with the original ERS tandem pairs and full digital documentation. The two Coherence images (called CAR and CFA) are resulting from a specialised processing of the ERS tandem images. This product will be published using the new coming Dimap/XML metadata standard that will provide both great ease of use of the products and a formalized framework for publishing technical auxiliary data about the images.

### KEYWORDS

ERS, Tandem pair, Coherence, metadata, Dimap, XML, browsing, catalog, geocoding, interferometric processing, Geotiff

### GLOSSARY

ERS	European Remote Sensing satellites (ERS-1 & ERS-2) of the European Space Agency
TANDEM	Configuration of ERS-1 & ERS-2 with a one day time difference between acquisitions
XML	eXtended Mark-up Language. The upcoming Internet standard.
XSL	An XML Style sheet language used to display XML data in a browser.
Dimap	Digital Image MAP metadata standard. Designed to fully describe, in a standard framework, any digital image map.
GeoTiff	Extension to Tiff that allows automatic geopositioning of images in GIS software
GCP	Ground Control Point. A location on the earth surface where ground co-ordinates are known at a high level of precision and which, when observed in an image, allows to build precise geometric models.
EPSG	European Petroleum Survey Group. A group of cartographers that published a reference set of tables describing world wide earth co-ordinate systems

**Table 1 : Glossary**

### INTRODUCTION

Spot Image has been working on format and data deliveries issues for many years. It is currently using two formats for its products: CEOS and GIS-Geospot®. The first one is mainly used for raw scenes deliveries whereas the latter is used for all the value added products image maps (SPOTView®).

Documenting both the contents of a delivery and its accompanying technical metadata has been a long term objective for Spot Image.

The work presented here provides information concerning the future metadata generation called Dimap. This format is about to be used for all image map products as well as raw satellite scenes when Spot5 will be launched (end of 2001).

The main goals of the format developments are:

- Data cataloguing and browsing (use of XML/XSL)
- Direct use format (load and go).
- Use of metadata concepts, specially tailored to imagery (data sources, specific processes, legend,
- Use of already existing standards for binary data storage
- Sensor and application independence
- Any geographic area coverage (including mosaicked images handling)
- Multiple data layers (raster, vector, DEM...)
- Humanly readable metadata
- 'e-commerce' compatibility

Dimap is an open metadata standard co-developed by SCC-Satellitbild and Spot Image.

### DIMAP FEATURES

Dimap is a collection of hierarchical metadata designed to hold contents and technical information about digital image maps. Its main features are :

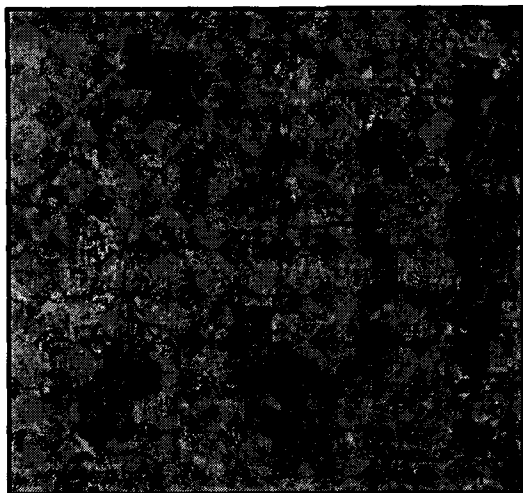
- XML and ASCII implementation provided
- Object oriented design
- Use of ISO rules when applicable for value
- Use of already existing standards for geodesy (EPSG/GeoTIFF)

- Metadata based on hierarchical keyword/value pairs.
- Digital packaging allowing multiple products, multiple layers, composite GIS data transfer.

#### AN EXAMPLE : THE COHERENCE PRODUCT

Spot Image has performed the analysis of user requirements for geographical information over the broad range of applications that a data provider has to face.

Based on the combination of Synthetic Aperture Radar (SAR) amplitude and interferometric correlation, or 'coherence', multi-band imagery can be generated that has a high potential as a complement to optical imagery. In the case of ERS SAR TANDEM data, multi-band amplitude/coherence imagery prove to be an effective solution as a complement to SPOT data products for a variety of land applications.



**Figure 1a - Coherence Product in CAR display (Red: coherence ; Green : amplitude average ; Blue : amplitude ratio)**



**Figure 1b - Multispectral SPOT XS extract**

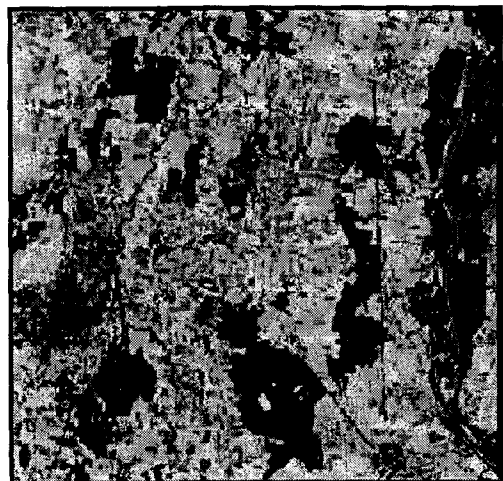
As a result of the development led by Spot Image in partnership with Gamma Remote Sensing (Bern) and the

European Space Agency, an in-house product is being released that is called the Spot Image Coherence Product.

The product is defined as the combination of amplitude and coherence using ERS SAR TANDEM data in the form of a series of four raster files encapsulated in DIMAP using the XML implementation.

The product is generated from SAR data in complex form using interferometric processing to exploit amplitude and phase information ; it may displayed as a RGB color composite in two forms :

- i) the CAR form (see Figure 1a) : coherence (Red), average amplitude of TANDEM pair, amplitude changes over one day - the TANDEM acquisition time difference (Blue) or
- ii) the CFA form : coherence (Red), despeckled amplitude of first - ERS-1 - acquisition (Green), despeckled amplitude of second - ERS-2 - acquisition (Blue).



**Figure 1c - Thematic map derived from Spot Image (Dark green : forest, Blue : water, Yellow & Red : urban)**

The Coherence Product is focussed on the exploitation of existing archives as ERS TANDEM programming is not being considered - apart from dedicated campaigns organised by the Agency.

Besides this limitation, the product offers unique capabilities as it allows the exploitation of radar imagery for image interpretation purposes whereas traditional radar data are hardly equivalent to optical data in terms of information content and radiometric aspect (see Figures 2 & 3).

The use of the Coherence Product in several application projects has been experienced successfully in a multi-sensor optical/radar approach.

The application of mapping and monitoring methods using such data has been evaluated by Spot Image and its partners. This has been analysed in depth in equatorial and tropical regions with high cloud coverage in the frame work of studies and through operational projects – a clear demonstration of the benefit of such a development.

## FUNDAMENTALS

Dimap is more a metadata standard rather than a data exchange format. Dimap may exist in several different forms called implementations. The very first implementation is a straightforward Ascii file structure. The recommended implementation is based on XML (the future Internet HTML). This implementation allows direct metadata browsing through standard XML enabled web browsers (such as Internet Explorer 5 by Microsoft). In addition, XML supports a fully structured document model which is very convenient for implementing the Group/Keyword structure of Dimap. Other object implementations will be proposed in the future: JavaBeans, OCX, Corba, etc...

The publication of the standard Dimap metadata is based on keywords. Keywords are fully documented, they are typed and value range checks can be performed. The keywords are themselves grouped semantically in Groups. The Groups can be composed of keywords and/or other sub-groups. The final level of structuration is called Containers, they provide a practical and standard way of using Dimap in the real life.

## METADATA & ENCAPSULATION

As stated above, Dimap is using metadata to describe the content of any geographic information data product. It proposes a set of well-defined keywords to provide the metadata.

Dimap allows the description of multiple layers of information of different types. For instance, it can give information about a volume, the products included in this volume, raster and vector paths to the real data attached to a product. And for each data product, it is possible to provide information on producing, framing, georeferencing and geopositioning, image content, quality assessment, image or vector sources.

The general mechanism used in Dimap is called encapsulation. It allows to define and handle complex data exchanges with any level of data nesting (hierarchical structuration).

In practice, a Dimap dataset can be composed of other datasets called Components. These Components can

themselves be described as Dimap datasets or through some other external formats such as DTMs or vectors.

Dimap makes use of existing data standard or de facto standards wherever possible (direct use of GeoTiff, DTEDs, DXF, MIF/MID, SHP, DGN, ...)

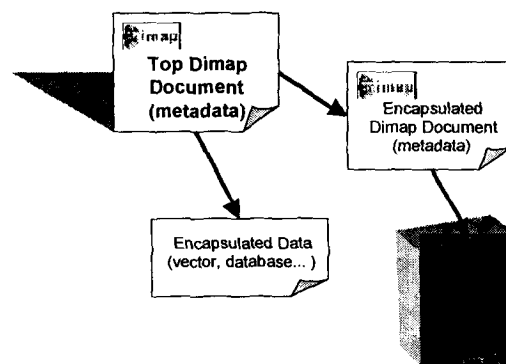


Figure 2 - Typical Dimap data file structure

## HETEROGENEOUS LAYERS

Dimap has been designed to handle heterogeneous datasets. Following the experience of Spot Image and SSC-Satellitbild, it appeared very early that the users often needed a ready-to-use collections of data. Such collections of data were forming digital maps composed of different layers, possibly of heterogeneous types. Therefore, it is possible to encapsulate any digital data into a Dimap product (see Digital packaging below). Consequently, the format is open to a broad variety of products, which can be tightened to some very specific needs, while using industry standards for the data storage itself.

For instance, it is possible to publish a product containing several layers of satellite images (different dates of acquisition, different sensors, etc...), other raster layers (landclass images, scanned maps, etc...), DEMs, vector layers (landcover maps, etc...), database exports... It is up to the data provider to guarantee the cross-consistency of the layers. For this reason, Dimap provides advanced structuring facilities.

## RASTER LAYERS DESCRIPTION

The designers of Dimap have put significant efforts on raster datasets. Therefore one will find many keywords dedicated to this sort of layers. From the data providers standpoint, an image is more than a simple raster file. An image is composed of a raster file plus a series of metadata providing information about the meaning of this raster file.

Multiple raster formats can be used along with Dimap, but it is highly recommended to use GeoTiff or BIL since most GIS or image processing software already implements these two formats. As well, Dimap provides a mechanism for describing multi-resolution images with a super-tiling support for very large images -; this topic will be covered in the Dimap reference documentation.

### IMAGE METADATA

The digital images provided in a Dimap delivery can result from complex image processing (image mosaicking, radiometric enhancements, geometric transformations, and thematic classifications...).

Therefore, it is essential for a user to be able to retrieve the processing history of an image in order for him to understand what he/she is looking at.

For instance, one can find the full listing and description of all the satellite scenes that have been used to generate the final image (including dates of acquisition, satellite identification, instrument(s) configuration, spectral mode, corner coordinates of original scenes...). Image metadata include :

- raster binary encoding scheme description
- georeferencing
- geopositioning
- raster layer thematic description
- colour coding and legend information if the raster layer is a pseudo-color file (landclass type products)
- load & go display parameters (eg brightness / contrast)
- information about the geometric and radiometric processing
- image sources

The following is an example of image metadata related to the Coherence Product :

```
<Data_Processing>
  <GEOMETRIC_PROCESSING>2A</GEOMETRIC_PROCESSING>
  <RADIOMETRIC_PROCESSING>CAR specific
    interferometric
    processing</RADIOMETRIC_PROCESSING>
</Data_Processing>
<Image_Interpretation>
  <BAND index="1">Degree of coherence
    (interferometric correlation between the two
    ERS scenes).
  </BAND>
  <BAND index="2">Average backscatter intensity
    of the ERS Tandem pair.
  </BAND>
  <BAND index="3">ratio (ABS(10*log10(i2/i1))
  </BAND>
</Image_Interpretation>
<Dataset_Use>
  <DATASET_CONTENT>Multiband Radar
  Imagery</DATASET_CONTENT>
```

```
<DATASET_COMMENTS>High value-added ERS-SAR
  based image product.</DATASET_COMMENTS>
</Dataset_Use>
```

### DATASET SOURCES

Dimap provides a series of standard keywords in order to describe the data sources. We believe that this piece of information is essential to the end-user for a good understanding of what he/she is looking at.

An image map is often resulting from the combination of several image acquisitions. Moreover external sources of information are also involved in interim processes. Therefore, the data sources information are repeatable, and thus allow to describe multiple sources. Each data source is composed of the following information :

- Dataset source identification and short description
- Dataset source corners (in order to spatially track the origin of the data)
- Dataset scene detailed information (mainly for satellite image data sources)

The above scheme allows the publication of data sources of many different types such as : satellite scenes, Ground Control Points, triangulation, paper maps, DTMs,...

Example :

```
<Dataset_Sources>
  <N_SOURCES>2</N_SOURCES>
  <Source_Information index="1">
    <SOURCE_ID>ERS2/19146/3609/1998-12-
    18</SOURCE_ID>
    <SOURCE_TYPE>SAR Radar image</SOURCE_TYPE>
    <SOURCE_DESCRIPTION>Reference ERS
    scene</SOURCE_DESCRIPTION>
    <Source_Corners>
    ...
  </Source_Corners>
  <Scene_Source>
    <IMAGING_DATE>1998-12-18</IMAGING_DATE>
    <MISSION>ERS 2</MISSION>
    <INSTRUMENT>AMI SAR</INSTRUMENT>
    <SCENE_PROC_LEVEL>ERS SAR
    RAW</SCENE_PROC_LEVEL>
    <SCENE_RECT_ELEV
    unit="M">0</SCENE_RECT_ELEV>
    <INCIDENCE_ANGLE
    DEG="">23.3193</INCIDENCE_ANGLE>
    <GRID_REFERENCE>19146/3609</GRID_REFER-
    ENCE>
    <THEORETICAL_RESOLUTION
    unit="M">25.0</THEORETICAL_RESOLUTION>
  </Scene_Source>
</Source_Information>
  <Source_Information index="2">
    <SOURCE_ID>ERS1/38819/3609/1998-12-
    17</SOURCE_ID>
    <SOURCE_TYPE>SAR Radar image</SOURCE_TYPE>
    <SOURCE_DESCRIPTION>Secondary ERS
    scene</SOURCE_DESCRIPTION>
    <Source_Corners>
    ...
  </Source_Corners>
  <Scene_Source>
```



```

<IMAGING_DATE>1998-12-17</IMAGING_DATE>
<MISSION>ERS 1</MISSION>
<INSTRUMENT>AMI SAR</INSTRUMENT>
<SCENE_PROC_LEVEL>ERS SAR
RAW</SCENE_PROC_LEVEL>
<SCENE_RECT_ELEV
unit="M">0</SCENE_RECT_ELEV>
<INCIDENCE_ANGLE
unit="DEG">23.3276</INCIDENCE_ANGLE>
<GRID_REFERENCE>38819/3609</GRID_REFEREN
NCE>
<THEORETICAL_RES
unit="M">25.0</THEORETICAL_RES>
</Scene_Source>
</Source_Information>
</Dataset_Sources>

```

## QUALITY ASSESSMENT

Currently there is no well identified and standard procedure to measure the geometric - and radiometric - precision or accuracy of an image. These subjects are under deep discussions among international standardization groups. An abstract set of keywords is being defined than can be used to describe quality assessment parameters that are yet to be defined.

```

<Quality_Assesment>
<QUALITY_TABLES>SPOT_IMAGE
1.0</QUALITY_TABLES>
<N_QUALITY_PARAMETERS>1</N_QUALITY_PARAMETERS
>
<Quality_Parameter>
<QUALITY_PARAMETER_DESC>Perpendicular base
line of the ERS Tandem
pair</QUALITY_PARAMETER_DESC>
<QUALITY_PARAMETER_VALUE unit="M">-
317.9</QUALITY_PARAMETER_VALUE>
</Quality_Parameter>
</Quality_Assesment>

```

Note that some raster sources information give indications about the currentness of the data, a topic that is often associated to precision and quality issues. Completness by itslef is not handled directly within Dimap.

However, an indication of the validity area may be given through the `Dataset_frame` support (exact dataset boundaries). In most situations this issue is relevant for very large data sets. Moreover, a specific mask layer may provide this information.

## OBJECT ORIENTED DESIGN

Dimap has a structured and modular design. Dimap is compliant with Object Oriented design style. The design has been made using the OMT method.

Following the OMT design method, a subtle distinction has been made between the metadata definition the use of it within a product. This means that many flavors of Dimap may exist whereas a single metadata standard does exist. Essentially, when a product is published using Dimap metadata :

- a keyword becomes a property because a value has been assigned to it
- a group becomes a body part because it is made of individual valued properties
- a container becomes a Document because it is composed of valued body parts

Further more, a toolbox, written in Java, has been developed to manipulate Dimap compliant products. The toolbox as well, is designed in an Object Oriented fashion. Therefore, encapsulation components of this toolbox with persistent Dimap datasets could easily lead to truly Object Oriented data exchanges as soon as GIS industry will support them.

## GEOCODING

All the products compliant with Dimap should be **geocoded**. This means that any geographic information belonging to a Dimap product should be published using a well-defined coordinate system and a set of localization parameters within this coordinate system for inserting the data.

**Geocoding**, for Dimap users, is about providing a way to georeference and geoposition a dataset. These subjects are covered in details in the following paragraphs.

Dimap recommends to use standard tables for identification of carto-geodetic parameters such as EPSG (also used by GeoTiff).

## GEOREFERENCING

Georeferencing allows to deliver precise description of the earth coordinate system used to attach the image geometry to the ground.

Cartographers have been using different coordinate systems since hundreds years which explains why there are so many different systems. Up to now, each GIS software has been using its own proprietary set of tables to describe the set of mathematical parameters used to parameterized a given coordinate system.

Recent work provided by EPSG [ 1] and reused by GeoTiff [ 3] and OpenGIS [ 4] allowed different vendors to share a common series of tables.

Although Dimap allows to use proprietary identification systems, we highly recommend to use the EPSG one. Such earth coordinate systems can be of two classes : cartographic (cartesian) and geographic (spherical).

## GEOPOSITIONING

Once the coordinate reference system (CRS) is identified, it is necessary to establish the relationship between the raster coordinate system (rows and columns) and the CRS. This is what we call geopositioning.

This operation can be performed through two techniques :

- Geoposition by points
- Geoposition by insertion.

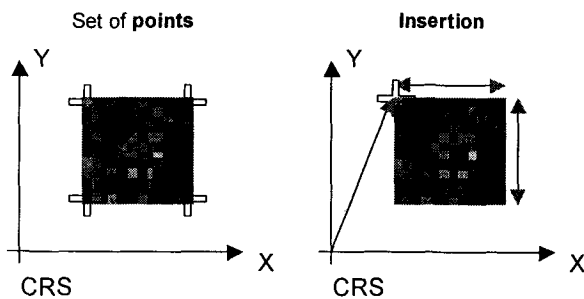


Figure 3 – Two geopositioning techniques

The first consist in identifying a set of points expressed in both CRS and Raster. Then, the user software builds a mathematical relationship between the two sets of coordinates and interpolates between these points. This technique is not very accurate and does not enable to control the geometric error budget. It can be used for approximate localization of raw imagery.

The second defines a precise insertion point for the top left corner of the raster image in the CRS and delivers the exact ground size along the two coordinate axes of a pixel. This technique is very accurate but requires that the image be rectified within the CRS (pixel axes and CRS axes are parallel to each other).

## USE OF XML TECHNOLOGY

XML is an international standard developed through the W3C (World Wide Web Consortium). It has reached its version 1.0 and is about to replace HTML in the next coming years. XML stands for eXtended Mark-up Language. Therefore its very nature lies in extensibility.

This feature has been used to directly transpose the Dimap dictionary into an XML structure.

XML also provides techniques (called DTDs: Document Type Declaration) that allow the parsers to check the structure of the document against a template.

An upcoming technique, not yet standardised, is currently being defined: XML-Schema. This will permit both

structural and syntax checks. In a very near future, the XML parsers will have the possibility to validate a Dimap document against the official specifications. This will greatly enhance the quality control tasks and ease data exchanges between producers and customers.

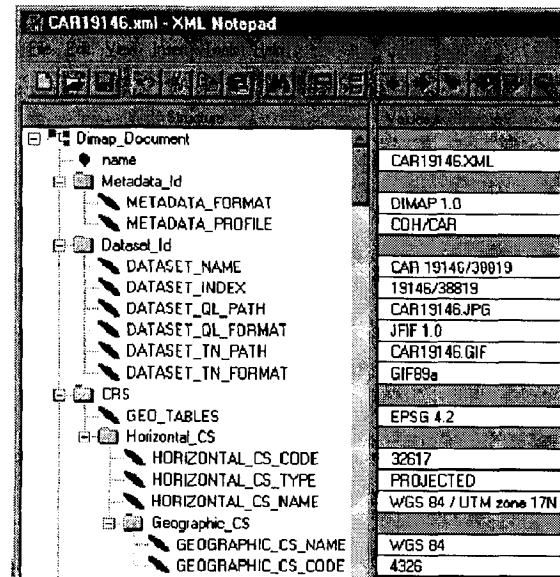


Figure 4 - Sample Dimap XML document

## XML BROWSING

XML alone, when displayed as a text file, is humanly readable. But XML allows a lot more than this: XSL. XSL, although not yet standardised, allows to transform an XML tree into any other XML tree.

The resulting tree can be based on HTML and therefore immediately displayable into a standard web browser.

At the time this article is being written, Internet Explorer 5 (IE5, see Figure 5) by Microsoft is the only widely distributed web browser which is fully implementing all the above described techniques.

Spot Image intends to develop this XML/XSL techniques in order to provide several levels of browsing of the very same Dimap-XML product.

For example, there could be :

- a "quick discovery" XSL for cataloguing applications,
- a "product browsing" XSL for end product customers display purposes and, finally,
- an "advanced" XSL that would show all the pieces of information provided with the product with on-line hyper-help.

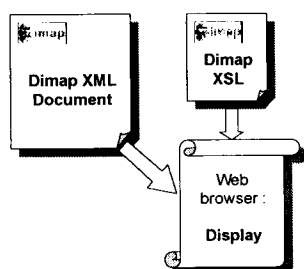


Figure 5 - XML/XSL browser display

All these applications are also directly compatible with on-line delivery and e-commerce issues.

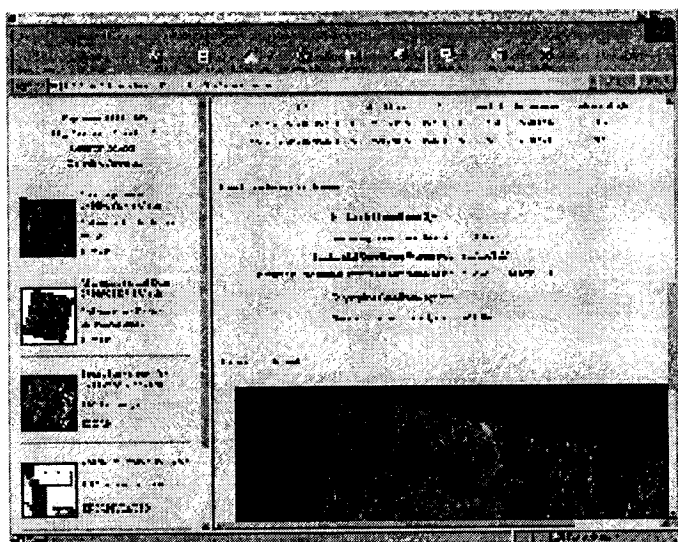


Figure 6 - Sample XML/XSL display in IE5

#### THE COHERENCE PRODUCT

The implementation of Dimap in the case of the ERS based Coherence Product has resulted in a structure that has the following main components (see Figure 7 from Left to Right):

- i) the CAR component,
- ii) the CFA component – both being the three band 24 bits rasters composing the main elements of the package,
- iii) and a third component comprising the source data, the product User Guide and Dimap Reference documents.

Navigation within the package composing the product is made easy and flexible through the proposed XML/XSL structure. The XML/XSL display associated to the product is as shown in Figure 6 ; see the second icon on the left - the CFA image - and the dynamic link to the associated CAR XML element.

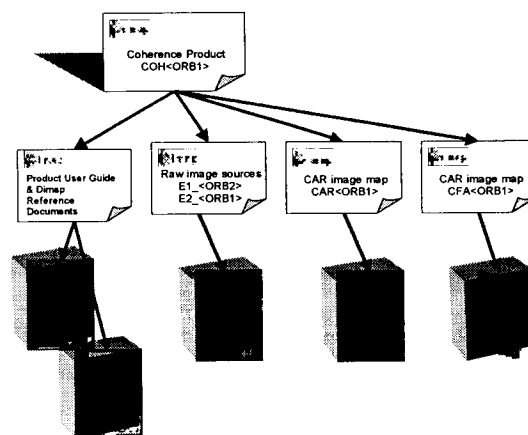


Figure 7 - Coherence Product XML implementation

On-line help is given via the documents associated to the product and its use and, secondly, through the Dimap reference documentation – both provided in HTML form.

#### CONCLUSION

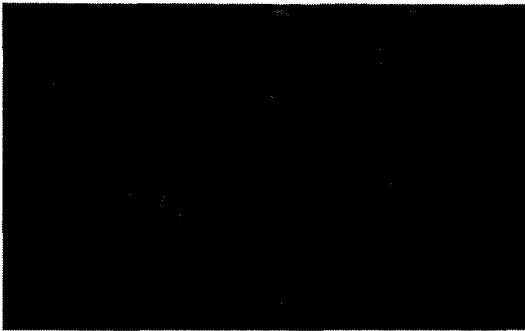
The work presented here shows that it is possible use up-to-date technology for satellite imagery metadata publishing.

Dimap is an open metadata standard, useable by any image data provider in its field of interest. The use of XML also permits to enhance the set of metadata for specific applications without disrupting the standard.

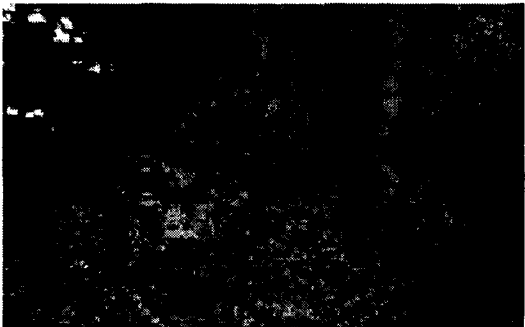
We expect to release a public documentation of Dimap by the end of 1999. We are currently working on a plan to maximise the penetration of Dimap among software vendors and customers.

The Spot Image Coherence Product is an innovative step in the development of new user-oriented remote sensing products and services resulting from new imaging techniques - based on interferometry and multi-band radar imagery.

Given utilisation procedures through the required spatial and temporal sampling and depending on the achievable spatial resolution, ERS TANDEM coherence imagery has a solid potential with respect to land applications.



**Figure 8 – Coherence Product over Fribourg area  
(CAR display mode)**



**Figure 9 – SPOT XS product over Fribourg area**

The Dimap format enables to provide new radar products in a form that is compatible with Spot Image's portfolio. The Spot Image Coherence Product was a valuable test for product designers with the aim to qualify the applicability and versatility of Dimap.

#### ACKNOWLEDGEMENTS

Special thanks to SSC-Satellitbild (especially Torbjorn Westin and Lars Nilsson) who co-authored the Dimap specifications.

#### REFERENCES

- [ 1 ] EPSG "European Petroleum Survey Group Geodetic database"  
<http://www.petroconsultants.com/products/geodetic.html>
- [ 2 ] XML specifications  
<http://www.w3.org/TR/1998/REC-xml-19980210> and  
<http://www.w3.org/XML>
- [ 3 ] GeoTiff specifications  
<http://www.remotesensing.org/geotiff/geotiff.html>
- [ 4 ] OpenGIS organization <http://www.opengis.org>

## A method for the automatic characterization of interferometric fringes free of atmospheric artifacts : application to the study of the subsidences on the city of Paris

Bénédicte FRUNEAU <sup>1</sup>, Francesco SARTI<sup>2</sup>

<sup>1</sup> Laboratoire des Géomatériaux, Institut Francilien des Géosciences (IFG)  
 Université de Marne-la-Vallée 5 Bd Descartes, Champs-sur-Marne  
 77454 Marne-la-Vallée cedex 2, France  
 Tel : 33.1.49.32.90.61 / Fax : 33.1.49.32.91.37 / e-mail: fruneau@univ-mlv.fr

<sup>2</sup> CNES, QTIS/SR,  
 18 avenue Edouard Belin, Bpi 811, 31401 Toulouse, France  
 Tel : 33.5.61.28.21.33 / Fax : 33.5 / e-mail: francesco.sarti@cnes.fr

### ABSTRACT

Differential SAR interferometry allows for the detection and mapping of ground subsidences, usually attributable to human activities, associated with the extraction of fluids beneath the surface, or underground mining... Limiting factors for monitoring slow subsidences are mainly temporal coherence loss and varying atmospheric conditions between the acquisitions of images. Such variations induce a path difference generating InSAR artifacts that cannot be corrected if only one interferogram is available. On urban areas, the coherence remains often high over long time scales. The main problem then appears to be the atmospheric heterogeneities. This kind of artifacts can be easily detected on the different interferograms we generated on the city of Paris. Significant phase variations are clearly visible, and can not be associated with topographic fringes, nor with displacements.

Several techniques exist in order to eliminate or reduce the effect of atmospheric artifacts: a solution consists in summing and averaging interferograms, but requires several interferograms over the same site. The advantages of a novel approach based on complex correlation of interferograms are presented here, in particular robustness when only a few interferograms are available (two interferograms are enough, under given hypotheses). These algorithms were tested in the context of automatic detection of atmospheric artifacts by means of correlation of interferometric triplets.

On the city of Paris, this method reveals 2 subsidening zones. One zone has the same location as an important underground working site, which took place from 1995 to 1997. The existence of subsidences in the area was known already from ground truth data. Their spatial extent can now be mapped by interferometry, and the temporal evolution of the subsidences is also examined here.

### INTRODUCTION

The use of SAR interferometry has now become essential for the detection of ground deformations caused by earthquakes, volcano activity, and ice motion, which are usually phenomena of large spatial extension. It has also proven to be a feasible tool for the detection and mapping of ground subsidences, associated with geothermal fields, oil fields, compaction of aquifer system, underground mining... Most of these studied subsidences occur either in non urban context, and are of small spatial extension (Carnec *et al.*, 1996), or concern urban areas, but are very large (Amelung, 1998; Fielding *et al.*, 1998; Wegmüller *et al.*, 1999). Here we examine the feasibility of SAR interferometry for the detection of slow deformations on urban areas with standard atmospheric conditions. We focus on the city of Paris, where displacements of a few hundred meters in extension and a few centimeters in amplitude occur. They are mainly due to the water pumping of working sites, and also to underground quarry.

### INTERFEROGRAMS

Ten interferograms of the city of Paris are derived from tandem SAR images acquired during the period of July 28 1993, August 10 1996 (Fig.1). Those interferograms are generated with the Diapason software developed at CNES, and have time separation ranging from 1 day to about 3 years (table 1).

The contribution of the topography is removed using a Digital Elevation Model provided by the Institut Géographique National, with a 25 m horizontal resolution. With an altitude of ambiguity larger than 400 m and a good quality DEM, we can affirm that coherent interferometric changes can only be due to surface deformations and/or changes in radar propagation

through the atmosphere between the acquisition of the 2 images.

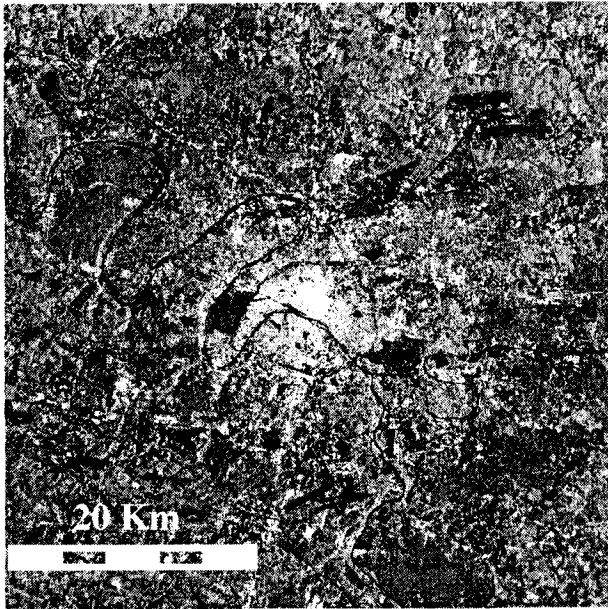


Fig.1: SAR amplitude image of Paris and surroundings

Significant phase variations as high as one fringe can be easily detected on all interferograms. Large scale bubbles (20 km diameter) are observed, as well as small ones (1 to 5 km diameter) (Fig. 2a and 2b).

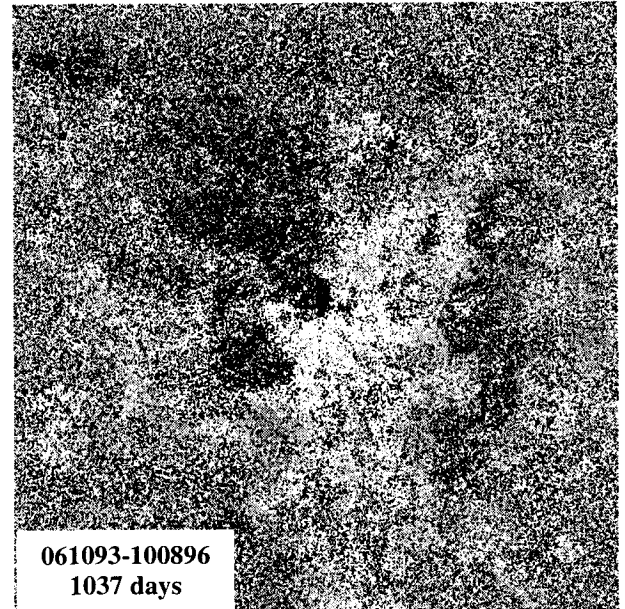


Figure 2a: 1037 days differential interferogram

280793 10631	061093 11633	210795 20995	220795 1322	100896 6833
71 d, h = 257 m				
723 d, h = -964 m				
724 d, h = 405 m				
1108 d, h = 348 m				
652 d, h = -203 m				
653 d, h = -705 m				
1037 d, h = -985 m				
1 d, h = 285 m				
385 d, h = 256 m				
384 d, h = 2474 m				

Table 1: Data selection

Data selection offers the opportunity to study the evolution of the coherence on a time scale of 3 years. Low values of baselines ensure there is no geometric decorrelation. As we expected, the coherence is shown to remain high over more than 3 years, thus indicating that the detection of very low subsidence rates over a long time span on urban areas is not limited by the coherence loss on the time scale required.

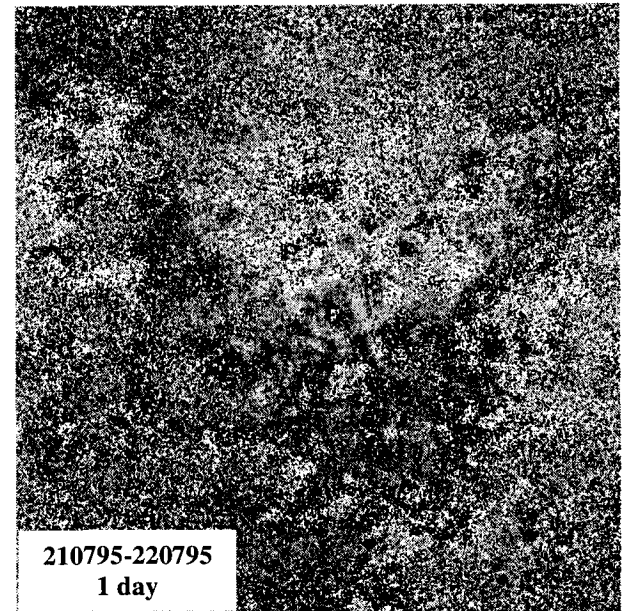


Figure 2b: 1 day differential interferogram

Most fringes can neither be associated with topography, nor with displacements, each fringe corresponding in this case to a half wavelength displacement. This phenomenon is even visible on the 1-day interferogram

and excludes the hypothesis of such displacements, distributed everywhere in Paris and surroundings (Fig.2b). Most of these bubbles are furthermore absolutely not stationary, their location changing from a day to another, and they do not have the size we expected for the deformations. Most of the signal may be attributed to tropospheric effects.

Using the logic of pair wise, we found that interferograms generated with the 06/10/93 image or with the 21/07/95 one show phase shifts similar in their geometry. Interferograms having the 21/07/95 image in common show little bubbles of small scale, everywhere in the image. This indicates the presence of convective cells. Interferograms containing the other one display an almost South-Northern fringe. This may be related to a frontal zone.

#### INFLUENCE OF TROPOSPHERIC HETEROGENEITIES

Atmospheric effects, as coherence preserving phase phenomenon, may be misinterpreted as subsidence on interferograms. Those effects are related to the variation of the refractive index distribution of the propagating medium. Homogeneous variations are highly correlated with altitude (Delacourt *et al.*, 1997) and can be neglected in our case (almost flat terrain). We are then only disturbed by the heterogeneous atmospheric component.

Those kind of artifacts are impossible to correct, since we need index profiles for almost each pixel of the images, that is for the 2 acquisition dates.

We tried to compare our interferograms with NOAA images (with a 1 km x 1 km resolution) in order to identify meteorological artifacts, and discriminate them from the signature of displacements. We intend to find common structures, and see if the spatial signature of the atmospheric effects in the interferograms could be correlated with the signal observed on NOAA images. The problem is that it is very difficult to have simultaneous acquisitions with SAR images, since they are acquired every 6 hours.

The 21 July SAR image was acquired at about 11 o'clock, between the first and second acquisition of NOAA. Therefore we can only derive qualitative conclusion. The only thing we can observe is the presence of many cumulus in the second NOAA image, corresponding to convective clouds development, which creates the most disturbing localized anomalies in the interferometric phase (Hanssen, 1998; Zebker *et al.*, 1997). This is also confirmed by MétéoFrance, which indicates a high humidity rate in the lower layers in the morning, and a high increase of the temperature. This led to convective developments.

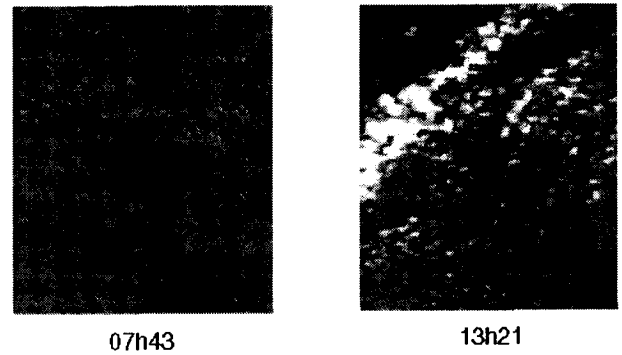


Figure 3: 21 July NOAA images

We also have 2 NOAA images for the August acquisition, but not at the time of SAR acquisition. Here, clouds are of stratocumulus type. Those kind of clouds are observed in frontal zones, which would be responsible of the parallel fringe.

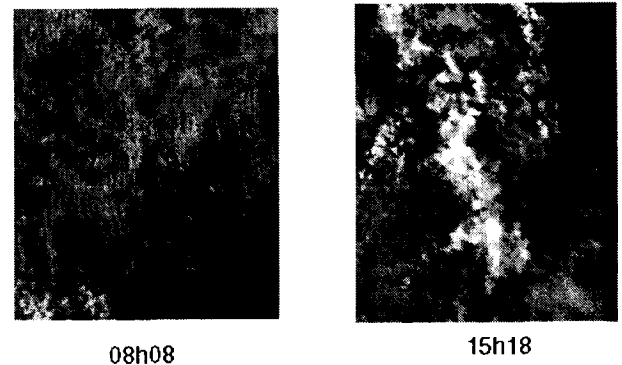


Figure 4 : 10 August NOAA images

#### DISPLACEMENTS DETECTED OVER PARIS

An usual solution to reduce the effect of the artifacts caused by atmospheric fluctuations consists in summing and averaging interferograms.

Here, we consider only a few interferograms:

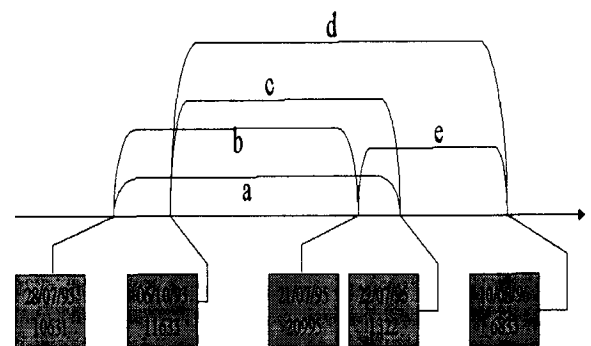


Figure 5 shows an example of the addition of interferograms a, b, c and d. It is possible to detect on the resulting image two areas of subsidence. But this method requires several interferograms over the same site, and atmospheric artifacts are still partially present.

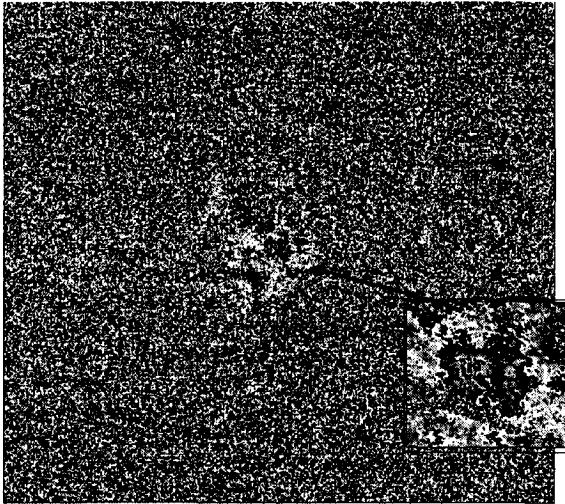


Figure 5: Sum of interferograms a, b, c and d, and zoom on the 2 areas of subsidence which are revealed by means of correlation

We propose here a **novel approach** based on complex correlation of interferograms. These algorithms were tested in the context of automatic detection of atmospheric artifacts by means of correlation of interferometric triplets (Sarti *et al.*, 1999).

The interferograms contain fringes due to the atmospheric conditions of the 2 SAR acquisitions, and due to ground displacements. By means of correlation between interferograms, we wish to isolate the deformation, that is the common fringes in the 2 interferograms.

Of course, we need to select for the correlation *two interferometric* pairs with no common dates (no common atmospheric artifacts) and containing the same subsidences (spanning a similar time period, except if the phenomenon is stable) : then, only common fringes (common displacements) will correlate.

From an interferogram AB, we construct a complex image, having a phase equal to the interferogram ( $\varphi$ ) and a modulus equal to the unity or to the coherence ( $\gamma$ ).

We then compute the correlation rate of pairs of interferograms AB and CD. The first formulation is:

$$\rho_1(AB, CD) = \text{corr}(1 \cdot e^{j\varphi_{AB}}, 1 \cdot e^{j\varphi_{CD}})$$

The second one, using the coherence norm, is:

$$\rho_2(AB, CD) = \text{corr}(\gamma_{AB} \cdot e^{j\varphi_{AB}}, \gamma_{CD} \cdot e^{j\varphi_{CD}})$$

An important parameter is the correlation window size: this should be adapted to the spatial scale of the expected displacements. In practice, we tested two different sizes (1500 m and 750m) (fig. 6 a and b) and we computed a multi-scale correlation, defined as the sum of the two correlation rates.

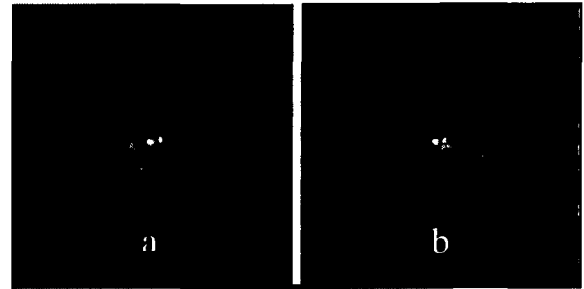


Figure 6: Correlation rates for different window sizes for interferograms b and c. (a) 1500 m - (b) 750 m.

Figure 7 shows the multiscale correlation rate between interferograms b and c, and a and d. These 2 correlations give consistent results. We obtain 2 areas, at the same position.

The first halo (from the left) is located south of the Saint-Lazare rail station. Its location is the same as that of the working site for the construction of an underground station "St-Lazare-Condorcet" for the Eole subway. Those entirely underground works took place from 1995 to 1997, and required to lower the piezometric level by pumping the phreatic water. Subsidence of the overlying ground surface, with an amplitude of the order of a few centimeters had been revealed already by ground truth. According to IFG, both correlation halos might therefore be linked to the construction of the subway.

The correlation rate is then used as a mask: we compute interferogram (b + c), masked with correlation (b,c), after application of an adequate threshold (fig. 8a), and interferogram (a + d), masked with correlation (a,d) (fig. 8b).

Despite the different time interval (2 years, 3 years), the observed phenomenon look similar on those two interferograms: it seems that no deformation occurred from July 1995 to august 1996.



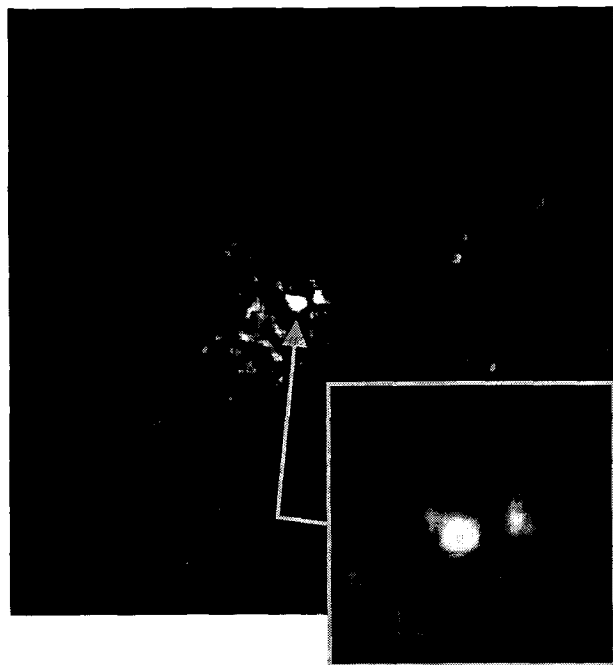


Figure 7a: Multi-scale correlation between interferograms b and c.

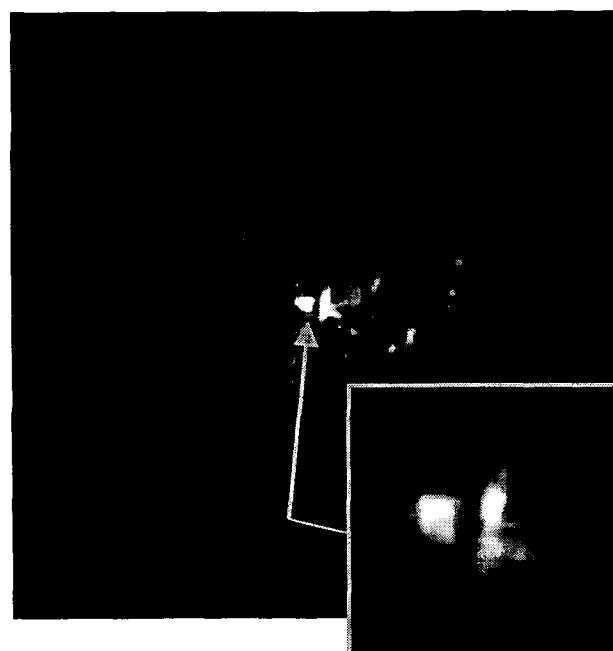


Figure 7b: Multi-scale correlation between interferograms a and d

In order to verify this conclusion, we used the difference of interferograms d-a , masked with correlation (a,d)

as a measure of the evolution/reversibility of phenomena (Fig.9).

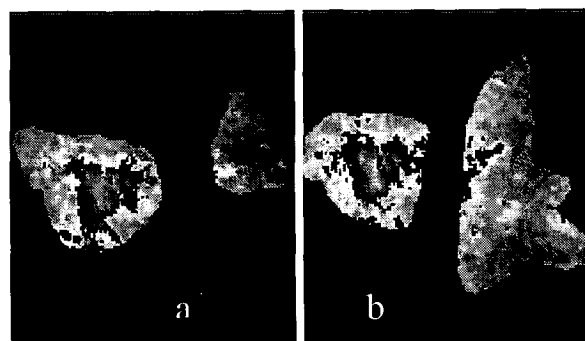


Figure 8:

(a) = Interferogram (b + c), masked with correlation (b,c) (zoom)  
 (b) = Interferogram (a + d), masked with correlation (a,d) (zoom)



Figure 9: Difference of interferograms d-a , masked with correlation (a,d) (zoom)

This difference is quite flat, as expected. It reveals no further evolution of the ground subsidences during the period July 1995 - August 1996

Furthermore, we know that the works started in 1995 in this area of Paris: the observed displacements are included in the time period October 1993 - July 1995. On the (b+c) and (a+d) interferograms, we can distinguish on the western area one fringe of displacement, corresponding to  $\frac{1}{2}$  fringe of real displacement. One fringe corresponds to 2.8 cm of deformation along the line of sight, or 3.1 cm of vertical deformation, so that displacements are of the order of 15,7 mm in 650 days.

We localized the two areas of deformation on the ERS amplitude image, using a Hue Intensity Saturation

composition with the amplitude image, the sum of interferograms, and the correlation (fig.10). We also superimposed the map of displacement on an airborne radar image (SETHI, C band, VV polarization, Onera/CNES), acquired the first December 1997 (fig.11). The leading localization error is estimated to be less than 50 m. It appears clearly that the western subsidence is centered on the Lycée Condorcet, whereas the second one contains in its central part the Rue Papillon. A whole building had to be evacuated in this street.

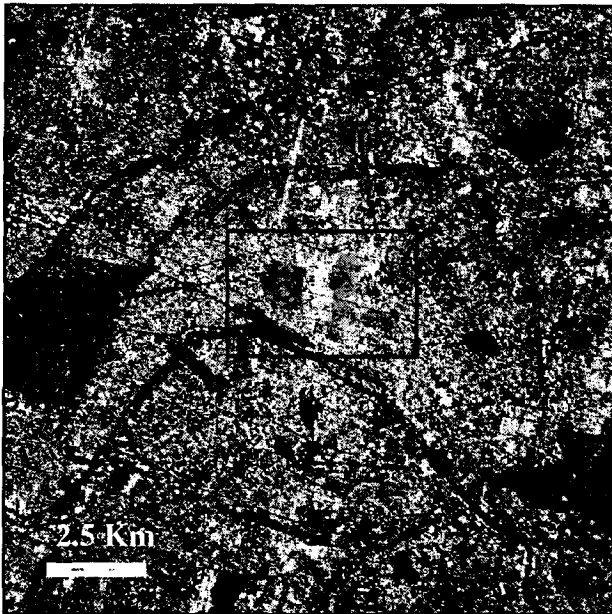


Figure 10 : HIS composition. Red rectangle corresponds to the extracted area of fig.11.

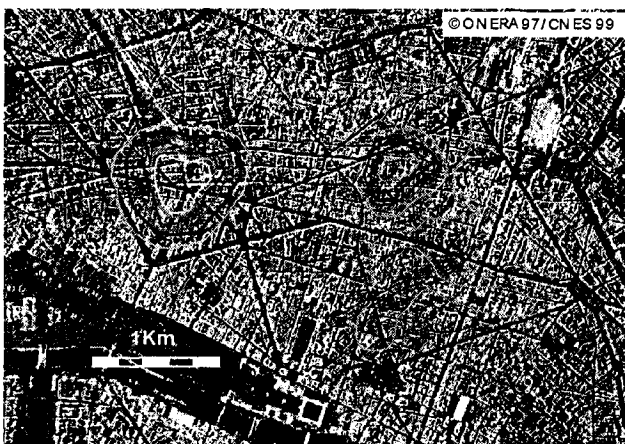


Figure 11 : Displacement map superimposed on an ONERA/CNES airborne radar image (SETHI) (copyright ONERA 1997; filtering by R.Touzi CCRS)

## CONCLUSION

We were able to detect slow deformations on the city of Paris, despite the atmospheric heterogeneities which introduce large artifacts in the interferograms, and constitute their principal limitation. The new method we presented allows to separate displacement fringes from (non-standard) atmospheric effects, using *only two interferograms*, when several conditions are verified. This method is valid under the hypotheses that there are no common standard atmospheric effects on the two interferograms used for correlation. In our application, this was certainly the case because of flat topography. Moreover, the time interval spanned by both interferograms should be the same, or the observed displacements should be stable.

The method was validated by correlating four different interferograms (a,d) and (b,c) without common acquisition dates : a similar result is obtained in both cases (two areas, same positions). A building located in the area to the west was evacuated. Subsidence in the area to the right were already known by ground truthing. According to IFG, they might be related to water pumping associated with the construction of an underground station (St.Lazare-Condorcet) for the *Eole* subway, started in 1995 and ended in 1997.

More acquisitions are necessary in order to delimit in time the beginning and the evolution of the ground displacements, notably after the end of the underground station construction and the water level re-establishment. We intend to find also, if any, other surface displacements on the city. The problem we are confronted with is that we are in the limits of ERS SAR resolution, which prevents to detect smaller events. We plan as well to test this method on different sites.

## ACKNOWLEDGMENTS

We thank ESA for providing the images, obtained within the framework of the tandem project AOT.F309, and project AO3.350. We thank IGN for the DEM. We are also grateful to the CNES, DGA and the GDR INSAR for their support. Warm thanks to D. Raymond, D. Aubert, H.Vadon and D.Massonnet.

## REFERENCES

- Amelung, F., Galloway, D., Bell, J., Zebker, H., and Laczniak, R., A sense of Las Vegas' ups and downs: New satellite maps reveal aquifer-system deformation and structural control of land subsidence, *Science*, unpublished.
- Carnec, C., Massonnet, D. and King, C., 1996, Two examples of the use of SAR interferometry on displacement fields of small spatial extension, *Geophys. Res. Lett.*, vol. 23, pp3579-3582.
- Delacourt, C., Briole, P., and Achache, J., 1998, Tropospheric corrections of SAR interferograms, *Geophysical Research Letters*, vol 25, pp 2849-2852.
- Fielding, E., Blom, R., Goldstein, R., 1998, Rapid subsidence over oil fields measured by SAR interferometry, *Geophys. Res. Lett.*, vol. 25, pp3215-3218.
- Hanssen, R., 1998, Assessment of the role of atmospheric heterogeneities in ERS tandem SAR interferometry, report in response to the statement of work for data quality analysis in support of the ERS tandem mission exploitation of the ESA, 145p.
- Massonnet, D., Rossi M., Carmona, C., Adragna, F., Peltzer, G., Feigl, K., and Rabaute T., 1993, The displacement field of the Landers earthquake mapped by radar interferometry, *Nature*, 364, pp138-142.
- Massonnet, D., Briole, P., and Arnaud, A., 1995, Deflation of Mount Etna monitored by spaceborne radar interferometry, *Nature*, pp567-570.
- Sarti, F., Vadon, H., Massonnet, D., A method for the automatic characterization of atmospheric artifacts in SAR interferograms by correlation of multiple interferograms over the same site, *Proceedings of IGARRS'99*, Hamburg, Germany, 28 june-2 july 1999
- Wegmüller, U., Strozzi, T., Bitelli, G., Validation of ERS differential SAR interferometry for land subsidence mapping: the Bologna case study, *Proceedings of IGARRS'99*, Hamburg, Germany, 28 june-2 july 1999.
- Zebker, H. A., Rosen, P.A., Hensley, S., 1997, Atmospheric effects in interferometric synthetic aperture radar surface deformation and topographic maps, *Geophysical Research Letters*, 102, pp7547-7563.



## Ship Detection Using Polarimetric SAR Data

Robert Ringrose, Nicola Harris  
 DERA Farnborough  
 Space Department, 1058 / A8  
 Hampshire, GU14 0LX, England  
 Tel: 44 1252 392663  
 Fax: 44 1252 396310  
 Email: rringrose@dera.gov.uk  
 WWW: www.dera.gov.uk

### ABSTRACT

Polarimetric techniques for the extraction of information from Synthetic Aperture Radar (SAR) data are becoming utilised increasingly by the scientific community. Significant research has been carried out over many years into methods of extracting target feature vectors from polarimetric data for use in classification algorithms. Analysis of the multi-polarimetric data collected by the Shuttle imaging radar - C (SIR-C) experiment during 1994 facilitated the production of land classification maps. The technique assumed that each type of land-use was characterised by a distinct polarimetric signature and imaged regions that exhibited unusual polarimetric behaviour corresponded to features of interest in the landscape, for example man-made structures. A different analysis technique for use on fully polarimetric data has been recently investigated. This method decomposes the full scattering matrix for each image pixel into three orthogonal components and then applies a series of matrix manipulations. The radar return from each image pixel is hereby characterised as corresponding to one of various physical elemental scatterer types. The advantage with this technique is that the polarimetric analysis is carried out for each individual image pixel. It is possible that the application of such a technique to ocean imaging could facilitate a viable approach to ship detection since areas of atypical polarimetric content may characterise the vessel well enough to mitigate it from the surrounding sea clutter. This analysis is believed to be of particular interest since the spatial resolution of the input data is not of primary importance to the scatterer classification. This allows the technique to be used for wide area surveillance.

This paper discusses the new analysis technique and investigates the implications for ship detection using fully polarimetric SAR data.

### INTRODUCTION

Multipolarimetric data from the SIR-C experiment in 1994 has been studied extensively. The different polarisations give indication of the types of features found in images of sea. A single-look complex SIR-C (L-band with rectangular pixels) image of the Gulf

Stream is shown in Fig. 1 where three polarization's have been fused together to give a colour image, HH polarisation is represented by red, VV by green and VH by blue.

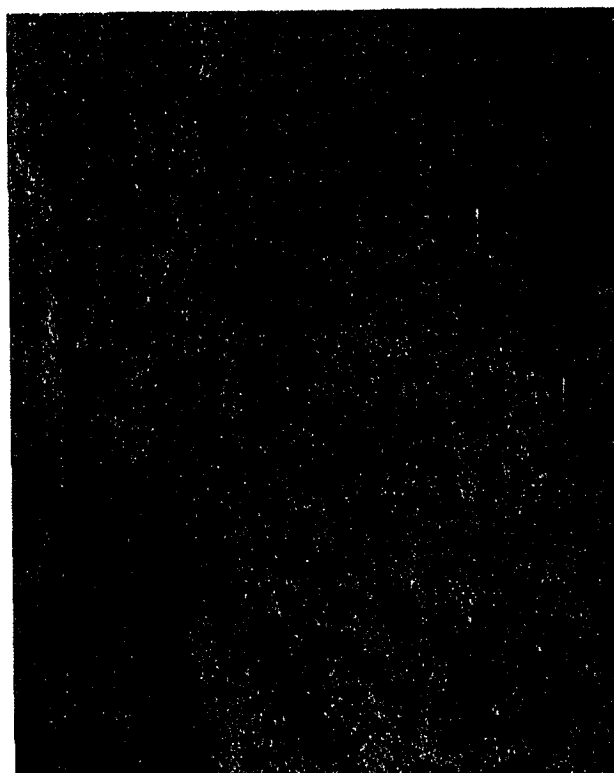


Fig. 1: Multi-polarimetric SIR-C image of the Gulf Stream

The ocean clutter gives a very significant return in the VV (green) channel. Given that a complicated (man made) target will generally give returns in all three channels, the response from such a target will be formed from contributions from all three channels giving a white response.

Fig. 1 shows many dark patches that are possible areas of low wind speed. Conventional CFAR detection algorithms do not perform as well on this sort of image as it has a large variation in backscatter. The large variation in backscatter from the ocean is significant in

the VV channel and is routinely seen in ESA's ERS-1/ERS-2 data. The variation is not nearly as significant in the HH channel as demonstrated in Radarsat data.

By examining the polarimetric content of a maritime scene the variation of backscatter is less important since the returns from each polarisation are compared relative to one another. With quad-polarisation data (ie HH, VV < HV and VH), the full scattering matrix can be derived. Association with those areas displaying similar polarimetric content can then characterize the ocean backscatter.

A target can be detected against the ocean backscatter if its polarimetric signature differs to that of the ocean. This paper discusses the methodology of polarimetric target detection and preliminary results.

This method has advantages in that once a threshold has been selected to determine the polarimetric properties of each pixel, there are no other user inputs required. For example, CFAR algorithms require a probability of false alarm so as to be able to generate a threshold. The polarimetric method does not link the threshold to a false alarm rate so there is no trade-off between false alarm rate and detection probability.

#### METHODOLOGY

Recent investigations were carried out to determine whether the full quad polarimetric content of ship and ocean data would allow full clutter mitigation and consequent reduction of false alarms. This polarimetric analysis was based on the methods developed by Cameron et al [1,2,3]. It was demonstrated that a scattering matrix could be decomposed into three orthogonal components. Further analysis of these components allows the classification of the scattering matrix as one of a number of classes corresponding to various physical scatterer types, e.g. Trihedral, Dihedral, Cylinder.

This technique enables us to decompose a fully polarimetric SAR image into elemental scatterer types, pixel by pixel. This could be a useful tool for ship detection since man-made objects are likely to exhibit different scatterer types to those of the ocean. This type of analysis could also be performed on lower resolution SAR data, enabling greater area coverage.

Here, we study different areas of ocean and quantify the main scatterer types. A simulated multi-polarimetric image of a ship will also be expressed as different scatterer types. By combining the two results, this will allow us to test whether polarimetric target detection is viable.

#### DATA SETS

The data sets considered here are the SIR-C experiment data from 1994 and simulated SAR data of ships.

The SIR-C data studied is the L-band fully polarimetric single-look complex data. Three areas of ocean have been taken from images of the Gulf Stream, the NE Atlantic and the North Sea.

The simulated SAR image is of a small commercial ship, in this case, a trawler, of approximately 50m length. This image is simulated with the same SAR parameters as the SIR-C image and at resolutions of 25m and 100m. The image is simulated every 10° aspect viewing angle over the full 360° circle.

#### DISCUSSION

A threshold is set when determining the scatterer types so that only those pixels lying above the threshold are considered. At higher thresholds, less clutter will be visible but also fewer target scatterers will be visible. An optimum threshold could be determined for optimal target detection.

Figs 2, 3, 4 show the distribution of scatterer types when varying the threshold for 3 different areas of ocean. The threshold is given in dBm. The main scatterer type for all three ocean areas is a cylinder. Each ocean area has an associated wind speed, 3 knots for the Gulf Stream image, 18-20 knots for the NE Atlantic image and 20-22 knots for the Denmark image. In all 3 cases, upto a threshold of -12dBm, at least 60% of the ocean image consist of cylinders. The wind speed does not have a large impact on the scatterer types, the slight difference being that the Gulf Stream image does not have such a wide variety of scatterers.

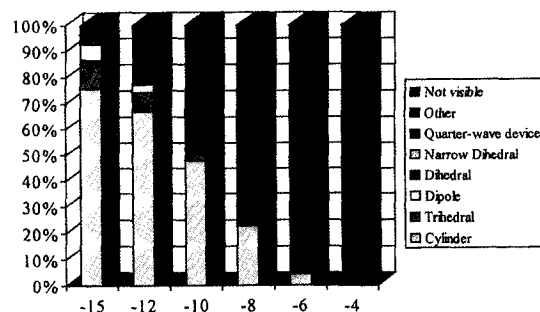


Fig. 2: Gulf Stream Scatterer Types

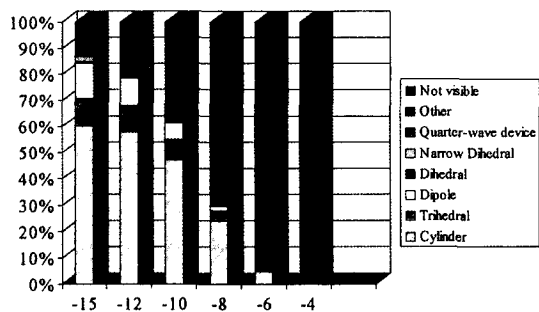


Fig. 3: NE Atlantic Scatterer Types

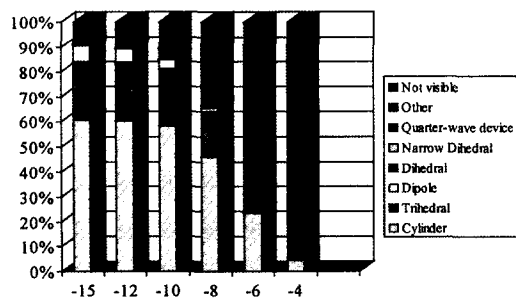


Fig. 4: Denmark Scatterer Types

The 36 simulated SAR ship images show the differences in scatterer type for different viewing angles and thresholds. For each aspect angle, the dominant scatterer type has been recorded. This data is displayed in Fig. 5 for a threshold of  $-15\text{dBm}$ . For most aspect angles, the dominant scatterer is trihedrals or dihedrals, however at some aspect angles, the dominant scatterer is a cylinder, the same scatterer type as typical ocean clutter.

At thresholds higher than  $-15\text{dBm}$ , the ocean clutter is composed of fewer scatterer types. This allows us to predict how much of the target is discernible from the ocean clutter at these thresholds. With respect to the Gulf Stream image at  $-10\text{dBm}$ , the only scatterers present are cylinders, trihedrals, dipoles and other.

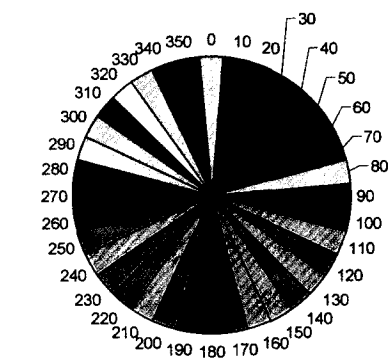


Fig. 5: Dominant Scatterers at  $-15\text{dBm}$

By calculating the percentage of scatterer types that are different to these types, an estimate of the detection probability can be made. This has also been performed for the  $-4\text{dBm}$  case (again for the Gulf Stream image) where the scatterer types present are cylinders only. Fig. 6 and Fig 7 show these results for different aspect angles.

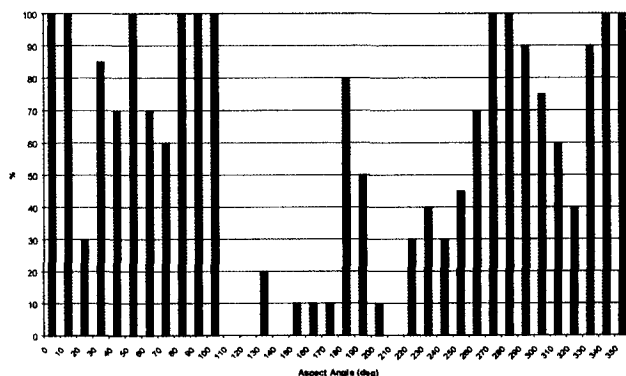


Fig. 6: Percentage of target scatterers discernible from ocean clutter at  $-10\text{dBm}$

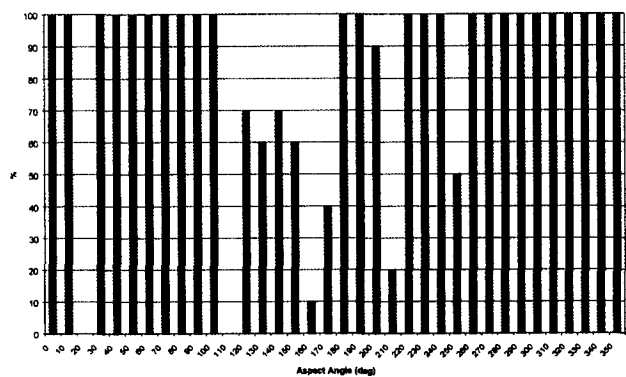


Fig. 7: Percentage of target scatterers discernible from ocean clutter at  $-4\text{dBm}$ .

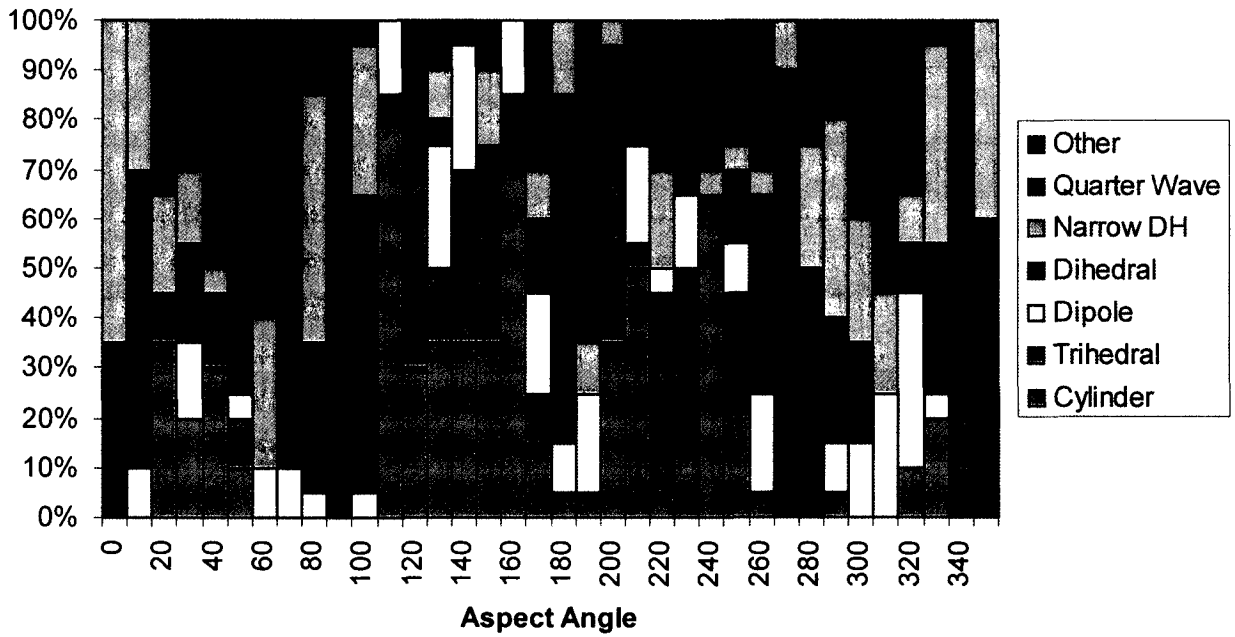


Fig. 8: -15dBm Target Scatterer Distribution

At certain aspect angles, Fig. 6 and Fig. 7 show the target cannot be distinguished from the clutter by these means. This would yield a less than perfect detection algorithm.

Fig. 8 shows the scatterer type for each aspect angle in the same manner as Figs. 2-4. It shows that the target is made up of different proportions of scatterer types to those of ocean areas. There is no straightforward relationship between the scatterer types of the different aspect angles. At 110 degree aspect, which was shown previously to be 0% discernible from the sea clutter, the proportion of trihedrals and dipoles is different to the proportions of these scatterers in the ocean areas. The most necessary scatterer for ship detection is the dihedral (or narrow dihedral) which is present in the target scatterer distribution at most aspect angles. This is a vital factor for target detection since it allows the construction of a rule for distinguishing between targets and ocean clutter.

The same polarimetric analysis as discussed above will be performed on Fig. 9, which is a zoom-in of part of Fig. 1. At least one target is visible.

Fig. 10 shows the result from performing the polarimetric analysis on Fig. 9, different scatterer types each denoted by a different colour. It can be seen that the ocean is primarily made up of cylinders. There are four targets clearly visible and these appear as combinations of dihedrals, narrow dihedrals and quarter

waves. Since the targets combine such differing scatterer types to the ocean, they are easily detected.

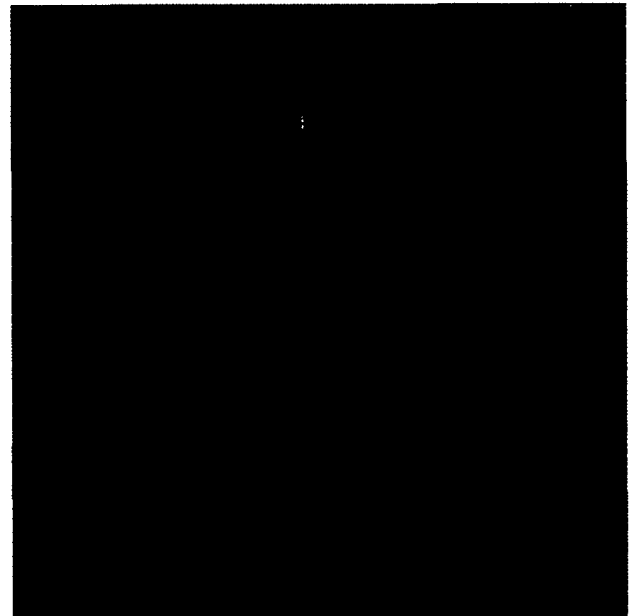


Fig. 9: A zoom-in of Fig. 1, the Gulf Stream SIR-C image



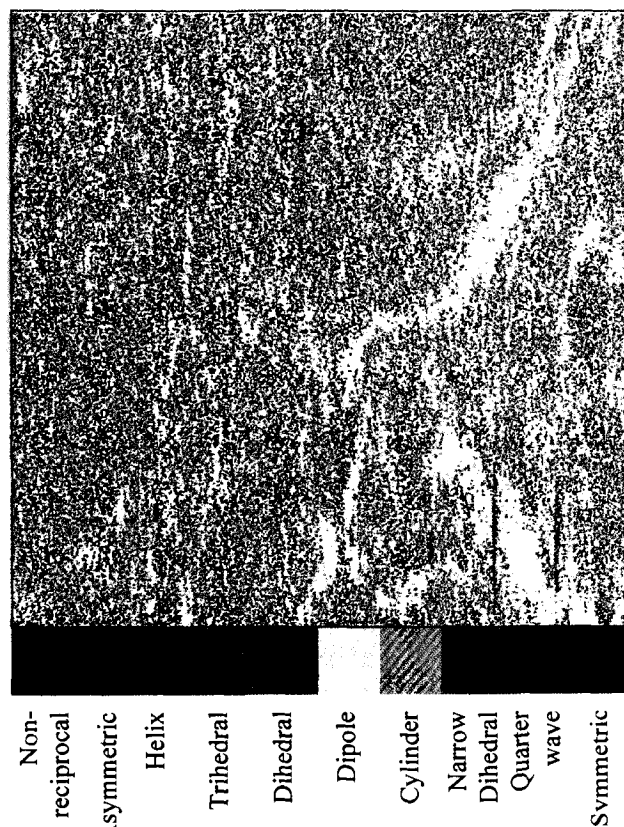


Fig. 10: Polarimetric Analysis of Fig. 9

### CONCLUSION

These results have shown that if a target is primarily made up of different scatterer types to those found in an ocean, then this is a reliable method of ship detection. The ship image shown was found to consist of dihedrals, narrow dihedrals and quarter waves, whereas the ocean data from SIR-C showed the ocean to consist primarily of cylinders at thresholds as low as  $-15\text{dBm}$  (where all ocean clutter is visible). Since the ship is at least as bright as this threshold then the ship's main scatterer types will be visible and become distinct from the ocean clutter.

The ship considered here is approximately 50m long and the simulated SAR images have been at resolutions of approximately half its length. The target is still distinct from the clutter despite being so small relative to the resolution. This has a large advantage in that a far greater swath width can be achieved using space-borne SAR and therefore greater areas of ocean can be observed.

By analyzing further images of ocean, a greater understanding of how the scattering matrix changes over the different sea states can be obtained. This could

then be fed back into the ship detection method to eliminate all sea clutter and leave only targets.

This system of ship detection requires a fully polarimetric SAR system to perform which is costly. However, a poorer resolution and hence, greater swath width can be accepted. The polarimetric method can be used for other applications and highlights that the requirement for fully polarimetric SAR is just as important as the requirement for better resolution.

This paper demonstrates that the preliminary results from this polarimetric target detection study look promising and are worthy of further investigation.

### REFERENCES

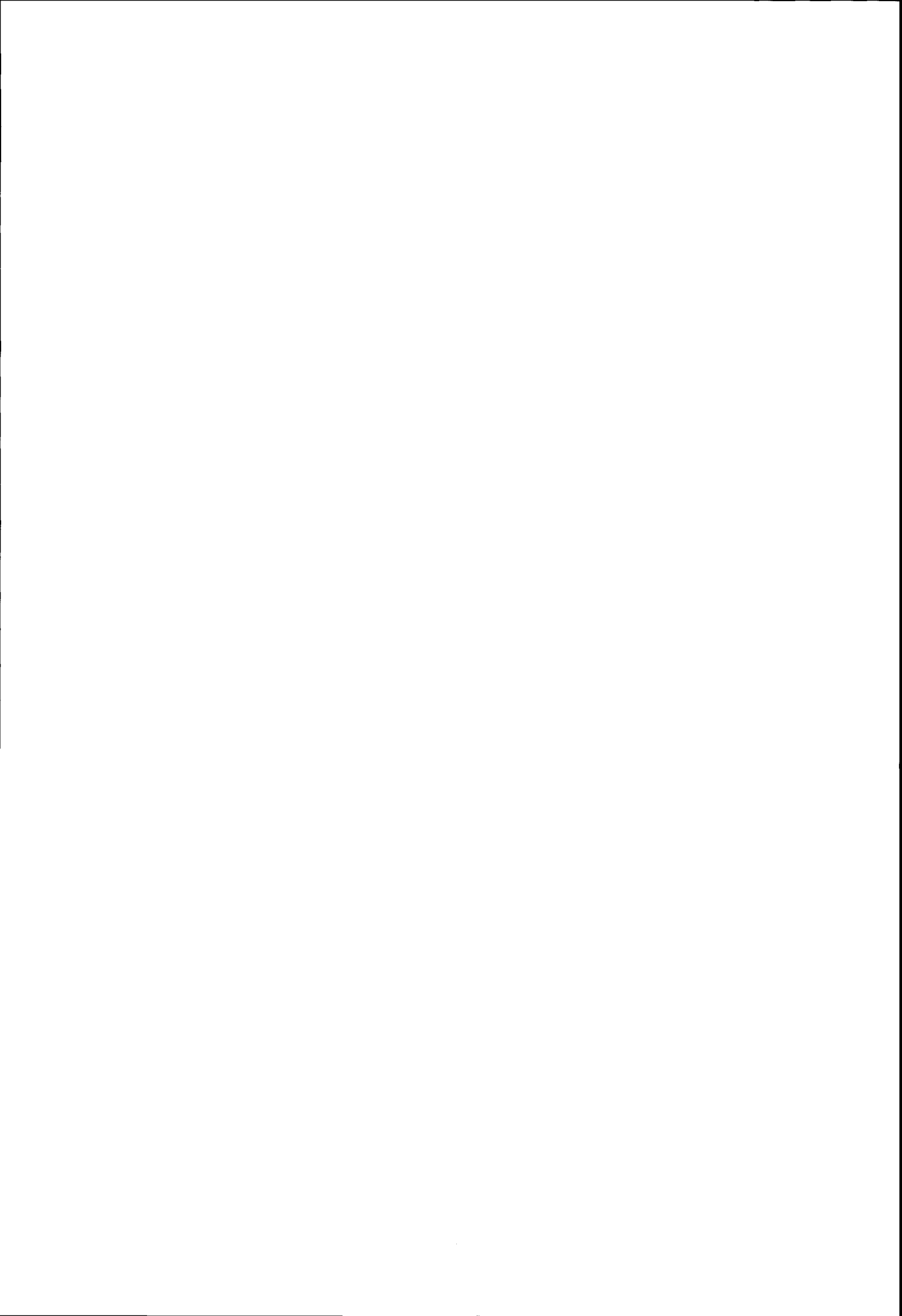
- [1] WL Cameron and LK Leung, "Feature-motivated Polarisation Scattering Matrix Decomposition". International Radar Conference. Proc. IEEE 1990.
- [2] WL Cameron and LK Leung, "Identification of Elemental Scatterer Responses in High-Resolution ISAR and SAR Signature Measurements". Secondes Journées Internationales de la Polarimétrie Radar, IRESTE. 1992, pp196-212.
- [3] PL Uslenghi, "Phenomenological Theory of Radar Targets", JR Huynen. Electromagnetic Scattering, New York: Academic. 1978.

#### Disclaimer:

Any views expressed are those of the authors and do not necessarily represent those of the department/HM government.

© British Crown Copyright 1999/DERA.

Published with the permission of the Controller of Her Britannic Majesty's Stationary Office.



## An Eigenvector Method for the Extraction of Surface Parameters in Polarimetric SAR

Shane R Cloude, Irena Hajnsek\*, & Konstantinos P Papathanassiou,

Applied Electromagnetics  
11 Bell Street, St Andrews, Fife, Scotland, KY16 9UR  
Tel/Fax : ++44 (0) 1334 477598/475570 e-mail :  
ael@fges.demon.co.uk

\*Deutsches Zentrum für Luft- und Raumfahrt  
Institut für Hochfrequenztechnik  
1116 Postfach, D-82230 Wessling, Germany  
Tel/Fax: ++49(0)815328 2305/1135 e-mail: irena.hajnsek@dlr.de

**ABSTRACT** - In this paper we introduce a new model for the inversion of surface roughness and moisture from polarimetric SAR data, based on the eigenvalues and eigenvectors of the coherency matrix. We demonstrate how three parameters, namely the polarimetric entropy, the anisotropy and the alpha angle can be used in order to decouple roughness from moisture content offering the possibility of a straightforward inversion of these parameters. We investigate the potential of the proposed model using fully polarimetric L-Band ESAR data (DLR) and ground truth measurements from the river Elbe test site.

### I. INTRODUCTION

One of the most important applications of scattering polarimetry is in quantitative surface roughness and moisture estimation. In the absence of any simple relationship between scalar reflectivity and surface parameters such as RMS height  $s$ , correlation length  $L$ , and complex permittivity  $\epsilon_r$ , several algorithms have been proposed based on multi-channel polarimetric data. Two main approaches have been employed in the literature based on empirical or semi-empirical relations: scattering amplitude ratio algorithms [1,2] and polarimetric coherence techniques [3,4]. As shown in [5,6] the relationship between surface roughness in scattering polarimetry and the eigenvalues of a coherency matrix have a physical significance in terms of scattering amplitudes and that their ratio represent generalised measures of polarimetric coherence.

A perfectly smooth surface has zero backscatter. However, considering the presence of slight roughness, particularly the case of  $ks \ll 1$  (Bragg scattering), the roughness can be seen as a perturbation of the smooth surface problem. In this case, we obtain the backscatter coefficients for a slightly rough surface using a small perturbation model from Maxwell's equations [3]. According to this model the backscatter from a surface is non-zero and depends on the component of the power

spectrum of the surface which matches the incident wavelength and angle of incidence (AOI). The scattering matrix for the surface has the form

$$[S] = \begin{bmatrix} R_s(\theta, \epsilon_r) & 0 \\ 0 & R_p(\theta, \epsilon_r) \end{bmatrix} \quad (1)$$

where the coefficients  $R_s$  and  $R_p$  are functions of the complex permittivity  $\epsilon_r$  and the local incident angle  $\theta$

$$R_s = \frac{\cos \theta - \sqrt{\epsilon_r - \sin^2 \theta}}{\cos \theta + \sqrt{\epsilon_r - \sin^2 \theta}} \quad (2)$$

$$R_p = \frac{(\epsilon_r - 1)(\sin^2 \theta - \epsilon_r(1 + \sin^2 \theta))}{(\epsilon_r \cos \theta + \sqrt{\epsilon_r - \sin^2 \theta})^2}$$

The scattering vector in its Pauli-basis representation becomes

$$\vec{k}_p = \begin{bmatrix} R_s + R_p \\ R_s - R_p \\ 0 \end{bmatrix} = m \begin{bmatrix} \cos \alpha * \exp i\phi_1 \\ \sin \alpha * \exp i\phi_2 \\ 0 \end{bmatrix} \quad (3)$$

where  $m$  denotes the absolute scattering amplitude. The corresponding coherency matrix results as

$$[T] = \left\langle \vec{k}_p \vec{k}_p^+ \right\rangle = \begin{bmatrix} \langle |R_s + R_p|^2 \rangle & \langle (R_s - R_p)(R_s + R_p)^* \rangle & 0 \\ \langle (R_s + R_p)(R_s - R_p)^* \rangle & \langle |R_s - R_p|^2 \rangle & 0 \\ 0 & 0 & 0 \end{bmatrix} \quad (4)$$

Note that the angle  $\alpha$ , as defined in Equation 3, is independent of roughness, and can be used to extract the dielectric constant if  $\theta$  is known.

The Bragg scattering model, as addressed in Equations 1-4, predicts zero cross-polarization and zero depolarisation. Real surfaces are characterised by non-zero cross-polarization backscattering as well as by depolarisation effects. However, real rough or smooth surfaces can always be represented in a generalisation of amplitude ratios in terms of their coherency matrix eigenvalue spectrum [7]

$$[T] = \begin{bmatrix} \lambda_1 & 0 & 0 \\ 0 & \lambda_2 & 0 \\ 0 & 0 & \lambda_3 \end{bmatrix} \quad \lambda_1 \geq \lambda_2 \geq \lambda_3 \quad (5)$$

By normalising the absolute scattering magnitudes we can interpret them as probabilities  $p_i$  such that

$$p_1 + p_2 + p_3 = 1 \Rightarrow p_i = \frac{\lambda_i}{\sum \lambda} \quad (6)$$

Equation 5 provides two parameters to describe the coherence properties of an arbitrary rough surface. One choice of such a pair may be the polarimetric Entropy  $H$  and Anisotropy  $A$  of the surface, defined as

$$H = -\sum_{i=1}^3 p_i \log_3 p_i \quad A = \frac{p_2 - p_3}{p_2 + p_3} \quad (7)$$

Both parameters varies between 0 and 1. For smooth surfaces,  $H$  becomes zero and increases with surface roughness. On the other hand,  $A$  can be zero even for rough surfaces, but  $A > 0$  generally indicates the presence of multiple scattering. In the limiting case of one-dimensional surfaces, where  $HV = 0$ ,  $A$  becomes 1. For azimuthally symmetric surfaces,  $A$  becomes by definition 0. Figure 1 shows the geometric representation of different rough surfaces in terms of their Entropy and Anisotropy values.

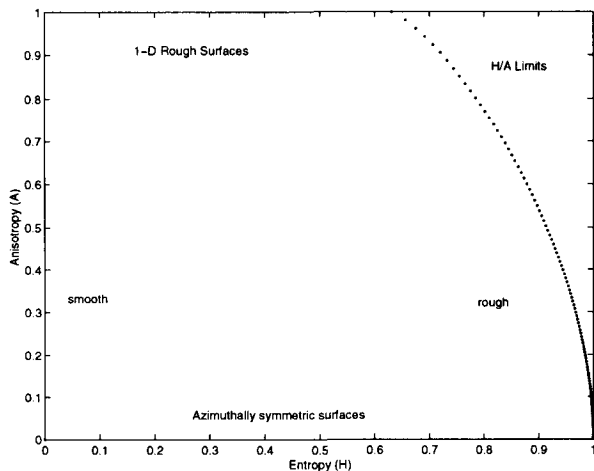


Figure 1 : Entropy/Anisotropy Plane Representation of Surface Scattering

## II. POLARIMETRIC SURFACE SCATTERING MODEL

In order to include a non-zero HV backscattering coefficient and depolarisation effects in the Bragg scattering model, we propose a configurational average of the above solution, to obtain a coherence less than one at the same time as generating cross polarized energy. The configurational averaging is taken over a uniform distribution about zero of the surface slope in the plane perpendicular to the scattering plane. If this slope is  $\beta$ , then we propose a uniform distribution of half-width  $\beta_1$  as shown in Figure 2

$$P(\beta) = \begin{cases} \frac{1}{2\beta_1} & |\beta| \leq \beta_1 \\ 0 & \text{otherwise} \end{cases} \quad (8)$$

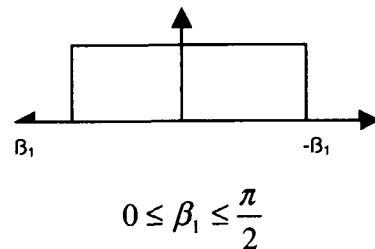


Figure 2 : Uniform Distribution of Surface Slope

Assuming now a non-coherent summation of energy across the distribution of  $\beta_i$ , then the coherency matrix for the surface becomes

$$[T] = \begin{bmatrix} A & B \text{sinc}(2\beta) & 0 \\ B^* \text{sinc}(2\beta) & C(1 + \text{sinc}(4\beta)) & 0 \\ 0 & 0 & C(1 - \text{sinc}(4\beta)) \end{bmatrix} \quad (9)$$

with  $\text{sinc}(x) = \sin(x)/x$ . The coefficients  $A$ ,  $B$  and  $C$  expressed in terms of the smooth surface solution are given by

$$\begin{aligned} A &= |R_s + R_p|^2 \\ B &= (R_s + R_p)(R_s^* - R_p^*) \\ C &= \frac{1}{2} |R_s - R_p|^2 \end{aligned} \quad (10)$$

According Equation 9 both the polarimetric coherence and the level of cross-polarized power is controlled by a single parameter ( $\beta_1$ ).

Figure 3 shows the variation of polarimetric coherence (dotted line) and normalised cross-polarized power (solid line). For  $\beta_1 = 0$  the HH-VV coherence is unity

and the HV power zero, as expected for the limiting case of a smooth surface, and the coherency matrix becomes the form of Equation 4. As  $\beta_1$  increases the HV power increases, while the coherence reduces monotonically from 1 for a smooth surface to zero for  $\beta_1 = 90$  degrees. In this second limiting case of high surface roughness the surface becomes azimuthally symmetric

$$[T] = \begin{bmatrix} \lambda_1 & 0 & 0 \\ 0 & \lambda_2 & 0 \\ 0 & 0 & \lambda_2 \end{bmatrix} \quad (11)$$

Note that the increase in HV power is faster than the fall off in coherence and so for small  $\beta_1$  the Anisotropy will be high (close to 1). As  $\beta_1$  increases so the anisotropy falls monotonically to zero.

Figure 4 shows how this fall in A occurs as a function of  $\beta_1$ . As shown in [6], A loses sensitivity to further increasing roughness above  $ks = 1$ . However, for  $ks < 1$  we can see an almost linear relation between A and  $ks$ . It is important to note that the value of A at any  $\beta_1$  is independent of the surface dielectric constant and of the AOI. The variation of A with dielectric constant is also shown to demonstrate the invariance of A to surface material. Similar studies show that A is also independent of the angle of incidence.

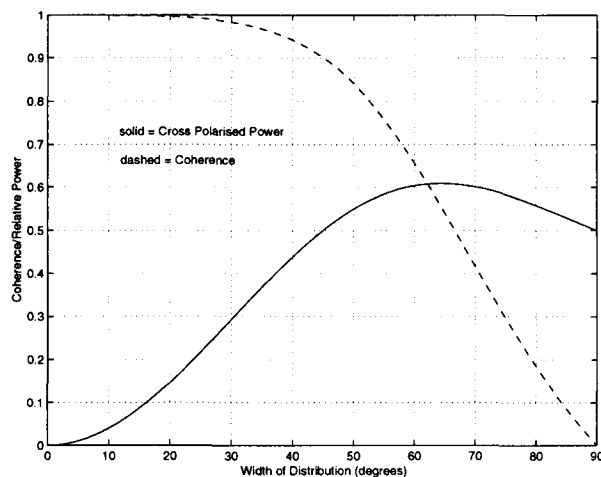


Figure 3 : Variation of Cross-Polarization and Depolarisation with model parameter  $\beta_1$

We can expose further structure in Equation 9 by plotting the Entropy/Alpha loci of points for dielectric constant  $\epsilon_r$  and half-width parameter  $\beta_1$  for fixed AOI  $\theta$ . Figure 5 shows the loci for 45 degrees AOI. The loci are best interpreted in a polar co-ordinate system centered on the origin. The radial co-ordinate is then the dielectric constant while the azimuthal angle represents changes in roughness. These loci provide an estimate of the surface dielectric constant, independent of surface

roughness. We do this by plotting the entropy/alpha value taken from a coherency matrix [T].

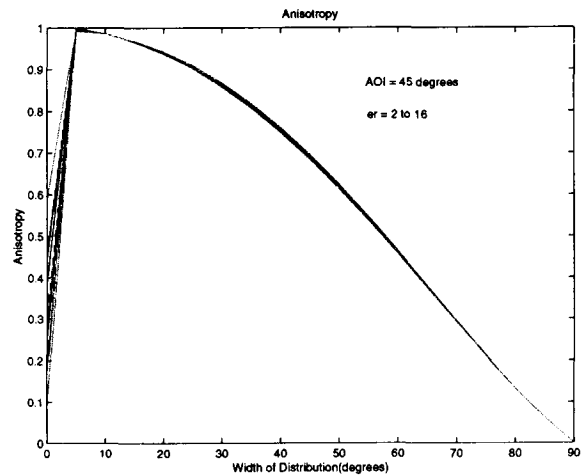


Figure 4 : Variation of Anisotropy with model parameter  $\beta_1$ .

In the limiting case of a smooth surface, this would be a zero entropy point and the alpha would correspond directly to a dielectric constant through Equation 3. However, as the entropy increases so the apparent mean alpha value reduces, causing error in the estimate of dielectric constant. By using Equation 9 we can compensate for this by tracking the loci of constant  $\epsilon_r$ , which reduces with increasing entropy. In this way both the entropy and alpha value are required in order to obtain a good estimate of the surface moisture.

Hence, by estimating three parameters, the entropy H, the anisotropy A and the alpha angle  $\alpha$ , we obtain a separation of roughness from surface dielectric constant. The roughness estimation comes from A and the dielectric constant estimation from combined H/ $\alpha$  values.

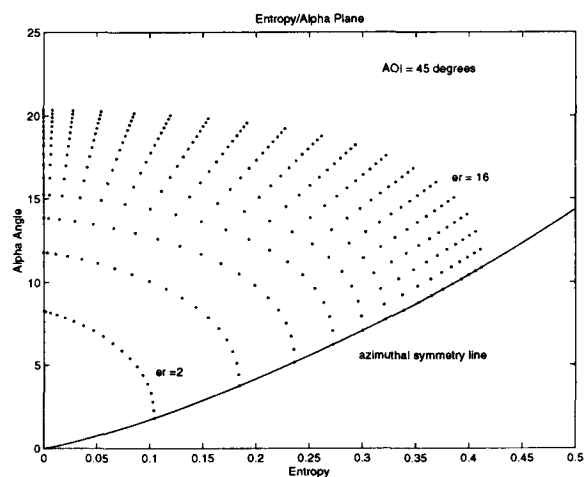


Figure 5 : Entropy/Alpha Diagram for 45 degrees AOI

### III. EXPERIMENTAL DATA ANALYSIS

For the validation of the proposed model fully polarimetric L-band data from the Elbe river test site in Germany, acquired by the experimental airborne E-SAR system of DLR in August 1997, are used. Figures 6 and 7 show the HV power image of the test site. During the data acquisition campaign, ground data have been collected over test fields with heterogeneous surfaces. Soil roughness was estimated with a needleboard in four directions: perpendicular and parallel to the ridges, and perpendicular and parallel to the flight direction. Soil moisture values were measured in depths of 0-4 cm and 4-8 cm using traditional gravimetric sampling and time domain reflectometry (TDR).

Because of the presence of vegetation, only four bare agricultural fields were available for validation. Nevertheless, as the four fields are located at different ranges (covering an incident angle range from 47 up to 52 degrees) with different roughness and moisture values (see Table 1) they are valuable for the validation of inversion results.

Field ID	$k_s$	$kl$	$\epsilon_r$ 0-4 cm	$\epsilon_r$ 4-8 cm
A5/10	0.549	1.841	10.79	9.28
A5/13	0.777	2.311	5.34	9.84
A5/14	0.795	3.203	4.51	10.82
A5/16	1.000	3.003	5.86	12.19

Tab. 1: Ground truth values for surface roughness, autocorrelation length and dielectric constant.

After SAR processing and polarimetric calibration, the scattering matrix data are transformed into a covariance matrix form and polarimetrically filtered [8]. Then the eigenvector decomposition is performed, followed by the computation of entropy, anisotropy, and alpha angle [7]. Figures 8,9,10 show the alpha-angle, the entropy and the anisotropy images of the test site respectively. Surface scattering is characterised by a strong dominant scattering mechanism, represented by the first eigenvalue. The amplitudes of the secondary scattering effects, expressed by the second and third eigenvalues, are in comparison very small and therefore, more affected by noise. Thus, in contrast to the entropy, the anisotropy is a more "noisy" parameter especially in low entropy areas as one can see in Figures 9 and 10, and its accurate estimation requires averaging over a large number of samples.

In a pre-selection step, areas where  $H > 0.45$  and  $\alpha > 45$  degrees have been masked out in order to select only surface scatterers. For the remaining areas the  $k_s$  values are evaluated directly from their anisotropy values. The result is shown in Figure 12. The correlation between the estimated and measured  $k_s$  values is shown in Figure

13. To reduce the estimation variation (mainly caused by the noisy character of A) the anisotropy A and the alpha angle  $\alpha$  have been estimated by averaging a minimum number of 1500 independent samples over each field. The high correlation of about 0.95, and the low RMS error of about 1.5 % underline the performance of the proposed method for roughness estimation.

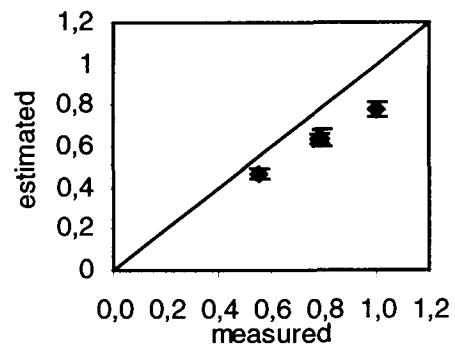


Figure 13: Estimated versus measured surface roughness values.

In a second step, the computed entropy and alpha images are used for the estimation of the dielectric constant. The estimation can be performed directly in terms of a lookup table which delivers the dielectric constant as a function of entropy/alpha values for each range line accounting in this way the variation of incident angle across the image. The resulting  $\epsilon_r$  map is shown in Figure 11. The correlation between the estimated and measured values for the four test fields is shown in Figure 14.

From Figure 14 results that the inverted  $\epsilon_r$  values correlate better with the  $\epsilon_r$  measurements in a depth of 4-8cm than with those measured in 0-4cm.

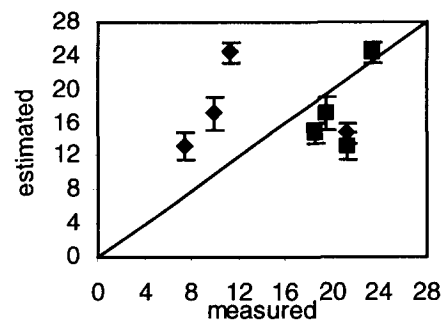


Figure 14: Estimated versus measured dielectric constant. The rhombuses indicate the 0-4 cm depth measurements while the quadrates the 4-8 cm depth measurements.

This is in accordance with the relatively low dielectric constant and the fact of using L-band data. The correlation is about 0.75, and the RMS error lies on the order of 5%. For converting dielectric constant to

volumetric moisture a polynomial relationship from [8] is used. After the polynomial conversion to volumetric moisture the results show the same trend with a correlation about 0.72 and a RMS error about 5% as shown in Figure 15.

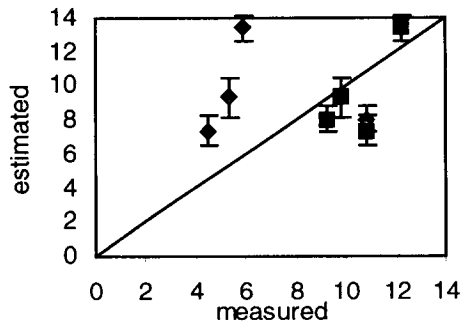


Figure 15: Estimated versus measured volumetric constant. The rhombuses indicate the 0-4 cm depth measurements while the quadrates the 4-8 cm depth measurements.

## V. DISCUSSION AND CONCLUSIONS

In this paper we have developed a new general parametric model which enables the quantitative estimation of roughness and dielectric constant for a wide range of natural bare surfaces up to  $ks = 1$  from polarimetric SAR data. The model assumes reflection symmetric surfaces, since by definition the surface normal imposes an orientation axis on the problem. It allows the HH and VV back-scattering coefficients to be different, and includes non-zero HV cross-polarized power as well as depolarisation. The application of the model to experimental data and the overall good agreement between the inverted values for  $ks$ ,  $\epsilon_r$  and  $\mu_v$  and the ground truth measurements prove that the structure of the data is in agreement with the predictions of the model over a large range of surface conditions.

The main advantage of the proposed inversion model lies in the separation of roughness and dielectric constant estimation which can be performed straightforwardly without the need for any data regression. Further, as the three key observables, the entropy the anisotropy and the alpha angle, are invariant under azimuth rotations the inversion becomes independent on azimuthal slope variations. This makes the application of the technique possible also for terrains with variable topography without the need of any additional topographic information.

Unknown is the influence of surface correlation length, as it is not appearing explicit in the model. Small correlation lengths lead to dihedral scattering effects which biases the alpha angle  $\alpha$  estimation increasing the  $Shh/Svv$  ratio. This bias can not be removed using the model alone. Fields characterised by eminently different correlation lengths in orthogonal directions, as for

example ploughed fields, violate the assumption of a rotation-symmetric roughness term and cannot be resolved by the model. The presence of vegetation cover on the one hand increases the entropy and decreases the anisotropy, leading to overestimation of the surface roughness, and on the other hand increases the alpha angle leading to underestimation of the dielectric constant.

Absolute calibration of the scattering matrix data is not strictly required. While for the  $ks$  estimation only cross-talk and relative channel calibration is sufficient, for the estimation of  $\epsilon_r$  copolar-phase calibration is essential. The high dependency of the  $\epsilon_r$  estimation on the alpha-angle values combined with the fact that any copolar-phase imbalance  $\Delta\phi$  affects directly the alpha-angle estimation ( $\Delta\alpha = \Delta\phi / 2$ ) forces the demand on very accurate phase calibration.

## VI. ACKNOWLEDGMENT

This work was performed in the frame of the EC-TMR and ONR-NICOP projects. The authors would like to thank J. S. Lee for filtering the polarimetric coherency matrix data.

## VII. REFERENCES

- [1] P. C. Dubois, J. J. van Zyl, T. Engman "Measuring Soil Moisture with Imaging Radars", IEEE Transactions on Geoscience and Remote Sensing, Vol.33, pp 916-926, 1995
- [2] Y. Oh, K. Sarabandi, F. T. Ulaby "An Empirical Model and an Inversion Technique for Radar Scattering from Bare Soil Surfaces", IEEE Transactions on Geoscience and Remote Sensing, Vol.30, pp 370-381, 1992
- [3] M. Borgeaud, J. Noll, "Analysis of Theoretical Surface Scattering Models for Polarimetric Microwave Remote Sensing of Bare Soils", International Journal of Remote Sensing, Vol 15, No. 14, pp 2931-2942, 1994
- [4] F. Mattia, T. Le Toan, J. C. Souyris, G. De Carolis, N. Floury, F. Posa, G. Pasquariello, "The effect of surface roughness on multi-frequency polarimetric SAR data", IEEE Trans GE-35, 1997, pp 954-965
- [5] S. R. Cloude and K.P. Papathanassiou, "Surface Roughness and Polarimetric Entropy", Proceedings IGARSS'99, pp. 2443-2445, Hamburg, 28 June - 2 July 1999.
- [6] S.R. Cloude "Eigenvalue Parameters for Surface Roughness Studies", Proceedings of SPIE Conference on Polarization: Measurement, Analysis and Remote Sensing II, Volume 3754, Denver, Colorado, USA, July 1999
- [7] S. R. Cloude, E. Pottier, "An Entropy Based Classification Scheme for Land Applications of Polarimetric SAR", IEEE Transactions on Geoscience and Remote Sensing], vol. 35, pp. 68-78, 1997.
- [8] J.S. Lee, M.R. Grunes, and G. De Grandi, "Polarimetric SAR Speckle Filtering and Its Impact on Classification", Proceedings IGARSS'98, pp. 1038-1040, Singapore, 3-8 August 1997.
- [9] G. C. Topp, J. L. Davis and A. P. Annan, "Electromagnetic Determination of Soil Water Content: Measurements in Coaxial Transmission Lines", Water Resources Research, vol. 16, no. 3, pp 574-582, 1980.

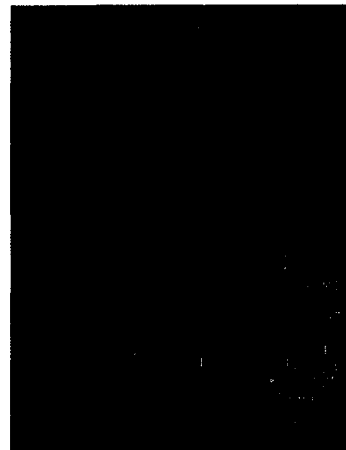
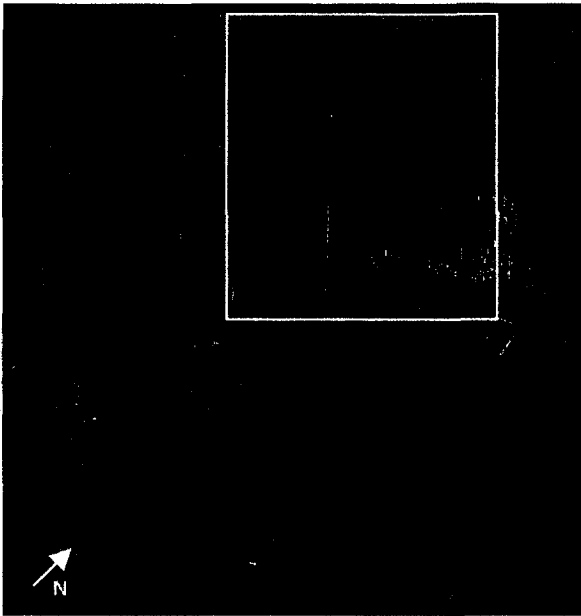


Figure 6: L band power image Elbe River 1997  
Figure 7: L band power image Elbe River part 1997

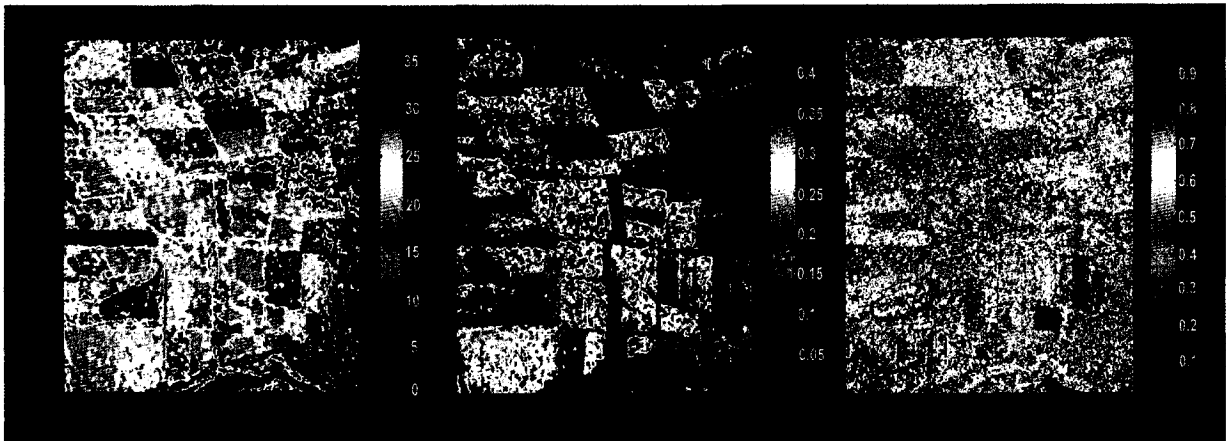


Figure 8: Alpha Angle  $\alpha < 43$  degree

Figure 9: Entropy  $H < 0.5$

Figure 10: Anisotropy  $A < 1$

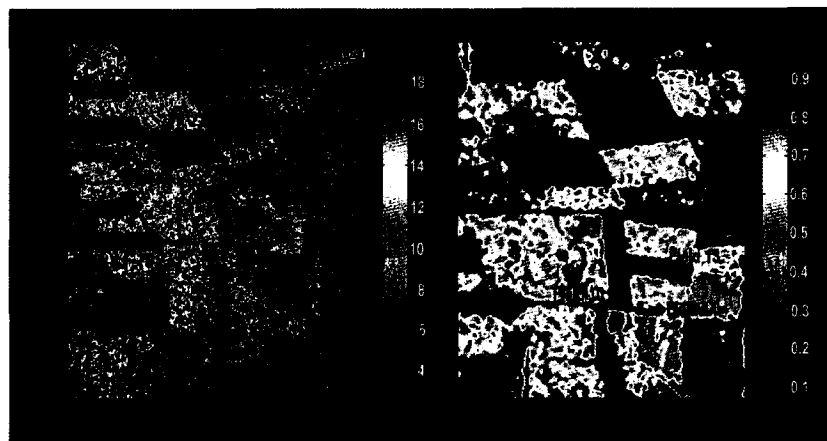


Figure 11: Dielectric constant  $\epsilon_r$

Figure 12: Surface roughness  $k_s$



## Polarimetric Calibration Results and Error Budget for SAR-580 System

RK Hawkins<sup>†</sup>, R Touzi<sup>†</sup>, A Wind<sup>†</sup>, K Murnaghan<sup>‡</sup>, and CE Livingstone<sup>¶</sup>

<sup>†</sup>Canada Centre for Remote Sensing, 588 Booth St, Ottawa, K1A 0Y7, Canada;  
Email: robert.hawkins@ccrs.nrcan.gc.ca, ridha.touzi@ccrs.nrcan.gc.ca, andrew.wind@ccrs.nrcan.gc.ca;

<sup>‡</sup>Isoceles Information Solutions, on contract to CCRS, Email: kevin.murnaghan@ccrs.nrcan.gc.ca;

<sup>¶</sup>Defense Research Establishment, Ottawa, 3701 Carling Ave, Ottawa, K1A 0K2, Canada;  
Email: Chuck.Livingstone@dreo.dnd.ca

### ABSTRACT

Polarimetric SAR capability was first demonstrated in the CCRS (Canada Centre for Remote Sensing) airborne SAR facility as an experimental X-band channel. Although this demonstration system had poor channel isolation, techniques were developed to show that under these conditions, it was possible to produce fully calibrated polarimetric data. That system was eventually abandoned in favour of a technically much improved C-band polarimeter. In November, 1996, the facility was transferred to Environment Canada who own and operate the facility. This paper reviews the technical implementation of the C-band polarimeter, the processing and calibration chain, and results from an extended period of stable operations. Calibration for this system involves use of external PARCs and trihedral corner reflectors deployed across the imaging swath. The paper also gives an error budget for the phase and amplitude calibration of the instrument.

### INTRODUCTION

The CCRS airborne SAR system [1,2] was transferred to Environment Canada in 1996 and is owned and operated by the Emergency Science Division there. CCRS and DND (Department of National Defense) continue to use and evaluate the facility and explore its use in a number of applications [3,4]. The system can collect SAR data in a number of modes including along-track and cross-track interferometry. This paper addresses only the polarimetric SAR mode at C-band.

The system can be configured in two slant range resolutions with flexible geometry. It was designed with range compression in hardware using analogue SAW/SAW<sup>-1</sup> devices followed by 6-bit ADCs. (This restricts the system's capability for point target measurements because of dynamic range limitations [5].) To cover the dynamic range across the swath due to the combination of range, antenna pattern, and target

backscatter, the system employs a sensitivity timing control (STC) that applies a range-dependent gain to the received signal train modelled to balance the expected falloff. Because STC also introduces accompanying phase rotations, this function is normally not used during polarimetric data collections.

Similarly, the SAR system has real-time motion compensation which performs three functions: dynamic antenna steering in azimuth and elevation to compensate for roll, pitch, and drift of the aircraft; PRF diversity to maintain the same ground sampling regardless of the ground speed; and phase rotation of the digitized signal to compensate for deviations from desired track. Due to inertial navigation system accuracy limitations, the phase rotation is normally not activated during polarimetric acquisitions in favour of post flight motion compensation.

To limit the calibration variables, we have recently adopted a 'standard' geometry that has good radiometric balance over a limited swath and is applicable to land targets using this mode. This is illustrated in Fig. 1.

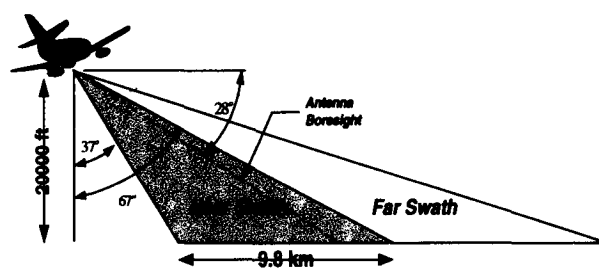


Fig. 1: Geometry for land applications with SAR

## AMPLITUDE CALIBRATION

The amplitude calibration follows the method based on internal and external calibration using trihedral corner reflectors and PARCs (Polarimetric Active Radar Calibrators) instituted at CCRS [6, 7] to establish the absolute calibration at a few discrete points within the swath. The calibration is then extended across the swath using the antenna pattern determined on an antenna range [8]. Extension to other data sets that do not have external calibration devices is achieved by reference to an internal calibration signal generated using the BITE facilities of the radar, and measurements of the inherent noise floor of the instrument. Figure 2 shows a typical data acquisition sequence. In the figure,  $DN_{tr}^2$ ,  $DN_n^2$ , and  $DN_n'^2$  are respective powers

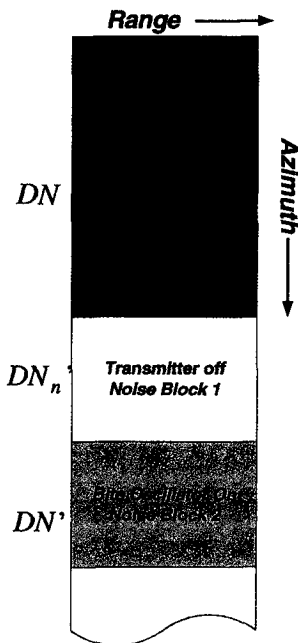


Fig. 2: Typical data acquisition sequence

of the processed scene and noise references before calibration. The basic radiometric calibration equation [7] used in the processing to radar brightness,  $\beta_{tr}^o$ , where  $tr$  indicates the transmit, receive polarization, is given by:

$$\beta_{tr}^o = \frac{DN_{tr}^2 - DN_n^2}{\langle DN^2 \rangle} \times \frac{v}{P_{av}} \times \frac{R^3}{G_{tr}(\vartheta)} \times \frac{g_{sys}}{g_{sys}} \times \frac{1}{K'_{tr}} \quad (1)$$

Here,  $\frac{v}{P_{av}}$  is the ratio of the ground speed to average radiated power;  $R$  is the range to the pixel;  $G_{tr}$  is the two-way antenna gain;  $\vartheta$  is the antenna departure angle

from boresight;  $\frac{g'_{sys}}{g_{sys}}$  is the ratio of the system gain

settings during the BITE acquisition to imagery acquisition; and  $K'_{tr}$  is the calibration constant dependent on polarization derived from point target measurements. Table 1 shows the results of a series of recent calibration measurements. The calibration constants here are the weighted mean of the individual targets, where the fading estimate is used as the weighting.

Table 1: List of amplitude calibration constants

Date	$K'_{HH}$	$K'_{HV}$	$K'_{VV}$	$K'_{VH}$
19-Jun-98	117.00	129.94	119.51	131.66
09-Jul-98	117.17	130.89	119.59	130.59
29-Jul-98	117.33	131.43	120.00	131.13
22-Oct-98	115.83	130.56	118.49	130.90
09-Mar-99	117.05	131.79	119.87	130.97
09-Mar-99	116.11	132.01	118.92	131.33
13-Apr-99	116.49	129.79	118.63	129.90
$\mu$	<b>116.71</b>	<b>130.92</b>	<b>119.29</b>	<b>130.93</b>
$\sigma$	<b>0.57</b>	<b>0.87</b>	<b>0.60</b>	<b>0.57</b>
$\sigma_\mu$	<b>0.22</b>	<b>0.33</b>	<b>0.23</b>	<b>0.21</b>

## PHASE CALIBRATION

Polarimetry was first tested at X-band in 1991 using a polarimetric switch with poor channel isolation. Investigation of the amplitude and phase calibration of this system led to a general formulation of the polarimetric calibration problem [9]. The methodology involves use of several trihedral reflectors and repeating, time delay PARCs in the image to be calibrated.

With the C-band polarimeter, the isolation between the channels is high as can be seen from Table 2, so that calibration of the later C-band polarimetric instrument could proceed with a much simpler method in which the channels could be considered independently with essentially no mixing [10].

The corner reflectors (CRs) provide results for the amplitude and phase of the like polarizations and the PARCs, deployed in a  $45^\circ \times 45^\circ$  orientation as shown in Fig. 4. This provides equal backscatter in all polarizations, and by comparison, allows determination of the cross-polarizations. Phase corrections relative to HH polarization determined in this way are then applied as a phase rotation to the complex data from the processor [11]. Table 3 shows recent results from this procedure.

Table 2: C-band polarimetric channel isolations

Property	$\frac{E_{HH}^2}{E_{HV}^2}$ (dB)	$\frac{E_{VV}^2}{E_{VH}^2}$ (dB)
Switch [12]	>50	>50
Antenna [13]	>37	>37
Total [14]	>35	>35

In these tables,  $\mu$  represents the weighted mean;  $\sigma$ , the standard deviation; and,  $\sigma_\mu$ , the standard deviation of the mean. These variations show that the calibration constants vary slightly from day to day, but are reasonably consistent. These difference may, however,

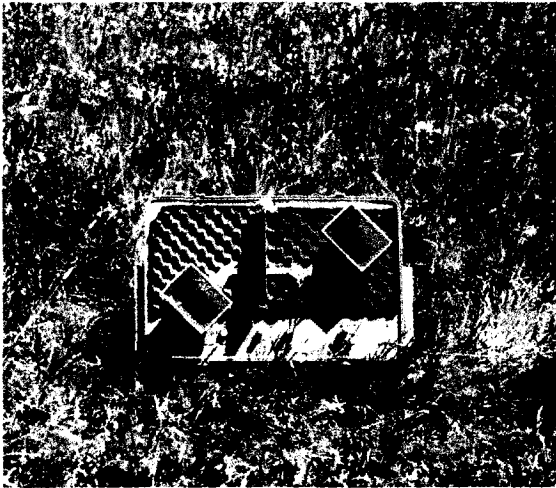


Fig. 3: PARC as deployed in a field situation

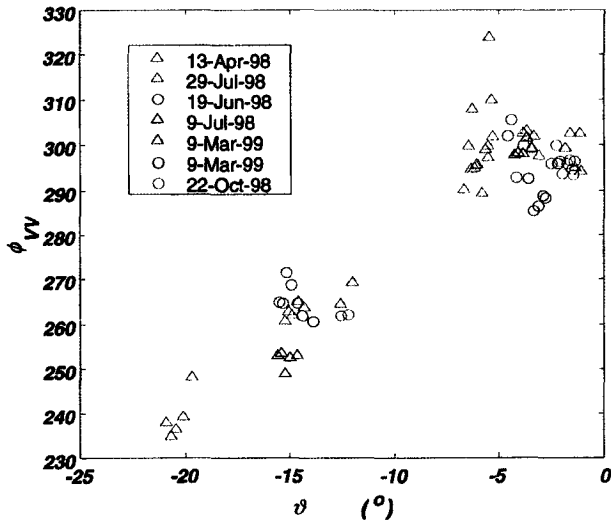


Fig. 4: Measured across track  $\phi_{VV}$  phase variation

be significant for some applications. Results from the cross polarization show more variation which may reflect the fact that fewer reflectors make up the mean for each day. In the case of parallel polarizations, approximately 20 reflectors may be used.

Table 3: Relative phase calibration constants

Date	$\phi_{HV}$ (deg)	$\phi_{VV}$ (deg)	$\phi_{VH}$ (deg)
19-Jun-98	102.63	287.65	85.78
09-Jul-98	90.04	286.87	82.38
29-Jul-98	94.60	296.43	87.23
22-Oct-98	110.95	297.69	98.13
09-Mar-99	106.91	288.32	84.35
09-Mar-99	97.32	302.10	89.02
13-Apr-99	103.53	290.45	93.15
$\mu$	100.85	292.79	88.58
$\sigma$	7.28	5.93	5.45
$\sigma_\mu$	2.75	2.24	2.06

The assessment of relative phase calibration across the swath has received less attention with this system since it was expected to be constant. Fig. 5 shows antenna angle dependence of the  $\phi_{VV}$  phase rotation. This variation shown near the peak of the pattern is modest, but away from the mainlobe, substantial correction is required. We do not know the cause of this effect but it appears to be antenna gain related, and cannot be due to phase centre displacements as the effect is too large. Figure 5 shows a simple model of the effect of phase centre displacements observed in other radars<sup>15</sup>. The trend measured above would require a 16 cm displacement. Clearly more systematic investigation is required.

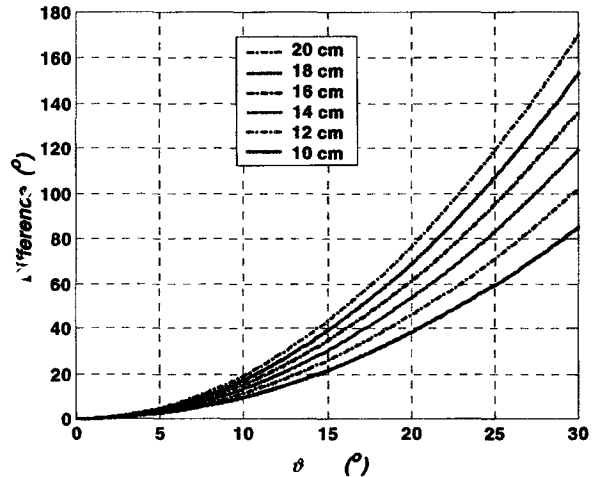


Fig. 5: Effect of phase centre displacement on  $\phi_{VV}$

## ERROR BUDGET

The error budget for the system can be assessed in a number of ways including, through the statistics of the individual calibration measurements. The methods employed at CCRS normally involve use of two calibration arrays in the Ottawa area for local flights, and a PARC/CR combination in at least one flight line of remote acquisitions. This means that, at best, the

overall calibration depends on the uncertainty in the associated calibration pass, our ability to extract and evaluate a set of  $\{K'_{PP}\}$  data, and the accuracy with which we can extrapolate this temporally (between passes) and spatially (across and along swath). This may depend on differences in configuration of the system and the flying conditions (altitude, aircraft attitude etc.).

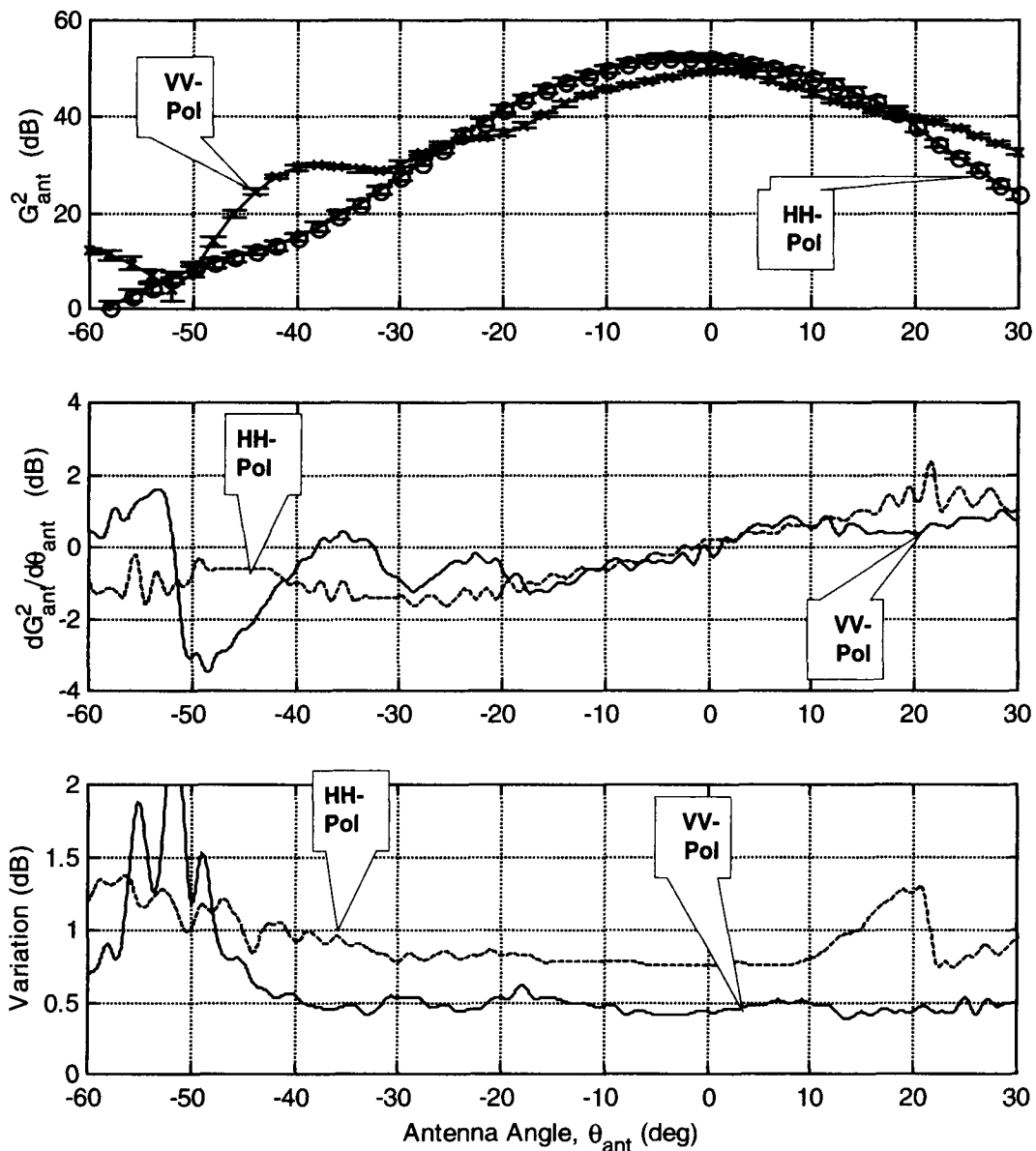


Fig. 6: Measured antenna gains for C-band SAR system. The error bars in the upper pane are shown as the variations at the bottom pane. The middle is the uncertainty in applied gain caused by a mask displacement of  $1^\circ$ .

## RADIOMETRIC ERROR BUDGET

Returning to (1) the two main contributing independent quantities come from the determination of the calibration constant  $K'$  itself and from  $G_{rr}^2(\vartheta)$ , the two-way antenna pattern. The other terms have small relative contributions.

$$\left(\frac{\Delta\beta^\circ}{\beta^\circ}\right)^2 = \left(\frac{\Delta K'}{K'}\right)^2 + \left(\frac{\Delta G_{rr}^2(\vartheta)}{G_{rr}^2(\vartheta)}\right)^2 + \dots \quad (2)$$

The determination of  $K'$  requires an inversion of the radar equation form of (1) for point targets and involves knowledge of all the associated terms including the application of  $G_{rr}^2(\vartheta_T)$  at the target, T, and its radar cross section. Let us assume that this uncertainty including background fading, and extraction error can all be determined from the relative spread in the measurements of the calibration constant,  $\frac{\Delta K'}{K'}$ .

Uncertainty in the antenna pattern,  $\frac{\Delta G_{rr}^2(\vartheta)}{G_{rr}^2(\vartheta)}$  comes in

two forms: the shape and size of the pattern; and the placement of the antenna mask over the illuminated swath. The antenna horn assembly is mounted in a radome beneath the aircraft near the tail on a three axis gimbal. The radiation path through the radome and the near field interaction of the antenna with the mounting faring and superstructure all depend on the aircraft attitude (pitch, roll, and yaw). As explained in [3], antenna range measurements were taken in the radome environment at various attitude configurations to assess these influences on  $G_{rr}^2$ ; these are plotted in Fig. 6.

Within  $\pm 20^\circ$  of the boresight, these are approximately constant in level at 0.7 dB for HH polarization and 0.5 dB for VV polarization.

We note that the dynamic range represented in an airborne image is especially high (50-60 dB) compared to typical spaceborne systems which cover much smaller angular ranges within their swaths. Placing this mask correctly over the resultant imagery requires accurate knowledge of the antenna pointing. Considerable effort [16] has been placed in matching the observed behaviour of CRs and distributed targets in the swath to determine the actual position of the antenna pattern relative to the readout and control information from the system. From this study, we believe that the mask can be placed within  $\pm 0.3^\circ$ . Returning to Fig. 5, this kind of uncertainty would lead to radiometric uncertainty which varies with angle to a maximum of 0.3 dB within  $\pm 20^\circ$  of the boresight.

Combining these ideas, we provide in Table 4 our estimates for the overall RMS errors expected from this system based on the calibration information derived from the data and presented above. Results from a particular line might be improved by site specific calibration. The results are over a region of  $\pm 20^\circ$  of the boresight of the antenna.

Table 4: Systematic error budget

Property	Unit	Within a Pass	Between Passes
$\frac{d}{d\vartheta} G_{rr}^2(\vartheta)\Delta\vartheta$	(dB)	0.70	0.70
$\Delta G_{rr}^2$	(dB)	0.30	0.30
$\Delta K'$	(dB)	0.30	0.70
Total	(dB)	<b>0.80</b>	<b>0.99</b>
$\Delta\phi$ within $\pm 10^\circ$ of peak	(deg)	3	10
$\Delta\phi$ beyond $\pm 10^\circ$ of peak	(deg)	30	30

## CONCLUSIONS

This paper has reviewed some recent polarimetric calibration results from the CV-580 C-band SAR. It shows the difficulty and importance of polarimetric calibration, even for a very well isolated system. This suggests that the engineering effort and procedures required for satellite systems need to be considered carefully.

## ACKNOWLEDGEMENTS

We thank the pilots and crew of the DOE CV-580 aircraft: Bryan Healey, Bill Chevrier, Reid Whetter, Doug Percy for their skills and efforts in making data acquisitions possible; Rob Gould, Rob Nelson and Paul Daleman for maintenance and support of this complex system. Ideas for processing and calibration with resultant operational code have been developed over an extended time by many individuals including: Paris Vachon, John Campbell, Laurence Gray, Tom Lukowski, Paul Daleman, John Wolfe, Mike Adair, Lana Ikkers (Teany), Ping Leung, Simon Methot, Gerrit Wessels, Peter Farris-Manning, Karim Mattar, Wendy Liu, Ian Neesan and Stephan Nedelcu to name only a few. Ronny Jean and Simon Austin assisted in

processing the data. It is a pleasure to acknowledge their contributions and accomplishments.

#### REFERENCES

- 1 Livingstone *et al.*, "The CCRS airborne SAR systems: Radar for remote sensing research," *Can. J. Rem. Sens.*, vol. 21, No. 4, 1995, pp. 468-491.
- 2 Minister of Supply and Services, Canada Centre for Remote Sensing Airborne C/X SAR, Cat. No M77-42/1994E, ISBN 0-662-22886-3, 1994.
- 3 Hawkins *et al.*, "Calibration and use of CV-580 airborne polarimetric SAR data," *Proc. 4<sup>th</sup> International Airborne Remote Sensing Conference and Exhibition/ 21<sup>st</sup> Canadian Symp. Rem. Sensing*, vol. 2, 1999, pp.32-40.
- 4 R Touzi, "On the use of polarimetric SAR data for ship detection," *IGARSS'99 Proceedings*, 1999, 4p.
- 5 RK Hawkins and PW Vachon, "C/X SAR Gain and Point Target Measurements – The Saturation Problem," CCRS internal documentation, CCRS-TN-1998-26, 1998, 10p.
- 6 LMH Ulander *et al.*, "Absolute Radiometric Calibration of the CCRS SAR," *IEEE Transactions on Geoscience and Remote Sensing*, November 1991, p. 922-933.
- 7 RK Hawkins and P Daleman, "Calibration Implementation for the CCRS Airborne SAR", DMD-TM-90-724, 1991, 100p.
- 8 SYK Tam *et al.*, "Calibration of the CCRS airborne SAR antenna –Final Report," SSC File No. 018SR.23413-8-4158, 1989, 151p.
- 9 R Touzi CE Livingstone, JRC Lafontaine, and TI Lukowski, "Consideration of antenna gain and phase patterns for calibration of polarimetric SAR data," *IEEE GSRS*, vol. 31, No. 6, 1993, pp. 1132-1145.
- 10 R Touzi and S Nedelcu, "Calibration of the polarimetric Convair-580 C-band SAR. Technical Report," CCRS/DREO agreement FY 97/98-98/99, Nov. 98, 20p.
- 11 A Wind, "Polarimetric calibration of the CCRS SAR data June 19 to July 29<sup>th</sup>, 1998," CCRS-TN-1999-010, 1999, 32p.
- 12 Acceptance testing done by COMDEV verified by DREO.
- 13 Notes from acceptance testing at COMDEV.
- 14 CE Livingstone, personal communication regarding 1993 field trials.
- 15 RJ Decker and A van den Broek, "Calibration of polarimetric Pharus data," CEOS SAR Workshop, ESA publication WPP-138, 1998, pp. 353-357.
- 16 RK Hawkins *et al.*, "C/X SAR, POLGASP, antenna pattern, and antenna pointing," CCRS internal technical note, CCRS-TN-1999-12, 1999, 12p.

## Radar polarimetry for vegetation observation

C. Titin-Schnaider  
ONERA-Palaiseau

Chemin de la Hunière, 91761 Palaiseau Cedex, France

Tel : 01 69 93 62 58 Fax : 01 69 93 62 69 Email : titin@onera.fr

### ABSTRACT

The purpose of this paper is to investigate the discriminating properties of the numerous polarimetric parameters and their potential to retrieve electromagnetic mechanisms. This discussion is based on two different approaches : a theoretical work and the knowledge acquired from the analysis of the database of full polarimetric SAR images provided by several RAMSES SAR airborne campaigns.

### INTRODUCTION

SAR images mainly contain two kinds of targets : single and distributed. On the one hand, single targets are generally man-made (like cars, trucks, buildings or landed aircraft...). The radar images of single targets are characterised by a reduced number of scattering centres. The waves returned by each scattering centre are quite completely polarised and add coherently. Each scattering centres is characterised by its scattering matrix. The deterministic theory of polarisation allows to identify the electromagnetic mechanisms which generate the main bright spots. On the other hand, distributed targets are generally extended areas (like crops, meadows, forests or urban areas...). In each resolution cell an indeterminate number of elementary mechanisms are adding in an incoherent way. The returned waves are therefore partially polarised. These area can only be characterised by second order statistical quantities. After averaging, these quantities can reveal some global properties.

Lots of parameters have been proposed in the open literature, in order to assist the analysis of polarimetric radar images. The objectives of this work are to introduce and discuss these numerous parameters, to demonstrate the links between some of them (especially between parameters belonging to different sets), to search and point out the parameters having genuine discriminating properties. This work has been conducted in two different ways : theoretical investigations and analysis on SAR full polarimetric images.

### THE VARIOUS SETS OF PARAMETERS

Nowadays, scientists can mainly use three sets of polarimetric parameters. These sets have been deduced from two second order statistical quantities: covariance and coherency matrices.

### General properties

These two matrices are built in the same way by averaging the direct product  $\langle \bar{S} \otimes \bar{S}^+ \rangle$  applied on the scattering vector  $\bar{S}$ .

Under the reciprocity assumption framework, the scattering vector has three components :

$$\bar{S} = (S_0, S_1, S_2)^t$$

and this kind of matrices can be written in the following form :

$$[M] = \begin{pmatrix} \langle S_0 S_0^* \rangle & \langle S_0 S_1^* \rangle & \langle S_0 S_2^* \rangle \\ \langle S_1 S_0^* \rangle & \langle S_1 S_1^* \rangle & \langle S_1 S_2^* \rangle \\ \langle S_2 S_0^* \rangle & \langle S_2 S_1^* \rangle & \langle S_2 S_2^* \rangle \end{pmatrix}$$

where  $\langle \rangle$  indicates an average. They depends on nine real parameters.

The difference comes exclusively from the base chosen to write the scattering vector. The h/v base :

$$\sigma_{hh} = \begin{pmatrix} 1 & 0 \\ 0 & 0 \end{pmatrix} \sigma_{hv} = \frac{1}{\sqrt{2}} \begin{pmatrix} 0 & 1 \\ 1 & 0 \end{pmatrix} \sigma_{vv} = \begin{pmatrix} 0 & 0 \\ 0 & 1 \end{pmatrix}$$

gives the scattering vector :

$$\bar{S} = (S_{hh} \quad \sqrt{2}S_{hv} \quad S_{vv})^t$$

and leads to the covariance matrix

The Pauli matrix base :

$$\sigma_0 = \frac{1}{\sqrt{2}} \begin{pmatrix} 1 & 0 \\ 0 & 1 \end{pmatrix} \sigma_1 = \frac{1}{\sqrt{2}} \begin{pmatrix} 1 & 0 \\ 0 & -1 \end{pmatrix} \sigma_2 = \frac{1}{\sqrt{2}} \begin{pmatrix} 0 & 1 \\ 1 & 0 \end{pmatrix}$$

gives the scattering vector :

$$\bar{S} = \frac{1}{\sqrt{2}} (S_{hh} + S_{vv} \quad S_{hh} - S_{vv} \quad 2S_{hv})^t$$

leading to the coherency matrix.

According to their mathematical way of building this kind of matrices have some specific properties :

-1) The Schwarz relationship :

$$\left| \langle S_a S_b^* \rangle \right|^2 \leq \langle S_a S_a^* \rangle \langle S_b S_b^* \rangle \quad a, b = \{0, 1, 2\} \quad a \neq b$$

applies on each off-diagonal terms giving three inequalities. In the deterministic case (any averaging is ineffective) the Schwarz relationships become equalities.

-2) Such matrices are hermitian and positive semi-definite. Therefore, firstly their eigenvalues  $\lambda_i (i = 1, 3)$  are real and

non-negative, and secondly the associated eigenvectors  $\vec{V}_i$  are orthogonal. This property leads merely to the Cloude decomposition [3] :

$$[M] = \sum_{i=1,3} p_i M_i \quad p_i = \lambda_i / \sum_{i=1,3} \lambda_i \quad \lambda_1 \geq \lambda_2 \geq \lambda_3 \geq 0$$

The original matrix  $[M]$  is decomposed into three orthogonal matrices :  $[M_i]$ . Each elementary matrix being built from a direct product applied on an eigenvector  $[M_i] = \vec{V}_i \otimes \vec{V}_i$  can only describe a deterministic mechanism (no average). By this way a non-deterministic mechanism can be decomposed into three deterministic mechanisms (weighted by the normalised eigenvalues  $p_i$ ).

It is necessary to be careful, when trying to give a physical meaning to this decomposition: the true elementary mechanisms may be neither orthogonal nor deterministic.

From the eigenvalues, two invariant parameters can be deduced: entropy and anisotropy.

The entropy:  $H = -\sum_{i=1,3} p_i \log_3 p_i$  is an indicator of the global state of the Schwarz inequalities. It quantifies the degree of randomness.

The anisotropy  $A = \frac{\lambda_2 - \lambda_3}{\lambda_2 + \lambda_3}$  must be used with caution especially in imaging: in quite deterministic cases (low value of H) the two smaller eigenvalues contains mainly measurement noise. In this case, very high values (without any physical meaning) of the anisotropy can be obtained.

*Covariance matrix*

The covariance matrix is often written in the form:

$$[C] = \sigma_{hH} \begin{pmatrix} 1 & \eta\sqrt{e} & \rho\sqrt{g} \\ \eta^*\sqrt{e} & e & \xi\sqrt{eg} \\ \rho^*\sqrt{g} & \xi^*\sqrt{eg} & g \end{pmatrix}$$

using the following parameters :

The hH RCS  $\sigma_{hH}$ , the copolarisation ratio  $g$ , the depolarisation ratio  $e$  :

$$g = \frac{\langle S_{vV} S_{vV}^* \rangle}{\langle S_{hH} S_{hH}^* \rangle} \quad e = \frac{2 \langle S_{hV} S_{hV}^* \rangle}{\langle S_{hH} S_{hH}^* \rangle}$$

and the three complex correlation coefficients between polarimetric channels :

$$\rho = Cor(hH, vV) \quad \eta = Cor(hH, hV) \quad \xi = Cor(vV, hV)$$

$$\text{with: } Cor(xY, aB) = \frac{\langle S_{xY} S_{aB}^* \rangle}{\sqrt{\langle S_{xY} S_{xY}^* \rangle \langle S_{aB} S_{aB}^* \rangle}}$$

The Schwarz inequality leads to the three inequalities:

$$|Cor(xY, aB)| \leq 1.$$

*Coherency matrix*

The coherency matrix is rather written using the parameters of the Mueller matrix :

$$[T] = \begin{pmatrix} 2A_0 & C - iD & H + iG \\ C + iD & B_0 + B & E + iF \\ H - iG & E - iF & B_0 - B \end{pmatrix}$$

The Schwarz inequality leads to the three inequalities :

$$2A_0(B_0 - B) \geq H^2 + G^2 \quad 2A_0(B_0 + B) \geq C^2 + D^2 \\ (B_0 + B)(B_0 - B) \geq E^2 + F^2$$

These parameters have the advantage of being all real and energy-like.

*Cloude-Pottier parameters*

The Cloude - Pottier [3] parameters are deduced from the Cloude decomposition theorem applied on the coherency matrix by writing each elementary eigenvector in the form :

$$\vec{V}_i = \left( \cos \alpha_i \quad \sin \alpha_i \cos \beta_i e^{j\delta_i} \quad \sin \alpha_i \sin \beta_i e^{j\gamma_i} \right)$$

It can be easily shown that the parameters  $\alpha$  and  $2A_0$  have a close meaning:  $2A_0 = (\cos \alpha)^2$  and that  $\beta$  is near the orientation angle  $2\psi$  of the Huynen theory. The representation  $\vec{\alpha} / H$  connecting physical and random properties illustrates the general principle: the more random is a mechanism and lesser it can be identified. The parameter  $\alpha$  allows a good separation between the three main kind of scattering which are nowadays of interest: surface, double-bounce and volume. For further works, it must be kept in mind that physical mechanisms depends in fact of the set of parameters:  $\alpha, \beta, \gamma, \delta$ . Therefore, a description of physical mechanisms restricted to the parameter  $\alpha$  can leads to some worrying ambiguities in the future, when the classification objectives will become more ambitious.

For instance, let us consider the scattering matrix depending on parameters  $x$  and  $\phi$  :

$$[S] = \frac{1}{\sqrt{1+x^2}} \begin{pmatrix} 1 & 0 \\ 0 & xe^{j\phi} \end{pmatrix}$$

It gives a parameter  $2A_0$  given by :

$$2A_0 = \frac{1}{2} \left( 1 + \frac{2x \cos \phi}{1+x^2} \right)$$

Therefore a given value of  $2A_0$  (or  $\alpha$ ) corresponds to an infinity of values of the pair  $(x, \phi)$  that is to say to an infinity of different scattering. In particular, a classification based only on this parameter cannot discriminate dihedrals from helices and dipoles from quater-wave dephasors ( $x=1, \phi = \pi / 2$ ) in the deterministic case.



*Links between two sets of parameters*

The parameters belonging to different sets are sometimes strongly related (the link between  $2A_0$  and  $\alpha$  have already been discussed). Interesting remarks can be deduced from the Mueller parameters written versus the covariance matrix parameters (in case of reflection symmetry for more simplicity).

Having put:  $\rho = Cor(hH, vV) = |\rho|e^{j\delta}$   
the following relations can be obtained:

$$2A_0 = \sigma_{hh} (1 + g + 2\sqrt{g}|\rho| \cos \delta)$$

$$B_0 + B = \sigma_{hh} (1 + g - 2\sqrt{g}|\rho| \cos \delta)$$

$$D = 2\sigma_{hh} \sqrt{g}|\rho| \sin \delta$$

$$C = \sigma_{hh} (1 - g)$$

$$B_0 - B = 2\sigma_{hh} e$$

It can be noticed that parameters  $2A_0, B_0 + B, D$  are all the more dependent on  $\delta$  as  $|\rho|$  is close to 1. Conversely, when  $|\rho|$  decreases down to zero, the range of variation of these parameters becomes more and more reduced. The classification diversity is strongly reduced. Therefore,  $|\rho|$  looks like a degree of order and  $\delta$  describes rather physical mechanisms (like the pair H,  $\alpha$ ).

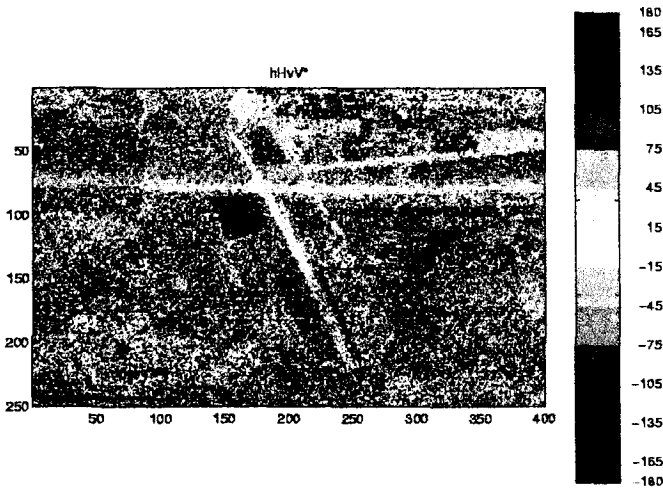


Fig. 1: Image of the phase of the correlation coefficient  $\delta = \arg(\rho)$

The image (Fig. 1) of the differential phase  $\delta = hh - vv$  (phase of the copolar correlation coefficient) highlight a dephasing near to  $\pi$  for a specific grassland (called 'dactyle'). Further investigations have shown that this important parameter is effective to discriminate mowed or not mowed grasslands.

Parameters C and D reveal an imbalance between the copolar components: C is connected to a magnitude

imbalance (its sign indicating the dominant polarisation hh or vv) and D reveals a phase imbalance. Parameter  $B_0 - B$  represents merely the crosspolar RCS.

SIGNIFICANT PARAMETERS IN SAR IMAGING

We have seen that a random media, can theoretically be described by nine parameters. The comparisons between mechanisms must be made without taking account of energy. Therefore, the span normalisation:

$$2A_0 + (B_0 + B) + (B_0 - B) = 1$$

must be applied at each pixel level.

In this part, we will try to investigate the number of truly useful parameters necessary to describe the random media in a SAR image.

Tree kind of mechanisms are mainly [2] met:

- 1) Volume scattering (vs) :

Volume scattering is known to give rise to a large cross polarised backscatter. This phenomena can be easily understood: the Mueller matrix parameters depending on the orientation angle  $\psi$ , become nulls after averaging on all directions. Therefore the coherency matrix of a cloud of randomly oriented elementary mechanisms is only characterised by the three remaining parameters:  $A_0, B_0, F$ . In practice F never appears, and the coherency matrix of a pure volume scattering is diagonal:

$$\langle [T]_{vs} \rangle = \begin{pmatrix} 2A_0 & 0 & 0 \\ 0 & B_0 & 0 \\ 0 & 0 & B_0 \end{pmatrix}$$

Furthermore, the unit span normalisation implies that:  $2A_0 + 2B_0 = 1$ . Therefore, in this case the coherency matrix depends only on a single parameter: the value of  $2A_0$ , for instance. From experimental data (in L-band), it can be observed that the model of randomly oriented dipoles applies very well to the volume scattering on vegetation (forest, in particular). The waves are scattered by branches and/or leaves (Fig.2) looking like a cloud of dipoles. According to that model:  $A_0 = B_0 = 1/4$ .

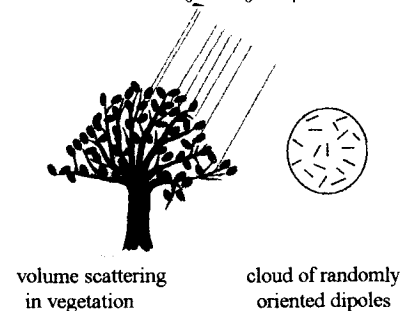


Fig. 2: Volume scattering in vegetation

In this case, it can be noticed that the volume scattering increases a lot the parameter  $B_0 - B = 2\sigma_{hv}$ , but never makes it dominating. It must be pointed out (Fig.3), that the area of volume interaction are clearly and merely localised on areas where the crosspolar magnitude  $hV$  is relatively high (forest, grown sunflower crops in June..).

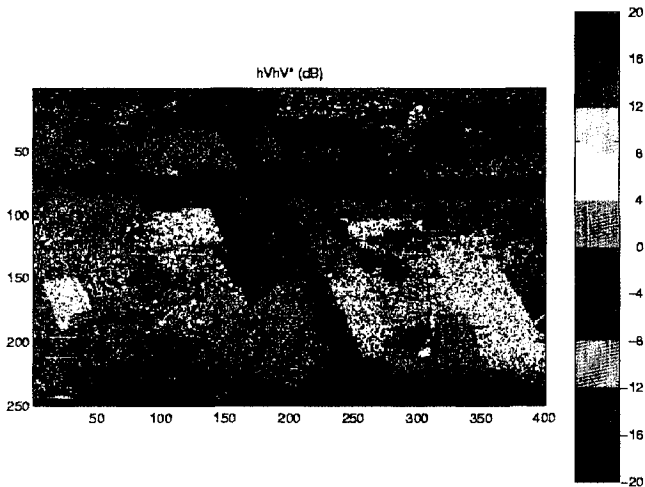


Fig. 3: Cross-polar RCS image (L-band)

Figure 4 shows that the main information given by entropy and  $hV$  images can be quite similar. Therefore a radar measuring only the crosspolar RCS can indicate in a satisfactory way, the vegetation volume scattering area.

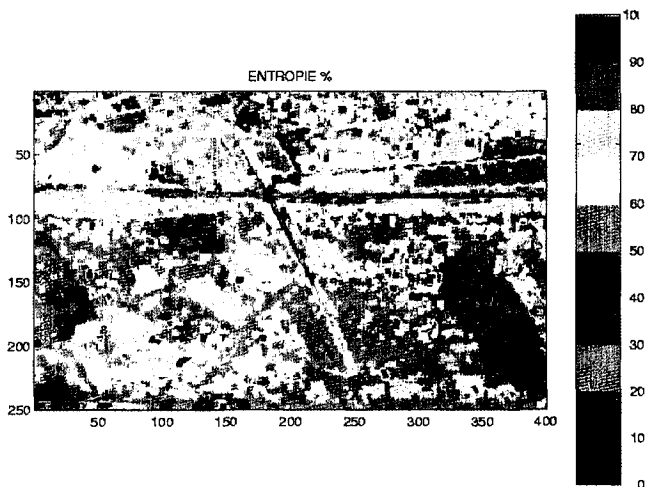


Fig. 4: Entropy image (L-band)

An imaging radar giving the crosspolar RCS can indicate well the vegetation volume scattering areas.

- 2) Surface scattering :

Another usual feature in SAR imaging is the surface scattering. The waves are reflected by an area behaving like a mirror. Few rays are returned to the radar (Fig.5) and the backscattered energy is very low (indicator). The waves

returned by most of the scattering centres add quite coherently. Therefore the returned signal is deterministic and its entropy is very low (indicator). A very low RCS is in many cases produced by a purely surface scattering. (low value of span and high value of  $2A_0$ ).

In practical cases, the coherency matrix of a surface scattering looks like to :

$$[T]_{ss} = \begin{pmatrix} |1+\beta|^2 & (1+\beta)(1-\beta^*) & 0 \\ (1+\beta^*)(1-\beta) & |1-\beta|^2 & 0 \\ 0 & 0 & 0 \end{pmatrix}$$

where  $\beta$  is not far from 1 .

The parameter  $2A_0$  is dominant but parameters C, D and  $B_0 + B$  can have significant values. In plain, the elementary surfaces are quite horizontal (roads, just sowed fields because they are compressed..). It is not true when the roughness RMS height is comparable or greater than the wavelength.

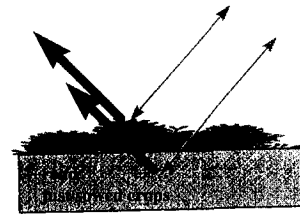


Fig. 5: Surface scattering

- 3) Double-bounce area :

The third usual feature in SAR imaging is double-bounce area. Looking at the drawing (Fig.6) representing the two main cases of double-bounce area : urban area and trunk (or stem) to ground interaction, it can be easily guessed that the orientation of the major part of the elementary dihedrals is quite horizontal. Therefore the double bounce area cannot be described by a cloud of randomly oriented dihedrals.

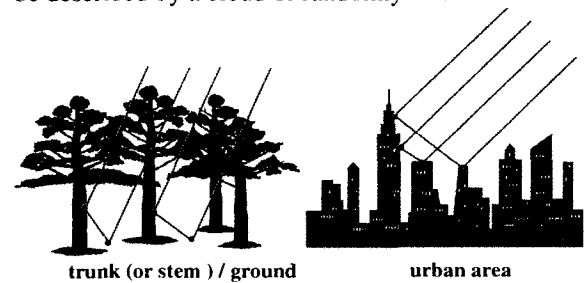


Fig. 6: Double-bounce scattering

The coherency matrix is :

$$[T]_{db} = \begin{pmatrix} |1-\beta|^2 & (1-\beta)(1+\beta^*) & 0 \\ (1+\beta)(1-\beta)^* & |1+\beta|^2 & 0 \\ 0 & 0 & 0 \end{pmatrix}$$

where  $\beta$  is a complex number not far from 1 .

The parameter  $B_0 + B$  is dominant but parameters  $C$ ,  $D$  and  $2A_0$  can have a significant value.

Urban areas also have large crosspolar contribution but not in the same way: their radar images show many strong bright spots on buildings generated by double bounce interactions (on average  $B_0 + B$  is quite large); the value of the parameter  $E$  is very often high proving that towns are typical areas where the reflection symmetry is not fulfilled.

It can be also noticed that in plain area, the variation coefficient which is sensible to the discontinuities (applied on the span, for instance) can also allow an easy discrimination of the location of man-made targets and in particular of urban areas.

The coherency matrix is often quite diagonal for vegetation area, but we have seen that non-diagonal parameters can have a significant value in some cases ( $E$  for town). Dielectric properties can be revealed by off-diagonal terms.

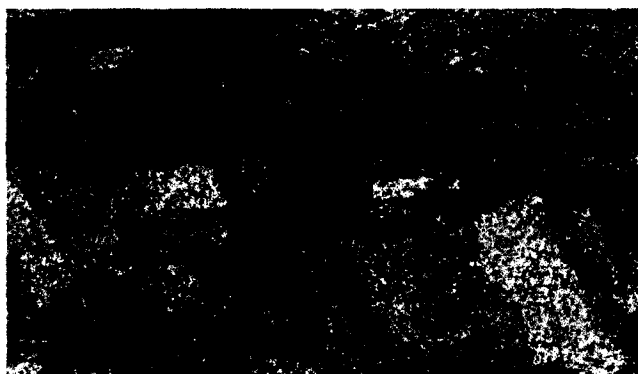


Fig. 7: RGB image of the three parameters  $B_0 + B$  (red),  $B_0 - B$  (green),  $2A_0$  (blue), after span normalisation.

In mountainous area, the elementary scatterer are rotated according the azimuthal slope of the terrain [4], and the coherency matrices cannot be diagonal.

The RGB imaging is generally made without extracting the overall energy. A better agreement with the polarisation theory is given by applying the span normalisation on each pixel. It gives images where physical mechanism can appear better. Figure 7 is an RGB mapping of the three diagonal terms of the coherency matrix. The span normalisation allows to show the area where each diagonal term is important. The drawback of this imaging are the area returning a very low energy. In this case, we must be careful because the analysis of pure noise might give sometimes a very coherent answer.

## CLASSIFICATION

In the framework of deterministic interactions (mainly man-made objects), the Huynen theoretical research [1] leads to extract from the nine Mueller parameters, the orientation angle and the desoriented Mueller parameters. These

interactions are theoretically described by 5 parameters. In [5] the interest for classification of this set after removing energy (span is normalised to the unity) is shown. On the other hand vegetation media have always some randomness and are described by the nine original Mueller parameters. In the preceding paragraph, it is shown that in practice the main interactions in plain area SAR imaging, have an horizontal mean orientation. In the two cases (deterministic or not) a few parameters have shown a real usefulness (high enough value above the noise, to be admitted as significant). But, one must remain cautious before excluding any parameter of the classification scheme under penalty of losing an important physical information. This is why, the images have been also analysed using another method: statistical analysis of homogeneous area.

The image of a parameter (unspecified) is displayed on the computer screen. Rectangular surfaces are drawn (in a way to select homogeneous area) interactively and a set of preselected polarimetric parameters are averaged and then stored for each area. In this way, tables giving for each vegetation a list of polarimetric parameters can be built.

Since a few years the French experimental airborne SAR radar RAMSES has been making full polarimetric measurements for several frequency bands (X,L,S...) and resolutions (ranging down to 0,5m). The results illustrating this paper were obtained from data acquired in L band on the ONERA test site in the south of Paris during two campaigns separated in time by 11 months: June 1997 and May 1998 in the framework of the RAMCAR campaign. We have a good ground truth thank to the information given by INRA (French establishment for agricultural research) who grows this area. This area contains a variety of targets: several urban area (U) and isolated buildings, several forests (F) of various surfaces, various kind of well controlled crops: great stem (S) crops (corn, sunflower), graminaceous (G) crops (wheat, barley, hybrid 'triticale'), small leaves (L) crops (flax, rape, peas), several kind of (M) meadow ('dactyle', 'fetuque') cut (10cm height) or not (30 cm height), and fallow lands.

The table 1 was obtained from the data acquired during the PRE-RAMCAR campaign. Fifteen kind of SAR surfaces are studied. They are sorted according to decreasing values of the parameter  $2A_0$ .

First of all, it is obvious that any classification method deduced from these data is premature, because the vegetation vary according to a number of parameters: state of growth, wetness degree, moment in the day ...

However, we can observe several things:

- 1) The off-diagonal terms of the coherency matrix show quite often significant values.
- 2) The coherency matrix is quite diagonal in two cases:
  - vegetation giving rise to a quite true volume scattering mechanism (eigenvalues close to the feature:  $\frac{1}{2} \frac{1}{4} \frac{1}{4}$ ): forest, sunflower, colza and flax. Very high entropy ( $>0.9$ )
  - runways giving a true surface scattering:  $2A_0$  dominant (0.9) and low entropy level ( $<0.5$ )

3) The parameters C and D are not negligible in several cases :

- the sign of C allow to separate the corn field according to the orientation of the furrows (parallel or perpendicular to the aircraft displacement defining the horizontal polarisation) ; It reveals a reversal of the imbalance between the level hh and vv.

- the parameter D is high for corn and 'fetuque' grass.

3) On the table 1, it can be observed that the diagonal terms of the coherency matrix cannot discriminate a specific grassland called 'dactyle' from urban area. The high value of parameter E (revealing that urban area have no reflection symmetry) must be used.

		Entro	$2A_0$	$B_0+B$	$B_0-B$	C	D	E
urban	U	0,9	0,32	0,52	0,16	0,14		-0,17
'dactyle' grass	M	0,8	0,32	0,57	0,11			
flax	L	0,9	0,42	0,32	0,26			
sun flower	S	0,95	0,46	0,30	0,24			
forest	F	0,95	0,47	0,28	0,25			
barley	G	0,80	0,48	0,40	0,12		-0,10	
'tritical'	G	0,85	0,52	0,28	0,20	0,15		
colza	L	0,9	0,55	0,25	0,20			
corn H	S	0,85	0,57	0,37	0,07	-0,13	0,20	
corn V	S	0,75	0,60	0,31	0,09	+0,15	0,27	
fetuque grass	M	0,8	0,60	0,30	0,10	0,10	0,20	
wheat	G	0,75	0,62	0,32	0,06	0,10		
peas	L	0,8	0,62	0,28	0,10			
fallow land	M	0,7	0,7	0,20	0,10			
not worked	M	0,4	0,90	0,10		-0,10	-0,10	
road	U	0,4	0,90	0,10				

Table 1 : Comb of Mueller parameters from pre-RAMCAR campaign for various kind of area

The span normalisation leads to the inequality ( equality in the deterministic case):

$$(2A_0)^2 + (B_0 + B)^2 + (B_0 - B)^2 + 2\{C^2 + D^2 + E^2 + F^2 + G^2 + H^2\} \geq 1$$

A learning memory filled with the reference Mueller parameters combs (normalised) describing all known interactions can be built. It can be updated and widened as the knowledge will improve. The combs can be easily compared between them using a correlation. In a general way, the classification algorithms will depend greatly on which targets have to be recognised, on the realism of the learning memory and consequently on the knowledge on electromagnetic interactions with targets and vegetation (dielectric, more or less dampness or dryness of surfaces ..)

## CONCLUSIONS

Classification algorithms using polarimetric parameters have to be matched to the targets of interest.

In this work many parameters are discussed with the aim of pointing out the true discriminating properties. It is shown that the off-diagonal terms of the coherency matrix can be significant . We have shown that the combs of Mueller parameters with a span normalisation:  $2A_0, B_0 + B, B_0 - B, C, D, E, F, G, H$  is a set well suited to a recognition software both for single and distributed targets. Although nondiagonal terms of the coherency matrix are often negligible, we have pointed out that in the current state of knowledge on electromagnetic mechanisms, one may be cautious under penalty of losing some significant information.

The general purpose of our investigations is to learn how to retrieve the electromagnetic mechanisms with vegetation and targets, from the polarimetric parameters which sometimes show very unexpected feature and behaviour. Further investigations will be needed, to be able to built a realistic reference memory of vegetation mechanisms. In many cases, a comparison with the results of theoretical model of vegetation will be fruitful to reach a better understanding.

## ACKNOWLEDGMENTS

The author wish to thank Mr Martineau from ONERA for his kind co-operation to the studies and Mr Galichet and Chevalier from INRA Bressonville for fruitful information on vegetation leading to a good ground truth.

## REFERENCES

- [1] J.R. Huynen, 'Phenomenological theory of radar targets', *Phd Thesis*, 1970.
- [2] A. Freeman, S. Durden, 'A three-component scattering model to describe polarimetric SAR data', *SPIE*, vol 1748, 1992
- [3] S.R. Cloude, E. Pottier, 'An entropy based classification scheme for land applications of polarimetric SAR', *IEEE Trans. Remote Sensing*, vol 35, n°1, jan 1997
- [4] D.L. Schuler, J.S. Lee, G. De Grandi, 'Measurement of topography using polarimetric SAR images', *IEEE Trans. Remote Sensing*, vol 34, n°5, jan 1996
- [5] C.Titin-Schnaider, 'Polarimetric analysis of RAMSES SAR images', *PIERS*, Nantes, July 1998.

## **List of Authors**



Achache J. ....	267	Closa J. ....	99, 317, 323
Adam N. ....	133	Cloude S. ....	347, 353, <b>693</b>
Adamovic M. ....	85, 531	Cochin C. ....	<b>563</b>
Adragna F. ....	167, 591, 663	Cookmartin G. ....	575
Aguttes J. ....	<b>263</b>	Corgier C. ....	5
Alessandrini B. ....	563	Crapolicchio R. ....	99
Angleraud C. ....	671	Crosetto M. ....	<b>367</b>
Arnaud A. ....	663	Crossley S. ....	575
Attema E. ....	99	Cumming I. ....	<b>159</b>
Bachelier E. ....	569	Davidson G. ....	545
Baghdadi N. ....	267	Davidson M. ....	467, 569
Bally P. ....	119, <b>671</b>	de Beaucoudrey N. ....	<b>631</b>
Balzter H. ....	509	De Carolis G. ....	467
Bamler R. ....	133	Dedieu J.P. ....	5
Banik B. ....	85, <b>531</b>	Defourny P. ....	443
Barba D. ....	631	Delhommeau G. ....	563
Baret F. ....	485	Desnos Y.-L. ....	59, <b>317, 323</b>
Barlaud M. ....	651	Dragoševi M. ....	<b>127, 545</b>
Baüer P. ....	645	Dreuillet P. ....	267
Beal R. ....	53	Droulers M. ....	487
Belgued Y. ....	<b>167</b>	Dubois P. ....	267
Bennett J. ....	575	Ducrot D. ....	455
Benz U. ....	203	Duesmann B. ....	323
Berges A. ....	587	Dufrêne E. ....	25
Bianchin A. ....	<b>497</b>	Dupuis X. ....	<b>651</b>
Blaes X. ....	<b>443</b>	 	
Blamont D. ....	503	Eineder M. ....	133, 657
Boerner W.-M. ....	<b>379</b>	Engen G. ....	59, <b>109</b>
Borderies P. ....	25, 551, 569	Espedal H. ....	71
Borgeaud M. ....	467, 569	Esteban Fernández D. ....	79, <b>597</b>
Braumann H. ....	241	 	
Breit H. ....	39, <b>133</b>	Farr T. ....	<b>361</b>
Brisson N. ....	485	Feigl K. ....	663
Brown M. ....	<b>183</b>	Fellah K. ....	455
Brown S. ....	575	Ferriti F. ....	<b>15</b>
Bruniquel J. ....	<b>455</b>	Ferro-Famil L. ....	<b>5</b>
Buck C. ....	183, 303, 323, <b>473</b>	Fischer J. ....	<b>203</b>
Burbidge G. ....	<b>293</b>	Foucher S. ....	213
 		Friedman K. ....	53
Cantalloube H. ....	<b>153, 581, 635</b>	Fröлинд P. ....	273
Carnec C. ....	113	Fruneau B. ....	437, <b>679</b>
Cathala T. ....	587	Furevik B. ....	71
Cavayas F. ....	479	 	
Caves R. ....	<b>449</b>	Gaillard C. ....	213
Cazuguel G. ....	199	Garello R. ....	173
Chakraborty M. ....	<b>31</b>	Gaveau D. ....	<b>509</b>
Chapron B. ....	59	Germain O. ....	<b>613</b>
Chauki H. ....	<b>485</b>	Geudtner D. ....	375
Chênerie I. ....	25, 551	Girard R. ....	245
Chust G. ....	455	Gobert S. ....	<b>119</b>
Classeau N. ....	<b>433, 437</b>	Goze S. ....	455
Clemente-Colón P. ....	53	Grandjean G. ....	<b>267</b>

- Gray R. .... 85  
 Guérif M. .... 485  
 Guijarro J. .... 303  
 Guillopé P. .... 433  
 Guneriussen T. .... 11  
  
 Hajji H. .... **513**  
 Hajnsek I. .... 693  
 Harris N. .... 687  
 Hawkins R. .... 85, **99**, 159, 519, 531, **539**, **699**  
 Henrion S. .... 141  
 Hensley S. .... 361  
 Herique A. .... **287**, **645**  
 Hervet E. .... 167  
 Høgda K.-A. .... 59  
 Holt B. .... 65  
 Horstmann J. .... **45**  
 Hubig M. .... 657  
  
 Imbo P. .... **341**, 663  
 Isoguchi O. .... 147  
  
 Jackson H. .... **311**  
 Jeanne I. .... 433  
 Jefferies W. .... 85  
 Johannessen O. .... **71**  
 Johnsen H. .... 11, **59**, 109  
  
 Knöpfle W. .... 657  
 Kobayashi T. .... 95  
 Kobrick M. .... 361  
 Koch W. .... 45  
 Kofman W. .... 645  
 Kwok R. .... **65**  
  
 Landeau T. .... 563  
 Landry P.-P. .... **245**  
 Lapierre L. .... 263  
 Latger J. .... 587  
 Lauknes I. .... 11  
 Laur H. .... 119, 317, 323, 455  
 Le Toan T. .... 467, 569  
 Le Tourneau F.-M. .... **487**  
 Lecomte P. .... 99  
 LeDantec V. .... 25  
 Lee J. .... 335  
 Lehner S. .... 39, 45  
 Lemaréchal C. .... 167  
 Li X. .... **53**  
 Lin C. .... **287**, **461**  
 Livingstone C. .... 699  
 Lopes A. .... 25, 341  
 Lukowski T. .... 85  
  
 Luscombe A. .... **89**  
  
 Maitre H. .... 497  
 Mametsa H. .... **587**  
 Mancini P. .... 79, 597  
 Marchionni D. .... **479**  
 Marthon P. .... 167, 341  
 Martin J. .... 361  
 Martin T. .... 273  
 Massonnet D. .... **251**  
 Mathew C. .... 293  
 Matsuoka T. .... 95  
 Matthieu P. .... 651  
 Mattia F. .... 467, **569**  
 Mavrocordatos C. .... 235  
 McDonald M. .... **575**  
 Meadows J. .... 99  
 Meadows P. .... **79**, **525**, 597, **607**  
 Meisl P. .... 317  
 Mercier G. .... **199**  
 Merlin L. .... **503**  
 Miyagawa H. .... 147  
 Moal C. .... 625  
 Monaldo F. .... 53  
 Monni S. .... 473  
 Morin X. .... 631  
 Morrison K. .... 575  
 Mouchot M.-C. .... 199  
 Mougín E. .... 25, 551  
 Murnaghan K. .... 85, 531, 699  
 Mvogo J. .... 199  
  
 Nadai A. .... 95  
 Nagler T. .... 449  
 Nahum C. .... 635  
 Narasimha Rao Ch. .... 235  
 Nezry E. .... **219**  
 Nicolas J.-M. .... 497, 503  
  
 Oddou M. .... **641**  
 Oliosio A. .... 485  
 Oriot H. .... 173  
  
 Paillou P. .... 267  
 Panigrahy S. .... 31  
 Papatthanassiou K. .... **347**, **353**, 693  
 Parihar J. .... 31  
 Pasquariello C. .... 467  
 Péraudeau S. .... 455  
 Pérez Aragues F. .... 367  
 Peskova S. .... **619**  
 Petit D. .... **591**, 663  
 Petz F. .... **235**



Phalippou L. ....	279, 287, 645	Suchandt S. ....	133
Pichel W. ....	53	Suess M. ....	557
Planès J.-G. ....	141, 625	Tadono T. ....	147
Plummer S. ....	509	Tam S. ....	311
Pottier E. ....	5, 335	Tannous I. ....	119
Pourthié N. ....	663	Taylor V. ....	147
Prati C. ....	15	Titin-Schnaider C. ....	705
Prévoit L. ....	485	Tonboe R. ....	45
Proisy C. ....	25, 551	Torres R. ....	303, 323
Quegan S. ....	449, 575	Touzi R. ....	225, 699
Ramamonjarisoa A. ....	513	Trebossen H. ....	433, 437
Ramongassie S. ....	287	Troufleau D. ....	485
Raucoules D. ....	113	Tupin F. ....	497
Réfrégier P. ....	613	Ulander L. ....	273
Reigber A. ....	347, 353	Umehara T. ....	95
Remy F. ....	645	Uratsuka S. ....	95
Ringrose R. ....	687	Vachon P. ....	519
Rocca F. ....	15	Verdi J. ....	379
Rodríguez E. ....	361	Vnotchenko S. ....	619
Rognant L. ....	167, 455	Wackerman C. ....	53
Rolleri E. ....	479	Wakabayashi H. ....	95, 147
Rosello-Guasch J. ....	235	Wegmüller U. ....	19
Rosengren M. ....	663	Wiesmann A. ....	19
Rosich B. ....	663	Wind A. ....	699
Rudant J.-P. ....	199, 433, 437, 487	Wingham D. ....	279
Ruiz C. ....	25, 551	Wismann V. ....	461
Saillard J. ....	5	Wolfe J. ....	519
Sandven S. ....	71	Wong F. ....	159
Sarti F. ....	25, 663, 679	Wright P. ....	607
Sassier H. ....	455	Yakam-Simen F. ....	219
Satake M. ....	95	Zagolski F. ....	213
Satalino G. ....	467	Zahn R. ....	241, 557
Savy L. ....	141, 625	Zink M. ....	375
Schaefer C. ....	557		
Schättler B. ....	39, 597, 657		
Schirinzi G. ....	193		
Schönenberg A. ....	303		
Schulz-Stellenfleth J. ....	39, 45		
Séguin G. ....	245		
Seren T. ....	631		
Shimada M. ....	95, 147		
Simonetto E. ....	173		
Simpson D. ....	293		
Sinclair I. ....	311		
Sole S. ....	513		
Somer Y. ....	671		
Souyris J. ....	267, 341		
Srivastava S. ....	85, 99, 531, 539		
Strozzi T. ....	19		
Suchail J.-L. ....	303, 323		



## **List of Participants**



<b>Frédéric Adragna</b>	CNES Radar Systems France	Frederic.Adragna@cnes.fr
<b>J.P. Aguttes</b>	CNES France	jean-paul.aguttes@cnes.fr
<b>Eve Antikidis</b>	France	eve.antikidis@free.fr
<b>Evert Attema</b>	ESA-ESTEC Earth Sciences Division The Netherlands	eattema@estec.esa.nl
<b>B. Badreddine</b>	DGA France	badri@ctme.etca.fr
<b>Philippe Bally</b>	SPOT IMAGE 31000 - France	philippe.bally@spotimage.fr
<b>Yifang Ban</b>	Stockholm University Remote Sensing Laboratory Department of Physical Geography Sweden	yifang@natgeo.su.se
<b>André Beaudoin</b>	Defence Research Establishment Aerospace Radar and Navigation Canada	riviere.beaudoin@dreo.dnd.ca
<b>Youssef Belgued</b>	Alcatel Space Industries IS France	Youssef.Belgued@space.alcatel.fr
<b>Xavier Blaes</b>	Université Catholique de Louvain Belgium	blaes@biom.ucl.ac.be
<b>Wolfgang-Martin Boerner</b>	University of Illinois EECS, Communications Sensing and Navigation Laboratory USA	wolfgang.m.boerner@uic.edu
<b>Pierre Borderies</b>	ONERA DEMR France	pierre.borderies@oncert.fr
<b>Maurice Borgeaud</b>	ESA-ESTEC Electromagnetics Division The Netherlands	maurice@xe.estec.esa.nl
<b>Helko Breit</b>	DLR Deutsches Fernerkundungsdatenzentrum (DFD) Germany	Helko.Breit@dlr.de
<b>Mike Brown</b>	Marconi Research Centre UK	mike.a.brown@gecm.com
<b>R. Bru</b>	Noveltis France	
<b>Jérôme Bruniquel</b>	Alcatel Space Industries Radar Image Quality France	Jerome.Bruniquel@space.alcatel.fr
<b>C.H. Buck</b>	ESA-ESTEC TOS-ETP The Netherlands	cbuck@estec.esa.nl

<b>Frédéric Cazaban</b>	Alcatel Space Industries Radar Image Quality Group France	Frederic.Cazaban@space.alcatel.fr
<b>R.K. Champati ray</b>	Indian Institute of Remote Sensing India	champati_ray@hotmail.com
<b>Elaine Chapin</b>	Jet Propulsion Laboratory Radar Science and Engineering Section USA	Elaine.Chapin@jpl.nasa.gov
<b>B. Chapron</b>	IFREMER France	
<b>Habiba Chauki</b>	INRA BIOCLIMATOLOGIE France	habiba@avignon.inra.fr
<b>Josep Closa</b>	ESRIN / Serco APP-APM Frascati Italy	Josep.Closa@esrin.esa.it
<b>Michele Crosetto</b>	Politecnico di Milano DIAR - Sez. Rilevamento Italy	miche@ipmtf4.topo.polimi.it
<b>Bruno Cugny</b>	CNES DTS/AE/INS/IR France	bruno.cugny@cnes.fr
<b>Ian Cumming</b>	DLR - DFD Germany	Ian.Cumming@dlr.de
<b>Valeria D'Acunti</b>	Parco Scientifico e Tecnologico di Salerno Italy	pstsa@xcom.it
<b>Malcolm Davidson</b>	CESBIO France	davidson@cesbio.cnes.fr
<b>Nicole De Beaucoudrey</b>	IRESTE Laboratoire SEI, EP CNRS 2018 France	ndebeauc@ireste.fr
<b>Louis Demargne</b>	SPOT IMAGE France	Louis.Demargne@Spotimage.fr
<b>Didier Dendal</b>	CESBIO France	dendal@cesbio.cnes.fr
<b>Leonard Denise</b>	Alcatel Space Industries IS/ISR France	Leonard.Denise@Space.Alcatel.fr
<b>Marc Deschaux</b>	Alcatel Space Industries France	Marc.Deschaux-Beaume@space.alcatel.fr
<b>Yves-Louis Desnos</b>	ESA-ESRIN Envisat User Support Section Italy	ydesnos@esrin.esa.it
<b>Marina Dragosevic</b>	Satlantic Inc. Info Systems Canada	marina@satlantic.com

<b>Philippe Dreuillet</b>	ONERA France	dreuil@onera.fr
<b>Pascale Dubois-Fernandez</b>	DGA France	Pascale@ctme.etca.fr
<b>Guy Duchossois</b>	ESA/HQ France	gduchoss@hq.esa.fr
<b>Philippe Durand</b>	CNES DSO/OT/QTIS/SR France	philippe.durand@cnes.fr
<b>Gonnie Elfering</b>	ESA-ESTEC The Netherlands	aelferin@estec.esa.nl
<b>Geir Engen</b>	Norut IT AS Forskningsparken i Tromsø Norway	geir.engen@itek.norut.no
<b>Daniel Esteban Fernandez</b>	GAEL Consultant Italy	desteban@esrin.esa.it
<b>Diane Evans</b>	Jet Propulsion Laboratory Earth Science Office USA	Diane.L.Evans@jpl.nasa.gov
<b>Tom Farr</b>	Jet Propulsion Laboratory Earth and Space Sciences USA	tom.farr@jpl.nasa.gov
<b>Kader Fella</b>	SERTIT France	kader@sertit.u-strasbg.fr
<b>Jean-Louis Fellous</b>	CNES DP/OT France	jean-louis.fellous@cnes.fr
<b>Lara Ferrigno</b>	Università 'degli studi di Salerno Ingegneria Elettronica Italy	lara@cesare.diiie.unisa.it
<b>Ferro-Famil</b>	SEI/IRESTE France	Lanvento.Ferro-Famil@ireste.fr
<b>Jens V. Fischer</b>	DLR Institute of Radio Frequency Technology Germany	jens.fischer@dlr.de
<b>Roger Fjortoft</b>	CESBIO France	Roger.Fjortoft@cesbio.cnes.fr
<b>Pierre-Louis Frison</b>	Université de Marne la Vallée Laboratoire des geomateriaux France	frison@cesbio.cnes.fr
<b>Benedicte Fruneau</b>	Université de Marne la Vallée Institut Francilien des Geosciences France	fruneau@univ-mlv.fr

<b>Jean-Marc Gaudin</b>	CNES Radar Systems Department France	Jean-Marc.Gaudin@cnes.fr
<b>D. Gaveau</b>	NERC Institute of terrestrial Ecology UK	dgav@wpo.nerc.ac.uk
<b>Olivier Germain</b>	ENSP Laboratoire Signal et Image France	germain@lsi.u-3mrs.fr
<b>S. Gobert</b>	Thomson CSF/SYSECA France	stephane.gobert@syseca.thomson-csf.com
<b>M<sup>a</sup> Del Carmen González Sampedro</b>	University of Valencia Termodinámica Spain	Maria.C.Gonzalez@uv.es
<b>Michael Gottwald</b>	Dornier - ST91 Satellitensysteme GmbH Germany	christoph.schaefer@dss.dornier.dasa.de
<b>Stéphane Goze</b>	Alcatel Space Industries France	Stephane.Goze@space.alcatel.fr
<b>Albert Guissard</b>	Universite Catholique de Louvain Electrical Engineering Belgium	guissard@tele.ucl.ac.be
<b>Hafedh Hajji</b>	MétéoMer R&D France	hhajji@meteomer.fr
<b>R.A. Harris</b>	ESA Publications Division The Netherlands	rharris@estec.esa.nl
<b>Nicola Harris</b>	DERA Space UK	nharris@scs.dera.gov.uk
<b>Bob Hawkins</b>	Canada Centre for Remote Sensing Applications Division Canada	Robert.Hawkins@ccrs.nrcan.gc.ca
<b>Stephane Henrion</b>	Alcatel Space Industries IS/ISR France	Stephane.Henrion@space.alcatel.fr
<b>Scott Hensley</b>	Jet Propulsion Laboratory Radar Science and Engineering USA	sh@kaitak.jpl.nasa.gov
<b>Alain Herique</b>	Laboratoire de Planétologie France	alain.herique@obs.ujf-grenoble.fr
<b>Benjamin Holt</b>	Jet Propulsion Laboratory Oceanography Element USA	ben@pacific.jpl.nasa.gov
<b>M.S. Hutchins</b>	DERA Space Department UK	mshutchins@scs.dera.gov.uk



<b>Patrick Imbo</b>	CESBIO France	imbo@cesbio.cnes.fr
<b>Harry Jackson</b>	SerCo FM BV ESA Estec TOS-ETP The Netherlands	hjackson@estec.esa.nl
<b>Muriel Jerome</b>	Alcatel Space Industries IRS France	muriel.jerome@space.alcatel.fr
<b>Harald Johnsen</b>	Norut Information Technology Remote Sensing Norway	harald.johnsen@itek.norut.no
<b>Y.K. Kato</b>	Kikusui Electronics Corp. Japan	ykato@kikusui.co.jp
<b>Gordon Keyte</b>	Defence Evaluation and Research Agency Space Department UK	gekeyte@scs.dera.gov.uk
<b>Ron Kwok</b>	Jet Propulsion Laboratory Polar Remote Sensing Group USA	ronald.kwok@jpl.nasa.gov
<b>Thierry Landeau</b>	CNRS IRESTE France	thierry.landeau@ireste.fr
<b>Pierre Paul Landry</b>	Agence Spatiale Canadienne Canada	neotech@videotron.ca
<b>Henri Laur</b>	ESA-ESRIN Italy	henri.laur@esrin.esa.it
<b>Thuy Le Toan</b>	CESBIO France	letoan@cesbio.cnes.fr
<b>François-Michel Le Tourneau</b>	CNRS France	fmlt@ens.fr
<b>Jong-Sen Lee</b>	Naval Research Laboratory Remote Sensing Division Code 7263 USA	lee@ccf.nrl.navy.mil
<b>Benoit Legresy</b>	CNES Observatoire Midi-Pyrenees France	benoit.legresy@cnes.fr
<b>S. Lehner</b>	DLR DFD-AP Germany	Susanne.Lehner@dlr.de
<b>Xiaofeng Li</b>	NOAA/NESDIS USA	xiaofeng.li@noaa.gov

<b>C.C. Lin</b>	ESA-ESTEC Earth Observation Future Programmes Noordwijk The Netherlands	clin@estec.esa.nl
<b>Jo Llewellyn</b>	DERA – Space England	jsllewellyn@scs.dera.gov.uk
<b>Armand Lopes</b>	CESBIO France	lopes@cesbio.cnes.fr
<b>Anthony Luscombe</b>	MacDonald Dettwiler Radarsat Canada	apl@mda.ca
<b>L. Magnapane</b>	Telespazio Italy	
<b>M. Majnsek</b>	Canadian Aerospace Centre Canada	
<b>Omar Malkawi</b>	Royal Jordanian Geographic Centre Planning Jordan	o.malkawi@usa.net
<b>Henri-Jose Mametsa</b>	ONERA-CERT DEMR France	mametsa@oncert.fr
<b>D. Marchionni</b>	Universidad Nacional de la Plata Instituto de Precusos Minerales Argentina	dmarchi@museo.fcnym.unlp.edu.ar
<b>Philippe Marthon</b>	ENSEEIH- Informatique France	marthon@enseeiht.fr
<b>Jean-Michel Martinez</b>	CESBIO France	martinez@cesbio.cnes.fr
<b>Robert Marx</b>	Alcatel Space Industries IS France	robert.marx@space.alcatel.fr
<b>Didier Massonnet</b>	CNES Qualité et Traitement de l'Imagerie Spatiale France	didier.massonnet@cnes.fr
<b>C.H. Mathew</b>	Matra Marconi Space UK	colin.mathew@mmsuk.co.uk
<b>Pierre Mathieu</b>	Université de Nice-Sophia Antipolis I3S France	mathieu@i3s.unice.fr
<b>Francesco Mattia</b>	Consiglio Nazionale delle Ricerche Istituto di Tecnologia Informatica Spaziale (ITIS) Italy	Mattia@itis.mt.cnr.it
<b>Peter Meadows</b>	Marconi Research Centre UK	peter.meadows@gecm.com
<b>Pierre Melon</b>	CESBIO France	melon@cesbio.cnes.fr

<b>Gregoire Mercier</b>	ENST Bretagne ITJ France	gregoire.mercier@enst-bretagne.fr
<b>K. Mermet</b>	Armée de l'Air France	
<b>Fang Miao</b>	University Chengau	
<b>Rémi Michel</b>	CEA Analyse Surveillance Environnement France	michel@ldg.bruyeres.cea.fr
<b>Nuno Miranda</b>	CESBIO France	miranda@cnes.cesbio.fr
<b>Y. Miyazaki</b>	Geological Survey of Japan Japan	miyazaki@gsj.go.jp
<b>N. Mognard</b>	CESBIO France	
<b>Eric Mougín</b>	CESBIO France	mougín@cesbio.cnes.fr
<b>Carole Nahum</b>	ONERA DEMR France	nahum@onera.fr
<b>E. Nezry</b>	Privateers NV Private Experts in Remote Sensing France	113247.1054@compuserve.com
<b>Michel Oddou</b>	StorageTek SBG Europe Marketing France	Michel_Oddou@storagetek.com
<b>Helene Oriot</b>	ONERA DTIM/TI France	tarayre@onera.fr
<b>Philippe Paillou</b>	Observatoire Astronomique de Bordeaux France	paillou@observ.u-bordeaux.fr
<b>Konstantinos Papathanassiou</b>	Applied Electromagnetics UK	kostas@fges.demon.co.uk
<b>Flavio Parmiggiani</b>	ISAO-CNR Italy	parmi@imga.bo.cnr.it
<b>Angela Peduto</b>	Parco Scientifico e Tecnologico di Salerno Italy	psta@xcom.it
<b>Jennifer Pellenq</b>	CESBIO France	Jennifer.Pellenq@cesbio.cnes.fr
<b>David Petit</b>	CNES Systeme Radar France	petit@irit.fr

<b>Laurent Phalippou</b>	Alcatel Space Industries RF Payload France	laurent.phalippou@space.alcatel.fr
<b>Ghislain Picard</b>	CESBIO France	picard@cesbio.cnes.fr
<b>William Pichel</b>	NOAA/NESDIS Office of Research and Applications USA	wpichel@nesdis.noaa.gov
<b>Jean-Guy Planes</b>	Alcatel Space Industries IS France	jean-guy.planes@space.alcatel.fr
<b>Eric Pottier</b>	Université de Rennes L.A.T - UPRESA CNRS 6075 "Structures Rayonnantes" France	eric.pottier@univ-rennes1.fr
<b>Nadine Pourthié</b>	CNES DSO/OT/QT/SR France	Nadine.Pourthie@cnes.fr
<b>Claudio Prati</b>	Politecnico di Milano DEI Italy	prati@elet.polimi.it
<b>Laurent Prevot</b>	INRA Bioclimatologie France	lprevot@avignon.inra.fr
<b>M. Prodhome</b>	CDAOA / Taverny France	
<b>Christophe Proisy</b>	CESBIO France	proisy@cesbio.cnes.fr
<b>S. Quegan</b>	University of Sheffield Sheffield Centre for Earth Observation Science UK	s.quegan@sheffield.ac.uk
<b>S. Ramongassie</b>	Alcatel Space Industries France	
<b>D. Raucoules</b>	BRGM France	raucoule@v24.brgm.fr
<b>Florence Ribbes</b>	CESBIO France	ribbes@cesbio.cnes.fr
<b>Loïc Rognant</b>	Alcatel Space Industries DI/IS/ISR France	Loic.Rognant@space.alcatel.fr
<b>Betlem Rosich</b>	ESA Italy	brosich@esrin.esa.it
<b>Jean Paul Rudant</b>	Université de Marne la Vallée Institut francilien des geosciences France	rudant@dedale.univ-mlv.fr
<b>Christian Ruiz</b>	ONERA DEMR France	ruiz@oncert.fr

<b>Stein Sandven</b>	Nansen Environmental & Rem. Sens. Center Edv. Griegsvei 3a Norway	stein.sandven@nrsc.no
<b>Francesco Sarti</b>	CNES OT/QTIS/SR France	Francesco.Sarti@cnes.fr
<b>Hugues Sassier</b>	Alcatel Space Industries DI/IS/ISR France	Hugues.Sassier@space.alcatel.fr
<b>Makoto Satake</b>	Communications Research Laboratory Earth Environment Div. Japan	satake@crl.go.jp
<b>Giuseppe Satalino</b>	CNR-IESI Italy	satalino@iesi.ba.cnr.it
<b>T. Sato</b>	Japan Resources Observation System Japan	sato@jaros.or.jp
<b>Laurent Savy</b>	Alcatel Space Industries Ingénierie Système Radar (IRS) France	laurent.savy@space.alcatel.fr
<b>Birgit Schättler</b>	DLR Deutsches Fernerkundungsdatenzentrum (DFD) Germany	Birgit.Schaettler@dlr.de
<b>J. Schulz-Stellenfleth</b>	DFD - DLR Deutsches Fernerkundungsdatenzentrum Germany	Johannes.Schulz-Stellenfleth@dlr.de
<b>Frank Martin Seifert</b>	Fokker Space EN-2 The Netherlands	fm.seifert@fokkerspace.nl
<b>Masanobu Shimada</b>	National Space Development Earth Observation Research Center Japan	shimada@eorc.nasda.go.jp
<b>Elisabeth Simonetto</b>	ONERA DTIM/TI France	simonetto@onera.fr
<b>Ian Sinclair</b>	MPB Technologies Inc. Canada	Ian.Sinclair@mpb-technologies.ca
<b>Domenico Solimini</b>	Tor Vergata University Ingegneria DISP Italy	solimini@disp.uniroma2.it
<b>Jean-Claude Souyris</b>	CNES Radar Systems Department France	souyris@cnes.fr
<b>S. Srivastava</b>	Canadian Space Agency Canada	Satish.Srivastava@space.gc.ca
<b>Oliver Stebler</b>	University of Zurich-Irchel Remote Sensing Laboratories (RSL) Switzerland	stebler@geo.unizh.ch
<b>J.L. Suchail</b>	ESA-ESTEC Noordwijk The Netherlands	jsuchail@estec.esa.nl

<b>Martin A. Suess</b>	Dornier Satellitensysteme GmbH Dept. ST 87 Germany	martin.suess@dss.dornier.dasa.de
<b>Sebastian Tam</b>	MPB Technologies Inc. Canada	Sebastian.Tam@mpb-technologies.ca
<b>Kevin Tansey</b>	University of Wales Department of Geography UK	K.J.Tansey@swansea.ac.uk
<b>Tove Tennvassås</b>	Kongsberg Spacetec Norway	tove@spacetec.no
<b>Cécile Titin-Schneider</b>	ONERA DEMR France	titin@onera.fr
<b>Ramón Torres</b>	ESA-ESTEC ENVISAT Noordwijk The Netherlands	rtorres@estec.esa.nl
<b>Ridha Touzi</b>	Canada Centre for Remote Sensing Application Division Canada	touzi@ccrs.emr.ca
<b>Hervé Trebossen</b>	SHOM Laboratoire géomatériaux France	trebosse@shom.fr
<b>F. Tupin</b>	ENST France	
<b>Hélène Vadon</b>	CNES OT:QTIS France	helene.vadon@cnes.fr
<b>Gaëtan Vinay</b>	CESBIO France	vinay@cesbio.cnes.fr
<b>Brian Whitehouse</b>	Alliance for Marine Remote Sensing Canada	brian@amrs.org
<b>Pierre Wiart</b>	University of Cambridge Geography UK	pw222@hermes.cam.ac.uk
<b>A. Wiesmann</b>	Gamma Remote Sensing AG Switzerland	wiesmann@gamma-rs.ch
<b>Francis Yakam Simen</b>	Privateers NV France	106341.2602@compuserve.com
<b>M. Yoxnon</b>		
<b>F. Zagolski</b>	Privateers NV Private Experts in Remote Sensing Canada	zagolski@interlinx.gc.ca
<b>Rudolf W. Zahn</b>	Dornier Satellitensysteme GmbH Dept. ST 87 Germany	rudolf.zahn@dss.dornier.dasa.de

**Manfred Zink**

DLR Oberpfaffenhofen  
Institut fuer Hochfrequenztechnik  
Germany

manfred.zink@dlr.de









**European Space Agency**  
**Agence spatiale européenne**

*Contact: ESA Publications Division*

c/o ESTEC, PO Box 299, 2200 AG Noordwijk, The Netherlands

Tel (31) 71 565 3400 - Fax (31) 71 565 5433